

Lecture Notes in Electrical Engineering 1054

Xuzhu Dong
Qingxin Yang
Weiming Ma *Editors*

The proceedings of the 10th Frontier Academic Forum of Electrical Engineering (FAFEE2022)

Volume II

 Springer

Lecture Notes in Electrical Engineering

Volume 1054

Series Editors

- Leopoldo Angrisani, Department of Electrical and Information Technologies Engineering, University of Napoli Federico II, Napoli, Italy
- Marco Arteaga, Departamento de Control y Robótica, Universidad Nacional Autónoma de México, Coyoacán, Mexico
- Samarjit Chakraborty, Fakultät für Elektrotechnik und Informationstechnik, TU München, München, Germany
- Jiming Chen, Zhejiang University, Hangzhou, Zhejiang, China
- Shanben Chen, School of Materials Science and Engineering, Shanghai Jiao Tong University, Shanghai, China
- Tan Kay Chen, Department of Electrical and Computer Engineering, National University of Singapore, Singapore, Singapore
- Rüdiger Dillmann, University of Karlsruhe (TH) IAIM, Karlsruhe, Baden-Württemberg, Germany
- Haibin Duan, Beijing University of Aeronautics and Astronautics, Beijing, China
- Gianluigi Ferrari, Dipartimento di Ingegneria dell'Informazione, Sede Scientifica Università degli Studi di Parma, Parma, Italy
- Manuel Ferre, Centre for Automation and Robotics CAR (UPM-CSIC), Universidad Politécnica de Madrid, Madrid, Spain
- Faryar Jabbari, Department of Mechanical and Aerospace Engineering, University of California, Irvine, CA, USA
- Limin Jia, State Key Laboratory of Rail Traffic Control and Safety, Beijing Jiaotong University, Beijing, China
- Janusz Kacprzyk, Intelligent Systems Laboratory, Systems Research Institute, Polish Academy of Sciences, Warsaw, Poland
- Alaa Khamis, Department of Mechatronics Engineering, German University in Egypt El Tagamoa El Khames, New Cairo City, Egypt
- Torsten Kroeger, Intrinsic Innovation, Mountain View, CA, USA
- Yong Li, College of Electrical and Information Engineering, Hunan University, Changsha, Hunan, China
- Qilian Liang, Department of Electrical Engineering, University of Texas at Arlington, Arlington, TX, USA
- Ferran Martín, Departament d'Enginyeria Electrònica, Universitat Autònoma de Barcelona, Bellaterra, Barcelona, Spain
- Tan Cher Ming, College of Engineering, Nanyang Technological University, Singapore, Singapore
- Wolfgang Minker, Institute of Information Technology, University of Ulm, Ulm, Germany
- Pradeep Misra, Department of Electrical Engineering, Wright State University, Dayton, OH, USA
- Subhas Mukhopadhyay, School of Engineering, Macquarie University, NSW, Australia
- Cun-Zheng Ning, Department of Electrical Engineering, Arizona State University, Tempe, AZ, USA
- Toyoaki Nishida, Department of Intelligence Science and Technology, Kyoto University, Kyoto, Japan
- Luca Oneto, Department of Informatics, Bioengineering, Robotics and Systems Engineering, University of Genova, Genova, Genova, Italy
- Bijaya Ketan Panigrahi, Department of Electrical Engineering, Indian Institute of Technology Delhi, New Delhi, Delhi, India
- Federica Pascucci, Dipartimento di Ingegneria, Università degli Studi Roma Tre, Roma, Italy
- Yong Qin, State Key Laboratory of Rail Traffic Control and Safety, Beijing Jiaotong University, Beijing, China
- Gan Won Seng, School of Electrical and Electronic Engineering, Nanyang Technological University, Singapore, Singapore
- Joachim Speidel, Institute of Telecommunications, University of Stuttgart, Stuttgart, Germany
- Germano Veiga, FEUP Campus, INESC Porto, Porto, Portugal
- Haitao Wu, Academy of Opto-electronics, Chinese Academy of Sciences, Haidian District Beijing, China
- Walter Zamboni, Department of Computer Engineering, Electrical Engineering and Applied Mathematics, DIEM—Università degli studi di Salerno, Fisciano, Salerno, Italy
- Junjie James Zhang, Charlotte, NC, USA
- Kay Chen Tan, Department of Computing, Hong Kong Polytechnic University, Kowloon Tong, Hong Kong

The book series *Lecture Notes in Electrical Engineering* (LNEE) publishes the latest developments in Electrical Engineering—quickly, informally and in high quality. While original research reported in proceedings and monographs has traditionally formed the core of LNEE, we also encourage authors to submit books devoted to supporting student education and professional training in the various fields and applications areas of electrical engineering. The series cover classical and emerging topics concerning:

- Communication Engineering, Information Theory and Networks
- Electronics Engineering and Microelectronics
- Signal, Image and Speech Processing
- Wireless and Mobile Communication
- Circuits and Systems
- Energy Systems, Power Electronics and Electrical Machines
- Electro-optical Engineering
- Instrumentation Engineering
- Avionics Engineering
- Control Systems
- Internet-of-Things and Cybersecurity
- Biomedical Devices, MEMS and NEMS

For general information about this book series, comments or suggestions, please contact leontina.dicecco@springer.com.

To submit a proposal or request further information, please contact the Publishing Editor in your country:

China

Jasmine Dou, Editor (jasmine.dou@springer.com)

India, Japan, Rest of Asia

Swati Meherishi, Editorial Director (Swati.Meherishi@springer.com)

Southeast Asia, Australia, New Zealand

Ramesh Nath Premnath, Editor (ramesh.premnath@springernature.com)

USA, Canada

Michael Luby, Senior Editor (michael.luby@springer.com)

All other Countries

Leontina Di Cecco, Senior Editor (leontina.dicecco@springer.com)

**** This series is indexed by EI Compendex and Scopus databases. ****

Xuzhu Dong · Qingxin Yang · Weiming Ma
Editors

The proceedings of the 10th Frontier Academic Forum of Electrical Engineering (FAFEE2022)

Volume II

 Springer

Editors

Xuzhu Dong
School of Electrical Engineering
and Automation
Wuhan University
Wuhan, China

Qingxin Yang
Tianjin University of Technology
Tianjin, China

Weiming Ma
Naval University of Engineering
Wuhan, Hubei, China

ISSN 1876-1100

ISSN 1876-1119 (electronic)

Lecture Notes in Electrical Engineering

ISBN 978-981-99-3407-2

ISBN 978-981-99-3408-9 (eBook)

<https://doi.org/10.1007/978-981-99-3408-9>

© Beijing Paiké Culture Commu. Co., Ltd. 2023

This work is subject to copyright. All rights are solely and exclusively licensed by the Publisher, whether the whole or part of the material is concerned, specifically the rights of translation, reprinting, reuse of illustrations, recitation, broadcasting, reproduction on microfilms or in any other physical way, and transmission or information storage and retrieval, electronic adaptation, computer software, or by similar or dissimilar methodology now known or hereafter developed.

The use of general descriptive names, registered names, trademarks, service marks, etc. in this publication does not imply, even in the absence of a specific statement, that such names are exempt from the relevant protective laws and regulations and therefore free for general use.

The publisher, the authors, and the editors are safe to assume that the advice and information in this book are believed to be true and accurate at the date of publication. Neither the publisher nor the authors or the editors give a warranty, expressed or implied, with respect to the material contained herein or for any errors or omissions that may have been made. The publisher remains neutral with regard to jurisdictional claims in published maps and institutional affiliations.

This Springer imprint is published by the registered company Springer Nature Singapore Pte Ltd. The registered company address is: 152 Beach Road, #21-01/04 Gateway East, Singapore 189721, Singapore

Contents

Communication Protocol Optimization of Electric Low Power Wireless Sensor Network Based on Active Wakeup	1
Chunyan An and Ziwei Huang	
Application of Scientific Hypothesis - Deductive Method in Analysis of Abnormal Swing Fluctuation of Hydropower Unit	11
Zhihua Li, Diancheng Liu, Nannan Xu, Mengshen Li, Jinsong Du, Keheng Zhou, Jin Li, and Hailin pei	
Optimization of Gear Ratio and Torque Density of Magnetic Gears Based on Genetic Algorithm	27
Zhiqiang Wang, Weinong Fu, Jiao Song, Peng Chen, Zhenyang Qiao, and Yanding Bi	
Simulation Study for the Influence of Electrical Trees on Electric Field Distribution Around 10 kV Cable Bushing	37
Zhichao Xiao, Baiwei Hu, Zhiqiang Chen, Xiaoqing Ji, and Gaohui He	
Novel Controllable Commutated Converter (CLCC) and Rapid Defense Method for Commutation Failure	47
Jun Yang, Caiwang Sheng, Chong Gao, Xiao Ding, Tingting Li, and Dongshan He	
An Uncertainty Analysis Method of Dimension Reduction for Multiconductor Transmission Line	57
Xutong Wang, Wenbing Wang, Feng Qin, and Yifu Zhou	
Magnetic Field Analysis and Magnetic Resistance Optimization of Moving Magnet Primary Segmented Permanent Magnet Synchronous Linear Motor	67
Haoyu Wang, Jie Zhang, Wenyuan Yan, and Hualin Huang	

Research on a Design Method of Composite Nano Generator Based on Rotation	87
Dong Yan, Chuangliang Zhao, Kai Zhang, and Jiuyuan Zhan	
Research and Application of Dry-Type Transformer Winding Material Detection Technology	97
Jiawei Wu, Guohua Chen, Donghui He, and Shunyao Li	
Prediction of Dissolved Gas Concentration in Transformer Oil Based on WPD-CSO-LSTM Model	109
Zhang Miao, Mo Wenjun, Fan Jingmin, Cao Yunfei, Feng Lutao, and Tan Zhichao	
Digital Twin Model of Air-Immersed Transformer Based on Electro-Thermal Simulations	121
Hui Qin, Xin Lin, Qideng Luo, Hengwang Zhou, Jing Fu, Danyang Qu, and Lidan Chen	
Simulation and Lead-In Design of Wall Bushings in Artificial Climate Chamber Under Complex Atmospheric Conditions	135
Junyi Xia, Ziyu Ma, Peiqi Xiong, Nanxuan Shen, Xuyuan He, Kun He, Li Cheng, and Xingming Bian	
Cascade Finite Control Set Model Predictive Control Research for Bearingless Switched Reluctance Motors	145
Jinlong Ma, Honghua Wang, Hao Li, and Zenan Qiu	
A Design of Voltage-PDM Type Torque Controller for Dual-Winding BSRM Based on Super-Twisting Algorithm	155
Zenan Qiu, Honghua Wang, Jinlong Ma, and Hao Li	
Harmonic Elimination in Inverter Using Modified GWO Algorithm	165
He Fei and Jiabei Shen	
Design and Application of Non-contact Voltage Acquisition Module for Dry Air Core Reactor	175
Zhiqin Ma, Gang Wang, Danyu Jiang, Xian Yang, Xiang Shu, and Shuo Jiang	
Experiment and Simulation Study on the Generation Process of Cable Carbonization Path	185
Xiaoyong Ye and Zhihong Xu	
Research on Thermal Runaway Behavior and Early Fire Detection Method of Lithium Battery	199
Zhilin Shan, Qixing Zhang, Yongmin Zhang, Shuping Wang, Yifeng Cheng, and Shiwei Guo	

Design of an Inductive Charging System Based on PCB-Resonator with Constant Current or Constant Voltage Output 211
 Huaqiang Xie, Zhaotian Yan, Yuan Shao, and Ruikun Mai

Bidirectional Converter-Based Decentralized Compensation Solution for Medium Voltage Networks in Urban Railways 221
 Zhe Wang and Shaobing Yang

Design of Polygonal Permanent Magnet Array in Magnetic Nanoparticle Imaging System 231
 Yide Huang, Li Ke, Qiang Du, Wannu Zu, and Kaicheng Wen

Fracture Toughness Measurement of GIS/GIL Epoxy Composites Based on Ultrasonic Testing Technology 241
 Xingwang Li, Zhuoyi Liang, Congwei Yao, Yanpeng Hao, Xiaofeng Pang, Shuai Sun, Xian Yang, Lin Liu, Yingying Zhang, and Yao Zheng

Active Gate Drive for Short-Circuit Current Suppression of SiC MOSFET in Hard Switching Fault 249
 Jingwei Zhang, Zhikang Guo, Yizhan Jiang, and Guojun Tan

Analysis and Research on an Equivalent Circuit of LiFePO₄ Battery Under a High Discharge Rate 259
 Liming Huang, Yihui Xia, and Yunxiang Jiang

Research on Orderly Charging Scheduling Strategies for Interactive Power Networks Through Cloud-Side-End Collaboration 273
 Bin Zhu, Min He, Yi Long, Xiujuan Yuan, Dong Yan, and Desheng Qian

Multi-objective Optimization of Motor Rotor Notches Based on Multi-Objective Particle Swarm Optimization 283
 Qiao Yan, Liu Jinglin, Qiao Yongming, and Wang Danqing

Analysis and Simulation of Electromagnetic Vibration Under Fault-Tolerant Control of Marine Six-Phase Permanent Magnet Synchronous Motor 293
 Lin Tan, Wei Xie, and Yunkai Guo

Research on PWM Rectifier Extending DC Working Voltage Range 307
 Danyang Xie, Gang Zhang, Yunda Wang, and Wei Wei

Deep Learning + Complex Physics Field Modeling: Illustrated by the Example of Numerical Investigation on Low Temperature Plasma 317
 Chaoqun Zhao, Jie Pan, Bin Li, and Yun Liu

Multi-objective Coordinated Charging Strategy for Electric Vehicles Considering Dynamic Time-of-Use Electricity Price	327
Zeyu Hou, Yong Li, Yixiu Guo, Xuebo Qiao, Zhenyu Zhang, and Yijia Cao	
Coordinated Control of Commutation Failure Prevention Under UHVDC Multi-infeed System	343
Zhiwei Wang, Yangchen Tan, Xin Liu, Wenzhuo Wang, Zheng Li, Zhaoyang Wei, Biao Su, and Jiahao Wang	
Research on Multi-modal Track Association and Fusion Algorithm in Air Defense Weapon System	353
Zhengzheng Yang, Tong Yao, Yong Hou, Xiaolong Su, Hao Bai, Xiutang Geng, and Binyi Wang	
Harmonic Analysis of Grid-Connected Electric Vehicle Charging Stations	363
Ziyi Yang	
Two-Tier Demand-Side Response for Hydrogen Producing and Hydrogen Selling Integrated Hydrogenation Station	377
Jiajia Huan, Xin Huang, Mintong Zhao, and Yunxia Xu	
Visual Defect Detection Method of High Voltage Overhead Transmission Line Based on rp-CenterNet	397
Wenhao Mo, Jie Tong, Yuanpeng Tan, Fangzhou Hu, and Zhuhan Tang	
Research of Image Recognition Technology Based on 3D Point Cloud Data in Locomotive Roof Detection	407
Jun Guo Wang, Nai Shu Yu, Yao He, and Ning Luan	
Review of Isolated DC-DC Converter for Wide Voltage Range Regulation	421
Ziyan Tang, Jin Wen, Jiajia Guan, Yiyang Yan, Cai Chen, Yong Kang, and Lei Yang	
Analysis on the Operating Condition of Electrical Contact Structure Used in Gas Insulated Switchgear	437
Wei Yang, Taiyun Zhu, Tao Xie, Shoufeng Jin, Ting Ren, Qingyu Wang, and Peng Liu	
Multi-objective Optimization and Research of the New Type Combined Excitation Permanent Magnet Motor for Electric Vehicle	449
Bingchang Lv, Liwei Shi, Jianning Jing, Kaiwen Liu, and Lintao Li	
Sensorless Control of Multiphase Permanent Magnet Synchronous Motor Considering Phase-to-Phase Coupling	461
Haoran Zhao, Dong Wang, Xinqiang Yi, and Pengfei Hu	

Analysis of Electromagnetic Loops Opening Scheme Based on Penalty Variable Weight Optimal Comprehensive Evaluation Model 473
 Yan Yang, Wantong Cai, Shixian Zou, Bo Peng, and Wei Xu

Application and Development of Active Distribution Grid Technology for Integrated Energy Systems in the Context of Industrial Internet 491
 Nuo Xu, Jinman Luo, Nuanqiang Ye, and Ming Zeng

Development of LDV-Based Length Measuring Equipment for Tension Stranding Construction Conductor 503
 Zheng Lv, Zhiming Huang, Qi Xiao, Zixin Li, Junfeng Guan, and Bo Tang

Achieving High Dielectric Constant, High Breakdown Strength, and High Efficiency in a Linear Polymethyl Methacrylate Composite for Energy Storage 513
 Yujiu Zhou, Hu Ye, Haohao Feng, Jiali Wu, Tao Chen, Qifeng Pan, Yuetao Zhao, and Jianhua Xu

Thermal Circuit Model of Oil-Immersed Distribution Transformer in Unbalanced Operation 523
 Yuqin Ding, Zhonglin Xu, Hengchi Ma, Kun Yuan, Yongpeng Yang, Haoxia Lei, Yang Feng, and Ye Tian

Improved Transformer Fault Diagnosis Method Based on Sparrow Search Algorithm-Optimized BP Network and Duval Pentagon 535
 Shicheng Zhang, Xiaofeng Tao, Hong Ding, Chunyan Lu, and Miaoxuan Shan

An Improved Low Voltage Ride Through Strategy for Wind Turbines Connected to the Weak Grid 545
 Chuanhao Liu and Jiaying Lei

Optimal Planning of Power-to-Hydrogen Unit Considering Electrical-Thermal Coupling in Power System with Offshore Wind 555
 Hao Yu, Honglin Chen, Zhengmin Zuo, Wenxin Liu, Yuheng Ying, and Xiaomeng Ai

Research and Application on Ferroresonance Suppression Effect of 6-35 kV Potential Transformer Current - Sensitive Harmonic - Free Device 571
 Yue Yang, Hongbing Guo, and Bo Chen

Delta Measurement Analysis Method Applicable to All-Parallel AT Traction Network of High Speed Railway 585
Dongdong Li and Zhengqing Han

Analysis and Research of Networked Traction Power Supply System 599
Qi Zhuo, Zhengqing Han, and Shibin Gao

Propagation Characteristics of High-Frequency Partial Discharge Current in Gas Insulated Equipment 609
Ke Zhao, Jingtian Ma, Tianxin Zhuang, Hongtao Li, Shan Gao, Jianjun Liu, Fanjun Kong, and Chaohai Zhang

Research on the Motion Behavior and Discharge Characteristics of Spherical Metal Particles in DC GIS 619
Hu Qiu, Yahui Sun, Chuanxian Luo, Jing Zhang, Hao Wen, Ziqiu Luo, and Kang Wang

A Comparison Study of Nonlinear Solvers in Transient Circuit Analysis Involving Power Diodes 631
Ming Chen, Xiaoping Sun, Yanmei Zhang, He Chen, Pengcheng Zhu, and Jiawei Wang

Application of VMD-Based Electromagnetic Railgun Launch Current Feature Extraction in the Measurement of Muzzle-Leaving Time 641
Yi Chen, Jie Yan, Kai Huang, Weisheng Ye, Juxiang Li, Yi Wang, Sui Wang, and Chengdong Liu

K-Means Based Multi-dimensional Charging Behavior Profiling Technique 655
Bin Zhu, Yulan Li, Zhi Li, Tingting Xu, Huicai Wang, Dong Yan, and Chongyang Luo

Turn-to-Turn Overvoltage Test Technology for Dry-Type Smoothing Reactor 665
Qingsong Liu, Jiajie Huang, and Chenlei Liu

Research on Target User Optimal Complex Path Technology for Regional Fault Scenario 675
Jianyi Cai, Zhiwei Chen, and Yuxin Lin

A Novel Design Method of Motor Speed Controller Based on Convex Optimization 685
Yiwei Tang, Xin Sun, Meng Zhang, and Xi Xiao

Fire Extinguishing Effect of Reignition Inhibitor on Lithium Iron Phosphate Storage Battery Module 703
Mingjie Zhang, Kai Yang, Jialiang Liu, Yilin Lai, Hao Liu, Hao Chen, Maosong Fan, and Mengmeng Geng

A Power Decoupling Strategy for Three-Phase Inverter Based on Mid-Leg Fundamental-Frequency Common-Mode Voltage Injection Under Unbalanced Conditions 713
 Rui Zhang, Lan Xiao, Zhiquan Deng, and Xin Cao

Terminal Sliding Mode Control of Permanent Magnet Motor Considering Saturation Effect 721
 Longfei Zhu, Jiani Liu, and Xueyan Han

An Equivalent Transformer Capacitance Model Analysis Method for CM Noise Conduction 731
 Kaining Fu, Zhiyong Qiu, Qiang Zhang, and Hanchao Zeng

Virtual Screening of New High Voltage Insulating Gases as Potential Candidates for SF6 Replacement 739
 Xiaodian Li, Dongwei Sun, Yongyan Zhou, Xiaopeng Fan, Li Li, Nian Tang, Zhuanglei Zou, and Gaokeng Xiao

Prediction of Global Warming Potential of Insulating Gases Using Random Forest Classifiers 753
 Dongwei Sun, Yongyan Zhou, Xiaopeng Fan, Li Li, Nian Tang, Zhuanglei Zou, and Gaokeng Xiao

Analysis of an Internal Fault of Main Transformer 767
 Zhou Xiu, Bai Jin, Ni Hui, Tian Tian, Chen Lei, Luo Yan, Sun Shangpeng, and Zhang Heng

Smooth Wind Power Fluctuation Based on Sliding Average and Low Pass Filtering 777
 Xingwu Fu and Yarui Hu

Research on Repetition Frequency Pulse Current Source Based on Solid State Switching Technology 789
 Xin Huang, Taixun Fang, Qiwen Zhou, Lei Zhang, Hui Chen, and Xingxing Huangfu

Monitoring Method of Power Data Asset Operation Platform Based on Visualization Technology 797
 Yingwei Liang and Zewu Peng

Primary Frequency Modulation Study of Receiver System with High Proportion Power Electronic Power Supplies 809
 Zexiang Zhu, Chao Fu, Junfeng Qi, Zhuo Liu, and Fei Tang

IGBT Module Status Monitoring Method Based on High-Speed Peak Holding 823
 Xiaoming Zhu, Jie Chen, Hui Wang, Xuefei Li, Jinpeng Li, Ruichang Qiu, and Zhigang Liu

An Abnormal Power Consumption Identification Method Considering User Psychology 833
Xiaoyi Xiong, Jinyu Wu, Zijie Rong, Pengwei He, Na Dong, Xiaoyong Jiang, Xuan He, and Yannan Ji

Bearing Fault Diagnosis Using 1D-CNN Combined with Multi-Dimensional Input and Self-Attention Mechanism 843
Lanlan Fang, Zicheng Liu, Dong Jiang, and Ronghai Qu

Interfacial Breakdown Voltage and Morphology of Cable Accessories Considering Different Interface States and Temperatures 853
Kai Wu, Tianfeng Zhang, Shaolei Wu, Yu Feng, and Yunxiao Zhang

Research on Critical Breakdown Distance of 110 kV/220 kV AC Transmission Lines with Trees Approaching 863
Kai Yang, Hong Wu, Shitao Liu, Jinpeng Hao, Yumeng Zeng, Haochen Zhang, Yu Wang, and Yeqiandeng

An Optimization Design Method of Multi-chip Parallel Power Module Based on Machine Learning 873
Jianing Wang, Yaodong Huang, Fuchen Wu, and Shaolin Yu

Low-Cost Modular Multilevel Converter Topology and Its Fault Control Strategy for Offshore Wind Power 887
Shuangfei Yang, Man Chen, Yongqi Li, Yuebin Zhou, Zhenkai Hu, Wenming Gong, and Yue Wu

Simulation Study on Thermal Effect of Multistage PIN Limiter 899
Mingxuan Gao, Yang Zhang, Lishan Zhao, and Jun Zhang

Hybrid Energy Storage System with Doubly Fed Flywheel and Coordination Control Strategy 911
Chenyu Wu, Zhengxiang Song, Junyue Wang, Kun Yang, Qiuyao Xiao, Weiquan Wang, and WenChao Liu

Multi-scenario Safe Operation Method of Energy Storage System for Cascade Utilization of Retired Power Batteries 925
Yan Wu, Peigen Tian, Xi Xiao, Yuan Cao, and Lu Yu

Research on Characteristics of Submersible Motor Under Fault Condition Based on Electromagnetic-Thermal Coupling 937
Tianle Li, Baichuan Xu, Yahui Zhang, Yi Wang, Yixiao Luo, and Kai Yang

Data-Driven Dynamic Modeling Methods for Offshore Wind Turbine Generators 947
Xinhu Ding and Haidong Chen

Electric Bicycle Charging Load Identification Technology Based on Non-intrusive Load Monitoring 957
 Ke Wu, Gan Zhou, and Feifei Zhu

An Approach to Approximate Evaluation of Shielding Effectiveness of Double-Cavity Structure with an Aperture Array Using BLT Equation 967
 Xin Zhang, Zhangpeng Zhou, Zonglin Wang, Hai Jin, and Kejian Chen

Power System Multi-oscillation Center Cut Sets Identification Method Based on Algebraic Graph Theory 977
 YanQiang Shi, Jing Li, Zhiyong Qiu, Haoyin Ding, Zhenyao Li, and Deqiang Gan

Research on the Adsorption Performance of β -Ga₂O₃ on C₂H₄ Gas in Transformer Oil 989
 Zhou Zemin, Wang Jialin, Pang Jianyou, Zhou Xiong, Huang Qianxiu, Shao Chen, and Guo Yuzheng

Research on Growth Characteristics of Water Tree in XLPE 997
 Hong Yang, Xiaokai Meng, Zhumao Lu, and Wei Wang

Pitch Angle Control of Wind Generation System Based on Wind Speed Prediction 1005
 Xia You, Bo Zhou, Youren Wang, Xiang'an You, Qingxi Zeng, and Honghao Guo

An Experiment on the Characteristics of Sturgeon Perceiving and Avoiding Current Fields in Water 1015
 Nan Liu, Ke Zhong, Yunfan Ye, Jiahao Chen, Bo Tan, Huiwu Wang, and Hailiang Lu

Research on Position Estimation Method of PMSM Based on SVPWM Control 1027
 Yu Ji, Zhe Chen, and Yue Hu

PMSM Vector Control System Based on NPC Three-Level Inverter and Fuzzy Control Algorithm 1039
 Pingjun Dai, Jinwu Gong, and Xiaoming Zha

An Optimized Fault-Tolerant Strategy Based on Uncoupled Zero-Sequence Voltage Injection for Cascaded Multilevel Converters 1049
 Ganlin Kong, Liming Shi, Fei Xu, Mingyuan Zhang, Jinhai Liu, and Shijiong Zhou

Wind Speed Estimation Based MPPT for WPGS 1057
 Xia You, Bo Zhou, Qingxi Zeng, Yajie Lin, and Honghao Guo

A Simplified Prediction Method of Magnetic Field Radiation of High-power Power Electronic Equipment	1067
Lei Zhang, GuiSheng Jie, Shan Gao, and ShengXian Ji	
Study on the Influence of Different Degrees of Deterioration of Oil-Paper Insulation on Partial Discharge Characteristics	1077
Li Longfei, Wu Tianbo, Liu Lei, Wang Xin, Zhang Fei, Ge Zhijie, Zhang Shuobo, and Liu Hongshun	
Power Grid State Assessment Method Based on RMT-PCA	1089
Kinzhi Ye, Lei Shang, Xuzhu Dong, Chengxi Liu, and Ye Tian	
Simulation of the Leakage Magnetic Field Under Inter-turn Short Circuit in the Transformer	1099
Meng Huang, Bo Qi, Wei Zheng, Mao Ji, Haomin Lv, Wenbing Zhu, and Jian Wang	
Sag Monitoring of Transmission Line Based on Motion Sensor	1109
Zhang Huiquan, Jiang Zelong, Ma Haoyu, Bi Ran, Pan Shi, He Jinliang, and Hu Jun	
Inversion of Transmission Line Icing State Based on Sag Monitoring	1123
Zhang Huiquan, Jiang Zelong, Jiang Hong, Zhang Huajie, Zhao Mengshi, He Jinliang, and Hu Jun	
Overvoltage Distribution Characteristics of Long Distance Gas Insulated Transmission Lines	1131
Qishen Lv, Gen Li, Zhiren Tian, Guoxing Wu, Shu Xu, Lin Zhang, and Yu Zheng	
500 KV GIL Fault Location Based on Single Terminal Transient Monitoring in Field Takeover Test	1139
Lin Zhang, Junqiang Gong, Zhiyi Luo, Fan Zhang, Jian Cheng, Gen Li, and Yu Zheng	
Channel Path Simulation and Channel Loss Calculation of 5G Substation	1149
Yifeng Li, Xingfa Liu, Bo Tang, Chenlin Cai, Longbin Zhang, and Yushan Yao	
5G Antenna Distribution in Substations Considering Electromagnetic Interference Factors	1157
Xingfa Liu, Bo Tang, Can Zhang, Daokun Qi, Yushan Yao, and Yifeng Li	
A New Distributed Intelligent Distribution Ring Main Unit Based on System on Chip Design	1167
Jiawen Chen, Chao Cai, Yang Lei, Gaohai Wang, Changsheng Sun, and Si Yang	

Research on Small Current Grounding Fault of Distributed Small Hydropower with Different Permeability when Connected to the Grid 1177
 Jiawen Chen, Chao Cai, Fan Yang, Lin Liu, Changsheng Sun, and Si Yang

Research Progress of New Multi-functional Transformer 1187
 Yu Dong, Feiyan Zhou, Yifan Wang, Lingyun Gu, Shingzhe Wang, and Yan Wu

Potential Development and Planning Method of Industrial Load Regulation 1195
 Chaoliang Wang, Wei Liu, Jiangming Zhang, and Hanqing Liu

Diagnosis Method for Inter-Turn Short Circuit in Winding Based on Feature Extraction of Traveling Wave 1205
 Haipeng Zhao, Mengjiao Xue, Chu Li, Jianpan Lyu, Liming Huang, Hongyue Men, E Yiyang, and Min Peng

Research on Output Characteristics of Vibrational Energy Harvesting Device Based on Double Crystal Piezoelectric Cantilever Beam Structure 1217
 Yuqing Sun, Zhiye Du, Mouyuan Chen, and Xinyi Huang

Numerical Study on Ultra-Low Specific Speed Pump as Turbine for Micro-hydropower System 1227
 Jiawei He, Peng Wang, Fanjie Deng, Wentao Sun, and Qiaorui Si

The Research on Ablation Characteristics of Oil and Gas Pipeline Under Power Frequency Current 1237
 Chunjiu Wu, Jianwei Jin, Lei Guo, Hailiang Lu, Zhibing Huang, Bo Tan, and Wenqiang Yang

Lightweight Object Detection Algorithm Based on Grid Site Work Dress Code Detection Method 1249
 Kexin Li, Jing Wang, and Liang Qin

Application and Research of Digital Twin Technology in Distribution Transformer Area 1259
 Chang Wu, Li Kong, and Hanmin Jiang

Application of Intelligent High Voltage Switchgear 1269
 Qin Zou, Hao Lei, Xushu Ye, Xiting Dong, Kezhen Yang, and Jin Chen

Research on Real-Time Data Acquisition of Flexible Distribution Network Based on SCU 1283
 Yi Yang

Deep Learning-Based Breakdown Voltage Prediction for Ball-to-Ball Discharge with an Air Gap Less Than 1.5 m 1293
Changzhi Peng, Xuzhu Dong, Jiangjun Ruan, Yanpu Zhao, Bing Luo, Tingting Wang, and Shucan Cheng

Remaining Useful Life Prediction Method of Lithium-Ion Batteries Based on Relevance Vector Machine 1303
Qiancheng Tian, Haitao Chen, Shuai Ding, Lei Wang, Jun Huang, and Ziwei Yang

Capacity Optimization of Haolebaoji-Ji'an Railway Freight Transportation 1315
Kai Xu and Xiaoning Zhu

Electric Field Simulation and Optimization of Environmentally Friendly ± 400 kV DC Wall Bushing 1325
Xiaohui Duan, Sai Liu, Yinghui Chai, Shuai Du, Xian Cheng, and Xiangyuan Dong

Communication Protocol Optimization of Electric Low Power Wireless Sensor Network Based on Active Wakeup



Chunyan An and Ziwei Huang

Abstract Most electric sensors are powered by battery and have strict requirements on energy consumption. The existing communication protocol of electric low power wireless sensor network (e-LPWSN) usually periodically wakes up sensors to save energy. This paper studies the communication protocol optimization of existing e-LPWSN based on active wakeup, where energy consumption is further reduced by minimizing not only the wake-up times, but also the retransmission due to channel collision. Besides, the proposed method can support both ACK and alarm transmission. Simulation results have shown that the proposed method can greatly improve data transmission success rate, and can reduce the energy consumption of sensors by more than 20%.

Keywords Electric Low Power Wireless Sensor Network (e-LPWSN) · Communication Protocol · Active wakeup · ACK

1 Introduction

The existing wireless sensor network technologies, such as LoRa [1], NB-IoT [2], BLE 5.0 [3] and ZigBee [4], are not designed for electric scenarios. Without modification, they cannot meet application requirements in scenarios such as substations and power transmission line. Modifications made by individual manufacturers may lead to products have poor compatibility and strong dependence on their original factory. As a result, State Grid Corporation of China has launched a series of standards [5, 6] for e-LPWSN communication protocol with the aim of interoperability.

C. An (✉) · Z. Huang
State Grid Smart Grid Research Institute Co., Ltd., Beijing 102209, China
e-mail: anchunyan@geiri.sgcc.com.cn

C. An
Electric Power Intelligent Sensing Technology and Application of State Grid Corporation Joint Laboratory, Beijing 102209, China

© Beijing Paiké Culture Commu. Co., Ltd. 2023
X. Dong et al. (eds.), *The proceedings of the 10th Frontier Academic Forum of Electrical Engineering (FAFEE2022)*, Lecture Notes in Electrical Engineering 1054, https://doi.org/10.1007/978-981-99-3408-9_1

Most electric sensors are powered by battery and have strict requirements on energy consumption. Besides, the services of e-LPWSN are usually data collection and metering, both of which are periodically. Communication protocols described in [5, 6] adopt periodic wake-up mechanism. In each service circle, sensors first complete data transmission/reception, and then fall asleep until the next service circle.

With the aim of minimizing the energy consumption of sensors, this paper studies the optimization of existing e-LPWSN communication protocol [5] based on active wakeup [7]. Firstly, we add active wake-up unit [8] to each sensor communication module, where sensors are waked up on demand instead of periodically, which can maximize the sensor sleep time. At the same time, channel collision is minimized by scheduling the wakeup of different sensors, which can reduce the average work time of sensors, thus to reduce energy consumption. Secondly, we optimize the communication protocol process, which makes it can support both ACK and alarm transmission.

2 Active Wakeup of Sensors

Active wake-up unit wakes up the sensor through internal interruption after receiving wakeup signal. Wakeup signal can be a simple energy burst that wakes up all sensors in the receiving range or includes address information that wakes up a specific sensor. The active wakeup unit should have the capability of low latency, high sensitivity, ultra-low power, and addressing.

A lot of research work has been done on active wakeup. Authors in [8] designed an ultra-low power wireless wakeup sensor. The energy consumption of the wireless wakeup module is only 0.07% of the communication module when it is idle. [9] presented the first demonstration of a sub-100 nW CMOS wakeup receiver with envelope detector, which was considered as the first architecture that operated at multigigahertz frequencies. [10] presented a 0.3-V, -75.8 -dBm differential wakeup receiver with temperature robustness for wireless sensor network applications. [11] proposed a wakeup receiver topology with addressing capability based on the innovative band-pass filter topology, and also proposed two new protocols, which used selective wakeup and dynamic address allocation to optimize system performance and realize directional wakeup of sensors. [12] developed a prototype with a novel addressing scheme for wakeup receivers which enabled broadcast, multicast, and unicast wakeups.

3 Communication Protocol Optimization

Assume the network topology of e-LPWSN is star, which is composed of one sink node and a large number of sensors directly connected to it.

With active wakeup technology, the sink node can wake up one or a certain number of sensors each time on demand, which enables better channel usage. In order to further reduce resource consumption and meet the requirements of radio management, it is considered that the e-LPWSN only uses one frequency channel. In addition, in order to eliminate the impacts of data losing during transmission, acknowledgement (ACK) mechanism is added to the optimized communication protocol.

Data transmission process of the optimized e-LPWSN communication protocol is shown in Fig. 1. Different to sensors wake up periodically of the existing communication protocol, sensors of the optimized e-LPWSN communication protocol are always asleep until they receive the wakeup signal transmitted by the sink node. When to wake up a certain sensor is up to the sink node, considering the sensor type, service requirements, and the channel condition. Besides, all the data transmission in the optimized e-LPWSN communication protocol should be acknowledged. Once receive ACK from the sink node, sensors fall asleep again.

The optimized communication protocol of e-LPWSN supports alarm transmission. When a sensor detects an alarm signal, it will wake up automatically, and then initiate the alarm transmission process as shown in Fig. 2.

Fig. 1. Data transmission process

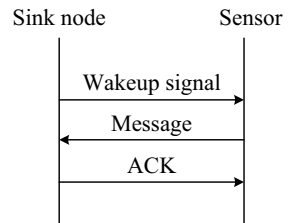
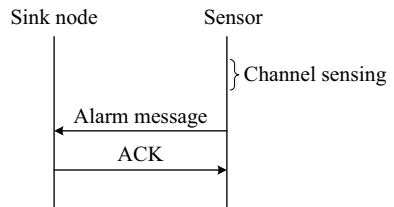


Fig. 2 Alarm transmission process



4 Theoretical Analysis

4.1 Existing Communication Protocol of e-LPWSN

The working flow chart of sensors after waking up is shown in Fig. 3. t_L is channel sensing time, t_b is the maximum delay before transmitting, t_t is message transmitting time, and t_r is the ACK receiving time. The length of each time slot is assumed to be $t = t_L + t_b + t_t + t_r$.

Both message and ACK may lost in the data transmission. Assume the data loss rate of a single transmission is η . Then the data loss rate during the whole transmission (including message transmission and ACK receiving) p_{loss} can be expressed as:

$$p_{loss} = 1 - (1 - \eta)^2 \quad (1)$$

Assume the service arrival obeys Poisson distribution, the probability that s sensors have message to transmit in a single time slot can be expressed as:

$$p(X = s) = \frac{\lambda^s}{s!} e^{-\lambda}, s = 0, 1, \dots, S \quad (2)$$

where λ is the arrival rate, and S is the total number of sensors.

Assume the maximum retransmission times is M . When at least 2 sensors (including retransmission) have message to transmit in a single time slot, channel will be detected to be busy. Channel busy rate p_{busy} can be expressed as:

$$p_{busy} = 1 - p(X = 0) - p(X = 1) + p(X = 1) \sum_{m=1}^M p_{loss}^m p(X = 1) \quad (3)$$

If channel is busy in the channel sensing phase, sensors will back off for w timeslots and then play channel sensing again. The maximum backoff times is assumed to be N . After N th backoff, if the channel is still busy, the message will be discarded. Besides, if sensors have transmitted message successfully but do not receive ACK, it will retransmit the original message. Then data transmission success rate $p_{success}$ can be expressed as:

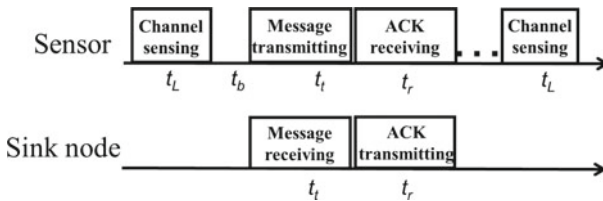


Fig. 3 Working flow chart of sensors after waking up

$$p_{success} = \sum_{n=0}^N p_{busy}^n (1 - p_{busy}) \sum_{m=0}^M p_{loss}^m (1 - p_{loss}) \quad (4)$$

Energy consumption of sensors consists of two parts: service message transmission and control message transmission. The transmission period of service message and control message are different.

The base energy consumption of sensors E_{base} without retransmission is defined as the total energy consumption of backoff, message transmitting and ACK receiving phase:

$$E_{base} = (t_b I_b + t_t I_t + t_r I_r) V \quad (5)$$

where I_b , I_t and I_r is the current in the waiting, message transmitting, and ACK receiving phase respectively. V is the working voltage of the transmitter.

For each retransmission, the extra energy consumption E_{extra} including the retransmitting and waiting energy consumption, can be expressed as:

$$E_{extra} = (t_t I_t + t_w I_b) V \quad (6)$$

where t_w is the waiting time to retransmit.

The average energy consumption of each message E_{ave_s} consists of three parts: channel sensing energy consumption, the base energy consumption and the extra energy consumption caused by data losing, and can be expressed as:

$$E_{ave_s} = t_L I_L V + (1 - p_{loss}^{M+1}) E_{base} + \sum_{m=1}^M m p_{loss}^m (1 - p_{loss}) E_{extra} + p_{loss}^{M+1} E_{extra} \quad (7)$$

Energy consumption of service message $E_{service}$ can be expressed as:

$$E_{service} = \begin{cases} (1 - p_{busy}) E_{ave_s} + p_{busy} t_L I_L V, & N = 0 \\ (1 - p_{busy}^{N+1}) E_{ave_s} + (N + 1) p_{busy}^{N+1} t_L I_L V + (1 - p_{busy}) \sum_{n=1}^N n p_{busy}^n t_L I_L V, & N \geq 1 \end{cases} \quad (8)$$

Different to the service message transmission, control message transmission of the existing e-LPWSN communication protocol consists of four parts: (a) channel sensing and random backoff; (b) control message requesting; (c) control message receiving; (d) ACK transmitting. Since data losing of control message has the same effect on the existing e-LPWSN communication protocol and the optimized one, here we do not consider the extra energy consumption caused by backoff and data losing for control messages. Energy consumption of control message $E_{control}$ can be expressed as:

$$E_{control} = (t_L I_L + t_b I_b + t_{t_message} I_t + t_r I_r + t_{t_ACK} I_t) V \quad (9)$$

where t_L , t_b , $t_{t_message}$, t_r and t_{t_ACK} represents the time of channel sensing, waiting, control message transmitting, control message receiving, and ACK transmitting respectively. I_L , I_b , I_t and I_r represents the current of sensors when sensing, waiting, transmitting and receiving respectively.

Energy consumption of sensors of the existing e-LPWSN communication protocol can be expressed as:

$$E_{existing} = \alpha E_{service} + \beta E_{control} \quad (10)$$

where α , β represents the weight of service and control message respectively, which varies inversely with transmitting cycle.

If backoff times $N = 0$, average transmitting delay is determined by p_{loss} , and can be expressed as:

$$T_1 = (1 - p_{busy}) \sum_{m=1}^M m p_{loss}^m (t_t + t_r) \quad (11)$$

If backoff times $N \geq 1$, average transmitting delay should take the backoff time into consideration, and can be expressed as:

$$T_z = (1 - p_{busy}) \sum_{n=1}^N n p_{busy}^n w t + (1 - p_{busy}^{N+1}) \sum_{m=1}^M m p_{loss}^m (t_t + t_r) \quad (12)$$

4.2 Optimized Communication Protocol of e-LPWSN

Data transmission success rate of the optimized communication protocol can be described as:

$$p_{success_opt} = \sum_{m=0}^M p_{loss}^m (1 - p_{loss}) \quad (13)$$

Energy consumption of sensors consists of service and control message transmission too. The energy consumption of control message of the optimized communication protocol is the same to that of the existing one. The energy consumption of service transmitting can be expressed as:

$$E_{service_opt} = (1 - p_{loss}^{M+1})E_{base} + \sum_{m=1}^M mp_{loss}^m (1 - p_{loss})E_{extra} + p_{loss}^{M+1}E_{extra} \quad (14)$$

The energy consumption of sensors can be described as:

$$E_{opt} = \alpha E_{service_opt} + \beta E_{control} \quad (15)$$

The average transmitting delay of the optimized communication protocol T_{opt} only contains the delay caused by data losing, which can be expressed as:

$$T_{opt} = \sum_{m=1}^M mp_{loss}^m (t_t + t_r) \quad (16)$$

5 Simulation Results

Simulation was done based on MATLAB. The weight of service and control message α and β is assumed to be 12 and 1 respectively. Backoff times of sensors w is assumed to be 5 time slots, and the maximum retransmission times M is set to be 3. Other simulation parameters are shown in Table 1.

From Fig. 4 (a) we can see that when the number of sensors is less than network capacity, data transmission success rate of the proposed method is close to 100%. When the number of sensors is 3500, the data transmission success rate of the proposed method is 99.8%, which is 27, 7 and 2% higher than that of the existing protocol when the backoff times $n = 0, 1$ and 2. From Fig. 4 (b), we can see that the average transmission delay increases with the number of sensors, and the proposed protocol can greatly reduce the average transmission delay.

Table 1 Simulation parameters

Type	Circuit/mA	Time/ms	Period
Service message transmitting	$I_1 = 15$	$t_1 = 15.2$	5 min
Service ACK receiving	$I_A = 7.7$	$t_A = 12.1$	5 min
Waiting because of data losing	$I_{A1} = 7$	$t_{A1} = 12.1$	\
Control message transmitting	$I_r = 15$	$t_r = 12.1$	1 h
Control ACK transmitting	$I_c = 15$	$t_c = 12.1$	1 h
Control message receiving	$I_a = 7.7$	$t_a = 16$	1 h
Transmitting delay for each packet	$I_d = 3$	$t_d = 16$	\
Channel sensing	$I_L = 7$	$t_L = 15.2$	\

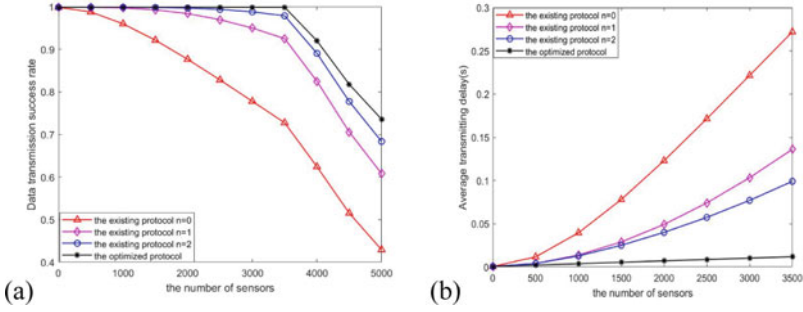


Fig. 4 Performance vs. the number of sensors **a** data transmission success rate **b** average transmission delay

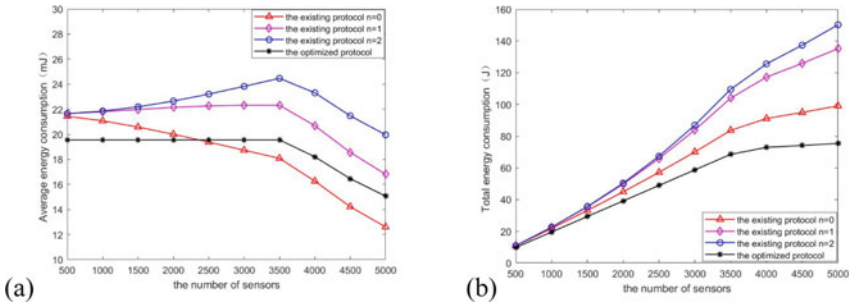


Fig. 5 Energy consumption vs. the number of sensors **a** Average **b** Total

From Fig. 5 (a) we can see that the average energy consumption of the proposed communication protocol is 19.55 mJ, which is 14.1 and 25.1% lower than 22.31 mJ with $n = 1$ and 24.46 mJ with $n = 2$ backoff times of the existing protocol. From Fig. 5 (b), we can see that total energy consumption of the proposed protocol is better than that of the existing protocol.

6 Conclusions

e-LPWSN plays an important role in data acquisition and transmission for monitoring and metering. However, there are still some open questions to be solved for practical application, such as ultra-low energy consumption, safe and reliable transmission. To address this problem, with the aim of further reducing energy consumption of sensors, this paper proposes a communication protocol optimization method of the existing e-LPWSN based on active wakeup, which can support both ACK and alarm

transmission. Simulation results have shown that the proposed optimized communication protocol not only greatly reduces energy consumption of sensors, but also improves the data transmission success rate and average transmission delay.

Acknowledgements This work was funded by science and technology projects of State Grid Corporation of China (Research on Lightweight Secure Connection Technologies for Electric Low Power Wireless Sensor Network with both Wide-band and Narrow-band Terminals, No.5500-202158416A-0-0-00)

References

1. Gehlot, A., Singh, R., Sharma, R.: LoRA and IoT Networks for Applications in Industry 4.0. Nova Science Publishers, New York (2020)
2. Hossam, F.: LTE Cellular Narrowband Internet of Things (NB-IoT): Practical Projects for the Cloud and Data Visualization. CRC Press, Boca Raton (2021)
3. Shan, G., Roh, B.: Performance model for advanced neighbor discovery process in bluetooth low energy 5.0-enabled IoT networks. *IEEE Trans. Ind. Electron.* **67**(12), 10965–10974 (2020)
4. Alberto, S., Javier, M., Ramon, F.: Smart Grid Telecommunications: Fundamentals and Technologies in the 5G Era. Wiley-IEEE Press, New York (2021)
5. State Grid Corporation of China: Micro-power wireless network communication protocol for the internet of power transmission and transformation equipment. *Q/GDW 12020–2019*, Beijing (2019). (in Chinese)
6. State Grid Corporation of China: Node device wireless networking protocol for the internet of power transmission and transformation equipment. *Q/GDW 12021–2019*. Beijing (2019). (in Chinese)
7. Djiroun, F., Djenouri, D.: MAC protocols with wake-up radio for wireless sensor networks: a review. *IEEE Commun. Surv. Tutor.* **19**(1), 587–618 (2017)
8. Lee, S., Bae, Y., Choi, L.: The design of an ultra-low power RF wakeup sensor for wireless sensor networks. *J. Commun. Netw.* **18**(2), 201–209 (2016)
9. Bassirian, P., Duvvuri, D., Liu, N.: Design of an S-band nanowatt-level wakeup receiver with envelope detector-first architecture. *IEEE Trans. Microw. Theory Tech.* **68**(9), 3920–3929 (2020)
10. Liu L., Xie S., Liao X.: A 0.3-V, -75.8 -dBm temperature-robust differential wake-up receiver for WSNs. *IEEE Sens. J.* **22**(21), 20593–20602 (2022)
11. Petrioli, C., Spenza, D., Tommasino, P., Trifiletti, A.: A novel wake-up receiver with addressing capability for wireless sensor nodes. In: 2014 IEEE International Conference on Distributed Computing in Sensor Systems, pp. 18–25 (2014)
12. Blobel, J., Krasemann, J., Dressler, F.: An architecture for sender-based addressing for selective sensor network wake-up receivers. In: 2016 IEEE 17th International Symposium on a World of Wireless, Mobile and Multimedia Networks (WoWMoM) (2016)

Application of Scientific Hypothesis - Deductive Method in Analysis of Abnormal Swing Fluctuation of Hydropower Unit



Zhihua Li, Diancheng Liu, Nannan Xu, Mengshen Li, Jinsong Du,
Keheng Zhou, Jin Li, and Hailin pei

Abstract This paper takes the abnormal fluctuation of the upper guiding shaft of a hydropower station as an example. Firstly, the independent variables of the abnormal fluctuation are determined. Assumptions about the main shaft shaking and the base change are made according to the measurement principle and scientific assumptions-deductive method. Then, different combinations of independent and dependent variables will reflect the changing law of peak-to-peak and gap values at the time of sampling overlap and non-overlapping time. According to the changing law and combined with the investigation method, the correlation is verified from the aspects of structural characteristics and numerical magnitude. By analyzing the combinations with “consistent” correlation verification, the reason for the abnormal fluctuation of the upper guiding shaft can be finally obtained. The proposed method can be applied in the complex multi-objective, multi-factor, multi-component, and multi-variable fault analysis, which can greatly reduce the analysis workload and provides appropriate direction for the fault analysis. The successful application of this method is expected to provide help for power station production technicians and scientific researchers.

Keywords Scientific hypothesis-deductive method · Cyclical fluctuation · The dependent variable · Verification of correlation · Arm creep

CLC Number: Document Identification Code:

Z. Li (✉) · N. Xu · J. Du · H. pei
Xi'an Thermal Power Research Institute Co., Ltd., Xi'an 710032, China
e-mail: lizhihua@tpri.com.cn

D. Liu · M. Li · K. Zhou · J. Li
HuanengLancang River Hydropower Inc., Kunming 650206, China

© Beijing Paiké Culture Commu. Co., Ltd. 2023
X. Dong et al. (eds.), *The proceedings of the 10th Frontier Academic Forum of Electrical Engineering (FAFEE2022)*, Lecture Notes in Electrical Engineering 1054,
https://doi.org/10.1007/978-981-99-3408-9_2

1 Introduction

Scientific hypothesis-deductive method is based on certain empirical facts and based on the existing scientific knowledge achievements. Use creative thinking to make scientific assumptions about some things that have not yet been known, and then use this assumption to deduce in the form of deduction. A method of broadly explaining known empirical facts or anticipating unknown facts [1]. Scientific hypothesis-deductive method is a methodology that is widely used in the understanding of objective laws in natural sciences, basic sciences, humanities and other disciplines. At the same time, this method is also accompanied by people's compulsory education stage, academic education stage, career growth stage, etc. It can be said that people apply this method all the time to solve practical problems and understand some objective laws [2–4].

In the existing literature, there are many discussions and solutions on the problems of the upper guide pendulum exceeding the standard and the vibration exceeding the standard. Such as unit load distribution, inter-turn short circuit, magnetic tension unbalance, insufficient frame stiffness, mass unbalance, etc. [5–10], and has been effectively solved, but there are relatively few literatures involving the periodic fluctuation of the upper guide pendulum.

Since the first unit of a hydroelectric unit was put into operation in 2017, the following abnormal fluctuations have been observed in the upward deflection of the 4 units in the whole station: The variation law of the peak-to-peak value of the upper lead swing with time is a sinusoidal variation law within 24 h. The peak of volatility appears in the period from 6:00 to 9:00, and the trough appears in the period from 17:00 to 19:30. It has been consistent with this rule since it was put into production.

The laws of performance in a short period of time after starting the grid connection are not the same during that the 4 units restarted after shutdown, but when continuous operation with load for more than 24 h, the swing peak-to-peak value of the upper guide pendulum fluctuates periodically. In addition, the longer the running time, the more consistent the fluctuation law and amplitude of the performance of the four units. Compare the swing data of the same generator set, summer/winter daytime fluctuations are about 70/100 μm . That is, the fluctuation range in summer is lower than that in winter. In order to reveal the essence of the problem, we try to use the scientific hypothesis-deduction method to analyze the problem, and finally draw a more reliable conclusion.

2 Analytical Application of the Methodology

The scientific hypothesis-deductive method can be divided into two stages, the formulation of the problem hypothesis and the verification of the hypothesis. Extract reasonably hypothesized related factors based on experience, and speculate on the basis of related factors that may cause changes in indirect dependent variables, through

different combinations of independent variables and dependent variables. Consistency verification is carried out with the change rules of the gaps at different positions respectively. If they are consistent, they are credible, and if they are inconsistent, they are not credible. Then re-validate the credible dependent variables to draw valid and credible conclusions.

2.1 Look for Relevant Factors

Generating state of the unit, reactive power, active power, terminal voltage, upper frame vibration, excitation current, upper lead oil temperature, upper lead cooling water flow, cooling water inlet and return water temperature difference, upper lead tile temperature, collector ring parameters such as room temperature are closely related. Therefore, first compare and analyze the correlation between the above parameters and the peak-to-peak fluctuation of the upper lead swing, among which the main parameter change curve is shown in Fig. 1.

Due to limited space, the oil temperature, water temperature, cold and hot air temperature, cooling water flow rate, water temperature, etc. are not drawn in Fig. 1. After inspection, the above parameters have no correlation or weak correlation with the swing peak-to-peak cycle fluctuation.

It can be seen from Fig. 1 that it is significantly related to the peak-to-peak fluctuation of the upper guide pendulum and the reproducible parameter of the periodic variation law is the temperature of the collector ring chamber. According to the location and structural characteristics of the measuring point arrangement, the fluctuation takes 24 h a day as a cycle, and it can be inferred that there is a strong correlation between the ambient temperature of the workshop and the peak-to-peak value of the upper guide swing. The relationship between temperature and peak-to-peak value is: the peak-to-peak value of the swing becomes smaller when the temperature is high, and the peak-to-peak value becomes larger when the temperature is low.

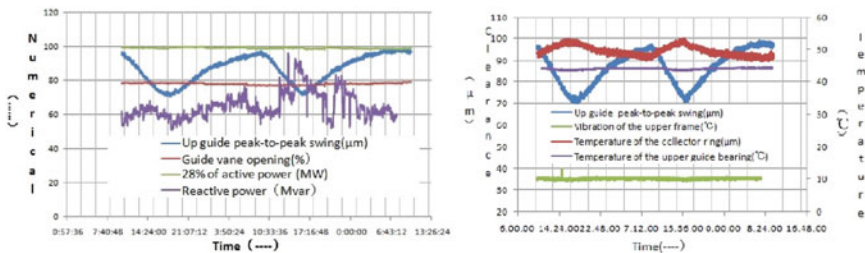


Fig. 1 #4Variation curve of operating parameters

2.2 Generation of Hypothesis

The peak-to-peak value of the upper guide pendulum varies with the temperature, and according to the calculation method and principle of the peak-to-peak value of the swing of the rotating object and the gap value (average value), it can be known that the peak-to-peak value of the pendulum becomes larger or smaller, that is, the gap of measured object and the probe becomes larger or smaller in a sampling period. There are three main forms. Assumption 1: The spindle shaking amplitude remains unchanged, and the position of the probe base changes; Assumption 2: The probe base position remains unchanged, and the spindle shaking amplitude changes; Assumption 3: The probe base position changes and the spindle shaking amplitude changes. In order to analyze the above assumptions, each assumption can be divided into condition 1: the main shaft does not shake; Condition 2: the base changes; Condition 3: the main shaft shakes; Condition 4: the base does not change. According to the structural characteristics and the composition of measuring equipment, the indirect-independent variables mainly include: sensor temperature drift problem, oil basin cover creep problem, upper frame center body creep problem, arm creep problem, spindle creep problem, bearing bush clearance, and a total of 7 indirect-independent variables in the problem. The independent variable is the collector ring room temperature or ambient temperature, denoted as independent variable 1. The dependent variable 1 is the peak-to-peak swing value of the upper lead swing, and the dependent variable 2 is the upper lead swing gap value. Due to the changes of the above independent variables and indirect independent variables, the swing peak-to-peak value and the gap value (dependent variable) will eventually be caused to change, which are called dependent variable 1 and dependent variable 2. The change process of the dependent variable is further divided into the peak-to-peak value and the value of the swing gap when the creep moment and the sampling time overlap, which are recorded as dependent variable 1. The swing peak-to-peak value of the dependent variable and the swing gap value when the creep time and the sampling time do not overlap, denoted as the dependent variable 2.

See Table 1 and Table 2 for the hypothesis combinations of specific independent variables, indirect-independent variables and dependent variables in Hypothesis 1 and Hypothesis 2. Assuming that the combinations in 3 are different combinations of Table 1 and Table 2, there can be 256 combinations, which are not listed one by one due to space problems of the paper. At the same time, some factors of Hypothesis 3 can be excluded in advance according to hypothesis testing to reduce the workload of analysis and comparison. Therefore, this paper focuses on the verification and analysis of Different combinations in hypothesis 1.

Table 1 Combination list of independent and dependent variables for Hypothesis 1

Condition 1	Independent variable 1	Indirect independent variable 2	Indirect independent variable 3	Indirect independent variable 4	Indirect independent variable 5	Dependent Variable 1 - Creep and Sampling Time Overlap		Dependent Variable 1 - Creep and Sampling Time do not Overlap		Correlation verification		The basis for the correlation test
						The swing peak-to-peak value trend	Change trend of swing clearance value	The swing peak-to-peak value trend	Change trend of swing clearance value	Peak-to-peak variation coupling results	Gap change coupling results	
The main shaft does not shake	Temperature change	The value of the probe changes with temperature	Creep value of oil basin roof	Upper frame center body creep	Rack arm creep	Constant	Smaller - on axis	Become smaller	Smaller - on axis	Consistent	Inconsistent	Figure 2-3 Table 2-3, Figure 2-3 Table 2-4 Figure 2-3, Figure 2-3 Table 2-1 and Formula 5 Figure 2-3 Table 2-3 Formula 1 and Formula 5 Figure 2-3 Table 2-3 Formula 1 and Formula 5
		Creep inward	Constant	Constant	Constant	Constant	Get bigger - on axis	Become bigger	Get bigger - on axis	Inconsistent	Consistent	
	Temperature rises	Creep outward	Constant	Constant	Constant	Constant	Smaller - on axis	Become smaller	Smaller - on axis	Inconsistent	Consistent	
		Creep inward	Constant	Constant	Constant	Constant	Get bigger - on axis	Become bigger	Get bigger - on axis	Consistent	Inconsistent	
	Temperature drop	Creep outward	Constant	Constant	Constant	Constant	Smaller - on axis	Become smaller	Smaller - on axis	Consistent	Inconsistent	
		Creep inward	Constant	Constant	Constant	Constant	Get bigger - on axis	Become bigger	Get bigger - on axis	Inconsistent	Consistent	
	Temperature drift	No temperature drift	Creep inward	Constant	Constant	Constant	Smaller - on axis	Become smaller	Smaller - on axis	Inconsistent	Consistent	
		No temperature drift	Creep outward	Constant	Constant	Constant	Get bigger - on axis	Become bigger	Get bigger - on axis	Consistent	Inconsistent	
	Temperature rises	No temperature drift	Constant	Creep inward	Constant	Constant	Bigger - on the base board	Become smaller	Bigger - on the base board	Consistent	Consistent	
		No temperature drift	Constant	Creep outward	Constant	Constant	Smaller - on the base board	Become bigger	Smaller - on the base board	Inconsistent	Inconsistent	
	Temperature drop	No temperature drift	Constant	Creep inward	Constant	Constant	Bigger - on the base board	Become smaller	Bigger - on the base board	Inconsistent	Inconsistent	
		No temperature drift	Constant	Creep outward	Constant	Constant	Smaller - on the base board	Become bigger	Smaller - on the base board	Consistent	Consistent	
	Temperature rises	No temperature drift	Constant	Constant	Creep inward	Constant	Bigger - on the base board	Become smaller	Bigger - on the base board	Consistent	Consistent	
		No temperature drift	Constant	Constant	Creep outward	Constant	Smaller - on the base board	Become bigger	Smaller - on the base board	Inconsistent	Inconsistent	
	Temperature drift	No temperature drift	Constant	Constant	Creep inward	Constant	Bigger - on the base board	Become smaller	Bigger - on the base board	Inconsistent	Inconsistent	
		No temperature drift	Constant	Constant	Creep outward	Constant	Smaller - on the base board	Become bigger	Smaller - on the base board	Consistent	Consistent	

Table 2 Combination list of independent and dependent variables for Hypothesis 2

Independent variable 1		Indirect - independent variable 2	Indirect - independent variable 6	Indirect - independent variable 7	Indirect - independent variable 8	Dependent Variable 1 - Creep and Sampling Time Overlap	Dependent Variable 1 - Creep and Sampling Time do not Overlap	Correlation verification		The basis for the correlation test		
Condition 3	Condition 4	The value of the probe changes with temperature	Creep of the shaft	Gap of shaft and guide bearing	Trajectory of the axis	The swing peak-to-peak value trend	Change trend of swing clearance value	The swing peak-to-peak value trend	Change trend of swing clearance value		Peak-to-peak variation coupling results	Gap change coupling results
Temperature rises	No temperature drift	Constant	Creep inward	Constant	Constant	Constant	Bigger - on axis	Become bigger	Bigger - on axis	Inconsistent	Consistent	Fig.2-5 、 Fig.2-4 、 Tab.2-3
	No temperature drift	Constant	Creep outward	Constant	Constant	Constant	Smaller - on axis	Become smaller	Smaller - on axis	Consistent	Inconsistent	
Temperature drop	No temperature drift	Constant	Creep inward	Constant	Constant	Constant	Bigger - on axis	Become bigger	Bigger - on axis	Consistent	Inconsistent	
	No temperature drift	Constant	Creep outward	Constant	Constant	Constant	Smaller - on axis	Become smaller	Smaller - on axis	Inconsistent	Consistent	
Temperature rises	No temperature drift	Constant	Constant	Gap gets bigger	Constant	Constant	Bigger - on axis	Become bigger	Bigger - on axis	Inconsistent	Consistent	
	No temperature drift	Constant	Constant	Gap gets smaller	Constant	Constant	Smaller - on axis	Become smaller	Smaller - on axis	Consistent	Consistent	Fig.2-5 、 Fig.2-4 、 Tab.2-3
Temperature drop	No temperature drift	Constant	Constant	Gap gets bigger	Constant	Constant	Bigger - on axis	Become bigger	Bigger - on axis	Consistent	Inconsistent	Formula 1 and Formula 5
	No temperature drift	Constant	Constant	Gap gets smaller	Constant	Constant	Smaller - on axis	Become smaller	Smaller - on axis	Inconsistent	Consistent	
Temperature rises	No temperature drift	Constant	Constant	Constant	Curvature becomes larger	Constant	Bigger - on axis	Become bigger	Bigger - on axis	Inconsistent	Consistent	Fig.2-5 、 Fig.2-4 、 Tab.2-3
	No temperature drift	Constant	Constant	Constant	Curvature becomes smaller	Constant	Smaller - on axis	Become smaller	Smaller - on axis	Consistent	Inconsistent	Formula 1 and Formula 5
Temperature drop	No temperature drift	Constant	Constant	Constant	Curvature becomes larger	Constant	Bigger - on axis	Become bigger	Bigger - on axis	Inconsistent	Consistent	
	No temperature drift	Constant	Constant	Constant	Curvature becomes smaller	Constant	Smaller - on axis	Become smaller	Smaller - on axis	Consistent	Inconsistent	

2.3 Verification of Hypotheses

2.3.1 Swing Peak-To-Peak and Gap Value Calculation

The calculation and reasoning of the peak-to-peak value of the swing of the conventional tested rotating body are all reasoned and demonstrated according to the constant probe base and the change of the spindle shaking amplitude. In order to facilitate the analysis and reveal the objective law of the periodic change of the upper lead swing caused by the changes of indirect-independent variable 3, indirect-independent variable 4, and indirect-independent variable 5. This paper deduces the process of the spindle sloshing unchanged and the base is subject to creep or periodic change that

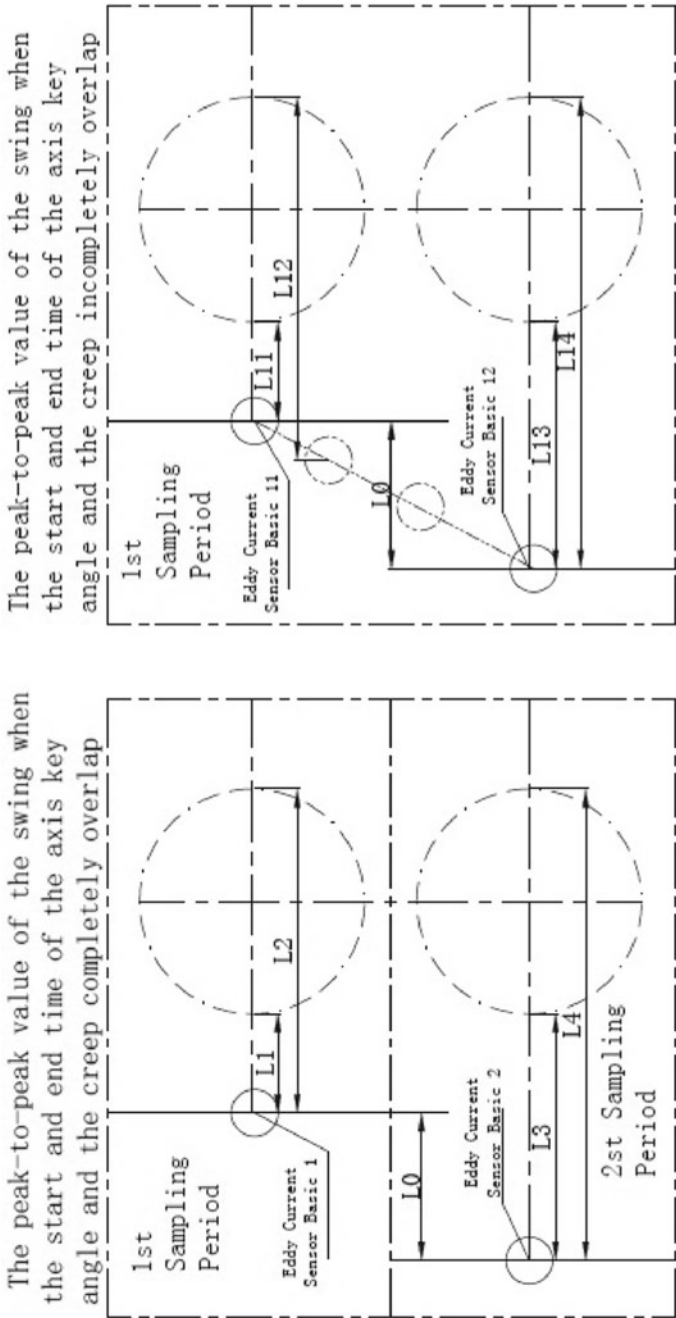


Fig. 2 Schematic diagram of extreme pendulum calculation

brings about the change of the peak-to-peak value and the gap value of the upper guide pendulum and the process is as follows:

The calculation formula of the clearance value of the upper guide swing:

$$hp = \frac{\sum_{i=1}^n h_i}{n} \quad (1)$$

The formula for calculating the peak-to-peak value of the upper lead swing:

$$h_{\max} = \max(h_1, h_2, \dots, h_n) - \min(h_1, h_2, \dots, h_n) \quad (2)$$

In the formula:

h_i : The gap between the measured object and the probe at different times when the generator set rotates once, μm ;

n : The number of measuring points recorded in one revolution of the generator set;

It can be seen from (Formula 1) that the swing gap value changes regardless of whether the creep time and sampling time of assumption 1 and assumption 2 overlap or not. If the creep time and sampling time of assumption 1 and assumption 2 overlap, then the measured value of formula 2 remains unchanged.

The peak-to-peak value and the gap value are regarded as the superposition of the gap values collected from time to time at different times in one circle, in any cylinder that rotates around its center. Then the gap values at different times can be expressed by the first cycle and the second cycle in Fig. 2. When analyzing the peak-to-peak value of the swing, each cycle can be regarded as the representation of the extreme value of the gap measured by one rotation of the cylinder.

- 1) Derivation of the calculation formula for the peak-to-peak value of the swing when the start and end time of the axis key angle and the creep in eddy current sensor base completely overlap:

$$\text{The peak - to - peak value of the swing in the first cycle is : } h_{\max 1} = L_1 - L_2 \quad (3)$$

In the formula:

L_1 : The minimum distance between the probe and the measured object for one rotation of the cylinder, μm ;

L_2 : The maximum distance between the probe and the measured object for one rotation of the cylinder, μm ;

The peak-to-peak value of the swing in the second cycle is:

$$h_{\max 2} = L_3 - L_4 = (L_1 + L_0) - (L_2 + L_0) = L_1 - L_2 = h_{\max 1} \quad (4)$$

In the formula:

L_3 : The minimum distance between the probe and the measured object for one rotation of the upper shaft, μm ;

L_4 : The maximum distance between the probe and the measured object for one rotation of the upper shaft, μm ;

L_0 : The relative distance of the base creep after the end of the first cycle of the upper end shaft and before the beginning of the second cycle, μm ;

It can be seen from formula (3) and formula (4) that although a relative displacement of $L_0 \mu\text{m}$ occurs at the creep position of the base, that is, a relative displacement of $L_0 \mu\text{m}$ occurs between the cylinder and the base gap, the peak-to-peak value of the cylinder pendulum does not change. There is no change that the first cycle and the second cycle swing peak-to-peak the same. The peak-to-peak swing of the upper end shaft does not change with the change of the gap between the upper end shaft and the base.

- 2) Derivation of the calculation formula for the peak-to-peak value of the swing when the start and end time of the axis key angle and the creep in eddy current sensor base incomplete overlap:

The start and end time of the axis key angle and the creep of the base do not completely overlap, that is, the creep of the base occurs in the middle of the two axis key angles. The upper end shaft changes the position of the base 11 to the base 12 in one cycle, and the position change is still $L_0 \mu\text{m}$. The changes of other parameters are shown in Fig. 2.

The peak-to-peak swing in a cycle is:

$$h_{\max} = \max(L_{11}, L_{12}, L_{13}, L_{14}) - \min(L_{11}, L_{12}, L_{13}, L_{14}) = L_{14} - L_{11} = h_{\max1} + L_0 \quad (5)$$

In the formula:

L_{11} : The minimum distance between the probe and the measured object in the first sampling time of the upper shaft to base movement. μm ;

L_{12} : The maximum distance between the probe and the measured object in the first sampling time of the upper shaft to base movement. μm ;

L_{13} : The minimum distance between the probe and the measured object in the second sampling time of the upper shaft to base movement, μm ;

L_{14} : The maximum distance between the probe and the measured object in the second sampling time of the upper shaft to base movement. μm ;

L_0 : The relative distance at which the base creeps during the cylinder makes one revolution in the first cycle. μm ;

According to formula (5), it can be known that the relative creep value $L_0 \mu\text{m}$ at the first moment, the second time...the nth time of the peak-to-peak value of the cylinder swing. It follows that when $L_0 > 0$, the swing peak-to-peak value of the swing measurement increases with the increase of the swing gap value, and the peak-to-peak value of the swing becomes smaller with the decrease of the swing

level gap value; When $L_0 < 0$, the swing peak-to-peak value becomes smaller as the swing gap value increases, and the swing peak-to-peak value becomes larger as the swing gap value decreases.

According to the derivation process of formula 1 to formula 5, it can be known that the rotating body under test does not shake, and the creep or periodic change of the sensor base will also bring about changes in the peak-to-peak value of the swing and the gap value.

2.3.2 Take Verification Measures and Data

Whether it is the change of the peak-to-peak value of the swing or the change of the gap value, it can be regarded as the change of the gap. Therefore, the gap between the main shaft and the oil basin cover of the #4 unit, the gap between the support arm and the base plate, and the gap between the support arm and the base plate are continuously and intermittently monitored to verify the Tables 1 and 2 assume content.

Measuring point 1: An eddy current sensor is arranged between the support arm and the base plate of the #4 unit to monitor the gap between the support arm and the base plate during static and transient processes. The transient process is shown in Figs. 3 and 4;

Measuring point 2: Add a mechanical dial indicator between the support arm and the base plate in the X and Y directions of the #4 unit to measure the change of the gap between the frame and the base plate and the symmetrical expansion of the support arm under the static state of the unit. The results are shown in Table 4;

Measuring point 3: Install a mechanical dial indicator at the sensor base in the $\pm X$ and $\pm Y$ directions of the main shaft of the #4 unit to measure the gap between the main shaft and the base and the symmetrical creep under the static condition of the unit. The measurement results are shown in Table 5.

Measuring point 4: Install a temporary probe at the bottom of the upper oil guide basin and replace the Y-direction fixed probe with a probe with temperature compensation characteristics. The results are shown in Fig. 5, in which the peak-to-peak value of "X-direction swing" in the figure is measured by the original probe data; "Y-direction swing" is the data measured by the newly installed probe in the X direction of the upper end axis; "Down-guided Y-direction" swing is the Y-direction swing replaced by an eddy current probe with temperature compensation.

(Note: X-direction swing: refers to the original probe and the peak-to-peak curve of the upper lead swing in the loop; Y-direction swing: refers to the actual peak-to-peak value of the actual swing of the upper shaft measured at the bottom of the oil basin; Downward Y-direction swing: refers to the replacement of the temperature compensation probe to measure the peak-to-peak value of the upper-lead Y-direction swing).

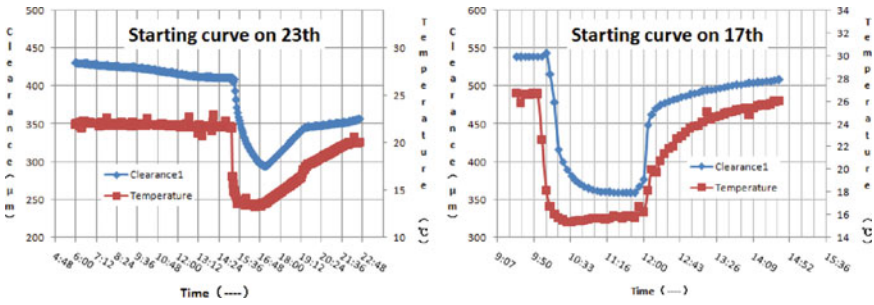


Fig. 3 #4 Relationship between clearance and temperature during start and stop

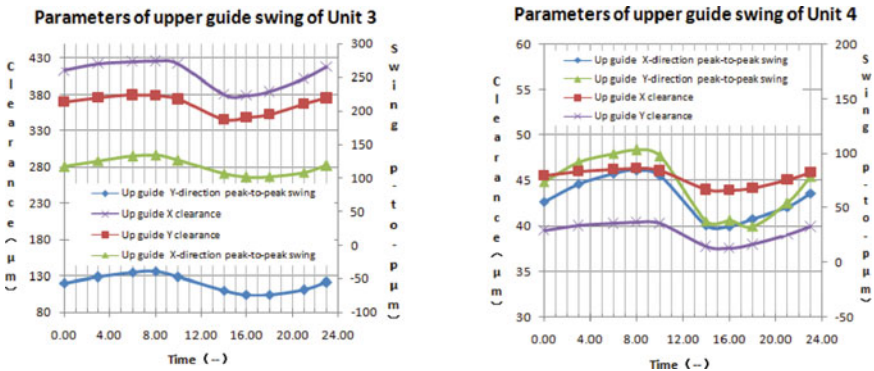


Fig. 4 #4 The curve of the relationship between the peak-to-peak value and the mean value of the swing of upper guiding shaft

Table 3 Rack to base plate clearance measurement record sheet

Date-time	Y direction clearance(mm)	X direction clearance(mm)	Temperature 1(°C)	Temperature 1(°C)	Remark
2022.2.16 9:50	0.00	0.00	28.53	29.17	Fom rack to base plate
2022.2.16 17:06	-0.07	-0.04	28.1	28.76	
2022.2.17 9:06	-0.1	-0.07	27.35	28.00	
2022.2.17 19:06	-0.13	-0.09	22.88	22.24	

2.3.3 Verification of Hypothesis

According to Fig. 3 and Table 3, the clearance between the arm and the foundation plate increases with the increase of temperature, and decreases with the decrease of temperature. The dependent variable combination that the clearance becomes smaller with the increase of temperature of the independent variable and that the temperature of the independent variable decreases with the increase of axis-clearance can

Table 4 Measuring record of oil basin cover plate to spindle clearance

Date-time	Y direction clearance(mm)	X direction clearance(mm)	-Y direction clearance(mm)	-X direction clearance(mm)	Temperature(°C)	Remark
2022.3.13 9:30	0.00	0.00	0.00	0.00	18.8	From the oil pan
2022.3.13 15:30	0.075	0.07	0.06	0.095	25.8	cover to the spindle

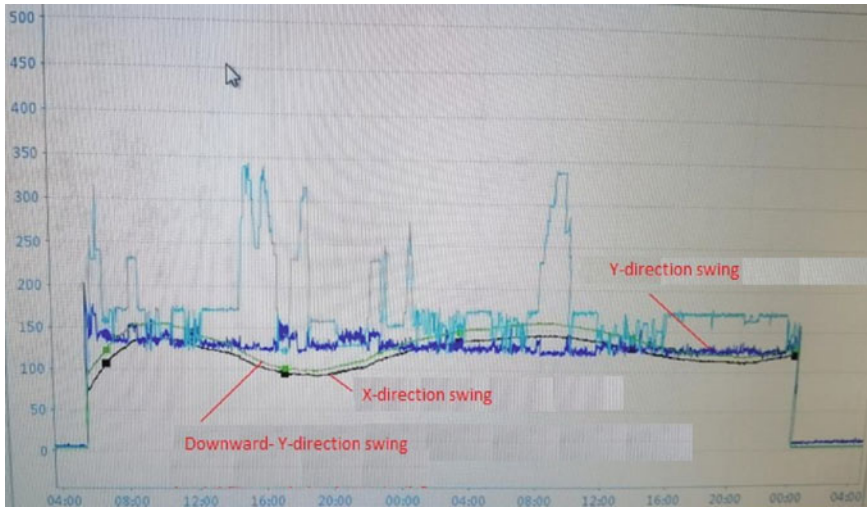


Fig. 5 #4Numerical changes at different measuring points

be excluded. According to Fig. 4 and Table 4, it can be seen that the gap between the base, that is, the probe to the main shaft increases with the increase of temperature, and decreases with the increase of temperature. It can be ruled out that the dependent variable increases with the temperature of the independent variable, and the gap between the shaft base and the independent variable temperature increases. Decrease the combination of dependent variables to reduce the axle base clearance. According to Fig. 5, each numerical curve is the peak-to-peak value of the gap between the main shaft and the base. In the figure, the “Y-direction swing of the lower lead” shows that the periodic fluctuation of the upper lead has not disappeared, and the “Y-direction swing” of the picture shows that the upper-lead periodic fluctuation disappears, and the “X-direction swing” in the figure shows that the periodic fluctuation does not disappear, which can exclude all indirect independent variable combinations of condition 3 main shaft shaking and condition 4 base unchanged. formula 4 and formula 5 respectively reveal the variation law related to the peak-to-peak value of the swing when the measured value of the gap becomes larger or smaller when the start and end time of the bond phase and the creep time do not overlap. According to the above assumptions and analysis, Tables 1 and 2 are lists of different indirect-independent variables and dependent variables that appear in different combinations from condition 1 to condition 4 due to temperature changes. Tables 3 and 4 and the objective laws of Formula 1 to Formula 5 are compared, i.e. correlation verification, and the two cases of peak-to-peak coupling and gap coupling are analyzed and compared respectively. The results are listed in Tables 1 and 2. As can be seen from Tables 1 and 2, according to the combination, the peak-to-peak value and the gap value coupling are consistent, indicating that the assumption is consistent with the objective actual results. If any of them are inconsistent, the assumption is

excluded. According to Tables 1 and 2, there are only 6 combinations with the same correlation verification results, while Tables 1 and 2 have a total of 32 combinations, so 26 combinations can be excluded, that is, the hypothesis 1 and hypothesis 2 reduce the number of combinations by 81%. It is only necessary to analyze and verify the hypotheses with the same correlation in Table 1, which greatly reduces the workload of investigation.

According to the “Y-direction swing” in Fig. 5 and the literature [11], the temperature difference between day and night collected from the field is about 5–8 °C, and the offset of the voltage change of the probe due to this temperature change can be ignored, so it is excluded that influence and combination of sensor temperature drift in Table 1. The free strain of the short and thin cylindrical shell due to temperature change should be axial creep, and the creep value of large metal parts is given as $1 \mu\text{m}/^\circ\text{C}$ per meter according to the experience of equipment materials. According to experience, it is estimated that the peak-to-peak fluctuation of the upper frame center body in one cycle is 29.38–47.00 μm , which is inconsistent with the 60–100 μm in the actual unit’s upper lead cycle fluctuation. The specific dimensions of the upper frame support arm are: diameter 14630 mm, I-shaped height 1070–1410 mm trapezoid, thickness 18 mm, arranged radially along the circumference, according to the creep value of large metal parts $1 \mu\text{m}/^\circ\text{C}$ to estimate its maximum and minimum. The creep values are 73.15 and 117.04 μm respectively, which are more consistent with the actual unit’s upward lead period fluctuation of 70–100 μm . Creep law analysis: In the short and thin cylindrical shell structure, the expansion is highly expanded along the axial direction, which is inconsistent with the on-site radial creep value. The I-shaped structure expands along the radial direction and the expansion law is consistent with the on-site radial creep value.

Therefore, from the numerical and quantitative relationship of periodic fluctuations and the structural characteristics of the frame, it can be seen that the radial creep or asymmetric creep of the support arm is transmitted through the center body to the base of the oil basin cover, which is fundamental the cause of the abnormal peak-to-peak fluctuation of the upper deflection of the unit.

3 Conclusion

Through the application of scientific hypothesis-deductive method in the analysis of periodic abnormal fluctuations of the upper guided pendulum, the following conclusions can be drawn:

- 1) It is more credible to use this method to analyze complex problems, especially for multi-objective, multi-factor, multi-component and multi-variable cases, that is, complex fault phenomena that cannot be described by analytical solutions;
- 2) Combined with formula derivation and on-site exclusion methods, more than 80% of the untrue factors can be excluded, greatly reducing the workload of investigation and special analysis;

- 3) The radial creep or asymmetric creep of the arm is transmitted to the base of the oil basin cap through the centrosome, which is the fundamental reason for the abnormal fluctuation of the peak-to-peak value of the guided swing on the unit.

Scientific hypothesis - deduction can well point out the direction for the analysis and investigation of complex problems in the field, and then take targeted verification means, can be very good to draw more credible conclusions. Therefore, this methodology can be widely used in the analysis and treatment of complex fault problems such as hydropower, thermal power, wind power and chemical industry.

References

1. Zheng, J.: A important method of research of the library theory: science hypothesis—the deductive method. *Library* (6), 13–15 (1998)
2. Zhang, C.: Some thoughts on mathematical meaning in economics. *Econ. Dyn.* **1**, 56–61 (2001)
3. Liu, D., Zhao, J.: Clavius' unified solutions by the method of twofold double false positions. *J. Northwest Univ. (Natl. Sci. Edn.)*, (49), 970–976 (2019)
4. Chen, G., Pan, D.M.: Analysis of the application of hypothesis testing thinking strategy in psychology. *Suppl. J. Sun Yatsen Univ.* (21), 243–245 (2001)
5. Yan, Z.G.: Research on stability of hydropower unit based on dynamic Load identification and numerical calculation. China Agricultural University, Beiiing (2013)
6. Shao, J., Liao, R., Xie, L., Chen, J.: cause analysis and treatment of the upper guide swing beyond standard on the generating unit of Ertan hydropower station. *Large Motor Technol.* **1**, 59–64 (2018)
7. Li, T.W., Wu, L.: Analysis and treatment of the cause of the upper lead swing exceeding the standard of the hydrogenerator. *Power Safety Technol.* (7), 13–16 (2009)
8. Wang, J.: Analysis and treatment of insufficient rigidity of upper bracket for a hydropower unit. *Hunan Electric Power* (3), 91–94 (2021)
9. Li, Y., Li, M., Ren, Y., Shang, H., GuBo. Vibration analysis and disposal of hydro-generating unit. *Water Power* (6), 67–69 (2021)
10. Mao, Z.: The Research of stiffness and dynamic Behavior of Upper Brack - stator system of hydroelectric Unit. Dalian University of Technology, Dalian (2010)
11. Fang, Q., Tian, X., Mao, P.: Study of the temperature drift compensation of eddy current transducers. *J. Southeast Univ.* (5), 47–51 (1995)

Optimization of Gear Ratio and Torque Density of Magnetic Gears Based on Genetic Algorithm



Zhiqiang Wang, Weinong Fu, Jiao Song, Peng Chen, Zhenyang Qiao, and Yanding Bi

Abstract Compared with traditional mechanical gears, coaxial magnetic gears (MG) have many advantages, including high gear ratio, high torque density, and low maintenance cost, so they are very suitable for industrial applications. In this paper, genetic algorithms are used to optimize three magnetic gears with different permanent magnet arrangements, including surface mounted, consequent-pole, and spoke-type array. To obtain the optimal design of magnetic gears in various applications, both gear ratio and unit mass torque density are taken as the optimization objectives. Furthermore, the performance of different aspects of the magnetic gears is compared and studied. The results show that the genetic algorithm can optimize the gear ratio and output torque simultaneously. Meanwhile, in this study, the relationship between the output torque and gear ratio is revealed. The output torque of the magnetic gears first increases with the gear ratio and then decreases greatly when the gear ratio is greater than a certain value due to the limitation of machining technology. After optimization, under the same constraints, both surface mounted MG and consequent-pole MG can achieve the characteristics of high gear ratio, but spoke-type array MG cannot. The torque of spoke-type array MG is the largest, which is 175.8% higher than that of surface mounted MG, but the volume of permanent magnets is exceeded by about 2 times. The torque of the consequent-pole MG is about 10.2% higher than that of surface mounted MG, but the torque ripple is larger.

Keywords Coaxial magnetic gear · Genetic algorithms · Gear ratio · Constraints · Optimization · Torque density

Z. Wang · W. Fu (✉) · J. Song · P. Chen · Z. Qiao · Y. Bi
Shenzhen Institute of Advanced Technology, Chinese Academy of Sciences, Shenzhen 518055, China
e-mail: wn.fu@siat.ac.cn

© Beijing Paiké Culture Commu. Co., Ltd. 2023
X. Dong et al. (eds.), *The proceedings of the 10th Frontier Academic Forum of Electrical Engineering (FAFEE2022)*, Lecture Notes in Electrical Engineering 1054, https://doi.org/10.1007/978-981-99-3408-9_3

1 Introduction

As mechanical transmission devices, mechanical gears are widely used in industrial applications. Traditional gears adopt the mechanical structure of mechanical meshing. However, this kind of structure is very complicated and has several drawbacks, including low gear ratio, low efficiency, and poor reliability. The magnetic gear (MG) transmits torque and power through a non-contact interaction between permanent magnets (PMs) on different parts. Compared with traditional mechanical gears, the MG can achieve a higher gear ratio, transmission efficiency, and reliability. Moreover, the MG has almost no mechanical wear and has a special overload protection mechanism, which makes its maintenance cost low. In addition, the low noise characteristic of the MG is more suitable for application in industrial production. In recent years, MG has attracted more and more attention from research institutions and industries [1].

The earliest MG is an electromagnetic spurred gear, which was proposed in 1901. The design structure of this MG is very similar to traditional mechanical gear, and the interaction between the permanent magnets replaces the force exerted by the meshing of the mechanical gear [1]. A novel high-performance MG was designed in [2], which is composed of inner and outer rotors and a flux modulator between them. An MG with a novel outer rotor structure was studied [3], it adopts a spoke-type outer PM rotor and introduces an auxiliary flux modulator placed in the outermost layer. A new flux focusing magnetic gear (FFMG) was designed in [4] with high torque performance. A comparison of torque density and cost-effectiveness of 15 MGs with simple coaxial radial topology was studied [5]. A taboo algorithm was used to optimize the MG with a traditional permanent magnet layout and finally obtained two new MG topologies with higher torque density [6]. A triple permanent magnet excitation (TPME) magnetic gear with an additional pinned layer of permanent magnets sandwiched between adjacent ferromagnetic segments was proposed [7]. A genetic algorithm was used to optimize MGs over a range of gear ratios at different temperatures [8]. The influence of different pole pair matching schemes on the performance of MGs under a certain gear ratio was studied [9]. High gear ratio capabilities of single-stage, series multistage, and compound differential coaxial magnetic gears were compared [10]. The influence of topological parameters of MGs on gear performance was studied [11]. The performances of three types of magnetic gears, which are radial-flux MGs, transverse-flux MGs, and axial-flux MGs were compared [12]. The two CMG topologies which are installed with radially magnetized and Halback magnetized PMs were quantitatively compared based on 3D FEM which takes the end effect into account [13]. Although many research results are showing that a high gear ratio will lead to a decrease in the output torque of MGs, in industrial applications, a high gear ratio, and high torque MG is required in numerous situations.

In this paper, a multi-objective genetic algorithm is used to optimize the parameters of three coaxial MGs with different PM arrangements, including surface mounted, consequent-pole, and spoke-type array arrangements. The gear ratio and unit mass torque density are designed as the optimization parameters and the torque performances between the different MGs under high gear ratio are compared.

2 MG Configuration

Figure 1 shows three radial flux MGs including, (a) Surface mounted MG (Topology I); (b) Consequent-pole MG (Topology II); and (c) Spoke-type array MG (Topology III). The magnetization direction of the PMs in Topology I and Topology II is radial, and the magnetization direction in Topology III is tangential. The pole-pair numbers of the inner and outer PMs are P_1 , P_3 , respectively. The number of flux modulators is P_2 . The magnetic field of the internal permanent magnet interacts with the magnetic field of the external permanent magnet to realize the transmission of torque through the modulation of the flux modulator. The relationship between the parameters of different parts is expressed as

$$P_2 = P_1 + P_3 \tag{1}$$

The speed relationship between the inner and outer rotors and the flux modulators is

$$P_1\omega_1 + P_3\omega_3 = P_2\omega_2 \tag{2}$$

where ω_1 , ω_2 , and ω_3 is the angular speed of the inner rotor, flux modulator, and the outer rotor, respectively.

Generally, the outer rotor and the inner rotor rotate, and the modulator is fixed. As a result, the relationship between the angular speed can be derived as

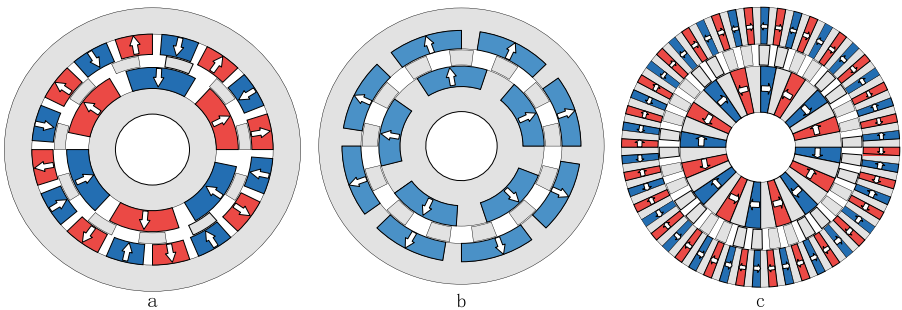


Fig. 1 Three radial flux MGs. (a) Surface mounted MG (Topology I). (b) Consequent-pole MG (Topology II). (c) Spoke-type array MG (Topology III)

$$\omega_2 = 0 \quad (3)$$

$$\omega_1 = -P_3\omega_3/\omega_1 \quad (4)$$

The pole pairs ratio P_3/P_1 between the outer and inner permanent magnets of the MG is the gear ratio. In the previous design, the gear ratio of the MG was often determined first, and then other parameters were set on this basis.

There are few reports using the gear ratio of the magnetic gear as an optimization target. In this paper, the gear ratio is taken as an optimization target of the MG, to quickly find a structural design with a high gear ratio and high torque density under a fixed outer dimension. In the optimization process, to prevent the torque fluctuation from affecting the operation, torque fluctuation is used as a constraint condition.

3 Optimize Settings

In this paper, the genetic algorithm is used to optimize the MGs. With the purpose to consider the manufacturing cost of the MGs, the optimization algorithm takes the torque density per unit mass of PM and the gear ratio of the MG as the objective functions. By changing the combination of the main structural parameters of the MG, topologies with a high gear ratio and high torque density per unit mass are obtained. Since the MGs of different structures have great differences in PM arrangements, and the optimization goal has a great relationship with the mass of the PMs, for a fair comparison, it is necessary to unify the three MG's specifications. As shown in Fig. 2, the air gap length of the magnetic gear is fixed at 0.5 mm. R_1 and R_2 are the inner air gap radius and outer air gap radius, respectively. If the air gap radius is not constrained in the optimization process, it will eventually lead to the optimization result of a deformed MG with a larger radius of the inner hollow part (R_{in}) and a smaller radial length of the permanent magnets (l_{i2} , l_{o2}). Therefore, in order to optimize the normal MG, the three types of MGs should have the same constraints on the length of the air gap during the optimization process.

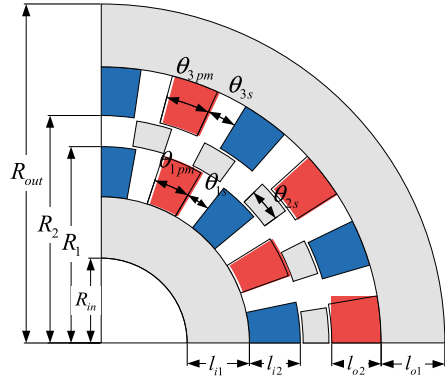
When the length of the air gap and the outer diameter of the MG are determined, to reduce the number of constraints in the optimization process, the duty ratio is used as the optimization variable to control the tangential width of each permanent magnet and flux modulator. The duty ratio of the inner and outer rotors (q_1 and q_3) is

$$q_1 = \frac{\theta_{1pm}}{\theta_{1s}} \quad (5)$$

$$q_3 = \frac{\theta_{3pm}}{\theta_{3s}} \quad (6)$$

where θ_{1pm} and θ_{1s} are the PM arc and air arc of the inner rotor; θ_{3pm} and θ_{3s} are the PM arc and air arc of the outer rotor.

Fig. 2 MG geometric parameters



And the duty ratio of the flux modulator (q_2) is

$$q_2 = P_2 \frac{\theta_{2s}}{360} \tag{7}$$

where θ_{2s} is the flux modulator arc.

At the same time, in order to optimize the usability of the results, a proportional relationship (k_i and k_o) is used to constrain the thickness of the PMs in the MG in the radial direction:

$$k_i = \frac{l_{i2}}{l_{i1}} \tag{8}$$

$$k_o = \frac{l_{o2}}{l_{o1}} \tag{9}$$

where l_{i1} and l_{i2} is the thickness of PMs and steel on the inner rotor and l_{o1} and l_{o2} is the thickness of PMs and steel on the outer rotor

The duty ratio of the inner and outer rotors of the Topology2 MG is fixed at 0.5 [8], and there is no permanent magnet thickness ratio constraint in the radial direction. After the relevant parameters of the MG are determined, the tangential width of the permanent magnets in the MG can also be determined. Taking the outer rotor of Topology I as an example, the width at the narrowest part of the permanent magnets of the outer rotor is

$$D_3 = 2\pi R_2 \frac{q_3}{2P_3} \quad (10)$$

where D_3 is the rear of the narrowest part of the single PM on the outer rotor.

If the number of pole pairs of the outer rotor is too large, the width of the single-piece PM will be too small, which is difficult to manufacture.

Taking MGs with a radius of 60 mm and a thickness of 80 mm as an example, the three types of MGs adopt the same layout design, the material used for PM is NdFe35, the material used for steel is 50DW310, and the design parameters are shown in Table 1.

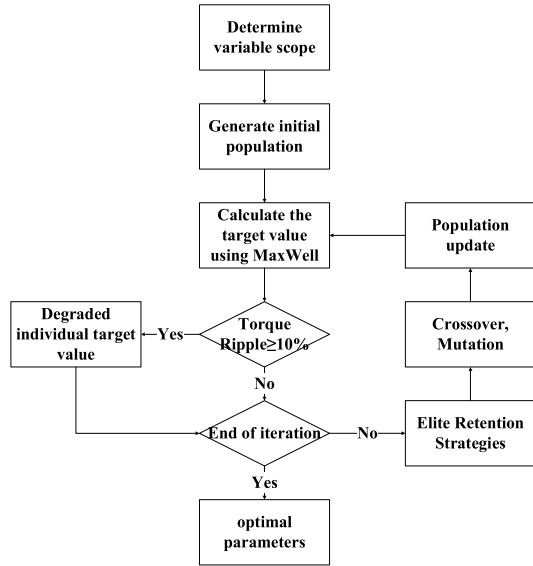
All constraints ensure that the width of the narrowest part of the PM of the MG is greater than 2 mm.

In the optimization calculation process, each combination of design parameters of the MGs is regarded as an individual. Since the optimization target is only the torque density per unit mass and the gear ratio, the torque ripple of the MG is not optimized. Consequently, the torque ripple of the individual may be too large to be used normally. Therefore, the optimization algorithm is modified. When the torque ripple of an individual exceeds 10%, the program will set the individual torque density and gear ratio to 0, so as to ensure that the genetic algorithm will discard the individual during the optimization process. In the process of crossover mutation, each gene of an individual crosses and mutates independently, and there is no influence between genes. When the population is selected, the Pareto level and crowding degree are calculated first, and the elite retention strategy is used to select the contemporary outstanding individuals for crossover mutation to generate a new generation of subgroups and enter the next iteration. The algorithm process is shown in Fig. 3.

Table 1 Optimize geometric parameters

Variable name	Description	Value
R_{out}	MG radial radius	60 mm
R_{in}	The internal hollow radius of MG	15 mm
R_1	Inner air gap radius	31–35 mm
R_2	Outer air gap radius	40–44 mm
P_1	Number of pole pairs of the inner rotor	1–8
P_3	Number of pole pairs of the outer rotor	1–20
P_2	Number of flux modulator	$P_1 + P_3$
q_1	The duty cycle of the inner rotor permanent magnet	0.3–0.7
q_2	The duty cycle of the flux modulator	0.4–0.95
q_3	The duty cycle of outer rotor permanent magnets	0.35–0.95
k_i	Inner rotor permanent magnet radial proportion	0.35–0.65
k_o	Outer rotor permanent magnet radial proportion	0.35–0.65

Fig. 3 The algorithm process after adding the fluctuation degradation module



4 Comparative Analysis

The individual with the highest torque density per unit mass under each gear ratio after optimization is extracted as the result. The optimization results of the three MGs are shown in Fig. 4. When the gear ratio is less than 10, the three MGs can achieve higher torque per unit mass. Topology II and Topology I have maximum torque per unit mass when the gear ratio is between 7.5 and 10, the Topology III has the largest torque when the gear ratio is 4. When the gear ratio is greater than 10, due to the constraint of the number of pole pairs of the outer rotor, in order to achieve a high gear ratio, the number of pole pairs of the inner rotor of the MG can only be 1. This constraint leads to a rapid reduction in the torque of the MGs, making it difficult to achieve the characteristics of high torque. At this time, the maximum torque per unit mass of Topology II and Topology I can reach 60 Nm/kg, while Topology III is only about 50 Nm/kg, so it is difficult for Topology II to maintain the characteristics of high torque when the gear ratio is too high.

Three MGs with the highest torque density per unit mass are selected for comparison. As shown in Table 2 the gear ratio of Topology III is 4, and the external torque (T_{avg}) is the largest. The gear ratio of Topology I and Topology II is both 10, and the torque of Topology II is relatively high. It can be seen that the torque performance of Topology I is the worst but the ripple (T_{rip}) is small. Although Topology III has the characteristics of high torque, it needs more PM mass (M_{PM}). Although the torque of Topology II is smaller than that of Topology III, the cost of Topology II is much lower because the PM is used less.

The use of different permanent magnet structures for the inner and outer rotors, as well as some other new structures, will also be further studied in future work.

Fig. 4 Optimization results of MGs with three topologies

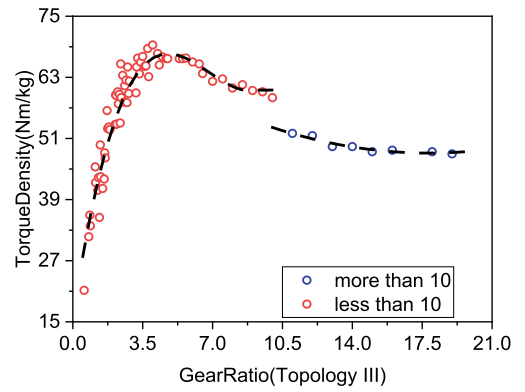
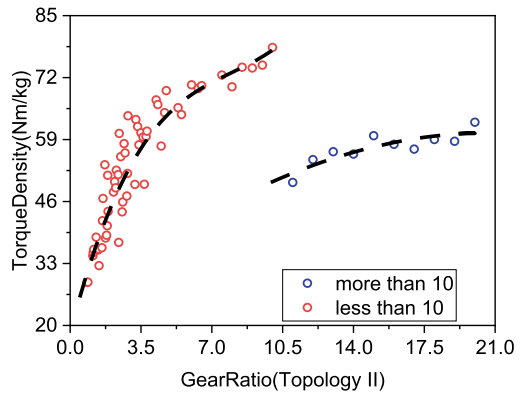
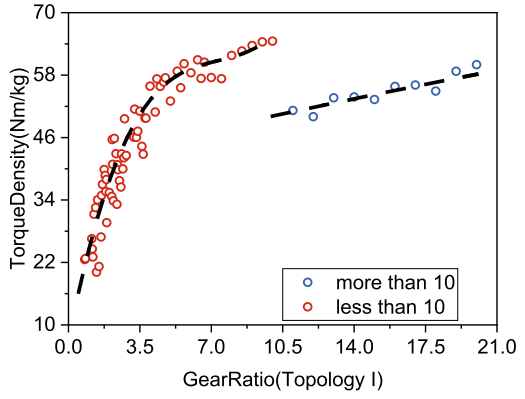
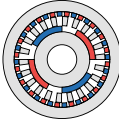
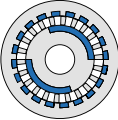
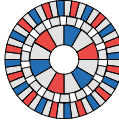


Table 2 Comparison of maximum torque density per unit mass performance of MGs with three topologies

Parameters			
R_1 (mm)	34.1	35	35
R_2 (mm)	43.9	44	44
P_1	2	2	3
P_2	22	22	15
P_3	20	20	12
q_1	0.69	0.61	0.5
q_2	0.46	0.42	0.6
q_3	0.67	0.58	0.5
k_i	0.3	0.3	—
k_o	0.3	0.3	—
Gear Ratio	10	10	4
T_{avg} (Nm)	61.56	67.83	169.80
M_{PM} (kg)	1.002	0.903	2.441
T_{rip} (%)	4.12	9.55	6.70
T_{avg}/M_{PM} (Nm/kg)	61.44	75.12	69.56

5 Conclusion

In this paper, a genetic algorithm is used to compare the MGs with three different PM arrangements with the optimization objectives of gear ratio and torque density per unit PM mass at the same time. It is found that Topology I has the characteristics of a high gear ratio, but the torque density per unit PM mass and the torque performance are low. Topology III provides extremely high torque performance. However, it is difficult to achieve a high gear ratio and requires a large number of permanent magnets to achieve high torque. Although the torque performance of Topology II is worse than Topology III, the cost of MGs is much lower than Topology III, and a high gear ratio can also be achieved. It can be known from the common phenomenon of the three MGs that when the gear ratio is too high, due to the limitation of processing technology and other factors, the number of pole pairs of the inner rotor can only be 1, which will lead to the decline of the torque performance of the MG.

References

1. Tlali, P.M., Wang, R.J., Gerber, S.: Technologies: a review. In: 2014 International Conference on Electrical Machines (ICEM), Berlin, Germany, pp. 544–550. IEEE (2014)
2. Atallah, K., Howe, D.: A novel high-performance magnetic gear. IEEE Trans. Magn. **37**, 2844–2846 (2001)

3. Zhang, X., Liu, X., Chen, Z.: A novel dual-flux-modulator coaxial magnetic gear for high torque capability. *IEEE Trans. Energy Convers.* **33**, 682–691 (2018)
4. Uppalapati, K.K., Bird, J.Z., Wright, J., Pitchard, J., Calvin, M., Williams, W.: A magnetic gearbox with an active region torque density of 239Nm/L. *IEEE Trans. Ind. Appl.* **54**, 1331–1338 (2018)
5. Shen, J.X., Li, H.Y., Hao, H., Jin, M.J., Wang, Y.C.: Topologies and performance study of a variety of coaxial magnetic gears. *IET Electr. Power Appl.* **11**, 1160–1168 (2016)
6. Fu, W.N., Li, L.: Optimal design of magnetic gears with a general pattern of permanent magnet arrangement. *IEEE Trans. Appl. Supercond.* **26**, 0606705 (2016)
7. Chen, Y., Fu, W.N., Li, W.: Performance analysis of a novel triple-permanent-magnet-excited magnetic gear and its design method. *IEEE Trans. Magn.* **52**, 8001304 (2016)
8. Gardner, M.C., Praslicka, B., Johnson, M., Toliyat, H.A.: Optimization of coaxial magnetic gear design and magnet material grade at different temperatures and gear ratios. *IEEE Trans. Energy Convers.* **36**, 2493–2501 (2021)
9. Praslicka, B., Gardner, M.C., Johnson, M., Toliyat, H.A.: Review and analysis of coaxial magnetic gear pole pair count selection effects. *IEEE J. Emerg. Sel. Top. Power Electron.* **10**, 1813–1822 (2022)
10. Gardner, M.C., Johnson, M., Toliyat, H.A.: Analysis of high gear ratio capabilities for single-stage, series multistage, and compound differential coaxial magnetic gears. *IEEE Trans. Energy Convers.* **34**, 665–672 (2019)
11. Evans, D.J., Zhu, Z.Q.: Influence of design parameters on magnetic gear's torque capability. In: *IEEE International Electric Machines & Drives Conference (IEMDC)*, Niagara Falls, ON, Canada, pp. 1403–1408. IEEE (2011)
12. Chen, Y., Fu, W.N., Ho, S.L., Liu, H.: A quantitative comparison analysis of radial-flux, transverse-flux, and axial-flux magnetic gears. *IEEE Trans. Magn.* **50**, 8104604 (2014)
13. Jian, L., Chau, K.T., Gong, Y., Jiang, J.Z., Yu, C., Li, W.: Comparison of coaxial magnetic gears with different topologies. *IEEE Trans. Magn.* **45**, 4526–4529 (2009)

Simulation Study for the Influence of Electrical Trees on Electric Field Distribution Around 10 kV Cable Bushing



Zhichao Xiao, Baiwei Hu, Zhiqiang Chen, Xiaoqing Ji, and Gaohui He

Abstract 10 kV ring main unit is widely used in urban distribution network due to its advantages of good airtightness, small size and convenient installation. However, the operating environment of 10 kV ring main unit is mainly open air, the cable wiring bushings in the ring main unit run in wet and dirty conditions for a long time, and it is easy to produce surface discharge on the surface of the bushings and form electrical tree. The appearance of electrical trees reduces the insulation performance of wiring bushings and seriously affects the reliability of power supply. In this paper, a finite element simulation model is established based on electrostatic field theory to study the distribution of electric field intensity around the surface of cable bushing in a 10 kV ring main unit when there are electrical trees. The influence of electric field intensity distribution on casing surface with different positions and different shapes is simulated and analyzed. The results show that the influence of electric field intensity distribution on casing surface is greater when the electric branch is generated at flange than at port. When other conditions are the same, the more complex shape and larger area of electrical trees will lead to more serious distortion of electric field intensity around casing. Through the study of the electric field distribution characteristics around the bushing when the electric branches appear, it can provide a theoretical basis for the insulation design, detection and repair of the bushing.

Keywords Ring main unit · Power cable · Wiring bushing · Electrical trees · Finite element model

Fund Project: Science and Technology Project of State Grid Chongqing Electric Power Company (SGCQSQ00YJJS2200342).

Z. Xiao · B. Hu · Z. Chen
State Grid Chongqing Electric Power Company Urban Power Supply Branch, Chongqing 400015, China

X. Ji · G. He (✉)
College of Engineering and Technology, Southwest University, Chongqing 400715, China
e-mail: hegaohui@swu.edu.cn

© Beijing Paiké Culture Commu. Co., Ltd. 2023
X. Dong et al. (eds.), *The proceedings of the 10th Frontier Academic Forum of Electrical Engineering (FAFEE2022)*, Lecture Notes in Electrical Engineering 1054, https://doi.org/10.1007/978-981-99-3408-9_4

1 Introduction

With the rapid development of economy and the deepening of urban power grid transformation, the requirements for power supply reliability are increasingly stringent. In order to improve the reliability of system power supply, the distribution network is usually connected to form a ring network, so that users can obtain power supply from at least two directions, and the ring network cabinet (RMU) plays a crucial role in the ring network. Due to the advantages of small size and low cost, ring network cabinet is especially suitable for power supply in large and medium-sized cities where land resources are increasingly strained [1]. However, the cable bushing of 10 kV ring network cabinet is mostly of integrated design and the operating environment is mainly open air, which make the working environment of ring network cabinet is relatively harsh [2–4]. The surface discharge often occurs on the insulating parts of the cable bushing (composed of epoxy resin), and electrical branch traces will be formed in serious cases. In recent years, power outages happened frequently due to insulation faults of cable bushing in ring network cabinet [5–7]. By 2014, the State Grid Corporation had installed 1.199,300 ring network cabinets, among which the Urban Power Supply Branch of State Grid Chongqing Electric Power Company alone installed 2143 10 kV ring network cabinets (nearly 37,956 cable bushing). It can be seen that 10 kV ring network cabinet plays an extremely important role in the urban power supply and distribution system. Once the ring network cabinet failure and lead to power outage, it will cause great negative social impact [8–10].

Several bushing burning accidents on site show that the cable bushing insulation layer is easy to age and damage during operation, mainly due to the internal discharge of the insulation leading to the formation of small channels by microcracks and the formation of electrical dendritic discharge traces on the bushing wall [11–13]. With the continuous improvement of the reliability requirements and the wide application of cables for distribution network, the study of the electrical branch characteristics of 10 kV cable bushing can provide relevant theoretical basis for the insulation design, detection and repair of distribution network cable bushing. In this paper, COMSOL software is used to establish a finite element simulation model to study the distribution of the surrounding electric field intensity when electrical branches appear on the surface of the cable connection bushing in the 10 kV ring main unit. In addition, the variation law of the electric field intensity when the location and shape of the electrical branches are different was carried out, and influence of the above factors on the distribution of electric field around the casing was summarized, thus providing a theoretical support for the repair technology of the 10 kV cable connection casing.

2 Finite Element Simulation Model of Cable Bushing

2.1 The Numerical Model

Electric field calculation in engineering is based on electrostatic field theory [14, 15], and the electric field strength is obtained by solving the electric potential of charge in the continuous distribution region of space. In isotropic, homogeneous and linear media, the electrostatic field is a vector field with flux source but no eddy current source. The basic equation of the electrostatic field is as follows [16–18]:

Differential form:

$$\begin{cases} \nabla \times \vec{E} = 0 \text{ or } (\vec{E} = -\nabla\Phi) \\ \nabla \cdot \vec{D} = 0 \end{cases} \quad (1)$$

Assuming that the bulk charge density is ρ , then the potential φ can be solved by Poisson's equation:

$$\nabla^2\Phi = \frac{\partial^2\Phi}{\partial x^2} + \frac{\partial^2\Phi}{\partial y^2} + \frac{\partial^2\Phi}{\partial z^2} = -\frac{\rho}{\varepsilon} \quad (2)$$

The electric field strength E is obtained:

$$E = -grad\Phi \quad (3)$$

2.2 The Numerical Model

When the finite element method is used to solve the electric field, the field in the continuous space position is transformed into the field in each discrete space, and the electric potential at each point in the field satisfies the Poisson Eq. (4), and the boundary of each field should also conform to one of the following three boundary conditions:

The first kind of boundary conditions:

$$\Phi|_s = f_1(s) \quad (4)$$

The second kind of boundary conditions:

$$\frac{\partial\Phi}{\partial n}|_s = f_2(s) \quad (5)$$

The third kind of boundary conditions:

$$\left[\frac{\partial \Phi}{\partial n} + h(\Phi - f_s) \right]_s = \text{const} \quad (6)$$

2.3 Model Building and Mesh Generation

The simulation object of this paper is 10 kV ring network cabinet and cable bushing inside the cabinet. Most of the cable bushing in the ring network cabinet adopts 630A European type bushing. According to the size standard of the bushing, the three-dimensional modeling software is used to establish the structural model of the ring network cabinet and the cable bushing in the cabinet. The length of the 3D model of the wiring sleeve is 255 mm, the maximum diameter of the flange is 125 mm, and the overall structure is axisymmetric. The inner conductor material of the sleeve is set as copper, and the outer insulating layer material is set as epoxy resin. The size of 10 kV ring network cabinet is set to $600 \times 400 \times 400$ mm, the material of ring network cabinet is set to steel, and the thickness is set to 5 mm. The wiring bushing is mainly used as the cable connection unit in the ring network cabinet. It is assembled with the ring network cabinet box body based on the established casing structure model, and the three bushing are evenly and symmetrically installed on the back wall of the box body.

Import the assembly formed by the wiring bushing and the ring network cabinet into the COMSOL software, and set the corresponding parameters of each material. The 10 kV AC voltage is applied to the port of the intermediate bushing, and the flange of the bushing and the cabinet body are set as ground, so as to establish the finite element simulation model of the cable bushing in the 10 kV ring network cabinet. The quality of grid cells is a measure of the quality of grid subdivision. The best case is 1, and when the value is less than 0.1, the results can hardly be solved. The average quality of grid cells in this model is 0.8, which meets the solving requirements. Then the finite element method is used to calculate. Firstly, the initial value and boundary conditions of the simulation model were set to obtain the initial electric potential and electric field distribution. Then Poisson equation is used to update the electric field distribution around the bushing. If the simulation results do not meet the error requirements, the updated electric field is used as the initial value for the next iteration. When the iteration results of this time step meet the requirements, it is judged whether the boundary conditions are set. If not, the initial value is reset for iterative update and solution. When the results converge and meet both the allowable error and boundary conditions, it is considered that the electric field intensity distribution around the wiring bushing is obtained.

3 Influence of Electric Branches on Electric Field Intensity Distribution Around Casing

3.1 Influence of Electric Branches at Different Locations on Electric Field Distribution

In order to study the influence of electric branches on the electric field distribution when they appear at different positions on the surface of the bushing, electric branch traces located at the flange and the port are added to the bushing surface of the simulation model. In order to control variables, the parameters and shapes of electric branches are consistent except for the location of occurrence. The electrical branch parameters were set as the length of 80 mm and the maximum ablative depth of the root of the tree was 0.8 mm. Electric branches in the simulation model gradually develop from the root of the tree and eventually form four branches to simulate the real development of electric branches, as shown in Fig. 1.

Under the premise that the shape and depth of electric branches are unchanged, the electric field distribution law under the influence of electric branches at different positions is simulated and analyzed. When the electrical branch is generated at the flange of the bushing and develops towards the port, the maximum electric field intensity generated at the flange is 4.85 kV/cm, and the minimum electric field intensity is about 3.22 kV/cm. However, when the electrical branch is generated at the terminal of the bushing and develops towards the flange direction, the maximum electric field intensity generated at the flange is 4.69 kV/cm, and the minimum electric field intensity is about 2.76 kV/cm. Compared with the well-insulated casing flange (the maximum electric field intensity is 4.54 kV/cm), the electric field strength around the casing is improved after the appearance of electric branches. In addition, it can be seen that the electric field intensity around the casing when the electric branch appears at the flange is greater than that when it appears at the port according to the

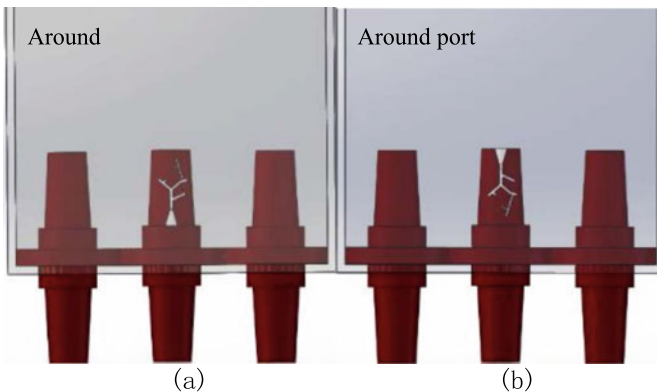


Fig. 1 Electric trees at different positions

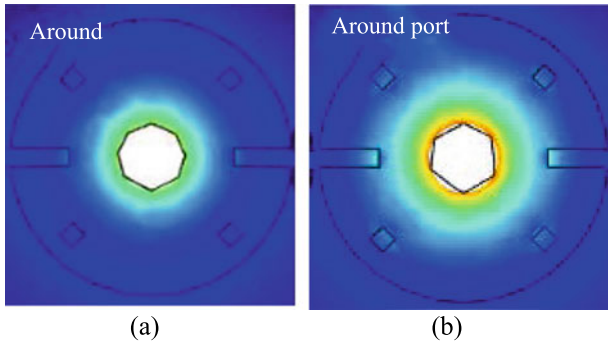


Fig. 2 Electric field intensity distribution when electrical trees is at different positions

simulation results, further indicating that the electric branch generated at the casing flange has a more obvious influence on the casing electric field than the electric branch generated at the casing port, as shown in Fig. 2.

3.2 Effects of Different Forms of Electric Branches on Electric Field Distribution

The influence of two different types of electrical branches on the electric field distribution was studied by manually setting the surface of the 10 kV cable bushing. The electrical branches are respectively set as: (1) a simple electrical branch shape with a length of 50 mm and an ablation depth of 0.8 mm located at the flange of the wiring sleeve and three branches; (2) Located at the flange of the wiring sleeve, the length is 80 mm, the ablation depth is 0.8 mm, and the four-branch complex electrical branch shape. The first simple form of electrical branch is generated at the flange position and extends outward, and stops at the middle of the casing. A second complex form of electrical branch is also generated at the flange position and extends outward, stopping near the casing port. After the electric branch is set, 10 kV voltage is applied to simulate the distribution law of electric field intensity under normal temperature and pressure environment.

Since the electric field distribution at the flange is isotropic along the radial direction, the radial direction of the flange is taken as the x direction (from the outer edge of flange to the outer edge of the conductor), and the influence law of different forms of electrical branches on the electric field intensity distribution in the x direction is compared and analyzed. As shown in Fig. 3, In the case of complex and simple electrical branches, the electric field intensity distribution in the radial direction is basically the same, showing a law of exponential increase. However, the electric field intensity under the complex electrical branch is slightly larger than that under the

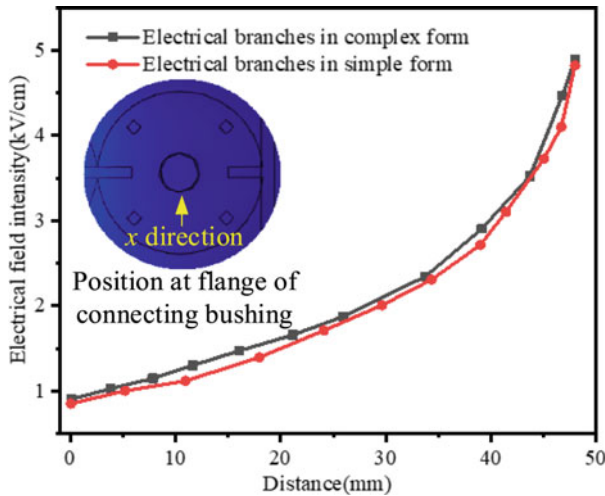
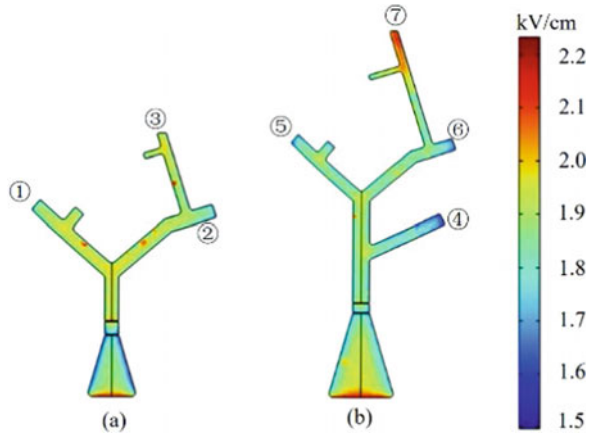


Fig. 3 The distribution of electric field intensity at flange with different shape of electric trees

simple electric branch. In addition, at the position with the largest electric field intensity, electric field intensity of complex shape electric branch is 4.85 kV/cm, and the intensity of electric fields generated by the simple form of about 4.82 kV/cm, which further shows that different in the form of electrical branches can electrically field distribution around the wire casing has more obvious effects, and the more complex shape, the more serious the casing around the electric field distortion.

Through the analysis of the electric field intensity in the regions of the two types of electrical branches, it was found that the electric field intensity at the branch ①–③ of the simple electric branch was about 1.9–2.0 kV/cm (as shown in Fig. 4(a)), while the electric field intensity at the branch ④–⑥ of the complex electric branch was close, about 1.6 kV/cm (as shown in Fig. 4(b)). It is slightly smaller than the electric field value at ①–③ of the simple electric branch. The electric field intensity at ⑦ of branch bifurcation at the most edge of the complex electric branch is the highest, which can reach 2.1 kV/cm. The main reason is that the electric branch with complex shape (④–⑥) is basically in the middle position of the wiring sleeve, which is far away from the port and flange. While the bifurcation ①–③ of the simple electric branch is far from the port, but close to the flange, which is easy to generate stronger electric field intensity. Because the distance between the fork and the bushing port is very close, the degree of unevenness increases, so the electric field intensity generated is significantly greater than that of other branches, which is also easy to cause the discharge of the bushing to the port direction, affecting the safety of the equipment.

Fig. 4 The field intensity of different electric branches



4 Conclusion

In this paper, the finite element calculation method and COMSOL software were used to quantitatively characterizing the trace of electrical branches of the cable bushing inside the 10 kV ring network cabinet. The influence of the position, shape and depth of the discharge ablation trace on the surface of the bushing on the electric field distribution of the bushing was discussed, and the following conclusions were obtained:

- (1) The simulation results of the electric field distribution around the well-insulated wiring bushing show that the electric field intensity is the largest at the metal flange of the bushing, which is the most prone to discharge breakdown of the bushing. Therefore, it is necessary to determine whether the bushing is still in the safe use range, the electric field strength variation at the casing flange should be focused on.
- (2) Changing the location and shape of the electrical tree traces will affect the distribution of the electric field intensity around the casing. The electrical tree generated at the flange has a greater impact on the electric field of the casing than the electrical tree at the port; in addition, the complex shape will lead to the increase of the electric field strength at the flange.
- (3) At the same time, it is considered that the change of the position of the electrical branch has a far greater influence on the distribution of the electric field intensity than the ablation shape.

References

1. Shao, S., Ma, X., Feng, R., et al.: Review of researches on power cables at home and abroad. *Wire Cable* **3**(3), 1–10 (2021)
2. Li, D., Wang, X., Wu, J., et al.: XLPE cable insulation aging based on feature detection life prediction method. *J. Electr. Power Sci. Technol.* **37**(1), 168–177 (2022)
3. Wang, K., Xiang, E., Cao, W., et al.: Identification of aging state of EPR cable insulation based on image feature and deep forest. *Electr. Meas. Instrum.* **59**(6), 32–36 (2022)
4. Yuan, Y., Li, S., Dong, J., et al.: A review on diagnostic testing technique of electrical power cables. *Electr. Mea. Instrum.* **53**(11), 1–7 (2016)
5. Wang, Y., Yao, Z., Xie, W., et al.: Research on fault location of high temperature superconducting cable based on time-frequency domain reflectometry. *Proc. CSEE* **41**(5), 1540–1547 (2021)
6. Wang, C., Li, Y., Shi, J., et al.: Failure analysis of 10 kV annular cabinet penetration casing pipe. *Electr. Saf. Technol.* **21**(8), 29–32 (2019)
7. Wang, Q., Zhu, Z., Jia, Z., et al.: Simulation and optimization of outdoor RMU ventilation effect. *High Volt. Appar.* **55**(3), 59–64 (2019)
8. Hou, C., Li, Q., Gao, Y.: Partial discharge analysis and structure design of solid insulated ring main units with 12 kV coated shield. *High Volt. Appar.* **54**(6), 241–247 (2018)
9. Li, T., Li, S.: Analysis of common faults and improvement measures of 10kV ring main units. *South Agric. Mach.* **50**(22), 179–180 (2019)
10. Tao, Y., Chen, H., Zhao, G., et al.: Electric field and local discharge characteristics of typical construction defects of 10 kV cable intermediate joint. *Electr. Power Eng. Technol.* **40**(5), 114–120 (2021)
11. Jia, M.: Research on Online Monitoring of Mechanical Characteristics and Insulation State Diagnosis of 10kV Ring Network Cabinet. Shenyang University of Technology, Shenyang (2019)
12. Han, X., Liu, B., Li, Y., et al.: A fault method for distribution automation switch cabinet based on fuzzy and gray correlation. *J. Electr. Power Sci. Technol.* **36**(2), 107–115 (2021)
13. Xiao, Y., Liu, X., Huang, Y., et al.: Analysis and exploration of 10kV switchgear maintenance and technical transformation strategy. *Power Saf. Technol.* **18**(6), 6–10 (2016)
14. Wen, T., Cui, X., Li, X., et al.: Finite element method in complex frequency domain for transient electric field intensity under electro-quasistatic field. *Proc. CSEE* **42**(7), 2776–2788 (2022)
15. Wang, Q., Wang, G., Wang, F., et al.: DC electric field simulation analysis for 10 kV AC XLPE cable melting joint. *Adv. Technol. Electr. Eng. Energy* **40**(10), 37–43 (2021)
16. Jin, Y.: Numerical Calculation Method of Solid Insulation External Synthetic Electric Field for DC Equipment. Wuhan University, Wuhan (2019)
17. Zhen, Y.Z., Cui, X., Lu, T.B., et al.: High efficiency FEM calculation of the ionized field under HVDC transmission lines. *IEEE Trans. Magn.* **48**(2), 743–746 (2012)
18. Liu, H.B., Liao, R.J., Liu, K.L., et al.: Research on corona discharge characteristics based on hybrid numerical algorithm. *IEEE Trans. Plasma Sci.* **46**(1), 4037–4043 (2018)

Novel Controllable Commutated Converter (CLCC) and Rapid Defense Method for Commutation Failure



Jun Yang, Caiwang Sheng, Chong Gao, Xiao Ding, Tingting Li, and Dongshan He

Abstract Commutation failure (CF) is an unique fault of traditional line commutated converter based high voltage direct current transmission system (LCC-HVDC). It is usually induced by AC system turbulence or fault, resulting in converter malfunction and swinging of power. For multi-infeed DC systems, CF may occur among several DC terminals, imposing significant safety threat on power grid. In order to solve CF completely, this paper proposed a novel converter topology, based on a combination of semi-controlled thyristors and fully-controlled IGBTs to aid the turning-off process of thyristors and realize forced commutation between bridge arms. Two operation modes were also designed and compared for the new converter. And a rapid detection strategy using the difference between arm current and its delay value is presented, which can identify the specific CF arm as fast as its commence, and triggering the mode switch, hence avoid CF at the early stage. Finally, a testing HVDC system model is developed from Cigre Benchmark model, adopting new CLCC converter at the inverter side. Using this model, AC grounding fault is simulated and the results shows that the proposed converter and its rapid defense strategy is efficient, and controllable commutation and relatively high power transmission is attained during fault, showing excellent fault ride-through and system support capacity.

Keywords Commutation failure · Converter topology · Thyristor · IGBT · Rapid detection

J. Yang · C. Sheng · C. Gao · X. Ding · T. Li (✉) · D. He
State Key Laboratory of Advanced Power Transmission Technology, (State Grid Smart Grid Research Institute Co., Ltd.), 102209 Beijing, China
e-mail: lmzzy@126.com

© Beijing Paiké Culture Commu. Co., Ltd. 2023
X. Dong et al. (eds.), *The proceedings of the 10th Frontier Academic Forum of Electrical Engineering (FAFEE2022)*, Lecture Notes in Electrical Engineering 1054, https://doi.org/10.1007/978-981-99-3408-9_5

1 Introduction

Line-commutated Converter based High-voltage direct current transmission technology (LCC-HVDC) has the advantages of large capacity, long transmission distance, high efficiency, low loss etc., and is widely used worldwide. In China, HVDC transmission is a key technology for bulk power transmission, accounting for more than 50% of the total capacity, from west to east. Among the more than 30 HVDC projects in operation nationwide, there are up to 11 in the east and 9 in the south, respectively, forming the densest multi-infeed HVDC systems in the world.

For the semi-controlled feature of the thyristor, LCC converter may fail to commute easily due to AC voltage disturbance, resulting in large fluctuations of active and reactive power in multi-infeed DC systems, threatening system stability.

In order to solve CF problem, some prevention methods have been proposed, which can be divided into two categories. One is to enhance the strength of the AC system with condenser, STATCOM or other reactive power compensation devices, reducing CF probability [1, 2]. The second is to optimize the DC system dynamics, including converter topology and control strategy improvement [3, 4].

Converter topology improvement is a promising solution for eliminating CF completely. In reference [5] and [6], Capacitor Commutation Converter (CCC) is put forward, which can decrease CF probability through increasing the extinction angle of the converter. However, in case of serious AC fault, the uneven charging of the capacitor will inevitably lead to CF. To make the capacitor voltage controllable, full-bridge sub-modules are adopted to enhance the commutation process in [7] and [8]. Due to the ratings limit of the fully-controlled devices such as IGBT, the full bridge module needs to be connected in series and parallel for 3000A application and above. So the total loss and cost of the converter will be high. Besides, the new converter need fast prediction of CF, in order to trigger the output of the full-bridge modules. In [9], a fast prediction and detection method of commutation failure is presented, but it can still not locate the bridge arm with commutation failure exactly.

This paper proposes a new type of controllable line-commutated converter (CLCC) topology with controllable turn-off capability, through mixing use of fully controlled device IGBT and semi-controlled device thyristor, realizing reliable recovery process and controllable commutation. A rapid detection method of commutation failure based on the current delay difference of the bridge arm is also proposed to make the new converter function properly. Finally, a remedied system model based on Cigre Benchmark HVDC system model is developed to showcase the transient characteristics of the new converter, verifying its powerful CF prevention capability.

2 Controllable Commutation Converter Topology

On the basis of conventional converter, the controllable commutation converter valve transformed each bridge arm into a parallel structure with a main and an auxiliary branches. The main branch is composed of thyristor valve V11 and IGBT valve V12, and the auxiliary branch is composed of IGBT valve V13 and diode valve V14. V11 is almost the same with conventional LCC valve. V12 is composed of a few IGBTs in series, and its main function is to turn off the main branch current and transfer it to the auxiliary branch. V13 is high voltage IGBT valve, it transfer the current to other bridge arms through active switching when the current of the bridge arm cannot extinguish naturally due to the AC fault. For suppressing voltage overshoot, V11 and V14 are paralleled with RC damping components, V12 and V13 are paralleled with RCD damping circuits and metal oxide varistors (MOV).

CLCC may work under two different control sequence, one is natural commutation control sequence, the other is forced commutation sequence, as shown in Fig. 2. For natural commutation sequence, V12 will turn on with V11, and turn off after arm current decay to zero. V13 keeps in block state. For forced commutation control sequence, V12 still turns on with V11, but turns off after 120 electrical degree of conduction when commutation starts. V13 will turn on at the turn-off instant of V12, and turn off after a short delay, as long as which is sufficient for V11 to regain block capability, i.e., several hundred microseconds.

In order to resist CF, CLCC must adopt forced commutation control sequence during AC fault, while both control sequences can be adopted during normal steady state. Therefore, there are two optional operation modes:

- (1) Temporary alternating operation mode: when the system is stable, the converter valve operates according to the natural commutation control sequence; when the AC system fails, the converter valve operates according to the forced commutation control sequence.
- (2) Continuous alternating operation mode: whether AC fault occurs or not, the converter valve operates in forced commutation control sequence.

Both operation modes can achieve the purpose of CF prevention, but which one is preferred will be analyzed in the next part (Fig. 2).

Fig. 2 Control sequence of CLCC

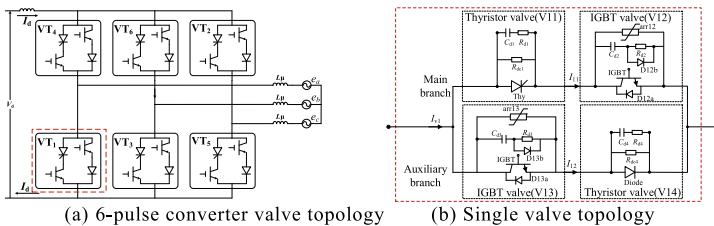


Fig. 1 Controllable commutation valve topology

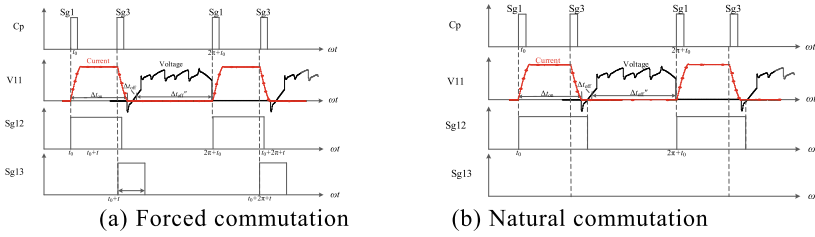


Fig. 2 Control sequence of CLCC

3 Parameter Design and Stress Analysis

3.1 Parameter Design of Converter Valve

A 6 pulse converter simulation model of CLCC is built for analysis, and the main system parameters are shown in Table 1.

The design idea of the main branch thyristor valve of the bridge arm is the same as that of the conventional LCC converter valve. Considering the high operational voltage stress, 60 series connected diodes are selected for V14. In order to suppress the reverse overshoot voltage, damping circuit is necessary. Since V11 and V14 are connected in parallel, the resistance and capacity after parallel connection is equivalent to that of conventional LCC thyristor valve, and the resistance and capacity are selected as 1.6 μ F and 32 Ω .

V12 plays the role of transferring current to the auxilliary branch. A few IGBTs in series can meet the requirements. In practical application, a certain amount of redundancy is taken into account. In this paper, the series number is selected as 8 levels. The series number of V13 is determined by the protection level of its parallel MOV. In order to ensure successful commutation under severe AC fault, the protection level should not be lower than the peak AC voltage. So, 1.2 p.u. of the peak AC system voltage is selected, and the series number is determined as 104.

Due to the existence of stray inductance in the circuit, the shutoff voltage overshoot will occur when V12 and V13 interrupt the current, as shown in Fig. 3. So, it is necessary to provide RCD damping circuit for the IGBT. The turn-off voltage overshoot increases with the stray inductance and the interrupted current, the average single-stage stray inductance is about 0.5 μ H according to the press-pack structure. Considering the turn-off delay between IGBT modules, the damping capacitor C_{ds} also needs to satisfy the following formula 1:

Table 1. System simulation parameters

DC Voltage	DC Current	AC Voltage	Leakage reactance	Extinction angle
500 kV	3kA	238 kV	0.171	19.5°

Fig. 3 Turn-off overshoot of IGBT

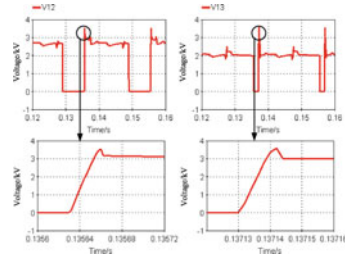
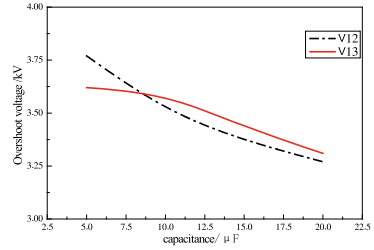


Fig. 4 Overshoot voltage variation with C_{ds}



$$C_{ds} \geq \frac{I_d \cdot \Delta t}{\Delta U} = \frac{3000 \times 1}{360} = 8.33 \mu F \tag{1}$$

where I_d is the maximum breaking current 3000A; ΔT is the maximum turn-off delay time among IGBTs, around 1 μs ; ΔU is the maximum voltage deviation of IGBTs (10% of the long-term service voltage 3.6 kV). So C_{ds} is determined to be 10 μF . The R_{ds} value is set as 4 Ω to ensure that damping capacitor can be discharged in tens of microseconds. The final parameters of each sub-valve are shown in Table 2.

Table 2 Main electrical parameters of CLCC Valve

Subvalve	Series number	$C_{ds}/\mu F$	R_{ds}/Ω
V11	60	1.6	32
V12	8	10	4
V13	104	10	4
V14	60	1.6	32

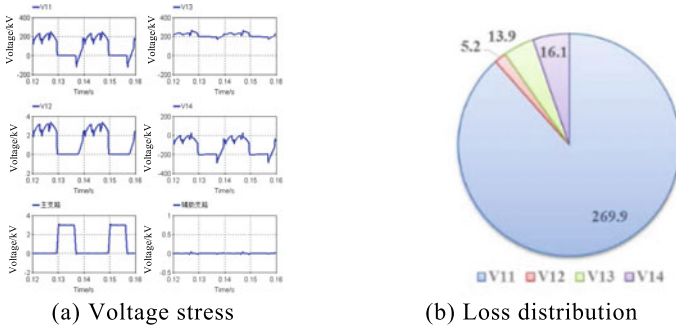


Fig. 5 Voltage and loss stress under temporary alternate operation mode

3.2 Stress Analysis

Because the switching control logic of each sub-valve of the bridge arm has obvious differences under two operation modes, its electrical stress may be quite different. So which is more appropriate needs to be determined through specific stress analysis.

(1) Temporary alternating operation mode

Under normal conditions, the valve voltage and loss distribution is shown in Fig. 5. Voltage across V11 is almost the same with the bridge arm voltage. V13 is in shut-off state constantly, so the voltage is almost flat with little ripples, and it will provide DC offset voltage for V14. The total loss of the valve is 305.1 kW, of which V11 accounts for 88.5%. Due to low working voltage, loss of V12 mainly comes from conduction loss. For different voltage variations, V13 has only a small amount of damping loss, which is much less than V14.

(2) Continuous alternating operation mode.

The voltage stress and loss distribution of CLCC are shown in Fig. 6(a). V12 turns off large current periodically, so it establishes turn-off voltage each cycle. Voltage of V13 rises with the total voltage of the bridge arm after it turns off, and its damping capacitance is much greater than V14, When the voltage rises to the peak, it basically remains stable. The total loss is 490.2 kW, 1.6 times that of the temporary alternating operation mode, the loss of the three sub-valves V12–V14 is significantly increased, as shown in Fig. 6(b).

(3) Stress comparison.

Table 3 lists the electrical stress and loss of each sub-valve under the two different modes. In terms sub-valve voltage peaks and total operation loss, CLCC should adopt temporary alternating operation mode during normal operation. When CF is about to occur, it should switch to continuous alternating operation mode quickly to fulfill forced commutation, and a special quick detection logic is needed as in Sect. 4.

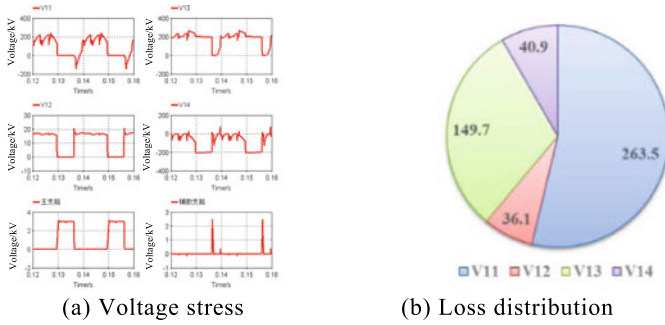


Fig. 6 Voltage and loss under continuous alternating operation mode

Table 3 Stress comparison of two modes

	Voltage/kV		Current/kA		Loss /kW	
	Temporary	Continuous	Temporary	Continuous	Temporary	Continuous
V11	267.9	274.8	3	3	269.9	263.5
V12	3.2	21.1	3	3	5.2	36.1
V13	264.8	274.5	0	2.3	13.9	149.7
V14	-296.1	-235.6	0	2.3	16.1	40.9

4 Rapid Detection Method of Commutation Failure

During normal operation, decline rate of arm current is determined by the instantaneous value of commutation voltage and the leakage reactance of the converter transformer [10]. After commutation, there is no conduction current in the bridge arm until the next cycle.

When AC fault occurs, the current drop rate will become lower due to the commutation voltage dip, or it will rise up again before the next triggering. Based on the this features, a CF observation window can be defined for each arm. Take bridge arm 1 as an example, the observation window can be set as shown in Fig. 7. It is a 90° interval since triggering of bridge arm 3. In order to avoid misjudgment due to the high sensitivity of the differential method, the strategy uses the delay differential method as shown in Fig. 8 to monitor the arm current i_v within the observation window. It contains two parts, in the first part the delay differential is used to obtain the current drop rate a certain delay time T, witch is reasonably selected between 200–300 μs. The second part is mainly set to eliminate the influence of the bridge arm damping circuit current, and the reference value I_{ref} is set as $0.2I_d$. Through the above two parts of judgment logic, the occurrence of CF can be accurately and quickly detected within the observation window time.

Fig. 7 Observation window of bridge arm commutation failure

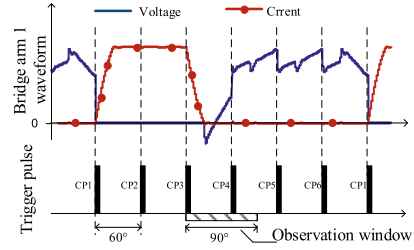
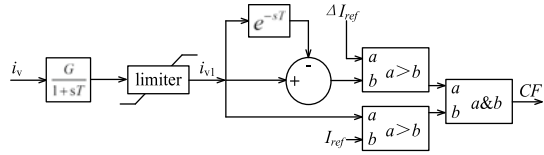


Fig. 8 Bridge arm current delay differential logic for commutation failure detection



5 Simulation Verification

In order to verify the effectiveness of CLCC converter valve and CF fast detection and defense startup method, a ± 500 kV/3000 MW DC system is built based on the CIGRE Benchmark DC system simulation model. The rectifier side, DC line and control strategy of the original model remain unchanged. CLCC converter is used to replace the inverter, and the CF detection module is added. The transient process of DC system under single-phase grounding fault and three-phase short circuit fault at the inverter side.

Simulation results is shown as in Fig. 9 and Fig. 10. It is shown that commutation between the bridge arms of CLCC is completed every cycle during AC fault. And maintains the DC voltage and the DC power basically maintains above 0.6p.u. level. The absorbed reactive power will decrease during the fault, and the system recovery time will be about 70 ms faster than LCC.

The above simulation results show that CLCC system can commute reliably in case of serious AC fault in AC power grid, providing strong active and reactive support for AC power grid.

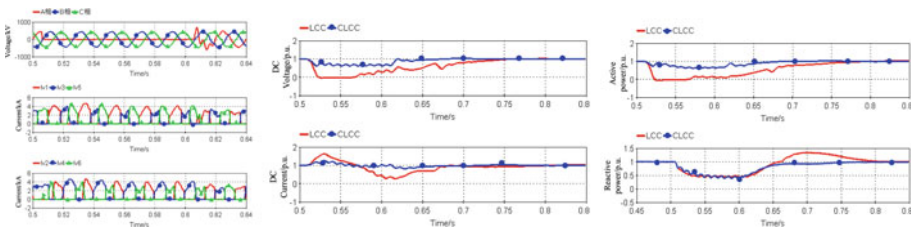


Fig. 9. CLCC Waveform & comparison with LCC during Single phase to ground fault

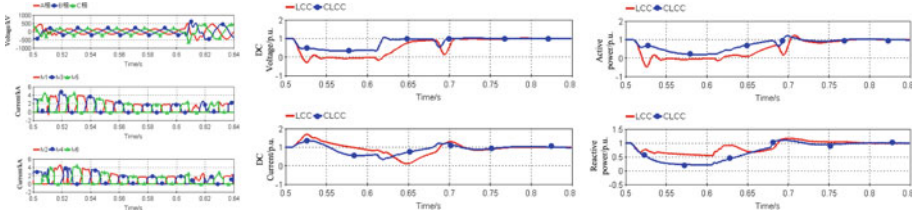


Fig. 10. CLCC Waveform & comparison with LCC during Three phase to ground fault

6 Conclusion

This paper proposes a new type of controllable grid commutation converter topology. In order to reduce the long-term operation loss, temporary alternate operation is selected as its operation mode through comparative analysis. In order to realize this mode, a fast detection method of CF based on leg current delay difference is proposed, and the topology and the fast start method of CF prevention are verified by simulation analysis, and the following conclusions are drawn:

- (1) A new type of controllable commutation converter topology is proposed, which can realize controllable commutation between bridge arms by mixing IGBT and thyristor;
- (2) Under long-term normal operation conditions, the temporary alternate operation mode can effectively reduce the overall operation loss of the converter. Compared with the conventional LCC converter, the total loss increases by only 13%.
- (3) The commutation failure detection method based on the difference analysis method of bridge arm current delay can quickly complete the determination and precise positioning of bridge arm at the early stage of commutation failure, and quickly start the resistance action;
- (4) The system has serious single-phase AC ground fault and three-phase short circuit fault. The new controllable commutation converter can provide strong active and reactive power support for the AC system, which is conducive to system stability.

Acknowledgements This work is supported by National Key Research and Development Program of China under Grant 2021YFB2400900.

References

1. Siye, R.U.A.N., Kai, X.U., Dan, L.I.U., et al.: Statistical analysis and suggestions on resistance measures for commutation failures of HVDC transmission system. *Autom. Electr. Power Syst.* **43**(18), 13–17 (2019). (in Chinese)

2. Xiaoxin, Z., et al.: Technology features of the new generation power system in China. *Proc. CSEE* **38**(7), 1893–1904 (2018). (in Chinese)
3. Wei, Z., Yuan, Y., Lei, X., et al.: Direct-current predictive control strategy for inhibiting commutation failure in HVDC converter. *IEEE Trans. Power Syst.* **29**(5), 2409–2417 (2014)
4. Chokhawala, R.S., Eric, I.C.: A snubber design tool for P-N junction reverse recovery using a more accurate simulation of the reverse recovery waveform. *IEEE Trans. Ind. Appl.* **27**(1), 74–84 (1991)
5. Yuan, Y., Li, X., Chen, Z., et al.: Parameter optimization strategy of commutation failure prevention control considering the influence of double bridge simultaneous commutation. *Electr. Autom.* **43**(4) (2021). (in Chinese)
6. Zhou, H., Yao, W., Li, C., Wen, J.: A predictive voltage dependent current order limiter with the ability to reduce the risk of first commutation failure of HVDC. *High Volt. Eng.* 1–9 (2021). (in Chinese)
7. Yang, Conghuan, Xue, et al.: Elimination of commutation failures of LCC HVDC system with controllable capacitors. *IEEE Trans. Power Syst. Publ. Power Eng. Soc.* **31**(4), 3289–3299 (2016)
8. Chunyi, G., Zhenggang, H., Bo, L., et al.: LCC converter adopting thyristor based energy dissipation full-bridge sub-module and its coordination control. *Proc. CSEE* **41**(4), 1398–1409 (2021). (in Chinese)
9. Minquan, C., et al.: Parameter optimization of commutation failure preventions between multiple DC links based on numerical approximation and value set. *Power Syst. Technol.* **45**(02), 776–784 (2021). (in Chinese)
10. Zhang, F., Xin, H., Wu, D., et al.: Assessing strength of multi-infeed LCC-HVDC systems using generalized short-circuit radiation. *IEEE Trans. Power Syst.* **34**(1), 467–480 (2019)

An Uncertainty Analysis Method of Dimension Reduction for Multiconductor Transmission Line



Xutong Wang , Wenbing Wang, Feng Qin, and Yifu Zhou

Abstract The position of wire bundle in electronic equipment is uncertain. Furthermore, the cables are numerous and the parameters of the cables are difficult to determine. Therefore, this paper presents a reduced-dimension interval analysis method with equivalent model. This method considers the uncertainties of the structure parameters and the load parameters of the wire bundle. In this paper, we deduce the structure parameters of equivalent model, which are independent of each other, and the equivalent parameters are used as input of interval analysis. The interval value of terminal coupling of transmission line can be obtained without the distribution of parameters. The validity of the proposed method is verified by a simulation case of random bundled wire bundle model. Simulation results show that the extended effect of this method is small, and the time-consuming of this method is much smaller than that of Monte Carlo method. The research provides a new way for the analysis of electromagnetic compatibility of random bundled wire harness.

Keywords Multiconductor transmission line · Uncertainty · Monte Carlo · Interval analysis

1 Introduction

With the development of information technology, more and more cables are used to transmit signal and power in electronic equipment. [1, 2] Cable is the main way of coupling electromagnetic energy. [3, 4] The problem of electromagnetic coupling of cable is the focus of the research of electromagnetic compatibility in electronic system. It plays an important role in the analysis of electromagnetic compatibility. This paper presents a new method of uncertainty analysis which can be applied to multi-dimensional variables.

X. Wang (✉) · W. Wang · F. Qin · Y. Zhou
State Key Laboratory of Intense Pulsed Radiation Simulation and Effect (Northwest Institute of Nuclear Technology), Xi'an 710024, China
e-mail: wangxutong@nint.ac.cn

© Beijing Paiké Culture Commu. Co., Ltd. 2023
X. Dong et al. (eds.), *The proceedings of the 10th Frontier Academic Forum of Electrical Engineering (FAFEE2022)*, Lecture Notes in Electrical Engineering 1054, https://doi.org/10.1007/978-981-99-3408-9_6

The spatial position of cable, the machining error of terminal impedance and the direction of incoming wave are uncertain. [5, 6] The existing uncertainty analysis methods mainly include the polynomial chaos method, the Monte Carlo method. The above methods need the probability distribution of the parameters. [7] In case the parameter distribution is difficult to obtain, the interval value of the coupled voltage can be obtained by applying the interval analysis method to the coupling analysis of the most conductor transmission lines.

In addition to the Monte Carlo method, all the above uncertainty analysis methods have the problem of calculating time index growth when dealing with multidimensional variables. [8] The method of line beam equivalent modeling (ECBM) is designed to equate a multi-conductor transmission line to a simplified model with no more than 4 wires. The main ideas are as follows: according to the comparison between the terminal impedance value of the wire bundle and its characteristic impedance value, the wire bundle can be divided into 4 groups; using the theory of multi-conductor transmission line, the composite section structure parameters of the wire bundle can be obtained; and the equivalent load of the terminal of the wire bundle can be established. [9, 10] Some researchers proposed a finite difference time domain method, and expanded the ECBM method to predict the crosstalk and radiation sensitivity of automobile lines. The method of wire bundle equivalent modeling solves the problem of the deterministic solution of multi-conductor wire bundle.

Based on interval analysis method and wire bundle equivalent modeling method, an interval analysis method based on wire bundle equivalent modeling is proposed in this paper. The correlations of equivalent unit length parameters obtained by wire-bundle equivalent modeling are considered. Based on the theory of multi-conductor transmission line, the number of variables is greatly reduced, and the interval values of the equivalent height and the equivalent line spacing and the equivalent line diameter are obtained. Finally, an example is given to verify the correctness and efficiency of the proposed method.

2 Interval Analysis Method

According to Weierstrass theorem, for any given $\varepsilon < 0$, there is a polynomial p makes $\|p - f\|_\infty < \varepsilon$, in which f is a real function defined above $[a, b]$. Therefore, the output of a complex system can be obtained by polynomial function approximation. Chebyshev polynomial has the property of optimal square approximation in interval range. When the uncertainty parameter is one-dimensional, $f(a)$ can be written as:

$$f(a) \approx p_k(a) = \sum_{j=0}^k f(a_j) C_j(a) \quad (1)$$

Here, $f(a_j)$ is polynomial coefficient, and $C_j(a)$ is Chebyshev polynomial basis function:

$$C_j(a) = \cos(j\theta) \quad (2)$$

$$\theta = \arccos\left(\frac{2a - (\underline{a} + \bar{a})}{\bar{a} - \underline{a}}\right) \quad (3)$$

\underline{a} , \bar{a} are Lower bound and upper bound of interval quantity, respectively. a_j is Chebyshev polynomial interpolation point:

$$a_j = \cos\theta_j, \theta_j = \frac{(2j-1)\pi}{2(k+1)}, j = 1, 2, \dots, k+1 \quad (4)$$

For the problem of multi-dimensional uncertainty parameters in the system, the tensor product of r-dimension k-order Chebyshev polynomial can be constructed directly, and the interpolation formula of r-dimension Chebyshev polynomial can be obtained.

$$f(a) \approx \sum_{i_1=0}^k \cdots \sum_{i_r=0}^k \left(\frac{1}{2}\right)^P f_{i_1, \dots, i_r} C_{i_1, \dots, i_r}(a) \quad (5)$$

Here, P is the number of 0 in subscripts of $C_{i_1, \dots, i_r}(a)$. f_{i_1, \dots, i_r} is Chebyshev polynomial coefficient:

$$f_{i_1, \dots, i_r} \approx \left(\frac{2}{k+1}\right)^r \sum_{j_1=1}^{k+1} \cdots \sum_{j_r=1}^{k+1} f(\cos\theta_{j_1}, \dots, \cos\theta_{j_r}) \cos i_1\theta_{j_1} \cdots \cos i_r\theta_{j_r} \quad (6)$$

The basic process of interval analysis is as follows:

- (1) The interpolation point is generated by formula (4)
- (2) Solve the induced voltage at each interpolating point.
- (3) The coefficients of Chebyshev polynomial are calculated by formula (6)
- (4) The interval function is constructed according to formula (5), and the upper and lower boundary of induction voltage is given.

3 Simplified Modeling Method for Stochastic Wire Bundle

3.1 Wire Bundle Grouping

The cable that needs to be pay attention to its terminal voltage is divided into the first group, and the other wire harness is divided into 4 groups according to Table 1, among which Z_{1i} and Z_{2i} are source impedance and load impedance respectively, and Z_{cm} are common mode impedance.

Table 1 Cable grouping rule

Group	Port 1	Port 2
2	$ Z_{1i} < Z_{cm}$	$ Z_{2i} < Z_{cm}$
3	$ Z_{1i} < Z_{cm}$	$ Z_{2i} > Z_{cm}$
4	$ Z_{1i} > Z_{cm}$	$ Z_{2i} < Z_{cm}$
5	$ Z_{1i} > Z_{cm}$	$ Z_{2i} > Z_{cm}$

Assuming that the wire bundle numbered 1 is the wire bundle of concern, then the first group contains N_1 conductors, and is numbered 1; The second group contains N_2 conductors, and are numbered as $2 \sim \alpha$; The third group contains N_3 conductors, and are numbered as $(\alpha + 1) \sim \beta$, The fourth group contains N_4 conductors, and are numbered as $(\beta + 1) \sim \gamma$; Group 5 contains N_5 conductors, and are numbered as $(\gamma + 1) \sim n$.

3.2 Simplified Wire Bundle Geometry Parameters

3.2.1 Height to the Ground

The height of each equivalent wire bundle is equal to the average height of all conductors in the wire bundle.

$$h_{eq} = \left[h_1 \frac{\sum_{p=2}^{\alpha} h_p}{N_2} \frac{\sum_{p=\alpha+1}^{\beta} h_p}{N_3} \frac{\sum_{p=\beta+1}^{\gamma} h_p}{N_4} \frac{\sum_{p=\gamma}^n h_p}{N_5} \right] \quad (7)$$

3.2.2 Horizontal Spacing of Cable

For a wire bundle model containing n ideal lossless conductors, the transmission line equation is as follows:

$$\begin{aligned} -\frac{\partial V}{\partial z} &= R_0 I(z, t) + L_0 \frac{\partial I}{\partial t} \\ -\frac{\partial I}{\partial z} &= G_0 I(z, t) + C_0 \frac{\partial V}{\partial t} \end{aligned} \quad (8)$$

The inductance matrix and horizontal spacing of the simplified wire bundle are as follows:

$$L_{eq} = \begin{bmatrix} L_{11} & \frac{\sum_{q=2}^{\alpha} L_{1q}}{N_2} & \frac{\sum_{q=\alpha+1}^{\beta} L_{1q}}{N_3} & \frac{\sum_{q=\beta+1}^{\gamma} L_{1q}}{N_4} & \frac{\sum_{q=\gamma+1}^n L_{1q}}{N_5} \\ \frac{\sum_{p=2}^{\alpha} L_{p1}}{N_2} & \frac{\sum_{p=2}^{\alpha} \sum_{q=2}^{\alpha} L_{pq}}{N_2^2} & \frac{\sum_{p=2}^{\alpha} \sum_{q=\alpha+1}^{\beta} L_{pq}}{N_2 N_3} & \frac{\sum_{p=2}^{\alpha} \sum_{q=\beta+1}^{\gamma} L_{pq}}{N_2 N_4} & \frac{\sum_{p=2}^{\alpha} \sum_{q=\gamma+1}^n L_{pq}}{N_2 N_5} \\ \frac{\sum_{p=\alpha+1}^{\beta} L_{p1}}{N_3} & \frac{\sum_{p=\alpha+1}^{\beta} \sum_{q=2}^{\alpha} L_{pq}}{N_3 N_2} & \frac{\sum_{p=\alpha+1}^{\beta} \sum_{q=\alpha+1}^{\beta} L_{pq}}{N_3^2} & \frac{\sum_{p=\alpha+1}^{\beta} \sum_{q=\beta+1}^{\gamma} L_{pq}}{N_3 N_4} & \frac{\sum_{p=\alpha+1}^{\beta} \sum_{q=\gamma+1}^n L_{pq}}{N_3 N_5} \\ \frac{\sum_{p=\beta+1}^{\gamma} L_{p1}}{N_4} & \frac{\sum_{p=\beta+1}^{\gamma} \sum_{q=2}^{\alpha} L_{pq}}{N_4 N_2} & \frac{\sum_{p=\beta+1}^{\gamma} \sum_{q=\alpha+1}^{\beta} L_{pq}}{N_4 N_3} & \frac{\sum_{p=\beta+1}^{\gamma} \sum_{q=\beta+1}^{\gamma} L_{pq}}{N_4^2} & \frac{\sum_{p=\beta+1}^{\gamma} \sum_{q=\gamma+1}^n L_{pq}}{N_4 N_5} \\ \frac{\sum_{p=\gamma+1}^n L_{p1}}{N_5} & \frac{\sum_{p=\gamma+1}^n \sum_{q=2}^{\alpha} L_{pq}}{N_5 N_2} & \frac{\sum_{p=\gamma+1}^n \sum_{q=\alpha+1}^{\beta} L_{pq}}{N_5 N_3} & \frac{\sum_{p=\gamma+1}^n \sum_{q=\beta+1}^{\gamma} L_{pq}}{N_5 N_4} & \frac{\sum_{p=\gamma+1}^n \sum_{q=\gamma+1}^n L_{pq}}{N_5^2} \end{bmatrix} \quad (9)$$

$$d_{eq(p,q)} = \sqrt{\frac{4h_{eq(p)}h_{eq(q)}}{\exp(\frac{4\pi L_{eq(p,q)}}{\mu_0}) - 1}} \quad (10)$$

Because of the correlation between L_{eq} and C_{eq} , L_{eq} and C_{eq} cannot be analyzed as interval numbers. Similarly, the formula (10) cannot be used for interval analysis because it contains L_{eq} , and the formula for horizontal spacing without L_{eq} is derived from formula (9) as follows:

$$d_{eq(p,q)} = \sqrt{\frac{K(h_{eq(p)} - h_{eq(q)})^2 - (h_{eq(q)} + h_{eq(q)})^2}{1 - K}} \quad (11)$$

When p is not equal to 1

$$K = \left[\prod_{i=1+\sum_{m=1}^{p-1} N_m}^{\sum_{n=1}^p N_n} \prod_{j=1+\sum_{y=1}^{q-1} N_y}^{\sum_{x=1}^q N_x} \frac{(h_i + h_j)^2 + d_{ij}^2}{(h_i - h_j)^2 + d_{ij}^2} \right]^{2/(N_p N_q)} \quad (12)$$

When p equals 1

$$K = \left[\prod_{j=1+\sum_{y=1}^{q-1} N_y}^{\sum_{x=1}^q N_x} \frac{(h_1 + h_j)^2 + d_{1j}^2}{(h_1 - h_j)^2 + d_{1j}^2} \right]^{2/N_q} \quad (13)$$

3.2.3 Cable Radius in Simplified Model

The radius of the equivalent wire bundle is given in the literature

$$r_{eq(p)} = \frac{h_{eq(p)}}{\exp\left(\frac{2\pi L_{eq(p,p)}}{\mu_0}\right)} \quad (14)$$

Similarly, the formula (14) cannot be used for interval analysis, and the formula for line diameter without L_{eq} is derived from formula (10) as follows:

$$r_{eq(p)} = \frac{2h_{eq(p)}}{K_1} \quad (15)$$

$$K_1 = \left[\prod_{\substack{i=1 \\ i=1+\sum_{m=1}^{p-1} N_m}}^{\sum_{n=1}^p N_n} \frac{2h_i}{r_i} * \prod_{\substack{i=1 \\ i=1+\sum_{m=1}^{p-1} N_m}}^{\sum_{n=1}^p N_n} \prod_{\substack{j=1 \\ j=1+\sum_{m=1}^{p-1} N_m}}^n \frac{\left((h_i + h_j)^2 + d_{ij}^2\right)}{\left((h_i - h_j)^2 + d_{ij}^2\right)} \right]^{1/(n-1)^2} \quad (16)$$

3.3 Terminal Load in Simplified Model

$$Z_{eq} = \left[Z_1 \frac{\sum_{p=2}^{\alpha} Z_p}{N_2} \frac{\sum_{p=\alpha+1}^{\beta} Z_p}{N_3} \frac{\sum_{p=\beta+1}^{\gamma} Z_p}{N_4} \frac{\sum_{p=\gamma}^n Z_p}{N_5} \right] \quad (17)$$

4 Stochastic Wire Bundle Simulation and Verification

In this paper, the improved interval analysis method is compared with the MC method and the traditional interval analysis method. The deterministic solution is obtained by using a finite-difference time domain method. Figure 1 gives a schematic diagram of 8 conductor bundled wire harness models. Table 2 gives the structural and load parameters of all conductors in a wire bundle. The incident direction of plane wave is perpendicular to the ground. The electric field direction is parallel to the wire bundle, and the plane wave source is the HEMP waveform recommended by IEC.

The simplified model with 2-order interval analysis method, 10,000 runs Monte Carlo method are used respectively. The terminal coupling voltage of cable 1 is given respectively.

Fig. 1 Model of 8-conductor transmission line bound under plane wave irradiation

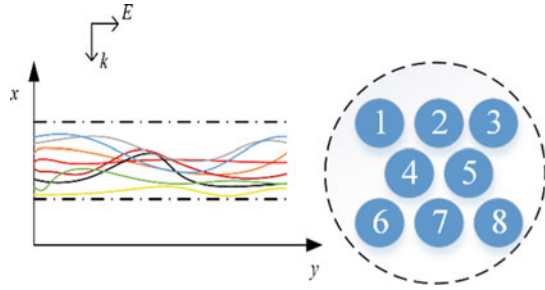


Table 2 Parameters of Transmission Line

number	h (m)	d (m)	L (m)	R (mm)	Z ₁ (Ω)	Z ₂ (Ω)
1	0.1 ~ 0.2	0.05 ~ 0.1	2	2	50	50
2	0.1 ~ 0.2		2	2	50	50
3	0.1 ~ 0.2		2	2	50	50
4	0.1 ~ 0.2		2	2	50	0
5	0.1 ~ 0.15		2	2	800	1000
6	0.1 ~ 0.15		2	2	600	1000
7	0.1 ~ 0.15		2	2	600	1500
8	0.1 ~ 0.2		2	2	1000	1000

From Figs. 2, 3, it can be seen that the terminal voltage is calculated by the wire bundle with different parameters respectively. In the whole time period, the interval analysis method is in good agreement with Monte Carlo method. In the acceptable range, the interval analysis method of dimension reduction has some extension effect.

Fig. 2 Left End Voltage of Cable 1

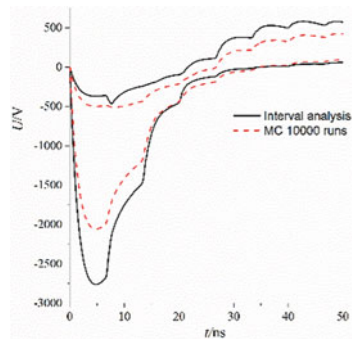


Fig. 3 Right End Voltage of Cable 1

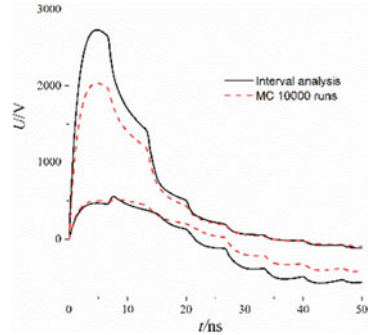


Table 3 Evaluation Results of FSV

Wire Voltage		ADM	FDM	GDM
Left	Upper bound	0.1245	0.2161	0.2592
	Lower bound	0.0562	0.2929	0.3098
Right	Upper bound	0.1202	0.2382	0.2725
	Lower bound	0.0819	0.2566	0.2875

4.1 Error Analysis

In this paper, feature selection verification technique (FSV) is used to evaluate the results of the improved interval analysis method and the 10,000 runs Monte Carlo method. The FSV technique shows the correlation between two groups of data according to amplitude and waveform. The evaluation indexes of FSV include total amplitude difference measure (ADM), total feature difference measure (FDM) and total global difference measure (GDM). The ratings were classified into three categories: excellent (0–0.1), very good (0.1–0.2), good (0.2–0.4), fair (0.4–0.8), poor (0.8–1.6), and very poor (> 1.6).

It can be seen from Table 3 that the rating of the comparison between the reduced dimension interval analysis method and Monte Carlo method is good, and the validity of this method is proved.

4.2 Computing Efficiency

Because the dimensions of variables are too many, the whole model interval analysis method is not given in this paper. By analyzing the whole model interval analysis, this paper simplifies the theoretical calculation time comparison of the model interval analysis method and the Monte Carlo method.

Table 4 Comparison of computing time

Calculation time		Full model	Simplified model	Monte Carlo
theory	$(k + 1)^n t_1$		$(k + 1)^m t_2$	10000 t_1
simulation			1660 s	37114 s

The computer configuration used in the simulation is: processor of Intel (R) Xeon (R) CPU E5-2690V4@2.60 GHz, RAM 192G, and operating system of Win7 64-bit.

The order of interval analysis method is k , and the Monte Carlo method is set as 10,000 times. Assuming that the whole model has n -dimensional variables, the time for a deterministic solution is t_1 , the equivalent model has m -dimensional variables, and the time for a deterministic solution is t_2 . Table 4 gives the theoretical calculation time and the practical simulation calculation time in the example.

As can be seen from Table 4, the reduced dimension interval analysis method proposed in this paper greatly reduces the modeling difficulty and effectively improves the simulation efficiency.

5 Conclusion

In this paper, a reduced dimension interval analysis method based on simplified model is proposed for complex wire bundle coupling modeling of electronic equipment, which simplifies the non-random bundled wire harness to the maximum 5-conductor wire bundle model, taking into account the uncertainty of wire bundle structure parameters and load parameters. Based on the equivalence relation between the whole model and the electrical parameters of the simplified model, the structural parameters of the simplified model are established, and the interval value of the terminal response is obtained by interval analysis. Finally, a numerical example of 8-conductor random bundled wire harness is given to verify the effectiveness of the method proposed in this paper. On the premise that the expansion effect is small, this method can effectively solve the difficulty of the uncertainty analysis of random bundled wire harness due to the difficulty of modeling and long calculation time caused by the number of variables, which provides an effective way for the electromagnetic compatibility analysis of random bundled wire harness of electronic equipment.

References

1. Liu S, Liu W.: Progress of relevant research on electromagnetic compatibility and electromagnetic protection. High Voltage Eng 40(6): 1605–1613 (2014)
2. Olsen RG, Tarditi AG.: EMP coupling to a straight conductor above ground: transmission line formulation based on electromagnetic reciprocity. IEEE Trans Electromagn Compat 61(3): 919–927 (2019)

3. Bellan D, Pignari AS, et al.: Statistical Superposition of Crosstalk Effects in Cable Bundles. *Wireless Commun Over Zigbee for Automotive Inclination Measur China Commun* 10(11): 119–128 (2013)
4. Wu, M., Beetner, D.G., Hubing, T.H., et al.: Statistical prediction of “reasonable worst-case” crosstalk in cable bundles. *IEEE Trans Electromagn Compat* **51**(3), 842–851 (2009)
5. Liu Z, Lesselier D, Sudret B, Wiart J.: Surrogate modeling based on resampled polynomial chaos expansions. *Reliab Eng Syst Safety* 202, 107008 (2020)
6. Fox, J, Ökten G.: Polynomial chaos as a control variate method. *SIAM J Sci Comput* 43(3): 2268–2294 (2021)
7. Xutong, W., Hui, Z., Yinhui, C.: Uncertainty analysis method of induced voltage of transmission line based on interval. *High Power Laser Particle Beams* **34**(4), 75–78 (2022)
8. Andrieu, G., Kone, L., Bocquet, F., et al.: Multiconductor reduction technique for modeling common-mode currents on cable bundles at high frequency for automotive applications. *IEEE Trans Electromagn Compat* **50**(1), 175–180 (2008)
9. Changqing G, Zhijiang S, Zhuo L, et al.: Equivalent method for analyzing crosstalk of cable bundles. *Chinese J Radio Sci* 26(3): 509–514 (2011)
10. Quandi, W., Yali, Z., Qingsong, L., et al.: Equivalent model for automotive cable bundle in electromagnetic radiation immunity simulation. *Trans China Electrotech Soc* **27**(7), 160–168 (2012)

Magnetic Field Analysis and Magnetic Resistance Optimization of Moving Magnet Primary Segmented Permanent Magnet Synchronous Linear Motor



Haoyu Wang, Jie Zhang, Wenyuan Yan, and Hualin Huang

Abstract In this paper, the moving-magnet segmented primary permanent magnet synchronous linear motor (SPPMSLM) with two primary stator units and one rotor is studied, the characteristics of magnetic field and force acting on the rotor during switching between two stator elements are analyzed. Firstly, the analytical expressions of the no-load air-gap magnetic field of SPPMSLM are derived by using the analytical method, and the results are verified by the finite element method, secondly, because the primary discontinuity in the structure of SPPMSLM results in the excessive magnetic resistance between the segments of the rotor, the size of the motor is simulated by the parameterized finite element method, the topology of adding auxiliary poles at both ends of the stator back iron is proposed, which is matched with the auxiliary teeth at the end of the primary stator unit, the effectiveness of the proposed structure in magnetic resistance reduction is evaluated by energy conversion method, which can provide some reference value for structure design and performance optimization of SPPMSLM.

Keywords Moving magnet · Permanent magnet synchronous linear motor · Air gap magnetic field analysis · Finite element analysis · Motor structure optimization

H. Wang (✉) · J. Zhang · W. Yan · H. Huang
Faculty of Mechanical Engineering and Mechanics, Ningbo University, Ningbo 315201, China
e-mail: wanghaoyu@nimte.ac.cn

J. Zhang
e-mail: zhangjie@nimte.ac.cn

W. Yan
e-mail: yanwenyuan@nimte.ac.cn

H. Wang · W. Yan · H. Huang
Ningbo Institute of Materials Technology and Engineering, Chinese Academy of Sciences,
Ningbo 315201, China

1 Introduction

In recent years, permanent magnet synchronous linear motor (PMLSM) has been widely concerned by related application industries because of its advantages such as light weight, small volume, simple structure, no intermediate drive device, high thrust density and fast response speed. PMLSM is usually run on the stator covered with permanent magnet steel by the actuator of the primary winding with iron core. The winding of the actuator needs to be powered by the trailing wire, which limits the movable range of the actuator. In addition, a large amount of magnetic steel is needed to meet the needs of the long stroke operation, and the cost is huge. In order to meet the needs of long and smooth operation of factory production lines or logistics lines, literature [1] proposed a moving magnetic primary segmented permanent magnet linear motor model. Literature [2–4] established the motor simulation model based on the application of the moving magnetic segmented primary synchronous linear motor in the vertical direction lifting system, carried out the finite element analysis of the electromagnetic characteristics of the motor model and proposed the corresponding analytical calculation formula. Based on the mutual verification of finite element method and analytical method, literature [5] put forward the design criteria and calculation formula for each size of the body structure of the moving magnetic segmented primary synchronous linear motor. In literature [6, 7], the finite element method was used to study both the magnetic resistance and the tooth groove force of the segmented primary synchronous linear motor, and the proposed theory was verified by experiments. Literature [8] proposed the analytical formula of air gap magnetic density of fractional slot permanent magnet linear motor. However, the derivation of the analytical formula of the air gap magnetic density of the moving magnetic piecewise linear motor model under no-load is not mature in the existing papers. This paper uses the finite element method to study the air gap magnetic density waveform of the primary piecewise model and deduces the calculation formula, and verifies the accuracy of the analytical formula of the air gap magnetic density of this model by comparing the results of the analytical method with the finite element method.

Because of the primary structure of the discontinuous segment, the end force of the moving magnetic resistance when the stator element is moving in and out is much greater than the tooth groove force when the stator is coupling. Therefore, noise and vibration will be generated when the moving stator is passing through the segment, which will affect the stability in operation. How to weaken the end force caused by the motor moving between segments is a particularly important point to improve the motor performance. In literature [9], Halbach array arrangement of permanent magnet was adopted, and the positioning force was modulated by the magnetic accumulation effect of the arranged array, thus reducing thrust fluctuation. In literature [10], it was proposed to change the length of the teeth at the primary two sides of the end and use the side end effect to modulate each other so as to effectively weaken the thrust fluctuation. Literature [11] proposed a method to weaken the end force by changing the height of several side teeth at both ends of the primary stator element.

Literature [12] proposed the method of changing the width of several side teeth at the end of the stator element to weaken the end force. Literature [11] proposed a way to divide the magnetic poles of permanent magnets to reduce the end force received during operation. The method used in literature [11–13] is mainly to optimize the structural size of the original model so as to weaken the end force on which the actuator runs in and out of the primary element. Literature [14] proposes a way of adding stepped auxiliary stages at both ends of the primary stator element to weaken the end force by adjusting the structural size of the auxiliary stages. Literature [15] further reduces the influence of the end force by combining the slanting pole arrangement of permanent magnets with the step type auxiliary teeth of the primary stator element. Literature [16] proposes a modified circular auxiliary stage placed on the end of the primary stator, which also has a very effective weakening effect on the end force of the secondary actuator running between segments. Literature [17] proposed a very advanced optimization method for thrust characteristics of flat permanent magnet linear motor. Literature [18, 19] proposed a new permanent magnet shape optimization method, which weakened the harmonic frequency of breath by modifying motor parameters to achieve performance optimization. The existing optimal design schemes all add auxiliary structure to the primary iron core. Since the motor under study is a moving magnetic setting, auxiliary poles can be added to both ends of the moving magnetic backplane to optimize the electromagnetic characteristics of the motor and weaken the positioning force by changing the structure of the magnetic backplane. In order to find an effective way to reduce the magnetic resistance, this paper proposed a method of adding auxiliary stages to both ends of the actuator back iron to weaken the end force received during operation between segments. Several auxiliary stage structures were designed and compared by finite element method, and then evaluated by energy conversion method to verify the effectiveness of reducing the magnetic resistance.

2 The Model of Discontinuous Sectional Primary Linear Motor

The SPPMLSM model studied in this paper is shown in Fig. 1. The stator of the linear motor is composed of primary units with windings, which are placed at certain intervals. The moving part consists of the secondary permanent magnet. The moving part starts to run after the primary winding is energized. The effective length of the stator element is L_1 , the spacing distance of the stator element is L_2 , and the effective distance of the actuator part is L . The effective distance of the actuator in the model is the sum of the effective length of the stator element and the length of the interval ($L = L_1 + L_2$). Such arrangement makes the total area of effective coupling between the moving part of the motor and the stator part constant in the process of moving, so that the three-phase current through each section of the stator element needs to be the same phase sequence and direction of each phase. When entering the next

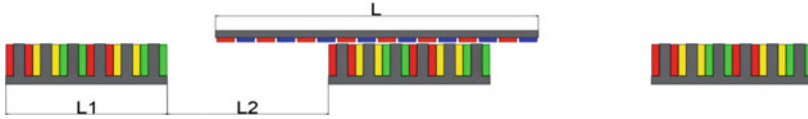


Fig. 1 Finite element model of moving magnetic segmented primary permanent magnet synchronous linear motor

stator, the actuator is partially counteracted by the end force of the entering end in the same direction as the moving direction and the end force of the leaving exit end in the opposite direction, which makes the actuator run more stable.

The moving magnetic segmented primary permanent linear motor has a moving length of 336 mm. It adopts a polar permanent magnet with the brand name NdFe42H16. The length of the permanent magnet is 18 mm, the width is 5 mm, the pole spacing is 21 mm, and the length of the primary stator element is 168 mm. The winding method adopted in this study is concentrated winding, with 200 turns per phase, 6 slots, slot spacing of 28 mm, and air gap between armature and starter of 2.5 mm. The specification of this motor model is shown in Table 1.

3 The Analysis of Air Gap Magnetic Field of Discontinuous Segmented Linear Motor

3.1 Analytical Formula of Air Gap Magnetic Density for Motor Model

The motor model with 4 poles and 3 slots studied in this paper belongs to fractional slot centralized winding. Because the repetition period of the magnet motive force waveform generated by the fractional slot winding group is not based on the distance between the poles, but on the distance between the unit motor, the number of slots occupied by each pole is different in a cycle. For this model, the number q per phase slot per pole is as follows:

$$q = \frac{Z}{2pm} = \frac{k}{j} \quad (1)$$

where: Z is the number of slots; p is the polar logarithm; m is the phase number; k and j are the numerator and denominator of the simplified fraction. The simplified denominator j is even, so the polar logarithm of the unit motor takes the same value as j .

The analytical expression of no-load airgap magnetic field of primary segment linear motor with moving magnetic is derived, that is, the analytical expression of magnetic density waveform of permanent magnet is studied when the moving stator

Table 1 The model parameters of the moving magnetic SPPMLSM

	Parameter	Numerical Value
Primary stator	Number of slots	6
	Slot width	16.5 (mm)
	Tooth width	11.5 (mm)
	Tooth height	39 (mm)
	Primary Length	168 (mm)
	Slot pitch	28 (mm)
	Winding method	Concentrated
	Winding turns	200
	Permanent Magnet	NdFe42
	Remanence intensity	1.25
Secondary mover	Pole number	16
	Pole inclination	0
	Pole width	5 (mm)
	Pole length	18 (mm)
	Pole distance	21 (mm)
	Back iron length	336 (mm)
	Back iron width	9 (mm)
Air gap length		2.5 (mm)
Model width		50 (mm)
Rated thrust		350 (N)
Rated current		5.3 (A)
Maximum speed		1 (m/s)

is coupled and the primary stator is not slotted. When the stator is not slotted, the air gap is evenly distributed, so the permeability per unit area in the air gap is:

$$\Lambda = \frac{\mu_0}{\delta} \tag{2}$$

That is:

$$\delta = h_m + \delta_0 \tag{3}$$

μ_0 is air permeability; δ is the sum of magnetization direction length h_m of permanent magnet and air gap length δ_0 when the stator is not slotted.

Take the unit motor with stator coupling as an example. Because the air gap magnetic field under each pole is different, the air gap magnetic field under a pair of magnetic poles cannot be deduced separately. Think of the entire magnetic pole as a whole. Figure 2 shows the air gap magnetic density distribution when the pole

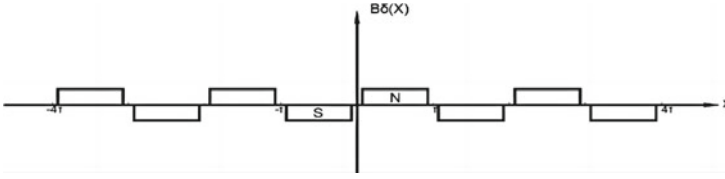


Fig. 2 Magnetic density distribution of stator air gap without grooving

number is 4, and the origin of coordinates is selected as the center point of the moving pole arrangement in the case of moving stator coupling.

Within the interval of $x \in [-4\tau, 4\tau]$, the air gap magnetic density can be expressed as follows:

$$B_{\delta}(x) = \begin{cases} -B_{\delta}, & 2k\tau + (\frac{3-\alpha}{2})\tau \leq x \leq 2k\tau + (\frac{3+\alpha}{2})\tau \\ B_{\delta}, & 2k\tau + (\frac{1-\alpha}{2})\tau \leq x \leq 2k\tau + (\frac{1+\alpha}{2})\tau \\ 0, & x \in \text{other position} \end{cases} \quad (4)$$

Among them, in the type τ : is pole distance; α is the polar arc coefficient; $k = 0, \pm 1, \pm 2$.

B_{δ} is the amplitude of magnetic density of square wave air gap generated by permanent magnet:

$$B_{\delta} = \frac{B_r h_m}{\delta} \quad (5)$$

where: B_r is the permanent magnetic strength of permanent magnet.

Since the magnetic density of the air gap is periodic, the Fourier transform can be applied to it. In the case that the stator is not grooved, the expression of the magnetic density of the air gap generated by the permanent magnet is:

$$B_{\delta}(x) = \frac{2B_{\delta}}{\pi} \left\{ \sum_{n=1}^{\infty} \left[\cos\left(\frac{n\pi(1-\alpha)}{2}\right) - \cos\left(\frac{n\pi(1+\alpha)}{2}\right) \right] \frac{\sin\left(\frac{n\pi x}{\tau}\right)}{n} \right\} \quad (6)$$

Among them $x \in [-4\tau, 4\tau]$.

When the stator is slotted, air gap magnetic field generated by the permanent magnet changed. Taking the whole number of slots as a whole, Fig. 3 shows the variation of the equivalent air gap length of the primary stator element of the motor with x after the stator is slotted. The origin of coordinates is selected at the center point of the tooth groove of the primary stator element.

Within the range of $x \in [-3t, 3t]$, the equivalent air gap length changes with x can be expressed as:

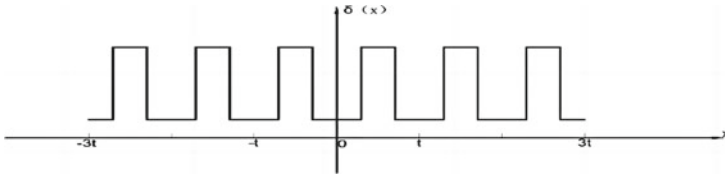


Fig. 3 Equivalent air gap length distribution of stator slotted

$$\delta_0(x) = \begin{cases} \delta, & kt \leq x \leq kt + \frac{b}{2} \\ \delta + h_s, & kt + \frac{b}{2} \leq x \leq kt + \frac{b}{2} + w \\ \delta, & kt + \frac{b}{2} + w \leq x \leq kt + b + w \end{cases} \quad (7)$$

where: it is the tooth pitch, b is the groove width, w is the tooth width, h_s is the groove depth; $k = 0, \pm 1, \pm 2, -3$.

Order $d_0(x) = \frac{1}{\delta_0(x)}$, then there is:

$$d_0(x) = \begin{cases} \frac{1}{\delta}, & kt \leq x \leq kt + \frac{b}{2} \\ \frac{1}{\delta + h_s}, & kt + \frac{b}{2} \leq x \leq kt + \frac{b}{2} + w \\ \frac{1}{\delta}, & kt + \frac{b}{2} + w \leq x \leq kt + b + w \end{cases} \quad (8)$$

The expression after the Fourier transform is:

$$d_e(x) = \frac{1}{t} \left(\frac{w}{\delta} + \frac{b}{\delta + h_s} \right) + \sum_{m=1}^{\infty} \left\{ \frac{2h_s}{(\delta^2 + \delta * h_s) \pi m} * \sin\left(\frac{n\pi * w}{t}\right) \cos\left(\frac{2n\pi * x}{t}\right) \right\} \quad (9)$$

Among them $x \in [-3t, 3t]$.

When the stator is slotted, since the air gap changes periodically and evenly, the permeability per unit area in the air gap is:

$$\Lambda(x) = \frac{\mu_0}{\delta(x)} \quad (10)$$

When the stator is slotted, the air gap magnetic density generated by the permanent magnet can be expressed as:

$$B(x) = \frac{B_\delta(x) * \delta}{\delta(x)} \quad (11)$$

In the type: $B(x)$ is the no-load air gap magnetic density under the stator slot; $B_\delta(x)$ is the no-load air gap magnetic density under unslotted stator.

Combining formula (8) and formula (11), the analytical formula of air gap magnetic density of the coupling part of the rotor at any position can be derived

as follows:

$$B_e(x) = \delta * d_e(x) * B_\delta(x - l) \tag{12}$$

where, l is the distance of the polar center line offset from the center line of the tooth groove.

3.2 The Comparison of Air Gap Magnetic Density Analysis and Finite Element Method

In order to verify the validity of the above analytical derivation of the airgap magnetic field, two primary stator elements and a secondary actuator were used as the model, Ansoft Maxwell 2D was used for finite element simulation of the airgap magnetic density of the two-dimensional model. The situation when the actuator runs between the stator elements is shown in Fig. 4:

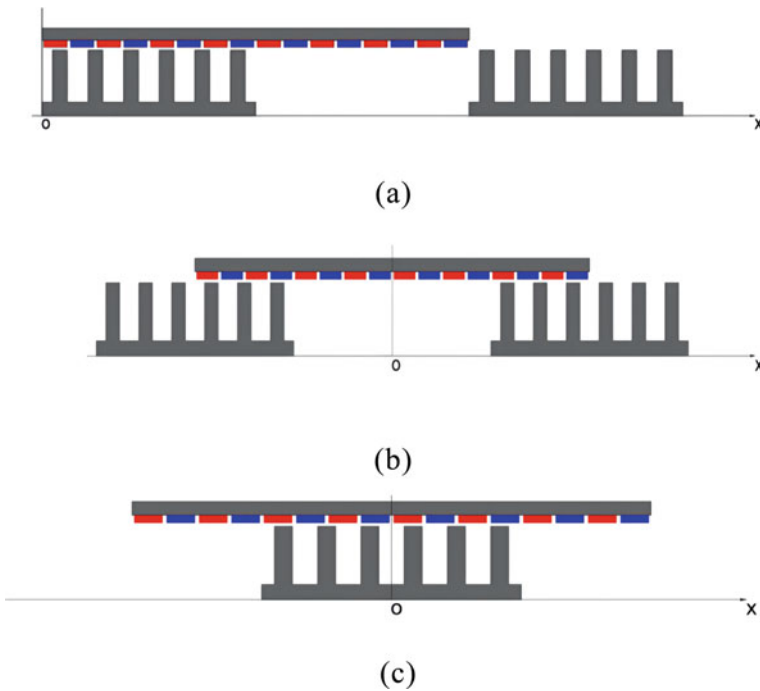


Fig. 4 Operation of the moving magnetic SPPMLSM **a** The mover is at the left end of two stator units **b** When the mover crosses two stator units **c** When the mover is coupled with a single stator unit

The electromagnetic field simulation function of Ansoft Maxwell 2D was utilized to conduct finite element two-dimensional numerical simulation of the magnetic density of the air gap between permanent magnet and primary stator element. The simulated results of the magnetic density of the air gap based on the three situations in Fig. 4 are shown in Fig. 5;

It can be seen from Fig. 4 and 5 that the total coupling area between the two primary stator elements is unchanged when the stator is running, and the air gap flux density in the part of the moving stator coupled with each other is shown as an irregular shape waveform with a period of 42 mm, while the air gap flux density in the uncoupled part of the moving stator is shown as a more regular waveform with a period of 42 mm. The waveforms of the coupled and uncoupled parts of the stator are compared by the analytical formula method.

Figure 6 shows the comparison between the results of the no-load airgap magnetic density analysis method and the finite element method when the dynamic stator is partially coupled in the motor model, and the reliability is verified by using the

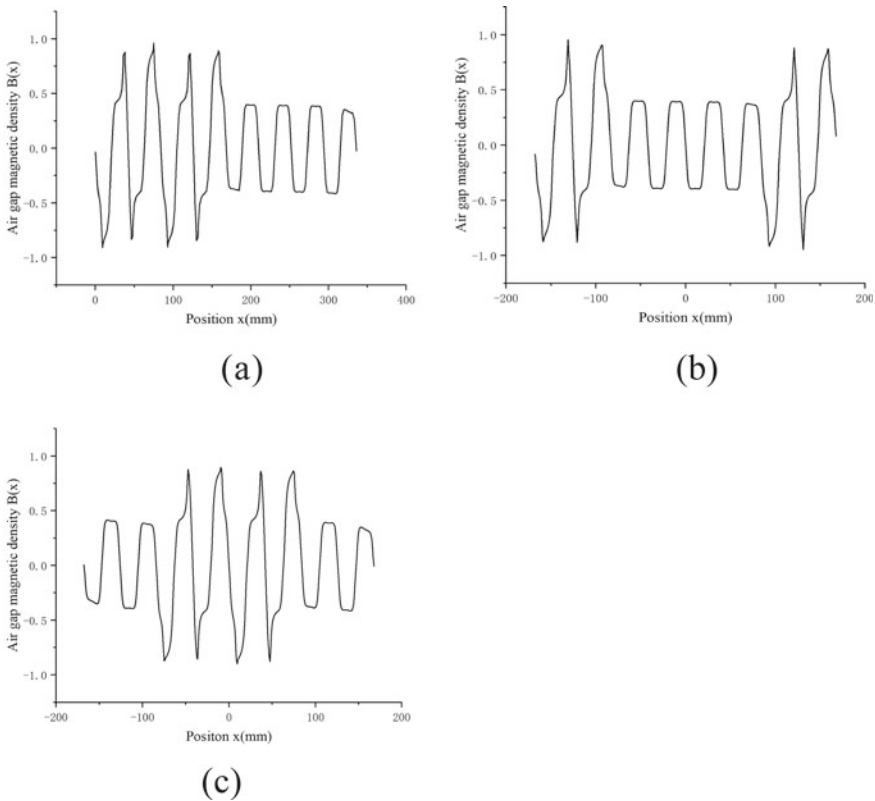


Fig. 5 Finite element analysis of air gap flux density of motor model **a**, **b** and **c** respectively correspond to the air gap magnetic density waveform of the mover at different positions in Fig. 4

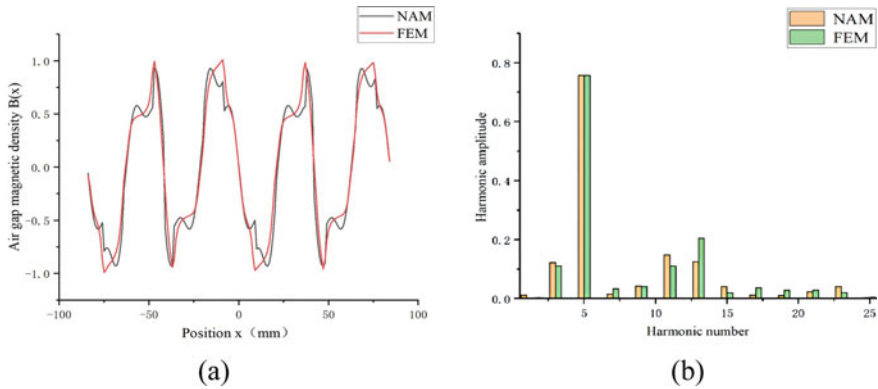


Fig. 6 **a** Comparison between analytical method and finite element method for no-load air gap flux density of motor with dynamic stator coupling **b** Comparison between analytical method and finite element method for time–space carrier air gap harmonic analysis of dynamic stator coupling

harmonics of the air gap part. It can be seen that the analytical formula derived above can more accurately reflect the no-load airgap magnetic field when the dynamic stator is coupled.

When the secondary actuator runs between the segments of the primary stator element, the air gap magnetic density formula of the uncoupled part can be derived from the air gap magnetic density formula when the stator is not slotted, that is, the value of the air gap length δ is increased. When the air gap length is large, the situation is the same as that of the uncoupled part of the moving stator. Figure 7 shows the comparison of the results of the no-load airgap magnetic density analysis method and the finite element method in the motor model when the moving stator part is not coupled, and the air gap harmonic analysis is used to verify the results.

According to the data shown in Fig. 6 and Fig. 7, there is a certain error between the analytical method and the finite element method of air gap harmonic analysis. In practice, because the magnetic permeability of the iron core is much greater than that of the air, and the magnetic density of the tooth groove or the edge of the end is affected by the change of the medium and the end effect, the magnetic density of the air gap increases abruptly. There is a difference between the analytical method and the finite element method in the direction of the magnetic field line in the tooth groove, so there will be some errors. Figure 7(a) shows that the 5th and 13th harmonics play a major role in the air gap magnetic density waveform through the simulation data of the finite element method. The amplitude of the number of major harmonics is effectively fitted by the analytical method, while the influence of the magnetic density of the air gap caused by the number of non-major harmonics is not fully fitted. In addition, only the first 10 harmonics were taken into account in the fitting with the finite element method in the analytical calculation, and the influence of the remaining harmonics on the magnetic density of the air gap was not fully considered. Therefore, there were errors in the two contrast curves in the image, namely the “burr” phenomenon in the curve of the analytical method.

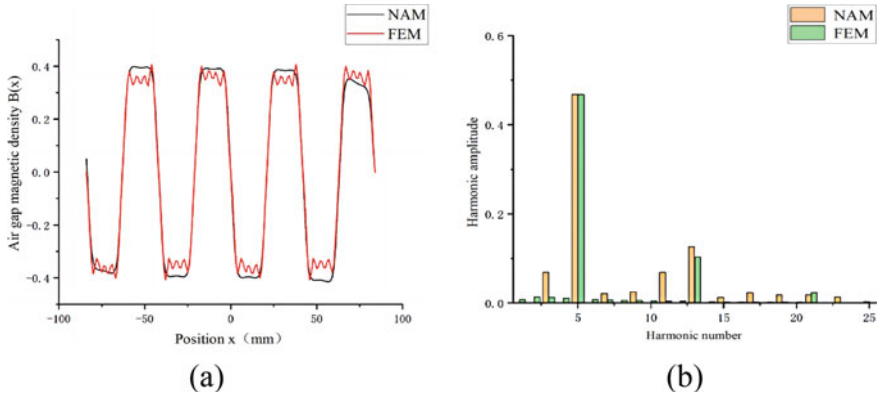


Fig. 7 a Comparison between analytical method and finite element method of the uncoupled no-load air gap magnetic density b Comparison of the results of the uncoupled no-load air gap harmonic analysis method and finite element method

4 Structure Optimization of SPPMLSM

The permanent magnet linear synchronous motor has obvious side end effect because the stator core is broken at both ends under static condition. And because the motor core is slotted, the tooth slotting effect is produced. The magnetic resistance of linear motor is composed of the groove force generated by the groove effect and the end force generated by the side end effect, which is the main reason for the thrust fluctuation of PMLSM. To improve the stability and reliability of the motor, we must try to reduce the magnetic resistance. When the secondary actuator moves in and out of the primary stator element, the finite element image of the magnetic resistance received by the actuator when it moves in and out of the primary stator element is shown in Fig. 8. As can be seen from the image, when the actuator enters and exits the stator, the end force is much greater than the tooth groove force. Therefore, this paper starts with the optimization of the motor body structure to reduce the end force of the actuator when running between segments.

Because the basic structure of the moving magnetic segmented primary permanent magnet synchronous linear motor studied in this paper is $L = L1 + L2$, the secondary actuator is affected by two stator elements at the same time between the switching stator segments. It enters one stator element and leaves the other one at the same time, and the coupling area of the moving stator is unchanged. The actuator is subjected to both the end force in the opposite direction when leaving the stator and the end force in the same direction when entering the stator, which can partially cancel each other. The force situation is shown in Fig. 9. The comparison between Fig. 8 and Fig. 9 shows that the arrangement of $L = L1 + L2$ can reduce the magnetic resistance by 20%.

It can be seen from Fig. 9 (b) that the magnetic resistance of the actuator moving between segments is an odd function with the symmetry axis formed by the middle

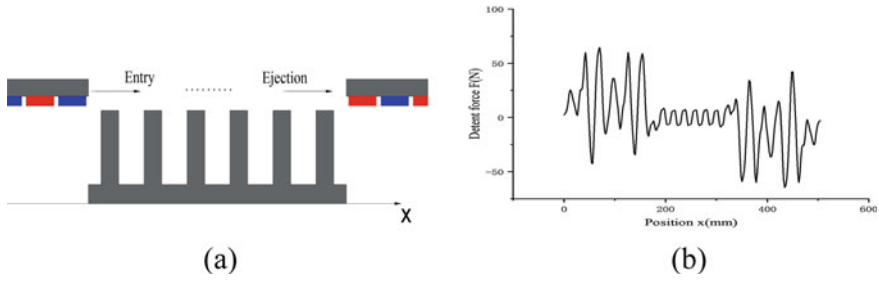


Fig. 8 a Schematic diagram of moving in and out of single stator b Magnetic resistance of moving in and out of single stator

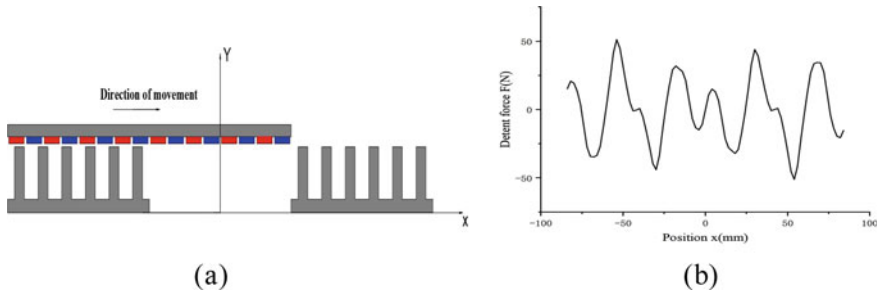


Fig. 9 a Two-dimensional model of PMLSM b Detent force of mover when switching between two stators

position of the two stator elements. In order to more clearly compare the weakening of each optimization model to the magnetic resistance with images, the finite element analysis of the magnetic resistance after structure optimization mainly analyzes the stress situation of $x \in [-84, 0]$.

We try to install auxiliary teeth at both ends of the primary stator element to reduce the magnetic resistance of the actuator when switching between segments. After parametric analysis and finite element simulation, it is finally found that the rectangular auxiliary tooth with width of 9 mm, height of 47 mm and material of steel_1008 has the best effect on magnetic drag weakening. Figure 10 shows the proposed model of the stator auxiliary teeth. Compared with the basic model in Fig. 9, the flux resistance of the actuator during operation is reduced by 41.6% when the primary stator element model with the primary stator auxiliary teeth is used compared to the one without the addition.

Adding auxiliary teeth to both ends of the primary stator on the initial model can play a significant role in the optimization. However, since the actuator is still subjected to a large magnetic resistance when switching between segments, further structural optimization is needed to reduce the end force caused by the primary stator breaking. Therefore, this paper attempts to optimize the structure of the secondary actuator back iron, adding auxiliary stages to both ends of the actuator back iron to

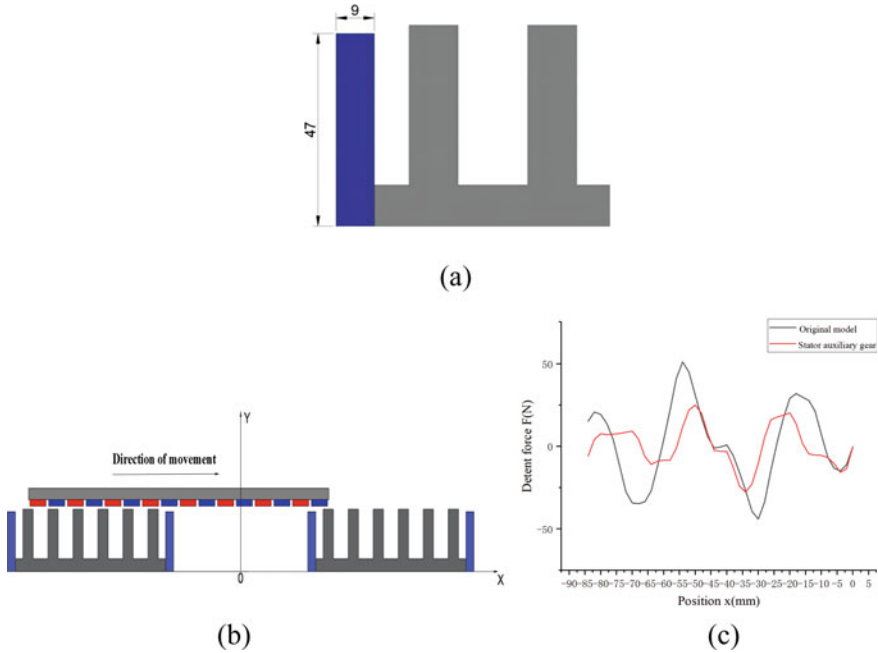


Fig. 10 **a** Schematic diagram of the size of stator auxiliary teeth **b** The two-dimensional model of the motor with stator auxiliary teeth **c** Comparison of detent force between primary optimization and original model

reduce the magnetic resistance during operation, and using the finite element two-dimensional numerical analysis of the force value of the actuator when switching between stator segments. By adding different auxiliary stages at both ends of the movable back iron to optimize its structure, the proposed model of changing the shapes of both ends of the movable back iron to reduce the end force is shown in Fig. 11.

By comparing the basic model in Fig. 9 with the model of the stator auxiliary teeth in Fig. 10 and the four auxiliary stage models in Fig. 11, the finite element two-dimensional numerical simulation was carried out to test the weakening of the magnetic resistance caused by the addition of the moving auxiliary stage. Figure 12 shows the waveform of the magnetic resistance of the motors of each model when switching between segments. It can be seen from Fig. 12 that the superposition of the actuator auxiliary stage and the stator auxiliary teeth is extremely effective in weakening the magnetic resistance. Compared with the magnetic resistance in the original model, the magnetic resistance is reduced by 76% in the finite element analysis results under the joint action of stator auxiliary teeth and moving auxiliary teeth.

As shown in Fig. 12, it can be proved that the magnetic resistance of the superposition effect of the actuator auxiliary pole and the stator auxiliary stage is smaller than

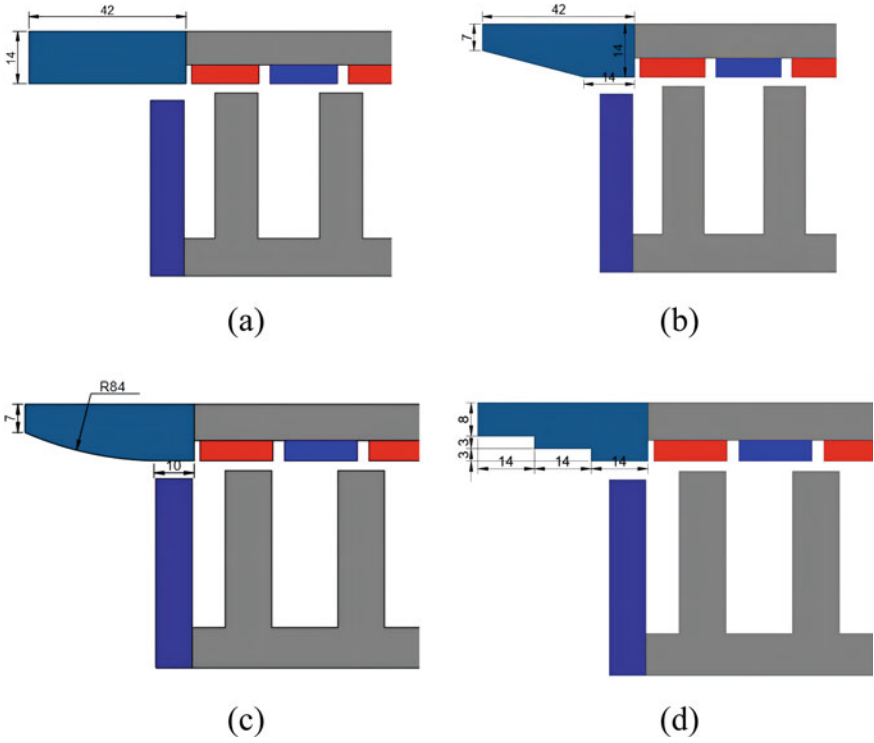


Fig. 11 **a** Model 1: Rectangular auxiliary level **b** Model 2: Wedge-shaped auxiliary stage **c** Model 3: Step-type auxiliary stage **d** Model 4: Cambered auxiliary stage

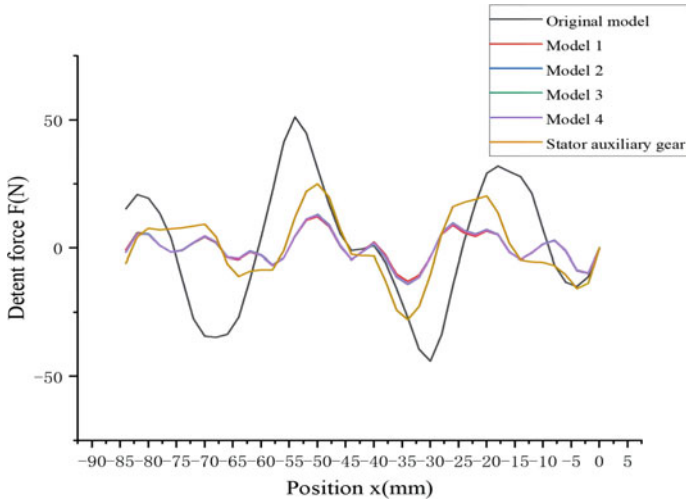


Fig. 12 Finite element comparison of detent force of various structures

that of the basic model and the proposed model with only the stator auxiliary teeth. The maximum magnetic resistance of the basic model is 51.44N, while the maximum magnetic resistance of the model with only stator auxiliary pole is proposed to be 27.32N. In the proposed model of superposition of stator auxiliary teeth and actuator auxiliary stages, the maximum magnetic resistance shown by the rectangular auxiliary stage of model 1 is only 12.5N.

Although the differences of magnetic drag values in various models can be compared in Fig. 12, it is difficult to judge the relative merits of each model. Therefore, energy conversion method is used to evaluate the effect of each model on magnetic drag weakening. The total energy value of each model's magnetic resistance after calculation is shown in Fig. 13. The energy is calculated as follows:

$$W_e = \int |F_c(x)|dx \tag{13}$$

where, W_e is the total energy of magnetic resistance received by the actor when switching between segments, and $F_c(x)$ is the magnetic resistance received by the actor at the corresponding time x , and the integral interval is $x \in [-84, 0]$.

In Fig. 13, the total magnetic resistance energy received by the moving segments of each model is 1691.18 J. The total magnetic resistance capacity of the model with only the stator auxiliary stage is 876.77 J, while that of model 1 with the minimum total magnetic resistance energy is only 389.79 J in the model with the stator auxiliary stage and the moving auxiliary teeth. By comparing the energy of the model with the superposition of the stator auxiliary teeth and the actuator auxiliary stages, it is found that the model with the rectangular auxiliary stages added at both ends of the

Fig. 13 Calculate the total detent force energy of each model by energy conversion

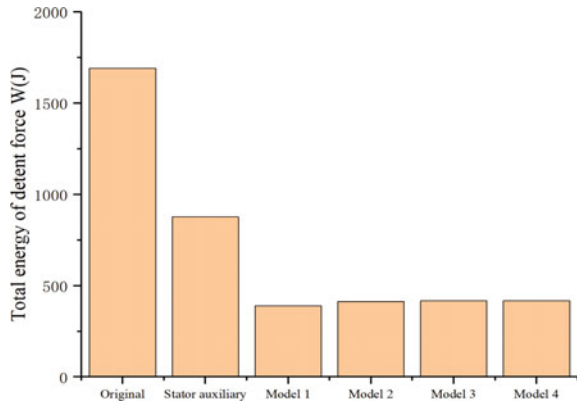


Fig. 14 Actuator motion process under rated load condition

secondary back iron can better reduce the magnetic resistance of the actuator when it moves between the stator segments.

5 Load Simulation Comparison of Motor Model Before and After Optimization

The first two parts of this paper are mainly based on the situation of the motor model under no-load, the electromagnetic characteristics of the no-load force of the motor before and after the structure optimization. As can be seen from Table 1, the rated working condition of the motor model studied in this paper is as follows: when the rated input current is 5.3 A, the actuator part of motor is subjected to rated thrust of 350 N and runs at the maximum speed of 1 m/s.

Under the rated load condition, the operation of the moving part is mainly divided into three processes: entering the stator, switching between the stator segments and leaving the stator. A two-dimensional numerical simulation model is constructed for the stator part composed of four discontinuous primary stators and the secondary permanent magnet as the moving part.

Using the simulation function of the force characteristics of the model with the finite element simulation software Ansoft Maxwell 2D, the dynamic parameters were set as the running speed was 1 m/s and the amplitude of three-phase AC current through the windings is 5.3 A. The thrust simulation under rated load was carried out on the original motor model before optimization and the motor optimization model after adding secondary auxiliary poles and primary auxiliary teeth. The thrust and thrust fluctuation of the two models in operation were explored, and the data were compared and analyzed.

As can be seen from Fig. 15, when the actuator enters the single-section stator, it will be attracted by the part of the stator, and the force will not become stable until the actuator is fully coupled with the single-section stator. When the two ends of the stator switch, there will be a large thrust fluctuation, which is the end force when the actuator enters and exits the stator section at the same time. In the process from coupling with the first stator to coupling with the last stator and not leaving ($x \in [0.3, 1.3]$), the thrust force received by the actuator fluctuates basically with a certain value as the average value. This average value is the average thrust received by the actuator when it is running, and the fluctuation of thrust value is the manifestation of thrust fluctuation.

According to the curve in Fig. 15 and the data in Table 2, before optimization, the average thrust received by the actuator in the original motor model is close to the rated thrust. However, during the inter-segment switch, due to the influence of the side end force, the thrust fluctuation rate is as high as 30.8%, which makes the motor unable to operate normally. After the motor model is optimized, the average thrust received by the actuator and the stator is reduced compared with that before the optimization, which may be because the increase of mass caused by the addition of auxiliary stage in

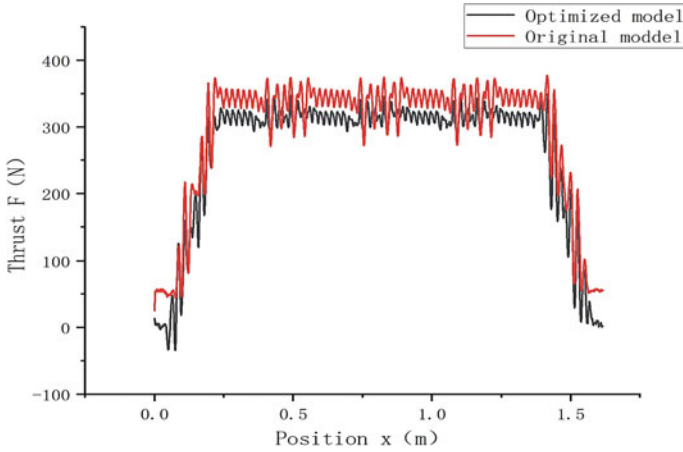


Fig. 15 Comparison of thrust of motor model before and after optimization

Table 2 Stress of the motor under rated working conditions before and after optimization

	Average thrust (N)	Magnetic drag (N)	Thrust fluctuation rate
Original model	340	105	30.8%
Optimized model	315	25	7.93%

the secondary back iron part will lead to the decrease of thrust during operation. Due to the addition of primary auxiliary teeth and secondary auxiliary stages, the force of the motor will be more stable during operation, and the thrust fluctuation during intersegment switching will be weakened a lot. The fluctuation rate only accounts for 7.93%, indicating that the motor motion characteristics and force characteristics have been greatly improved after structural optimization compared with that before optimization. The structural optimization method tried in this paper is effective.

6 Conclusion

The research object of this paper is the primary moving magnetic discontinuous segmented permanent magnet synchronous linear motor. In order to solve the problem that the motor suffers too much magnetic resistance when switching between two stator segments, two-dimensional finite element simulation analysis is carried out on the motor model to understand its electromagnetic and mechanical characteristics, and structural optimization is carried out to reduce the magnetic resistance. By adding

auxiliary poles to both ends of the primary stator element and auxiliary teeth to both ends of the moving magnetic backplane, the amplitude of the magnetic resistance is reduced from 52.3N to 12.5N, which effectively weakens the influence of the magnetic resistance without affecting the electromagnetic performance and makes the motor have a more stable and reliable operating condition. According to the finite element comparison simulation under the rated load condition, the motion characteristics and mechanical characteristics of the motor after optimization are greatly improved compared with that before optimization. This method does not change the effective area of the stator coupling, nor does it change the electromagnetic performance of the motor during operation. It not only improves and optimizes the structure design of the motor, but also provides the simulation basis for the switching part between the stator segments in the subsequent drive experiment.

Acknowledgements This study was supported by the Zhejiang Provincial Key R&D Program (2021C01069), Zhejiang Provincial Natural Science Foundation Major Project (LD21E070002), Ningbo Science and Technology Innovation 2025 Major Project (2020Z070) and Ningbo Science and Technology Innovation 2025 Major Project (2019B10070).



References

1. Seki, K., Watada, M.: INSTITUTE OF ELECTRIC AND ELECTRONIC ENGINEER. Discontinuous arrangement of long stator linear synchronous motor for transportation system. In: 1997 International Conference on Power Electronics and Drive Systems, 1997. Proceedings. vol. 2, pp. 697–702 (1997)
2. Shangguan, X.F., Li, Q., Yuan, S.: Running process analysis of discontinuous stator permanent magnet linear synchronous motor. *J. Xi 'an Jiaotong Univ.* **38**(12), 1292–1295, 1300 (2004). (in Chinese)
3. Shangguan, X.F., Li, Q., Yuan, S.: Overall modeling and simulation of multi-stage primary permanent magnet linear synchronous motor drive system. *Trans. China Electrotech. Soc.* **21**(3), 52–57 (2006). (in Chinese)
4. Shangguan, X.F., Li, Q., Yuan, S.: System modeling and braking simulation of multi-stage primary permanent magnet linear synchronous motor. *J. Xi 'an Jiaotong Univ.* **40**(6), 694–698 (2006). (in Chinese)
5. Shangguan, X.F., Li, Q., Yuan, S.: Vertical lifting system driven by multi-stage primary permanent magnet linear synchronous motor. *Proc. CSEE* **27**(18), 7–12 (2007) (in Chinese)
6. Wang, S.-H., Xiong, G.-Y.: Design of segmented vertical motion permanent magnet linear synchronous motor. *J. China Coal Soc.* **35**(3), 520–524 (2010) (in Chinese)
7. Shuhong, W., Guangyu, X.: Magnetic resistance of segmented permanent magnet linear synchronous motor. *Electric Mach. Control* **14**(10), 56–60 (2010). (in Chinese)
8. Liu, W., Cui, J., Li, B., et al.: Analysis of no-load air gap flux density of fractional slot permanent magnet synchronous linear motor. *Electric Mach. Control Appl.* **201**, **48**(4), 65–70, 109. (in Chinese)
9. Fengyang, G., Xiaodong, Qi., Xiaofeng, Li., Cheng, Y., Shengxian, Z.: Optimization design of partial segment halbach permanent magnet synchronous motor. *Trans. China Electro. Soc.* **36**(4), 787–800 (2021). (in Chinese)
10. Zhang, C., Chen, F., et al.: A low detent force DS-PMSLM based on the modulation of cogging and end forces. *IEEE Trans. Ind. Electron.* 1–1 (2022)

11. Yong-Jae, K., Masaya, W., Hideo, D.: Reduction of the cogging force at the outlet edge of a stationary discontinuous primary linear synchronous motor. *IEEE Trans. Mag.* **43**(1 Pt.1), 40–45 (2007)
12. Kim, Y.-J., Hideo, D.: Cogging force verification by deforming the shape of the outlet edge at the armature of a stationary discontinuous armature PMLSM. *IEEE Trans. Mag.* **43**(6), 2540–2542 (2007)
13. Kim, Y.-J., Hwang, S., Jeong, Y.-S.: Cogging force reduction of a stationary discontinuous armature PM-LSM by magnet segmentation. *IEEE Trans. Magn.* **45**(6), 2750–2753 (2009)
14. Kim, Y.-J., Sang-Yong, J.: Minimization of outlet edge force using stair shape auxiliary teeth in a stationary discontinuous armature linear permanent magnet motor. *IEEE Trans. Magnet.* **47**(10), 3228–3231 (2011)
15. Eui-Jong, P., Yong-Jae, K., Jung, S.-Y.: Edge effect minimization of stationary discontinuous armature PMLSM using skewed magnets and stair shape auxiliary teeth. In: 2013 International Conference on Electrical Machines and Systems: 2013 International Conference on Electrical Machines and Systems (ICEMS), 26–29 Oct. 2013, Busan, Korea (South): Institute of Electrical and Electronics Engineers, pp. 1958–1961 (2013)
16. Kim, S.J., Park, E.J., Jung, S.Y., et al.: Optimal design of reformed auxiliary teeth for reducing end detent force of stationary discontinuous armature PMLSM. *IEEE Trans. Appl. Supercond.* **26**(4), 1–5 (2016)
17. Liu, C., Yongxiang, X., Zou, J., Guodong, Y., Zhuo, L.: Permanent magnet shape optimization method for PMSM air gap flux density harmonics reduction. *China Electro. Soc. Trans. Electr. Mach. Syst.* **5**(4), 284–290 (2021)
18. Xionsong, L., Cui Hesong, H., Chunfu, L.X., Shoudao, H.: Optimal design of thrust characteristics of flat plate permanent magnet linear synchronous motor. *Trans. Chin. Soc. Electron. Technol.* **36**(5), 916–923 (2021). (in Chinese)
19. Fei, G., Qiu, C., Chunyan, L., Tao, M.: Research on influence of motor parameters on the negative-salient permanent magnet synchronous motor. *China Electro. Soc. Trans. Electr. Mach. Syst.* **6**(1), 77–86 (2022)

Research on a Design Method of Composite Nano Generator Based on Rotation



Dong Yan , Chuangliang Zhao, Kai Zhang , and Jiuyuan Zhan

Abstract The self powered technology has become a research hot spot at home and abroad. In view of the problem that the electrode contact mode of the traditional rotary composite nano generator will bring more mechanical energy loss due to sliding friction, an electromagnetic friction composite nano generator based on rolling friction is designed, which has low friction loss and high output power. The generator is experimentally verified. The results show that the output power of the friction nano generator reaches 129 μ W and the output voltage reaches 80 V at the speed of 500r/min and the load of 20m Ω . The coil type electromagnetic generator has an output power of 33.28mW and an output voltage of 3 V at a speed of 500r/min and a load of 100m Ω . The output current of the composite nano generator can light 150 LED lamps at a rotational speed of 600r/min, which is three times larger than the driving current of the traditional rotary composite nano generator. The rotary composite nano generator can drive a temperature sensor. The rotating composite nano generator designed in this paper has important practical significance for the self powered working scheme of wireless sensor networks.

Keywords Rotating composite nano generator · Composite energy collection · Self powered

D. Yan · C. Zhao

Chongqing University of Posts and Telecommunications School Automation/Industrial Internet School, Chongqing 400065, China

e-mail: yandong@cqupt.edu.cn

K. Zhang (✉)

Chongqing University of Posts and Telecommunications School of Media and Art, Chongqing 400065, China

e-mail: 915883126@qq.com

J. Zhan

State Grid Chongqing North Power Supply Company, Chongqing 400065, China

© Beijing Paike Culture Commu. Co., Ltd. 2023

X. Dong et al. (eds.), *The proceedings of the 10th Frontier Academic Forum of Electrical Engineering (FAFEE2022)*, Lecture Notes in Electrical Engineering 1054, https://doi.org/10.1007/978-981-99-3408-9_8

1 Introduction

Fluid energy is a kind of energy widely existing in nature [1], which can drive wireless sensor networks under the background of self powered technology, and has become a research hot spot at home and abroad [2]. The motor contact mode of traditional rotary composite nano generator brings more mechanical energy loss for sliding friction [3]. Zhang L. B et al. designed an electromagnetic energy collector using rolling magnets [4], which can significantly improve the magnetic flux when cutting coils compared with the electromagnetic energy collector with sliding magnets. However, compared with mechanical movement, the electromagnetic field caused by it changes irregularly, reducing the stability [5, 6]. Wang Beihong et al. designed an electromagnetic friction composite nano generator based on sliding friction [7, 8]. To solve this problem, this paper optimizes the structure of the motor and matches the impedance of the power management circuit [9, 10]. The driving current output is increased through the power management circuit. Compared with the unmatched circuit, the circuit current can be increased by 2 times.

2 Design of Rotary Composite Nano Generator

2.1 Mechanism of Frictional Nano Power Generation

Under the action of external mechanical force, the electrodes of the friction nano generator contact each other, which in turn drives electrons to move in the external circuit to form a current. According to Maxwell displacement current equation:

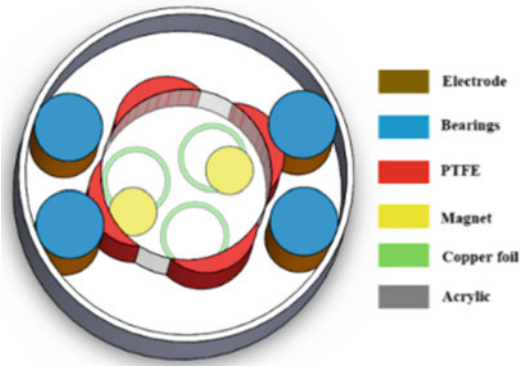
$$J_D = \frac{\partial D}{\partial t} = \varepsilon \frac{\partial E}{\partial t} + \frac{\partial P_s}{\partial t} \quad (1)$$

D represents the displacement field, E represents the electric field, ε represents the vacuum dielectric constant, and represents the polarization field.

$$V_{\text{out}} = -\frac{1}{C(d)} Q_{EFER} + V_{OC}(d) \quad (2)$$

$C(d)$ indicates that the capacitance between the two electrodes is a function of the distance, Q_{EFER} indicates the amount of charge transferred between the two electrodes, and $V_{OC}(d)$ indicates the open circuit voltage caused by the static charge generated by friction.

Fig. 1 Composite nano generator based on roller structure



2.2 Structural Design of Composite Nano Generator

According to the characteristics of rolling friction form⁹, a composite nano generator based on double drum structure is designed. The overall structure is shown in Fig. 1. The composite nano generator is divided into three parts: Coil permanent magnet electromagnetic induction power generation unit and mechanical energy capture unit.

The diameter of the central drum is 40 mm, the height is 80 mm, the diameter of the shell is 100 mm, and the diameter of the drum electrode barrel is 20 mm. The above components are made of acrylic materials. There is a 3 mm hole on the upper and lower cover plates of the central roller. The distance between the center of the roller electrode and the edge of the shell is 12.5 mm, and the spacing between the rollers is 8 mm.

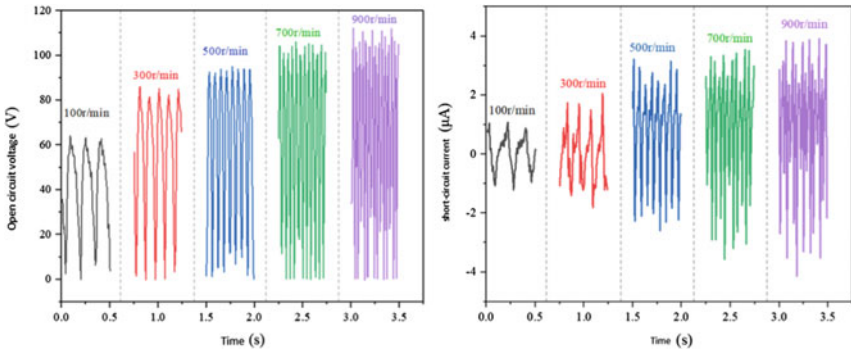
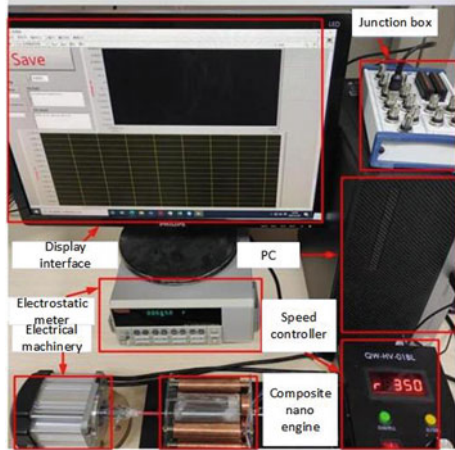
2.3 Structural Design of Composite Nano Generator

In order to study the output characteristics of the hybrid generator, a test system is designed. The desktop computer is responsible for processing the collected data with the running program, and the display interface displays the data waveform. Picture Fig. 2 of the test system:

Physical picture of motor test system In the experiment, adjust the speed of induction motor to simulate the strength of fluid energy in nature. The motor test takes 100 r/min as the starting point, 200 as the step size, and 900 r/min as the open circuit voltage and short circuit current under the final condition. The measured results are shown in Fig. 3.

It can be seen from Fig. 3 (a) that the open circuit voltage increases from 60 V at the initial 100r/min to 110 V at 900r/min. Figure 4 shows the load characteristic curve of the friction nano generator. These two points prove that the friction nano generator is a voltage source with “high internal resistance”.

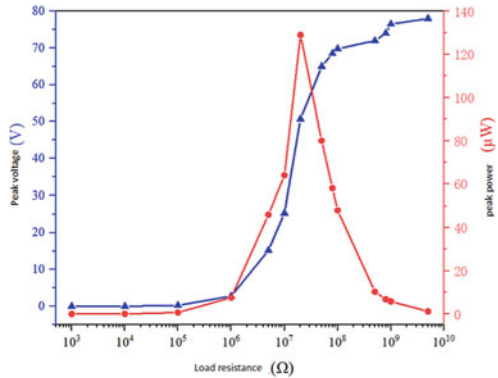
Fig. 2 Physical Drawing of Motor Test System



(a) Open circuit voltage of friction nano generator (b) Short circuit current of friction nano generator

Fig. 3 Test Results of Friction Nano generator

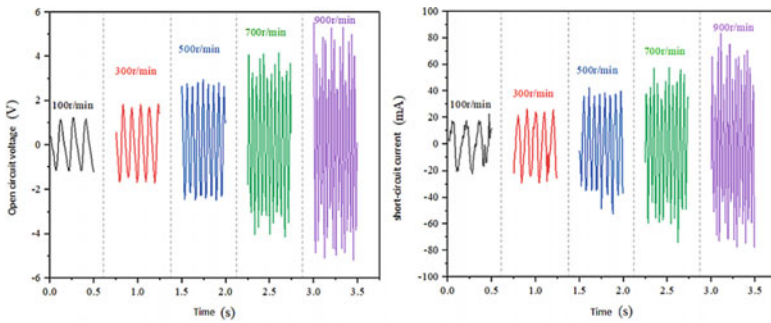
Fig. 4 Load characteristics of friction nano generator



It can be seen from Fig. 5 (a) that the open circuit voltage has increased from 2 V at the initial 100r/min to 10 V at 900r/min, and the open circuit voltage has increased by 5 times. This proves that the coil type electromagnetic generator is a current source with “low internal resistance” (Fig. 6).

Through the above output characteristic test, we can know that the characteristics of friction nano generator and coil electromagnetic generator are different. In this paper, the experiment of driving LED is done and the circuit connection scheme is optimized, which greatly increases the driving capacity of the friction nano generator. The test principle is shown in the figure.

As shown in Fig. 8, the friction nano generator can light up 10 LEDs at 100r/min and before the rectifier bridge is ungrounded, and the measured current after rectification is 1.8 μ A. After the ground cathode of the rectifier bridge is connected to the ground, the friction nano generator can light up 50 LEDs under the same conditions, and the output current increases to 3.8 μ A.



(a) Open circuit voltage of coil type electromagnetic generator (b) Short circuit current of coil type electromagnetic generator

Fig. 5 Test Results of Coil type Electromagnetic Generator

Fig. 6 Load characteristics of coil type electromagnetic generator

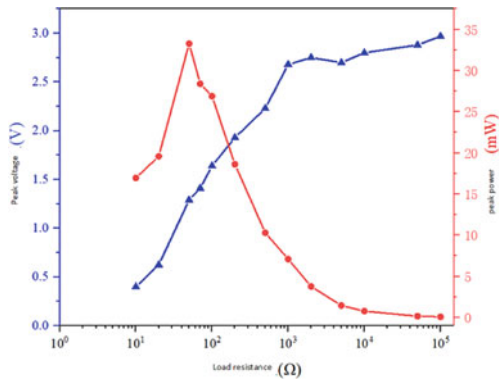
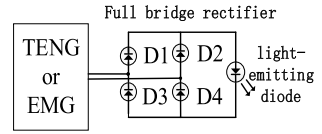


Fig. 7 Schematic diagram of driving LED circuit



Therefore, the LED starts to light up when the motor speed is increased to 600r/min, as shown in Fig. 8 (a). Figure 8 (b) shows the optimized total output of the composite nano generator at 600r/min, which can light up 150 LEDs, achieving the goal that the total output power is greater than that of a single generator, and greatly improving the practicability of the composite nano generator (Fig. 9).

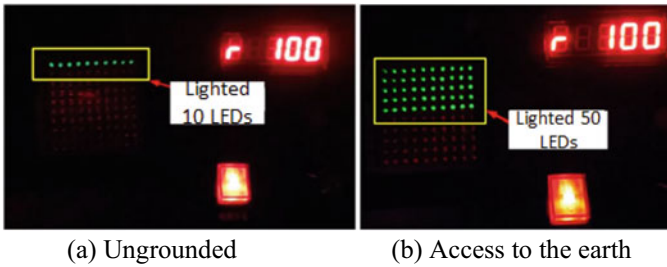


Fig. 8 Comparison of Lighting of Friction Nano generator before and after Grounding

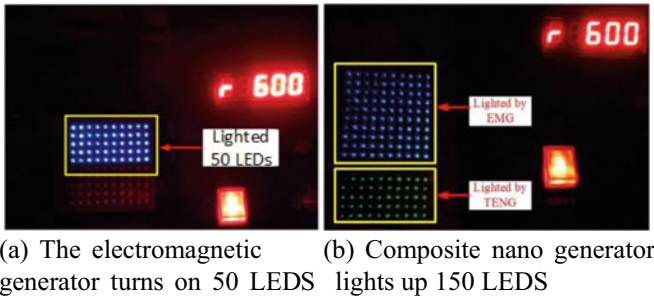


Fig. 9 Physical picture of electromagnetic generator and composite nano generator lighting LED

Fig. 10 Schematic Diagram of AC/DC

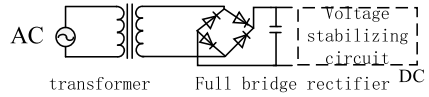
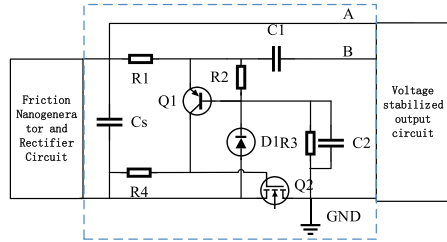


Fig. 11 Charging and discharging control circuit structure



3 Power Management Circuit Design

3.1 Rectifier Circuit Design

The generator output voltage signal used for energy collection is in AC mode. The back-end circuit is required to have the function of converting AC voltage into DC voltage. The conversion schematic diagram is as follows:

This stage is AC/DC conversion. Therefore, based on the AC/DC structure, capacitors are introduced to realize the function of energy storage10. (Fig. 10).

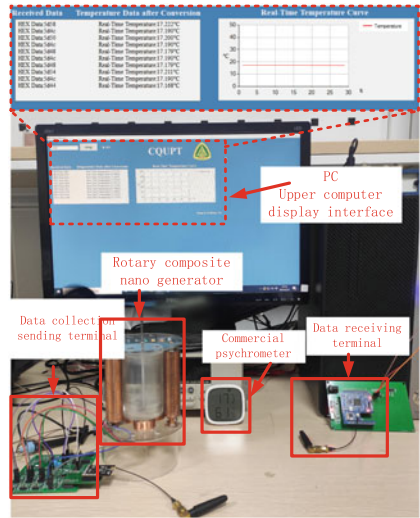
3.2 Charging and Discharging Circuit Design

Disconnect the energy storage capacitor and the voltage stabilizing output circuit again to make the energy storage capacitor return to the state of charging and energy storage. According to the literature, Fig. 11. Shows the charge discharge control circuit designed by using three semiconductor devices in this paper.

4 Simulation and Experimental Verification

Under laboratory conditions, the Bosch hand-held blower is used to simulate the natural wind energy to drive the rotary composite nano generator, and the generated electric energy is transformed through the power management circuit and then supplied to the data collection and transmission terminal for use. The sending end of data acquisition sends the obtained temperature data to the receiving end of data, and finally verifies the practicability of the whole system through the display of the upper computer. The test results are shown in Fig. 12.

Fig. 12 Actual measurement of wireless temperature measurement system



In the actual test, the distance between the hand-held blower and the wind cup is 2 m. The rotary composite nano generator can be quickly started, 1800 μ F. The voltage of energy storage capacitor can reach 3.3 V in a short time. In Fig. 12, the real-time temperature data converted by the upper computer is about 17.1 $^{\circ}$ C, which is very close to the 17.2 $^{\circ}$ C displayed on the commercial thermometer. Therefore, the practicability of the rotary composite nano generator and the wireless temperature measurement system has been verified (Fig. 12).

5 Conclusion

To sum up, The experimental verification shows that the output power of the friction nano generator reaches 129uW and the output voltage reaches 80 V at the speed of 500r/min and the load of 20M Ω . At the speed of 500r/min and the load of 100M Ω , the output power of the coil type electromagnetic generator reaches 33.28mW and the output voltage is up to 3 V. The output current of the composite nano generator can light up 150 LED lights at the speed of 600r/min. The research results can provide technical reference for the power supply of passive low-power devices, and have practical application value for the application of self powered sensor networks.

References

1. Herbert, G.M.J., Iniyan, S., Sreevalsan, E., et al.: A review of wind energy technologies. *Renew. Sustain. Energy Rev.* **11**(6), 1117–1145 (2007)
2. Mohanty, A., Parida, S., Behera, R.K., et al.: Vibration energy harvesting: a review. *J. Adv. Dielectr.* **9**(04), 1930001 (2019)
3. Kulah, H., Najafi, K.: Energy scavenging from low-frequency vibrations by using frequency up-conversion for wireless sensor applications. *IEEE Sens. J.* **8**(3), 261–268 (2008)
4. Zhang, L.B., Dai, H.L., Yang, Y.W., et al.: Design of high-efficiency electromagnetic energy harvester based on a rolling magnet. *Energy Convers. Manage.* **185**, 202–210 (2019). (in chinese)
5. Eghbali, P., Younesian, D., Farhangdoust, S.: Enhancement of piezoelectric vibration energy harvesting boosters. *Int. J. Energy Res.* **44**(2), 1179–1190 (2020)
6. Beihong, W., Lun, P., Jiyu, W., et al.: An ultra-low-friction triboelectric electro-magnetic hybrid nano generator for rotation energy harvesting and self-powered wind speed sensor. *ACS Nano* **12**(9), 9433–9440 (2018). (in chinese)
7. Fan, F., Tian, Z., Wang, Z.: Flexible Tribo electric generator. *Nano energy* **1**(2), 328–334 (2012). (in chinese)
8. Simiao, N., Ying, L., Sihong, W., et al.: Theory of sliding-mode Tribo electric Nano generators. *Adv. Mater.* **25**(43), 6184–6193 (2013). (in chinese)
9. Simiao, N., Ying, L., Xiangyu, C., et al.: Theory of freestanding Tribo electric-layer-based Nano generators. *Nano Energy* **12**, 760–774 (2015). (in chinese)
10. Zhong, Y., Zhao, H., Guo, Y., et al.: An easily assembled electric magnetic tribo electric hybrid nano generator driven by magnetic coupling for fluid energy harvesting and self-powered flow monitoring in a smart home/city. *Adv. Mater. Technol.* **4**(12), 1900741 (2019). (in chinese)

Research and Application of Dry-Type Transformer Winding Material Detection Technology



Jiawei Wu, Guohua Chen, Donghui He, and Shunyao Li

Abstract Based on the principle of thermoelectric effect, by detecting the thermoelectric potential at different temperatures at both ends of dry-type transformer windings combined with the difference of relative Seebeck coefficients between different metals, the inner winding material can be detected without destroying the whole insulation of epoxy resin of dry-type transformer, and the hidden danger of aluminum transformer pretending to be copper transformer can be found in time. For transformers in operation, the same method can be used to detect and make targeted operation and maintenance strategies for aluminum transformers that have been found and have not experienced insulation deterioration for the time being, so as to effectively reduce the fault risk.

Keywords Dry-type transformer · Winding · Thermoelectric effect · Aluminum transformer · Grid operation and maintenance

1 Introduction

In recent years, as the increasing scale of distribution network, the growth rate of distribution transformer gradually increases. Due to its small size, convenient installation, simple operation and maintenance, dry-type transformer has become the first choice for distribution transformers. However, due to the fierce competition caused by the low threshold of the industry, the price of bulk commodities rises constantly in recent years. Some manufacturers have adopted bad fraud means of ‘aluminum instead of copper’, in order to maximize the profits, so that some transformers which are marked as copper winding and actually are aluminum winding flow into the distribution network.

J. Wu (✉) · G. Chen · D. He · S. Li
Dongguan Power Supply Bureau of Guangdong, Power Grid Co., Ltd., Dongguan 523008,
Guangdong, China
e-mail: 407960325@qq.com

© Beijing Paiké Culture Commu. Co., Ltd. 2023
X. Dong et al. (eds.), *The proceedings of the 10th Frontier Academic Forum of Electrical Engineering (FAFEE2022)*, Lecture Notes in Electrical Engineering 1054,
https://doi.org/10.1007/978-981-99-3408-9_9

The aluminum core transformer produced according to the standard technical process is not inferior products [1]. However, the nameplate is identified as a copper core transformer. In fact, the copper core transformer is a material fraud. According to the national standard requirements of transformer nameplate information, the winding material is distinguished by letter code in the model. The copper material is not marked the letter code, and the aluminum material must be marked the letter code 'L' [2]. Because the thermal conductivity, electrical conductivity, tensile strength and Brinell hardness of metal aluminum are lower than those of metal copper, the electrical and mechanical properties of metal aluminum are worse than those of metal copper. Therefore, aluminum transformers need to formulate special operation and maintenance strategies to improve the reliability of aluminum transformers to a reasonable range [3]. The purchase price, applicable scenarios and operation and maintenance points of transformers with different materials are significantly different. Material fraud would directly bring the hidden dangers to the operation and maintenance of distribution network.

This paper studies the detection effect and application of thermoelectric effect detection method on dry-type transformers, studies the operation and maintenance points of transformers with different materials, and provides experience and reference for product acceptance and actual operation and maintenance.

2 Thermoelectric Effect Method

2.1 Principle of Thermoelectric Effect

The Seebeck effect is also called the first thermoelectric effect, and the Thomson effect is also called the third thermoelectric effect. The Seebeck effect means that if two different conductors are connected into a loop. And when the temperature of the two joints is different, the electromotive force is generated in the loop, and there will be a current. The Thomson effect refers to the phenomenon of heat absorption or heat release on a single conductor or semiconductor, when there is a temperature difference between the two ends of a single conductor or semiconductor and there is a current passing.

The reason for the Seebeck effect is that when there is a temperature gradient in the conductor, the carriers at the hot end migrate to the cold end, and the charge accumulation causes the self-built electric field in the conductor, to form a electric potential difference at both ends of the conductor. The main reason for the thermoelectric effect is the diffusion of carriers from the hot end to the cold end. However, since the carrier concentration of the metal and the position of the Fermi energy level basically do not change by the temperature [4], therefore, the Seebeck effect of the metal is generally less than $10 \mu\text{V}/\text{K}$, which is much smaller than hundreds of $\mu\text{V}/\text{K}$ of the semiconductor.

The mechanism which generated the thermoelectric effect of metal could be analyzed from two aspects. First is the free electronic of diffusion from the hot end of conductor towards to cold end. The diffusion is not generated because of electron concentration gradient (The electron concentration in metal is not relevant to the temperature altitude), but is generated because that the electronic of hot end has higher energy and speed. Obviously, if the function is major, the coefficient of Seebeck effect generated should be negative.

The second is the influence of electron free path. Although there are many free electrons in the metal, the contribution to the conduction is mainly the so-called conduction electrons in the range of $2kT$ near the Fermi level [5]. However, the average free path of these electrons is related to the condition of suffering scattering (phonon scattering, impurity and defect scattering) and the change of density of states with energy.

If the average free path of hot electrons increases with the increase of electron energy, the hot electrons will have a large energy on the one hand, and there is a large average free path on the other hand. The transport of hot electrons to the cold end is the main process, which will generate the Seebeck effect with negative Seebeck coefficient. This is true for metals of Al, Mg, Pd and Pt, etc.

On the contrary, if the average free path of hot electrons decreases with the increase of electron energy, the hot electrons have a large energy, but their average free path is very small, so the electron transport will be mainly from the cold end to the hot end, which will produce the Seebeck effect with positive Seebeck coefficient. This is true for metals of Cu, Au, Li, etc.

Transformer winding are generally made of a single metal (i.e., all copper or all aluminum), but for counterfeit manufacturers, metal copper is generally used in the direct observation part of conductive rods and leads. And metal aluminum is used in the winding wrapped by epoxy resin, so as to achieve the purpose of cost savings. For products with unknown winding material, there are three possibilities of metal combination, namely pure copper, pure aluminum and copper aluminum.

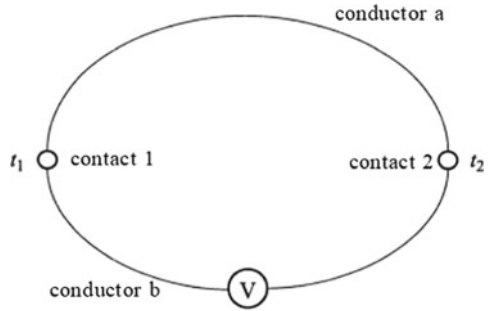
For a single metal, that is, pure copper or pure aluminum transformer. The winding side is heated, and the potential difference between the two ends of the winding is generated according to the Thomson effect due to different temperatures. The calculation formula of thermoelectric potential of single metal a is as follows:

$$U = S_a(t_1 - t_2) \quad (1)$$

Since the average free path of electrons in copper and aluminum varies with temperature is opposite, which causes the direction of motion of electrons between the hot end and the cold end is also opposite. Therefore, the direction of the thermoelectric potential can be detected to determine whether the conductive metal is copper or aluminum.

For the transformer whose conductive rod and lead row material is copper and the transformer winding material is aluminum, the detection principle is shown in Fig. 1, and the calculation formula of the Seebeck effect potential difference is as follows:

Fig. 1 Schematic diagram of thermoelectric effect



$$U = \int_{t_1}^{t_2} (S_a(t) - S_b(t)) dT \quad (2)$$

In the formula:

S_a —Seebeck coefficient of conductor a, $\mu\text{V/K}$

S_b —Seebeck coefficient of conductor b, $\mu\text{V/K}$

t_1 —Temperature of contact 1, $^{\circ}\text{C}$

t_2 —Temperature of contact 2, $^{\circ}\text{C}$

If S_a and S_b do not change with temperature, the above formula can be expressed as follows

$$U = (S_A - S_B)(t_1 - t_2) \quad (3)$$

When the transformer winding material is aluminum, the thermal potential formed at both ends of the winding is:

$$U = S_{\text{Cu-Al}}(t_1 - t_2) \quad (4)$$

Since the Seebeck coefficient of copper and aluminum is opposite, the absolute value of the relative Seebeck coefficient will be greater than the absolute value of the single metal. And the potential difference between the hot and cold ends will be larger than the single metal potential difference, so as to identify the transformer with false winding material.

2.2 Detection Method of Thermoelectric Effect of Dry-Type Transformer

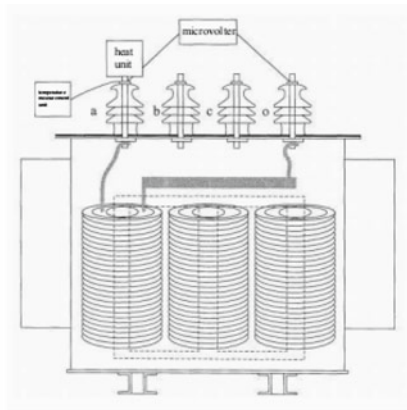
The heating unit and temperature measurement unit are installed on the conductive rod of the dry-type transformer, and the microvolt meter is installed at the end of the conductive rod and the winding. The heating unit is installed on the conductive rod at one end of the tested winding and is in close contact with the conductive rod.

The temperature measurement unit monitors the temperature on the conductive rod below the heating unit. The microvoltmeter is connected between the conductive rods at both ends of the tested winding. The thermoelectric potential measurement point should be the same as the temperature measurement position. The thermoelectric effect wiring of star-connected winding and delta-connected winding is shown in Fig. 2.

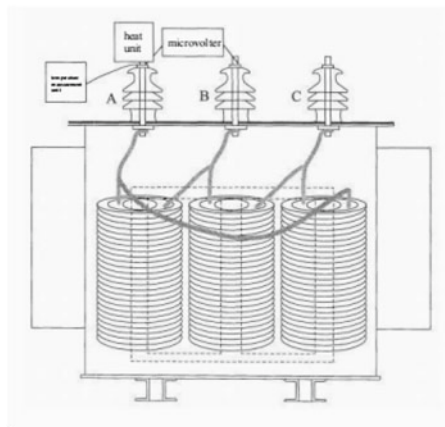
Turn on the power supply of the heating unit to heat the conducting rod of the tested winding, and use heat conduction to form a temperature difference between the two ends of the tested winding. Heating can be stopped when one of the following conditions is met:

- 1) The temperature on the conductive rod is $120\text{ }^{\circ}\text{C} \pm 2\text{ }^{\circ}\text{C}$.
- 2) The thermoelectric power is greater than $100\text{ }\mu\text{V}$.

Fig. 2 Connecting scheme of thermoelectric effect



(a) star connection



(b) delta connection

- 3) The temperature change within 3 min is not more than 5 °C.
- 4) The change of thermoelectric potential value within 3 min is not more than 5 μV .

2.3 Test Result and Judgment Standard

The Seebeck coefficients of copper and aluminum are calculated by Boltzmann equation [6]. It is known that the Fermi energies of copper and aluminum are 7.00 eV and 11.7 eV at 273 K [7]. Theoretical values of Seebeck coefficients of copper and aluminum at 273 K are 1.908 9 $\mu\text{V/K}$ and $-2.142\ 1\ \mu\text{V/K}$ [8], respectively, and the relative Seebeck coefficient between copper and aluminum is 4.051 0 $\mu\text{V/K}$. The above calculations are for pure metal materials. Transformer windings generally use enameled copper and enameled aluminum wires. The Seebeck coefficient is slightly different from the theoretical value. The measured values are shown in Table 1.

It can be seen that the Seebeck coefficient of the combination between copper and aluminum is greater than 4 $\mu\text{V/K}$, and the Seebeck coefficient between enameled copper and enameled aluminum can reach 4.213 $\mu\text{V/K}$. Pure copper combinations are less than 1 $\mu\text{V/K}$. Due to the short length of the transformer winding and the small specific heat capacity of the metal[9], the temperature difference between the two ends of the winding should not exceed 30 K after heating, that is, the potential difference between the copper windings should not be greater than 30 μV . If the potential difference exceeds 100 μV , it can be basically judged that the transformer is aluminum instead of copper false winding.

In the case of reasonable consideration of the margin, it is considered that when the heating stop condition is satisfied [10], the thermoelectric potential value is less than 40 μV to be judged as copper material and higher than 100 μV to be judged as aluminum material [11].

Table 1 Relative Seebeck coefficient

Metal material	Relative Seebeck coefficient ($\mu\text{V/K}$)
Copper conductive rod-pure copper wire	0.4411
Copper conducting rod - enamelled copper winding	07,182
Enameled copper winding-pure copper wire	0.1241
Copper conductive rod-pure aluminum wire	4.053
Copper conductive rod - enamelled aluminum winding	4.213
Enameled copper winding - enamelled aluminum winding	4.001

3 Detection Example of Dry-Type Transformer Thermoelectric Effect Method

In 2022, a power supply bureau in South China disassembled several faulty transformers produced by Guangzhou dry-type transformers to check their internal winding materials. It was found that the winding was made of aluminum except for the conductive rod and lead bar, and the fault transformer nameplate was not marked as aluminum winding transformer. Subsequently, a typical in-service transformer of the manufacturer was selected for routine project and thermoelectric effect material detection, and the winding material and operation situation were comprehensively analyzed to formulate corresponding control measures.

3.1 Thermoelectric Effect Detection Method of Winding Material

According to the method described above, the thermoelectric effect is detected. According to the judgment basis, the thermoelectric potential at the end of heating is lower than $40 \mu\text{V}$ for copper material, higher than $100 \mu\text{V}$ for aluminum material, and the thermoelectric potential is $40 \mu\text{V}$ - $100 \mu\text{V}$, which should be judged comprehensively with examples. When the winding of the transformer stops heating up, the thermoelectric potential is $142 \mu\text{V}$, and the thermoelectric potential is always higher than $40 \mu\text{V}$ during the cooling process. It is judged that the transformer is an aluminum transformer (Table 2).

3.2 Electrical Test Items

The conventional electrical testing items such as insulation resistance, DC resistance, ratio and withstand voltage of the transformer are carried out. According to the requirements of 'China Southern Power Grid Power Equipment Maintenance Test Regulations [9] and' Technical Parameters and Requirements of 6 kV ~ 35 kV Dry Aluminum Winding Power Transformer [10], the direct resistance and ratio of each gear of the transformer meet the relevant requirements. There is no significant change in insulation before and after AC withstand voltage, and the conventional test items are judged to be qualified.

Table 2 Measured data of dry-type transformer by thermoelectric effect method

Testing time	2022.5.20	Ambient temperature / humidity	28°C/50%
Transformer model	SCB10-400/10	manufacturer	Guangzhou Dry type
Transformer number	110S02F3	Test winding	AB winding
Test equipment model	BY200	Test equipment number	00,112
Stop heating time	Temperature difference at both ends	Thermoelectric power value	Remark
0	39	142	The phase A conductive rod was heated to 120 °C and then stopped heating. The temperature difference and thermopower of the phase AB conductive rod were monitored
3	34	131	
6	29	120	
9	25	115	
12	22	89	
15	20	81	
18	18	73	
21	16	71	
24	12	66	
27	11	59	
30	10	54	

3.3 Transformer Temperature Rise and Capacity Verification

According to the judgment basis of ‘Part 2 temperature rise of power transformer, the normal temperature rise limit of transformer with insulation heat resistance grade F under continuous rated capacity steady state is 100 K, and the temperature rise results meet the requirements. The temperature rise results are shown in Table 3.

According to the ‘ 35 kV and below voltage level power transformer capacity evaluation guidelines, the deviation between the measured short-circuit impedance of 3.9844% and the standard short-circuit impedance of 4% corresponding to the preset capacity (400 kVA) is within $\pm 10\%$, and the temperature rise results meet

Table 3 Temperature rise test results

High voltage winding temperature rise	Temperature rise of low voltage winding	Iron core temperature rise
88.17 K	85.33 K	72.4 K

the requirements. It is judged that the preset capacity of 400kVA is the transformer capacity.

However, the measured no-load loss is 1043.71 W, which is higher than the requirement that the technical parameters and requirements of the 6 kV ~ 35 kV dry aluminum winding power transformer are not more than 980 W. The no-load loss of the transformer exceeds 6.5%, which will cause the transformer loss and heat. If the transformer load is not controlled and the cooling device is used reasonably, the insulation aging speed will be accelerated and eventually lead to failure.

3.4 Silicon Steel Sheet and Epoxy Resin Detection

The silicon steel sheet of the dry-type transformer was sampled and tested. The vernier caliper was used to measure the average thickness of the silicon steel sheet to be 0.35 mm. The silicon steel sheet sample of 3 cm × 3 mm was cut out, and the two sides of the sample were ground with sandpaper to remove the insulating layer and expose the metal luster. The treated silicon steel sheet was subjected to a direct reading spectral composition analysis test, and the test results are shown in Table 4.

The test results meet the relevant technical requirements for the thickness, roughness and composition content of silicon steel sheet in ‘full process cold rolled electrical steel.

Trichloromethane was used as solvent for epoxy resin sampling and detection, and epoxy equivalent was detected by 0.1 N perchloric acid standard titration solution. The content of inorganic chlorine was determined by titration with 0.002 N silver nitrate solution using acetone as solvent. The content of easily saponified chlorine was determined by 0.01 N silver nitrate titration using butyloxyethanol as solvent. The test results are as follows: Table 5.

Table 4 Chemical composition content of silicon steel sheet (Unit wt%)

	C	Si	Mn	P	S	Cu	Fe
Sample 1	0.0410	3.1434	0.2301	0.0087	0.0047	0.4505	Margin
Sample 2	0.0245	2.9330	0.1911	0.0128	0.0096	0.3208	Margin
Average	0.0327	3.0382	0.2106	0.0107	0.0072	0.3857	Margin

Table 5 Test results of epoxy resin

	Epoxide equivalent g/mol	Inorganic chlorine W/%	Easy saponification chlorine W/%
Sample 1	213.5	0.0051	0.2101
Sample 2	222.1	0.0049	0.1933
Average value	217.8	0.005	0.2017

The test results meet the relevant technical requirements of epoxy resin for EP01551 310 pouring in 'bisphenol A epoxy resin'.

4 Operation and Maintenance Strategy of Aluminum Core Transformer

Through the analysis of multiple faults and the detection of the equipment in operation, it is found that the nine dry-type transformers produced by Guangzhou Dry-Type Transformer Factory are all aluminum-core transformers. The transformers produced by the factory in operation have the hidden danger of winding material fraud. It is necessary to formulate a special operation and maintenance strategy for the batch of transformers to reduce the recurrence of similar faults. At the same time, it is necessary to strengthen the control of network access detection to avoid similar equipment flowing into the distribution network again.

4.1 Strengthen Dry Operation and Maintenance

Strengthen load rate monitoring. When the monthly average load rate of dry-type distribution transformers exceeds 60%, an infrared temperature measurement monitoring equipment status should be carried out.

Shorten the infrared temperature monitoring cycle. Focusing on the winding temperature of dry distribution transformer, infrared imaging temperature measurement is carried out once a month for dry transformers over 100 °C, and infrared imaging temperature measurement is carried out once a quarter for other dry transformers. When the relative temperature difference is greater than 35%, general defect treatment should be reported. When the hot spot temperature exceeds 130 °C (SC type) or 140 °C (SG type), emergency defect treatment should be reported.

Carry out partial discharge test. Conditional units, complete a dry distribution transformer dry partial discharge test every six months.

Implement cooling device operation and maintenance. Check the dry-type distribution transformer fan, and deal with the fault as soon as possible to ensure that the cooling device is available. Before the fault fan is completed, the field should be equipped with an additional fan to help the transformer cool down. At the same time, the temperature controller is checked and adjusted, and the starting temperature is adjusted to 80 °C.

4.2 *Strengthen the Control of Dry Transformer Access Network*

The technical specifications of the 10 kV dry-type transformer of the network company do not clearly require that the dry-type transformer must cool the fan, which is selected by the user and responded by the manufacturer. The normal operation of the fan helps to reduce the operating temperature of the dry change. Therefore, the transformer standardization working group of the network company is reported, and it is proposed that the dry-type transformer must be equipped with a cooling fan.

At present, there is no requirement for testing materials in dry-type transformer network test. In order to prevent similar risks, the control gate is moved forward, and the dry transformer of the new network is carried out. Each batch of products of each manufacturer carries out the thermopower material test to eliminate the aluminum generation of copper transformer.

5 Conclusions

Aiming at the problem that the dry-type transformer generally needs to destroy the external epoxy resin insulation layer to detect the internal winding material, this paper studies the dry-type transformer winding material detection technology based on the thermoelectric effect, and proposes a method and its judgment standard for detecting the internal winding material without destroying the dry-type transformer insulation.

The material analysis, capacity check, epoxy resin silicon steel sheet detection and other tests were carried out on the transformer with batch winding material fraud found in a power supply bureau in South China. Combined with the test results, the corresponding control measures were put forward for the batch transformer. In summary, the feasibility of the detection method demonstrated in this paper provides a detection example and corresponding risk control measures, which provides an effective method for the detection and application of dry-type transformer winding materials.

References

1. Sun, D.H., Li, S.L.: Discussion on the characteristics of aluminum transformer and others. *Transformer* **52**(1), 15–19 (2015). (in Chinese)
2. Identification method of transformer' s product type: JB/T 3837—2010. China Standard Press, Beijing, China (2010). (in Chinese)
3. Du, L., Yu, X.X., Zhou, N.R., Wang, K., Tang, K.: Transformer winding material identification method based on thermoelectric effect. *High Voltage Eng.* **26**(10), 2275–2280 (2011). (in Chinese)

4. Zhenyao, X., Qingguo, Y., Zhang, F.: Design and analysis of asymmetric rotor pole type Bearingless switched reluctance motor. *China Electrotech. Soc. Trans. Electr. Mach. Syst.* **6**(1), 3–10 (2022)
5. Olivares, J.C., Leon, F.D.: Selection of copper against aluminium windings for distribution transformers. *IET Electr. Power Appl.* **4**(6), 474–485 (2010)
6. Li, L.B., Sun, Y.F.: *Metal material physical properties of the manual*. Mechanical Industry Press, Beijing, China, pp. 173–175 (2011). (in Chinese)
7. Orr, W.W.: Aluminum and its future in power transformers. *Electr. Eng.* **78**(7), 737 (1959)
8. Wu, Y.Z., Ma, Y.Q.: Study on performance calculation of copper-clad aluminum wire. *Electric Mater.* **3**, 15–19 (2008). (in Chinese)
9. Zhang, Z., Liu, Y., Wang, J.: Optimal design of multi-channel water cooled radiator for motor controller of new energy vehicle. *China Electrotech. Soc. Trans. Electr. Mach. Syst.* **6**(1), 87–94 (2022)
10. Xiang, Z., Weiling, P., Zhu, X., Quan, L.: Design and analysis of a v-shaped permanent magnet vernier motor for high torque density. *China Electrotech. Soc. Trans. Electr. Mach. Syst.* **6**(1), 20–28 (2022)
11. Zhang, H., Wenfei, Y., Hua, W.: Design and key technology of oil-free centrifugal air compressor for hydrogen fuel cell. *China Electrotech. Soc. Trans. Electr. Mach. Syst.* **6**(1), 11–19 (2022)

Prediction of Dissolved Gas Concentration in Transformer Oil Based on WPD-CSO-LSTM Model



Zhang Miao, Mo Wenjun, Fan Jingmin, Cao Yunfei, Feng Lutao, and Tan Zhichao

Abstract Power transformers are important equipment in the grid system. The dissolved gas in the transformer oil can be used as an important basis for transformer condition prognosis. In order to solve the problems that the hyperparameters of the traditional recurrent neural network model are difficult to determine and the number of subseries of the original gas concentration decomposition is too large, which leads to large errors in the prediction results, this paper proposes a method to predict the dissolved gas concentration in transformer oil based on wavelet packet decomposition and crisscross optimization to optimize the long short-term memory model. Firstly, wavelet packet decomposition is used to decompose the original concentration sequences of dissolved gases. Then, the hyperparameters of long short-term memory network are optimized by crisscross optimization. Finally, the WPD-CSO-LSTM model is constructed to predict the subseries and obtain the final predicted values. The analysis results show that the model overcomes the premature phenomenon of particle swarm optimization. With the same number of iterations, the proposed model can accurately predict the trend of dissolved gas concentration in transformer oil and has a better fit than other optimization algorithm models.

Keywords Dissolved gas in oil · Wavelet packet decomposition · Long short-term memory network · Crisscross optimization · Concentration prediction

1 Introduction

Power transformer is one of the most critical equipment in power system, ensuring the safe and stable operation of transformer is an important subject in the field of power equipment [1]. When the transformer works, the insulating oil and solid materials inside the transformer are affected by high temperature, strong electric field and oxidation, which will produce a small amount of gas dissolved in the insulating

Z. Miao · M. Wenjun · F. Jingmin (✉) · C. Yunfei · F. Lutao · T. Zhichao
School of Automation, Guangdong University of Technology, Guangzhou 510012, China
e-mail: fanjingmin2004@163.com

© Beijing Paiké Culture Commu. Co., Ltd. 2023
X. Dong et al. (eds.), *The proceedings of the 10th Frontier Academic Forum of Electrical Engineering (FAFEE2022)*, Lecture Notes in Electrical Engineering 1054, https://doi.org/10.1007/978-981-99-3408-9_10

oil, including H_2 , CH_4 , C_2H_6 , C_2H_2 , C_2H_4 , CO and CO_2 . Therefore, it is of great significance to evaluate the future operation status of power transformers, predict the latent faults of transformers and master the development trend of transformer health status to establish a prediction model of dissolved gas in oil and predict the future operation data of transformers by using the historical monitoring data in the operation process of transformers. Dissolved Gas Analyses (DGA) is widely used to detect incipient faults in oil filled power transformers [2]. At present, DGA has become the most mainstream method for early fault diagnosis of transformers. Prediction of dissolved gas concentration in transformer oil can predict the operation status of transformer and reduce the incidence of accidents, which has important engineering significance.

Scholars at home and abroad have conducted a series of studies on the prediction of dissolved gas concentration in transformer oil, mainly using traditional prediction methods and artificial intelligence algorithms. The traditional prediction methods mainly include gray model [3] and time series model [4], etc. Artificial intelligence algorithms mainly include support vector machines [5] and extreme learning machines [6], etc. With the development of deep learning, neural networks have also been applied in DGA. Ke-jin Liu et al. proposed a combined prediction method of dissolved gas concentration in transformer oil using particle swarm optimization (PSO) and LSTM networks [7].

The combination of pattern decomposition algorithm and machine learning can further explore the potential information of the original data sequence. Chen Tie et al. proposed a method for predicting dissolved gas in transformer oil combining empirical modal decomposition, granger causality test, and long-short time memory network network, which can improve the prediction accuracy of dissolved gas in oil [8]. All of the above literature can achieve the prediction of dissolved gas in transformer oil, but there are two problems: on the one hand, the hyperparameters of the LSTM model are difficult to determine, and the number of iterations to optimize the parameters of the LSTM neural network using PSO is time-consuming. At the same time, PSO also has the disadvantage of converging to a locally optimal solution. On the other hand, the combined “decomposition-prediction-reconstruction” model is widely used in DGA research, but the common time series decomposition methods, such as wavelet decomposition (WD), have too many decomposed subsequences, greatly increasing the model complexity and calculation scale.

In view of the above research background, this paper proposes a combination prediction model based on wavelet packet decomposition (WPD) and crisscross optimization (CSO) algorithm to optimize the LSTM network model. Firstly, the WPD algorithm is used to decompose the original gas concentration into subsequences of multiple frequency components. Then, two key parameters in the LSTM model are optimized iteratively using CSO algorithm. Finally, the model is used to predict each subsequence and reconstructed to obtain the final predicted gas concentration. The results of numerical examples show that the prediction model proposed in this paper can have higher prediction accuracy and track the variation trend of dissolved gas concentration more accurately under the same number of iterations.

2 Wavelet Packet Decomposition

The content of dissolved gas in transformer oil is an important index to judge the running state of transformer oil. The content of dissolved gas in transformer oil is an important index to judge the running state of transformer oil. However, under the action of high temperature and strong electric field, the dissolved gas is non-stationary and nonlinear. Therefore, it is necessary to decompose and reconstruct the dissolved gas sequence in transformer oil. However, common time series decomposition methods decompose too many subsequences, greatly increasing the model complexity, which is not conducive to the prediction of gas content in a short time.

WD is a widely used time–frequency analysis tool, mainly through the telescopic translation operation to gradually multi-scale refinement of the signal, and finally achieve the purpose of time subdivision at high frequencies and frequency subdivision at low frequencies. However, WD ignores the high frequency part of the signal. WPD is derived from WD. WPD decomposes the low frequency subsets of the signal while continuing to decompose the high frequency subsets. WPD provides more accurate signal analysis, and it divides the time–frequency plane more accurately than WD. It has been used in various temporal data decomposition [9, 10].

Wavelet packet in WPD is defined as: $\{h_{0k}\}_{k \in \mathbb{Z}}$ and $\{h_{1k}\}_{k \in \mathbb{Z}}$ is an orthogonal mirror filter, the two-scale formula is shown in formula 1:

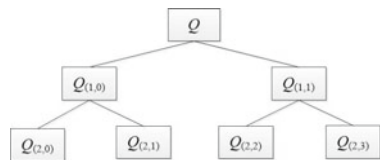
$$\begin{cases} W_{2n}(t) = \sqrt{2} \sum_{k \in \mathbb{Z}} h_{0k} W_n(2t - k) \\ W_{2n+1}(t) = \sqrt{2} \sum_{k \in \mathbb{Z}} h_{1k} W_n(2t - k) \end{cases} \quad (1)$$

when $n = 0$, $W_0(t)$ is the scale function, and the function sequence $\{W_n(t)\}_{n \in \mathbb{Z}}$ corresponding to the scale function is the wavelet packet.

A typical two-layer wavelet packet decomposition is used in this paper, and its schematic diagram is shown in Fig. 1.

As shown above, Q is the original gas concentration sequence, and $Q_{(2,0)}$, $Q_{(2,1)}$, $Q_{(2,2)}$ and $Q_{(2,3)}$ are the components after undergoing two decompositions.

Fig. 1 Two-layer wavelet packet decomposition



3 Long Short-Term Memory

Long short-term memory Network is a special implementation of Recursive Neural Network (RNN). Since RNN tends to produce gradient disappearance during back propagation, its hidden layer is improved. The concept of time sequence is introduced on the basis of RNN neural network, so that the output of the last moment can directly affect the input of the next moment. Thus, LSTM networks with significant application in processing and predicting time series with long intervals and delays are obtained.

LSTM is updated on the basis of RNN, and input gate, forgetting gate and output gate are added in the hidden layer. It can compare the memory information with the current information, and learn the information by setting the valve size to control the degree of memory or forgetting, so as to alleviate the problem of gradient explosion and disappearance in the process of RNN model training [11]. The unit structure diagram is shown in Fig. 2.

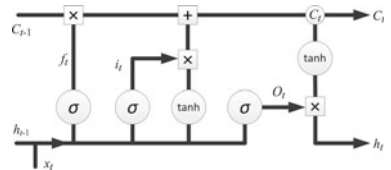
The model contains three inputs: the input sample x_t at the current time, the short-term memory information h_{t-1} at the previous time and the long-term memory information C_{t-1} at the previous time. There are three input gates for the current information and the output gate for the left information. They are the forgetting gate f_t , the input gate i_t and the output gate O_t . The calculation formula (2) is as follows:

$$\begin{cases} f_t = \sigma(w_f \cdot [h_{t-1}, x_t] + b_f) \\ i_t = \sigma(w_i \cdot [h_{t-1}, x_t] + b_i) \\ O_t = \sigma(w_o \cdot [h_{t-1}, x_t] + b_o) \end{cases} \quad (2)$$

where w, b is the weight matrix and bias vector of the control gate, σ is the Sigmoid activation function. After the outputs of the three control gates are calculated from the above formula, the long-term memory information C_t , short-term memory information h_t and the final output y_t of the unit can be further calculated. Tanh is hyperbolic tangent activation function and $*$ is Hadamard product. The calculation formula (3) is as follows:

$$\begin{cases} \tilde{C}_t = \tanh(w_c \cdot [h_{t-1}, x_t] + b_c) \\ C_t = f_t * C_{t-1} + i_t * \tilde{C}_t \\ h_t = o_t * \tanh(C_t) \\ y_t = w_y h_t + b_y \end{cases} \quad (3)$$

Fig. 2 Long short-term memory network structure



4 Crisscross Optimization Algorithm

Crisscross optimization algorithm is a newly developed heuristic algorithm proposed by Meng, A [12, 13]. Its main characteristics are two kinds of interactional crossover operators, namely horizontal crossover operator and vertical crossover operator. The former uses half of the population to search for new solutions in an independent hypercube with a high probability, while searching in their respective peripherals with a low probability. This cross-border search method can reduce the search blind spots and enhance the global search capability. The latter plays an important role in maintaining population diversity and promoting stagnation dimension to jump out of local minimum through a unique transboundary way. In CSO algorithm, the population in which the 2 operators alternately breed offspring individuals at each iteration is called the mean solution, and only those offspring individuals who are more suitable than the parent can survive in the new generation. Obviously, CSO algorithm maintains the individual optimal solution from generation to generation, greatly speeding up the convergence process of the population.

Horizontal crossover is a cross-boundary search mechanism that ensures global search capability and operates on all dimensions between two different individuals. Suppose there is a population H , the i -th parent H_i and the j -th parent H_j perform transverse crossover operation in the d dimension, The expression (4) and (5) of the mean solution (descendant individual) obtained by the crossover is:

$$S_h(i, d) = r_1 H(i, d) + (1 - r_1) H(j, d) + c_1 (H(i, d) - H(j, d)) \tag{4}$$

$$S_h(j, d) = r_2 H(j, d) + (1 - r_2) H(i, d) + c_2 (H(j, d) - H(i, d)) \tag{5}$$

where r_1 and r_2 are random numbers between $[0,1]$; c_1 and c_2 are random numbers between $[-1,1]$. $S_h(i, d)$ and $S_h(j, d)$ are two newly generated mean solutions.

Longitudinal crossover is aimed at two random dimensions of all individuals, and the crossover operator is used to complete the crossover operation with a certain probability p_v . The most important characteristic of this crossover method is to keep the diversity of the population and prevent the population from convergence stagnation and falling into local optimum. Supposing that d_1 and d_2 are two different dimensions of individual i . According to Eq. (6), the mean solution is generated through longitudinal crossover.

$$S_v(i, d_1) = r H(i, d_1) + (1 - r) H(i, d_2) \tag{6}$$

where $r \in (0,1)$; $i \in (1, M)$; $d_1, d_2 \in N(1, D)$; M is population quantity; D is the dimensional quantity of the population. $S_v(i, d_1)$ is the newly generated mean solution.

The competitive operator mainly gives the opportunity of competitive selection between offspring population and parent population. The offspring can only be preserved when they have better performance than the parent, so that the population can quickly converge and achieve global optimization. It is this kind of double cross and competition mechanism that makes CSO algorithm have powerful searching ability. The number of hidden layer nodes m and the initial learning rate r_{lr} in LSTM network have great influence on the prediction results. The crisscross algorithm performs better than other swarm intelligence algorithms in the optimization process. Therefore, the crisscross algorithm is proposed to optimize the m and r_{lr} parameters of LSTM.

5 Network Prediction Model Based on WPD-CSO-LSTM

The previous section decomposed the nonlinear gas concentration into multiple subsequences, which are now input into the CSO-LSTM network prediction model. The specific modeling process is shown in Fig. 3. Where i is the number of iterations and i_{\max} is the maximum number of iterations.

The specific steps are as follows:

Step 1: The data of 7 gases dissolved in transformer oil are used as the input of the model and decomposed into multiple sub-series using the WPD algorithm.

Step 2: Normalize the subsequence and map the data between $[0,1]$; Further, divide the data samples into the training set and test set according to the ratio of 9:1. The normalized formula (7) is

$$x^* = \frac{x - x_{\min}}{x_{\max} - x_{\min}} \quad (7)$$

where x^* is the normalized data; x_{\max} , and x_{\min} are the maximum and minimum values of the data set respectively, and x is the original data.

Step 3: Initialize the number of LSTM neurons m , the range of values of the learning rate r_{lr} , and the CSO parameters.

Step 4: The model is trained using the training set, and the average root mean square error of the prediction results is used as the fitness value of each particle.

Step 5: The particles are crossed horizontally and vertically in turn. The location and information of the optimal particle, as well as the optimal local solution, and global optimal solution of each iteration, are recorded.

Step 6: If the maximum number of iterations is reached, output the optimal parameters m and r_{lr} ; otherwise, return to Step 4.

Step 7: The optimal parameters are applied to the LSTM model, and the subsequences are reconstructed to obtain the true predicted values of the seven gases.

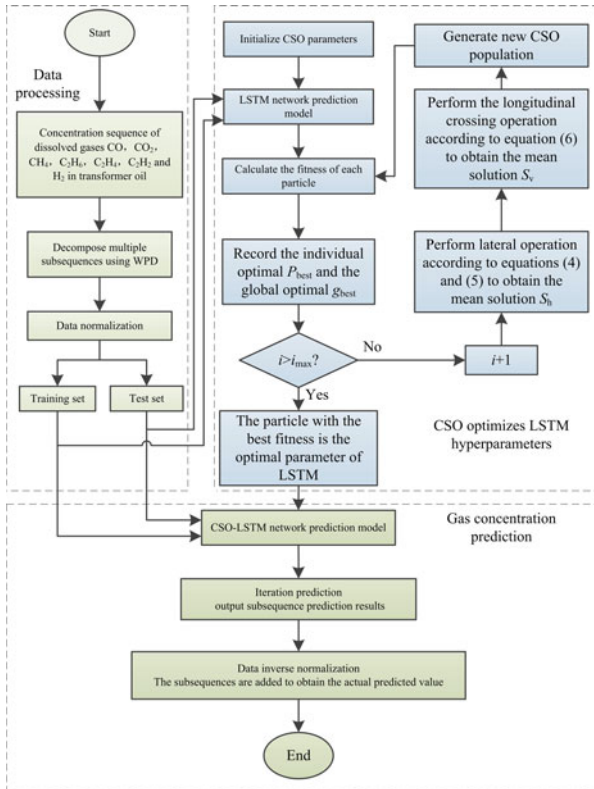


Fig.3 Flow chart of WPD-CSO-LSTM

6 Example Analysis

6.1 Prediction Model Evaluation Index

In this paper, three evaluation indexes were selected to verify the prediction effect of the WPD-CSO-LSTM network model and other network models, including root mean square error (RMSE) and mean absolute percentage error (MAPE). The calculation formula is shown in formulas (8) to (9):

$$E_{RMSE} = \sqrt{\frac{1}{n} \sum_{i=1}^n (y_{pre} - y)^2} \quad (8)$$

$$E_{MAPE} = \frac{1}{n} \sum_{i=1}^n \left| \frac{y_{pre} - y}{y} \right| \quad (9)$$

where: y_{pre} is the predicted value, y is the real value, and \bar{y} is the average value of the real value.

6.2 Partition of Data Sets

To verify the accuracy of the WPD-CSO-LSTM prediction model, chromatographic monitoring data of a 330 kV transformer oil are selected as an example. A total of 629 groups of monitoring data from January 10, 2020 to September 30, 2021 with a monitoring period of 24 h are selected as data samples. In this study, the gas concentration units are unified as ppmv.

The data set is divided into 10-time steps. 576 sets of monitoring data from January 10, 2020 to August 7, 2021 are used as the training set, and 53 sets of monitoring data from August 8, 2021 to September 30, 2021 are used as the test set. Limited by space, this paper takes the time series data of dissolved C_2H_2 concentration in oil as an example for detailed analysis.

6.3 Data Processing

The WPD algorithm is used to decompose the concentration of ethylene gas into four subsequences, as shown in Fig. 4.

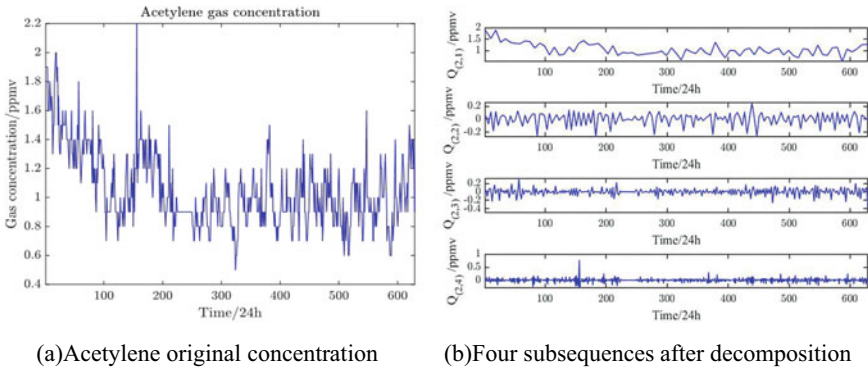


Fig. 4 WPD decomposition of C_2H_2

6.4 Experimental Results and Analysis

To verify the effectiveness of the model, the same training set, and the same number of iterations are used to train WPD-PSO-LSTM, WD-CSO-LSTM, and WPD-LSTM models respectively. Figure 5 shows a line graph of the predicted versus actual values for the 53 test sets from different algorithmic models.

As can be seen from the figure, all the four algorithm models involved have good predictive performance. The WPD-CSO-LSTM prediction model proposed in this paper has a better prediction effect, and a better fitting ability for the actual data. The prediction curve obtained has the highest accuracy, and is consistent with the actual gas content change trend.

The proposed model in this paper is compared with WPD-PSO-LSTM, WD-CSO-LSTM, and WPD-LSTM, and the evaluation metrics are shown in Table 1. From the analysis, it can be obtained that compared to the WD-CSO-LSTM prediction model, the metrics E_{RMSE} and E_{MAPE} of the WPD-CSO-LSTM prediction model are reduced by 35.29% and 35.45%, respectively. This indicates that in WPD is better than WD algorithm in this paper.

Compared with the WPD-LSTM prediction model, the WPD-CSO-LSTM prediction model and WPD-PSO-LSTM prediction model have reduced the E_{RMSE} metrics by 77.24% and 48.97%, and the E_{MAPE} metrics by 78.08% and 49.40%, respectively. This indicates that optimizing the LSTM prediction model using the optimization

Fig. 5 Prediction results of different models

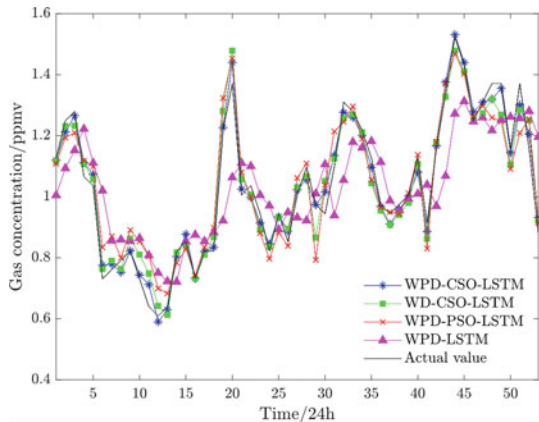


Table 1 Evaluation index values of four models

Prediction model	E_{RMSE}	$E_{MAPE}/\%$
WPD-CSO-LSTM	0.033	2.640
WD-CSO-LSTM	0.051	4.090
WPD-PSO-LSTM	0.074	6.094
WPD-LSTM	0.145	12.044

Table 2 Evaluation indexes for each model prediction

Type of gas		Index	Prediction model			
			WPD-CSO-LSTM	WD-CSO-LSTM	WPD-PSO-LSTM	WPD-LSTM
1	CH ₄	E_{RMSE}	0.084	0.166	0.146	0.227
		$E_{MAPE}/\%$	1.334	2.187	1.916	3.669
2	C ₂ H ₆	E_{RMSE}	0.026	0.058	0.084	0.098
		$E_{MAPE}/\%$	0.406	0.914	1.420	1.577
3	C ₂ H ₄	E_{RMSE}	0.025	0.041	0.068	0.080
		$E_{MAPE}/\%$	0.995	1.782	2.680	3.077
4	H ₂	E_{RMSE}	0.063	0.102	0.086	0.174
		$E_{MAPE}/\%$	0.996	1.843	1.445	3.077
5	CO	E_{RMSE}	2.697	4.202	4.773	5.278
		$E_{MAPE}/\%$	0.592	0.915	1.062	1.314
6	CO ₂	E_{RMSE}	9.020	18.036	21.847	31.065
		$E_{MAPE}/\%$	0.430	0.978	1.157	1.599

algorithm has better prediction results in dealing with time series problems, which reflects the necessity of parameter optimization for LSTM models.

The WPD-CSO-LSTM prediction model has 55.41% and 56.68% lower E_{RMSE} and E_{MAPE} , respectively, compared with the WPD-PSO-LSTM prediction model. This indicates that the LSTM prediction model optimized by CSO algorithm improves the prediction accuracy under the same number of iterations.

6.5 Experimental Results of Other Gas Concentration Prediction

As can be seen from Table 2, compared with WPD-PSO-LSTM, WD-CSO-LSTM, and WPD-LSTM models, the prediction accuracy of dissolved gases in other oils is also higher.

7 Conclusion

This paper combines the current research hotspots in the field of deep learning, addresses the problems of insufficient accuracy of dissolved gas prediction in transformer oil and long prediction time of neural networks, and proposes a network model based on wavelet packet decomposition and longitudinal crossover algorithm

to optimize the long and short term memory for tracking and predicting the change pattern of dissolved gas concentration in transformer oil in order to discover potential transformer faults faster. The following conclusions are drawn.

- 1) The WPD method is used to decompose the original gas sequence in transformer oil, and both high-frequency components and low-frequency components are properly processed to reduce the mutual interference between different time information. The overall prediction performance of the network model is improved, and the features of the original sequence are mined at a deeper level to reduce the prediction difficulty.
- 2) Optimization of hyperparameters in the temporal attention mechanism LSTM network model using the CSO algorithm to improve the prediction accuracy of the LSTM network. The disadvantages of the PSO algorithm such as long iteration time and local convergence are solved.
- 3) The experiments show that using the same dissolved gas concentration data set in oil and under the same iteration conditions, the WPD-CSO-LSTM model proposed in this paper can reach the optimal solution faster, with lower average relative error and higher prediction accuracy than the WD-CSO-LSTM, WPD-PSO-LSTM and WPD-LSTM model.

Acknowledgements This research is supported by the National Natural Science Foundation of China (Grant NO.62073084).

References

1. Li, G., Yu, C., Liu, Y., Fan, H., Wen, F., Song, Y.: Challenges and prospects of fault prognostic and health management for power transformer. *Autom. Electric Power Syst.* **41**(23), 156–167 (2017) (in Chinese)
2. Singh, S., Bandyopadhyay, M.N.: Duval triangle: a noble technique for DGA in power transformers. *Int. J. Electr. Power Eng.* **4**(3), 193–197 (2012)
3. Liu, X., Zhang, P., Zhou, J., Tian, Y., Wang, F., Ling, X.: Gray model based on $\cos(x^\alpha)$ transformation and its application in the prediction of gas concentration in transformer oil. *J. Xihua Univ. (Nat. Sci. Edn.)* **32**(02), 79–83(2013) (in Chinese)
4. Deng, Y., Zhang, W., Liang, J., Wu, R.: Prediction of the trends in the data of dissolved gas production in transformer oil based on time series analysis. *Smart Grid* **4**(08), 744–748 (2016) (in Chinese)
5. Wei, C., Tang, W., Wu, Q.: Dissolved gas analysis method based on novel feature prioritisation and support vector machine. *Electric Power Applications Let* **8**(8), 320–328 (2014)
6. Malik, H., Tarkeshwar, R.K.J.: Make use of DGA to carry out the transformer oil-immersed paper deterioration condition estimation with fuzzy-logic. *Procedia Engineering* **30**, 569–576 (2012)
7. Liu, K., Gou, J., Luo, Z., Wang, K., Xu, X., Zhao, Y.: Prediction of dissolved gas concentration in transformer oil based on PSO-LSTM model. *Power Syst. Technol.* **44**(07), 2778–2785 (2020) (in Chinese)
8. Chen, T., Chen, W., Li, X., Zhang, H., Zhou, Z.: Dissolved gas prediction in transformer oil based on EMD and GCT. *High Volt. Apparatus* **58**(04), 70–79 (2022). (in Chinese)

9. Sun, Y., Cao, Y., Li, P.: Fault diagnosis for train plug door using weighted fractional wavelet packet decomposition energy entropy. *Accident Anal. Prevent.* **166**, 106549 (2022)
10. Wang, H., Wang, W., Du, Y.J., et al.: Improving annual precipitation prediction using extreme learning machine with wavelet packet decomposition (2021)
11. Chuye, Hu., Zhong, Y., Yiqi, Lu., Luo, X., Wang, S.: A prediction model for time series of dissolved gas content in transformer oil based on LSTM. *J. Phys. Conf. Ser.* **1659**(1), 012030 (2020)
12. Yin, H., Wu, F., Meng, X., Lin, Y., Fan, J., Meng, A.: Crisscross optimization based short-term hydrothermal generation scheduling with cascaded reservoirs. *Energy* **203**, 117822 (2020)
13. Meng, A., Chen, S., Zuhong, Ou., Ding, W., Zhou, H., Fan, J., Yin, H.: A hybrid deep learning architecture for wind power prediction based on bi-attention mechanism and crisscross optimization. *Energy* **238**, 121795 (2022)

Digital Twin Model of Air-Immersed Transformer Based on Electro-Thermal Simulations



Hui Qin, Xin Lin, Qideng Luo, Hengwang Zhou, Jing Fu, Danyang Qu,
and Lidan Chen

Abstract A model-driven digital twin (DT) model of a certain type air-immersed transformer is proposed. First, a three-dimensional geometric model of the power transformer is built based on ANSYS Maxwell platform, including the iron core, windings, etc. Then, a digital model of the characteristic parameterization of the transformer in the digital space is established. The electromagnetic field and the temperature field based on ANSYS Workbench platform are coupled. Also, The temperature distribution of the air-immersed transformer core-winding module under six typical different working conditions is studied, and the hot spot location and temperature distribution rule under different working conditions are obtained. The simulation results of magnetic flux density, voltage and current under different operating conditions, losses and theoretical values show that the proposed DT model can effectively reflect the physical mechanism of the transformer. In addition, the

H. Qin · X. Lin · Q. Luo · H. Zhou
Power Grid Planning Research Center, Guangxi Power Grid Co., Ltd., Nanning 530023, China
e-mail: 517544316@qq.com

X. Lin
e-mail: lin_xin@gx.csg.cn

Q. Luo
e-mail: luo_qd@gx.csg.cn

H. Zhou
e-mail: zhou_hw@gx.csg.cn

J. Fu
Energy Planning Research Center, China Energy Engineering Group Guangxi Electric Power Design Institute Co., Ltd., Nanning 530007, China
e-mail: 2270406696@qq.com

D. Qu
Guangzhou Development New Energy Co., Ltd., Guangzhou 510623, China
e-mail: 1093800167@qq.com

L. Chen (✉)
Department of Maritime Engineering, Guangzhou Maritime University, Guangzhou 510725, China
e-mail: chenld@gcu.edu.cn

simulated results show that the iron core temperature does not rise with the increase of the load rate and the winding temperature rises with the increase of the load rate.

Keywords Air-immersed transformer · Digital twin (DT) · Electromagnetic thermal coupling · Finite element analysis

1 Introduction

With the in-depth integration of information technology and energy fields, the construction of digital power grid has become a current hot spot, which puts forward new requirements for power equipment [1]. The digital twin (DT) is considered to be one of the key technologies to promote the digital and intelligent development of the power equipment field [2]. The construction of a DT model of power equipment can realize the functions of self-diagnosis [3, 4], life cycle management [5], predictive maintenance and other functions of power equipment, and can use DT model to simulate hundreds of future scenarios to understand the performance impact of different working conditions and other factors [6], so as to ensure power grid security, improve the level of power grid operation, promote the construction of digital power grid, and inject new vitality into the power system [7]. The research on DT of the power equipment is still in its infancy [8], and how to achieve digital twins of power equipment has become an urgent problem to be solved.

At present, a lot of research on digital twins of power equipment has been carried out. In China, the joint team of Guizhou Power Grid Corporation and Xi'an Jiaotong University conducted a temperature field study on a distribution switchgear based on DT technology against the background that abnormal temperature status during the operation of the distribution switchgear would lead to safety hazards and affect the reliability of power supply. The authors in [9] established the DT calculation process and simulation model of the side casing of the converter transformer valve-side bushing based on the field data, and verified the accuracy of the model through the temperature rise test. In [10], the authors propose a reconstruction method of the GIS barrel DT model based on real site cloud data, and establish four typical fault conditions, then the temperature change is simulated based on ABAQUS software.

As one of the important power grid equipment, relevant enterprises and researchers have also carried out research on the DT model of power transformers. The authors of [11] proposed a multi-physics DT implementation method for oil-immersed transformer based on Microsoft Azure IoT and ANSYS Twin Builder, which calculated the real-time temperature field distribution of transformer cores and windings by using the real-time simulation results of the DT model. Considering the transformer electrothermal characteristic parameters such as transformer winding current, winding hot spot temperature and oil temperature, a short-circuit fault identification method between turns of oil-immersed transformer based on electrothermal characteristic fusion analysis is proposed in [12].

This paper applies the DT technology to the construction of the working characteristic model of the air-immersed transformer. The core-winding module of the air-immersed transformer is modeled and simulated by coupling the electromagnetic field and the temperature field based on ANSYS Workbench platform. The magnetic flux and loss parameters of the air-immersed transformer core and the winding module under different working conditions and the distribution of the temperature field are obtained, and the DT simulation model of the operating characteristics of the air-immersed transformer is realized.

2 DT Modeling Scenario and Parameters

2.1 The Overall Scenario for DT Modeling and Simulation

The overall scenario flowchart for digital twin modeling and simulation of air-immersed transformer is shown in Fig. 1.

The development of the digital twin of the power transformer was completed in four main steps. First, physical object is selected, then the structural parameters and electrical parameters are obtained. Second, the three-dimensional geometric model of the power transformer will be built by ANSYS Maxwell software in which the ‘RMxprt’ module is used. In addition, to derive the mechanism of the transformer, we adopt the automatic meshing. Third, the electrical and temperature field simulation are proposed. Finally, the 2th level DT integration model of the transformer is completed based on the above three steps. The electromagnetic characteristics and temperature characteristics and geometric modeling are modeled and verified.

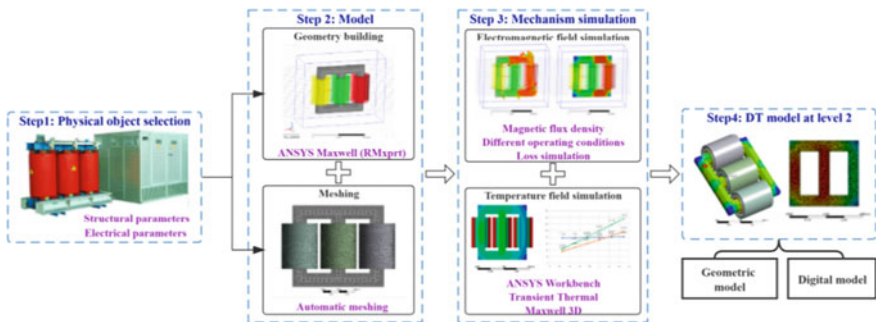


Fig. 1 The overall flowchart for model-driven DT model of the air-immersed transformer

Table 1 Detailed electrical parameters of the air-immersed transformer

Type	Value	Type	Value
Rated voltage	6.3/20 kV	Rated capacity	1770 kVA
Number of phases	3	Rated current	93/47 A
Number of the junction group	YNd11	Rated frequency	50 Hz
Tap range	$\pm 4 \times 2.5\%$	Heat resistance rating of insulation	F

Table 2 Detailed structural parameters of the air-immersed transformer

Low voltage windings	Value	High voltage windings	Value	Iron core	Value
Winding height /mm	1460	Winding height /mm	1460	The iron leg to the center distance/mm	1200
Inner radius /mm	283	Inner radius /mm	440	Core height/mm	2196
Outer radius /mm	370	Outer radius /mm	555		
Turns	113	Turns	223		

2.2 The Parameters of the Air-Immersed Transformer

In this work, we build a DT model for an air-immersed transformer at level 2 [13]. We selected an air-immersed transformer with rated voltage of 6.3/20 kV and rated capacity of 1770kVA. The electrical parameters and structural parameters of the air-immersed transformer used in this paper are shown in Table 1 and Table 2.

3 Digital Twin Model of Air-Immersed Transformers

The operating characteristics of air-immersed transformers mainly include electromagnetic characteristics and temperature characteristics [14]. This section models these two operating characteristics by ANSYS Maxwell software and ANSYS Thermal modules.

3.1 Model Building and Meshing

To reduce the workload of pre-modeling and optimize modeling efficiency, the ANSYS Maxwell platform's built-in module library "RMxpvt" [15] is used, which provides users with dozens of common design templates such as iron cores and coils. It is modeled according to the core-winding parameters in Table 1 and Table 2. This paper uses the element length-based method for meshing, the solution area (blue

rectangular box) sets the maximum value of the meshing element to 8000, and the core-winding model sets the maximum value of the meshing element to 80,000.

Load and Boundary Conditions Setting. The heat source of the air-immersed transformer is mainly determined by the internal core-winding loss. Maxwell 3D's calculated loss values are transmitted from the Solution to the Transient Thermal module as heat inputs via a coupling link. The heat dissipation method is mainly based on air convection heat dissipation, which mainly sets the convective heat dissipation setting of the iron-winding model as a whole, and sets the heat dissipation coefficient to $10W/m^2 \cdot ^\circ C$, and the initial temperature is set to $22\ ^\circ C$. With reference to the temperature field simulation principle, the model is set for thermal radiation, and two main aspects are mainly set: 1) thermal radiation of the iron core to the low-voltage winding; 2) Low-voltage winding to high-pressure winding thermal radiation.

3.2 Modeling of Electromagnetic Characteristics

Electromagnetic Calculations Based on Finite Element Analysis. The finite element analysis method is used to calculate the electromagnetic field, which divides the magnetic field to be studied into multiple sub-magnetic fields, and combines the Maxwell equation and the initial and boundary conditions to calculate these sub-magnetic fields independently, thereby simplifying the electromagnetic problem and improving the efficiency of the solution. When solving the problem of the edge value of the electromagnetic distribution in the electromagnetic field, the partial differential equation used is derived from Maxwell's equation, which is shown in (1).

$$\left\{ \begin{array}{l} \oint_S \vec{D} d\vec{S} = q \\ \oint_S \vec{B} d\vec{S} = 0 \\ \oint_S \vec{E} d\vec{l} = - \oint_S \frac{\partial \vec{B}}{\partial t} d\vec{S} \\ \oint_S \vec{H} d\vec{l} = I + \oint_S \frac{\partial D}{\partial t} d\vec{S} \end{array} \right. \quad (1)$$

where D is the electrical induction intensity; B is the magnetic induction intensity; E is field strength; H is the magnetic field strength; q is the amount of charge in the electromagnetic field, and I is the current.

Core Loss. Core losses consist mainly of hysteresis losses, eddy current losses, and additional losses. In general, the value of the additional loss is very small compared to the above two losses, so the additional loss value is generally ignored in the calculation. The formula for calculating iron loss is shown in (2).

$$P_{Fe} = P_h + P_e = K_h B_{\max}^2 f + K_c (B_{\max} f)^2 \quad (2)$$

where P_{Fe} is the iron loss; P_h is the hysteresis loss; P_e is the eddy current loss; K_h is the hysteresis loss coefficient; B is the magnetic flux density; f is for frequency; K_c is the eddy current loss coefficient.

Winding Loss. The windings of air-immersed transformers are mainly made of copper materials, so the loss of the windings generally refers to the loss caused by the resistance of the copper material. Its loss is proportional to the resistor R and proportional to the square of the current (I^2). Then, the winding loss calculation formula can be shown in (3).

$$P_{DC} = 3I_{1n}^2 R_{1,120^\circ\text{C}} + 3I_{2n}^2 R_{2,120^\circ\text{C}} \quad (3)$$

where P_{DC} is for the winding coil loss; I_{1n} is the primary side current; I_{2n} is the secondary side current; $R_{1,120^\circ\text{C}}$ is a primary side resistor; $R_{2,120^\circ\text{C}}$ is a secondary side resistor.

3.3 Modeling of the Temperature Characteristics

The temperature characteristic modeling is divided into two categories: steady-state and transient, and the temperature field is mainly an analysis of its heat transfer [14]. In general, heat transfer is divided into three forms, and the model is constructed as follows:

Heat Conduction. Heat transfer exists between two units that are in contact with each other and have different temperatures. For air-immersed transformers, it refers to the process of transmitting heat production between the core and windings of the loss, which can be described in thermodynamics by Fourier's law of heat transfer, as shown in Eq. (4).

$$q = -\lambda \frac{\partial t}{\partial x} n \quad (4)$$

where q is the heat flow density, in W/m^2 ; λ is the thermal conductivity, in $\text{W}/\text{m} \cdot \text{K}$.

Thermal Convection. Thermal convection occurs in fluids (such as air, liquids, etc.), where heat transfer occurs due to the intermingling of fluids with different temperatures. Due to the large temperature difference between the gas and the air on the heat-producing surface of the air-immersed transformer, the phenomenon of thermal convection occurs. Thermal convection processes can be described in thermodynamics by Newton's law of cooling, as shown in (5) and (6).

$$q = h \cdot (t_w - t_f) \dots (t_w > t_f) \quad (5)$$

$$q = h \cdot (t_f - t_w) \dots (t_w < t_f) \quad (6)$$

where q is the convection heat transfer coefficient, in $W/m^2 \cdot k$; t_w is the solid temperature; t_f is the fluid temperature.

Thermal Radiation. Thermal radiation dissipates heat in the form of electromagnetic waves. For air-immersed transformers, the thermal radiation process mainly occurs in two aspects: 1) the iron core radiates heat to the low-voltage windings; 2) Low-voltage windings radiate heat to high-pressure windings. The description of thermal radiation in thermodynamics is shown in Eq. (7).

$$P = \varepsilon \delta T^4 \quad (7)$$

where P is radiated power; ε is the emissivity; δ is the Stefan-Boltzmann constant.

4 Simulation Analysis

4.1 Electromagnetic Field Simulation

Settings. The excitation settings of low-voltage windings and high-voltage windings is shown as Fig. 2. In addition, the ANSYS Maxwell 3D solver is used, the simulation time is set to 40 ms, the simulation step is 0.0005 s, a total of 80 simulation cycles, at this time the air-immersed transformer is considered to have reached a stable operating state.

Electromagnetic Field Simulation Analysis. Through an ANSYS Maxwell 3D analysis, the magnetic flux density and magnetic field line distribution are obtained.

In this paper, the simulation models of six typical working conditions (25% load rate to 150% load rate) are set by external circuit excitation, and the simulation values and theoretical values of the secondary lateral line voltage and secondary lateral current under the six operating conditions are shown in Table 3 and Table 4.

The core loss simulation results are shown in Fig. 3, and it can be seen that the eddy current loss and hysteresis loss change periodically from 20 ms (40 cycles), and the core loss begins to stabilize.

4.2 Temperature Field Simulation

Combined with the operation of the air-immersed transformer and the complexity of this model, in order to make the simulation effect fully presented, the simulation is

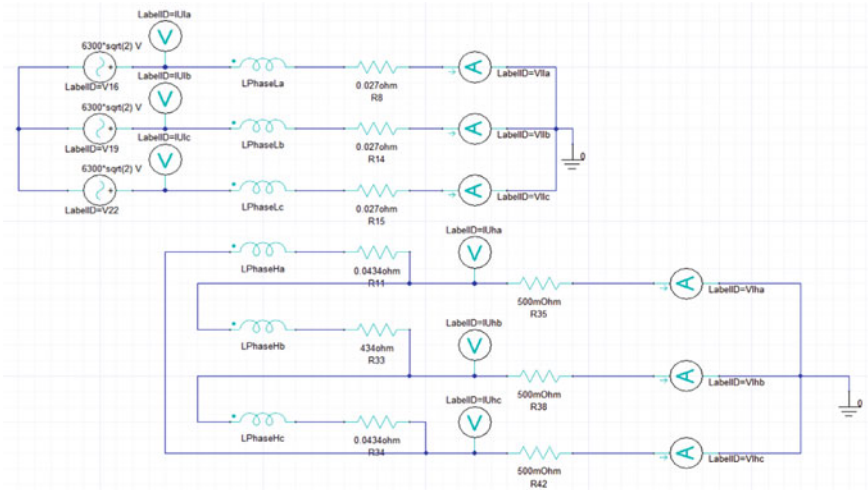


Fig. 2 External circuit excitation settings

Table 3 Line voltage of the secondary lateral

Load rate	The simulated value (kV)	Theoretical value (kV)	Relative error (%)
25%	20.61	20	3.05
50%	20.65	20	3.25
75%	20.86	20	4.3
100%	20.66	20	3.3
125%	20.61	20	3.05
150%	20.97	20	4.85

Table 4 Line current of the secondary lateral

Load rate	The simulated value (kV)	Theoretical value (kV)	Relative error (%)
25%	12.14	11.9	2.02
50%	25.1	23.8	5.46
75%	35.2	35.6	1.12
100%	48.78	47	3.78
125%	59.52	59.4	0.202
150%	72.7	71.3	1.96

controlled by transient Thermal’s built-in program, and the simulation time is set to 1.44e+005 s, the minimum step size is 0.001 s, and the maximum step size is 1800 s.

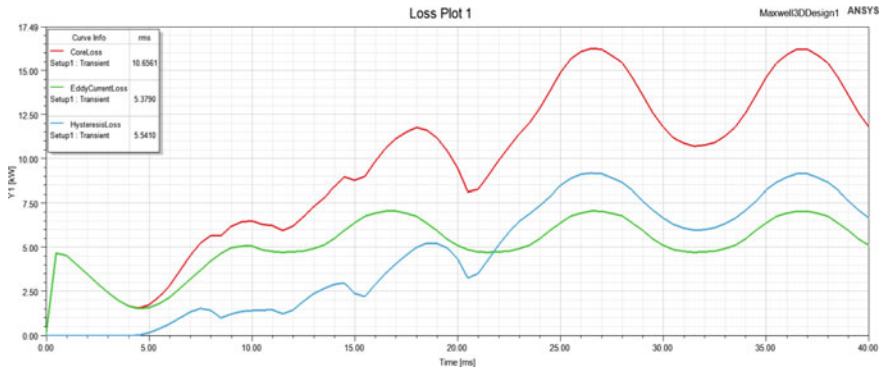


Fig. 3 Simulation results for core loss

Model Coupling and Division. Due to the asymmetry of the electromagnetic field analysis part, the loss of thermogenesis is asymmetrical, and then the temperature field analysis part is also asymmetrical, so it is necessary to use Maxwell 3D for direct coupling with Transient Thermal. The direct coupling method uses coupled variables to solve all physics at once to obtain results for all physics. The geometry, material properties, and losses of the Maxwell 3D platform are coupled to the Transient Temperature Field Analysis Module in the form of data.

In order to improve the accuracy of the transient temperature field calculation and analysis, the core-winding is meshed. This paper uses automatic meshing, which is divided into 115,248 nodes and 64,907 cells, as shown in Fig. 4. The quality factor of the unit of the meshing quality index ranges from 0 to 1, and the value of 1 is the best. The unit mass factor of 90.45% in this paper is greater than 0.6, which is basically concentrated near 0.85, so it is considered to be calculatable.

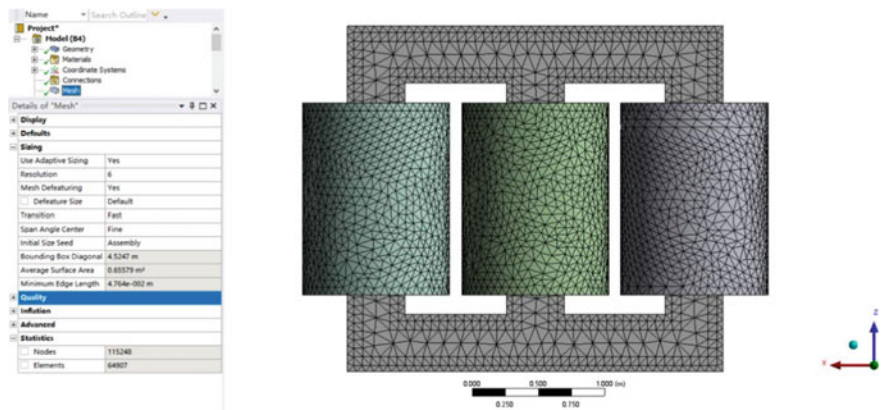
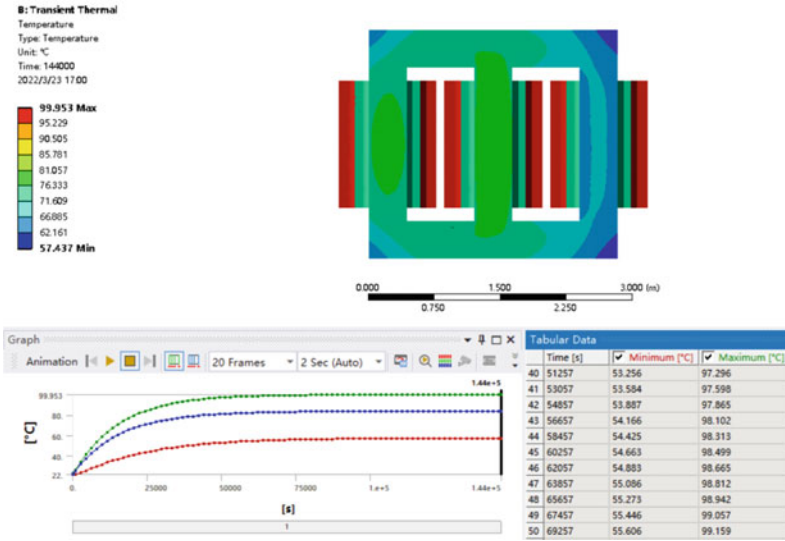


Fig. 4 Meshing for the transformer

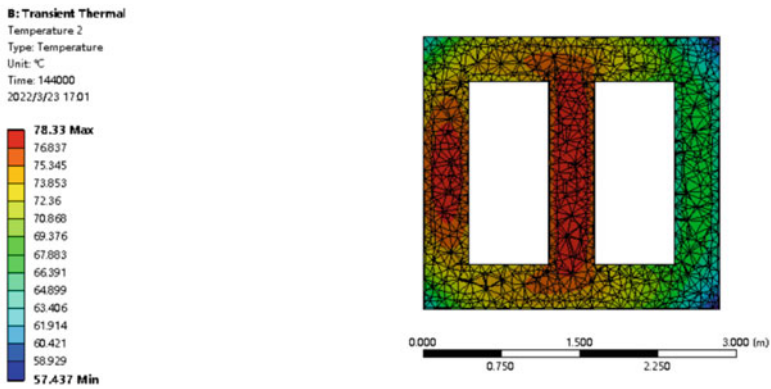
Temperature Field Simulation Analysis. Through transient thermal analysis, the overall temperature distribution of the air-immersed transformer is obtained. The overall temperature, core temperature, low-voltage winding temperature and high-voltage winding temperature distribution of the rated working conditions of the air-immersed transformer are shown in Fig. 5. It can be seen that the overall temperature tends to stabilize when the simulation reaches $5e+004$ s. The maximum overall temperature is $99.953\text{ }^{\circ}\text{C}$ while the minimum temperature is $57.437\text{ }^{\circ}\text{C}$. The maximum temperature of the iron core is $78.33\text{ }^{\circ}\text{C}$, the minimum temperature is $57.437\text{ }^{\circ}\text{C}$. The maximum temperature of the low-voltage winding is $72.932\text{ }^{\circ}\text{C}$, the minimum temperature is $72.148\text{ }^{\circ}\text{C}$, and the maximum temperature of the high voltage winding is $99.953\text{ }^{\circ}\text{C}$, and the minimum temperature is $98.511\text{ }^{\circ}\text{C}$.

From the temperature distribution of the transformer, it can be seen that the air density is proportional to the temperature in the vertical direction, thus the hot air will rise to take away the heat. For the winding, the bottom temperature is low due to the rise of hot air, and the top temperature is low due to better heat dissipation conditions, so the middle of the winding has more heat and the temperature is higher. The temperature field simulation is also carried out for different working conditions, and the highest and lowest temperature data of the core and winding under different working conditions are obtained as shown in Table 5.

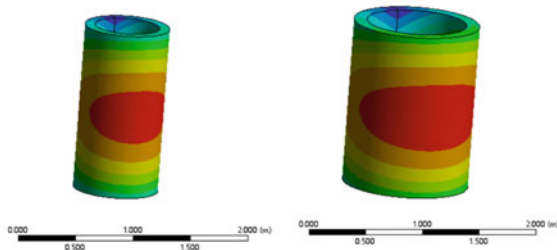
From Table 5, it can be seen that the core loss does not rise with the increase of the load rate during the operation of the air-immersed transformer, and the core temperature is basically unchanged. The winding temperature is positively correlated with the load rate and rises with the load rate.



(a) Overall temperature distribution of the air-immersed transformer



(b) Temperature distribution of iron core



(a) Temperature distribution of low voltage winding and high voltage winding

Fig. 5 Temperature distribution of the simulated transformer

Table 5 Temperature distribution under different work conditions

Load rate	Core temperature (°C)	Low voltage windings temperature (°C)	High voltage windings temperature (°C)
25%	77.322/59.221	35.402/35.195	42.341/41.965
50%	77.52/58.926	48.351/47.945	62.125/61.384
75%	78.001/58.481	60.857/60.259	81.334/80.236
100%	78.33/57.437	72.932/72.148	99.953/98.511
125%	80.191/57.082	84.593/83.63	117.98/116.2
150%	81.481/55.999	95.853/94.718	135.42/133.32

5 Conclusion

In recent years, digital twin technology has been widely used in industrial fields due to its high fidelity, scalability, and operability. In this paper, the electric, magnetic and temperature fields of the air-immersed transformer are simulated by ANSYS Maxwell 3D module and Transient Thermal modules for the purpose of realizing the DT biochemical level 1 and 2 specifications of air-immersed transformer digitization. By analyzing and simulating the magnetic flux density, magnetic field line, voltage, current, loss, temperature distribution and other indicators of the air-immersed transformer, the rationality of the mechanism model is verified, and the temperature distribution of the core and winding under different load rates is obtained: 1) The iron core temperature does not rise with the increase of the load rate; 2) The winding temperature rises with the increase of the load rate. The results of this air-immersed transformer modeling provide a reference for the realization of digital twins of electrical equipment. On the basis of this work, according to the five levels of DT chemistry, we can continue to improve the level 2 DT model, the improvement idea is to extract the node data of the mechanism model proposed in this paper by using the ANSYS Dynamic ROM Pre add-on module, and to downgrade the model in three dimensions through the ANSYS Twin Builder platform.

References

1. Tao, F., Zhang, H., Liu, A., et al.: Digital twin in industry: state-of-the-art. *IEEE Trans. Industr. Inf.* **15**(4), 2405–2415 (2018)
2. Shen, C., Cao, Q., Jia, M., et al.: Concepts, characteristics and prospects of application of digital twin in power system. *Proc. CSEE* **42**(02), 487–498 (2022). (in Chinese)
3. Yang, Y., et al.: State evaluation of power transformer based on digital twin. In: *International Conference on Service Operations and Logistics, and Informatics (SOLI)*, Zhengzhou, pp. 230–235. IEEE (2019)
4. Kolesnikov, I.E., Korzhov, A.V., Gorshkov, K.E.: Digital program for diagnosing the status of a power transformer. In: *Global Smart Industry Conference (GloSIC)*, Chelyabinsk, pp. 315–321. IEEE (2020)

5. Jing, Y., Zhang, Y., Wang, X., Li, Y.: Research and analysis of power transformer remaining life prediction based on digital twin technology. In: 3rd International Conference on Smart Power & Internet Energy Systems (SPIES), Shanghai, pp. 65–71. IEEE (2021)
6. Moutis, P., Alizadeh-Mousavi, O.: Digital twin of distribution power transformer for real-time monitoring of medium voltage from low voltage measurements. *IEEE Trans. Power Deliv.* **36**(4), 1952–1963 (2021)
7. Zhou, M., Yan, J., Feng, D.: Digital twin framework and its application to power grid online analysis. *CSEE J. Power Energy Syst.* **5**(3), 391–398 (2019)
8. Zhang, Z., Jiang, J., Cheng, X.: Research on digital twin model of energy equipment. In: 2nd International Conference on Power, Electronics and Computer Applications (ICPECA), Shenyang, pp. 264–268. IEEE (2022)
9. Lin, M., Liu, K., Wang, N., et al.: Characteristics establishment of digital twin model of converter transformer valve-side bushing and analysis of its thermal characteristics. *High Volt. Eng.* **48**(5), 1653–1662 (2022). (in Chinese)
10. Wang, H., Xu, H., Du, Y., et al.: Research on temperature change behavior of key components of GIS barrel based on digital twin model. *High Volt. Eng.* **47**(5), 1584–1594 (2021). (in Chinese)
11. Yang, F., Wu, T., Liao, R., et al.: Application and implementation method of digital twin in electric equipment. *High Volt. Eng.* **47**(05), 1505–1521 (2021). (in Chinese)
12. Zhang, L., Sheng, G., Hou, H., et al.: Detection method of interturn short-circuit faults in oil-immersed transformers based on fusion analysis of electrothermal characteristic. *Power Syst. Technol.* **45**(7), 2473–2482 (2021). (in Chinese)
13. Tao, F., Liu, W., Zhang, M., et al.: Five-dimension digital twin model and its ten applications. *Comput. Integr. Manuf. Syst.* **25**(01), 1–18 (2019). (in Chinese)
14. Susa, D., Lehtonen, M., Nordman, H.: Dynamic thermal modelling of power transformers. *IEEE Trans. Power Deliv.* **20**(1), 197–204 (2005)
15. Wang, L., Zhou, L., Yuan, S., et al.: Improved dynamic thermal model with pre-physical modeling for transformers in ONAN cooling mode. *IEEE Trans. Power Deliv.* **34**(4), 1442–1450 (2019)

Simulation and Lead-In Design of Wall Bushings in Artificial Climate Chamber Under Complex Atmospheric Conditions



Junyi Xia, Ziyu Ma, Peiqi Xiong, Nanxuan Shen, Xuyuan He, Kun He, Li Cheng, and Xingming Bian

Abstract In order to explore the effects of atmospheric conditions on corona discharge under AC/DC composite voltage, it is proposed to build an artificial climate chamber that can simulate complex atmospheric conditions (0.5 ~ 1 atm, $-30 \sim 80^{\circ}\text{C}$, 10 ~ 95% relative humidity) and lead in AC 100 kV (peak voltage) and DC ± 100 kV into the chamber with wall bushings. For the operation safety of the experiment under complex atmospheric conditions, the breakdown voltage is corrected, and the electric field intensity is controlled within corona control value. The finite element method is adopted to calculate the electric field distribution of three wall bushings with different installation positions. According to the simulation results, the best installation position is set to 0.6 m away from the upper wall. This paper provides a useful reference for the lead-in design of equipment insulation structure under complex atmospheric conditions.

Keywords Corona · Artificial climate chamber · Complex atmospheric conditions · Wall bushings · Finite element method

J. Xia · Z. Ma · P. Xiong · N. Shen · X. He · X. Bian (✉)
State Key Laboratory of Alternate Electrical Power System With Renewable Energy Sources,
North China Electric Power University, Beijing 102206, China
e-mail: bianxingming@ncepu.edu.cn

J. Xia · K. He · X. Bian
Tibet Yangbajing High Altitude Electrical Safety and Electromagnetic Environment National
Observation and Research Station, Lhasa 851500, China

L. Cheng
State Key Laboratory of Power Transmission Equipment & System Security and New
Technology, Chongqing University, Chongqing 400044, China
e-mail: chengl16@cqu.edu.cn

© Beijing Paiké Culture Commu. Co., Ltd. 2023
X. Dong et al. (eds.), *The proceedings of the 10th Frontier Academic Forum of
Electrical Engineering (FAFEE2022)*, Lecture Notes in Electrical Engineering 1054,
https://doi.org/10.1007/978-981-99-3408-9_12

1 Introduction

Because the distribution of energy center and load center in China is unbalanced, it is necessary to speed up construction of large-capacity and long-distance transmission system. In order to save the line corridor, the transmission mode of hybrid AC/DC transmission lines [1–3] has been proposed. Corona discharge, radio interference and other electromagnetic environment problems of transmission lines will be affected by the line conditions and environmental factors [4, 5].

In order to effectively and conveniently simulate the electromagnetic environment problems faced by power equipment under complex atmospheric conditions, it is proposed to build an artificial climate chamber that can consider the conditions of air pressure, humidity, and temperature. The outside and inside dimension of the artificial climate chamber are $5.5\text{ m} \times 5.4\text{ m} \times 3.5\text{ m}$ and $4.5\text{ m} \times 4.4\text{ m} \times 2.5\text{ m}$, respectively, with the steel thickness (d_s) of 0.5 m. Different from the previous climate chamber construction [6–8], it is planned to lead AC 100 kV (peak voltage) and DC $\pm 100\text{ kV}$ into the chamber instead of just one type of voltage. The air pressure, temperature and humidity are adjustable in the range of $0.5 \sim 1\text{ atm}$, $-30 \sim 80^\circ\text{C}$ and $10 \sim 95\%\text{RH}$, respectively.

Wall bushings are applied to lead in high voltage from outdoor to indoor. Monga [9] used a 2-D model to optimize the design of high-voltage bushings and found that the optimum design consisted of an internal metal electric field shaper and one grading ring at the top. Nie [10] put forward the method of adding a grading ring to the flange side to reduce the field intensity around the surface of shed and sheath. Zhang [11] built a 3-D model of wall bushing and found that high electric field intensity (E) mainly occurred in metal shield structure and outer grading ring.

Different from the above simulation of wall bushings, the impact of atmospheric factors on the lead-in design of wall bushings is also considered in this paper. The installation position of three wall bushings under complex atmospheric conditions is of great significance for controlling E , preventing breakdown and corona discharge, and ensuring the safety and reliability of the experiment.

2 Breakdown Voltage Correction and Corona Control Value

2.1 Breakdown Voltage Correction

Under complex atmospheric conditions, breakdown may occur when high voltage is applied. Therefore, it is necessary to correct the breakdown voltage. In order to comprehensively consider the effects of air pressure, temperature and humidity on the breakdown voltage, the g -parameter method is used [12]. The method involves air pressure correction coefficient K_1 and humidity correction coefficient K_2 .

K_1 and K_2 are defined as

$$\begin{cases} K_1 = \delta^m \\ K_2 = K^w \end{cases} \quad (1)$$

where δ is the relative density of air, K is a parameter related to the type of test voltage. The K - H/δ relationship diagram should be referred to get the specific value of K . H is absolute humidity, g/m^3 . m and w are related to g .

The parameter g is defined as

$$g = \frac{U_{50}}{500d\delta K} \quad (2)$$

where U_{50} is the 50% breakdown voltage in the actual atmospheric environment. d is the required minimum discharge distance, m.

The breakdown voltage (U) under complex atmospheric conditions is obtained by multiplying the breakdown voltage value (U_0) under standard atmospheric conditions [12] by the atmospheric correction coefficient K_1 ($K_1 = K_1 K_2$), which is supposed to be less than the maximum voltage (100 kV) led into the chamber.

2.2 Corona Control Value

Under complex atmospheric conditions, the corona onset voltage on the conductor surface decreases, and partial discharge may occur. E on the conductor surface at 0.5 atm is calculated by using peek formula corrected by humidity [13]:

$$E_{\text{ons}} = m_0 E_0 \delta \left(1 + \frac{H - 11}{100} \right) \left(1 + \frac{K_0}{\sqrt{\delta r}} \right) \quad (3)$$

where E_{ons} is the corona onset electric field intensity, kV/cm ; m_0 is the roughness coefficient, taken as 0.8; r is the radius of the conductor, taken as 2 cm; K_0 and E_0 is related to the type of applied voltage [13].

According to Eq. (3), under the conditions of 0.5 atm, $t = -30^\circ\text{C}$ and 10% RH, E_{ons} under different types of applied voltage reaches the minimum value. In consideration of humidity fluctuation, conductor cleanliness and other problems, a certain margin coefficient shall be confirmed, which is set as 0.8 in this paper. Consequently, the corona control value of conductors under DC voltage inside the chamber is 13.69 kV/cm , and that under AC voltage indoor is 13.09 kV/cm .

3 Simulation Settings

Composite dry wall bushing is used to lead high voltage into the chamber. Figure 1 shows the sectional view of the FCGW-126 wall bushing. Figure 2 shows the grading measure. An artificial climate chamber with three wall bushings is built in Solid-Works. The geometry file of the model is imported into the finite element simulation software, and a 10 m × 10 m × 10 m air area is established outside the chamber model. The conductivity and relative permittivity of the material are shown in Table 1.

The distribution of E under AC and DC can be obtained by Gauss theorem and two current continuity equations [14]. The artificial climate chamber model is divided by free tetrahedral grid. The maximum cell size is set to 0.55 m, the minimum cell size is set to 5 mm, and the maximum cell growth rate is 1.4. The steel structure is grounded.

Fig. 1 Profile of composite dry wall bushing

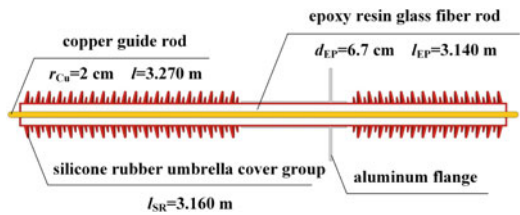


Fig. 2 Wall bushing with grading measure

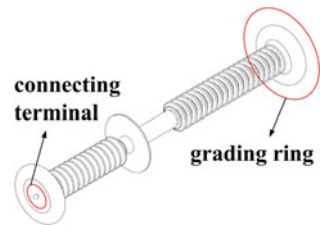


Table 1 Conductivity and dielectric constant of materials

Materials	Air	Cu	Al	Steel	EP	Silicone rubber
Conductivity (S/m)	0.2	5.7×10^7	3.5×10^7	1×10^7	1×10^{-15}	1×10^{-14}
Relative permittivity	1	1×10^{10}	1×10^{10}	1×10^{10}	3.4	3.7

4 Design of Installation Position

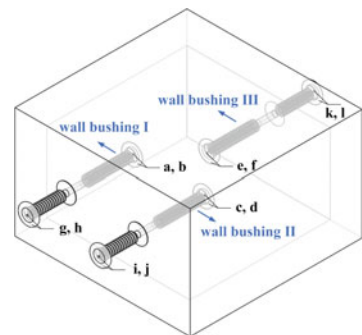
Considering the load-bearing capacity of the wall, as shown in Fig. 3, three wall bushings are installed on two opposite walls, and the bushings are evenly distributed on the same horizontal plane, that is, the distance between wall bushing I and the left wall, the distance between wall bushing II and the right wall and the distance between wall bushing III and the other bushings are 1.125 m. A high electric field area will exist if the distance between wall bushings and the upper wall is too short, which is prone to discharge or even breakdown. Therefore, the distance between wall bushings and the upper wall needs to be carefully considered.

The placement order of three different types of voltage is needed to be considered at first. The total of six cases are shown in Fig. 4. Because of the polarity reversal of AC, it needs to be divided into peak voltage + 100 kV and peak voltage -100 kV. After combining symmetrical electric fields, only case 1 and case 2 marked blue in Fig. 4 are considered when applying potential boundary conditions.

The vertical distance between axes of bushings and the upper wall is set as 0.4 m ~ 1 m, and simulations are conducted every 0.1 m with a total of 7 groups.

E_{max} at No.1–6 ends and on No.1–6 grading rings (marked in Fig. 3) with different vertical distance is simulated, and the data are drawn in Fig. 5, 6. E_{max} outside the chamber is larger than that inside the chamber, but the difference between E_{max} inside and outside the chamber is no that obvious in case 2 than that in case 1. It can be seen that no matter how + DC, -DC and AC are placed, they can meet the requirements of corona control value. At the same time, with the increase of vertical distance, E_{max} decreases, and the decrease rate at the end and on the grading rings inside the chamber is faster than that outside. Comparing the data at 0.4 m and 1 m, the value at ends and on the grading rings decrease by about 10% and 50%, respectively. The change of E_{max} on the grading rings is more obvious than that at the end. Figure 6 show that when the distance is greater than 0.6 m, E_{max} on grading rings tends to be stable. Overall, the bushings can be installed at a distance of 0.6 m from the upper wall.

Fig. 3 Three bushings on two opposite walls. (a, b-No.1 end, grading ring; c, d- No.2 end, grading ring; e, f- No.3 end, grading ring; g, h- No.4 end, grading ring; i, j- No.5 end, grading ring; k, l- No.6 end, grading ring)



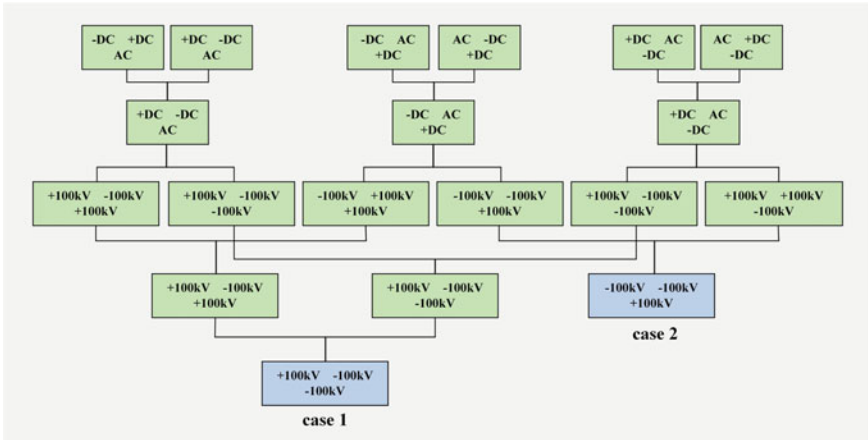


Fig. 4 Considering the placement sequence of three different types of voltage. (The order in the box is wall bushing I, II and III in the order from left to right and from top to bottom)

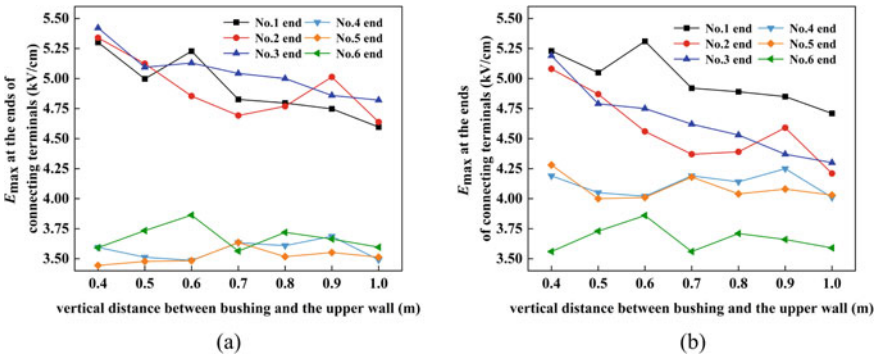


Fig. 5 E_{max} at the end of connecting terminals under different vertical distance between bushings and the upper wall. **a** case 1; **b** case 2

5 Final Design Scheme Verification

5.1 Breakdown Voltage Correction

D is taken as 0.6 m (rod-plane air gap); In the atmosphere of 0.5 ~ 1 atm, 10 ~ 95% RH and $-30 \sim 80^{\circ}\text{C}$, the value of K_1 is 0.445. The breakdown voltage under complex atmospheric conditions is calculated and listed in Table 2.

The corrected DC and AC breakdown peak voltage are greater than 100 kV, so the vertical and horizontal distance listed in the table can meet the requirements. Breakdown will not occur under complex atmospheric conditions.

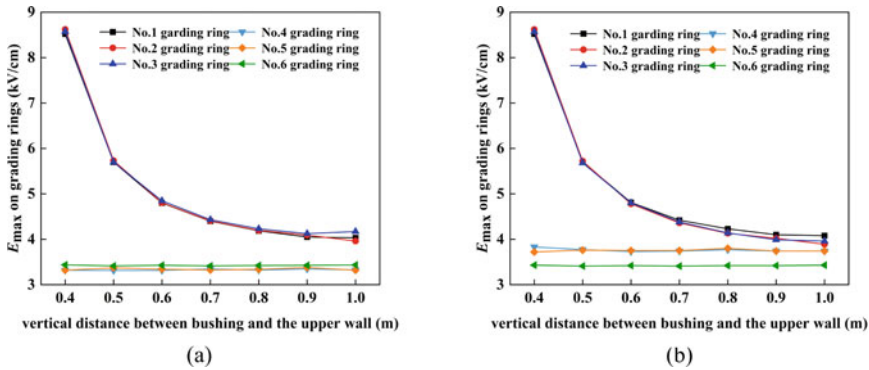


Fig. 6 E_{max} on grading rings under different vertical distance between bushings and the upper wall. **a** case 1; **b** case 2

Table 2 Breakdown voltage correction of different types of air gap under complex atmospheric conditions

d (m)	Meaning of d	Breakdown voltage under standard atmospheric conditions (kV)		Breakdown voltage under complex atmospheric conditions (kV)	
		DC	AC	DC	AC
1.125	Horizontal distance between axes of wall bushing I and III, II and III	625	450	278.1	200.3
2.25	Horizontal distance between axes of wall bushing I and II	1180	980	525.1	436.1
0.6	Vertical distance between axes of wall bushings and the upper wall	260	225	115.7	100.1

5.2 Corona Discharge Verification

E_{max} at the end and on the grading rings are 5.31 kV/cm and 4.81 kV/cm, respectively, which are within the corona control value (13.69 kV/cm indoor under DC voltage, and 13.09 kV/cm indoor under AC voltage), so corona discharge will not occur.

5.3 Final Design Scheme

The distance between the bushing axes and the upper wall is set to 0.6 m. The distance between two wall bushing axes is 1.125 m.

The maximum E_{max} at key parts are listed in Table 3. The overall E_{max} appears at the interface between the copper guide rod and the internal insulation, and the value is

Table 3 Maximum E_{\max} at key parts

Key parts	Maximum E_{\max} (kV/cm)	Key parts	Maximum E_{\max} (kV/cm)
End of copper guide rod and surface of connecting terminal	5.31	Surface of grading ring	4.81
Rod contacted with epoxy	42.30	Silicone rubber contacted with air	9.41

42.68 kV/cm, which is far less than the breakdown strength of the internal insulation [15]. It can be seen from Table 3 that the electric field is uniformly distributed without local abnormal issues. At the same time, the final design scheme has met the requirements of preventing breakdown and corona discharge. Therefore, the final design scheme can ensure the operation safety under complex atmospheric conditions.

6 Conclusions

Firstly, the corona control value is calculated and the breakdown voltage is corrected under complex atmospheric conditions, which provide theoretical support for the design of wall bushings. An artificial climate chamber which can lead in three different types of voltage (+DC, -DC, AC) is designed to provide conditions for corona discharge experiment under composite voltage.

Secondly, the wall bushings with different installation positions are simulated by FEM. The results shows that the bushings should be installed at a distance of 0.6 m from the upper wall.

Acknowledgements This work was supported by the National Natural Science Foundation of China (51877082), 2022 Annual Open Funds of Tibet Yangbajing High Altitude Electrical Safety and Electromagnetic Environment National Observation and Research Station (Grant No. GYB51202201516)

References

1. Ma, Z.Y., et al.: Experimental and numerical study on corona onset threshold under combined AC-DC voltages in wire-plane electrodes. *Int. J. Electr. Power Energy Syst.* **143**, 108479 (2022)
2. He, X.Y., et al.: The role of space charge on corona inception threshold conditions in rod-plane air gaps at DC/AC combined voltage. *IEEE Access* **9**, 125496–125507 (2021)
3. He, Z.C., Zhu, J.Y., Zhu, J., Bian, X.M., Shen, B.Y.: Experiments and analysis of corona inception voltage under combined AC-DC voltage at various air pressure and humidity in rod to plane electrodes. *CSEE J. Power Energy Syst.* **7**(4), 875–888 (2020)

4. Xu, P., Ma, Y.X., Zhu, J., Zhao, L.X., Shen, B.Y., Bian, X.M.: Effect of TiO₂ coating on the surface condition and corona characteristics of positive DC conductors with particle matters. *High Volt.* **7**(1), 147–157 (2022)
5. Huang, C.W., Yin, H., Xu, P.F., Zhang, B., He, J.L., Liu, J.B.: Prediction of radio interference from HVDC transmission lines based on corona discharge characteristics. *High Volt.* **5**(6), 679–687 (2020)
6. He, G.H., Hu, Q., Wu, B., Shu, L.C., Jiang, X.L., Xiao, L.F., Yu, Z.: Influence of freezing water conductivity on the positive corona performance of soft rime ice-covered conductor. *Int. J. Electr. Power Energy Syst.* **112**, 137–143 (2019)
7. Xu, P.F., Zhang, B., Chen, S.M., He, J.L.: Influence of humidity on the characteristics of positive corona discharge in air. *Phys. Plasmas* **23**(6), 063511 (2016)
8. Zhang, B., He, J.L., Ji, Y.M.: Prediction of average mobility of ions from corona discharge in air with respect to pressure, humidity and temperature. *IEEE Trans. Dielectr. Electr. Insul.* **26**(5), 1403–1410 (2019)
9. Monga, S., Gorur, R.S., Hansen, P., Massey, W.: Design optimization of high voltage bushing using electric field computations. *IEEE Trans. Dielectr. Electr. Insul.* **13**(6), 1217–1224 (2006)
10. Nie, D.X., Zhang, H.L., Chen, Z., Shen, X., Du, Z.Y.: Optimization design of grading ring and electrical field analysis of 800 kV UHVDC Wall wall bushing. *IEEE Trans. Dielectr. Electr. Insul.* **20**(4), 1361–1368 (2013)
11. Zhang, S.L., Peng, Z.R., Liu, P., Li, N.Y.: Design and dielectric characteristics of the ± 1100 kV UHVDC wall bushing in China. *IEEE Trans. Dielectr. Electr. Insul.* **22**(1), 409–419 (2015)
12. Zhou Z.C., Shen Q.G., Fang Y., Wang D.Z.: *High Voltage Technology*. 3rd edn. China Electric Power Press, Beijing (2007). (in Chinese)
13. Hartmann, G.: Theoretical evaluation of Peek's law. *IEEE Trans. Ind. Appl.* **20**(6), 1647–1651 (1984)
14. Volpov, E.: Electric field modeling and field formation mechanism in HVDC SF₆ gas insulated systems. *IEEE Trans. Dielectr. Electr. Insul.* **10**(2), 204–221 (2003)
15. Lü, F.C., Song, J.X., Ruan, H.O., Zhu, M.Y., Wang, S.S., Lü, P., Xie, Q.: Enhanced direct-current breakdown strength of Al₂O₃/epoxy resin composites through plasma fluoridation of fillers interface. *Polym. Compos.* **43**(1), 347–357 (2022)

Cascade Finite Control Set Model Predictive Control Research for Bearingless Switched Reluctance Motors



Jinlong Ma, Honghua Wang, Hao Li, and Zenan Qiu

Abstract There is a nonlinear and strong coupling relationship between torque and levitation force of 12/8-pole three-phase double winding bearingless switched reluctance motors. In order to realize decoupling control of torque and levitation force, a cascade finite control set model predictive control for bearingless switched reluctance motors is designed. Firstly, the discrete state space model of bearingless switched reluctance motor is established, the motor torque and levitation force are predicted based on the state space model; Secondly, the cost function is designed, and the optimal voltage vector which makes the tracking error of torque and levitation force minimum is selected by minimizing the cost function to realize the coordinated control of torque and levitation force. The simulation results show that the cascade finite control set model predictive control algorithm has good decoupling and coordinated control ability.

Keywords Bearingless switched reluctance motor · State space model · Cost function · Optimal voltage vector · Model predictive control

1 Introduction

Bearingless switched reluctance motor (BSRM) is a new type of motor that combines switched reluctance motor (SRM) and magnetic bearing technology. It has broad application prospects in flywheel energy storage, aerospace and other fields. However, there is a nonlinear and strong coupling relationship between torque and levitation force of BSRM. Finite control set model predictive control (FCS-MPC) is widely used in power electronic converter and motor control [1–4] because of its advantages of processing coupling and multi-objective coordinated control.

Finite control set model predictive control has been used for SRM. Applying different voltage vectors in different sectors can effectively reduce the computational

J. Ma · H. Wang (✉) · H. Li · Z. Qiu

College of Energy and Electrical Engineering, Hohai University, Nanjing 211100, China
e-mail: wanghonghua@263.net

© Beijing Paiké Culture Commu. Co., Ltd. 2023

X. Dong et al. (eds.), *The proceedings of the 10th Frontier Academic Forum of Electrical Engineering (FAFEE2022)*, Lecture Notes in Electrical Engineering 1054, https://doi.org/10.1007/978-981-99-3408-9_13

burden of embedded processors [3]. Moreover, the finite control set of SRM can be expanded to reduce the torque ripple in SRM [5]. Direct torque control (DTC) can also be applied to single winding BSRM in combination with FCS-MPC to calculate the cost function of torque and levitation force respectively [6]. In view of the nonlinear and strong coupling relationship between the torque and levitation force, a BSRM control algorithm for three-phase 12/8-pole double winding BSRM based on finite control set model predictive control is designed in this paper, which has certain decoupling and coordinated control ability for the torque and levitation force.

2 Cascade FCS-MPC Algorithm for BSRM

For three-phase 12/8-pole double winding BSRM, the average torque reaches the maximum when the conduction interval of the main winding is $[-15^\circ, 0^\circ]$, and the average levitation force reaches the maximum when the conduction interval of levitation winding is $[-7.5^\circ, 7.5^\circ]$. In order to give consideration to torque and suspension force control[7], taking phase A as an example, the conduction intervals of its suspension winding and main winding are fixed as $[-11.5^\circ, 3.5^\circ]$, $[-18.5^\circ, 3.5^\circ]$, then the overlapping conduction intervals of the main windings of phase A and B, phase A and C, phase B and C are $[-3.5^\circ, 3.5^\circ]$, $[-18.5^\circ, -11.5^\circ]$, $[11.5^\circ, 18.5^\circ]$, respectively. Since the prediction model of the overlapping conduction interval of the main windings of phase A and C, phase B and C can be derived from the prediction model of the overlapping conduction interval of the main windings of phase A and B. Therefore, taking the angle range of $[-11.5^\circ, -3.5^\circ]$ and $[-3.5^\circ, 3.5^\circ]$ as examples, the motor prediction model is established and the model predictive control algorithm is described.

2.1 Prediction Model of BSRM

Ignoring the mutual inductance between motor windings, the voltage balance equation of a single winding is [8]:

$$U = Ri + (L + i \frac{\partial L}{\partial i}) \frac{di}{dt} + i \frac{\partial L}{\partial \theta} \frac{d\theta}{dt} \quad (1)$$

where U is the winding terminal voltage, R is the winding resistance, L is the winding self inductance, i is the winding current, θ is the rotor angular position. Ignoring the magnetic circuit saturation and radial displacement, the state space equation of a single winding can be obtained according to Eq. (1):

$$\frac{di}{dt} = \frac{1}{L} \left(U - Ri - i \frac{dL}{d\theta} \omega \right) \quad (2)$$

where ω is the rotor angular velocity.

Taking the sampling period as T_s , the forward Euler method is used to discretize Eq. (2). According to the discretized Eq. (2) and BSRM mathematical model [9, 10], the discrete state space model of the motor can be established, as shown in Eqs. (3) and (4). When $\theta \in [-11.5^\circ, 3.5^\circ]$, the suspension winding and main winding of phase A are conducted, and all the windings of phase B and C are turned off. The current of phase B winding has decreased to 0, while the current of phase C winding is turned off at $\theta = -11.5^\circ$, the free wheeling current of its winding still needs to be predicted. When $\theta \in [-3.5^\circ, 3.5^\circ]$, the suspension winding and the main winding of phase A are kept in conduction, the main winding of phase B is conducted, and all windings of phase C are kept off.

$$\left\{ \begin{array}{l} \theta(k+1) = \theta(k) + T_s \omega(k) \\ i_{mA}(k+1) = i_{mA}(k) + \frac{T_s}{L_{mA}(\theta(k))} \left\{ \left(-R_m - \omega(k) \frac{dL_{mA}}{d\theta} \Big|_{\theta=\theta(k)} \right) i_{mA}(k) + U_{mA}(k) \right\} \quad -11.5^\circ \leq \theta < 3.5^\circ \\ i_{sA\alpha}(k+1) = i_{sA\alpha}(k) + \frac{T_s}{L_{sA\alpha}(\theta(k))} \left\{ \left(-R_s - \omega(k) \frac{dL_{sA\alpha}}{d\theta} \Big|_{\theta=\theta(k)} \right) i_{sA\alpha}(k) + U_{sA\alpha}(k) \right\} \quad -11.5^\circ \leq \theta < 3.5^\circ \\ i_{sA\beta}(k+1) = i_{sA\beta}(k) + \frac{T_s}{L_{sA\beta}(\theta(k))} \left\{ \left(-R_s - \omega(k) \frac{dL_{sA\beta}}{d\theta} \Big|_{\theta=\theta(k)} \right) i_{sA\beta}(k) + U_{sA\beta}(k) \right\} \quad -11.5^\circ \leq \theta < 3.5^\circ \\ i_{mB}(k+1) = \begin{cases} 0 & -11.5^\circ \leq \theta < -3.5^\circ \\ i_{mB}(k) + \frac{T_s}{L_{mB}(\theta(k))} \left\{ \left(-R_m - \omega(k) \frac{dL_{mB}}{d\theta} \Big|_{\theta=\theta(k)} \right) i_{mB}(k) + U_{mB}(k) \right\} & -3.5^\circ \leq \theta < 3.5^\circ \end{cases} \\ i_{mC}(k+1) = i_{mC}(k) + \frac{T_s}{L_{mC}(\theta(k))} \left\{ \left(-R_m - \omega(k) \frac{dL_{mC}}{d\theta} \Big|_{\theta=\theta(k)} \right) i_{mC}(k) - \text{sign}(i_{mC})V_{cc} \right\} \quad -11.5^\circ \leq \theta < 3.5^\circ \\ i_{sC\alpha}(k+1) = i_{sC\alpha}(k) + \frac{T_s}{L_{sC\alpha}(\theta(k))} \left\{ \left(-R_s - \omega(k) \frac{dL_{sC\alpha}}{d\theta} \Big|_{\theta=\theta(k)} \right) i_{sC\alpha}(k) - \text{sign}(i_{sC\alpha})V_{cc} \right\} \quad -11.5^\circ \leq \theta < 3.5^\circ \\ i_{sC\beta}(k+1) = i_{sC\beta}(k) + \frac{T_s}{L_{sC\beta}(\theta(k))} \left\{ \left(-R_s - \omega(k) \frac{dL_{sC\beta}}{d\theta} \Big|_{\theta=\theta(k)} \right) i_{sC\beta}(k) - \text{sign}(i_{sC\beta})V_{cc} \right\} \quad -11.5^\circ \leq \theta < 3.5^\circ \end{array} \right. \quad (3)$$

$$\left\{ \begin{array}{l} \begin{bmatrix} F_x(k+1) \\ F_y(k+1) \end{bmatrix} = i_{mA}(k+1) \begin{bmatrix} K_1(\theta(k+1)) & -K_2(\theta(k+1)) \\ K_1(\theta(k+1)) & K_2(\theta(k+1)) \end{bmatrix} \begin{bmatrix} i_{sA\alpha}(k+1) \\ i_{sA\beta}(k+1) \end{bmatrix} + \begin{bmatrix} \cos(\pi/6) & \sin(-\pi/6) \\ \sin(\pi/6) & \cos(\pi/6) \end{bmatrix} \cdot \\ \quad i_{mC}(k+1) \begin{bmatrix} K_1(\theta(k+1)+15^\circ) & -K_2(\theta(k+1)+15^\circ) \\ K_1(\theta(k+1)+15^\circ) & K_2(\theta(k+1)+15^\circ) \end{bmatrix} \begin{bmatrix} i_{sC\alpha}(k+1) \\ i_{sC\beta}(k+1) \end{bmatrix} \\ T_{eAC}(k+1) = J_r(\theta(k+1)) \left[2N_m^2 i_{mA}^2(k+1) + N_s^2 i_{sA\alpha}^2(k+1) + N_s^2 i_{sA\beta}^2(k+1) \right] + \\ \quad J_i(\theta(k+1)+15^\circ) \left[2N_m^2 i_{mC}^2(k+1) + N_s^2 i_{sC\alpha}^2(k+1) + N_s^2 i_{sC\beta}^2(k+1) \right] \\ T_{eB}(k+1) = J_r(\theta(k+1)-15^\circ) \left[2N_m^2 i_{mB}^2(k+1) \right] \end{array} \right. \quad (4)$$

In the discrete state space model, Eq. (3) is the state equation and Eq. (4) is the output equation. Where i_{mA} , i_{mB} , i_{mC} is the main winding current of phase A, B and C respectively. $i_{sA\alpha}$, $i_{sC\alpha}$ is the α direction suspension winding current of phase A and C respectively. $i_{sA\beta}$, $i_{sC\beta}$ is the β direction suspension winding current of phase A and C respectively. V_{cc} is motor DC bus voltage, U_{mA} , $U_{sA\alpha}$, $U_{sA\beta}$ are the main winding and α and β direction levitation winding terminal voltage of phase A, U_{mB}

is the main winding terminal voltage of phase B; F_x is the total levitation force in the x direction, F_y is the total levitation force in the y direction, T_{eAC} is the sum of the electromagnetic torques of phases A and C, and T_{eB} is the electromagnetic torque of phase B; N_m and N_s are the number of turns of main winding and suspension winding respectively; $\text{sign}(x)$ is a sign function, $K_1(\theta)$ and $K_2(\theta)$ is the coefficient of levitation force; $J_l(\theta)$ is the phase torque coefficient. L_{mA} , L_{mB} , L_{mC} is the main winding inductance of phase A, B and C respectively. $L_{sA\alpha}$, $L_{sC\alpha}$ is the α direction suspension winding inductance of phase A and C respectively. $L_{sA\beta}$, $L_{sC\beta}$ is the β direction suspension winding inductance of phase A and C respectively. R_m is the main winding resistance, and R_s is the suspension winding resistance; The specific expression of each coefficient in Eq. (4) can be found in [9, 10].

The vector–matrix form of the discrete state space model can be expressed as:

$$\begin{cases} \mathbf{x}(k+1) = \mathbf{f}(\mathbf{x}(k), \mathbf{U}(k)) \\ \mathbf{y}(k+1) = \mathbf{g}(\mathbf{x}(k)) \end{cases} \quad (5)$$

where state vector $\mathbf{x}(k) = [\theta(k) \ i_{mA}(k) \ i_{sA\alpha}(k) \ i_{sA\beta}(k) \ i_{mB}(k) \ i_{mC}(k) \ i_{sC\alpha}(k) \ i_{sC\beta}(k)]^T$, output vector $\mathbf{y}(k) = [F_x(k) \ F_y(k) \ T_{eAC}(k) \ T_{eB}(k)]^T$, input vector \mathbf{U} is as shown in Eq. (6).

$$\begin{aligned} \mathbf{U}(k) &= \begin{cases} U_{1n}(k) & -11.5^\circ \leq \theta < -3.5^\circ \\ [U_{1n}^T(k) \ U_{2h}(k)]^T & -3.5^\circ \leq \theta < 3.5^\circ \end{cases} \\ U_{1n}(k) &= [U_{mA}(k) \ U_{sA\alpha}(k) \ U_{sA\beta}(k)]^T, n = 1, 2, \dots, 27 & -11.5^\circ \leq \theta < 3.5^\circ \\ U_{2h}(k) &= U_{mB}(k), h = 1, 2, 3 & -3.5^\circ \leq \theta < 3.5^\circ \end{aligned} \quad (6)$$

The power converters of BSRM main winding and suspension winding respectively adopt asymmetric half bridge and H-type bridge circuits. Within the conduction interval, there are three voltage balance states for a single winding: taking the main winding of phase A as an example, the ‘+’ state, ‘-’ state and ‘0’ state respectively correspond to its terminal voltage $U_{mA} = +V_{CC}, -V_{CC}, 0$ V. As shown in Eq. (6), when $\theta \in [-11.5^\circ, 3.5^\circ]$, different terminal voltage of main winding and α , β direction suspension winding of phase A constitute a total of $3^3 = 27$ voltage vectors, and the vector is written as $U_{1n} = [U_{mA} \ U_{sA\alpha} \ U_{sA\beta}]^T$, ($n = 1, 2, \dots, 27$); When $\theta \in [-3.5^\circ, 3.5^\circ]$, different terminal voltage of main winding of phase B have a total of 3 voltage values, and the value is written as $U_{2h} = U_{mB}$, ($h = 1, 2, 3$).

2.2 BSRM Optimal Voltage Vector Selection

Figure 1 is the overall control block diagram of the system. As shown in Fig. 1, the angular velocity error is converted into torque reference T_{ref} by PI controller, the x direction and y direction radial displacement error are converted into levitation force reference F_{xref} and F_{yref} by PID controller respectively. Model predictive control is

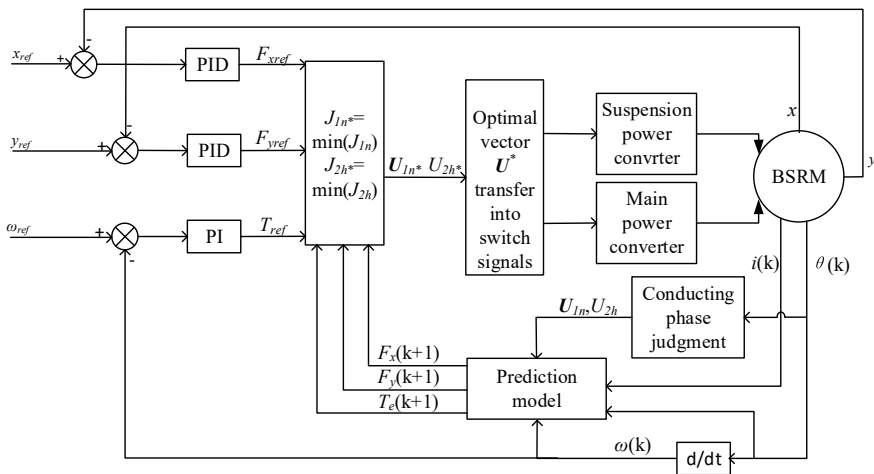


Fig. 1 System control block diagram

used as the torque and levitation force inner loop control algorithm to track the torque reference T_{ref} , levitation force reference F_{xref} and F_{yref} , and select the optimal voltage vector that minimizes the cost functions J_1 and J_2 . Finally, the optimal voltage vector is transferred into the switch signals of the power converter to obtain the minimum torque and levitation force tracking error.

As shown in Eq. (7), the cost function J_1 is the weighted sum of the square of the torque tracking error of phase A and C, the square of the levitation force tracking error, and the square of the main winding current of phase A; The cost function J_2 is the square of the torque tracking error of phase B. Selecting reasonable weights k_t, k_{fx}, k_{fy} and k_i will obtain good coordination control ability for multiple control objectives.

$$\begin{aligned}
 J_{1n} &= k_t (T_{ref} - T_{eACn}(k+1))^2 + k_{fx} (F_{xref} - F_{xn}(k+1))^2 + k_{fy} (F_{yref} - F_{yn}(k+1))^2 + k_i (i_{mAn}(k+1))^2 \\
 J_{2h} &= ((T_{ref} - T_{eAC}^*) - T_{eBh}(k+1))^2
 \end{aligned} \tag{7}$$

$$\begin{cases}
 n = 1, 2 \dots 27 & -11.5^\circ \leq \theta < 3.5^\circ \\
 h = 1, 2, 3 & -3.5^\circ \leq \theta < 3.5^\circ
 \end{cases}$$

As shown in Fig. 2, the cascade finite control set model predictive control is based on the current measurement value $i(k)$, the rotor angle $\theta(k)$ and angular velocity $\omega(k)$ at time kT_s . First, $U_{1n}(n = 1, 2 \dots 27)$ are sequentially substituted into the phase A part of Eq. (3) to calculate the current value $i_n(k + 1)$ and the rotor position $\theta(k + 1)$ at time $(k + 1)T_s$, then calculate $T_{eACn}(k + 1)$, $F_{xn}(k + 1)$, $F_{yn}(k + 1)$ and $J_{1n}(n = 1, 2 \dots 27)$ according to Eq. (4) and Eq. (7) respectively. J_{1n}^* ($n^* \in [1, 2 \dots 27]$) can be obtained from minimizes $J_{1n}(n = 1, 2 \dots 27)$. When the corresponding voltage vector U_{1n}^* ($n^* \in [1, 2, \dots 27]$) is used as input vector, the total torque of phase A and phase C is T_{eAC}^* .

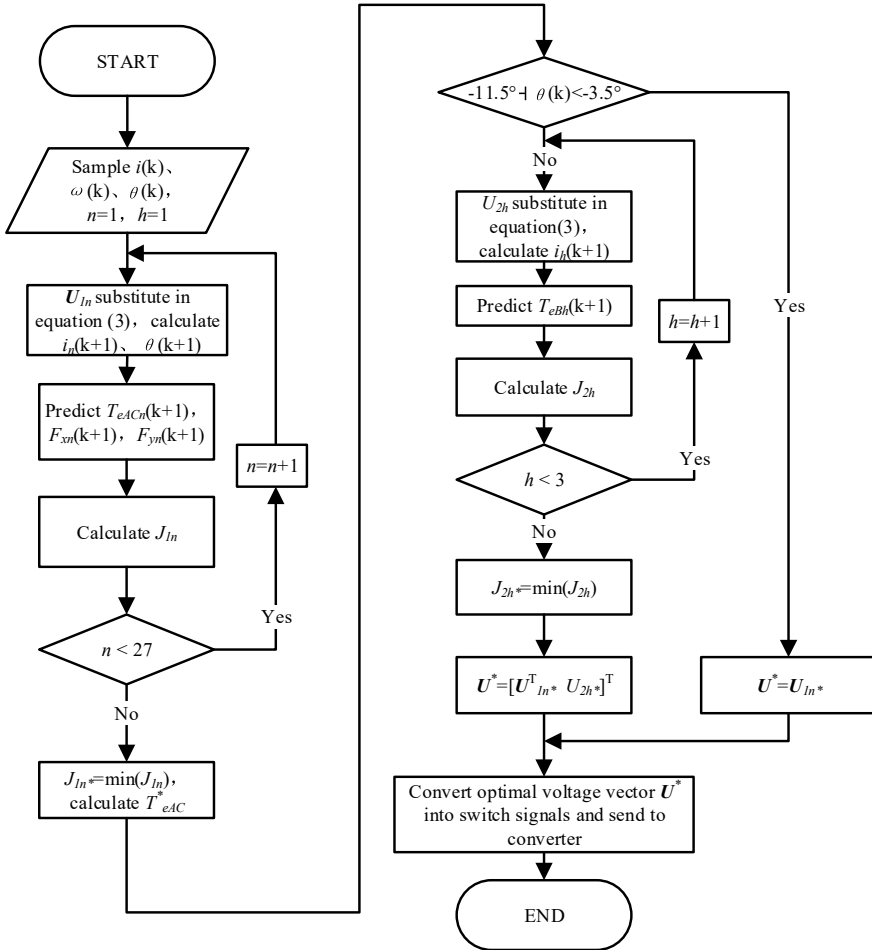


Fig. 2 Flow chart of cascade finite control set model predictive control algorithm for BSRM

Second, determine the interval of θ . When $-3.5^\circ \leq \theta(k) < 3.5^\circ$, U_{2h} ($h = 1, 2, 3$) are sequentially substituted into the phase B part of Eq. (3) to calculate the current value $i_h(k+1)$, then calculate $T_{eBh}(k+1)$ and J_{2h} ($h = 1, 2, 3$) according to Eq. (4) and Eq. (7) respectively. J_{2h}^* can be obtained from minimizes J_{2h} ($h = 1, 2, 3$). So, U_{In^*} ($n^* \in [1, 2 \dots 27]$) and U_{2h^*} ($h^* \in [1, 2, 3]$) constitute the optimal voltage vector $U^* = [U_{In^*}^T U_{2h^*}^T]^T$; When $-11.5^\circ \leq \theta(k) < -3.5^\circ$, the optimal voltage vector $U^* = U_{In^*}$.

As the selected input vector of the system, U^* is finally converted into the switch signals of the power converter.

3 Simulation and Analysis of Cascade FCS-MPC Algorithm

The simulation model is built in MATLAB according to the system control block diagram, where $x_{ref} = 0$ mm, $y_{ref} = 0$ mm, $\omega_{ref} = 150$ rad/s. The parameters of three phase 12/8-pole double winding BSRM can be found in the parameters of motor prototype 2 in reference [9]. In the simulation, when $t = 0$, the radial position in x direction is -0.2 mm, the radial position in y direction is -0.3 mm, the angular velocity is 0 rad/s, the load torque is 0.3 N.m, and the suspended loads in the x and y directions are 0 N and 25.48 N respectively. The weight coefficients k_t , k_{fx} , k_{fy} and k_i in Eq. (7) are chosen as 300, 0.01, 0.017 and 0.58 respectively. In order to verify the decoupling and coordinated control ability of predictive control algorithm under different working conditions, the dynamic response of radial displacement and angular velocity are simulated with suddenly changes of suspension load in y directions. The simulation results are shown in Fig. 3(a–d).

The suspension load in y direction suddenly changes to 15.48 N at 0.2 s and 45.48 N at 0.3 s. As shown in Fig. 3(a–d). The radial displacement in the y direction can be quickly tracked to y_{ref} after being adjusted by controller. But adjusting the radial

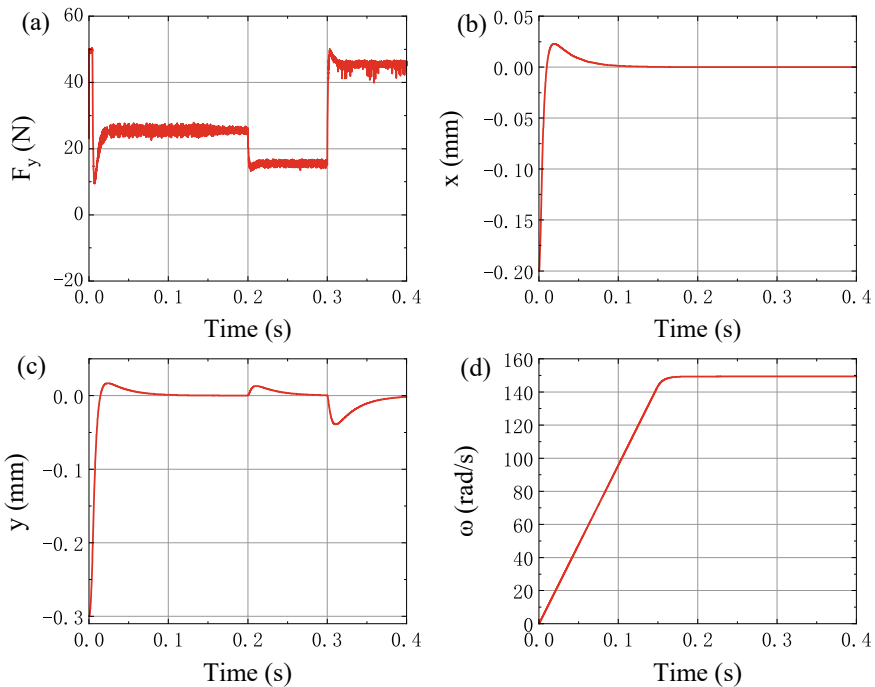


Fig. 3 Simulation results of FCS-MPC for BSRM **a** Levitation force in y direction, **b** Radial displacement in x direction, **c** Radial displacement in y direction, **d** Rotor angular velocity

displacement in the y direction has almost no effect on the rotor angular velocity and the radial displacement in the x direction. The above simulation results show that the cascade finite control set model predictive control algorithm has good decoupling and coordinated control performance.

4 Conclusion

BSRM is a typical MIMO system. The cascade finite control set model predictive control algorithm designed in this paper directly considers the coupling relationship in the established predictive model, and then selects the optimal voltage vector as the system input vector under the consideration of the tracking effect of multiple controlled targets such as torque and levitation force. The simulation results show that the control algorithm effectively solves the problem that multiple controlled targets of BSRM are difficult to control independently, and realizes the high performance suspension control of BSRM.

Acknowledgements This work was supported by the National Natural Science Foundation of China (51477042).

References

1. Valencia, D.F., Tarvirdilu-Asl, R., Garcia, C., Rodriguez, J., Emadi, A.: A review of predictive control techniques for switched reluctance machine drives. Part I: fundamentals and current control. *IEEE Trans. Energy Conv.* **36**, 1313–1322 (2021)
2. Valencia, D.F., Tarvirdilu-Asl, R., Garcia, C., Rodriguez, J., Emadi, A.: A review of predictive control techniques for switched reluctance machine drives. Part II: torque control, assessment and challenges. *IEEE Trans. Energy Conv.* **36**, 1323–1335 (2021)
3. Li, Y., Wang, G.-F., Li, C.-H., Fan, Y.-S., Xu, A.-D.: Finite control set predictive torque control method for switched reluctance motor drives. *Dianji yu Kongzhi Xuebao/Electric Mach. Control* **23**, 49–58 (2019). (in Chinese)
4. Yang, Y., Wen, H.Q., Fan, M.D., Zhang, X.A., He, L.Q., Chen, R., Xie, M.X., Norambuena, M., Rodriguez, J.: Low complexity finite-control-set mpc based on discrete space vector modulation for T-Type three-phase three-level converters. *IEEE Trans. Power Electron.* **37**, 392–403 (2022)
5. Villegas, J., Vazquez, S., Carrasco, J.M., Gil, I.: IEEE: model predictive control of a switched reluctance machine using discrete space vector modulation. In: *IEEE International Symposium on Industrial Electronics (ISIE)*, pp. 3139–3144 (2010)
6. Yu, Q.: *The Research on Control Strategy of Bearingless Switched Reluctance Motor Based on Direct Control*, vol. Master. Nanjing University of Aeronautics and Astronautics Nanjing, China (2020). (in Chinese)
7. Liu, C.H., Cao, X., Yuan, R., Deng, Z.Q., Zhou, J.X.: IEEE: torque sharing and predictive current control of dual-winding bearingless switched reluctance motors for torque ripple reduction. In: *19th International Conference on Electrical Machines and Systems (ICEMS)* (2016)
8. Wang, H.: *Speed Adjustment and Control Technology for Switched Reluctance Motor Drives*. China Machine Press, Beijing, China (2014). (in Chinese)

9. Chen, L.: Basis Research on Suspension, Variable Speed and Vibration Control for the Rotor of Bearingless Switched Reluctance Motor. vol. Doctor. Hohai University, Nanjing, China (2017) (in Chinese)
10. Sun, Y., Liu, X., Wang, D., Mao, J.: Extension of mathematical model to full angle for bearingless switched reluctance motors based on finite-element analysis. *Diangong Jishu Xuebao/Trans. China Electrotechn. Soc.* **22**, 34–39 (2007). (in Chinese)

A Design of Voltage-PDM Type Torque Controller for Dual-Winding BSRM Based on Super-Twisting Algorithm



Zenan Qiu, Honghua Wang, Jinlong Ma, and Hao Li

Abstract During the operation of the dual-winding bearingless switched reluctance motor (BSRM), the coupling of torque and suspension force will affect the performance of the motor. According to the winding voltage equation and combining the characteristics of the super-twisting algorithm (STA) and the pulse density modulation (PDM), a torque controller that treats one of the main winding as the controlled object, while the suspension winding of the phase and the winding of other phases are treated as disturbance terms is designed. The controller improves the robustness of the control system and limits switching frequency of the inverter. Simulation results verified the effectiveness of the controller.

Keywords Dual-winding bearingless switched reluctance motor · Sliding mode control · Super-twisting algorithm · Pulse density modulation

1 Introduction

The traditional control method of BSRM requires the solution of the winding current [1], which has the disadvantages of poor robustness and takes much time [2]. In order to overcome these shortcomings, some new strategies have been proposed. BSRM direct torque and force control (DTC&DFC) [3] has the drawbacks of low torque-ampere ratio and high switching frequency of inverter [4]. Although BSRM direct instantaneous torque and force control (DITC&DFC) [5] reduced the switching frequency and improved the torque-ampere ratio, the existence of hysteresis band reversed the disadvantages of poor robustness and uncontrollable switching frequency of inverter [6].

With the goal of improving the torque control of BSRM, according to the winding voltage equation, combined with the anti-disturbance characteristics of STA [7] and

Z. Qiu · H. Wang (✉) · J. Ma · H. Li
College of Energy and Electrical Engineering, Hohai University, Nanjing 211100, China
e-mail: wanghonghua@263.net

© Beijing Paiké Culture Commu. Co., Ltd. 2023
X. Dong et al. (eds.), *The proceedings of the 10th Frontier Academic Forum of Electrical Engineering (FAFEE2022)*, Lecture Notes in Electrical Engineering 1054, https://doi.org/10.1007/978-981-99-3408-9_14

155

the discrete output characteristic of PDM [8], a torque controller is designed in this paper, which has no torque hysteresis band and limits the switching frequency.

2 BSRM Control Principle

2.1 Torque Control Principle

The mathematical model of BSRM when one phase is working is shown in (1) and (2) [1], i.e.

$$T = K_t(2N_m^2 i_m^2 + N_s^2 i_{s1}^2 + N_s^2 i_{s2}^2) \quad (1)$$

$$\begin{bmatrix} F_1 \\ F_2 \end{bmatrix} = i_m \begin{bmatrix} K_1 & -K_2 \\ K_2 & K_1 \end{bmatrix} \begin{bmatrix} i_{s1} \\ i_{s2} \end{bmatrix} \quad (2)$$

where T is the electromagnetic torque, F_1 and F_2 are the suspension forces under the phase coordinate system, N_m and N_s are the number of turns of winding, i_m is the current of main winding, and i_{s1} and i_{s2} are the currents of suspension winding. The electromagnetic torque coefficient K_t is shown in (3) and (4), i.e.

$$K_t = \begin{cases} \frac{\mu_0 h r}{\eta^2} \left[\frac{-\pi r \theta}{l_0(2l_0 - \pi r \theta)} \right] & -15^\circ < \theta < 0^\circ \\ -\frac{\mu_0 h r}{\eta^2} \left[\frac{\pi r \theta}{l_0(2l_0 + \pi r \theta)} \right] & 0^\circ \leq \theta < 15^\circ \end{cases} \quad (3)$$

$$K_t = \begin{cases} \frac{2\mu_0 h r^2}{\pi - 2} \left\{ \begin{array}{l} \frac{\pi(\pi - 4)(2\theta + \pi/4)}{[\pi r(\theta + \pi/6) + 2l_0][-\pi r(\theta + \pi/12) + 2l_0]} \\ + \frac{2\theta + \pi/4}{[r(\theta + \pi/6) + l_0][-\pi r(\theta + \pi/12) + l_0]} \end{array} \right\} & -22.5^\circ \leq \theta \leq -15^\circ \\ \frac{2\mu_0 h r^2}{\pi - 2} \left\{ \begin{array}{l} \frac{\pi(\pi - 4)(2\theta - \pi/4)}{[\pi r(\pi/6 - \theta) + 2l_0][\pi r(\theta - \pi/12) + 2l_0]} \\ + \frac{2\theta - \pi/4}{[r(\pi/6 - \theta) + l_0][r(\theta - \pi/12) + l_0]} \end{array} \right\} & 15^\circ \leq \theta \leq 22.5^\circ \end{cases} \quad (4)$$

where μ_0 is the permeability of vacuum, h is the length of rotor flake, r is the radius of rotor, η is the coefficient of air gap, l_0 is the length of air gap. The levitation force coefficients K_1 and K_2 are shown in (5) and (6), i.e.

$$K_1 = \begin{cases} \frac{2N_m N_s \mu_0 h}{\eta^2} \left[\frac{r(\tau_r + \theta)}{l_0^2} - \frac{4r\theta}{l_0(2l_0 - \pi r\theta)} + \frac{\sin(\tau_r/2)(4l_0 - \pi r\theta)}{l_0(2l_0 - \pi r\theta)} \right] & \theta < 0^\circ \\ \frac{2N_m N_s \mu_0 h}{\eta^2} \left[\frac{r(\tau_r - \theta)}{l_0^2} + \frac{4r\theta}{l_0(2l_0 + \pi r\theta)} + \frac{\sin(\tau_r/2)(4l_0 + \pi r\theta)}{l_0(2l_0 + \pi r\theta)} \right] & \theta \geq 0^\circ \end{cases} \quad (5)$$

$$K_2 = \begin{cases} \frac{2N_m N_s \mu_0 h}{\eta^2} \left[\frac{r(\theta^2 + \tau_r\theta)}{2l_0^2} - \frac{2r\theta^2}{l_0(2l_0 - \pi r\theta)} + \frac{\cos(\tau_r/2)(-\pi r\theta)}{l_0(2l_0 - \pi r\theta)} \right] & \theta < 0^\circ \\ -\frac{2N_m N_s \mu_0 h}{\eta^2} \left[\frac{r(\theta^2 - \tau_r\theta)}{2l_0^2} - \frac{2r\theta^2}{l_0(2l_0 + \pi r\theta)} + \frac{\cos(\tau_r/2)(\pi r\theta)}{l_0(2l_0 + \pi r\theta)} \right] & \theta \geq 0^\circ \end{cases} \quad (6)$$

The winding state equation for one phase is shown in (7), i.e.

$$\begin{aligned} \dot{i}_m &= -\frac{1}{L_m} (R_m + \frac{dL_m}{dt}) i_m + \frac{1}{L_m} u_m \\ \dot{i}_{s1} &= -\frac{1}{L_s} (R_s + \frac{dL_s}{dt}) i_{s1} + \frac{1}{L_s} u_{s1} \\ \dot{i}_{s2} &= -\frac{1}{L_s} (R_s + \frac{dL_s}{dt}) i_{s2} + \frac{1}{L_s} u_{s2} \end{aligned} \quad (7)$$

It can be seen that the control of the motor torque and suspension force comes down to the regulation of the winding voltage ultimately. In the dual-winding BSRM, each stator tooth pole is wound with a main winding and a suspension winding. In this paper, voltage source inverter is used to supply power to each winding, of which the main winding adopts an asymmetrical half-bridge topology and the suspension winding adopts a H-bridge topology.

2.2 Suspension Force Control Principle

Direct force control is an efficient BSRM suspension force control method that achieves the control of instantaneous suspension force by constantly switching the voltages across the suspension winding [3]. The suspension winding power converter adopts a H-bridge circuit with three possible voltage states for a bidirectional current, i.e., the positive bus voltage, the zero voltage and the negative bus voltage.

As stated in (2), when one phase is providing suspension force, the main winding of the phase should have a current flowing through too. (5) and (6) show that the phase whose angle is in $[-7.5^\circ, 7.5^\circ]$ produce the most suspension force. However, if the main winding of the phase within $[0^\circ, 7.5^\circ]$ is in conduction, it will produce negative torque. In order to reduce the negative torque as much as possible, considering the needs of torque and suspension force comprehensively, this paper adjust the suspension force conduction interval to the angle of $[-11.25^\circ, 3.75^\circ]$, when the rotor is in the angle of $[0^\circ, 3.75^\circ]$, the main winding generates negative torque through current chopping.

In order to generate as little negative torque as possible, this paper adopts the method of nonlinear programming. The current of main winding during the negative

torque region that can provide suspension force sufficiently and produce negative torque at a minimum under different working conditions is calculated offline, and these parameters are fitted with the linear interpolation method. When the motor runs into the negative torque area, the chopping current of the main winding is adjusted dynamically according to different loads and rotor angles to obtain the optimal torque-ampere ratio.

3 Implementation of Super-Twisting Torque Controller

3.1 Design of Super-Twisting Controller

Known by (1) and (2), the BSRM torque and suspension force are highly coupled. Considering only the torque provided by the main winding of one phase, the torque generated by the suspension winding of this phase and other phases is regarded as perturbation term, there are

$$\begin{aligned} \dot{i}_m &= -\frac{1}{L_m} \left(R_m + \frac{dL_m}{dt} \right) i_m + \frac{1}{L_m} u_m \\ T &= 2K_t N_m^2 i_m^2 + d \end{aligned} \quad (8)$$

The problem is to design a feedback control law u_m that can drive the output T follow the tracks of the reference input T^* asymptotically. For such system the control problem is challenging since asymptotic convergence is to be achieved in the presence of the unknown disturbance d . The sliding mode controller can achieve the desired control goal [9]. According to the principle of sliding mode control, (8) is rewritten as follow

$$\begin{aligned} \dot{x} &= a(t, x) + b(t, x)u \\ \sigma &= \sigma(t, x) \end{aligned} \quad (9)$$

where the state variable $x = i_m$, the control input $u = u_m$ and the output σ is

$$\sigma = 2K_t N_m^2 i_m^2 + d - T^* \quad (10)$$

where the perturbation term d is the torque generated by the suspension winding of current phase and the winding of other phases, the reference input T^* is the torque that needs to be tracked. Obviously, these two parameters are bounded. In this way, the problem translates into how to make the output σ converge to 0 in finite time via the feedback control [9]. Assume that σ has the necessary derivative of time, we can get

$$\begin{aligned} \dot{\sigma} = & \dot{d} - \dot{T}^* + \frac{dK_t}{d\theta} \omega \cdot 2N_m^2 i_m^2 \\ & + \frac{4K_t N_m^2 i_m}{L_m} \left[(R_m + \frac{dL_m}{d\theta} \omega) i_m + u_m \right] \end{aligned} \quad (11)$$

Apparently, this is a system of relative degree 1 that requires super-twisting algorithm to control [9]. According to the principle of STA, (11) is rewritten as follow

$$\dot{\sigma} = h(t, x) + g(t, x)u \quad (12)$$

$$h = \left[\frac{dK_t}{d\theta} \omega + \frac{2K_t}{L_m} (R_m + \frac{dL_m}{d\theta} \omega) \right] \cdot 2N_m^2 i_m^2 + \dot{d} - \dot{T}^* \quad (13)$$

$$g = \frac{4K_t N_m^2 i_m^2}{L_m} \quad (14)$$

Furthermore, assume that the reference input torque T^* is constant during the motor motion, and the main winding inductor adopts a linear model, we can obtain a series of normal numbers C , K_m , K_M , U_M , which satisfying

$$|\dot{h}| + U_M |\dot{g}| \leq C \quad (15)$$

$$0 \leq K_m \leq g \leq K_M \quad (16)$$

$$\left| \frac{h}{g} \right| < q U_M \quad (0 < q < 1) \quad (17)$$

Therefore, with the parameters α , λ satisfies $K_m \alpha > C$ and λ is sufficiently large, the super-twisting controller (18) can achieve the control of (9) in finite time [9], so that the instantaneous torque will track reference input.

$$\begin{aligned} u = & -\lambda |\sigma|^{1/2} \text{sign}(\sigma) + u_1 \\ \dot{u}_1 = & \begin{cases} -u & , |u| > U_M \\ -\alpha \text{sign}(\sigma) & , |u| \leq U_M \end{cases} \end{aligned} \quad (18)$$

where the control law u of the super-twisting controller will remain in it once it enters the segment $[-U_M, U_M]$.

3.2 Pulse Density Modulation Principle

Pulse density modulation allow us to translate continuous feedback controller design options into implementable switch-controlled strategies with practically the same closed loop behavior [10]. (19) is the system equation of the modulation system, where $\mu(t)$ is the continuous input signal and q is the modulated switching signal.

$$\begin{aligned} \dot{e} &= \mu(t) - q \\ q &= \begin{cases} \frac{1}{2}(1 + \text{sign}(e)) & , \mu > 0 \\ -\frac{1}{2}(1 - \text{sign}(e)) & , \mu \leq 0 \end{cases} \end{aligned} \quad (19)$$

The control input u provided by the super-twisting algorithm is multiplied by a quantization factor to give $\mu(t)$, and the output q obtained by PDM is taken value from the set $\{1, 0, -1\}$, corresponding to three voltage states acceptable to the asymmetric half-bridge circuit: “-1”, “0”, “+1”. In addition, it is vital to note that the switching frequency of PDM signal depends on the system sampling frequency, which is set to 1 MHz in the simulation of this paper, while the switching frequency of IGBTs is usually less than 50 kHz [11], this paper limits the output signal frequency to less than 20 kHz.

4 Control Block Diagram

Figure 1 is a control block diagram of BSRM drive system based on the control algorithm designed in this paper. The commutation controller obtains the working state of main winding of each phase according to the rotor angle: the phase needs to work in the positive torque region is controlled by the controller designed in this paper, the phases need to work in the negative torque region are controlled by current chopper.

5 Simulation Analysis

Based on MATLAB/Simulink, two dynamic simulation model of BSRM drive system using direct torque direct suspension force control (DTC&DFC) strategy or the controller designed in this paper is established. Among them, the torque hysteresis band width of DTC&DFC is 0.1 Nm. The motor speed is set at 600 rpm.

With the settled simulation conditions, the switching frequency of the main winding power converter controlled by DTC&DFC is as high as 100 kHz, while the same condition using STA voltage-PDM method is not higher than 20 kHz, and the torque ripple is significantly less than that of the DTC&DFC strategy (Fig. 2).

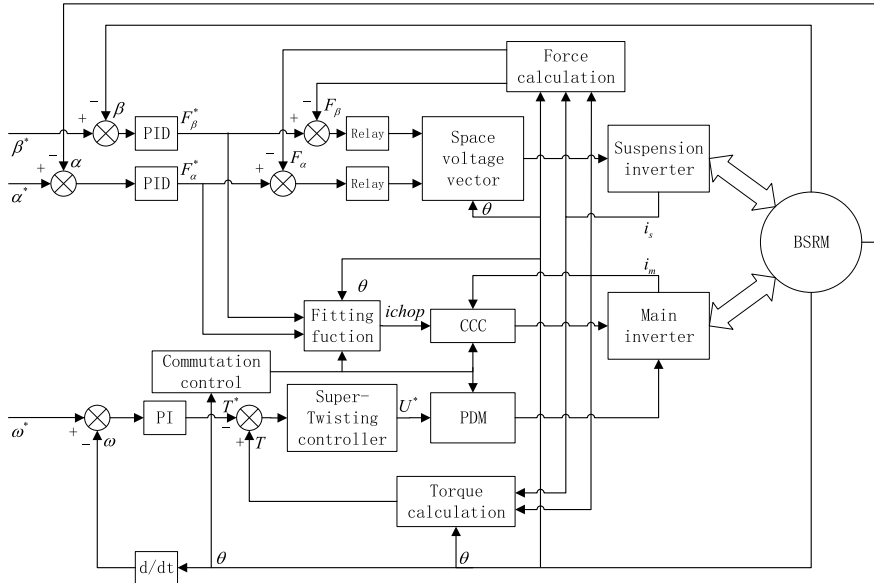
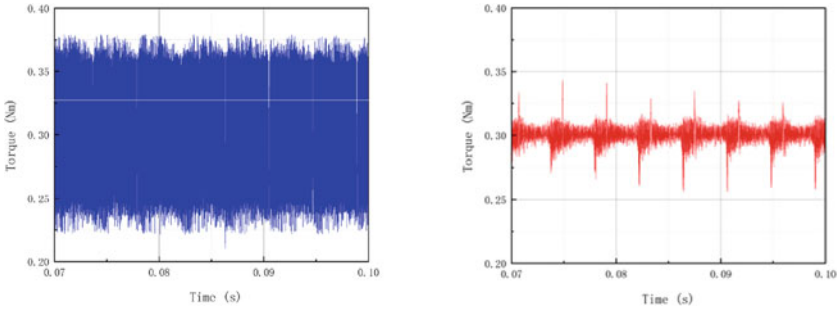


Fig. 1 Control block diagram of BSRM drive system

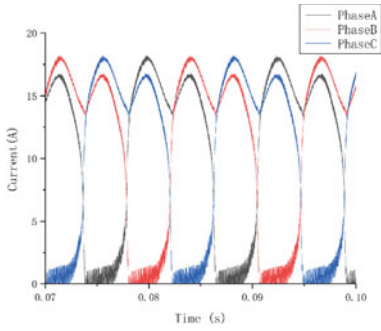


(a) With DTC&DFC

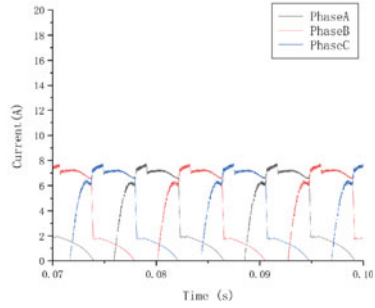
(b) With Controller designed in this paper

Fig. 2 Torque simulation results using different methods

Figure 3 shows that the current of controller designed in this paper is significantly less than the DTC&DFC method. Figure 4 and 5 show that compared with the DTC&DFC method, the ripple of suspension force is reduced largely by the controller designed in this paper.

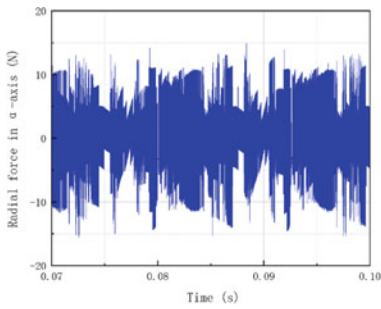


(a) With DTC&DFC

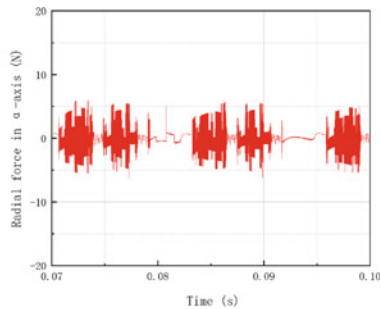


(b) With Controller designed in this paper

Fig. 3 Main winding current simulation results using different methods

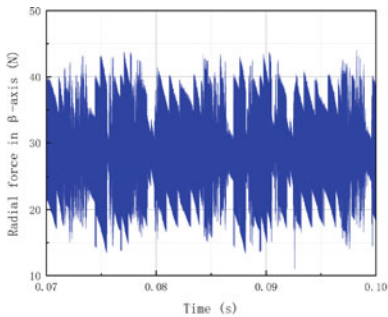


(a) With DTC&DFC

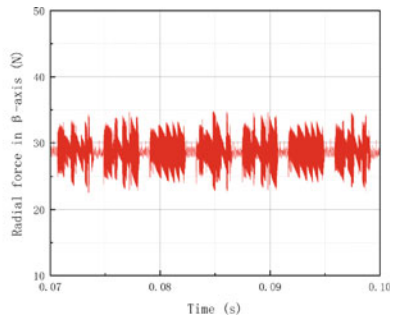


(b) With Controller designed in this paper

Fig. 4 α -axis levitation force simulation results using different methods



(a) With DTC&DFC



(b) With Controller designed in this paper

Fig. 5 β -axis levitation force simulation results using different methods

6 Conclusions

On the basis of the traditional direct suspension force control, this paper designs a torque control algorithm, which can adjust the main winding current during negative torque area dynamically due to different working conditions. The super-twisting algorithm and the pulse density modulation is applied to the torque control to improve the robustness of the control system and limits switching frequency of the inverter.

Acknowledgements This work was supported by the National Natural Science Foundation of China (51477042).

References

1. Cheng, L.: Basis Research on Suspension, Variable Speed and Vibration Control for the Rotor of Bearingless Switched Reluctance Motor. College of Energy and Electrical Engineering, vol. Doctor. Hohai University, Nanjing (2017) (in Chinese)
2. Preethishri, R.S., Roseline, J.A., Murugesan, K., Kumaran, M.S.: Optimized power factor correction for high speed switched reluctance motor. *Intell. Autom. Soft Comput.* **35**, 997–1014 (2023)
3. Cao, X., Sun, Q., Liu, C.H., Zhou, H., Deng, Z.Q.: Direct control of torque and levitation force for dual-winding bearingless switched reluctance motor. *Electric Power Syst. Res.* **145**, 214–222 (2017)
4. Hao, Z., Yu, Q., Cao, X., Deng, X., Shen, X.: An improved direct torque control for a single-winding bearingless switched reluctance motor. *IEEE Trans. Energy Convers.* **35**, 1381–1393 (2020)
5. Zhang, L.: The Research of Direct Instantaneous Torque Control for Bearingless Switched Reluctance Motor. College of Automation Engineering, vol. Master. Nanjing University of Aeronautics and Astronautics, Nanjing (2018) (in Chinese)
6. Wang, S.H., Hu, Z.H., Cui, X.P.: Research on novel direct instantaneous torque control strategy for switched reluctance motor. *IEEE Access* **8**, 66910–66916 (2020)
7. Scalcon, F.P., Fang, G.L., Vieira, R.P., Grundling, H.A., Emadi, A.: Discrete-time super-twisting sliding mode current controller with fixed switching frequency for switched reluctance motors. *IEEE Trans. Power Electron.* **37**, 3321–3333 (2022)
8. Zong, X., Chai, Y., Wang, P., Hu, X.: Improved pulse density modulation power conversion control method. *Power Electronics* **54**, 51–53 (2020). (in Chinese)
9. Shtessel, Y., Edwards, C., Fridman, L., Levant, A.: *Sliding Mode Control and Observation*. Birkhäuser New York, New York (2014)
10. Sira-Ramírez, H.: *Sliding Mode Control: The Delta-Sigma Modulation Approach*. Birkhäuser Cham, Cham (2015)
11. Volke, A., Hornkamp, M.: *IGBT Modules: Technologies*. China Machine Press, Beijing, Driver and Application (2016). (in Chinese)

Harmonic Elimination in Inverter Using Modified GWO Algorithm



He Fei and Jiabei Shen

Abstract Aiming at the problems of low accuracy and easy precocity of grey wolf optimization algorithm for solving nonlinear equations of multi-level inverter SHEPWM, a multi-strategy fusion grey wolf optimization algorithm is proposed. Firstly, chaos is used to initialize the individual positions of gray wolves for increasing the individual diversity of the population; Then, a nonlinear dynamic variation parameter based on trigonometric function and beta distribution is given to realize the good transition of the algorithm from exploration to development; Finally, by introducing the idea of particle swarm optimization, the gray wolf's individual experience optimal value and the population optimal value are combined to update the gray wolf's position information for accelerating the algorithm convergence speed. Simulation and experimental results verify the correctness and feasibility of the algorithm.

Keywords Selective harmonics elimination · Inverter · Pulse width modulation · Gray Wolf optimization algorithm · Nonlinear control parameter

1 Introduction

SHEPWM has the advantages of high conversion efficiency, good output voltage waveform and high voltage utilization rate by optimizing the switch angle and eliminating specified low frequency harmonics [1].

Newton iterative method [2], homotopy algorithm [3], Walsh function [4] are commonly used to solve SHEPWM nonlinear transcendental equations. However, the solution of numerical method depends on the selection of initial values, which will lead to the algorithm falling into local optimal solution. In algebraic methods, such as Wu's method [5], Groebner's basis [6], algebraic polynomial [7], resultant

H. Fei
Liaoning Technical University, Fuxin 123000, China

H. Fei · J. Shen (✉)
Liaoning Technical University, Huludao 125000, China
e-mail: s1696647865@163.com

© Beijing Paiké Culture Commu. Co., Ltd. 2023

X. Dong et al. (eds.), *The proceedings of the 10th Frontier Academic Forum of Electrical Engineering (FAFEE2022)*, Lecture Notes in Electrical Engineering 1054, https://doi.org/10.1007/978-981-99-3408-9_15

elimination method [8], harmonic elimination equations are converted into polynomial equations to solve them, but the computation is large, so it is not suitable for multilevel inverters. With the rapid development of intelligent algorithms in recent years, more and more intelligent algorithms are used in SHEPWM. Genetic Algorithm (GA), which is adopted in the literature [9], has flexible searching ability, and its iterative process is random, but its convergence speed is slow and it is easy to fall into “premature”. Particle Swarm Optimization (PSO) used in references [10], although its steps are simple, convergence is fast and computational complexity is low, but its diversity is lost and it is easy to fall into local optimum. The Sine Cosine Algorithm (SCA) used in reference [11] has few parameters and fast convergence speed, but it also has the characteristics of low calculation accuracy and easy prematurity. The Grey Wolf Optimizer (GWO) used in [12] has simple principle and strong global optimization ability, but its linear decreasing convergence function leads to the imbalance of exploration and development ability and slow convergence speed in the later period.

Aiming at the problems in GWO, this paper uses multi-strategy fusion gray wolf optimization algorithm (PGWO) to solve the SHEPWM equations of five-level inverter. Grey wolf optimization algorithm is the main solution process, sine chaotic map is introduced to initialize the population, trigonometric function and beta distribution are used instead of grey wolf optimization algorithm to control the linear decreasing strategy of parameters, and balance the global optimization and local exploration ability of the algorithm; Inspired by the individual memory function of particle swarm, this paper will enable the individual of gray wolf to remember the optimal value of its own experience, and finally compare with the optimal value of population, so that the algorithm can converge to the optimal solution faster for solving SHEPHWM equations. The correctness and feasibility of PGWO are verified by simulation and experiment.

2 Grey Wolf Optimization Algorithm

In traditional GWO algorithm, assume search in D-dimensional space, position of the i gray wolf $X_i = (X_i^1, X_i^2, \dots, X_i^D)$, $i = 1, 2, \dots, N$, N is population size. In the GWO population, alpha (α) is considered to be the best solution between wolves. Therefore, the second and third-best solutions are called beta (β) and delta (δ), respectively. The remaining solutions are assumed to be omega (ω). The position of the prey corresponds to that of the alpha Wolf. Mathematically, the model explains the behavior of hunting prey as:

$$X_i^d(t+1) = X_p^d(t) - A_i^d \cdot |C_i^d \cdot X_p^d(t) - X_i^d(t)| \quad (1)$$

where: equations t denotes iteration, equations $A_i^d \cdot |C_i^d \cdot X_p^d(t) - X_i^d(t)|$ denotes the distance between a gray Wolf and its prey, equations X_p^d and X_i^d represents the prey and the gray Wolf, A_i^d is the convergence factor, C_i^d is the oscillation factor. The calculation formula is as follows:

$$A_i^d = 2a \cdot rand_1() - a \tag{2}$$

$$C_i^d = 2 \cdot rand_2() \tag{3}$$

$$a = 2 \left(1 - \frac{t}{T_{\max}} \right) \tag{4}$$

where: $rand_1, rand_2$ is a random number between $[0, 1]$, a is the linear control parameter, $a_{\text{initial}} = 2, a_{\text{final}} = 0, T_{\max}$ is the maximum number of iterations.

When gray wolves find prey, the three wolves closest to the prey are α, β, δ , and the remaining wolves X_i surround the prey under the leadership of the three wolves. Therefore, positions $X_\alpha, X_\beta, X_\delta$ are regarded as prey positions:

$$\begin{cases} X_{i,\alpha}^d(t+1) = X_\alpha^d(t) - A_{i,1}^d \cdot |C_{i,1}^d X_\alpha^d(t) - X_i^d(t)| \\ X_{i,\beta}^d(t+1) = X_\beta^d(t) - A_{i,2}^d \cdot |C_{i,2}^d X_\beta^d(t) - X_i^d(t)| \\ X_{i,\delta}^d(t+1) = X_\delta^d(t) - A_{i,3}^d \cdot |C_{i,3}^d X_\delta^d(t) - X_i^d(t)| \end{cases} \tag{5}$$

$$X_i^d(t+1) = \frac{X_{i,\alpha}^d(t+1) + X_{i,\beta}^d(t+1) + X_{i,\delta}^d(t+1)}{3} \tag{6}$$

According to “Eq. (5)”, the distance between gray Wolf individuals and wolves α, β, δ and the moving direction of gray wolves are calculated. Finally, the positions of gray wolves are updated according to “Eq. (6)”.

3 Improved Grey Wolf Optimization Algorithm

3.1 Chaotic Population Initialization

In the swarm intelligence algorithm, the initial population distribution plays an important role in the subsequent optimization results. The random generation of initial population in GWO may lead to the aggregation of initial population within a certain range, which is easy to lead to too small search space and reduced search efficiency in the iterative process, resulting in premature convergence of the algorithm. Therefore, when initializing the population, it should be evenly distributed in the search space.

Chaos is a common nonlinear natural phenomenon in nature, which is characterized by randomness and ergodicity; Chaos initialization makes the population

more evenly distributed in the search space, makes the search space wider and more uniform, avoids falling into the local optimal state, and makes the algorithm easier to find the optimal solution. Therefore, sine chaotic mapping was used to initialize the gray Wolf population in this paper, and the mathematical model of sine chaotic mapping was as follows:

$$x_{n+1} = \mu \sin(\pi x_n) \quad (7)$$

3.2 Improved Nonlinear Convergence Factor

It can be seen from “Eq. (2)” that the change ability of convergence factor A is controlled by parameter a, that is, the global optimization and local search ability of GWO algorithm largely depends on parameter a. However, the process of finding the optimal solution of GWO algorithm is complex. It can be seen from “Eq. (4)” that the control parameter a decreases linearly, which is inconsistent with the complex search and optimization process of GWO algorithm. Therefore, this paper introduces trigonometric function and beta distribution²² into control parameter A. It can be seen from literature that nonlinear control parameters can better reflect the optimization process of GWO algorithm than linear control parameters.

Beta distribution is a density function and satisfies Bernoulli distribution and binomial distribution. The distribution interval is (0, 1) The mathematical expression of beta distribution is:

$$B(b_1, b_2) = \int_0^1 t^{b_1-1} (1-t)^{b_2-1} dt, b_1 > 0, b_2 > 0 \quad (8)$$

$$f(x) = \frac{x^{b_1-1} (1-x)^{b_2-1}}{B(b_1, b_2)}, 0 < x < 1 \quad (9)$$

Therefore, the parameter of nonlinear convergence factor proposed in this paper is:

$$a = 1 - \cos\left(2\pi \cdot \frac{t}{T_{\max}}\right) + 0.2B(b_1, b_2) \quad (10)$$

where: equations t denotes iteration, equations T_{\max} denotes maximum number of iterations; $a > 0, b > 0$.

3.3 Position Updating Formula Based on Particle Swarm Optimization

According to “Eq. (5)” and “Eq. (6)”, GWO algorithm only considers the location information exchange between each gray wolf individual when updating the location, and moves and iterates in the search space to converge to the optimal solution. However, it does not take into account the comparison between the gray wolf individual and the best location information of his own experience, which shows that it is an algorithm that lacks the individual’s own location memory.

In the particle swarm optimization algorithm, each particle retains its own historical optimal location information, finds a global optimal solution from these individual optimal solutions, and selects the optimal solution compared with the historical optimal solution. Therefore, this paper introduces the optimal information of its own experience history retained in the particle swarm optimization algorithm into the gray wolf optimization algorithm, and proposes a location update formula based on the individual’s own memory is:

$$X_i^d(t + 1) = w \left(\frac{X_{i,\alpha}^d(t + 1) + X_{i,\beta}^d(t + 1) + X_{i,\delta}^d(t + 1)}{3} \right) + rand \cdot (X_{ibest}^d - X_i^d(t)) \tag{11}$$

$$\omega = (\omega_{ini} - \omega_{end})(G_k - X_{ibest}^d) / G_k + \omega_{end} \tag{12}$$

where, X_{ibest}^d is the optimal position experienced by the gray Wolf individual, $rand$ is the random number between [0, 1], ω is the inertia weight coefficient, ω_{ini} is the initial inertia weight, G_k is the maximum number of iterations, and ω_{end} is the inertia Performance test and analysis of PGWO algorithm

4 Establishment of Five-Level SHEPWM Equations

Figure 1 shows the voltage waveform of cascaded Five-Level Inverter. The waveform is 1/4 even symmetrical in half cycle. The output nonlinear SHEPWM equations of Five-Level Inverter are:

$$\begin{cases} \frac{4}{\pi} \sum_{k=1}^N p_k \cos \alpha_k = 2m \\ \frac{4}{n\pi} \sum_{k=1}^N p_k \cos(n\alpha_k) = 0, n = 5, 7, 11, 13 \dots \end{cases} \tag{13}$$

where: when α_k is the rising edge, p_k is 1; When α_k is the falling edge, p_k is - 1. m is the adjustment system; N is the number of switching angles in 1/4 cycle; n is the number of harmonics; α_k is the switching angle and shall meet:

$$0 < \alpha_1 < \alpha_2 < \dots < \alpha_N < \frac{\pi}{2} \tag{14}$$

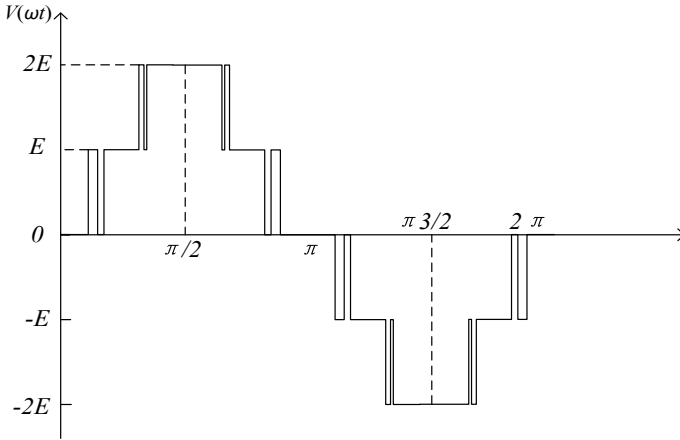


Fig. 1 Five-level voltage waveform

5 Improved Grey Wolf Algorithm for Solving Nonlinear Equations

The fitness function equation is established from “Eq. (13)”, as shown in “Eq. (15)”

$$\begin{cases} f_1(\alpha) = \frac{4}{\pi} \left[\sum_{k=1}^3 (-1)^{k+1} \cos \alpha_k + \sum_{k=4}^6 (-1)^k \cos \alpha_k \right] - 2m = \varepsilon_1 \\ f_2(\alpha) = \frac{4}{5\pi} \left[\sum_{k=1}^3 (-1)^{k+1} 5 \cos \alpha_k + \sum_{k=4}^6 (-1)^k 5 \cos \alpha_k \right] = \varepsilon_2 \\ \cdot \\ \cdot \\ \cdot \\ f_6(\alpha) = \frac{4}{17\pi} \left[\sum_{k=1}^3 (-1)^{k+1} 17 \cos \alpha_k + \sum_{k=4}^6 (-1)^k 17 \cos \alpha_k \right] = \varepsilon_6 \end{cases}$$

The fitness function is defined as:

$$f(\alpha) = \frac{1}{1 + \varepsilon_1^2 + \varepsilon_2^2 + \varepsilon_3^2 + \varepsilon_4^2 + \varepsilon_5^2 + \varepsilon_6^2} \tag{16}$$

When $f(\alpha) = 1$, the values of $\varepsilon_1, \varepsilon_2, \varepsilon_3, \varepsilon_4, \varepsilon_5, \varepsilon_6$ are all 0. At this time, it is considered that the PGWO algorithm converges to the optimal solution. Run GWO and PGWO programs respectively to solve the nonlinear equations under different modulation systems, and the obtained switching angle value and fitness function value are shown in Table 1 and Table 2.

The comparison between Table 1 and Table 2 shows that the fitness function value $f(\alpha)$ obtained by PGWO can be taken as 1, which is better than GWO algorithm. Compared with GWO, PGWO has better computational accuracy and global search ability, so better optimization results can be obtained.

Table 1 GWO switch angle between modulation 0.8 to 1.0

m	α_1	α_2	α_3	α_4	α_5	α_6	$f(\alpha)$
0.8	29.959	38.287	46.482	50.698	54.966	65.133	0.999
0.9	20.422	25.662	34.012	58.821	83.381	85.721	0.999
1.0	16.975	20.169	41.433	56.170	73.461	89.852	1

Table 2 PGWO switch angle between modulation 0.8 to 1.0

m	α_1	α_2	α_3	α_4	α_5	α_6	$f(\alpha)$
0.8	18.188	23.682	34.337	61.351	71.549	76.355	1
0.9	19.955	26.720	31.338	56.969	60.547	62.532	1
1.0	13.769	18.026	21.069	41.688	46.742	56.141	1

6 Simulation and Experimental Verification

6.1 Simulation Study

Taking the single-phase five level voltage source inverter as an example, the effect of SHEPWM selective harmonic elimination is verified. The system simulation parameters are as follows: the DC voltage source voltage is 24 V, the inverter load $L = 5 \text{ mh}$, $r = 5 \Omega$, and the fundamental frequency is 50 Hz. Figure 2 show the comparative analysis of PGWO and GWO voltage spectrum, voltage fundamental amplitude and harmonic distortion rate (THD) when modulation $m = 0.7$ and 0.9 .

Through the spectrum analysis of Fig. 2, it can be seen that the 5th, 7th, 11th, 13th and 17th harmonics in the voltage are basically eliminated, and the harmonic elimination effect of PGWO is better than that of GWO. Therefore, it can be proved

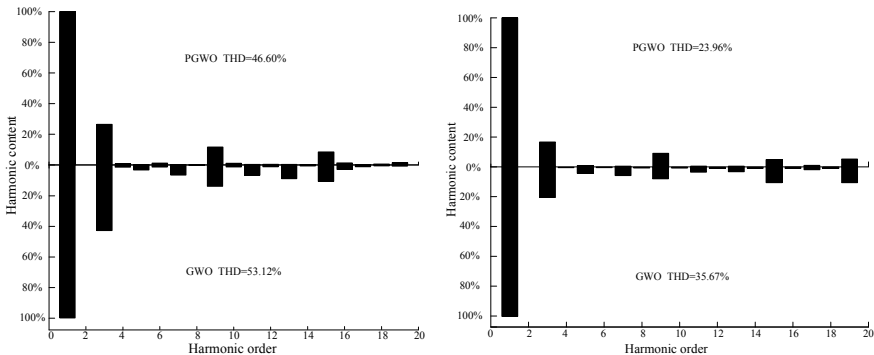


Fig. 2 Simulation spectrum comparison between modulation system $m = 0.7, 0.9$ PGWO and GWO voltage

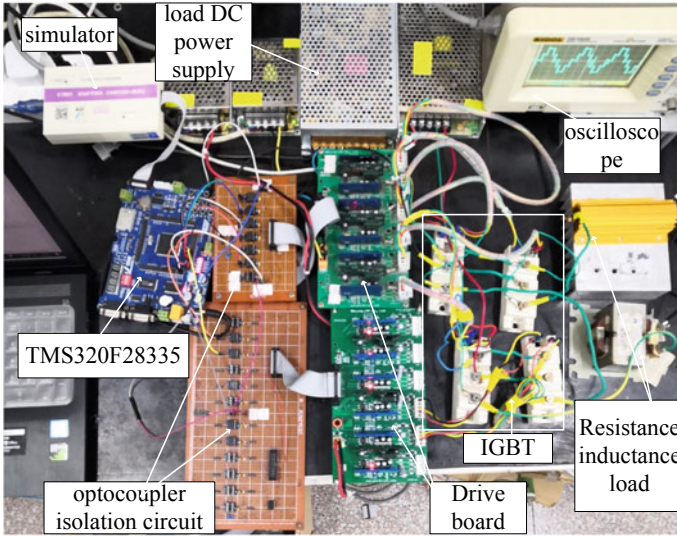


Fig. 3 Experimental circuit diagram

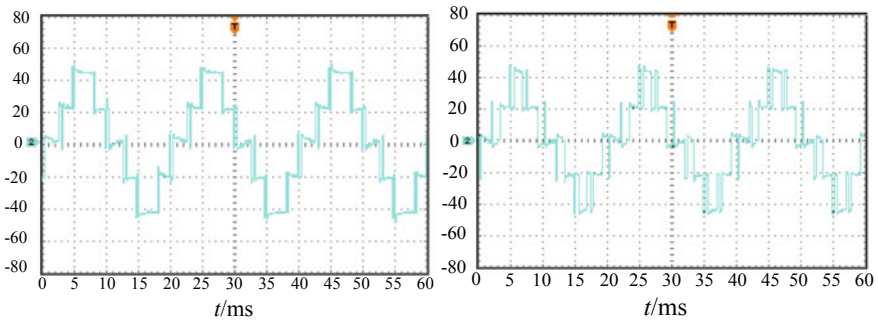


Fig. 4 Voltage waveform of modulation system $m = 0.7, 0.9$

that the improved gray wolf optimization algorithm proposed in this paper is correct and effective in solving the switching angle of SHEPWM.

6.2 Experimental Analysis

The parameters of the cascaded five-level experimental platform built in this paper are consistent with the simulation parameters. DSP (TMS320F28335) is used as the main chip, the main circuit module adopts the IGBT with the model of BSM50GB120DN2, the driving module adopts the logwood source integrated driving IGBT to drive

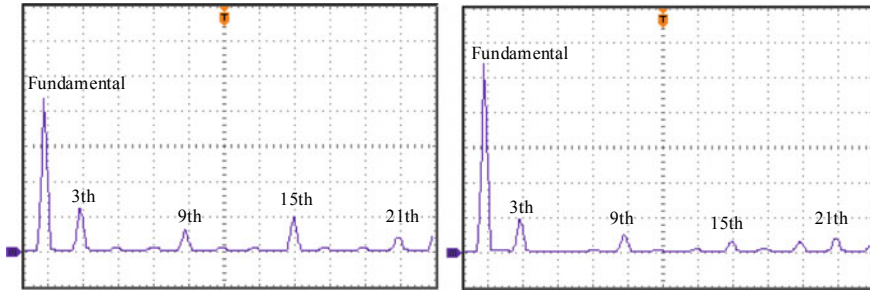


Fig. 5 Experimental spectrum of $m = 0.7, 0.9$ voltage modulation

DA962D6, and the oscilloscope model is DS1052E. The modulation ratio is 0.7 and 0.9. The experimental prototype is shown in Fig. 3 (Figs. 4 and 5).

7 Conclusions

In this paper, an improved grey wolf optimization algorithm is proposed to solve the switching angle of SHEPWM, and the grey wolf population is initialized by sine chaotic map; The nonlinear control parameters are introduced to realize the good transition of the algorithm from exploration to development; Inspired by the idea of PSO, a location update formula based on individual self memory is proposed. Compared with GWO, PGWO has higher precision, wider search range and is easier to jump out of the local optimum. The simulation and experimental results prove the accuracy and feasibility of PGWO in solving SHEPWM equations.

References

1. Yan, X., Guan, B., Du, X.: Multi-mode hybrid modulation strategy for three-level converters based on half-wave symmetric SHEPWM. In: 2021 IEEE 12th Energy Conversion Congress & Exposition - Asia (ECCE-Asia), Singapore, pp. 349–354 (2021)
2. Liu, C., Tian, X., Cao, Y., et al.: Specific harmonic elimination of cascaded multilevel inverters based on stochastic Newton method. *Power Syst. Prot. Control* **45**(5), 96–102 (2017)
3. Yang, K., Lu, D., Kuang, X., Yuan, Z., Yu, W.: Harmonic elimination for multilevel converters with unequal DC levels by using the polynomial homotopy continuation algorithm. In: 2016 35th Chinese Control Conference (CCC), Chengdu, China, pp. 9969–9973 (2016)
4. Zheng, C., Zhang, B.: SHEPWM technology of inverter based on Walsh transform. *Trans. China Electrotech. Soc.* (05), 65–71 (2005)
5. Zheng, C., Zhang, B.: Application of Wu elimination method to harmonic elimination techniques. In: *Proceedings of the CSEE*, vol. 25, no. 15, pp. 40–45 (2005)
6. Yang, K.-H., Wei, W., Wang, C., et al.: Complete algorithm solving switching angles for SHEPWM inverters. *Electr. Mach. Control* **18**(12), 24–30 (2014)

7. Ye, M., Li, S., Cai, H.: All solutions of the three-level inverter SHEPWM technology. In: Proceedings of the CSU-EPSA, **29**(10), 18–21, 29 (2017)
8. Yang, K., Chen, L., Yuan, Z., et al.: Parallel complete algorithm for solving switching angles of SHEPWM inverters. *Autom. Electr. Power Syst.* **39**(13), 87–93 (2015)
9. Chatterjee, A., Rastogi, A., Rastogi, R., Saini, A., Sahoo, S.K.: Selective harmonic elimination of cascaded H-bridge multilevel inverter using genetic algorithm. In: 2017 Innovations in Power and Advanced Computing Technologies (i-PACT), Vellore, India, pp. 1–4 (2017)
10. Sahu, J.K., Mishra, S.K., Hariharan, K.: Harmonic analysis of three phase inverter by using particle swarm optimization technique. In: 2019 International Conference on Smart Systems and Inventive Technology (ICSSIT), Tirunelveli, India, pp. 1158–1162 (2019)
11. Sahu, N., Londhe, N.D.: Selective harmonic elimination in five level inverter using sine cosine algorithm. In: 2017 IEEE International Conference on Power, Control, Signals and Instrumentation Engineering (ICPCSI), Chennai, India, pp. 385–388 (2017)
12. Nalcaci, G., Ermis, M.: Effect of grey wolf optimization on THD of 3- phase voltage source inverter with selective harmonic elimination base. In: 2019 4th International Conference on Power Electronics and their Applications (ICPEA), Elazig, Turkey, pp. 1–5 (2019)

Design and Application of Non-contact Voltage Acquisition Module for Dry Air Core Reactor



Zhiqin Ma, Gang Wang, Danyu Jiang, Xian Yang, Xiang Shu,
and Shuo Jiang

Abstract During the operation of dry-type air core reactor, the event of failure or even burning has always existed, which seriously threatens the safe and stable operation of the power grid. At present, there is no protection and monitoring method for the fault of dry-type air core reactor, and the monitoring method is very limited for the fault. Based on the principle of non-contact optical measurement, a non-contact voltage waveform acquisition method is proposed in this paper. The sampling rate is more than 20 MHz and the sampling channels are not less than 3. It fills the gap of fault monitoring method for dry-type air core reactor. And the dynamic response test of the contactless voltage acquisition module in the time domain and frequency domain was carried out. On the basis of meeting the needs of strong electric field measurement in sensitivity, dynamic range and frequency response, the on-site test of reactor overvoltage switching was carried out. The results show that the module has good accuracy in measuring overvoltage based on the contactless principle. It can meet the requirements of on-site testing, and is convenient to enrich the databases of different reactor equipment. It provides technical support for reactor insulation detection and fault warning research.

Keywords Dry air-core reactor · Fault monitoring · Non-contact type · Acquisition module

Z. Ma (✉) · G. Wang · D. Jiang · X. Yang · X. Shu · S. Jiang
Guangdong Electric Power Equipment Reliability Key Enterprise Laboratory,
Guangzhou 510080, China
e-mail: mzhqcqu@163.com

Z. Ma · G. Wang · X. Yang · X. Shu · S. Jiang
Electric Power Research Institute of Guangdong Power Grid Co., Ltd., Guangzhou 510080, China

© Beijing Paike Culture Commu. Co., Ltd. 2023
X. Dong et al. (eds.), *The proceedings of the 10th Frontier Academic Forum of Electrical Engineering (FAFEE2022)*, Lecture Notes in Electrical Engineering 1054,
https://doi.org/10.1007/978-981-99-3408-9_16

1 Introduction

With the large number of dry-type air core reactors put into operation in the power grid and the wide application of large capacity dry-type air core shunt reactors, the faults are exposed constantly [1, 2]. There are many encapsulated branches of dry-type air core reactor, which may cause inter turn short circuit, strand breakage or turn number deviation during manufacturing and transportation. During operation, winding insulation breakdown is caused by winding damp, partial discharge, partial overheating insulation burning and other reasons, as well as loss and heating of surrounding metal framework, grounding grid, wiring terminals in high-voltage cabinet caused by magnetic leakage. According to incomplete statistics of power sector, interturn short circuit fault accounts for more than 70% of total reactor faults [3]. When the inter turn short circuit fault occurs in the dry reactance, the local temperature at the short circuit location rises sharply, accelerating the insulation aging near the short circuit turn, making the short circuit fault develop continuously, and then expand to multi turn short circuit fault. The reactor will catch fire in a short time, and can no longer be maintained and used [4, 5].

For reactor faults, the existing diagnostic methods mainly include the measurement of reactor DC resistance, infrared temperature measurement and loss measurement [6–8]. However, due to the absence of some power frequency anti-interference measures for relevant measuring instruments, the measurement results caused by strong power frequency interference during field measurement are inaccurate, which will seriously lead to the burning of measuring instruments, and it is impossible to accurately determine the fault type and find the fault point. At the early stage of turn to turn short circuit fault of dry-type air core reactor, due to the lack of obvious changes in electrical parameters, the existing monitoring methods for turn to turn short circuit fault have the problem of poor sensitivity, which can not detect the initial turn to turn short circuit fault of the reactor in time and take pre control measures [9–11]. With the more and more heavy task of reactor in power system, it is very urgent to solve the problem of reactor fault monitoring. Therefore, it is necessary to study the fault development characteristics under typical reactor defects and propose a highly reliable, highly sensitive and portable reactor fault diagnosis method and device.

The number of dry-type air core reactor equipment is huge, and the switching times are frequent. Considering the simplicity and feasibility of on-site switching overvoltage test, this paper proposes a non-contact voltage waveform acquisition method (the line does not need to power off to install a voltage divider). With the non-contact field sensor as the front end, research and build a collection module suitable for the test of reactor switching overvoltage waveform, which provides effective help for the collection of reactor transient overvoltage waveform.

2 Testing Principle and Testing Equipment

2.1 Architecture of Non-contact Voltage Waveform Acquisition Module

As shown in Fig. 1, the non-contact optical measurement principle is adopted in this paper. The photoelectric integrated electric field measurement system consists of the following parts: laser source, polarization maintaining fiber, sensor, optical receiver, acquisition and processing module. The laser source is used to generate linearly polarized light with constant power. It is transmitted to the sensor through the polarization maintaining fiber and modulated under the effect of electric field. The optical power signal is input into the optical receiver through the polarization maintaining fiber to convert the optical power signal into a voltage signal. The voltage signal containing the electric field information is obtained with the acquisition card, and is observed and measured through the processing module.

The two modes of light in the sensor are affected by the electric field, resulting from the phase difference of the linear correlation of the electric field. When the waveguide is output, the two modes of light interfere, and the phase difference signal is converted into light intensity signal. The optical receiver converts the light intensity signal into voltage signal, which is recorded by the oscilloscope. This voltage signal is portable with the electric field signal sensed by the sensor. The transfer function of the measurement system is:

$$V_{out} = A \cdot [1 + b \cdot \cos(\varphi_0 + \frac{E}{E_{\pi}}\pi)] \tag{1}$$

where, A is the power loss of the optical path and the photoelectric conversion coefficient of the receiver; b is the extinction ratio of the sensor; φ_0 is the phase difference caused by natural infringement; E_{π} is defined as the half wave electric field of the sensor, that is, when the applied electric field is E_{π} , the phase difference is

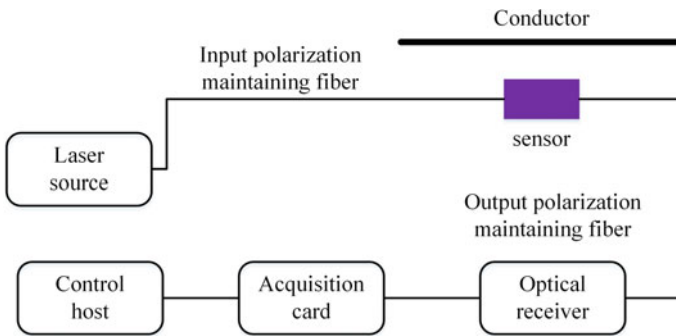
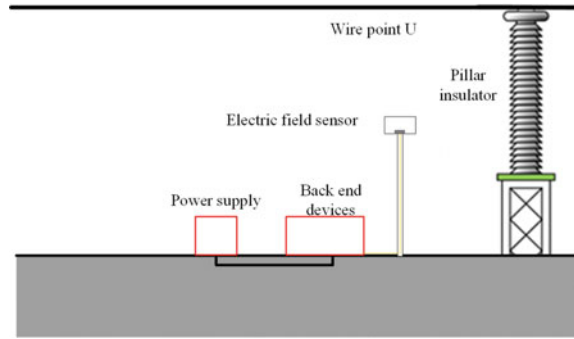


Fig. 1 Schematic diagram of the designed galloping test system

Fig. 2 Schematic diagram of voltage sensing terminal system



π . Generally, through production process control φ_0 is approximately $\pi/2$. When the measured electric field E is far less than E_π , the transfer function can be approximately expressed as:

$$V_{out} = A \cdot [1 + b \cdot \frac{E}{E_\pi} \pi] \quad (2)$$

It can be seen that the response output of the measurement system is linear with the electric field within a certain range. The installation implementation scheme of voltage sensing terminal is shown in Fig. 2. It mainly consists of three parts: all optical electric field sensor, support frame and back-end equipment.

2.2 Construction of Non-contact Voltage Acquisition Module

The final acquisition module is shown in Fig. 3, including non-contact optical electric field sensor, support frame, polarization maintaining fiber, light source module, acquisition card and acquisition host. The integrated optical electric field sensor has a measuring range of 5–500 kV/m. The multi-channel PCI-E acquisition card corresponding to ADLINK is proposed to be selected in the design, with the maximum sampling rate of 100 MHz and the accuracy of 16bit, meeting the requirements that the sampling rate is not less than 20 MHz and the sampling channel is not less than 3. The front end uses an optical sensor to detect the voltage signal, and the back end directly transmits the voltage signal to the high-speed acquisition card or oscilloscope, and collects data through a micro PC.



Fig. 3 Physical object of voltage acquisition module

3 The Non-contact Voltage Acquisition Module Test

3.1 Time Domain Response Speed Test of Sensor

(1) ms level response

The power frequency response of the sensor can be obtained by using the experimental device. The normalized input and output waveforms are shown in Fig. 4(a). The correlation coefficient between V_{out} and electric field E is output by the sensor $\rho(V_{out}, E)$ to characterize the degree of the sensor's following the original electric field. The correlation coefficient of the waveform shown in Fig. 4 is 0.999, indicating that the sensor has a good power frequency response [12].

Use the operation wave generator and the spherical plate electrode to generate a 250/2500 μs long wave head operation wave electric field, place the sensor between the spherical plate electrodes, and normalize the input and output waveforms as shown in Fig. 4(b), with a correlation coefficient of 0.996. Both power frequency

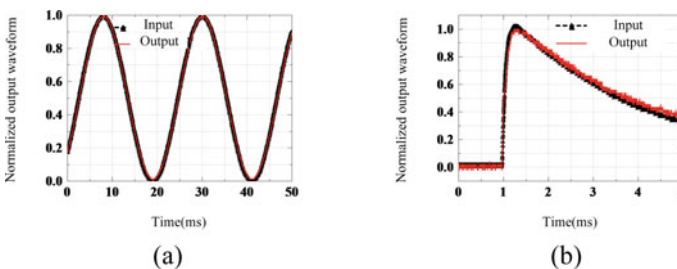


Fig. 4 Power frequency (a) and Long wave head (b) operation wave response of sensor

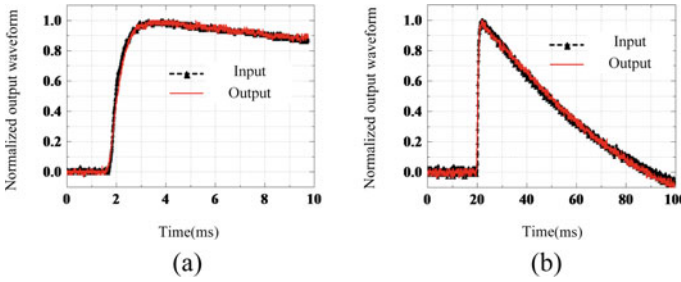


Fig. 5 Lightning wave response of sensor (wave head **(a)** and full wave **(b)**)

response and long wave head operation wave response indicate that the sensor can follow the ms level waveform well.

(2) μs level response

The high-voltage power supply is replaced by a lightning wave generator (EMCpro), which can output lightning waves with a peak value of 0.2–6 kV. The lightning wave head and full wave response of the sensor are shown in Fig. 5, and their correlation coefficients are 0.998 and 0.996 respectively.

3.2 Response Speed Test of Sensor

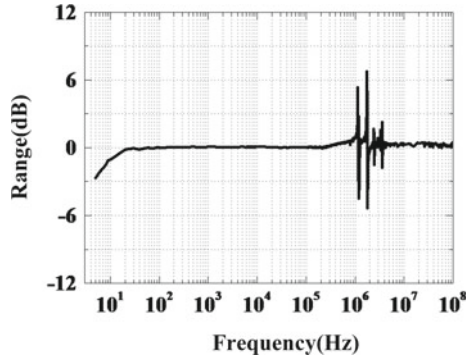
When the high-voltage power supply is replaced by a low-frequency signal generator, the peak value of the electric field signal generated is about 2.5 kV/m, and the frequency range is 5–10 kHz.

High frequency signal generator, power amplifier, TEM cell and spectrometer are used to investigate the high frequency response of the sensor. The test range of the frequency sweep device is 250 kHz–100 MHz, and the amplitude of the electric field signal is about 300 V/m.

The existing experimental devices cannot generate sweep signals in the frequency band of 10–250 kHz. The amplitude frequency response in the range of 5 kHz–1 MHz is analyzed by using fast Fourier transform.

Synthesizing the frequency response characteristics of each frequency band, the amplitude frequency response characteristics of the sensor in the range of 5 Hz–100 MHz are obtained, as shown in Fig. 6. The 3 dB lower cut-off frequency of the sensor is about 5 Hz, and the 3 dB upper cut-off frequency is greater than 100 MHz. Except for the resonant frequency point in the 1.2–3.5 MHz frequency band, the sensor has flat frequency response characteristics from 20 Hz to 100 MHz.

Fig. 6 Amplitude frequency response (5 Hz–100 MHz)



4 The Non-contact Voltage Acquisition Module Test

4.1 On Site Switching Test of Test Station

Based on the built acquisition module, the field test of the test station was carried out. The test architecture and on-site installation are shown in Figs. 7 and 8. The sensor is fixed below the bus, the circuit breaker conducts switching test, and the switching overvoltage waveform is collected through the acquisition module.

The switching overvoltage waveform is shown in Fig. 9. The switching overvoltage waveform is an attenuated oscillation waveform. The oscillation period is related to the electrical parameters of the circuit breaker shunt reactor system. Multiple switching tests show that the frequency of the oscillation waveform is shown in Table 1, indicating that the acquisition module has good stability. At the same time, it is found that the switching overvoltage at the end of the circuit breaker is consistent with that of the reactor bus.

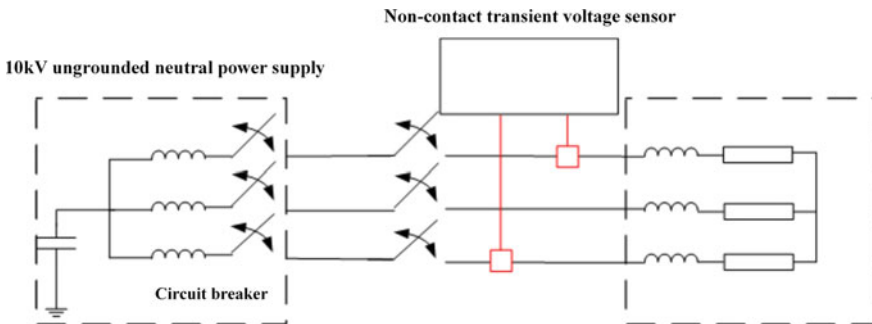


Fig. 7 Field test framework of three-phase switching test

Fig. 8 Field installation test

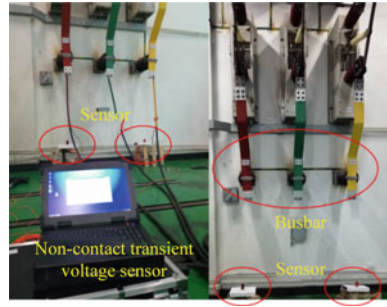


Fig. 9 Test results of switching test

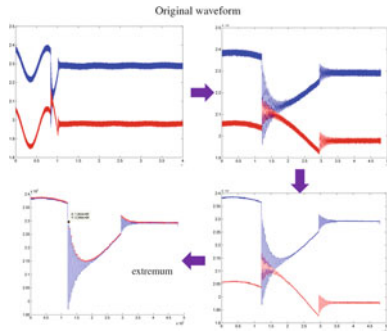


Table 1 Oscillation waveform frequency

	The first transient process	The second transient process
1	9.5 kHz	11 kHz
2	5.5 kHz	6.5 kHz

4.2 On Site Switching Overvoltage Test of Substation

On site switching overvoltage test was carried out for circuit breaker to cut off shunt air core reactor [13].

In order to verify the accuracy of the non-contact acquisition module, the non-contact acquisition module and the voltage divider are used to test and compare in the field. The data waveform collected by the non-contact acquisition module is shown in Fig. 10(a), and the data waveform collected by the voltage divider acquisition module is shown in Fig. 10(b).

Compare the overvoltage waveform measured by voltage divider with that measured by non-contact method, and the voltage envelope, overvoltage multiple and frequency are consistent. The frequency and overvoltage multiple of the collected switching overvoltage waveform are analyzed, and the comparison between the measurement results of the non-contact acquisition module and the voltage divider is

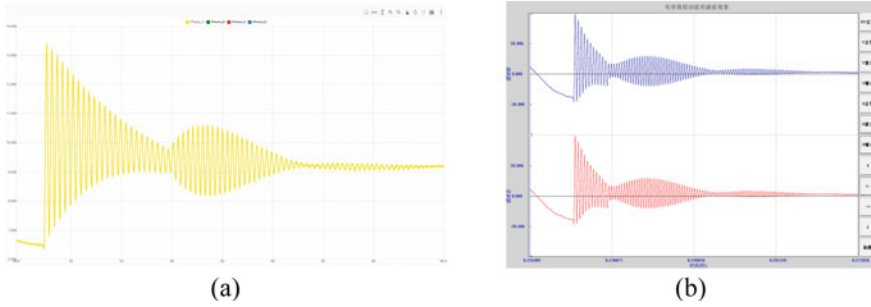


Fig. 10 Results of non-contact acquisition module (a) and divider acquisition module (b)

Table 2 Overvoltage multiple and oscillation waveform frequency

	Overvoltage multiple	Oscillation frequency
Reactor 1	1.18	2 ± 0.05 kHz
Reactor 2	1.21	6.5 kHz
Error ratio	2.48%	0–3.7%

shown in Table 2. It can be seen from the comparison that the error between the non-contact measurement method and the voltage divider measurement results is small, the over-voltage multiple measurement error is 2.48%, and the maximum error of the oscillation frequency is 3.7%, which shows that the over-voltage accuracy measured based on the non-contact principle is good and meets the requirements of on-site test.

5 Conclusion

In this paper, the research on switching oscillation overvoltage test of dry-type air core reactor is carried out, the non-contact acquisition module of switching oscillation overvoltage waveform is built, the non-contact voltage waveform acquisition architecture is developed.

- (1) The response test of the non-contact voltage acquisition module in time domain and frequency domain is carried out. On the basis of verifying that its sensitivity, dynamic range, frequency response and other aspects meet the requirements of strong electric field measurement.
- (2) Three phase overvoltage switching test of reactor and on-site switching overvoltage test of substation are carried out, and the overvoltage measured by voltage divider is compared. The results show that the over-voltage accuracy of the module based on the non-contact principle is good, and it meets the on-site test requirements.

- (3) This module can effectively collect the overvoltage data of reactor switching, which is convenient to enrich the database of different reactor equipment, and facilitate the comprehensive analysis of data. It provides strong technical support for reactor insulation detection and fault early warning research.

Acknowledgements This work was funded by Guangdong Power Grid Science and Technology Project, (GDKJXM20198252) China.

References

1. Li, W., et al.: Research on fault types and causes of dry-type air core reactor. *Power Equip. Manag.* **36**(1), 63–64 (2020). (in Chinese)
2. Lin, H., et al.: A preliminary study on the formation mechanism of microcracks in dry-type air-core shunt reactors. In: *International Conference on High Voltage Engineering and Application (ICHVE)*, Beijing, China, pp. 1–4. IEEE (2020)
3. Nie, H.Y., et al.: Breaking overvoltage of dry-type air-core shunt reactors and its cumulative effect on the interturn insulation. *IEEE Access* **7**, 55707–55720 (2019)
4. Chen, J.S., et al.: Common faults and rectification measures of 35kV dry type air core reactor. *Electr. Technol.* **19**(1), 77–79 (2018). (in Chinese)
5. Li, R.X., et al.: Diagnosis and analysis of abnormal heating fault for 35kV dry air core reactor. In: *5th Advanced Information Technology, Electronic and Automation Control Conference (IAEAC)*, Chongqing, China, pp. 431–434. IEEE (2021)
6. Wang Y.H. et al.: Analysis of influencing factors on site fault diagnosis of inter-turn short circuit fault of dry-type air-core shunt reactor. In: *International Conference on the Properties and Applications of Dielectric Materials (ICPADM)*, Xi'an, China, pp. 713–716. IEEE (2018)
7. IEEE Draft Standard Requirements, Terminology, and Test Code for Dry-Type Air-Core Series-Connected Reactors, pp. 1–117. IEEE PC57.16/D9 (2011)
8. Xue, S.W., et al.: Analysis and research on insulation data of dry air core reactor based on fuzzy theory. In: *18th International Conference on Computer and Information Science (ICIS)*, Beijing, China, pp. 306–309. IEEE (2019)
9. Ru, Q.S., et al.: Research status and prospect of dry air core reactor fault monitoring and early warning technology. *Power Equip. Manag.* **3**(7), 218–219 (2021). (in Chinese)
10. Zhuang, Y.A., et al.: Monitoring method of inter-turn insulation fault for dry-type air-core shunt reactor. In: *International Conference on the Properties and Applications of Dielectric Materials (ICPADM)*, Xi'an, China, pp. 700–703. IEEE (2018)
11. Zhu, Y.C., et al.: Research and application of on-line monitoring device for dry-type air-core reactor. In: *International Conference on Electron Devices and Solid-State Circuits (EDSSC)*, Xi'an, China, pp.1–2. IEEE (2019)
12. Dong, C., et al.: Broadband voltage measurement and sensor performance test based on capacitive transformer bushing. *Chongqing University* (2021). (in Chinese)
13. Juan, A., et al.: Switching overvoltage measurements and simulations—Part I: field test overvoltage measurements. *IEEE Trans. Power Deliv.* **29**(6), 2502–2509 (2014)

Experiment and Simulation Study on the Generation Process of Cable Carbonization Path



Xiaoyong Ye and Zhihong Xu

Abstract Power cable carbonization path fault arc in the cause of electrical fires occupies a large proportion. It has the characteristics of difficult prevention, strong concealment, and great harm. Based on the arc fault characteristics experimental device, a high-speed camera was used to take pictures of the cable carbonization path generation process, and the mechanism of the process is analyzed in stages. An orthogonal experiment was used to obtain the primary and secondary influencing order of each factor on the results, and the optimal level combination. Finally, based on Magnetohydrodynamics (MHD) theory, a simulation model of the BVVB cable notch arc was established by Comsol software to simulate the dynamic trend of the arc in the early carbonization process. By comparing the simulation results with the actual images captured by the high-speed camera, the feasibility of the model is verified, and it provides ideas for further research on the cable carbonization path process.

Keywords Cable arc · Carbonization path · Orthogonal experiment · Magneto-hydrodynamics

1 Introduction

According to national statistics on house fires in China from 2012 to 2021, electrical fires topped the list with a proportion of 42.7%, posing a serious challenge to people's lives and property. As a necessary part of the electrical circuit, wires and cables are the main factors causing fires, and the percentage of electrical fires in 2020 caused by

X. Ye · Z. Xu (✉)

College of Electrical Engineering and Automation, Fuzhou University, Fuzhou 350108, China
e-mail: 641936593@qq.com

Fujian Key Laboratory of New Energy Generation and Power Conversion, Fuzhou 350108, China

Fujian Province University Engineering Research Center of Smart Distribution Grid Equipment, Fuzhou 350108, China

© Beijing Paiké Culture Commu. Co., Ltd. 2023

X. Dong et al. (eds.), *The proceedings of the 10th Frontier Academic Forum of Electrical Engineering (FAFEE2022)*, Lecture Notes in Electrical Engineering 1054, https://doi.org/10.1007/978-981-99-3408-9_17

wiring problems reached 68.9% [1]. The reasons of fires caused by lines themselves can be divided into two main aspects, current factor and fault arc factor [2]. The current factor mainly refers to the current overload in the line, so that the internal heating causes the insulating material to overheat and burn; the fault arc factor mainly refers to the local overheating caused by the fault arc, resulting in the insulation material or flammable materials around the cable on fire.

At present, for arc fault fire prevention, research is mainly focused on the detection of low-voltage arc fault. It's relevant standards UL1699 and GB/T 31,143-2014 pointed out that the detection process requires the generation of arc fault waveform in arc fault detection device [3]. There are two main methods to generate the arc waveform: one is to add a fault arc generator in the circuit to generate an actual arc, including arc pulling device and cable carbonization path specimen. [4] proposed two types of cutouts and one type of articulated pretreatment were performed for different cable types, and it was concluded that different treatments can have a direct effect on the arc waveform after cable carbonization. [5] proposed a method to improve the carbonization success rate by using a fixed bending angle, quantifying the creepage distance on the process of the cable specimen cutting. Another way to generate waveforms is to simulate the arc through electronic devices and digital signals. [6] proposed a closed-loop controlled constant-current output fault arc waveform generation device that can output an arc with a maximum RMS value of 10 A. [7] established a fault arc waveform database, which can be used to find the corresponding current source waveform during testing, which improves the waveform generation efficiency to a certain extent. Although the arc waveform simulation device has the advantages of small size, high speed and strong flexibility, however, the analog waveform still cannot restore all the actual information. Therefore, misoperations or inactions are prone to occur in the inspection process of the arc fault detection device, which effects the accuracy. Cable carbonization path as a natural carrier of the fault arc, its waveform information is the most complete and accurate, so the in-depth study of the cable carbonization path still has greater relevance and necessity.

Currently, other scholars have conducted partial studies on the generation of charged pyrolysis and carbonization paths in cables. [8] studied the pyrolysis process of low-voltage flame-retardant cables in substations, and summarized the difference between the pyrolysis reaction mechanism of actual cables and pure PVC. [9] proposed a carbonization path generation mechanism for the flashover inside and on the surface of the cable, causing by the combined action of overcurrent and water absorption of the cable CaCO_3 filler. [10] combined the one-dimensional heating model of the cable with the Arrhenius expression to establish a combustion pyrolysis model of the cable in an external heating source. [11] proposed two mechanisms for the generation of fault arc in cables: one is that in a twin-core conductor where a single conductor is severed, the conductor heats up. The broken conductor pierces the outer skin layer and connect with another one, eventually leading to fault arc. The other is that the arc discharge phenomenon generates directly when the conductor of the complete component is disconnected.

In this paper, a high-speed camera was used to capture the dynamic evolution process image of the cable notch arc in the arc fault characteristic experimental

device, so as to analyze the generation mechanism of the cable carbonization path. On this basis, an orthogonal experiment was designed to analyze the different influencing factors on the success rate of cable carbonization path generation, the primary and secondary order of the influencing factors and optimal level combination were determined. Finally, based on magnetohydrodynamics (MHD), a model of the cable notch arc was built in the Comsol software, and the dynamic characteristics of the arc were analyzed. At the same time, the simulation results were compared with the arc images to verify the feasibility of the simulation model.

2 Analysis of Cable Carbonization Process Based on High-Speed Camera

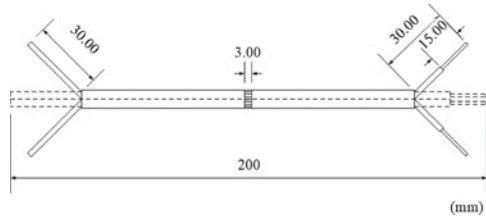
The discharge early stage of the carbonization path generation process is rapid and short, conventional image acquisition instruments are difficult to collect information. High-speed camera has the characteristics of short shooting interval, non-contact acquisition, low exposure at high frame rate, etc., which can quickly capture the discharge phenomenon of high brightness, and use the brightness difference to effectively exclude the interference of other non-luminous objects for the identification of features related to the discharge phenomenon. Therefore, in this paper, a high-speed camera is used to photograph the carbonization path generation process and analyze related phenomena.

2.1 Experimental Design

The high-speed camera used in this paper is Phantom MIRO M310. The experimental sample is a $2 \times 1.5 \text{ mm}^2$ BVVB-Copper core PVC insulated and sheathed flat cable, and the cutting treatment is shown in Fig. 1. The carbonization path experimental equipment is the JD-DHGZ-1 arc fault characteristic experimental device designed according to the national standard GB/T31143-2014 "General Requirements for Arc Fault Protection Devices (AFDD)" [12]. According to the design, the carbonization experimental energization voltage and current in the experimental device were set to 7 kV, 30 mA and 2 kV, 300 mA, respectively, in order to quickly generate the carbonization path.

2.2 Analysis of the Carbonization Process

Wire and cable are subject to external forces such as bending, pulling and squeezing, resulting in rupture of the insulation sheath and copper core. The copper core is

Fig. 1 Cable sample

exposed to the air and the exposed part is prone to electric breakdown and discharge phenomenon when energized. Under the effect of discharge, the insulation sheath is thermally decomposed and turns into a conductive channel mixed with carbon and organic semiconductors. However, the discharge process in actual conditions is random and strong, while the entire generation process is slow, leading to difficulties in capturing focused information, so this paper uses a high-speed camera to shoot and analyze the carbonization path generation process that occurs in the carbonization device of the arc fault characteristic experimental equipment. The actual shooting parameters of the high-speed camera were set as resolution 256×128 , frame rate 6000 fps and exposure time $160 \mu\text{s}$.

Figure 2 shows the high-speed camera image of the arc burning at the cable notch at an energized voltage of 2 kV. Because the electric intensity of the sharp part between the exposed copper cores is extremely high to produce electric breakdown, an arch-shaped arc is formed between the exposed copper cores at the cable notch, and the arc root spot is bright and clearly visible, as shown in Fig. 2(a), so this moment is recorded as the arc burning moment of 0 ms. Because the pyrolysis temperature of PVC, the main component of the insulation skin, is 543 K [8], and the temperature of the arc is mostly above 3000 K. Broken non-dense insulation sheath debris at the cut is the first to be pyrolyzed, producing HCl gas and benzene gas [8]. The gas blows the arc, which gradually elongates and expands, but is always not pulled off and blown out. Along with the change of current RMS, the arc burning also shows a corresponding change from violent to gradually extinguished, the burning duration is 7.5 ms, see Fig. 2(b)–(e). Thereafter, the arc reignites after the first burning arc of 9.8 ms, and enters the next burning arc cycle, as shown in Fig. 2(f).

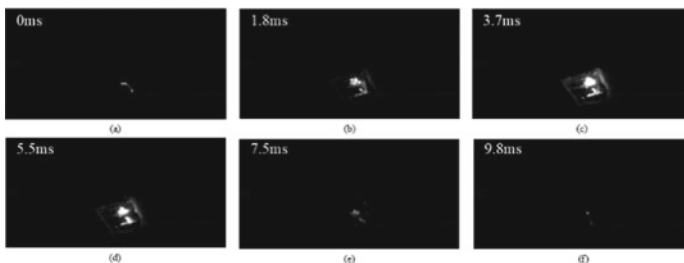
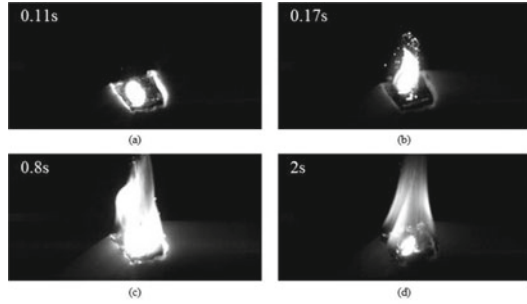
**Fig. 2** Arc burning image of cable notch

Fig. 3 Cable notch carbonization path generation image



With the continuous reignition of the arc heating and its own thermal inertia, the temperature at the cable notch gradually increases. More PVC around the copper core undergoes pyrolysis and begins to form a carbon layer covering the incision surface, and a bright flame begins to appear at the incision along with some molten copper splashes, see Fig. 3(a)–(b). Thereafter, the arc continued to emit energy. With the flame at the incision extending from the local to the whole incision, the PVC sheath accelerates the pyrolysis and a large amount of loose carbon chain structure can be observed to accumulate in Fig. 3(d).

2.3 Carbonization path Generation Mechanism

The generation process of the high voltage carbonization path within the cable carbonization equipment can be divided into two main stages, the first stage is the arc discharge stage. Initially the discharge phenomenon occurs at the location of the broken copper core, which in turn forms an arc between the two bare copper cores. The arc heats the surrounding PVC and copper debris. When PVC is pyrolyzed, HCl and benzene gases are released, which cause the arc to shift in shape and perhaps cause the arc root to migrate over the exposed copper core. The pyrolysis residual carbon begins to gradually cover the incision surface. The second stage is the burning stage of the sheath by heat. When the incision accumulates heat to the ignition point of the sheath material in the first stage, the PVC starts to be on fire, and a bright flame appears. Sufficient heat promotes the pyrolysis and combustion of the sheath. Generally, the PVC in the insulating layer is mixed with flame retardant, which mainly produces dense carbon slag and loose carbon layer during combustion to isolate the heat exchange between the flame and the sheath, so a large amount of loose carbon layer will accumulate at the incision. These layers of carbon with semiconducting properties are concentrated in the incision, which provides excellent conditions for the existence and development of the arc while isolating the heat source, for example: when the carbon content of the carbon layer reaches the “Percolation Threshold” [13], the resistivity will drop rapidly and the current flow more easily through the carbon layer; the carbon has hot ion emission properties when

heated [14], which facilitates the arc initiation. Eventually, a stable structure like carbon-carbon or carbon-copper electrode with certain internal gap will be formed at the incision, and the carbonization path will be generated.

3 Multi-factor Analysis of Carbonization Path Generation

The success criteria of cable carbonization are mainly determined by the arc waveform morphology after energization and the luminescence of the series-connected 100 W bulb. Carbonization path waveform according to the shape of the arc waveform can be divided into three kinds: Arc waveform intermittently missing and the presence of a sine wave is called under-carbonization, in this case the bulb flickers; arc waveform continues without a sine wave is called normal-carbonization, in this case the bulb continues to shine; arc waveform completely missing and only the presence of a sine wave is called over-carbonization, in this case the bulb continues to shine and be high brightness. The specific waveform can be seen in Fig. 4. The above three cases only when the normal carbonization represents a stable carbonization path successfully generated.

Considering the enforceability and determinacy of various factors in practice, this paper chooses to investigate the influence of the following factors on the carbonization success rate using orthogonal analysis experiments, including the cable structure (that is, whether the cable is fixed with PVC filler between the inner double cores or not, structure A with filler and structure B without filler), the notch width, the energization time at different voltages. The cable specimens are treated in the same way as in Fig. 1, only need to wrap two turns of electrical insulation tape and glass fiber flame retardant tape at the notch. The number of cable specimens for each group of orthogonal experiments was 10. The above experimental was in the cable carbonization device of JD-DHGZ-1 arc fault characteristics experimental device.

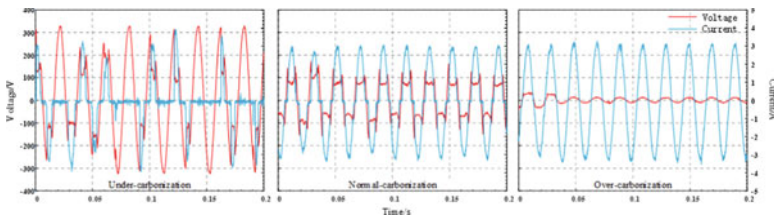


Fig. 4 Different arc waveforms of carbonization paths

Table 1 Factor level table

	Structure	Notch width (mm)	7 kV energization time (s)	2 kV energization time (s)
1	A	1	0.5	0.5
2	B	2	1	1
3		3	2	1.5
4		4	3	2
5			4	2.5

3.1 Orthogonal Experimental Design

The effect of each factor on the success of carbonization can be investigated through orthogonal design experiments. The success rate mainly focuses on four factors: cable structure, notch width, and energization time of different voltages, as shown in Table 1.

Ignoring the interaction level effect between the factors, the orthogonal table L25 (5⁶) was selected. Considering the inconsistent levels of the factors, the orthogonal scheme of this experiment was obtained after using the quasi-level horizontal and the combination method.

3.2 Range Analysis in Orthogonal Experiments

The range analysis is a common method in orthogonal experiments. This method can be used to obtain the primary and secondary influencing order of each factor and level on the results, and to analyze the optimal level combination.

Based on the experimental data in Table 2, the *K* values and *k* values were calculated for each factor level. Because of the inconsistent level of this orthogonal experiment, the *R'* value needs to be calculated, and the calculation results were shown in Table 3.

1. According to the comparison of *R'* values in Table 3, the main influencing order of each factor on the success rate of carbonization is: 2 kV energization time > notch width > structure > 7 kV energization time, and 2 kV energization time has the most significant influence on the success rate.
2. According to the comparison of *k* values in Table 3, the optimal level combination of each factor was determined as structure A (the cable is fixed with PVC filler between the inner double cores), notch width 1 mm, 7 kV energizing time 4 s, 2 kV energizing time 2.5 s.

Table 2 Orthogonal experimental data

	Structure	Notch width (mm)	7 kV energization time (s)	2 kV energization time (s)	Success rate
1	A	1	0.5	0.5	0.5
2	A	2	2	2	0.5
3	A	3	4	1	0.6
4	A	4	1	2.5	0.8
5	A	1	3	1.5	0.6
6	B	1	4	2	0.9
7	B	2	1	1	0.7
8	B	3	3	2.5	0.8
9	B	4	0.5	1.5	0.2
10	B	2	2	0.5	0.4
11	A	1	3	1	0.7
12	A	2	0.5	2.5	0.6
13	B	3	2	1.5	0.4
14	B	4	4	0.5	0.1
15	A	3	1	2	0.5
16	B	1	2	2.5	1
17	A	2	4	1.5	0.6
18	B	3	1	0.5	0
19	A	4	3	2	0.6
20	A	4	0.5	1	0.3
21	A	1	1	1.5	0.7
22	B	2	3	0.5	0.1
23	B	3	0.5	2	1
24	B	4	2	1	0.2
25	B	1	4	2.5	0.9

4 Cable Notch Arc Model Simulation

Before building the simulation model, the following assumptions were made for conditions in order to facilitate convergence and solution.

1. The arc for the simulation solution is assumed to be an equilibrium plasma, satisfying local thermodynamic equilibrium.
2. The magnetic field is a uniform steady-state field and the flow of the arc is laminar.
3. The effect of the arc on the ablation of the contact region and the sheath layer in the near-polar region is not considered.

Table 3 Range analysis datasheet

Item	Level	Structure	Notch width (mm)	7 kV energization time (s)	2 kV energization time (s)
K_i	1	7	5.3	2.6	1.1
	2	6.7	2.9	2.7	2.5
	3	–	3.3	2.5	2.5
	4	–	2.2	2.8	3.5
	5	–	–	3.1	4.1
k_i	1	0.58	0.76	0.52	0.22
	2	0.52	0.48	0.54	0.5
	3	–	0.55	0.5	0.5
	4	–	0.37	0.56	0.7
	5	–	–	0.62	0.82
R		0.07	0.39	0.12	0.6
R'		0.17	0.43	0.11	0.54

4.1 Arc Magnetohydrodynamic Equation Set

The stable combustion of arc plasma is a complex multi-physics field coupling process involving electric, magnetic, and fluid fields, so the coupling process needs to be considered in the simulation calculation [15].

The mass conservation equation:

$$\frac{\partial \rho}{\partial t} + \nabla \cdot (\rho \mathbf{U}) = 0 \quad (1)$$

where ρ is the arc plasma density as a function of temperature; t is time; and \mathbf{U} is the arc plasma velocity vector.

The momentum conservation equation:

$$\rho \frac{\partial \mathbf{U}}{\partial t} + \rho \mathbf{U} \cdot \nabla \mathbf{U} = \nabla \cdot \left[\mu (\nabla \mathbf{U} + (\nabla \mathbf{U})^T) - \frac{2}{3} \mu (\nabla \cdot \mathbf{U}) \mathbf{I} - p \mathbf{I} \right] + \mathbf{F} \quad (2)$$

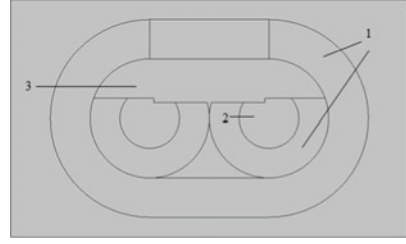
$$\mathbf{F} = \mathbf{J} \times \mathbf{B} \quad (3)$$

where p , μ , \mathbf{I} , \mathbf{F} , \mathbf{J} and \mathbf{B} are, respectively, pressure, dynamic viscosity, unit matrix, Lorentz force, current density vector, magnetic induction vector.

The energy conservation equation:

$$\frac{\partial (\rho H)}{\partial t} + \nabla \cdot (\rho H \mathbf{U}) = \nabla \cdot \left(\frac{\lambda}{C_P} \nabla H \right) + S_H \quad (4)$$

Fig. 5 Geometric model of Cable notch arc simulation **1** PVC insulation sheath, **2** copper core, **3** notch



$$S_H = \frac{1}{\sigma} \mathbf{J}^2 + S_\varphi - S_{rad} \quad (5)$$

$$S_\varphi = \frac{\partial}{\partial T} \left(\frac{k_B T}{2q} \left(\frac{\lambda}{C_P} + 5 \right) \right) (\nabla T \cdot \mathbf{J}) \quad (6)$$

where H , λ , C_p , T , σ , S_H , S_φ , S_{rad} , k_B and q are, respectively, enthalpy, thermal conductivity, constant pressure heat capacity, temperature, electrical conductivity, arc heat source energy, current electron enthalpy, overall radiation energy, Boltzmann's constant, charge.

Maxwell's equations:

$$\begin{cases} \mathbf{E} = -\nabla\phi - \frac{\partial \mathbf{A}}{\partial t} \\ \nabla \cdot (-\sigma \nabla\phi) = 0 \\ \nabla \times \mathbf{A} = \mathbf{B} \\ \mathbf{J} = \sigma \mathbf{E} \\ \nabla^2 \mathbf{A} = -\mu_0 \mathbf{J} \end{cases} \quad (7)$$

where \mathbf{E} is the electric field strength; \mathbf{A} is the vector magnetic potential and ϕ is the electric potential.

4.2 Simulation Model

Based on Comsol software, a model of arc in the BVVB cable notch was established in this paper, as shown in Fig. 5.

4.3 Simulation Analysis

Current Density Distribution Analysis. Figure 6 shows the trend of current density changes in the dynamic process of the cable arc. After 2 ms of energization, the current density distribution begins to appear in the arch discharge channel, and this

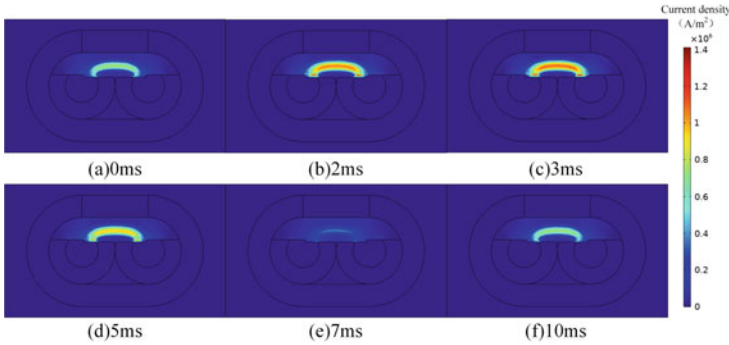


Fig. 6 Variation of arc current density at cable notch

time recorded as the arc burning time 0 ms. Thereafter, the current density changes with the current waveform, increasing and then decreasing. The arc continues to burn 7 ms and then extinguished. After 3 ms current zero-crossing time, the arc reignites.

Temperature Distribution Analysis. Figure 7 shows the trend of the arc temperature field in the cable notch. The arc temperature in the beginning is relatively low, with the increasing current, the arc temperature gradually increases and spreads to the surrounding area, the temperature reaches the maximum value at 3 ms. Then, the arc temperature decreases with current changing. At 7 ms, the current reaches zero-crossing, the arc tends to extinguish, the arch shape recedes. But due to the thermal inertia of the arc, the incision area temperature did not recover. At 10 ms, the arc continues to reignite.

The cable insulation sheath is heated rapidly by the high temperature of the incision arc, especially the sharp part of the outer sheath, where the temperature change is most obvious, see Fig. 8(a). After one arc-burning cycle, the temperature of the inner sheath reaches the pyrolysis temperature of PVC.

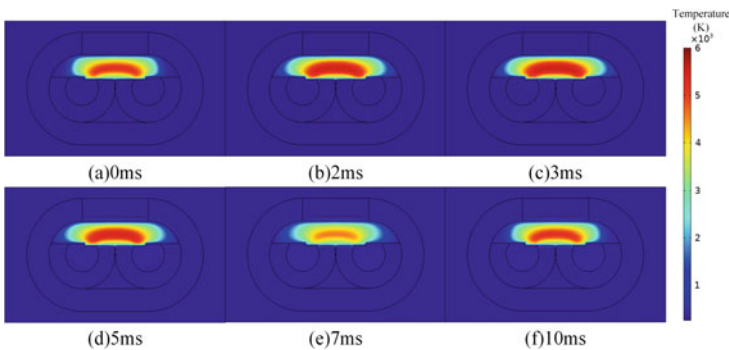


Fig. 7 Variation of arc temperature field at cable notch

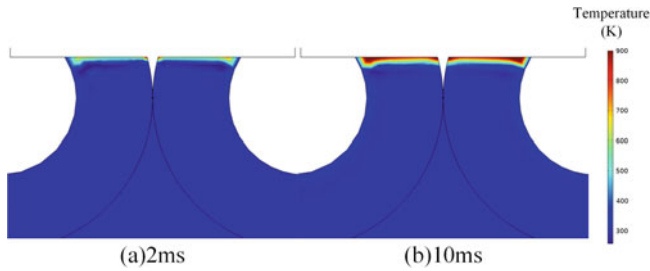


Fig. 8 Variation of temperature field at cable notch insulating sheath

After comparing the simulation results with the images taken by the high-speed camera, the simulation of the early burning morphology and dynamic change trend of the arc at the cable incision is basically consistent with the actual one, which can reflect the early process of discharge at the cable incision. However, due to the lack of numerical simulation of the phase change of PVC material, the process of carbon layer generation cannot be simulated for the time being, and there is still room for improvement.

5 Conclusion

In this paper, a high-speed camera was used to photograph the carbonization process of the cable notch in the arc fault characteristics experimental device and analyze the mechanism of its carbonization path generation process, which is divided into two stages: the arc discharge stage and the heat combustion stage of the insulation sheath. Secondly, through orthogonal experimental design, the influencing order of different factors on the success rate of carbonization path generation is determined: 2 kV energization time > notch width > structure > 7 kV energization time, and a set of optimal levels are obtained: structure A (cable inner double core with PVC filler fixed between the cores), notch width 1 mm, 7 kV energization time 4 s, 2 kV energization time 2.5 s. Finally, a simulation model of arc in the cable incision was established by using magnetohydrodynamic (MHD), the results are basically consistent with the actual results of the high-speed camera, which has some practical reference value.

Acknowledgements This research is supported by the Fujian Provincial Department of Science and Technology University Industry-University Cooperation Project under Grant 2021Y4002, and the Fujian Province Science and Technology Innovation Leading Talent Funding Project under Grant 00387024.

References

1. Anon: National fire situation remains stable in 2020. *China Fire* (1), 12–14 (2021). (in Chinese)
2. Lu, L., Duan, C., Ji, S.C., et al.: Overview of ignition mechanism and combustion characteristic of wire and cable. *High Volt. Eng.* **48**(2), 612–625 (2022). (in Chinese)
3. Xie, Z.H., Su, J.J., Fu, B., et al.: Comparative analysis of two standards for arc fault detection device. *Electr. Eng.* **21**(12), 62–67 (2020). (in Chinese)
4. Shi, Q., Shi, W.Y., Tu, D.P., et al.: Introduction on the sample(s) cable production in testing arc fault detection device. *Electr. Energy Manag. Technol.* (21), 41–46+73 (2015). (in Chinese)
5. Juan, C.M., Fu, K.L., Jin, C., et al.: Research of methods to improve cable carbonization in AFDD test. *Electr. Energy Manag. Technol.* **10**, 54–59 (2018). (in Chinese)
6. Wang, T.S.: Research on arc fault simulator. Doctor, Hebei University of Technology (2019). (in Chinese)
7. Qi, Z.B., Xu, K.L., Gao, W.: Low voltage AC arc fault test and the establishment of database. *Fire Sci. Technol.* **33**(11), 1351–1353 (2014). (in Chinese)
8. Zhang, J.Q., Guo, Y., Feng, R., et al.: Solid-gas products and reaction mechanism of pyrolysis of the sheath material of a typical flame-retardant low-voltage cable in substations during a fire. *J. Tsinghua Univ.* **62**(01), 33–42 (2022). (in Chinese)
9. Babrauskas V.: How do electrical wiring faults lead to structure ignitions. In: *Proceedings of the Fire and Materials 2001 Conference*, pp. 39–51 (2001)
10. Courty, L., Garo, J.P.: External heating of electrical cables and auto-ignition investigation. *J. Hazard. Mater.* **321**, 528–536 (2017)
11. Takenaka, K., Ishikawa, Y., Mizuno, Y., et al.: Fundamental investigation of discharge-induced fire from damaged AC power supply cord. In: *2019 IEEE Conference on Electrical Insulation and Dielectric Phenomena (CEIDP)*, pp. 158–161. IEEE (2019)
12. Du, L.W., Xu, Z.H.: Analysis and judgment of cable carbonization path based on arc fault test system. *Electr. Power Autom. Equip.*, 1–14 (2022). <https://doi.org/10.16081/j.epae.202204077>. (in Chinese)
13. Zhang, Z.B.: Preparation and properties of soft antistatic PVC composites. Doctor (2017). (in Chinese)
14. Carvou, E., Le Garrec, J.L., Mitchell, J.B.A.: Characteristics of arcs between porous carbon electrodes. *IEEE Trans. Plasma Sci.* **41**(11), 3151–3158 (2013)
15. Shi, Y., Chen, P., Tian, H., et al.: Arc simulation analysis of a new high voltage DC relay based on Comsol multiphysics. *J. Beijing Univ. Chem. Technol. (Nat. Sci. Ed.)* **49**(01), 90–97 (2022). (in Chinese)

Research on Thermal Runaway Behavior and Early Fire Detection Method of Lithium Battery



Zhilin Shan , Qixing Zhang, Yongmin Zhang, Shuping Wang, Yifeng Cheng, and Shiwei Guo

Abstract The fire safety of energy storage lithium batteries has become the key technology that most needs to make breakthroughs and improvement. During the development and evolution process of thermal runaway of power lithium ion battery, and based on the thermal runaway gas production mechanism of lithium ion batteries, the development law of heat and gas production, and the analysis of gas production components of lithium batteries with different materials, this paper studies the thermal runaway behavior of lithium ion batteries and its detection methods, explores the early behavior characteristics and detection methods of thermal runaway of lithium batteries, and provides a research basis for the safety monitoring of electrochemical energy storage. The research shows that during the thermal runaway evolution of lithium-ion batteries. The thermal runaway process can be divided into exhaust stage and thermal runaway fire stage. Both stages will emit a large amount of thermal runaway characteristic gases including CO₂, CO, H₂, CH₄ and other alkanes. The detection method based on characteristic gases is the key technology to monitor electrochemical energy storage fire.

Keywords Thermal runaway of lithium battery · Gas behavior · Analysis of characteristic parameters detection method

Z. Shan · Q. Zhang (✉) · Y. Zhang · S. Guo
State Key Laboratory of Fire Science, University of Science and Technology of China,
Hefei 230031, China
e-mail: qixing@ustc.edu.cn

S. Wang · Y. Cheng
State Grid Anhui Electric Power Research Institute, Hefei 230601, China

Z. Shan
Institute of Advanced Technology, University of Science and Technology of China, Hefei 230031,
China

1 Introduction

In the process of thermal runaway development and evolution of electrochemical energy storage power lithium ion battery, a large amount of heat is released from internal side reactions, and a large amount of combustible and toxic gases are generated. Gas chromatography and other equipment were used to analyze the collected gas and thermal runaway temperature, and it was concluded that the peak thermal runaway temperature of 100% SOC lithium iron phosphate battery was about 400 °C. The volume fraction of hydrogen and carbon dioxide in the gas generated accounted for about 25.34% and 25.39% [1]. Lithium battery thermal runaway fire safety, the focus is on prevention and control, monitoring and early warning is especially important. The study of thermal runaway behavior characteristics of lithium batteries is the starting point of its monitoring and early warning. Thermal runaway behavior characteristics and the anode materials, lithium battery capacity and SOC, thermal runaway environment, etc. are linked. Based on the market mainstream lithium ion batteries, such as lithium iron phosphate batteries, ternary lithium batteries, lithium titanate batteries, etc., this paper deeply studied the thermal runaway behavior of lithium ion batteries and its detection methods from mechanism of gas generation, hot and gas production characteristics, gas properties of different anode materials etc., of lithium ion battery, which provides a research basis for the early detection and warning methods of thermal runaway of electrochemical energy storage lithium batteries.

2 Analysis of Thermal Runaway Gas Production Mechanism of Lithium Battery

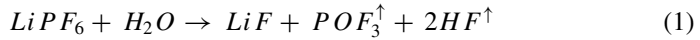
In the process of thermal runaway development of lithium battery, physical and chemical reactions will occur inside, and heat release and gas release will accompany the reaction process. A large amount of heat accumulation leads to intensified chemical reactions inside the battery, and finally triggers thermal runaway [1].

Lithium battery electrolytes contain certain organic solvents as shown in Table 1 below. This kind of solvent has a certain volatility, wherein DMC, DEC, EMC flash point within 35 °C, boiling point within 130 °C. Under certain conditions, it is easy to volatilize and form electrolyte vapor, which exists in the battery internal environment in the form of gas.

Table 1 Flash point and boiling point data of electrolyte solvent

Item	DMC	DEC	EMC	EC	PC
Flash point	17 °C	31.1 °C	26.7 ± 7.8 °C	160.0 °C	132.2 °C
Boiling point	90.5 °C	126.8 °C	107.5 °C	248.2 °C	241.7 °C

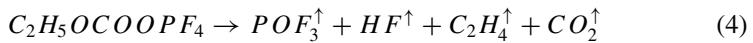
In the process of thermal runaway, a variety of chemical reactions occur and characteristic gases are produced. Among them, LiPF_6 can start hydrolysis reaction at 30 °C or even lower temperature under appropriate conditions if the environment contains appropriate water [2]:



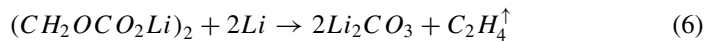
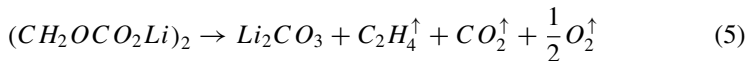
The initial pyrolysis temperature of LiPF_6 is about 110 °C, and its pyrolysis reaction [3] is as follows:



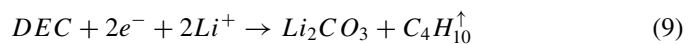
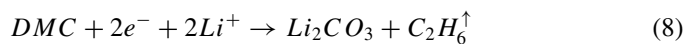
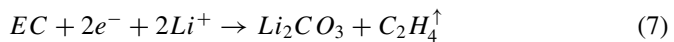
POF_3 , HF and PF_5 gases are produced in the chemical reactions of hydrolysis and pyrolysis.



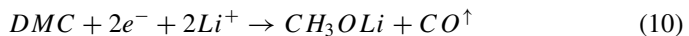
In addition, studies have shown that SEI diaphragm $(\text{CH}_2\text{OCO}_2\text{Li})_2$ will decompose near 100 °C [4] and produce a certain amount of O_2 gas, as follows:



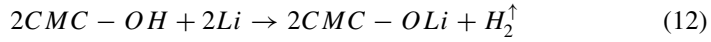
With the increase of temperature and the chemical reaction of SEI film, SEI film cannot protect the cathode, Li contacts with electrolyte and reacts chemically, producing hydrocarbon gases as follows [5]:



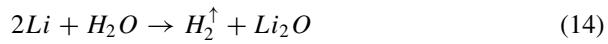
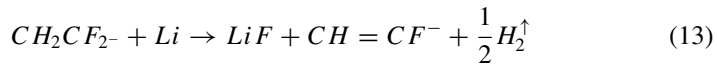
At the same time, reduction reaction [6] can take place to generate CO gas:



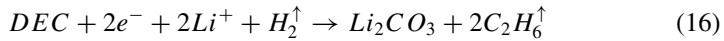
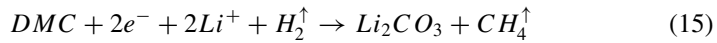
Lithium ion battery binder commonly used materials are polyvinylidene fluoride (PVDF), sodium carboxymethyl cellulose (CMC), is one of the main factors to produce hydrogen (H₂). When the temperature exceeds 230 °C, the graphite particles on the cathode fall off, and lithium metal is in direct contact with the binder [7]. The chemical reaction between CMC and lithium ions is:



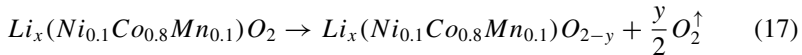
The reaction between PVDF and Li and the self-decomposition reaction are as follows [8]:



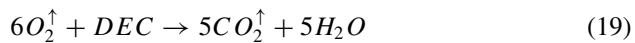
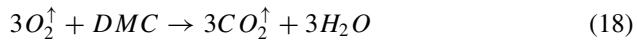
Under the action of H₂, Li ions undergo reduction reactions with DMC and DEC, producing gases such as CH₄ and C₂H₆:



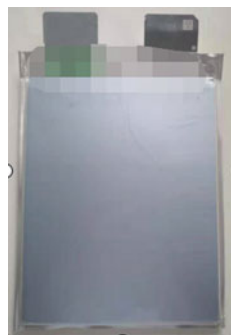
When the temperature reaches about 200 °C, the autopyrolysis reaction of cathode materials such as Li(Ni_{0.1}Co_{0.8}Mn_{0.1})O₂ is intensified [9], and a certain amount of O₂ is produced:



The oxygen produced is oxidized and rapidly combines with the electrolyte solvent or hydrocarbon small molecules inside the battery to undergo reduction reaction [10], generating CO₂ and H₂O. The released heat will further accelerate the decomposition reaction of the electrolyte.



From the above analysis, during the thermal runaway process of lithium ion batteries, physical and chemical reactions are generated, and the gases produced include VOCs, CO₂, H₂, CO, CH₄, C₂H₄, POF₃, HF, NH₃ and other gases.

Fig. 1 The battery

3 Experimental Design

3.1 Samples of the Battery

In this experiment, the same batch of soft package lithium titanate cells provided by the supplier were used. Cell capacity: 40 Ah; SOC: 100%; Voltage: 2.35 V; AC internal resistance: ≤ 0.55 m Ω , DC internal resistance: ≤ 1.2 m Ω ; Operating temperature -25 – 55 °C; The size is 161 * 227 * 11.3 mm; 0.92 kg (Fig. 1).

3.2 Design of Experimental Apparatus and Methods

As shown in the figure above, the mixed gas, smoke particles, moisture and other mixed substances generated by thermal runaway enter the gas pool through the filter and the minitype gas pump. The sensor design in the multi-feature gas detection channel includes CO gas sensor, H₂ gas sensor, VOCs gas sensor and other characteristic gas sensors (Fig. 2).

A variety of ways can be designed to trigger the thermal runaway of lithium battery in the sealed chamber of the reaction kettle, including heating, overcharging, nail penetration, etc. The experimental conditions of this experimental design are shown in the following table (Table 2):

According to GB/T 31,485-2015 “Safety Requirements and Test Methods for Traction Batteries for Electric Vehicles”, heating and overcharging thermal runaway methods were adopted, and each method was repeated for three times to analyze the behavior and development process of lithium titanate batteries in different thermal runaway ways.

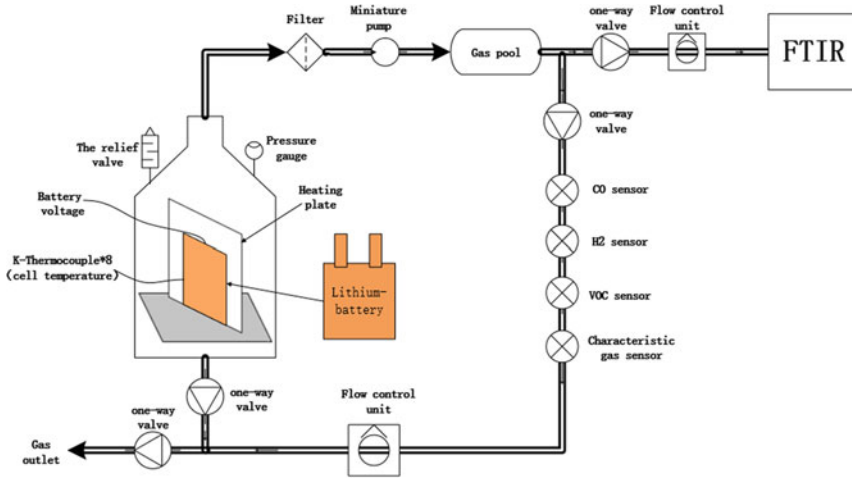


Fig. 2 Multi-characteristic parameters measurement system

Table 2 Table of experimental conditions

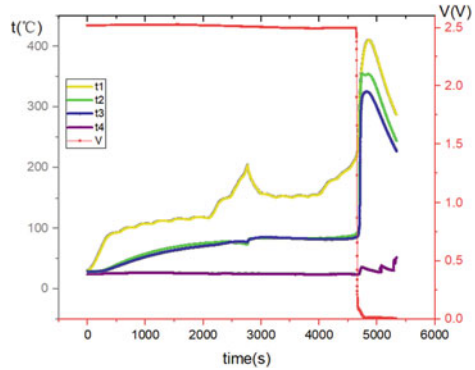
Working condition	1	2	3	4	5	6
Trigger method	Heating			Overcharging		

4 Study and Analysis of Thermal Runaway Behavior

4.1 Analysis of Heat Production Behavior

The experimental process of thermal runaway triggered by heating is analyzed. The following figure shows the voltage and temperature curves of the process. $t_1/ t_2/ t_3/ t_4$ are the temperature measurement at different points. V is the voltage value. After heating 2500 s, the temperature rise rate of the battery gradually accelerates. In the experiment, the temperature approached 200 °C and a rapid flue gas emission process was observed. When the temperature dropped to 150 °C, it remained at a temperature platform and then continued to rise. When it is heated to 4640 s and the surface temperature of the battery reaches 220 °C, the battery voltage begins to drop, and in the following 20 s, the voltage drops from 2.498 V to 0.2 V and finally to 0 V. 10 s after the voltage change, the battery surface temperature (t_1, t_2, t_3) increased significantly, and the temperature on one side of the heating plate rose rapidly first. The temperature peaks within 1 min of thermal runaway. According to the t_4 temperature curve analysis, the temperature rose twice, indicating that after the first thermal runaway, the battery experienced two more thermal runaway see Fig. 3.

Fig. 3 Curve of heating temperature and voltage of lithium battery



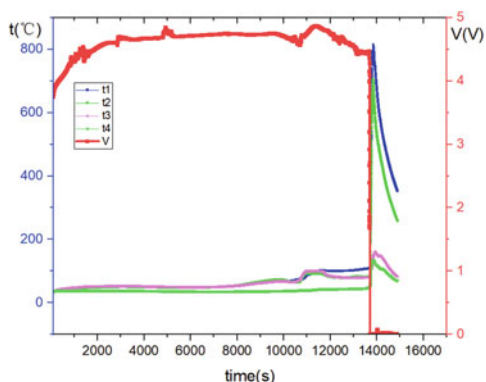
In thermal runaway stage, voltage mutation is earlier than temperature mutation, and the time advance is 3–10 s. After the occurrence of thermal runaway, the temperature value of the battery surface on the heating plate side is the highest, and the order of the temperature peak value everywhere is $t_1 > t_2 > t_3 > t_4$, indicating that the thermal runaway on the heating plate side is the most intense development degree, and the heat generated is the largest. The peak temperature at the top of the sealing chamber of the heating kettle is around 52 °C.

The Fig. 4 above shows the voltage and temperature curves of the overcharge heat runaway process. With the progress of battery charging, t_1 and t_3 rose significantly at 10800 s with exhaust, and then t_3 dropped slowly. When the voltage reaches the maximum 4.79 V, the battery voltage V tends to decline. At 13703 s, the voltage instantly drops from 4.2 V to 0 V, and thermal runaway generation. The temperature change lags behind the voltage change. When the voltage drops to 0 V for 10 s, the battery surface temperature (t_1, t_2) increases. The battery surface temperature rises from 100 °C to 400 °C within 5 s. The electrode ear temperature is higher than the surface temperature of the battery. The maximum temperature of the battery pole ear reaches about 800 °C, and combustion and flame ejection occur in the process of overcharging. The lithium battery accumulates more energy in the process of thermal runaway, and the change rate of temperature, voltage and gas generation in thermal runaway is greater than that of heating thermal runaway.

4.2 Analysis of Gas Production Behavior

H2 and FTIR gas analysis equipment were used to analyze the thermal runaway gas of lithium battery. The gas conduit in the sealed chamber of the reaction kettle was connected to the FTIR equipment, and the gas flow meter was used to control the gas flow into the analysis equipment, and the composition and concentration of the thermal runaway gas were analyzed online in real time. After the thermal runaway

Fig. 4 Curve of overcharge temperature and voltage of lithium battery



is triggered by overcharging, the gas is collected in a sealed gas bag, and then use the analysis equipment for gas composition and concentration analysis.

Heating thermal runaway can be simply divided into two stages, exhaust stage and thermal runaway stage. The gas composition of the two stages is basically the same, but the content is different. A large amount of EMC gas is produced, up to 6047 ppm. The gas and smoke take away the heat, the battery temperature drops, and thermal runaway of the battery does not occur after the exhaust. An even greater amount of gas is released during the thermal runaway stage and some gas concentrations is about 20 times that of the exhaust phase. The gases generated in the exhaust and thermal runaway phase mainly include CO, CO₂, EMC, HF, C₃H₆, CH₄, POF₃, C₄H₈, COS, H₂, etc. The contents of EMC, CO₂, CO and H₂ are relatively large. In the process of thermal runaway during heating, The gas concentration curve is shown in the Fig. 5 below:

So the exhaust stage as the early stage of lithium battery thermal runaway has produced a large number of electrolyte vapor and a small amount of characteristic gas. Analyze from the gas generation mechanism: in the exhaust stage, the temperature of the battery heating surface is less than 200 °C, the average temperature of the whole cell is less than 200 °C. SEI separator decomposition reaction and electrolyte decomposition reaction occurred in the lithium battery, which produced a large amount of electrolyte vapor, a certain amount of C_xH_y alkane gas and HF/POF₃ gas. At this time, the chemical reaction between the cathode material and the electrolyte inside the battery and the electrolyte decomposition did not start or only a small amount of chemical reaction occurred, and the thermal runaway was not fully triggered. In the thermal runaway stage, the highest temperature reaches more than 400 °C. From the analysis of gas generation mechanism, it can be inferred that the types and intensity of chemical reactions in the battery increase, and a large amount of electrolyte steam, CO, H₂, O₂, CH₄, C_xH_y, HF/POF₃, etc.. The composition of the gas is consistent with the above analysis.

The classified statistics of gas concentration are shown in the Fig. 6 below:

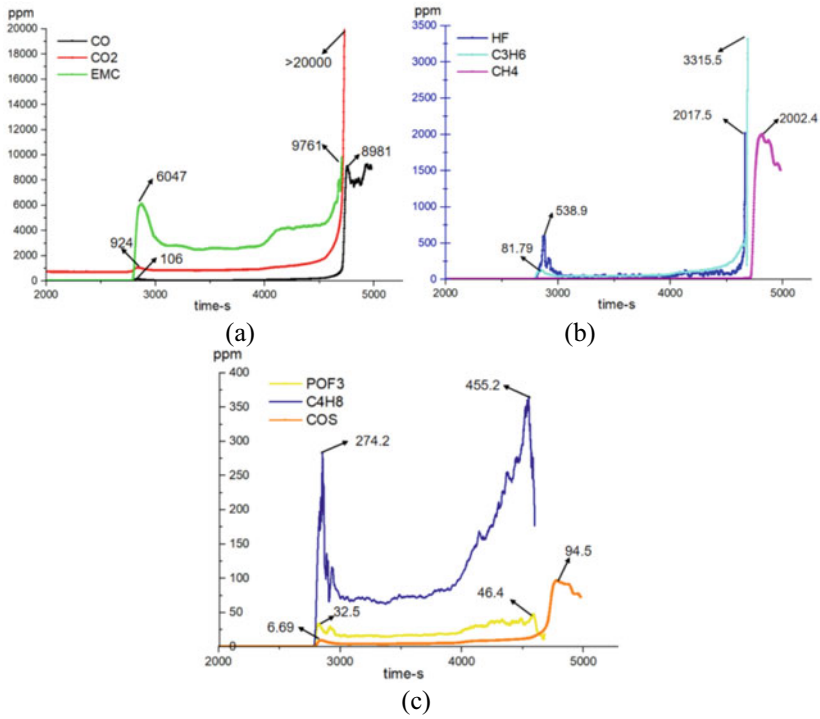
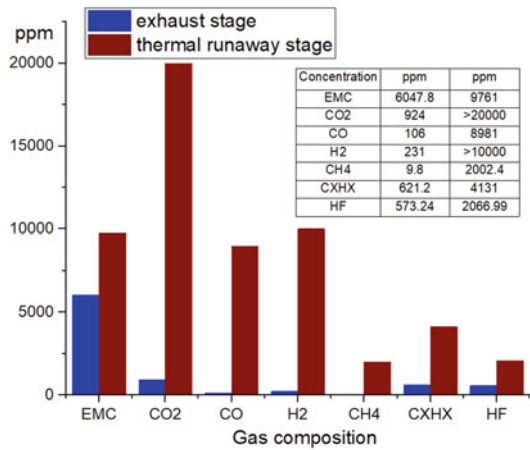


Fig. 5 Heating thermal runaway characteristic gas concentration curve

Fig. 6 Bar chart of gas components characteristic of heating thermal runaway



5 Conclusion

By analyzing the gas generation mechanism of lithium ion battery, adopting thermal runaway multi-characteristic parameter measurement system of lithium ion battery. The gas composition and concentration of lithium battery were analyzed by in situ online method and sampling and collection method. We conducted in-depth research and analysis on the thermal runaway heat production and gas production behavior of lithium ion battery:

- a) The degree of thermal runaway heat generation and gas production induced by overcharge of a single cell is stronger than that induced by heating. The thermal runaway behavior analysis shows that temperature, voltage and characteristic gas can be used as the determination characteristics of thermal runaway.
- b) In the thermal runaway process of lithium ion battery with different types and SOC contents, the characteristic gases generated mainly include electrolyte vapor, such as DMC, DEC, EMC, PC and EC, which are $C_xH_yO_z$ gases and belong to VOCs gases; Alkane gases, such as C_xH_y gases; Easy to cause combustion and explosion or flammable and explosive gases, such as H_2 , CO, O_2 ; Other gases, such as CO_2 , POF_3 , HF, PF_5 , C_2H_5F , etc. CO_2 , H_2 and CO account for more than 60%.
- c) The thermal runaway of the battery is divided into the early exhaust stage and the full eruption stage. The gas produced in the exhaust stage is mainly electrolyte vapor. The characteristic gases produced by thermal runaway mainly include CO_2 , H_2 , CO and so on.

Acknowledgements Supported by Anhui Provincial Natural Science Foundation (2021 Anhui Energy Internet Joint Fund Project, 2108085UD04)

References

1. Yuan, L.M., Dubaniewicz, T., Zlochower, I., et al.: Experimental study on thermal runaway and vented gases of lithium-ion cells. *Process Saf. Environ. Prot.* **144**, 186–192 (2020)
2. Jiang, X., Zuo, X., Cai, F., et al.: Study on thermal decomposition kinetics of lithium hexafluorophosphate. *Chin. J. Power Sour.* (4), 467–469 (2012)
3. Ping, P., Wang, Q., Sun, J., Xiang, H., Chen, C.: Thermal stabilities of some lithium salts and their electrolyte solutions with and without contact to a $LiFePO_4$ electrode. *J. Electrochem. Soc.* **157**, A1170-A6 (2010)
4. Spotnitz, R., Franklin, J.: Abuse behavior of high-power, lithium-ion cells. *J. Power Sour.* **113**, 81–100 (2003)
5. Dedryvère, R., Martinez, H., Leroy, S., et al.: Surface film formation on electrodes in a $LiCoO_2$ /graphite cell: a step by step XPS study. *J. Power Sour.* **174**, 462–468 (2007)
6. Aurbach, D., Ein-Eli, Y., Markovsky, B., Zaban, A., Luski, S., Carmeli, Y., Yamin, H.: *J. Electrochem. Soc.* **142**, 2882 (1995)
7. Huang, Z., Qin, P., Shi, H., Wu, J., Yao, L., Wang, Q.: Study on thermal runaway behavior of 86 Ah lithium iron phosphate battery under overheat condition. *High Volt. Eng.* **48**(03), 1185–1191 (2022)

8. Golubkov, A.W., Scheikl, S., Planteu, R., et al.: Thermal runaway of commercial 18650 Li-ion batteries with LFP and NCA cathodes-impact of state of charge and overcharge. *RSC Adv.* **5**(70), 57171–57186 (2015)
9. Li, H., Tang, X., Shao, D., Liang, J.: Research progress in thermal runaway gas of Li-ion battery. *Battery Bimon.*, 1–5 (2022)
10. Zhang, Q., Qu, Y., Hao, C., Liu, T., Chen, D.: In-situ analysis of thermal runaway gas in ternary lithium-ion battery. *High Volt. Eng.* (2022). <https://doi.org/10.13336/j.1003-6520.hve.20211850>

Design of an Inductive Charging System Based on PCB-Resonator with Constant Current or Constant Voltage Output



Huaqiang Xie, Zhaotian Yan, Yuan Shao, and Ruikun Mai

Abstract An inductive power transfer (IPT) system based on PCB-resonators with CC and CV output characteristics is proposed, which can be used to charge low-power devices such as sensors. A compact PCB-resonator based on the double helical coil is constructed, and its distributed parameter equivalent circuit is proposed. Based on the port impedance of the resonator, the equivalent relationship between each resonant frequency point and the series resonance (parallel resonance) lumped circuit is explained. The CC and CV outputs can be realized naturally without external compensation elements in the system. The whole system does not need to use switches and complex control strategies. Besides, the system meets zero voltage switching (ZVS) conditions. The experimental results demonstrate that when the operating frequency is 1.340 MHz, the constant charge current and constant charge voltage fluctuates less than 7% in a wide load range.

Keywords Inductive power transfer · PCB resonator · Distributed parameter · Constant current · Constant voltage

1 Introduction

At present, a large number of sensors are buried in railways, tunnels and mines to ensure the monitoring of ambient temperature, pressure and harmful gases [1]. For sensor power supply, adopting IPT technology can improve system reliability and flexibility. However, due to the limited installation space of the power supply system, the designed coupling mechanism should be lightweight. In order to ensure the voltage, current and temperature stability of all parts of the system, high-quality

H. Xie (✉) · Z. Yan · Y. Shao · R. Mai
School of Electrical Engineering, Southwest Jiaotong University, Chengdu 611756, Sichuan,
China
e-mail: xhq111997@163.com

R. Mai
e-mail: mairk@swjtu.edu.cn

© Beijing Paiké Culture Commu. Co., Ltd. 2023
X. Dong et al. (eds.), *The proceedings of the 10th Frontier Academic Forum of Electrical Engineering (FAFEE2022)*, Lecture Notes in Electrical Engineering 1054,
https://doi.org/10.1007/978-981-99-3408-9_19

coils and relatively stable circuit structure are also necessary. In addition, it is recommended to use constant current (CC) and constant voltage (CV) for battery charging to prolong the battery life [2]. Therefore, it is necessary to realize the system's constant voltage and current conversion according to the charging demand of the sensor.

In order to obtain CC and CV output characteristics of the system, scholars have conducted research on the topology [3], the number of coils [4], and control methods [5]. Nevertheless, the above method requires the connection of passive components such as inductance or capacitance in the transmitter (TX) or receiver (RX), resulting in poor consistency of system parameters. Moreover, coil stacking takes up much space, and too many connection points will affect the system's reliability. To solve the above problems, PCB coils can be used. It has the characteristics of consistent parameters, light and thin structure, small installation space and convenient mass production. Moreover, using the parasitic capacitance of the coil as the compensation capacitance to realize the self-resonance of the coil can avoid the use of physical capacitance [6–10]. One of the difficulties in realizing coil self-resonance is quantifying and extracting parasitic capacitance. [6] proposed a method to measure parasitic capacitance using electric field energy distribution and gave a calculation model. Furthermore, [7] proposed the equivalent circuit of parasitic capacitance, which verified the feasibility of using parasitic capacitance between adjacent planar coil layers as compensation capacitance. Optimizing the coil structure can improve the coupling mechanism's compactness to meet the application requirements of PCB coils [8]. In addition, it is necessary to analyze its resonance characteristics to obtain a more perfect equivalent model of PCB coil, which can be obtained by measuring the port impedance [9]. To explain the resonance characteristics of PCB coils, a research method combining partial element equivalent circuit and finite element method is proposed in [10]. The parasitic parameters of the coil and the circuit model of high-frequency loss are established, and the main factors of high-frequency loss are discussed.

In a word, these works have fully discussed PCB coils. To make the IPT system have CC and CV output characteristics, this paper proposes the PCB-resonator based on the advantages of PCB coil, and illustrates its resonant characteristics using the distributed parameter equivalent model.

2 Analysis of PCB-Resonator

2.1 Equivalent Model

In this paper, the double-layer printed spiral coil is studied. Figure 1 (a) is a three-dimensional view of the proposed PCB-resonator. The copper channel on the top layer is wound clockwise, internally connected to the bottom layer through vias, and the copper channel on the bottom layer is also wound clockwise. Figure 1 (b) is a cross-sectional view of the R - Z axis of the PCB-resonator, showing the coupling path

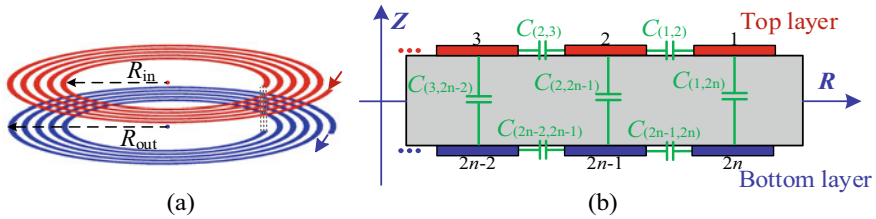


Fig. 1 (a) The 3D view of the PCB-resonator. (b) The cross section of R-Z axis of the PCB-resonator and shows the equivalent model of coupling capacitance

between each turn copper channel and the dielectric layer. Where $C_{(i,i+1)}$ is the unit equivalent inter-turn capacitance between i copper channel and $i + 1$ copper channel ($i = 1, 2, 3 \dots 2n - 1$). $C_{(i,j)}$ is the unit equivalent inter-layer capacitance between i copper channel and j copper channel ($j = 2n, 2n - 1, 2n - 2 \dots n + 1$).

The circuit model of a single-turn copper channel can be equivalent to an inductor in series with a resistor. In order to simplify the analysis, the influence of mutual capacitance between non-adjacent copper tracks is ignored. Considering the adjacent inter-turn capacitance and adjacent inter-layer capacitance between all copper channels, the distributed parameter circuit model of the PCB-resonator can be obtained, as shown in Fig. 2. Where L_i and R_i are the equivalent inductance and equivalent internal resistance of the i -th turn copper channel. I_i is the equivalent current flowing through the i -th turn of the copper channel ($i = 1, 2, 3 \dots 2n$).

To obtain the frequency characteristics of PCB-resonators, it is necessary to analyze the impedance characteristics of A-B ports in their distributed parameter equivalent circuit. Assuming that all copper channels' adjacent inter-turn capacitance (inter-layer capacitance) is equal, set it as $C_1(C_2)$. The equivalent inductance and equivalent internal resistance of each turn of the copper channel are also equal, set as L and R . Z_n is the equivalent impedance of the A-B port. ω is the operating angular frequency of the PCB-resonator. According to the recursive formula, Z_n can be expressed as

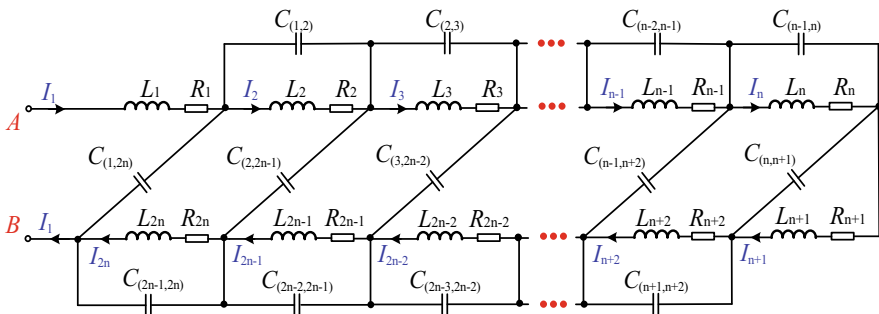


Fig. 2 The equivalent circuit of the distribution parameters of the proposed PCB resonator

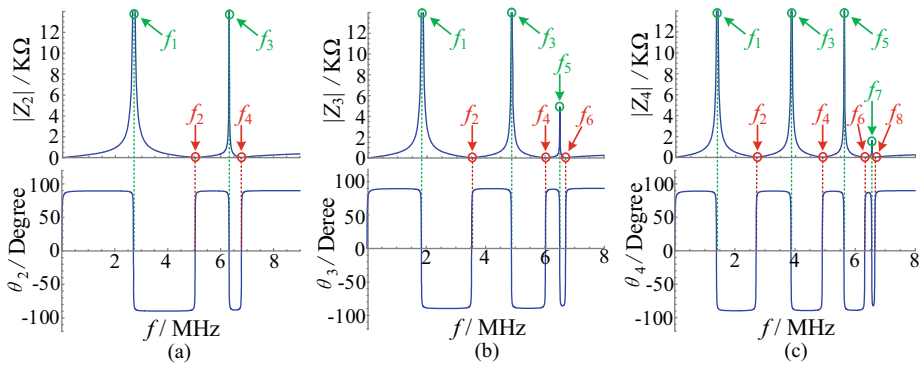


Fig. 3 (a) The amplitude and phase Angle of Z_2 . (b) The amplitude and phase Angle of Z_3 . (c) The amplitude and phase Angle of Z_4

$$\begin{cases} Z_2 = R + j\omega L + \frac{1}{j\omega C_2} \parallel \left[\frac{2}{j\omega C_1} \parallel (R + j\omega L) + \frac{1}{j\omega C_2} \parallel (R + j\omega L) \right] \\ Z_3 = R + j\omega L + \frac{1}{j\omega C_2} \parallel \left[\frac{2}{j\omega C_1} \parallel (R + j\omega L) + Z_2 - (R + j\omega L) \right] \\ \vdots \\ Z_n = R + j\omega L + \frac{1}{j\omega C_2} \parallel \left[\frac{2}{j\omega C_1} \parallel (R + j\omega L) + Z_{n-1} - (R + j\omega L) \right] \end{cases} \quad (1)$$

According to Eq. (1), impedance amplitude and phase angle curves of Z_2 , Z_3 , and Z_4 can be obtained, as shown in Fig. 3 (a), Fig. 3 (b), and Fig. 3 (c). The number of resonant frequency points increases with the increase of turns. For PCB-resonators with single-layer turns of n , there are $2n$ resonance frequency points in theory. Among them, n resonance frequency points (f_1, f_3, f_5, \dots) have large impedance amplitudes, which can be defined as parallel resonance points. On the contrary, the impedance amplitude of the other n resonance frequency points (f_2, f_4, \dots) is close to zero, which can be defined as the series resonance point. The lumped parameter circuit of the PCB resonator under the series resonance point and the parallel resonance point can be equivalent to Fig. 4 (a) and Fig. 4 (b). $L_e(C_e)$ is the PCB-resonator's equivalent inductance (equivalent capacitance). r_e is the equivalent series resistance (ESR). $L_{m1}(L_{m2})$ and $r_{m1}(r_{m2})$ represent the inductance and resistance tested from the PCB-resonator port in the series resonance (parallel resonance) circuit.

2.2 Port Impedance

The value of the self-resonant frequency f_0 of the proposed PCB-resonator is mainly affected by parameters such as coil turns, layer spacing, copper channel width, and copper channel spacing. It can be measured by equivalent inductance L_e and equivalent capacitance C_e . As shown in Fig. 4, whether the PCB-resonator is in a series

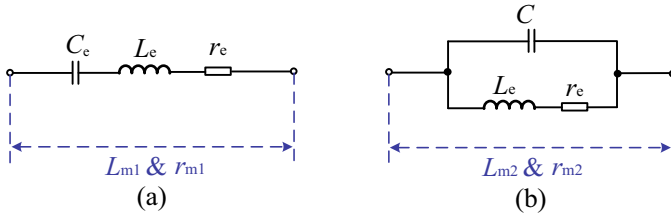


Fig. 4 The lumped parameter circuit. (a) Series resonance. (b) Parallel resonance

resonance state or parallel resonance state, f_0 can be expressed as

$$f_0 = \frac{1}{2\pi \sqrt{C_e L_e}} \tag{2}$$

The port impedance of the PCB-resonator can be obtained by lumped parameter circuit. Z_{m1} (Z_{m2}) is the port impedance of the PCB-resonator in the series resonance (parallel resonance) circuit.

(1) According to Fig. 4 (a), the Z_{m1} can be expressed as

$$Z_{m1} = r_{m1} + j\omega L_{m1} = j\omega L_e + r_e + \frac{1}{j\omega C_e} \tag{3}$$

where r_e and L_e in the series resonant circuit can be calculated as

$$\begin{cases} r_e = r_{m1} \\ L_e = L_{m1} \frac{f^2}{f^2 - f_0^2} \end{cases} \tag{4}$$

(2) According to Fig. 4 (b), the Z_{m2} can be expressed as

$$Z_{m2} = r_{m2} + j\omega L_{m2} = \frac{\frac{j\omega L_e + r_e}{j\omega C_e}}{j\omega L_e + r_e + \frac{1}{j\omega C_e}} \tag{5}$$

where r_e and L_e in the parallel resonant circuit can be calculated as

$$\begin{cases} r_e = r_{m2} \left[1 - \left(\frac{f}{f_0} \right)^2 \right]^2 \\ L_e = L_{m2} \left[1 - \left(\frac{f}{f_0} \right)^2 \right]^2 \end{cases} \tag{6}$$

3 Analysis of IPT System with CC-CV Output

The IPT system of the sensor mentioned in this paper is shown in Fig. 5. In this system, TX, RX, and relay coil are composed of independent PCB-resonators. According to the analysis in the previous section, adjusting the resonant frequency of the resonator can be equivalent to S-type or P-type topology. When the resonator is equivalent to an S-type topology, a closed relay coil with both ends is placed between TX and RX, and the system is a CV power supply. When the relay coil is moved away, the system will be a CC power supply. The equivalent circuit in CC mode is shown in Fig. 6 (a), and the equivalent circuit in CV mode is shown in Fig. 6 (b).

- (1) CC mode. When the PCB-resonator works at the serial resonant frequency point, the IPT system can be equivalent to an S-S type circuit, the system can realize CC output, as shown in Fig. 6 (a). According to Kirchhoff's Voltage Law (KVL), the relationship between voltage and current of each loop can be given as follows

$$\begin{bmatrix} r_P + X_P & -j\omega M_{PS} \\ -j\omega M_{PS} & r_S + X_S + R_{eq} \end{bmatrix} \cdot \begin{bmatrix} \dot{I}_P \\ \dot{I}_S \end{bmatrix} = \begin{bmatrix} \dot{U}_P \\ 0 \end{bmatrix} \quad (7)$$

- (2) CV mode. Add a relay coil between TX and RX to form an S-S-S circuit. At this time, the system can realize CV output, as shown in Fig. 6 (b). According to KVL, the relationship between voltage and current of each loop can be given as follows

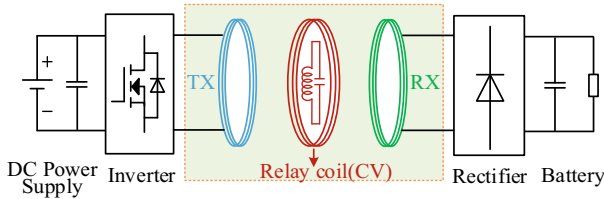


Fig. 5 The circuit diagram of the IPT system for sensor

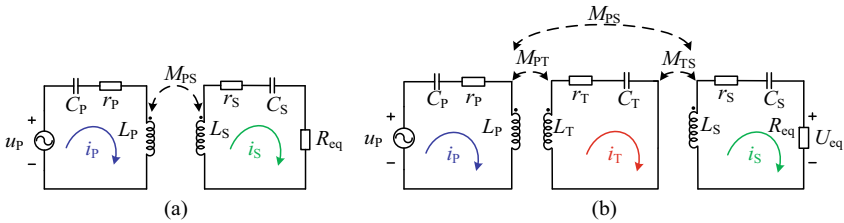


Fig. 6 (a) The equivalent circuit in CC mode. (b) The equivalent circuit in CV mode

$$\begin{bmatrix} r_P + X_P & -j\omega M_{PT} & -j\omega M_{PS} \\ -j\omega M_{PT} & r_T + X_T & -j\omega M_{TS} \\ -j\omega M_{PS} & -j\omega M_{TS} & r_S + X_S + R_{eq} \end{bmatrix} \cdot \begin{bmatrix} \dot{I}_P \\ \dot{I}_T \\ \dot{I}_S \end{bmatrix} = \begin{bmatrix} \dot{U}_P \\ 0 \\ 0 \end{bmatrix} \quad (8)$$

4 Experiment

4.1 Experimental Setup

The experimental prototype is shown in Fig. 7. The dimension parameters of the proposed PCB-resonator are shown in Table 1.

The port impedance amplitude and phase angle of the proposed PCB-resonator are obtained by scanning the frequency, as shown in Fig. 8. Where f_1 and f_3 are parallel resonant frequency points, and f_2 and f_4 are series resonant frequency points. The amplitudes of coil port impedance at f_2 and f_4 frequencies are 28.21 Ω and 110.55 Ω , respectively. Therefore, to reduce the coil’s internal loss, the frequency f_2 can be used for the experiment.

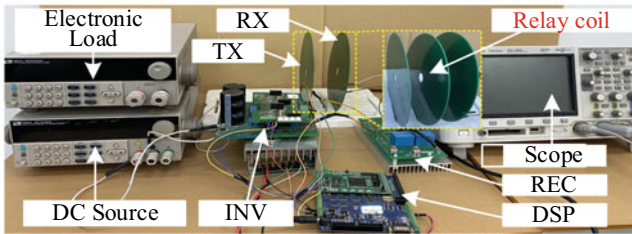


Fig. 7 The experimental prototype of the IPT system

Table 1 Dimension parameters

Parameter	Describe	Value
w	Copper traces clearance	40 mil
s	Copper traces width	60 mil
z	Dielectric laminate thickness	1.4 mm
d	Copper thickness	2 OZ
R_{in}	Inner radius	11 mm
R_{out}	Outer radius	100 mm
n	Number of turns of a single layer	36

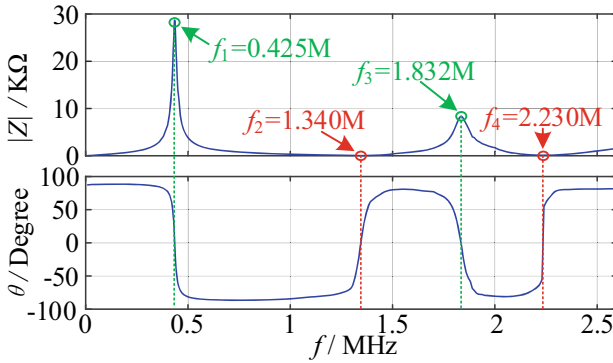


Fig. 8 The port impedance amplitude and phase Angle diagram of PCB board

4.2 CC Mode Experiment Results

The self-resonant frequency of the PCB-resonator is f_2 (1.340 MHz), the input voltage is 50 V, and the load resistance is set to 50 Ω . To facilitate the experimental record, four operating frequencies were selected for the experiment. The relationship between the system output current I_{out} and the load resistance R_{LDC} is shown in Fig. 9(a). The experimental waveforms of inverter output voltage U_p , inverter output current i_p , load voltage U_{out} and load current I_{out} are shown in Fig. 9(b). When the operating frequency is 1.340 MHz, the output current fluctuation is only 6.28% when the load resistance transitions from 30 Ω to 80 Ω . The system has good CC characteristics under light load, and the U_p and i_p waveforms of the inverter show that MOSFET realizes ZVS.

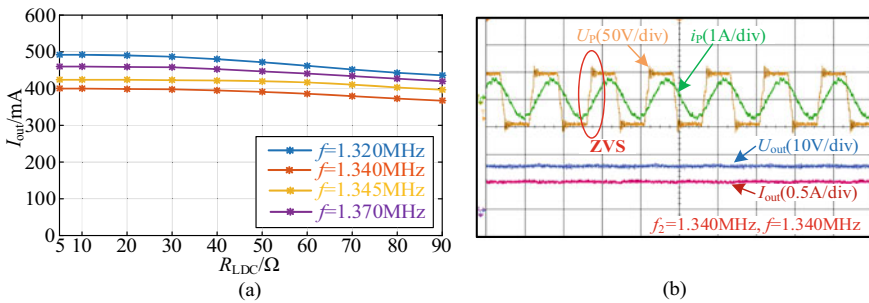


Fig. 9 (a) The output current varies with the load. (b) The waveform of U_p , i_p , U_{out} , and I_{out}

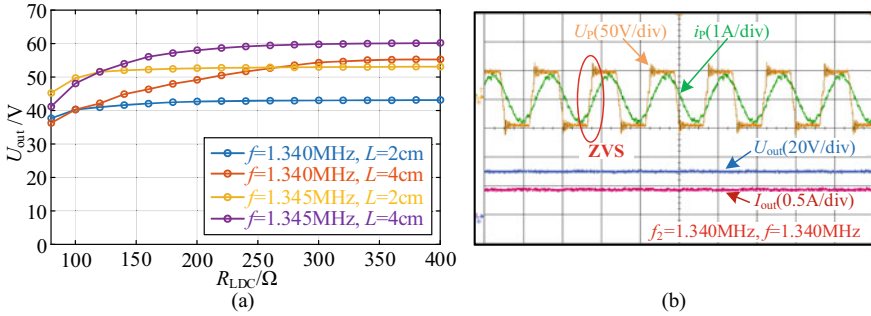


Fig. 10 (a) The output voltage varies with the load. (b) The waveform of U_p , i_p , U_{out} , and I_{out}

4.3 CV Mode Experiment Results

For the convenience of experimental records, different operating frequencies (1.340 MHz and 1.345 MHz) and air gap distances (2 cm and 4 cm) were selected for experiments. The input voltage is 50 V, and the load resistance is set to 120 Ω . The experimental results are shown in Fig. 10. When the load resistance jumps to 300 Ω from 100 Ω , the output voltage fluctuates only 6.88%. The system has excellent CV characteristics, and the inverter meets ZVS conditions.

5 Conclusion

This paper presents a compact IPT system suitable for sensor battery charging. The introduction of self-resonant PCB coils, without passive compensation components, can naturally achieve CC or CV output only by changing the number of coils. Avoid using switches and complex control strategies. The distributed parameter model of the PCB-resonator is proposed, and the amplitude and phase characteristics of the port impedance are analyzed. Moreover, the equivalent relationship between the resonant frequency points and the series resonant (parallel resonant) lumped circuit is illustrated. In addition, the circuit characteristics of S-S and S-S-S topologies are also discussed. The inverter switch tube can realize the ZVS condition. Finally, an experimental prototype is built to verify the system performance at the resonant frequency point (1.340 MHz). The experimental results show that the fluctuations of output current and output voltage in CC and CV mode are 6.28% and 6.88%, respectively.

References

1. Lande, S., Chabukswar, P., Bhope, V.: An efficient implementation of wireless sensor network for performing rescue & safety operation in underground coal mines. In: 2020 International Conference for Emerging Technology (INCET), Belgaum, India, pp 1–6. IEEE (2020)
2. Li, Y., Hu, J., Liu, M., et al.: Reconfigurable intermediate resonant circuit based WPT system with load-independent constant output current and voltage for charging battery. *IEEE Trans. Power Electron.* **34**(3), 1988–1992 (2019)
3. Mai, R., Chen, Y., Li, Y., et al.: Inductive power transfer for massive electric bicycles charging based on hybrid topology switching with a single inverter. *IEEE Trans. Power Electron.* **32**(8), 5897–5906 (2017)
4. Mai, R., Dai, R., Zhu, Z., et al.: Optimization of time-weighted average efficiency for reconfigurable IPT battery charging system. *IEEE Access* **7**, 43092–43099 (2019)
5. Qu, X., Han, H., Wong, S.C., et al.: Hybrid IPT topologies with constant current or constant voltage output for battery charging applications. *IEEE Trans. Power Electron.* **30**(11), 6329–6337 (2015)
6. Lee, C.K., Su, Y.P., Ron Hui, S.Y.: Printed spiral winding inductor with wide frequency bandwidth. *IEEE Trans. Power Electron.* **26**(10), 2936–2945 (2011)
7. Lee, Y.D., Kim, K.W., Moon, G.W.: A self-compensated planar coil with integrated single-switch regulator for wireless power transfer (WPT) systems. *IEEE Trans. Power Electron.* **36**(10), 10954–10958 (2021)
8. Yi, Z., Li, M., Muneer, B., et al.: Self-resonant antisymmetric planar coil for compact inductive power transfer system avoiding compensation circuits. *IEEE Trans. Power Electron.* **36**(5), 5121–5134 (2021)
9. Li, J., Costinett, D.: Analysis and design of a series self-resonant coil for wireless power transfer. In: 2018 IEEE Applied Power Electronics Conference and Exposition (APEC), TX, USA, pp. 1052–1059. IEEE (2018)
10. Chen, K., Zhao, Z.: Analysis of the double-layer printed spiral coil for wireless power transfer. *IEEE J. Emerg. Sel. Top. Power Electron.* **1**(2), 114–121 (2013)

Bidirectional Converter-Based Decentralized Compensation Solution for Medium Voltage Networks in Urban Railways



Zhe Wang and Shaobing Yang

Abstract In urban rail transit, bidirectional converters can be used for reactive power compensation, but coordinating compensation is still a difficult problem, so it is necessary to install compensation devices in the main substation as insurance, which increases the system investment and maintenance cost. In order to save investment and improve the device utilization rate, a decentralized compensation scheme based on bidirectional converters is proposed, which eliminates main substation compensation device. The scheme includes communication system and compensation system. The communication system collects the medium voltage (MV) network structure and load information, and sends control information to each unit based on the compensation strategy. Taking a railway as an example, the advantages and disadvantages of the two solutions, decentralized compensation using bidirectional converter and centralized compensation using SVG, are quantitatively compared, and the results show that decentralized compensation using bidirectional converter is technically fully competent for reactive power compensation needs and is more economically advantageous.

Keywords Urban rail transit · Reactive power compensation · Bidirectional converter · Decentralized compensation · Power factor

1 Introduction

Bidirectional converters can combine traction power supply, regenerative energy feed and other functions, and have significant advantages in terms of improving energy utilization and stabilizing network voltage, and have been installed and used in urban rail transit in recent years. Thanks to the maturity of power electronics and control

Z. Wang (✉) · S. Yang
School of Electrical Engineering, Beijing Jiaotong University, Beijing 100044, China
e-mail: 20121501@bjtu.edu.cn

© Beijing Paiké Culture Commu. Co., Ltd. 2023
X. Dong et al. (eds.), *The proceedings of the 10th Frontier Academic Forum of Electrical Engineering (FAFEE2022)*, Lecture Notes in Electrical Engineering 1054, https://doi.org/10.1007/978-981-99-3408-9_20

strategies, bidirectional converter units can be converted into reactive power generators during non-operating hours to achieve decentralized reactive power compensation in the AC network, thereby reusing equipment and improving equipment utilization. However, given the changing operating conditions and load fluctuations of the MV network, it is still difficult to maintain the grid-side power factor (PF) by completely eliminating the compensation devices in the main substation and only using bidirectional converters for decentralized compensation.

Power system reactive power compensation is divided into two aspects: compensation equipment and compensation strategy. In terms of equipment, [1] proposed a smart transformer to improve the voltage distribution in MV grids by injecting reactive power, and [2] developed a hybrid submodule modular multilevel converter (MMC) for multi terminal direct current (MTDC) transmission systems, which can apply voltage balancing strategies for reactive power management; in terms of management strategies, [3] combined two data communication methods for DSTATCOM to improve PF, deep learning [4], PSO [5], multi-objective differential evolutionary algorithms [6], and other intelligent algorithms have also been applied. In urban rail reactive power compensation, capacity allocation and system operation strategy are two key issues that need to be addressed. [7] proposed a method to evaluate the compensation effect based on the load level, and the reactive power compensation capacity of the bidirectional converter was estimated based on the evaluation results. These studies used a hybrid compensation scheme in which the main substation reactive power compensation unit is the primary and the bidirectional converter is the secondary. The advantage of such schemes is that no cooperative control strategy is required. With the popularization of bidirectional converter units, many studies have explored the feasibility of removing the main substation reactive power compensation device with a bidirectional converter-based reactive power compensation scheme. [8] discussed the compensation strategy considering local and global effects from the perspective of engineering applications, pointing out that the decentralized compensation relying on bidirectional converters can meet the PF assessment requirements of the power sector, and arguing that centralized compensation can be eliminated when certain conditions are met. [9] adopted a zonal compensation scheme and proposed the idea of calculating the compensation amount based on the measurement data of the dispatching system according to the low real-time requirement of reactive power compensation, thus realizing zonal control but not considering the existence of a voltage reduction institute in the line.

With the intelligent development of urban rail power supply systems and the widespread use of bidirectional converters, decentralized compensation has gradually become available for collaborative control. It is expected that the redundant capacity of bidirectional converters can be fully applied for compensation. In this paper, we study a decentralized compensation method based on bidirectional converters and propose a compensation strategy. Firstly, the operation mode and key parameters of the MV AC network are known from SCADA, then the compensation scheme is obtained based on the compensation strategy, and finally the compensation scheme is synchronized to the bidirectional converter for reactive power compensation. The paper first proposes the decentralized compensation topology and control process,

then introduces the case-by-case compensation strategy and calculation method, then improves the tide calculation for reactive power compensation, and finally compares the effect and economy of centralized and decentralized compensation with a real line example.

2 Decentralized Compensation Solution

2.1 Compensation Network Topology

Urban rail MV network is the AC transmission network from the city grid to each station, line capacitive reactive power dominant makes the system PF down under non-operating hours traction, endanger the health of equipment will also be fined by the power operation department. To solve the problem of low PF under non-operating hours, this paper proposes a decentralized compensation system structure topology as shown in Fig. 1. The system includes two parts: compensation system and communication system. The compensation system cancels the traditional compensation devices (such as SVC/SVG) in the main substation, and the stations are divided into traction station/buck station according to whether the bidirectional converter is set up or not; the communication system collects data information such as load, PF and compensation device switching situation in each station by SCADA, and sends the control information such as compensation power to each station after calculation.

This paper adopts bidirectional converter as compensation device, which can also be used for traction power supply, energy-feed absorption and other functions to replace rectifier unit and inverter feedback device and reduce construction investment; in terms of information acquisition and communication, urban rail has SCADA to collect electrical information, and provide efficient and reliable data communication services for each subsystem, which can ensure communication continuity, reliability and real-time. For urban rail transit, the system load and line structure will not change significantly during non-operating hours, so frequent and large information updates are not required, and a small amount of communication resources can be used to meet communication needs.

2.2 Compensation Control Method

Based on the proposed decentralized compensation topology, the reactive power compensation control process of urban rail is developed as shown in Fig. 2. Based on the SCADA system to collect information and update the system network structure, parameters and the power load of each station [10], compensation control information is sent to each station to adjust the compensation power of each station after the

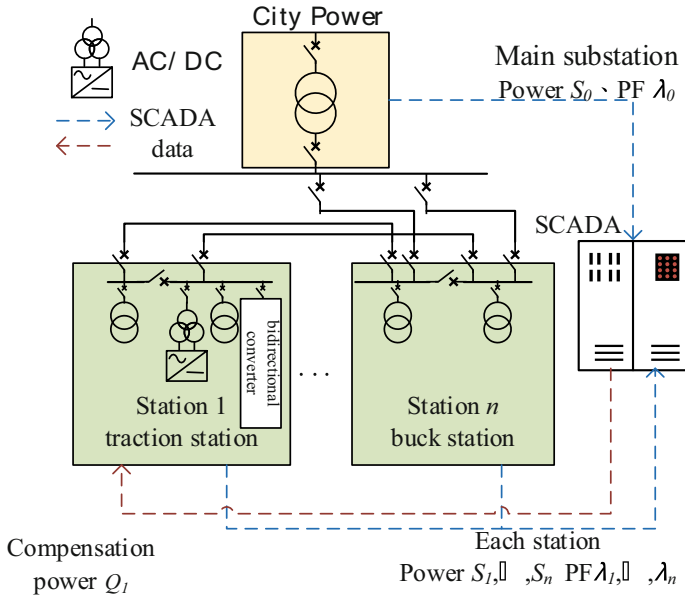
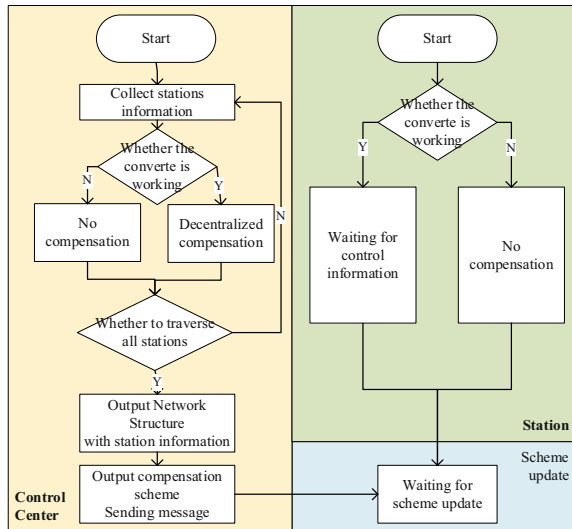


Fig. 1 Decentralized compensation system diagram

compensation scheme is obtained according to the compensation strategy. Considering that the power supply station may shutdown due to maintenance or fault, the control process judges whether the power supply station is involved in compensation according to the unit status.

Fig. 2 Decentralized compensation control flow chart



During non-operating hours, the system network structure and load level are stable, and the update interval can be set to two to three times per hour to avoid frequent adjustment of system reactive power distribution and reduce the requirement for real-time communication. When a large change in system is detected, the reactive power distribution can be forcibly updated.

3 Reactive Power Compensation Strategy

In order to achieve the desired compensation effect, the compensation scheme needs to be adjusted according to the system reactive power distribution. The source of reactive power in the system is divided into two parts—the reactive power generated by the power load of the station and the cable. The ideal reactive power compensation is local balanced by decentralized compensation, which can reduce the losses. A decentralized compensation strategy based on bidirectional converter is proposed.

First, a number of nearby buck stations (the main substation is regarded as a buck station) and the connected cables are regarded as a compensated unit, and the compensated power is the sum of the buck station load and the cable reactive power. Then the compensation range is divided by the midpoint of the nearby traction station and the compensation unit. The buck station merger and compensation range are divided as shown in Fig. 3 and 4.

Assuming sufficient compensation capacity, for each compensation range to achieve the set PF λ_s , for a traction station in compensation range, the reactive power Q_{need} needs to issue can be expressed as

$$Q_{need} = Q_{line} + Q_{self} + Q_{close} \tag{1}$$

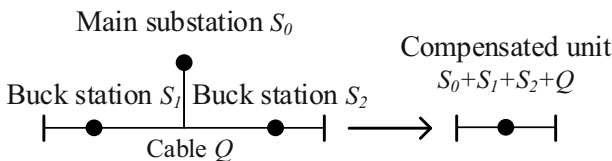
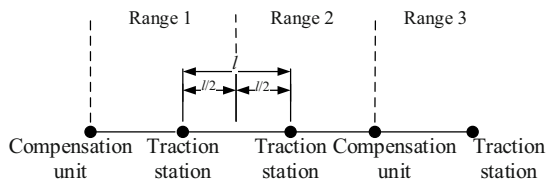


Fig. 3 Diagram of the combining bucking institute

Fig. 4 Diagram of the compensation range division



where Q_{line} , Q_{self} , Q_{close} is the reactive power required by the cable, the traction station itself, the nearby compensation unit. Based on the system measurements to obtain the power S_i with PF λ_i , Q_{self} can be expressed as

$$Q_{self} = \frac{S_i \lambda_i}{\lambda_s} \sqrt{1 - \lambda_s^2} - S_i \sqrt{1 - \lambda_i^2} \quad (2)$$

Similarly, with the compensation unit the power S_i and PF λ_i , Q_{close} can be expressed as

$$Q_{close} = \frac{S_c \lambda_c}{\lambda_s} \sqrt{1 - \lambda_s^2} - S_c \sqrt{1 - \lambda_c^2} \quad (3)$$

When the compensation unit is connected to one unit, Q_{close} is fully assumed by the connected unit; when it is connected to two units, it is divided into Q_{c1} and Q_{c2} to two units according to the length of the cable with the compensation unit. Assume that the distance of compensation unit from both units is l_1 , l_2 , ignore the cable resistance, the reactance per unit length of the connected cable is x , the system voltage is rated voltage U . The power loss P_{loss} caused by the transmission of reactive power in the line can be expressed as follows

$$\begin{cases} P_{loss} = \frac{Q_c^2}{U^2} l_1 x + \frac{Q_c^2}{U^2} l_2 x \\ Q_{close} = Q_{c1} + Q_{c2} \end{cases} \quad (4)$$

When $Q_{c1} = \frac{l_2}{l_1+l_2} Q_{close}$, $Q_{c2} = \frac{l_1}{l_1+l_2} Q_{close}$, the power loss P_{loss} takes the minimum value. Thus Eq. (1) can be written as.

$$Q_{need} = \frac{L}{L_{sum}} Q_L + \frac{S_i \lambda_i}{\lambda_s} \sqrt{1 - \lambda_s^2} - S_i \sqrt{1 - \lambda_i^2} + r \left(\frac{S_c \lambda_c}{\lambda_s} \sqrt{1 - \lambda_s^2} - S_c \sqrt{1 - \lambda_c^2} \right) \quad (5)$$

where, r is the proportion of the compensation power of the nearby compensation unit, which is determined according to the network structure and cable length.

4 Analysis of Reactive Power Compensation Optimization Examples

4.1 Reactive Power Compensation Example

Take a MV network of railway as an example, the schematic diagram of the network and the compensation range division are shown in Fig. 5. When centralized compensation is adopted, SVG (not shown in the figure) is installed in the main substation

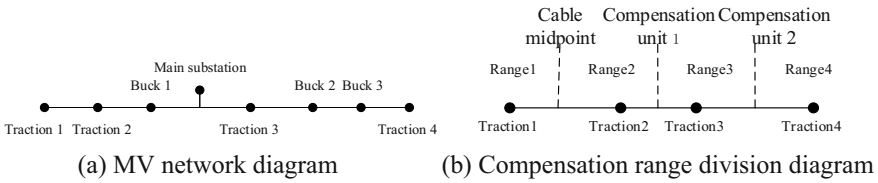


Fig. 5 Diagram of the network structure and compensation division

Table 1 Bidirectional converter working condition division

No.	Traction 1	Traction 2	Traction 3	Traction 4
I	On	On	On	On
II	On	On	On	Off
III	On	On	Off	On
IV	On	Off	On	On
V	Off	On	On	On

to adjust the PF, and when decentralized compensation is adopted, the PF is adjusted by the bidirectional converter in the traction station.

The bidirectional converter in the line is divided into different combinations of on/off states as shown in Table 1 to check the compensation effect when unit out of work.

4.2 Comparison of Reactive Power Compensation Effect

The reactive power compensation constraint sets the voltage deviation value not exceeding 5%, and the lower limit of PF at the main substation is 0.95, and the reactive power compensation capacity for each operating condition is obtained as shown in Table 2.

Table 2 Compensation capacity in each working condition

No.	Centralized/(MVar)	Decentralized/(MVar)			
		Traction 1	Traction 2	Traction 3	Traction 4
I	1.322	-0.073	0.398	0.664	0.267
II		-0.073	0.398	0.931	/
III		-0.073	0.683	/	0.632
IV		0.213	/	0.774	0.267
V		/	0.325	0.664	0.267

Table 3 Reactive power compensation effect

No.	Main substation PF	System loss/(kW)
No compensation	0.7339	69.011
Centralized	0.9508	75.073
Decentralized I	0.9506	68.460
Decentralized II	0.9504	68.407
Decentralized III	0.9506	68.697
Decentralized IV	0.9504	69.210
Decentralized V	0.9501	68.522

The comparison of loss and main substation PF after compensation is shown in Table 3. In adjusting the PF of the main substation, the decentralized compensation is close to the centralized compensation, and it shows the centralized compensation can be replaced by decentralized; in the power consumption, the centralized compensation requires additional equipment SVG, and the system loss is higher.

5 Conclusion

In this paper, a decentralized compensation topology and compensation strategy for urban railways is proposed. Taking the actual network as an example, the compensation effect of centralized and decentralized compensation is quantitatively compared, and the following conclusions are drawn by comparing the PF, system loss:

- (1) The compensation scheme obtained by applying compensation strategy can significantly improve the PF, which verifies the feasibility of the compensation system and the effectiveness of the compensation strategy.
- (2) Both centralized compensation and decentralized compensation can raise the PF of the main substation above the set value. When the PF is close, the decentralized compensation loss is lower. The decentralized compensation fully meet demand for reactive power compensation, can cancel the centralized compensation to save construction and operation costs.

References

1. Zhu, R., et al.: Smart transformer/large flexible transformer. *CES Trans. Electr. Mach. Syst.* **4**(4), 264–274 (2020)
2. Chen, Y., et al.: MMC-MTDC transmission system with partially hybrid branches. *CES Trans. Electr. Mach. Syst.* **5**(2), 124–132 (2021)
3. Kumar, C., et al.: A new voltage control strategy to improve performance of DSTATCOM in electric grid. *CES Trans. Electr. Mach. Syst.* **4**(4), 295–302 (2020)

4. Li, T., Hu, W., et al.: Intelligent economic dispatch for PV-PHS integrated system: a deep reinforcement learning-based approach. *Trans. China Electrotech. Soc.* **35**(13), 2757–2768 (2020). (in Chinese)
5. Xie, Y., Zhai, S., Li, W., et al.: Active-reactive power coordinated optimization of distribution network with photovoltaic based on PSO-CSA algorithm. In: 2022 7th International Conference on Power and Renewable Energy (ICPRE), Shanghai, China, pp. 313–318. IEEE Press (2022)
6. Liu, M., Wang, Z., Xing, Y.: Enhanced multi-objective differential evolutionary algorithm based optimal power flow calculation for integrated electricity and gas systems. *Trans. China Electrotech. Soc.* **36**(11), 2220–2232 (2021). (in Chinese)
7. Zhou, Z.: Analysis of reactive power compensation capacity in urban mass transit power supply system. *Electr. Drive Locomot.* (04), 68–70 (2015). (in Chinese)
8. Xiang, W., Jun, L.: On scheme of distributed reactive power compensation system using a bidirectional converter. *High Speed Railw. Technol.* **12**(03), 91–96+116 (2021). (in Chinese)
9. Zhu, S., Ruan, B., Quan, H., et al.: Study of urban rail reactive power compensation strategy based on energy-fed traction power supply equipment. *Adv. Technol. Electr. Eng. Energy* **32**(02), 16–19+23 (2013). (in Chinese)
10. Fan, D., Chen, H., Yi, X.: Application of multiple SCADA integrated supervision and control system in urban rail transit. *Urban Rapid Rail Transit* **30**(05), 99–102+113(2017). (in Chinese)

Design of Polygonal Permanent Magnet Array in Magnetic Nanoparticle Imaging System



Yide Huang, Li Ke, Qiang Du, Wannu Zu, and Kaicheng Wen

Abstract Magnetic nanoparticle imaging (MPI) is a novel medical imaging technology with the advantages of high sensitivity, high spatial resolution, short imaging time, and no ionizing radiation. The permanent magnet array with Halbach layout using field-free line (FFL) scanning in MPI has the advantages of high magnetic field uniformity and no thermal power consumption. Currently Halbach permanent magnet arrays use the same rectangular magnets and are positioned and oriented in a specific way to generate the field-free line needed to select the field. In order to optimize the performance of the field-free line, in this paper, the shape of the magnet of Halbach array is expanded from square to polygon, and the magnet layout of mandhala structure is used to form field-free line with different gradients. Finally, the simulation results show that by increasing the number of sides of a single polygon, the magnetic field strength in each direction is continuously enhanced, and the gradient of the field-free line is becoming larger and larger. When the polygon becomes a circle, the field-free gradient reaches 12.09 T/m, which is about 30% higher than that of a square magnet. The feasibility of using polygon permanent magnet array to optimize FFL in MPI and improve the resolution of MPI imaging is proved.

Keywords Magnetic nanoparticle imaging · Permanent magnet array · Field-free line

1 Introduction

Magnetic nanoparticle imaging (MPI) is a new medical imaging technology using magnetic nanoparticles as tracers to image the spatial concentration distribution. Compared with traditional medical imaging techniques such as CT and NMR, MPI has the advantages of high spatial resolution, short imaging time, and no ionizing radiation [1]. It has broad application prospects in cell tracing, tumor imaging, and

Y. Huang · L. Ke (✉) · Q. Du · W. Zu · K. Wen
School of Electrical Engineering, Shenyang University of Technology, Shenyang 110870, China
e-mail: keli@sut.edu.cn

© Beijing Paiké Culture Commu. Co., Ltd. 2023
X. Dong et al. (eds.), *The proceedings of the 10th Frontier Academic Forum of Electrical Engineering (FAFEE2022)*, Lecture Notes in Electrical Engineering 1054, https://doi.org/10.1007/978-981-99-3408-9_21

231

angiography [2, 3]. As a tracer for MPI imaging, magnetic iron oxide nanoparticles (SPION) will produce a nonlinear magnetization response, which is particle signal, in an external alternating magnetic field when it is around the zero magnetic field [4]. Then an external receiving coil is used to receive the induced voltage signals of the particles, the induced voltage signals directly reflect the particle concentration information around the zero magnetic field, and finally the spatial coding of the magnetic nanoparticles is realized by changing the position of the zero magnetic field [5].

In MPI, zero-field lines are commonly used to scan particles. FFL can be generated in two main ways: electromagnetic coils or permanent magnets. Compared with electromagnetic coils, MPI systems built with permanent magnets have the advantages of high magnetic field uniformity, large magnetic field gradient, and not producing thermal power consumption like electromagnetic coils [6]. In 2013, Saritas and Goodwill et al. designed a structure [7] in which six permanent magnets with the same magnetization direction were oppositely placed, thus forming an FFL of 2.3 T/m. In 2018, Matthias Weber et al. proposed a 5 T/m FFL formed by a magnet array ring consisting of 90 rectangular permanent magnets [8]. In 2020, Bakenecker et al. proposed to use multiple Halbach rings to generate an FFL of 8.7 T/m [9].

At present, most MPI systems still use electromagnetic coils to generate FFL. However, electromagnetic coils usually need to large current of tens of amperes to generate high-gradient FFL, which will lead to a large amount of thermal power consumption and more intense Brownian motion of magnetic particles, which affects the image resolution of MPI systems. At the same time, most MPI systems are closed structures, limiting the volume of imaging targets. In addition, the existing permanent magnet arrays all use a structure of a bar magnet, and the permanent magnet array of this structure cannot generate a sufficiently strong FFL gradient in a limited space, so that a high-resolution imaging effect cannot be obtained. Therefore, it is of great practical significance to design a novel MPI field-free system with permanent magnet array, which can enlarge the detection aperture, reduce the system power consumption and generate high-performance FFL.

Based on the above problems, firstly, the Halbach permanent magnet array is constructed by using polygonal permanent magnets. Second, the arrangement of the magnet array is made more compact by the Halbach layout using the mandhala structure to allow the array to produce a higher flux density to obtain the best performance FFL. Finally, the performance of FFL is analyzed by COMSOL multi-physical field simulation software, which proves the feasibility of using polygon permanent magnet array to optimize FFL-MPI.

2 Theoretical Basis of Halbach Permanent Magnet Array

The ideal Halbach permanent magnet array is shown in Fig. 1(a). The magnetization direction of the permanent magnet cylinder is continuously changed according to a specific angle, but in reality, it is difficult to realize the continuous change of

the magnetization direction along the circumferential direction of the ring. Therefore, in practical application, the discrete form shown in Fig. 1(b) is often used to approximately replace [10].

The magnetic flux density B generated for the continuous Halbach cylinder of Fig. 1(a) is

$$B = B_R \ln\left(\frac{r_{out}}{r_{in}}\right) \tag{1}$$

where B_R is the residual magnetic flux density of the permanent magnet, r_{in} is the inner diameter of the magnet ring and r_{out} the outer diameter of the magnet ring. The magnetic flux density $B(n)$ generated for a Halbach cylinder consisting of n segment discrete structures is

$$B(n) = K(n)B_R \ln\left(\frac{r_{out}}{r_{in}}\right) \tag{2}$$

$$K(n) = \sin\frac{(2\pi/n)}{2\pi/n} \tag{3}$$

According to this principle and the references [10, 11], the functional expression of the magnetic field strength of the discrete dipole along the z axis with the distance from the center plane is obtained:

$$B(z) = \frac{\mu_0 n}{8\pi} \frac{3mr^2}{(r^2 + z^2)^{5/2}} \begin{pmatrix} 0 \\ 0 \\ 1 \end{pmatrix} \tag{4}$$

where $\mu_0 = 4\pi \times 10^{-7} Tm/A$ is permeability of vacuum, m is the magnetic moment, r is the central radius of the magnet ring and z is the distance of the magnet array from the x - y plane. Where the magnetic moment m is

$$m = M * V \tag{5}$$

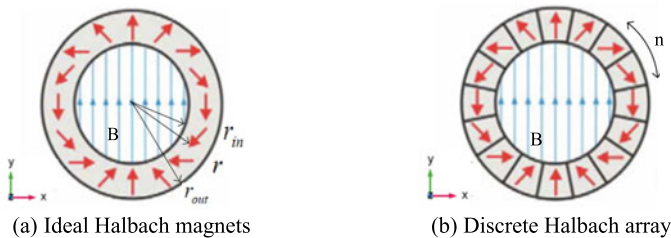


Fig. 1 Ideal Halbach magnet and discrete Halbach array

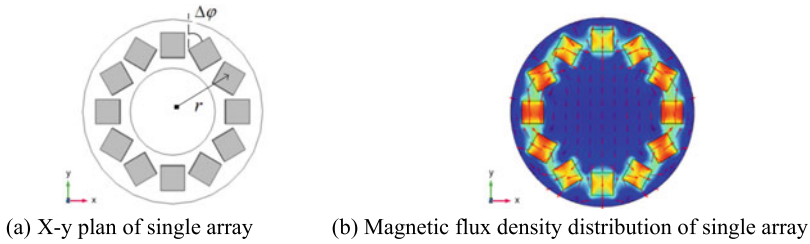


Fig. 2 Square permanent magnet array plan and magnetic flux density distribution

where M is the magnetization, V is the magnet volume, by changing the magnet shape to change the volume contribution in the magnetic flux density B , so that for any specific shape of the magnet the above formula can be simplified as

$$B_y(z) = \frac{3n}{8\pi} \frac{V \cdot r^2}{(r^2 + z^2)^{5/2}} B_R \quad (6)$$

Figure 2 shows the planar structure of a single square Halbach permanent magnet array, where r is the central radius of the annular permanent magnet array. Halbach permanent magnet array is arranged by n permanent magnets rotating in space around the axis of symmetry [12], where the change angle of the magnetization direction of adjacent magnets $\Delta\varphi$ meets the following equation:

$$n \cdot \Delta\varphi = (k + 1) \cdot 360^\circ, \quad k \in n \quad (7)$$

where n is the number of magnets and $\Delta\varphi$ is the change in magnetization direction of adjacent magnets, k is the number of pairs of magnetic poles, Fig. 2 is the system structure of a single array at $k = 1$, and the arrow in Fig. 2(b) is the direction of the generated magnetic field.

3 Design of Permanent Magnet Array Linear Field-Free Line System

The selection field of the magnetic nanoparticle imaging system of the permanent magnet array can be generated by placing two pairs of Halbach annular arrays in parallel with each other, and the magnetization directions of the magnets at the positions corresponding to the upper and lower arrays are different by 180 degrees. In the z direction, the magnetic field near the position of the arrays is stronger, until the positions in the middle of the two arrays are reached, the field strengths at two sides are almost symmetrically attenuated to zero. In the positions in the middle of the two arrays, along the x direction, the field strengths are attenuated to zero, to form FFL, as shown by the dotted line in Fig. 3(a).



Fig. 3 FFL generated by permanent magnet array

Table 1 Mandhala layout parameter of different magnets

	Square	Polygon	Circle
$a(\text{mm})$	$2 \cdot r \cdot \Omega(n)$	$2 \cdot r \cdot \theta(n)$	$2 \cdot r \cdot \sin(\pi/n)$

In order to make the magnetic field generated by the permanent magnet array as strong as possible, the structure of the permanent magnet array is designed as Mandhala structure commonly used in magnetic resonance. Mandhala structure is a simple, economical and efficient method to generate a high-intensity uniform magnetic field [13]. In order to make better use of the space on the ring, adjacent magnets should contact each other as much as possible to obtain a strong magnetic field as possible, as shown in Fig. 5.

Given the number of magnets n and their center radius r , their size can be calculated for all adjacent magnet contact arrangements, as shown in Table 1.

Among them,

$$\Omega(n) = \frac{\cos(\frac{2\pi}{n}) - \sin(\frac{2\pi}{n}) - \sqrt{2} \cdot \sin(\frac{\pi}{4} - \frac{4\pi}{n})}{2 \cdot \cos(\frac{\pi}{4} - \frac{4\pi}{n}) + \sqrt{2}} \tag{8}$$

$$\theta(n) = \begin{cases} \frac{1}{2} \tan\left(\frac{2\pi}{n}\right) & n \text{ is even number} \\ \frac{2 \sin(\frac{\pi}{n})}{\cos(\frac{2\pi}{n}) + 1} & n \text{ is odd number} \end{cases} \tag{9}$$

In this paper, the height h of each permanent magnet, the distance d between the upper and lower Halbach arrays, and the number of individual permanent magnet arrays are constant. In this paper, the number of magnets $n = 12$, the center radius $r = 38 \text{ mm}$ as an example, the height of each permanent magnet $h = 20 \text{ mm}$, the distance between the upper and lower two Halbach array $d = 30 \text{ mm}$, as shown in Fig. 4.

As shown in Fig. 5 shows the different polygonal magnet configurations used and the corresponding geometric parameters. Suppose that the magnetic flux density generated by the square magnet is B_0 , and the comparison of area, volume and magnetic flux density of different polygons is shown in Table 2.

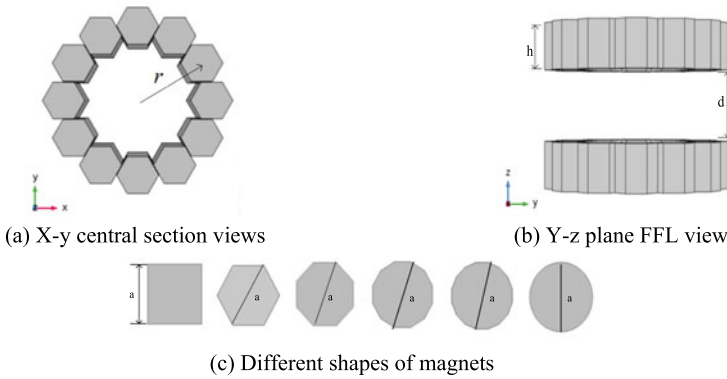


Fig. 4 Structure diagram of permanent magnet array system







	Square	Hexagon	Octagon	Dodecagon	Hexadecagon	Circle
n=12 r=38mm	 a=16.62mm	 a=21.94mm	 a=21.94mm	 a=21.94mm	 a=21.94mm	 a=19.67mm

Fig. 5 Configuration of different polygons and corresponding geometrical parameters

Table 2 Different polygon areas, volumes, magnetic flux densitiesets

	Square	Hexagon	Octagon	Hexadecagon	Circle
Area(mm ²)	275.2	312.7	340.4	368.4	372
Volume(mm ³)	5504.3	6253.1	6807.5	7368.4	7458.3
Magnetic flux	B ₀	1.14B ₀	1.24B ₀	1.34B ₀	1.35B ₀

4 Analysis of Simulation Results of Different Polygon

According to the designed different polygonal permanent magnet array system structures, the COMSOL5.5 multi-physical field simulation software was used to construct the three-dimensional model of the permanent magnet array system and the simulation analysis was performed. The axial flux density distribution, the y directional flux density distribution, and the gradient of the generated FFL are calculated, including the center of the upper and lower permanent magnet arrays.

Figure 6 is a field-free line formed by the square permanent magnet array obtained through simulation. Figure 6(a) is a view in the y-z plane FFL, and Fig. 6(b) is a view in the x-y plane FFL. The dotted line in the figure is FFL generated by the system.

The magnetization direction and magnetic field distribution shown in Fig. 6 are the same for magnets of different shapes.

The magnetic flux density of each Halbach permanent magnet array along the y axis is shown in Fig. 7(a). From the curves drawn according to the simulation results, it can be seen that from the square permanent magnet array to the circular permanent magnet array, the magnetic flux density shows an increasing trend and is distributed along the axis symmetry until $y = 0$, the attenuation at the field-free line position is 0. The slope of the magnetic flux density curve increases continuously, the zero magnetic field gradient increases continuously.

In addition, according to the y axial flux density meter obtained in Fig. 7(a), the field-free line gradient values obtained by different polygonal permanent magnet arrays are calculated, as shown in Fig. 7(b). Where number of sides 0 is circular. The FFL gradient increase gradually from square to polygon to circle, from 9.19 T/m for square to 12.09 T/m for circle. As the number of sides of the polygon increases, the shape of the magnet gradually approaches the circular shape, and the FFL gradient increases gradually and becomes gentle, with the gradient increased by about 30%.

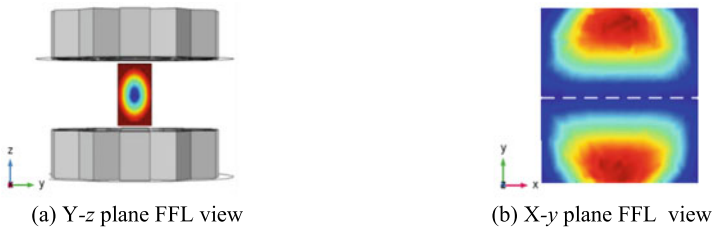


Fig. 6 FFL generated by square permanent magnet array

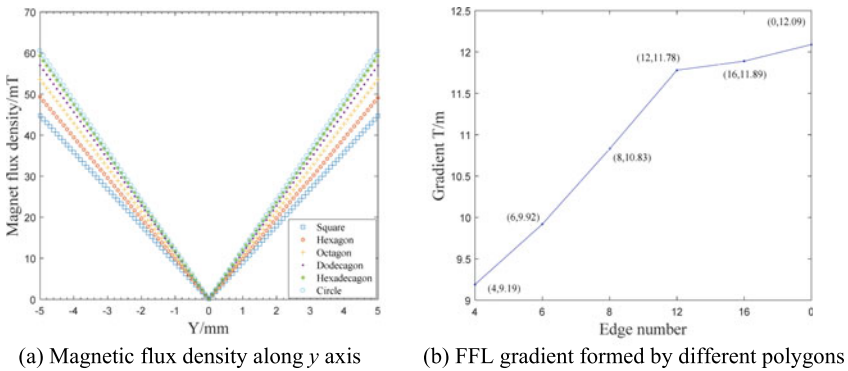


Fig. 7 Magnetic flux density along y axis and FFL gradient

5 Conclusions

In this paper, aiming at the problems of large heating power consumption, small magnetic field gradient, low spatial resolution and so on in the existing magnetic nanoparticle imaging system, a structure using different polygonal permanent magnet arrays to generate the field-free line required by the magnetic nanoparticle imaging system is designed. By placing two Halbach permanent magnet arrays in antiparallel, a field-free line can be created in the center plane, and no thermal power dissipation occurs because the field-free line is created by the permanent magnets. In addition, the arrangement of Halbach using mandela structure makes the arrangement of magnet array more compact to make the array produce higher magnetic flux density. Simulation results show that by extending the structure of the field-free line generated by Halbach square magnet to the polygon (hexagonal, octagonal, dodecagonal, hexagonal, circular) structure, a higher magnetic flux density is obtained. the field-free gradient increases from 9.19 T/m in a square to 12.09 T/m in a circle, and the FFL gradient increases by about 30%. Since the larger the zero magnetic field gradient of the magnetic nanoparticle imaging system is, the higher the spatial resolution of the system is, this paper proves the feasibility of using polygon permanent magnet array to achieve high resolution imaging in the MPI system.

Acknowledgements The research was supported by National Natural Science Foundation of China (52077143) and the Liaoning Province Department of Education (LJKZ0131).

References

1. Billings, C., Langley, M., Warrington, G., et al.: Magnetic particle imaging: current and future applications, magnetic nanoparticle synthesis methods and safety measures. *Int. J. Molecular Sci.* **22**(14), 7651 (2021)
2. Mimura, A., Inaoka, Y., Asakawa, S., et al.: A novel cellular imaging method using Hemagglutinating Virus of Japan-Envelope (HVJ-E) vector and magnetic particle imaging. *J. Nanoence Nanotechnol.* **20**(4), 2007–2017 (2020)
3. Wang, Q.Y., Ma, X.B., Liao, H.W., et al.: Artificially engineered cubic iron oxide nanoparticle as a high-performance magnetic particle imaging tracer for stem cell tracking. *ACS Nano* **14**(2), 2053–2062 (2020)
4. Zhang, Y., Li, K., Qiang, D., et al.: Research on magnetic particle imaging algorithm based on wavelet sparse. *Beijing Biomed. Eng.* **40**(04), 337–345.(2021) (in Chinese)
5. Ergor, M., Bingolbali, A., et al.: Field-free line magnetic particle imaging magnet design using nested halbach cylinders. *IEEE Magn. Lett.* (99), 1–1 (2022)
6. Jiang, C., Li, K., Qiang, D., et al.: Research on the magnetic field-free line system based on ring magnet array. *Chin. J. Sci. Inst.* **42**(9), 192–201 (2021) (in Chinese)
7. Saritas, E.U., Goodwill, P.W., Croft, L.R., et al.: Magnetic particle imaging (MPI) for NMR and MRI researchers. *J. Magn. Reson.* **229**(Complete), 116–126 (2013)
8. Weber, M., Beuke, J., Gladi, A.V., et al.: Novel Field Geometry Using Two Halbach Cylinders for FFL-MPI (2018)
9. Bakenecker, A.C., Schumacher, J., Blumler, P., et al.: A concept for a magnetic particle imaging scanner with Halbach arrays. *Phys. Med. Biol.* (2020)

10. Soltner, H., Blumler, P.: Dipolar Halbach magnet stacks made from identically shaped permanent magnets for magnetic resonance. *Concepts Magn. Reson. Part A* **36A**(4), 211–222 (2010)
11. Tretiak, O., Blumler, P., Bougas, L.: Variable single-axis magnetic-field generator using permanent magnets for magnetic resonance. *AIP Adv.* **2019**(11) (2019)
12. Meribout, M., Kalra, M.: A portable system for two dimensional magnetic particle imaging. *Measurement* **152**, 107281 (2020)
13. Raich, H., Blumler, P.: Design and construction of a dipolar Halbach array with a homogeneous field from identical bar magnets: NMR Mandhalas. *Concepts Magn. Reson.* **23B**, 16–25 (2004)

Fracture Toughness Measurement of GIS/GIL Epoxy Composites Based on Ultrasonic Testing Technology



Xingwang Li, Zhuoyi Liang, Congwei Yao, Yanpeng Hao, Xiaofeng Pang, Shuai Sun, Xian Yang, Lin Liu, Yingying Zhang, and Yao Zheng

Abstract Accurate evaluation of fracture toughness of epoxy composites for GIS/GIL insulators affects the safety and reliability of insulators. In order to achieve effective evaluation of fracture toughness of epoxy composites for GIS/GIL insulators, the epoxy composite samples containing prefabricated cracks were prepared firstly. An ultrasonic detection platform was built, and the size of the prefabricated crack of the specimens were measured by the ultrasonic reflection method. The results were compared with vernier caliper measurements, showing that the ultrasonic detection technology can assist in measuring the prefabricated crack length of epoxy specimens. Then the critical load at break of the epoxy specimen was measured by a three-point bending test. Finally, the K_{IC} and G_{IC} values of the fracture toughness evaluation index of the epoxy material was calculated. The critical load values of epoxy composites for GIS/GIL insulators were measured at 333.211 N. The average values of K_{IC} and G_{IC} were respectively $0.932 \text{ MPa}\cdot\text{m}^{1/2}$ and 60.7 J/m^2 .

Keywords Fracture toughness · Prefabricated cracks · K_{IC} · G_{IC} · Ultrasonic reflection method

1 Introduction

Gas insulated metal-enclosed switchgear (GIS) and gas insulated transmission line (GIL) have the advantages of high reliability, good integration, small footprint, long service life, low maintenance, and environmental friendliness [1].

X. Li · C. Yao (✉) · X. Pang · S. Sun · X. Yang
Electric Power Research Institute, Guangdong Power Grid Co. Ltd., Guangzhou, China
e-mail: yaocongwei1990@163.com

Guangdong Key Laboratory of Electric Power Equipment Reliability, Guangzhou, China

Z. Liang · Y. Hao · L. Liu · Y. Zhang · Y. Zheng
School of Electric Power Engineering South, China University of Technology, Guangzhou, China

Three-pillar insulators and basin insulators are thermosetting insulating products made of epoxy resin, curing agent and filler pouring and curing, which have excellent electrical properties, good chemical stability, excellent resistance to alkali, acid, salt and other media corrosion [2], is the key electrical component of GIS/GIL. However, with the increase in the volume of high-voltage switch-gear, the amount of insulation failure shows an upward trend. Since it was put into operation in 2013, the 500 kV GIL equipment of a converter station has caused four electrical insulation failures and two pipeline noises due to the unqualified quality of the GIL tube mother insulator [3]. In 2020, a 252 kV GIS basin insulator leaked air, and a total of 19 cracks were found in 7 intervals of 15 basin insulators [4], and the study found that the waterproof structure design and process of the basin insulator were unreasonable, and the assembly process of the basin insulator tightening bolt was unqualified, resulting in stress concentration, which reduced the mechanical properties of the insulator.

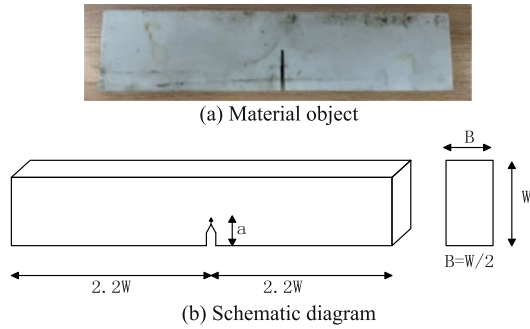
With the development of China's power system towards ultra-high voltage, ultra-high voltage and large capacity, higher requirements are put forward for the performance of insulators, and the mechanical properties of epoxy casting materials are also getting higher and higher. For a long time, the focus of fracture mechanics research was mainly on metallic materials. With considerable development, fracture mechanics has been used to analyze fracture problems in ceramic materials, composites, polymer materials, biomedical materials, and rock concrete materials, and has achieved many achievements [5, 6].

The fracture toughness measurement method of materials is based on the theory of fracture mechanics, and the K_{IC} and G_{IC} values are quantitative indicators for evaluating the toughness and crack expansion ability of materials.

At present, the fracture toughness measurement methods of materials at home and abroad are: prefabricated crack method (SEPB), standard compact tension (CT) specimen [7] and cut beam method [8]. Among them, the SEPB method [9] is difficult to prefabricated cracks simply and conveniently. The incision beam method includes the unilateral incision beam method (SENB), the mountain type incision beam method (CNB) [10] and the unilateral V-shaped cut beam method (SEVNB) [11, 12]. It is generally believed that the sample preparation of the SENB method [13] is simple, the preparation of prefabricated cracks is easier and the comprehensive cost is lower than that of CNB method or SEVNB method, and the test method is simpler and more convenient than the CT method, so this method is more commonly used. In summary, the accuracy of the material fracture toughness measurement is subject to the sharpness of the prefabricated crack incision, and the sharper the incision, the closer the measured value is to the true fracture toughness. However, the direction and length of the propagation of the material prefabricated cracks are often difficult to determine, which seriously affects the measurement accuracy of fracture toughness.

In this paper, the standard sample of epoxy resin composite materials for GIS/GIL epoxy insulation were taken as the research object, and the ultrasonic measurement method was proposed in this paper for the fracture toughness measurement of epoxy composites to measure the prefabricated crack size of the specimen. And the critical

Fig. 1 Standard test block for epoxy composites for GIS/GIL insulators



load of fracture is measured on the sample using a three-point bending test. Finally, the K_{IC} and G_{IC} values of epoxy composites are calculated using the SENB empirical formula to achieve effective evaluation of the fracture toughness of epoxy composites.

2 Experiments

2.1 Epoxy Specimens

In this paper, epoxy specimens were prepared according to standard ASTM D5045-99, and three epoxy specimens (#1, #2 and #3) were prepared according to the standard ASTM D5045-99, with a length of 90 mm, a width of W of 20 mm, and a thickness of 10 mm.

The standard specimen for fracture toughness test is made of epoxy resin, curing agent, filler, etc. by pouring and curing. The size of the standard specimen should meet the following specific requirements: thickness $B = W/2$ (W is the width of the specimen), crack length $a = (0.45-0.55)W$, see Fig. 1.

2.2 Prefabricated Crack Ultrasonic Testing Platform

K_{IC} and G_{IC} are quantitative indicators for evaluating the fracture toughness of materials, and the measurement accuracy of the length of the prefabricated crack in the specimen determines the accuracy of the K_{IC} and G_{IC} values. The SENB method is widely used to evaluate the fracture toughness of materials due to its high measurement accuracy. But there is still the problem of inaccurate measurement of prefabricated crack length. Ultrasonic reflection method has the advantages of high sensitivity, simple measurement, convenient and easy to implement, and can measure the length of prefabricated cracks, which is an effective prefabricated crack detection method.

The ultrasonic testing platform consists of an ultrasonic pulser, an oscilloscope, a probe adaptation line, and a high impedance transmission line. Among them, the ultrasonic pulse generator is an improved CTS-23 with negative square wave excitation, pulse amplitude and width adjustment. And the ultrasonic probe is a narrow strip longitudinal wave ultrasonic probe, with a diameter of 6 mm on the bottom surface of the probe and a probe height of H 20 mm.

The oscilloscope model Tektronix MDO3012 has a bandwidth of 100 MHz, a sample rate of 2.5 GS/s, and a sampling point of 100 k.

During the test, the probe is placed vertically in the upper part of the specimen where there are cracks and no cracks to measure twice. Ultrasonic longitudinal waves travel in a straight line in the specimen, encounter reflections at the bottom of the specimen, and return to the probe along the original path. Record the timing of the oscilloscope reflected wave signal peaking in both measurements t_0 (with cracks) and t_1 (without cracks), as shown in Fig. 2.

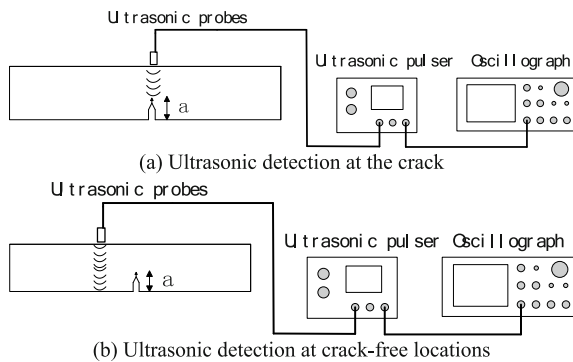
The propagation velocity of ultrasonic longitudinal waves in epoxy composites V is to 3000 m/s [14], then the prefabricated crack a and geometric factor f are obtained by Eqs. (1) and (2).

$$a = \frac{V(t_1 - t_0)}{2} \tag{1}$$

$$f(k) = \frac{6(k)^{\frac{1}{2}}(1.99 - k)(1 - k)(2.15 - 3.93k + 2.7k^2)}{(1 + 2k)(1 - k)^{\frac{3}{2}}} \tag{2}$$

Wherein, a is the length of the prefabricated crack, the unit is mm; V is the ultrasonic longitudinal sound velocity, the unit is m/s; t_0 is the time at the crack in the specimen, t_1 is the time without crack in the specimen, the unit is s; k is the ratio of the length of the prefabricated crack a to the width W .

Fig. 2 Schematic diagram of prefabricated crack length measurement of standard test blocks based on ultrasonic scanning principle



2.3 Three-Point Bending Test

In this paper, the SANS microcomputer-controlled electronic universal testing machine CMT 5105 was used to perform a three-point bending test on the standard specimen of epoxy composites, as shown in Fig. 3.

In this paper, the standard sample of epoxy composites is repeated three times. Adjust the crack position and align the prefabricated natural crack of the specimen with the tester indenter. Fine-tune the indenter of the tester so that it has a certain distance from the specimen to be pressed. Zeroing is performed on the computer that controls the testing machine, the testing machine is turned on, and the indenter is loaded at a constant speed of 0.5 mm/min.

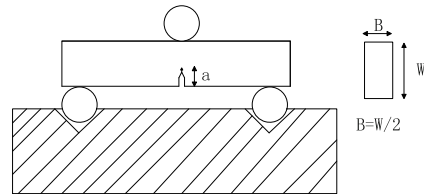
Collect the data of the external force load and indenter displacement of the specimen in the whole process from the opening of the testing machine to the fracture of the specimen, determine the critical load value of the specimen at break, and calculate the K_{IC} and G_{IC} values of the epoxy composite material according to the SENB empirical formula (3) and the fracture mechanics formula (4).

$$K_{IC} = \frac{P_C}{BW^{1/2}} f(k) \tag{3}$$

$$G_{IC} = \frac{K_{IC}^2 (1 - \nu^2)}{E} \tag{4}$$

Wherein, P_C is the critical load value of the epoxy composite, in N. B and W are the thickness and width of the epoxy specimen, respectively, in mm. E is the elastic

Fig. 3 Three-point bending test of epoxy composite standard test block



(a) Material object



(b) Schematic diagram

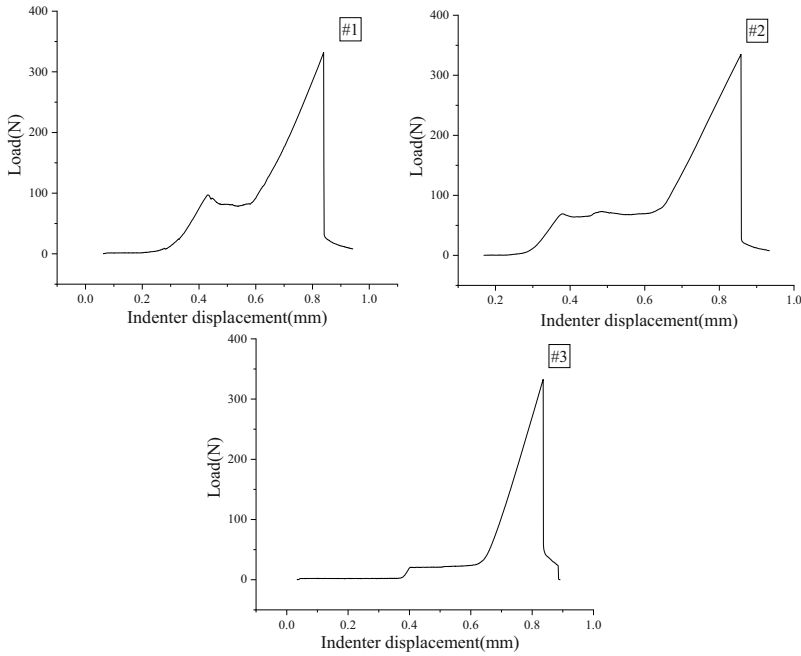


Fig. 4 Three-point bending test data

modulus of the epoxy composite, taking 12.25 GPa [15]. The Poisson ratio of the epoxy composite is 0.32 [15].

3 Results and Analysis

3.1 Ultrasonic Detection of Prefabricated Crack Lengths

The ultrasonic testing platform measured the propagation time t_0 and t_1 of the ultrasonic detection platform in 3 epoxy samples containing prefabricated cracks, and the length and geometric factors of the prefabricated cracks of the 3 specimens were calculated by Eqs. (1) and (2), as shown in Table 1. At present, the prefabricated crack length of epoxy specimens is usually measured using a vernier caliper, and the measured prefabricated crack length is shown in Table 1.

As can be seen from Table 1, the deviation of the prefabricated crack length measurement between the vernier caliper and the ultrasonic detection platform is 4.6%. The ultrasonic testing platform provides a digital interface-assisted prefabricated crack length measurement. The results were compared to vernier calipers that require measurement after the epoxy specimen breaks, showing that the ultrasonic

Table 1 Ultrasonic detection of prefabricated cracks in epoxy specimens

Method	Epoxy samples	#1	#2	#3
Ultrasonic Testing	acoustic-path difference $\Delta t(s)$	6.4×10^{-6}	6.4×10^{-6}	6.5×10^{-6}
	Crack length $a(mm)$	9.6	9.6	9.7
	Geometric factors f	3.933	3.933	3.910
Vernier Calipers	Crack length $a(mm)$	10.06	10.09	10.14
	Geometric factors f	3.832	3.825	3.815

Table 2 Critical load at break of epoxy specimen and calculation of K_{IC} and G_{IC}

Epoxy samples	#1	#2	#3
Critical Load(N)	332.04	334.9	332.7
$K_{IC}(MPa \cdot m^{1/2})$	0.929	0.937	0.931
$G_{IC}(J/m^2)$	60.3	61.3	60.5

testing platform can non-destructively measure the prefabricated crack length of the epoxy specimen.

3.2 Fracture Toughness Measurement

The fracture critical load values of three epoxy specimens measured by the three-point bending test are shown in Table 2, and the K_{IC} and G_{IC} values are calculated according to Eqs. (3) and (4). The K_{IC} measurements of sample #1, #2 and #3 were 0.929, 0.937 and 0.931, respectively, and the average of the three was 0.932 $MPa \cdot m^{1/2}$ as the K_{IC} result of fracture toughness of the epoxy composite. The G_{IC} measurement results were 60.3, 61.3, and 60.5, respectively, and the average of the three was 60.7 J/m^2 as the fracture toughness G_{IC} results of the epoxy composite.

4 Conclusion

In order to evaluate the fracture toughness of epoxy resin composites for GIS/GIL insulators, an ultrasonic detection method was proposed in this paper for measuring the prefabricated crack size of the sample for the fracture toughness of epoxy composites. And the ultrasonic testing technology can assist in the nondestructive measurement of the length of the prefabricated cracks of epoxy samples.

The epoxy specimen was then measured using the three-point bending method, and the mean fracture critical load P_C of the three epoxy specimens was 333.211N. The mean values of K_{IC} and G_{IC} for epoxy composites were 0.932 $MPa \cdot m^{1/2}$ and 60.7 J/m^2 , respectively, calculated from the empirical formula of the SENB method.


Acknowledgements Project supported by the China Southern Power Grid Corporation Science and Technology Project Funding (GDKJXM20201965).

References

1. Yong, Y., Rui, Y., Hongchuan, W.: Comparison of stress classification and verification standards between gas-insulated closed metal equipment and gas-insulated transmission lines. *Electric Technol.* **21**(12), 87–91 (2020)
2. Manling, S.: The application principle and technology of epoxy resin (2002)
3. Jingfei, W., Qiang, Z., Xiangbin, L., et al.: Fault analysis and improvement measures of GIL three-pillar insulator in UHVDC transmission project. *High Voltage Appar.* **56**(1), 246–252 (2020.)
4. Wenyao: GIS basin insulator cracking cause analysis and treatment measures. *Hubei Electric Power* **45**, 40–46 (2021)
5. Suo, Z., Hutchinson, J.W.: Interface crack between two elastic layers. *Int. J. Fract.* **43**(1), 1–18 (1990)
6. Jianghong, G., Zhenduo, G.: Research progress of fracture toughness test technology of ceramic materials in China. *Silicate Notific.* **15**(1), 53–57 (1996)
7. Xiangxi, S.: The Effect of Prefabricated Crack Offset Angle on Dynamic Fracture Toughness of Materials. Harbin Engineering University, Harbin (2016)
8. Zhenduo, G., Xinmin, D.: Comparison of test methods for fracture toughness KIC of ceramic materials and analysis of influencing factors. *J. Silicate* **3**, 24–33 (1982)
9. Kaur, S., Cutler, R.A., Shetty, D.K.: Short-crack fracture toughness of silicon carbide. *J. Am. Ceram. Soc.* **92**(1), 179–185 (2009)
10. Shuangyin, Z.: Mountain notch specimens and methods for determination of fracture toughness of brittle materials. *J. Inorg. Mater.* **4**(4), 289–298 (1989)
11. Liu, H., Zhao, W., Ji, Y., Cui, J., Chu, Y., Rao, P.: Determination of fracture toughness of zirconia ceramics with different Ytria concentrations by SEVNB method. *Ceram. Int.* **43**(13), 10572–10575 (2017)
12. Zhao, W., Cui, J., Rao, P.: Effect of molten zone ablated by femtosecond lasers on fracture toughness of Si₃N₄ measured by SEVNB method. *J. Eur. Ceram. Soc.* **38**(4), 2243–2246 (2018)
13. Kim, B.C., Park, S.W., et al.: Fracture toughness of the nano-particle reinforced epoxy composite. *Compos. Struct.* **86**(1–3), 69–77 (2008)
14. Fangyuan, T., Yanpeng, H., Zhouchio, Z.: Ultrasonic critical refraction longitudinal wave method for the detection of microcracks on the surface of epoxy composite insulation. *Guangdong Electric Power* **32**, 106–112 (2019)
15. Zhouzhiao, Z.: the theory and method of GIS basin insulator stress ultrasonic detection based on acoustic elastic effect. Guangzhou South China University of Technology (2020)

Active Gate Drive for Short-Circuit Current Suppression of SiC MOSFET in Hard Switching Fault



Jingwei Zhang , Zhikang Guo, Yizhan Jiang, and Guojun Tan

Abstract Most of researches on short-circuit protection of power devices focus on reducing the detection time of gate drives. In order to further reduce the effect of SC event, this paper presents an active gate drive (AGD) for SiC MOSFET based on short-circuit current suppression under hard switching fault (HSF). While performing conventional short-circuit protection method, the AGD is achieved to suppress short-circuit current by providing a lower positive gate voltage, decided by detecting the drain–source voltage. In addition, the key parameters of driving circuit are calculated and adjusted to guarantee typical high turn-on speed characteristic. The advantage and reliability of the proposed AGD are verified experimentally on 1.2 kV/80 A SiC MOSFET in short-circuit test. Comparing with the conventional gate drive (CGD), AGD achieves at most 46% reduction in short-circuit current, and 51% reduction in short-circuit loss at identical dc-bus voltage. With the increase of blanking time, the value of short-circuit current and loss decrease more greatly.

Keywords Silicon carbide MOSFET · Hard switching fault · Current suppression · Active gate drive

1 Introduction

Wide band gap semiconductor devices represented by SiC MOSFETs contribute to the development of new energy power generation, radio energy transmission, household appliances and other industries [1, 2]. In order to reduce the impact of short circuit fault on SiC MOSFETs, gate drives are required to detect it quickly and shorten the duration of short circuit [3, 4]. Desaturation protection is the most widely used method at present [5, 6]. It can be seen from the practical application that the detection rate of this method can meet the protection requirements.

J. Zhang (✉) · Z. Guo · Y. Jiang · G. Tan
School of Electrical Engineering, China University of Mining and Technology, Xuzhou 221116, China
e-mail: TB19130011B4@cumt.edu.cn

However, the designed short-circuit blanking time is long, so that the short-circuit loss and junction temperature are relatively high. In order to further reduce the short circuit detection time, many researches have improved the short-circuit protection circuit. Horiguchi et al. [7] proposed PCB Rogowski coil with its sensing circuit to directly detect short circuit current. Xue et al. [8] and Lee et al. [9] proposed a short-circuit current changing rate judgement method by extracting the induced voltage of stray inductance between power-source and auxiliary-source terminals. Horiguchi et al. [10] proposed a fast short-circuit diagnosis method using gate charge characteristics. The improved methods can reduce the short circuit fault detection time of SiC MOSFET drive to hundreds of nanoseconds. However, the corresponding short circuit detection circuit requires high hardware requirements and is vulnerable to interference. At present, they are not suitable for commercial applications and have no universality. However, in addition to improving the detection rate of the gate drive, the way to improve the short circuit withstanding capability of SiC MOSFET by reducing the short circuit current is conducive to reduce the design requirements for fast short circuit protection of gate drives. At present, there are few researches on the driving circuit of short-circuit current suppression. In this paper, an active gate drive (AGD) which can suppress short-circuit current during hard switching fault (HSF) is proposed. The two-level positive driving voltage switching method is adopted for SiC MOSFET to make the gate voltage higher during normal conduction process and lower gate voltage with small gate resistor during turn-on transient and short-circuit process so as to reduce short-circuit current without affecting normal turn-on process.

2 Gate Drive circuit and Parameters design

The hard switching fault (HSF) occurs in turn-off transient of power devices. Although many researches have verified that the reduction of positive driving voltage can restrain short-circuit current [11], few gate drives uses this method to deal with short-circuit. This paper designs an active gate drive (AGD) based on CPLD logical control for SiC MOSFET. The proposed AGD mainly consists of three circuit units as depicted in Fig. 1.

In the driving amplifier unit, it is composed of four switches M_1 , M_2 , M_3 and M_4 . Among them, M_1 and M_2 are used to provide positive voltage V_{CC} and negative voltage V_{EE} respectively. M_4 is used to soft turn-off SiC MOSFET during short-circuit protection, and the gate resistance $R_{g\text{soft}} > R_{g\text{off}}$. Different from the traditional driving circuit, the amplifier adds a lower positive voltage V_{CC1} , which is powered by M_3 . The diode D_{g1} is used to block the current loop of V_{CC} and V_{CC1} .

In the drain-source voltage V_{DS} detection unit, traditional desaturation method is adopted for short-circuit protection. In order to avoid the false protection in turn-on transient, the detection method needs a certain blanking time. When the SiC MOSFET is turned off, the analog switch SW remains closed. When the gate drive receives turn-on signal, the SW is cut off. The blanking time Δt_{blank} is

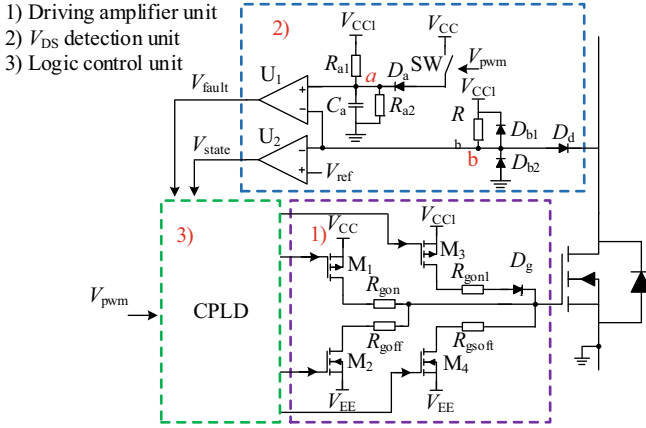


Fig. 1 Detail circuit schematic diagram of the proposed gate driver

$$\Delta t_{\text{blank}} = -n \ln \frac{V_{CC1}(1 - m)}{V_{CC} - mV_{CC1}} \tag{1}$$

where $n = \frac{R_{a1}R_{a2}C_a}{R_{a1} + R_{a2}}$ and $m = \frac{R_{a2}}{R_{a1} + R_{a2}}$.

The detection principle of comparator U_1 is shown in Fig. 2. During normal turn-on transient, the voltage V_a at the positive input terminal “a” of U_1 is greater than the voltage V_b at the negative input terminal “b”, the short circuit fault signal V_{fault} remains low level. When HSF fault occurs, since the voltage at “a” and “b” points intersects after the blanking time, as shown in Fig. 2(b), V_{fault} is converted to high level. Comparator U_2 judges the drain-source voltage V_{DS} state by comparing the voltage at point “b” with the reference value V_{ref} . At the beginning of turn-on transient, when V_{DS} stays at high voltage, the output signal V_{state} of U_2 is low level, and after entering the normal conduction, V_{DS} drops to conduction voltage, V_{state} is converted to high level. AGD will judge whether V_{CC} or V_{CC1} should be provided to the gate of SiC MOSFET according to the drain source state.

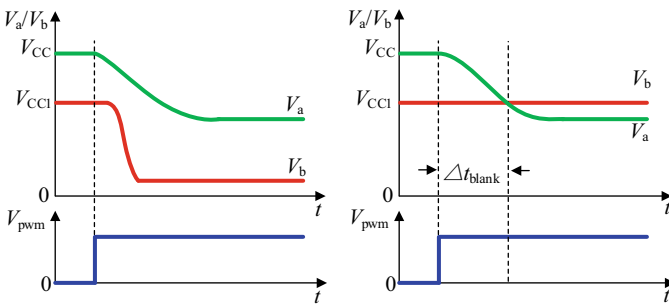


Fig. 2 The principle of desaturation method

In the logic control unit, in order to realize the high-speed processing capability of various signals in the gate drive, the working frequency of CPLD reaches 100 MHz. After receiving V_{pwm} , V_{fault} and V_{state} signals, CPLD quickly judges the operating state of SiC MOSFET, and then controls the switching timing of M_1 – M_4 .

Figure 3 shows the detail circuit implementation of the AGD. When CPLD receives turn-on signal V_{pwm} at t_{x0} (high level in the figure), the drive amplifier circuit switches M_3 , and the gate is converted from the turn-off voltage V_{EE} to V_{CC1} . During the normal turn-on transient, as shown in Fig. 3(a), V_{DS} drops to conduction voltage before the blanking time. V_{state} is converted to high level, causing AGD switches M_1 . The gate is converted from V_{CC1} to V_{CC} , which reduces the conduction loss of SiC MOSFET. When HSF happens, as shown in Fig. 3(b), due to the desaturation effect, V_{DS} is always at high bus voltage, thus, the V_{state} remains low. Due to the lower positive voltage V_{CC1} switches to the gate, the short-circuit current is suppressed. After the blanking time, V_{fault} is converted to high level. The short circuit fault is detected and M_4 is switched immediately to soft turn-off SiC MOSFET.

According to the transfer characteristics of SiC MOSFET, the lower the gate voltage is, the smaller the maximum current allowed by SiC MOSFET. Therefore, it seems that the smaller the value of V_{CC1} is, the lower the short-circuit current will be suppressed. However, in order to ensure the normal and rapid switching speed of SiC MOSFET, V_{CC1} cannot be too small. During the normal turn-on process, when the gate rises to threshold voltage V_{th} , the drain current starts to rise. When drain current rises to the load current I_L . V_{DS} starts to drop, and the gate voltage rises slowly due to the charging characteristics of Miller capacitor, forming the Miller platform V_p

$$V_p = V_{th} + \frac{I_L}{g_m} \tag{2}$$

High load current will increase V_p . Therefore, the maximum voltage of Miller platform V_{pmax} will be generated when the drain current reaches the maximum load current required by the system. Since the driving voltage is V_{CC1} at this time, V_{CC1}

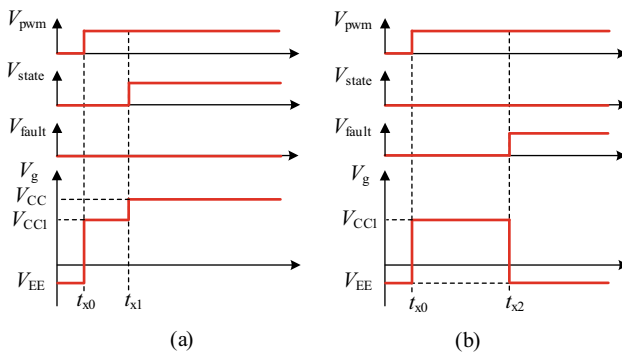
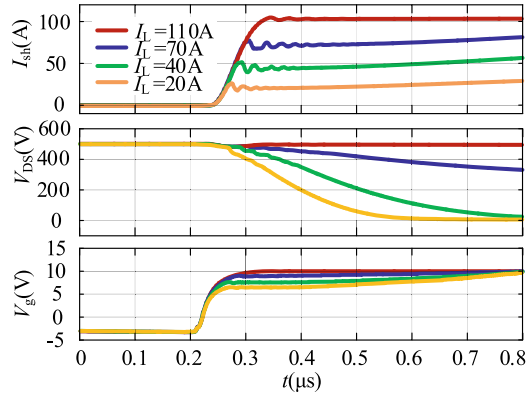


Fig. 3 Driver behavior and signal feedback (a) common turn-on process (b) the HSF process

Fig. 4 The turn-on transient simulation waveforms of SiC MOSFET with $V_{CC1} = 10$ V



must be higher than V_p in order to turn-on the SiC MOSFET normally. Figure 4 shows the transient simulation waveform of SiC MOSFET (Rohm's BSM080D12P2C008) when V_{CC1} is 10 V. When I_L is at low value ($I_L = 20$ A or 40 A), SiC MOSFET can normally turn-on at fast speed. However, when I_L approaches the rate current ($I_L = 70$ A), V_{DS} drops slowly, seriously affecting the switching rate. When I_L reaches to 110 A, V_{DS} maintains a high value. the load current cannot continue to rise, indicating that this current is the maximum drain current that flow through SiC MOSFET when the gate voltage is 10 V.

By looking up the Miller platform voltage of different SiC MOSFETs under twice the rated current, it is found that the range of V_{pmax} is about 10–14 V. In order to ensure the universality and reliability of the gate driver, a certain V_{CC1} margin must be reserved. However, V_{CC1} should not be set too high to suppress the short circuit current as much as possible. Therefore, the positive voltage V_{CC1} is set to 15 V in this paper. The SiC MOSFET module is BSM080D12P2C008 in Rohm.

3 Experiment

A SiC MOSFET pulse test platform is built to verify the short-circuit current suppression performance of the AGD, as shown in Fig. 5. T_1 is the device to be test, T_2 is used as freewheeling diode. T_2 still remains at off state. L_s is the stray inductance, L_{load} the load inductor. In normal double pulse test, the value of L_{load} is selected according to the required load current and pulse width. While in HSF test, the load should be replaced by a short copper wire which has small inductance.

In order to verify the suppression effect of the AGD designed in this paper, the testing results are compared with the traditional driver (CGD) as shown in Fig. 6. Both the AGD and CGD use the same desaturation detection circuit for short circuit protection, and the drive parameters are basically the same. However, CGD has no V_{CC1} switching circuit and V_{DS} state detection circuit. In addition, due to the high

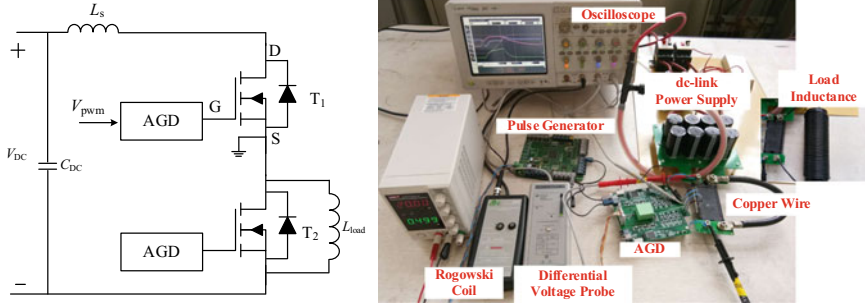


Fig. 5 Schematic diagram and hardware prototype of SiC MOSFET switching characteristic test platform

short-circuit current of CGD, the gate resistance R_{gsoft} for soft turn off is higher than that of AGD to ensure the same voltage overshoot. The experimental results are shown in Fig. 6. The blanking time is $1.2 \mu s$. In CGD, the gate voltage finally rises to 20 V, causing the short-circuit reaches to 690 A, which is 8 time more than the rated current. The loss E_s of SiC MOSFET caused by short circuit fault is 284 mJ. Comparing with CGD, in AGD, the gate voltage rises to 15 V, and the maximum short circuit current is 390 A, which is less than 5 times of the rated current, reducing by 46%. The loss E_s is 139 mJ, reduced by 51%.

The blanking time of desaturation protection method is an important factor affecting the HSF protection. It can be known from Eq. (1) that Δt_{blank} has a linear relationship with the capacitance C_a . By changing C_a , the short-circuit waveforms and the losses of SiC MOSFET between different blanking times (800 to 1800 ns) are shown in Figs. 7 and 8 respectively. The short-circuit current I_{sh} keeps rising with the increase of blanking time. However, the rising rate of short-circuit current of AGD is lower than that of CGD, which greatly reduces the loss. When the blanking time

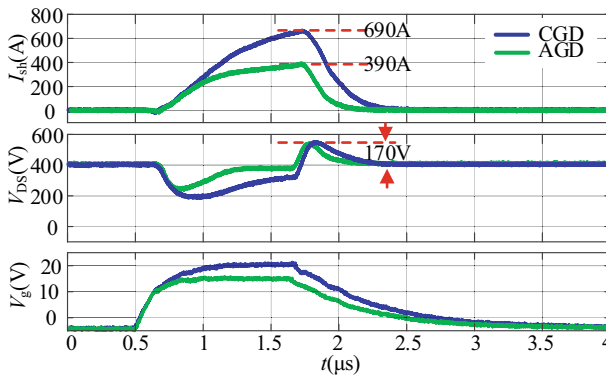


Fig. 6 HSF protection performance comparison of SiC MOSFET between proposed and conventional method

is 800 ns, the short-circuit current caused by CGD and AGD are 520 A and 320 A respectively, the current of AGD is reduced by 200 A, and the total loss is reduced by 120 mJ. When the blanking time is 1800 ns, the short-circuit current of CGD and AGD is 800 A and 410 A respectively, the current of AGD is reduced by 390 A, and the total loss is reduced by 200 mJ. Therefore, it can be known from the above experimental results that AGD can effectively suppress the short circuit current and reduce the short circuit loss when HSF occurs, thus reducing the impact of the short circuit current on the device.

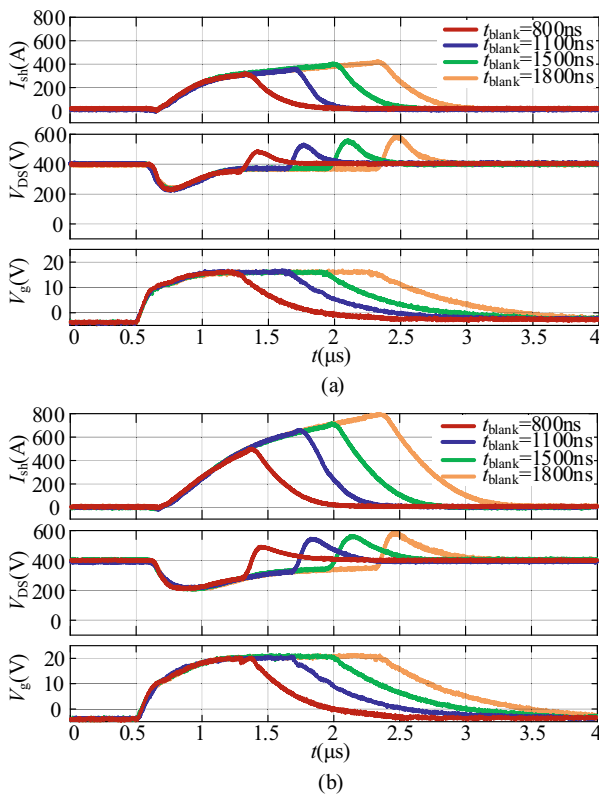


Fig. 7 HSF protection performance with different blanking time (a) proposed method and (b) conventional method

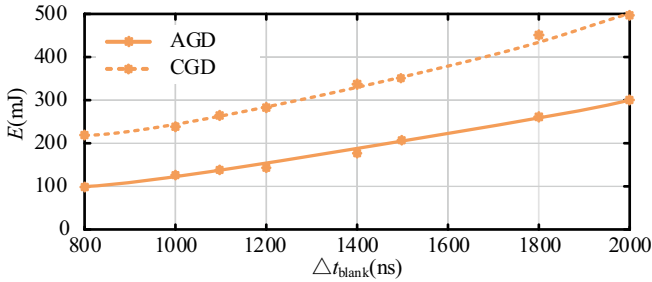


Fig. 8 Short-circuit loss of SiC MOSFET between AGD and CGD

4 Conclusion

In this paper, an active gate drive (AGD) based on current suppression of hard switching fault is proposed. The gate drive can effectively reduce the short circuit current by changing the gate voltage. By detecting the state of drain source voltage of SiC MOSFET when in turn-on transient, the positive drive voltage is switched, so that the gate voltage of SiC MOSFET is 20 V when it is normally turned on to reduce the conduction loss, and 15 V when in short circuit to suppress the short circuit current. The short circuit processing effect of AGD is compared to CGD in experiments. AGD can significantly suppress the short circuit current at any blanking time, thereby reducing the short circuit loss and reducing the impact of HSF fault on SiC MOSFETs. The short circuit treatment method proposed in this paper provides some reference for the reliable application of SiC MOSFET.

References

1. Guan, Q.X., Li, C., Zhang, Y., et al.: An extremely high efficient three-level active neutral-point-clamped converter comprising SiC and Si hybrid power stages. *IEEE Trans. Power Electron.* **33**(10), 8341–8352 (2018)
2. Han, Y., Lu, H.F., Li, Y.D., et al.: Analysis and suppression of shaft voltage in SiC-based inverter for electric vehicle applications. *IEEE Trans. Power Electron.* **34**(7), 6276–6285 (2019)
3. Sadik, D.-P., Colmenares, J., Lim, J.-K., Bakowski, M., Nee, H.-P.: Comparison of thermal stress during short-circuit in different types of 1.2-kV SiC transistors based on experiments and simulations. *IEEE Trans. Indust. Electron.* **68**(3), 2608–2616 (2021). <https://doi.org/10.1109/TIE.2020.2972442>
4. Yao, K.L., Yano, H., Iwamuro, N.: Investigations of short-circuit failure in double trench SiC MOSFETs through three-dimensional electro-thermal-mechanical stress analysis. *Microelectron. Reliabil.* **122** (2021)
5. Sadik, D.P., Colmenares, J., Tolstoy, G., et al.: Short-circuit protection circuits for silicon-carbide power transistors. *IEEE Trans. Indust. Electron.* **63**(4), 1995–2004 (2016)
6. Shi, Y., Ren, X., Lu, W., et al.: Short-circuit protection of 1200 V SiC MOSFET T-type module in PV inverter application. *Energy Conversion Congress and Exposition* (2016)

7. Horiguchi, T., Kinouchi, S., Nakayama, Y., et al.: Comparison and discussion on shortcircuit protections for silicon-carbide MOSFET modules: desaturation versus rogowski switch-current sensor. *IEEE Trans. Indust. Appl.* **56**(3), 2880–2893 (2020)
8. Xue, J., Xin, Z., Wang, H., et al.: An improved di/dt-RCD detection for short-circuit protection of SiC mosfet. *IEEE Trans. Power Electron.* **36**(1), 12–17 (2021)
9. Lee, S., Kim, K., Shim, M., et al.: A digital signal processing based detection circuit for short-circuit protection of SiC MOSFET. *IEEE Trans. Power Electron.* **36**(12), 13379–13382 (2021)
10. Horiguchi, T., Kinouchi, S., Nakayama, Y., et al: A fast short-circuit protection method using gate charge characteristics of SiC MOSFETs. *IEEE Energy Conversion Congress and Exposition*, pp. 4759–4764 (2015)
11. Zhang, J W., Zhang, T., Feng, Y., et al: Dynamic characterization assessment on series short-circuit of SiC MOSFET. *Trans. China electrotechn. Soc* **36**(12), 2446–2458 (2021) (in Chinese)

Analysis and Research on an Equivalent Circuit of LiFePO₄ Battery Under a High Discharge Rate



Liming Huang, Yihui Xia, and Yunxiang Jiang

Abstract This paper proposed a model parameter identification method for lithium iron phosphate batteries under high discharge magnification, used the identification results under 10 C discharge conditions instead of 30 C model parameters, and compared the actual output voltage observations of the LiFePO₄ battery with the output voltage values of the established simulation model, which proved that the parameters under 10 C discharge conditions were still applicable under 30 C conditions, and the second-order RC model was more accurate than the first-order RC model. The results show that the proposed parameter identification method can solve the problem that the battery parameters identified by the Forgetting Factor Recursive Least Squares (FFRLS) at high discharge rate are not physically significant, and obtain a second-order RC model with higher accuracy, which provides a basis for subsequent state of charge (SOC) estimation of LiFePO₄ battery.

Keywords LiFePO₄ battery · High discharge rate · Least squares · Parameter identification

1 Introduction

As a result of the advantage of good safety, long service life, and high power density, lithium iron phosphate battery has been widely applied in energy storage systems, electric vehicles, and so on [1–3]. To satisfy the requirement of energy storage system capacity, the LiFePO₄ battery usually forms an energy storage module with a series–parallel connection, which further configures energy storage systems. It's necessary to real-time monitor the LiFePO₄ battery information such as the SOC to know the condition of a single battery or module battery in real time and prevent faults such as over charge, over discharge, and over temperature when works. However, the SOC of high precision needs a battery model of high precision. At present, the battery

L. Huang · Y. Xia (✉) · Y. Jiang
College of Electric Engineering, Naval University of Engineering, Wuhan 430033, China
e-mail: xiayihui2005@163.com

© Beijing Paiké Culture Commu. Co., Ltd. 2023
X. Dong et al. (eds.), *The proceedings of the 10th Frontier Academic Forum of Electrical Engineering (FAFEE2022)*, Lecture Notes in Electrical Engineering 1054, https://doi.org/10.1007/978-981-99-3408-9_24

modeling methodologies mainly include electrochemistry, artificial neural networks and equivalent circuit model [4–6]. The equivalent circuit model has been widely used in practical engineering projects because many advantages such as intuitive, moderate calculation amount, straightforward identification of model parameters, high accuracy of estimation of the SOC, suitable for circuit simulation experiments, and easy to achieve.

Currently, the research on equivalent circuit model of lithium iron phosphate battery mainly focuses on low rate conditions such as electric vehicles. However, a load capacitor is required to charge to high voltage immediately on the occasion of High Energy Pulse Weapons for Ships and Electromagnetic Launch [7, 8]. At this time, the lithium iron phosphate battery needs to be in the discharge condition of 30–50 C. The internal chemical reaction is intense, and the battery capacity and internal resistance will change, which brings difficulties to parameter identification [9, 10].

Taking the discharge process of LiFePO₄ battery as an example, the battery negative electrode generate the lithium ions that enter the electrolyte, and combine with the positive electrode. Because of the difference of ion concentration in the solution, there are unreacted positive and negative charges at the interface between the electrolyte and the positive and negative electrodes, forming a double layer [11]. Therefore, there is a dynamic process of polarization-depolarization in the lithium iron phosphate battery [12–14]. Polarization refers to the change of voltage caused by the accumulation of charge on the electrode surface due to the existence of a double layer, in which the polarization reaction includes ohmic polarization, electrochemical polarization, and concentration difference polarization [15]. Depolarization is the electrode reaction, which makes the accumulated charge react with lithium ions, and the battery electrode potential returns to normal. The principle of a double electric layer is shown as follow.

In research, polarization plays a leading role in the working process of lithium batteries [16]. As before, taking the discharge process of LiFePO₄ battery as an example, because of polarization, the electron flowing speed in the electrolyte is faster than the electrode reaction speed of the positive electrode. At this time, the potential difference between positive and negative becomes smaller. After discharge, because of depolarization, the potential of positive and negative return to equilibrium, and the potential difference between positive and negative becomes bigger [17]. Therefore, under high discharge rate conditions, it needs further study whether the commonly equivalent circuit model and parameter identification method are still applicable.

Firstly, this paper used FFRLS to identify the parameters of the first-order RC model and the second-order RC model under 30 C discharge conditions and solves the problem of whether FFRLS is still applicable in the battery parameter identification under high rate conditions [21, 22]. Secondly, a parameter identification method is proposed to solve the problem that FFRLS identification results do not have physical meaning at 30 C rate. Based on this method, the first-order RC model and the second-order RC model are compared and analyzed to obtain a second-order RC model with higher accuracy.

2 Typical Equivalent Circuit

The process of the capacitor accumulating charge is similar to polarization when the terminal voltage of the capacitor exists, and the process of the capacitor releasing charge through a resistor is similar to depolarization [18]. Therefore, the electrode can be equivalent to a capacitor when the change of voltage is occurring due to polarization, and the electrode can be equivalent to an RC parallel link when the voltage re-rises due to depolarization. Since the ohmic polarization response time is instantaneous, the electrochemical polarization response time is microsecond level, and the concentration difference polarization response time is second level [19, 20], when ohmic polarization and electrochemical polarization are considered, a resistor is used to simulate ohmic polarization, and an RC parallel link is used to simulate electrochemical polarization, which is first-order RC equivalent circuit; when ohmic polarization, electrochemical polarization, and concentration difference polarization are considered, internal resistance and two RC parallel links are used to simulate ohmic polarization, electrochemical polarization and concentration difference polarization, which is second-order RC equivalent circuit.

2.1 First-Order RC circuit

Based on the internal resistance model, the first-order RC model adds a polarization circuit composed of a capacitor and a resistor. Compared with other models, the model structure is relatively simple, but it can accurately describe the changes in battery terminal voltage during charging and discharging. The equivalent circuit is shown in Fig. 2. U_{OC} represents the battery open circuit voltage (OCV), R_0 represents the ohmic internal resistance, C_P represents the polarization capacitance, R_P represents the polarization resistance (Fig. 1).

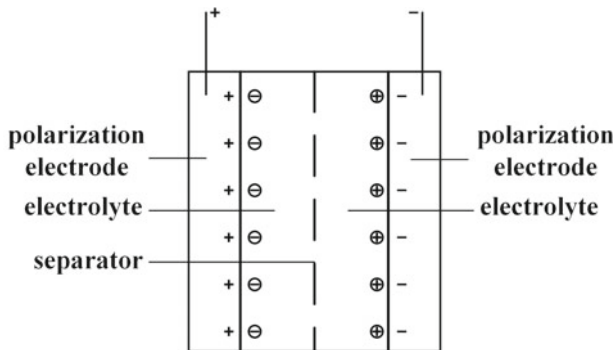
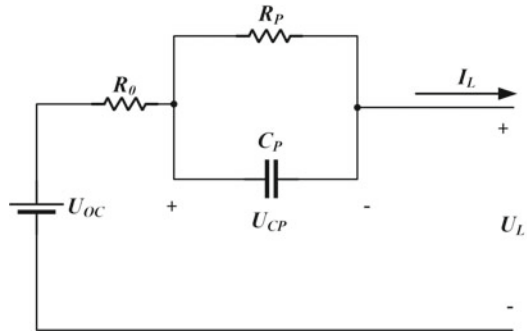


Fig. 1 Schematic of a double electric layer

Fig. 2 First-order RC model



On the base of Fig. 2, the state space equation of the first-order RC circuit model is as follows:

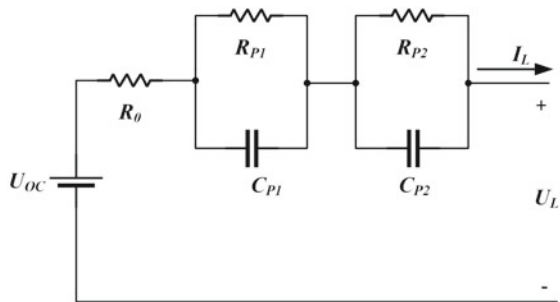
$$\begin{cases} U_{CP}^* = -\frac{1}{R_p C} U_{CP} + \frac{1}{C_p} I_L \\ U_{OC} = R_0 I_L + U_{CP} + U_L \end{cases} \quad (1)$$

2.2 Second-Order RC circuit

On the base of the first-order RC battery model, there are two RC parallel circuits used in the second-order RC model to describe the electrochemical polarization with a small time constant and the concentration difference polarization with a large time constant, to obtain higher modeling accuracy, as shown in Fig. 3.

U_{OC} represents the OCV, R_0 represents the ohmic internal resistance, R_{P1} and C_{P1} represent electrochemical polarization internal resistance and electrochemical polarization capacitance. R_{P2} and C_{P2} represent concentration difference polarization internal resistance and concentration difference polarization capacitance. The state space equation is as follows:

Fig. 3 Second-order RC model



$$\left\{ \begin{aligned} \begin{pmatrix} U_{P1}^* \\ U_{P2}^* \end{pmatrix} &= \begin{pmatrix} -\frac{1}{R_{P1}C_{P1}} & 0 \\ 0 & -\frac{1}{R_{P1}C_{P2}} \end{pmatrix} \begin{pmatrix} U_{P1} \\ U_{P2} \end{pmatrix} + \begin{pmatrix} \frac{1}{C_{P1}} \\ \frac{1}{C_{P2}} \end{pmatrix} I_L \\ U_{OC} &= R_0 I_L + U_{P1} + U_{P2} + U_L \end{aligned} \right. \quad (2)$$

3 Parameter Identification Based on the FFRLS Algorithm

3.1 Algorithm Principle

Recursive Least Squares (RLS) is extensively used in the field of system identification. The following is the principle of RLS.

For linear systems, the mathematical description expression is as follows:

$$Y(k) = \varphi(k)\theta(k)^T + e(k) \quad (3)$$

where,

$$\varphi(k) = [-Y(k-1) \cdots -Y(k-n)u(k) \cdots u(k-n)] \quad (4)$$

$Y(k)$ represents the output at time k of the system, $u(k)$ is the input at time k of the system, $\theta(k)$ is the parameter vector to be identified of the system, $e(k)$ is the system noises. The recursive formula of RLS is as follows:

$$\left\{ \begin{aligned} \hat{\theta}(k+1) &= \hat{\theta}(k) + K(k+1)[Y(k+1) - \varphi^T(k+1)\hat{\theta}(k)] \\ K(k+1) &= P(k+1)\varphi(k+1) \\ P(k+1) &= P(k) - \frac{P(k)\varphi(k+1)\varphi^T(k+1)}{1+P(k)\varphi(k+1)\varphi^T(k+1)} \end{aligned} \right. \quad (5)$$

$P(k)$ represents a covariance matrix, $K(k)$ represents a gain matrix. In the recursive process, RLS uses the deviations between the estimated and measured values of the system output and the gain matrix $K(k)$ to correct $\hat{\theta}(k)$. When initializing, the initial value can be any value, $P(0) = \alpha I$, α represents a constant as large as possible, and I is a unit matrix. To weaken the role of past data and give new data a larger weight, the forgetting factor λ ($0 < \lambda < 1$) is added to obtain the FFRLS. The recursive formula is as follows:

$$\left\{ \begin{aligned} \hat{\theta}(k+1) &= \hat{\theta}(k) + K(k+1)[y(k+1) - \varphi^T(k+1)\hat{\theta}(k)] \\ K(k+1) &= \frac{P(k)\varphi(k+1)}{\lambda + \varphi^T(k+1)P(k)\varphi(k+1)} \\ P(k+1) &= \frac{1}{\lambda} [1 - K(k+1)\varphi^T(k+1)]P(k) \end{aligned} \right. \quad (6)$$

α is generally between 0.95–1. The value of the forgetting factor λ is inversely proportional to the weight of the new data. When $\lambda = 1$, it degenerates to ordinary recursive least squares.

3.2 Online Identification of First-Order RC Circuit Parameters

According to Kirchhoff law, the circuit structure of the first-order RC model is analyzed, and the circuit KVL relationship is as follows:

$$U_{OC} = U_{CP} + R_0 I_L + U_L \tag{7}$$

Do Laplace transform on both sides, as follows:

$$U_{OC}(s) = R_0 I(s) + \frac{R_P I(s)}{\tau_P s + 1} + U_L \tag{8}$$

where $\tau_P = R_P C_P$. After reduction of fractions to a common denominator, calculate the first-order backward difference, as follows:

$$U_{OC}(k) - U_L(k) = \frac{\tau_P}{\tau_P + T} (U_{OC}(k - 1) - U_L(k - 1)) + \frac{T(R_0 + R_P) + \tau_P R_0}{\tau_P + T} I(k) - \frac{\tau_P R_0}{\tau_P + T} I(k - 1) \tag{9}$$

Let:

$$\begin{cases} k_1 = \frac{\tau_P}{\tau_P + T} \\ k_2 = \frac{T(R_0 + R_P) + \tau_P R_0}{\tau_P + T} \\ k_3 = -\frac{\tau_P R_0}{\tau_P + T} \end{cases} \tag{10}$$

Get:

$$\begin{cases} Y(k) = [U_{OC}(k - 1) \ I(k) \ I(k - 1)] \\ \theta(k) = [k_1 \ k_2 \ k_3] \end{cases} \tag{11}$$

After the accessed value obtained by FFRLS, the first-order RC model parameters of can be calculated by the following formula.

$$\begin{cases} R_0 = -\frac{k_3}{k_1} \\ R_P = \frac{(\tau_P + T)(k_2 + k_3)}{T} + \frac{k_3}{k_1} \\ C_P = \frac{\tau_P}{R_P} \end{cases} \tag{12}$$

3.3 Online Identification of Second-Order RC Circuit Parameters

The circuit structure of the second-order RC model is analyzed according to Kirchhoff law, and the circuit KVL relationship is as follows:

$$U_{OC} = U_{P1} + U_{P2} + R_o I_L + U_L \tag{13}$$

Do Laplace transform on both sides, as follows:

$$U_{OC}(s) = \left(\frac{R_{P1}}{R_{P1}C_{P1}s + 1} + \frac{R_{P2}}{R_{P2}C_{P2}s + 1} + R_0 \right) I(s) + U_L(s) \tag{14}$$

Let time constant $\tau_{P1} = R_{P1}C_{P1}$, $\tau_{P2} = R_{P2}C_{P2}$, and let $a = \tau_{P1}\tau_{P2}$, $b = \tau_{P1} + \tau_{P2}$, $c = R_{P1} + R_{P2} + R_0$, $d = R_{P1}\tau_{P2} + \tau_{P1}R_{P2} + R_0(\tau_{P1} + \tau_{P2})$. The above equation can be simplified to:

$$aU_{OC}s^2 + bU_{OC}s + U_{OC} = aR_0I_s^2 + dI_s + cI + aU_s^2 + U_L \tag{15}$$

After the difference, Eq. (15) is discretized to obtain:

$$U(k) = \frac{-bT-2a}{T^2+bT+a}U(k-1) + \frac{a}{T^2+bT+a}U(k-2) + \frac{cT^2+dT+aR_0}{T^2+bT+a}I(k) + \frac{-dT-2aR_0}{T^2+bT+a}I(k-1) + \frac{aR_0}{T^2+bT+a}I(k-2) \tag{16}$$

where $U(k) = U_{OC}(k) - U_L(k)$. The above equation can be simplified to:

$$U(k) = k_1U(k-1) + k_2U(k-2) + k_3I(k) + k_4I(k-1) + k_5I(k-2) \tag{17}$$

Equation (17) can be substituted into FFRLS to identify the estimated value, then the circuit model parameters are derived from the identification results, as follows:

$$\begin{cases} \tau_{P1} = \frac{T}{2(k_1+k_2+1)} \left(\sqrt{k_1^2 - 4k_2} - k_1 - 2k_2 \right) \\ \tau_{P2} = -\frac{T}{2(k_1+k_2+1)} \left(\sqrt{k_1^2 - 4k_2} + k_1 + 2k_2 \right) \end{cases} \tag{18}$$

And

$$\begin{cases} R_0 = \frac{k_5}{k_2} \\ R_{P1} = \frac{\tau_{P1} \frac{k_3+k_4+k_5}{k_1+k_2+1} + \tau_{P1}R_0 + \frac{T(k_4+2k_5)}{k_1+k_2+1}}{\tau_{P1}-\tau_{P2}} \\ R_{P2} = \frac{k_3+k_4+k_5}{k_1+k_2+1} - R_{P1} - R_0 \\ C_{P1} = \frac{\tau_{P1}}{R_{P1}} \\ C_{P2} = \frac{\tau_{P2}}{R_{P2}} \end{cases} \tag{19}$$

4 Experimental Validation

4.1 Calibration Experiment of OCV-SOC Function

According to Eqs. (9) and (17), the OCV, operating voltage, and operating current data are required for battery model parameter identification, where OCV is the terminal voltage of the battery after the lithium battery is fully shelved. Therefore, OCV data cannot be obtained in real-time during the online identification of lithium battery parameters. However, there is a one-to-one correspondence between OCV and battery SOC, so the relationship between them can be obtained by fitting the OCV and SOC measurement points, then OCV can be calculated by the SOC. Firstly, the HPPC experiment was carried out on a 13 Ah lithium iron phosphate battery to obtain its SOC and OCV data. The lithium battery is first discharged at 1C for 10 s and then charged at 0.75 C for 10 s after being held for 40 s. When the SOC drops by 0.1, it is held for 45 min. After the OCV at this time is measured, the next stage of the cycle test is performed until the battery is discharged and the SOC is 0.06.

The SOC sampling points were selected as 1.00, 0.90, 0.80, 0.70, 0.60, 0.60, 0.50, 0.40, 0.30, 0.20, 0.10 and 0.06 for OCV-SOC curve fitting. Figure 4(a) is the OCV-SOC sampling point and fitting curve, the fitting function sampling nine polynomial fitting, the number of fitting coefficients from high to low is 1419.16469768676, -6717.95444590820 , 13,624.0494483225, $-15,486.0532500591$, 10,836.3905382773, -4821.81020435755 , 1356.90924240580, -231.379692258040 , 21.8783325576193, 2.31024798710441. When the SOC of a lithium battery is between 10 to 90%, the deviation between the fitting value and the true value is less than 0.01 V from Fig. 4(b). When the SOC of a lithium battery is close to 0 or 100%, the deviation is large. The reason is that the voltage in these two stages changes greatly, increasing fitting deviation. The battery data used for parameter identification is measured when the battery SOC is 40%–70%, so the parameter identification can use the OCV value to estimate the battery SOC according to the OCV-SOC function.

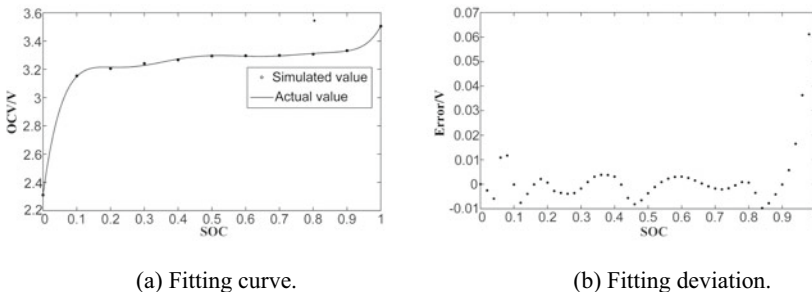


Fig. 4 SOC-OCV fitting

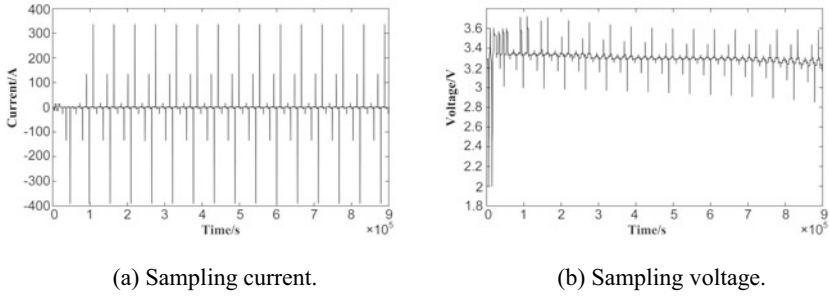


Fig. 5 Sampling current and voltage waveforms

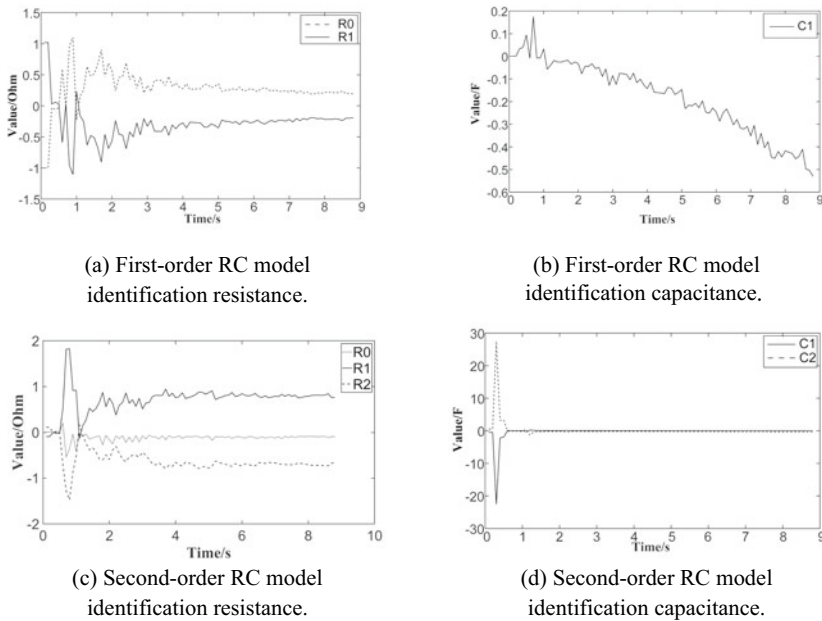
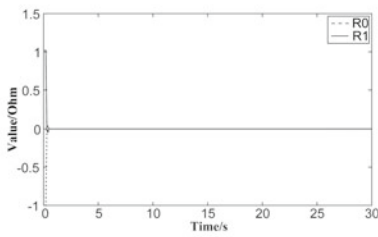


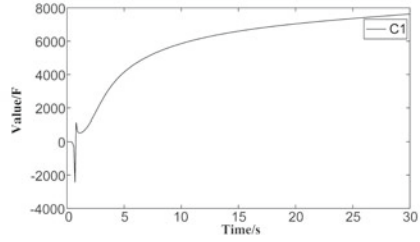
Fig. 6 FFRLS identification results under 30 C working conditions

4.2 Model Parameter Identification Experiment

Experimental lithium iron phosphate battery capacity is 13Ah, rated voltage is 3.2 V, under the condition of 25 °C, 0.5 C, 1 C, 2 C, 10 C, 30 C charge and discharge experiments, the sampling interval is 0.1 s, each charge and discharge after the end for 1.5 h to obtain OCV data, according to the OCV–SOC function to estimate the initial SOC. The waveforms sampled in the actual test of voltage and current are shown as follows (Fig. 5):

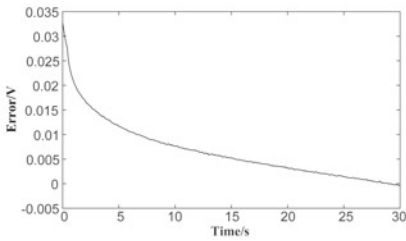


(a) First-order RC model identification resistance.

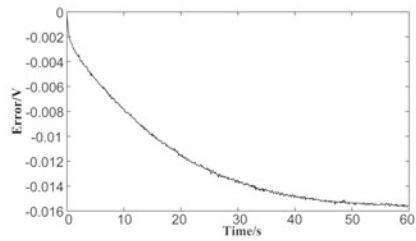


(b) First-order RC model identification capacitance.

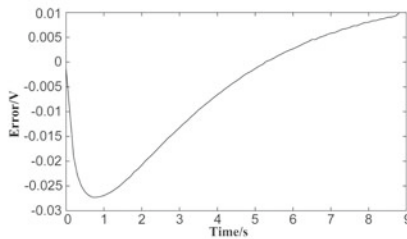
Fig. 7 First-order RC model identification results



(a) Condition of 10C.



(b) Condition of 2C.



(c) Condition of 30C.

Fig. 8 Terminal voltage deviation

The principle of the FFRLS algorithm for lithium battery model parameter identification is used to find a set of parameters to minimize the estimation deviation of the system. The identification results only need to meet the deviation requirements and do not need to consider the identification result physical meaning. The RC parallel link of the first-order RC model simulates the electrochemical polarization process of the battery, and the response time is microsecond level. The two RC parallel links of the second-order RC model simulate the electrochemical polarization and concentration difference polarization process, and the response time is microsecond

level and second level. The RC parallel link time constants of both models are small. When the battery operating current is large, the capacitor of the RC parallel link will soon be fully charged. At this time, the voltage of the RC parallel link will no longer change. Due to the existence of ohmic internal resistance, the terminal voltage will still change. To meet the deviation requirements, there will be a situation where the RC parallel link resistor and capacitor parameter identification results are negative, which is inconsistent with its physical meaning, and the identification results cannot be used. Under the condition of 30C, the FFRLS algorithm is used to perform simulation calculations in MATLAB with a forgetting factor of 0.999. The identification results are shown as follows. Whether it is a first-order RC model or a second-order RC model, there are cases where the identification results are negative (Fig. 6).

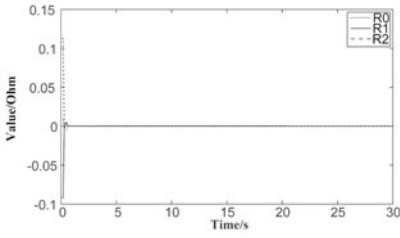
To solve the problem of FFRLS parameter identification under 30C condition, this paper proposed a method of using 10 C identification results as 30 C model parameters. Firstly, using FFRLS to identify the parameters of lithium batteries under 10 C discharge condition in MATLAB, and the forgetting factor is set to 0.999. Based on the identification parameters, to verify the discharge conditions of 10, 2, and 30 C, building a simulation model in Simulink. The output voltage and measurement voltage of the simulation model are compared to analyze whether the model parameters identified under the discharge condition of 10 C can be used under the discharge conditions of 2 and 30 C. Identification results and deviations are shown as follows (Figs. 7 and 8):

From Figs. 9 and 10, it can be seen that under the 10C discharge condition, when the model parameters identified by FFRLS are substituted into the simulation model in Simulink and given the same current excitation as the sampling current, the first-order RC model deviation finally converges to 0.005 V, and the second-order RC model deviation is also 0.005 V. Under 2 and 30 C conditions, using 10 C identification parameters, on the first-order RC model, the deviations are 0.016 and 0.01 V, but on the second-order RC model, the deviations are 0.016 and 0.005 V. Under the condition of 30 C, the estimation deviation of the first-order RC model is 0.50%, the estimation deviation of the second-order RC model is 0.16%, and the deviation of the two models under the condition of 2 C is the same, both of them are 0.50%. The reason is that the second-order RC model takes into account the effect of the concentration difference polarization of the battery and uses an RC parallel link for simulation, giving it a higher fitting accuracy.

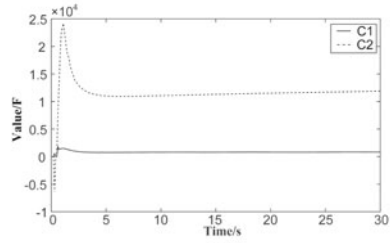
5 Conclusion

Through simulation analysis, it is verified that the parameter identification results of the FFRLS algorithm under high rate conditions have no physical meaning and cannot be used in subsequent work.

A parameter identification method is proposed, which solves the problem of model parameter identification at a high discharge rate by using the identification results under 10 C as the model parameters under 30 C. This method has the advantages of a

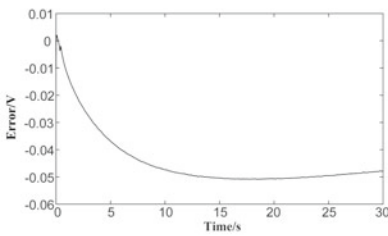


(a) Second-order RC model identification resistance.

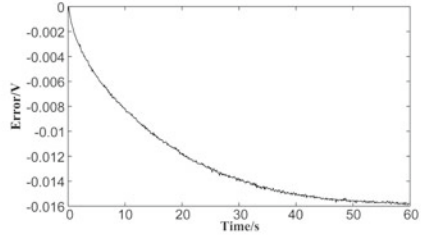


(b) Second-order RC model identification capacitance.

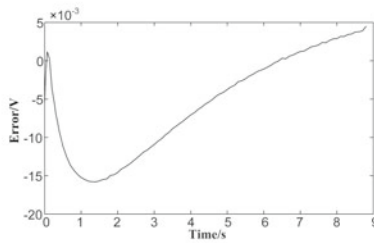
Fig. 9 Second-order RC model identification results



(a) Condition of 10C.



(b) Condition of 2C.



(c) Condition of 30C.

Fig. 10 Terminal voltage deviation

simple process and the parameters under 10 C can also be used under 2 C conditions. Comparing the first-order RC model with the second-order RC model, a second-order RC model with higher accuracy is obtained. Experimental and simulation results prove the effectiveness of the proposed method.

Acknowledgements This work is supported by the National Natural Science Foundation of China under Grant 51777177.

References

1. Doyle, M.: Modeling of galvanostatic charge and discharge of the lithium/polymer/insertion cell. *J. Electrochem. Soc.* **6**, 13–21 (2019)
2. Hu, X.: Review of modeling techniques for lithium-ion traction batteries in electric vehicles. *J. Mech. Eng.* **53**(16), 20 (2017). <https://doi.org/10.3901/JME.2017.16.020>
3. Tseng, S.: Hybrid converter with multiple sources for lithium battery charger applications. *Electronics* **11**(4), 616 (2022). <https://doi.org/10.3390/electronics11040616>
4. Yan, K.: Simplified mechanism modeling and discharge characteristics analysis of high rate lithium iron phosphate battery. *Trans. China Electrotechn. Soc.* **37**(3), 599–609 (2022). (in Chinese)
5. Li, C.: An approach to lithium-ion battery simulation modeling under pulsed high rate condition based on LSTM-RNN. *Proc. CSEE* **40**(9), 3031–3042 (2020). (in Chinese)
6. Zhang, Z.: State of charge estimation of LiFePO₄ battery under the condition of high rate pulsed discharge. *Trans. China Electrotechn. Soc.* **34**(8), 1769–1780 (2019). (in Chinese)
7. Long, X.: Application on lithium batteries for electromagnetic launch. *J. Natl. Univ. Defense Technol.* **41**(4), 66–72. (2019). (in Chinese)
8. Li, C.: Charging strategy amelioration of multilevel hybrid energy storage for electromagnetic launch. *Trans. China Electrotechn. Soc.* **32**(13), 118–124 (2017). (in Chinese)
9. Zhang, Y.: Research of internal and external temperature field of lithium power battery discharged at high rate. *Chin. J. Power Sources* **41**(5), 699–701 (2017). (in Chinese)
10. Luo, H.: The relationship between internal resistance and discharge rate of LiFePO₄ batteries. *Energy Storage Sci. Technol.* **6**(4), 799–805 (2017). (in Chinese)
11. Wang, H.: Electrochemical modeling of lithium ion battery based on double layer structure. *Battery Bimonth.* **48**(04), 244–248 (2018). (in Chinese)
12. Chen, L.: State estimation of lithium ion battery in energy storage system based on real time circuit model. *J. Central South Univ. (Sci. Technol.)* **52**(02), 458–464 (2021). (in Chinese)
13. Wang, S.: Online dynamic equalization adjustment of high-power lithium-ion battery packs based on the state of balance estimation. *Appl. Energy* **166**, 44–58 (2016)
14. Xin, Z.: Modeling of battery dynamics and hysteresis for power delivery prediction and SOC estimation. *Appl. Energy* **180**, 823–833 (2016)
15. Liu, L.: Modeling of lithium battery pack for energy storage system considering internal parameter inconsistency. *Autom. Electric Power Syst.* **45**(19), 15–23 (2021). (in Chinese)
16. Liu, W.: Modeling method of lithium-ion battery considering commonly used constant current conditions. *Trans. China Electrotechn. Soc.* **36**(24), 5186–5200 (2021). (in Chinese)
17. Zhu, R.: Lithiumion battery modeling and parameter identification based on decentralized least squares method. *J. Mech. Eng.* **55**(20), 85–93 (2019). (in Chinese)
18. Wang, G.: Improvement of battery equivalent circuit modeling combined with thevenin and PNGV models. *Process Autom. Instrument.* **42**(2), 45–49+55 (2021). (in Chinese)
19. Gao, Y.: Modeling of Liion battery at high rate condition. *Battery Bimonth.* **51**(6), 563–567 (2021). (in Chinese)
20. Nejad, S.: A systematic review of lumped-parameter equivalent circuit models for real-time estimation of lithiumion battery states. *J. Power Sources* **316**, 183–196 (2016).
21. Liu, C.: A new method of modeling and state of charge estimation of the battery. *J. Power Sources* **320**, 1–12 (2016)
22. Li, Z.: On state-of-charge determination for lithiumion batteries. *J. Power Sources* **348**, 281–301 (2017)

Research on Orderly Charging Scheduling Strategies for Interactive Power Networks Through Cloud-Side-End Collaboration



Bin Zhu, Min He, Yi Long, Xiujuan Yuan, Dong Yan , and Desheng Qian

Abstract Aiming at the poor real-time performance of the current orderly charging scheduling strategy for EV, and the difficulty in balancing user experience and balance of grid power, an orderly charging scheduling strategy based on three element hierarchical progressive optimization through cloud-side-end collaboration is proposed. First of all, a three-layer coordinated orderly charging scheduling system is built, including ECS, orderly charging coordinator and power controller. Secondly, the real-time load in the substation area is taken as the first element, the short-term load forecasting in the future is taken as the second element, and the user experience is taken as the third element to formulate the scheduling strategy step by step, and is deployed in the side orderly charging coordinator. Finally, an orderly charging scheduling test platform was built for testing. The results show that the system can achieve real-time adjustment of charging power of charging piles under the station area by cloud-side-end collaboration and reduce the peak valley difference of load in the station area and improve the user experience on the basis of stable power grid.

B. Zhu · M. He · Y. Long · X. Yuan

State Grid Chongqing Electric Power Company Marketing Service Center (Metering Center),
Chongqing 400023, China
e-mail: 13098681679@163.com

M. He

e-mail: hemin_1991@163.com

Y. Long

e-mail: 156376604@qq.com

X. Yuan

e-mail: 717035520@qq.com

D. Yan (✉) · D. Qian

Chongqing University of Posts and Telecommunications School of Automation/Industrial Internet
School, Chongqing 400065, China
e-mail: yandong@cqupt.edu.cn

D. Qian

e-mail: qds_gongyong@163.com

© Beijing Paiké Culture Commu. Co., Ltd. 2023

X. Dong et al. (eds.), *The proceedings of the 10th Frontier Academic Forum of Electrical Engineering (FAFEE2022)*, Lecture Notes in Electrical Engineering 1054, https://doi.org/10.1007/978-981-99-3408-9_25

Keywords EV · Orderly charging · Cloud-side-end collaboration · Three element hierarchical progressive optimization · Balance of grid power

1 Introduction

With the world's attention to environmental and energy issues, EV has ushered in popularization [1]. With the rapid development of new EV, the balance between the increasing demand for charging and the grid load has become a key problem to be solved.

At present, many scholars at home and abroad have carried out relevant research on EV orderly charging. Haoming, R, Wu Fangzhu and others proposed an orderly charging guidance scheme based on time-sharing price [2, 3], and this kind of scheme only considers the consumer experience, and does not consider the grid side load. X. Yuan, X. Peng et al. proposed a scheduling strategy based on grid side load and user demand [4, 5], and this strategy is based on the intelligent algorithm itself and has no practical engineering application. Dou Yali and others put forward a scheme that charging piles directly receive cloud power regulation instructions to complete power regulation [6], and this method relies too much on the cloud, which is greatly restricted by public network communication. Meng Huanping, W Liu et al. proposed a dispatching system based on energy router and energy controller [7–11], which comprehensively considered the load on the grid side and the needs of users, but such systems have long data flow paths and poor real-time control. The above orderly charging scheduling strategies all have certain limitations.

In today's Internet of Things, an orderly charging scheduling strategy for multi-indicator optimization through cloud-side-end collaboration emerge.

As shown in Fig. 1, this paper designs an orderly charging system with a three-layer communication architecture of "cloud", "edge" and "end". Among them, the power controller is connected in series between the AC charging pile and EV as an intermediate device, which can complete the orderly charging function upgrade without changing the original charging pile structure. The orderly charging coordinator takes the real-time station load as the first consideration to formulate the initial power regulation plan, and fine-tunes the power regulation plan with the station load forecast in the next 10 min as the second consideration, and on the basis that the first two factors meet the conditions, the charging power of the charging pile is not reduced as much as possible to ensure the user experience.

2 System Scheduling Strategy

2.1 Orderly Charging Scheduling Strategy Based on Three Elements

The structure diagram of the orderly charging dispatching system under a single station area is shown in Fig. 2. First, the orderly charging coordinator collects the real-time load data of the substation area from the measuring elements in real time.

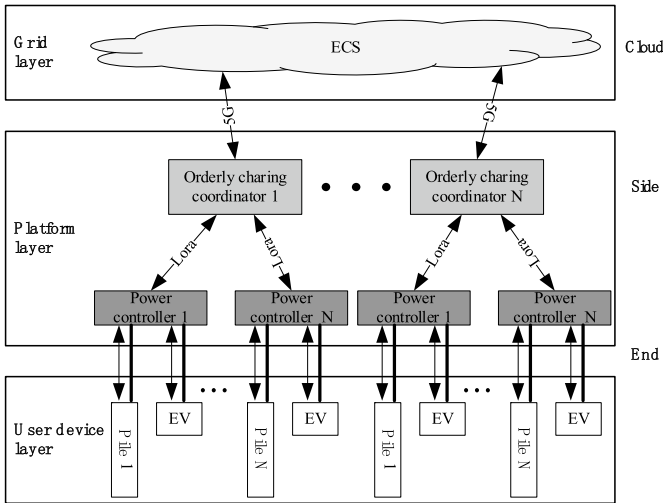


Fig. 1 Structure diagram of orderly charging scheduling system of “cloud”, “side” and “terminal”

According to the preset upper and lower limits of the substation area load, the substation area load state is divided into three states: high load state (higher than the upper limit of the load rate), alert state (lower than the upper limit of the load rate, higher than the lower limit of the load rate), and normal state (lower than the lower limit of the load rate). The three states correspond to the initial strategies for power regulation of the charging piles under the three stations: CP duty cycle is reduced to 10%, CP duty cycle is reduced to 30%, and CP duty cycle remains unchanged (Table 1).

Then, the orderly charging coordinator receives the average load forecast for the next hour issued by the cloud in 10 min. $T_{i,j}$ represents the i th hour and the j th ten minute period of a day. The calculation formula of ECS load forecast for each time period is shown in Formula (1).

$$P_{i,j} = \frac{\sum_{k=1}^7 P_{i,j,k}}{7} \tag{1}$$

Fig. 2 Structure diagram of orderly charging scheduling system in a single area

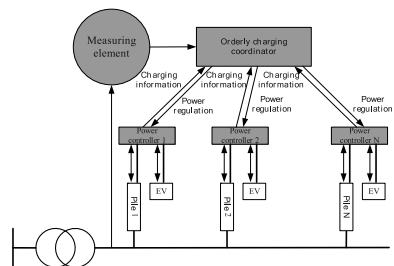


Fig. 3 Comparison of the detection flow and control flow path of the mainstream scheme (left) and the scheme proposed in this paper (right)

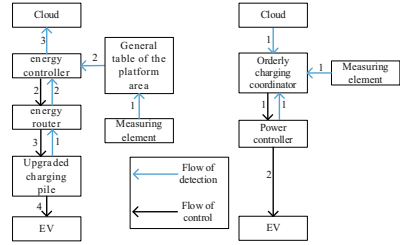
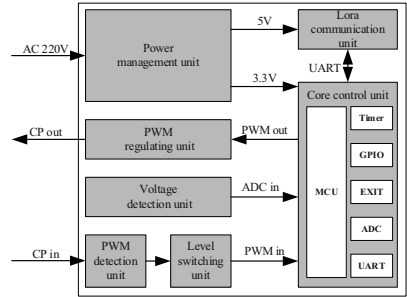


Fig. 4 Hardware system structure diagram of power controller



where $P_{i,j}$ represents the load forecast in $T_{i,j}$ time period, represents the actual load of the platform area at time k days before the current day. The cloud calculates the average value of the station area load in the first 7 days of each period, and sends it to the orderly charging coordinator in 10 min. The preliminary scheduling strategy is adjusted based on the load forecast value according to the corresponding relationship in Table 2.

Finally, the adjusted final power regulation strategy is based on three principles: first, if the load forecast in the next period is the same as the current substation load, the original scheme will be maintained; Second, when the current station load is normal, no matter what the load forecast in the next period is, the charging power of the charging piles under the station area will not be changed to ensure the user’s experience; Third, when the above two points are not met, fine tune the original charging strategy.

Table 1 The relationship between the load state of the station area and the initial power adjustment strategy of the coordinator to adjust the CP duty cycle

State of load	CP duty cycle
High load state	10%
Alert state	30%
Normal state	No change

Table 2 Adjustment and comparison of power regulation strategy based on load forecasting in station area

State of load	Forecast of load state in the next period	Font size and style
High load state	High load state	10%
Alert state	High load state	20%
Normal state	High load state	No change
High load state	Alert state	20%
Alert state	Alert state	30%
Normal state	Alert state	No change
High load state	Normal state	20%
Alert state	Normal state	No change
Normal state	Normal state	No change

2.2 The Characteristics of Detection Flow Data and Control Flow Data

At present, the mainstream design idea of orderly charging scheduling system is to upgrade charging piles, introduce energy routers, and introduce energy controllers [10, 11]. The orderly charging scheduling system built in this way has the characteristics of too long path of data detection flow and control flow.

Compared with the current mainstream “energy router + energy controller” scheme, the system designed in this paper has shorter data detection flow and control flow paths (Fig. 3).

Obviously, the detection stream data in the system does not need to be forwarded, which ensures the reliability of the detection stream and shorter data transmission delay.

In terms of control flow data, in the system designed in this paper, the generation of control strategy is migrated from the “cloud” to the “edge”, giving full play to the edge device’s advantage of being close to the terminal, and using the edge computing capability of the edge device to reduce the burden of cloud computing. After the side equipment has formulated the scheduling strategy, it will directly send it to the power controller to complete the real-time regulation of charging power. Shorter detection and control flow paths for more timely charging power regulation of the system.

3 System Hardware

3.1 Power Controller Hardware

The power controller, as the actuating terminal in the system, plays an important role in the final control of the charging power in the system. This requires that it must have fast execution capability, stable operating characteristics and timely data processing capability (Fig. 4).

The PWM detection unit for the analogue vehicle end interface (BMS unit) is designed using signal relays, precision sampling resistors and diodes. The MCU transmits the vehicle end status to the pile by means of the on–off signal relays that determine the access to the resistors and diodes, and detects the control information sent from the pile by means of the PWM duty cycle.

The 12 V voltage level PWM regulating unit is constructed by using analog switch and post stage resistance capacitance filter circuit. After processing 3.3 V voltage level PWM wave output by MCU, 12 V voltage level CP signal is generated and connected to EV. In addition, because the information interaction between the charging pile and the electric vehicle is conducted through the CP single signal line, the charging pile needs the AD detection unit to receive the feedback information from the vehicle end. The power controller, as the intermediate of information transmission between vehicle end and pile end, also needs to add an AD detection unit at the signal output end to receive the vehicle end signal.

Lora communication is a long-range, highly reliable wireless communication. Therefore, the Lora module is used as the communication module for the power controller and is responsible for communicating with the orderly charging coordinator.

3.2 Orderly Charging Coordinator Hardware

The orderly charging coordinator, which is responsible for the development of the orderly charging scheduling strategy and the issuance of power regulation commands in the system, as well as the information interaction with the power controller and the cloud server, is the core of the whole system. Figure 5 gives a diagram of the hardware system structure of the orderly charging coordinator.

The Lora communication unit undertakes the important task of receiving charging information reported by the power controller and issuing power regulation commands to the power controller.

The orderly charging coordinator uses an industrial 5G module for 5G communication, which enables high-speed data transmission without connecting to a network cable. The orderly charging coordinator uses Gigabit Ethernet as a backup NIC.

Fig. 5 Hardware system structure diagram of orderly charging coordinator

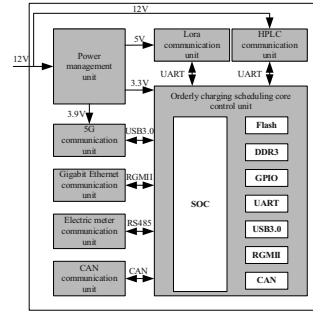
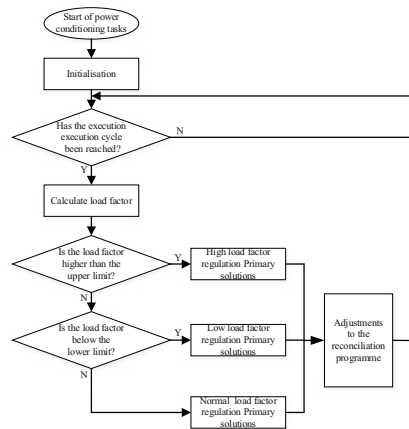


Fig. 6 Orderly charging coordinator power regulation software flow chart

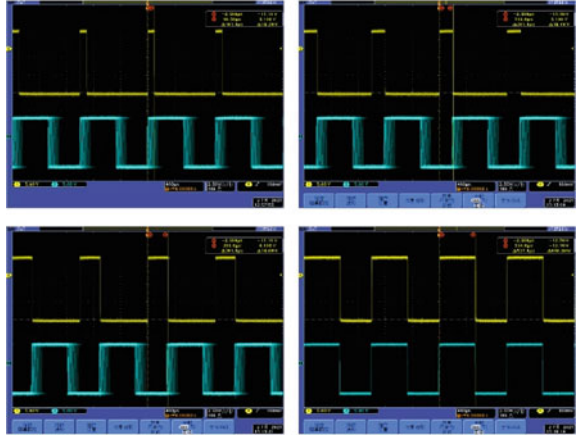


4 System Software

In the orderly charging scheduling system designed in this paper, the core task of orderly charging coordinator is the power regulation task (Fig. 6).

The power regulation task is the process of periodically regulating the charging power of the station charging piles by formulating a scheduling strategy based on the three elements of real-time station load, forecast station load and user demand. The execution process is as follows: firstly, if the execution cycle has arrived, the real-time load of the station area is first calculated based on the data transmitted by the measurement elements, the state of the station area load at this time is analyzed and the corresponding primary solution for power regulation is generated. Then, the power regulation scheme is adjusted according to the load forecast data from the cloud. Finally, power regulation is carried out. This is done by regulating the charging power of the charging posts in the station area in a polling manner based on the scheduling scheme.

Fig. 7 The results of power regulation



5 System Test

From the above introduction, it can be seen that the final execution effect of the power regulation of the AC charging pile in the station area is in four states: CP duty cycle to 10%, CP duty cycle to 20%, CP duty cycle to 30%, and no change in CP duty cycle. The ordered charging power regulation test platform was built using a BMS simulator, an AC charging pile, a power controller, an orderly charging coordinator and an oscilloscope.

We can leave the coordinator in various power regulation states and use an oscilloscope at the input and output of the power controller CP signal for waveform detection, which can directly reflect the power regulation effect by the duty cycle of the oscilloscope PWM wave. In Fig. 7, from top to bottom are the four cases where the duty cycle of the CP signal is adjusted to 10%, 20%, 30% and no change in CP duty cycle, respectively. The results show that the system is able to accomplish specific power regulation and complete orderly charging scheduling.

6 Conclusion

The strategy takes into account the real-time load of the station area, the load forecast of the station area in future periods, and the user experience. On this basis, the specific implementation of the scheduling is deployed to the edge-side and end-side devices. The system offers significant advantages in terms of real-time, meeting multi-factor metrics, and ease of implementation.

Acknowledgements This research work is supported by State Grid Chongqing Electric Power Company Science and Technology Project (522000220004) and Research on Key Technologies and Device Development of Orderly Charging of Electric Vehicle Charging Pile based on Multidimensional Data Perception.

References

1. Li, C., et al.: A review of the progress of research on load forecasting of electric vehicles into the grid and their interaction with the grid. *Smart Power* **50**(07), 96–103(2022). (in Chinese)
2. Haoming, Wei, R., Jie, L., Xinwei, M.: Orderly charging strategy of charging stations based on dynamic time-sharing charging price response. In: 18th International Conference on AC and DC Power Transmission, pp. 1181–1187 (2022)
3. Wu, F., Tian, Y.: Research on the orderly charging and discharging strategy of electric vehicles based on time-sharing tariff. *Electric. Eng. Electric.* (04), 21–25(2022). (in Chinese)
4. Yuan, X., Li, J., Wang, Y., Cai, H., Liu, Y., Ren, H.: Optimization strategy design of distribution network based on orderly charging control of electric vehicles. In: 2021 International Conference on Power System Technology (POWERCON), pp. 771–777 (2021)
5. Peng, X., Chen, C., Zheng, T., Tang, W., Xiong, Z., Ouyang, G.: Improved Ant Lion Algorithm for orderly charging of electric vehicles. In: 2021 IEEE 12th International Symposium on Power Electronics for Distributed Generation Systems (PEDG), pp. 1–7 (2021)
6. Yali, D., Xiuyun, N., Wang, L., Li, Z.: STM32F407-based orderly AC charging pile control system design. *Electric. Appl.* **41**(06), 81–89 (2022). (in Chinese)
7. Liu, W., Liu, Y., Chen, L.: Design of controller and router for orderly charging system of electric vehicle. In: 2021 China International Conference on Electricity Distribution (CICED), pp. 915–918 (2021)
8. Li, M., Liu, G., Chen, H., Huang, B.: An orderly charging module design for the Internet of Things. In: 2022 IEEE 6th Information Technology and Mechatronics Engineering Conference (ITOEC), pp. 135–138 (2022)
9. Meng, H., Long, H., Xiao, J., Hao, Q.: Research and application of orderly charging system for electric vehicles. *Build. Electric.* **40**(06), 22–26 (2021). (in Chinese)
10. Gao, H., Liu, Y.: Applied research on the orderly charging of large-scale electric vehicles in residential areas. In: 2021 China International Conference on Electricity Distribution (CICED), pp. 1091–1098 (2021)
11. Guang, C., Shen, G., Zhao, Y., et al.: Electric vehicle orderly charging control strategy comprehensively considering charging cost and load fluctuation. In: 2019 IEEE Sustainable Power and Energy Conference (iSPEC), 900–905 (2019)

Multi-objective Optimization of Motor Rotor Notches Based on Multi-Objective Particle Swarm Optimization



Qiao Yan, Liu Jinglin, Qiao Yongming, and Wang Danqing

Abstract In response to the national carbon neutral strategy, the electric vehicle industry has developed rapidly in recent years, and users are increasingly concerned about the NVH performance of electric vehicles. In this paper, to reduce the electromagnetic vibration noise of the motor, an improvement measure of adding notches on the rotor surface is proposed, and the rotor notches are modelled parametrically and sensitivity analysis is carried out. The effectiveness of the optimisation solution is verified by comparing the results of the electromagnetic performance, mechanical performance, electromagnetic force and noise before and after optimisation.

Keywords Multi-objective optimisation · Particle swarm optimization · NVH

1 Introduction

At present, carbon-neutralization has become the consensus and mission of the world. For China, the goal of carbon-neutralization 30/60 will be one of the most deterministic trends in the next 40 years [1]. Therefore, the electric vehicle industry has received strong support from the country. The built-in permanent magnet synchronous motor (IPMSM) with good speed regulation performance, high power density and high efficiency has also been used extensively in the electric drive system of electric vehicles and has become the heart of electric vehicles. To meet the user's needs for comfort when driving and riding, it is a requirement to keep motor cogging

Q. Yan (✉) · L. Jinglin · W. Danqing
School of Automation, Northwestern Polytechnical University, Xi'an 710000, China
e-mail: 467347932@qq.com

L. Jinglin
e-mail: JinglinL@nwpu.edu.com

Q. Yongming
AVIC Xingxiang Aviation Industry (Group) Co., Ltd., Xin Xiang 410700, China

torque, torque pulsation, air gap counter-electromotive force harmonic content, electromagnetic vibration and noise as low as possible while ensuring high motor power density and high torque density.

In the past, the motor optimization method was to optimize a single parameter until all the parameters needed to be optimized were traversed. However, the optimization of the motor was a problem of designing multiple physical fields, multiple objectives and multiple parameters [2]. This optimization method did not take into account the mutual influence of different parameters. The optimal solution for the current target may not be suitable for another target, So at present, many scholars have introduced artificial intelligence algorithm into the motor optimization problem, and have achieved good success.

In the literature [3], a new DTFM applied to industrial robots is proposed, and an optimisation strategy incorporating neural networks and multi-objective particle swarm algorithms is used to study the optimal design of this type of motor and to verify the superiority of the motor performance. In the literature [4], for asymmetric V-shaped IPMSM, a multi-objective optimisation method based on a mixture of parametric hierarchical design and response surface methods is proposed, with the optimisation objectives of reducing torque pulsation and increasing output torque, and it is verified that the improved scheme can increase torque density while reducing torque pulsation.

In this paper, a rotor optimisation structure with notches on the motor rotor is proposed for a built-in 8-pole 48-slot PMSM for an electric vehicle. The average torque, torque pulsation and electromagnetic vibration noise of the motor are used as optimisation targets, sensitivity analysis is carried out on different structural parameters of the notches to study the influence of different structural parameters on different optimisation targets, and the multi-objective optimisation of the motor is carried out using Particle Swarm Optimization (PSO) with the aid of simulation platforms such as Ansys Maxwell and Optislang.

2 Analytical Calculation of Electromagnetic Force

Electromagnetic vibration noise is known to be the most significant origin of motor vibration noise [5]. Electromagnetic vibration is generated by the electromagnetic force acting on the surface of the motor stator teeth. For the study of electromagnetic vibrations in electric motors, we should first use the analytical method to derive the analytical formula of the electromagnetic force of the motor. Since the permeability of ferromagnetic materials used in the stator core is about 2000–6000 times of the air permeability, the magnetic density of the tangential air gap is negligible compared to the magnetic density of the radial air gap. Therefore, Based on Maxwell's tensor method, the radial electromagnetic force can be given by the expression [6]:

$$f_r = \frac{B_r^2 - B_t^2}{2\mu_0} \approx \frac{B_r^2}{2\mu_0} \quad (1)$$

Among them, f_r denotes the density of radial electromagnetic force; B_r and B_t are the radial and tangential portions of the air gap flux density of the motor; μ_0 represents the vacuum permeability.

The air-gap magnetic density is denoted as the product of the magnetomotive force F and the equivalent air-gap magnetic conductivity λ_δ , where the magnetomotive force F is generated by the superposition of the air-gap magnetomotive force of the permanent magnetic field F_R and the armature reaction magnetomotive force F_S .

$$B_r = F\lambda_\delta = F_R\lambda_\delta + F_S\lambda_\delta \tag{2}$$

For integer slot PMSM, the number of harmonics in the permanent magnet field of the rotor is $v_R = (2k + 1)p, k = 0, 1, 2, \dots$, where p is the number of motor poles. After the three-phase sine current is supplied to the stator winding of the motor, the harmonic number of the armature reaction magnetic field is $v_s = (6k_s + 1)p, k_s = 0, \pm 1, \pm 2, \dots$, and the spatial order of the EMF wave is $n = v_R \pm v_s$. It is a common knowledge that the main source of electromagnetic vibration noise in motors is caused by the interaction of the v_R harmonic of the permanent magnet field of the rotor with the first order permeability harmonics. According to $V_i = p \pm iZ (i = 1, 2, \dots)$, the number of pole pairs of the first harmonic of the stator teeth of the 8 pole 48 slot motor is 52 and -44 . Therefore, for the 8 pole 48 slot permanent magnet synchronous motor, the 0 order $12f$, -8 order $10f$, 8 order $14f$ and 0 order $12f$ electromagnetic force waves generated by the interaction of the first-order tooth harmonic $V_1 = 52$ or $V_1 = -44$ and the rotor permanent magnet magnetic field $v_R = 44$ or $v_R = 52$ harmonics are the main reasons for the electromagnetic vibration noise of the motor under no-load and load conditions. As shown in Table 1, it is the spatial order of radial electromagnetic force versus frequency for this motor with spatial order no greater than eight.

The minimum non-zero order of the electromagnetic force wave from for a PMSM with an integer number of slots can be expressed as:

$$r_{\min} = GCD(Z/m, 2p) \tag{3}$$

Table 1 Spatial order and frequency of radial electromagnetic force

v_R	v_s				
	4	-20	28	-44	52
4	0/0				
12	8/2f	-8/4f			
20		0/6f	-8/4f		
28		8/8f	0/6f		
36			8/8f	-8/10f	
44				0/12f	-8/10f
52				8/14f	0/12f

where GCD represents the largest common divisor; Z represents the number of stator slots; m is the number of phases. Therefore, the minimum non-zero order of 8 pole 48 slot motor is 8. Also, Since the stator deformation is in inverse proportion to the fourth power of the spatial order of the electromagnetic force, the smaller the order of the electromagnetic force, the greater the deformation caused and the greater the noise generated. Therefore, it is only necessary to consider the $r_{\min} = 0$ order electromagnetic force corresponding to the breathing mode [7]. From Table 1, we can see that the primary frequencies of the 0-order electromagnetic force are $12f$ and $6f$, which correspond to the 48 order and 24 order noise respectively. It can be seen from literature [8] that torque ripple and zero-order radial force wave both originate from the same order air-gap magnetic density and have the same frequency characteristics. For the built-in integral slot motor, the torque ripple is related to the important harmonic component in the zero-order radial force wave and the tooth harmonic component in the airgap magnetic density. Therefore, the radial and tangential force wave components can be suppressed simultaneously by weakening the tooth harmonic of the rotor magnetic potential to decrease the electromagnetic vibration noise.

3 Optimum Design of Motor Rotor Structure

This paper is about a double U-rotor IPMSM, and a notch is added between the two adjacent poles on the rotor surface as the optimization design. The radial schematic illustration of the motor is shown in Fig. 1, and the main parameters of the motor are shown in Table 2. Where l_1 is the radial depth of the notch, l_2 is the external arc length width of the notch expressed by the electrical angle, and l_3 is the internal arc length width of the notch expressed by the electrical angle.

Fig. 1 Schematic diagram of motor radial direction

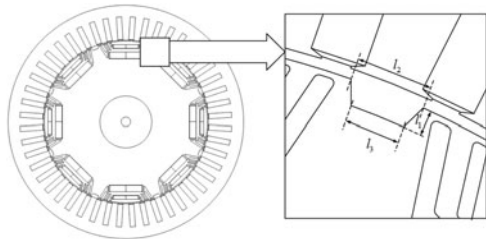


Table 2 Basic motor design parameters

Parameter	Value	Parameter	Value
Number of slots/poles slots/poles	48/8	Stator core length, mm	100
Stator outer diameter, mm	250	Stator inner diameter, mm	175
Rotor outer diameter, mm	174	Voltage rating, VDC	400
Power rating, kW	150	Continuous torque, Nm	240
Rated speed, rpm	6000	Phase number	3

4 Multi-objective Optimization Algorithm Based on Particle Swarm Optimization

4.1 Multi-objective Optimization and Particle Swarm Optimization Theory

Multi-objective optimization (MOP) was first proposed by economist V. Pareto [9]. The core idea is that multiple optimization objectives can be optimized within a given range. The solution for multi-objective optimization is usually an optimal collection of many Pareto optimal solutions. Each element of the collection is described as either a Pareto optimal solution or a non-inferior optimal solution [10]. PSO was first developed by Eberhart and Kennedy in 1995 [11]. It was designed by simulating the predation of birds. Assuming that there is only one piece of food in a certain area (that is, the optimal solution), the task of birds is to search for this food.

4.2 Multi-objective Optimization Process

Theoretically, all parameters of the motor can be used as optimization variables, but doing so will increase the workload of calculation. From the above, it is observed that the zero-order radial force wave is the main cause of the electromagnetic vibration of the motor. Torque ripple and zero-order radial force wave are derived from the same order airgap magnetic density and have the same frequency characteristics. Therefore, the torque ripple can be directly optimized to reduce the electromagnetic vibration noise. Throughout this paper, to explore the effect of adding notches on electromagnetic performance, electromagnetic vibration noise and other performances of the motor rotor surface, the efficiency and torque ripple are set as the optimization objectives, and the constraint conditions of the optimization objectives are defined as the maximum torque at the rated speed. With the help of Ansys Optislang multi-objective optimization software, the three parameters of the motor rotor surface notch shown in Fig. 1 are selected as the optimization variables for parametric modeling. Following the principle that the size of the rotor notch does not affect the size of the

magnetic isolation bridge, the values of the optimization variables are determined as illustrated in Table 3.

As shown in (a), (b) and (c) of Fig. 2, the response surfaces of l_1 , l_2 , l_3 and torque ripple T_{Ripple} are obtained. Under the premise of ensuring the average torque at rated speed, the purpose of optimizing torque ripple T_{Ripple} can be achieved by selecting the optimal structural parameters of l_1 , l_2 and l_3 . As shown in (d) of Fig. 2, through the multi-objective optimization based on PSO, it is evident that the results of rotor notch optimization and Pareto front (shown in the red line), it can be seen that the efficiency of the motor basically shows a downward trend with the increase of torque ripple. After considering various factors, the corresponding point at the five-pointed star in the figure is taken as the best solution. At this time, the corresponding values of rotor notch optimization parameters l_1 , l_2 and l_3 are 1.51, 24.27 and 17.36 respectively.

Table 3 Optimize parameters

Optimize variables	Initial value	Value range
Depth of concave diameter l_1 /mm	0	0–3
Outer arc length width of notch l_2 (ED)/(°)	0	0–30
Internal arc length width of notch l_3 (ED)/(°)	0	0–30

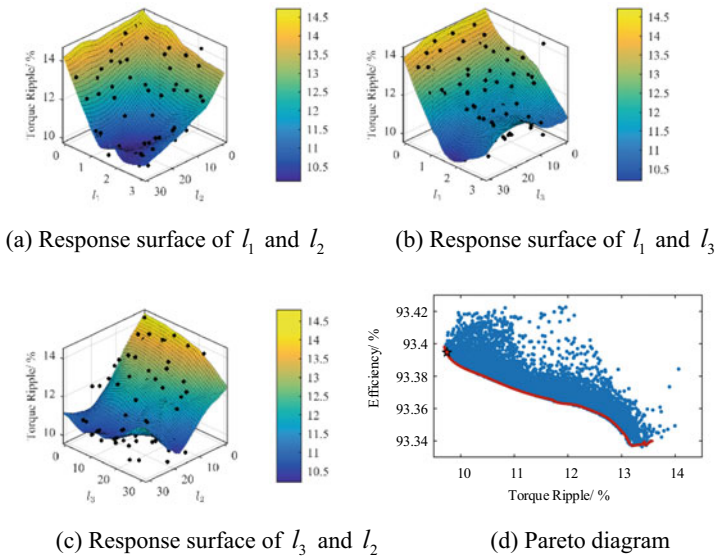


Fig. 2 Optimized parameter response surface and Pareto Diagram

4.3 Comparison of Optimization Effects

According to the above, the design without notch on the rotor surface of the motor is selected as the pre-optimization scheme, and the corresponding point of the five-pointed star in Fig. 2(d) is selected as the post-optimization scheme. The two solutions were compared with the assistance of the FEM simulation software. The main electromagnetic performance comparison diagram is shown in Fig. 3.

From Fig. 3(a) it can be seen that the radial magnetic density of the motor changes as the rotor structure changes. Simultaneously, the radial air gap magnetic density of the load decreases in amplitude from 1.50 to 1.11 T, the amplitude of the radial airgap magnetic density of the load decreases from 1.50 to 1.11 T, and the average

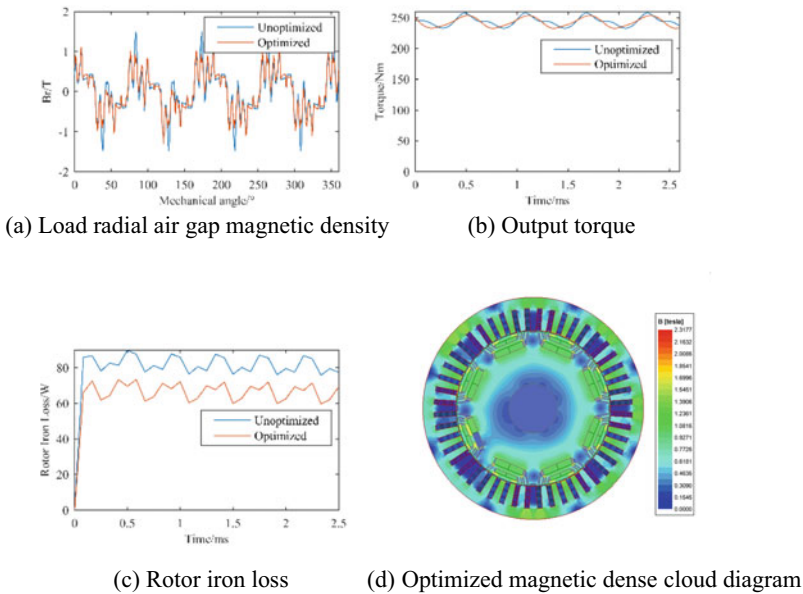


Fig. 3 Comparison of main electromagnetic properties before and after optimization

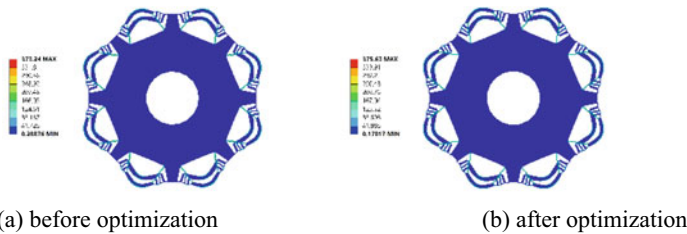


Fig. 4 Cloud diagram of rotor stress distribution

value of the air gap magnetic density greater than 0 is 0.448 and 0.443 T, respectively. The electromagnetic force will also decrease according to Maxwell tensor method. In Fig. 3(b), the average torque after optimization is 242.70 Nm, which is almost the same as the average torque before optimization 243.97 Nm, but the torque ripple decreases from 9.71 to 7.61%, which proves that the optimized structure has a minor effect on output torque of the motor and has a noticeable improvement effect on the torque ripple of the motor. Because the structural optimization involved in this paper is mainly for the rotor, it has the greatest impact on the rotor iron loss. From Fig. 3(c), It is evident that the optimized motor rotor iron loss amplitude has decreased from 86.69 to 73.29 W, which has played a positive role in improving the motor efficiency and reducing the motor temperature rise. It is evident from Fig. 3(d) that the magnetic density of the stator and rotor yoke of the motor is less than the material saturation point, and there are few saturation areas at the stator teeth, but they are within the acceptable range (Fig. 4).

Because the notch of the motor rotor is located between the two adjacent poles and is relatively close to its magnetic isolation bridge, it will make its stress more concentrated to a certain extent. As shown in Fig. 5, the stress nephogram distribution of the motor rotor structure before and after optimization is shown. At the maximum speed of 10,000 rpm, the maximum stress of the motor rotor structure before and after optimization is 373.24 and 375.63 MPa, respectively, which are smaller than the yield strength of the material 455 MPa, Therefore, the rotor structure before and after optimization meets the mechanical requirements.

Through the FEM element simulation software, Images of the density of radial electromagnetic forces on the stator teeth before and after optimisation of the motor under rated working conditions are obtained as illustrated in Fig. 5(a) and (b), and vary with time and space, and perform an FFT decomposition to obtain a time-harmonic Fourier specification of the radial electromagnetic force density, as shown in Fig. 5(c). The amplitude of radial electromagnetic force density decreased from 9.79×10^5 N/m² to 7.16×10^5 N/m² before and after motor optimization. The second harmonic component after optimization is slightly larger than that before optimization, but the sixth harmonic component that plays a major role is significantly decreased, and the 12th harmonic component is also slightly decreased. The optimised structure has been proven to weaken the electromagnetic radial forces on the stator tooth surfaces.

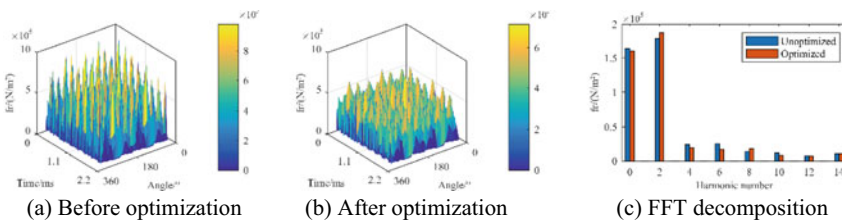
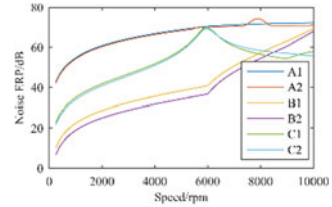


Fig. 5 Comparison of radial electromagnetic force before and after optimization

Fig. 6 Order analysis of noise at full speed



Through the coupling calculation of the structural field and the sound field, the order analysis diagram of the noise at the full speed of the motor before and after optimization is obtained. As shown in Fig. 6, A1–C2 represent the noise curve of the whole after optimization, the whole before optimization, the 0 order $6f$ before optimization, the 0 order $6f$ after optimization, the 0 order $12f$ before optimization, and the 0 order $12f$ after optimization as the speed changes. As can be seen from the graph, the noise profile relative to the optimised 0th order $6f$ has dropped significantly, and the optimized 0-order $12f$ has a downward trend before 6000 rpm, and then slightly increased, but the impact is very small, which is completely consistent with the conclusion analyzed in Fig. 5. As for the motor as a whole, the optimized noise curve significantly decreased, and the amplitude decreased from 74.40 to 72.29 dB. Because every 10 dB increase in the decibel value means that the volume increases by 10 times [12], so the effect of this optimization scheme is obvious.

5 Conclusion

This paper is based on an 8-pole 48-slot IPMSM for electric vehicles, and the electromagnetic force on the surface of the stator teeth is calculated and analyzed analytically. The improvement measure of adding slots to the rotor surface is proposed in order to reduce electromagnetic vibration and noise, and a multi-objective optimisation design method based on PSO is used to optimise the motor with torque ripple and efficiency as the optimisation objectives and the maximum value of the average torque at rated operating conditions as the constraint. Finally, an optimal scheme is obtained. Through simulation analysis, the optimisation can be seen to reduce torque ripple, radial air gap magnetic density and rotor iron loss, weaken the stator tooth surface radial electromagnetic force and also decrease the vibration noise, while satisfying the condition of basically constant average torque, proving that the optimisation is effective and feasible.

References

1. Chai, Q.: On global carbon neutrality and new energy revolution under complex new situation. *Yuejiang Acad. J.* **14**(04), 89–93+173 (2022). (in Chinese)
2. Ullah, W., Khan, F., Umair, M.: Multi-objective optimization of high torque density segmented PM consequent pole flux switching machine with flux bridge. *China Electrotechn. Soc. Trans. Electric. Mach. Syst.* **5**(1), 30–40 (2021). (Author, F., Author, S., Author, T.: Book title. 2nd edn. Publisher, Location (1999))
3. Zhang, W., Xu, Y., Li, S.: The structural principle and design optimization of a new type of disk-type transverse flux permanent magnet brushless motor. *J. Electric. Technol.* **36**(14), 2979–2988. (in Chinese)
4. Liu, G., Wang, Y., Chen, Q.: Multi-objective optimization design of asymmetric V-type built-in permanent magnet synchronous motor. *J. Electric. Technol.* **33**(S2), 385–393. (in Chinese)
5. Zhu, S., Lu, J., Zeng, F.: Fast calculation of electromagnetic forces in IPMSMs under PWM VSI supply based on small-signal time-harmonic finite element method. *China Electrotechn. Soc. Trans. Electric. Mach. Syst.* **6**(1), 67–76 (2022)
6. Wang, X., He, X., Gao, P.: Research on electromagnetic vibration and noise reduction method of permanent magnet motor with V-shaped magnetic steel rotor for electric vehicle. *Chinese J. Electric. Eng.* **39**(16), 4919–4926+4994. (in Chinese)
7. Qian, Z., Tang, G., Wang, Q., Li, D., Cheng, Y.: Rotor structure optimization weakens vibration noise of permanent magnet synchronous motor for vehicle. *J. Motor Control* **25**(10), 122–129 (2021)
8. Lanhua Research on electromagnetic force wave and electromagnetic vibration of permanent magnet synchronous motor. Harbin Institute of Technology, Harbin (2019). (in Chinese)
9. Premkumar, M., Pradeep Jangir, R., Sowmya, H.H., Alhelou, S.M., Santhosh Kumar, B.: Multi-objective equilibrium optimizer: framework and development for solving multi-objective optimization problems. *J. Comput. Design Eng.* **9**(1), 24–50 (2021). <https://doi.org/10.1093/jcde/qwab065>
10. Li, M., Sun, H., Peng, L.: Fisher–Rao geometry and Jeffreys prior for Pareto distribution. *Commun. Statist. Theory Meth.* **51**(6), 1895–1910 (2022). <https://doi.org/10.1080/03610926.2020.1771593>
11. Khan, R.A., Yang, S., Fahad, S., Khan, S., Khan, J.A.: A modified particle swarm optimization for the applications of electromagnetic devices. In: *Proceedings of 2021 2nd International Conference on Electronics, Communications and Information Technology (CECIT 2021)*, pp. 127–132 (2021)
12. Li, W., Li, S.: Understanding digital sound – a review of computer hearing based on general audio/ambient sound. *J. Fudan Univ. (Natl. Sci. Edn.)* **58**(03), 269–313 (2019). (in Chinese)

Analysis and Simulation of Electromagnetic Vibration Under Fault-Tolerant Control of Marine Six-Phase Permanent Magnet Synchronous Motor



Lin Tan, Wei Xie, and Yunkai Guo

Abstract Six-phase permanent magnet synchronous motors are often used in marine electric propulsion systems because of their strong fault tolerance and other advantages. In order to ensure that the ship's electric propulsion system can still output torque smoothly in the case of open-phase, the six-phase permanent magnet synchronous motor often uses a fault-tolerant control algorithm. In this paper, by setting fault-tolerant control current with minimum copper loss as compensation target, establishing a two-dimensional electromagnetic field model, the Maxwell stress tensor method is used to calculate the electromagnetic force density of the motor with open-phase. Then, the electromagnetic force is imported into the three-dimensional model of the motor stator core to solve the vibration response spectrum of the motor. Comparing the vibration values under operational load, open-phase, and fault-tolerant control, it is found that the electromagnetic force density is the largest and the vibration velocity is the smallest, and the distribution of the maximum vibration velocity is relatively scattered under full load. The electromagnetic force density is reduced and the vibration speed increases, and the maximum vibration speed is distributed in one place under the open-circuit of phase and fault tolerance. The research results show that machine fault-tolerant control algorithm needs to consider the relevant performance index of vibration response.

Keywords Six-phase PMSM · electromagnetic vibration · open-phase · fault-tolerant control

L. Tan (✉)

Department of Mechanical Engineering, Shanghai Maritime University, Shanghai 201306, China
e-mail: tanlin219@sina.com

W. Xie · Y. Guo

Department of Electrical Automation, Shanghai Maritime University, Shanghai 201306, China
e-mail: weixie@shmtu.edu.cn

Y. Guo

e-mail: 18186470862@163.com

© Beijing Paiké Culture Commu. Co., Ltd. 2023

X. Dong et al. (eds.), *The proceedings of the 10th Frontier Academic Forum of Electrical Engineering (FAFEE2022)*, Lecture Notes in Electrical Engineering 1054, https://doi.org/10.1007/978-981-99-3408-9_27

1 Introduction

In recent years, multiphase motors are widely used in marine electric propulsion systems, of which multiphase PMSM are the most reliable. In the absence of phase, this motor can still have a smooth output torque driven by the fault-tolerant control algorithm [1, 2]. At present, the fault-tolerant current optimization constraint method of multiphase PMSM has been improved. Ref. [3] solves the fault-tolerant control current based on the principle of constant magnetomotive force of the stator, aiming at the minimum copper loss. Ref. [4] proposes a fault-tolerant control strategy after a full-range minimum loss fault for a multi-phase motor with sinusoidally distributed windings to minimize the loss of the entire motor. In this paper, the minimum copper loss criterion is used to solve the fault-tolerant current.

The three-phase permanent magnet motor should stop running immediately when the phase is missing, otherwise it will cause huge vibration [5]. The vibration and noise performance indicators of the motor must be tested when the motor leaves the factory. Long-term high specification vibration of the motor reduces motor insulation and bearing life [6]. Ref. [7, 8] proposes that radial electromagnetic force in this motor is the main cause of electromagnetic vibration and noise. The electromagnetic forces of motors with sinusoidal and non-sinusoidal sources are calculated and exported to the structural field model to solve the electromagnetic vibration spectrum [9]. Ref. [10] introduces a fast calculation method of electromagnetic force of built-in permanent magnet synchronous motor powered by a voltage source inverter, and uses a small-signal time-harmonic finite element algorithm. Ref. [11] establishes the internal relationship between electromagnetic force, stator structure mode and electromagnetic vibration. The vibration of the motor is simulated by the modal superposition method, and a 10-pole 12-slot permanent magnet motor is used to carry out the no-load electromagnetic vibration experiment, and the experimental data and the simulation data are well matched [12]. Ref. [13] analyzes the electromagnetic force of a two-phase induction motor in the absence of phase tolerance.

The reliability and service life requirements of marine multiphase permanent magnet motors are different from those of ordinary three-phase motors. In this paper, the vibration of surface-mount six-phase permanent magnet synchronous motors under different working conditions when used as marine electric propulsion motors is studied. In the face of complex offshore environments, multiphase permanent magnet motors operate reliably even in the absence of phase. Although the vibration of a three-phase PMSM is studied in the absence of phase in [5], the vibration of a multiphase PM under fault-tolerant control is not studied. Therefore, it is necessary to study the vibration of multiphase permanent magnet motors. In this paper, the fault-tolerant current is solved by the fault-tolerant control algorithm, substituted into the two-dimensional electromagnetic field finite element model of the motor,

Table 1 Details of the motor

Parameter	Value
Outer diameter of the stator core	1101 mm
Inner diameter of the stator core	881 mm
Air gap length	2 mm
Outer diameter of the rotor core	877 mm
Inner diameter of the rotor core	390 mm
Permanent magnet thickness	10.98 mm
Number of stator slots	72
Core length	411 mm
Number of permanent magnets	20

the electromagnetic force is solved, and then the electromagnetic force is derived to the structural finite element analysis module to find the response spectrum of the motor vibration. For the selection of the corresponding surface mechanical properties of the insulation winding as a reference.

2 Analysis of the Structure and Electromagnetic Vibration Mechanism of Six-Phase Permanent Magnet Synchronous Motor

2.1 Modeling of the Motor

The ship's electric propulsion system requires a low-speed, high-torque motor, so the rotor structure of the marine motor is surface-mounted. There are two types of neutral points in the six-phase PMSM's winding structure: single and double. This paper only analyzes a motor with a single neutral point, and the winding uses an asymmetrical structure to shift the double Y phase by 30° , which can eliminate the 5th and 7th harmonics and 6th torque pulsations in the operation of the motor. The motor parameters are shown in Table 1.

2.2 Electromagnetic Vibration Mechanism Analysis

Under the condition of the sine wave power supply, the magnetic field harmonics generated by the stator current and the magnetic field harmonics generated by the rotor permanent magnet are coupled with each other to form an air gap magnetic field. The air gap magnetic field interacts with the stator core, which in turn generates an

electromagnetic force, which acts directly on the stator tooth root. Both radial and tangential electromagnetic forces exist, with radial electromagnetic forces serving as the primary sources of electromagnetic vibration [7, 8].

According to the Maxwell stress tensor method, the radial electromagnetic force per unit area is calculated as follows:

$$F_r = \frac{B_r^2 - B_t^2}{2\mu_0} \quad (1)$$

The following formula is used to compute the tangential electromagnetic force per unit area:

$$F_t = \frac{B_r B_t}{\mu_0} \quad (2)$$

where: F_r is the radial electromagnetic force density; F_t is the tangential electromagnetic force density; B_r is radial air gap flux density; B_t is tangential air gap flux density; μ_0 is the air gap permeability.

Radial air gap flux density [14]:

$$B_r = B_x \cos \theta + B_y \sin \theta \quad (3)$$

Tangential air gap flux density [14]:

$$B_t = B_y \cos \theta - B_x \sin \theta \quad (4)$$

where: B_x is the air gap magnetic density along the x-axis at a certain point in the air gap; B_y is the air gap magnetic density along the y-axis at a certain point in the air gap; θ is the circumferential angle.

They are calculated by editing the above formula in the electromagnetic field finite element software calculator.

3 Electromagnetic Solutions Under Different Working Conditions

3.1 Motor Excitation Source Setting Under Load

The electromagnetic solution of the simulation motor is completed in the two-dimensional electromagnetic field calculation software. The air gap magnetic tightness may be properly calculated using the finite element approach. In order to simulate the operation of the ship motor, the speed is now set to 300 r/min under three operating conditions.

In the process of solving, the current excitation is first set in the calculation software, and the excitation expression is as follows:

$$i_A = \sqrt{2}I_m \sin 100\pi t \quad (5)$$

$$i_B = \sqrt{2}I_m \sin(100\pi t - \frac{4\pi}{3}) \quad (6)$$

$$i_C = \sqrt{2}I_m \sin(100\pi t - \frac{2\pi}{3}) \quad (7)$$

$$i_D = \sqrt{2}I_m \sin(100\pi t - \frac{5\pi}{6}) \quad (8)$$

$$i_E = \sqrt{2}I_m \sin(100\pi t - \frac{\pi}{6}) \quad (9)$$

$$i_F = \sqrt{2}I_m \sin(100\pi t + \frac{\pi}{2}) \quad (10)$$

The I_m is the rated current. $I_A, I_B, I_C, I_D, I_E, I_F$ is the excitation current of the six-phase windings.

3.2 Motor Excitation Source Setting After Open-Phase

In this paper, the six-phase PMSM has six windings. When setting up a phase loss fault, this article sets normal full load operation, A or AF phase open circuit faults respectively, and then solves the electromagnetic field model. When phase A is open, the phase A current is set to zero. When the AF phase fails, the AF phase current is set to zero. The above method is used as an excitation source to solve the electromagnetic force density.

3.3 Motor Excitation Source Setting After Single-Phase Open-Circuit Fault-Tolerant Control

After the phase failure of the six-phase PMSM, the fault-tolerant control system was quickly put into operation. When phase is missing, the current of phase F drop to zero. The fault-tolerant control algorithm is based on the principle of constantly composite magnet-motive force. The magnet-motive force of the remaining 5 phase windings is added up to the composite magnet-motive force before phase loss. Then the 4 equations are listed. A constraint equation is listed according to the single neutral point current relationship. Finally, the compensation equation is listed with

the minimum copper loss as the compensation goal [15]. The equation is solved by constructing the Lagrange function to find a five-phase current expression. The expression is as follows:

$$\begin{cases} i_A = 1.554I_m \sin(\omega t + 0.1022\pi) \\ i_B = 1.656I_m \sin(\omega t + 0.5872\pi) \\ i_C = 1.217I_m \sin(\omega t - 0.6344\pi) \\ i_D = 1.421I_m \sin(\omega t - 0.8333\pi) \\ i_E = 1.405I_m \sin(\omega t - 0.1667\pi) \end{cases} \quad (11)$$

3.4 Excitation Source Setting After Two-Phase Open-Circuit Fault-Tolerant Control

In the event of a two-phase open-circuit fault, the AF-phase current excitation is set to zero. Again, use the single-phase fault-tolerant current solving process to calculate the fault-tolerant current after the two-phase open-circuit fault. Set the following currents in the winding excitation:

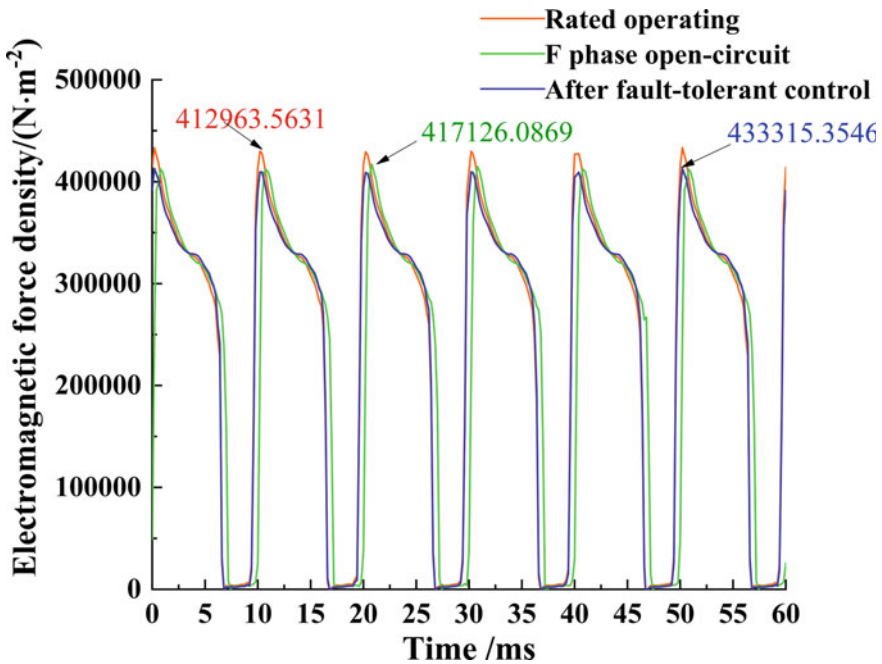


Fig. 1 F phase open-circuit fault electromagnetic force

$$\begin{cases} i_B = 1.694I_m \sin(\omega t + 0.5266\pi) \\ i_C = 1.132I_m \sin(\omega t - 0.6522\pi) \\ i_D = 1.132I_m \sin(\omega t - 0.8477\pi) \\ i_E = 1.694I_m \sin(\omega t - 0.0266\pi) \end{cases} \quad (12)$$

3.5 Comparative Analysis of Radial Electromagnetic Force Finite Element Solution Results

We set the solution time to 0.06 s with a step size of 0.0002 s. By solving the two-dimensional electromagnetic transient field finite element model, a time-domain waveform graph of the electromagnetic force density in Fig. 1 and Fig. 2 is obtained. The green curve in Fig. 1 is the density of the concentrated electromagnetic force of one of the individual tooth roots after the F phase is absent. The peak electromagnetic force density at full load and after fault tolerance is 433315.3546 N/m² and 412,963.5631 N/m², respectively. After the single-phase phase is missing, the peak electromagnetic force density decreases by 3.74% to 417,126.0869 N/m², and the

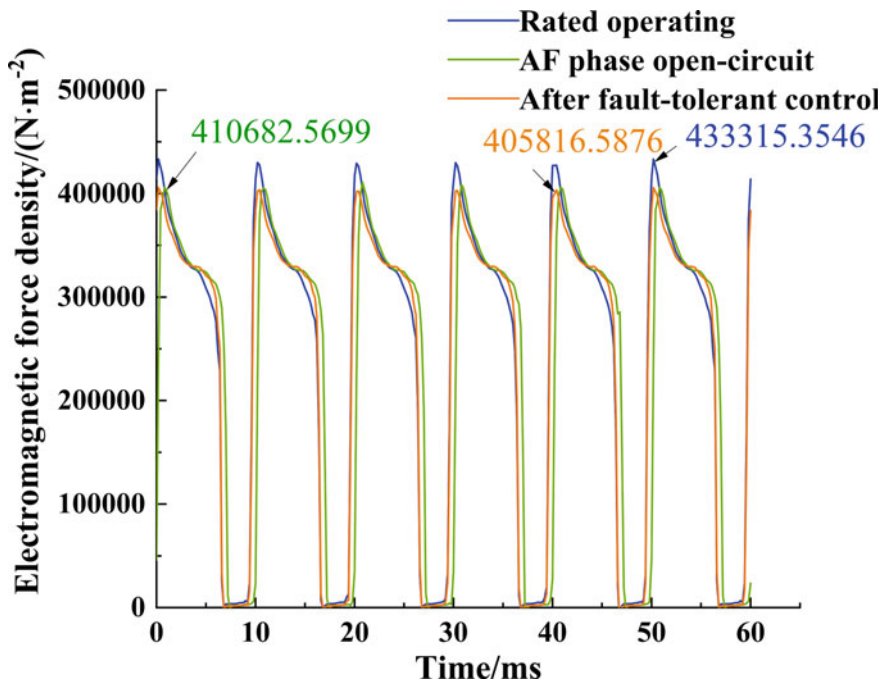


Fig. 2 AF phase open-circuit fault electromagnetic force

fault tolerance decreases by 1.43% compared with full load. The peak electromagnetic force density after fault-tolerant control decreases by 0.10% compared with the absence of phase. Its phase shift after phase loss. After fault-tolerant control, the phase is almost synchronized with the motor which is fully loaded. Through comparison with Ref. [13], it is found that the electromagnetic force loss of the simulation model motor is much lower than that of the double three-phase asynchronous induction motor. The percentage of electromagnetic force lost in the double three-phase asynchronous induction motor is 16.7%.

Figure 2 shows the electromagnetic force density before and after AF phase loss, and the dark green curve indicates that peak electromagnetic force density when the AF phase fault is 410682.5699 N/m², and its peak after fault tolerance is 405816.5876 N/m². The peak in full load is 433315.3546 N/m², which is 5.22% higher than when AF is out of phase. This peak electromagnetic force density after fault tolerance is 1.18% lower than the peak electromagnetic force density at full load. The ratio of missing two phases to single phase: Even the minimum copper loss compensation target fault-tolerant control algorithm cannot compensate for the loss of electromagnetic force caused by the increase in the number of missing phases.

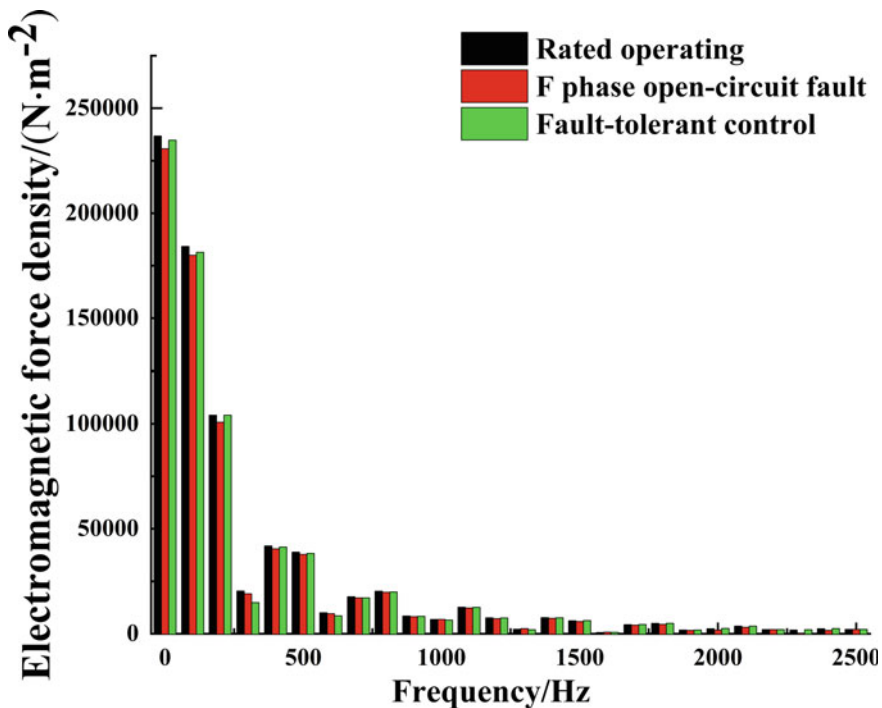


Fig. 3 Spectrum of electromagnetic force density before and after F phase open-circuit fault

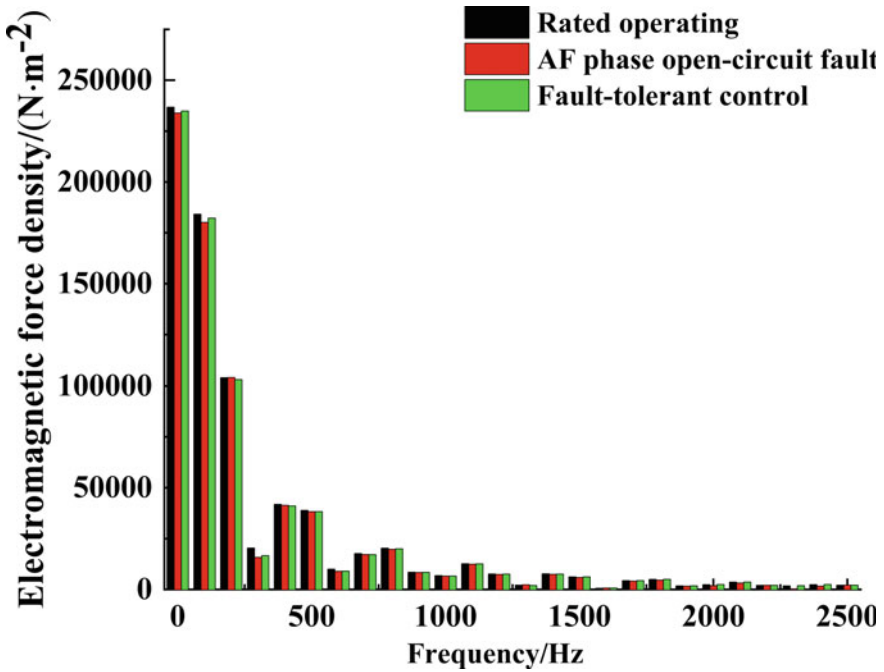


Fig. 4 Spectrum of electromagnetic force density before and after AF phase open-circuit fault

Figure 3 shows the Fourier analysis of the electromagnetic force density before and after the F-phase is absent. Filter out frequency bands with large amplitudes. The fundamental frequency is 100 Hz. The fundamental electromagnetic force density at full load is 179969.80 N/m². When the F phase is absent, the electromagnetic force density becomes 230,737.83 N/m². It is 181383.74 N/m² after fault tolerance.

Figure 4 shows the results of the Fourier analysis of the electromagnetic force before and after the two-phase open circuit failure. The fundamental electromagnetic force at full load is 184218.38 N/m². When the AF phase is absent, the electromagnetic force becomes 180,105.02 N/m². Post-fault tolerant 182,280.47 N/m². The fundamental electromagnetic force density is higher when two are missing than when the one-phase winding fails. But they are all lower than the peak of electromagnetic force density in rated operation.

4 Magneto-Solid Interaction Physics Field Simulation

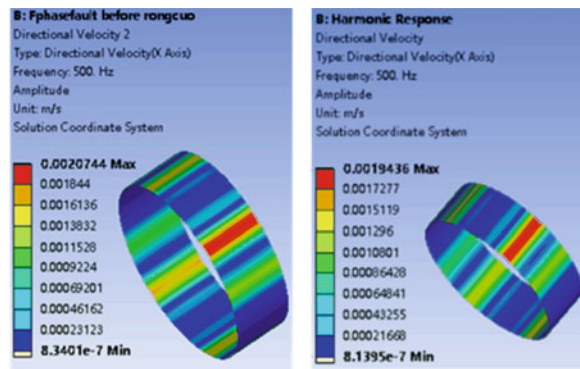
4.1 Stator Core Surface Vibration Response Analysis

In the three-dimensional structural harmonic response analysis, the stator core material DW465 Poisson ratio is set to 0.28; Young’s modulus is 1.683×10^{11} Pa; density is 7600 kg/m^3 . Since the introduced radial electromagnetic force is a concentrated force, the root plane of the tooth is selected as the introduction position of the force, and when the point of action of the force is not in the center of the root surface of the tooth, the point of action is offset to the center of the root surface of the tooth by setting the distant force. The core surface velocity response is calculated by the complete method.

Figure 5 shows that the maximum vibration speed of the F phase is 0.0020744 m/s , which is significantly higher than the vibration speed of 0.0017758 m/s in rated operation in Fig. 7. Through the velocity cloud map, it is found that the maximum speed in rated operation is distributed in three places on the surface of the core. The maximum velocity cloud map after F-phase absence and fault-tolerant control is distributed in only one place. Figure also shows that the maximum vibration speed decreases after fault-tolerant control.

Figure 6 shows that the maximum vibration rate when the AF is out of phase is also higher than the maximum vibration speed in rated operation in Fig. 7. In Fig. 6, it shows that the maximum vibration speed is 0.0032264 m/s in rated operation. In the same condition, the maximum vibration speed is distributed in only one place. The maximum vibration speed is reduced to 0.0021054 m/s by fault-tolerant control. At this point the frequency is 500 Hz .

Fig. 5 F phase open-circuit fault vibration velocity before and after fault-tolerant control nephogram



(a) F phase open-circuit (b) Fault-tolerant control fault

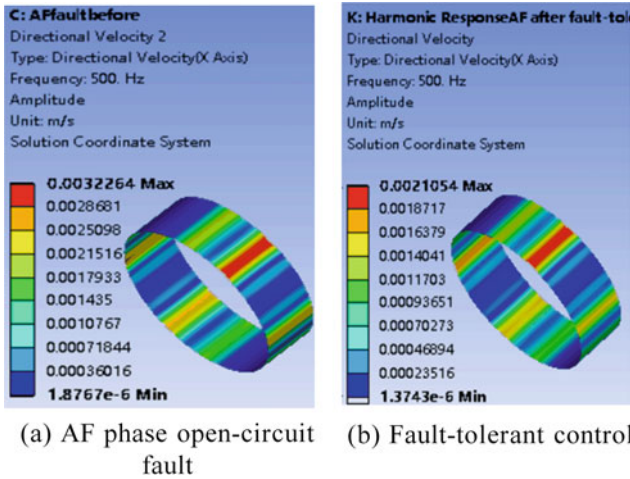


Fig. 6 AF phase open-circuit fault vibration velocity before and after fault-tolerant control nephogram

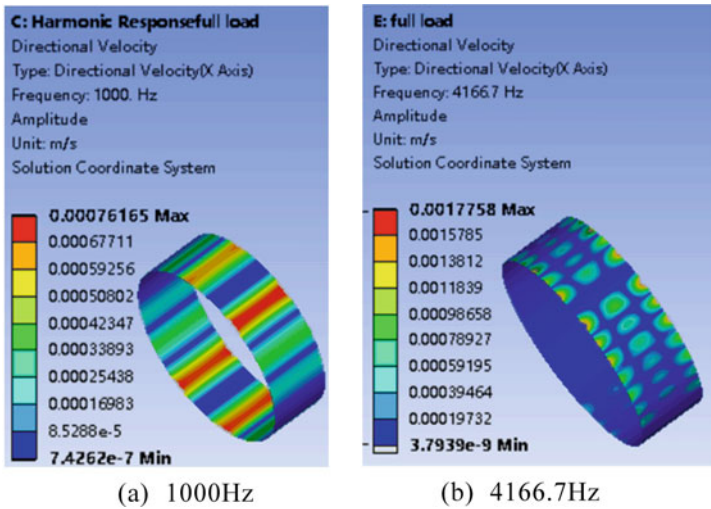


Fig. 7 Rated operating vibration velocity nephogram

5 Conclusions

For marine motors, the reduction of air gap magnetic density when the phase is missing and after fault tolerance leads to a decrease in radial electromagnetic force density and uneven distribution, which in turn leads to a severe vibration response. When it is in open phase, after the fault-tolerant control, its density should be less than

the electromagnetic force density at rated operation. The density value of the two-phase open circuit is lower than the electromagnetic force density of the single-phase open circuit, which also includes in fault-tolerant. The maximum vibration speed in full load is distributed on multiple core surfaces, and the maximum vibration speed is concentrated in one place when the single-phase or the two-phase is lost. In rated operation, the vibration speed is less than that of single-phase open circuit and two-phase open circuit. When the two phases are open, the vibration is abnormal, and the vibration speed has been significantly reduced in the low frequency band after fault-tolerant control.

References

1. Munim, W.N.W.A., Duran, M.J., Che, H.S., et al.: A unified analysis of the fault tolerance capability in six-phase induction motor drives. *IEEE Trans. Power Electron.* **32**, 7824–7836 (2017)
2. Wang, X., Wang, Z., Xu, Z., et al.: Comprehensive diagnosis and tolerance strategies for electrical faults and sensor faults in dual three-phase PMSM drives. *IEEE Trans. Power Electron.* **34**, 6669–6684 (2019)
3. Wang, Y., Wen, X., Zhao, F.: The fault tolerant control for six-phase permanent magnet synchronous machines with one phase failure. *Trans. China Electrotechnical Soc.* **30**(5), 49–58 (2015). (in Chinese)
4. Yepes, A.G., Doval-Gandoy, J., Baneira, F., et al.: Postfault strategy for dual three-phase machines with minimum loss in the full torque operation range under two open phases. In: 2018 IEEE Energy Conversion Congress and Exposition (ECCE), Portland, OR, USA, pp. 3380–3385. IEEE (2018)
5. Han, H., Deng, M., Zhang, H., et al.: Dynamic characteristics analysis of electromagnetic radial force of permanent magnet synchronous motor under phase failure. *Modular Mach. Tool Autom. Manuf. Tech.* **11**, 102–106 (2020). (in Chinese)
6. Zhen, Y.: Analysis and treatment of motor vibration. *Technol. Innov. Appl.* **16**, 6 (2013). (in Chinese)
7. Islam, R., Husain, I.: Analytical model for predicting noise and vibration in permanent-magnet synchronous motors. *IEEE Trans. Ind. Appl.* **46**, 2346–2354 (2010)
8. Islam, M.S., Islam, R., Sebastian, T.: Noise and vibration characteristics of permanent-magnet synchronous motors using electromagnetic and structural analyses. *IEEE Trans. Ind. Appl.* **50**(5), 3214–3222 (2014)
9. Zuo, S., Liu, X., Yu, M., et al.: Numerical prediction and analysis of electromagnetic vibration in permanent magnet synchronous motor. *Trans. China Electrotechnical Soc.* **32**(1), 159–167 (2017). (in Chinese)
10. Zhu, S., Lu, J., Zeng, F.: Fast calculation of electromagnetic forces in IPMSMs under PWM VSI supply based on small-signal time-harmonic finite element method. *Trans. Electr. Mach. Syst.* **6**, 67–76 (2022)
11. Zhang, L., Xu, J., Meng, D.: Effect of tangential electromagnetic force on electromagnetic vibration of permanent magnet synchronous in-wheel motor. *J. TongJi Univ. (Nat. Sci.)* **47**(S1), 126–132 (2019). (in Chinese)
12. Hong, J., Wang, S., Sun, Y., et al.: The influence of high-order force on electromagnetic vibration of permanent magnet synchronous motors. *Trans. China Electrotechnical Soc.* **37**(10), 2446–2458 (2022). (in Chinese)
13. Ge, B., Zhou, X., Tao, D., et al.: Electromagnetic force analysis of double three-phase induction motor operating in fault-tolerant state. *J. Harbin Univ. Sci. Technol.* **26**(2), 75–82 (2021). (in Chinese)

14. Wang, B.: Magneto-mechanical coupling vibration analysis of motor considering the influence of shell deformation. Chongqing University of Technology (2018). (in Chinese)
15. Zheng, D., Liu, Y.: Fault-tolerant control of dual three-phase permanent magnet synchronous motors under open winding faults. *Electr. Mach. Control Appl.* **47**(5), 28–32+38 (2020). (in Chinese)

Research on PWM Rectifier Extending DC Working Voltage Range



Danyang Xie, Gang Zhang, Yunda Wang, and Wei Wei

Abstract PWM rectifier has the excellent characteristics of bidirectional energy transmission and controllable power factor, which becomes the key equipment for constructing flexible traction power supply system. The PWM rectifier based on the traditional unit power factor control is a boost converter. Its DC side voltage has a minimum limit, which can not maintain normal operation when the DC voltage falls due to sudden conditions. It has become a technical difficulty that must be broken through. In this paper, based on the original control strategy, constant power control and power reduction control methods are introduced to broaden the voltage range of the DC side of the PWM rectifier, ensure that during the DC voltage sag period, the PWM rectifier keeps running in the network, and provides active power output to the maximum extent, assist the DC network voltage recovery, and realize the low voltage through the DC side. Through simulation, the method can effectively broaden the DC side voltage range of PWM rectifier, and has practical application significance.

Keywords PWM rectifier · constant power control · reduced power control · low voltage through

1 Introduction

PWM rectifier has many excellent performance, in the converter process can achieve two-way power transmission, grid side current is sine wave, unit power factor control, and has a good dynamic control response [1].

With the growing size of urban rail system, traction power supply system with PWM rectifier as the core is also faced with some challenges [2]. When multiple trains pull at the same time, the required power will be greater than the power provided by

D. Xie · G. Zhang (✉) · Y. Wang · W. Wei
School of Electrical Engineering, Beijing Jiaotong University, Beijing 100044, China
e-mail: ngzhang@bjtu.edu.cn

G. Zhang
Beijing Rail Transit Electrical Engineering Technology Research Center, Beijing 100044, China

© Beijing Paiké Culture Commu. Co., Ltd. 2023
X. Dong et al. (eds.), *The proceedings of the 10th Frontier Academic Forum of Electrical Engineering (FAFEE2022)*, Lecture Notes in Electrical Engineering 1054, https://doi.org/10.1007/978-981-99-3408-9_28

the PWM rectifier, and then the DC voltage will drop rapidly. The network topology of PWM rectifier determines that it is a booster converter, so the DC side voltage has a minimum value. When the output power cannot meet the load demand, it cannot cope with the DC voltage drop caused by the multi-train traction condition, and then the grid withdrawal, which further worsens the situation.

To solve this problem, Ren Zengtian et al. [3] improved the circuit topology and changed the booster structure into the booster structure by adding circuit components. Zhang Xingliang et al. [4] broadened the range of output voltage regulation by controlling the power factor on the AC side.

In this paper, on the premise of not changing the topology structure of the PWM rectifier circuit, constant power control and power reduction control are adopted. In different control stages, different voltage ranges are adjusted to ensure that during the DC voltage drop period, the PWM rectifier keeps running on the network, and provides maximum active power output to assist the DC network voltage recovery.

2 Modeling and Control of PWM Rectifier

The main topology of the PWM rectifier is shown in Fig. 1 [5]. e_a , e_b and e_c are respectively the electromotive force of the AC side power supply, R is the line equivalent resistance, L is the AC inductance, C is the DC side capacitance, a, b and c are the midpoint of each phase bridge arm, and O is the midpoint of the AC side power supply.

Three-phase PWM rectifier adopts PWM modulation when it works normally. According to the basic principle of PWM modulation strategy, the state of two full control tubes on each bridge arm cannot be the same at any time. Therefore, a binary logic switching function can be established for each full control tube, as Eq. (1) is shown:

$$s_k = \begin{cases} 1 & \text{The upper bridge arm is on, and the lower bridge arm is off} \\ 0 & \text{The upper bridge arm is off, and the lower bridge arm is on} \end{cases} \quad (1)$$

The mathematical model of three-phase PWM rectifier based on switching function model in d-q coordinate system is shown in Eq. (2) [6].

Fig. 1 Main topology of PWM rectifier

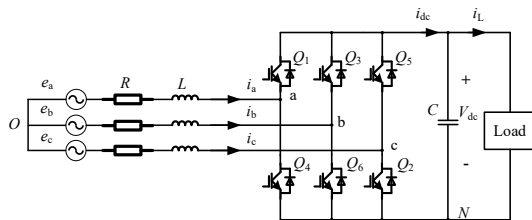
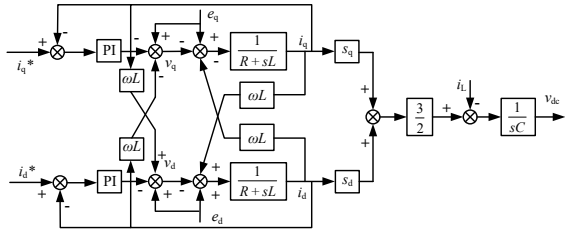


Fig. 2 Schematic diagram of decoupling control of PWM rectifier



$$\begin{cases} L \frac{di_q}{dt} + \omega Li_d + Ri_q = e_q - v_{dc}s_q \\ L \frac{di_d}{dt} - \omega Li_q + Ri_d = e_d - v_{dc}s_d \\ C \frac{dv_{dc}}{dt} = \frac{3}{2}(i_qs_q + i_ds_d) - i_L \end{cases} \quad (2)$$

As can be seen from Eq. (2), the mathematical model of PWM rectifier located in the rotating coordinate system still has the effect of coupling between d and q axis components [7]. Therefore, it is necessary to design the control system for decoupling control.

The current state feedback method is selected for decoupling, and the grid side voltage disturbance is considered, and the grid voltage vector e_q and e_d feedforward are used to eliminate the disturbance and the governing Eq. (3) is: [8]

$$\begin{cases} v_q = -(K_{ip} + \frac{K_{il}}{s})(i_q^* - i_q) - \omega Li_d + e_q \\ v_d = -(K_{ip} + \frac{K_{il}}{s})(i_d^* - i_d) + \omega Li_q + e_d \end{cases} \quad (3)$$

where K_{ip} and K_{il} are the proportional gain and integral gain of the current loop PI regulator respectively. i_q^* and i_d^* are the command values of the current component i_q and i_d .

The decoupling control of PWM rectifier is shown in Fig. 2.

3 Method Analysis of Broadening DC Side Voltage Range of PWM Rectifier

The PWM rectifier can control the amplitude and phase of the three-phase alternating current at the output end by using the pulse-width modulation technology. Figure 3 shows the single-phase equivalent circuit of PWM rectifier [9].

The mathematical expression of single-phase equivalent circuit of PWM rectifier is as follows:

$$e_a - u_a = L \frac{di_a}{dt} \quad (4)$$

Fig. 3 Single phase equivalent circuit of PWM rectifier

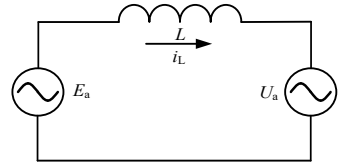
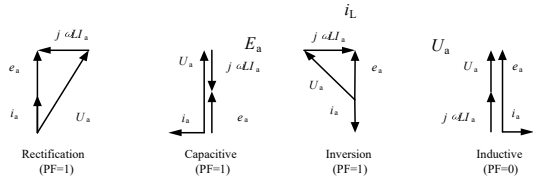


Fig. 4 PWM rectifier single phase equivalent circuit vector diagram



The vector diagram corresponding to the single-phase equivalent circuit of the PWM rectifier is shown in Fig. 4.

It can be seen that the PWM rectifier has the ability to work in four quadrants. By adjusting U_a , the working mode of the PWM rectifier can be adjusted, which provides the basis for regulating the DC side voltage.

The PWM rectifier that adopts the SVPWM modulation strategy has the relation shown in Eq. (5) [10]:

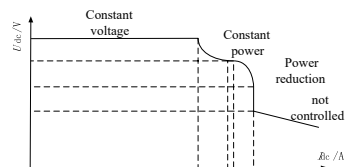
$$U_a = \frac{mU_{dc}}{\sqrt{6}} \tag{5}$$

where, U_a is the effective value of the AC side phase voltage of the PWM rectifier, m is the modulation ratio ($m \leq 1$), and U_{dc} is the DC side voltage [11].

With the increase of the demand traction power, a low voltage crossing control strategy is derived. The control strategy divides the working area of the PWM rectifier into four parts: constant voltage area, constant power area, power reduction area and uncontrolled rectifier area. The external characteristic curve is shown in Fig. 5

Under the constant voltage control strategy and the constant power control strategy, in order to ensure that the PWM rectifier output as much as possible with active power, unit power factor control should be adopted, as shown in Fig. 6(a) and (b). Under the power reduction control strategy, in order to further reduce the DC side voltage and broaden the adaptive range, the power reduction control strategy

Fig. 5 The low voltage traverses the characteristic curve outside the control policy



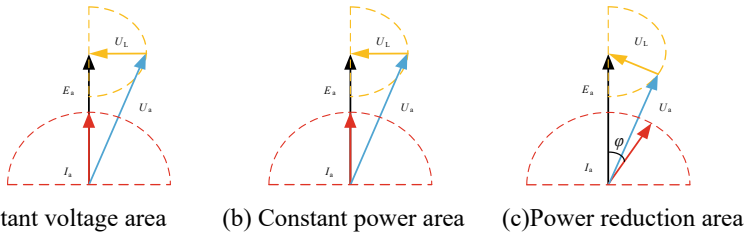
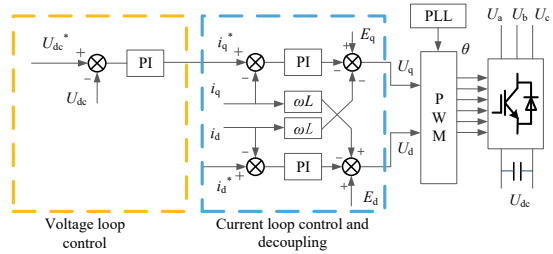


Fig. 6 Working principle of PWM rectifier

Fig. 7 Block diagram of voltage-current double closed-loop control strategy



should be adopted to make the PWM rectifier work in the non-unit power factor rectification state, as shown in Fig. 6(c).

The realization of the switching of the three working areas is based on the voltage-current double closed-loop control strategy [12]. The control block diagram is shown in Fig. 7. The values of U_{dc}^* , I_d and i_q are determined through the calculation of boundary conditions, and the sub-regional control varies with the load is realized. Due to space limitation, the calculation process will not be described here.

4 Simulation Analysis

The simulation model was built according to the topology shown in Fig. 1. The parameters of the simulation model were set as shown in the table below. Regardless of the influence of the resistance on the AC side, the controlled current source was selected for the load to simulate the load of the train (Table 1).

As can be seen from Fig. 8, with the increase of load current, the output of PWM rectifier appears to be unchanged after the first increase in power, while its DC side voltage is first constant and then gradually decreases, experiencing constant voltage zone, constant power zone, reduced power zone and uncontrolled rectifier zone.

Table 1 Simulation model parameters

Parameter	Value
The rated power of PWM rectifier is S/MW	3
Grid voltage amplitude Ea/V	367.42
Grid voltage frequency f1/Hz	50
Ac side filter inductance L/mH	0.001
Power source load slope k/(A/s)	500
Switching frequency f2/Hz	2000

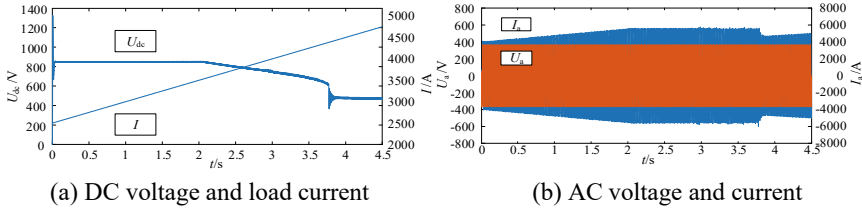
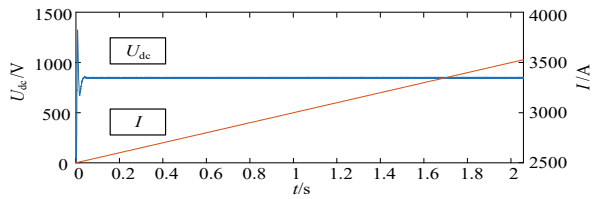


Fig. 8 Curve of voltage and current

Fig. 9 Curve of DC voltage and load current in constant voltage region



4.1 Constant Voltage Region

It can be seen from Fig. 9 that in the constant-voltage region, DC voltage maintains a constant value of 850 V with the increase of load current. It can be seen from Fig. 10 that in the operating range of the constant-voltage region, the current at the AC side is in the same phase as the voltage, and the current at the AC side increases with the increase of load current.

4.2 Constant Power Region

It can be seen from Fig. 11 that in the constant power region, as the power of the PWM rectifier has reached the upper limit, the DC voltage changes in reverse proportion with the increase of load current, and the modulation ratio m gradually increases.

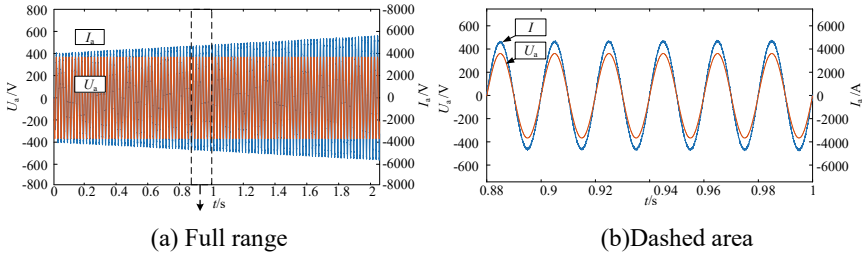


Fig. 10 Curve of AC voltage and current in constant voltage region

Fig. 11 Curve of DC voltage and load current in constant power region

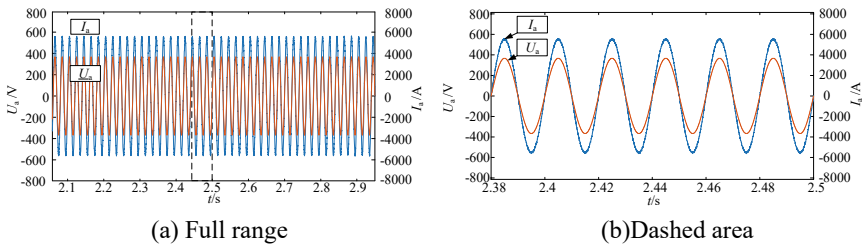
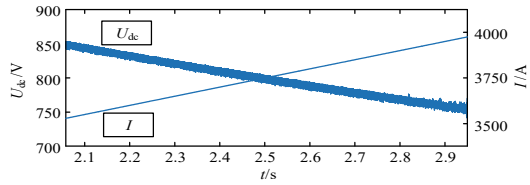


Fig. 12 Curve of AC voltage current in constant voltage region

Considering the safety margin, when it increases to 0.93, the DC voltage decreases to the lowest value 750 V.

It can be seen from Fig. 12 that in the constant voltage working range, the current at the AC side is in the same phase as the voltage, and the current at the AC side does not increase with the increase of the load current.

4.3 Power Reduction Region

As can be seen from Fig. 13(a), DC voltage of PWM rectifier drops rapidly with the increase of load current in the working section of the power reduction zone. When DC voltage drops to 608 V, PWM rectifier is in a critical state in the working section of the power reduction zone. After that, the output active power cannot meet the

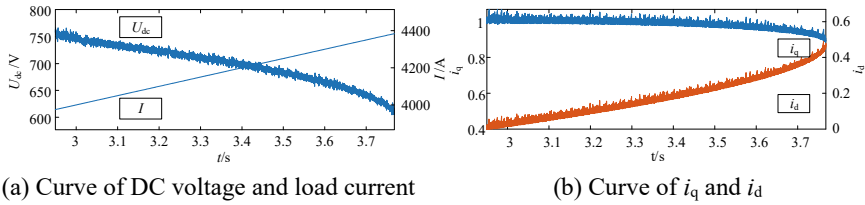


Fig. 13 Curve of DC voltage and load current in power reduction region

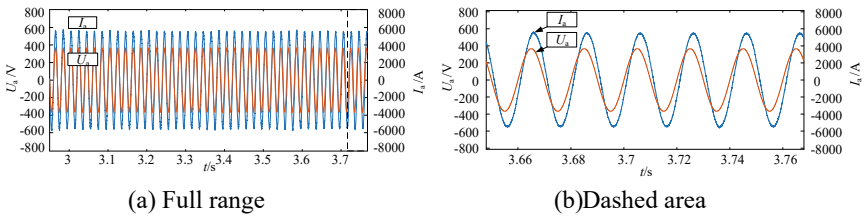


Fig. 14 Curve of AC voltage and current in power reduction region

needs of the load, so it is necessary to block the pulse of IGBT module and adopt diode uncontrolled rectifier mode.

It can be seen from Fig. 14 and Fig. 13(b) that in the working interval of the power reduction zone, the current of the AC side does not change, but lags the AC voltage at a certain phase. At this time, the PWM rectifier works in the state of non-unit power factor. With the continuous decrease of DC voltage, the i_q of active current decreases and the i_d of reactive current increases, and the power factor decreases to further broaden the range of DC voltage. The phase of AC current lagging behind AC voltage also becomes larger and larger.

5 Conclusion

In this paper, on the basis of the original PWM rectifier control, the method of constant power control and power reduction control is introduced to broaden the DC side voltage range of the PWM rectifier, and realize the low voltage crossing.

The simulation results show that the PWM rectifier including constant power control and power reduction control strategy is adopted to realize the switching work in multiple working intervals under the condition that the load demand current is gradually increasing.

References

1. Wang, G.X., Jin, S.Y.: Research on control strategy based on three-phase voltage PWM rectifier. *Electr. Drive* **49**(10), 34–38+74 (2019). (in Chinese)
2. Zhang, G., Hao, F.J., Wang, Y.D., et al.: Flexible urban rail traction power supply system and optimization control study. *Trans. China Electrotechnical Soc.* **37**(S1), 153–162 (2022). (in Chinese)
3. Zeng, Z.T.: Research on charge and discharge system based on PWM rectifier technology. Harbin Engineering University (2012). (in Chinese)
4. Zhang, X.L., Meng, G.W., Xiang, D., et al.: A way of broadening the scope of PWM rectifier voltage regulator research. *Micromotors* **53**(03), 44–48+54 (2020). (in Chinese)
5. Zhang, Y., Gao, J., Qu, C.: Relationship between two direct power control methods for PWM rectifiers under unbalanced network. *IEEE Trans. Power Electron.* **32**(5), 4084–4094 (2017)
6. Zhang, C.W., Zhang, X.: *PWM Rectifier and Its Control*. China Machine Press, Beijing (2012). (in Chinese)
7. Zou, Y., Zhang, L., Xing, Y., et al.: Generalized clarke transformation and enhanced dual-loop control scheme for three-phase PWM converters under the unbalanced utility grid. *IEEE Trans. Power Electron.* **37**(8), 8935–8947 (2022)
8. Kakkar, S., Maity, T., Kumar Ahuja, R., et al.: Design and control of grid-connected PWM rectifiers by optimizing fractional order PI controller using water cycle algorithm. *IEEE Access* **9**, 125941–125954 (2021)
9. Wang, X., Liu, S., Li, Q.: Research on control strategy of PWM rectifier technology based on DSP. In: 2017 IEEE International Conference on Information and Automation (ICIA), Macao, China, pp. 1050–1053 (2017)
10. Zhang, X., Wu, X., Geng, C., et al.: An improved simplified PWM for three-level neutral point clamped inverter based on two-level common-mode voltage reduction PWM. *IEEE Trans. Power Electron.* **5**(10), 11143–11154 (2020)
11. Chen, J., Li, J., Qiu, R.C., et al.: Research on synchronous overmodulation strategy of space vector pulse width modulation for traction system of rail transit. *Trans. China Electrotechnical Soc.* **35**(S1), 91–100 (2020). (in Chinese)
12. Zhao, H., Hu, R.J.: Space-vector pulse width modulation and its simulation based on simulink. *Trans. China Electrotechnical Soc.* **30**(14), 350–353 (2015). (in Chinese)

Deep Learning + Complex Physics Field Modeling: Illustrated by the Example of Numerical Investigation on Low Temperature Plasma



Chaoqun Zhao , Jie Pan, Bin Li, and Yun Liu

Abstract In deep learning field, the appropriate selection of constraints directly affects the learning efficiency and learning results of a network. Partial differential equations (PDEs) which are extremely accurate compared to the constraint methods employed in traditional neural networks are natural constraint models in complex physical fields. In this paper, based on this premise we propose a new method to solve complex physical field simulation problems. We approximate the variables in a complex physical field by building a feedforward deep neural network while applying the chain rule of calculus to encode the corresponding PDEs into the loss function to add constraints. It is worth noting that we have only used part of the equations of the physical process rather than all of them. In other words, instead of solving the equations we learn the whole physical process via the partial PDEs constraints and a few data points. We verify the effectiveness of the deep learning method via learning low-temperature plasma model that is composed of complex physical processes. This technique presents a paradigm for the simulation of complex physical field problems.

Keywords Deep Learning · Complex Physics Field · Partial Differential Equations · Low Temperature Plasma · Numerical Investigation

1 Introduction

Currently, with the development of Moore's Law, the computing power of computers has increased dramatically, while deep learning algorithms for artificial neural networks have emerged in the field of artificial intelligence [1–3]. Recently, deep learning has made considerable achievements in different industries, such as residential, medical, education, finance, industry and agriculture fields, while relatively little research has been done in basic science, especially in complex physical fields that are

C. Zhao · J. Pan (✉) · B. Li · Y. Liu
School of Physics and Electronics, Shandong Normal University, Jinan, China
e-mail: sdnupanjie@163.com

© Beijing Paiké Culture Commu. Co., Ltd. 2023
X. Dong et al. (eds.), *The proceedings of the 10th Frontier Academic Forum of Electrical Engineering (FAFEE2022)*, Lecture Notes in Electrical Engineering 1054, https://doi.org/10.1007/978-981-99-3408-9_29

in initial research stages [4]. Interdisciplinary complex physical fields that mix mathematics, physics, scientific and engineering applications, and applied topics in numerical analysis are processes or systems coupled with multiple simultaneous physical features [5, 6]. They contain several complex physical processes and complex partial differential equations (PDEs), including fluid dynamics equations, electrodynamics equations, and electromagnetic field equations [7, 8]. Due to the very large computational effort required by traditional simulation methods, such as the finite difference method (FDM), finite element method (FEM) and finite volume method (FVM), whether deep learning can be applied to complex physical fields has become the main topic of our research [1].

Solving scientific problems with deep learning is not a new inspiration but neural networks have made significant progress in solving PDEs are shown by current experience [4, 9–12]. Physics-informed neural networks, as function approximators, are the most important of these networks, and the key is to reasonably add physical information to the neural network [13]. According to the differentiation function within a program, the partial differential terms of the equations in complex physical fields can be conveniently calculated and incorporated the equations as constraints in the iterative process. A partial differential equation is extremely accurate as a natural constraint term. Instead of neural networks solving equations, our model adds physical information into a program as constraints which enhance the learning ability of neural networks on data [1]. More importantly, we are unaware of the full equations of physical quantities involved in physical processes under experimental conditions. Our approach proves that only some of the equations are required to be programmed into the neural network as physical constraints to obtain fairly accurate results with the addition of a small amount of data. The method has made significant progress in modeling problems in complex physical fields. Compared with traditional numerical simulation methods, this approach not only saves simulation time but also breaks the curse of dimensionality [14].

To demonstrate this framework, the chapters of the paper are arranged as follows. In Sect. 2, A general complex physical field model construction algorithm based on deep learning is described in detail. In Sect. 3, the validity of the framework is verified by examples of numerical studies of low-temperature plasma. Finally, conclusions and further research are provided in Sect. 4.

2 Methodology

A complex physical field that is mathematically represented as multiple nonlinear and parameterized partial differential equations is a multidimensional space–time system. Its general form is as follows:

$$f(t, x, u, v, u_t, u_x, v_t, v_x, \dots, \nabla u, \nabla \cdot u, \nabla v, \nabla \cdot v, \dots; \lambda) = 0 \quad (1)$$

where $u = u(x, t)$ and $v = v(x, t) \in R^{2 \times n}$ are the potential multidimensional characteristic solutions of the equation. u and v denote the first-order derivative of the space-time domain, where $t \in [0, T]$ indicates time and $x \in \Omega^{m \times n}$ indicates space. $f(\cdot)$ is a complex nonlinear equation formed by u, v, u and v after permuting and weighting. The λ parameters represent physical properties, e.g., the mass density, diffusion coefficient, electrical conductivity, thermal conductivity, and reaction rate coefficient. ∇ is the Hamiltonian operator. Due to the specificity of solving PDEs, the constraints of the initial and boundary conditions are needed.

$$B(t, x, u, v) = 0, I(x, u, v) = 0 \quad t \in [0, T], x \in \Omega^{m \times n} \tag{2}$$

In complex physical fields, the expressions of Eq. (1) are often complex and coupled. For simplicity, we can treat Eq. (1) as the sum of several equations $f(\cdot) = \sum_i f_i(\cdot)$, in which $f_i(\cdot)$ can denote equations of specific physical significance, e.g., continuity equation, conservation of momentum equations, and conservation of energy equations.

With the development of the TensorFlow framework, an open-source machine learning library developed and maintained by Google Brain, the automatic differential solver in TensorFlow makes it easy to program complex partial differential equations. As illustrated in Fig. 1, we developed a neural network topology based on this theory. The neural network outputs the characteristic solution $h^* = (t, x, \theta)$ for $f(\cdot)$ when x and t are randomly selected as the total input in the space-time domain. The parameter θ is $\theta = (w, b)$, where w is a set of weights randomly initialized or employed some specific techniques in the neural network, such as the Xavier initialization is applied before training the neural network, and b is a set of biases that are initialized as a zero matrix. These are all parameters in the neural network, and their values are continuously optimized through network iteration.

To involve physical constraints in the neural network iterative process, we define the loss function as [15]:

$$L(\theta) = \frac{1}{\sqrt{N_u}} \sum_m \alpha_m \|h^*(t_i, x_i, \theta) - h(t_i, x_i)\|_2 + \frac{1}{\sqrt{N_f}} \sum_n \beta_n \|f_n(t_j, x_j)\|_2 + \gamma \|\Lambda\|_2 \tag{3}$$

where $\{t_i, x_i\}_{i=1}^{N_u}$ and $\{t_j, x_j\}_{j=1}^{N_f}$ denote the sets of corresponding initial and boundary points. n and m are the number of characteristic solutions of h and equation $f(\cdot)$, respectively. $\|\cdot\|_2$ denotes the second-order norm. $(\alpha, \beta) \in R$ are relative weights. Λ is the regularization parameter whose coefficient γ is set to zero in this study. The L-BFGS algorithm is finally chosen to optimize the loss function [16, 17].

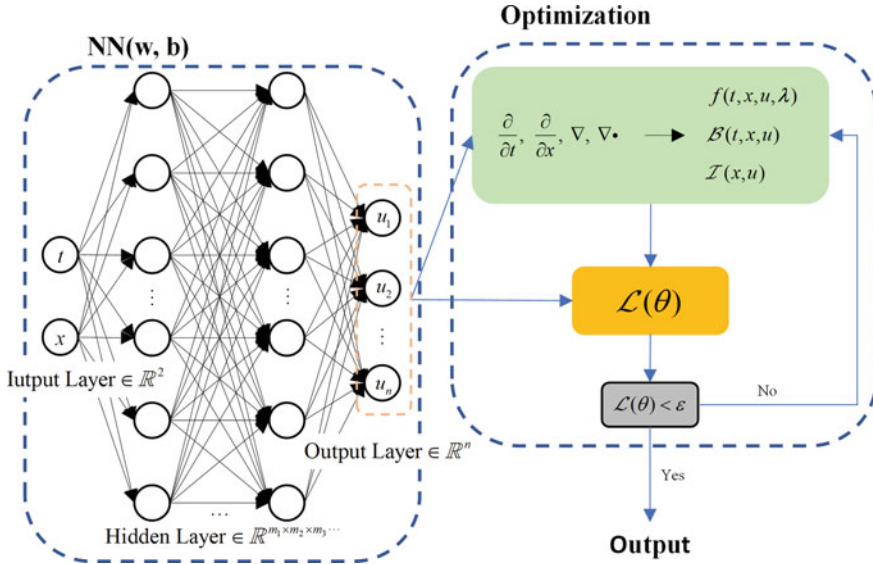


Fig. 1 Diagram of the neural network for complex physical fields. The main body is a neural network topology with two inputs and multiple outputs. The output is used to represent the solution of the equation

At this point, the neural network design is completed while the neural network and PDEs are optimized in coordination. With the help of automatic differentiation, PDEs provide the neural network with an exact physical model as a constraint while the neural network in turn finds the corresponding closed-form solution for the PDEs.

3 Deep Learning for Low Temperature Plasma Simulation

Low-temperature plasma has an applied electric field, a constantly changing internal electric field, and numerous and complex physicochemical reactions [7, 8], which are hard to solve using classical methods. The advantages of our method are demonstrated as an example of a complex physical field in a low-temperature plasma model.

In the complex physical field of low temperature plasma, we model the electric field, electron density and electron temperature with the following PDEs:

$$\frac{\partial(\frac{3}{2}K_B T_e(x, t)N_e(x, t))}{\partial t} + \nabla \cdot \mathbf{W}(x, t) = -e\mathbf{\Gamma}_e(x, t) \cdot \mathbf{E}(x, t) \quad (4)$$

where

$$\mathbf{W}(x, t) = -\lambda_e(x, t)\nabla T_e(x, t) + \frac{5}{2}K_B T_e(x, t)\mathbf{\Gamma}_e(x, t)$$

$$\lambda_e(x, t) = \frac{5}{2}K_B D_e N_e(x, t)$$

and

$$\mathbf{\Gamma}_e(x, t) = -\mu_e \mathbf{E}(x, t)N_e(x, t) - D_e \nabla N_e(x, t)$$

where K_B is the Boltzmann constant, μ_e is the migration rate, D_e is the diffusion coefficient, \mathbf{W} is the electron energy flux density, \mathbf{E} is the electric field intensity, N_e the electron density, and T_e is the electron temperature. Because the method in this paper is more locally applicable, the space-time region for our simulations is $x : 0.06 \sim 0.5$ cm and $t : 6.5 \times 10^{-5} \sim 2.6 \times 10^{-4}$ μs , and these values are chosen randomly. We define the boundaries of the selected region as the initial and boundary conditions.

Since the low-temperature plasma reaction process is complex and the PDEs in it are numerous and coupled, we employ 8-hidden-layer with 130 neurons per layer deep neural networks to simulate this complex physical field. All the source data are obtained via FEM using a program we wrote in Fortran. After several attempts, we determined the activation functions of all neural networks as hyperbolic tangent functions. A randomly selected eight hundred points in the space-time domain are employed as training data while PDEs are used as loss function constraints. The comparison of the learning results of our method and the various types of results are shown in Fig. 2, 3 and 4, the electric field intensity, electron density and electron temperature of the low-temperature plasma are chosen as outputs. It can be seen that the curves of the three physical quantities simulated by the method overlap with the curves of the exact results to a high degree, even in the region near the boundary where the data vary drastically. To make the results more convincing, we give the errors of electric field strength, electron density, and electron temperature, which are 6.93×10^{-4} , 2.15×10^{-3} and 2.14×10^{-3} . In contrast to PINN under the same conditions [4], even though PINN is relatively strong in solving PDEs, it becomes weak when encountering problems with more coupled and incomplete equations, especially in regions with abrupt changes. Similarly, classical deep learning without PDE constraints learns well in smooth regions but not in regions with abrupt changes

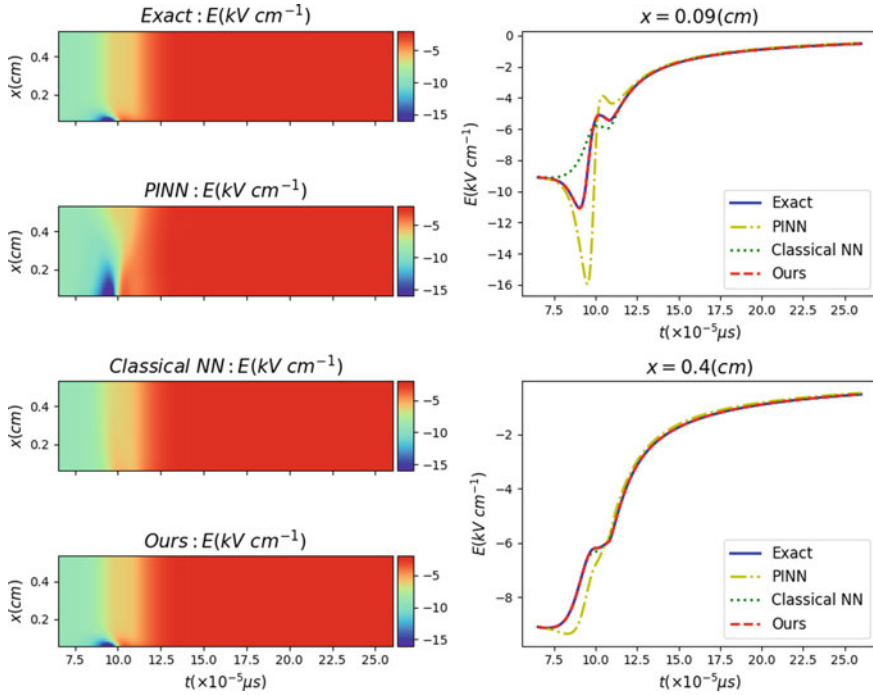


Fig. 2 Prediction of the electric field intensity of low temperature plasma via our method while comparing with those obtained by other methods. PINN is a physics-informed neural network that solves equations. The classical solution is obtained by a standard feedforward neural network without an equation

under the same conditions. In summary, our approach is superior to other methods in modelling complex physical fields [12].

We further analyze the performance of the network from three aspects. The effects of the number of hidden layers, the number of neurons and the number of training data on the electric field intensity, electron density and electron temperature accuracy were studied by using the control variable method.

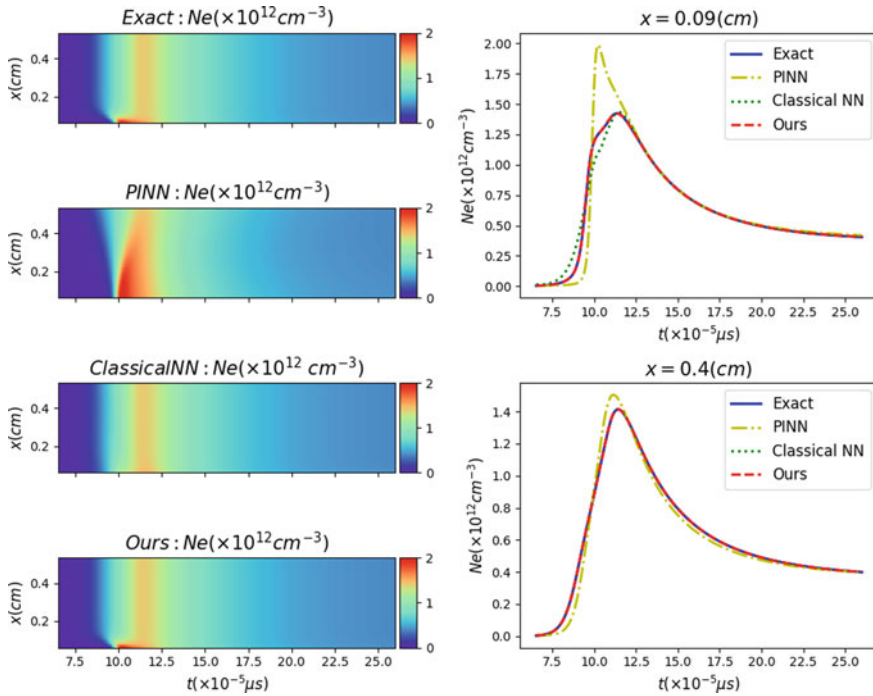


Fig. 3 Prediction of the electron density of low temperature plasma via our method while comparing with those obtained by other methods

Firstly, as shown in Fig. 5(a), we explore the effect of varying the number of training points on the final error, holding all other conditions constant. Obviously, the error changes significantly as the number of points increases with a low number of training data. This is because a highly robust deep learning model requires sufficient data to learn. However, as the amount of training data increases, the model becomes more computationally heavy, and the performance gain when increasing the number of points is slight. Secondly, as shown in Fig. 5(b) and Fig. 5(c), we explore the effect of varying the number of training points and neurons on the final error, holding all other conditions constant. From these two figures, it can be seen that the prediction accuracy does not change significantly with the number of hidden layers and neurons increasing. A qualitative change in the results cannot be achieved by the above parameters, but by exploring a better topologic structure of the network.

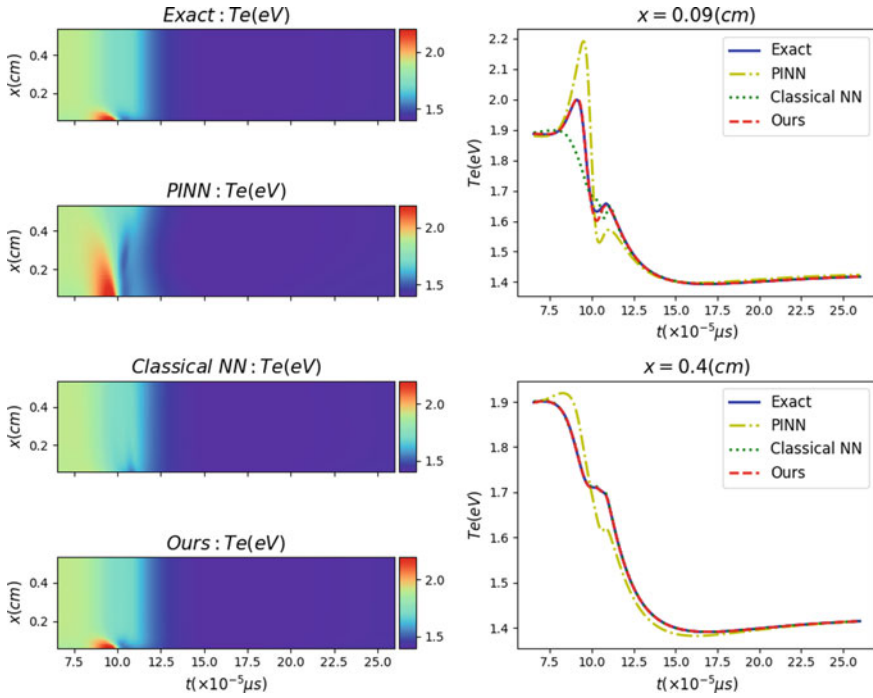


Fig. 4 Prediction of the electron temperature of low temperature plasma via our method while comparing with those obtained by other methods

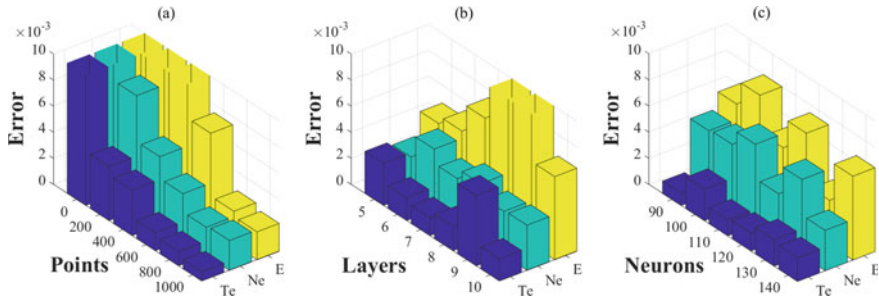


Fig. 5 **a** Effect of the amount of training data on the error for simulating low temperature plasma with the deep learning method. **b** Effect of the number of hidden layers on the error. **c** Effect of the number of neurons in each hidden layer on the error

4 Conclusion

In this paper, we present a deep learning method for complex physical field simulation. Treating the partial differential equation as a natural constraint brings machine learning more in line with the laws of physics. The power of our method in this kind of task is illustrated by modeling numerical investigations on low-temperature plasma. This approach could provide a prospective and new numerical tool for complex physical fields. In future work, simulations based on this method could be extended from local to global simulations while maintaining the simulation performance in areas with abrupt changes.

Acknowledgements This work has been supported by the National Science Fund for Distinguished Young Scholars (Grant No. 51925703) and the National Natural Science Foundation of China (Grant Nos. 51637010, 52077129 and 51807190).

References

1. Thuerey, N., Holl, P., Mueller, M., et al.: Physics-based deep learning. arXiv preprint [arXiv:2109.05237](https://arxiv.org/abs/2109.05237) (2021)
2. Saxena, D., Cao, J.: Generative adversarial networks (GANs) challenges, solutions, and future directions. *ACM Comput. Surv. (CSUR)* **54**(3), 1–42 (2021)
3. Han, Z., Yu, S., Lin, S.B., et al.: Depth selection for deep ReLU nets in feature extraction and generalization. *IEEE Trans. Pattern Anal. Mach. Intell.* **44**(4), 1853–1868 (2020)
4. Raissi, M., Perdikaris, P., Karniadakis, G.E.: Physics-informed neural networks: a deep learning framework for solving forward and inverse problems involving nonlinear partial differential equations. *J. Comput. Phys.* **378**, 686–707 (2019)
5. Xia, W., Liu, D.: Discharge characteristics and bactericidal effect of ar plasma jet treating ethanol aqueous solution. *Trans. China Electrotechnical Soc.* **36**(4), 765–776 (2021)
6. Xu, H., Chen, Z., Liu, D.: Aqueous solutions treated by cold atmospheric plasmas: a review of the detection methods of aqueous reactive species. *Trans. China Electrotechnical Soc.* **35**(17), 3561–3582 (2020)
7. Wang, R., Li, Z., Hu, P., Yang, Y., Xia, Z.: Review of research progress of plasma chemical warfare agents degradation. *Trans. China Electrotechnical Soc.* **36**(13), 2767–2781 (2021)
8. Zhan, Z., Ruan, H., Lü, F., Liu, W., Li, Z., Xie, Q.: Plasma fluorinated epoxy resin and its insulation properties in C₄F₇N/CO₂ mixed gas. *Trans. China Electrotechnical Soc.* **35**(8), 1787–1798 (2020)
9. Lu, L., Jin, P., Karniadakis, G.E.: DeepONet: learning nonlinear operators for identifying differential equations based on the universal approximation theorem of operators. arXiv preprint [arXiv:1910.03193](https://arxiv.org/abs/1910.03193) (2019)
10. Lu, L., Meng, X., Mao, Z., et al.: DeepXDE: a deep learning library for solving differential equations. *SIAM Rev.* **63**(1), 208–228 (2021)

11. Li, Z., Kovachki, N., Azizzadenesheli, K., et al.: Fourier neural operator for parametric partial differential equations. arXiv preprint [arXiv:2010.08895](https://arxiv.org/abs/2010.08895) (2020)
12. Zhong, L., Gu, Q., Wu, B.: Deep learning for thermal plasma simulation: solving 1-D arc model as an example. *Comput. Phys. Commun.* **257**, 107496 (2020)
13. Zhong, L., Wu, B., Wang, Y.: Low-temperature plasma simulation based on physics-informed neural networks: frameworks and preliminary applications. *Phys. Fluids* **34**(8), 087116 (2022)
14. Pang, G., Lu, L., Karniadakis, G.E.: fPINNs: fractional physics-informed neural networks. *SIAM J. Sci. Comput.* **41**(4), A2603–A2626 (2019)
15. Sirignano, J., Spiliopoulos, K.: DGM: a deep learning algorithm for solving partial differential equations. *J. Comput. Phys.* **375**, 1339–1364 (2018)
16. Liu, D.C., Nocedal, J.: On the limited memory BFGS method for large scale optimization. *Math. Program.* **45**(1), 503–528 (1989)
17. Byrd, R.H., Hansen, S.L., Nocedal, J., et al.: A stochastic quasi-Newton method for large-scale optimization. *SIAM J. Optim.* **26**(2), 1008–1031 (2016)

Multi-objective Coordinated Charging Strategy for Electric Vehicles Considering Dynamic Time-of-Use Electricity Price



Zeyu Hou, Yong Li, Yixiu Guo, Xuebo Qiao, Zhenyu Zhang, and Yijia Cao

Abstract Large-scale electric grid connection of electric vehicles will affect the reliable and economic operation of power grid. Meanwhile, the traditional time-of-use price is relatively fixed and not flexible. Aiming at the above problems, the paper comprehensively considers the time-of-use price, load variation and users' willingness to charge, and proposes a multi-objective coordinated charging strategy for electric vehicles (EVs) considering dynamic time-of-use electricity price. Firstly, the EVs charging behavior characteristics are analyzed using the measured EVs charging data of a public charging station in Hunan Province, and the dynamic time-of-use price model is given. Secondly, an EV orderly charging optimization model is constructed, which is aimed at minimum peak-valley difference, minimum daily load variance, minimum user charging cost of distribution network. Then, a Genetic Simulated Annealing Particle Swarm Optimization (GSAPSO) algorithm based on adaptive inertial weight is proposed. Finally, the rationality and effectiveness of the proposed strategy are verified by simulation of typical scenarios. The simulation results show that the coordinated charging strategy solved by dynamic time-of-use price and GSAPSO algorithm can better reduce the peak-valley difference, the daily

Z. Hou (✉) · Y. Li · Y. Guo · X. Qiao · Z. Zhang · Y. Cao
College of Electrical and Information Engineering, Hunan University, Changsha 410082, China
e-mail: zeyuhou@hnu.edu.cn

Y. Li
e-mail: yongli@hnu.edu.cn

Y. Guo
e-mail: yixiuguo@hnu.edu.cn

X. Qiao
e-mail: xbq1992@hnu.edu.cn

Z. Zhang
e-mail: zhenyuzhang@hnu.edu.cn

Y. Cao
e-mail: yjcao@hnu.edu.cn

load variance, and the charging cost of users. As the responsiveness of electric vehicles participating in the coordinated charging strategy increases, the optimization effect is more obvious.

Keywords Electric vehicles · Dynamic time-of-use price · coordinated charging · GSAPSO algorithm

1 Introduction

Under the strategy of “carbon peak and carbon neutrality”, our country is actively building a low-carbon energy system to reduce carbon emissions. At the same time, it is imperative to implement green transportation. On the one hand, the promotion of EVs can reduce the use of traditional fossil energy, on the other hand, it can effectively regulate the demand-side energy structure [1, 2]. According to statistics, the scale of EVs in my country is developing rapidly every year. The number of EVs in 2020 is about 4 million units. In 2021, the number of EVs is about 6.4 million units. Due to the uncertain and intermittent characteristics of EV users’ charging behavior [3, 4], EVs charging is regarded as a new form of power load. Large-scale EVs unordered access to power grid charging will have an impact on the reliable and economic operation of the grid. It is prone to problems such as the increase of power grid peak value due to the coincidence of load peak period, the transformer load exceeding the limit, and the load fluctuation increasing. Therefore, formulating an orderly charging strategy for EVs will help to improve the security and reliability of the grid and promote its economic operation [5–7].

It is usually necessary to consider various factors such as electricity price type, optimization model and solving algorithm in order to realize EVs coordinated charging. In terms of electricity price types, the reference [8] proposed a dual-sequence valley period orderly charging method considering time-of-use electricity price. This method effectively reduced the peak-valley difference and user charging costs. Reference [9] realizes EVs optimal scheduling through dynamic non-cooperative game. The dynamic electricity price proposed in this paper is jointly determined by parameters such as total load, transformer load rate and electricity price coefficient. Reference [10] proposes a distributed control method for EVs charging based on a multi-agent system, and iteratively corrects the virtual electricity price to realize EVs orderly charging. In terms of optimization model and solution algorithm, reference [11] establishes a dual-objective optimization model to control charging costs and reduce grid fluctuations, and used the TOPSIS ranking method to quantitatively analyze the charging demand of users, realizing orderly charging and reducing users’ charging costs and power grid fluctuations. Reference [12] propose a charging model that takes the owners’ charging demand and the safe operation of distribution equipment as constraints, and aims to “peak cutting and valley filling” and improves operators’ profits, and finally achieves EVs orderly charging optimization. Reference [13, 14] all start from the interests of both the power grid and users,

and build EVs coordinated charging optimization methods related to the owners' demand and distribution network load, and use the improved CS algorithm and GA to solve the problem.

In terms of electricity price types, most of the above literature only consider the orderly charging strategy guided by the traditional time-of-use price, while the orderly charging strategy guided by the dynamic price does not fully consider EV users' willingness to charge and load changes. In terms of optimization model and solution algorithm, some literatures currently use traditional optimization algorithms, which have certain limitation in solving optimization models. The solution process is easy to stay in local optimum, resulting in the final result is not the best result.

Therefore, this paper proposes a multi-objective coordinated charging strategy for electric vehicles considering dynamic time-of-use electricity price. Firstly, using the actual charging data of EV users in a public charging station in Hunan Province, the characteristics of charging behavior are analyzed. Secondly, considering the dynamic time-of-use price, the EV coordinated charging optimization model is established to reduce the load peak-valley difference, reduce the variance of daily load, and reduce the users' charging cost. Then, the paper proposes a GSAPSO algorithm based on adaptive inertia weight, and the algorithm is used to solve the charging strategy. Finally, the effectiveness and feasibility of the proposed method are verified for several typical scenario simulations.

2 EV Charging Behavior Characteristics and Dynamic Time-of-Use Electricity Price

2.1 The EV Charging Behavior Characteristics

The data used in this experiment is the EV charging data measured by a public charging station in a certain area of Hunan Province. The data mainly include start charging time, end charging time, the initial state of charge (SOC), end charging SOC, charging capacity, charging current, etc. By sorting and analyzing the measured data, the following four main EV charging behavior characteristics are obtained.

1. The EVs starting charging time t_s in one day approximately obeys $N(\mu_{T_i}, \sigma_{T_i})$ distribution. Its expression is as follows:

$$f_T(t_s) = \sum_{i=1}^n \frac{\alpha_i}{\sigma_{T_i} \sqrt{2\pi}} e^{\left[-\frac{(t_s - \mu_{T_i})^2}{2\sigma_{T_i}^2} \right]} \quad (1)$$

where, the mean values μ_{T_1} , μ_{T_2} , and μ_{T_3} of EV charging time are 33.65, 61.42, and 80.98, respectively; the standard deviations σ_{T_1} , σ_{T_2} , and σ_{T_3} are 8.70, 4.52, and 6.47, respectively; the coefficients α_1 , α_2 , and α_3 are 0.352, 0.208, and 0.440.

2. The EVs start charging SOC approximately obeys $N(\mu_s, \sigma_s)$ distribution. Its expression is as follows:

$$f_s(SOC_s) = \frac{1}{\sigma_s \sqrt{2\pi}} e^{\left[-\frac{(SOC_s - \mu_s)^2}{2\sigma_s^2}\right]} \quad (2)$$

where, the mean value μ_s of the start charging SOC is 0.47; the standard deviation σ_s is 0.22.

3. The EVs end charging SOC approximately obeys Beta distribution. Its expression is as follows:

$$f_e(SOC_e) = \frac{\Gamma(a+b)}{\Gamma(a)\Gamma(b)} SOC_e^{a-1} (1 - SOC_e)^{b-1} \quad (3)$$

where, a and b are respectively expressed as parameters of the Gamma function, a is 127.46, and b is 0.19.

4. The EV charging time is calculated as follows:

$$T_i = \frac{(SOC_{i,end} - SOC_{i,start})C_i}{\eta_c P_c} \quad (4)$$

where, T_i represents the charging time of the i -th EV; $SOC_{i,start}$ represents the SOC of the i -th EV at the start charging; $SOC_{i,end}$ is the SOC after the expected charging end of the i -th EV; C_i represents the rated battery capacity of the i -th EV; P_c represents the charging power of the charging pile to charge EV; η_c represents the charging efficiency.

2.2 The EV Charging Behavior Characteristics

The traditional time-of-use price is usually divided into three periods, consisting of peak period, normal period and valley period, and the price flexibility is not high. Compared the traditional price, the dynamic time-of-use price is more flexible and accurate. It can change with the changes of load and other factors.

This paper uses the time-of-use price in Table 1 as the basis to formulate the dynamic time-of-use price. This price combines the time-of-use price, the current load change and the users' willingness to charge, so that the feedback between the users' charging choice and the electricity price becomes bidirectional. The dynamic time-of-use price model consists of Eqs. (5)–(7). The electricity price floating factor in the model consists of the ratio of the overall load to the maximum capacity of the transformer and the EV charging willingness. In addition, EV charging willingness also considers the proportion of disordered charging in the entire charging. When the overall load and disordered charging proportion are too high, the electricity price will increase accordingly, and vice versa.

Table 1 Division of time-of-use price

Time divisions	Periods	The time-of-use price (¥/ kWh)
valley period	00:00–08:00	0.365
normal period	12:00–14:30 、 21:00–24:00	0.687
peak period	08:00–12:00 、 14:30–21:00	0.869

$$\xi_{i,w}(t) = 1 - \frac{SOC_{i,w}(t)}{SOC_{i,wend}} \tag{5}$$

$$\xi_{EV}(t) = \frac{\sum_{i=1}^{N_w} \xi_{i,w}(t)}{\sum_{i=1}^N x_{i,t}} \tag{6}$$

$$R(t) = R_S(t) + \left(\frac{P_b(t) + \sum_{i=1}^N P_e x_{i,t}}{P_{max}} + \xi_{EV}(t) \right) R_S(t) \tag{7}$$

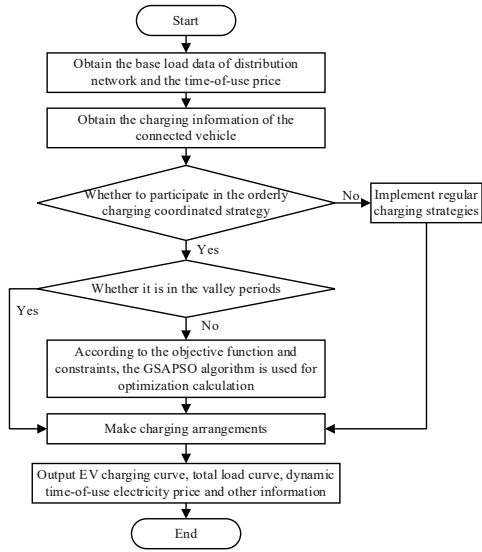
where, $SOC_{i,w}(t)$ represents the SOC of the i -th disordered charging EV at time t ; $SOC_{i,wend}$ represents the SOC after the expected charging end of the i -th disordered charging EV; $\xi_{i,w}(t)$ represents the personal charging willingness of the i -th disorderly charging EV at time t ; $\xi_{EV}(t)$ is the overall vehicle charging willingness at time t ; $R_S(t)$ represents the time-of-use price at time t ; $P_b(t)$ represents the grid base load at time t ; P_e represents the EV charging power; N is the total number of EVs; N_w represents the total number of disordered charging EVs; P_{max} is the maximum capacity value of the transformer; $R(t)$ is the dynamic time-of-use price at time t ; $x_{i,t}$ is the EV charging state.

3 EVs Coordinated Charging Strategy Model

3.1 EVs Coordinated Charging Strategy

In the first stage, users choose whether to participate in the coordinated charging strategy according to the price information and their own charging habits. If EV user does not participate in the coordinated charging, the conventional charging strategy is implemented. If the user participates in the coordinated charging, it is judged whether EV enters the charging station and starts charging whether it is in

Fig. 1 Flow chart of coordinated charging strategy



the valley period. If it is in the valley period, it will arrange to charge; otherwise, it will enter the second stage of charging optimization. In the second stage, the second-stage is charging optimization for all the remaining EVs, and the GSAPSO algorithm is used to optimize the charging according to the objective functions and constraints. Through two-stage process, the entire EV charging strategy is realized. The coordinated charging strategy flow is shown in Fig. 1.

3.2 EVs Coordinated Charging Strategy

The Objective Functions. This paper starts from the impact of the charging cost of users and large-scale EVs on the distribution network. Based on the dynamic time-of-use price, EVs coordinated charging optimization model is constructed, which is aimed at minimum peak-valley difference, minimum daily load variance, minimum user charging cost of distribution network.

1. The minimum peak-valley difference

$$F_1 = \min \left(\max_{t \in [1, T]} \left(P_b(t) + \sum_{i=1}^N P_e x_{i,t} \right) - \min_{t \in [1, T]} \left(P_b(t) + \sum_{i=1}^N P_e x_{i,t} \right) \right) \quad (8)$$

2. The minimum daily load variance

$$F_2 = \min \left(\frac{1}{T} \sum_{t=1}^T \left(P_b(t) + \sum_{i=1}^N P_e x_{i,t} - \frac{1}{T} \sum_{t=1}^T \left(P_b(t) + \sum_{i=1}^N P_e x_{i,t} \right) \right)^2 \right) \quad (9)$$

3. The minimum charging cost for users

$$F_3 = \min \left(\sum_{t=1}^T \sum_{i=1}^N P_e T_c R(t) x_{i,t} \right) \quad (10)$$

This paper normalizes the above three objective functions F_1 , F_2 , and F_3 to form a consistent objective function.

$$\min F(x) = \sum_{k=1}^n \lambda_k f_k(x) \quad (11)$$

$$s.t. \begin{cases} 0 \leq \lambda_k \leq 1 \\ \sum_{k=1}^n \lambda_k = 1 \end{cases} \quad (12)$$

where, $f_k(x)$ is the normalized function; λ_k is the weight coefficient.

The Constraints

1. The constraint on the number of charging EVs

$$N(t) \leq N \quad (13)$$

2. The constraint on EVs charging time

$$\frac{(SOC_{i,end} - SOC_{i,s})B_i}{\eta P_e} \leq T_{i,end} - T_{i,start} \quad (14)$$

where, $T_{i,end}$ is the charging end time of the i -th EV; $T_{i,start}$ represents the charging start time of the i -th EV; B_i represents the rated capacity of the i -th EV battery.

3. The constraint on EVs battery capacity

$$SOC_{i,s} B_i \leq SOC_{i,s} B_i + \sum_{j=1}^T P_e T_c x_{i,t} \eta \leq B_i \quad (15)$$

where, $SOC_{i,s}$ represents the initial SOC of the i -th EV; η represents the charging efficiency.

4. The constraint on the maximum capacity of transformers

$$P_b(t) + \sum_{i=1}^N P_e x_{i,t} \leq P_{max} \quad (16)$$

4 Genetic Simulated Annealing Particle Swarm Optimization

4.1 The Algorithm Improvement

Particle Swarm Optimization (PSO) is a traditional optimization algorithm based on the simulation of bird predation behavior. PSO has some advantages of fast convergence speed and high precision in the solution process, but the particles are easy to “premature” and stay in the local optimum.

This paper is to solve the shortcomings of PSO, a Genetic Simulated Annealing Particle Swarm Optimization (GSAPSO) algorithm based on adaptive inertia weights is proposed. The algorithm introduces the Genetic Algorithm (GA) and the Simulated Annealing (SA) into the PSO algorithm. Through the crossover and variation in GA, the population becomes diverse. The Metropolis criterion in SA enables particles to jump out of the local optimal solution, so as to improve the ability of the algorithm to search for the global optimal solution. At the same time, the inertia weight ω in PSO algorithm is adjusted to an adaptive mechanism, so that the particle swarm movement speed is more suitable. The flow chart of GSAPSO algorithm is shown in Fig. 2.

4.2 The Algorithm Parameter Setting

1. Inertia weight setting

$$\omega = \omega_{max} - (\omega_{max} - \omega_{min}) \left(\frac{k}{k_{max}} \right)^2 \quad (17)$$

where, ω_{max} and ω_{min} are respectively the maximum values and minimum values of inertia weights in GSAPSO. Set ω_{max} and ω_{min} to 0.9 and 0.4 respectively; k is the k -th iteration number; k_{max} is the total number of iterations.

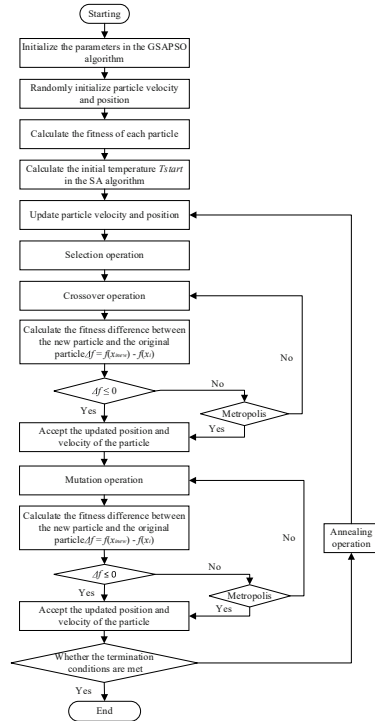
2. Initial temperature setting

$$T_{start} = \frac{f(G_{best})}{\ln 5} \quad (18)$$

where, $f(G_{best})$ represents the optimal fitness of the initial particle swarm.

3. Annealing coefficient setting

Fig. 2 Flow chart of GSAPSO algorithm



$$T = \delta t \tag{19}$$

In order to enhance the probability of finding the global optimum, the simulated annealing process was slowed down, and the annealing coefficient δ was set to 0.95.

5 Analysis of Examples

In the simulation case, the typical conventional load data of a region in Hunan Province is used as the basic load. Considering the charging characteristics of the actual EVs, the EV charging start time, the starting charging SOC, and the ending charging SOC satisfy the EV charging behavior characteristics in Sect. 1.1, and are obtained by sampling. The maximum capacity of the transformer is set to 1200kVA. In addition, according to the actual situation, the EV time-sharing charging fee consists of the electricity purchase cost and the service cost. The electricity purchase cost is the time-of-use prices in Table 1. The charging service fee is ¥0.6. The prices for EV charging during peak periods, normal periods, and valley periods are ¥1.469, ¥1.287, and ¥0.965, respectively. In order to verify the feasibility and effectiveness of the proposed method, four typical scenarios with different electricity price strategies,

different vehicle numbers, different responsiveness and different algorithms are set up for comparative analysis.

5.1 Optimization Results Under Different Electricity Price Strategies

Based on a setting scenario of 800 EVs and 70% responsiveness, the orderly charging strategy under the time-of-use price and the dynamic time-of-use price are simulated. The time-of-use price and dynamic time-of-use price curve are shown in Fig. 3. The ordered charging load curves under the guidance of two different electricity price strategies are shown in Fig. 4, the comparison results are shown in Table 2.

According to Fig. 3, compared with the time-of-use price, the dynamic time-of-use price is more flexible. During the valley periods, due to the low current load and a small proportion of disordered charging, the dynamic time-of-use price is lower.

Fig. 3 The time-of-use price curve and the dynamic time-of-use price curve

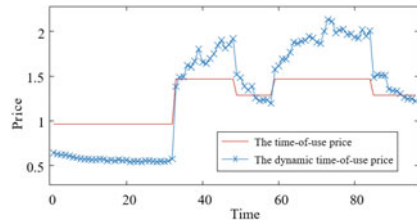


Fig. 4 Coordinated charging load curves under different electricity price strategies

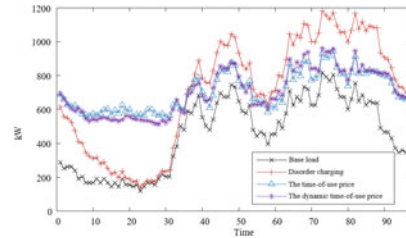


Table 2 Optimization comparison results under different electricity price strategies

Parameters	The dynamic time-of-use price	The time-of-use price
The peak valley difference/kW	391.79	447.89
The user charging cost/¥	24,766.62	28,129.38
The load variance/kW ²	1.27×10^4	1.81×10^4

During the peak periods, due to the large proportion of disordered charging and the peak load period, the dynamic time-of-use price is higher. During the normal periods, the two electricity prices are equal. From the perspective of the whole-day prices, the average of the two prices is similar.

As can be seen from Fig. 4 and Table 2, the two different electricity price strategies can effectively reduce daily load variance, the peak-valley difference and user charging cost. However, the peak-valley difference of the dynamic time-of-use price is smaller, which is reduced by 12.53% compared with the other one. The variance of daily load is smaller, which is reduced by 29.83% compared with the time-of-use price. The charging cost for users are lower, which is 11.95% less than the other one. During the peak periods, the load of the dynamic time-of-use price is almost lower than the other price. During the valley periods, the load is basically higher than that of the time-of-use price. The coordinated charging effect under the guidance of the dynamic time-of-use price is better, and the effect of peak regulation and load fluctuation is better.

5.2 Optimization Results for Different Numbers of Vehicles

In the future, EVs will continue to increase and the scale will gradually expand. In this paper, 500, 800 and 1000 EVs are analyzed under disordered charging and ordered charging with 70% responsiveness. The coordinated charging load curves under different numbers of vehicles are shown in Fig. 5, and the comparison results of disordered charging and coordinated charging are shown in Table 3.

According to Fig. 5 and Table 3, with the continuous expansion of EVs scale, the coordinated charging strategy has a more obvious effect, and the charging load during the peak periods is effectively transferred to the valley periods. Under the setting of 1,000 EVs, the peak-valley value of coordinated charging is reduced by 775.10 kW, and the charging cost is reduced by 31.54%. In the case of 500 EVs, the peak-valley value of coordinated charging is reduced by 422.36 kW, and the charging cost is reduced by 38.41%. In addition, when the EVs scale is larger, the larger the range of which can be used as a regulated load, the more obvious the peak regulation effect, the more stable the load change, and the more conducive to regulating the load size of the distribution network.

Fig. 5 Coordinated charging load curves under different numbers of vehicles

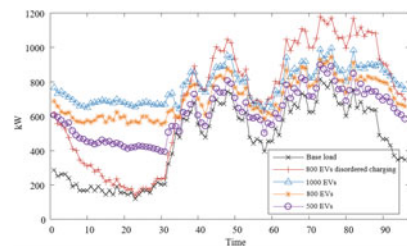


Table 3 Optimization comparison results under different numbers of vehicles

Parameters	500 EVs disordered charging	800 EVs disordered charging	1000 EVs disordered charging
The peak valley difference/kW	925.01	1042.09	1139.09
The user charging cost/¥	24,084.76	40,030.69	51,695.76
The load variance/kW ²	8.28×10^4	1.09×10^5	1.32×10^5
Parameters	500 EVs coordinated charging	800 EVs coordinated charging	1000 EVs coordinated charging
The peak valley difference/kW	502.65	391.79	363.99
The user charging cost/¥	14,834.82	24,766.62	35,389.01
The load variance/kW ²	1.91×10^4	1.27×10^4	1.02×10^4

5.3 Optimization Results Under Different Responsiveness

Based on the setting of 800 EVs, the coordinated charging strategies under three scenarios of responsiveness of 30%, 50% and 70% are analyzed. The coordinated charging load curves under different responsivities are shown in Fig. 6, the comparison results are shown in Table 4.

Fig. 6 Coordinated charging load curves under different responsivities

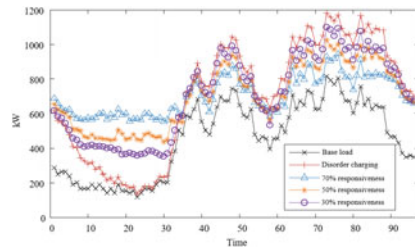


Table 4 Optimization comparison results under different responsivities

Parameters	30% responsiveness	50% responsiveness	70% responsiveness
The peak valley difference/kW	747.23	589.46	391.79
The user charging cost/¥	35,315.97	29,873.23	24,766.62
The load variance/kW ²	5.80×10^4	3.44×10^4	1.27×10^4

According to Fig. 6 and Table 4, compared with disordered charging, the coordinated charging strategy proposed can effectively transfer of charging load. It can significantly reduce the peak-valley difference and the load variance. The operating pressure of the transformer is effectively reduced. When the EVs responsivity is higher, the peak-valley difference is smaller, the load variance is smaller, and the charging cost of the user is reduced. In a scenario of 70% responsiveness, the peak-valley difference is 391.79 kW, which is 62.40% lower than the case of disordered charging, and the user cost is saved by ¥15,264.07. When the responsivity is 30%, the peak-valley difference, load variance, and user charging cost are reduced by 28.30%, 46.79%, and 11.78% respectively. To a certain extent, the effect of “peak cutting and valley filling”, load fluctuation leveling and user charging cost saving can be achieved.

5.4 Optimization Results Under Different Algorithms

In order to verify the effectiveness of the GSAPSO algorithm, the optimization results of the proposed GSAPSO algorithm, GAPSO algorithm and PSO algorithm are respectively compared under the scenario setting of 800 EVs and 70% responsiveness. The coordinated charging load curves under different algorithms are shown in Fig. 7, the comparison results are shown in Table 5.

As can be seen from Fig. 7 and Table 5, the peak-valley difference after the optimization of the GSAPSO algorithm reduces by 23.36% compared with the PSO optimization result, and reduces by 16.32% compared with the GAPSO optimization result. In terms of user charging cost, it is ¥1179.56 less than the GAPSO algorithm result, and ¥1821.18 less than the PSO algorithm result. In terms of load variance,

Fig. 7 Coordinated charging load curves under different algorithms

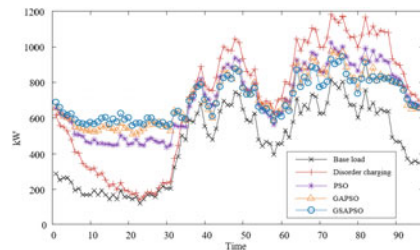


Table 5 Optimization comparison results under different algorithms

Parameters	PSO	GAPSO	GSAPSO
The peak valley difference/kW	511.24	468.22	391.79
The user charging cost/¥	26,587.80	25,946.18	24,766.62
The load variance/kW ²	2.22×10^4	1.88×10^4	1.27×10^4

the result of GSAPSO algorithm is 32.45% lower than that of GAPSO algorithm, and 42.79% lower than that of PSO algorithm. In general, the optimization effect of the GSAPSO algorithm is better than the other two algorithms, which enhances the global search ability, and can avoid staying in the local optimum and find the global optimum. The effectiveness of the proposed GSAPSO algorithm is verified.

6 Conclusion

This paper proposes a multi-objective coordinated charging strategy for EVs considering dynamic time-of-use prices. Based on the measured data of a charging station in Hunan Province, the 24 h EV load demand was simulated. The coordinated charging scenarios under different electricity price strategies, different numbers of vehicles, different responsiveness and different algorithms are analyzed, and the feasibility and effectiveness of the proposed coordinated charging strategy are verified. The simulation analysis draws the following conclusions:

- 1) Compared with the coordinated charging based on the time-of-use price, the proposed dynamic time-of-use price strategy is more flexible and accurate. It can better guide EVs to participate in the coordinated charging, reduce the peak-valley difference, save users' charging cost, and make the load curve smoother.
- 2) Using the proposed GSAPSO algorithm based on adaptive inertia weight, the optimization effect is significantly improved compared with the PSO and GAPSO algorithms, and it effectively avoids staying in local optimum.
- 3) As the responsiveness of EVs participating in coordinated charging increases or the increase of vehicle size, the greater the range of EVs as regulated load, the better the optimization effect, and the more obvious the "peak cutting and valley filling" of the grid.

In future research, the authors will analyze the coordinated charging of large-scale EVs in complex scenarios such as different charging modes. In order to improve the utilization rate of each charging station, the information exchange of multiple public area charging stations will be considered, and unified management will guide EVs to achieve more economical and safe coordinated charging.

Acknowledgements This research is supported by the International Science and Technology Cooperation Program of China (2018YFE0125300), the Excellent Innovation Youth Program of Changsha (KQ2009037), and the National Nature Science Foundation of China (52061130217).

References

1. Wang, Z.: Research on interactive technology of orderly charging and vehicle network for electric vehicles under dual carbon goals. *Electr. Power Eng. Technol.* **40**(05), 1 (2021). (in Chinese)
2. Pradhan, P., Ahmad, I., Habibi, D., et al.: Reducing the impacts of electric vehicle charging on power distribution transformers. *IEEE Access* **8**, 210183–210193 (2020)
3. Jahangir, H., Gougheri, S.S., Vatandoust, B., et al.: Plug-in electric vehicle behavior modeling in energy market: a novel deep learning-based approach with clustering technique. *IEEE Trans. Smart Grid* **11**(6), 4738–4748 (2020)
4. Gan, L., Chen, X., Yu, K., Zheng, J., Du, W.: A probabilistic evaluation method of household EVs dispatching potential considering users' multiple travel needs. *IEEE Trans. Ind. Appl.* **56**(5), 5858–5867 (2020)
5. Guo, J., Wen, F.: Impact of electric vehicle charging on power system and relevant countermeasures. *Electr. Power Autom. Equipment* **35**(06), 1–9 (2015). (in Chinese)
6. Al-Ogaili, A.S., Juhana, T., Rahmat, N.A., et al.: Review on scheduling, clustering, and forecasting strategies for controlling electric vehicle charging: challenges and recommendations. *IEEE Access* **7**(1), 128353–128371 (2019)
7. Habib, S., Khan, M.M., Abbas, F., et al.: A comprehensive study of implemented international standards, technical challenges, impacts and prospects for electric vehicles. *IEEE Access* **6**, 13866–13890 (2018)
8. Su, H., Liang, Z.: Orderly charging control based on peak-valley electricity tariffs for household electric vehicles of residential quarter. *Electr. Power Autom. Equipment* **35**(06), 17–22 (2015). (in Chinese)
9. Chen, L., Pan, Z., Yu, T., et al.: Real-time optimal dispatch of large-scale electric vehicles based on dynamic non-cooperative game theory. *Autom. Electr. Power Syst.* **43**(24), 32–40+66 (2019). (in Chinese)
10. Yu, N., Yu, F., Huang, D., et al.: Multi-agent system based charging and discharging of electric vehicles distributed coordination dispatch strategy. *Power Syst. Prot. Control* **47**(5), 1–9 (2019). (in Chinese)
11. Shen, G., Chen, G., Zhao, Y., et al.: Orderly charging optimization strategy of an electric vehicles based on double objective hierarchical optimization and TOPSIS ranking. *Power Syst. Prot. Control* **49**(11), 115–123 (2021). (in Chinese)
12. Chen, K., Ma, Z., Zhou, S., et al.: Charging control strategy for electric vehicles based on two-stage multi-target optimization. *Power Syst. Prot. Control* **48**(1), 65–72 (2020). (in Chinese)
13. Li, J., Yang, X., Zhang, L., et al.: Research on hierarchical control strategy of orderly charging of large-scale electric vehicles. *Electr. Measur. Instrum.* **58**(5), 168–175 (2021). (in Chinese)
14. Wu, J., Qiu, X., Pan, Y., et al.: Research on orderly charging strategy of electric vehicle based on improved chicken swarm optimization. *Electr. Measur. Instrum.* **56**(9), 97–103 (2019). (in Chinese)

Coordinated Control of Commutation Failure Prevention Under UHVDC Multi-infeed System



Zhiwei Wang, Yangchen Tan, Xin Liu, Wenzhuo Wang, Zheng Li, Zhaoyang Wei, Biao Su, and Jiahao Wang

Abstract Firstly, this paper analyzes the impact of AC failure at different electrical distance on the start-up time of commutation failure prevention control (CFPREV). It is found that the startup time of CFPREV far from the AC failure point is later than the time of commutation failure of the inverter valve group, so the commutation failure can not be effectively suppressed. Based on the research above, this paper puts forward a coordinated control of CFPREV in UHVDC multi-infeed system. The coordinated controller uses the information of CFPREV near the AC fault point to advance the startup time of CFPREV far from the AC fault point. So it can improve the effect of CFPREV far from the AC fault point to suppress the commutation failure of the inverter valve group. A simulation model is built with reference to a UHVDC multi-feed system in construction. The example results verify the effectiveness of the coordinated controller.

Keywords UHVDC transmission · commutation failure · CFPREV

Z. Wang · Y. Tan (✉) · X. Liu · W. Wang · Z. Li · Z. Wei · B. Su · J. Wang
Northwest Branch of State Grid Corporation of China, Xian 710048, China
e-mail: yangchen_tan@163.com

Z. Wang
e-mail: wangzw@nw.sgcc.com.cn

X. Liu
e-mail: linx2@nw.sgcc.com.cn

W. Wang
e-mail: wangwz@nw.sgcc.com.cn

Z. Li
e-mail: liz0501@nw.sgcc.com.cn

Z. Wei
e-mail: weizy@nw.sgcc.com.cn

B. Su
e-mail: sub@nw.sgcc.com.cn

J. Wang
e-mail: wangjh@nw.sgcc.com.cn

1 Introduction

The electric power generation resources of China are concentrated in the western region, and the load center is located in the eastern coastal area. The mismatch of resources and demand has led to flourishing the UHVDC transmission whose advantages are large transmission capacity and long transmission distance. With the extensive construction of UHVDC transmission in China, multiple UHVDC lines are fed into the same AC system. Power Grid of east China has become a typical UHVDC multi-infeed system.

The receiving end of the UHVDC multi-infeed system is located in the same AC grid, and the electrical coupling between different DC systems is close. At present, relevant literatures have studied the mutual coupling mechanism between UHVDC multi-infeed systems. In reference [1], the reactive power coupling relationship between the inverter stations of adjacent DC systems was studied after the fault of the receiver AC system of the multi-infeed DC system. In reference [2], the influence of sending and receiving end AC system fault on inverter valve groups commutation failure was analyzed. [3] proposed that the CFPREV increases the reactive power demand of the DC system on the receiving AC system. The CFPREV action will affect the adjacent DC system through the electrical coupling of the AC system. [4] and [5] proposed that the control aim of DC current is ambiguous in stage 2 and sending end AC faults can both cause commutation failure.

The detection and suppression methods of commutation failure have been studied in some literatures. [6] used the short circuit ratio of DC multi-infeed system and the critical commutation failure impedance boundary to determine whether the inverter valve groups fail commutation or not. [7] analyzed the influence of DC current and inverter bus voltage on the turn off angle comprehensively, and calculated the critical voltage change rate that caused commutation failure. [8] proposed an improved CFPREV method based on waveform similarity detection. [9] proposed a new LCC-UHVDC topology, which uses controllable capacitors to generate reactive power during commutation to help commutation. In reference [10], the interaction mechanism of commutation failure of high and low end valve groups under UHVDC hierarchical connection to AC grid was studied, and a coordinated CFPREV was proposed. [11] proposed a commutation failure suppression method based on voltage time commutation area prediction. In reference [12], a dynamic compensation control method for turn off angle is proposed by comprehensively considering the influence of DC current, commutation failure voltage amplitude and commutation voltage offset angle to suppress subsequent commutation failure.

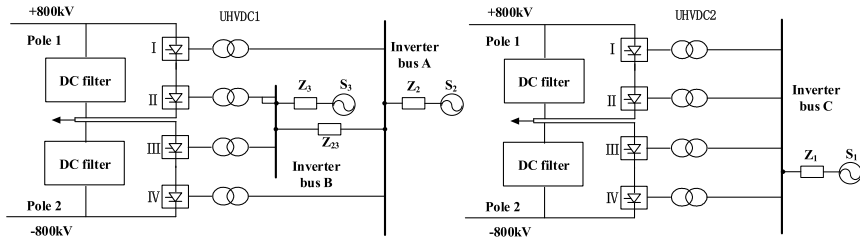


Fig. 1 UHVDC multi-infeed structure

2 Structure and Control Strategy of UHVDC Multi-infeed System

2.1 Structure of UHVDC Multi-infeed System

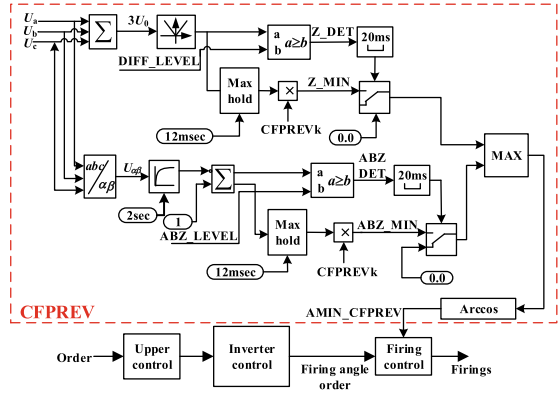
The research model is based on the UHVDC project under planning and construction which is shown in Fig. 1. UHVDC1 and UHVDC2 are fed into the same AC system. HVDC1 is a unique structure that high end inverter valve groups are fed into inverter bus A, meanwhile low end inverter valve groups are fed into inverter bus B. UHVDC2 is normal UHVDC structure that all inverter valve groups are fed into one same inverter bus C.

2.2 CFPREV Control Strategy of UHVDC Multi-infeed System

The function of CFPREV is to prevent commutation failure by advancing the trigger time of the valve group control system when the inverter bus voltage is detected to reduce. Under normal circumstances, every inverter valve group has independent valve group control system. Considering that CFPREV is a part of the inverter valve group control system, the CFPREV of each valve group in the UHVDC system are also independent.

The basic structure of CFPREV is shown in Fig. 2. U_a, U_b and U_c are the instantaneous AC voltage values of the converter bus connected to the valve group; DIFF_LEVEL and ABZ_LEVEL are the threshold value of asymmetric fault detection and symmetric fault detection respectively; CFPREV $_k$ is the proportion coefficient of CFPREV output and voltage drop degree; AMIN_CFPREV is the output of CFPREV, which can determine the trigger angle phase shift of inverter valve group.

Fig. 2 Structure of CFPREV



Symmetric fault detection and asymmetric fault detection are used to detect AC faults. If the voltage drop of inverter bus reaches the action threshold after a AC fault, CFPREV sends an advance trigger signal to the trigger control of valve group, which is determined by the voltage drop of inverter bus (Table 1).

The fault detection of CFPREV is divided into two parts: asymmetric fault detection and symmetrical fault detection. The principle of asymmetric fault detection is to judge an asymmetric fault of AC system by monitoring the zero sequence voltage drop.

$$3U_0 = U_a + U_b + U_c \tag{1}$$

where: $3U_0$ is the zero sequence voltage of three-phase voltage instantaneous value; U_a , U_b and U_c are the instantaneous values of three-phase voltage of the converter bus.

The principle of symmetrical fault detection is to judge a symmetrical fault of AC system according to the drop of the root mean square of U_α and U_β under the two-phase coordinate system which are converted by the instantaneous value of three-phase voltage.

$$\begin{cases} U_\alpha = \frac{2}{3}U_a - \frac{1}{3}(U_b + U_c) \\ U_\beta = \frac{\sqrt{3}}{3}(U_b - U_c) \\ U_{\alpha\beta} = \sqrt{U_\alpha^2 + U_\beta^2} \end{cases} \tag{2}$$

where: U_α is α phase coordinate under two-phase coordinate system; U_β is β phase coordinate under two-phase coordinate system; $U_{\alpha\beta}$ is the root mean square of the above two coordinates.

3 The Coordinated Control of CFPREV in UHVDC Multi-infeed System

3.1 The Strategy of Coordinated Control of CFPREV in UHVDC Multi-infeed System

According to the different electrical distance between the inverter valve group and the AC fault point, this paper names the inverter valve group that is close to the AC fault point as the near fault inverter valve group, and the inverter valve group that is far from the AC fault point as the far fault inverter valve group. The fault of AC system will lead to voltage drop of inverter bus, which will cause commutation failure of inverter valve group. The influence of AC fault on the near fault inverter valve group is greater than that on the far fault inverter valve group, which leads to that the start time of CFPREV of the near fault inverter valve group is earlier than that of the far fault inverter valve group. In extreme cases, the start time of CFPREV of the far fault valve group is later than the time of commutation failure, so that the CFPREV can not be able to effectively suppress the occurrence of commutation failure. In order to improve the suppression effect of the commutation failure of the far fault valve group CFPREV, this paper uses the information of the near fault inverter valve group CFPREV to increase the start time of the far fault inverter valve group CFPREV, which will effectively improve the suppression effect of the commutation failure of the far fault valve group.

The coordinated control of CFPREV in UHVDC multi-infeed system is shown in Fig. 3.

CO_CFPREV1 and CO_CFPREV2 are the output of the coordinated CFPREV, k_{a1} and k_{a2} are the coordinated control coefficients between CFPREV1 and CFPREV1 respectively. For example, CO_CFPREV1 is the maximum value of AMIN_CFPREV1 and AMIN_CFPREV2 multiplied by k_{a1} .

Fig. 3 Coordinated CFPREV under UHVDC multi-infeed system

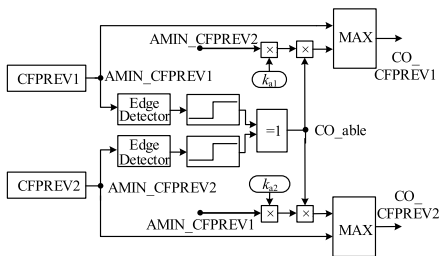
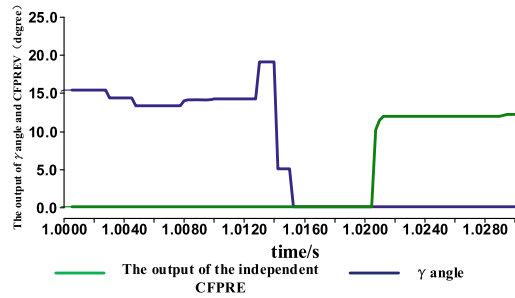


Fig. 4 The comparison diagram of the output of independent CFPREV and γ



3.2 The Effect of the Coordinated Control on Suppressing Commutation Failure under Symmetric Faults

In example 1, the CFPREVs of inverter valve groups of the UHVDC multi-infeed system are independent from each other. Three phase grounding short circuit fault is set near 500 kV converter bus C. The electrical distance between the AC fault point and the 500 kV converter bus C is equivalent to 0.36H reactor. The time of fault occurrence is 1.000 s, and the fault duration is 0.1 s.

The inverter valve groups of UHVDC1 are far from the AC point. The output of the independent CFPREV and the γ angle of the far fault inverter valve groups are shown in Fig. 4.

The γ angle is an important parameter reflecting commutation failure, and the commutation failure occurs to the valve group after the γ angle drops to 0. The simulation results show that the inverter valve group has a commutation failure at 1.014 s, and the start time of CFPREV is 1.021 s. The start time of CFPREV is later than the time of commutation failure, so that the commutation failure cannot be suppressed.

In example 2, the inverter valve groups of UHVDC multi-infeed system adopts the coordinated CFPREV, and the fault is consistent with example 1. Figure 5 shows the comparison between the output of the coordinated CFPREV and the independent CFPREV. The start time of the coordinated CFPREV is 1.006 s, and the start time of the independent CFPREV is 1.021 s. The startup time of the coordinated CFPREV is advanced by 15 ms.

Figure 6 shows the comparison of γ angles between inverter valve group with the independent CFPREV and that with the coordinated CFPREV. The coordinated CFPREV advances the start time, which makes the trigger time of inverter valve groups earlier, so that the commutation failure of inverter valve groups is suppressed effectively.

Fig. 5 Comparison of the output of independent CFPREV and coordinated CFPREV

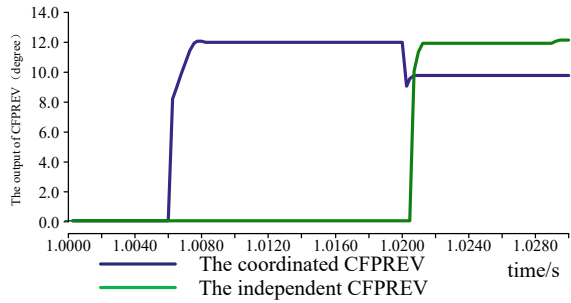
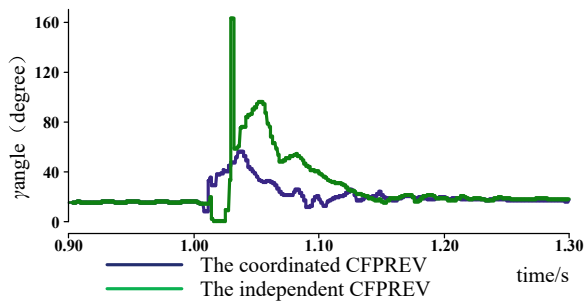


Fig. 6 Comparison of γ between independent CFPREV and coordinated CFPREV



In order to get more simulation examples for verification, the paper sets a series of comparison examples of the coordinated CFPREV and the independent CFPREV. The controller parameters of the above examples are the same as those of examples 1 and 2, and only different three-phase grounding fault parameters are set. Considering that the occurrence time and severity of the AC system fault will affect the commutation failure of the inverter valve groups, the time range of the AC system fault is 1.000–1.009 s, and the equivalent electrical distance between the AC fault point and the near fault converter bus is 0.2–0.5H.

Figure 7 is a comparison diagram of the effect of the coordinated CFPREV and the independent CFPREV in suppressing commutation failure in a series of simulation examples of three-phase ground fault. The white square represents that CFPREVs with or without coordinated control both can avoid commutation failure of far fault inverter valve groups. The light blue square represents that the coordinated CFPREV avoids commutation failure of far fault inverter valve groups, while the independent CFPREV cannot avoid commutation failure. The dark blue square represents that CFPREVs with or without coordinated control cannot avoid commutation failure of far fault inverter valve groups either. For the examples shown in the light blue, the coordinated CFPREV is superior to the independent CFPREV in suppressing commutation failure of inverter valve groups. In the above series of simulation examples, the coordinated CFPREV of most examples is more effective in suppressing commutation failure.

Fig. 7 Comparison of suppression effect of commutation failure between coordinated CFPREV and independent CFPREV under a series of examples

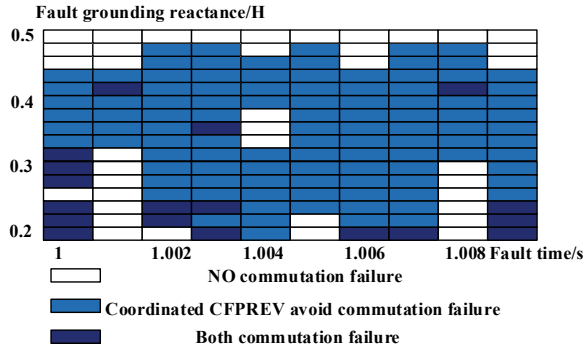


Table 1 Main CFPREV parameters of inverter valve group

DIFF_LEVEL	ABZ_LEVEL	CFPREV _k
0.1405	0.15	0.075

4 Conclusion

Based on the analysis of CFPREV mechanism, a coordinated CFPREV strategy for UHVDC multi-infeed system is proposed. A large number of comparative examples are studied for the above coordinated CFPREV, and the following conclusions are obtained:

- For the independent CFPREV under UHVDC multi-infeed system, the far fault inverter valve groups are less affected by AC fault, and the start time of CFPREV may be later than the time of commutation failure, which cannot effectively suppress the occurrence of commutation failure.
- This paper proposes a coordinated CFPREV under UHVDC multi-infeed system. The controller uses the CFPREV information of the near fault valve group to accelerate the start time of the CFPREV of far fault valve group, which improves the suppression effect of commutation failure of the far fault valve group effectively.


References

1. Ouyang, J., Ye, J., Zhang, Z., et al.: Mechanism and characteristics of successive commutation failure of multi infeed DC transmission system under power grid fault. *Autom. Electr. Power Syst.* **45**(20), 93–99 (2021). (in Chinese)
2. Lin, S., Lei, Y., Liu, J., et al.: Analysis of receiving-side commutation failure mechanism caused by HVDC sending-side system fault. *Proc. CSEE* **42**(5), 1669–1679 (2022). (in Chinese)
3. Li, C., Tan, Y., Xiong, Y., et al.: Coordinated control of commutation failure prevention in UHVDC multi-infeed system. *Power Syst. Technol.* **43**(10), 3532–3542 (2019). (in Chinese)

4. Liu, L., Lin, S., Liu, J., et al.: Analysis and prevention of subsequent commutation failures caused by improper inverter control interactions in HVDC systems. *IEEE Trans. Power Delivery* **35**(6), 2841–2852 (2020)
5. Xiao, H., Li, Y., Lan, T.: Sending end AC faults can cause commutation failure in LCC-HVDC inverters. *IEEE Trans. Power Delivery*. **35**(5), 2554–2557 (2020)
6. Shao, Y., Tang, Y.: Fast evaluation of commutation failure risk in multi-infeed HVDC systems. *IEEE Trans. Power Syst.* **33**(1), 646–653 (2018)
7. Wang, L., Li, F., Yin, C., et al.: Analysis of asymmetric fault commutation failure in A HVDC system with DC current variation. *Power Syst. Prot. Control* **49**(1), 17–22 (2021). (in Chinese)
8. Liu, J., Liu, L., Lin, S.: Improved commutation failure predictive control method based on waveform similarity detection. *Autom. Electr. Power Syst.* **45**(10), 132–139 (2021). (in Chinese)
9. Xue, Y., Zhang, X.: Reactive power and AC voltage control of LCC HVDC system with controllable capacitors. *IEEE Trans. Power Syst.* **32**(1), 753–763 (2017)
10. Xin, J., Shu, Z., Tan, Y., et al.: Coordinated control of commutation failure prevention for UHVDC hierarchical connection to AC grid. *Power Syst. Technol.* **43**(10), 3543–3551 (2019). (in Chinese)
11. Zhu, R., Zhou, X., Luo, A., et al.: Commutation failure suppression method based on voltage time commutation area prediction. *Autom. Electr. Power Syst.* **46**(3), 156–161 (2022). (in Chinese)
12. Zhu, L., Niu, C., Wang, Z., et al.: An extinction angle dynamic compensation control method for suppressing continuous commutation failure. *Proc. CSEE* **41**(22), 7621–7629 (2021). (in Chinese)

Research on Multi-modal Track Association and Fusion Algorithm in Air Defense Weapon System



Zhengzheng Yang , Tong Yao, Yong Hou, Xiaolong Su, Hao Bai, Xiutang Geng, and Binyi Wang

Abstract In the air defense integrated cooperative operation, a multi-modal track association and fusion algorithm is proposed to meet the needs of multi-sensor data fusion of air defense weapon systems. The algorithm constructs a virtual point on a known two-dimensional vector, and then constructs a space triangle with known coordinates of the three vertices based on the point and the vector. Based on the space triangle, calculate the distance from the space point to the straight line, and then obtain the correlation coefficient between any three-dimensional coordinate point in space and two-dimensional vector, and then complete the multi-mode track association fusion processing between three-dimensional air situation and two-dimensional air situation. Simulation experiments show that the algorithm has high track association accuracy, small fusion error, fast processing speed, and advanced technical indicators. It can effectively deal with multi-mode track association and fusion problems in different application scenes, improve the situation awareness and information sharing ability of air defense weapon system, and provide useful reference for the intelligent development of air defense weapon system.

Keywords Air Defense Weapon System · Multi-modal · Track Association and Fusion · Triangle Method

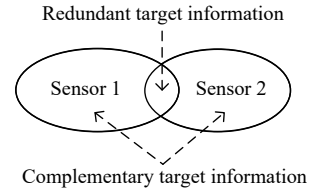
1 Introduction

The air defense weapon system is composed of air defense missiles and anti-aircraft guns, which is an important terminal defense weapon equipment in the air defense system [1–3]. With the rapid development and application of information technology and high-precision fixed point strike technology, as well as the development and improvement of airspace combat mode, the traditional air defense weapon system is

Z. Yang (✉) · T. Yao · Y. Hou · X. Su · H. Bai · X. Geng · B. Wang
Northwest Institute of Mechanical and Electrical Engineering, Xianyang 712099, China
e-mail: yangzzheng2020@163.com

© Beijing Paiké Culture Commu. Co., Ltd. 2023
X. Dong et al. (eds.), *The proceedings of the 10th Frontier Academic Forum of Electrical Engineering (FAFEE2022)*, Lecture Notes in Electrical Engineering 1054, https://doi.org/10.1007/978-981-99-3408-9_32

Fig. 1 Schematic diagram of multi-sensor track association and fusion



facing severe challenges, such as the integration of air and ground multiple equipment, the increasingly complex battlefield geographical environment and electromagnetic interference [4, 5]. In the future information battlefield, the integrated and cooperative operation of air ground multiple equipment and the complex battlefield geographical environment and electromagnetic environment have put forward higher requirements for the air defense weapon system to achieve rapid association and fusion of target air information within the defense area [6]. Multi-mode track association and fusion is a multifunctional process that uses multi-sensor data fusion technology to associate and fuse information and intelligence detected by different types of sensors of multiple equipment. Therefore, more accurate and complete target information and battlefield situation can be obtained, providing better decision information for commanders, as shown in Fig. 1 [7]. At present, research shows that three-dimensional track and three-dimensional track association and fusion algorithm have been applied in air defense weapon system, and basically meet the requirements. However, there are few researches in the association and fusion algorithms of three-dimensional track and two-dimensional track. Therefore, it is necessary to propose effective algorithms to solve the challenge faced by multi-sensor data fusion in air defense system [8, 9].

In this paper, we present a multi-mode track association and fusion algorithm to solve the problem of three-dimensional and two-dimensional target track association and fusion in air defense weapon system. The proposed algorithm is based on the triangle method to complete the three-dimensional and three-dimensional target track fusion. The application of this algorithm in air defense weapon system can effectively improve the situation awareness and information sharing capabilities of air defense weapon system, and provide a useful reference for the future development of air defense weapon system informatization and intelligence.

2 Background

The air defense weapon system consists of anti-aircraft guns, air defense missiles, command vehicles and other equipment. In the system, the target information can be detected through a variety of different types of sensors, such as the three-dimensional information (range, azimuth, elevation) of the target can be detected by the target indication radar, and the two-dimensional information (azimuth, elevation) of the target can be detected by the photoelectricity sensor. Track association and fusion

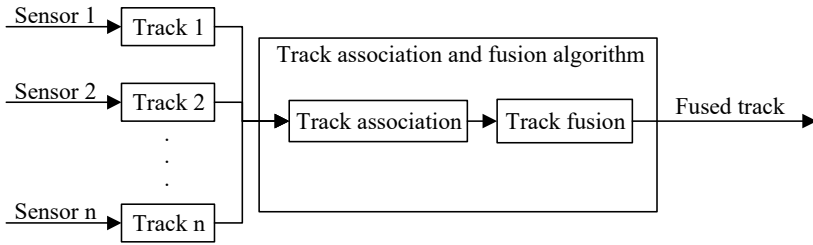


Fig. 2 Track association and fusion structural framework

technology is associate and fuse target information detected by different sensors to obtain more stable and reliable information data closing the real target, as shown in Fig. 2. In the air defense weapon system, track association and fusion technology is used to associate and fuse the target air information detected by multi-sensor to obtain target location, situation awareness and other information. Thus, it can provide strong support for commander to conduct command and decision on the battlefield, and further improve the combat capability of the air defense weapon system [10].

In the cooperative operation of air defense weapon system, the important problem to be solved is multi-mode track association and fusion, which is an important research field of the system. In a multi-sensor target detection environment, each sensor has collected a large amount of target track information. How to determine whether multiple tracks from different sensors are from the same target is the problem of track association and fusion [11]. The track association problem is easy to solve when the tracks are far away from each other and there is no interference or clutter. However, when multiple targets appear in the scene and there are many interference, clutter or forked tracks, the problem of track association becomes quite difficult. In addition, the difference of detection data dimension (three-dimensional or two-dimensional), deployment location and detection accuracy between different sensors, coordinate transformation error and other factors make effective track association and fusion more challenging [12].

3 Multi-modal Track Association and Fusion Algorithm

When the air defense weapon system cooperates with multiple equipment, the vehicle not only receives the three-dimensional air information from the target indication radar, but also receives the two-dimensional air information data from other sensors. Therefore, the vehicle needs to perform track association and fusion for the received three-dimensional tracks and two-dimensional tracks. For the problem, the multi-mode track association and fusion algorithm is proposed in this paper. The proposed algorithm is composed of a three-dimensional and two-dimensional track association and fusion model based on the triangle method, which can realize the track association and fusion of three-dimensional and two-dimensional track, as shown in Fig. 3.

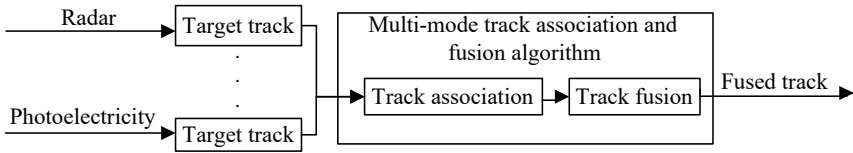


Fig. 3 Multi-modal track association and fusion algorithm

3.1 Three-Dimensional and Two-Dimensional Track Association Fusion Model Based on Triangle Method

By constructing a virtual point on a known two-dimensional vector, a spatial triangle with known coordinates of three vertices based on the point and vector is constructed. Based on the space triangle, the distance from the space point to the straight line can be calculated, and then we can obtain the correlation coefficient between any three-dimensional coordinate point in space and two-dimensional vector. Thus, the multi-mode track association fusion processing between three-dimensional air situation and two-dimensional air situation can be completed.

The processing flow of this model is shown in Fig. 4.

The model takes the radar position, photoelectric position, three-dimensional position information of the target detected by radar, two-dimensional position information of the target detected by photoelectric as the input, and the associated and fused track points as the output. Finally, the multi-mode track association and fusion can be effectively completed. The specific steps are as follows:

Fig. 4 Model processing flow

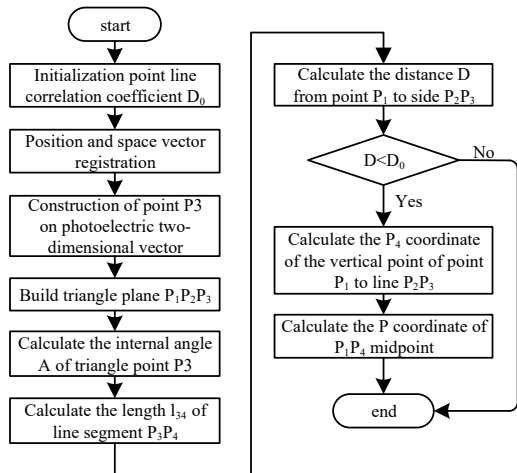
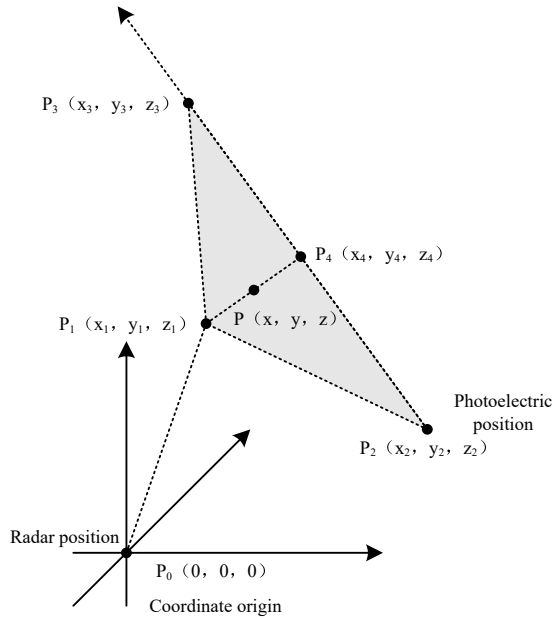


Fig. 5 Spatial relationship diagram



Step 1: Initialize the model.

Set the correlation coefficient as D_0 , and establish a new three-dimensional rectangular coordinate system, that is, take the radar position coordinate as the origin of the new three-dimensional rectangular coordinate system. It is known that under the geodetic rectangular coordinate system, the radar position is $P_0'(x_0', y_0', z_0')$, the corresponding detected three-dimensional target point position is $P_1'(x_1', y_1', z_1')$, the photoelectric position is $P_2'(x_2', y_2', z_2')$, and the corresponding detected target azimuth is α' and the elevation is β' .

Step 2: Conduct position and vector space registration [13].

Let the origin of the new three-dimensional rectangular coordinate system be $P_0(0, 0, 0)$.

Then the three-dimensional coordinate of the detected target is $P_1(x_1, y_1, z_1)$, the position of the photoelectric is $P_2(x_2, y_2, z_2)$, and the corresponding detected target azimuth angle is α , and the elevation angle is β . The formula is converted as follows:

$$\begin{aligned}
 P_1(x_1, y_1, z_1) &= P_1(x_1' - x_0', y_1' - y_0', z_1' - z_0') \\
 P_2(x_2, y_2, z_2) &= P_2(x_2' - x_0', y_2' - y_0', z_2' - z_0') \\
 \alpha &= \alpha' \\
 \beta &= \beta'
 \end{aligned}
 \tag{1}$$

Step 3: Build a point on the photoelectric two-dimensional coordinate vector P_3 .

Here, the distance from point P_3 to point P_2 is l , which is about twice the distance from the real detected target point P_1 to the photoelectric position P_2 . The spatial

relationship is shown in Fig. 5. The formula of point P_3 is as follows.

$$\begin{aligned}x_3 &= x_2 + l \times \cos \beta \times \cos \alpha \\y_3 &= y_2 + l \times \cos \beta \times \sin \alpha \\z_3 &= z_2 + l \times \sin \beta\end{aligned}\quad (2)$$

Step 4: Build a spatial triangle plane $P_1P_2P_3$.

The spatial triangle plane is shown in Figure 6, and the three side l_a, l_b, l_c are described as follows.

$$\begin{aligned}l_a &= \sqrt{(x_1 - x_3)^2 + (y_1 - y_3)^2 + (z_1 - z_3)^2} \\l_b &= \sqrt{(x_1 - x_2)^2 + (y_1 - y_2)^2 + (z_1 - z_2)^2} \\l_c &= \sqrt{(x_2 - x_3)^2 + (y_2 - y_3)^2 + (z_2 - z_3)^2}\end{aligned}\quad (3)$$

Step 5: Calculate the internal angle of the point P_3 .

$$A = \arccos\left(\frac{l_b^2 + l_c^2 - l_a^2}{2l_b l_c}\right)\quad (4)$$

Step 6: Calculate the length l_{34} of the line segment P_3P_4 .

Let the intersection point of point P_1 and vertical side P_2P_3 be $P_4(x_4, y_4, z_4)$. The length of l_{34} is calculated as follows.

$$l_{34} = l_a \cos A\quad (5)$$

Step 7: Calculate the distance D from the point P_1 to the straight line P_2P_3 .

$$D = \sqrt{l_a^2 - l_{34}^2}\quad (6)$$

Step 8: Judge the correlation between point P_1 and vector P_2P_3 .

If $D < D_0$, point P_1 is related to vector P_2P_3 , go to step 9; Otherwise, point P_1 and vector P_2P_3 are irrelevant, and multi-mode track association and fusion is completed.

Step 9: Calculate the coordinate of the shortest distance point $P_4(x_4, y_4, z_4)$ from point P_1 to line P_2P_3 .

$$\begin{aligned}x_4 &= x_2 + (x_3 - x_2) \frac{(l_c - l_{34})}{l_c} \\y_4 &= y_2 + (y_3 - y_2) \frac{(l_c - l_{34})}{l_c} \\z_4 &= z_2 + (z_3 - z_2) \frac{(l_c - l_{34})}{l_c}\end{aligned}\quad (7)$$

Step 10: Calculate the coordinates $P(x, y, z)$ of the midpoint P_1P_4 .

$$\begin{aligned}
 x &= \frac{(x_4 + x_1)}{2} \\
 y &= \frac{(y_4 + y_1)}{2} \\
 z &= \frac{(z_4 + z_1)}{2}
 \end{aligned}
 \tag{8}$$

Here $P(x, y, z)$ is the track point after association and fusion.

4 Simulation Experiment

In order to verify the effectiveness of the multi-mode track association and fusion algorithm proposed in this paper, simulation experiments are carried out. Set the following two typical application scenes, as shown in Fig. 7. The computer hardware configuration of the simulation experiment is 3.2 GHz CPU and 8.0 GB memory.

Application Scene I:

- (a) Detection point 1 is the location of radar detection equipment, detection point 2 is the location of photoelectric detection equipment, and the distance between radar detection point and photoelectric detection point is 4 km;
- (b) Simulate that the three target tracks are parallel to each other and parallel to the X axis. The starting position is shown in Fig. 7. There are five kinds of simulated tracks, with the step size of 200 m to 1000 m in horizontal and vertical directions.

Fig. 6 Space triangle plan.

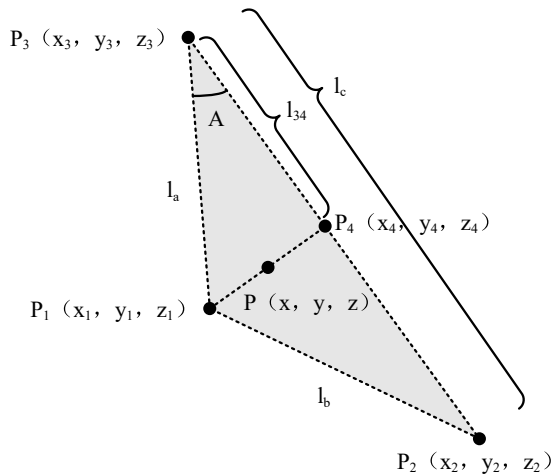
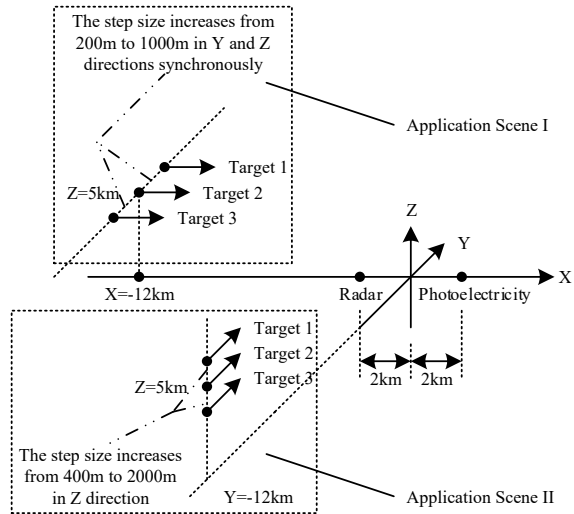


Fig. 7 Application scenes



Application Scene II:

- (a) The position settings of radar detection points and photoelectric detection points are consistent with the application scene I;
- (b) Simulate that the three target tracks are parallel to each other and parallel to the Y axis. The starting position is shown in Fig. 7. There are five kinds of simulated tracks, with the step size of 400 m to 2000 m in vertical direction.

According to the position coordinates of radar detection points and photoelectric detection points in the two application scenes, and the detected target tracks, multi-mode track association and fusion algorithm is used to calculate track association and fusion on the simulation computer. The final experimental data are shown in Table 1. The simulation experiment indicators in this paper include the association accuracy of three-dimensional track and two-dimensional track (point-line), the measurement average deviation distance, the association fusion processing time, etc. [14].

As is shown in Table I, the multi-mode track association and fusion algorithm proposed in this paper can effectively process the association and fusion of three-dimensional and two-dimensional tracks, in which the point an line association accuracy is more than 94%, the fusion deviation distance is less than the average detection deviation distance of a single three-dimensional detection equipment, and the average processing time is 0.01 Ms. Therefore, the proposed algorithm can deal with the multi-mode track association and fusion problem in air defense weapon system effectively, in real time and quickly.

Table 1 Performance indicators of multi-modal track association fusion algorithm in two application scenes

Examples		Accuracy of point-line association	Average deviation distance		Processing time
Scene	Spacing distance		Average deviation of three-dimensional detection	Fusion deviation distance	
Scene I: Distance increase in horizontal and vertical directions	200 m	94.1957%	90.3973 m	74.4841 m	0.011 ms
	400 m	100.000%	90.5235 m	69.2853 m	0.009 ms
	600 m	100.000%	90.7034 m	69.3424 m	0.011 ms
	800 m	100.000%	90.9373 m	69.4419 m	0.009 ms
	1000 m	100.000%	91.2257 m	69.5840 m	0.010 ms
Scene II: Distance increase in vertical direction	400 m	97.6783%	91.6435 m	71.3335 m	0.010 ms
	800 m	100.000%	91.8386 m	69.0268 m	0.010 ms
	1200 m	100.000%	92.1067 m	69.2132 m	0.010 ms
	1600 m	100.000%	92.4494 m	69.4576 m	0.010 ms
	2000 m	100.000%	92.8694 m	69.7630 m	0.010 ms

5 Conclusion

In this paper, a multi-mode track association and fusion algorithm is proposed to solve the multi-mode track association and fusion problem derived from multi-sensor target detection trick in the field of air defense weapon system. The proposed algorithm first constructs a virtual point on a known two-dimensional vector. Then, a space triangle with known coordinates of three vertices based on the point and the vector. Based on the triangle, the distance from the point to the line in space can be calculated, and the correlation coefficient between a three-dimensional coordinate point and a two-dimensional vector can be obtained. Finally, multi-mode track association and fusion can be completed. We evaluate the effectiveness of the proposed algorithm in dealing with multi-mode track association and fusion in different application scenes by simulation experiments. The simulation results show that the algorithm has high track association accuracy, small fusion track error, fast processing speed and advanced technical indicators when dealing with three-dimensional and two-dimensional track association and fusion. This algorithm can provide reference for multi-modal data fusion in air defense weapon system, and it should be further verified and optimized in real air defense operations. This algorithm can effectively improve the situation awareness and information sharing ability of air defense weapon system when applied to air defense weapon system, and provide useful reference for the modernization and intelligent development of air defense weapon system.

References

1. Chen, L.G., Zhang, Y., Liu, X.L.: Analysis of multi aerial targets threaten degree on terminal Defense system. In: Proceedings of 2015 International Conference on Computer Information Systems and Industrial Applications (CISIA), pp. 1020–1023 (2015)
2. Gao, K., Xiao, H., Qu, L., Wang, S.: Optimal interception strategy of air defence missile system considering multiple targets and phases. *Proc. Inst. Mech. Eng. Part O: J. Risk Reliab.* **236**(1), 138–147(2022)
3. Yuan, C.: Research on target track fusion and distribution technology in terminal air Defense weapon system. Beijing University of Technology (2020). (in Chinese)
4. Zhang, Q., Guo, S., Wu, N., Deng, J.: Research on dynamic display of radar detection range in complex electromagnetic environment based on GIS. In: IOP Conference Series: Earth and Environmental Science, vol. 474, no. 4, pp. 593–597(2020)
5. Ricciardi, S., Souque, C.: Modern electromagnetic spectrum battlefield. *PRISM* **9**(3), 122–139 (2021)
6. Shen, X.: Present development situation of foreign moving air-defense system. *Shipboard Electron. Countermeasure* **33**(2), 49–55 (2010)
7. Shivanand, G., Reddy, K.V.K., Prasad, D.B.N.: An innovative asynchronous, multi-rate, multi-sensor state vector fusion algorithm for air Defence applications. *IFAC Papers OnLine* **49**(1), 337–342 (2016)
8. Zhang, K., Wang, Z., Guo, L., Peng, Y., Zheng, Z.: An asynchronous data fusion algorithm for target detection based on multi-sensor networks. *IEEE Access* **8**, 59511–59523 (2020)
9. Hao, R., Yang, R.: Current research status of multi-sensor data fusion technology and its military applications. *Armament Autom.* **26**(4), 16–23 (2007). (in Chinese)
10. Hao, X., Xia, Y., Yang, H., Zuo, Z.: Asynchronous information fusion in intelligent driving systems for target tracking using cameras and radars. *IEEE Trans. Industr. Electr.* **70**(3), 2708–2717 (2023)
11. Shi, D., Xue, P., Yang, W., Wang, Y.: Research on the air information processing method in small area air defense operation. *J. Gun Launch Control* **41**(4), 23–31 (2020). (in Chinese)
12. Tian, W.: Multisensor track-to-track association and bias removal in complex environments. Tsinghua University (2014). (in Chinese)
13. Gao, L., Battistelli, G., Chisci, L., Wei, P.: Distributed joint sensor registration and target tracking via sensor network. *Inf. Fusion* **46**, 218–230 (2019)
14. Wan, Y.: Data analysis and assessment system of multi-radar. Southeast University (2017). (in Chinese)

Harmonic Analysis of Grid-Connected Electric Vehicle Charging Stations



Ziyi Yang

Abstract With the strong support of national policies, wholesale grid connection of this new type of load electric vehicles, will inject harmonics into the distribution network. Based on this, this article examines the grid-connected harmonic characteristics of electric vehicle charging stations(EVCSs) and analyzes its corresponding suppression measures under various charging scenarios in urban EVCSs.

Firstly, based on the construction status of EVCSs in China and the different scale and capacity of EVCSs and geographical locations, more typical charging station categories are selected for analysis and research. To realize the simulation of these different charging scenarios, an EVCS model is built, and then the harmonic characteristics are simulated and analyzed after its connection to the city distribution network. By studying the harmonic characteristics under different charging scenarios, the impact of charging stations access on the power quality of the power grid after connection is analyzed, and effective measures for harmonic suppression are proposed, and suggestions for the configuration of compensation and treatment devices are given to provide a basis for the further building of charging facilities and the planning and operation of distribution grid.

Keywords Electric Vehicle Charging Station · Distribution Network · Harmonics

1 Introduction

As the world's largest energy-consuming country and an important force in environmental protection, China actively implements electric vehicle science and technology strategies, promotes the upgrading of the industrial structure of the automobile industry and the transformation of the electric power system, cultivates and develops the electric vehicle market, and the electric vehicle industry has been elevated to a national strategy, becoming one of the strategic emerging industries that the country

Z. Yang (✉)

College of Electrical and New Energy, Three Gorges University, Yichang 443002, China
e-mail: 3113780577@qq.com

© Beijing Paiké Culture Commu. Co., Ltd. 2023

X. Dong et al. (eds.), *The proceedings of the 10th Frontier Academic Forum of Electrical Engineering (FAFEE2022)*, Lecture Notes in Electrical Engineering 1054, https://doi.org/10.1007/978-981-99-3408-9_33

363

focuses on developing [1]. With national policy support and the progress of social development, the growth of electric net cars, electric official cars, and electric shuttle buses in scenic spots is also becoming more and more rapid, and the demand for charging stations will also increase significantly.

Electric vehicle charger are nonlinear loads consisting of electrical and electronic devices, which can inject harmonics into the distribution network and cause harm to the secure and stable operation of power grid and equipment. [2–4]. In large and medium-sized charging stations, there are many harmonic source chargers, which will cause harmonic pollution and other adverse effects on the grid after large-scale grid connection [5]. The literature [6] analyzes the characteristics of harmonics in terms of both equivalent load changes in electric vehicle charging and changes in the number of charging piles connected to the grid, and proposes a method based on an improved wavelet neural network to meet the accurate detection of harmonics in EVCSs, laying the foundation for electric vehicle harmonic suppression. Literature [7] obtained that charging piles mainly increase the 5th and 7th harmonics based on the modeling and simulation analysis of EV charging piles, and proposed the introduction of active power filters to suppress harmonics. [8] proposes two methods to manage harmonics and reduce their impact on power quality, based on the analysis of the system of charging stations connected to the grid and the design of switching stations, with multi-pulsation rectification techniques and filtering techniques. The literature [9] analyzes the impact of some uncertainties associated with nonlinear residential loads and electric vehicles on voltage harmonic distortion and voltage imbalance in distribution networks, thus proposing a probabilistic approach to comprehensively assess the impact of power quality in networks with electric vehicles, nonlinear loads and photovoltaics. The literature [10] evaluates and alleviates the impact of different EV chargers on distribution transformers and distribution system voltage quality based on weighted arithmetic mean and optimal harmonic power flow algorithms. [11] studied the impact of large-scale EV penetration on low-voltage distribution and proposed several charging schemes for EV integration into the utility grid, considering power demand, voltage profile, power quality and system adequacy. The literature [12] pointed out that an adaptive neuro-fuzzy controlled distribution static compensator can effectively improve the power quality in the electric vehicle distribution grid and designed a sustainable bi-directional EVCS in the distribution grid based on this.

Therefore, in order to reduce the harmonic pollution to the electricity network grid and improve the power quality of the distribution network, it is necessary to study the harmonic influence on the distribution network when charging EVCSs is connected to the grid, especially the change law and characteristics of the harmonics generated during the charging process, and to formulate a reasonable harmonic management plan, so as to provide a theoretical basis for the construction of large-scale EVCS and power quality management, and to ensure the secure, economic and reliable operation of the power grid. In this article, we investigate the harmonics changes in different charging scenarios. In this paper, we study the harmonics characteristics of grid-connected EVCSs under different charging scenarios and analyze the corresponding suppression measures. Firstly, we analyze the construction status of EVCSs in China,

and select several typical charging stations, such as urban public charging stations, bus charging stations and highway charging stations, according to the different scale and capacity of EVCSs and geographical locations. Further, a model of EVCS is built to realize the simulation of these different charging scenarios, and the harmonic characteristics of different types of charging stations after grid connection are simulated and analyzed. Then, according to the harmonic limitation standards of public power grid and electrical equipment, the impact of charging stations on the power quality of power grid after connection is analyzed by studying the harmonic characteristics of different charging scenarios, and effective measures for harmonic suppression and suggestions for the configuration of harmonic compensation treatment devices are proposed.

2 Typical City Electric Vehicle Charging Station

2.1 Classification of EV Charging Stations in Typical Cities

The development of electric vehicles has been strongly supported by national policies in recent years, and a series of national and local policies have been introduced to promote new energy vehicles and charging infrastructure. 2012 saw the State Council issue the “Energy Conservation and New Energy Vehicle Industry Development Plan (2012–2020)”, and in 2013 four ministries and commissions jointly issued the “Notice on Continuing the Promotion and Application of New Energy Vehicles”. In 2014, the country has intensively introduced policies to increase the promotion efforts. Five ministries and commissions issued the Implementation Plan for the Purchase of New Energy Vehicles by Government Agencies and Public Institutions, the General Office of the State Council issued the Guiding Opinions on Accelerating the Promotion and Application of New Energy Vehicles, the Development and Reform Commission issued the Notice on Issues Related to Electric Vehicle Pricing Policy, and four ministries and commissions issued the Notice on Incentives for the Construction of New Energy Vehicle Charging Facilities. In November 2015, four ministries and commissions jointly issued the “Electric Vehicle Charging Infrastructure Development Guide (2015–2020)”[13] and the General Office of the State Council issued the “Guidance on Accelerating the Construction of Electric Vehicle Charging Infrastructure”, China will accelerate the construction of charging infrastructure.

EVCSs can be divided into special charging stations, urban public charging stations and intercity traffic charging stations according to the scale capacity and geographic location, etc. Special charging stations serve the charging needs of vehicles for environmental protection, logistics and police; urban public charging stations serve the charging needs of social electric vehicles; intercity traffic charging stations serve the charging needs of electric vehicles to and from highways.

Table 1 Electric vehicle charging station classification and its characteristics

Classification	Service Users	Charging mode	Charging features
Urban public charging stations	Service for social vehicles	Regular and fast charging	More electric vehicles charging at the same time, less power battery power
Bus charging station	Dedicated to bus service	General charging	The power battery has a large capacity and requires a relatively high voltage and current for charging
Highway charging stations	Service for vehicles passing through the highway	Fast charging	Longer distance from substation and longer distribution lines

Urban public charging stations are oriented to social electric vehicles with large demand and different scales, among which the large-scale grid connection of electric vehicles will change the load characteristics and structure of the distribution network and have a large impact on the urban power grid; buses, as an electric vehicle that occupies a certain position in public travel, and bus charging stations are mostly built in bus hubs and other places with large charging demand, and the charging power is large, which will inject large harmonics into the power grid. Considering the intercity travel and travel charging demand for tourism, vacation, sightseeing and leisure, highway charging stations, as an important member of intercity transportation charging stations, also need to be studied for their grid-connected harmonic characteristics (Table 1).

2.2 EV Charger Model

The current working principle of widely used chargers is that the three-phase bridge rectifier carries out uncontrolled rectification and filtering of the three-phase AC voltage, and then passes through a high-frequency DC/DC power converter, and then provides DC power to the power battery after output filtering, as shown in Fig. 1.

Among them, the high-frequency power conversion device is complicated to model and computationally intensive, which needs to be approximated as equivalent. The charging process of an electric vehicle can take as fast as half an hour, and conventional charging generally takes 4–6 h, so the output voltage U_0 and output current I_0 of the charger can be considered as constant DC in the industrial frequency cycle, i.e., the DC/DC power converter is in a constant power operation during this period. Therefore, a nonlinear time-varying resistive element R_c can be equated to the equivalent input impedance of this power converter [14]. The simplified equivalent model of an electric vehicle charger is shown in Fig. 2. The nonlinear time-varying

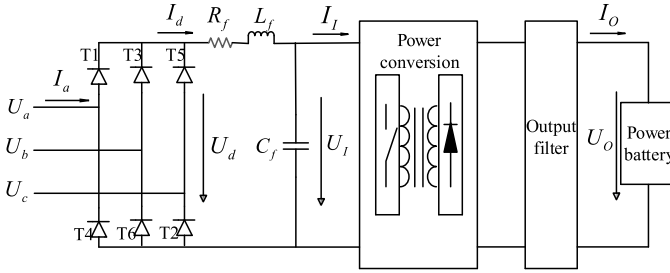
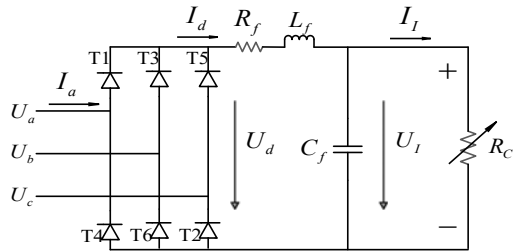


Fig. 1 Single charger charging schematic

Fig. 2 Charger Equivalent Circuit



resistor is equivalent to the electric vehicle battery charging characteristics and its analytical equation is shown in Eq. (1).

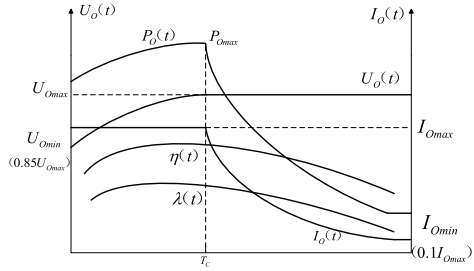
$$R_c = \frac{U_i}{I_i} = \frac{U_i^2}{U_i I_i} = \frac{U_i^2}{P_i} = \frac{\eta U_i^2}{P_o} = \frac{\eta U_i^2}{U_o I_o} \tag{1}$$

where η is the charger efficiency. Based on the above analysis, it is clear that building the charger equivalent circuit model requires studying the charging characteristics of the EV battery to obtain the specific variation of the nonlinear time-varying resistance.

In order to improve charging efficiency and save charging time, a two-stage constant-current voltage-limiting/constant-voltage current-limiting charging method (CC/CV) is widely used [15], i.e., the current first charges the battery at a constant current at the beginning, when the voltage is gradually rising, and when the charging voltage rises to a certain stage, it enters the constant-voltage charging mode, and the charging current slowly decreases to prevent the excessive current from damaging the battery at the late stage of charging. The specific charger output parameters change as shown in Fig. 3 below, and the nonlinear resistance R_c will also change with the change of charging output power.

For conventional charging, the typical charger conventional charging output power curve was obtained in the literature [16] based on the battery data recorded during the actual charging process and then by data fitting, where the maximum output power was 9 kW and the variation law is shown in Fig. 3, where the output power is a segmentation function that rises in the first half and drops significantly after

Fig. 3 Typical curves of power cell charging parameters during charging



reaching the maximum value. Therefore, the relationship between the charger output power and charging time under two-stage charging mode is obtained as shown in the following equation.

$$P_o(t) = \begin{cases} 0.79 P_{Omax} t^{0.048}, & 0 < t \leq T_C \\ P_{Omax} e^{-0.021(t-T_C)}, & T_C \leq t \leq T \end{cases} \quad (2)$$

where P_{Omax} is the maximum output power of the charger, T_C and T are the constant current charging time and complete charging cycle of the charger, respectively.

The electric vehicle charging pile model built based on the equivalent simplified model of the charging station above is shown in Fig. 4, taking a typical 9 kW conventional charger as an example [16], the power supply is supplied at 10 kV, the transformer is of 10/0.4 kV voltage level, dy11 connection, the inductor-capacitor value is used a common charger parameter, and the harmonic analysis is performed using the FFT module with each harmonic analysis module.

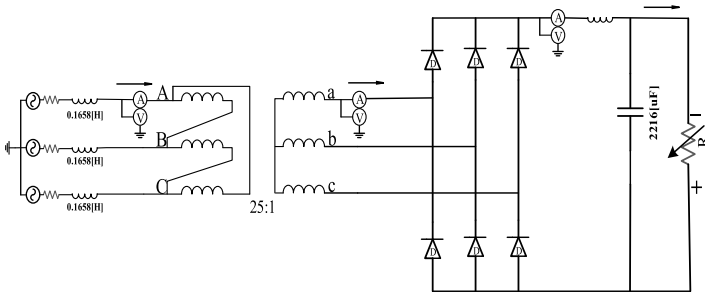


Fig. 4 Charger simulation model

3 The Impact of Urban Charging Station Access on the Harmonics of the Distribution Network

3.1 Harmonic Analysis Model for Urban EVCSs

Due to the different charging objects and geographical locations, they can be divided into various types of charging stations such as urban public charging stations, bus charging stations, highway charging stations, etc. The characteristics of the service areas of the distribution networks accessed by these charging stations are very different, including:

1. Various load types and different load levels such as residential, commercial and industrial.
2. Different total three-phase and single-phase loads.
3. Network topology variations including different single-phase and three-phase line lengths and differences between total lengths.
4. Different network voltage levels, substation MVA ratings, etc.

When electric vehicles are charged through the charging pile’s access to the grid, the impact caused by battery charging can be expressed as the impact of the charging pile or charging station on the grid from the perspective of the grid side. The power supply voltage of large electric vehicle charging station is 10 kV, usually using special line or double-loop way to supply power; medium-sized charging station uses 10 kV single-way often supplying special transformer power supply; small charging station can usually directly connect to 0.4 kV low-voltage line. In this paper, we mainly study the harmonic influence generated by urban EVCSs connected to the medium and low voltage distribution network, whose structure is shown in Fig. 5.

Fig. 5 The overall layout structure of EVCSs connected to the city distribution network

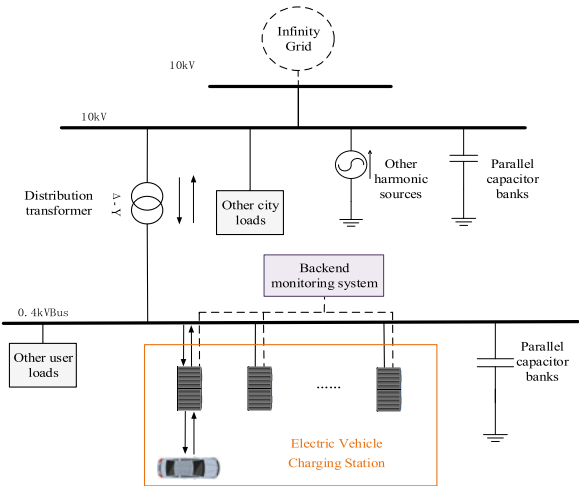


Table 2 Electric vehicle charging station parameters and grid connection location

Parameter	Charging pile power/kW	Maximum number of charging stations/pc	Charging method	Access location
Urban public charging station	5	8	Conventional charging, fast charging	380 V busbar
Bus charging station	90	4	Conventional charging	10 kV busbar
Highway charging station	15	4	Fast charging	Long distance transmission line

With reference to the actual parameters of charging facilities currently under construction in Huzhou City, this paper builds a simulation model of different charging stations connected to the distribution network, and the capacity configuration of each type of electric vehicle charging station, as well as the grid connection location, are shown in Table 2 below.

3.2 Harmonic Analysis of Different Charging Scenarios

According to the electric vehicle charger model built above and different types of charging station parameters, build charging station grid-connected models for different charging scenarios, simulate the operation to the peak electric vehicle charging period, measure the harmonic voltage and current on the 10 kV common connection point and 380 V bus of the distribution network, and use the FFT module to analyze the voltage content of each harmonic, the simulation results are as follows (Fig. 6) and (Table 3).

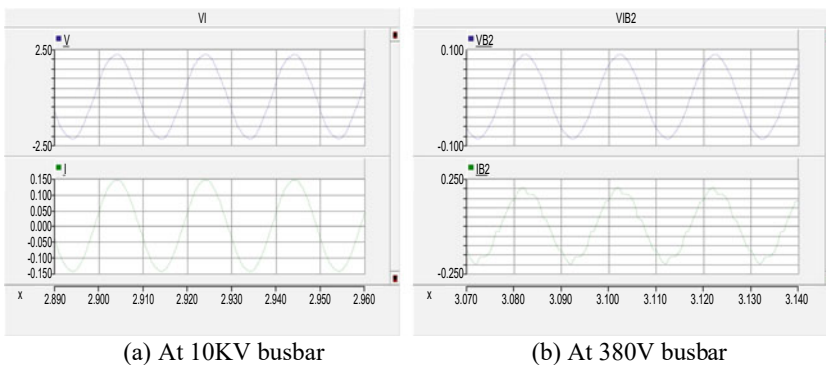


Fig. 6 Harmonic voltage and current diagram of urban public charging stations

Table 3 Harmonic voltage content of 10 kV and 380 V in urban public charging stations

Urban public charging stations	Voltage harmonic content/%				
	5 times	7 times	11 times	13 times	THD
10 kV	2.18%	0.33%	0.09%	0.12%	2.21%
380 V	0.53%	0.82%	0.32%	0.54%	1.22%

- (1) Urban public charging stations.
- (2) Bus charging station.
- (3) Highway charging station.

The total harmonic distortion rate of voltage on the common connection point of 10 kV and 380 V bus of the distribution network is measured and compared with GB/T 14,549–1993 standard to compare and analyze the harmonic pollution of the charging station grid-connected to the distribution network under different charging scenarios, and the comparison of the results is shown in Figs. 9 and 10.

As can be seen the main number of AC side voltage harmonics during the charging process of EVCSs are the 5th, 7th, 11th and 13th harmonics i.e. the 5th harmonic, of which the 5th harmonic voltage content is the largest. Among different charging scenarios, the bus charging station connected to the grid causes the most serious harmonic pollution, which exceeds the allowable value of 10 kV bus harmonic voltage content in GB/T 14,549–1993 standard. It can be seen that bus charging stations, as high-power charging stations, need to be equipped with special distribution transformers for power supply, and their harmonic impact on the grid is more serious, and centralized management measures should be taken to cope with the harmonic problem of charging loads (Fig. 7) and (Table 4).

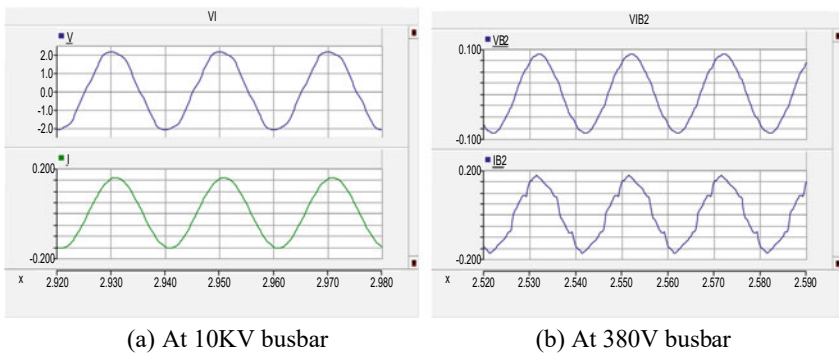


Fig. 7 Harmonic voltage and current diagram of bus charging station

Table 4 Harmonic voltage content of 10 kV and 380 V in bus charging station

Bus charging station	Voltage harmonic content/%				
	5 times	7 times	11 times	13 times	THD
10 kV	4.01%	0.79%	0.55%	0.34%	4.15%
380 V	1.95%	1.00%	1.06%	0.89%	2.64%

Table 5 Harmonic voltage content of 10 kV and 380 V in highway charging station

Bus charging station	Voltage harmonic content/%				
	5 times	7 times	11 times	13 times	THD
10 kV	2.95%	0.16%	0.30%	0.25%	2.98%
380 V	0.80%	0.20%	0.58%	0.66%	1.21%

Comparing with the bus charging station, it is easy to find that the harmonic voltage content of 10 kV and 380 V bus after the city public charging station and highway charging station are connected to the distribution grid does not exceed the standard allowable value. Therefore, the simulation of the scenario where the city public charging station and the highway charging station are connected to the grid at the same time is carried out, and the results are shown in the table (Fig. 8) and (Table 5).

As the data in the table shows, when urban public charging stations and highway charging stations are connected to the distribution network at the same time, the harmonic voltage content of 10 kV bus is greatly increased compared with that without charging stations, far exceeding the national standard value. Therefore, when a large number of urban EVCSs are connected to the grid, the harmonic pollution problem to the distribution network cannot be ignored, and reasonable construction planning of charging stations should be adopted to study how to achieve the best configuration of charging stations with the least impact on the distribution network;

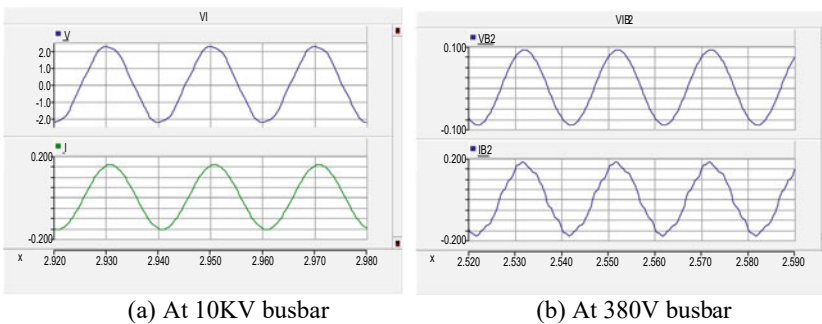


Fig. 8 Harmonic voltage and current diagram of highway charging station

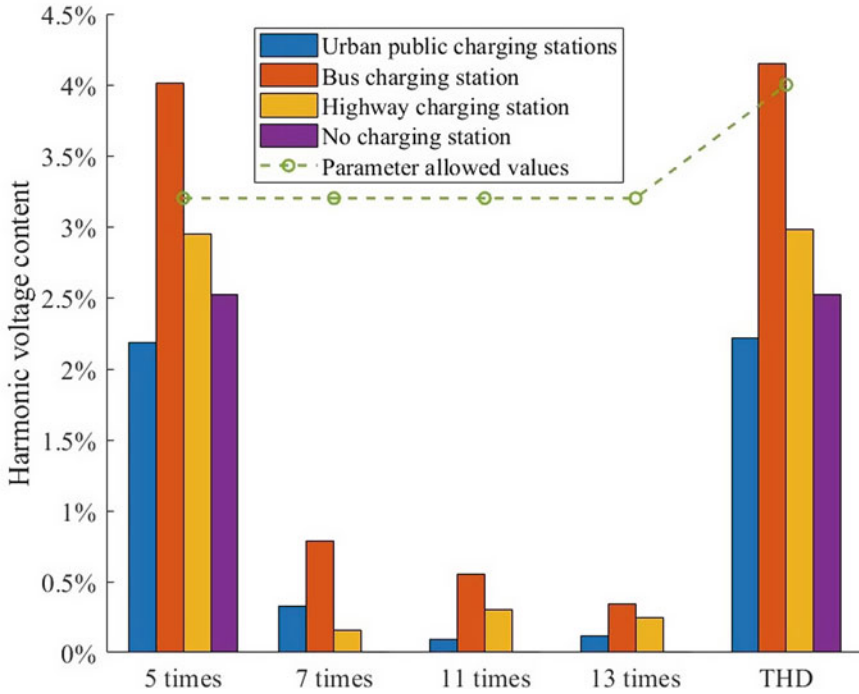


Fig. 9 Harmonic voltage content at 10 kV under different charging scenarios

and appropriate compensation and treatment devices should be configured to meet the harmonic requirements of the connected network (Table 6).

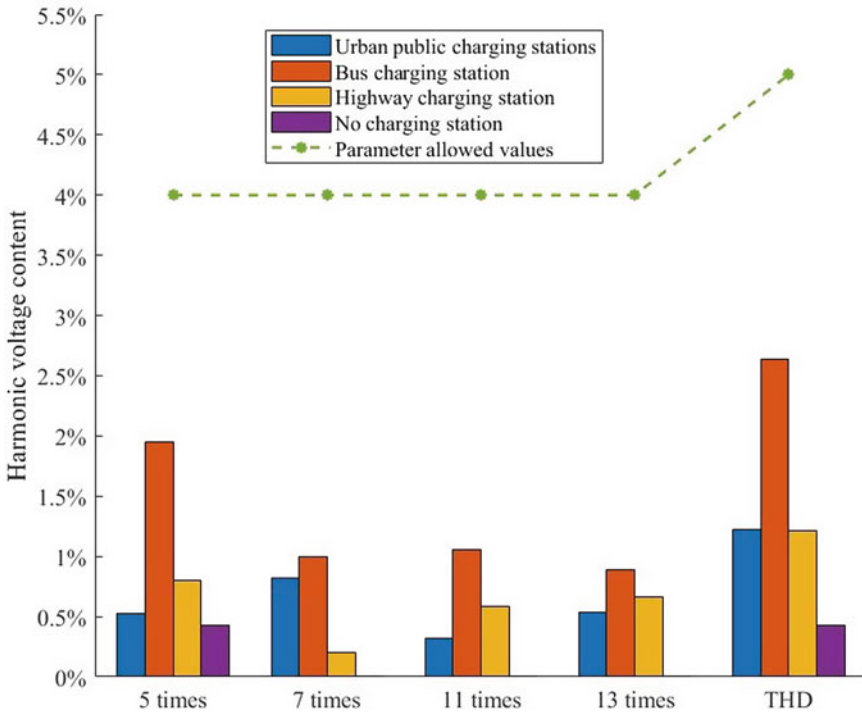


Fig. 10 Harmonic voltage content at 380 V under different charging scenarios

Table 6 10 kV bus charging harmonic voltage under different charging scenarios.

Charging scene	Voltage harmonic content/%				Total voltageharmonic distortion rate/%
	5 times	7 times	11 times	13 times	
City and highway charging station	26.7	0.08	0.11	0.19	26.7
No charging station	2.52	0	0	0	2.52
Parameter allowance	3.2	3.2	3.2	3.2	4.0

4 Conclusion

In this paper, according to the construction status of EVCSs in China and the difference of their scale capacity and geographical location, representative urban public charging stations, bus charging stations and highway charging stations are selected for analysis and research. Then a model of electric vehicle charging station is built to simulate and analyze the harmonic characteristics of different types of charging stations after they are connected to the city distribution network. The harmonic

characteristics of urban EV charging stations under different charging scenarios are studied and analyzed to obtain the impact of charging stations on the power quality of the power grid after connection, and effective measures for harmonic suppression are proposed, and suggestions for the configuration of compensation and treatment devices are given to provide a basis for the further construction of charging facilities and the planning and operation of the distribution grid.

References

1. Liu, Z., Chen, J., Lin, K., Zhao, Y., Xu, H.: Current status and trends of electric vehicle development at home and abroad. *Electric Power Constr.* **36**(7), 25–32 (2015). (in Chinese)
2. Zhang, Q., Han, W., Yu, J., Li, C., Shi, Y.: Simulation model of electric vehicle charging station and its impact on grid harmonics. *J. Electr. Eng.* **27**(2), 159–164 (2012). <https://doi.org/10.19595/j.cnki.1000-6753.tces.2012.02.024>. (in Chinese)
3. Moses, P.S., Deilami, S., Masoum, A.S., Masoum, M.A.: Power quality of smart grids with plug-in electric vehicles considering battery charging profile. In: *Innovative Smart Grid Technologies Conference*, pp 1–7. IEEE, Europe (2010)
4. Bonner, A., Grebe, T., Gunther, E., Hopkins, L.: Xu, W: Modeling and simulation of the propagation of harmonics in electric power networks Part I: concepts, models, and simulation techniques. *IEEE Trans Power Deliv.* **11**(1), 452–460 (1996). <https://doi.org/10.1109/61.484130>
5. Hu, Z., Song, Y., Xu, Z., Luo, Z., Zhan, K., Jia, L.: Impact and utilization of electric vehicle access to power grid. *Chin. J. Electr. Eng.* **32**(04), 1–10 (2012). <https://doi.org/10.13334/j.0258-8013.pcsee.2012.04.006>. (in Chinese)
6. Yang, L., Pazilai, M.: Improved wavelet neural network based harmonic detection for charging stations. *Modern Electr. Technol.* **44**(05), 156–160 (2021). <https://doi.org/10.16652/j.issn.1004-373x.2021.05.032>. (in Chinese)
7. Zhou, Z.W., Yan, X.H.: Simulation analysis of harmonic suppression for AC charging pile of electric vehicle. In: *Journal of Physics: Conference Series*, vol. 1848, no. 1 (2021). <https://doi.org/10.1088/1742-6596/1848/1/012159>.
8. Zhang, F.: Research on electric vehicle charging and switching station technology and harmonic control. *Mechatron. Inf.* (27), 22–23 (2020). <https://doi.org/10.19514/j.cnki.cn32-1628/tm.2020.27.011>. (in Chinese)
9. Rodríguez-Pajarón, P., Hernández, A., Milanović, J.V.: Probabilistic assessment of the impact of electric vehicles and nonlinear loads on power quality in residential networks. *Int. J. Electr. Power Energy Syst.* **129** (2021). <https://doi.org/10.1016/j.ijepes.2021.106807>.
10. Alame, D., Azzouz, M., Kar, N.: Assessing and mitigating impacts of electric vehicle harmonic currents on distribution systems. *Energies* **13**(12) (2020). <https://doi.org/10.3390/en13123257>.
11. Khan, M.M.H., et al.: Integration of large-scale electric vehicles into utility grid: an efficient approach for impact analysis and power quality assessment. *Sustainability* **13**(19), 10943 (2021). <https://doi.org/10.3390/SU131910943>
12. Balasundar C., Sundarabalan C.K., Sharma J., Srinath N.S., Guerrero J.M.: Design of power quality enhanced sustainable bidirectional electric vehicle charging station in distribution grid. *Sustain. Cities Soc.* **74** (2021). <https://doi.org/10.1016/J.SCS.2021.103242>.
13. Electric vehicle charging infrastructure development guide (2015–2020). In: *National Development and Reform Commission of the People's Republic of China* (2015). (in Chinese)
14. Ma, L., Yang, J., Fu, C., Liu, P., Sun, Y.: A review of the impact of electric vehicle charging and discharging on the power grid. *Power Syst. Prot. Control* **41**(3), 140–148 (2013). (in Chinese)
15. Guo, J.-L., Wen, F.-S.: Impact of electric vehicle charging on power system and its countermeasures. *Power Autom. Equipment* **35**(6), 1–9 (2016). <https://doi.org/10.16081/j.issn.1006-6047.2015.06.001>. (in Chinese)

16. Gao, C.W., Zhang, L: A review of the impact of electric vehicle charging on power grid. A review of the impact of electric vehicle charging on power grid. *Power Grid Technol.* **35**(2), 127–131 (2011). (in Chinese). <https://doi.org/10.13335/j.1000-3673.pst.2011.02.020>

Two-Tier Demand-Side Response for Hydrogen Producing and Hydrogen Selling Integrated Hydrogenation Station



Jiajia Huan, Xin Huang, Mintong Zhao, and Yunxia Xu

Abstract As a kind of clean secondary energy, hydrogen energy has the advantages of extensive acquisition methods, low carbon terminal energy and abundant application scenarios. The development of hydrogen energy has been promoted to national energy strategy, and studying the economy of hydrogen energy development and utilization is currently one of the urgent needs to optimize energy consumption structure and energy transformation in China. This paper presents a demand-side response model for hydrogen generation and hydrogenation integrated parent station of hydrogen fuel cell vehicle. Electrolysis of water system is adopted in the model of methanol and hydrogen production link, and consider the peak valley price and methanol prices external environment, build a hydrogen mother standing demand side response behavior model of integrated energy system, accounting mother hydrogen filling station integrated energy system for demand side response of the peak valley price analysis, for the hydrogen fuel cell car hydrogen production for the cost optimization of hydrogenation mother standing support, It provides decision support for hydrogen production and hydrogenation parent station to face methanol price fluctuation and electricity price change.

Keywords Demand response · Hydrogen production and sales integration · The Peak valley price · Hydrogen energy

J. Huan (✉) · X. Huang
Guangdong Power Grid Co., Ltd. Power Grid Planning Research Center, Guangzhou 510000, China
e-mail: winnie5983@126.com

M. Zhao
Guangdong Power Grid Co., Ltd., Guangzhou 510000, China

Y. Xu
Tsinghua Sichuan Energy Internet Research Institute, Chengdu 610000, China

1 Introduction

With the deterioration of the global environment, the world has launched a series of discussions on economic development and environmental protection, and China has pledged to lay out a comprehensive green energy industry and implement the two major goals of carbon peaking and carbon neutrality in order to help solve global environmental problems [1]. In the context of double carbon, various production industries are looking for clean energy to achieve the emission reduction target and seek the possibility of low carbon emission reduction energy transition. As a renewable energy source, hydrogen has the advantages of wide access, low carbon end-use, and rich application scenarios, and will become a secondary energy source that cannot be ignored in the future low-carbon energy transition, and is an effective alternative to fossil energy for achieving deep decarbonization in difficult emission reduction areas such as power, industry, and transportation sectors [2]. The transportation sector, as one of the important areas to achieve carbon emission reduction, countries have continuously replaced the existing fossil energy vehicles by clean energy vehicles to achieve zero carbon transportation, and the development of new energy vehicles has become a possibility of replacement [3]. Among the ranks of new energy vehicles, hydrogen-fueled tram cars, which use hydrogen energy as a power source, have become an important part of hydrogen energy development and have been developed and applied by many countries and companies.

The main energy consumed by hydrogen fuel cell vehicles is hydrogen. Nowadays, the main ways of hydrogen production are coal to hydrogen, natural gas to hydrogen, methanol to hydrogen, industrial by-production of hydrogen, and electrolysis of water to hydrogen [4]. While hydrogen is used as an energy source for fuel cells, the supply of hydrogen to transportation fuel mainly adopts centralized hydrogen supply mode and distributed hydrogen supply mode. The distributed hydrogen supply model adopts the ready-to-use concept and is present in most of the hydrogen refueling stations because of its abundant hydrogen production methods, low safety risk, and better total cost of hydrogen use than the centralized hydrogen supply. In terms of raw materials, distributed hydrogen production can be divided into three categories: natural gas hydrogen, methanol hydrogen, and electrolytic water hydrogen, among which methanol hydrogen is the preferred source of distributed hydrogen supply because of its lower cost compared with the other two, while electrolytic water hydrogen can achieve zero carbon emission compared with the other two and has been further developed and applied [5]. Currently, there are different new models for the operation of hydrogen refueling stations. For example, in the literature [6], the concept of mother-son station is proposed, where the mother station is integrated with hydrogen production and hydrogen refueling, and the son station is used as a pure hydrogen refueling station. For example, the paper [6] proposed the concept of child-mother station, where the mother station is integrated with hydrogen production and refueling, and the child station is a pure hydrogen refueling station.

At present, the hydrogen production mode in hydrogen refueling stations mainly adopts proton exchange membrane electrolytic water production, i.e., the conversion of electrical energy into hydrogen energy. With the difference between peak and valley prices in the peak-to-valley tariff, this PEM hydrogen production has the potential to respond to the fluctuation of electricity prices and to reduce the peaks and fill the valleys. However, the fluctuation of hydrogen demand makes hydrogen production demand-side responsive mainly because of the fluctuation of electricity price. Currently, studies on the demand-side response of hydrogen energy are mainly covered in integrated energy systems. For example, literature [7] proposed a wind-light-hydrogen multi-energy complementary microgrid optimal configuration method that takes into account demand-side response to solve the problem of optimal economic cost of multi-energy complementary microgrid; literature [8] proposed a multi-objective optimization model of regional integrated energy system that takes into account integrated demand response to solve the problem of balancing multiple scheduling objectives such as energy cost, pollution emission and wind power consumption in regional integrated energy system. However, the demand-side response research for the integrated hydrogen production and hydrogen processing mother station is less, and the demand-side response mechanism and model for the integrated hydrogen production and hydrogen processing mother station need further research.

Accordingly, this paper proposes a demand-side response model for an integrated hydrogen production and hydrogen refueling mother station for hydrogen fuel cell vehicles, which is relatively little studied and analyzed in hydrogen production and hydrogen refueling mother stations. The model uses electrolytic water and methanol reforming to produce hydrogen, and takes into account the external price environment of peak and valley electricity prices and methanol prices to build a demand-side response behavior model for the integrated energy system of hydrogen production and hydrogen refueling mother station, to realize the demand-side response analysis of the integrated energy system of hydrogen production and hydrogen refueling mother station for peak and valley electricity prices, to support the cost optimization of hydrogen production and hydrogen refueling mother station for hydrogen fuel cell vehicles, and to provide a decision for the hydrogen production and hydrogen refueling mother station for methanol price fluctuations and electricity price changes. The model provides decision support for the price fluctuation of methanol and electricity price change.

2 Two-Tier Demand-Side Response System Structure and Demand-Side Response Mechanism

2.1 Integrated Energy System Structure of the Integrated Hydrogen Production and Hydrogen Refueling Mother Station

At present, hydrogen refueling stations in China are mainly integrated energy supply stations with refueling, hydrogen refueling, charging and photovoltaic power generation [9], and hydrogen refueling stations with integrated hydrogen production, transportation and sale in a “child and mother station”. For hydrogen production and hydrogen refueling mother stations actively participate in the peak and valley tariff mechanism in the demand to change the electricity consumption behavior. The system constructed in this paper is an integrated energy system for hydrogen production and sale “mother station” hydrogen refueling station to meet hydrogen demand through electrolytic water hydrogen production system and methanol hydrogen production system, as well as considering energy storage unit and hydrogen production link to participate in demand-side response. The energy flow diagram of this integrated energy system is shown in Fig. 1.

In the system, the electrolytic water hydrogen production system adopts the proton exchange membrane electrolytic water hydrogen production equipment, which is supplied by the photovoltaic power generation unit, the energy storage unit and the superior power grid, and the hydrogen produced is directly supplied to the hydrogen load; the methanol hydrogen production system adopts the methanol and water vapor reforming hydrogen production process, and the hydrogen produced is

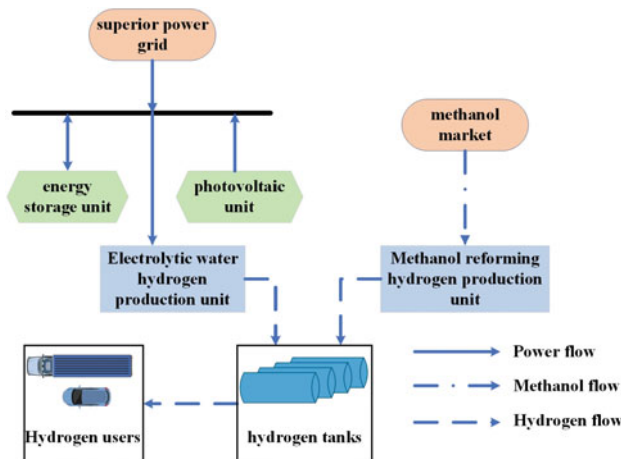


Fig. 1 Energy flow diagram of integrated energy system

directly supplied to the hydrogen load, and the raw material for hydrogen production, methanol, comes directly from the methanol market.

2.2 Link Model of Integrated Energy System Structure of Hydrogen Production and Hydrogen Refuelling Integrated Mother Station

2.2.1 Hydrogen Production by Electrolysis of Water.

The electrolyzer in the electrolytic water hydrogen production system converts electrical energy into hydrogen by electrolyzing water. Hydrogen production from electrolytic water is the most promising hydrogen production technology because of its high purity and no carbon dioxide emission during the process. According to the different diaphragms, electrolytic water technology can be divided into alkaline electrolytic water hydrogen production, proton exchange membrane electrolytic water hydrogen production and solid oxide electrolytic water hydrogen production, among which alkaline electrolytic water hydrogen production is the most mature and highly commercialized; proton exchange membrane electrolytic water hydrogen production has high current density and good input dynamic response, which is suitable for renewable energy generation with obvious fluctuations, but the investment cost of equipment is high, and it has been initially commercialized. The solid oxide electrolytic water hydrogen production has high conversion efficiency, but requires high temperature heat source and high requirement for material anti-aging ability in high temperature environment [10–12].

In this paper, the mathematical model of [13] is proposed to be used for hydrogen production by electrolysis of water using a proton exchange membrane, as shown in Eq. (1).

$$m_t^{P2H} = \varepsilon \eta^{P2H} P_t^{P2H} \quad (1)$$

where m_t^{P2H} is the hydrogen production of the electrolyzer at time t , in kg/h . ε is the electro-hydrogen conversion factor in $Nm^3/(kWh)$. η^{P2H} is the efficiency of electrolyzer. P_t^{P2H} is the input power of the electrolyzer at time t , in kW .

2.2.2 Methanol Reforming to Hydrogen

Methanol hydrogen production has the advantages of flexible hydrogen production scale, low construction investment cost, easy to obtain raw materials, and high energy density per unit of methanol, easy to store and transport, and low carbon emission in the process of hydrogen production, which is “blue hydrogen”. Methanol water vapor reforming is a relatively mature methanol to hydrogen technology, which is a

reaction between methanol and water vapor under certain pressure and temperature conditions, using Cu, Pd, etc. as catalysts to convert to hydrogen and carbon dioxide. This type of hydrogen production has the advantages of mild reaction conditions, high hydrogen yield, and low CO content [14]. Methanol reforming for hydrogen production is not only applied in hydrogen refueling stations for hydrogen production, but also in some new energy vehicles where on-board methanol reforming for hydrogen production is adopted to supply hydrogen fuel cell consumption directly [14].

The mathematical model proposed in this paper [15] is shown in Eq. (2).

$$m_t^{M2H} = \eta^{M2H} m_t^{in} \quad (2)$$

where m_t^{M2H} is the methanol reformer hydrogen production at time t , in kg/h . η^{M2H} is the efficiency of methanol reformer hydrogen production. m_t^{in} is the mass of methanol consumed by methanol reformer hydrogen production at time t , in kg/h .

2.3 Two-Layer Demand-Side Response Mechanism of the Integrated Hydrogen Production and Hydrogen Refueling Mother Station

The two-layer demand-side response of the integrated hydrogen production and hydrogen refueling mother station proposed in this paper is not only reflected in the demand-side response of traditional electric energy storage, but also in the demand-side response of cross-energy forms.

The energy storage unit serves as the first layer of a two-tier demand-side response for the integrated hydrogen production and hydrogen refueling mother station. In the price-based demand-side response [10] the batteries of the energy storage unit are charged at the valley price of the peak-valley tariff to obtain electricity from the grid, and discharged at the peak price of the peak-valley tariff to provide electricity to the electricity-using load, which does not obtain electricity from the grid until the batteries are completely discharged. Such a response can, on the one hand, help the load to reduce the cost of electricity and, on the other hand, reduce the peak-to-valley difference of the power system.

The second layer of the two-tier demand-side response of the integrated hydrogen production and refueling mother station is reflected in the cross-energy form of demand response. This layer of demand response occurs only when the peak hydrogen cost is higher than the methanol reforming cost and when the valley hydrogen cost is lower than the methanol reforming cost. When the peak-to-valley tariff is in the peak range, the customer will be motivated to use electrolytic water to produce hydrogen; when the peak-to-valley tariff is in the valley range, the customer will be motivated to use methanol reforming to produce hydrogen.

3 Two-Tier Demand-Side Response Model

The two-tier demand-side response model proposed in this paper considers the factors of electricity price and methanol price, and the integrated hydrogen production and hydrogenation mother station operates the system with the pursuit of minimizing its own operation cost. Therefore, the two-tier demand-side response model given in this section will find the appropriate independent variables to construct the objective function with the objective of minimizing the system operation cost and determine the optimal decision scheme.

3.1 Objective Function

In this model, three independent variables are selected to construct the objective function. These include the battery charging and discharging power P_t^b at time t . The input power P_t^{P2H} of the electrolyzer at time t . And the methanol mass m_t^{in} consumed in methanol reforming for hydrogen production at time t .

The objective function of this paper is to minimize the sum of the operating cost F_1 of electric hydrogen production and the operating cost F_2 of methanol hydrogen production, and the detailed formula is shown in Eq. (3).

$$\begin{cases} \text{Min } F = F_1 + F_2 \\ F_1 = C_{Ph} + C_B + C_{P2H} \\ F_2 = C_M \end{cases} \tag{3}$$

where $\text{Min}F$ is the sum of objective functions F_1 and F_2 , and C_{Ph} , C_B and C_{P2H} are the operating costs of PV unit, energy storage unit and electrolyzer, respectively. C_M is the operating cost of methanol to hydrogen.

Where C_{Ph} , C_B , C_{P2H} and C_M , the detailed equations are shown in Eq. (4).

$$\begin{cases} C_{Ph} = - \sum_{t=1}^T C_t^P \cdot P_t^V \cdot \Delta t \\ C_B = - \sum_{t=1}^T C_t^P \cdot P_t^B \cdot \Delta t \\ C_{P2H} = \sum_{t=1}^T C_t^P \cdot P_t^{P2H} \cdot \Delta t \\ C_M = \sum_{t=1}^T C_t^M \cdot m_t^{in} \cdot \Delta t \end{cases} \tag{4}$$

where T is the dispatch period in h . C_t^P is the purchased power price in time period t . P_t^V is the PV output in time period t in kW . Δt is the dispatch time per unit in h . C_t^M is the purchased power price in time period t .

3.2 Constraints

3.2.1 Energy Storage Device Constraints

The operation of the two-tier demand-side response system model needs to satisfy three constraints on the battery operating state of the energy storage equipment, the charging and discharging power constraints, and the energy storage capacity.

Among them, the first constraint is the battery operation state constraint, as shown in Eq. (5), which indicates that the total discharge of the battery in a dispatch cycle is equal to the total charge.

$$\sum_{t=1}^T P_t^B \cdot \Delta t = 0 \quad (5)$$

The second constraint is the battery charging and discharging power constraint, as shown in Eq. (6), which indicates that the battery charging and discharging power must not exceed certain upper and lower boundaries during t time periods.

$$-P_{\max}^B \leq P_t^B \leq P_{\max}^B \quad (6)$$

where, P_{\max}^B is the upper and lower limits of battery charging and discharging power in kW .

The third constraint is the battery storage capacity constraint, as shown in Eq. (7), which indicates that the battery capacity must not exceed certain upper and lower boundaries.

$$0 \leq Init^B + \sum_{t=1}^k P_t^B \leq BE_{\max}, \forall k \in 1, 2, \dots, T \quad (7)$$

where, $Init^B$ is the initial storage capacity of the battery in $kW \cdot h$. BE_{\max} is the upper capacity limit of the battery in $kW \cdot h$.

3.2.2 Hydrogen Production and Storage Equipment Constraints

The constraints to be satisfied by the hydrogen production equipment model in the two-layer demand-side response model are three constraints: hydrogen supply

and demand balance constraint, electrolyzer input power constraint, and methanol reforming hydrogen production power constraint. As well as the operating state constraint of the hydrogen storage equipment, and the stock constraint.

Among them, the hydrogen supply and demand balance constraint of the hydrogen production equipment model, as shown in Eq. (8), which indicates that the total amount of hydrogen produced by the hydrogen production equipment in a dispatch cycle is equal to the hydrogen demand.

$$\sum_{t=1}^T (m_t^{P2H} + m_t^{M2H}) = \sum_{t=1}^T m_t^{HR} \tag{8}$$

where, m_t^{HR} is the hydrogen demand in kg for time period t .

The electrolyzer input power constraint for the hydrogen production equipment model is shown in Eq. (9), which indicates that the electrolyzer input power in time period t must not exceed a certain upper and lower bound.

$$P_{\min}^{P2H} \leq P_t^{P2H} \leq P_{\max}^{P2H} \tag{9}$$

where P_{\min}^{P2H} and P_{\max}^{P2H} are the lower and upper limits of the input power of the electrolyzer.

The methanol reformer hydrogen production power constraint constraint for the hydrogen production equipment model, shown in Eq. (10), indicates that the methanol input to the methanol reformer hydrogen production at time t must not exceed a certain upper and lower bound.

$$P_{\min}^{P2H} \leq P_t^{P2H} \leq P_{\max}^{P2H} \tag{10}$$

where m_{\min}^{in} and m_{\max}^{in} are the lower and upper limits of methanol input per unit time to the methanol reforming hydrogen plant.

The operating state constraint of the hydrogen storage equipment, as shown in Eq. (11), indicates that the input quantity of the hydrogen storage equipment is equal to the output quantity in one scheduling cycle.

$$\sum_{t=1}^T S_t^H = 0 \tag{11}$$

where S_t^H is the net intake of hydrogen storage equipment at time t , in kg.

The stock constraint of the hydrogen storage equipment, as shown in Eq. (12), which indicates that the hydrogen stock in a dispatch cycle must not exceed a certain upper and lower bound.

$$0 \leq Init^H + \sum_{t=1}^k S_t^H \leq S_{\max}^H, \forall k \in 1, 2, \dots, T \tag{12}$$

where $Init^H$ is the initial hydrogen storage capacity in kg, and S_{max}^H is the upper limit of hydrogen storage capacity in kg of the hydrogen storage equipment.

4 Example Analysis

4.1 Background of the Algorithm

To test the validity of the model proposed in Sect. 2, two typical numerical studies are conducted in this section, namely, feasibility experiments and sensitivity experiments. The feasibility experiment is used to test the reasonableness of the model and the solution algorithm, and to obtain relevant data for evaluating the enhancement effect of the model. The sensitivity experiments are used to analyze how the change of some important variables in the model will affect the demand-side response and to analyze the feasible range of the model. In the sensitivity analysis experiment of this paper, the volatility of methanol price is considered, and the change of demand-side response is observed by adjusting the methanol price from ¥0.5 to ¥5 continuously, and the feasible range of the demand-side response model proposed in this paper is obtained.

This example takes into account the actual situation of peak and valley tariffs of the power grid, sets the dispatching period to 24 h, the unit dispatching time to 1 h, and the tariff adopts the peak and valley tariff of Guangzhou City set by the Development and Reform Commission of Guangdong Province, the tariff for peak hours (10–12, 14–19) is 1.1008 Yuan/(kWh); the tariff for low hours (0–8) is 0.2461 Yuan/(kWh) The tariff is 0.6475 Yuan/(kWh) for the rest of the day. The daily hydrogen output is set at 1000 kg/day with reference to the daily demand of a hydrogen refueling station in Guangzhou. The peak-valley tariff curve and hydrogen demand curve are shown in Fig. 2 below, the PV output curve is shown in Fig. 3, and the basic data of the calculation case are shown in Table 1.

4.2 Feasibility Experiment Results and Analysis

In the experiments, we obtained the changes of various data of the system under two demand-side responses by scheduling the system with the objective of the lowest production cost while satisfying the production tasks of the users. The specific changes of each data of the system in the feasibility experiment are shown in Table 2, and the changes of various parameters and variables are shown in Figs. 4, 5, 6 and 7.

As can be seen from Table 2, compared with the traditional demand-side response model, the two-tier demand-side response model proposed in this study reduces the total daily power purchase from 22,947 kWh to 17,761 kWh, a reduction of up to

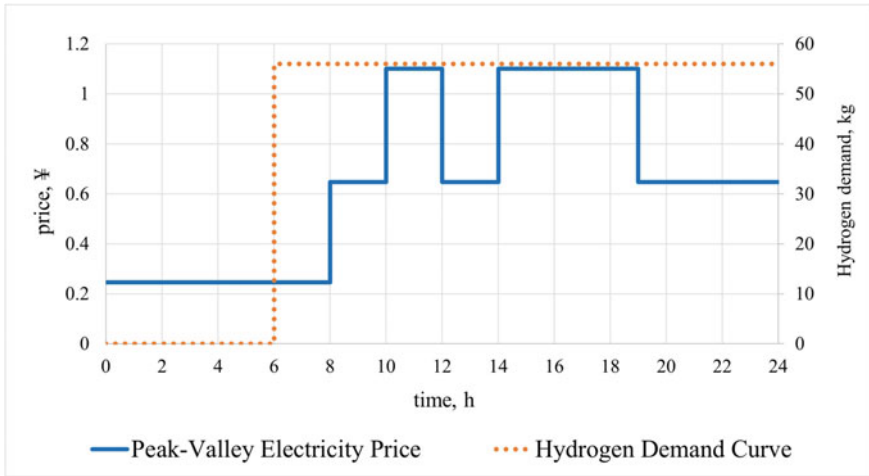


Fig. 2 Peak-valley electricity price and hydrogen demand curve

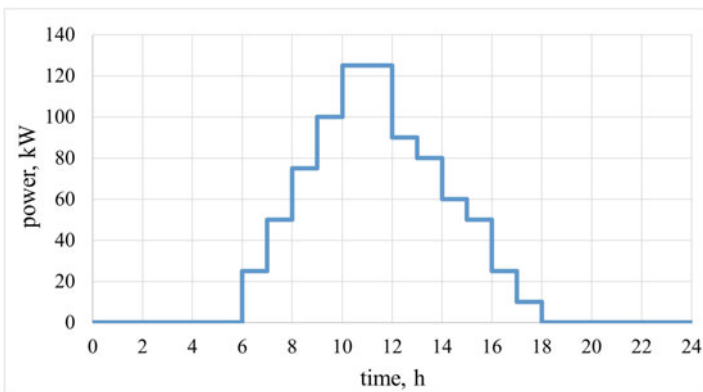


Fig. 3 PV output curve

5,186 kWh, while the methanol consumption increases from 5,644 kg to 6,876 kg, an increase of 1,232 kg. The maximum daily peak-to-valley difference increases from 185 to 1985 kW, indicating that the system will have a large amount of electrical load demand shifted from the peak to the trough section of the tariff, and the effect of peak reduction and valley filling is more obvious. As for the cost, the daily power purchase cost of the system is reduced by 8,857 Yuan, while the methanol cost is increased by 3,079 Yuan, thus the total cost is reduced by 5,778 Yuan, and thus the unit cost of hydrogen production is reduced from 28.4 Yuan to 22.6 Yuan, and the production cost of 1 kg of hydrogen is reduced by up to 5.8 Yuan.

From the charging and discharging power curves of the energy storage unit in Fig. 4, it can be seen that under both demand-side responses the energy storage unit

Table 1 Basic data of the algorithm

Battery capacity limit	300 kW.h
Initial energy storage of the battery	30 kW.h
Battery charging and discharging power limit	± 30 kW/h
Electric hydrogen power upper and lower limits	lower limit:200 kW upper limit:2000 kW
Methanol to hydrogen power upper and lower limits	lower limit:20 kg/h upper limit:1000 kg/h
Storage limit of hydrogen tank in the station	312 kg
Storage limit of hydrogen tank in the station	18 kg

Table 2 Comparison of results under two-tier demand-side responses

Project	Traditional demand-side response model	Two-tier demand-side response model	Amount of change
Total daily power purchase of the system (kWh)	22,947	17,761	reduce 5186
Total daily methanol consumption of the system (kWh)	5644	6876	Increase 1232
Total system electricity consumption at the peak of the daily tariff (kWh)	6326	795	reduce 5531
Total system electricity consumption at the peak of the daily tariff (kWh)	8086	15,541	Increase 7455
Maximum peak-to-valley difference of daily electrical load of the system (kW)	185	1985	Increase 1800
System day power purchase cost (Yuan)	14,480	5623	reduce 8857
System day methanol cost (Yuan)	14,110	17,189	Increase 3079
Total system day cost (Yuan)	28,590	22,812	reduce 5778
System hydrogen production unit cost (Yuan/kg)	28.4	22.6	reduce 5.8

is charged at maximum power in the valley section of the tariff, and then discharged at maximum power after reaching the peak section of the tariff, and the excess electricity continues to be released in the flat section until the energy storage unit resumes its initial energy storage situation. Therefore, under the two-tier demand-side response model proposed in this study, the energy storage unit still maintains the charging and discharging situation under the traditional demand-side response model, which is not affected by the hydrogen production link.

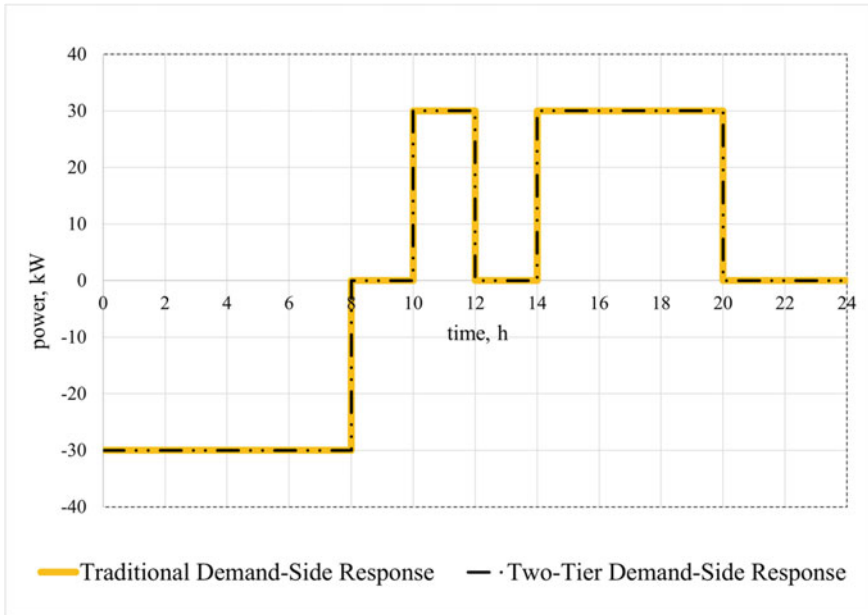


Fig. 4 Charging and discharging power of energy storage unit under two-tier demand-side responses

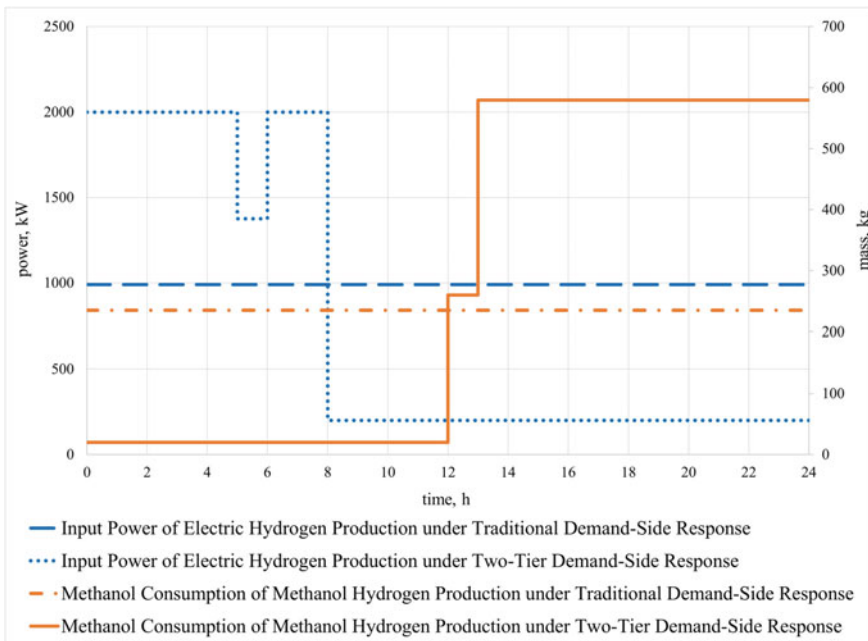


Fig. 5 Changes of input electric power and methanol consumption in hydrogen production link

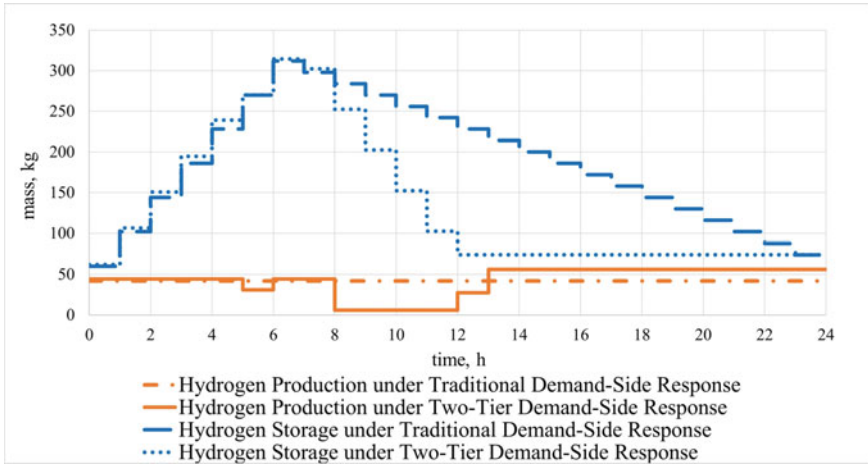


Fig. 6 Hydrogen production and stock under two-tier demand-side responses

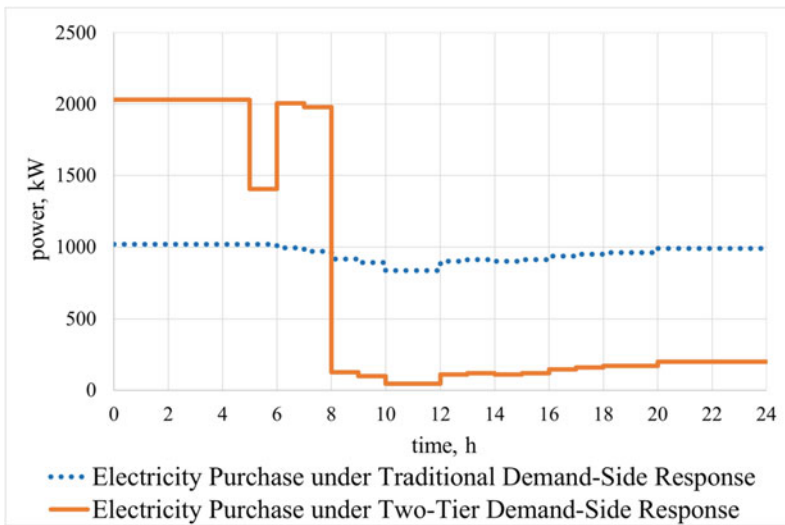


Fig. 7 Purchasing power of the system under two-tier demand-side responses

Combining Figs. 5 and 6, it can be seen that under the traditional demand-side response model, the input electric power of the hydrogen production link and the methanol consumption in each time period remain the same throughout the day, so the hydrogen production remains constant, while the hydrogen stock rises continuously from 0:00 to 6:00, and then decreases gradually from 6:00 to 24:00. In the two-layer demand-side response mode, the algorithm automatically identifies the lowest cost of hydrogen production in the valley of electricity price, so from 0:00 to 6:00, although

the hydrogen demand is 0, the electric hydrogen production runs at full power and the methanol hydrogen production runs at the lowest power, and the hydrogen is produced in advance and stored in the storage tank, and the hydrogen stock keeps increasing until all the storage tanks are full, and the hydrogen is mainly produced by the electric hydrogen production in this period. From 6:00 to 8:00, when the electricity price is still in the trough, the electric hydrogen production runs at full power and consumes part of the hydrogen stock to meet the hydrogen demand, while the methanol hydrogen production still runs at the lowest power. From 8:00 to 12:00 both electric and methanol hydrogen production run at minimum power and hydrogen demand is mainly met by hydrogen stock during this period, which is decreasing. At 12:00 to 24:00, the hydrogen stock will reach a low point, and hydrogen demand will be mainly met by methanol hydrogen production during this period, with electric hydrogen production running at the lowest power.

From the system power purchase in Fig. 7, it can be seen that, compared with the traditional demand-side response model, most of the electrical loads in the flat and peak segments are shifted to the valley segment of the tariff under the two-layer demand-side response model proposed in this study, and the peak-valley difference is more obvious, which results in better peak-shaving and valley-filling effects.

The conclusions we can draw from the feasibility experiments are as follows:

The demand-side response model proposed in this study, the response of the energy storage unit to the tariff curve is consistent with the results under the traditional demand-side response model, so the model does not change the demand-side response of the energy storage unit.

In addition, the model enables the energy storage unit and the hydrogen production link to participate in demand-side response at the same time, realizing cross-energy form of demand-side response. Since hydrogen production consumes more electricity, compared with the traditional demand-side response, the participation of hydrogen production in the demand-side response shifts a large amount of electrical load to the tariff valley section, and the electricity consumption in the tariff peak section is significantly reduced, and the peak-valley difference increases from 1,442 kW to 1,920 kW, which is more effective in cutting the peak and filling the valley. For users, the cost of hydrogen production without affecting the normal supply of hydrogen is reduced from 28.4 Yuan/kg to 22.6 Yuan/kg, which is 20.4% lower than that under the traditional mode, and can bring greater economic benefits to users and meet the interests of users. Combining all the above results, the model proposed in this study is proved to be effective.

4.3 Analysis of Sensitivity Test Results

With the change in methanol prices [15], the various types of data presented in this study for the two-layer demand-side response are shown in Table 3 below.

From Table 3, it can be seen that the total daily cost of the system increases with the increase of methanol price, while the results such as the daily power purchase of

Table 3 Various types of demand-side response data under different methanol prices

Methanol Price (Yuan)	0.5	1.0	1.1	2.5	2.8	4.6	4.7	5.0
Total daily power purchase of the system (kWh)	3985	3985	17,761	17,761	33,961	33,961	44,689	44,689
Total daily consumption of methanol in the system (kg)	10,148	10,148	6876	6876	3028	3028	480	480
Total system electricity consumption in the peak period of daily tariff (kWh)	795	795	795	795	795	795	11,523	11,523
Total system electricity consumption in the valley section of the daily tariff (kWh)	1765	1765	15,541	15,541	15,541	15,541	15,541	15,541
Maximum peak-to-valley difference of daily electrical load of the system (kW)	185	185	1985	1985	1985	1985	1985	1985
Total system day cost (Yuan)	7306	12,380	13,186	22,812	24,590	30,041	30,177	30,321

the system can be divided into three cases according to the change of methanol price as follows.

In the case that the cost of methanol hydrogen production is lower than the cost of electric hydrogen production in the valley of electricity price, as the cost of electric hydrogen production is always higher than the cost of methanol hydrogen production, the total daily power purchase of the system is only 3985kWh. The hydrogen demand of the system is mainly met by methanol hydrogen production, and the methanol consumption is up to 10,148 kg. At this time, electric hydrogen production operates at the lowest power with a small peak-to-valley difference of 185 kW.

In the case that the cost of methanol hydrogen production is between the cost of electric hydrogen production in the valley and peak segments of the electricity tariff, the daily power purchase of the system increases more than the daily power purchase when the cost of methanol hydrogen production is lower than the cost of electric hydrogen production in the valley segment of the electricity tariff, from 3985 kWh to 17,761 kWh. When the cost of methanol hydrogen production is above the cost of electric hydrogen production in the flat segment of the electricity tariff, the power purchase further changes to 33,961 kWh when the cost of methanol hydrogen production is lower than the cost of electric hydrogen production in the flat segment of the electricity tariff. At this time, according to the change of electricity price and methanol price, the system will meet the hydrogen demand with electricity when the electricity hydrogen cost is low, and will meet the hydrogen demand with methanol when the methanol hydrogen cost is low, and the power consumption in the valley

section is larger, 15541kWh, and the maximum peak-to-valley difference changes from 185 to 1985 kW.

In the case that the cost of methanol hydrogen production is higher than the cost of electric hydrogen production in the peak section of the electricity tariff, the total daily power purchase of the system reaches the maximum value of 44,689 kW-h because the cost of electric hydrogen production is always lower than the cost of methanol hydrogen production, and the hydrogen demand of the system is mainly met by electric hydrogen production, and the methanol hydrogen production is maintained at the lowest power operation possible, and the daily methanol consumption is only 480 kg. At this time, the power consumption in the peak section of the electricity tariff is higher than the cost of methanol hydrogen production. The electricity consumption and the maximum peak-to-valley difference of the system are still the same as the corresponding values when the cost of methanol hydrogen production is between the cost of electricity in the valley and the cost of electricity in the peak section of the tariff, which are 11,541 kW-h and 1985 kW-h, respectively. kW-h and 1985 kW.

From the analysis of the above three cases, it can be seen that when the cost of methanol hydrogen production is lower than the cost of electric hydrogen production in the trough of electricity price or higher than the cost of electric hydrogen production in the peak of electricity price, electric hydrogen production or methanol hydrogen production will operate at the lowest possible power in any time, and the hydrogen production link will not participate in the demand-side response. Therefore, the demand-side response model proposed in this paper is feasible when the cost of methanol hydrogen production is located at the cost of electric hydrogen production in the electricity price valley and the electricity price peak.

5 Conclusion

In this paper, we develop a two-tier demand-side response system model for hydrogen production and sale integrated hydrogen refueling station. The system mainly consists of renewable energy distributed generation unit, energy storage unit, electrolytic water hydrogen production system, and methanol hydrogen production system. The model is divided into four parts: mathematical model of equipment, establishment of independent variables, establishment of objective function and constraints. Combined with the analysis of the arithmetic results, the following conclusions are drawn.

- The two-layer demand-side response proposed in this paper has a significant participation response effect compared to the traditional electric storage demand-side response. Under the double-layer demand-side response, the peak-section electricity consumption is reduced and the valley-section electricity consumption is increased significantly. Most of the peak section electric load is shifted to the valley section of the electricity price, which is conducive to the power system load

to achieve peak shaving and valley filling, alleviating the peak-valley difference and achieving stable operation of the power system.

- The two-tier demand-side response proposed in this paper takes into account the electricity price and methanol price factors to provide a decision solution for the integrated hydrogen production and hydrogen refining mother station to reduce the operating cost of the integrated hydrogen production and hydrogen refining mother station. When the peak price hydrogen production cost is greater than the methanol reforming hydrogen production cost, methanol reforming hydrogen production cost is selected; when the valley price hydrogen production cost is less than the methanol reforming hydrogen production cost, electrolytic water hydrogen production is selected.

Acknowledgements This research was partially funded by the Guangdong Power Grid Corporation Electricity Planning Theme Study Project 031000QQ00210018.

References

1. Cao, Y., Cheng, N., Luo, D.: New role of hydrogen energy industry under the trend of energy transition. *Pet. Petrochem. Green Low-carbon* **7**(01), 1–5 (2022). (in Chinese)
2. Yang, Y., Ge, X.: Research on innovation and development of China's new energy vehicle industry under the background of "double carbon." *Energy Storage Sci. Technol.* **11**(07), 2406–2407 (2022). (in Chinese)
3. Shao, Z., Yi, B.: Development status and prospect of hydrogen energy and fuel cells. *Bull. Chin. Acad. Sci.* **34**(04), 469–477 (2019). (in Chinese)
4. Xu, D., Liu, Y., Li, Z., Ding, S., Chen, S.: Review on the economics of hydrogen energy development and utilization. *Oil Gas New Energy* **33**(02), 50–56 (2021). (in Chinese)
5. Ma, Z.-C., Feng, H., Yan, Y.-D.: Selection of hydrogen supply mode and research status analysis of hydrogen production technology in hydrogenation station. *Guangzhou Chem. Ind.* **47**(16), 132–134 (2019). (in Chinese)
6. Wang, Y., Du, W., Ye, G., He, Q., Yi, L.: Hydrogen production hydrogenation "mother standing" construction planning makes analysis. *J. Chem. Eng.* **33**(S2)6, 121–127 (2020). 10.16085/j.iSSN.1000–6613.2020–1314. (in Chinese)
7. Chen, W.-R., Fu, W.-X., Han, Y., Li, Q., Huang, L.-J., Xu, C.-P.: Optimal configuration of wind-light-hydrogen multi-energy complementary microgrid considering demand side. *J. Southwest Jiaotong Univ.* **56**(03), 640–649 (2021). (in Chinese)
8. Wei, Z., Ren, X., Huang, Y.: Multi-objective optimal scheduling of regional integrated energy system considering integrated demand side response. *Electr. Power Const.* **41**(07), 92–99 (2020). (in Chinese)
9. The first hydrogenation station in Hubei province of Sinopec was built. *Chlor-alkali industry* **57**(12), 47 (2021). (in Chinese)
10. Wang D.-R.: Power demand response. Xinhua Press (2018). (in Chinese). 201808.171
11. Yu, H., Shao, Z., Hou, M., Yi, B., Duan, F.-W., Yang, Y.-X.: Research progress and suggestions on hydrogen production from water electrolysis. *Eng. Sci. China* **23**(02), 146–152 (2021). (in Chinese)
12. He, Z., et al.: Development status and prospect of water electrolysis for hydrogen production by proton exchange membrane. *Chem. Ind. Prog.* **40**(09), 4762–4773 (2021). (in Chinese)
13. Li, C., Li, X., Song, L.: Numerical simulation and analysis of hydrogen production system by methanol reforming. *Power Supply Technol.* **2006**(11), 898–900 (2006). (in Chinese)

14. Sun, X., Sha, Q., Wang, C., Zhou, D.: Research progress of cu-based catalysts for hydrogen production from methanol reforming. *Acta Chemica Sinica* **72**(12), 5975–6001 (2021). (in Chinese)
15. Chen, S.: China methanol industry market analysis report 2021–2022 (middle). *Guangzhou Chem. Ind.* **50**(04), 1–3 (2022). (in Chinese)

Visual Defect Detection Method of High Voltage Overhead Transmission Line Based on rp-CenterNet



Wenhao Mo, Jie Tong, Yuanpeng Tan, Fangzhou Hu, and Zhuhan Tang

Abstract Regression box target detection technology based on deep learning is widely used in high-voltage overhead line inspection and has been widely used. However, the existing detection technology usually has some problems, such as a low recall rate and the decline of positioning accuracy with the change of shooting angle, especially in the detection of equipment with small size and large length-width ratio. In this paper, we propose a direction adaptive anchor-free detection method called rp-CenterNet. The main improvements of the network include: 1) To implement rotated device detection, we proposed a direction point schema to form rotated bounding boxes. 2) Meanwhile, we replaced the fixed-shape Gaussian kernel with a category-wise adaptive kernel, which captured devices' varied appearance features better. 3) Use ResNet as a backbone and add the fusion weight of the feature graph. We achieved the best speed-accuracy-recall trade-off on the custom dataset TRANS2021, which aims at four kinds of defects: falling off of shockproof hammer, a self explosion of insulator, corrosion of conductor, and damage of cable joint skin with 61% AP and 77% Recall.

Keywords Patrol inspection · Equipment detection · Direction adaptive detection · Anchor-free method

1 Introduction

Equipment detection is an important research direction in the field of automatic detection of high-voltage overhead lines. At present, the transmission line UAV patrol inspection generally adopts the method of combining the edge side UAV acquisition with the cloud defect detection and identification [1]. The transmission line tower and main equipment images are taken by the operation inspection personnel or the UAV independent acquisition method, uploaded to the cloud AI computing platform

W. Mo · J. Tong (✉) · Y. Tan · F. Hu · Z. Tang
China Electric Power Research Institute Co., Ltd., Beijing 100000, China
e-mail: tongjie1@epri.sgcc.com.cn

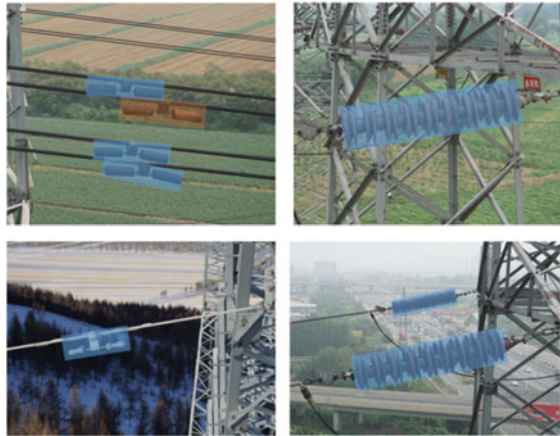
© Beijing Paiké Culture Commu. Co., Ltd. 2023
X. Dong et al. (eds.), *The proceedings of the 10th Frontier Academic Forum of Electrical Engineering (FAFEE2022)*, Lecture Notes in Electrical Engineering 1054, https://doi.org/10.1007/978-981-99-3408-9_35

through the business platform, and then processed and analyzed through the GPU server.

According to the network structure, it can be divided into one stage detection method [2–4], two stage detection method [5–7] and Anchor-free method. As a representative Anchor-Free method, CenterNet has simple network structure and good scalability. For rotating target detection, reference [8] adds a rotating detection branch to the multitask branch of CenterNet, reference [9] uses the attention pyramid block to optimize the feature extraction network, the reference [10] proposes the rotating target detection network RCNet based on CenterNet, and proposes to set all sampling points in the detection frame when generating the feature heat map. The above method realizes rotation detection by adding rotation branches, and has been verified on DOTA and other satellite remote sensing image data sets, but has not been further studied and improved for the rotation task.

This paper proposes a directional adaptive high voltage overhead line equipment detector rp-CenterNet based on anchored frame network. The detector adopts an improved dynamic label allocation strategy, expands an additional rotation angle prediction branch, and realizes the rotation angle prediction of the regression box; The sample generation method of FCOS is adopted to effectively alleviate the impact of the imbalance of positive and negative samples in the data set on the training effect; At the same time, a dynamic label allocation strategy is developed to reduce the impact of sample imbalance on equipment and defect detection accuracy. On the data set TRANS2021, this method achieves the best speed-accuracy-recall tradeoff. The AP and recall rates are 61% and 77% respectively. Some test results are shown in Fig. 1.

Fig. 1 Schematic diagram of rp-CenterNet



2 Directional Adaptive Visual Defect Detection Framework for High-Voltage Overhead Transmission Lines

2.1 Application of Directional Adaptive Target Detection in Transmission Line Defect Detection

The directional adaptive target detection technology is applied to the fields of transmission and distribution line inspection, substation equipment status monitoring, cable tunnel inspection, etc., which can solve the problems of low accuracy of detection results, scarcity of defect data, and partial defects relying on business logic judgment.

The scarcity of negative samples is a common problem in the detection of power equipment. In engineering, the defect detection task is often divided into multiple subtasks in a cascade way to improve the recognition accuracy. Taking the self-explosion of insulator as an example, the insulator can be located through a large number of normal insulator images, and then whether there is self-explosion can be identified based on it. In this task, rotating target detection can effectively reduce background information interference and improve defect recognition accuracy.

2.2 TRANS2021 Dataset

At present, the research on transmission line direction adaptive detection technology is relatively small, and no large-scale public data set has been formed. Based on the data of overhead transmission lines and cable tunnels collected in Liaoning, Shandong, Zhejiang, Tianjin and other places, the data set TRANS2021 is constructed by combining horizontal annotation and rotation annotation, which is used for the training and verification of the model algorithm. The TRANS2021 data set contains 6200 images of normal equipment and 2500 images of equipment defects, including 548 pieces of shockproof hammer falling off, 664 pieces of pin missing, 472 pieces of insulator self-explosion, 139 pieces of wire corrosion, 489 pieces of bird's nest, and 188 pieces of cable joint skin damage.

In terms of defect type selection, shockproof hammer falling off, insulator self-explosion, wire corrosion, cable joint skin damage are equipment defects with large aspect ratio, which are used to detect the accuracy of the algorithm for angle prediction; The length and width ratio of bird's nest defect is small, which is used to detect the accuracy of location prediction of the algorithm; The pin missing character is small, which is used to detect the small target detection ability of the algorithm. Take the pin missing, shockproof hammer falling off and wire corrosion defects in the data set as an example to count the aspect ratio and rotation angle of the rotating label box, as shown in Fig. 2. Among them, the average length–width ratio of pin missing is 1.28, the average value of shockproof hammer falling off is 4.82, and the average

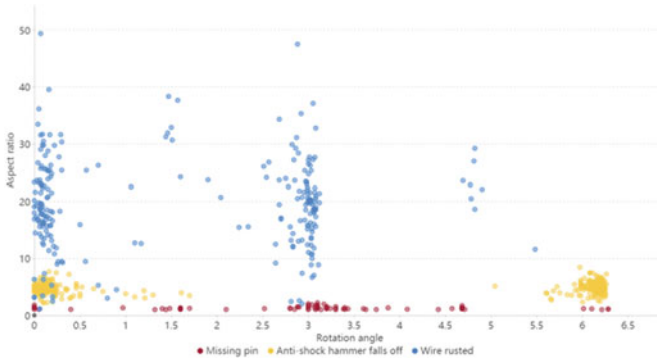


Fig. 2 Defect Shape Characteristics of TRANS2021

value of wire corrosion is 20.6. There are obvious distribution differences between different categories.

3 Visual Defect Detection of Transmission Equipment Based on rp-CenterNet

3.1 Network Structure

The overall framework of rp-CenterNet takes CenterNet as the benchmark, and forms a boundary box by predicting the center point, object size and offset of the object to be detected. The network uses ResNet-50 with FPN structure as the backbone network. In order to realize the detection of rotating equipment, the direction prediction branch is introduced to establish the rotating boundary frame network. It should be pointed out that the network structure has better scalability and applicability, and can be flexibly deployed in a variety of side devices. The network output characteristic map is obtained from the original input image after 4 times of down-sampling.

The ResNet50 feature extraction network based on improved FPN is adopted, the feature map fusion weight α_q^p is set to improve the target detection rate, and the deformable convolution is combined to solve the problem of mismatch between the orientation of the receptive field of the feature extraction network and the actual target position. An adaptive feature map fusion weight α_q^p is proposed, which is defined as follows:

$$\alpha_q^p = k_{pq} * \frac{\overline{f_p}}{f_q} \tag{1}$$

where k_{pq} is the preset fusion weight, $\overline{f_p}$ is the mean value of non-zero point in the feature layer f_p , and $\overline{f_q}$ is the mean value of non-zero point in the target feature layer f_q .

Another challenge in the design of direction adaptive target detector is the rotation alignment of features. The standard convolution kernel extends the receptive field horizontally and vertically, and cannot accurately cover the target area. Referring to DCN [11], this paper proposes a rotation convolution network with adaptive direction:

$$R = \{(-1, -1), (-1, 0), \dots, (1, 1)\} \quad (2)$$

$$y(p_0) = \sum_{p_n \in R} w(p_n) \cdot x(p_0 + \vartheta_{p_0} p_n) \quad (3)$$

Among them, R is the sample point set of standard convolution, w is the convolution kernel parameter, and ϑ is the rotation angle prediction at the center point of the current convolution. Its size is the same as that of the feature map. The input feature map is predicted by 3×3 convolution.

By presetting or adaptively adjusting the distribution of convolution kernel sampling points, the receptive field can be extended to the specified area, which can achieve the effect of fitting with the target shape and improve the rotation detection accuracy.

3.2 Equipment Category Prior Check

Considering the non-uniformity of the distribution of power equipment in aspect ratio, this paper proposes a priori kernel of equipment category on the generation method of characteristic heat map, optimizes the generation method of characteristic map based on Gaussian distribution, and solves the problem of too little effective information of characteristic map generated by Gaussian kernel.

The prior kernel $P_m(x, y) = \exp\left(-\frac{(x-x_0)^2}{2\sigma_x^2} - \frac{(y-y_0)^2}{2\sigma_y^2}\right)$ is used to generate the next boundary box parameters and rotation parameters, where (x_0, y_0) represents the true position of the center of the boundary box of the object to be detected, and $\sigma = (\sigma_x, \sigma_y)$ is a learnable parameter that affects the shape of the prior distribution. Like CenterNet, in order to achieve feature alignment on the low-resolution feature map, (x_0, y_0) is the equivalent representation calculated by dividing the step size of the feature map.

As shown in Fig. 3 (a), the distribution of the characteristic heat map without a priori check of the equipment category has nothing to do with the size and shape of the detection target. Moreover, due to the small range of the Gaussian kernel, most of the generated heat map points are zero points, which will greatly increase the difficulty of model learning. However, the priori kernel of the equipment category

expands the coverage of the characteristic heat map and is closer to the shape of the target itself to increase the learnable information of the model.

Meanwhile, the direction point prediction method is used to describe the rotation angle of the equipment. Different from the direct regression angle value, the direction point method reduces the instability of IoU by using the periodic change of the angle value, and using the offset prediction method instead of using another thermal diagram to predict the direction point can solve the problem of matching the direction point with the center point and reduce the calculation amount. As shown in Fig. 4, the connection between the shock hammer and the conductor is used as the direction point for the shock hammer, and the upper edge of the self-explosion insulator is used as the direction point for the self-explosion of the insulator.

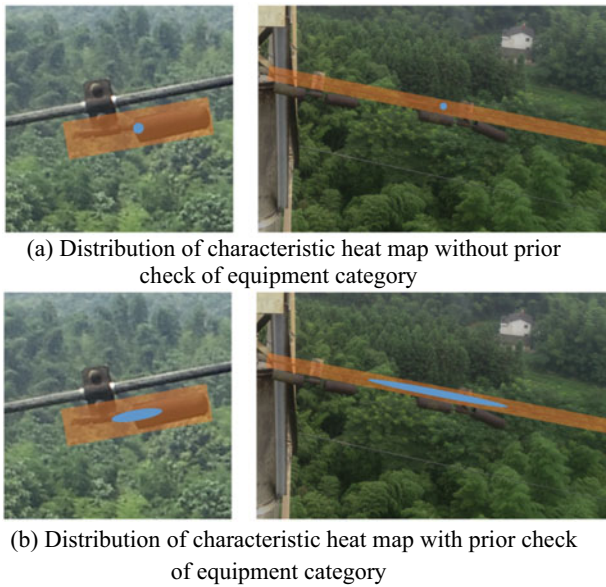


Fig. 3 Comparison of adding device prior kernels

Fig. 4 Rotation Detection Frame Based on Pole

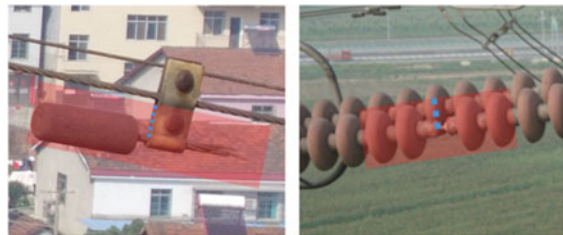


Table 1 Ablation experimental of Adding Prior kernel on Different Branches

Classification branch	Regression branch	AP50	AP90
		0.52	0.24
✓		0.56	0.25
	✓	0.53	0.27
✓	✓	0.57	0.27

4 Simulation Experiment and Result Analysis

4.1 Dataset and Experimental Environment

The ablation experiment was carried out on the customized data set TRANS2021. The training set and verification set (2000 images) were used for training and the test set (500 images) was used for evaluation.

The experimental training server uses Ubuntu 18.04 system, and is based on two Yingweida V100 32G GPUs for training. The experimental test equipment adopts Ubuntu 16.04 system and is based on Nvidia 2080 GPU for reasoning test.

4.2 Analysis of Simulation Results

The validity of rp-CenterNet is verified by adding a device prior module to the benchmark method. The fourth row of Table 1 shows that the average accuracy of the equipment prior module in the classification branch and regression branch is increased from 0.52 to 0.57.

FCOS, CenterNet, R3Det and YOLOX, which have good performance in general data sets and are widely used, are selected as the comparison model for the overall experiment. After experiments, the accuracy of the method proposed in this paper has been significantly improved, especially in terms of recall rate, which is more than 0.2 compared with other networks. The recall rate reaches 0.77, and the mAP reaches 0.61 (Table 2).

Table 2 Comparison Between rp-CenterNet with Rotation Detection Model on TRANS2021

Method	Anti-shock hammer falls off	Missing pin	Insulator self-explosion	Wire rusted	Nest	Cable joint skin damage	FPS	Recall	mAP
FCOS [12]	0.51	0.25	0.43	0.28	0.64	0.23	22.7	0.40	0.39
CenterNet [13]	0.48	0.26	0.37	0.26	0.59	0.28	15.4	0.26	0.37
R3Det [14]	0.60	0.44	0.48	0.29	0.71	0.38	13.6	0.57	0.48
YOLOX [15]	0.68	0.46	0.53	0.31	0.80	0.42	19.9	0.66	0.53
rot-CenterNet	0.65	0.41	0.52	0.36	0.74	0.44	14.8	0.48	0.52
rp-CenterNet*	0.73	0.58	0.65	0.42	0.81	0.47	14.2	0.77	0.61

5 Conclusions

In this paper, a high voltage overhead equipment and its defect detection method based on rp-CenterNet are proposed. Through the design of rotation detection module and nuclear branch module, a directional adaptive high voltage overhead line target detection method is realized. The network has made a great improvement in the accuracy of equipment detection and positioning. In the TRANS2021 test set, the mAP is 0.61, the recall rate is 0.77, and it is more than 0.13 higher than other common target detection methods. It solves the problem that the detection error increases and the positioning accuracy decreases with the change of shooting angle in the detection of transmission line equipment defect target.

Acknowledgements This work was funded by China Electric Power Research Institute Project “Research on transmission line patrol inspection technology based on airborne intelligent terminal”, China (No. AI84-22-003).

References

1. Xu, X., Hao, H., Zhong, P., et al.: Design and implementation of UAV autonomous inspection system for transmission line. *Hebei Electr. Power* **40**(05), 11–14+32 (2021). (in Chinese)
2. Liu, W., Anguelov, D., Erhan, D., et al.: SSD: Single Shot MultiBox Detector. In: Leibe, B., Matas, J., Sebe, N., Welling, M. (eds) *Computer Vision – ECCV 2016*. ECCV 2016. Lecture Notes in Computer Science(), vol. 9905, pp. 21–37. Springer, Cham. https://doi.org/10.1007/978-3-319-46448-0_2
3. Redmon, J., Farhadi, A.: Yolov3: an incremental improvement. arXiv preprint: [arXiv:1804.02767](https://arxiv.org/abs/1804.02767) (2018)
4. Lin, T.Y., Goyal, P., Girshick, R., et al.: Focal loss for dense object detection. In: *Proceedings of the IEEE International Conference on Computer Vision*, pp. 2980–2988 (2017)
5. Girshick, R.: Fast R-CNN. In: *Proceedings of the IEEE International Conference on Computer Vision*, pp. 1440–1448 (2015)
6. Ren, S., He, K., Girshick, R., et al.: Faster R-CNN: towards real-time object detection with region proposal networks. In: *Advances in Neural Information Processing Systems*, vol. 28, pp. 91–99 (2015)
7. Cai, Z., Vasconcelos, N.: Cascade R-CNN: delving into high quality object detection. In: *Proceedings of the IEEE Conference on Computer Vision and Pattern Recognition*, pp. 6154–6162 (2018)
8. Wang, M., Wang, J., Liu, C.: Detection of rotating targets in remote sensing images based on key points. *J. Electr. Measur. Instrum.* **35**(06), 102–108 (2021). (in Chinese)
9. Yang, Z., Ding, S., Zhang, L.: Anchor-free remote sensing image detection method for dense objects with rotation. *J. Comput. Appl.* **42**(06), 1965–1971 (2022). (in Chinese)
10. Jiang, G., Hu, C., Ye, H., et al.: Remote sensing target accurate detection algorithm based on rotation center point estimation. *Appl. Res. Comput.* **38**(09), 2866–2870 (2021). (in Chinese)
11. Jifeng, D., Haozhi, Q., Yuwen, X., Yi, L., et al.: Deformable convolutional networks. In: *Proceedings of the IEEE International Conference on Computer Vision*, pp. 764–773 (2017)
12. Tian, Z., Shen, C., Chen, H., et al.: FCOS: fully convolutional one-stage object detection. In: *Proceedings of the IEEE/CVF International Conference on Computer Vision*, pp. 9627–9636 (2019)
13. Zhou, X., Wang, D., Krähenbühl, P.: Objects as points. arXiv preprint [arXiv:1904.07850](https://arxiv.org/abs/1904.07850) (2019)

14. Yang, X., Yan, J., Feng, Z., et al.: R3Det: Refined single-stage detector with feature refinement for rotating object. In: Proceedings of the AAAI Conference on Artificial Intelligence, vol. 35, no. 4, pp. 3163–3171 (2021)
15. Ge, Z., Liu, S., Wang, F., et al.: YOLOX: Exceeding yolo series in 2021. arXiv preprint [arXiv: 2107.08430](https://arxiv.org/abs/2107.08430) (2021)

Research of Image Recognition Technology Based on 3D Point Cloud Data in Locomotive Roof Detection



Jun Guo Wang, Nai Shu Yu, Yao He, and Ning Luan

Abstract The loco locomotive roof foreign object detection system uses 3D image detection technology, 2D/3D image fusion technology and anti-sunlight interference technology to collect 2D/3D images of locomotive roofs in an open-air environment. The key components of the main locomotive models such as HXD2, HXD3, HXD3C, HXD3D are characterized and accurately positioned, so as to realize the recognition of foreign objects/abnormal states on the roof, solve the problem that there are many types of locomotive models that cannot be recognized by conventional patterns, and manually climb the roof. Aim to explore the gradual conversion of the manual summit preparation process to human-machine joint inspection.

Keywords Locomotive Roof Foreign Object Detection · Feature Recognition · Image Algorithm · Deep Learning

1 Introduction

The presence of foreign bodies on the roof of the locomotive is a safety hazard in the operation of the train, such as the damage caused to the inherent equipment of the roof, so that the equipment cannot operate normally [1]. Foreign objects on the roof include gloves used by staff, forgotten tools, animal carcasses, etc. [2]. We need to detect the state of the locomotive roof, correctly analyze and judge the roof foreign bodies, and take effective preventive measures to improve the quality of locomotive operation [3].

J. G. Wang · N. S. Yu

QingDao Locomotive Maintenance Section of China Railway Jinan Bureau Group Co., Ltd.,
Qingdao 266000, Shandong, China

Y. He (✉) · N. Luan

Sifang Rolling Stock Research Institute Co., Ltd., Qingdao 266000, Shandong, China
e-mail: 253192951@qq.com

© Beijing Paiké Culture Commu. Co., Ltd. 2023

X. Dong et al. (eds.), *The proceedings of the 10th Frontier Academic Forum of Electrical Engineering (FAFEE2022)*, Lecture Notes in Electrical Engineering 1054, https://doi.org/10.1007/978-981-99-3408-9_36

At present, there are several main methods for detecting the condition of non-contact roofs without manual work [4]:

- Frame of camera video detection.
- Area or line array 2D image detection.

The detection method of using camera dynamic video frame extraction is subject to the image accuracy limitation of the camera itself, and it is difficult to output a stable single frame image for image recognition. Due to the long body of the locomotive, the solution using an area scan camera often requires multiple images to be stitched together into a vehicle image, and the texture of the locomotive roof is complex and the image collected in the open air environment has more noise, which is easy to produce deviation after image stitching [5]. At the same time, the recognition system based on two-dimensional images needs to be calibrated regularly, and post-maintenance is more difficult [6].

In this paper, a fully automatic detection system is proposed based on non-contact 3D image processing technology and automatic control technology. The system can collect 2D and 3D images of locomotive roofs, collect and process images in real time, and finally upload the inspection data to the database. Through the software control platform based on B/S architecture, the remote control center can be manually inspected by the roof key components and the roof status.

2 System Design

The system plan can cover the locomotive roof improvement inspection work of the assembly station, according to the structural characteristics of the maintenance section and the maintenance station, the system is designed as three main components: site image detection unit, site control unit, remote control center. The site control unit is used to collect 3D point cloud and 2D image data of locomotive roof, train speed and vehicle number information. The site control unit is used for the logic control of the system, equipment power supply, data processing, and the unattended detection process of the system. The remote control center is located in the dispatching room and the computer room is mainly composed of server units, which are used for the storage of image data and the operation of the software platform. The system topology is shown in the following figure (Fig. 1).

2.1 System Workflow

When the vehicle arrives, the wheel flange contacts the vehicle magnet, the image acquisition module, doppler radar, and vehicle number recognition device will be triggered into standby. Two symmetrical magnets triggered by the same wheel flange contact, the controller captures the rising edge generated by the magnet for delayed

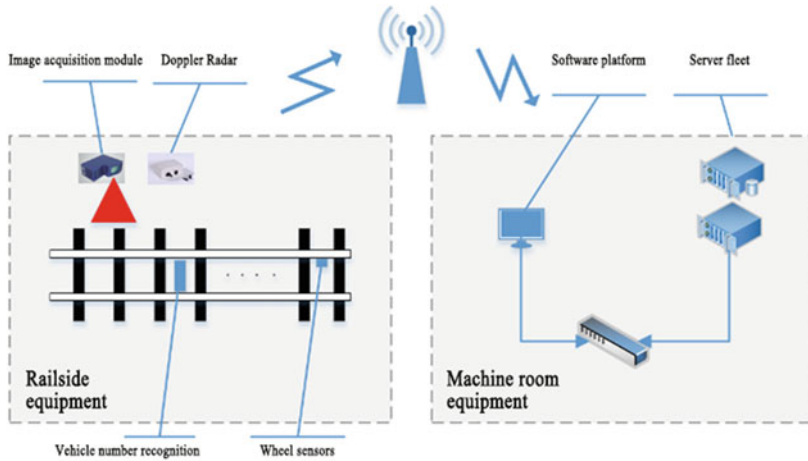


Fig. 1 System Topology

start. Whenever the wheel flange touches the magnet, the number of axes recorded by the system increases by one. When the axle number record reaches the threshold, it is judged that the vehicle is driving away. Moreover, the identification logic of separate magnet false trigger and reverse entry false trigger is added to accurately identify the driving state of the locomotive. When Doppler radar detects that a vehicle is passing, it triggers the image acquisition module to scan the roof of the locomotive at a collection gap of one millimeter. The vehicle number is collected to the current vehicle number and binds to the image data and excludes the model that is not the identification target, such as the engineering vehicle. After the roof image is identified in the recognition computer, the recognition results are uploaded to the server unit. The maintenance personnel access the server on the WEB side to access the image recognition results and print the work order for troubleshooting (Fig. 2).

2.2 3D Reconstruction of the Roof Image

Laser triangulation approximates the surface of a three-dimensional object through a set of contour lines containing height information. Laser triangulation mainly uses Sheet-of-light technology, the basic principle is that by projecting a slender light-emitting line (such as a laser line), the laser line is illuminated to the surface of the object, so that the surface of the irradiated part of the object is reconstructed, and then the laser line image projected onto the surface of the object is obtained with the camera. In order to reconstruct the entire surface of an object, a laser is required to scan the entire surface of the object. And the camera takes as many images of laser lines projected to various locations of the object as possible to obtain a set of object

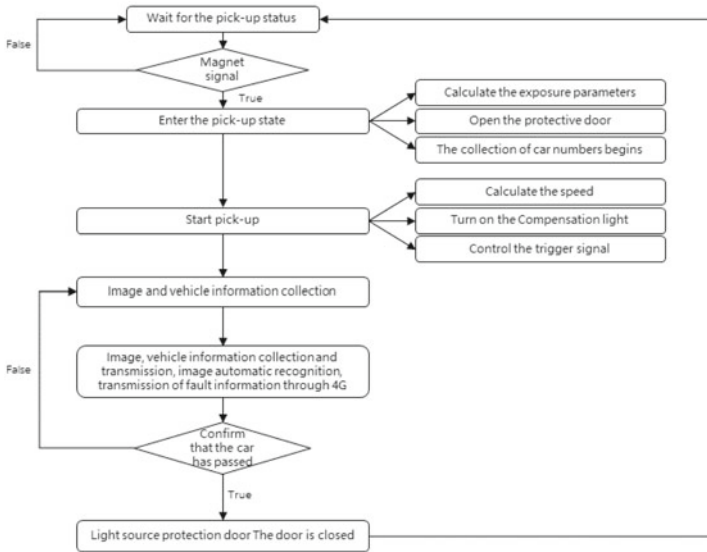


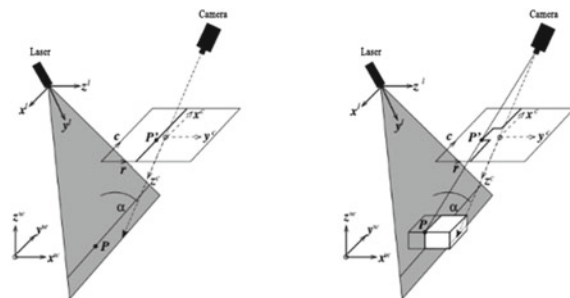
Fig. 2 System Work Flow Chart

height profiles, so that the object must move relative to the measurement system composed of the laser and the camera [7].

First, the laser constructs a plane, called the light plane, as shown in Fig. 3. The optical axis and light plane of the camera form an angle, called the triangulation angle. The intersection of the laser line and the camera viewpoint depends on the height of the object’s surface. Therefore, if the laser line is projected to the object at a change in height, due to the movement of the intersection of the laser line and the camera viewpoint, the imaging of the laser line on the surface of the object captured by the camera is not a straight line, but the outline of the surface of the object. Using this profile, we can get the height difference of the object.

Then, by moving the object relative to the laser and camera, the camera can obtain a contour of a certain horizontal line on the surface of the object with each

Fig. 3 Basic Principles of Laser Triangulation



shot. The laser line image (i.e., the outline image) acquired by the camera is stored as a row in the image in turn to obtain a parallax image, as shown in Fig. 4. If the measurement system is calibrated, the coordinates of each point in the parallax image and its grayscale value represent the X, Y, and Z coordinates of the points on the corresponding object surface in the world coordinates. According to the X, Y, Z coordinates of each point, the points are drawn in the three-dimensional coordinates, and the three-dimensional model of the object can be obtained and visualized.

During a 3D reconstruction, you need to convert point p^w in the world coordinate system into a pixel coordinate system.

First, to transform point $p^w = (x^w, y^w, z^w)^T$ in the world coordinate system into the camera coordinate system using the homogeneous transformation matrix cH_w , represented by $p^c = (x^c, y^c, z^c)^T$:

$$p^c = {}^cH_w \cdot p^w$$

Then:

$$\begin{bmatrix} x \\ y \\ z \\ 1 \end{bmatrix} = \begin{bmatrix} \cos \beta \cos \gamma & -\cos \beta \sin \gamma & \sin \gamma & t_x \\ \cos \alpha \sin \gamma + \sin \alpha \sin \beta \cos \gamma & \cos \alpha \cos \gamma - \sin \alpha \sin \beta \sin \gamma & -\sin \alpha \cos \beta & t_y \\ \sin \alpha \sin \gamma - \cos \alpha \sin \beta \cos \gamma & \sin \alpha \cos \gamma + \cos \alpha \sin \beta \sin \gamma & \cos \alpha \cos \beta & t_z \\ 0 & 0 & 0 & 1 \end{bmatrix} \cdot \begin{bmatrix} x^w \\ y^w \\ z^w \\ 1 \end{bmatrix}$$

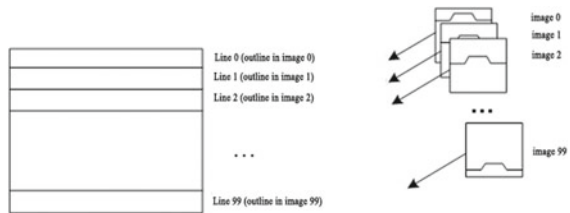
The homogeneous transformation matrix cH_w is determined by six elements, namely the translation component t_x, t_y, t_z on the X, Y, Z axis and the rotation angle α, β, γ , also known as the external parameters of the camera.

Then, convert 3D point p^c in the camera coordinate system to point $p^i=(u, v)^T$ in the image plane coordinate system:

$$\begin{pmatrix} u \\ v \end{pmatrix} = \frac{f}{z^c} \begin{pmatrix} x^c \\ y^c \end{pmatrix}$$

The f in formula is the focal length of the camera lens.

Fig. 4 Parallax Image Formation



2.3 Image Recognition Algorithms

The system recognition algorithm registers the current figure with the 2D and 3D images of the historical map, combines the 3D depth data comparison, and performs fault determination criteria at a certain threshold, which can be used for the identification of fault types such as key component shedding and surface foreign objects. First of all, the template image of each car is collected, and the characteristic area marked on the image is saved in the template directory. After the vehicle to be inspected passes through the identification system, the identification software parses the annotation file, obtains the ROI area of the image to be tested, sets the peripheral search box on the basis of this area and extracts the contour characteristics of the key components in the area, establishes the image pyramid, traverses step by step, realizes SIFT feature matching, and obtains the zoom factor. According to the matching results, on the basis of the precise positioning of key components, the intercepted new depth map will make the difference (depth) between the map to be tested and the template map, and automatically generate fault labels in the areas where the difference exceeds the threshold (Fig. 5).

2.4 Image Acquisition Module

The image acquisition module used in the system uses a 2D line scan camera with a 3D area scan camera solution. 2D line scan camera with uniform line laser light source to achieve long-distance high-speed image acquisition. Laser light source using near-infrared band and the light form is a linear band. Besides, light energy concentration with the filter can achieve anti-sunlight interference function. The 3D area scan camera is equipped with high-brightness structured light, the shape of the light is linear light, the light energy is concentrated, the laser line width is < 1 mm, the uniformity is high. And the three-digit measurement data is obtained by the movement of the measured object relative to the light sheet to reconstruct its shape. The 3D structured light uses the 915 nm band to prevent mutual interference with the 2D camera light source. The resolution of the 2D line scan camera reached 4096×2000 pix. The resolution of the XY axis of the 3D area scan camera was 1.3 mm, and the average accuracy of the Z-axis in the depth of field range was not ± 5 mm (Fig. 6).

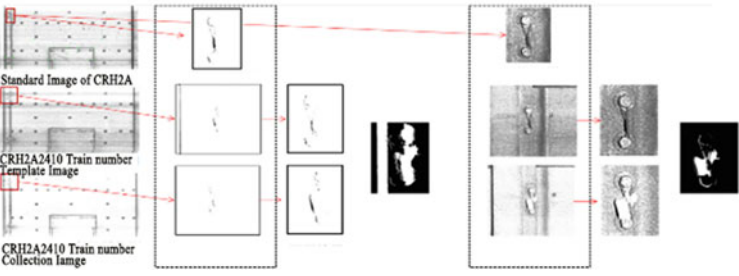
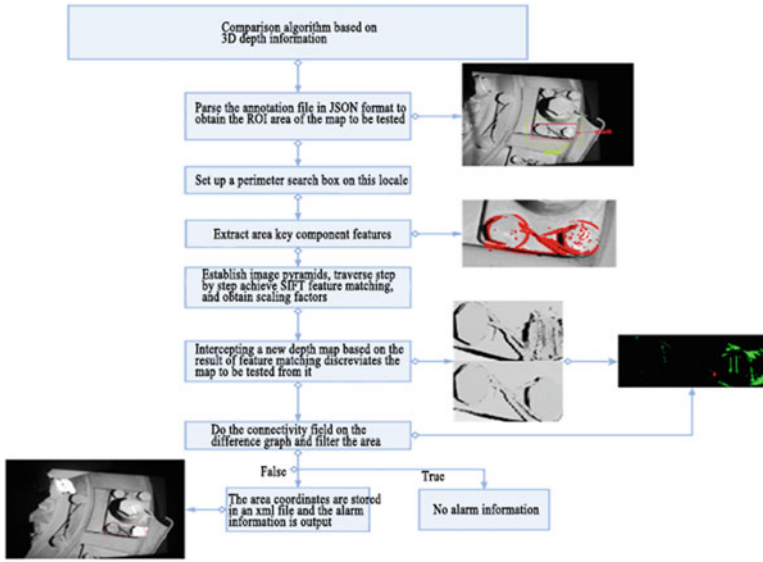


Fig. 5 Image Algorithm Flow

Fig. 6 Image Recognition Module

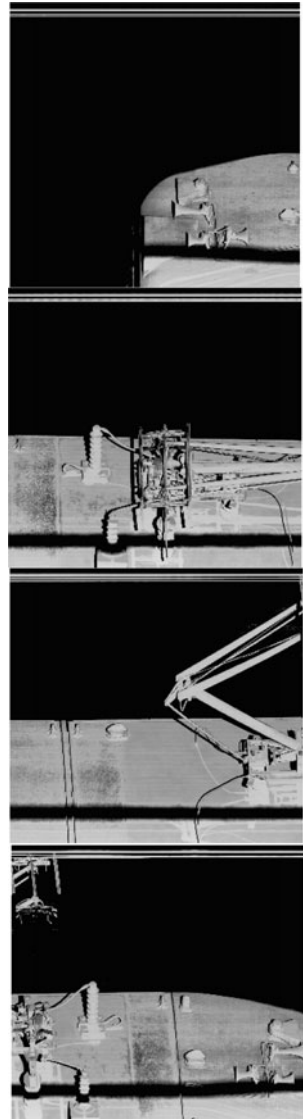


2.5 Vehicle Number Recognition Module

The vehicle number recognition module is used to identify the vehicle number of the incoming vehicle. The vehicle number recognition adopts passive electronic tag for identification, and the selected label meets the standards of “TB/T 3021–2001

Railway Locomotive and Rolling Stock Electronic Device” and “TB/T 3070–2002 Technical Conditions for Automatic Identification Equipment for Railway Locomotive and Rolling Stock”. The passive label does not contain a battery, and is powered by the programmer when programming, and is powered by RF excitation feeds when read out by the ground reading device. The car number, vehicle type, manufacturing information, etc. will be writing in the label (Fig. 7).

Fig. 7 Roof 2D Image



2.6 *Speed Measurement Module*

The speed measurement module is used to monitor the speed of incoming vehicles in real time and trigger 2D and 3D cameras to acquire roof images in real time. Speed measurement module using Doppler radar. The movement of the locomotive as it approaches and moves away from the detection point is parallel to the radial component of the radar. The amount of frequency shift produced by moving toward and away from radar is the same, but the symbol is reversed. According to this feature of Doppler radar, can identify the direction and speed of the locomotive movement (Fig. 8).

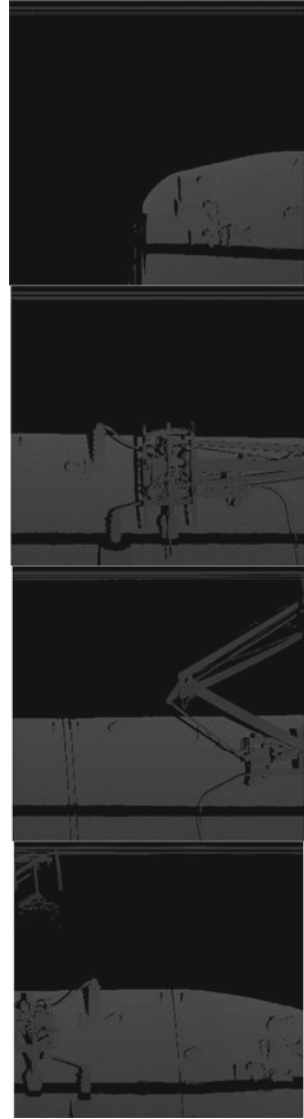
2.7 *Control Module*

Control Module

The control module adopts the solution of the embedded control board based on sbRIO. The sbRIO-based hardware combines modular, multi-threaded software design ideas [8], The following features are implemented: camera control, light source control, network communication, real-time data display, data management and task configuration functions, real-time reception of AEI messages, radar speed pulses processing, communication protocol conversion.

The entire control software can be divided into three parts, FPGA code, the Real-Time (RT) code, and the Host code [9]. The FPGA code runs on the FPGA, which mainly implements the underlying driver function of the camera. The RT code runs in a real-time controller, which mainly implements the UDP communication of data and receive instructions and feedback status. Host code runs on the host computer, such as PC, Touch Panel, etc., mainly to achieve human-computer interaction functions, such as displaying data, sending commands, managing data, etc. Both FPGA and RT are integrated in sbRIO, often referred to as the lower computer, and communication between the upper and lower host computer is carried out through the standard UDP protocol (Fig. 9).

Fig. 8 Roof Depth Image



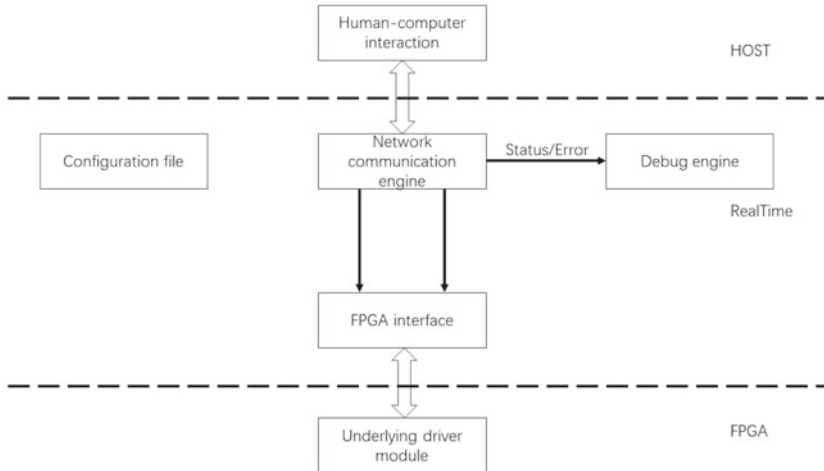


Fig. 9 Control Board Topology

Fig. 10 Control Board



3 System Testing

A total of three fault simulation tests were carried out in the system trial run, and a total of 14 foreign body fault points were made for HXD3C and HXD3D models, with an identification accuracy rate of 100%, but due to the limited field experimental conditions of engineering applications, there are fewer dispatching vehicles available for experimentation, and there is too few negative samples for testing, and the follow-up research will focus on the collection and identification verification of a large number of negative samples (Fig. 10).

During the actual operation of the system, the real bird carcasses appeared on the roof, and the system separated the point clouds of the bird carcasses based on the 3D image of the original roof and realized accurate positioning and alarm, as shown in Fig. 11.

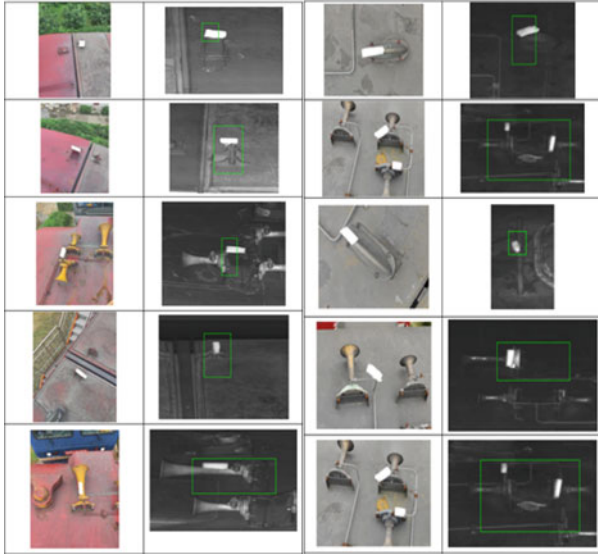


Fig. 11 Foreign Body Recognition Results



Fig. 12 True Fault Identification Results

4 Conclusion

This paper proposes a roof foreign body detection system scheme based on two-dimensional combined with three-dimensional image, which gives the identification process and mode, which can realize the online dynamic detection of the roof of the main locomotive models in the current maintenance section, and can quickly and accurately locate the key components and find foreign objects. However, due to the large number of key components of the roof and the complexity of the structure, the occluded position is prone to visual blind spots, resulting in missing depth data in some key areas and missing detection. In subsequent studies, further research is needed on better image acquisition protocols.

References

1. Qian, C., Cai, Q.: Status quo and development of locomotive roof equipment status and foreign body detection technology. *Electr. Meas. Technol.* **44**(10), 7 (2021). (In Chinese)
2. Lei, L.I.U.: Analysis of causes and countermeasures of discharge of HX_D3 locomotive roof high-voltage equipment. *Railway Locomotives EMUs* **11**, 3 (2017). (In Chinese)
3. Cao, C.: Locomotive pantograph and roof condition detection system. *Nanjing University of Aeronautics and Astronautics*, Nanjing, vol. 12 (2017). (In Chinese)
4. Meizhou, H.E., Jin, T.A.O.: Fault analysis and standardization of SS3 locomotive roof insulation detection system. *Guangxi Railway School* **1**, 18–20 (2020). (In Chinese)
5. Zhu, Y.: Detection of foreign body on locomotive roof based on laser scanning system. *South China University of Technology*, Guangzhou, vol. 12 (2016). (In Chinese)
6. Changsheng, R.O.N.G., Bo, L.I.U.: Background data processing technology of remote monitoring and diagnosis system (CMD System) of Chinese locomotive. *China Railways* **000**(003), 28–34 (2017). (In Chinese)
7. Zhang, J., Jing, J.: Research on three-dimensional reconstruction method of coal mine roadway based on stereo vision. *J. Xi'an Polytech. Univ.* **11** (2020). (In Chinese)
8. Zemin, G.A.O.: Research and Application of Railway Locomotive Running Fault Monitoring and Diagnosis Technology. *Eng. Technol. Chin. Sci. Technol. J. Database (Abstracts Edition)* **9**, 00328–00328 (2016). (In Chinese)
9. Gan, J., Zhang, W.: Fault classification and operation and maintenance monitoring design of locomotive traction motor. *Electromech. Inf.* (18), 2 (2016). (In Chinese)

Review of Isolated DC-DC Converter for Wide Voltage Range Regulation



Ziyan Tang, Jin Wen, Jiajia Guan, Yiyang Yan, Cai Chen, Yong Kang, and Lei Yang

Abstract In wide input and output voltage applications, resonant converters have received broad attention due to their high efficiency and high power density. This article will provide a topology summary and comparison from single-stage topology and other topologies. The topologies are applicable to wide input and output voltage range scenarios. For the single-stage topology, the existing voltage regulation improvement strategies will be introduced separately on the primary side, transformer side, and secondary side. For other topologies, this paper introduces the voltage regulation improvement strategies of two-stage topology, quasi-single-stage topology and LCLC resonant topology. This article will compare the advantages and disadvantages of different topologies in detail, and provide a reference for wide range voltage regulation topology applications.

Keywords Modified Strategy · Resonant Converter · Wide Range Voltage Regulation

Z. Tang (✉) · J. Wen · J. Guan · Y. Yan · C. Chen · Y. Kang
School of Electrical and Electronic Engineering, Huazhong University of Science and Technology, Wuhan 430074, China
e-mail: tang_ziyan@hust.edu.cn

J. Wen
e-mail: m202171915@hust.edu.cn

J. Guan
e-mail: jiajiaguan@hust.edu.cn

Y. Yan
e-mail: yanyiyang@hust.edu.cn

C. Chen
e-mail: caichen@hust.edu.cn

Y. Kang
e-mail: ykong@hust.edu.cn

L. Yang
Beijing Institute of Precision Mechatronics and Controls, Beijing 100044, China

© Beijing Paiké Culture Commu. Co., Ltd. 2023
X. Dong et al. (eds.), *The proceedings of the 10th Frontier Academic Forum of Electrical Engineering (FAFEE2022)*, Lecture Notes in Electrical Engineering 1054, https://doi.org/10.1007/978-981-99-3408-9_37

1 Introduction

In recent years, as the energy situation becomes tenser, renewable energy sources, for example, wind and solar have rapid development. Due to the fast voltage fluctuations in applications such as electric vehicles, wide range voltage regulation and high-efficiency isolated DC-DC plays an important role [1]. For example, on-board chargers for electric vehicles require wide range voltage regulation converter to control the conversion of 650–1170 V input to 250–450 V output [2]. Due to the influence of weather, control system, and so on, the output voltage of new energy power generation fluctuates up to 100% [3]. 200–400 V DC power distribution systems require wide input voltage range DC-DC converters to achieve low output voltage [4]. In a communication power system, the input is generally 90 to 264 V AC, while its output is 42 to 58 V DC. Generally speaking, converters that operate under wide input and output voltage conditions have lower efficiency than that of narrow input and output voltage ranges.

Resonant converters are the most common wide voltage range regulation DC-DC converters at present. Dual Active Bridge converters don't need resonant components and can realize ZVS (zero voltage switching) over a wide range with a simple design. DAB can adjust the output voltage through single-phase-shift control, double-phase-shift control, and three-phase-shift control. It's widely used in energy storage systems and microgrid applications. However, while the voltage has a great change, it is difficult for DAB to achieve ZVS, and the circulating power increases sharply, which will result in current stress increasing and efficiency decreasing [5–7].

LLC and CLLC resonant converters can achieve the primary side ZVS and the secondary side ZCS within the full load range and achieve wide range voltage regulation through frequency modulation control with high efficiency and high power density. LLC and CLLC converters are widely used in DC distribution grids, on-board chargers, and fuel cell electric vehicles because of their advantages such as wide voltage regulation range, high efficiency, and low EMI [8–10].

However, LLC and CLLC resonant converters are complex in design. The converter gain range is greatly affected by the values of k (L_m/L_r) and Q (quality factor) [11–13]. The smaller the k , the larger the maximum voltage gain, but the smaller the magnetizing inductance, the bigger the magnetizing current, and the bigger the loss; the bigger the k , the smaller the maximum voltage gain and the position where the maximum value of the voltage gain occurs moves away from the resonant frequency, and the voltage gain curve becomes more and more stable. As the Q value raises, the voltage gain at the same frequency becomes smaller. When the voltage regulation range is too wide, the frequency regulation range becomes too wide, which is not conducive to the design of magnetic components; while the switching frequency is far from the resonant frequency, the soft switching may be lost, the loss will increase, and the efficiency will decrease [14].

Therefore, for the above problems and applications, existing literature has proposed many methods to widen the voltage regulation range of the isolated DC-DC converter to realize high efficiency and wide-range voltage regulation.

In this paper, the wide-range voltage regulation topologies proposed in the existing literature are reviewed and compared. It is divided into single-stage topology and other topology forms for a detailed introduction. The single-stage topology is split into three stages: primary side, transformer side, and secondary side. The structure of this research is arranged as follows: Sect. 2 introduces the improvement strategies of single-stage topology; Sect. 3 introduces other topologies of wide-range voltage regulation; Sect. 4 compares and summarizes the topologies mentioned in the literature, which provides a reference for the selection of wide range voltage regulation topology. Finally, Sect. 5 provides a summary of the full text.

2 Single-Stage Topology

For single-stage topology, the improvements to widen the voltage regulation range mentioned in the existing literature can be divided into three types: primary side, transformer side, and secondary side.

2.1 Primary Side Modified Resonant Converter

The primary side modified strategies of resonant converters for widening voltage regulation range include variable resonant parameter, bridge arm switching, and reconfigurable bridge with the asymmetric resonant tank.

Variable Resonant Parameter. J. Lee et al. proposed a half-bridge LLC with additional switches and capacitors on the primary side [15], as shown in Fig. 1. The structure switches the on or off of the auxiliary switch tube according to the input voltage to change the value of the resonant capacitor. When Q_A is off, the resonant capacitor is C_{RC} ; when Q_A is on, the resonant capacitor is $C_{RC} + C_{RA}$, which means Q decreases and maximum voltage gain increases. This structure can narrow the frequency modulation range and improve efficiency. However, this circuit introduces additional components and switching losses.

Y. Wei et al. proposed a topology that adjusts the magnetizing inductance to achieve high efficiency and wide range voltage regulation [16], as shown in Fig. 2. The structure controls the connection of the auxiliary magnetizing inductor by adjusting the on-off of the auxiliary switch. While the auxiliary switch is on, the auxiliary magnetizing inductor is connected, the magnetizing inductance decreases, the k value decreases, and the voltage gain increases, so that the voltage regulation range is widened, the frequency regulation range is narrowed, and the efficiency is improved.

Bridge Arm Switching. U. Khalid et al. proposed a bridge arm switching CLLC converter [17], as shown in Fig. 3. This structure changes the converter into a half-bridge or full-bridge structure by controlling the on-off of the additional switch

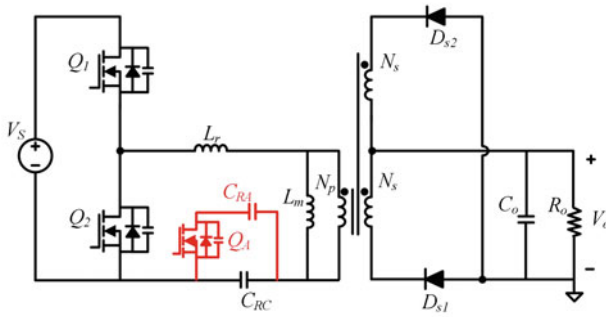
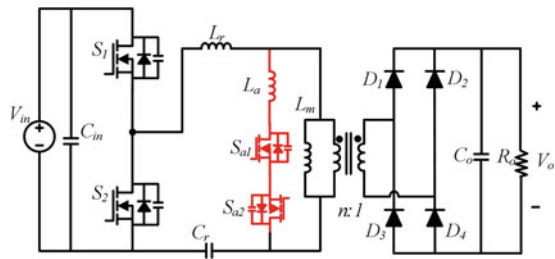


Fig. 1 Topology in [15]

Fig. 2 Topology in [16]



tubes. It adopts frequency modulation and phase shift control to narrow the frequency modulation range, broaden the system input and output voltage range, and improve efficiency. However, this structure introduces four additional switching tubes, and the control is complicated.

The bridge arm switching topology improvement strategy proposed by Z. Liang et al. [18] is shown in Fig. 4. This structure controls the primary side bridge arm structure by changing the on or off state of S3 and S4 switches. When S3 and S4 work at high frequency, it operates in full-bridge mode; when S3 is constantly off and S4 is constantly on, it operates in half-bridge mode. The structure is simple to control, and the voltage range can be widened without additional devices.

Fig. 3 Topology in [17]

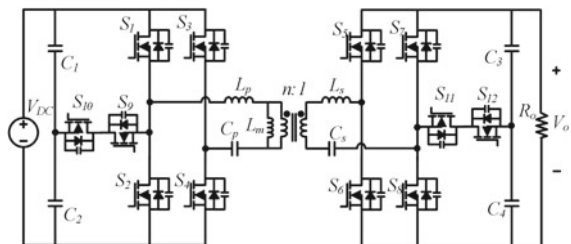


Fig. 4 Topology in [18]

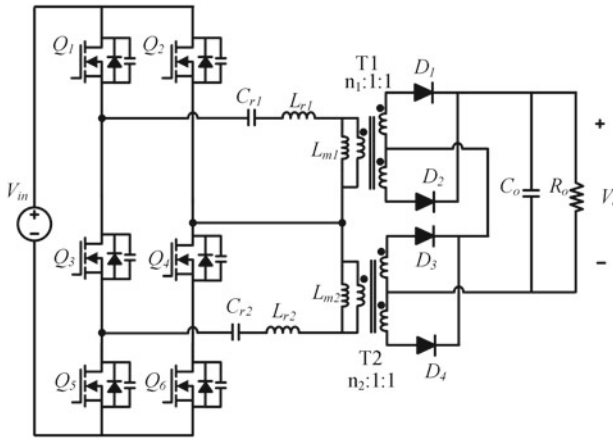
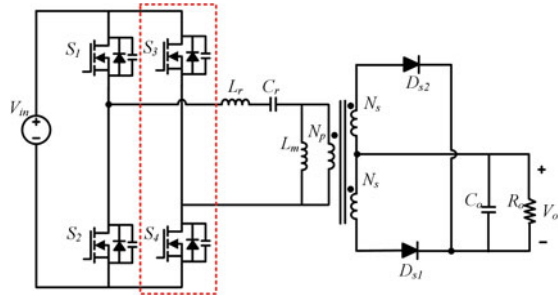


Fig. 5 Topology in [19]

Reconfigurable Bridge and Asymmetric Resonant Tank. The reconfigurable bridge arm topology proposed by C. Li et al. consists of six switches on the primary side and two asymmetric resonant tanks [19], as shown in Fig. 5. By controlling the on–off of the primary switch tubes, the circuit can work in six modes: T2 half bridge; T1 half bridge; double half bridge; T1 half-bridge, T2 full-bridge; T1 full-bridge, T2 half-bridge, and double full bridge. Therefore, the structure can realize six kinds of gain curves, greatly widen the voltage regulation range, and realize high efficiency.

2.2 Transformer Modified Resonant Converter

The basic principle of the transformer modified resonant converter mentioned in the existing literature is to change the transformer’s turn ratio in two ways: winding switching and connection way of multiple transformers.

H. Hu et al. proposed a resonant converter structure with two transformers in series and two output modules in parallel, as shown in Fig. 6. This structure controls whether TR2 and Rectifier2 are connected to the circuit by controlling the on or off of the auxiliary switch tube to modify the gain of the converter [20]. At the same time, the circuit also adopts bridge arm switching to further widen the voltage regulation range.

C. Kim et al. proposed a topology that employs transformer switching for wide-range voltage regulation [21], as shown in Fig. 7. The circuit can work in two modes by controlling auxiliary switch tubes: two transformers and resonant tanks in parallel, and two transformers and resonant tanks in series. Compared with the traditional LLC, this circuit can design a larger magnetizing inductance, reduce power loss and improve efficiency. However, the structure of the two transformers increases the volume of the system and the complexity of the circuit.

H.-G. Han et al. researched an LLC resonant converter with an adaptive turn ratio transformer [22], as shown in Fig. 8. By controlling the auxiliary switches SA1 and SA2 on or off, the topology can realize two different transformation ratios and increase the gain range of the converter. However, this structure still requires a large

Fig. 6 Topology in [20]

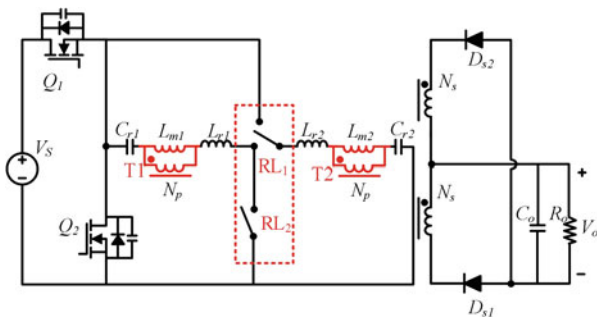
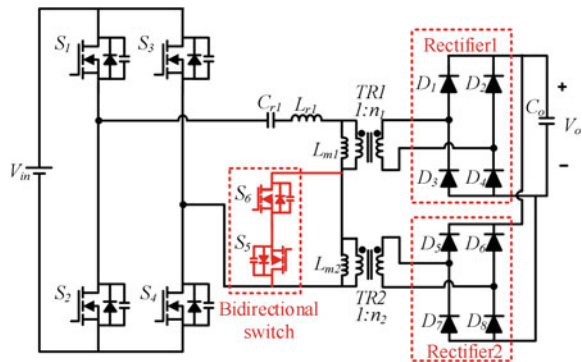


Fig. 7 Topology in [21]

Fig. 8 Topology in [22]

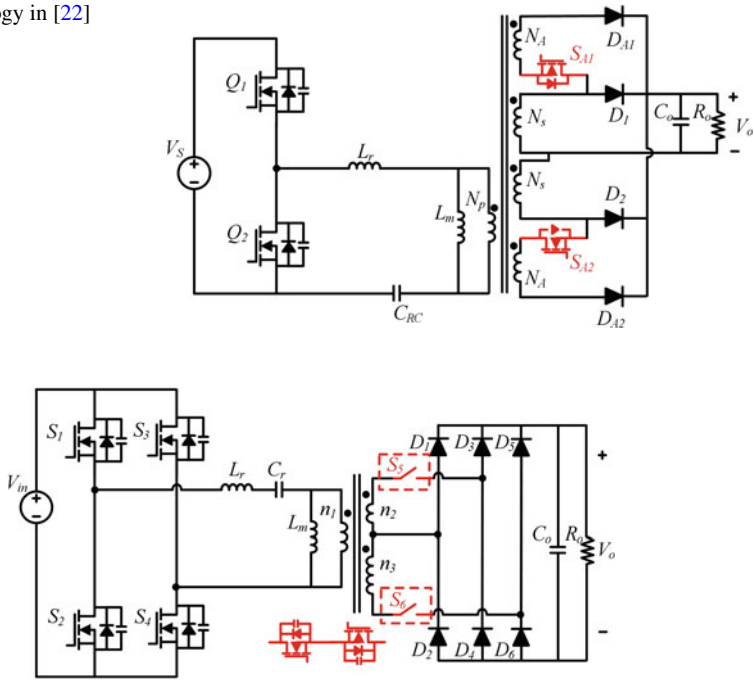


Fig. 9 Topology in [23]

excitation current to achieve ZVS, and the multi-winding structure makes the volume of the transformer increased and the difficulty of design optimization raised.

D. Shu et al. proposed a LLC converter with an adjustable turns ratio transformer [23], as shown in Fig. 9. In this circuit structure, three different turn ratios can be realized by switches S5 and S6, and the switching frequency range of each mode is compressed to a range close to the resonant frequency, which improves the efficiency.

2.3 Secondary Side Modified Resonant Converter

The secondary side modified resonant converter can be split into the output series-parallel switching type and the bridge arm switching type.

Output Series-Parallel Switching. H. Dang et al. proposed an output side adjustable converter [24], as shown in Fig. 10. The circuit uses D3, D4, and S5 to control the output in series and parallel. When S5 is on, the output is connected in series to achieve double the gain; when S5 is off, the output is connected in parallel. The output voltage can be controlled by controlling the duty cycle of S5. Like traditional LLC, S1-S4 can realize ZVS in a wide range, and D1, D2 realize ZCS. Compared with traditional LLC-Buck, the structure’s loss is smaller. However,

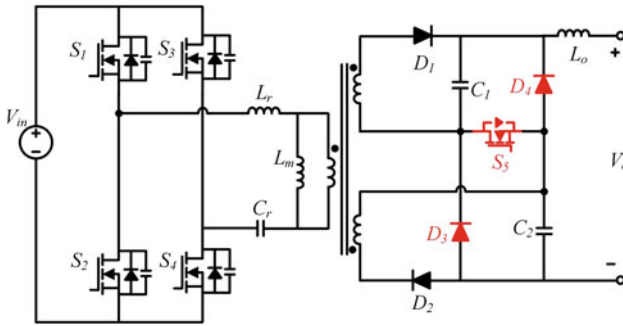


Fig. 10 Topology in [24]

this circuit adds an output capacitor and an extra switch, which is not good for the improvement of power density.

H. Wang et al. proposed an improved LLC resonant converter of bridge arm switching type, as shown in Fig. 11. The primary side of the topology works in a quasi-resonant state, and the output voltage is adjusted by regulating the duty cycle of the additional switch S5. When S5 is on, only an output capacitor is working; when S5 is off, two capacitors are in series to obtain twice the output voltage [25]. The fixed-frequency operation of this circuit can realize soft switching, but the additional components introduce additional loss and volume.

H. Wu et al. proposed a two-phase interleaved LLC resonant converter [26] with uncontrolled rectification, as shown in Fig. 12. This topology adopts frequency modulation and phase shift control. When the output voltage is high, the secondary windings are connected in series, and the output voltage is controlled by frequency modulation; when the output voltage is low, the secondary side can be switched in series or parallel by constant frequency phase shift control to adjust the output voltage. This topology can realize full-range soft switching. Compared with the traditional LLC, the additional conduction loss caused by the magnetizing inductance is smaller.

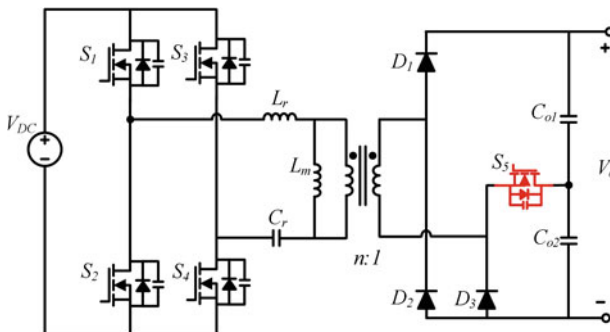


Fig. 11 Topology in [25]

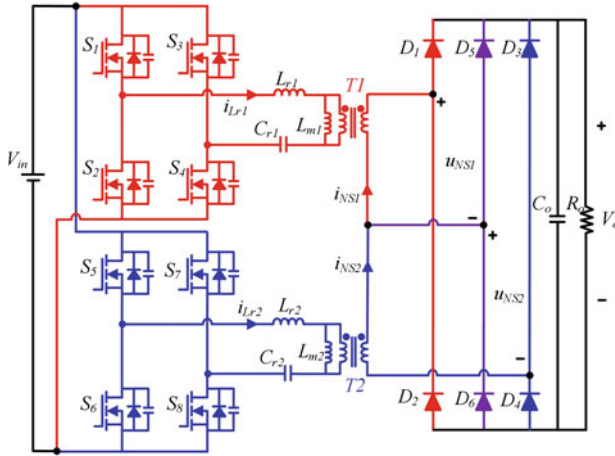


Fig. 12 Topology in [26]

However, in the phase shift control, the circulating current increases and the loss increases.

Bridge Arm Switching. The switching strategy of the bridge arm of the secondary side is similar to that of the primary side, both of which can switch the bridge arm through additional switches [17], or control the two switches of one bridge arm to be consistently on and consistently off [18].

3 Other Topologies

3.1 Two-Stage Topology

To solve two problems that resonant converters may face under wide-range voltage regulation: too wide frequency modulation range leads to low efficiency and difficult design of magnetic components, in addition to the single-stage topology modified strategies summarized in the previous section of this paper, a two-stage topology can be used to widen the voltage regulation range and achieve high efficiency and high power density. Commonly used two-stage topologies are DC/DC + DCX or DCX + DC/DC.

Y. Wang et al. proposed a Buck-Boost + LLC two-stage converter structure with bridge arm multiplexing [27], as shown in Fig. 13. The Buck + Boost shares a bridge arm with LLC, which reduces the number of a group of switches. The bipolar modulation strategy is adopted, and ZVS is realized by using the chopping inductor current, so the magnetizing current of the transformer can be very small, which can

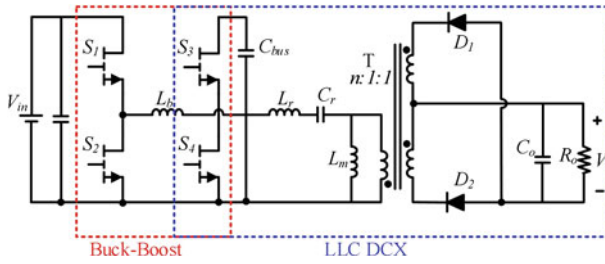


Fig. 13 Topology proposed by [27]

realize the non-gap transformer and reduce the winding loss; in addition, the resonant current is reduced, and the conduction loss of the switch tubes is reduced. As a result, this topology can realize a wide range of voltage regulation, high efficiency, and high power density.

3.2 Quasi-Single-Stage Topology

Z. Wu et al. proposed a novel partial power regulation topology [28], as shown in Fig. 14. This topology consists of two parts: DCX for main power flow and DCX + PWM Converter for auxiliary partial power flow. The topology is simple to control and can achieve low losses and high efficiency due to partial power regulation.

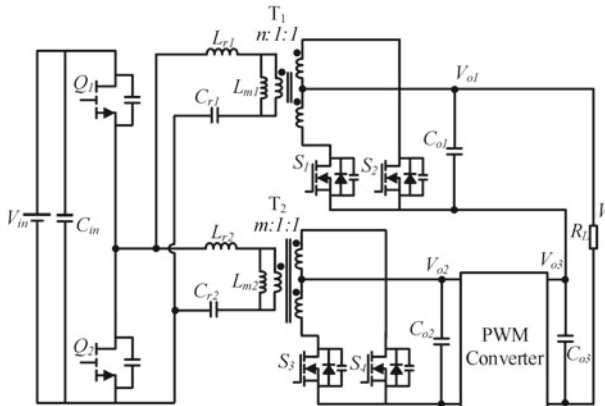


Fig. 14 Topology proposed by [28]

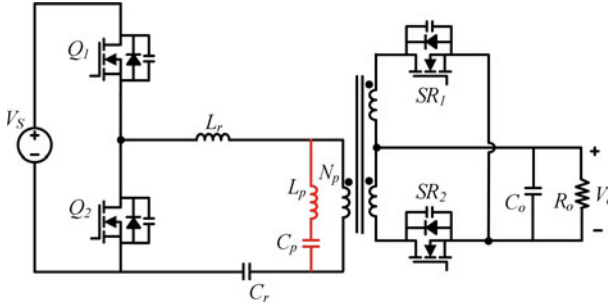


Fig. 15 Topology proposed by [29]

3.3 LCLC Resonant Converter

Z. Chen et al. proposed an LCLC resonant converter [29], as shown in Fig. 15. Based on the traditional LLC, this topology improves the magnetizing inductance and uses the inductance in series with a capacitor to be equivalent to the actual magnetizing inductance. The converter is equivalent to an LLC converter with variable magnetizing inductance. As the input voltage decreases, the equivalent magnetizing inductance will decrease as the switching frequency decreases, allowing the converter to achieve high k_{eak} gain. However, this circuit requires additional magnetizing inductance components, which increases the volume of the system and isn't conducive to the improvement of power density.

4 Topology Summary and Comparison

The second and third sections of this paper respectively list the modified strategies for single-stage topology and other topologies to achieve high efficiency and wide range voltage regulation. For single-stage topology, topology modified strategies include resonant parameter switching, bridge arm switching, reconfigurable bridge arm mode, transformer winding switching, and series-parallel switching. The bridge arm switching can achieve twice the voltage range through full-bridge and half-bridge switching. The resonant parameter switching can achieve different maximum voltage gains by changing the k and Q of the resonant converter. The reconfigurable bridge arm mode can obtain several sets of the gain curves to narrow the frequency modulation range. Transformer winding switching can change the turns ratio of the converter and greatly adjust the voltage regulation range. Series-parallel switching introduces N modules, adjusting modules series and parallel to achieve N times the voltage gain. In addition to the single-stage topology, there are still many forms of topology that can achieve high efficiency and wide range voltage regulation. In the third section of this paper, three representative wide range voltage regulation topologies are listed: two-stage topology, quasi-single-stage topology, and LCLC

topology, which can be as a design reference. The topology comparison results are shown in Table 1.

Table 1 Topology Comparison

	Input	Output	f_s	Modulation	Frequency range	Efficiency	Notes
[15]	325–385 V	56 V	90 k	FM	34–95 k	95%	Additional capacitor and switch
[16]	100–180 V	20 V	90 k	FM	65–90 k	-	Additional inductor and switch
[17]	400 V	100–440 V	100 k	PWM + FM	-	-	Additional switching loss and complex control
[18]	125–550 V	500 V	60 k	FM	40–120 k	97.7%	Safe transition needs to be considered
[19]	390 V	80–420 V	100 k	FM	70–130 k	97.4%	Low power density
[20]	25–100 V	210 V	140 k	FM	80–140 k	98%	Increased size and design complexity
[21]	127–380 V	16.5 V	160 k	FM	75–155 k	96.2%	Increased size and design complexity
[22]	311 V	25–42 V	130 k	FM	-	95%	Multiple windings; complex design
[23]	390 V	126–420 V	140 k	FM	130–220 k	97.2%	Additional switches and windings
[24]	100 V	100–200 V	20 k	PWM	-	95.5%	Additional output capacitor and switch The regulation range is only up to 2 times

(continued)

Table 1 (continued)

	Input	Output	f_s	Modulation	Frequency range	Efficiency	Notes
[25]	390 V	250–420 V	100 k	PWM	-	96.7%	Additional switches The regulation range is only up to 2 times
[26]	400 V	150–500 V	1000 k	PWM + FM	-	98%	Many components; low power density
[27]	360–440 V	24 V	500 k	PWM	-	97.6%	Complex control
[28]	360–460 V	12 V	460 k	PWM	-	96.5%	Efficiency decreases when the voltage range is too wide
[29]	250–400 V	12 V	256 k	FM	135–250 k	96.4%	Additional inductor and capacitance Large system size

5 Conclusion

This paper summarizes and compares topologies applied to wide input and output voltage range from single-stage and other topologies, and provides a reference for the design of wide range voltage regulation converters. Table 1 lists the electrical parameters, efficiency, and advantages and disadvantages of all converters mentioned in this paper. In general, to realize wide range of input and output voltage regulation, reduce the frequency modulation range, and improve efficiency, the modification strategies of single-stage topology include bridge arm switching, resonant parameter switching, reconfigurable bridge arm mode, transformer winding switching, and series or parallel switching. It is worth noting that the combination of different modification strategies can obtain a wider voltage regulation range. When designing, the most suitable topology can be selected according to various factors such as voltage regulation requirements, control complexity, design complexity, cost, and efficiency.

References

1. Chen, D., Deng, J., Wang, W., Wang, Z., Wang, S., Dorrell, D.G.: A novel control method for a primary triple bridges dual active bridge dc-DC converter with minimum RMS current optimization. In: 2020 IEEE Energy Conversion Congress and Exposition (ECCE), Michigan, pp. 2592–2597. IEEE (2020)
2. Wei, C., Zhu, D., Xie, H., Liu, Y., Shao, J.: A SiC-based 22kW bi-directional CLLC resonant converter with flexible voltage gain control scheme for EV on-board charger. In: PCIM Europe Digital Days 2020, pp. 1–7 (2020)
3. Chen, D., Deng, J., Wang, W., Wang, Z., Wang, S.: A novel voltage-fed hybrid bridge combining semiactive rectifier converter for wide voltage gain. *IEEE Trans. Industr. Electron.* **69**(1), 365–375 (2022)
4. Yu, Y., Masumoto, K., Wada, K., Kado, Y.: Power flow control of a triple active bridge DC-DC converter using GaN power devices for a low-voltage DC power distribution system. In: 2017 IEEE 3rd International Future Energy Electronics Conference and ECCE Asia (IFEEC 2017 - ECCE Asia), Kaohsiung, pp. 772–777. IEEE (2017)
5. Ye, W., Shao, S., Guo, Q., Zhang, J., Sheng, K.: A phase shift control of minimal circulating current and ZVS turn-on for DAB converter. In: 2018 IEEE 2nd International Electrical and Energy Conference (CIEEC), Beijing, pp. 682–686. IEEE (2018)
6. Carvalho, E.L., Felipe, C.A., Bellinaso, L.V., de Oliveira Stein, C.M., Cardoso, R., Michels, L.: Asymmetrical-PWM DAB converter with extended ZVS/ZCS range and reduced circulating current for ESS applications. *IEEE Trans. Power Electron.* **36**(11), 12990–13001 (2021)
7. Liu, P., Duan, S.: A hybrid modulation strategy providing lower inductor current for the DAB converter with the aid of DC blocking capacitors. *IEEE Trans. Power Electron.* **35**(4), 4309–4320 (2020)
8. Jiang, T., Zhang, J., Wu, X., Sheng, K., Wang, Y.: A bidirectional LLC resonant converter with automatic forward and backward mode transition. *IEEE Trans. Power Electron.* **30**(2), 757–770 (2015)
9. Li, B., Lee, F.C., Li, Q., Liu, Z.: Bi-directional on-board charger architecture and control for achieving ultra-high efficiency with wide battery voltage range. In: 2017 IEEE Applied Power Electronics Conference and Exposition (APEC), Da Nang, pp. 3688–3694. IEEE (2017).
10. Chu, A.: Evaluation and Design of a SiC-Based Bidirectional Isolated DC/DC Converter (2018)
11. He, P., Mallik, A., Sankar, A., et al.: Design of a 1-MHz high-efficiency high-power-density bidirectional GaN-based CLLC converter for electric vehicles. *IEEE Trans. Veh. Technol.* **68**(1), 213–223 (2019)
12. Sun, S., Fu, J., Wei, L.: Optimization of high-efficiency half-bridge LLC resonant converter. In: 2021 40th Chinese Control Conference (CCC), Shanghai, pp. 5922–5926. IEEE (2021)
13. Lu, X., Wang, H.: Three-port bidirectional CLLC resonant converter based onboard charger for PEV hybrid energy management system. In: 2017 IEEE Energy Conversion Congress and Exposition (ECCE), Cincinnati, OH, pp. 1432–1438. IEEE (2017)
14. Musavi, F., Craciun, M., Gautam, D.S., Eberle, W., Dunford, W.G.: An LLC resonant DC-DC converter for wide output voltage range battery charging applications. *IEEE Trans. Power Electron.* **28**(12), 5437–5445 (2013)
15. Lee, J., Kim, J., Baek, J., Kim, J., Moon, G.: Resonant capacitor on/off control of half-bridge LLC converter for high-efficiency server power supply. *IEEE Trans. Industr. Electron.* **63**(9), 5410–5415 (2016)
16. Wei, Y., Mantooh, A.: Magnetizing inductor ON/OFF control for LLC resonant converter with wide input voltage range. In: 2020 IEEE 11th International Symposium on Power Electronics for Distributed Generation Systems (PEDG), Croatia, pp. 386–390. IEEE (2020)
17. Khalid, U., Shu, D., Wang, H.: Hybrid modulated reconfigurable bidirectional CLLC converter for V2G enabled PEV charging applications. In: 2019 IEEE Applied Power Electronics Conference and Exposition (APEC), pp. 3332–3338 (2019)

18. Liang, Z., Guo, R., Wang, G., Huang, A.: A new wide input range high efficiency photovoltaic inverter. In: 2010 IEEE Energy Conversion Congress and Exposition, United States, pp. 2937–2943. IEEE (2010)
19. Li, C., Wang, H.: A wide gain range LLC resonant converter based on reconfigurable bridge and asymmetric resonant tanks. In: 2019 IEEE Applied Power Electronics Conference and Exposition (APEC), pp. 3281–3286 (2019)
20. Hu, H., Fang, X., Shen, J., Chen, F., Shen, Z.J., Batareseh, I.: A modified high-efficiency LLC converter with two transformers for wide inputvoltage range applications. *IEEE Trans. Power Electron.* **28**(4), 1946–1960 (2013)
21. Kim, C., Baek, J., Lee, J.: High-efficiency single-stage LLC resonant converter for wide-input-voltage range. *IEEE Trans. Power Electron.* **33**(9), 7832–7840 (2018)
22. Han, H.-G., Choi, Y.-J., Choi, S.-Y., Kim, R.-Y.: A high efficiency LLC resonant converter with wide ranged output voltage using adaptive turn ratio scheme for a li-ion battery charger. In: 2016 IEEE Vehicle Power and Propulsion Conference (VPPC), Hangzhou, pp. 1–6. IEEE (2016)
23. Shu, D., Wang, H.: An adjustable turns ratio transformer based LLC converter for deeply-depleted PEV charging applications. In: 2020 IEEE Applied Power Electronics Conference and Exposition (APEC), pp. 860–864. IEEE (2020)
24. Dang, H., Du, S., Zhang, Y., Liu, J.: A novel LLC resonant converter with configurable capacitors in output stage for wide output voltage range operation. *IEEE Trans. Power Electron.* **37**(6), 6233–6236 (2022)
25. Wang, H., Li, Z.: A PWM LLC type resonant converter adapted to wide output range in PEV charging applications. *IEEE Trans. Power Electron.* **33**(5), 3791–3801 (2018)
26. Wu, H., Zhan, X., Xing, Y.: Interleaved LLC resonant converter with hybrid rectifier and variable-frequency plus phase-shift control for wide output voltage range applications. *IEEE Trans. Power Electron.* **32**(6), 4246–4257 (2017)
27. Wang, Z., Wu, Z., Liu, T., Chen, C., Kang, Y.: A high efficiency and high power density integrated two-stage DC-DC converter based on bipolar symmetric phase shift modulation strategy. *IEEE Trans. Power Electron.* **37**(4), 4358–4373 (2022)
28. Wu, Z., Wang, Z., Zhang, Y., Xu, W., Chen, C., Kang, Y.: A high efficiency and high power density DC transformer topology with output regulation capability. *IEEE Trans. Power Electron.* **37**(7), 8232–8247 (2022)
29. Chen, Y., et al.: LCLC converter with optimal capacitor utilization for hold-up mode operation. *IEEE Trans. Power Electron.* **34**(3), 2385–2396 (2019)

Analysis on the Operating Condition of Electrical Contact Structure Used in Gas Insulated Switchgear



Wei Yang, Taiyun Zhu, Tao Xie, Shoufeng Jin, Ting Ren, Qingyu Wang, and Peng Liu

Abstract In recent years, gas insulated switchgear (GIS) has been widely used in power systems. As an important part of GIS equipment, its operation reliability is directly related to the stability of electrical equipment operation. Therefore, analyzing the operating condition of electrical connection structures in GIS equipment is necessary. In this paper, the spring contact is taken as the research object, the electric field, thermal field, and flow field distribution were simulated, the surface of the spring contact after prolonged use was observed by scanning electron microscopy. It is found that the operating temperature of the spring contact is 339.07 K. When deterioration occurs due to poor contact, the temperature of the conductor can reach 415.59 K. In addition, the long-term operation will cause significant wear on the contact surface, which will degrade electrical contact performance. The research in this paper can provide a theoretical basis for the analysis of GIS overheating faults.

Keywords Wear · Electrical contact · Temperature distribution · Overheating faults

1 Introduction

Energy security is related to the national economy and people's livelihood. With the increase of power grid transmission capacity and the proposal of China's carbon peaking and carbon neutrality, UHV power equipment's operation stability is becoming increasingly important [1, 2]. Gas insulated switchgear (GIS) has been widely used in power system for its high reliability, high current breaking capability and small footprint (Fig. 1).

W. Yang · T. Zhu
State Grid Anhui Electric Power Research Institute, Hefei 230601, China

T. Xie (✉) · S. Jin · T. Ren · Q. Wang · P. Liu
State Key Laboratory of Electrical Insulation and Power Equipment, Xi'an Jiaotong University,
Xi'an 710049, Shaanxi, China
e-mail: 1528037633@qq.com

Fig. 1 Application scenarios of GIS equipment



In GIS equipment, electrical contact structures such as spring connectors and plum connectors are usually used in the busbar joint. Under the comprehensive action of electric, thermal and mechanical stress for a long time [3, 4]. Therefore, the deterioration phenomenon is easy to occur, which leads to the overheating fault of the bus joint, and seriously affects the operation stability of GIS equipment (Fig. 2). However, the contact part can't be measured directly because of the narrow space [5, 6], so it is necessary to carry out the simulation analysis of the temperature field distribution of the contact structure.

In this paper, the temperature calculation model of the GIS bus connector is established based on the finite element analysis of multi-field coupling. The distributions of current and temperature fields in the GIS bus connection area were calculated when the contact resistance of the spring connector was changed. In addition, the contact area of the spring connector was analyzed by scanning electron microscopy (SEM). The research in this paper can provide a theoretical basis for bus overheating fault analysis and a reference for the deterioration mechanism of the electrical connection structure.



Fig. 2 Overheat failure of busbar joint.

2 Theoretical Basis

2.1 GIS Busbar Joint Modeling

GIS busbar joint is a connection structure used to connect conductors in GIS. Its function is to enable the conductor to move at the joint and weaken the damage to the basin insulator caused by external environmental stress. In this paper, the spring contact of 252 kV GIS is selected as the research object, its structure is shown in Fig. 3. The outer diameter of the spring connector is 115 mm. When the busbar joint is connected, interference fit provides contact pressure to ensure electrical connection. To increase the conductivity, the busbar plug and connector are plated with silver.

In this paper, the refinement model of the spring is first constructed. Compared with ordinary springs, the coil of the inclined coil spring has a tilt angle, so the cross-section of the spring is oval. The parametric equation of the inclined coil spring can be obtained from the equation related to the ordinary spring as shown in Eq. 1.

Where a is the length of the long axis of the inclined coil spring, b is the length of the short axis of the inclined coil spring, d is the diameter of the spring, R is the radius of the whole spring, and θ is the Angle of the inclined coil spring. In this paper select a 30° inclined coil spring as the research object. n is the number of turns of spring. The values of the preceding parameters are as follows (Table 1):

Fig. 3 Structure of GIS bus connector

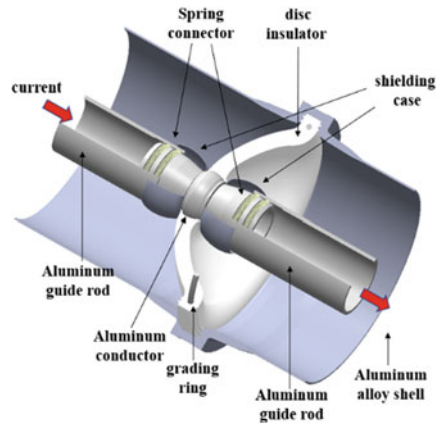


Table 1. Values of key parameters

Name	<i>a</i> (mm)	<i>b</i> (mm)	<i>d</i> (mm)	<i>R</i> (mm)	<i>n</i>
Value	6.3	5.3	1.5	52.5	108

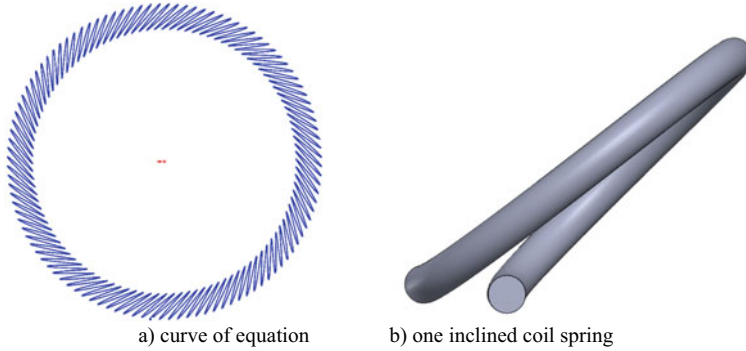


Fig. 4 Model of inclined spring

$$\begin{cases}
 x(t) = -\frac{2a-d}{2} \cdot \sin\theta \cdot \cos(2\pi t)\cos\left(\frac{2\pi t}{n}\right) \\
 \quad + \left[\frac{2b-d}{2}\cos(2\pi t) + R\right] * \sin\left(\frac{2\pi t}{n}\right) \\
 z(t) = \frac{2a-d}{2} \cdot \sin\theta \cdot \cos(2\pi t)\sin\left(\frac{2\pi t}{n}\right) \\
 \quad + \left[\frac{2b-d}{2}\cos(2\pi t) + R\right] * \cos\left(\frac{2\pi t}{n}\right) \\
 y(t) = \frac{2a-d}{2} \cdot \sin(2\pi t)
 \end{cases} \tag{1}$$

In SOLIDWORKS, the inclined coil spring model is established by the curve driven by the equation as follows (Fig. 4).

2.2 Electrical Contact Theory

The GIS busbar joint is subjected to the simultaneous action of electricity, mechanical stress, and heat in the working condition. Since mechanical stress mainly affects the change of contact resistance, the calculation can be simplified into electrothermal coupling analysis by adjusting the value of contact resistance in the electrical calculation.

The following assumptions exist in this model

1. The parts far away from the busbar joint or the geometric structures that have little influence on the electric calculation are simplified. For example, the shield ring in the basin insulator was not modeled. In addition, the small chamfered geometric features on the part surface in the solid model are ignored.
2. Materials are homogeneity
3. the spring contacts are free from stress relaxation and creep under contact conditions
4. the insulating gas inside the GIS busbar joint is considered to be chemically stable under normal operating conditions and no chemical corrosion occurs. The film resistance of the contact surface is ignored and only the contact resistance is considered. The number and size of the conductive and mechanical contact points are kept constant.
5. Ignore the displacement current and the thermoelectric effect of the material.

2.3 Theoretical Basis

The surface of a conductor is not flat, even if the surface has been carefully treated, under microscopic observation, the surface is made up of many different sizes of convex bodies. In the process of contact between two planes, even if the normal force between the two contact surfaces is great, they are compressed each other and seem to fit perfectly, but in fact, there are only a small number of points or surfaces in the contact surface to achieve real complete contact. It is on a few points or surfaces that are actually in contact that all the external force is applied.

As the current passes through the contact surface, it is pooled through these actual contact points (i.e., conductive spots). Due to the small area of the conductive spots, the current is contracted and an additional resistance is generated. In addition, electrons crossing the film will create additional resistance, often referred to as film resistances, which together form the contact resistance. Film resistance is usually ignored because of its small resistance values.

According to Holm contact resistance theory [7], the resistance value of contact resistance is

$$R_c = \frac{\rho_1 + \rho_2}{2a} \quad (2)$$

where ρ_1, ρ_2 is the resistivity of contact material, $\Omega \cdot m$, a is the radius of the contact point, m.

In the above formula, the contact radius is related to the force on the contact surface. According to the relationship between contact resistance and contact force established in the literature [8], the contact resistance can be calculated as follows:

$$R_c = \frac{E^* \rho \sigma_s}{3.7F} \quad (3)$$

In the above equation, E^* is the equivalent elastic model of the contact material, σ_s is the mean square error value of the height of the micro-convex on the rough surface.

2.4 Calculation Method of Thermal Field and Flow Field

In the GIS busbar joint, the current flowing through the Aluminum guide rod generates joule heat, which is the main internal heat source [9, 10]. Due to the small leakage current, the joule heat generated by the epoxy material is small and negligible. Therefore, according to Maxwell's equation, the electromagnetic field control equation can be expressed as:

$$\nabla \times \frac{1}{\mu} \times (\nabla \times A) = J_s - \varepsilon \frac{\partial E}{\partial t} \quad (4)$$

where μ is the conductivity coefficient, A is the magnetic vector, J_s is the current density in the conductor, ε is the dielectric constant and E is the electric field intensity.

In the cylindrical conductive rod model, the cylindrical coordinate system is established with the conductor axis as the Z-axis. In this coordinate system, the electric field intensity E and current density have only axial components. In this paper, the heating power of conductors and electrically connected components is calculated by the following equation.

$$J_s^2 / \gamma \quad (5)$$

where γ is the volume conductivity of the conductor. In GIL equipment, both gas and solid exist, and the heat conduction equation can be written as follows:

$$\rho c_p \frac{\partial T}{\partial t} = \lambda \left(\frac{\partial^2 T}{\partial x^2} + \frac{\partial^2 T}{\partial y^2} + \frac{\partial^2 T}{\partial z^2} \right) + Q \quad (6)$$

where T is temperature, c_p is the specific heat of the material, Q is the heating power per unit volume, x , y and z are the directions, ρ is the density, and t is the time. As the fluid flows, these parts produce heat exchange. Convection is usually the main form of heat transfer in liquids and gases. In GIL, the governing equations of the three-dimensional flow field and thermal field of material with incompressible and constant properties are as follows:

$$\nabla \rho v = 0 \quad (7)$$

$$\rho \frac{\partial v}{\partial t} = F - \nabla p + \mu \nabla^2 v \quad (8)$$

$$\rho c_p \frac{\partial T}{\partial t} = \nabla^2(\lambda T) + Q \tag{9}$$

3 Simulation and Analysis

Based on the establishment of the model, this paper calculated the current flow path of GIS equipment, verified the current contraction phenomenon of electrically connected parts, and calculated the temperature field distribution under the fluid–structure coupling condition, the calculation results are as follows.

Firstly, the calculation of the current contraction of GIS spring contact was carried out. The current module was selected in COMSOL to simulate the contraction current, and the operating current 2545A of the GIS equipment was input to analyze the change of conductor current density.

An inclined coil spring has 108 turns in total, 108 contacts with the outer guide rod, and 216 contacts with the inner conductor. Along the direction of the current flow, there are two springs on one side. When the current flows through the spring contact, its contact area shrinks, which causes the current to shrink.

The simulation model shows that the current density changes when the current flows through the touch part, and a significant current contraction occurs. At the same time, considering the current contraction of the contact surface and the existence of contact resistance, poor contact at the contact point can easily affect the stability of the whole (Fig. 5).

Based on the calculation results of the electric field, the heating power of the conductor is calculated through electromagnetic heating, and the fluid–solid coupling thermal field is analyzed in ANSYS CFX. The calculation results are shown in Fig. 6.

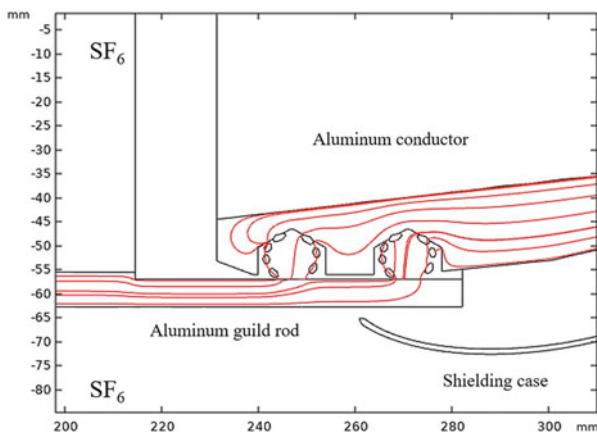


Fig. 5 Current direction of the connector

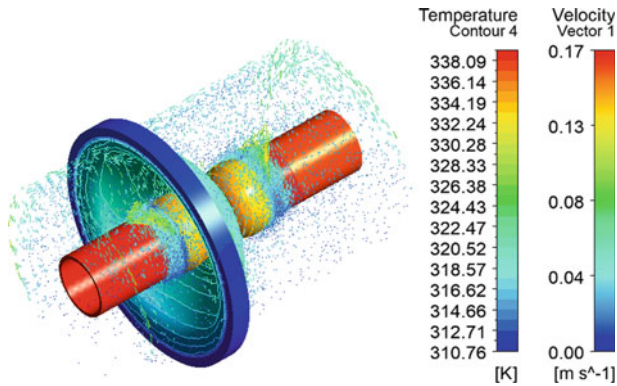


Fig. 6 The temperature distribution of GIL

The simulation results show that when the current of 2545A passes through the conductor, the temperature of the conductor is the highest, which can reach 338.09 K. In the fluid–structure interaction, considering the gas flow and gravity, the gas with high temperature has a low density and moves upward, while the gas with low temperature sinks. As can be seen from the velocity vector diagram in Fig. 6, a large amount of hot gas is emitted from the top of the shield ring, and the hot gas cools down in the process of rising, and then moves down from the surrounding circle, starting the cycle in this way.

When bad contact or deterioration occurs in the connector part, the contact resistance between the contact finger and the conductor part will increase, and the contact resistance may reach about 100 times of normal operation. When the contact resistance changes by 100 times, the temperature distribution of the contact is shown in the figure below.

It is obvious that the highest temperature area is transferred to the spring contact, and the overall maximum temperature rises to 416.23 K degrees. Therefore, the decline of contact performance of the touch finger will greatly affect the overall operation stability of GIS equipment (Fig. 7).

Based on the simulation, the deterioration phenomenon of electrical contact components was investigated in this paper. One turn of the used connector was observed by scanning electron microscope, and the surface of the connector is shown in Fig. 8. The back of the spring contact finger is a non-contact area, such as area 2 in Fig. 8, which is relatively smooth on the whole. The front side is the contact area, and area 2 in Fig. 8 has a rough surface.

With the increase in service time, the spring contact is subjected to multiple physical quantities for a long time so that its surface becomes rough and the contact effect is weakened. The deterioration of the contact surface will cause the contact resistance to increase. The increase in contact resistance will raise the heating power of the contact section, which in turn will raise the temperature of the contact section. The temperature increase of the contact part will accelerate the deterioration of the

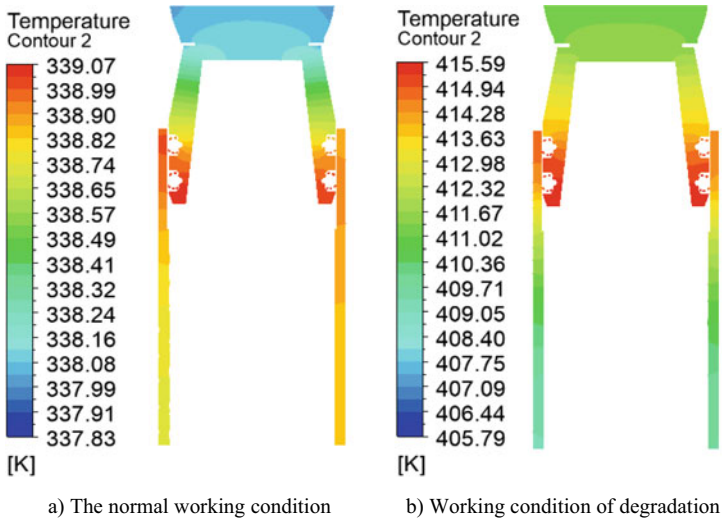
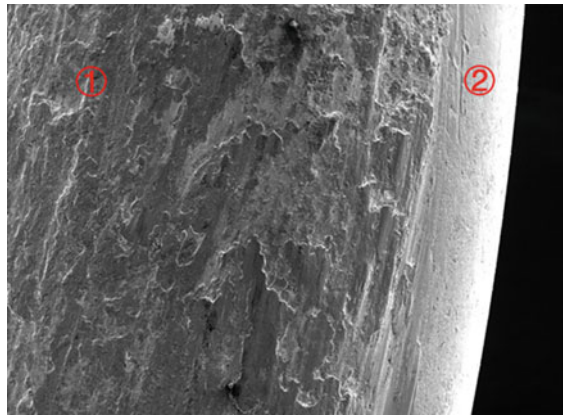


Fig. 7 The temperature distribution of the contact and guide rod

Fig. 8 Surface of connector



contact surface. Eventually a vicious circle is formed, and the long-term development will lead to the overheating failure of the busbar connection part.

4 Conclusion

In this paper, the 3D simulation model of the GIS bus joint is established, and the contact resistance, heat convection, heat conduction, and heat radiation are considered to complete the simulation analysis of the GIS bus joint. Through simulation analysis, it is found that:

- 1) When the current is 2545 A, the highest temperature of the GIS equipment occurs on the conductor, which is 338.09 K. Considering factors such as the change in gas density, the temperature rise near the conductor causes the gas to flow, resulting in a temperature difference between the upper and lower parts.
- 2) When poor contact or deterioration occurs, the temperature of the contact structure rises and the maximum conductor temperature rises to 415.59 K through the action of heat transfer. Prolonged operation at high temperatures will seriously affect the safety of the equipment.
- 3) The observation of the contact surfaces reveals that wear occurs on the contact surfaces due to the long-term electrical heating effect. Wear deteriorates the contact condition of the contact parts and further contributes to the increase in operating temperature.

In summary, the deterioration of electrically connected components is the result of the long-term influence of several factors. The temperature of the contact area can be used as an important indicator to evaluate the working condition. The research in this paper can provide a basis for the analysis of the deterioration mechanism of the electrical connection components of GIS equipment.

Acknowledgements This work is supported by the science and technology project of State Grid Anhui (B3120521000Z).

References

1. Han, X., Sun, X., Chen, H., et al.: The overview of development of UHV AC transmission technology in China. *Proc. CSEE* **40**(14), 4371–4386+4719 (2020). (in Chinese)
2. Zhong, J., Chen, G., Tan, S., et al.: Key technology and development trend of high-voltage switchgear. *High Voltage Eng.* **47**(08), 2769–2782 (2021). (in Chinese)
3. Tian, H., Jin, S., Gong, A., et al.: Analysis on the deterioration behavior of electrical contact structure used in converter transformer RIP bushings. *Proc. CSEE* **41**(03), 1146–1156 (2021). (in Chinese)
4. Jin, S., Tian, H., Wang, Q., et al.: Corrosion reaction kinetics and high-temperature corrosion testing of contact element strips in ultra-high voltage bushing based on the phase-field method. *IET Gener. Transm. Distrib.* **16**(15), 2947–2958 (2022)
5. Cong, H., Li, Q., Qi, B., et al.: Online GIS switch contact temperature monitoring based on IR sensing. *Electr. Power Autom. Equip.* **34**(03), 144–148+161 (2014). (in Chinese)
6. Qi, C., Li, Q., Cong, H., et al.: On-line temperature monitoring for GIS disconnecting switch contacts based on multipoint-distributed fiber bragg grating. *Trans. China Electrotech. Soc.* **30**(12), 298–306 (2015). (in Chinese)

7. Holm, R.: *Electrical Contacts*. Springer, New York (1979)
8. Liu, P., Ren, T., Xie, T., et al.: Numerical calculation of contact resistance of strap contacts of the bushing on the side of the converter valve. *High Voltage Eng.* 1–10 (2022). (in Chinese)
9. Xie, G., Shi, S., Wang, Q., et al.: Simulation and experimental analysis of three-dimensional temperature distribution of ± 400 -kV converter transformer valve-side resin impregnated paper bushing under high current. *IET Gener. Transm. Distrib.* **16**, 2989–3003 (2022)
10. Jin, S., Tian, H., Gong, A., et al.: Research on the temperature and flow velocity characteristic of GIL based on multi-field coupling. In: *2019 IEEE Conference on Electrical Insulation and Dielectric Phenomena (CEIDP)*. IEEE (2019).

Multi-objective Optimization and Research of the New Type Combined Excitation Permanent Magnet Motor for Electric Vehicle



Bingchang Lv , Liwei Shi , Jianning Jing, Kaiwen Liu, and Lintao Li

Abstract A new combined excitation permanent magnet motor (CEPMM) is proposed to reduce the amount of rare earth materials and the cogging torque of the traditional permanent magnet motor (TPMM). By combining the energy method and the Fourier decomposition method, the influence mechanism of the combined excitation structure on the cogging torque is revealed. On this basis, in order to further obtain the optimal parameter values of the motor, an efficient multi-objective hierarchical optimization strategy suitable for CEPMM is proposed. Based on the orderly combination of parametric hierarchical design and multiple optimization algorithms to achieve the comprehensive optimization among multiple optimization objectives. The performance of TPMM and CEPMM is analyzed using the finite element method, and it can be seen that the cogging torque and rare earth dosage of CEPMM are reduced by 79.9% and 19%, respectively, compared with TPMM. Finally, the correctness of the structure and the effectiveness of the optimization method are verified by the prototype experiment.

Keywords Permanent magnet motor · Combined excitation · Multi-objective optimization · Finite element analysis

1 Introduction

Permanent magnet synchronous motors have the advantages of high ratio power and high efficiency, and are now widely used in the field of electric vehicles [1, 2]. However, the built-in permanent magnet motor generates high cogging torque due to its structure, which leads to a rise in torque ripple and has a certain impact on the running performance of the vehicle [3, 4]. The rising price of rare earths has led to

B. Lv · L. Shi (✉) · J. Jing · K. Liu · L. Li
School of Transportation and Vehicle Engineering, Shandong University of Technology,
Shandong 255049, China
e-mail: shiliwei@sdut.edu.cn

© Beijing Paiké Culture Commu. Co., Ltd. 2023
X. Dong et al. (eds.), *The proceedings of the 10th Frontier Academic Forum of Electrical Engineering (FAFEE2022)*, Lecture Notes in Electrical Engineering 1054, https://doi.org/10.1007/978-981-99-3408-9_39

the increase in the cost of permanent magnet motors, thus limiting the development of permanent magnet motors [5, 6].

Numerous scholars have conducted in-depth studies to address these issues. In terms of improving motor output performance, the literature [7] proposes a method of shifting between magnetic poles to reduce the cogging torque and the torque ripple of the motor and improve the output performance of the motor, while introducing the concept of repeating unit to reveal this mechanism. In addition to changing the motor structure, optimization algorithms can also be used to determine the optimal values of motor parameters to improve the electromagnetic performance. The literature [8] uses the experimental design method for single objective optimization, which has a large number of experiments and the interaction between parameters is easily ignored, making it difficult to determine the optimal parameter values. The literature [9] proposed the Taguchi multi-objective optimization algorithm, which can significantly reduce the number of simulations, but its optimization results are limited by the selection of the initial values of the parameters, which has certain limitations. For the reduction of rare earth materials, scholars have proposed to use cheap ferrite instead of neodymium iron boron (NdFeB) [10], but the small magnetic energy product of ferrite will cause the decrease of motor output torque, so the hybrid excitation [11] becomes an effective solution.

A hierarchical multi-objective optimization strategy suitable for combined excitation-type permanent magnet motors is proposed, which can quickly and accurately obtain the optimal parameter values of the motor, reduce the mutual influence between optimization objectives, and improve the optimization efficiency. The TPMM and CEPMM are simulated and compared, and the correctness of the structure and the effectiveness of the optimization method are verified by prototype experiments.

2 Motor Topology Analysis

The topological structure of the CEPMM is shown in Fig. 1.

The structure has the following characteristics: 1) the angle and width of the permanent magnets are asymmetric; 2) the rotor has a non-uniform air gap. α : rotation angle NdFeB1 to d -axis, β : rotation angle NdFeB2 and Ferrite to d -axis, W_{pm3} :

Fig. 1 Topology of CEPMM

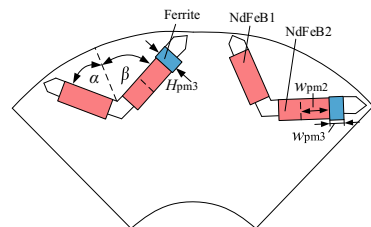
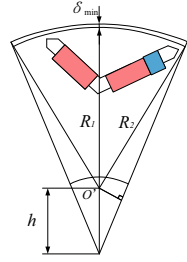


Fig. 2 Non-uniform air-gap rotor structure



increased width of the Ferrite, H_{pm3} : thickness of Ferrite, W_{pm2} : reduced width of NdFeB2. Figure 2 shows a model of the non-uniform air-gap structure of the motor. R_1 : radius of stator; R_2 : outer diameter of rotor; δ_{\min} : the minimum air-gap length of the CEPMM; h : eccentric distance.

The cogging torque of the CEPMM can be expressed as:

$$T_{\text{cog}} = -\frac{\partial W}{\partial \gamma} \quad (1)$$

where, W is the magnetic field energy, γ is the relative position angle of the permanent magnet to the armature. The formula for the distribution of the air-gap magnetic density along the surface of the rotor is as follows:

$$B_g(\theta, \gamma) = B_r(\theta) \frac{h_m(\theta)}{h_m(\theta) + \delta(\theta, \gamma)} \quad (2)$$

where, $B_g(\theta, \gamma)$ is the air-gap magnetic density; B_r is the PM residual magnet; $h_m(\theta)$ is the PM thickness at the angle θ of the magnetic pole centerline; $\delta(\theta, \gamma)$ is the distribution function of the air-gap along the circumference direction.

The magnetic field energy is calculated as follows:

$$W = \frac{1}{2\mu_0} \int_V B_r^2(\theta) \left[\frac{h_m(\theta)}{h_m(\theta) + \delta(\theta, \gamma)} \right]^2 dV \quad (3)$$

The Fourier decomposition of B_r as follows:

$$\begin{cases} B_r^2(\theta) = \alpha_p B_r^2 + \sum_{n=1}^{\infty} \frac{2}{n\pi} B_{rn} \cos(2np\theta) \\ B_{rn} = \frac{2}{n\pi} B_r^2 \sin(n\alpha_p\pi) \end{cases} \quad (4)$$

The Fourier decomposition of $\left[\frac{h_m(\theta)}{h_m(\theta) + \delta(\theta, \gamma)} \right]^2$ as follows:

Table 1 Main optimization parameters and variation range

Parameters	Range	Unit
α	45.5–47.5	°
β	63–65	°
W_{pm3}	1–3	mm
H_{pm3}	4.5–4.9	mm
h	2–6	mm
W_{pm2}	1–4	mm

$$\left[\frac{h_m(\theta)}{h_m(\theta) + \delta(\theta, \gamma)} \right]^2 = G_0 + \sum_{n=1}^{\infty} G_n \cos n\zeta(\theta + \gamma) \tag{5}$$

The cogging torque can be transformed as:

$$T_{cog}(\gamma) = \frac{\pi z L}{4\mu_0} (R_1^2 - R_2^2) \sum_{n=1}^{\infty} n G_n B_{r, \frac{n\zeta}{2p}} \sin(nZ\gamma) \tag{6}$$

The cogging torque is related to the α_p and δ of CEPMM, and the α_p of CEPMM is determined by the angle, width, and material ratio of the permanent magnet.

3 Motor Parameter Optimization

3.1 Optimization Goals and Parameters

Table 1 shows the design variables and corresponding variation ranges. The range of values of the optimization variables is derived from the single variable analysis. Considering the performance of the CEPMM in operation, minimizing the cogging torque (T_{cog}), the torque ripple (T_{rip}) and the no-load back-EMF waveform total harmonic distortion (THD) are selected as design objectives for motor multi-stage optimization. It is also necessary to consider the output torque of the CEPMM in the process of replacing NdFeB with Ferrite, so the output torque of the motor is used as a constraint.

3.2 Sensitivity Analysis

In order to effectively identify the influence weight of parameters on the objective, the comprehensive sensitivity function $S(x_i)$ can be expressed as:

Table 2 Results of sensitivity indices of optimization parameters to optimization objectives

Parameters	$I_{\text{cog}}(x_i)$	$I_{\text{rip}}(x_i)$	$I_{\text{THD}}(x_i)$	$S(x_i)$
α	-0.177	-0.144	-0.257	0.185
β	-0.162	-0.096	-0.165	0.146
$W_{\text{pm}2}$	-0.727	-0.745	-0.792	0.747
$W_{\text{pm}3}$	-0.456	0.066	-0.083	0.265
h	-0.237	-0.575	0.261	0.327
$H_{\text{pm}3}$	0.018	0.045	0.055	0.034

$$\begin{cases} I(a_i) = V(I(b/a_i)) / V(b) \\ S(a_i) = \lambda_1 |I_{\text{cog}}(a_i)| + \lambda_2 |I_{\text{rip}}(a_i)| + \lambda_3 |I_{\text{THD}}(a_i)| \end{cases} \quad (7)$$

where, b is objective, $I(b/a_i)$ is the average value, $I(b)$ and $V(I(y/x_i))$ are the variance of b and $I(b/a_i)$, respectively. $|I_{\text{cog}}(a_i)|, |I_{\text{rip}}(a_i)|$ and $|I_{\text{THD}}(a_i)|$ are the sensitivity indices, respectively. The values for λ_1, λ_2 , and λ_3 are 0.5, 0.25, and 0.25, respectively.

According to the data obtained in Table 2, these parameters can be divided into two layers. The Level 1 is $\alpha, W_{\text{pm}2}, h$ and $W_{\text{pm}3}$ for parameters with high-sensitivity, and the Level 2 is β and $H_{\text{pm}3}$ for parameters with low-sensitivity.

3.3 High-Sensitivity Parameters Optimization

The RSM can effectively reduce the number of experiments and use polynomial functions instead of the required designed model. The BBD method is chosen in this paper. The multiple quadratic regression fitted polynomial is shown in Eq. (8).

$$G(t) = \beta_0 + \sum_{i=1}^4 \beta_i t_i + \sum_{i=1}^4 \beta_{ii} t_i^2 + \sum_{i=1}^3 \sum_{j>i}^4 t_i t_j + \varepsilon \quad (8)$$

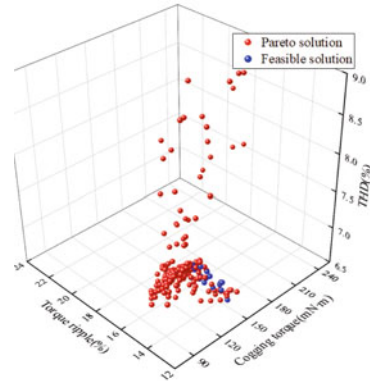
where, $G(t)$ is the response value; β_0 is the constant, β_i is the first-order coefficient, and β_{ii} is the second-order coefficient; t_i and t_j are two different optimization variables; ε is the fitting error. The first level of optimization contains four optimization variables and generally requires $3^4 = 81$ experiments. A total of 25 experiments are required using the BBD method, and the response matrix and results are shown in Table 3.

In order to obtain the global optimal solution of the three optimization objectives, Multi-Objective Genetic Algorithm-II (MOGA-II) is introduced into the optimization process of high-sensitivity parameters. The mathematical model is shown in Eq. 9. The Pareto solution of the high sensitivity parameters are shown in Fig. 3.

Table 3 Response matrix and results

Model	α ($^{\circ}$)	W_{pm3} (mm)	h (mm)	W_{pm2} (mm)	T_{cog} (mN·m)	T_{rip} (%)	THD (%)
1	45.5	2	2.5	6	142.43	14.49	8.41
2	46.5	3	2.5	2	141.39	17.65	6.87
3	47.5	3	2.5	4	141.01	15.67	6.63
...
25	47.5	1	2.5	2	161.48	18.37	6.88

Fig. 3 Pareto solution of the high-sensitivity parameters



$$\text{Constrains } T_{cog} \leq 140 \text{ mN} \cdot \text{m}, T_{rip} \leq 15.5\%, THD \leq 7\%, T_{avg} \geq 15.16 \text{ N} \cdot \text{m} \tag{9}$$

3.4 Low-Sensitivity Parameters Optimization

The single variable sweep method is used for the low-sensitivity parameters, and the influence of the optimized parameters on the optimization objective is shown in Table 4. The final design parameters are determined as $\beta = 65^{\circ}$ and $H_{pm3} = 4.5 \text{ mm}$.

4 Performance Comparison

4.1 CEPMM Structure Parameters

The CEPMM models were established based on the motor dimensional parameters shown in Table 5.

Table 4 Impact of β and H_{pm3} on optimization objectives

Parameters	Value	T_{cog} (mN·m)	T_{rip} (%)	THD (%)
$\beta(^{\circ})$	63	146.13	18.39	6.98
	64	120.14	16.23	7.07
	65	113.06	15.07	7.15
H_{pm3} (mm)	4.5	113.06	15.07	7.39
	4.6	116.53	15.52	7.18
	4.7	117.84	15.86	6.98

Table 5 The key parameters of CEPMM

Parameters	Value (mm)
Outer diameter of the stator	160
Inner diameter of the stator	107.6
Minimum air-gap length	0.8
Iron stack length	91
Thickness of the Ferrite	4.5
Width of the Ferrite	7
Thickness of the NdFeB	4.3
Width of the NdFeB1/NdFeB2	10.5/6.5

4.2 Analysis of No-Load Condition

The flux density distribution of TPMM and CEPMM under no-load conditions is given in the Fig. 4, and the results show that the flux density generally does not exceed 1.4 T, except for the magnetic saturation phenomenon in a small area, such as the magnetic field strength near the spacer bridge exceeds 2 T, when the silicon steel sheet is fully saturated, which is beneficial to suppress the leakage phenomenon. In general, the flux density distribution of CEPMM is relatively uniform, which reduces the additional losses caused by the aggregation effect to a certain extent.

Fig. 4 The magnetic filed map analysis

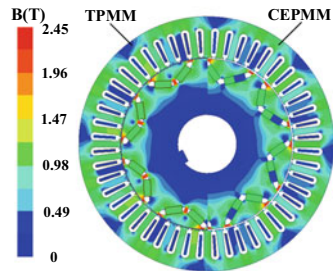
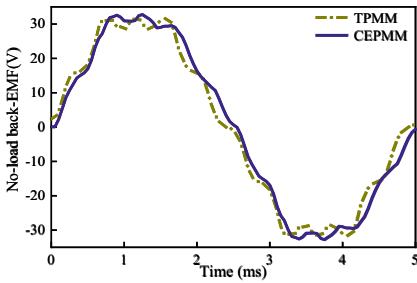
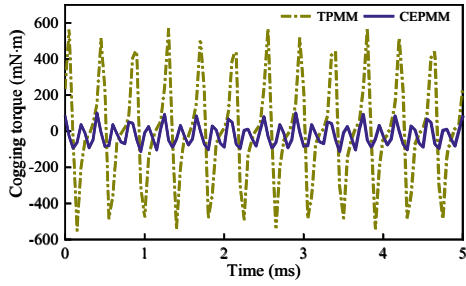
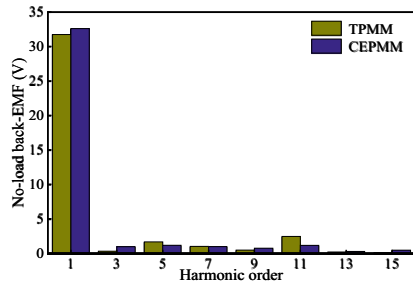


Fig. 5 The cogging torque analysis



(a) The no-load back-EMF waveform.



(b) The harmonic analysis.

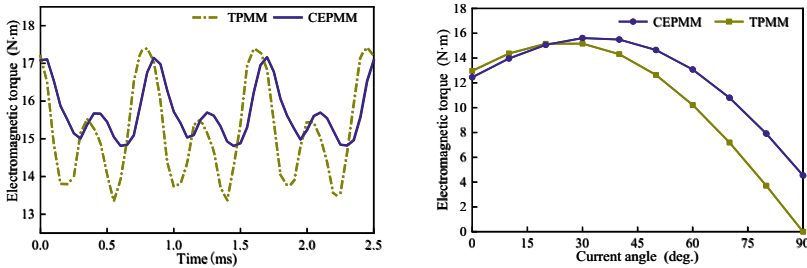
Fig. 6 The no-load back-EMF waveform and the harmonic analysis

The cogging torque comparison results of the TPMM and the CEPMM are shown in Fig. 5. The cogging torque peak-to-peak difference of the TPMM is 1.16N·m and the maximum value is 563.77 mN·m. The cogging torque peak-to-peak difference of the CEPMM is 0.21N·m, and the maximum value is 113.39 mN·m, which is 79.9% lower than the TPMM. It can be concluded that the cogging torque of the CEPMM is significantly lower than the TPMM.

The no-load back-EMF waveforms of the TPMM and the CEPMM are shown in Fig. 6(a). The waveforms of the CEPMM have good symmetry with those of the TPMM. To study the sinusoidality of the waveforms of the motor more accurately, the waveform is analyzed by FFT, and the results are shown in Fig. 6(b). The harmonic distortion rate of TPMM is 9.92%, while the harmonic distortion rate of CEPMM is 6.98%.

4.3 Analysis of Electromagnetic Torque

The electromagnetic torque performance of the TPMM and the CEPMM is shown in Fig. 7(a). The average output torque of TPMM is 15.16N·m, and the average torque of CEPMM is 15.68 N·m, so the torque output capacity of CEPMM is higher than that of TPMM. In addition, the torque ripple of TPMM is 26.87%, compared



(a) The electromagnetic torque waveform. (b) The torque curves with respect to current angle.

Fig. 7 The electromagnetic torque analysis

with TPMM, the torque ripple of the CEPMM is greatly reduced, and its value is 15.03%, which is conducive to improving the stability of electric vehicles and meeting the requirements of low torque ripple when actually driving. To compare the torque characteristics of the TPMM and the CEPMM, analyze the variation law between the output torque and the current angle, the results are shown in Fig. 7(b). The electromagnetic torque of the two motors has similarity with the change of the current angle, and the peak of the output torque of the CEPMM corresponds to the current angle around 30° , while the current angle of TPMM is near 20° .

4.4 Analysis of Efficiency

For the simulation analysis of the efficiency of the motor, Fig. 8 gives the map diagram of the two motors, it can be seen that although the efficiency of the two motors exceeds 90%, the maximum efficiency of the CEPMM is higher than that of the TPMM, and the high efficiency area is wider, which also verifies that the loss of the CEPMM is lower than that of the TPMM. For the maximum output torque, the CEPMM is slightly higher than the TPMM. Therefore, it can be seen that the CEPMM has better operating characteristics.

4.5 Analysis of Demagnetization

As can be seen from Fig. 9, the magnetic densities of the ferrite materials are above 0.2 T under rated load, indicating that the ferrite permanent magnet materials have no demagnetization phenomenon. Considering that the vehicle will be overloaded during the driving process, the magnetic density of the ferrite material when the load current is increased to 1.5 times of the rated current is analyzed. From Fig. 9, it can be seen that the phenomenon of 0.2 T below the magnetic density value occurs at the outer edge of the ferrite, which indicates that the ferrite is irreversibly demagnetized,

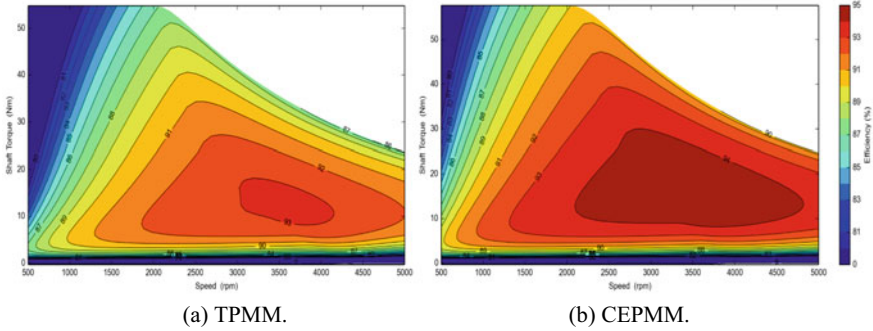
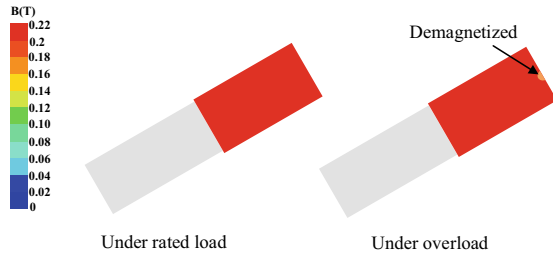


Fig. 8 Motor efficiency analysis

Fig. 9 Demagnetization area of the ferrite PMs



but the demagnetization area is small. Therefore, the CEPMM has a high resistance to demagnetization.

5 Experiment Verification

In order to verify the correctness of CEPMM and the effectiveness of optimization strategy, a prototype of the CEPMM was fabricated. The prototype and experimental platform are shown in Fig. 10.

The cost comparison between TPMM and CEPMM for PM is shown in Table 6. The price of NdFeB is considered to be \$100/kg and the price of ferrite is considered to be \$7/kg.

The measured values of the cogging torque of the prototype in different rotational directions are shown in Fig. 11(a) and Fig. 11(b). The peak-to-peak values of the prototype in different rotational directions are basically the same, with slight differences from the finite element simulation values of CEPMM. The measured three-phase no-load back-EMF waveform is shown in Fig. 11(c), which shows that the amplitudes of the waveforms are basically equal and the phase difference is 120°, with good symmetry and high consistency between the waveforms and the simulation results, with an error of 4.8%. This test of the mechanical characteristics of the

Fig. 10 Photo of the prototype and experimental platform



Table 6 PM cost comparison

	TPMM	CEPMM
Price NdFeB PM (pu)	1	0.81
Price ferrite PM (pu)	0	0.17×10^{-4}
Total Price (pu)	1	0.810017

motor uses the dynamometer test bench. The result is shown in Fig. 11(d). Under rated load, the maximum torque is 56.4N·m, and the maximum efficiency is higher than 90%.

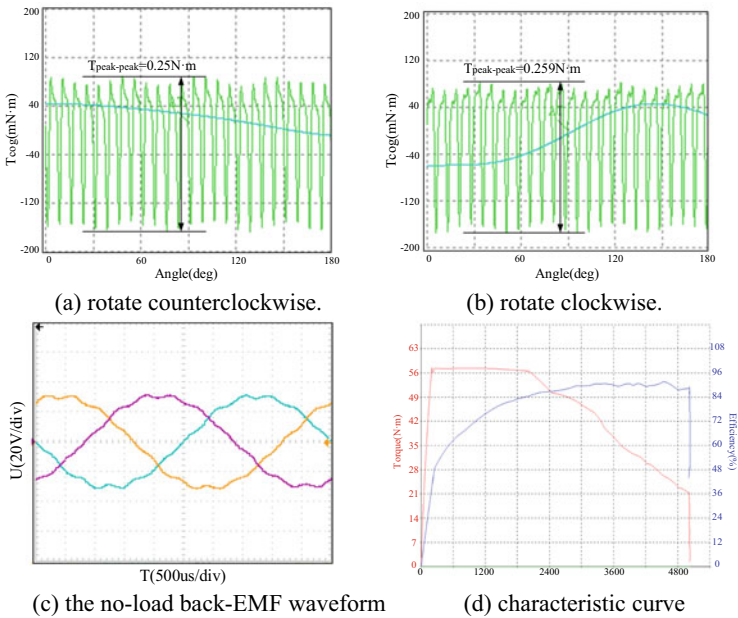


Fig. 11 The measured results of the prototype

6 Conclusion

- (1) The CEPMM is excited by two different permanent magnet materials to reduce the amount of rare earth materials by 19%, and the asymmetric placement structure design of hybrid permanent magnet materials reduces the cogging torque by 79.9%, while having the lower torque ripple and the higher efficiency.
- (2) Aiming at the relatively complex structure of the motor, a hierarchical optimization method suitable for this motor is proposed. This optimization method can reduce the optimization time and improve the optimization efficiency while ensuring the accuracy.

Acknowledgements This work was supported by the Nation Natural Science Foundation of China (51975340).

References

1. Onsal, M., Cumhur, B., Demir, Y., Yolacan, E., Aydin, M.: Rotor design optimization of a new flux-assisted consequent pole spoke-type permanent magnet torque motor for low-speed applications. *IEEE Trans. Magn.* **54**(11), 1–5 (2018)
2. Hu, W., Zhang, X., Geng, H., Gao, T., Shi, L., You, D.: Electromagnetic design and flux regulation analysis of new hybrid excitation generator for electric vehicle range extender. *J. Electr. Comput. Eng.* **2021**(18), 1–13 (2021)
3. Ren, W.: A technique of torque ripple compensation for interior permanent magnet machines by using an asymmetrical V-type rotor configuration. In: *IECON 2017–43rd Annual Conference of the IEEE Industrial Electronics Society*, pp. 8744–8749 (2017)
4. Jo, I.H., Lee, H.W., Jeong, G., Ji, W.Y., Park, C.B.: A study on the reduction of cogging torque for the skew of a magnetic geared synchronous motor. *IEEE Trans. Magn.* **55**(2), 1–5 (2019)
5. Ma, Q., El-Refaie, A., Lequesne, B.: Low-cost interior permanent magnet machine with multiple magnet types. *IEEE Trans. Ind. Appl.* **56**(2), 1452–1463 (2020)
6. Shi, L., Guo, Y., Xiao, D., Han, Z., Zhou, X.: Design, optimization, and study of a rare-earth permanent-magnet generator with new consequent-pole rotor for extended-range electric vehicle. *IEEE Trans. Electr. Electron. Eng.* **14**(6), 917–923 (2019)
7. Liu, G., Du, X., Zhao, W., Chen, Q.: Reduction of torque ripple in inset permanent magnet synchronous motor by magnets shifting. *IEEE Trans. Magn.* **53**(2), 1–13 (2017)
8. Wang, X., Yuan, L., Zhan, Y., Chen, H., Wardach, M., Palka, R., Orabi, M.: Sensitivity analysis on novel U-shape dual-stator switched reluctance motor. *IEEE Trans. Appl. Supercond.* **31**(8), 1–5 (2021)
9. Zhang, W., Shi, L., Liu, K., Li, L., Jing, J.: Optimization analysis of automotive asymmetric magnetic pole permanent magnet motor by Taguchi method. *Int. J. Rotating Mach.* **2021**(71), 1–9 (2021)
10. Kim, H.J., Kim, D.Y., Hong, J.P.: Structure of concentrated-flux-type interior permanent-magnet synchronous motors using ferrite permanent magnets. *IEEE Trans. Magn.* **50**(11), 1–4 (2014)
11. Du, Z.S., Lipo, T.A.: Cost-effective high torque density bi-magnet machines utilizing rare earth and ferrite permanent magnets. *IEEE Trans. Energy Convers.* **35**(3), 1577–1584 (2020)

Sensorless Control of Multiphase Permanent Magnet Synchronous Motor Considering Phase-to-Phase Coupling



Haoran Zhao, Dong Wang, Xinqiang Yi, and Pengfei Hu

Abstract The traditional sensorless control method often uses lumped inductance parameters to estimate the flux linkage generated by the stator. When the number of motor phases is small, this method has high accuracy. However, in a multiphase motor, due to the increase of the coupling between phase windings, the influence of all phase currents on the flux linkage cannot be taken into account when calculating the stator flux linkage by lumped parameters. When the torque fluctuates, the flux linkage calculation results will produce certain errors, which adversely affects the accuracy of the sensorless control algorithm. In order to improve the calculation accuracy of flux linkage in the control algorithm, a position-sensorless control method for twelve-phase permanent magnet synchronous motor is studied in this paper. First, the mathematical model of twelve-phase permanent magnet synchronous motor is deduced. Secondly, the rotor position calculation method considering multi-phase coupling is proposed, and the motor speed is estimated based on the phase-locked loop (PLL). Finally, the effectiveness of the control method is verified by Matlab/Simulink simulation. The results show that the proposed sensorless control method has higher accuracy and better control performance than the traditional control method. It can still provide accurate rotor position angle under the condition of asymmetric multiple windings.

H. Zhao · D. Wang · X. Yi (✉) · P. Hu
National Key Laboratory of Electromagnetic Energy,
Naval University of Engineering, Wuhan 430033, China
e-mail: yixinqiang86@163.com

East Lake Laboratory, Wuhan, China

H. Zhao
e-mail: haoranzhaoh@163.com

D. Wang
e-mail: wangdongl@vip.sina.com

P. Hu
e-mail: 785141654@qq.com

Keywords Twelve-phase permanent magnet synchronous motor · Position-sensorless control · Phase-locked loop · Rotor position detection

1 Introduction

The development of China's key equipment in energy, transportation, high-end manufacturing and national defense and military industry has raised the goal of "four Hs, one L and one M" for the performance of motor system, namely: high power density, high adaptability, high reliability, high accuracy, low emissions and multi-function composite [1]. Permanent magnet synchronous motor (PMSM) has the merit of high-power density, low torque ripple [2] and is helpful to enhance the redundancy of the system [3]. Besides, PMSMs have more control resources and possess giant potential in advanced transmission system and advanced marine electric propulsion system [4–6].

Precise control of PMSM relies on accurate rotor position [7–10], while rotor position is usually detected by position sensor. However, in some special cases, submarine shaftless propeller, for example, rotor position sensor cannot be installed due to the special structure of the rotor. To solve this problem, position-sensorless control technology can take the place of traditional rotor position sensor, and by analyzing the motor's voltage and current, the rotor position and speed can be calculated at actual time.

Different from three-phase motor, multiphase motor has its own characteristics in control due to the diversity in winding arrangement. So, it is necessary to conduct research on the position-sensorless control method multiphase motor.

This paper proposes a position-sensorless control method for a twelve-phase PMSM based on flux observation, and phase-to-phase coupling is considered. And phase-locked loop is used to estimate the rotor position and speed. The simulation result shows that the proposed method can accurately detect the rotor position and speed.

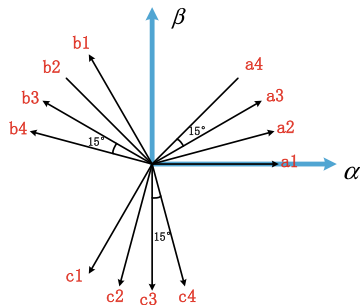
2 Mathematical Model of Twelve-Phase PMSM

2.1 Mathematical Model in *abc* Coordinate System

Take twelve-phase PMSM for example, the winding vector direction is shown as Fig. 1. The twelve-phase winding is composed of four sets of three-phase windings with phase shift of 15° electrical angle in turn.

In *abc* coordinate system, the voltage function of twelve-phase PMSM can be shown as [11, 12]:

Fig. 1 Twelve-phase PMSM winding vector



$$u_{abc} = Ri_{abc} + \frac{d\psi_{abc}}{dt} \tag{1}$$

where u_{abc} , R , i_{abc} and ψ_{abc} represent stator winding's phase voltage vector, phase resistance, phase current vector, and flux vector respectively.

$$u_{abc} = [u_{a1} \ u_{b1} \ u_{c1} \ u_{a2} \ u_{b2} \ u_{c2} \ u_{a3} \ u_{b3} \ u_{c3} \ u_{a4} \ u_{b4} \ u_{c4}]^T$$

$$R = \text{diag}(\underbrace{r \ r \ \dots \ r}_{12})^T$$

$$i_{abc} = [i_{a1} \ i_{b1} \ i_{c1} \ i_{a2} \ i_{b2} \ i_{c2} \ i_{a3} \ i_{b3} \ i_{c3} \ i_{a4} \ i_{b4} \ i_{c4}]^T$$

$$\psi_{abc} = [\psi_{a1} \ \psi_{b1} \ \psi_{c1} \ \psi_{a2} \ \psi_{b2} \ \psi_{c2} \ \psi_{a3} \ \psi_{b3} \ \psi_{c3} \ \psi_{a4} \ \psi_{b4} \ \psi_{c4}]^T$$

where r represents stator winding's phase resistance.

Flux function can be shown as:

$$\psi_{abc} = L_{abc}i_{abc} + \psi_p \tag{2}$$

where L_{abc} represents the inductance vector in abc coordinate system, and ψ_p represents each phase's flux linkage of the stator winding.

$$L_{abc} = \begin{bmatrix} L_{11} & M_{12} & M_{13} & M_{14} \\ M_{21} & L_{22} & M_{23} & M_{24} \\ M_{31} & M_{32} & L_{33} & M_{34} \\ M_{41} & M_{42} & M_{43} & L_{44} \end{bmatrix}$$

$$\psi_p = \psi_f [\cos \theta \ \cos(\theta - \frac{2\pi}{3}) \ \cos(\theta - \frac{4\pi}{3}) \ \cos(\theta - \frac{\pi}{12}) \ \cos(\theta - \frac{3\pi}{4}) \ \cos(\theta - \frac{17\pi}{12}) \ \cos(\theta - \frac{\pi}{6}) \ \cos(\theta - \frac{5\pi}{6}) \ \cos(\theta - \frac{3\pi}{2}) \ \cos(\theta - \frac{\pi}{4}) \ \cos(\theta - \frac{11\pi}{12}) \ \cos(\theta - \frac{19\pi}{12})]^T$$

where L_{ii} and M_{ij} ($i, j = 1, 2, 3, 4$) represent the self-inductance of the i th set of winding and the mutual-inductance between the i th and the j th set of winding. ψ_f represents the amplitude of the flux generated by magnet and θ represents electrical angle.

$$L_{ii} = \begin{bmatrix} L_{a_i a_i} & M_{a_i b_i} & M_{a_i c_i} \\ M_{b_i a_i} & L_{b_i b_i} & M_{b_i c_i} \\ M_{c_i a_i} & M_{c_i b_i} & L_{c_i c_i} \end{bmatrix} \quad i, j = 1, 2, 3, 4$$

$$M_{ij} = \begin{bmatrix} M_{a_i a_j} & M_{a_i b_j} & M_{a_i c_j} \\ M_{b_i a_j} & L_{b_i b_j} & M_{b_i c_j} \\ M_{c_i a_j} & M_{c_i b_j} & L_{c_i c_j} \end{bmatrix}$$

2.2 Mathematical Model in $\alpha\beta 0$ Coordinate System

Based on equal amplitude transformation, the Clark transformation of twelve-phase motor can be expressed as:

$$C_{\alpha\beta 0}^{abc} = \begin{bmatrix} C_{11} & & & \\ & C_{22} & & \\ & & C_{33} & \\ & & & C_{44} \end{bmatrix}$$

$$C_{ii} = \frac{2}{3} \begin{bmatrix} \cos(i-1)15^\circ & \cos[(i-1)15^\circ + 120^\circ] & \cos[(i-1)15^\circ - 120^\circ] \\ \sin(i-1)15^\circ & \sin[(i-1)15^\circ + 120^\circ] & \sin[(i-1)15^\circ - 120^\circ] \\ \frac{1}{2} & \frac{1}{2} & \frac{1}{2} \end{bmatrix} \quad i = 1, 2, 3, 4$$

The inverse transformation of Clark transformation can be expressed as:

$$C_{abc}^{\alpha\beta 0} = \begin{bmatrix} C_{11}^{-1} & & & \\ & C_{22}^{-1} & & \\ & & C_{33}^{-1} & \\ & & & C_{44}^{-1} \end{bmatrix}$$

$$C_{ii}^{-1} = \begin{bmatrix} \cos(i-1)15^\circ & \sin(i-1)15^\circ & 1 \\ \cos[(i-1)15^\circ + 120^\circ] & \sin[(i-1)15^\circ + 120^\circ] & 1 \\ \cos[(i-1)15^\circ - 120^\circ] & \sin[(i-1)15^\circ - 120^\circ] & 1 \end{bmatrix} \quad i = 1, 2, 3, 4$$

Applying Clark transformation to Eq. (1) and the voltage function in $\alpha\beta 0$ coordinate system can be got:

$$u_{\alpha\beta 0} = R i_{\alpha\beta 0} + \frac{d\psi_{\alpha\beta 0}}{dt} \quad (3)$$

where:

$$\begin{aligned} u_{\alpha\beta 0} &= [u_{\alpha_1} \ u_{\beta_1} \ u_{0_1} \ u_{\alpha_2} \ u_{\beta_2} \ u_{0_2} \ u_{\alpha_3} \ u_{\beta_3} \ u_{0_3} \ u_{\alpha_4} \ u_{\beta_4} \ u_{0_4}]^T \\ i_{\alpha\beta 0} &= [i_{\alpha_1} \ i_{\beta_1} \ i_{0_1} \ i_{\alpha_2} \ i_{\beta_2} \ i_{0_2} \ i_{\alpha_3} \ i_{\beta_3} \ i_{0_3} \ i_{\alpha_4} \ i_{\beta_4} \ i_{0_4}]^T \\ \psi_{\alpha\beta 0} &= [\psi_{\alpha_1} \ \psi_{\beta_1} \ \psi_{0_1} \ \psi_{\alpha_2} \ \psi_{\beta_2} \ \psi_{0_2} \ \psi_{\alpha_3} \ \psi_{\beta_3} \ \psi_{0_3} \ \psi_{\alpha_4} \ \psi_{\beta_4} \ \psi_{0_4}]^T \\ \psi_{\alpha\beta 0} &= C_{\alpha\beta 0}^{abc} L_{abc} C_{abc}^{\alpha\beta 0} i_{\alpha\beta 0} + C_{\alpha\beta 0}^{abc} \psi_p \end{aligned}$$

When the four sets of three-phase winding are symmetric and their neutral points are not led out, the zero-sequence component can be neglected and the following can be got:

$$\psi_{\alpha\beta} = L_{\alpha\beta} i_{\alpha\beta} + \psi_{p\alpha\beta} \quad (4)$$

$$\psi_{\alpha\beta} = [\psi_{\alpha_1} \ \psi_{\beta_1} \ \psi_{\alpha_2} \ \psi_{\beta_2} \ \psi_{\alpha_3} \ \psi_{\beta_3} \ \psi_{\alpha_4} \ \psi_{\beta_4}]^T$$

where the structure of $L_{\alpha\beta}$ can be seen in Appendix A1.

3 Rotor Flux Observation Method Considering Phase-to-Phase Coupling

The principle of rotor flux observation method is to calculate the rotor position and speed through the relationship between stator voltage, stator winding current and air gap flux. Since the air-gap magnetic linkage $\psi_{\alpha\beta}$ contains rotor position information, the rotor position angle can be estimated by calculating the components of the magnetic linkage generated by the permanent magnet on the $\alpha\beta$ shafts [13, 14]:

$$\psi_{\alpha\beta} = \int (u_{\alpha\beta} - R_s i_{\alpha\beta}) dt \quad (5)$$

$$\psi_{p\alpha\beta} = \psi_{\alpha\beta} - L_{\alpha\beta} i_{\alpha\beta} \quad (6)$$

During the operation of multiphase motor, there are non-ideal factors such as the asymmetry of multiple sets of winding parameters. If the permanent magnet magnetic linkage $\psi_{p\alpha\beta}$ is calculated only by the single set of winding current and the lumped

inductance parameters, the calculated rotor position angle and rotor speed are easy to produce large errors, which will adversely affect the control performance.

Therefore, when calculating the rotor flux linkage, it is necessary to consider the coupling between each phase winding to improve the calculation accuracy of the rotor position. The calculations are as follows:

$$\cos \theta_{est} = (\psi_{\alpha_1} - L_{\alpha_1} i_{\alpha\beta}) / \psi_f \tag{7}$$

$$\sin \theta_{est} = (\psi_{\beta_1} - L_{\beta_1} i_{\alpha\beta}) / \psi_f \tag{8}$$

$$L_{\alpha_1} = [L_{\alpha_1\alpha_1} \ M_{\alpha_1\beta_1} \ M_{\alpha_1\alpha_2} \ M_{\alpha_1\beta_2} \ M_{\alpha_1\alpha_3} \ M_{\alpha_1\beta_3} \ M_{\alpha_1\alpha_4} \ M_{\alpha_1\beta_4}]$$

$$L_{\beta_1} = [M_{\beta_1\alpha_1} \ L_{\beta_1\beta_1} \ M_{\beta_1\alpha_2} \ M_{\beta_1\beta_2} \ M_{\beta_1\alpha_3} \ M_{\beta_1\beta_3} \ M_{\beta_1\alpha_4} \ M_{\beta_1\beta_4}]$$

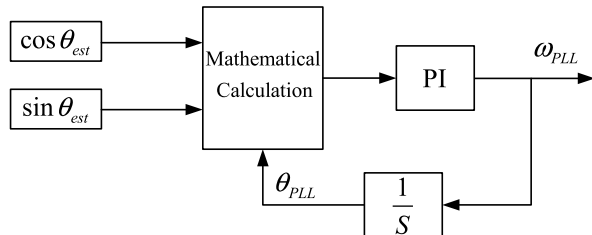
$$i_{\alpha\beta} = [i_{\alpha_1} \ i_{\beta_1} \ i_{\alpha_2} \ i_{\beta_2} \ i_{\alpha_3} \ i_{\beta_3} \ i_{\alpha_4} \ i_{\beta_4}]^T$$

4 Rotor Position and Speed Observation Based on PLL

If the arctangent function is directly used to calculate θ_{est} from Eq. (7) and Eq. (8), the calculation result is easily affected by torque ripple, so PLL is used to estimate the phase angle and speed [15–17].

The input of PLL is the difference between the rotor position angle θ_{est} estimated by position-sensorless control method and the rotor position angle θ_{PLL} estimated by PLL. PLL tracks the estimated rotor position angle θ_{est} at actual time, so when PLL is at steady state, θ_{est} approximately equals to θ_{PLL} [18], and $\theta_{est} - \theta_{PLL}$ approximately equals to $\sin(\theta_{est} - \theta_{PLL})$. The mathematical calculation part in Fig. 2 is: $\sin\theta_{est}\cos\theta_{PLL} - \cos\theta_{est}\sin\theta_{PLL}$.

Fig. 2 PLL calculation process



5 Simulation Verification

In this paper, a simulation model of a 240 kW twelve-phase semi-symmetrical winding PMSM is built in Matlab/Simulink to verify the control effect of the sensorless control method considering phase-to-phase coupling. The parameters of the motor are shown in Table 1. The inductance in $\alpha\beta$ coordinate system is calculated by finite element analysis and the results are shown in Table 2.

5.1 Simulation of Typical Load Conditions

In order to verify the accuracy of sensorless control method under load condition, the simulation is carried out under the condition that the motor speed is set at 160 r/min and 300 r/min. The load is water and the load torque at the corresponding speed is 146.6 Nm and 515.4 Nm respectively. When speed reaches 100 r/min, the control mode is switched from IF [19, 20] control to sensorless control and the simulation results at steady state are shown in Fig. 3 and Fig. 4.

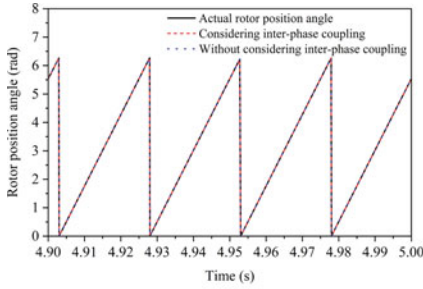
Table 1 Parameters of twelve-phase PMSM

Parameter	Value
Number of phase m	12
Number of pole pairs p_n	15
Rated speed (r/min)	300
Stator winding resistance r (Ω)	0.162
Permanent magnet flux ψ_f (Wb)	0.66325

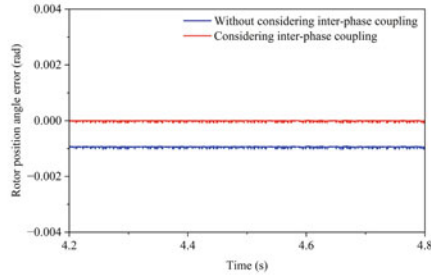
Table 2 Inductance parameters in $\alpha\beta$ coordinate system

Parameter	Value
$L_{\alpha 1\alpha 1}$	0.815
$M_{\alpha 1\alpha 2}$	0.468
$M_{\alpha 1\beta 2}$	-0.124
$M_{\alpha 1\alpha 3}$	0.607
$M_{\alpha 1\beta 3}$	-0.350
$M_{\alpha 1\alpha 4}$	0.342
$M_{\alpha 1\beta 4}$	-0.343

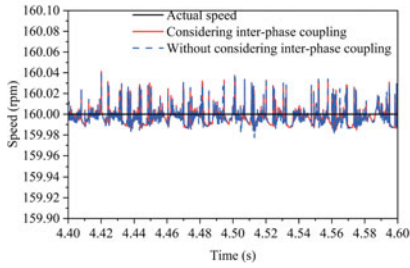
5.1.1 160 r/min Load Condition



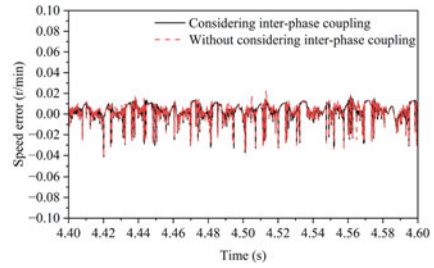
(a) Rotor position estimation.



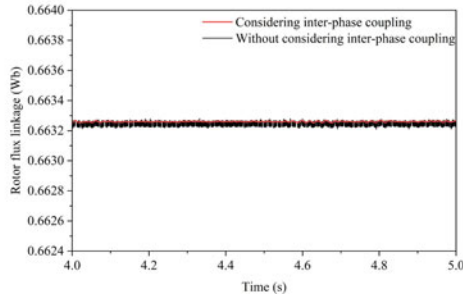
(b) Rotor position error.



(c) Speed estimation.



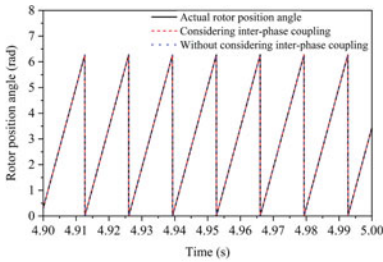
(d) Speed error.



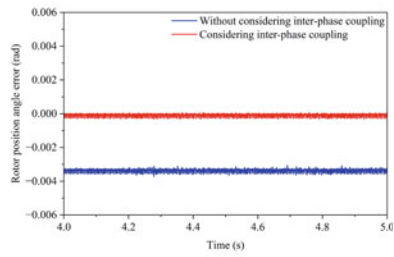
(e) Rotor flux linkage estimation result.

Fig. 3 Load simulation results at 160 r/min

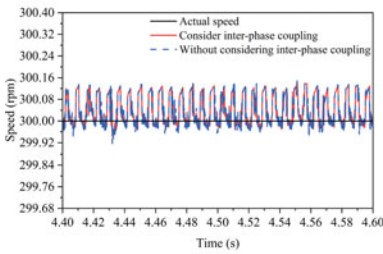
5.1.2 300 r/min Load Condition



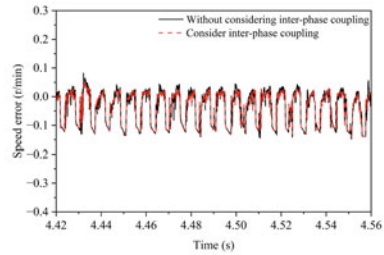
(a) Rotor position estimation.



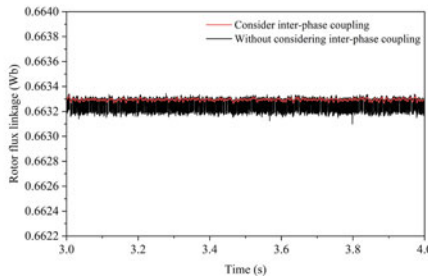
(b) Rotor position error.



(c) Speed estimation.



(d) Speed error.



(e) Rotor flux linkage estimation result.

Fig. 4 Load simulation results at 300 r/min

5.1.3 Asymmetry Working Condition at 160 r/min

Under this working condition, the first set of three-phase winding is normally powered, and the other three sets of winding are not powered, so as to simulate the extreme situation of multiple sets of winding asymmetry.

5.2 Comparative Analysis

From the simulation results, it can be seen that the designed sensorless control method can accurately track the rotor position, and the rotor position angle error is within 0.001 rad. And the motor speed can be accurately estimated by PLL, with the error within ± 0.15 r/min.

By comparing Fig. 3(b) and Fig. 4(b), it can be seen that the rotor position angle error calculated by the control method considering phase-to-phase coupling is smaller, which is 78% less than that calculated by the control method without considering phase-to-phase coupling. Comparing Fig. 3(e) and Fig. 4(e), it is found that the rotor flux fluctuation calculated by the positionless control method considering phase-to-phase coupling is smaller. Comparing the rotor position angle calculation error of the two control methods in Fig. 5, under the same load condition, the rotor position angle error of the control method proposed in this paper is reduced by about 100% compared with the position-sensorless control method without considering the phase coupling. It can be proved that the position-sensorless control method proposed in this paper has higher control accuracy than the position-sensorless control method commonly used in engineering under the influence of non-ideal factors of multiple sets of winding asymmetry. The simulation results above prove that the proposed position-sensorless control method has good control performance and calculation accuracy.

At present, the twelve-phase PMSM has been manufactured (Fig. 6), and relevant tests will be carried out to verify the performance of the proposed position-sensorless control method.

Fig. 5 Load simulation results at 160r/min when stator windings are asymmetrical

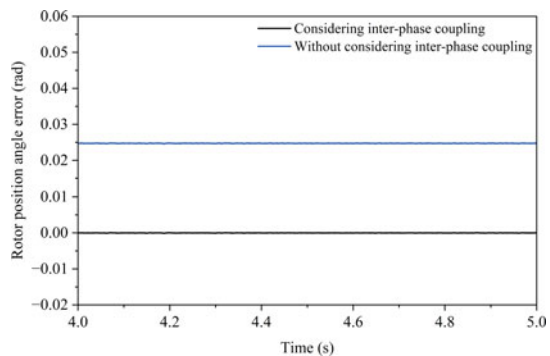


Fig. 6 Twelve-phase PMSM



6 Conclusion

In this paper, a position-sensorless control method of multi-phase PMSM considering phase-to-phase coupling is proposed. This method uses PLL and the characteristics of the motor, and considers the influence of the coupling between multi-phase currents on the control method. The simulation results show that the proposed method has higher accuracy and better control performance than the position-sensorless control method based on lumped parameters, and provides an optimized design scheme for rotor position estimation of multi-phase PMSM in shaftless propulsion system.

Acknowledgements This paper was partially funded by the National Natural Science Foundation of China under Grant 51807202 and Young Elite Scientists Sponsorship Program by CAST under Grant 18-JCJQ-QT-003.

Appendix

$$L_{\alpha\beta} = \begin{bmatrix} L_{\alpha_1\alpha_1} & M_{\alpha_1\beta_1} & M_{\alpha_1\alpha_2} & M_{\alpha_1\beta_2} & M_{\alpha_1\alpha_3} & M_{\alpha_1\beta_3} & M_{\alpha_1\alpha_4} & M_{\alpha_1\beta_4} \\ M_{\beta_1\alpha_1} & L_{\beta_1\beta_1} & M_{\beta_1\alpha_2} & M_{\beta_1\beta_2} & M_{\beta_1\alpha_3} & M_{\beta_1\beta_3} & M_{\beta_1\alpha_4} & M_{\beta_1\beta_4} \\ M_{\alpha_2\alpha_1} & M_{\alpha_2\beta_1} & L_{\alpha_2\alpha_2} & M_{\alpha_2\beta_2} & M_{\alpha_2\alpha_3} & M_{\alpha_2\beta_3} & M_{\alpha_2\alpha_4} & M_{\alpha_2\beta_4} \\ M_{\beta_2\alpha_1} & M_{\beta_2\beta_1} & M_{\beta_2\alpha_2} & L_{\beta_2\beta_2} & M_{\beta_2\alpha_3} & M_{\beta_2\beta_3} & M_{\beta_2\alpha_4} & M_{\beta_2\beta_4} \\ M_{\alpha_3\alpha_1} & M_{\alpha_3\beta_1} & M_{\alpha_3\alpha_2} & M_{\alpha_3\beta_2} & M_{\alpha_3\alpha_3} & M_{\alpha_3\beta_3} & M_{\alpha_3\alpha_4} & M_{\alpha_3\beta_4} \\ M_{\beta_3\alpha_1} & M_{\beta_3\beta_1} & M_{\beta_3\alpha_2} & M_{\beta_3\beta_2} & M_{\beta_3\alpha_3} & L_{\beta_3\beta_3} & M_{\beta_3\alpha_4} & M_{\beta_3\beta_4} \\ M_{\alpha_4\alpha_1} & M_{\alpha_4\beta_1} & M_{\alpha_4\alpha_2} & M_{\alpha_4\beta_2} & M_{\alpha_4\alpha_3} & M_{\alpha_4\beta_3} & L_{\alpha_4\alpha_4} & M_{\alpha_4\beta_4} \\ M_{\beta_4\alpha_1} & M_{\beta_4\beta_1} & M_{\beta_4\alpha_2} & M_{\beta_4\beta_2} & M_{\beta_4\alpha_3} & M_{\beta_4\beta_3} & M_{\beta_4\alpha_4} & L_{\beta_4\beta_4} \end{bmatrix} \quad (A1)$$

$$\begin{cases} L_{\alpha_i\alpha_i} = L_{\beta_j\beta_j} \\ M_{x_m x_{m+1}} = M_{y_n y_{n+1}}(x, y = \alpha, \beta)(m, n = 1, 2, 3)(i, j = 1, 2, 3, 4) \\ M_{\alpha_i\beta_j} = -M_{\beta_j\alpha_i}, M_{x_i x_j} = M_{x_j x_i} \end{cases}$$

References

1. Ma, W., Wang, D., Cheng, S., et al.: Common basic scientific problems and development of leading-edge technology of high-performance motor system. *Proc. CSEE* **36**(8), 2025–2035 (2016). (in Chinese)
2. Pillay, P., Krishnan, R.: Application characteristics of permanent magnet synchronous and brushless DC motor for servo drives. *IEEE Trans. Ind. Appl.* **27**(5), 986–996 (1991)
3. Wang, D., Ma, W., Guo, Y., et al.: Modelling of multiphase induction motor with non-sinusoidal supply. *Trans. China Electrotech. Soc.* **25**(2), 6–14 (2010). (in Chinese)
4. Ma, W.: Electromechanical power conversion technologies in vessel integrated power system. *J. Electr. Eng.* **10**(4), 3–10 (2015). (in Chinese)
5. Li, C.: *Adjusting Speed System of Synchronous Machine*, 2nd edn. China Science Publishing & Media Ltd., Beijing (2013). (in Chinese)
6. Liu, J., Xiao, F., Shen, Y., et al.: Position-sensorless control technology of permanent-magnet synchronous motor—a review. *Trans. China Electrotech. Soc.* **32**(16), 76–88 (2017). (in Chinese)
7. Zhou, S.: Rotor position estimation method for PMSM based on improved flux linkage observer. *Electric Drive* **50**(6), 15–21 (2020). (in Chinese)
8. Paul, P.A., John, F.W.: Review of position-sensorless operation of brushless permanent-magnet machines. *IEEE Trans. Industr. Electron.* **53**(2), 352–362 (2006)
9. Gu, S., He, F., Tan, G., et al.: A review of sensorless control technology of permanent magnet synchronous motor. *Trans. China Electrotech. Soc.* **24**(11), 14–20 (2009). (in Chinese)
10. Li, H., Wang, P.: Sensorless control of surface mounted permanent magnet synchronous motor drive system. *Trans. China Electrotech. Soc.* **31**(S1), 85–91 (2016). (in Chinese)
11. Xu, W., Jiang, Y., Mu, C., Blaabjerg, F.: Improved nonlinear flux observer-based second-order SOIFO for PMSM sensorless control. *IEEE Trans. Power Electron.* **34**(1), 565–579 (2019)
12. Yang, J., Yang, G., Li, T.: Modeling and vector control for dual three-phase PMSM. *Electric Mach. Control* **14**(6), 1–7 (2010). (in Chinese)
13. Shen, J.X., Zhu, Z.Q., Howe, D.: Improved speed estimation in sensorless PM brushless AC drives. *IEEE Trans. Ind. Appl.* **38**(4), 1072–1080 (2002)
14. Gao, R., Husain, I., Su, J., Yang, G.: An improved rotor flux estimation strategy for position-sensorless control of surface-mount permanent magnet synchronous motor. In: 40th Annual Conference of the IEEE Industrial Electronics Society, Dallas, TX, pp. 404–409. IEEE (2014)
15. Mai, Z., Liu, J., Xiao, F., et al.: Permanent magnet synchronous motor sensorless control based on PLL. *Power Electron.* **51**(7), 97–99 (2017). (in Chinese)
16. Wang, G., Li, Z., Zhan, H., et al.: Phase-locked-loop rotor position observer for IPMSM considering inverter nonlinearity. *Trans. China Electrotech. Soc.* **29**(3), 172–178 (2014). (in Chinese)
17. Wei, H., Wei, H., Zhang, Y., et al.: New rotor position estimation strategy for permanent magnet synchronous motor based on rotor flux model. *Trans. China Electrotech. Soc.* **33**(13), 2963–2971 (2018). (in Chinese)
18. Tao, X., Li, Y., Sun, M., et al.: A novel single-phase locked loop algorithm based on synchronous reference frame. *Trans. China Electrotech. Soc.* **27**(6), 147–152 (2012). (in Chinese)
19. Liu, J., Xiao, F., Mai, Z., et al.: Position-sensorless startup strategy for permanent magnet synchronous motor based on double DQ space. *Trans. China Electrotech. Soc.* **33**(12), 2676–2684 (2018). (in Chinese)
20. Wang, M., Yang, J., Zhang, X., et al.: An I/F control method with closed-loop regulation of current vector for surface permanent magnet synchronous motor drives. *Proc. CSEE* **35**(10), 2513–2521 (2015). (in Chinese)

Analysis of Electromagnetic Loops Opening Scheme Based on Penalty Variable Weight Optimal Comprehensive Evaluation Model



Yan Yang, Wantong Cai, Shixian Zou, Bo Peng, and Wei Xu

Abstract The electromagnetic loop is a transitional network frame for the transmission network to develop to a higher voltage level. The power grid should gradually untie the electromagnetic loop to achieve layered and partitioned operation. Based on the idea of variable weight, this paper proposes a punitive variable weight algorithm, which not only considers the role of weights, but also considers the role of index values. The weight of indicators changes with the changes of index values. It is possible to “punish” the situation that an index value of the power grid is too low after the loop is opened (closed) to avoid the situation that a certain index value of the power grid is too low, but the comprehensive evaluation result is higher, and its physical background is more in line with the actual power system. The electromagnetic loop de-looping scheme determined by this model can comprehensively consider the evaluation function of each index, determine a comprehensive index, and evaluate the advantages and disadvantages of the electromagnetic ring network de-looping scheme through this index. The simulation results of the Shaanxi power grid de-looping scheme prove the effectiveness and superiority of the penalty variable weight algorithm.

Keywords Punitive variable weight · Electromagnetic loops · Loop opening · Optimal comprehensive evaluation · Multi-objective decision

Y. Yang · B. Peng · W. Xu

Grid Planning & Research Center, Guangdong Power Grid Corporation, CSG, Guangzhou, China

W. Cai (✉)

Electric Power Research Institute, CSG, Guangzhou, China

e-mail: caiw2@csg.cn

S. Zou

Electric Power Institute, South China University of Technology, Guangzhou, China

© Beijing Paiké Culture Commu. Co., Ltd. 2023

X. Dong et al. (eds.), *The proceedings of the 10th Frontier Academic Forum of Electrical Engineering (FAFEE2022)*, Lecture Notes in Electrical Engineering 1054, https://doi.org/10.1007/978-981-99-3408-9_41

1 Introduction

High and low voltage electromagnetic loops is a transitional network structure in the development process of power grid. This operation mode generally has problems such as large short-circuit current, complex power flow distribution and safety protection devices, and difficulty in dispatching operation and management. The "Guidelines for Safety and Stability of Electric Power Systems" clearly requires that with the gradual improvement of the grid structure, the power grid should gradually untie the electromagnetic loops to achieve layered and partitioned operation.

In order to disconnect the electromagnetic loops reasonably, it is necessary to calculate the power flow, stability, short-circuit current, network loss and other aspects, and then make a decision after synthesizing the advantages and disadvantages. At present, the main indicators for selecting de-loop points and evaluating the pros and cons of de-loop schemes at home and abroad include power flow, short-circuit capacity, N-1 index, and transient stability. Reference [1] considers short-circuit capacity index, power flow index and transient stability index; Reference [2] considers N-1 index and transient stability index; Reference [3] considers power flow, N-1 index and transient stability index; Reference [4] mainly considers the power flow on the power tie line.

Although the above indicators can comprehensively evaluate the advantages and disadvantages of the electromagnetic ring network, the evaluation indicators may contradict each other. How to comprehensively consider the evaluation function of each index, determine a comprehensive index, and use this index to evaluate the advantages and disadvantages of the electromagnetic loops opening scheme is an urgent problem to be solved. At present, there are two main methods: AHP and Principal Component Analysis [5]. Analytic hierarchy process (AHP) decomposes a complex factor into several different simple factors, and quantitatively considers the dominating relationship between them, and finally forms a multi-level structure. However, the expert scoring link of the AHP is restricted by the level and knowledge of the experts themselves. Even the same expert may have different scoring results at different periods, so it is highly contingent and subjective. The principal component analysis method is based on the mathematical algorithm of dimensionality reduction, which converts seemingly unrelated multiple indicators into a few indicators (principal components). The weight of the comprehensive factors is not artificially determined, and is relatively objective and reasonable. However, the calculation process of the principal component analysis method is cumbersome, and the original more indexes are replaced by less indexes, so there are problems of information distortion and imperfect indexes.

In the field of mathematics and finance, the above problem of obtaining comprehensive indicators is also called "multi-objective decision-making" problem [6]. For the above problems, each evaluation index can be quantified according to a certain method, and the weight of each index can be obtained, and then the total evaluation value can be obtained by weighted synthesis according to a certain synthesis model. However, once the weight of each indicator is determined, no matter how

each indicator changes, the weight will not change, that is, the weight will not change accordingly with each indicator. In response to the above problems, Professor Wang Peizhuang first proposed the idea of changing power [7]. On the basis of systematically studying the theory of factor space, Professor Li Hongxing gave a comprehensive model of variable weights [8–10].

Inheriting the idea of variable weights, this paper first proposes an optimal comprehensive evaluation model with constant weights. This model combines the idea of principal component analysis and multi-objective decision-making to obtain the weights of the running indicators of the loops opening scheme completely and objectively, avoiding subjectivity and chance. On this basis, combined with the variable weight theory of the factor space, the optimal comprehensive evaluation model of punitive variable weight is proposed, which considers both the role of the weight and the role of the index value. It is achieved by making the weight of the indicator change as the indicator value changes. The grid opening scheme determined by this model can “penalize” the situation that a certain index value is too low after the grid opening (closing), so as to avoid a grid index value that is too low, but the comprehensive evaluation result is higher. Its physical background is more in line with the actual power system.

2 Operation Index of Opening Scheme

The principles of the operation of electromagnetic loops disengagement and closing include power grid security, power supply reliability, short-circuit current size, and economy. Therefore, this paper proposes six indicators of power flow distribution (including weighted power flow entropy and network loss), power grid safety, short-circuit current, section transmission power limit, and power balance at the transmission and receiving end, as operational indicators for quantitative analysis of the merits of the electromagnetic loops opening scheme [11–14].

2.1 Subsection Sample Flow Distribution Index

The electromagnetic loops is easy to generate circulating power in the closed loop operation mode, which affects the economy of the power grid operation; after the electromagnetic loop is de-looped, the circulating current can be eliminated and the loss can be reduced, but at the same time, it will also have a great impact on the load rate of the line.

Compared with the average load rate, the weighted power flow entropy proposed in reference [15] can describe the unbalance of line power flow distribution. In this paper, the weighted power flow entropy is used to quantitatively characterize the rationality of the power flow distribution before and after the power grid disintegration. For the specific algorithm, please refer to reference [15]. At the same time, the total

network loss value of the whole network is proposed to quantitatively characterize the network loss before and after the disengagement of the power grid.

Assuming that the maximum active power transmission capacity of line i is F_i^{\max} , and the actual power flow of line i during system operation is F_i^0 , the load rate w_i of line i is

$$w_i = |F_i^0 / F_i^{\max}|, i = 1, 2, \dots, N_l \tag{1}$$

In the formula, N_l is the total number of lines.

Given a constant sequence $U = [U_1, U_2, \dots, U_n]$, use l_k to represent the number of lines with the load rate $w_i \in (U_k, U_{k+1}]$, then the probability $P(k)$ that the line load rate is in the $(U_k, U_{k+1}]$ interval for

$$P(k) = l_k / \sum_{k=1}^{n-1} l_k \tag{2}$$

Then the calculation formula of the line weighted power flow entropy H_l is:

$$H_l = - \sum_{i=1}^{n-1} W(k) P(k) \ln P(k) \tag{3}$$

In the formula, $W(k)$ represents the average load rate of all lines of the load rate $w_i \in (U_k, U_{k+1}]$. If there are t lines in interval $(U_k, U_{k+1}]$, then

$$W(k) = \frac{1}{t} \sum_{i=1}^t w_{ki} \tag{4}$$

The calculation formula of the total network loss value ΔP of the whole network is:

$$\Delta P = \sum_{i=1}^N \Delta P_i \tag{5}$$

2.2 Grid Security Indicators

The grid security index is defined as τ_{ji} : when a certain line i flows through a unit current and is disconnected, the ratio of the power flow transfer amount to the transmission capacity of this line j . Its calculation formula is

$$\tau_{ji} = \frac{P_j^1 - P_j^0}{P_j^n P_i^0} \tag{6}$$

In the formula: P_j^1 is the active power flow flowing through line j after line i is disconnected; P_j^0 is the active power flow before disconnection; P_j^n is the rated transmission capacity of line j ; P_i^0 is the active power flow through line i before line i is disconnected.

2.3 Short Circuit Current Index

Let the average out-of-limit short-circuit current level indicator \overline{I}_{sc} be

$$\overline{I}_{sc} = \frac{1}{N_{sc}} \sum_{i=1}^{N_{sc}} \frac{I_{sc,i}}{I_{sc,N}} \tag{7}$$

In the formula: N_{sc} represents the number of busbars whose short-circuit current exceeds the limit before unlooping; $I_{sc,i}$ represents the short-circuit current of busbar i ; $I_{scN,i}$ represents the short-circuit current interrupting capacity corresponding to busbar i . The after de-looping still selects these buses whose short-circuit current exceeds the limit before de-looping to calculate the average short-circuit current. If $N_{sc} = 0$ before and after the loop is disengaged, it means that there is no busbar whose short-circuit current exceeds the limit before and after the disengagement of the power grid. Then, let N_{sc} be the number of all busbars in the power grid, and calculate the average short-circuit current level of all the busbars in the whole network.

2.4 Section Transmission Power Limit Index

Set the ratio \overline{K} of the section limit of the whole network after the loop is closed to the section limit of the initial operation mode

$$\overline{K} = \frac{1}{N_{sec}} \sum_{i=1}^{N_{sec}} \frac{P_{secmax,i}^1}{P_{secmax,i}^0} \tag{8}$$

In the formula: N_{sec} is the number of sections; $P_{secmax,i}^1$ is the section limit of section i after the loop is disengaged; $P_{secmax,i}^0$ is the section limit of section i in the initial operation mode.

2.5 Sending and Receiving End Power and Power Balance Indicators

Set the power balance margin P_{margin} in the power supply area

$$P_{margin} = P_{in,max} + P_{G,sum} - P_{L,sum} - P_{out,max} \tag{9}$$

In the formula: $P_{in,max}$ represents the power limit of the incoming section in the power supply area; $P_{out,max}$ represents the outgoing section; $P_{G,sum}$ represents the maximum power generation capacity in the power supply area; $P_{L,sum}$ represents the maximum active load in the power supply area. There are many partition methods for power supply partition, this paper refers to reference [16].

With the above six evaluation indicators, a comprehensive evaluation model can be established, and the rationality of the electromagnetic loops opening scheme can be quantitatively analyzed.

3 Optimal Comprehensive Evaluation Model of Penalty Variable Weight

3.1 Inverse Quotient Transform and De-dimensioning

Assuming that a power grid has $n/2$ loop decoupling schemes, and each scheme has 2 evaluation targets (loop decoupling and loop closure), the total evaluation target is n . For any target, there are 6 evaluation indicators, namely network loss, weighted power flow entropy, static safety, short-circuit current, section limit and power capacity margin. Let the value of the evaluation index corresponding to each evaluation target be $X_{ij}(i = 1, 2, \dots, n; j = 1, 2, \dots, 6)$, as shown in Table 1.

Suppose the weight coefficient of the evaluation index is $W_j(j = 1, 2, \dots, 6)$, then the comprehensive evaluation result of each evaluation target is.

Table 1. Evaluation index of each target

Target	Network loss	Weighted power flow entropy	Static security	Short circuit current	Section limit	Power margin
Target 1	X_{11}	X_{12}	X_{13}	X_{14}	X_{15}	X_{16}
Target 2	X_{21}	X_{22}	X_{23}	X_{24}	X_{25}	X_{26}
...
Target n	X_{n1}	X_{n2}	X_{n3}	X_{n4}	X_{n5}	X_{n6}

$$Y_i = \sum_{j=1}^6 W_j X_{ij} \tag{10}$$

In the formula: i is the serial number of the evaluation target; Y_i is the comprehensive evaluation index; X_{ij} is the value of each evaluation index. In descending order of the comprehensive evaluation index Y_i , the larger the index value is, the better the loop decoupling scheme corresponding to the index is.

From the definitions of Eqs. (1)–(10), it can be seen that the larger the section limit and the power and electricity margin, the higher the security of the power grid, and these indicators are called positive indicators; static security, network loss, weighted power flow entropy, short-circuit current. The larger the value of these four indicators of current is, the more unfavorable it is to the safety or economy of the power grid. Such indicators are called negative indicators. In order to make the comprehensive evaluation index Y_i and each index value X_{ij} always positively correlated, the negative index is firstly subjected to “steering inverse transformation”. The most direct transformation is to take the reciprocal of the negative index, that is, the inverse quotient transformation, which can be written as the formula

$$X_{ij\text{new}} = \begin{cases} \frac{1}{X_{ij\text{old}}}, & X_{ij\text{old}} \text{ is positive} \\ X_{ij\text{old}}, & X_{ij\text{old}} \text{ is negative} \end{cases} \tag{11}$$

In the formula: $X_{ij\text{old}}$ is the original index; $X_{ij\text{new}}$ is the new index obtained by inverse quotient transformation. When all indicators are processed by formula (11), Y_i and all indicators are positively correlated. For the convenience of description, the X_{ij} mentioned later are all new indexes obtained after inverse quotient transformation.

The new index obtained after the inverse quotient transformation has a positive correlation with Y_i , but due to the six indexes of network loss, weighted power flow entropy, static safety, short-circuit current, section limit and power margin. Therefore, by directly comparing each other and calculating the weight of each index, the results obtained may not truly reflect the relationship between each index. Therefore, each indicator needs to be de-dimensionalized, or standardized. Its formula is

$$X_{ij}^s = \frac{X_{ij}}{\sum_{i=1}^n X_{ij}} \tag{12}$$

In the formula, X_{ij}^s is the new index obtained after de-dimensioning. For the convenience of description, the X_{ij} mentioned in the following are all new indicators obtained after de-dimensioning.

3.2 Constant Weight Optimal Comprehensive Evaluation

It can be seen from formula (10) that to obtain the comprehensive index size of each evaluation target, it is also necessary to determine the weight W_j of each evaluation index. The principle of determining the weight coefficient is: try to distinguish each evaluation object as much as possible. If a certain evaluation index has a high degree of discrimination, it has a greater impact on the comprehensive evaluation ranking, that is, the higher the weight of this evaluation index. The degree of discrimination of the evaluation index can be measured by the amount of variance information. Therefore, according to the above-mentioned principles and known conditions for calculating the weight coefficient, the weight coefficient W_j should meet two conditions: 1) Y_i is as dispersed as possible (maximum mean square error); 2) The sum of W_j is 1.

The mathematical model for weight calculation is

$$\left\{ \begin{array}{l} \max D^2 = \frac{1}{n} \sum_{i=1}^n (Y_i - Y)^2 \\ Y_i = \sum_{j=1}^6 W_j X_{ij} \\ Y = \frac{1}{n} \sum_{i=1}^n Y_i \\ \sum_{j=1}^6 W_j = 1 \end{array} \right. \quad (13)$$

In the formula: D is the mean square error; Y is the average value of each column of indicators.

Let $(\mathbf{X}_1, \mathbf{X}_2, \mathbf{X}_3, \mathbf{X}_4, \mathbf{X}_5, \mathbf{X}_6)$ be a column vector with X_{ij} as an element, and the covariance of any \mathbf{X}_i and \mathbf{X}_j is R_{jk} , then the $n \times 6$ matrix with R_{jk} as an element is called the covariance matrix of the random vector, denoted as \mathbf{R} , the expression is

$$\mathbf{R} = \begin{bmatrix} R_{11} & R_{12} & R_{13} & R_{14} & R_{15} & R_{16} \\ \cdot & \cdot & \cdot & \cdot & \cdot & \cdot \\ R_{i1} & R_{i2} & R_{i3} & R_{i4} & R_{i5} & R_{i6} \\ \cdot & \cdot & \cdot & \cdot & \cdot & \cdot \\ R_{n1} & R_{n2} & R_{n3} & R_{n4} & R_{n5} & R_{n6} \end{bmatrix}_{n \times 6} \quad (14)$$

The formula for calculating the covariance R_{jk} is

$$R_{jk} = \text{cov}(\mathbf{X}_i, \mathbf{X}_j) = E(\mathbf{X}_i - E(\mathbf{X}_i))(\mathbf{X}_j - E(\mathbf{X}_j)) \quad (15)$$

In the formula $\text{cov}(\mathbf{X}_i, \mathbf{X}_j)$, is the mathematical expression of the covariance of the column vectors \mathbf{X}_i and \mathbf{X}_j .

Therefore, Eq. (13) can be converted into matrix form

$$\begin{cases} \max D^2 = \frac{1}{n} \mathbf{WRW}^T \\ \mathbf{W} = (W_1, W_2, \dots, W_6) \\ \mathbf{R} = \{R_{jk}\}_{n \times 6} \\ R_{jk} = \sum_{i=1}^6 (X_{ij} - X_j)(X_{ik} - X_k) \\ X_j = \frac{1}{n} \sum_{i=1}^n X_{ij} \end{cases} \quad (16)$$

However, the weight coefficient matrix $\mathbf{W} = (W_1, W_2, \dots, W_6)$ obtained according to the above method is a constant matrix, that is to say, when \mathbf{W} is determined, the weight of each indicator is determined, and the specific size of each indicator will no longer affect \mathbf{W} . At this time, the weight W_j is called constant power. This approach of "remaining unchanged" (constant weight) in response to change (indicator value) is somewhat one-sided. Therefore, it can be considered to process the constant weight coefficients.

3.3 Optimal Comprehensive Evaluation Model of Penalty Variable Weight

Combining factor space theory and variable weight theory of principal component analysis [6–10], this paper proposes an optimal comprehensive evaluation model based on penalty variable weight. Redefine formula (10) as

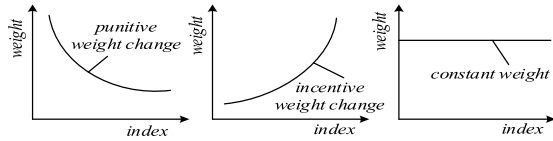
$$Y_i = \sum_{j=1}^6 W_j(\mathbf{X}_1, \mathbf{X}_2, \mathbf{X}_3, \mathbf{X}_4, \mathbf{X}_5, \mathbf{X}_6) X_{ij} \quad (17)$$

In the formula: the matrix $\mathbf{X}_1, \mathbf{X}_2, \mathbf{X}_3, \mathbf{X}_4, \mathbf{X}_5, \mathbf{X}_6$ is the column vector corresponding to the element X_{ij} ; $W_j(\mathbf{X}_1, \mathbf{X}_2, \mathbf{X}_3, \mathbf{X}_4, \mathbf{X}_5, \mathbf{X}_6)$ is the variable weight related to the six state quantities of $\mathbf{X}_1, \mathbf{X}_2, \mathbf{X}_3, \mathbf{X}_4, \mathbf{X}_5, \mathbf{X}_6$, which is different from the aforementioned "constant weight", which is called "variable weight" here.

The most commonly used weight change methods are punitive weight change and incentive weight change. Figure 1 can visualize the above weights.

The definition of penalty variable weight refers to the following 6 mappings $W_j: [0, 1]^m \rightarrow [0, 1] (m = 1, 2, 3, 4, 5, 6), (\mathbf{X}_1, \mathbf{X}_2, \mathbf{X}_3, \mathbf{X}_4, \mathbf{X}_5, \mathbf{X}_6) \mapsto$

Fig. 1 Common variable weights



$W_j(\mathbf{X}_1, \mathbf{X}_2, \mathbf{X}_3, \mathbf{X}_4, \mathbf{X}_5, \mathbf{X}_6)$ ($j = 1, 2, 3, 4, 5, 6$), This map satisfies the following 2 conditions:

- 1) Normalization $\sum_{j=1}^6 W_j(\mathbf{X}_1, \mathbf{X}_2, \mathbf{X}_3, \mathbf{X}_4, \mathbf{X}_5, \mathbf{X}_6) = 1$
- 2) Punishment $W_j(\mathbf{X}_1, \mathbf{X}_2, \mathbf{X}_3, \mathbf{X}_4, \mathbf{X}_5, \mathbf{X}_6)$ monotonically decreases with respect to the varying element \mathbf{X}_j ($j = 1, 2, 3, 4, 5, 6$)

Then $W_j(\mathbf{X}_1, \mathbf{X}_2, \mathbf{X}_3, \mathbf{X}_4, \mathbf{X}_5, \mathbf{X}_6)$ ($j = 1, 2, 3, 4, 5, 6$) is called a penalty variable weight vector.

In short, the penalized variable weight comprehensive evaluation is a kind of evaluation method to punish shortcomings. In order to obtain a better comprehensive evaluation value, each single factor state (evaluation value) must not be too low, which is consistent with the requirements of the power grid for each index. Compared with the constant weight, the penalized variable weight can make a punitive comprehensive evaluation on the case that a certain index value is too low after the solution (combined) loop of the power grid, which can more reasonably reflect the actual situation of the power grid.

Define the variable weight ratio $\eta_{i,j}(\mathbf{X}_i, \mathbf{X}_j)$ ($i, j = 1, \dots, m$) of each pair of indicators, let $\{\mathbf{W}_j\}(1 \leq j \leq m)$ be a set of constant weights, and define the calculation of the penalty variable weight vector of network loss, weighted power flow entropy, static safety, short-circuit current, section limit and power allowance. The formula is

$$W_j(\mathbf{X}_1, \mathbf{X}_2, \mathbf{X}_3, \mathbf{X}_4, \mathbf{X}_5, \mathbf{X}_6) = (W_{1j}, W_{2j}, W_{3j}, W_{4j}, W_{5j}, W_{6j})^T \tag{18}$$

$$W_{ij} = \frac{\frac{w_j^{(0)}}{X_{ij}}}{\sum_{j=0}^6 \frac{w_j^{(0)}}{X_{ij}}} \tag{19}$$

It can be verified that the variable weight vector defined according to Eq. (19) satisfies normalization and punishment. For the specific proof, please refer to [10], which will not be repeated here. If written in matrix form, the penalty variable weight matrix is

$$\mathbf{W}_{n \times 6} = \begin{bmatrix} \frac{w_1^{(0)}}{X_{11}} & \dots & \frac{w_6^{(0)}}{X_{16}} \\ \sum_{j=1}^6 \frac{w_j^{(0)}}{X_{1j}} & & \sum_{j=1}^6 \frac{w_j^{(0)}}{X_{1j}} \\ \vdots & \ddots & \vdots \\ \frac{w_1^{(0)}}{X_{n6}} & \dots & \frac{w_6^{(0)}}{X_{n6}} \\ \sum_{j=1}^6 \frac{w_j^{(0)}}{X_{nj}} & & \sum_{j=1}^6 \frac{w_j^{(0)}}{X_{nj}} \end{bmatrix} \tag{20}$$

In the formula: $\mathbf{W}_{n \times 6}$ is the penalty variable weight matrix; $w_j^{(0)}$ ($j = 1, 2, 3, 4, 5, 6$) is the constant weight obtained according to formula (16).

It can be seen from Eq. (20) that the penalized variable weight matrix is an $n \times 6$ matrix, that is to say, the weight coefficients are in one-to-one correspondence with the indicators in Table 1, and each indicator has a unique weight. Compared with the constant weight matrix $\mathbf{W} = (W_1, W_2, \dots, W_6)$, the penalized variable weight can “penalize” the situation that the value of a certain index is too low after the power grid is opened (closed) loop, that is, increase the weight of the low index. In this way, the situation where a certain index value of the power grid is too low, but the comprehensive evaluation result is high can be avoided.

To sum up, the calculation method of the weight coefficient is as follows: 1) Perform inverse quotient transformation on the original evaluation index value. 2) De-dimensionalize the new index obtained after the inverse quotient transformation. 3) Find the covariance matrix. 4) Obtain the unitized eigenvector corresponding to the largest eigenvalue of the covariance matrix, that is, the constant weight coefficient. 5) Use formula (20) to penalize the constant weight coefficient to obtain the final weight coefficient.

After obtaining the weight result of punitive variable weight according to Eq. (20), substitute it into Eq. (10) to calculate the final comprehensive evaluation index value of punitive variable weight for each electromagnetic loop in the operation mode of loop disengagement and loop closure. If the index under the closed loop operation mode is greater than the index under the open loop operation mode, it is considered that the power grid should operate under the closed loop; otherwise, if the index under the closed loop operation mode is smaller than the index under the open loop operation mode, it is considered that the power grid should operate under the open loop; if the difference in size is less than 1%, it is considered that both modes of operation are acceptable.

4 Case Analysis

4.1 Introduction to Shaanxi Power Grid

By the planning level year of 2017, the 750 kV backbone grid of the power grid in the region will be formed, and it will be ready to untie the 750/330 kV electromagnetic loops. However, new problems such as the power balance of each 750 kV substation as the power supply partition, the operation mode of disengagement and closure between different power supply partitions, the determination of new transmission sections and the formulation of operation control schemes have followed. Therefore, it is necessary to propose a comprehensive evaluation method, which comprehensively considers the influence degree of these operation indicators, and determines the operation scheme of decoupling.

4.2 Simulation Analysis of Power Grid Decoupling Scheme

According to the formulas (1)–(9), the six indexes of the seven electromagnetic loops in Shaanxi under the condition of loop disengagement and loop closure are calculated. Inverse quotient transformation and de-dimensioning are performed on the indicators, and the results are shown in Table 2.

Substitute the data in Table 2 into Eq. (16) to obtain a constant weight vector $W_{\text{常}} = (0.080, 0.005, 0.109, 0.177, 0.168, 0.460)$. Substitute the data in Table 2 and the calculation result of the constant weight vector into Eq. (20), the penal variable weight matrix is obtained as

$$W_{\text{变}} = \begin{bmatrix} 0.083 & 0.005 & 0.110 & 0.175 & 0.165 & 0.461 \\ 0.079 & 0.005 & 0.112 & 0.182 & 0.171 & 0.450 \\ 0.097 & 0.005 & 0.107 & 0.173 & 0.170 & 0.448 \\ 0.078 & 0.005 & 0.110 & 0.182 & 0.179 & 0.446 \\ 0.076 & 0.004 & 0.107 & 0.175 & 0.168 & 0.468 \\ 0.078 & 0.005 & 0.114 & 0.189 & 0.169 & 0.446 \\ 0.075 & 0.004 & 0.101 & 0.171 & 0.166 & 0.483 \\ 0.081 & 0.005 & 0.111 & 0.184 & 0.171 & 0.449 \\ 0.072 & 0.004 & 0.097 & 0.150 & 0.142 & 0.534 \\ 0.082 & 0.005 & 0.111 & 0.183 & 0.170 & 0.449 \\ 0.089 & 0.005 & 0.108 & 0.175 & 0.171 & 0.452 \\ 0.078 & 0.005 & 0.110 & 0.179 & 0.165 & 0.464 \\ 0.079 & 0.005 & 0.114 & 0.181 & 0.171 & 0.450 \\ 0.077 & 0.005 & 0.117 & 0.183 & 0.170 & 0.446 \end{bmatrix} \quad (9)$$

In order to prove the validity and superiority of the optimal comprehensive evaluation model of penalized variable weights, this paper uses the principal component analysis method and the analytic hierarchy process used in the literature [5] to calculate the comprehensive evaluation index value. Among them, the AHP method needs to construct a relative importance matrix. After a pairwise comparison, the relative importance matrix constructed in this paper is:

Table 2 Processed indexes of seven electromagnetic loops of Shaanxi grid

Loop name	Close/ Open	Power flow entropy	Network loss	Safety	Short circuit current	Power limit	Power margin
Baoji - Qian County	Open	1.000	1.018	1.027	1.052	1.054	1.035
	Close	1.027	0.960	0.990	0.990	1.001	1.040
Qian County - South Xi'an	Open	0.833	1.003	1.027	1.036	0.994	1.035
	Close	1.027	1.000	0.990	0.972	0.935	1.029
Qian County - North One of Xi'an	Open	1.027	1.000	1.000	0.990	0.978	0.962
	Close	1.036	1.003	0.966	0.942	0.994	1.035
Qian County - Xi'an North Second	Open	1.027	1.000	1.040	0.990	0.968	0.913
	Close	1.004	1.006	0.998	0.974	0.994	1.035
Xi'an North - Luochuan	Open	1.027	1.000	1.036	1.089	1.093	0.796
	Close	0.982	1.003	0.998	0.981	0.994	1.035
Xi'an North - Xinyi	Open	0.911	1.010	1.027	1.030	0.994	1.035
	Close	1.027	1.000	0.990	0.986	1.011	0.985
Xinyi - South Xi'an South	Open	1.027	1.000	0.968	0.990	0.994	1.035
	Close	1.045	0.999	0.942	0.977	0.994	1.035

$$A = \begin{bmatrix} 1.00 & 1.00 & 0.33 & 0.23 & 0.33 & 1.00 \\ 1.00 & 1.00 & 0.33 & 0.23 & 0.33 & 1.00 \\ 3.00 & 3.00 & 1.00 & 0.70 & 1.00 & 3.00 \\ 4.35 & 4.35 & 1.43 & 1.00 & 1.43 & 4.35 \\ 3.00 & 3.00 & 1.00 & 0.70 & 1.00 & 3.00 \\ 1.00 & 1.00 & 0.33 & 0.23 & 0.33 & 1.00 \end{bmatrix}$$

Its maximum eigenvalue $\lambda_{max} = 6.687$, and the average consistency ratio index $CR = 0.068 < 0.1$, which meets the requirements of the consistency ratio index. Therefore, the weight $W_{Floor} = (0.257, 0.257, 0.085, 0.060, 0.085, 0.257)$ is obtained by the AHP. In actual operation, a judgment matrix can be constructed by combining expert experience and focus to change the relative importance of each element.

Therefore, according to the weight calculation results W_{Floor} , W_{normal} , $W_{penalty}$ of the three evaluation methods of AHP, PCA, and penal variable weight method, the comprehensive evaluation index values in the case of ring disassembly and ring closure are finally obtained as shown in Table 3.

In order to verify the rationality of the above evaluation results, this paper compares the loop decoupling scheme obtained by the three evaluation methods with the preliminary operation scheme. The preliminary operation plan is a decoupling plan determined by Shaanxi dispatching on the basis of the operation principle

Table 3. Comprehensive evaluating indexes of each method

Loop name	Close/ Open	Weighted power flow entropy	Principal Component Analysis Index	Penalty weighted optimal composite value
Baoji - Qian County	Open	1.024	1.037	1.037
	Close	1.005	1.017	1.017
Qian County - South Xi'an	Open	0.971	1.011	1.007
	Close	1.006	0.999	0.997
Qian County - North One of Xi'an	Open	0.995	0.979	0.979
	Close	1.012	1.004	1.002
Qian County - Xi'an North Second	Open	0.985	0.959	0.957
	Close	1.009	1.010	1.010
Xi'an North - Luochuan	Open	0.971	1.021	0.923
	Close	1.003	1.010	1.009
Xi'an North - Xinyi	Open	0.992	1.016	1.015
	Close	1.002	0.993	0.993
Xinyi - South Xi'an	Open	1.012	1.008	1.005
	Close	1.013	1.012	1.011

of decoupling described in Sect. 1 in combination with the actual situation and operation experience of the power grid, so it is more authoritative. If the index under the closed loop operation mode is greater than the index under the open loop operation mode, it is considered that the power grid should operate under the closed loop, and vice versa; if the difference between the index sizes is less than 1%, the two operation modes are considered acceptable. Table 4 shows the comparison results of the final decoupling scheme of Shaanxi power grid.

From the results in Table 4, it can be seen that in the results obtained by the AHP, the results of the combined ring of Qianxian-Xi'an South and Xi'an North-Xinyi are different from the initial operation plan; The results of the combined loop of the network are different from the preliminary operation scheme; while the results of the penalty weighted optimal comprehensive evaluation scheme are basically consistent with the preliminary operation scheme.

Therefore, there is a big gap between the results obtained by the AHP and the actual power grid, because the relative importance matrix of the AHP is determined by expert experience and focus, and its subjectivity is relatively large; the same is an objective weighting method., the results obtained by the principal component analysis method and the penalty weighted optimal comprehensive evaluation scheme have a small gap with the actual power grid, but the evaluation effect of the penalty weighted optimal comprehensive evaluation scheme is better. The reasons for these differences are analyzed in detail below.

Table 4. Comparison results of final design for opening electromagnetic loops of Shaanxi grid

Ring name	Preliminary operating plan	Analytic Hierarchy Process Evaluation Scheme	Principal Component Analysis Evaluation Scheme	Penalty Weighted Optimal Comprehensive Evaluation Scheme
Baoji - Qian County	open	open	open	open
Qian County - South Xi'an	open	close	open	open
Qian County - North One of Xi'an	close	close	close	close
Qian County - Xi'an North Second	close	close	close	close
Xi'an North - Luochuan	close	close	open	close
Xi'an North - Xinyi	open	close	open	open
Xinyi - South Xi'an	close	close or open	close or open	close or open

Table 5 shows the comparison results of the power and electricity margins before and after the operation of the Xi'an North-Luochuan electromagnetic loop before and after the disengagement and closure of the loop. It can be seen from Table 5 that compared with the closed-loop operation, the power and electricity margin of the Baoji power supply area decreases very seriously during the open-loop operation. According to the calculation method of formula (9), the margin is -620 MW, while the load is only 760 MW, and the de-loop operation may have a relatively bad impact on the normal supply of electricity in Baoji area. Therefore, the Xi'an North-Luochuan electromagnetic loop should be operated in a closed loop.

From the previous calculation results, the constant weight result of the power and electricity margin is 0.46. After the punitive weight change, the weight of the power and electricity margin of the Xi'an North-Luochuan electromagnetic loop is significantly increased, reaching 0.534; Therefore, the optimal comprehensive evaluation result is reduced, so that the comprehensive evaluation index value of the unlooped operation is smaller than the comprehensive evaluation index value of the closed loop operation, and the power grid should be operated in a closed loop. This is consistent with the analysis results in Table 5 and above. And this is the improvement of the optimal comprehensive evaluation method of penalty variable weight compared with the principal component analysis method.

In addition, it should be noted that in the planned power system, when the combined loop scheme is determined, some "safety indicators" of the power grid, such as short-circuit current, N-1 static safety and other indicators will exceed the

Table 5. Comparison results of electric power and energy margin for opening electromagnetic loops of Xi'an North - Luochuan

Power supply area name	Power supply area load/MW	Power margin/MW during de-looping operation	Power margin/MW during closed loop operation
Baoji	760	- 620	- 120
Qian County	2828	200	200
Xi'an North	1992	4020	6260
South Xi'an - Xinyi	6137	1200	1200
Northern Shaanxi	7460	740	740
Southern Shaanxi	3570	3930	3930

allowable range. Makes the power grid operate in an unsafe condition. However, the security of the power grid is determined by multiple indicators, and it is impossible to completely abandon this scheme because one indicator exceeds the limit. The significance of this paper is to determine a combined loop scheme, so that under this scheme, most of the power grid indicators are in the optimal state; and for the indicators that do not meet the safety requirements, this can be solved in the future planning of the power grid. For example, for the busbar whose short-circuit current exceeds the standard, measures such as replacing a circuit breaker with a larger breaking capacity can be used to solve this problem. In the final scheme for de-closing the loop determined by the calculation example, the short-circuit level of the 750 kV busbar in Shaanxi Power Grid meets the requirements, and the N-1 calibration also fully meets the requirements; however, the short-circuit level of the 330 kV busbar is relatively high, and the result that the short-circuit current of the 330 kV busbar exceeds the standard listed, as shown in Table 6.

Table 6. The short-circuit current exceeding the regulation of final design for opening electromagnetic loops

Serial number	Bus name	Short circuit current/A		Switch rated breaking capacity/MVA	percentage/%
		Three-phase	Single-phase		
1	Shaanxi Anbei 31	66.74	74.10	63	117.62
2	Shan Nie Liu 31	64.88	69.20	50	138.40
3	Northern Shaanxi Suburbs 31	48.01	46.49	40	116.23
4	Shaanxi Caotan 31	47.95	49.11	45	109.13

Therefore, targeted reinforcement can be made for the above 330 kV bus short-circuit current exceeding the standard. Due to space limitations, this paper does not list specific measures.

To sum up, the power grid decomposing loop scheme based on the penalty weighted optimal comprehensive evaluation model can “penalize” the situation that a certain index value of the power grid is too low, but the comprehensive evaluation result is high can be avoided. Its physical background is more in line with the actual power system, and the advantages and disadvantages of the electromagnetic loop decoupling scheme can be quantitatively analyzed.

5 Epilogue

1. Aiming at the shortcomings of AHP and PCA, this paper proposes a constant-weight optimal comprehensive evaluation model. This model combines the ideas of PCA and multi-objective decision-making. The de-dimensioning process can completely and objectively obtain the weight of the operation index of the loop closure scheme, avoiding subjectivity and contingency.
2. The weights in the constant-weight optimal comprehensive evaluation model will not change correspondingly with each index. In order to take into account the roles of weights and index values in the comprehensive evaluation at the same time, combined with the variable weight theory of factor space, this paper proposes a penalty for the first time. The optimal comprehensive evaluation model of the variable weight is adopted, so that the weight of the index changes with the change of the index value. The grid decoupling scheme determined by this model can “penalize” the situation that a certain index value is too low after the grid decoupling (closing). In this way, it can avoid the situation that a certain index value of the power grid is too low, but the comprehensive evaluation result is high.
3. The actual calculation example of Shaanxi Power Grid shows that the operation scheme obtained by the AHP cannot provide an effective reference for the decoupling of the loop. The results obtained by the punitive weighted optimal comprehensive evaluation scheme are more consistent with the initial operation scheme, and meet the actual safe and stable operation requirements of the power system.
4. Although the punitive weighted optimal comprehensive evaluation model is used in the analysis of the electromagnetic ring network decoupling scheme in this paper, its application scope is by no means limited to this. This model can be applied to the problem of multi-index comprehensive evaluation. This model can be applied to issues involving multi-index comprehensive evaluation, such as power quality assessment, power grid transient safety margin, and subsequent fault line identification of cascading failures.

5. The penal variable weight calculation formula proposed in this paper is relatively simple, and a variable weight formula more suitable for the actual situation of the power grid can be proposed according to the actual situation of the power grid, which will be the next research direction.

References

1. Li, J., Teng, H., Guo, N., et al.: An optimal decision to restrain short circuit current for 500 kV power grids with combinatorial weighting method of relative entropy. *Power Syst. Technol.* **40**(6), 1811–1817 (2016). (in Chinese)
2. Tang, X., Cheng, Z., Zhang, X., et al.: An on-line voltage stability evaluation system for AC/DC hybrid power system. *Power Syst. Technol.* **38**(5), 1175–1180 (2014). (in Chinese)
3. Cui, M., Sun, Y., Yang, J., et al.: Power grid security comprehensive assessment based on multi-level grey area relational analysis. *Power Syst. Technol.* **37**(12), 3453–3460 (2013). (in Chinese)
4. Shen, Y., Peng, X., Mao, X., et al.: Comprehensive evaluation indexes framework and evaluation method on location layout of UHV substations. *Power Syst. Technol.* **36**(12), 44–53 (2012). (in Chinese)
5. Zhang, W., Yang, J.: Analysis on 500 kV/220 kV electromagnetic loops in north China. *North China Elect. Power* **7**, 28–30 (2004). (in Chinese)
6. Li, Y.: Variable weight synthesis theory and multi-objective decision-making. Kunming University of Science and Technology, Kunming (2008)
7. Wang, P.: Simplified definition and property of random sets and fuzzy shadows distribution. *J. Xi'an Jiaotong Univ.* **6**, 114–119 (1982). (in Chinese)
8. Li, H.: Factor spaces and mathematical frame knowledge representation(I)-axiomatic definition of factor spaces and description frames. *J. Beijing Normal Univ. (Nat. Sci.)*. **32**(4), 452–459 (1996). (in Chinese)
9. Li, H.: Factor spaces and mathematical frame knowledge representation (VII)-multifactorial decision-making with multiple objectives. *Fuzzy Syst. Math.* **2**, 16–24, 10 (1995) (in Chinese)
10. Li, H.: Factor spaces and mathematical frame knowledge representation (VIII)-variable weights analysis. *Fuzzy Syst. Math.* **3**, 1–9 (1995). (in Chinese)
11. Cheng, L.: Analysis and control of electromagnetic ring network disengagement and control. North China Electric Power University, Beijing (2007)
12. Tang, W.: Research on the optimal solution method of electromagnetic ring network. Chongqing University, Chongqing (2013)
13. Dan, H.: Liaoning Power Grid Electromagnetic Ring Network Solution Research. North China Electric Power University, Beijing (2014)
14. Zhang, D.: Research on comprehensive evaluation of electromagnetic ring network de-ring scheme. Chongqing University, Chongqing (2011)
15. Liu, W., Cai, W., Zhang, N., et al.: The evolution of grid's self-organizing critical state based on united weighted entropy theory. *Power Syst. Technol.* **35**(6), 1363–1370 (2015). (in Chinese)
16. Liu, G., Li, X.: Partition principles and methodology for cross-section of transmission line. *Northeastern Elect. Power Technol.* **11**, 15–18 (2005). (in Chinese)

Application and Development of Active Distribution Grid Technology for Integrated Energy Systems in the Context of Industrial Internet



Nuo Xu, Jinman Luo, Nuanqiang Ye, and Ming Zeng

Abstract The new round of energy revolution is deepening under the impetus of Internet technology, and an integrated energy system as an important trend in the development of energy and electricity has become an initial decision. As different types of new technologies and models are gradually applied in the integrated energy system distribution network, the traditional distribution network technology can no longer fully adapt to the increasingly complex external environment. This paper considers the overall characteristics of the integrated energy system and its impact on the planning and operation of the distribution network based on the deep integration of the industrial Internet and the energy and power industry, studies the typical application model and synergy mechanism of active distribution network technology in the integrated energy system, and designs and constructs a typical model from multiple dimensions such as demand response, collaborative planning, energy management and monitoring and control of the distribution network, analyzes the overall trend and key areas of active distribution network technology in the future, and forms the development path of active distribution network technology in the integrated energy system under the industrial Internet, summarizes the key initiatives appropriate to the development of integrated energy systems in different development stages, and provides rationalization suggestions for the operation of distribution networks in the promotion of integrated energy systems.

Keywords Industrial internet · Integrated energy · Active distribution grid · Synergy mechanism · Development path

N. Xu (✉) · J. Luo · N. Ye
Guangdong Power Grid Limited Liability Company, Dongguan Power Supply Bureau
Information Center, Dongguan 523120, Guangdong, China
e-mail: 121224376@qq.com

M. Zeng
North China Electric Power University, Changping, Beijing 102206, China

© Beijing Paiké Culture Commu. Co., Ltd. 2023
X. Dong et al. (eds.), *The proceedings of the 10th Frontier Academic Forum of Electrical Engineering (FAFEE2022)*, Lecture Notes in Electrical Engineering 1054, https://doi.org/10.1007/978-981-99-3408-9_42

1 Introduction

In recent years, the integrated energy service system has been moving forward, The rapid development of integrated energy systems will have many implications for the planning and operation of distribution networks, a large number of distributed power sources with volatility and uncertainty are beginning to be connected to the distribution network, demand-side customer energy use patterns and demand response methods are also changing to a greater extent, the reliability and security of the distribution network has been challenged in many ways, traditional distribution network technologies need to be adapted to a greater extent and scope to meet the reasonable requirements of distribution network planning and operation in the new environment. In the research of integrated energy systems, the reference [1] analyzes the key elements and development directions of multi-energy coordinated control technology in the process of realizing integrated energy coordination and optimization by combining typical integrated energy system projects at home and abroad. The reference [2] analyzes the dimensions of different energy types, interest subjects and user-side energy use characteristics for integrated energy system multi-scenario planning and design, which provides reference for integrated energy planning and layout. The reference [3] analyzes the economy and rationality of different types of energy storage methods in combination with the operation mode of the overall architecture of the integrated energy system area, and realizes the orderly planning of energy storage devices in the integrated energy system. The reference [4] combines demand-side resources for the construction of a collaborative optimization model of power generation, transmission, loading, and storage to achieve efficient and rational utilization of energy in the region. The reference [5] provides collaborative control of integrated energy systems in a hierarchical and distributed manner to achieve an effective balance of supply and demand resources in the region. In general, an integrated energy system is a hierarchical system covering multiple types of collaborative optimization approaches and control and regulation devices [6–9]. In terms of research on active distribution networks, the reference [10] combines multiple types of influencing factors to perform the analysis of constructing an optimal configuration model for intermittent distributed power sources in distribution networks to find the most optimal layout. In the reference [11], the dispatch optimization analysis of distributed energy sources in active distribution networks is carried out in two stages, day-ahead and real-time, to provide a reasonable operation of active distribution networks. The reference [12–14] analyzes the development trends and optimization strategies of active distribution networks from the key technologies and core elements of active distribution networks. The reference [15] and [16] considered factors such as access to distributed power sources and distributed generators' interests in the process of distribution network planning and optimization, respectively. The reference [17] and [18] consider the application and development of energy storage devices in active distribution networks. Overall, the application and development of active distribution networks will involve multiple types of factors, and factors such as access to

distributed power sources, load forecasting and demand-side response will be key concerns in the construction process of active distribution networks.

Research on the application of active distribution grid technologies has been carried out in some areas, but a systematic analysis is still lacking, in particular, as the interaction and integration between industrial Internet and energy and power industry deepens, the application of “cloud computing, big data, Internet of things, mobile Internet, artificial intelligence” and other Internet technologies in energy and power systems will bring new possibilities for the development and improvement of the distribution grid technology system of integrated energy systems, while the analysis of the application and development of active distribution grid technology of integrated energy systems under the industrial Internet is still lacking in focus at this stage, and the application and development of active distribution grid technology of integrated energy systems need to be studied from a comprehensive and systematic perspective to achieve efficient and reasonable operation of regional distribution networks. In this paper, on the basis of describing the impact of industrial Internet on the distribution network of integrated energy system, from the characteristics and development trend of active distribution network technology, combined with the typical models and experiences of active distribution development at home and abroad, this paper analyzes the application and development prospects of active distribution grid technologies for integrated energy systems, realizes the analysis of typical patterns of active distribution networks in the area of integrated energy systems, discusses the appropriate distribution grid model in the process of building an integrated energy system, and forms a path for the application of active distribution grid technology in the field, proposes a strategy for synergistic optimization of integrated energy systems and active power distribution to help realize the optimization and enhancement of power distribution networks in the new context.

2 Typical Model of Active Distribution Network of Integrated Energy System in the Context of Industrial Internet

At present, the traditional distribution network can no longer effectively adapt to the access of large-scale distributed energy in integrated energy systems, the volatility and intermittency of new energy sources will also make the traditional distribution network face new challenges, and the difficulties are mainly focused on five aspects, one is the increase of short-circuit current, the second is the lack of new energy consumption capacity, the third is the relatively low level of energy efficiency of the overall traditional distribution network, and the fifth is the difficulty of power quality control will increase, all the above difficulties need to be corrected by optimizing the traditional distribution network planning and operation methods. In addition, in today’s rapidly developing integrated energy system, the development of the distribution network is starting to be closely related to the power management on the

customer side, the diversified energy use patterns and alternative energy use systems on the user side will largely influence the demand-side response and control, the operation and control mode of the distribution network needs to be better coordinated with the demand-side load resources, and the active distribution network technology is used to achieve rapid response and active participation for the demand side.

As a new industrial ecology, key infrastructure and new application model for the deep integration of new-generation information technology and manufacturing industry, the Industrial Internet can realize the comprehensive connection of the whole industrial element, the whole industrial chain and the whole value chain through the comprehensive interconnection of people, machines and things, which brings the possibility of optimizing the operation of the distribution network of comprehensive energy system and its mutual coordination with the demand side. Therefore, the construction of the industrial Internet and the promotion and application of related technologies will facilitate the integrated management of distributed resources in the area of integrated energy systems and effectively support the wide access to distributed energy sources based on the effective control of tidal currents.

In summary, the integrated energy system distribution grid technology will give full play to its initiative in planning, forecasting, control and response of the distribution network through the application of Internet-related technologies to achieve rapid and flexible access to distributed energy sources. In addition, using the technical characteristics of open interconnection and intelligent interaction of people, machines and things in the Industrial Internet, active distribution grid technology will further improve the energy efficiency management of demand-side users, use controllable resources and adjustable loads to participate in output power balancing and demand-side load balancing, efficiently solving the problems of load dynamic monitoring, fault crisis handling and demand-side response within the area of integrated energy system, and comprehensively improving the security and economy of the distribution network.

3 Typical Model of Active Distribution Network of Integrated Energy System in the Context of Industrial Internet

Active distribution grid technology should consider the design and optimization of active distribution grid management scheme in the area of integrated energy system in the context of reliability, economy and distributed energy access capability, combined with the actual situation of investors, while the mode of active distribution grid will directly affect the new energy consumption capability, fault response capability, load control capability and safety and stability of distribution network in the area. Therefore, in the process of constructing and analyzing the active distribution network model, the factors that need to be considered comprehensively cover four main dimensions, which are the planning and layout dimension of the distribution network,

the monitoring and forecasting dimension of the distribution network, the feedback control dimension of the distribution network, and the active response dimension of the distribution network, the details of which are shown in Table 1.

As can be seen from Table 1, the construction and design of a typical model of an active distribution network for an integrated energy system must take into account the access of distributed energy sources on the power side, take into account the promotion of electric vehicles and demand-side response at the customer side, among others, provide real-time monitoring and sharing of load conditions, equipment conditions and operational data, improve the ability of the distribution network to respond and serve proactively, so as to better control the load in the region, regulate the energy resources in the region, and improve the overall energy efficiency of the integrated energy system region.

For the time being, the model of urban active distribution network needs to be coordinated with the overall layout of the urban area distribution network, covering distributed power module, energy storage system module, load response module, system module and monitoring and prediction module, the typical active distribution grid model will gradually integrate with new businesses and technologies in the context of integrated energy, forming a new energy source that guarantees new energy on the supply side, therefore, the main framework of a typical model of an active distribution network can be specifically summarized as shown in Fig. 1 below.

From the above figure, it can be seen that the typical mode of active distribution network of integrated energy system under industrial Internet will have many functions such as active prediction, active planning, active response and active control, among them:

- 1) In the demand forecasting system, the load change in the active distribution grid area in the integrated energy system is significantly different from the load growth in the traditional area, and the access of distributed power sources, the

Table 1 Influencing factors considered in the construction process of the active distribution network

No	Considerations	Specific content
1	Planning layout	In the context of integrated energy systems, large-scale distributed power sources and electric vehicles are beginning to be connected, and the access of new types of factors need to be considered during the planning and layout of distribution networks
2	Monitoring Forecast	The influx of new factors means the need for more accurate load forecasting, load monitoring, and real-time monitoring of equipment and operational data
3	Feedback control	The application of active distribution network technology means that the distribution network is more intelligent in real time, allowing for better feedback and regulation control for different scenarios
4	Proactive Response	Integrated energy systems require more efficient energy efficiency management and demand response, and the proactive responsiveness of the distribution network is of great importance for balanced coordination within the region

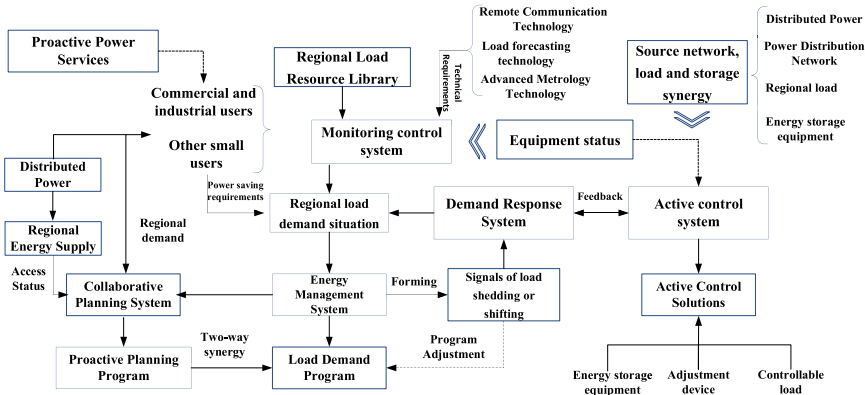


Fig. 1 Typical mode of active distribution network in integrated energy system

integrated energy service model and business system in the distribution grid area, and the uncertainty risk of demand-side user energy use will become new factors affecting the regional load, therefore, the active distribution grid needs to emphasize the consideration of Therefore, in the process of load forecasting, it is necessary to emphasize the spatial dynamic load forecasting that takes into account the risk of fluctuation in demand measurement, which means that in the process of load forecasting, the uncertainty factors such as fluctuation of distributed power supply and the randomness of customer demand-side response are considered, and the energy consumption patterns and characteristics of customers in the spatial region are summarized in combination with the energy service system and types of customers in the spatial region, so as to realize the dynamic and reasonable load forecasting in the spatial region and provide basic data reference for the planning and response control of the active distribution network. The data can be used to provide basic reference for active distribution network planning and response control.

- 2) In the active planning system, compared with the traditional distribution network planning, the planning of the active distribution network of the integrated energy system under the industrial Internet takes into account the new factors of regional new supply and demand for the layout and optimization of the network, which improves the rationality of the planning scheme in the technical dimension. In addition, the active planning system will consider to a greater extent the integration of technical and economic, will consider the economic benefits of grid investment while planning and optimizeng the distribution network, taking the market structure of the planning area and the benefits of investment behavior of grid enterprises as the key elements in the active planning process, emphasizing that the active planning system will achieve the optimization of the comprehensive benefits of the planning scheme under multiple scenarios.
- 3) In the monitoring and feedback system, the active distribution network of the integrated energy system under the industrial Internet will focus on two areas,

one is equipment operation condition monitoring and response, which means extensive access and summary analysis of equipment operation and monitoring data in the whole distribution network area, and real-time early warning and situation reporting of equipment that fails in the course of distribution network operation. The second is the rapid monitoring response to the load fluctuations caused by the demand changes on the demand side and the generation of new business models, so as to support the design and selection of solutions for the active control system of the distribution network.

- 4) In the active control system, the data and feedback provided in the monitoring feedback system and demand forecasting system will be combined to provide feasible solutions to the actual problems encountered in the distribution network. The active control system makes judgments and deals with faults and problems that may be encountered in the distribution area through data analysis, and performs scenario simulations and demonstrations of multiple scenarios to make optimal choices and action responses to ensure the safe and economic operation of the distribution network area.
- 5) In the interactive response system, the sharing and interaction between the active distribution grid and the regional users is emphasized, which means that the grid is emphasized to participate more actively in the demand response with the user side, provide energy service solutions for customers, and actively construct interoperability and sharing of energy use information with customers, allow the customer to also play its important role as a participating subject in the interactive response process, ensuring that the load resources on the customer side are used efficiently.

4 The Development Path of Active Distribution Network of Integrated Energy System in the Context of Industrial Internet

The development of a comprehensive energy system active distribution network cannot be achieved overnight, and the active distribution network will show a staged development trend, in this study, the development of urban active distribution networks is divided into three stages, which are the pre-basic construction stage, the mid-term focused development stage, and the full-scale application stage in the mature period. Their details are shown in Fig. 2.

As can be seen from the above figure, in each stage, the development of the active distribution network of the integrated energy system under the industrial Internet has its own focus and attention, the first stage of the foundation building stage mainly emphasizes the access to more types of distributed power sources in the distribution network, the means of regulation of the power grid is gradually expanding from a single to a diversified one, users begin to participate in the grid's interactions on the demand side, the focus of this stage is for the distribution network to begin to achieve local balancing and consumption of distributed power sources within a

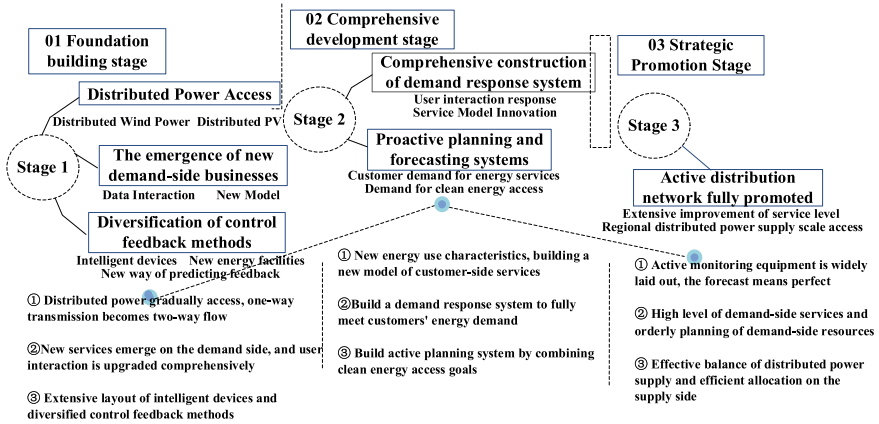


Fig. 2 Development path analysis of active distribution network in integrated energy system

certain range, helping the distribution network to better coordinate the emergence of new types of factors. The key development stage in the middle term mainly emphasizes the increasing diversification of user-side energy use patterns and the relative improvement of demand response mechanisms and systems, by improving its own control mechanism and system, the distribution network can better meet customers' demand for energy services and the extensive access to regional distributed energy.

1) Pre-stage: Foundation building stage

This stage is the preliminary stage of the development of the distribution network in the integrated energy system, which is mainly characterized by the increasing degree of intelligence and interaction of the distribution network, in this stage the concept and operation service model of active distribution network started to emerge, and new factors such as distributed power and electric vehicles became the focus of attention of the distribution network, at the same time, the distribution network is facing various types of new problems are gradually arising, distributed energy consumption will also be integrated into the planning of active distribution grids through a new model, the new initiatives for the control and operation of the distribution network in this stage are shown in Table 2.

2) Mid-term stage: comprehensive development stage

This stage is the middle stage of the development of the distribution network of the integrated energy system, the main feature of this stage is the increased emphasis on proactive services and proactive participation in the distribution network, the demand-side users' energy use patterns and demand response methods are transformed, the interactivity between the distribution network and customers reaches a certain level, the distribution network gradually improves the timeliness and effectiveness of customer demand response by improving the prediction and response mechanism on the demand side, so that the distribution network can achieve coordinated development on the demand side, the new

Table 2 New initiatives for the active distribution network in the basic construction stage

No	Key Initiatives	Specific effects
1	Distributed power and grid co-optimization	Enhance the construction and access of distributed facilities
2	Application promotion of demand-side energy storage technology	Improving demand-side energy storage synergy with the grid
3	New distribution network planning and dispatching system	Promote comprehensive coordination of power generation transmission, loading, storage and active planning of distribution network
4	Intelligent monitoring system and response mechanism	Enhance the active response and control capability of distribution network
5	Operational control strategies for active distribution networks	Improve the overall operation and control level of the distribution network

initiatives for the control and operation of the distribution network in this stage are shown in Table 3.

(3) Maturity stage: Extension application stage

This stage belongs to the stage of relatively perfect construction of the active distribution network of the integrated energy system, at this stage, the overall operation and control mechanism of the distribution network has matured, and the overall operation of the active distribution network in the region is orderly and reasonable, the focus of the distribution network development is to promote the application of a comprehensive network, so that the original active distribution network in a small area can be expanded to a large-scale active distribution area, so that the resources on the supply side and demand side can be balanced on a

Table 3 New initiatives for the active distribution network in the comprehensive development stage

No	Key Initiatives	Specific effects
1	Active Distribution Grid Interaction Demonstration Area	Strengthen demand-side interactivity and realize information sharing
2	Integrated energy service system construction	Build a flexible and diverse energy use model on the user side
3	User-side demand response market	Improve the ability of regional load balancing conditions in the distribution network
4	The promotion and application of smart home	Promoting the transformation and development of household energy use patterns
5	Coordinated optimization mechanism of power generation transmission, loading, and storage	Promote supply-side and demand-side synergy and the consumption of new energy

Table 4 New initiatives for active distribution networks in the application and promotion stage

No	Key Initiatives	Specific effects
1	Power IOT network construction	Enables wide range of communication and business data transmission and feedback control
2	Building a strong smart grid	Support multiple energy consumption modes and distributed power access for users in the region
3	Energy Sharing Platform Promotion	Create a shared energy model and provide a hub-and-spoke network platform

larger scale, the novel initiatives of the active distribution network in the stage are as follows (Table 4):

5 Conclusion

Under the trend of deepening interaction between industrial Internet and energy and electricity, the active distribution grid technology of integrated energy system will be further promoted and developed, the promotion and application of active power distribution network will also provide strong support for the consumption of distributed energy in the region and the timely and effective satisfaction of customers' demand for electricity, this paper combines the characteristics of integrated energy systems and active distribution grids, conducts design analysis of typical application modes of active distribution grids, explores the stages and initiatives for the development and promotion of active distribution grids, and promotes the rational and orderly construction of active distribution grids under integrated energy systems, this paper draws the following conclusions in the course of research on the application and development of active distribution grid technologies for integrated energy systems.

- 1) The promotion and application of active distribution network technology will be more adapted to the development needs of the new distribution network, with the gradual development of the integrated energy system, the emergence of new factors such as distributed power sources, electric vehicles and demand-side response models will have an impact on the single mode of the traditional distribution network, the promotion and application of active distribution network technology enables intelligent and dynamic control feedback and two-way flow in the distribution network, which plays an important role in promoting the access to distributed power sources and meeting the new energy consumption patterns of customers in the region.
- 2) The mode of active distribution network will directly affect the new energy consumption capacity, fault response capacity, load control capacity and the security and stability of the distribution network in the region, at present, a typical active power distribution model can be developed through the application of Internet technology to achieve diversified system functions including demand

forecasting, monitoring feedback, active planning, active control and interactive response, the design and construction of the distribution network model will fully reflect the characteristics of new network active planning, active control, active participation and active service.

- 3) The development of an integrated energy system active distribution network is a dynamic staged process, in this paper, we divide it into the basic construction stage in the early stage, the comprehensive development stage in the middle stage and the promotion and application stage in the mature period, in this regard, the focus of the foundation building stage is to integrate the emergence of new factors into the planning and construction process of the distribution network, the focus of the comprehensive development stage is to further consider the demand-side energy use model and system construction in the process of operation and control of the distribution network, the focus of the full-scale promotion stage is to promote the relatively mature management mechanism and operation mode on a wider scale to meet the diversified needs of supply-side distributed power access and user-side while improving the service level.

References

1. Peng, K., Zhang, C., Xu, B.Y., et al.: Status and prospect of pilot projects of integrated energy system. *Elect. Power Autom. Equip.* **7**(6), 3–10 (2017)
2. Cheng, L., Zhang, J., Huang, R.L., et al.: Case analysis of multi-scenario planning based on multi-energy complementation for integrated energy system. *Elect. Power Autom. Equip.* **37**(6), 282–287 (2017)
3. Xiong, W., Liu, Y.Q., Su, W.H., et al.: Optimal configuration of multi-energy storage in regional integrated energy system considering multi-energy complementation. *Autom. Elect. Power Syst.* **9**(1), 118–126 (2019)
4. Zeng, M., Yang, Y.Q., Xiang, H.W., et al.: Optimal dispatch model based on coordination between “gene-ration-grid-load-energy storage” and demand-side resource. *Elect. Power Autom. Equip.* **36**(2), 102–111 (2016)
5. Zhao, Y.H., Peng, K., Xu, B.Y., et al.: Hierarchical and distributed coordination control of integrated energy system. *Elect. Power Autom. Equip.* **37**(6), 253–259 (2017)
6. Hao, R., Ai, Q., Zhu, Y.C., et al.: Hierarchical optimal dispatch based on energy hub for regional integrated energy system. *Elect. Power Autom. Equip.* **37**(6), 171–178 (2017)
7. Saboori, H., Hemmati, R., Abbasi, V.: Multistage distribution network expansion planning considering the emerging energy storage systems. *Energy Convers. Manage.* **105**, 938–945 (2015)
8. Wang, X., Gu, R.T., Ji, Y.F.: Ring-like reliable PON planning with physical constraints for a smart grid. *Opt. Fiber Technol.* **27**, 24–34 (2016)
9. Wang, W.L., Wang, D., Jia, H.J., et al.: Review of steady-state analysis of typical regional integrated energy system under the background of energy internet. *Proc. CSEE* **36**(12), 3292–3305 (2016)
10. Zhang, S.X., Li, K., Cheng, H.Z., et al.: Optimal allocation of intermittent distributed generator in active distribution network. *Elect. Power Autom. Equip.* **35**(12), 45–51 (2015)
11. Zeng, M., Peng, L.L., Wang, L.H., et al.: Two-stage dual-level dispatch optimization model of distributed energy system in active distribution network. *Elect. Power Autom. Equip.* **36**(6), 108–115 (2016)

12. You, Y., Liu, D., Zhong, Q., et al.: Study on day-ahead dispatch strategy of active distribution network. *Autom. Elect. Power Syst.* **38**(9), 177–183 (2014)
13. Fan, M.T., Zhang, Z.P., Su, A.X., et al.: Enabling technologies for active distribution systems. *Proc. CSEE* **33**(6), 12–17 (2013)
14. You, Y., Liu, D., Yu, W.P., et al.: Technology and its trends of active distribution network. *Autom. Elect. Power Syst.* **36**(6), 10–16 (2012)
15. Liu, B.L., Huang, X.L., Li, J., et al.: Multi-objective planning of distribution network containing distributed generation and electric vehicle charging stations. *Power Syst. Technol.* **39**(2), 450–456 (2015). (in Chinese)
16. Zeng, M., Shu, T., Shi, H., et al.: An active distribution network planning taking interest of distributed Genco into account. *Power Syst. Technol.* **39**(5), 1379–1383 (2015). (in Chinese)
17. Carr, S., Premier, G.C., Guwy, A.J., et al.: Energy storage for active network management on electricity distribution networks with wind power. *IET Renew. Power Gener.* **8**(3), 249–259 (2014)

Development of LDV-Based Length Measuring Equipment for Tension Stranding Construction Conductor



Zheng Lv, Zhiming Huang, Qi Xiao, Zixin Li, Junfeng Guan, and Bo Tang

Abstract In the construction of traditional force erection wire, when using sag observation, the wire is often unable to reach the position in one step, resulting in low construction efficiency. However, the existing wire length measuring equipment is difficult to be applied in the wire erection construction, and the measurement accuracy also needs to be improved. Therefore, based on laser Doppler velocimetry (LDV), a calculation model of double beam irradiation is proposed, and the construction characteristics of tension wire are closely combined. Wire length measuring equipment for wireline construction. The developed wire length measuring equipment has been successfully applied to the 110 kV outer Jiao line project of Jiangmen Hongxing (Shengli) power transmission and transformation project, and the sag observation value of the wire displayed according to this equipment meets the engineering requirements.

Keywords Tension wire construction · Wire Length Measuring Equipment · Laser Doppler Velocimetry · Dual beam illumination model

1 Introduction

The tension wire construction method has become an important construction method in the construction of overhead transmission lines because of its high speed of spreading the wires and can effectively avoid the friction damage of the wires [1].

Z. Lv · Q. Xiao

Guangdong Power Grid Company Ltd., Guangzhou 510000, China

e-mail: learlui@hotmail.com

Z. Huang · Z. Li · J. Guan

Jiangmen Power Supply Bureau, Guangdong Power Grid Company Ltd., 529000 Jiangmen, China

B. Tang (✉)

College of Electrical Engineering and New Energy, China Three Gorges University,

Yichang 443000, China

e-mail: 20776237@qq.com

© Beijing Paiké Culture Commu. Co., Ltd. 2023

X. Dong et al. (eds.), *The proceedings of the 10th Frontier Academic Forum of Electrical Engineering (FAFEE2022)*, Lecture Notes in Electrical Engineering 1054, https://doi.org/10.1007/978-981-99-3408-9_43

503

However, in the process of laying out the wire, it is often difficult to directly lay the wire in place in one step, and it is necessary to carry out repeated adjustment work in strict accordance with the requirements of the design sag. At present, the total station is usually used to observe the sag of overhead transmission lines [2], but this observation method is inefficient. With the development of science and technology, high and new technologies such as video image processing technology [3, 4], aerial sequence image technology [5, 6], and laser point cloud technology [7] are widely used in the field of overhead transmission line construction. But these technologies are mostly used for operation monitoring after the completion of the line, and it is difficult to apply and guide the adjustment range in real time during construction.

In fact, some Reference [8, 9] have obtained sag data indirectly through real-time measurement of easily measurable parameters. Therefore, according to the relationship model between the line length and the sag of the overhead transmission line, and based on the principle of laser Doppler length measurement, a length measurement device suitable for the construction of the tension wire is developed. The application of this equipment in the Jiangmen Hengjian access system engineering project proves that it can accurately control the line sag by measuring the length of the wire, thereby eliminating the tedious and complicated process of loosening and tightening the wire and greatly simplifying the process. process to improve construction efficiency.

2 Functional Requirements of Tension Wire Length Measuring Equipment

2.1 Tension Wire Construction Features

Tension wiring refers to the use of tensioning equipment and pre-laid traction wires to pull conductors during wireline construction [10], which is widely used in the construction of transmission lines.

The size of sag of overhead transmission line has an important influence on the safe operation of the line. In order to ensure that the line sag meets the design requirements, a total station is usually used to observe the sag in actual construction [11], but this method is easily restricted by objective conditions such as weather and terrain, which affect the observation results. After the preliminary laying of the wires is completed, according to the observation results, the loosening and tightening of the wires shall be repeatedly adjusted. As a result, the construction steps are cumbersome and complicated.

Since the size of the line sag is closely related to the length of the line, it can be considered to realize the control of the sag of the overhead transmission line by measuring the line length in real time during the construction of the tension wire.

2.2 Tension Wire Construction Features

According to the construction characteristics and functional requirements, select the appropriate method of measuring the length of the line to measure the length of the line. In the existing method for estimating the wire length by calculating the number of revolutions of the wire disc, when the wire disc is rotated repeatedly, the radius of rotation is gradually reduced [12], resulting in a large error. In the production process of cables and wires, this method uses the friction between the cable and the pulley to drive the pulley to rotate [13]. Other circumstances lead to inaccurate length measurement. Therefore, the above two length measurement methods are difficult to be effectively applied in construction.

Laser Doppler Velocimetry is a non-contact, high-precision measurement method, which is widely used in the measurement of speed and length [14]. Therefore, according to the principle of laser Doppler velocity measurement and combined with other equipment in construction, the design of the overhead transmission line length measurement system based on non-contact length measurement is completed, which realizes the online real-time measurement of conductors during wireline construction.

3 Establishment of Non-Contact Length Measurement Model

The basic principle of laser Doppler measurement technology is shown in Fig. 1(a). The laser transmitter emits a beam of laser light with frequency f and wavelength λ , which is irradiated on the particle O and received by the photodetector after being reflected. \vec{a} and \vec{b} are the unit velocity vectors in the receiving and incident directions of the laser, respectively.

When the particle O is in a static state, the frequency of the scattered light does not change, and the frequency f_1 of the scattered light received by the receiver is

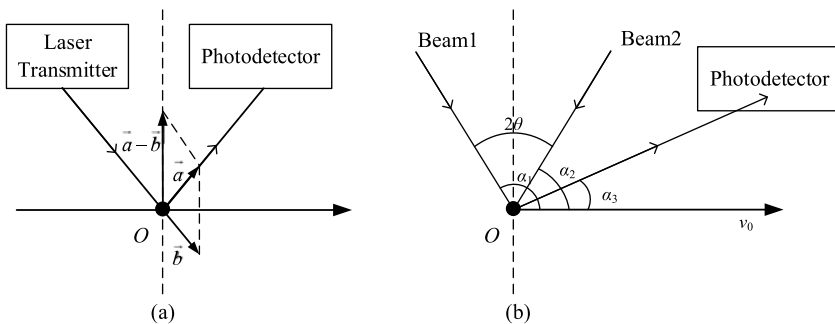


Fig. 1 Laser Doppler Velocimetry Schematic. (a) Single beam irradiation model. (b) Dual beam illumination model

$$f_1 = f = \frac{c}{\lambda} \quad (1)$$

where c is the speed of light. When the particle O moves at the speed v_0 , the frequency f_2 of the scattered light received by the receiver is

$$f_2 = f \left[1 + \frac{v_0 \cdot (\vec{a} - \vec{b})}{c} \right] \quad (2)$$

From this, the Doppler frequency shift Δf can be obtained as

$$\Delta f = f_2 - f_1 = \frac{1}{\lambda} v_0 \cdot (\vec{a} - \vec{b}) \quad (3)$$

The principle of the laser Doppler velocimetry model of double beam irradiation is shown in Fig. 1(b). The included angles between the two beams of frequency f_0 and wavelength λ , beam 1 and beam 2, and the direction of the velocity of the measured particle with velocity v_0 are α_1 and α_2 , respectively, the angle between the receiving direction of the photodetector and the moving direction of the measured particle is α_3 . From the formula (3), the Doppler frequency shift difference f_d of the scattered light of the two laser beams can be obtained as

$$f_d = \Delta f_2 - \Delta f_1 = \frac{f_0 v}{c} (\cos \alpha_1 - \cos \alpha_2) \quad (4)$$

When the moving object vertically passes through the angle bisector of the two incident lights, by $\pi = \alpha_1 + \alpha_2$, then there is

$$f_d = 2 \frac{v \sin \theta}{\lambda} \quad (5)$$

In view of the current situation in the construction of tension wire, the laser Doppler velocimetry model irradiated by double beams of light should be selected. As shown in Fig. 2.

Therefore, when the wavelength λ of the laser and the incident direction 2θ of the two laser beams are known, the instantaneous velocity v of the wire can be obtained by measuring f_d . After integrating the instantaneous velocity v by time, the length L of the wire is obtained, which is

$$v = \frac{\lambda f_d}{2 \sin \theta} \quad (6)$$

$$L = \int_0^t v dt$$

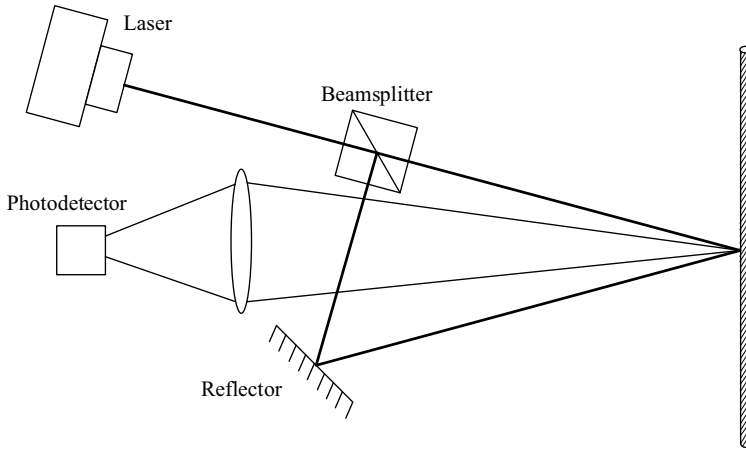


Fig. 2 Optical path diagram of double beam irradiation model

This model does not require the position of the photodetector, and has high applicability in the construction environment with complex working conditions.

4 Development of Wire Length Measuring Equipment

4.1 Overall Structure Scheme of Length Measuring Equipment

According to the actual situation in the construction of tension wire and the functional requirements of the system, the design of the length measuring system can be divided into hardware structure design and software program design for discussion. The hardware structure mainly includes data acquisition, processing and wireless transmission modules, and a power supply module is also required to supply power to the above modules. According to the hardware structure design, the software program design of the length measuring equipment can be divided into two parts: one is the data acquisition and processing software program design, and the other is the terminal driver program design. To sum up, the design process of the entire length measuring equipment is shown in Fig. 3.

4.2 Hardware Structure Design of Length Measuring System

Install the LDV length measuring device at the outlet of the tension machine to realize the accurate length measurement of the wire. The system selects the HL6326MG laser

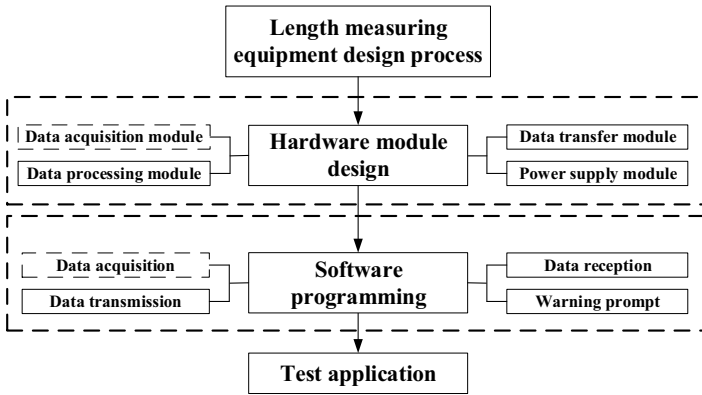


Fig. 3 Length measuring equipment design flow chart

diode as the system light source, and selects the C12702-11 type photodiode as the photodetector. In order to avoid the interference caused by wire jitter, the OPA841 integrated signal amplifier is selected to amplify and filter the signal collected by the photodetector. And select ADS1256 analog-to-digital converter for analog-to-digital conversion of the signal. Finally, the data processing is completed by the STC12LE5A60S2 single-chip microcomputer. The signal acquisition and processing module is shown in Fig. 4.

After the length data information is collected and processed, it needs to be sent to each receiving end through wireless transmission. The LoRa-based SX1278 wireless serial port module has strong anti-interference and wireless penetration capabilities, and its transmission distance can reach more than 10 km. Therefore, the transmission module of the length measurement system uses LoRa technology for wireless data transmission.

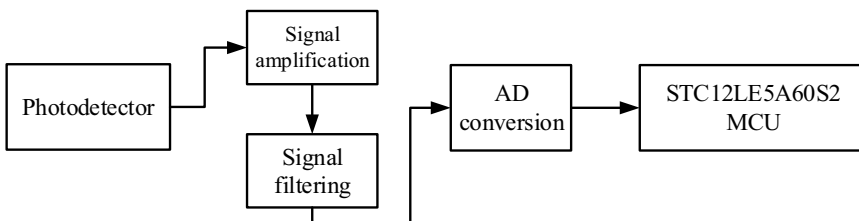


Fig. 4 Signal acquisition and processing module

4.3 System Software Programming

According to the relevant formulas of overhead transmission lines, the mathematical relationship model of the line length and sag is obtained, and the program is written according to this. The construction personnel can obtain the wire length that should be spread after inputting the relevant parameters according to the on-site working conditions, that is, the drawing threshold. Considering that the reaction time is reserved for the braking of the stretcher and the drawing and printing of the equipment, the warning threshold is generally set about 10 m before the drawing and printing threshold.

The terminal receiving equipment is responsible for receiving the information transmitted by the transmitter of the length measuring equipment, and displaying and warning the received data. The staff can directly issue corresponding instructions through the handheld terminal device to control the speed of the stretcher and the start and stop work. The signal transmission module is set to transmit the collected measurement data every 10 ms to ensure that the receiving terminal can grasp the length information of the released wire in real time. The program flow of the transmitter of the length measuring equipment information is shown in Fig. 5.

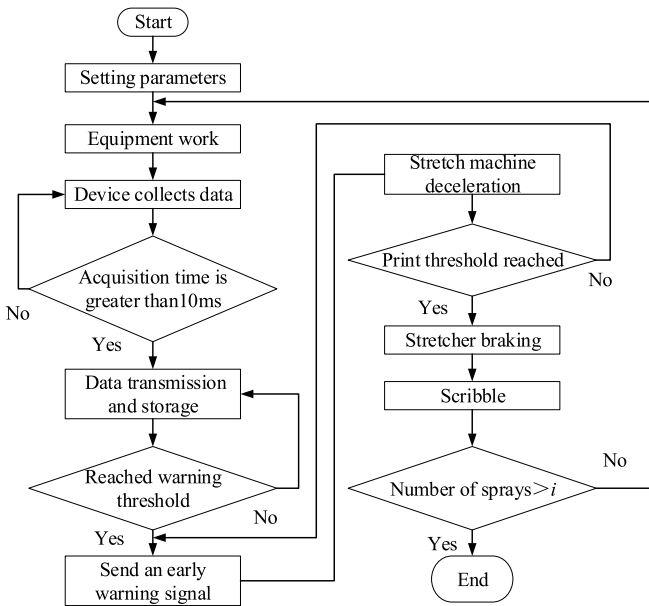


Fig. 5 Equipment software program flow chart

Table 1 The length of each line in the construction section (unit: m)

Name	Span	Height difference	Calculate line length
12–13#	299	+ 5	299.646
13–14#	251	+ 3	251.364
14–15#	350	−2	350.966
15–16#	400	−2	401.450

5 Engineering Applications

The developed tension wireline construction wire length measurement system was successfully applied in the Jiangmen Hengjian access system project in April 2021. The engineering parameters are shown in Table 1. According to the calculation, the sag of the observation stall is 11.228 m, and the sag of the observation stall after the installation is measured according to the calculated line length is 11.642 m, and the error is 3.7%, which meets the design requirements.

6 Conclusion

The designed wire length measuring equipment can measure the length of the wire in real time during the construction of the tension wire, which saves the tedious and complicated technological process and improves the construction efficiency.

Acknowledgements This work is supported by China Southern Power Grid Corporation Technology Project (GDKJXM20200710).

References

1. Zeng, L.: Discussion on tension stringing construction technology for overhead transmission lines. *Value Eng.* **37**(26), 252–254 (2018). (in Chinese)
2. Yan, B.: Research on construction technology of 32kV transmission line under tension. *China High New Technol.* **2021**(22), 47–48 (2021). (in Chinese)
3. Chen, S., Wang, B., Sheng, G., Wang, W., Jiang, X.: Application of digital image processing and photogrammetric technology to sag measuring method. *High Volt. Eng.* **37**(4), 904–909 (2011). (in Chinese)
4. Huang, X., Zhang, X., Li, L., Luo, B.: Measurement of transmission lines conductor sag using image processing. *High Volt. Eng.* **37**(8), 1961–1966 (2011). (in Chinese)
5. Lu, Q., Chen, W., Wang, W.: SAG measurement of transmission line based on aerial image. *Comput. Appl. Softw.* **36**(4), 108–111 (2019). (in Chinese)
6. Tong, W., Li, B., Yuan, J., Zhao, S.: Method of transmission line sag measurement based on aerial image sequence. *Proc. CSEE.* **31**(16), 115–120 (2011). (in Chinese)
7. Ma, W., Wang, J., Wang, C., Ma, Y.: Transmission line sag simulation from airborne LiDAR point cloud data. *J. Geom. Sci. Technol.* **36**(4), 394–399+405 (2019). (in Chinese)

8. Xu, Q., Ji, H., Wang, M.: Real-time monitoring of transmission line sag. *High Volt. Eng.* **2007**(7), 206–209 (2007). (in Chinese)
9. Qin, J., Liu, C., Qi, Z., Qiao, L.: Calculation method and engineering test for continuous process of tension stringing based on catenary method. *Southern Power Syst. Technol.* **15**(6), 36–42 (2021). (in Chinese)
10. Chen, H., Sun, L., Liu, W., Zhang, B.: The research of a intelligent monitor control system for tension string equipment. *Mach. Tool Hydr.* **39**(17), 89–91 (2011). (in Chinese)
11. Ding, Z.-W., et al.: Phi-OTDR based on-line monitoring of overhead power transmission line. *J. Lightwave Technol.* **39**(15), 5163–5169 (2021)
12. Khawaja, A.H., Huang, Q.: Estimating sag and wind-induced motion of overhead power lines with current and magnetic-flux density measurements. *IEEE Trans. Instrum. Measure.* **66**(5), 897–909 (2017). <https://doi.org/10.1109/TIM.2017.2676140>
13. Jeong, S., Kim, D., Kim, S., Ham, J.-W., Lee, J.-K., KiYong, O.: Real-time environmental cognition and sag estimation of transmission lines using UAV equipped with 3-D lidar system. *IEEE Trans. Power Deliv.* **36**(5), 2658–2667 (2021). <https://doi.org/10.1109/TPWRD.2020.3024965>
14. Zhao, X., Zhou, H., Shi, D., Zhao, H., Jing, C., Jones, C.: On-line PMU-based transmission line parameter identification. *CSEE J. Power Energy Syst.* **1**(2), 68–74 (2015). <https://doi.org/10.17775/CSEEJPES.2015.00021>

Achieving High Dielectric Constant, High Breakdown Strength, and High Efficiency in a Linear Polymethyl Methacrylate Composite for Energy Storage



Yujiu Zhou, Hu Ye, Haohao Feng, Jiali Wu, Tao Chen, Qifeng Pan, Yuetao Zhao, and Jianhua Xu

Abstract Electrostatic capacitors are widely used due to their relatively high voltage, high power density, and high reliability. However, its energy density is very low and unable to meet the growing demand. Moreover, it is usually difficult for a single material to satisfy high dielectric constant, high breakdown strength, and high efficiency simultaneously. Herein, we reported an all-organic composite by using linear polymethyl methacrylate (PMMA) as the matrix. The film was fabricated through a scalable solution casting method for industrial application. Due to good compatibility between the PMMA matrix and poly(vinylidene fluoride-co-hexafluoropropylene) (P(VDF-HFP)), the composite exhibit improved high dielectric constant, enhanced breakdown strength, and maintain excellent energy storage efficiency. After introducing a proper proportion of ferroelectric P(VDF-HFP), a high energy density of 4.43 J/cm^3 could be reached, while that of pristine PMMA is only 1.82 J/cm^3 . Moreover, the efficiency of P-15 is still maintained at 83.4% even under 4500 kV/cm, and the decline of efficiency is very low (5.3% from 500 kV/cm to 4500 kV/cm). This work provides a case to enhance the energy density of PMMA based all-organic polymer composite.

Y. Zhou · H. Ye · H. Feng · J. Wu · T. Chen · Q. Pan (✉) · Y. Zhao
Department of Film Capacitors, Xin Yun Electronic Components Company of China Zhen Hua Group, Guiyang 550018, China
e-mail: phoenix4326@163.com

Y. Zhao
e-mail: zhaoyuetao@just.edu.cn

H. Ye · Y. Zhao · J. Xu
State Key Laboratory of Electronic Thin Films and Integrated Devices, School of Optoelectronic Science and Engineering, University of Electronic Science and Technology of China, Chengdu 610054, China

Y. Zhao
Ocean College, Jiangsu University of Science and Technology, Zhenjiang 212100, China

Keywords PMMA composite · Breakdown strength · Dielectric films · Energy storage efficiency

1 Introduction

With the decline of non-renewable energy sources, clean energy (e.g. solar power and wind power) is attracting more and more attention [1]. With the use of those clean energy, energy conversion, storage, and transmission devices are very important. However, the volume and weight of the new energy equipment are very huge, and one of the factors is caused by the low energy density of capacitors [2–4]. Compared with ceramic capacitors and electrolytic capacitors, organic film capacitor act as an irreplaceable role in the power system due to their ability to withstand large current and high voltage. The performance of the organic film capacitors is mainly depended on the organic dielectric materials. The most common materials are biaxially oriented polypropylene (BOPP), and the intrinsic dielectric constant is 2.2 which hinders the further improvement of the energy density of BOPP capacitors [4]. To meet the high energy density requirements of the client, the only way is to explore new materials. New materials mainly consist of linear materials and non-linear materials.

Poly(vinylidene fluoride) (PVDF) is a typical ferroelectric polymer and belongs to non-linear material. It has attracted extensive attention attributes to its very high dielectric constant (~ 10) among polymers and strong structural designability [5]. Hence, PVDF has plenty of co-polymers, such as poly(vinylidene fluoride-chlorotrifluoroethylene) (P(VDF-CTFE)), (P(VDF-HFP)) with various electrical, mechanical, and thermal performances [6–8]. However, due to the strong coupling between polar dipoles for ferroelectric materials, the energy storage efficiency of those PVDF-based materials is always lower than 70% (even lower than 40%) which means that about 60% of energy was lost. On the other hand, linear materials also are troubled by their low dielectric constant despite their high efficiency [9, 10]. A common and simple method is to composite the advantages of linear materials and non-linear materials, to obtain a composite material with high dielectric constant, high efficiency, and relatively high breakdown strength. Because composite is the mixing of two or more component, hence the electrical properties is determined by the type, distribution, and compatibility of the composite phase. Poor compatibility will cause rapid deterioration of electrical performance.

PMMA is a kind of linear material with weakly polar and shows good compatibility with PVDF [11]. The dielectric constant of PMMA is 3.6, higher than that of BOPP. In addition, the amorphous structure could avoid the coupling of polar dipoles, which affords enough space for rotation. Based on the excellent compatibility and electrical performance complementarity of PVDF and PMMA, their composite is widely studied and have been obtained some meaningful results [12–16]. However, most of them are using PMMA as the additive component, and PMMA seldom is used as the matrix. This is mainly attributed to the PMMA is fragile and the improvement is not obvious (even performance deteriorates). For instance, Lu fabricated the

PMMA/Ba_{0.5}Sr_{0.5}TiO₃ composite, but the maximum energy density and breakdown strength of the composite films are even much lower than the pristine film [17]. Recently, we found that the PMMA with higher molecular weight can make flexible self-supporting film formation, and then designed a sandwich structure nanocomposite [18]. But the energy storage properties of the PMMA matrix did not meet the expectation, that is the dielectric constant and the breakdown strength are relatively low. In that nanocomposite embedded structure, a polymer matrix with lower dielectric needs to tolerate a higher electric field which is attributed to the extremely high dielectric constant of the mid-layer. Therefore, it is very important to optimize the polymer matrix.

In this paper, a PMMA/P(VDF-HFP) nanocomposite is fabricated and analyzed. After the introduction of an appropriate proportion of P(VDF-HFP), the composite not only shows a higher dielectric constant and breakdown strength, but also the η is higher than the pristine PMMA. For instance, the breakdown strength and the dielectric constant of the composite with 15% P(VDF-HFP) (P-15) present 15.6% and 16.6% higher than those of the PMMA matrix, respectively. This work provides a scalable method for linear materials with low polarity in the application of capacitors.

2 Experimental

2.1 Materials

The PMMA powder was obtained from Sigma Aldrich and the P(VDF-HFP) was purchased from Solvay, respectively. The solvent N-methyl-2-pyrrolidone (NMP, AR grade) was provided by Chengdu Kelong Reagent. All the materials were used as received.

2.2 Preparation of the PMMA Composite Films

PMMA and P(VDF-HFP) powders with a certain percentage (95:5, 90:10, 85:15, and 80:20 weight ratio) were dissolved in NMP solution, and the solid content in composite solutions was maintained at 15 wt.%. Subsequently, the composite solution was stirred overnight with a magnetic stirrer to obtain a clear solution. The solution with different composite ratios was cast on the glass plate and the thickness was controlled through the scraper slit. After the wet solution preparation, then the glass plates were heated at 90 °C overnight. After that, PMMA/P(VDF-HFP) composite with different components was obtained. For simplicity, the composite sample with 5%, 10%, 15%, and 20% P(VDF-HFP) was named P-5, P-10, P-15, and P-20, respectively.

2.3 Characterization

The thickness was measured by DUALSCOPE MPO (Fischer, Germany), and the surface morphology was observed by SEM (Hitachi, Japan). Before the electric characterization, the aluminum electrode was evaporated on the film surface. The dielectric properties were tested by Agilent 4294A. The breakdown strength dates were obtained by a high-voltage device (Tonghui, China). And the P-E loop was measured by radiant multiferroic equipment.

3 Results and Discussion

The surface morphology of the composite films is shown in Fig. 1. The composite films present a very smooth surface as PMMA and no obvious characteristic can be observed. A smooth surface is a benefit to fabricated capacitor films which is attributed that the breakdown process always occurring in the thin part. Based on the research result that the amorphous PMMA segments could decrease the crystalline of PVDF-based polymer [19]. Here in, PMMA segments and HFP elements hinder the formation of large grains which might form smaller domains.

Dielectric spectroscopy is used to uncover how P(VDF-HFP) affects the dielectric properties of blending composite, as shown in Fig. 2. The dielectric constant of the composite is enhanced with the increasing of high dielectric constant P(VDF-HFP) content. For instance, the dielectric constant of P-20 reached 4.3, which is almost twice that of BOPP (2.2) and 20% higher than the PMMA matrix (3.6). Due to the relatively low addition amount, the effect on dielectric loss is small from 1 to 100 kHz.

To explore a substitute material for capacitor applications, evaluating their high voltage properties is very essential. Figure 3 shows the breakdown strength properties. Sixteen points were tested and then analyzed by Weibull distribution [20]. The shape parameter of the composite exhibit higher than the pristine PMMA, which presents

Fig. 1 SEM results of PMMA composite (a) P-5, (b) P-10, (c) P-15, (d) P-20

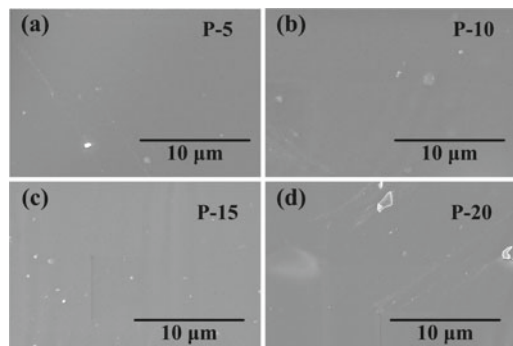


Fig. 2 Dielectric spectrum of the composite films

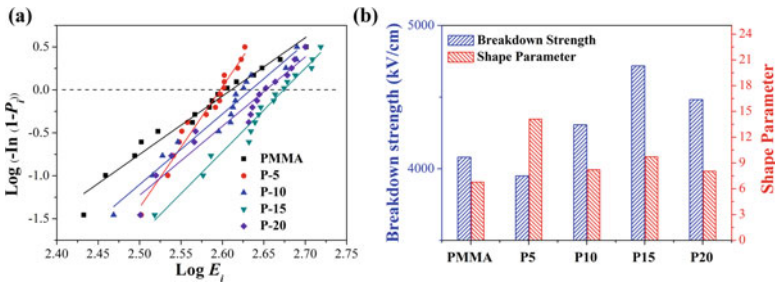
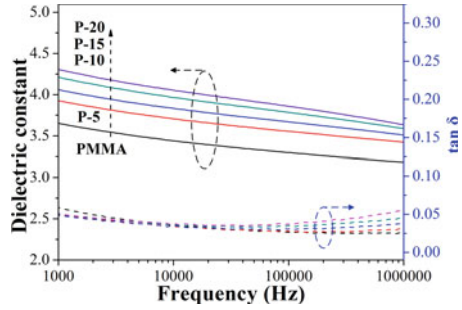
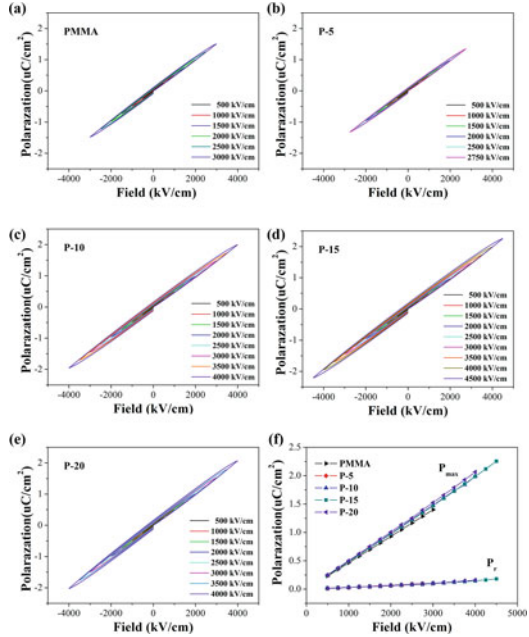


Fig. 3 The (a) breakdown strength point and (b) bar graph results of composite

higher reliability. The breakdown strength of PMMA is 4080 kV/cm, which is higher than our previous work (The critical key factor is the solvent, and the influence of the solvent will not discuss in this paper). The greatly improved value of 4718 kV/cm could be achieved in P-15, which is 15% higher than the PMMA matrix. It is well known that the breakdown strength is square in proportion to the energy density. Hence, the higher dielectric constant and higher breakdown strength of P-15 are promising to exhibit higher energy storage properties.

Figure 4 shows the P-E loop of the PMMA/P(VDF-HFP) composites, and the test step is 250 kV/cm until the film is broken. All the composites could keep good linearity of the PMMA matrix. The difference is mainly in the max electric field due to different breakdown strength. For instance, the max electric field of PMMA and P-15 is 4500 kV/cm and 3000 kV/cm, respectively. It should be noted that the breakdown strength results are commonly higher than those of P-E loop results. The breakdown strength of PMMA and P-15 is 4718 kV/cm and 4080 kV/cm, respectively. This is mainly attributed to the electrode area of P-E (1.44 cm²) being much bigger than that of 0.314 cm² of breakdown strength. In this paper, the use of big electrodes for P-E has two reasons. On the one hand, our purpose is aim to find a usable material. On the other hand, we found that the little electrode area would introduce many errors, which will cause the experimental results to be misestimated. The effective dielectric constant ϵ_r of linear materials can be calculated by Eq. (1,2), where D is the electric displacement, E is the applied field and ϵ_0 is the vacuum dielectric constant, P is the

Fig. 4 P-E loops of (a) PMMA, (b) P-5, (c) P-10, (d) P-15 and (e) P-20; (e) Pmax and Pr



polarization [21]

$$\epsilon_r = \frac{1}{\epsilon_0} \cdot \frac{dD}{dE} \tag{1}$$

$$D = \epsilon_0 E + P \tag{2}$$

As for the big electrode in this paper, ϵ_r can be calculated by the P and E. For P-15, the Pmax is $2.2 \mu C/cm^2$, so the ϵ_r under 4500 kV/cm is 4.9 which is consistent with the value measured with dielectric spectroscopy (4.3). A high field will drive more dipole switching to generate polarization which causes a higher ϵ_r under the high field. However, for small electrodes such as 2 mm diameter, the P_{max} of pristine PMMA is about $5 \mu C/cm^2$ at 3500 kV/cm, so the calculated ϵ_r is 14.3, even 3 times than its dielectric spectroscopy results [22]. The remanent polarization P_r still remains at a low level, as shown in Fig. 4f.

The energy storage properties such as charged energy density and efficiency are shown in Fig. 5. P-15 presents the largest enhanced discharged energy density $4.42 J/cm^3$ among all samples, which is caused by the higher dielectric constant and higher breakdown strength. Because of the high electric field, the energy density of P-15 is 143% higher than that of $1.82 J/cm^3$. Moreover, the efficiency of P-15 at 4500 kV/cm is 83.4%, and the superiority of linear PMMA is still maintained at high fields. It should be noted that the absolute value of the efficiency decrease from 500 kV/cm to 4500 kV/cm is very low. For instance, the efficiency of P-15 at 500 kV/cm

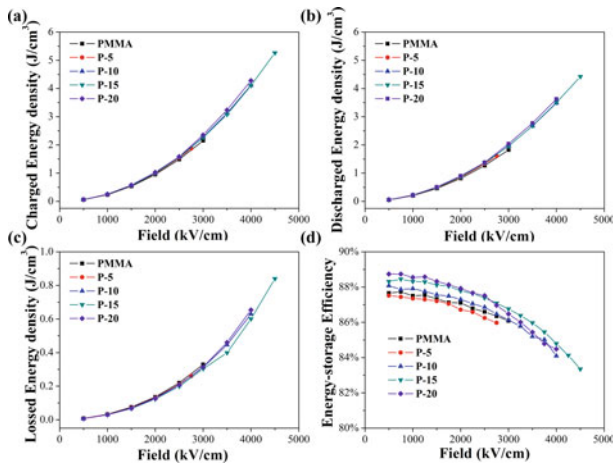


Fig. 5 Energy storage properties of the composites

and 4500 kV/cm is 88.7% and 83.4%, respectively. The absolute decline is 5.3%, indicating a very excellent linear retention rate. This also presents that there are low ferroelectric loss and conduction loss (a major source of efficiency decline) of the composite film [23]. Further work will focus on improving the initial efficiency (at the low field) of the PMMA matrix through purification or copolymerization.

4 Conclusion

In summary, a linear polymer PMMA composite for high energy storage is fabricated through a simple solution casting method. The experimental results confirm that PMMA and P(VDF-HFP) exhibit good compatibility, and could combine the advantages of a high dielectric constant for P(VDF-HFP) and high efficiency for PMMA. After introducing a proper proportion of ferroelectric P(VDF-HFP), a high energy density of 4.43 J/cm^3 could be reached, while that of pristine PMMA is only 1.82 J/cm^3 . Moreover, the efficiency of P-15 is still maintained at 83.4% under 4500 kV/cm.

Acknowledgements The financial support of this work by the University Natural Science Research Project of Jiangsu Province (Grant No. 19KJB470035), the China Postdoctoral Science Foundation (Grant No. 2022MD713827) and the National Natural Science Foundation of China (Grant No. 62201231 & 61971112) is greatly appreciated.

References

1. Whittingham, M.S.: Materials challenges facing electrical energy storage. *MRS Bull.* **33**(4), 411–419 (2008)
2. Jiang, Y., Shen, Z., Zhang, X.: Ferroelectric polymers and their nanocomposites for dielectric energy storage applications. *APL materials.* **9**, 4020905 (2021)
3. Zhou, Y., Wang, Q.: Advanced polymer dielectrics for high temperature capacitive energy storage. *J. Appl. Phys.* **127**(24), 240902 (2020)
4. Zhang, G.Q., Li, Q., Allahyarov, E., Li, Y., Zhu, L.: Challenges and opportunities of polymer nanodielectrics for capacitive energy storage. *ACS Appl. Mater. Interfaces.* **13**(32), 37939–37960 (2021)
5. Zha, J.-W., Zheng, M.-S., Fan, B.-H., Dang, Z.-M.: Polymer-based dielectrics with high permittivity for electric energy storage: a review. *Nano Energy* **89**, 106438 (2021). <https://doi.org/10.1016/j.nanoen.2021.106438>
6. Chu, B., et al.: A dielectric polymer with high electric energy density and fast discharge speed. *Science* **313**(5785), 334–336 (2006)
7. Guo, M.F., et al.: High-energy-density ferroelectric polymer nanocomposites for capacitive energy storage: enhanced breakdown strength and improved discharge efficiency. *Mater. Today* **29**, 49–67 (2019)
8. Guan, F., Pan, J., Wang, J., Wang, Q., Zhu, L.: Crystal orientation effect on electric energy storage in poly(vinylidene fluoride-co-hexafluoropropylene) copolymers. *Macromolecules* **43**(1), 384–392 (2010)
9. Tong, H., et al.: Sulfonyl-containing polyimide dielectrics with advanced heat resistance and dielectric properties for high-temperature capacitor applications. *Macromol. Mater. Eng.* **304**(4), 1800709 (2019)
10. Zhu, L.: Exploring strategies for high dielectric constant and low loss polymer dielectrics. *J. Phys. Chem. Lett.* **5**(21), 3677–3687 (2014)
11. Sun, S., et al.: Achieving concurrent high energy density and efficiency in all-polymer layered paraelectric/ferroelectric composites via introducing a moderate layer. *ACS Appl. Mater. Interfaces* **13**(23), 27522–27532 (2021)
12. Kang, S.J., et al.: Printable ferroelectric PVDF/PMMA blend films with ultralow roughness for low voltage non-volatile polymer memory. *Adv. Func. Mater.* **19**(17), 2812–2818 (2009)
13. Chu, B.J., Zhou, Y.: Energy storage properties of PVDF terpolymer/PMMA blends. *High Volt.* **1**(4), 171–174 (2016)
14. Mohamadi, S., SharifiSanjani, N.: Effect of thermal annealing on the crystalline structure of PVDF/PMMA-modified graphene nanocomposites. *J. Macromol. Sci. Part A* **55**(11–12), 775–784 (2018). <https://doi.org/10.1080/10601325.2018.1528848>
15. Meng, N., Zhu, X.J., Mao, R., Reece, M.J., Bilotti, E.: Nanoscale interfacial electroactivity in PVDF/PVDF-TrFE blended films with enhanced dielectric and ferroelectric properties. *J. Mater. Chem. C* **5**(13), 3296–3305 (2017)
16. Nie, R.P., et al.: PVDF/PMMA dielectric films with notably decreased dielectric loss and enhanced high-temperature tolerance. *J. Polym. Sci. Pt. B-Polym. Phys.* **57**(16), 1043–1052 (2019)
17. Lu, X., et al.: High energy density with ultrahigh discharging efficiency obtained in ceramic-polymer nanocomposites using a non-ferroelectric polar polymer as matrix. *Nano Energy* **70**, 104551 (2020)
18. Zhou, Y., et al.: Gradient dielectric constant sandwich-structured BaTiO₃/PMMA nanocomposites with strengthened energy density and ultralow-energy loss. *Ceram. Int.* **47**(4), 5112–5122 (2020)
19. Faria, L.O., Moreira, R.L.: Structural and kinetic transitions in P(VDF–TrFE)/PMMA blends. *Polymer* **40**(16), 4465–4471 (1999). [https://doi.org/10.1016/S0032-3861\(98\)00686-7](https://doi.org/10.1016/S0032-3861(98)00686-7)
20. Prateek, B.R., Siddiqui, S., Garg, A., Gupta, R.K.: Significantly enhanced energy density by tailoring the interface in hierarchically structured TiO₂-BaTiO₃-TiO₂ Nanofillers in PVDF-based thin-film polymer nanocomposites. *ACS Appl. Mater. Int.* **11**(15), 14329–14339 (2019)

21. Li, B., Yuan, M.X., Zhang, S.H., Rajagopalan, R., Lanagan, M.T.: Abnormal high voltage resistivity of polyvinylidene fluoride and implications for applications in high energy density film capacitors. *Appl. Phys. Lett.* **113**(19), 5 (2018)
22. Chen, J., Wang, Y., Chen, W.: Excellent comprehensive energy storage capabilities achieved in linear polymer composites via inserting acrylic rubber dielectric elastomers. *J. Mater. Chem. C* **9**(14), 5000–5007 (2021)
23. Khanchaitit, P., Han, K., Gadinski, M.R., Li, Q., Wang, Q.: Ferroelectric polymer networks with high energy density and improved discharged efficiency for dielectric energy storage. *Nat. Commun.* **4**, 2845 (2013)

Thermal Circuit Model of Oil-Immersed Distribution Transformer in Unbalanced Operation



Yuqin Ding, Zhonglin Xu, Hengchi Ma, Kun Yuan, Yongpeng Yang, Haoxia Lei, Yang Feng, and Ye Tian

Abstract This paper mainly focuses on two subjects. One is to establish the thermal circuit model of oil-immersed distribution transformer to calculate the hot spot temperature of transformer in unbalanced operation. To validate the model, special temperature rise test is designed to simulate the unbalanced operation of transformer with the Dyn11 type oil-immersed distribution transformer in different capacity works as the test objects. The other one is to do investigation on the change rule of nonlinear thermal resistance, through the analysis of large amount of data, the empirical value of the hot spot to oil and oil to ambient thermal resistance nonlinearity exponent for ONAN oil-immersed distribution transformer in cold start is proposed. Besides, through further analysis, the thermal resistance coefficient, which given the symbol M , is defined for the calculation of thermal resistance under different operating conditions, and the approach to get M is also introduced. M is a parameter that reflects the intrinsic structure of transformer. The proposed M makes the transformer parameters required for modeling significantly decrease, which further simplifies the modeling and calculation process for thermal circuit model method. The verification of experimental data shows the accuracy and convenience of the thermal circuit model based on M .

Keywords Oil-Immersed Distribution Transformer · Thermal Circuit Model · Unbalanced Temperature Rise Test · Nonlinear Thermal Resistance · Nonlinearity Exponent · Thermal Resistance Coefficient

Y. Ding (✉) · Z. Xu · H. Ma · K. Yuan · Y. Yang · H. Lei · Y. Feng · Y. Tian
Chengdu Power Supply Company, State Grid Sichuan Power Supply Company, Chengdu 610041, Sichuan, China
e-mail: dingyuqindeng@163.com

© Beijing Paiké Culture Commu. Co., Ltd. 2023
X. Dong et al. (eds.), *The proceedings of the 10th Frontier Academic Forum of Electrical Engineering (FAFEE2022)*, Lecture Notes in Electrical Engineering 1054, https://doi.org/10.1007/978-981-99-3408-9_45

1 Introduction

Oil-immersed distribution transformers are essential for the power system. There are various loads applied on the distribution side, which leads to the uneven distribution of loads for the three phases, that is, the imbalance in operating conditions of transformers. Unbalanced operation would exacerbate the transformer losses, induce local overheating and even cause burnout [1]. In order to protect the transformers from severe overheating, it is necessary to investigate the characteristics of temperature distribution when the transformer works under unbalanced operating conditions.

As one of the most significant parameter needed to characterize the internal thermal state of the transformer, the hot spot temperature is also the deciding factor in transformer loading [2]. For the safe operation of transformers, it is often necessary to measure the temperature of the hot spot during operation of the transformer. The thermal circuit model, which is based on thermoelectric analogy theory, has been widely applied to calculate the hot spot temperature of transformers, showing the advantages like high accuracy, easy calculation and excellent real-time performance [3–7].

The key to applying thermal circuit model is the establishment of a model that can not only reflect the heating and cooling process in the transformer but also enable the accurate calculation of various model parameters such as thermal resistance. When the transformer is in unbalanced operation, the heat transfer process is made more complex by the interphase thermal coupling effect. In this paper, the thermal circuit model of oil-immersed distribution transformers is established under the context of unbalanced operation, which is based on the actual heat transfer process. To validate the model, the thermal test is performed to simulate the unbalanced operation of distribution transformers. Besides, a further investigation is conducted into the pattern of changes in nonlinear thermal resistance, including the proposed empirical value of thermal resistance nonlinearity exponent and the definition of thermal resistance coefficient, which is denoted as M . All of these findings have contributed to simplifying the modeling and computational processes.

2 The Thermal Circuit Model of Transformer in Unbalanced Operation

When transformers work in balanced operation, the heat generation and dissipation conditions of each phase are basically the same. Therefore, the three-phase transformer can be simplified as a single-phase transformer when calculate the hot spot temperature using the thermal circuit model method, as shown in Fig. 1 [8].

Where, q_{ld} is the heat generated by load losses; q_{fe} is the heat generated by core losses; C_{wd} is thermal capacitance of the winding; C_{fo} is thermal capacitance of the core and oil; θ_{hs} is the hot spot temperature; θ_{oil} is the top oil temperature; θ_{amb} is the ambient temperature; R_{hs_oil} is the hot spot to oil thermal resistance; R_{oil_amb}

Fig. 1 The thermal circuit model of transformer in balanced operation

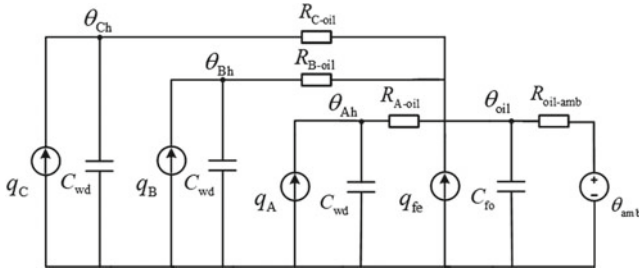
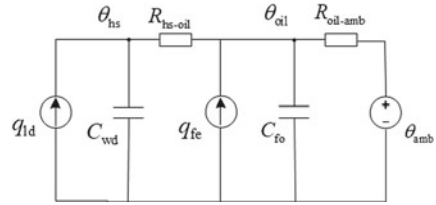


Fig. 2 The thermal circuit model of transformer in unbalanced operation

is the oil to ambient thermal resistance. Since the core and winding are separated through oil-paper insulation, the core losses have no immediate impact on winding temperature but oil temperature. For this reason, the heat sources are deployed for the model in a way as shown in Fig. 1.

When a transformer is in unbalanced operation, the heating conditions vary between different phases. The heat exchange between phases with the transformer oil functions as the main medium and the difference in the losses causes the thermal resistances of each phase to vary. With this taken into account, the thermal circuit model of transformer in unbalanced operation is established, as shown in Fig. 2.

Where, $q_{A(B/C)}$ is the load losses of A(B/C) phase; $\theta_{A(B/C)h}$ is the hot spot temperature in A(B/C) phase; $R_{A(B/C)_{oil}}$ is the hot spot of A(B/C) phase to oil thermal resistance.

Analogy to Kirchoff’s law, (1) is obtained according to Fig. 2 and we can get the hot spot temperature of each phase by solving the differential equation.

$$\begin{cases} \frac{d\theta_{Ah}}{dt} = \frac{1}{C_{wd}} \left(-\frac{\theta_{Ah}}{R_{A_{oil}}} + \frac{\theta_{oil}}{R_{A_{oil}}} + q_A \right) \\ \frac{d\theta_{Bh}}{dt} = \frac{1}{C_{wd}} \left(-\frac{\theta_{Bh}}{R_{B_{oil}}} + \frac{\theta_{oil}}{R_{B_{oil}}} + q_B \right) \\ \frac{d\theta_{Ch}}{dt} = \frac{1}{C_{wd}} \left(-\frac{\theta_{Ch}}{R_{C_{oil}}} + \frac{\theta_{oil}}{R_{C_{oil}}} + q_C \right) \\ \frac{d\theta_{oil}}{dt} = \frac{1}{C_{fo}} \left[\frac{\theta_{Ah}}{R_{A_{oil}}} + \frac{\theta_{Bh}}{R_{B_{oil}}} + \frac{\theta_{Ch}}{R_{C_{oil}}} - \theta_{oil} \left(\frac{1}{R_{A_{oil}}} + \frac{1}{R_{B_{oil}}} + \frac{1}{R_{C_{oil}}} + \frac{1}{R_{oil_{amb}}} \right) + \frac{\theta_{amb}}{R_{oil_{amb}}} + q_{fe} \right] \end{cases} \tag{1}$$

3 The Calculation Method of Model Parameters

3.1 The Losses

To solve (1) the parameters, which includes the losses and thermal resistances and thermal capacitance, should be solved firstly.

The only internal heat source of the transformer is the losses caused during operation, the core losses q_{fe} and the load losses q_{ld} . The core losses under rated operating conditions can be determined through the no-load test, with the iron losses being proportional to the square of current within a certain range. Therefore, the core losses under different operating conditions can be calculated by (2).

$$q_{fe} = q_{Rfe}(I/I_R)^2 \quad (2)$$

where q_{Rfe} is the core losses under rated conditions, W; I_R is the rated current of transformer, A; I is the load current, A.

The load losses include winding loss q_{wd} and additional loss q_{ad} . The former is the Joule heating of the winding and the latter is mainly eddy loss and stray loss. All of the losses are correlated with transformer loading and temperature, while the losses under rated operating conditions can be determined through the short-circuit test. Under different operating conditions, winding loss and additional loss are calculated by (3):

$$\begin{cases} q_{wd} = q_{Rwd}(273 + \theta)/(273 + \theta_R)(I/I_R)^2 \\ q_{ad} = q_{Rad}(273 + \theta_R)/(273 + \theta)(I/I_R)^2 \end{cases} \quad (3)$$

where q_{Rwd} is the winding losses in the rated operating conditions, W; q_{Rad} is additional losses in the rated operating conditions, W; θ is the average winding temperature and is estimated according to [5], °C; θ_R is the winding temperature in the short-circuit test, °C.

3.2 The Thermal Capacitance

Thermal capacitance equals to the product of mass and specific heat capacity. Therefore, C_{wd} and C_{fo} in the model can be calculated by (4) and (5)

$$C_{wd} = \frac{m_{wd}C_{p_Cu}}{3} \quad (4)$$

$$C_{fo} = m_{fe}c_{p_fe} + 0.85m_{oil}c_{p_oil} + 0.67m_{tank}c_{p_fe} \quad (5)$$

where m_{wd} , m_{fe} , m_{oil} , and m_{tank} is the mass of the winding, the core, the transformer oil and the tank, kg; C_{p_Cu} , C_{p_fe} , and C_{p_oil} is the specific heat capacity of the winding, the core and the transformer oil, J·(kg/m³). The correction factor 0.85 and 0.67 is empirical and is proposed according to the previous research [8].

3.3 The Thermal Resistances

The thermal resistances in the model consist of hot spot to oil thermal resistances (R_{A_oil} , R_{B_oil} , and R_{C_oil}) and oil to environment thermal resistance (R_{oil_amb}). The hot spot to oil thermal resistances are related to many factors such as the material and layout of the transformer winding, the structure of the oil ducts and the speed of the oil flow. Usually, these parameters are difficult to obtain and the structural differences between transformers cannot be ignored, so it is difficult to solve these thermal resistances analytically. In this paper, the hot spot to oil thermal resistances are solved through the results of temperature rise tests which simulate the unbalanced working condition of the transformers, and the variation law of which are explored.

The thermal resistance between oil and the ambient is the series connection of the transformer oil's conduction thermal resistance, the natural convection thermal resistance between the oil and the inner wall of the tank, the tank's conduction thermal resistance and the natural convection thermal resistance of the air. Among them, the last one is much larger than other parts, so we focus on the analysis of the natural convection thermal resistance of air. In this paper, it is solved based on the experimental data and the theory of heat transfer. The variation law of this kind of thermal resistance is also explored.

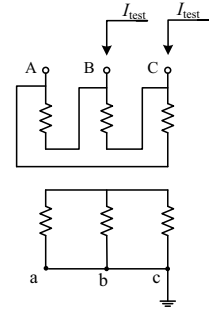
4 The Thermal Resistance Calculation

4.1 The Unbalanced Temperature Rise Test

In order to calculate the thermal resistance of each part and evaluate the accuracy of the model, the temperature rise test of oil-immersed distribution transformer, hereafter referred to as unbalanced temperature rise test, was carried out under the context of unbalanced operation with Dyn11 type column transformers as the experimental objects. Figure 3 shows the wiring diagram for the temperature rise test that satisfies the condition of unbalanced operation.

There are multiple thermocouples embedded in the transformers to monitor the temperature and measure the hot spot temperature accurately. Under the experimental conditions, A-phases and C-phase are completely symmetrical, with the current in the B-phase being about twice that in the other two phases. With the 400 kVA, 315 kVA,

Fig. 3 The temperature rise test wiring diagram



and 100 kVA transformers as the experimental objects, the unbalanced temperature rise test was conducted at different test currents.

The rated current of the 400 kVA transformer is 23.1/577.4 A. And the current I_{test} in Fig. 3 were set as 9 A, 11.5 A, 21 A, 23 A in the temperature rise tests. The measured hot spot temperature rise during different current tests is shown in Fig. 4. Where $\Delta\theta_A$ and $\Delta\theta_B$ denotes to the hot spot temperature rise in A-phase and B-phase respectively. By fitting the curve in Fig. 4, it is found that the change of the hot spot temperature rise with time can be expressed by two time constants. Equation (6) shows the change of the hot spot temperature rise of A and B phases with time when I_{test} equals to 23 A:

$$\begin{cases} \Delta\theta_A = 35.8 - 8.3e^{-\frac{t}{28.7}} - 27.2e^{-\frac{t}{178}} \\ \Delta\theta_B = 55 - 28e^{-\frac{t}{15}} - 27e^{-\frac{t}{180}} \end{cases} \quad (6)$$

According to the definition in GB 1094.2–1996 [9], it can be deduced that the constant term in (6) refers to the steady-state temperature rise; the larger time constant in the exponential term reflects the heat capacity of the oil and the coefficient of which is the top oil temperature rise in steady-state; the smaller time constant reflects the

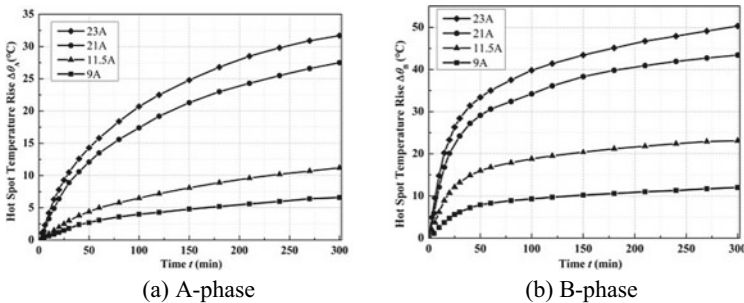


Fig. 4 The hot spot temperature rise change with time of the 400 kVA transformer

delay of temperature varies between the hot spot and the oil and the coefficient of which is the temperature difference between the hot spot and oil in steady-state.

4.2 The Parameters Calculation Results

The thermal resistance of each part under different experimental conditions can be calculated by combining the definition of thermal resistance and the steady-state temperature rise of the hot spot and top oil obtained from the temperature rise test (6), and the calculation formula of the thermal resistances are given by (7).

$$R_{A(B)_{oil}} = \Delta\theta_{A(B)_{oil}}/q_{A(B)}, R_{oil_{amb}} = \Delta\theta_{oil_{amb}}/q_t \tag{7}$$

where q_t is the total losses, which is the sum of core losses and load losses, W; $\Delta\theta_{A(B)_{oil}}$ refers to the temperature gradient between hot spot in A(B) phase and top oil, °C; $\Delta\theta_{oil_{amb}}$ refers to the temperature gradient between top oil and ambient, °C.

Table 1 shows the losses of 400 kVA transformer under different testing condition, and Table 2 shows the thermal resistances.

The losses and thermal resistances in the table above are substituted into (1). Then, the temperature rise of hot spot is calculated by solving the equation with Runge–Kutta method. The calculated temperature rise of the hot spot is compared with the measured values, as shown in Fig. 5.

It should be noted that there is only calculated top oil temperature rise presented in Fig. 5 as the measured top oil temperature in different regions are quite different when transformers in unbalanced operation so it is meaningless to present the measured value.

Table 1 The losses of 400kVA transformer under different testing conditions

I/A	q_{Cu_A}/W	q_{Cu_B}/W	q_{fe}/W	q_t/W
9	66.8	267.3	14.9	416
11.5	107	428.3	23.5	665.8
21	363.1	1408.3	72.3	2206.8
23	435.8	1719.7	77.7	2669

Table 2 The thermal resistances of 400kVA transformer under different testing conditions

I/A	$R_{A_{oil}}/(^{\circ}C \cdot W^{-1})$	$R_{B_{oil}}/(^{\circ}C \cdot W^{-1})$	$R_{oil_{amb}} / (^{\circ}C \cdot W^{-1})$
9	0.022	0.028	0.0152
11.5	0.0246	0.0266	0.0167
21	0.0193	0.017	0.0106
23	0.019	0.0163	0.0102

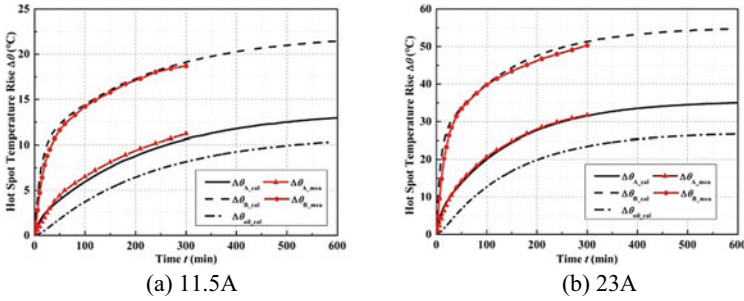


Fig. 5 Comparison of the calculated hot spot temperature rise with the measured value

As shown in Fig. 5, the measured hot spot temperature rises, the calculated value remains unchanged under different operating conditions and the steady-state values are comparable. Despite the thermal resistance caused by the measured temperature rise, the accuracy of other parameters such as thermal capacitance and losses also affects the calculation result of hot spot temperature rise. Therefore, the comparison result can be used to reflect the accuracy of the whole calculation process.

The calculated hot spot temperature rise is also in good agreement with the measured value for 315 kVA and 100 kVA transformers.

5 The Variation Law of Thermal Resistances

5.1 The Nonlinearity Exponent of Thermal Resistances

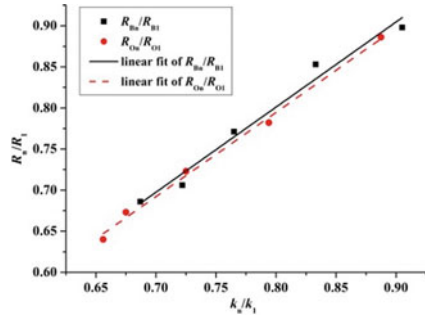
The hot spot to oil thermal resistance is mainly the natural convection thermal resistance of the oil, which is inversely proportional to the product of the area and the convective heat dissipation coefficient. According to the theory of heat transfer, the coefficient of heat convection h can be calculated by (8)

$$h = M_1 \left(\frac{\Delta\theta}{\mu_{oil}} \right)^n \tag{8}$$

where $\Delta\theta$ is the temperature gradient in $^{\circ}\text{C}$; μ_{oil} is the viscosity of the oil in Pa·s; n is the nonlinearity exponent representing the nonlinear characteristic of thermal resistance and is fully empirical; M_1 is a transformer structure-related parameter, with small changes in temperature and can be regarded as a constant. The oil viscosity can be calculated according to (9) [10].

$$\mu_{oil} = 0.0000013575e^{\frac{2797.3}{\theta_{oil} + 273}} \tag{9}$$

Fig. 6 The variation law of thermal resistances



It can be implied that the thermal resistances in different oil temperature T_1 and T_2 (R_{T1} and R_{T2}) satisfy the following relationship:

$$R_{T2}/R_{T1} = h_1/h_2 = (\mu_2/\Delta\theta_2)^n/(\mu_1/\Delta\theta_1)^n \tag{10}$$

As mentioned before, the main part of the oil to ambient thermal resistance is the natural convection thermal resistance of the air. And the relation of thermal resistances in different ambient temperature also behaves as shown in (10) with the nonlinearity exponent set as m .

This paper statistics and analyze a large amount of data, and the result is that: for distribution transformer in cold start, the nonlinearity exponent for winding to oil thermal resistance is 0.2 and is 0.3 for oil to environment thermal resistance. In the following content, this conclusion will be elaborated based on the relevant data of 400 kVA transformer. Defining k_{oil} and k_{air} as (11):

$$k_{oil} = (\mu_{oil}/\Delta\theta_{ht_oil})^n, k_{air} = (\mu_{air}/\Delta\theta_{oil_amb})^m \tag{11}$$

where μ_{air} is the viscosity of air, Pa-s; $\Delta\theta_{ht_oil}$ is the temperature gradient between hot spot and top oil, °C. $k_1 \sim k_6$ represent k 's value when I_{test} is 9 A, 11.5 A, 15 A, 18 A, 21 A and 23 A respectively and $R_1 \sim R_6$ is the thermal resistance in the corresponding test current. Substituting $n = 0.2$ and $m = 0.3$ when calculating k_{oil} and k_{air} . In Fig. 6, the abscissa is k_n/k_1 and the ordinate is R_n/R_1 . The fitting curve in the graph is a straight line with a slope of one and a zero crossing. Therefore, it is obvious that the relations of thermal resistance at different temperatures in (10) is satisfied when n is 0.2 and m equals 0.3.

5.2 The Thermal Resistance Coefficient

The calculation of convection thermal resistance is shown in (12) which can be derived from (8).

$$R = M(\mu/\Delta\theta)^n \tag{12}$$

where $M = 1/A/M_1$, which is defined as the thermal resistance coefficient and A is the area of heat convection. M is a parameter that is related to the structure of transformer and is a constant for transformers in specific type. Apparently, it is easier to calculate the thermal resistance under different operating condition with the premise that the value of M is known, which would reduce the transformer parameters required in the application of the thermal model significantly and automatically make the modeling and calculation process simplified. Therefore, it is of importance to make research on M . And M 's value of 100 kVA, 315 kVA and 400 kVA transformers are calculated and shown in Table 3.

Where M_o is the coefficient of oil to ambient thermal resistance when transformer in balanced operation; M_o' is the coefficient of oil to ambient thermal resistance when transformer in unbalanced operation; M_h is the coefficient of hot spot to oil thermal resistance when transformer in balanced operation; M_A and M_B is the coefficient of hot spot to oil thermal resistance when transformer in unbalanced operation which corresponds to R_{A_oil} and R_{B_oil} in Fig. 2. It can be seen from the Table 3 that the values of M_o and M_o' are close, that is, the thermal resistance coefficient between the transformer oil and the ambient under different operating conditions remain unchanged. However, there is no obvious mathematical relationship between M_A , M_B , and M_h . In summary, the data of the regular transformer temperature rise test can be used to calculate M_o' ; M_A and M_B can be calculated through an unbalanced temperature rise test. Finally, the hot spot temperature and top oil temperature of transformer under unbalanced operation can be obtained by solving (13)

$$\begin{cases} \frac{d\theta_{Ah}}{dt} = \frac{1}{C_{wd}} \left[-\frac{(\theta_{Ah}-\theta_{oil})^{n+1}}{M_A\mu_{oil}^n} + q_A \right] \\ \frac{d\theta_{Bh}}{dt} = \frac{1}{C_{wd}} \left[-\frac{(\theta_{Bh}-\theta_{oil})^{n+1}}{M_B\mu_{oil}^n} + q_B \right] \\ \frac{d\theta_{Ch}}{dt} = \frac{1}{C_{wd}} \left[-\frac{(\theta_{Ch}-\theta_{oil})^{n+1}}{M_C\mu_{oil}^n} + q_C \right] \\ \frac{d\theta_{oil}}{dt} = \frac{q_{fe}}{C_{fo}} + \frac{1}{C_{fo}} \left[\frac{(\theta_{Ah}-\theta_{oil})^{n+1}}{M_A\mu_{oil}^n} + \frac{(\theta_{Bh}-\theta_{oil})^{n+1}}{M_B\mu_{oil}^n} + \frac{(\theta_{Ch}-\theta_{oil})^{n+1}}{M_C\mu_{oil}^n} - \frac{(\theta_{oil}-\theta_{amb})^{m+1}}{M_O\mu_{air}^m} \right] \end{cases} \tag{13}$$

It should be noted that μ_{oil} is a function of oil temperature, and (9) needs to be taken into account when solving (13). It can be seen from (13) that when the parameter M is introduced in the application of the thermal model, the transformer parameters required calculating the hot spot temperature only consists two types. One is the thermal capacitance related parameters, mass and specific heat capacity included.

Table 3 M ' Value of transformers in different capacity

capacity/kVA	M_o	M_o'	M_h	M_A	M_B
100	1.72	1.67	0.06	0.127	0.129
315	1.03	0.99	0.0353	0.0736	0.133
400	0.72	0.735	0.0408	0.0788	0.0877

The other one is the losses related parameters, resistance and current included. In a word, the introduced M greatly reduces the transformer parameters required in the application of thermal circuit model method.

5.3 Verification

The experimental data on temperature rise of 200kVA transformer, whose rated current is 11.55/288.7 A, is used to verify the above model. Table 4 shows the parameters related to the transformer regular temperature rise test and the value of M_o . Table 5 shows the parameters related to the unbalanced temperature rise and the value of M_A and M_B , as calculated under the condition that the I_{test} is equal to 12.06A. Then, the hot spot temperature under different conditions is obtained by inputting the value of M_o , M_A , and M_B into (13). Figure 7 shows the results of comparison between the calculated hot spot temperature and the measurement value. Apparently, the results are sufficient to validate the successful use of thermal resistance coefficient, that is, the symbol M used in this paper.

Table 4 Regular temperature rise test related parameters and the value of M_o for 200kVA transformer

q_l/W	q_t/W	$\Delta\theta/^\circ C$	R_{oil_amb}	M_o
2124	2238	35	0.0158	1.2

Table 5 Unbalanced temperature rise test related parameters and the value of M_A and M_B for 200kVA transformer

	q_l/W	$\Delta\theta/^\circ C$	R_{hs_oil}	$M_{A/B}$
phase A	258.2	7.2	0.0279	0.073
phase B	1032.8	27	0.0262	0.088

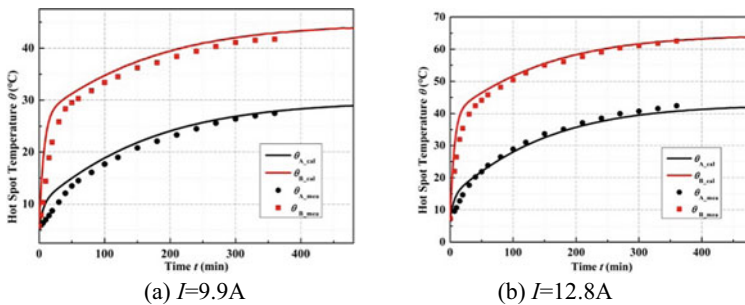


Fig. 7 The comparison of calculated hot spot temperature with the measured value

6 Conclusion

In the present study, the thermal circuit model of oil-immersed distribution transformers is established under the context of unbalanced operation and then validated through the unbalanced temperature rise experiment. Besides, the nonlinear characteristics of thermal resistance are further studied. Through data analysis, it is concluded that the nonlinearity exponent of distribution transformer in cold start is 0.2 for hot spot to oil thermal resistance and is 0.3 for oil to ambient thermal resistance. At the same time, the concept of thermal resistance coefficient is proposed and denoted as M , for the calculation of thermal resistance under different working conditions. The thermal resistance coefficient can be used to reflect the intrinsic structure of the transformer. The coefficient M of the thermal resistance between oil and environment can be obtained through the regular temperature rise test while the hot spot to oil one can be calculated through an unbalanced temperature rise test. With the thermal resistance coefficient obtained, it is easy to solve the hot spot temperature and top oil temperature of transformer under different working conditions. Due to the introduction of M , the model is made more concise.

References

1. Yang, Y.L., Wang, F.Q.: Additional loss and voltage deviation caused by unbalanced operation of distribution transformer and countermeasures. *Power Syst. Technol.* **28**(8), 73–76 (2004). (in Chinese)
2. IEEE Guide for Loading Mineral-oil-Immersed Power Transformers: IEEE **C57**, 91 (1995)
3. Swift, G., Molinski, T.S., Lehn, W.: A fundamental approach to transformer thermal modeling. I. theory and equivalent circuit. *IEEE Trans. Power Deliv.* **16**(2), 171–175 (2001)
4. Susa, D., Lehtonen, M.: Dynamic thermal modeling of power transformers: further development-part II. *IEEE Trans. Power Deliv.* **21**(4), 1971–1980 (2006)
5. Luo, H., Lai, W., Jiang, G.: Modification and experimental verification of oil-immersed transformer thermal circuit model. *High Volt. Appar.* **55**(1), 0220–0225 (2019). (in Chinese)
6. Ding, Y., Zhang, Q., Gao, M.: Distributed thermal circuit model of oil-immersed distribution transformers. *High Volt. Eng.* **45**(3), 968–974 (2019). (in Chinese)
7. Du, J., Huang, X., Guo, S.: Research on hot spot location of transformer winding based on thermal circuit model. *Transformer* **58**(3), 44–49 (2021). (in Chinese)
8. Blume, L., Boyajian, A., Camilli, G.: *Transformer Engineering*, 1st edn. Wiley, New York (1938)
9. Loading guide for oil-immersed power transformers, GB/T 15164–1994 (1994). (in Chinese)
10. Hao, Y., Shi, H., Fan, R.: Study on temperature rise of distribution transformer under overload condition based on dynamic thermal circuit model. *Transformer* **57**(12), 22–26 (2020). (in Chinese)

Improved Transformer Fault Diagnosis Method Based on Sparrow Search Algorithm-Optimized BP Network and Duval Pentagon



Shicheng Zhang, Xiaofeng Tao, Hong Ding, Chunyan Lu,
and Miaoxuan Shan

Abstract Accurate diagnosis of the transformer fault type can effectively improve the stability of the power system. In order to improve the accuracy of transformer fault type diagnosis and solve the problem that the fault area division of the Duval pentagon method is too absolute, a combination method based on Duval pentagon 1 and SSA-BP is proposed. Firstly, the Duval pentagon method is used to extract the characteristic gas characteristics, and then SSA-BP is input for fault diagnosis. The final experiment shows that the correct rate of the diagnostic effect of the combined method reaches 89.6%, which can effectively complete the diagnosis of transformer fault types and provide reference to the operation and maintenance personnel.

Keywords Duval pentagon · Sparrow search algorithm · BP neural network · Fault diagnosis · Transformer

1 Introduction

Transformers play an important role in the power system for the stable operation of the grid. Because of their high cost, they require regular inspection and maintenance to ensure proper operation, as damage can affect local electricity consumption. In the case of oil-immersed transformers, which are widely used today, the insulating oil will deteriorate and decompose to produce the corresponding gases depending on the situation. Previous studies have found that the gas decomposition during a transformer failure is closely related to the type of failure. Therefore, the dissolved gas analysis (DGA) method is currently the most applied, effective and widely studied method [1, 2] in transformer fault detection.

S. Zhang · X. Tao · H. Ding · C. Lu · M. Shan (✉)
NARI Group Corporation (State Grid Electric Power Research Institute), Nanjing 211106, China
e-mail: shan18252039798@163.com

© Beijing Paiké Culture Commu. Co., Ltd. 2023
X. Dong et al. (eds.), *The proceedings of the 10th Frontier Academic Forum of Electrical Engineering (FAFEE2022)*, Lecture Notes in Electrical Engineering 1054,
https://doi.org/10.1007/978-981-99-3408-9_46

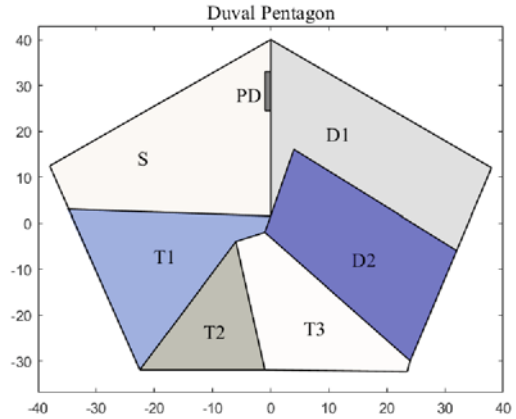
With the rapid development of artificial intelligence technology, the model combining techniques such as neural network [3, 4], extreme learning machine, support vector machine (SVM) and rough set with DGA method has been proved to be effective in improving the accuracy rate of transformer fault diagnosis. Li et al. [1] used an improved sparrow search algorithm (ISSA) optimized support vector machine (SVM) method for transformer fault classification and identification, which improved the correct rate; Wei et al. [2] proposed an improved BP network classification method for transformer faults; He et al. [5] established a quantum immune BP neural network (QIA-BP) method, which used QIA to optimize the parameters of the BP network. Then the transformer is diagnosed for faults, which effectively improves the accuracy of predicting faults. Benmahamed et al. [6] used a particle swarm algorithm optimized support vector machine (PSO-SVM) and K nearest neighbor algorithm (KNN) for the fault diagnosis method of the improved Duval pentagon method, which has relatively weak mining and global search capabilities compared to the sparrow search algorithm. Wang et al. [7] used the kernel principal-form analysis algorithm in Elman neural network to improve the diagnostic accuracy. It was found that the artificial intelligence method based on neural networks has received a lot of attention in transformer fault diagnosis due to its extremely strong self-learning capability, nonlinear relationship handling ability, and better robustness.

Duval pentagon is a graphical fault diagnosis method based on DGA proposed by Duval [6], which is widely used in engineering. The transformer will decompose H_2 , CH_4 , C_2H_4 , C_2H_6 , C_2H_2 and other gases when it fails. Since the decomposed gas is related to the fault type, the fault type of the transformer is displayed by calculating the population distribution relationship of the centroid on the pentagon. However, the Duval pentagon has the problem that the fault area is too absolute, and the judgment result is correct only when the transformer is faulty. Sparrow Search Algorithm (SSA) is a new type of swarm intelligence optimization algorithm which was proposed in 2020. The algorithm has strong local search ability and convergence.

In order to improve the accuracy of transformer fault diagnosis and solve the problem that fault division area of Duval pentagon is too absolute, a method based on Duval pentagon and SSA-BP is proposed. Firstly, the characteristic gas characteristics are extracted by Duval pentagon, and then the fault types are divided by the SSA-BP method. The final simulation experiment shows that the combined method proposed in this paper can effectively divide the fault types of transformers and provide reference for operation and maintenance personnel.

2 Duval Pentagon Method

The traditional methods for transformer fault diagnosis are Duval triangle and IEC triple ratio method, etc. Duval pentagon is a supplementary description method to analyze the DGA results, including Duval pentagon 1 and 2. Duval pentagon 1 classifies the fault types into: low temperature overheating (T1), medium temperature

Fig. 1 Duval pentagon 1

overheating (T2), high temperature overheating (T3), partial discharge (PD), low-energy discharge (D1), and high-energy discharge (D2). In addition to this, the Duval pentagon method considers faults in the S-domain of stray gases, i.e., when the transformer temperature is between 120° and 200° , the oil decomposes and produces some stray gases, such as CO [8]. Also the Duval pentagon 2 classifies the fault types in a more advanced way, including not only partial discharge (PD), low energy discharge (D1), high energy discharge (D2), but also high temperature superheat in oil only (T3-H), paper carbonation heat fault (C), low temperature heat fault (O), and stray gas fault (S). In this paper, we mainly use Duval 1 method to classify the faults according to the fault types in IEEE/IEC, and classify the medium temperature thermal faults and low temperature thermal faults as medium and low temperature faults. When using the Duval pentagon to calculate the center of mass, even if the gas concentration of one is 100% and the others are 0%, the location of the center of mass is calculated according to the formula and is restricted to the pentagon formed at 40% of the gas axis [8]. The graph of the Duval pentagon1 is shown in Fig. 1.

3 Sparrow Search Algorithm to Optimize BP Neural Network

3.1 Sparrow Search Algorithm

The sparrow search algorithm is a novel intelligent optimization algorithm proposed in 2020 [1]. Similar to other swarm intelligence methods such as genetic algorithm (GA) [9, 10] and particle algorithm (PSO) [11, 12], the sparrow search algorithm is inspired by sparrow foraging and with anti-predation. The optimal parameters are found by simulating the behavior of predation and anti-predation and continuously updating the position [13]. The sparrow search algorithm requires the existence of a

set of valid solutions in the search space, and the search is performed in the solution space according to the size of the adaptation value, by continuously updating the position of the solution until the optimal solution is found. Compared with traditional optimization algorithms, the sparrow search algorithm has fewer parameters and better local search capability. In the performance of the benchmark function, the stability, convergence speed, and the ability to avoid local optima outperform algorithms such as PSO [14].

3.2 BP Neural Network

The main structure of BP neural network consists of three parts: the input layer, the hidden layer, and the output layer. If the number of input neurons of the network is M and the number of output neurons is N , the neural network structure can be considered as a mapping from an M -dimensional Euclidean space to an N -dimensional Euclidean space [15]. The hidden node $s = 5$ is chosen according to the empirical formula as well as the simulation results.

The BP neural network training process is as follow:

Let the weight of the input to the hidden layer be ω_{ij} and the weight of the hidden to the output layer be ω_{jk} . The output, threshold and transfer function of the hidden layer are Y_j, θ_j, f_1 respectively. The threshold and transfer function of the output layer are θ_k, f_2 . Let the input sample be (x_k, b_k) where, $K \in \{1, 2 \dots N\}$, N is the number of input samples. According to the formula:

$$Y_j = f_1\left(\sum_{i=1}^n \omega_{ij}x_i - \theta_j\right) (i = 1, 2, \dots, n; j = 1, 2 \dots s) \tag{1}$$

$$Y_k = f_2\left(\sum_{j=1}^s \omega_{jk}b_j - \theta_k\right) (j = 1, 2, \dots, s; k = 1, 2 \dots m) \tag{2}$$

Get the output Y_j of the hidden layer nodes, and the network output Y_k .

The error of the output layer nodes is obtained from the expected value T_k :

$$\varphi_k = -(T_k - Y_k)Y_k(1 - Y_k) \tag{3}$$

Node errors in the hidden layer:

$$\varphi_j = Y_j(1 - Y_j)\sum_{k=1}^m \varphi_k\omega_{jk} \tag{4}$$

The gradient descent method is used to trim the weights that the error function E reaches the minimum result, The formula is as follow:

$$\Delta\omega = \eta \frac{\partial E}{\partial \omega} \tag{5}$$

Table 1 Sample number and distribution

Fault type	T1&T2	D1	D2	T3	PD
Fault Number	1	2	3	4	5
Number of case	28	42	79	108	52

η and ω represent the learning rate and weights. At the end of training, the test set is input to the network to obtain the predicted classification results.

4 Improved Fault Diagnosis Model Based on Duval's Pentagonal Method and SSA-BP

The experimental data are based on the dissolved gas data in the oil taken from the transformer operation at a site of the power grid company. A total of 309 sets of data were used, and the first 250 sets of data were used as the training set, and the remaining data were used as the test set. In order to verify the feasibility of the method, single Duval pentagon, SSA-BP and PSO-SVM are selected for comparison. The fault numbers and sample distribution are shown in Table 1:

The flowchart of the algorithm is shown in Fig. 2. First, the DGA gas data of the fault is processed by the David pentagon, and the centroid of each fault is obtained; training, the final output fault type.

The following graphs show the predicted results compared to the true results:

Figure 3, 4, and 5 show the diagnostic results of the three methods, and Table 2 and Table 3 show the comparison of the accuracy and recall of the three methods respectively. From Table 2, it can be seen that compared with the traditional Duval pentagon, Duval-SSA-BP improves the accuracy of fault type diagnosis by 9.1%. Compared with the supplementary method of PSO-SVM, the accuracy improves by 4.5%. From the perspective of accuracy, SSA-BP can effectively supplement the traditional Duval pentagon.

It can be seen from Table 3, for the fault types of medium and low temperature overheating, the diagnostic recall rate of the improved method based on Duval pentagon and SSA-BP is equal to that of Duval pentagon, which is slightly higher than Duval pentagon and Duval-PSO-SVM. For low-energy discharge fault types and high-energy discharge fault types, the diagnostic recall rate of Duval-SSA-BP is higher than the other two models. All three models are correctly diagnosed on the high temperature and overheating fault types. For the types of partial discharge faults, the fault boundary division of the traditional Duval pentagon method is too absolute, so the overall diagnostic recall rate is lower than the other two models.

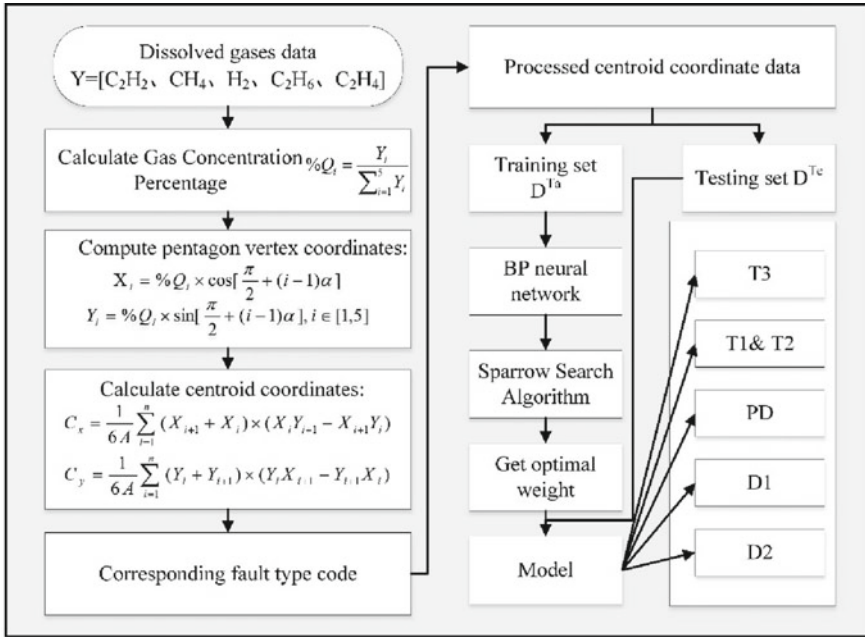


Fig. 2 Algorithm Flow Diagram

Fig. 3 The prediction results of the improved method based on SSA-BP and the Duval pentagon method

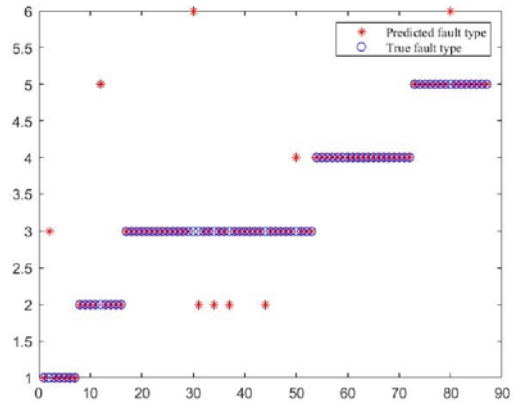


Fig. 4 The prediction results of the improved method based on PSO-SVM and the Duval pentagon method

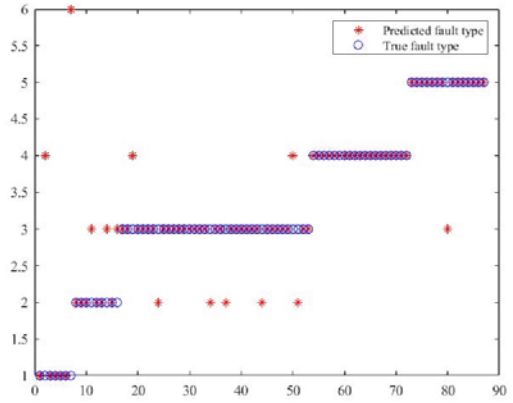


Fig. 5 Prediction results of Duval pentagon method

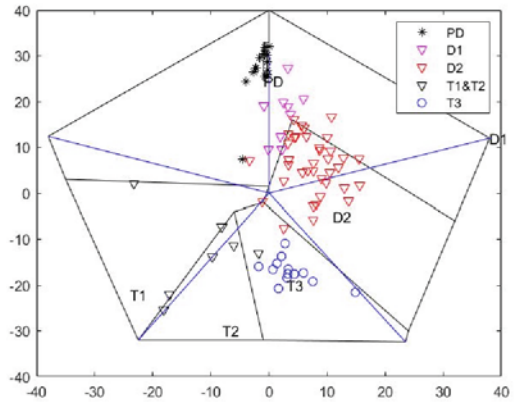


Table 2 Comparison of prediction results

Algorithm	Precision
Duval-SSA-BP	89.6%
Duval-PSO-SVM	85.1%
Duval Pentagon	80.5%

Table 3 The recall of fault type diagnosis

Fault type	Duval-SSA-BP	Duval Pentagon	Duval-PSO-SVM
T1&T2	83.3%	83.3%	71.4%
D1	88.9%	77.8%	66.7%
D2	83.7%	81.1%	81.1%
T3	100%	100%	100%
PD	93.3%	60.0%	93.3%

5 Conclusion

A transformer fault diagnosis model based on Duval pentagon method and sparrow search algorithm to optimize the BP neural network is proposed. Firstly, the Duval pentagon is used to extract the characteristics of the fault gas data, and then the SSA optimization method of BP parameters is introduced to complete the fault type diagnosis, which can fully combine the fault mechanism with the artificial intelligence technology to complete the diagnosis. Through the comparative analysis of multiple models, it is found that the combined model diagnosis Duval-SSA-BP has higher accuracy in diagnosing fault types, and has strong diagnostic ability in actual scenarios, which can be used in transformer fault type diagnosis. Provide effective diagnosis, reduce costs, save resources, and provide a guarantee for safe power supply.

References

1. Li, H., Zhang, Y., Zhang, Y.: Research on transformer fault diagnosis based on ISSA optimized SVM. *J. Electron. Measur. Instrum.* **35**(03), 123–129 (2021). (in Chinese)
2. Wei, L., Xu, S.: Research on transformer fault diagnosis method based on improved BP neural network. *Hebei Elect. Power Technol.* **40**(02), 25–28 (2021). (in Chinese)
3. Li, C., Fei, X., Fan, Y., Yang, G., Xin, T.: An approach to lithium-ion battery SOH estimation based on convolutional neural network. *Trans. China Electrotechn. Soc.* **35**(19), 4106–4119 (2020). (in Chinese)
4. Wang, T., Zhao, X., Jin, H.: Intelligent second-order sliding mode control based on recurrent radial basis function neural network for permanent magnet linear synchronous motor. *Trans. China Electrotechn. Soci.* **36**(6), 1229–1237 (2021). (in Chinese)
5. He, N., et al.: Transformer fault diagnosis based on QIA-BP neural network algorithm. *Transformer* **58**(03), 50–56 (2021). (in Chinese)
6. Benmahamed, Y., Teguair, M., Boubakeur, A.: Application of SVM and KNN to Duval Pentagon 1 for transformer oil diagnosis. *IEEE Trans. Dielectr. Electr. Insul.* **24**(6), 3443–3451 (2017)
7. Wang, Y., Cao, T.: Transformer fault diagnosis method based on improved Elman neural network. *J. Shenyang Univ. Technol.* **43**(03), 254–258 (2021). (in Chinese)
8. Duval, M., Lamarre, L.: The Duval pentagon—a new complementary tool for the interpretation of dissolved gas analysis in transformers. *IEEE Elect. Insul. Mag.* **30**(6), 9–12 (2014). <https://doi.org/10.1109/MEI.2014.6943428>
9. Wang, L., Bi, X.: Risk assessment of knowledge fusion in an innovation ecosystem based on a GA-BP neural network. *Cogn. Syst. Res.* **66**, 201–210 (2021)
10. Peng, Y., Xiang, W.: Short-term traffic volume prediction using GA-BP based on wavelet denoising and phase space reconstruction. *Physica A* **549**, 123913 (2020)
11. Huang, W., et al.: Railway dangerous goods transportation system risk identification: comparisons among SVM, PSO-SVM, GA-SVM and GS-SVM. *Appl. Soft Comput.* **109**, 107541 (2021). <https://doi.org/10.1016/j.asoc.2021.107541>
12. CuongLe, T., et al.: An efficient approach for damage identification based on improved machine learning using PSO-SVM. *Eng. Comput.* **38**(4), 3069–3084 (2022). <https://doi.org/10.1007/s00366-021-01299-6>
13. Ma, C., et al.: Optimized support vector machines for rolling bearing fault diagnosis based on sparrow search algorithm. *Sci. Technol. Eng.* **21**(10), 4025–4029 (2021). (in Chinese)

14. Xue, J., Shen, B.: A novel swarm intelligence optimization approach: sparrow search algorithm. *Syst. Sci. Control Eng.* **8**(1), 22–34 (2020)
15. Xu, N., Dang, Y., Gong, Y.: Novel grey prediction model with nonlinear optimized time response method for forecasting of electricity consumption in China. *Energy* **118**, 473–480 (2017)

An Improved Low Voltage Ride Through Strategy for Wind Turbines Connected to the Weak Grid



Chuanhao Liu and Jiaying Lei

Abstract Low Voltage Ride Through (LVRT) is a necessary function of modern wind turbines. However, it is found that in the extremely weak power grid scenario, the existing LVRT control strategy will generate a large current reference value jitter near the voltage threshold, which will cause the machine terminal voltage to oscillate. In order to solve this problem, this paper establishes a mathematical model of wind power grid-connected converters suitable for weak grid scenarios. On this basis, the mechanism of voltage oscillation generated by existing LVRT is analyzed, and the discontinuity of weight coefficient of the reactive current reference value i_q^* is the cause of current jitter is pointed out. In order to solve this problem, an improved LVRT control strategy is proposed, so that when the terminal voltage amplitude is near the threshold value, the weight coefficient of i_q^* remains continuous, thereby eliminating the sudden change of i_q^* and ensuring the smoothness of the terminal voltage during low voltage ride through. Finally, the effectiveness of the proposed control strategy is verified in the Matlab/Simulink simulation model.

Keywords Wind power · Weak grid · Low voltage ride through · Current control

1 Introduction

With the increase in the scale of wind power access, the relationship between wind power and grid has become more and more close. The access of large-scale power electronic converters has changed the dynamic characteristics of the grid, and the related dynamic problems have gradually emerged [1]. In order to cope with the grid voltage drop, the wind power grid-connected system usually needs to have low voltage ride-through capability and reactive power support capability.

C. Liu · J. Lei (✉)
Southeast University, Nanjing 210096, Jiangsu, China
e-mail: jxlei@seu.edu.cn

© Beijing Paiké Culture Commu. Co., Ltd. 2023
X. Dong et al. (eds.), *The proceedings of the 10th Frontier Academic Forum of Electrical Engineering (FAFEE2022)*, Lecture Notes in Electrical Engineering 1054, https://doi.org/10.1007/978-981-99-3408-9_47

In previous studies, the LVRT strategy was mainly designed under the strong grid, thinking that the voltage at the grid-connected point remained constant. With the grid becomes weaker, the assumption is no longer applicable [2, 3]. Therefore, it is urgent to carry out in-depth research on the voltage and current stability control of the grid connection point of wind turbines under weak grid faults.

In order to maximize the support capacity of the grid during grid faults, [4] proposes a dynamic coordinated control strategy to enhance the overall safety and power support ability of the wind turbine. [5] proposed an improved low voltage ride-through control strategy based on reactive current distribution. [6] proposed a control method based on Riccati equation, which improves the support capability of wind power generation systems for the grid.

Existing research focuses on the improvement of grid voltage support capability of new energy sources during the fault period, but there are few studies on the stability of the wind power grid-connected system caused by the grid fault. [7] proposed a concurrent control scheme of active and reactive power to reduce the active power shortage caused by faults as much as possible. [8] proposed an active and reactive current injection control strategy with adaptive priority for wind turbines to alleviate the frequency problem caused by grid voltage dips. [9] studied the synchronous instability problem caused by voltage deep drop, and proposes a criterion for the existence of equilibrium point, which provides a reference for analysis and control design.

This paper proposes a current control strategy suitable for LVRT in weak grid. Firstly, the grid-connected converter is modeled, and the voltage equation and power equation are obtained. On this basis, the control strategy of the whole system is proposed. Then the improved LVRT control strategy is proposed, which ensures the reactive power support and the stability of the system during the fault period. Finally, the effectiveness of the proposed control strategy is verified in the Matlab/Simulink simulation model.

2 System Modeling and Control

2.1 Low Voltage Ride Through Weak Grid

The strength of the grid can be represented by the Short Circuit Ratio (SCR) [10]:

$$SCR = \frac{S_{SC}}{S_N} = \frac{3U_g^2}{Z_g S_N} \quad (1)$$

In the formula, S_{SC} is the short-circuit capacity of the power grid, S_N is the rated capacity of the converter connected to the power grid, U_g is the rms phase voltage of the power grid, and Z_g is the fundamental impedance of the grid.

It is generally considered that a grid with an SCR value less than 3 is a weak power grid [11]. The impedance of the weak grid is large, and it can no longer be equivalent to an ideal voltage source with infinite capacity. It may lead to unstable grid-connected current and cause grid-connected current distortion, especially when LVRT occurs in the grid.

2.2 Control of System

The Control strategy of grid-side converter in weak grid is shown in Fig. 1. Among it, u_{iA} , u_{iB} and u_{iC} are the output voltages on the bridge arm of the inverter, L_f is the filter inductance of the inverter, u_{gA} , u_{gB} and u_{gC} are the grid-connected voltages, and L_g is the grid inductance. From Kirchhoff's voltage law:

$$\begin{bmatrix} u_{iA} \\ u_{iB} \\ u_{iC} \end{bmatrix} = L_f \frac{d}{dt} \begin{bmatrix} i_{gA} \\ i_{gB} \\ i_{gC} \end{bmatrix} + \begin{bmatrix} u_{gA} \\ u_{gB} \\ u_{gC} \end{bmatrix} \tag{2}$$

Use Park transformation to transform formula (2) into the dq coordinate system:

$$\begin{bmatrix} u_{id} \\ u_{iq} \end{bmatrix} = L_f \frac{d}{dt} \begin{bmatrix} i_{gd} \\ i_{gq} \end{bmatrix} + \begin{bmatrix} -\omega_g L_f i_{gq} + u_{gd} \\ \omega_g L_f i_{gd} + u_{gq} \end{bmatrix} \tag{3}$$

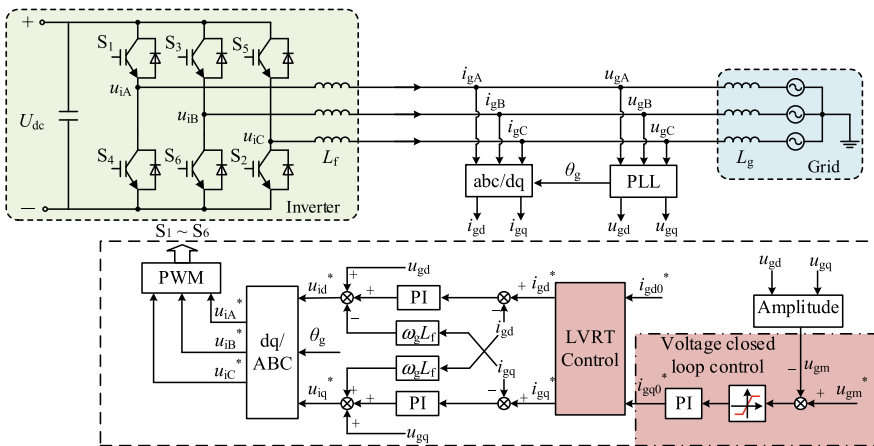


Fig. 1 Control strategy of wind turbine grid-side converter in weak grid

The phase angle θ_g used by the Park transform is obtained by phase-locked loop and is oriented with the d-axis voltage, the active and reactive power injected by the grid-side converter into the grid are [12]:

$$P_g = 1.5u_{gm}i_{gd}, \quad Q_g = -1.5u_{gm}i_{gq} \quad (4)$$

It can be seen that i_{gd} is the active current and i_{gq} is the reactive current.

For the current inner loop, the reference voltage of the bridge arm of the inverter can be obtained from formula (2):

$$\begin{bmatrix} u_{id}^* \\ u_{iq}^* \end{bmatrix} = \begin{bmatrix} G_i(s)(i_{gd}^* - i_{gd}) - \omega_g L_f i_{gq} + u_{gd} \\ G_i(s)(i_{gq}^* - i_{gq}) + \omega_g L_f i_{gd} + u_{gq} \end{bmatrix} \quad (5)$$

In the formula, $G_i(s)$ is the transfer function of the current inner loop PI controller.

For the reference current, the active reference current i_{gd0}^* can be used to control the DC bus voltage of the grid-side converter. The DC bus voltage of the converter studied in this paper takes a constant value, so i_{gd0}^* is constant. In the weak grid, a certain reactive current must be provided to enhance the reactive power support capability of the grid during the LVRT period. The voltage amplitude of the grid-connected point is controlled by the voltage outer loop.

3 LVRT Current Control Strategy

3.1 Current Limiting Strategy

Considering the limitation of inverter capacity and the requirement of reactive power support, i_{gd0}^* and i_{gq0}^* need to be controlled by LVRT control to obtain i_{gd}^* and i_{gq}^* that act on the PI controller. The current amplitude has a maximum value [13]:

$$i_{gd}^{*2} + i_{gq}^{*2} \leq I_{\max}^2 \quad (6)$$

The calculation of i_{gd}^* and i_{gq}^* is related to the current amplitude and the voltage amplitude of the grid connection point. The normal range of the voltage amplitude at the grid-connected point is $0.9 < u_{gm}(\text{pu}) < 1.1$, and there are the following situations:

- State1: $i_{gd0}^{*2} + i_{gq0}^{*2} \leq I_{\max}^2$

In this case, the reference current amplitude is less than the maximum value, no matter whether the voltage of the grid-connected point is within the normal range, let

$$i_{gd}^* = i_{gd0}^*, i_{gq}^* = i_{gq0}^* \tag{7}$$

- State2: $i_{gd0}^{*2} + i_{gq0}^{*2} > I_{max}^2, 0.9 < u_{gm}(pu) < 1.1$

In this case, the amplitude of the reference current is greater than I_{max} , but the voltage is still within the normal range, it only needs to perform equal-scale normalization on the reference current:

$$i_{gd}^* = \frac{i_{gd0}^*}{\sqrt{i_{gd0}^{*2} + i_{gq0}^{*2}}} I_{max}, i_{gq}^* = \frac{i_{gq0}^*}{\sqrt{i_{gd0}^{*2} + i_{gq0}^{*2}}} I_{max} \tag{8}$$

- State3: $i_{gd0}^{*2} + i_{gq0}^{*2} > I_{max}^2, u_{gm}(pu) < 0.9$ or $u_{gm}(pu) > 1.1$

This situation generally occurs during LVRT period, the reference current amplitude is greater than the maximum value, and the voltage is not within the normal range. In order to quickly restore the u_{gm} to the normal range, the control of reactive current should be ensured first, so try Make i_{gq}^* close to i_{gq0}^* , at which time equal-scale normalization is no longer applicable, which is described in detail below.

3.2 Traditional Method

When the system is in State 3, the traditional method assigns the available current to the reactive current first and the rest to the active current without exceeding the current limit. The reference current command is calculated as follows:

$$\left| i_{gq}^* \right| = \min \left\{ \left| i_{gq0}^* \right|, I_{max} \right\}, i_{gd}^* = \sqrt{I_{max}^2 - i_{gq}^{*2}} \tag{9}$$

Although this method can try to satisfy the control of reactive current during the LVRT period, but in the critical state when $u_{gm}(pu) = 0.9$ or $u_{gm}(pu) = 1.1$, the calculated reference currents of formulas (8) and (9) are not equal. During the LVRT period, the voltage of the grid-connected point will fluctuate within normal and abnormal range, that is, the State 2 and State 3 will be continuously switched, which will cause the reference current to jump, further causing the grid-connected active and reactive current, affecting the operation of the entire system.

3.3 The Proposed Method

In order to take into account the control of reactive current and the continuity of reference current, when the system is in State 3, first amplify i_{gq0}^* , and then normalize it with i_{gd0}^* . When the system is in State 1 and State 2, then keep i_{gq0}^* unchanged, and ensure that the reactive power reference current i_{gq}^* is uninterrupted during state switching. To do this, change the weights of i_{gq0}^* in different states, let

$$i_{gq1}^* = k_q i_{gq0}^*, k_q = \begin{cases} k_1(u_{gm} - 0.9) + 1, & u_{gm}(\text{pu}) < 0.9 \\ 1, & 0.9 \leq u_{gm}(\text{pu}) \leq 1.1 \\ k_2(u_{gm} - 1.1) + 1, & u_{gm}(\text{pu}) > 1.1 \end{cases} \quad (10)$$

where $k_1 < 0, k_2 > 0$, the change curve of k_q with u_{gm} is shown in Fig. 2, and the current vector diagram under different conditions when the reference current exceeds the limit is shown in Fig. 3.

Normalize i_{gq1}^* and i_{gd0}^* to get the reference current command:

$$i_{gd}^* = \frac{i_{gd0}^*}{\sqrt{i_{gd0}^{*2} + i_{gq1}^{*2}}} I_{\max}, i_{gq}^* = \frac{i_{gq1}^*}{\sqrt{i_{gd0}^{*2} + i_{gq1}^{*2}}} I_{\max} \quad (11)$$

It can be seen from Fig. 3 that the more the voltage at the grid-connected point deviates from the normal range, the greater the magnification k_q of i_{gq0}^* , and more current will be allocated to the reactive current, so that the voltage can quickly recover. In the critical state $u_{gm}(\text{pu}) = 0.9$ or $u_{gm}(\text{pu}) = 1.1$, $k_q = 1$ and there is continuity, so when the State 2 and State 3 are constantly switching, the reference

Fig. 2 Variation curve of k_q with u_{gm}

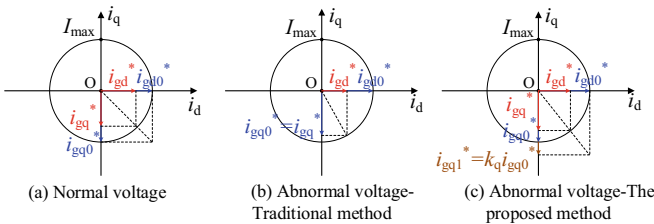
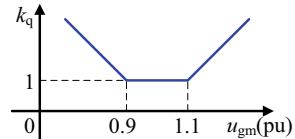


Fig. 3 Current vector diagrams under different conditions

Table 1 System parameters

Parameters	Value
Grid-connected converter rated power/MW	3.0
Grid rated voltage (line voltage rms)/kV	0.69
Rated current (phase current amplitude)/kA	3.55
DC bus voltage/kV	1.27
System frequency/Hz	50
Inverter filter inductor/ μ H	25

currents i_{gd}^* and i_{gq}^* are continuous and do not occur jump to ensure the smoothness of the grid-connected current.

4 Simulation Verification

4.1 Simulation Parameters

The system model is built in Matlab/Simulink to verify the effectiveness of the proposed control strategy. Take the SCR of the grid as 1.7, the active reference current is given as $i_{gd0}^*(pu) = 0.7$, and the main parameters are set as shown in Table 1.

4.2 Simulation Results and Analysis

Figure 4 and Fig. 5 show the simulation results before and after the proposed LVRT control strategy. The system operation has reached a steady state before 3 s, and the three-phase LVRT occurs at 3 s, and it returns to normal at 5 s. When using the traditional LVRT control strategy, the three-phase voltage waveforms at the grid-connection point are shown in Fig. 4(a). It can be seen that the voltage oscillates during the LVRT period. The three-phase and dq-axis current are shown in Fig. 4(b)(c), and the reference current waveforms are shown in Fig. 4(d). The voltage amplitude fluctuates greatly, that is, the State 2 and the State 3 are continuously switched, which makes i_{gd}^* and i_{gq}^* discontinuous, causing the current and voltage to oscillate, affecting the stable operation of the system.

The voltage and current waveforms when the proposed LVRT control strategy is adopted are shown in Fig. 5, where the waveforms shown in each sub-figure have the same meaning as Fig. 4. It can be seen from Fig. 5(a) that the voltage no longer oscillates during LVRT period. It can be seen from Fig. 5(c)(d) that the proposed method can ensure the continuity of the reference current, ensuring the stability of the grid-connected current is improved.

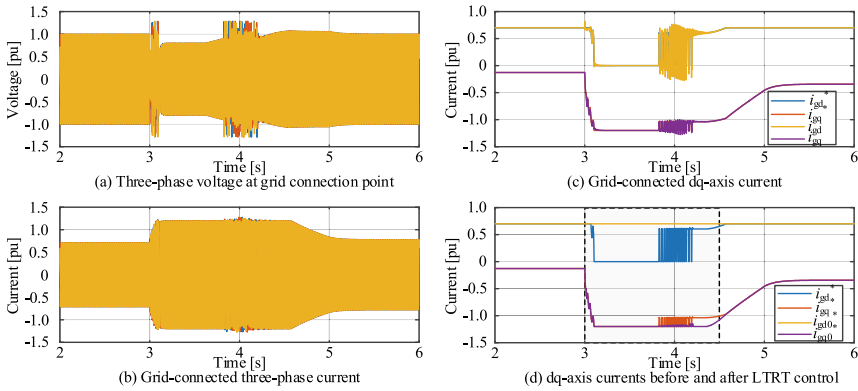


Fig. 4 Grid-connected voltage and current waveforms under traditional LVRT control strategy

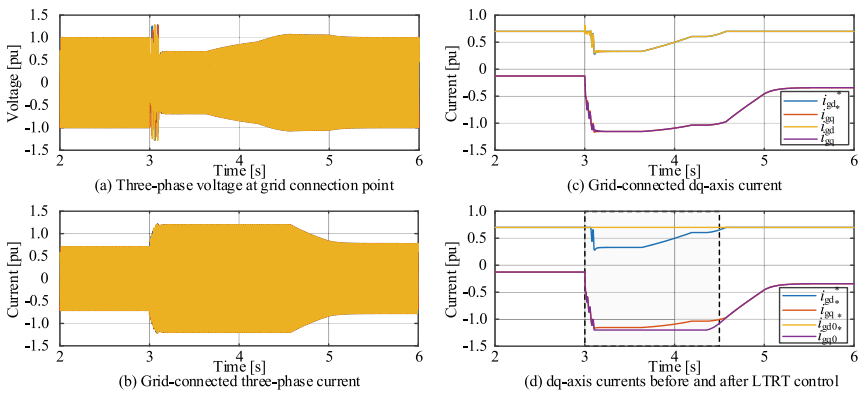


Fig. 5 Grid-connected voltage and current waveforms under proposed LVRT control strategy

5 Conclusion

This paper proposes a LVRT control strategy for wind turbines connected to the weak grid. The reactive power reference current is obtained by feeding back the voltage at the grid-connected point, which can provide reactive power support to the grid. The proposed LVRT control strategy is used to calculate the active and reactive reference current, by properly amplifying the reactive reference current and then normalizing it with the active reference current, the continuity of the reference current can be guaranteed, thus ensuring that the system can still run stably during the fault.

Acknowledgements This research is supported by the National Key R&D Program of China (2021YFB2400500).

References

1. Zhang, Y., Cai, X., Zhang, C., et al.: Transient Synchronization stability analysis of voltage source converters: a review. *Proc. CSEE* **41**(5), 1687–1702 (2021). (in Chinese)
2. Liu, Y., et al.: Transient stability enhancement control strategy based on improved PLL for grid connected VSC during severe grid fault. *IEEE Trans. Energy Convers.* **36**(1), 218–229 (2021). <https://doi.org/10.1109/TEC.2020.3011203>
3. He, X., Geng, H., Li, R., Pal, B.C.: Transient stability analysis and enhancement of renewable energy conversion system during LVRT. *IEEE Trans. Sustain. Energy* **11**(3), 1612–1623 (2020). <https://doi.org/10.1109/TSTE.2019.2932613>
4. Ghosh, S., Isbeih, Y.J., Bhattarai, R., et al.: A dynamic coordination control architecture for reactive power capability enhancement of the DFIG-based wind power generation. *IEEE Trans. Power Syst.* **35**(4), 3051–3064 (2020)
5. Li, H., Fu, B., Yang, C., et al.: Reactive current allocation and control strategies improvement of low voltage ride through for doubly fed induction wind turbine generation system. *Proc. CSEE* **32**(22), 24–31+ 22 (2012). (in Chinese)
6. Zhang, R., Qin, B., Li, H., et al.: Low voltage ride-through control strategy for DFIG-based wind turbine based on disturbance attenuation. *Autom. Electr. Power Syst.* **44**(20), 112–120 (2020). (in Chinese)
7. Lyu, X., Jia, Y., Liu, T., He, Y.: Concurrent optimal Re/Active power control for wind farms under low-voltage-ride-through operation. *IEEE Trans. Power Syst.* **35**(6), 4956–4959 (2020). <https://doi.org/10.1109/TPWRS.2020.3021582>
8. Karbouj, H., Rather, Z.H.: A novel wind farm control strategy to mitigate voltage dip induced frequency excursion. *IEEE Trans. Sustain. Energy* **10**(2), 637–645 (2019). <https://doi.org/10.1109/TSTE.2018.2842232>
9. Göksu, Ö., Teodorescu, R., Bak, C.L., Iov, F., Kjær, P.C.: Instability of wind turbine converters during current injection to low voltage grid faults and PLL frequency based stability solution. *IEEE Trans. Power Syst.* **29**(4), 1683–1691 (2014). <https://doi.org/10.1109/TPWRS.2013.2295261>
10. Liu, R., Yao, J., Wang, X., Sun, P., Pei, J., Hu, J.: Dynamic stability analysis and improved lvr control schemes of DFIG-based wind turbines during a symmetrical fault in a weak grid. *IEEE Trans. Power Electron.* **35**(1), 303–318 (2020). <https://doi.org/10.1109/TPEL.2019.2911346>
11. Maganti, S., Padhy, N.P.: Analysis and design of PLL less current control for weak grid-tied LCL-type voltage source converter. *IEEE J. Emerg. Sel. Top. Power Electron.* **10**(4), 4026–4040 (2022). <https://doi.org/10.1109/JESTPE.2021.3129804>
12. Ran, X., Xu, B., Liu, K., Zhang, J.: An improved low-complexity model predictive direct power control with reduced power ripples under unbalanced grid conditions. *IEEE Trans. Power Electron.* **37**(5), 5224–5234 (2022). <https://doi.org/10.1109/TPEL.2021.3131794>
13. Mahamedi, B., Eskandari, M., Fletcher, J.E., Zhu, J.: Sequence-based control strategy with current limiting for the fault ride-through of inverter-interfaced distributed generators. *IEEE Trans. Sustain. Energy* **11**(1), 165–174 (2020). <https://doi.org/10.1109/TSTE.2018.2887149>

Optimal Planning of Power-to-Hydrogen Unit Considering Electrical-Thermal Coupling in Power System with Offshore Wind



Hao Yu, Honglin Chen, Zhengmin Zuo, Wenxin Liu, Yuheng Ying,
and Xiaomeng Ai

Abstract The power-to-hydrogen (PtH) units serve as flexible load in power system, which can consume surplus offshore wind power and avoid network congestion. PtH units are modeled with constant efficiency between electrical power input and hydrogen production currently, ignoring the internal physical processes. In this paper, an electrical-thermal coupling model is proposed to consider the temperature effect. A planning model for PtH units is established and transformed into a mixed-integer linear programming problem by piecewise linear approximation. The proposed model is verified by a 10-bus power system with offshore wind farms. The operation results show that PtH units can assist in the integration of wind power and the temperature affects the performances. Besides, sensitivity analysis of PtH unit planning is conducted, including curtailment coefficient, selling price, and unit transfer cost.

H. Yu · H. Chen · Z. Zuo

Power Grid Planning Research Center, Guangdong Power Grid Co., Ltd., Guangzhou 510080,
Guangdong, China
e-mail: yuhao@gd.csg.cn

H. Chen

e-mail: chenhonglin@gd.csg.cn

Z. Zuo

e-mail: zuozhengming@gd.csg.cn

W. Liu (✉) · Y. Ying · X. Ai

School of Electrical and Electronic Engineering, Huazhong University of Science and
Technology, Wuhan 430074, Hubei, China
e-mail: liuwenxin@hust.edu.cn

Y. Ying

e-mail: yingyuheng@hust.edu.cn

X. Ai

e-mail: xiaomengai@hust.edu.cn

© Beijing Paiké Culture Commu. Co., Ltd. 2023

X. Dong et al. (eds.), *The proceedings of the 10th Frontier Academic Forum of
Electrical Engineering (FAFEE2022)*, Lecture Notes in Electrical Engineering 1054,
https://doi.org/10.1007/978-981-99-3408-9_48

555

Keywords Power-to-hydrogen · Power system planning · Electrical-thermal coupling

1 Introduction

Hydrogen is regarded as a distinguished energy carrier for carbon neutrality for high energy density and broad industry applications [1]. Among various hydrogen production methods, water electrolysis is a mature method with commercial projects, which is also called power-to-hydrogen (PtH). Especially, water electrolysis by renewable energy can achieve a carbon-free process of hydrogen production, known as green hydrogen [2]. Although PtH only accounts for a small share of global hydrogen production, it has widely attracted research attention from both academia and industry [3]. On the one hand, green hydrogen production can assist the integration of renewable energy sources, such as wind farms and photovoltaic stations [4]. On the other hand, green hydrogen is a major raw material in industry sectors [5], including chemical synthesis, petroleum refining, and metallurgy production, which are currently dominated by hydrogen produced from fossil fuels. The rapid development of PtH using renewable energy can accelerate decarbonization in the above sectors [6].

Due to these distinguished advantages, several studies on the PtH unit in electrical power system with high penetration of renewable energy are carried out. In [7], a hydrogen storage system consisting of PtH unit and fuel cell is established to resolve power quality issues raised by wind turbines. Besides, the PtH unit also has the ability of frequency support in power system [8]. In [9], hydrogen produced by PV-PtH system is optimized by the coordinated control of DC/DC converter and water flow. The above studies mainly focus on the operation of PtH units instead of the planning. In [10], the PtH unit serves as a part of hybrid storage system in the microgrid and its capacity is optimized. PtH units can also serve as a part of hydrogen supply chain, which includes the transmission and storage of hydrogen. A flexible supply chain can be achieved by the scheduling of PtH units and other components [11]. However, the electrical-thermal coupling in water electrolysis reaction is a significant part in PtH units, which is hardly considered in the planning stage [12]. Ignoring the coupling may cause inaccurate performance evaluation, affecting the optimality of planning options.

To address this problem, this paper proposes a model of PtH unit to consider the electrical-thermal coupling. Then, an optimization model is established for the PtH unit planning in power system with renewable energy. The model is transformed into a MILP problem using piecewise linear approximation for a convenient solution. At last, the proposed model is verified through the case study. And the result shows that the PtH unit can assist in the integration of renewable energy and economical operation.

2 Planning Model of Power-to-Hydrogen Unit Considering Electrical-Thermal Coupling

2.1 Electrical-Thermal Coupling Model of PtH Unit

In industrial PtH unit, the electrolyzer is the core component, where water electrolysis reaction occurs. During the reaction, the electrical power is converted into chemical energy in hydrogen, which can be expressed by the voltage-current(U - I) characteristic of electrolysis cells.

The voltage supplied to a single electrolysis cell consists of reversible voltage, ohmic overvoltage, and activation overvoltage. These voltages are mainly affected by the temperature and current of the cell, as shown in (2)-(4).

$$U_t^{\text{cell}} = U_t^{\text{rev}} + U_t^{\text{ohm}} + U_t^{\text{act}} \quad (1)$$

$$U_t^{\text{rev}} = U^{\text{rev}.0} - k^{\text{rev}}(T_t^{\text{ele}} - 298.15) \quad (2)$$

$$U_t^{\text{ohm.}} = R_t^{\text{ohm}} I_t^{\text{ele}} \quad (3)$$

$$U_t^{\text{act}} = \frac{RT_t^{\text{ele}}}{z\alpha F} \sinh^{-1}\left(\frac{I_t^{\text{ele}}}{2j_t^0 A}\right) \quad (4)$$

$$R_t^{\text{ohm}} = R^{\text{ohm}.0} \exp\left(\frac{\delta}{T_t^{\text{ele}}} - \frac{\delta}{T^0}\right) \quad (5)$$

$$j_t^0 = a^0 \exp\left(-\frac{b^0}{T_t^{\text{ele}} - 273.15}\right) \quad (6)$$

where U_t^{cell} , I_t^{ele} , and T_t^{ele} represents voltage, current, and temperature of the cell at time t , respectively, U_t^{rev} is reversible voltage at time t , which is linear to temperature, $U^{\text{rev}.0}$ represents the reversible voltage at 298.15 K, equal to 1.23 V, k^{rev} is the coefficient between the reversible voltage and temperature, U_t^{ohm} is ohmic overvoltage at time t , which is proportional to current, R_t^{ohm} is the resistance of the cell at time t , determined by (5), U_t^{act} is activation overvoltage at time t , given by Butler-Volmer equation, R is the ideal gas constant, z is the number of transferred electrons in the reaction, α is electrode exchange coefficient, F is Faraday constant, A is the electrode plate area, j_t^0 represents the exchange current density of catalysts, as shown in (6), $R^{\text{ohm}.0}$ is the resistance at temperature T^0 and δ is the temperature coefficient, a^0 and b^0 are experimental coefficients of the exchange current density.

The industrial electrolyzer has several electrolysis cells in series to expand the scale. In this paper, each electrolysis cell in series is assumed to have the same current and temperature. The power consumption and hydrogen production of the

electrolyzer can be calculated.

$$P_t^{\text{ele}} = n^{\text{cell}} U_t^{\text{cell}} I_t^{\text{ele}} \quad (7)$$

$$M_t^{\text{PtH}} = n^{\text{cell}} \frac{m_{\text{H}_2}}{2F} I_t^{\text{ele}} \Delta t \quad (8)$$

where n^{cell} represents the number of electrolysis cells in the industrial electrolyzer, m_{H_2} is the molar mass of hydrogen, Δt is the time interval, which is 1 h in this paper.

Obviously, the temperature affects the relationship between power consumption and hydrogen production. To describe the process of temperature change in the PtH unit, this paper proposes the thermal dynamic model, considering internal energy conservation. The thermal unbalance consists of the reaction heat (9), heat dissipation from cooling equipment (10), and heat dissipation to the environment (11). Besides, the derivative of temperature should be proportional to the thermal unbalance, as shown in (12).

$$Q^{\text{reaction}} = P^{\text{ele}} - n^{\text{cell}} U^{\text{rev}} I^{\text{ele}} \quad (9)$$

$$Q^{\text{cooling}} = P^{\text{cool}} \cdot \eta^{\text{cool}} \quad (10)$$

$$Q^{\text{loss}} = k^{\text{ex}}(T - T^{\text{en}}) \quad (11)$$

$$C_p \frac{dT}{dt} = Q^{\text{reaction}} - Q^{\text{cooling}} - Q^{\text{loss}} \quad (12)$$

where P^{cool} and η^{cool} represent electrical power and efficiency of cooling equipment, k^{ex} is ambient heat dissipation coefficient, T^{en} is the environment temperature (25°C), C_p is the heat capacity of PtH unit.

By differencing the above Eq. (12), the temperature change between two time slots is obtained, as shown in (13).

$$T_t^{\text{ele}} - T_{t-1}^{\text{ele}} = \frac{\Delta t}{C_p} (P_t^{\text{ele}} - n^{\text{cell}} U_t^{\text{rev}} I_t^{\text{ele}} - P_t^{\text{cool}} \cdot \eta^{\text{cool}} - k^{\text{ex}}(T_t^{\text{ele}} - T^{\text{en}})) \quad (13)$$

The cooling equipment is used to prevent the temperature rise due to the water electrolysis reaction, which increases electrical power consumption of the PtH unit, as shown in (14).

$$P_t^{\text{PtH}} = P_t^{\text{ele}} + P_t^{\text{cool}} \quad (14)$$

From the above model, the relationship between power consumption and hydrogen production of PtH unit is affected by the temperature. Meanwhile, the intensity of water electrolysis reaction may lead to various temperature changes. In a word, the

electrical-thermal coupling has a significant impact on the characteristics of PtH units.

2.2 Planning Model of Power System with PtH Units

In the planning model, the location and capacity of PtH units should be determined to integrate renewable energy, such as offshore wind. Because the industrial PtH unit has various types based on power level, the capacity of PtH units is determined by the number of different types. Besides, hydrogen produced by PtH units needs devices for storage and the capacity of hydrogen storage (HS) devices should also be planned. In conclusion, the planning option of proposed model includes the number of industrial PtH units with different types and the capacity of HS devices at any node. And the optimal planning option can achieve renewable energy integration and economical system operation.

A. Objective Function

The objective function of proposed planning model is to minimize the annual cost of power system with PtH unit. The annual cost includes the investment cost C^{inv} and the operation cost C^{op} , as shown in (15).

$$\min J = C^{inv} + C^{op} \quad (15)$$

The annual investment cost is determined by the planning option of PtH units and HS devices (16), while the annual operation cost is determined by the scheduling of electrical power system and hydrogen system under the planning option (17). We select several typical scenarios in this paper to reduce the computational effort. Then, the annual operation cost can be simulated by the operation cost in these scenarios.

$$C^{inv} = CRF * (C^{PtH.inv} + C^{HS.inv}) \quad (16)$$

$$C^{op} = 365 * \sum_{s=1}^{N_s} (p_s * (C_s^E + C_s^H)) \quad (17)$$

$$CRF = \frac{\gamma(1 + \gamma)^{N^{year}}}{(1 + \gamma)^{N^{year}} - 1} \quad (18)$$

$$\sum_s p_s = 1 \quad (19)$$

where CRF represents the capital recovery factor, which is calculated by (18), γ is the discount rate, N^{year} is the lifecycle of devices, equal to 20 years in this paper, N_s is the number of typical scenarios, p_s is the probability of scenario s .

$C^{PtH.inv}$ and $C^{HS.inv}$ represent the investment cost of power-to-hydrogen units and hydrogen storage devices, respectively. For PtH units, the investment cost is related to the number of PtH units, as shown in (20). For HS devices, the investment cost is proportional to the storage capacity, as shown in (21).

$$C^{PtH.inv} = \sum_{h=1}^{N_h} \sum_i c_i^{PtH.inv} N_{h,i}^{PtH} \quad (20)$$

$$C^{HS.inv} = \sum_{h=1}^{N_h} c^{HS.inv} Cap_h^{HS} \quad (21)$$

where N_h is the number of nodes for planning, $c_i^{PtH.inv}$ is the unit investment cost of type i PtH unit, $N_{h,i}^{PtH}$ is the planning number of type i PtH unit on node h , $c^{HS.inv}$ is the unit capacity investment cost of HS device, Cap_h^{HS} is the planning capacity of HS device on node h .

C_s^E and C_s^H represent the operation cost of electrical power system and hydrogen system in scenario s , respectively. For power system, the cost includes fuel cost, startup cost, and shutdown cost of generators, as well as wind curtailment cost. For hydrogen system, the cost includes storage cost, transfer cost, and selling profits of hydrogen.

$$C_s^E = \sum_{t=1}^T \left(\sum_{g=1}^{N_g} (F_g^{fuel}(P_{g,t,s}) + C_{g,t,s}^{su} + C_{g,t,s}^{sd}) + \sum_{w=1}^{N_w} (k^{cur} * (P_{w,t,s}^a - P_{w,t,s})) \right) \quad (22)$$

$$C_s^H = \sum_{t=1}^T \left(\sum_{h=1}^{N_h} (k^{HS} * SOH_{h,t,s} + k^{trans} * M_{h,t,s}^{trans} - k^{H2} * M_{h,t,s}^{load}) \right) \quad (23)$$

where T represents the number of total time slots, N_g is the number of generators, F_g^{fuel} represents the fuel cost function of generator g , $P_{g,t,s}$, $C_{g,t,s}^{su}$, $C_{g,t,s}^{sd}$ represent the power, startup cost, and shutdown cost of generator g at time t in scenario s , respectively, N_w is the number of offshore wind farms, k^{cur} represents the curtailment coefficient, $P_{w,t,s}^a$ and $P_{w,t,s}$ represent the available and actual power of wind farm w at time t in scenario s , respectively, k^{HS} , k^{trans} , and k^{H2} represent the unit storage cost, unit transfer cost, and selling price, $SOH_{h,t,s}$ is the mass of stored hydrogen on node h at time t in scenario s , $M_{h,t,s}^{trans}$ and $M_{h,t,s}^{load}$ represent the mass of hydrogen in the transfer or selling process on node h at time t in scenario s .

B. Constraints

The constraints of proposed planning model can be divided into two categories: planning constraints and operation constraints. The planning option including the number of PtH units and the capacity of HS devices should be constrained due to technical factors, such as limited space. For each type of PtH units, the planning number cannot

exceed the maximum value (24). For HS devices, the planning capacity cannot exceed the upper limit (25)

$$0 \leq N_{h,i}^{\text{PtH}} \leq N_i^{\text{PtH,max}} \quad (24)$$

$$0 \leq \text{Cap}_h^{\text{HS}} \leq \text{Cap}^{\text{HS,max}} \quad (25)$$

where $N_i^{\text{PtH,max}}$ is the maximum planning number of type i PtH units, $\text{Cap}^{\text{HS,max}}$ is the capacity limit of HS devices.

The operation constraints involve PtH units, HS devices, generators, and power flow. In addition to the electrical-thermal coupling model, the operation of PtH units also satisfies the following constraints: the planning number Eq. (26), the power consumption limit of electrolyzers (27), the power consumption limit of cooling equipment (28), the temperature limit (29), and the current limit (30).

$$N_{h,i}^{\text{PtH}} = \sum_{j=1}^{N_i^{\text{PtH,max}}} U_{h,i,j}^{\text{PtH}} \quad (26)$$

$$U_{h,i,j}^{\text{PtH}} P_{\min}^{\text{ele},i} \leq P_{h,t}^{\text{ele},i,j} \leq U_{h,i,j}^{\text{PtH}} P_{\max}^{\text{ele},i,j} \quad (27)$$

$$U_{h,i,j}^{\text{PtH}} P_{\min}^{\text{cool},i} \leq P_{h,t}^{\text{cool},i,j} \leq U_{h,i,j}^{\text{PtH}} P_{\max}^{\text{cool},i} \quad (28)$$

$$T_{\max}^{\text{ele}} \leq T_{h,t}^{\text{ele},i,j} \leq T_{\max}^{\text{ele}} \quad (29)$$

$$I_{\max}^{\text{ele}} \leq I_{h,t}^{\text{ele},i,j} \leq I_{\max}^{\text{ele}} \quad (30)$$

where $U_{h,i,j}^{\text{PtH}}$ represents whether the j -th PtH unit of type i on node h is planned, \min and \max in the subscript represent the minimum and maximum value of variables.

Hydrogen produced by PtH unit should be stored in HS devices and transferred to hydrogen load for selling. The constraints include hydrogen mass limit in HS devices (31), hydrogen mass variation between two time slots (32), hydrogen production rate limit (33), and hydrogen supply rate limit (34).

$$0 \leq \text{SOH}_{h,t} \leq \text{Cap}_h^{\text{HS}} \quad (31)$$

$$\text{SOH}_{h,t} = \text{SOH}_{h,t-1} + \left(\sum_i \sum_{j=1}^{N_i^{\text{PtH,max}}} M_{h,t}^{\text{PtH},i,j} - M_{h,t}^{\text{load}} \right) \quad (32)$$

$$0 \leq \sum_i \sum_{j=1}^{N_i^{\text{PtH,max}}} M_{h,t}^{\text{PtH},i,j} \leq M_h^{\text{max}} \quad (33)$$

$$0 \leq M_{h,t}^{\text{load}} \leq M_h^{\text{max}} \quad (34)$$

The operation constraints of generators include generation capacity, ramp limit, startup/shutdown power limit, and minimum on/off time. Besides, DC power flow is adopted in this paper to express the node active power balance, upward/downward spinning reverse, and branch flow limit in power system. The above constraints have been widely used in power system optimization and they are not shown in detail in this paper to save manuscript pages.

2.3 Model Linearization

The aforementioned planning model is a nonlinear programming problem because the relationship between the power consumption P_t^{ele} and current I_t^{ele} of electrolyzers (1)-(7) is nonlinear. As a result, the proposed optimization model is hard to solve and the global optimal planning option cannot be guaranteed. In this paper, piecewise linear functions are used to approximate the nonlinear characteristic of electrolyzers [13], which is mainly affected by temperature, as shown in (35).

$$P_t^{\text{ele}} = f(I_t^{\text{ele}}, T_t^{\text{ele}}) \quad (35)$$

According to the upper and lower limit, the current (temperature) range is divided into several segments using breakpoints in (36) and (37). Then, power consumption of the electrolyzer at corresponding breakpoints can be calculated by (35).

$$\mathbf{I}^{\text{ele}} = [I_0^{\text{ele}}, I_1^{\text{ele}}, \dots, I_M^{\text{ele}}] \quad (36)$$

$$\mathbf{T}^{\text{ele}} = [T_0^{\text{ele}}, T_1^{\text{ele}}, \dots, T_N^{\text{ele}}] \quad (37)$$

where 0 and $M(N)$ in the subscript represents the lower and upper limit.

Based on these breakpoints, the temperature, current, and power at time t can be expressed as the linear combination of corresponding values.

$$I_t^{\text{ele}} = \sum_{j=0}^M \sum_{k=0}^N w_{t,j,k}^{\text{ele}} I_j^{\text{ele}} \quad (38)$$

$$T_t^{\text{ele}} = \sum_{j=0}^M \sum_{k=0}^N w_{t,j,k}^{\text{ele}} T_k^{\text{ele}} \quad (39)$$

$$P_t^{\text{ele}} = \sum_{j=0}^M \sum_{k=0}^N w_{t,j,k}^{\text{ele}} P_{j,k}^{\text{ele}} \quad (40)$$

where $w_{t,j,k}^{\text{ele}}$ is the weight coefficient of breakpoint $(I_j^{\text{ele}}, T_k^{\text{ele}})$ and $P_{j,k}^{\text{ele}}$ is the power consumption corresponding to the breakpoint.

To ensure the uniqueness and rationality of linear combinations, any variable value should only be expressed by the nearest two breakpoints. The following constraints is needed to achieve this goal:

$$\sum_{j=0}^M \sum_{k=0}^N w_{t,j,k}^{\text{ele}} = 1 \quad (41)$$

$$0 \leq w_{t,j,k}^{\text{ele}} \leq 1 \quad (42)$$

$$\sum_{j=0}^M \sum_{k=0}^N (h_{t,j,k}^{\text{ele.up}} + h_{t,j,k}^{\text{ele.down}}) = 1 \quad (43)$$

$$w_{t,j,k}^{\text{ele}} \leq h_{t,j,k}^{\text{ele.up}} + h_{t,j,k}^{\text{ele.down}} + h_{t,j+1,k+1}^{\text{ele.up}} + h_{t,j+1,k+1}^{\text{ele.down}} + h_{t,j,k+1}^{\text{ele.up}} + h_{t,j+1,k}^{\text{ele.down}} \quad (44)$$

where $h_{t,j,k}^{\text{ele.up}}$ and $h_{t,j,k}^{\text{ele.down}}$ are respectively associated with the upper left and lower right triangles with the line between $(I_{j-1}^{\text{ele}}, T_{k-1}^{\text{ele}})$ and $(I_j^{\text{ele}}, T_k^{\text{ele}})$ as the hypotenuse.

After linearization, the proposed planning model for PtH units is a mixed-integer linear programming (MILP) problem, which can be solved by commercial solvers, such as Cplex and Gurobi.

3 Case Study

3.1 System Description

A modified 10-bus system is used to validate the proposed planning model, as shown in Fig. 1. The system includes 3 generators and 1 offshore wind farm, which is located at bus 10 with 350 MW installed capacity. The PtH unit and HS device can be planned at bus 10 to integrate offshore wind. Technical parameters of PtH units with different types are listed in Table 1. The cooling efficiency of cooling equipment η^{cool} is set to 95%. In this case, 4 typical scenarios are selected to represent the operation characteristic of 10-bus system in spring, summer, autumn, and winter. The hourly forecasted load and offshore wind power are obtained from actual operation. Besides, each scenario has the same probability of 25%.

Fig. 1 Topology of a 10-node power system with offshore wind

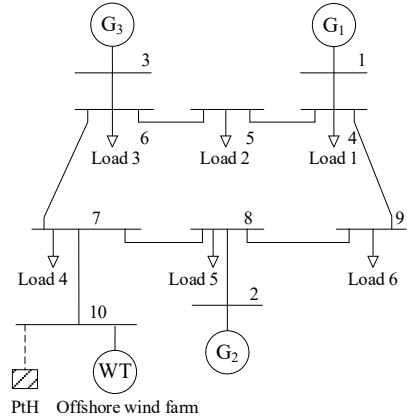


Table 1 Technical Parameters of different types of electrolyzers

Type	$N^{PtH.max}$	$C^{PtH.inv}$ (RMB)	$p^{ele.max}$ (MW)	$p^{cool.max}$ (MW)	n^{cell}
1	5	1.4×10^7	6	3	300
2	6	1.0×10^7	4	2	250
3	8	5×10^6	2	1	150
4	10	2×10^6	0.5	0.25	50

4 Influence of PtH Units on Offshore Wind Integration

A. Offshore Wind Consumption Without PtH Units

Firstly, the system operation without PtH unit is analyzed. The curtailment coefficient of offshore wind is $1000RMB/(MW \cdot h)$ and the selling price of hydrogen is $60RMB/kg$. In addition, the unit transfer cost of hydrogen is set to $1.4RMB/kg$ considering the distance from the shore of wind farms. The optimization results of each typical scenario are shown in Fig. 2.

When there is no PtH unit on offshore wind farms, wind curtailment of each typical scenario is 0%, 5.1879%, 0%, and 3.5413%, the average is 2.1823%. The annual operating cost of the system is $8.2884 \times 10^8 RMB$, namely, the daily operation cost is $2.27 \times 10^6 RMB$. When wind curtailment cost is $1000RMB/(MW \cdot h)$, the average daily wind curtailment cost is $7.816 \times 10^4 RMB$, accounting for 3.44% of daily operating cost. In most cases, when k^{cur} increases, the tolerance to wind curtailment declines, and the renewable energy accommodation capacity increases. However, in this case, when k^{cur} varies from 1000 to 5000, there is no obvious change in wind curtailment. The main reason is that in some periods, the available power of offshore wind exceeds the transmission capacity limitation of the grid-connected channel (line 7–10). For this problem, expanding the transmission capacity by constructing extra grid-connected channels may be a possible solution. But the investment and system stability are easily affected by the environment, especially in deep-sea systems. The

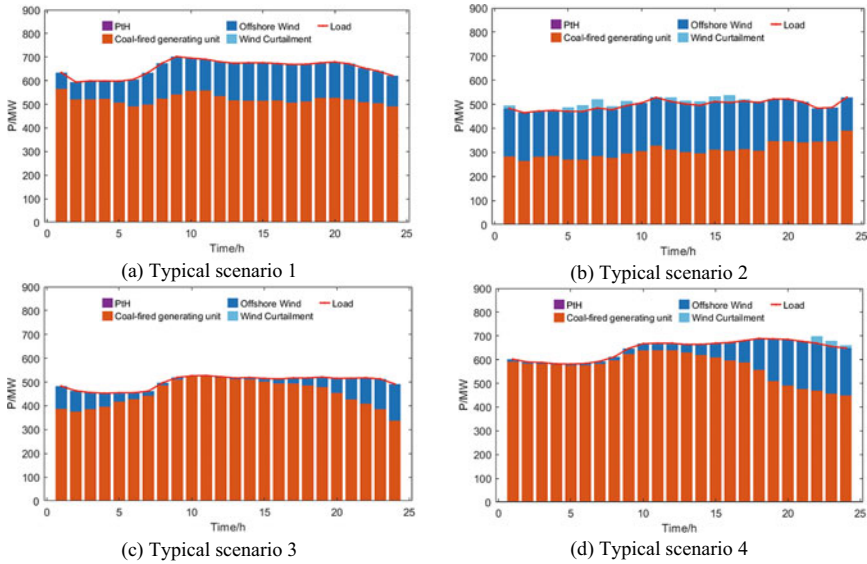


Fig. 2 System operation without PtH unit

planning of PtH unit can promote renewable resource consumption. PtH unit can act as a flexible load to consume electrical power and produce hydrogen when wind resource is abundant, relaxing the constraint of real-time power transmission balance and realizing flexible access to offshore wind power.

B. Offshore Wind Consumption with PtH Units

According to the solution results of the proposed programming optimization model, the configuration scheme of the electric hydrogen production unit is to configure two 6 MW and four 2 MW electrolyzers at the node (node 10) where the offshore wind farm is located, with a total capacity of 20 MW. In addition to the power consumption of auxiliary equipment, the maximum power of the configured electric hydrogen production unit can reach 30 MW.

According to the optimization result, two 6 MW and four 2 MW electrolyzers are configured. The wind curtailment rate is 0%, 0.1695%, 0% and 0.0242%, the average is 0.048%. The average daily operation cost is 2.245×10^6 RMB, and the average daily wind curtailment cost is only 2.128×10^3 RMB. Compared with the case without PtH unit, the rate decreases by 97.7%. It demonstrates that introducing PtH can reduce the wind curtailment caused by randomness, intermittence, and reverse peak regulation characteristics, and reduce the overall system operation cost (Fig. 3).

PtH units mainly operate in typical scenario 2, and the temperature of electrolyzers and hydrogen storage are shown in Fig. 4. When the electrolyzers are producing hydrogen, auxiliary cooling equipment start operation, and heat imbalance causes temperature drop. Then the hydrogen is stored in a high-pressure tank and sold

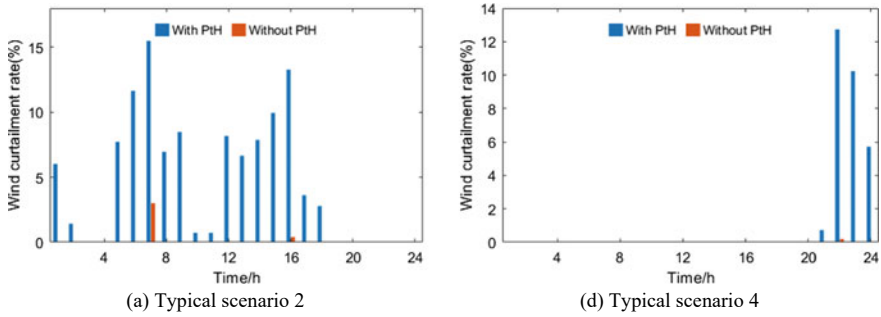


Fig. 3 System operation with PtH unit

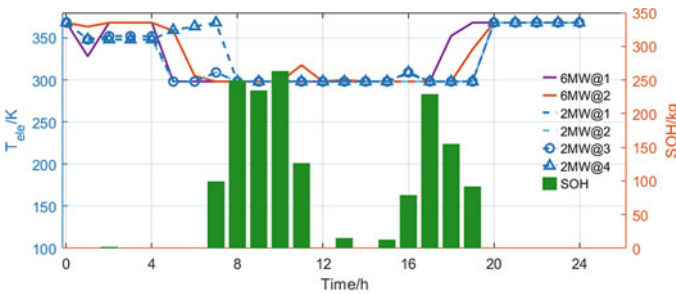


Fig. 4 Temperature and hydrogen storage in typical scenario 2

for economic effectiveness. The model considering electrical-thermal coupling will reflect the system state more accurately.

5 Sensitivity Analysis

To explore the influence of different factors on the absorption of offshore wind power in the planning of PtH units, the following cases are set.

A. Influence of Wind Curtailment Coefficient k^{cur} Figure 5 Variation of wind curtailment rate with wind curtailment cost shows the optimal operation results of the system with wind curtailment cost coefficients varying. When k^{cur} reduces from 2000 to 500, the tolerance to wind curtailment increases. To minimize the sum of investment and operating cost, the capacity of the offshore PtH unit decreases from 22 to 18 MW. And the average wind curtailment rate increases from 0.03% to 0.105%.

B. Influence of Hydrogen Selling Price k^{H2}

Figure 6 reflects the influence of hydrogen price in the system. In the example, the variation range of hydrogen selling price is 0 ~ 100RMB/kg. When k^{H2} increases,

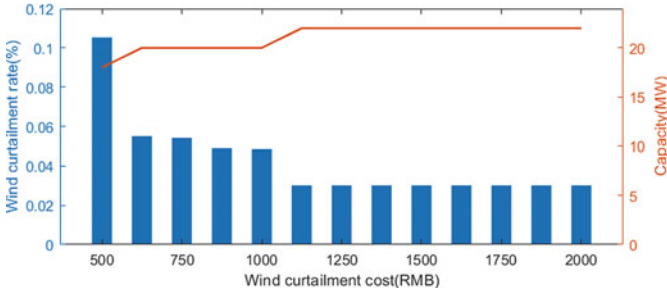


Fig. 5 Variation of wind curtailment rate with wind curtailment cost

the cost of construction investment and electricity is lower than hydrogen price, and there tend to be more PtH units for more profit. In this case, the capacity of PtH units remains unchanged because k^{H_2} is not. When k^{H_2} is lower than 40, although it is less than the cost, the capacity of planned PtH units remains approximately unchanged. The reason is that the wind curtailment cost encourages energy storing devices to consume surplus wind power. But the planning of PtH units changes from two 6 MW and four 2 MW to one 6 MW and seven 2 MW, wind curtailment rate decreases accordingly owing to the flexibility of small capacity units.

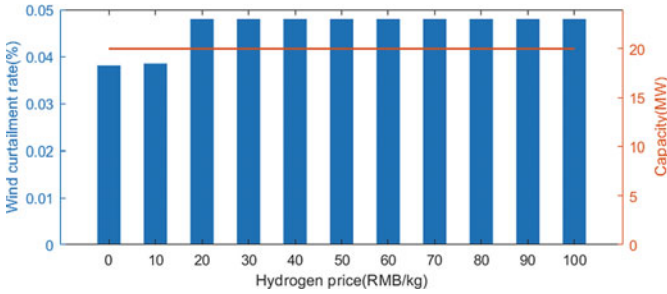


Fig. 6 Variation of wind curtailment rate with hydrogen price

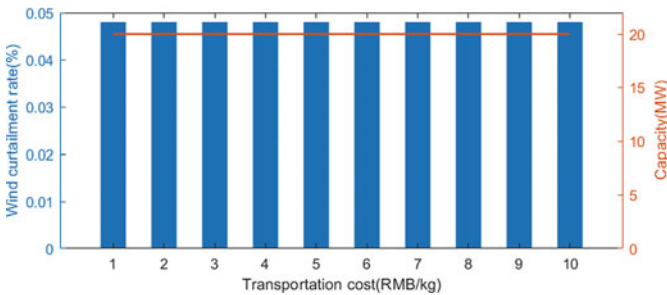


Fig. 7 Variation of wind curtailment rate with transportation cost

C. Influence of Hydrogen Unit Transfer Cost k^{trans}

According to Reference [14], k^{trans} varies with distance and transportation methods, which affects the overall profit of the system. The increase in the transportation price is equivalent to a decrease in the profit of hydrogen sales. However, since the transportation price is much lower than the price of hydrogen, there is no significant change in the configuration plan (Fig. 7).

6 Conclusion

In this paper, an electrical-thermal coupling model is proposed to demonstrate the effect of temperature on the performance of PtH units. Based on this, a planning model of power system with PtH units is established and it is transformed into a MILP problem using piecewise linear functions. Through the case study, it can be concluded that PtH units in power system significantly improve the integration of renewable energy and reduce wind curtailment phenomenon caused by line congestion. Furthermore, the influence of curtailment coefficient, unit transfer cost, and selling price of hydrogen are analyzed. When the selling profit exceeds the investment and operation cost, there will be more PtH units and HS devices in the planning option solved by the model. Only the deterministic case is considered in the current work and the uncertainties of renewable energy will be included in future work with corresponding algorithms, such as robust optimization.

Acknowledgements This work is supported by the China Southern Power Grid Electricity Planning Special Project (031000QQ00210019) and Research and development plan in key areas of Guangdong Province (2021B0101230004).

References

1. Tu, H.: Hydrogen energy: a global trend and China's strategy. *Engineering* **7**(6), 703 (2021)
2. Ursua, A., Gandia, L.M., Sanchis, P.: Hydrogen production from water electrolysis: current status and future trends. *Proc. IEEE* **100**(2), 410–426 (2012). <https://doi.org/10.1109/JPROC.2011.2156750>
3. Mazloomi, K., Chandima, G.: Hydrogen as an energy carrier: Prospects and challenges. *Renew. Sustain. Energy Rev.* **16**(5), 3024–3033 (2012)
4. Glenk, G., Reichelstein, S.: Economics of converting renewable power to hydrogen. *Nat. Energy* **4**(3), 216–222 (2019). <https://doi.org/10.1038/s41560-019-0326-1>
5. Li, Z., Zhang, R., Sun, H., Zhang, W., Mei, C.: Review on key technologies of hydrogen generation, storage and transportation based on multi-energy complementary renewable energy. *Trans. China Electrotechn. Soc.* **36**(3), 446–462 (2021). (in Chinese)
6. Griffiths, S., Sovacool, B.K., Kim, J., et al.: Industrial decarbonization via hydrogen: A critical and systematic review of developments, socio-technical systems and policy options. *Energy Res. Soc. Sci.* **80**, 102208 (2021)

7. Esmaeilian, H.R., Fadaeinedjad, R.: Resolving power quality issues raised by aerodynamic aspects of wind turbine in isolated microgrids using fuel cell/electrolyzer system. *IEEE Trans. Sustain. Energy* **7**(3), 1274–1283 (2016). <https://doi.org/10.1109/TSTE.2016.2544102>
8. Tuinema, B.W., Adabi, E., Ayivor, P., et al.: Modelling of large-size electrolyzers for real-time simulation and study of the possibility of frequency support by electrolyzers. *IET Gener. Transm. Distrib.* **14**(10), 1985–1992 (2020)
9. Dahbi, S., Aziz, A., Benazzi, N., et al.: Optimised hydrogen production by a photovoltaic - electrolysis system DC/DC converter and water-flow controller. In: 2015 3rd International Renewable and Sustainable Energy Conference (IRSEC). IEEE (2016)
10. Li, Q., Zhao, S., Pu, Y., Chen, W., Yu, J.: Capacity optimization of hybrid energy storage microgrid considering electricity-hydrogen coupling. *Trans. China Electrotechn. Soc.* **36**(3), 486–495 (2021). (in Chinese)
11. He, G., Mallapragada, D.S., Bose, A., Heuberger, C.F., Gencer, E.: Hydrogen supply chain planning with flexible transmission and storage scheduling. *IEEE Trans. Sustain. Energy* **12**(3), 1730–1740 (2021). <https://doi.org/10.1109/TSTE.2021.3064015>
12. Shen, X., Nie, C., Hong, L.: Coordination control strategy of wind power-hydrogen alkaline electrolyzer bank considering electrothermal characteristics. *Trans. China Electrotechn. Soc.* **36**(3), 463–472 (2021). (in Chinese)
13. Oikonomou, K., Parvania, M.: Optimal coordination of water distribution energy flexibility with power systems operation. *IEEE Trans. Smart Grid* **10**(1), 1101–1110 (2019)
14. Shan, T., Song, P., Li, Y.: Cost analysis of hydrogen from the perspective of the whole industrial chain of production, storage, transportation and refueling. *Nat. Gas Chem. Ind.* **45**(01), 85–90+96 (2020). (in Chinese)

Research and Application on Ferroresonance Suppression Effect of 6~35 kV Potential Transformer Current - Sensitive Harmonic - Free Device



Yue Yang, Hongbing Guo, and Bo Chen

Abstract The existing harmonic elimination devices in Mengxi Power Grid generally have the problem of insufficient fuse capacity, and ferromagnetic resonance has become one of the main reasons for the faults of voltage transformers. This paper analyzes the overvoltage principle of Potential transformer ferromagnetic resonance, summarizes the characteristics of ferromagnetic resonance in the voltage transformer circuit, lists some ferromagnetic resonance control measures, and proposes a flow-sensitive electromagnetic voltage based on PTC material. Transformer harmonic elimination device. The device maintains a low-resistance state during normal operation, does not affect the system or Potential Transformer, and can automatically adjust to an appropriate resistance range during ferromagnetic resonance to destroy the resonance condition. The practical application shows that the current-sensing harmonic elimination device can suppress the excitation inrush current in a short harmonic elimination time, which provides a new idea for the ferromagnetic resonance management of the transformer.

Keywords Distribution Network · Potential Transformer · Ferroresonance · Flow-sensitive resistance

Y. Yang (✉) · H. Guo · B. Chen
Inner Mongolia Power (Group) Co., Ltd., Inner Mongolia Power Research Institute Branch,
Hohhot 010020, China
e-mail: Y18548139798@163.com

Inner Mongolia Enterprise Key Laboratory of High Voltage and Insulation Technology,
Hohhot 010020, China

© Beijing Paiké Culture Commu. Co., Ltd. 2023
X. Dong et al. (eds.), *The proceedings of the 10th Frontier Academic Forum of
Electrical Engineering (FAFEE2022)*, Lecture Notes in Electrical Engineering 1054,
https://doi.org/10.1007/978-981-99-3408-9_49

1 Introduction

For a long time, resonant overvoltage in power system has seriously threatened the safety of power grid. Especially in the distribution network of 6~35 kV, because the neutral point of the system is not grounded, when the bus switch closing operation or failure occurs, the generated transient impact will cause series effect between Electromagnetic Potential Transformer (PT) and the capacitor in the system, resulting in serious ferroresonance overvoltage in the system. This kind of overvoltage is one of the internal overvoltage that cause many accidents. It may lead to misoperation of ground indicator and rupture of primary PT fuse, or burn PT, or even blow up the insulator and arrester of the system, resulting in system outage [1–3].

In the second quarter of 2022, 39 cases of 6~35 kV PT faults and defects occurred in Mengxi Power Grid, among which 18 cases were caused by resonance and insufficient capacity of harmonic eliminators, accounting for 46.15%. there were 6 cases of fuse burn, 8 cases of breakdown, and 4 cases of deharmonizer deterioration. although pt is basic configuration stake power grid harmonic elimination device, but due to the lack of the net harmonic elimination device testing link, and as the continuous expansion of grid, harmonic elimination device is widespread fusing existing the problem of insufficient capacity, not enough to prevent ferroresonance PT fault, to that end, this paper proposes a flow sensitive type harmonic free installation of ferromagnetic resonance suppression method, the method can effectively eliminate the ferroresonance generated by PT and ground capacitance in 6~35 kV distribution network.

2 Principle and Characteristics of PT Ferromagnetic Resonance Overvoltage

2.1 *Harm of Ferromagnetic Resonance Overvoltage in Distribution Network*

In the neutral point ungrounded system, a Y_0 type electromagnetic PT is usually connected to the bus. The system ground parameters include the excitation inductance L of the transformer in addition to the ground capacitance C of the power conductor and the equipment. When the power system is in normal operation, the three phases are basically balanced, the operating point of the PT is in the non-saturation region, the excitation inductance of each phase is basically the same, and the displacement voltage of the neutral point is small. When the single-phase grounding of the line, the sudden change of the system operation mode or the switching of electrical equipment, the large fluctuation of the system load, the unbalanced change of the load and other disturbances, the neutral point displacement will generate zero-sequence voltage, and the increasing line current will cause the core of PT is gradually magnetically

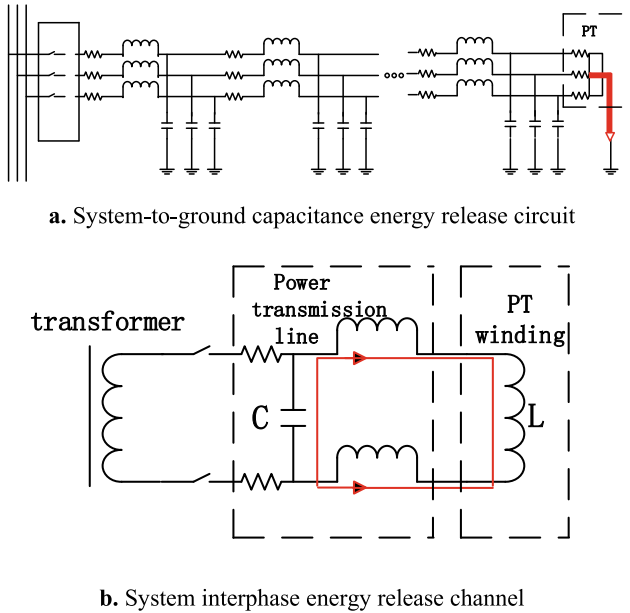


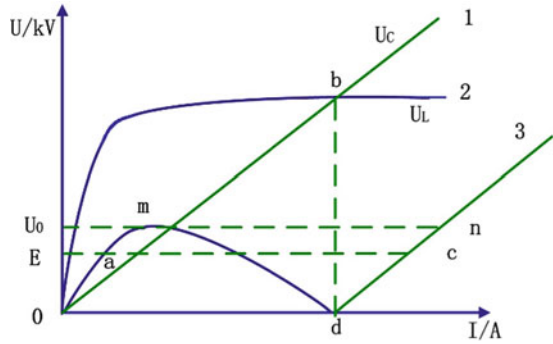
Fig. 1 System capacitance energy release channel

saturated. When the parameter matching of the capacitor and the inductor meets the excitation conditions of the series resonance, a resonance circuit is formed with the line-to-ground capacitance, the excitation causes the resonance overvoltage. Since the neutral point of the distribution network system is not grounded, the grounded neutral point of the high-voltage winding of the electromagnetic PT connected to Y_0 becomes the only energy release channel for the three phases of the system. The excitation energy generated by the overvoltage will be released through the PT primary neutral point (as shown in Fig. 1(a)), and the excitation energy release loop is shown in Fig. 1(b).

2.2 PT Ferromagnetic Resonance Overvoltage Principle

The volt-ampere characteristics of the nonlinear resonant tank are shown in Fig. 2. Ray 1 represents the volt-ampere characteristics of the capacitor, curve 2 represents the volt-ampere characteristics of the inductor, and ray 3 is the algebraic difference between the two. When there is the excitation of external conditions, the system shows that the current increases, the iron core is saturated, and the inductance decreases. The ray 1 and the curve 2 intersect at point b, resulting in ferromagnetic resonance. At the resonant frequency, the circuit is purely resistive to the outside, and the inductive reactance of the system is equal to the capacitive reactance. The whole process

Fig. 2 The volt-ampere characteristics of the nonlinear resonant tank



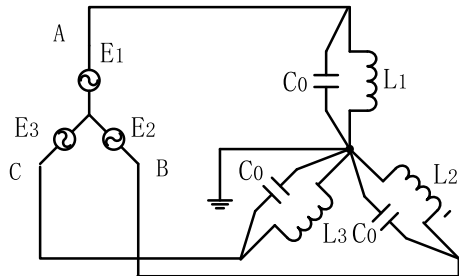
includes three characteristic points: the resonance at the point a has not yet occurred, which is a stable point; resonance occurs at point b, but the capacitance and inductive reactance are still developing, which is an unstable point; when the power supply voltage increases $\Delta U > U_0$, the operating point changes from Point m jumps to point n, with the disappearance of excitation energy, when the voltage returns to the normal operating voltage, the system is stable at point c.

The non-linear characteristics of PT cause the iron core to saturate, and the loop in which it is located then produces a transition from the capacitive state to the inductive state. During this transition, the current surges and the voltage also increases, resulting in overvoltage. The generated ferromagnetic resonance is self-sustaining, that is, the duration of the ferromagnetic resonance overvoltage is generally very long, and it can even exist stably.

L_1, L_2, L_3 are nonlinear excitation inductances in PT, and the capacitance to ground can be regarded as C_0 equivalently. The resonance of the two generates overvoltage. Figure 3 shows the ferromagnetic resonance oscillation circuit.

The non-linear characteristics of PT cause the iron core to saturate, and the loop in which it is located then produces a transition from the capacitive state to the inductive state. During this transition, the current surges and the voltage also increases, resulting in overvoltage. The generated ferromagnetic resonance is self-sustaining, that is, the duration of the ferromagnetic resonance overvoltage is generally very long, and it can even exist stably.

Fig. 3 Ferromagnetic resonance oscillator circuit



During normal operation, the load of the three-phase circuit is balanced to the ground, the neutral point is regarded as zero potential, and no displacement occurs, that is, the neutral point voltage. When the line resonates, displacement occurs, and the corresponding zero-sequence current flows in the PT loop. Due to the small loop resistance and the large zero-sequence current, the generated zero-sequence voltage and the original three-phase voltage are superimposed, forming a serious overvoltage. Assuming that the A-phase resonates at this time, the A-phase nonlinear voltage drops, the other two-phase voltages rise, and the excitation current also rises, causing the PT core to saturate. And the A-phase admittance Y_1 is inductive, and the B-phase admittance Y_2 and C-phase admittance Y_3 are still capacitive. According to Kirchhoff's First Law, there is:

$$U_N = \frac{\sum_{i=1}^3 E_i Y_i}{\sum_{i=1}^3 Y_i} \quad (1)$$

After resonance, $\sum_{i=1}^3 Y_i$ will probably approach to zero and U_N grows larger, so the series resonance after disturbance is usually very serious.

2.3 Characteristics of Ferromagnetic Resonance in PT Circuit

According to the division of the resonance region by Peterson H.A, [4–6] the ferromagnetic resonance of PT loop can be divided into three resonance modes: fundamental wave, frequency division and frequency doubling:

- (1) When the fundamental wave resonance occurs, the overvoltage does not exceed 3.2 times of the phase voltage, and the three-phase voltage appears as two-phase increase and one-phase decrease, which may issue a false grounding signal;
- (2) When frequency division resonance occurs, the overvoltage does not exceed 2.5 times of the phase voltage. The PT opening voltage is generally concentrated between 85 and 95 V, and the three-phase voltage increases in turn. Due to the large overcurrent, it is easy to cause fuses. fuse;
- (3) When high frequency resonance occurs, the resonance frequency is 3 times or 5 times of the rated frequency of the power grid, the opening voltage generally exceeds 100 V, the three-phase voltage of the system increases at the same time, and the overcurrent is small. In the process of high frequency resonance, a large amount of heat is accumulated, which is easy to cause vicious accidents such as PT insulation breakdown and even explosion.

3 Research and Analysis on Treatment Measures of Ferromagnetic Resonance

3.1 *Change the Resonance Parameters*

(1) Adopt PT with good excitation performance

The neutral point displacement overvoltage is closely related to the volt-ampere characteristics of the PT. The worse the excitation characteristic is, the easier it is to excite the neutral point displacement overvoltage. Therefore, improving the excitation characteristics of PT is a measure to eliminate ferromagnetic resonance overvoltage. Although the method of increasing the saturation of PT reduces the probability of resonance, once resonance occurs, the overvoltage and overcurrent generated will be greater, and the harm will be greater.

(2) Increase the ground capacitor bank

The circuit capacitance is increased by putting in the backup line and installing a group of three-phase-to-ground capacitors on the bus, thereby destroying the resonance condition. However, if there are multiple PTs on the line, this method is usually not used because of the large capacity required to be installed.

(3) The neutral point is grounded through the arc suppression coil.

This method is equivalent to connecting an inductance in parallel with the excitation inductance of each phase of the PT, which breaks the parameter matching relationship and reduces the probability of arc overvoltage, but the capacity of the arc suppression coil needs to change with the development of the power grid. For smaller systems, if the neutral point through the arc suppression coil is installed in order to suppress the ferromagnetic resonance, the economy will not be satisfied.

(4) 4PT wiring method.

The essence of this wiring method is to add a zero-sequence PT to the neutral point of each single-phase PT. When the neutral point of the system is displaced, the single-phase PT is still under the phase voltage, and the iron core is still in the linear region (unsaturated). So as to achieve the effect of suppressing ferromagnetic resonance. However, when multiple groups of PTs are connected, each group of PT must be wired in this way to be effective, and the neutral point-to-ground voltage (zero sequence voltage) of the three-phase PT is also raised, requiring higher dielectric strength and occupying a larger space.

3.2 *Increase System Damping*

The principle is that the PT resonance of the distribution network has zero-sequence properties, and positive sequence parameters such as system load and interphase capacitance do not participate in the resonance. The generation and development of

resonance can be damped by adding resistance in the zero-sequence loop. The main practices are:

(1) Add a damping resistor to the open delta winding

This method has a certain effect on suppressing resonance, but the size of the resonance elimination resistor is not easy to choose. The smaller the resistance, the more conducive to suppressing the resonance. However, when the system fails, it will cause the PT to be overloaded and increase the possibility of PT burning. If it is larger, it will not have the effect of suppressing resonance. At present, the common application in engineering is microcomputer harmonic elimination.

(2) PT neutral point is grounded through nonlinear varistor.

When the grounding resistance of the neutral point on the primary side of the PT is large enough, the excitation inrush current of the primary winding can be limited to avoid saturation of the transformer core. Obviously, the larger the neutral point grounding resistance, the better the harmonic cancellation effect. When the system resonates and the overvoltage amplitude is low, the varistor is in a high-resistance state and is effective at the initial stage of resonance; but when the system fails, it is in a low-resistance state, the flowing current increases, and thermal breakdown is likely to occur; During normal operation, the impedance of the varistor is extremely large, reaching the megohm level, which affects the measurement accuracy of the PT.

4 Flow-Sensitive Intelligent Harmonic Elimination Management Technology

To sum up, this paper proposes a flow-sensitive harmonic elimination device based on PTC (Positive Temperature Coefficient) material. Its function is to maintain a low resistance state during normal production operation without affecting the system or PT; when ferromagnetic resonance Can automatically adjust to the appropriate resistance range to break the resonance condition [11].

4.1 *The Working Principle of the Flow-Sensitive Harmonic Elimination Device*

The current-sensitive harmonic elimination device mainly uses the characteristics of PCT to form an automatic control function, and its characteristics include: resistance-temperature characteristics, current-voltage characteristics, and current-time characteristics. In actual operation, when the flow-sensitive intelligent harmonic elimination device reaches a certain transformation temperature (Curie temperature point), the temperature coefficient can reach $+(15 \sim 60)\%/^{\circ}\text{C}$ or more, and the mutual transformation of semiconductor and insulator occurs, and the resistance value occurs.

Jump (3 to 7 orders of magnitude), reducing the system current, and suppressing the resonance; in the normal operation state, the harmonic elimination device returns to a low resistance state due to the temperature rise; the applied voltage has a large initial current and sudden continuous decay part, that is, the greater the resonance energy, the faster the varistor heats up, and the shorter the time it takes to stabilize.

4.2 Simulation

Build a 3PT ferromagnetic resonance simulation model (as shown in Fig. 4). The PT neutral point is grounded through the flow-sensitive harmonic elimination device in the loop, and the resistance is raised to a high-resistance state for a short time after resonance. Set the PT neutral point to be grounded through a 40 kΩ resistor during normal operation. After the ferromagnetic resonance occurs, the neutral point is set to a resistance of 400 kΩ, when $t = 0.1$ s is set in the model.

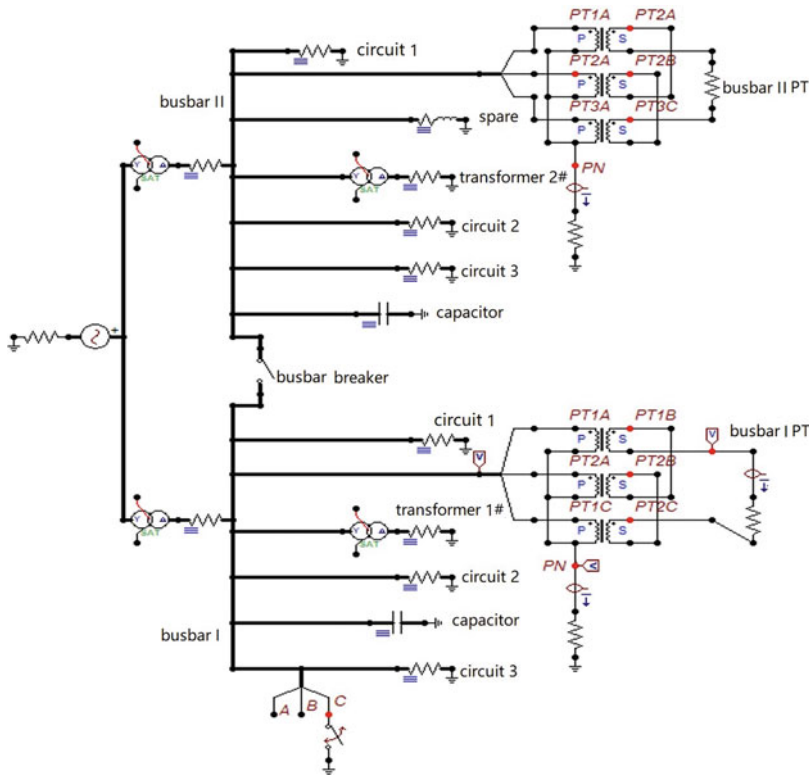


Fig. 4 Ferromagnetic resonance oscillator circuit

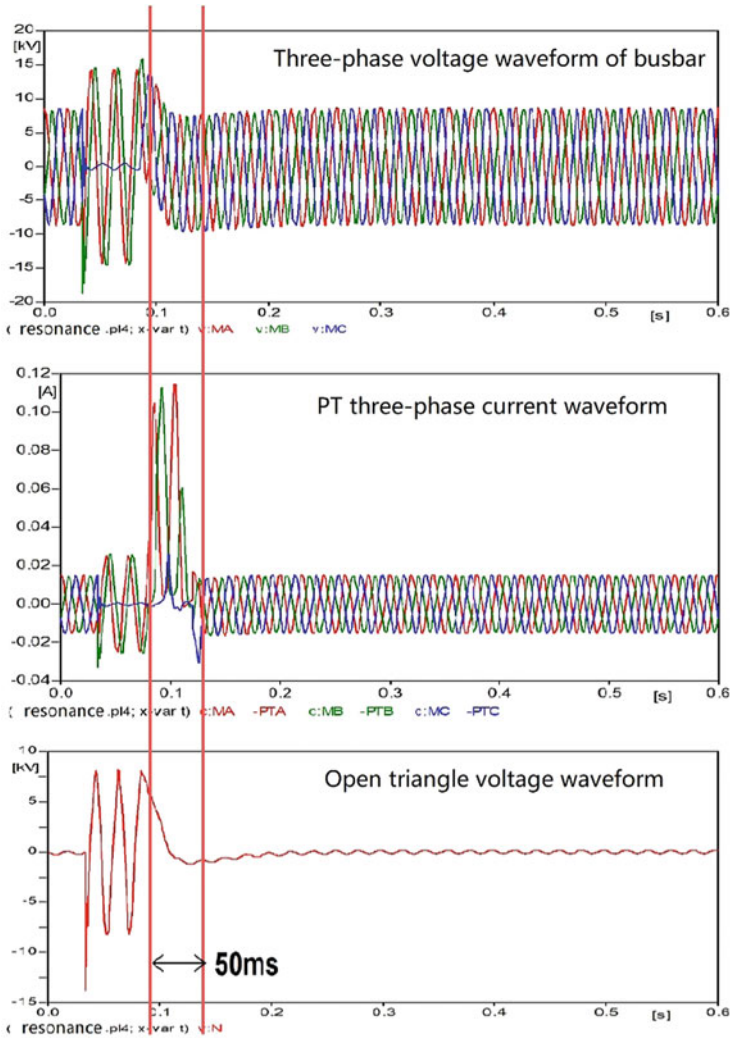


Fig. 5 Flow-sensitive intelligent harmonic elimination simulation waveform

The waveform of each feature quantity is obtained as shown in the Fig. 5. After the PT neutral point is put into a large resistance, it can be seen from the waveform that the three-phase voltage of the system bus is close to normal after about 50 ms, and the open delta voltage and the three-phase current flowing through the PT gradually tend to normal operation, which means that the flow of the neutral point in series. The sensitive intelligent comprehensive harmonic elimination device has a good suppression effect on the PT ferroresonance. The PT three-phase current is suppressed below 200 mA, and the harmonic elimination time is short, which has a good harmonic elimination effect.

5 Flow-Sensitive Intelligent Harmonic Elimination Management Technology

From January 1st to March 29th, 2022, in one 110 kV substation, DS I No.314 circuit and DS II No.313 circuit, pulled a total of 12 times. When the voltage is abnormal, the regulator will notify the on-duty personnel in the station to check the equipment. After several inspections, the equipment in the station is normal, and then the voltage of the pull-out circuit returns to normal after regulation.

At 00:19 on March 29, 2022, the monitoring showed that the bus voltage of the 35 kV I section of the station was abnormal. The station personnel checked the abnormal voltage of the 35 kV busbar I on the side of the monitoring machine, U_a : 32.7 kV, U_b : 37.8 kV, U_c : 14.7 kV. At 00:23, the DS II No.313 circuit breaker was opened by regulation and control, and the abnormality of the bus bar did not disappear. At 00:28, the regulation and control opened the DS I No.314 circuit breaker, and the voltage returned to normal. At 00:32, the voltage of the 35 kV busbar I was abnormal again U_a : 5.5 kV, U_b : 37.3 kV, U_c : 15.4 kV. The dispatcher notified that the grounding of the 35 kV busbar I needs to check the equipment on site. The station personnel checked the auxiliary control equipment and found that the A and C phases of No.381 PT were smoking and catching fire. At 00:42, the No.351 circuit breaker was opened by regulation and control. The station personnel went to the site to check and found that the A and C phases of No.381 PT bodies burst, the three-phase burst of the primary melting tube, and the three-phase porcelain bottle of the arrester all had burn marks of varying degrees, as shown in Fig. 6.

The operation mode of the station is double-column in parallel, the PT connection mode is 3PT grounding through the harmonic elimination coil, the 35 kV system capacitance current test results are consistent with the two parallel operation test



Fig. 6 PT is seriously damaged

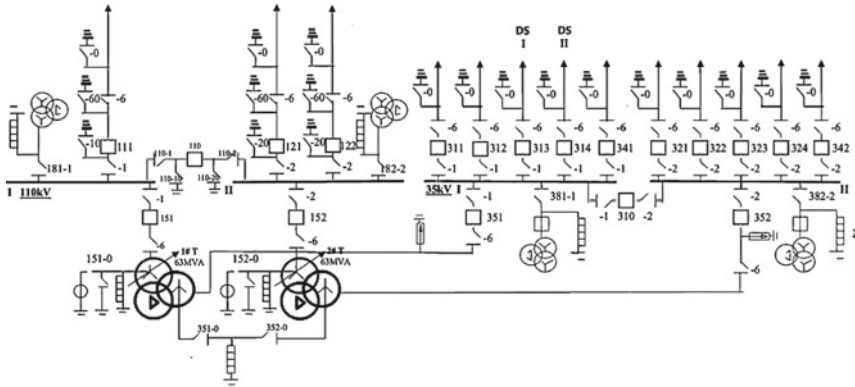


Fig. 7 110 kV substation high voltage equipment wiring diagram

results, and the 10 kV system capacitance current test shows that the two parallel operation test results are different but both less than 10 A (Fig. 7).

The cause of the fault is that the PT circuit has multiple ground faults in a short period of time, and the harmonic elimination coil cannot absorb the energy of the accumulated resonance. The cumulative effect of the fault makes the harmonic elimination device abnormal performance and cannot protect the PT. Eventually, the PT bursts due to the impact of the resonant voltage and the accumulation of thermal effects. The solution is to replace the PT and install a flow-sensitive harmonic-free device and an active harmonic elimination device, as shown in Fig. 8. After 4 months of operation, the line runs smoothly, and no more PT burning and fuse blown phenomenon happened.

Fig. 8 Replace PT and install flow-sensitive harmonic eliminator



6 Conclusion

Since the neutral point of the distribution network is not grounded, it is very easy to cause disturbance and then generate resonance overvoltage. If the configured harmonic elimination device has the defect of insufficient fusing capacity, it will cause PT fault. In this paper, the principle and characteristics of ferromagnetic resonance overvoltage generated by PT are analyzed, and a ferromagnetic resonance suppression method based on a flow-sensitive harmonic free device is proposed by comparing the common harmonic elimination measures in the network. The length of the resonance elimination time of this type of device is related to the neutral current and the resonance energy. The greater the neutral point current during resonance, the faster the resonance disappears. When the single-phase grounding occurs in the system, the amplitude of the PT open triangle voltage will not change significantly. Practice has shown that this type of harmonic-free device can effectively solve the problems of fuse blowing and PT explosion caused by intermittent grounding of the system.

References

1. Wang, L., Li, W., Shi, W.: Study on the computer simulation of ferroresonance overvoltage in 10 kV distribution system. *High Volt. Appar.* **40**(4), 269–271 (2004)
2. Wang, X., Li, B., Pang, C.: Research review on ferroresonance in power systems. *Elect. Power Sci. Eng.* **4**, 49–51 (2002)
3. Zhang, X., Zhang, H., Li, Y.: Danger, distinction and prevention and cure treatment on ferroresonance in electricity system. *J. Elect. Power.* **2002**(4), 283–286 (2002)

4. Liang, Z., Zhao, M., Niu, S., et al.: Sizing and siting of BESS for grid connected microgrid with electric vehicles. *Elect. Power Autom. Equip.* **36**(9), 17–24 (2016)
5. Chen, X.: The analysis on excitation characteristics of electromagnetic transformer. Shandong University, Jinan (2013)
6. Yang, Q.: The digital simulation if Simulation analysis of ferroresonance in power system and wavelet analysis. North China Electric Power University (2001)
7. State Grid Corporation. Eighteen major power grid anti-accident measures of State Grid Corporation (State Grid Health [2012] No. 352) (2012)
8. He, L., Wu, J., Zhang, L., et al.: Researches on ferromagnetic resonance calculation and harmonic elimination measures in substation based on EMTP - ATP. *High Volt. Appar.* **54**(5), 210–216 (2018)
9. He, Z., Li, X., Fan, M., et al.: Research on suppression of ferromagnetic resonance overvoltage based on harmonic elimination. *Insul. Surge Arrest.* **2017**(5), 77–84 (2017)
10. Zhang, Y., Liu, S.: Study of comprehensive suppression method for distribution network ferromagnetic resonance. *High Volt. Appar.* **52**(11), 137–142 (2016)
11. Wu, X., AI, S., Fan, Y., et al.: The study and application of the primary current limiting harmonic excluder for the type of the thermal resistor. *Ningxia Elect. Power* **2008**(6), 35–38 (2008)

Delta Measurement Analysis Method Applicable to All-Parallel AT Traction Network of High Speed Railway



Dongdong Li and Zhengqing Han

Abstract At present, the superimposed (delta) measurement protection is used as backup protection in the traction power supply system, mainly using the superimposed current to form the protection criterion, lacking the theoretical analysis basis of delta measurement in the traction power supply system. The parameter correspondence between the autotransformer (AT) traction network and the equivalent network is investigated, and the distribution of fault current is deduced by analyzing the equivalent circuit of all-parallel AT traction network. This paper proves the adaptability of the fault component method for nonlinear components such as electric multiple units, introduces the fault component method to analyze the all-parallel AT traction network, gives fault component equivalent circuit diagrams for all-parallel AT traction networks, derives the delta measurement expressions at each circuit breaker (CB), analyzes the distribution characteristics of delta measurement in traction networks, and gives constraints to unify the phase characteristics of delta measurement for no-load and on-load conditions. The simulation results verify the correctness of the theoretical analysis.

Keywords All-parallel autotransformer · Fault component method · Delta measurement · Nonlinear components

1 Introduction

All-parallel autotransformer railway system (AARS), provide a single-phase 2×25 kV, 50 Hz AC supply to high-speed electric multiple units (EMU) in China. High ridership, high departure density and heavy load are the features of high-speed EMU. In order to reduce the impedance of traction network, enhance the power supply

D. Li · Z. Han (✉)
Southwest Jiaotong University, Chengdu 610031, China
e-mail: hanzhengqing@home.swjtu.edu.cn

D. Li
e-mail: lddswjtu@163.com

© Beijing Paiké Culture Commu. Co., Ltd. 2023
X. Dong et al. (eds.), *The proceedings of the 10th Frontier Academic Forum of Electrical Engineering (FAFEE2022)*, Lecture Notes in Electrical Engineering 1054, https://doi.org/10.1007/978-981-99-3408-9_50

capacity and meet the power demands of EMU, the up and down lines are connected at AT post (ATP) and section post (SP) through busbars in AARS. However, when a fault occurs, multiple circuits will appear to supply power to the fault point with large fault current at the same time because of the parallel branch. Compared with the general speed railway, high-speed railway load current is greater, usually more than twice the general speed railway load current. But the current, impedance and other protection principles do not change, which leads to high-speed railway protection sensitivity is lower compared to the general speed railway. When the line has a high resistance fault, the traditional current and impedance protection cannot act, can only rely on the delta measurement protection as a backup protection. At present, the delta measurement protection in the traction power supply system mainly uses the superimposed current to form the protection criterion. the theoretical analysis basis of delta measurement is lacking for the structure of AARS and the nonlinearity of EMU.

A large number of studies exist on the fault component method in power systems, and protection methods such as the energy function method [1, 2], the sequence component method [3–7], the phase comparison method [8], and waveform similarity method [9] have been proposed, which are based on the characteristics of the voltage and current fault components to discriminate faults. Reference [10] investigated the effect of grid-connected distributed generation on the fault component method. However, due to the EMU draws current in the range of AARS, the characteristics of the delta measurement in the traction power supply system are not exactly the same as in the power system. Meanwhile, there is no sequence component in the single-phase railway system because of its topology and physical properties. Therefore, the above research results of fault components in power systems cannot be directly applied to AARS.

There are few theoretical studies on delta measurement in traction power supply systems. Reference [11] used the correlation coefficient method to calculate the delta measurement waveforms at three posts on the same line, and the results were used to discriminate between in-phase and reverse-phase to select the faulty line. This reference only studied the method of using the delta measurement to select the faulty line in case of traction network fault in no-load condition, and has not studied the distribution law of the delta measurement in the AARS from the theoretical level by combining the fault component method in the power system.

In order to solve the above problems, this paper introduces the analysis method of fault components [6], investigates the influence of EMU, a nonlinear element, on the fault component method, analyzes the fault component equivalent network of the AARS, derives the expression for the delta measurement at each breaker, and studies the distribution law of the delta measurement in the AARS.

2 Fault Current Analysis

AARS Schematic diagram is shown as Fig. 1. Traction catenary (T), rail (R) and feeder (F) of the up and down lines are connected in parallel at the SS, ATP and SP busbars. CB1 to CB6 are the circuit breakers installed at SS, ATP and SP, which can be tripped by relay1 to relay6. The autotransformers are connected to the busbar, and the length of feeding section between SS and SP is usually 20 to 30 km. We take the busbar-to-line direction as the positive direction. \dot{I}_{Tn} , \dot{I}_{Rn} and \dot{I}_{Fn} denote the T-line current, R-line current, and F-line current at the relays, respectively, n is the number 1 to 6. In AARS, the fault current is the difference between the T-line current and the F-line current at the relays, i.e. $\dot{I}_n = \dot{I}_{Tn} - \dot{I}_{Fn}$.

The equivalent network derived in the Reference [9] is the equivalent of the AT traction network shown in Fig. 2 as a circuit composed of the equivalent self-impedance of the T, R, and F lines and the transformer leakage resistance (shown in Fig. 3). In Fig. 2, I is the fault current, I_T , I_R , and I_F , are the currents flowing through the first end of T, R, and F lines respectively in the original circuit diagram. Z_T , Z_R , Z_F , Z_{TR} , Z_{TF} , Z_{FR} are the self-impedance and mutual impedance of T, R and F lines respectively in the original circuit diagram. In Fig. 3, I'_T , I'_R and I'_F are the currents at the first ends of T, R and F lines in the equivalent circuit diagram, Z_1 , Z_2 and Z_3 are the equivalent self-impedances of the equivalent T, R and F lines, respectively. Z_g is the leakage reactance of the traction transformer and Z'_g is the leakage reactance of AT. Take any 1 km long section of the AT network and write the T ~ F loop equation as follow [12]:

$$\dot{U}_1 - \dot{U}_2 = \frac{Z_T - Z_{TF}}{2} \cdot \dot{I}_T + \frac{Z_{TR} - Z_{FR}}{2} \cdot \dot{I}_R + \frac{Z_{TF} - Z_F}{2} \cdot \dot{I}_F \quad (1)$$

The parameter correspondence between the AT traction network and the equivalent circuit is obtained by deriving formula (1) according to Davinan's theorem [12], as follows:

Fig. 1 Schematic diagram of AARS

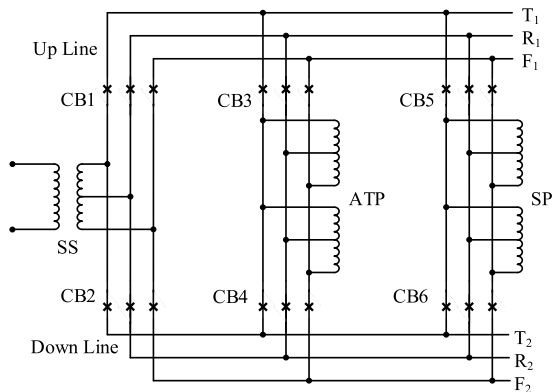


Fig. 2 AT traction network original circuit diagram

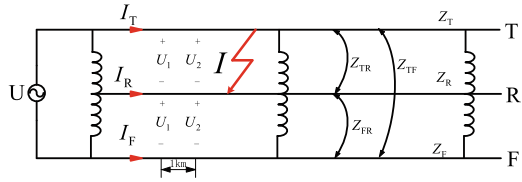
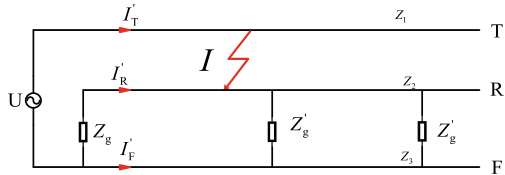


Fig. 3 AT traction network equivalent circuit diagram



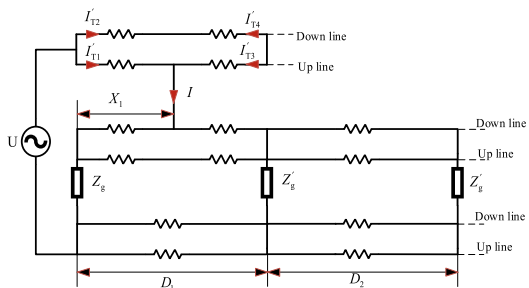
$$\begin{cases} \dot{I}'_T = \dot{I}_T - \dot{I}_F \\ \dot{I}'_R = \dot{I}_R \\ \dot{I}'_F = 2\dot{I}_F \end{cases} \quad (2)$$

$$\begin{cases} Z_1 = \frac{1}{2}(Z_T + Z_{FR} - Z_{TR} - Z_{TF}) \\ Z_2 = Z_R + \frac{1}{2}(Z_T + Z_{TF} - 3Z_{TR} - Z_{FR}) \\ Z_3 = \frac{1}{4}(Z_F - Z_T) + \frac{1}{2}(Z_{TR} - Z_{FR}) \end{cases} \quad (3)$$

Three types of faults usually occur in the all-parallel AT traction network: **T-R fault**, **F-R fault** and T-F fault. When a T-R fault occurs between the SS and the ATP on the up line, the equivalent circuit of AARS can be derived based on the AT traction network equivalent circuit at the time of the fault, as shown in Fig. 4. In Fig. 4, X_1 is the distance from the fault point to SS, D_1 is the length from the SS to the ATP, and D_2 is the length from the ATP to the SP.

Since $\dot{I}'_T = \dot{I}_T - \dot{I}_F$, the equivalent T-line current is the measured current, i.e. $\dot{I}'_n = \dot{I}'_{Tn}$. According to Fig. 4, the equivalent T-line current can be deduced from the distribution law of the fault current at each breaker, as follow:

Fig. 4 T-R fault equivalent circuit diagram for first AT section of AARS



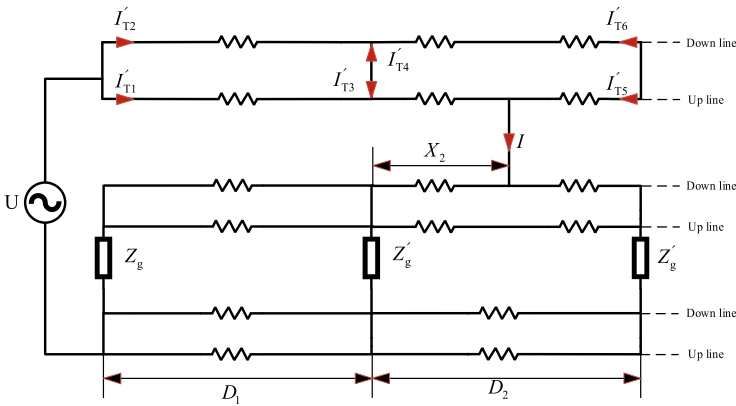


Fig. 5 T-R fault equivalent circuit diagram for second AT section of AARS

$$\begin{cases} i_1 = \frac{2D_1 - X_1}{2D_1} i \\ i_2 = i_3 = -i_4 = \frac{X_1}{2D_1} i \\ i_5 = i_6 = 0 \end{cases} \quad (4)$$

When the fault occurs between the ATP and the SP of the up line, the equivalent circuit of AARS can be obtained as shown in Fig. 5. In Fig. 5, X_2 is the distance of the fault point from the ATP of the second AT section.

Similarly, the relationship between the measured current at each circuit breaker and the fault current can be introduced according to the equivalent circuit diagram in Fig. 5, as follow:

$$\begin{cases} i_1 = i_2 = \frac{1}{2} i \\ i_3 = -i_4 = \frac{D_2 - X_2}{2D_2} i \\ i_5 = -i_6 = \frac{X_2}{2D_2} i \end{cases} \quad (5)$$

From (4) and (5), when a fault occurs between SS and ATP, the delta measurement of the up and down lines at the SS are of different magnitude and in the same direction, and the delta measurement of the up and down lines at the ATP are of the same magnitude and in different direction. And when a fault occurs between ATP and SP, the delta measurement of the up and down lines at the SS are of the same magnitude and direction, and the delta measurement of the up and down lines at the ATP and the SP are of the same magnitude and in different direction.

3 Delta Measurement Analysis

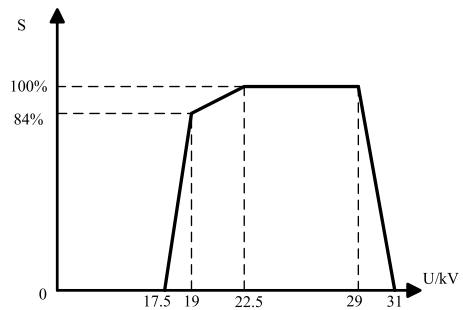
The EMU will move at high speed in the AARS, and is a typical nonlinear load. Since the fault component method is based on the superposition principle and is only applicable to linear systems, it is necessary to consider the adaptability of the fault component method in the AARS. Take CRH2 as an example, its voltage–power characteristic curve is shown in Fig. 6.

According to the characteristic curve in Fig. 1, the function between power and network voltage can be written as follow:

$$S_* = \begin{cases} 0 & U_L \in (0, 17.5)kV \\ 0.84 \times \frac{U_L - 17.5}{19 - 17.5} & U_L \in (17.5, 19)kV \\ 0.84 + 0.16 \times \frac{U_L - 19}{22.5 - 19} & U_L \in (19, 22.5)kV \\ 1 & U_L \in (22.5, 29)kV \\ 1 - \frac{U_L - 29}{31 - 29} & U_L \in (29, 31)kV \\ 0 & U_L \in (31, +\infty)kV \end{cases} \quad (6)$$

where, U_L is the effective value of the traction network voltage at the EMU, S_* is the standard value of the EMU power. According to the formula of apparent power calculation, the train current variation law under different traction network voltage range can be deduced, expressed by segment function as:

Fig. 6 Traction characteristics of CRH2



$$I_{L*} = \begin{cases} 0 U_L \in (0, 17.5)kV \\ 14 - \frac{245}{U_L} U_L \in (17.5, 19)kV \\ 1.1429 - \frac{0.7143}{U_L} U_L \in (19, 22.5)kV \\ \frac{25}{U_L} U_L \in (22.5, 29)kV \\ -12.5 + \frac{387.5}{U_L} U_L \in (29, 31)kV \\ 0 U_L \in (31, +\infty)kV \end{cases} \quad (7)$$

where I_{L*} is the standard value of the EMU current.

The load current of the EMU has less harmonic content and can be approximated as a standard sine wave with a frequency of 50 Hz. For the EMU, the power factor $\cos \varphi$ is determined, the phase difference between voltage and current is φ , and the PWM rectifier module of the EMU adjusts the phase of the load current according to the phase of the network voltage. In summary, the amplitude and phase of load current \dot{I}_L are determined by the network voltage at the EMU, which can be equated to the voltage controlled current source equivalent model. It can be expressed as:

$$\dot{I}_L = f(\dot{U}_L) \quad (8)$$

When the superposition principle is used in the presence of a controlled source in the circuit, the controlled source cannot act alone and must always remain in the circuit. Therefore, the fault component method can be used properly in AARS.

The fault component method is used to analyze the short-circuit conditions of the AARS at no load, and the faulty traction network is decomposed into the pre-fault system state and the fault component state by the superposition principle to obtain the fault component additional network equivalent circuit diagram of the AARS as shown in Fig. 7. In Fig. 7, $\Delta \dot{E}_k$ is the network voltage before the fault at the fault point, and $\Delta \dot{I}$ represents the delta measurement of the system. Since it originates from the same voltage source, it can be seen from Fig. 7 that the delta measurement at all breakers are in the same phase or differ by 180° .

The delta measurement at each breaker in Fig. 7 are expressed as:

$$\begin{cases} \Delta \dot{I}_1 = \frac{(2D_1 - X_1)}{2D_1} \Delta \dot{I} \\ \Delta \dot{I}_2 = \Delta \dot{I}_3 = -\Delta \dot{I}_4 = \frac{X_1}{2D_1} \Delta \dot{I} \\ \Delta \dot{I}_5 = \Delta \dot{I}_6 = 0 \end{cases} \quad (9)$$

where $\Delta \dot{I}_1 \sim \Delta \dot{I}_6$ denotes the delta measurement at relay1 ~ relay6, respectively.

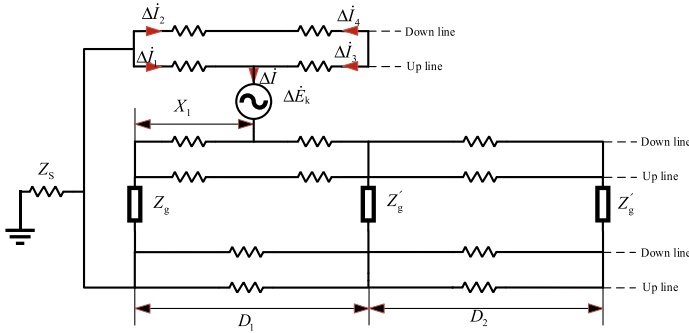


Fig. 7 Fault component equivalent circuit diagram of AARS at no load

It can be seen from (9) that when the traction network is no-load, after the fault occurs between the SS and the ATP, the delta measurement at the SS on the up and down lines are of different magnitude and in the same direction, and the delta measurement at the ATP on the up and down lines are of the same magnitude and in different direction. Combining with (4), we can see that when the traction network is no-load, the delta measurement and the fault current show the same law. Similarly, when the fault occurs in the ATP and the SP, the delta measurement and the fault current also have the same law, and the expression of delta measurement is:

$$\begin{cases} \Delta i_1 = \Delta i_2 = \frac{1}{2} \Delta i \\ \Delta i_3 = -\Delta i_4 = \frac{D_2 - X_2}{2D_2} \Delta i \\ \Delta i_5 = -\Delta i_6 = \frac{X_2}{2D_2} \Delta i \end{cases} \quad (10)$$

From (4), (5), (9) and (10), it can be seen that when a fault occurs in the traction network at no load, the delta measurement and the fault current change in the same pattern, but when there is an EMU in traction network, the delta measurement change is more complicated. When a fault occurs in the traction network which is under load conditions, the voltage controlled current source model is used instead of the EMU, and the fault component method is used to obtain the fault component equivalent circuit diagram of AARS as shown in Fig. 8. ΔI_L in the figure indicates the load current change before and after the fault. Usually the traction network voltage will fall to a lower level after the fault occurs, and the EMU will stop taking current from the traction network because of pulse latching, so ΔI_L is generally equal to the load current before the fault.

When a fault occurs in the traction network under load conditions, the delta measurement needs to consider both the fault current and the load current, and the delta measurement at each breaker in Fig. 8 is expressed as:

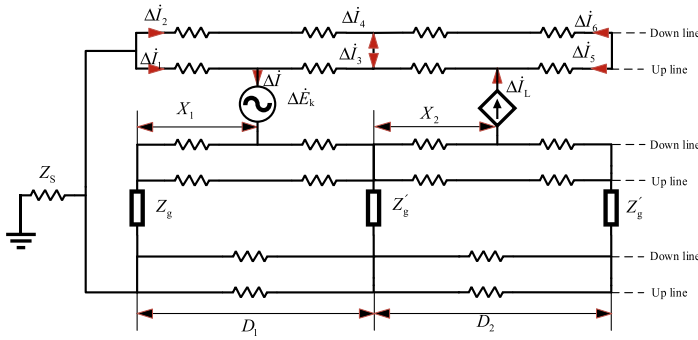


Fig. 8 Fault component equivalent circuit diagram of AARS with load

$$\begin{cases} \Delta i_1 = \frac{(2D_1 - X_1)}{2D_1} \Delta i - \frac{1}{2} i_L \\ \Delta i_2 = \frac{X_1}{2D_1} \Delta i - \frac{1}{2} i_L \\ \Delta i_3 = -\Delta i_4 = \frac{X_1}{2D_1} \Delta i - \frac{(D_2 - X_2)}{2D_2} i_L \\ \Delta i_5 = -\Delta i_6 = -\frac{X_2}{2D_2} i_L \end{cases} \quad (11)$$

As can be seen from (9) and (11), unlike no-load lines, the mobility of EMU can lead to variable load current measurements at the relays and more complex delta measurement changes when there is an EMU. Taking the fault condition in Fig. 8 as an example, according to Eqs. (4) and (11), it is known that after the fault, the measured current at SP is close to 0. The delta measurement consists entirely of load currents, resulting in a negative directional delta measurement at CB5. This is because the uncertainty of the load location and fault location lead to uncertainty in the magnitude and phase of the load current and fault current at the relays. Four combinations of different load currents and fault currents will be in existence before and after the fault. The delta measurement is in reversed-phase with the fault current only when the fault current amplitude is less than the load current amplitude and both are in phase. Due to the uncertainty of the load location and fault location, the reversed-phase delta measurement may occur at each relay, resulting in the phase characteristics of the delta measurement being inconsistent with the no-load condition. Therefore, in order to unify the phase characteristics of

delta measurement under load and no-load conditions, the phase characteristics of delta measurement are not considered when the fault current amplitude is smaller than the load current.

4 Simulation Validation

We employed the model as shown in Fig. 1 to verify the correctness of delta measurement analysis. The model was built on MATLAB/Simulink with parameters described as follows: the capacity of traction transformer is 40MVA, and the ratio of the transformer is 220 kV/27.5 kV/27.5 kV. The AT capacity is 10MVA. The self-impedance of T, R and F are $0.1465 + j0.589 \Omega/\text{km}$, $0.0842 + j0.407 \Omega/\text{km}$ and $0.1452 + j0.713 \Omega/\text{km}$, the mutual impedance between T and R, R and F, T and F are $0.05 + j0.315 \Omega/\text{km}$, $0.05 + j0.332 \Omega/\text{km}$, $0.05 + j0.3 \Omega/\text{km}$. The length of feeding section between SS and ATP, ATP and SP are 12 km, 13 km. The load current is set to 800A.

In order to verify the correctness of the theoretical analysis of delta measurement, different locations of T-R faults are set for the traction network under no-load condition and load condition, where only the load under f4 condition is located on the down line and the rest of the load and faults are located on the up line, the theoretical calculation and simulation results are shown in Table 1. The phase angle of $\Delta \dot{E}_k$ in the theoretical calculation is set to -150° , assuming that the EMU power factor is 1. Since $\Delta \dot{I}_3$ and $\Delta \dot{I}_4$, $\Delta \dot{I}_5$ and $\Delta \dot{I}_6$ are of equal magnitude and opposite direction, the theoretical calculation and simulation results of $\Delta \dot{I}_4$ and $\Delta \dot{I}_6$ are not shown in the table.

From Table 1, it can be seen that the theoretical and simulated results of the delta measurement amplitude are consistent with each other, taking into account certain errors existing in the simulated and theoretical calculations. It can be seen that the simulation results of phase angle at each relay are consistent with the theoretical calculation results, and the phase simulation results of $\Delta \dot{I}_3$ of f5 and $\Delta \dot{I}_5$ of f6 are somewhat different from the other relays, respectively, which are consistent with the possible reversed-phase delta measurement phase characteristics when there is an EMU as discussed in the previous section. The simulation results in Table 1 prove the correctness of the theoretical analysis of the delta measurement of AARS.

Table 1 Theoretical calculation and simulation results of delta measurement

Fault conditions	Fault location /km	EMU Location /km	$\Delta I_1/kA$		$\Delta I_2/kA$		$\Delta I_3/kA$		$\Delta I_5/kA$	
			calculation	simulation	calculation	simulation	calculation	simulation	calculation	simulation
f1	11	-	4.62 ∠125°	4.61 ∠128°	3.9 ∠125°	3.9 ∠128°	3.9 ∠125°	3.9 ∠125°	-	-
f2	24	-	3.4 ∠129°	3.68 ∠132°	3.4 ∠129°	3.68 ∠132°	0.26 ∠129°	0.28 ∠132°	3.14 ∠129°	3.4 ∠132°
f3	18	8	3.71 ∠136°	3.4 ∠126°	3.66 ∠132°	3.46 ∠129°	1.99 ∠135°	1.83 ∠126°	1.66 ∠127°	1.63 ∠132°
f4	18	11 (down line)	3.68 ∠133°	3.44 ∠128°	3.69 ∠134°	3.42 ∠127°	1.93 ∠116°	2.02 ∠139°	1.66 ∠127°	1.63 ∠132°
f5	24	11	3.49 ∠136°	3.54 ∠126°	3.47 ∠135°	3.55 ∠127°	0.48 ∠177°	0.31 ∠174°	3.14 ∠129°	3.37 ∠131°
f6	11	24	4.67 ∠130°	4.53 ∠123°	3.97 ∠130°	3.81 ∠122°	3.91 ∠125°	3.93 ∠127°	0.37 ∠-150°	0.31 ∠-147°

5 Conclusion

This paper introduces the fault component method in the power system to theoretically analyze the faults in AARS under no-load and loaded conditions, respectively, and derives the delta measurement expression formula at each circuit breaker, and draws the following conclusion: the nonlinear EMU can be equated to a voltage-controlled current source, which can be applied to the fault component method. The delta measurement at all the posts of the faulty line is in the positive direction, and the non-faulty line, except for the SS, is in the negative direction. If the load current amplitude is greater than the fault current under loaded condition, the phase characteristics of the corresponding delta measurement are not considered.

In this paper, the modeling simulation of AARS is performed to verify the correctness of the theoretical analysis of the delta measurement about AARS. The delta measurement analysis of AARS in this paper lays the theoretical foundation for delta measurement protection, which is conducive to further research on the delta measurement protection scheme that integrates fault identification and fault line identification.

Acknowledgements This study was supported by the National Natural Science Foundation of China (Grant No. 52177116) and the National Key Research and Development Program of China (No. 2021YFB2601500).

References

1. He, B., Jin, H., Li, J.: Principle and property research of the energy directional protection. *Proc. CSEE* **17**(03), 23–27 (1997). (in Chinese)
2. Yang, J., Wu, H., Dong, X., Chen, J., Liu, Y.: Transmission line fault type identification based on the characteristics of current fault components and random forest. *Power Syst. Protect. Control* **49**(13), 53–63 (2021). (in Chinese)
3. Muda, H., Jena, P.: superimposed adaptive sequence current based microgrid protection: a new technique. *IEEE Trans. Power Deliv.* **32**(2), 757–767 (2017)
4. Zhu, J., Mu, L., Guo, W.: Fault control of inverter interfaced distributed generator considering fault direction identification of the grid-connected microgrid. *Trans. China Electrotechn. Soc.* **37**(03), 634–644 (2022). (in Chinese)
5. Song, G., Chang, P., Hou, J., Zhang, C., Lyu, J.: Adaptability analysis of fault component directional component in AC/DC multi-terminal infeed system. *Autom. Elect. Power Syst.* **45**(09), 136–145 (2021). (in Chinese)
6. Gao, S.P., Song, G.B., Ma, Z.B., Jin, X.F.: Novel pilot protection principle for high-voltage direct current transmission lines based on fault component current characteristics. *IET Gener. Transm. Distrib.* **9**(05), 468–474 (2015)
7. Thomas, D.W.P., Jones, M.S., Christopoulos, C.: Phase selection based on superimposed components. *IEEE Proc. Gener. Transm. Distrib.* **143**(3), 295–299 (1996)
8. Yang, H., Yin, X., Chen, W., Liu, Y., Liu, B.: Wide area protection based on phase comparison of segregated current fault component. *Power Syst. Protect. Control.* **40**(23), 1–6 (2012). (in Chinese)
9. Dai, Z., Liu, X., Liu, Z., Li, Y., Chen, S.: Pilot protection scheme for flexible DC distribution grids based on superimposed current. *High Volt. Eng.* **47**(05), 1684–1695 (2021). (in Chinese)

10. Pan, G., Zeng, D., Wang, G., Zhu, G., Li, H.: Fault analysis on distribution network with inverter interfaced distributed generations based on PQ control strategy. *Proc. CSEE* **34**(04), 555–561 (2014). (in Chinese)
11. Lin, G., Gao, S.: Selective-tripping scheme for power supply arm on high-speed railway based on correlation analysis between feeder current fault components in multisite. *IEE J. Trans. Elect. Electron. Eng.* **14**(5), 773–779 (2019)
12. Xin, C.: AT power supply system equivalent circuit derivation method. *Elect. Railway.* **01**, 18–21+36 (1999). (in Chinese)

Analysis and Research of Networked Traction Power Supply System



Qi Zhuo, Zhengqing Han, and Shibin Gao

Abstract In order to solve the shortcomings of the existing traction power supply system and further optimize the operation quality of the AC traction power supply system, scholars have proposed a networked traction power supply system. This paper analyzes the system structure and operation principle of the networked traction power supply system, constructs a simulation model of the networked traction power supply system, and explores the performance and application prospects of the networked traction power supply system. The analysis shows that the established model can reflect the operating characteristics of the networked traction power supply system. The simulation analysis shows that the networked traction power supply system has enhanced power supply capacity compared with the traditional single-sided traction power supply system, and the system has performance advantages and feasibility, which provides a theoretical basis for further research and practice of the networked traction power supply system.

Keywords Networked Traction Power Supply System · Traction Substation · Converter

1 Introduction

The traction power supply system of Chinese electric railway adopts single-phase power frequency AC system, which has the advantages of simple structure and strong power supply capacity, but it will cause power quality problems in industrial three-phase power supply systems, such as increased line loss and undervoltage at the end of the contact line, grid current imbalance and so on [1]. At present, the traction power supply system is usually connected to the three-phase power supply system by commutation connection, receiving current from the three phases A, B, and C in turn, and setting an electrical split between the ends of two adjacent power supply

Q. Zhuo · Z. Han (✉) · S. Gao

School of Electrical Engineering, Southwest Jiaotong University, Chengdu 611756, China

e-mail: hanzhengqing@home.swjtu.edu.cn

© Beijing Paiké Culture Commu. Co., Ltd. 2023

X. Dong et al. (eds.), *The proceedings of the 10th Frontier Academic Forum of Electrical Engineering (FAFEE2022)*, Lecture Notes in Electrical Engineering 1054, https://doi.org/10.1007/978-981-99-3408-9_51

599

arms to prevent short-circuit between phases. In order to avoid the interphase short circuit caused by live running and phase splitting, the pantograph must be lowered and the power must be cut off when the train passes through the phase splitting. Therefore, the phase splitting will form a power supply dead zone in the traction power supply system, causing the train speed loss, increasing energy consumption, reducing the performance of high-speed railway, affecting the ability of heavy haul freight trains to grow up the slope, and even causing parking in serious cases. At the same time, the existence of electric phase separation makes it impossible to fuse the power between power supply arms, and the traction power cannot be transferred and mutually supported between different power supply arms. In addition, when the train passes through the electric phase separation, it will also produce voltage impact, current impact, pantograph catenary arc, etc., endangering the normal and safe operation of the catenary and electric locomotive [2, 3].

In order to solve the shortcomings of the existing traction power supply system, relevant scholars have proposed the in-phase power supply technology, which can be divided into two categories [4, 5]. The first is to use symmetrical compensation technology to achieve in-phase power supply, and the second is to form the in-phase power supply system based on the power flow controller [6–9]. However, the current technical scheme may generate balanced current and electromagnetic loop network in the traction power supply system. Therefore, some scholars put forward the concept of networked traction power supply system, and optimized the structure of traction power supply system with the help of power electronics technology to solve the problem of phase insulator of traction power supply system and improve the power quality of the system [10, 11].

The networked traction power supply system is based on power electronics technology, with reference to flexible transmission and energy interconnection technologies, and integrates railway regenerative braking energy utilization technology to realize the power controllability and transmissibility of the traction power supply system and improve the power supply quality.

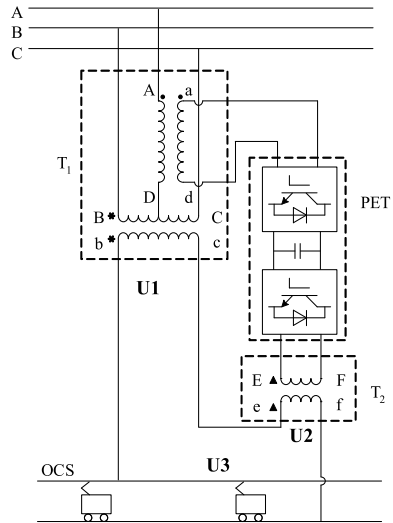
Based on the networked traction power supply system proposed by scholars, this paper analyzes the system structure and operation principle of the networked traction power supply system, establishes the system simulation model using MATLAB/Simulink simulation platform, and studies the performance of the networked traction power supply system.

2 Networked Traction Power Supply System

2.1 System Structure

In the networked traction power supply system, the structure of the traction substation is shown in Fig. 1. The traction substation adopts a fully controlled structure, and its three-phase/single-phase voltage transformation part includes Scott transformer

Fig. 1 The structure of traction substation of networked traction power supply system



and power electronic transformer (PET). The incoming lines of the power system are connected to the primary side of the substation in the same phase sequence. The output end of the PET matching transformer is connected with the direct secondary output of the traction transformer through the traction network to supply power to the traction network. At the same time, the intermediate DC link of PET can also be connected to the energy storage device and the new energy power generation device to realize the interconnection of the electrical network and the new energy.

The two adjacent traction substations all adopt the fully controlled structure, and the electric sections are still retained at the exit of the traction substation, and the power supply arms between the substations adopt the bilateral power supply mode, with the upstream and downstream running in parallel.

2.2 System Operation Principle

As shown in Fig. 1, in the traction substation of the networked traction power supply system, the T-block winding of the Scott transformer supplies the 110 kV (or 220 kV) level voltage of the bus bar to the AC/DC converter, the rectifier unit of the converter turns the AC power into DC power, and then the inverter unit of the converter turns the DC power into single-phase AC power, so that the output voltage of the converter can match the frequency and phase of the output voltage of the M-block of the Scott transformer. The output voltage of the converter is stepped up by the transformer and then connected in series with the M block of Scott transformer to provide 27.5 kV/50 Hz for the traction load.

When the system is working normally, the converter tracks the secondary voltage of Scott transformer M block to adjust its own output voltage, and then controls the secondary voltage of the matching transformer to ensure that the feeder outlet voltage between traction substation groups remains stable, and also adjusts the power tide between traction substations to realize the power controllability and transferability of the traction power supply system, improve the quality of power supply, and enhance the adaptability of power supply capacity and traffic organization.

As the inverter unit of the converter is mainly composed of power electronics, which is expensive, the normal operating current of the traction load, overcurrent and short-circuit current of the feeder all have to pass through the inverter unit of the converter. Therefore, when a short-circuit fault occurs in the traction network, the converter should adopt the current limiting mode to avoid the short-circuit current from damaging the power electronics, and at the same time make the protection sense the occurrence of the fault, discover the fault and remove it in time.

3 The Working Principle of PET

3.1 Basic Structure of PET

In the networked traction power supply system, the power electronic transformer of the traction substation is mainly composed of power switching tubes, as shown in Fig. 2. The grid-side inductor L_1 of the rectifier unit plays the role of transferring and storing energy and suppressing high harmonics, while the filter capacitor C_d plays the role of suppressing high harmonics and reducing DC voltage ripple; the inductor L and capacitor C of the inverter unit form a series resonant circuit for filtering the harmonic components of the output voltage.

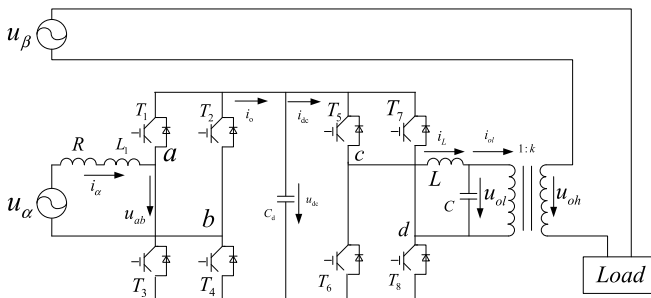


Fig. 2 The working principle circuit diagram of PET

3.2 Control Strategy for PET

As shown in Fig. 1, the secondary voltage vector of Block M of Scott transformer T1 and the secondary voltage vector of transformer T2 are combined to form the output voltage vector of the traction substation of the networked traction power supply system, and the secondary voltage vector of transformer T2 is changed by changing the output voltage of PET to make the output voltage of different traction substations consistent, so as to realize the bilateral power supply of the inter-station arm.

In the traction substation of the networked traction power supply system, the schematic circuit diagram of the PET operation is shown in Fig. 2, u_α and u_β are the low voltage side voltages of the traction transformer M block and T block, u_{ol} is the AC output voltage of the PET, u_{oh} is the load side output voltage of the converter matching transformer, and k is the ratio of the matching transformer.

According to the working principle of the traction substation of the networked traction power supply system, let u_{set} be the desired output voltage of the traction substation, then the voltage relationship between Scott transformer and PET is shown as follows:

$$\begin{cases} u_\alpha(t) = \sqrt{2}U_\alpha \sin \omega t \\ u_\beta(t) = \sqrt{2}U_\beta \sin(\omega t - 90^\circ) \\ u_{ol}(t) = u_{oh}(t) / k \\ u_{set}(t) = u_\beta(t) + u_{oh}(t) \end{cases} \quad (1)$$

During the normal operation of the networked traction power supply system, the output voltage of the low voltage side of the Scott transformer's M block is detected, and the output voltage of the PET is calculated according to the set output voltage of the traction substation, and the PET uses this as the control target of the output voltage, and the voltage of the low voltage side of the T block of the Scott transformer is AC/DC transformed so that the traction substation can steadily output 27.5 kV/50 Hz to provide power to the traction load.

As a grid-side converter of PET, the rectifier unit is essentially an intermediate medium for energy exchange between the AC grid and the DC intermediate circuit. The rectifier unit converts the input AC energy into DC energy for the inverter unit. In the process of energy exchange, the rectifier unit uses algorithms to achieve control characteristics such as stable DC intermediate voltage, grid power factor close to 1, and grid current waveform close to sinusoidal, so as to improve the power quality of the traction power supply system as much as possible.

The inverter unit adjusts the output of AC voltage according to the output voltage of the low voltage side of Scott transformer M block, and inverts the intermediate DC voltage to AC voltage that meets the demand, so that the traction substation can steadily output 27.5 kV/50 Hz voltage.

For the inverter unit of the converter, in order to keep the output voltage of the traction substation stable, the output voltage of the inverter unit requires high steady-state accuracy and fast dynamic response, therefore, the dual-loop control scheme of voltage outer loop and current inner loop is selected. The current inner loop of the dual-loop control scheme expands the bandwidth of the inverter control system, which makes the dynamic response of the inverter faster and reduces the harmonic content of the output voltage, and improves the adaptability to nonlinear loads. The current inner loop of the dual-loop control scheme expands the bandwidth of the inverter control system.

Meanwhile, since the Scott transformer and PET are connected in series, both traction load current and short-circuit fault current have to pass through the converter. Therefore, when a short-circuit fault occurs in the traction network and the short-circuit current will exceed the capacity of the PET devices, in order to avoid the damage of the power electronics of the PET due to the high current, the PET should enter the current limiting and voltage reduction mode to control the current within the capacity of the devices.

4 Simulation Model Analysis

4.1 Simulation Model

According to the analysis of traction substation topology and PET control strategy of networked traction power supply system, the model of PET in MATLAB and the simulation model of networked traction power supply system are shown in Fig. 3.

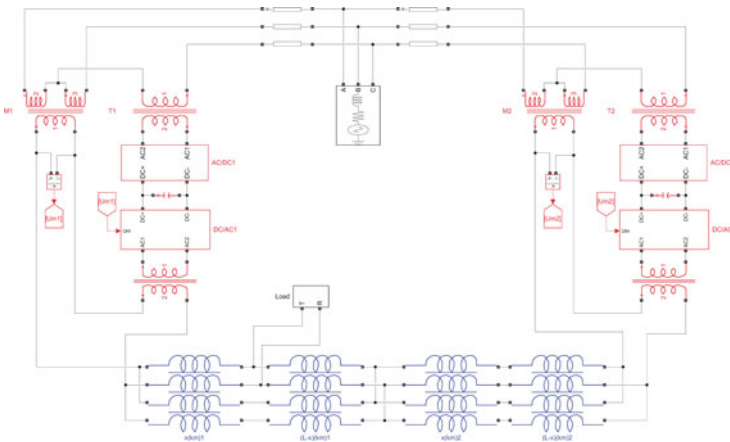
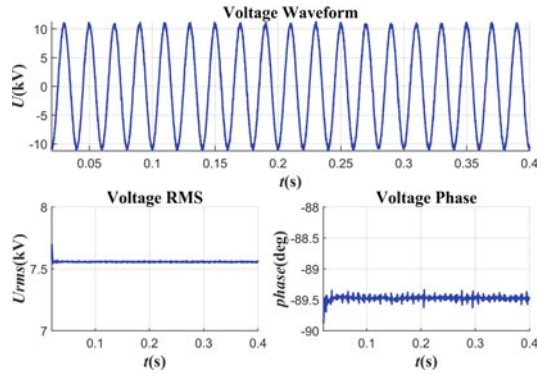


Fig. 3 Simulation model of traction substation for networked traction power supply system

Fig. 4 Transformer output voltage simulation of PET



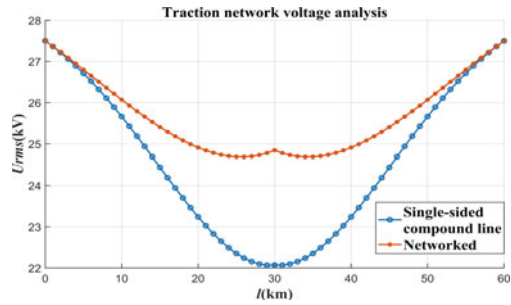
4.2 System Performance Analysis

The desired output voltage of the traction substation has a magnitude of 27.5 kV and a phase angle of -90° ; the primary and secondary voltage ratio of Block M of Scott transformer is 110 kV/20 kV, and the simulated output voltage of the secondary output voltage of Block M has a magnitude of 19.9 kV and a phase angle of -90.28° . According to Eq. (1), the output AC voltage from the PET is 7.51 kV with a phase angle of -89.25° after the transformer step-up. The voltage waveform simulation is shown in Fig. 4.

According to Fig. 4, after the PET is stepped up by the transformer, the RMS value of the output voltage is 7.52 kV and the phase angle is -89.31° , which can realize the control of the output voltage of the traction substation. The networked traction power supply system makes the output voltage of adjacent traction substations achieve the same amplitude, frequency and phase through the regulating effect of PET, and thus the system does not produce equalization current and electromagnetic ringing problem.

According to the established system simulation model, comparing the voltage loss of the traditional single-sided complex traction power supply system and the networked traction power supply system, the impedance per unit length of the traction network is taken to be $0.131 + 0.366i$ (Ω/km), the length of the power supply arm of the traction substation is 30 km, and the traction load current is taken to be 1000 A. The change of the traction network voltage with the movement of the traction load position is shown in Fig. 5.

Fig. 5 Traction network voltage analysis of traction power supply system



5 Conclusion

This paper analyzes the system structure and operation principle of the networked traction power supply system, establishes a simulation model based on MATLAB/Simulink simulation platform, verifies the feasibility of the networked traction power supply system, explores the performance advantages of the system, and provides a basis for further research and practice of the networked traction power supply system.

The networked traction power supply system is based on power electronics technology, drawing on flexible transmission and energy interconnection technology, and integrating railroad regenerative braking energy utilization technology. Through the regulation of PET, it can ensure that the feeder outlet voltage between groups of traction substations remains stable and of the same frequency and phase, avoiding the phenomenon of electromagnetic ring network in the system and reducing the impact of the traction power supply system on the power system, while also regulating the power tide between traction substations, improving the power tide characteristics of the traction network, realizing the power controllability and transferability of the traction power supply system, improving the quality of power supply, and increasing the utilization rate of new energy.

Acknowledgements This work was supported by the National Key Research and Development Program of China (No. 2021YFB2601500) and the National Natural Science Foundation of China (Grant No. 52177116).

References

1. Li, Q., He, J.: Analysis of Traction Power Supply System. 3rd edn. Southwestern Jiaotong University Press, Chengdu (2012). (in Chinese)
2. Zhou, F., Chen, P., Wu, L.: Status and development of the technology for electrified railway traction power supply system. Railway Stand. Des. **63**(01), 133–137 (2019). (in Chinese)
2. Li, Q., Wang, H., Huang, W., Xie, S., Ma, Q.: Interconnected power supply system of traction substation group and its key technologies for the electrified railway. Trans. China Electrotech. Soc. **36**(05), 1064–1074 (2021). (in Chinese)

4. Zhang, L., Li, X., Liang, S., Han, D.: Research on the influence of electric railway bilateral power supply on power system and countermeasures. *Int. J. Electr. Power Energy Syst.* **137**(2022)
5. Arabahmadi, M., Banejad, M., Dastfan, A.: Hybrid compensation method for traction power quality compensators in electrified railway power supply system. *Global Energy Interconnection* **4**(2), 158–168 (2021)
6. Wu, S., Wu, M., Wang, Y.: A novel co-phase power-supply system based on modular multilevel converter for high-speed railway AT traction power-supply system. *Energies* **14**(1), 253–253 (2021)
7. Li, Y., Hu, J., Tang, Z., Xie, Y., Zhou, F.: Feedforward compensation of railway static power conditioners in a V/v traction power supply system. *Electronics* **10**(6), 656–656 (2021)
8. Sun, P., Li, K., Xing, C.: A partial compensation scheme for MMC-based railway Cophase power supply. *Transp. Saf. Environ.* **2**(4), 305–317 (2020)
9. Zhou, J., Yan, T., Zhang, X., Chen, Y.: Topology and control of multi-level trough-type Cophase power supply device for electrified railway. *Proc. CSU-EPSC* **34**(06), 42–53 (2022). (in Chinese)
10. Li, Q.: On new generation traction power supply system and its key technologies for electrification railway. *J. Southwest Jiaotong Univ.* **49**(04), 559–568 (2014). (in Chinese)
11. Wang, X., Tu, C., Guo, Q., Xiao, F., Li, J.: Review of through-type power supply system for electrified railways. *Electr. Drive Locomotives* (03), 17–28(2022). (in Chinese)

Propagation Characteristics of High-Frequency Partial Discharge Current in Gas Insulated Equipment



Ke Zhao, Jingtian Ma, Tianxin Zhuang, Hongtao Li, Shan Gao, Jianjun Liu, Fanjun Kong, and Chaohai Zhang

Abstract As a simple and low-cost partial discharge (PD) detection method, high-frequency current (HFCT) method has wide application prospects in the field maintenance of gas insulated equipment. However, the propagation law of high-frequency PD current in gas insulated equipment is still unclear, which limits the application of HFCT method to field PD detection. In this paper, the equivalent circuit of gas insulation equipment was analyzed, the distribution parameters were calculated, and then the simulation circuit of the gas insulated equipment was built in MATLAB/Simulink, the influence of the distance, signal frequency and discharge position on the propagation characteristics was studied. The results show that the discharge amplitude decreases nonlinearly with the increase of the distance between the detection point and discharge position. For the same propagation distance, the higher the signal frequency, the greater the amplitude attenuation. The high-frequency signal decays quicker than the low frequency signal. When discharge position changes, the maximum value of the discharge amplitude is located at the discharge point, and decreases to both sides. The research results can provide theoretical and data support for the improvement of the effectiveness of PD detection and the optimization of the design and layout of high-frequency current sensors.

Keywords High-frequency current · Gas insulated equipment · Partial discharge · Propagation characteristics

K. Zhao · J. Ma · T. Zhuang · H. Li · S. Gao · J. Liu
State Grid Jiangsu Electric Power Research Institute, Nanjing, China
e-mail: jsepcgs@aliyun.com

F. Kong (✉) · C. Zhang
Department of Electrical Engineering, Nanjing University of Aeronautics and Astronautics,
Nanjing, China
e-mail: kongfj@nuaa.edu.cn

C. Zhang
e-mail: zhangchaohai@nuaa.edu.cn

1 Introduction

Gas insulated equipment includes gas insulated switchgears (GIS) and gas insulated transmission lines (GIL). It has become a key component of the power system owing to its advantages of small footprint, easy installation and high reliability [1–3]. Insulation defects are easily generated during the production, installation and operation of gas insulated equipment, which can lead to local electric field distortion. Once the local field strength reaches the breakdown field strength, the partial discharge (PD) will occur [4]. With the development of PD, equipment insulation will deteriorate, which will eventually lead to insulation failure, endanger power grid security, and cause social and economic losses.

Commonly used PD detection methods mainly include acoustic emission (AE) method, ultra-high-frequency (UHF) method and high-frequency current (HFCT) method [5, 6]. Although AE method is simple in operation and low in cost, it is easily disturbed by the external environment and has low detection sensitivity for void and surface discharges [7]. UHF method has the advantages of strong anti-interference and high sensitivity, but it is easy to detect defects incorrectly [8, 9]. In addition, some devices are not installed with built-in UHF sensors, which will greatly reduce the sensitivity of the UHF method. HFCT method detects discharge by installing a high-frequency current sensor at the ground point to detect the current signal generated by PD. This method is easy to operate and requires little experience, making it suitable for use in conjunction with other methods in the field [10]. However, the propagation of high-frequency current in gas insulated equipment has an important impact on the detection effectiveness of HFCT method. Therefore, it is necessary to study the propagation characteristics of the high-frequency current signal in the gas insulated equipment, which is of great significance for optimizing sensor design and improving the sensitivity of PD detection.

In this paper, the equivalent circuit of gas insulation equipment is established, and the distribution parameters of gas insulation equipment are theoretically calculated. Then, the simulation circuit is built in MATLAB/Simulink, and the influence of the propagation distance, signal frequency and discharge position on the propagation characteristics of high-frequency current in gas insulating equipment is simulated. The research results can provide reference for optimizing sensor design and improving the sensitivity of PD detection.

2 Equivalent Circuit Analysis and Parameters Calculation

2.1 Equivalent Circuit Analysis

As shown in Fig. 1, gas insulated equipment is a coaxial cylindrical structure, in which both the conductor and the enclosure are cylindrical, and insulating gas is filled in the middle. The enclosure and conductor are made of aluminum alloy material, so

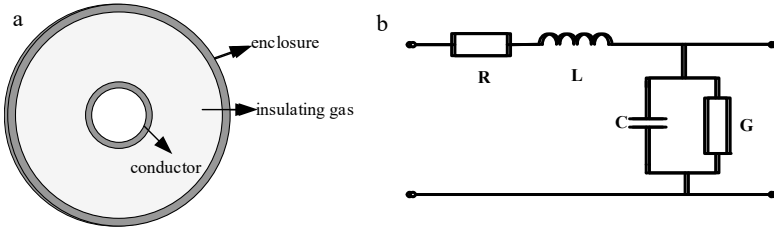


Fig. 1 Schematic diagram (a) and equivalent circuit (b) of gas-insulation equipment

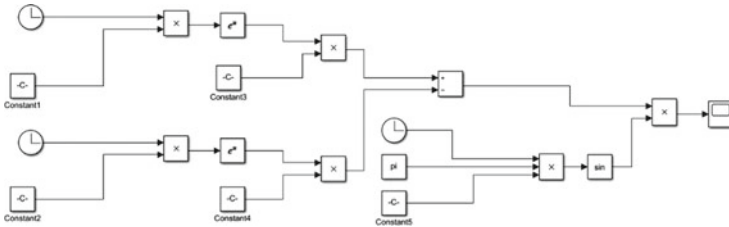


Fig. 2 Simulation model of high-frequency current signal

there is resistance in both enclosure and conductor, which is distributed over the entire length, and is not concentrated at one point. When the conductor is energized, the electromagnetic field will be generated around the conductor, and the magnetic flux is distributed over the entire length of the device, so the inductance is also a distributed inductance. When the external voltage is applied to the conductor, there will be an electric field between the conductor and the enclosure, so there will be a distributed capacitance. In summary, the equivalent circuit of gas insulation equipment is shown in Fig. 2, where R is resistance, L is inductance, C is capacitance, and G is conductance. The conductance of gas insulating equipment is so small that it can be neglected. The transmission characteristics of high-frequency current signals in gas insulated equipment are affected by resistance, capacitance, and inductance, so these parameters are calculated in detail below.

2.2 Distribution Parameters Calculation

Taking a 126 kV GIS bus as an example, the relevant parameters required for the calculation are shown in Table 1.

(1) resistance

The resistance can be calculated according to Eqs. (1):

Table 1 Structural parameters of 126 kV GIS bus

Parameter name	Value
enclosure outer diameter/mm	366
enclosure inside diameter/mm	360
conductor outer diameter/mm	30
conductor inside diameter/mm	24
height of conductor center to ground/mm	583

$$R = \rho \frac{L}{\pi(r_2^2 - r_1^2)} \quad (1)$$

where ρ is resistivity, the resistivity of aluminum alloy is $2.8598 \times 10^{-8} \Omega/\text{m}$, L is length, r_2 is conductor outer radius, and r_1 is conductor inside radius.

It is calculated that the conductor resistance is $1.1238 \times 10^{-4} \Omega/\text{m}$.

(2) Inductance

The inductance can be calculated according to Eq. (2):

$$L = \frac{\mu_0}{2\pi} \ln \frac{R_1}{r_2} \quad (2)$$

where μ_0 is magnetic permeability, $\mu_0 = 4\pi \times 10^{-7} \text{H/m}$.

It is calculated that inductance is $4.9698 \times 10^{-7} \text{H/m}$.

(3) capacitance

The capacitance can be calculated according to Eq. (3):

$$C = \frac{2\pi \varepsilon_r \varepsilon_0}{\ln(R_1/r_2)} \quad (3)$$

where ε_r is relative dielectric constant, ε_0 is vacuum dielectric constant, $\varepsilon_0 = 8.85 \times 10^{-12} \text{F/m}$.

It is calculated that capacitance is $2.2378 \times 10^{-11} \text{F/m}$.

3 Simulation of High-Frequency Current Propagation Characteristics

3.1 Simulation Model of High-Frequency Current

Firstly, the PD model is constructed in MATLAB/Simulink. In this paper, the double exponential oscillation attenuation pulse is selected as the PD source, and its specific expression is shown in Eq. (4):

Fig. 3 Simulation waveform of high-frequency current signal

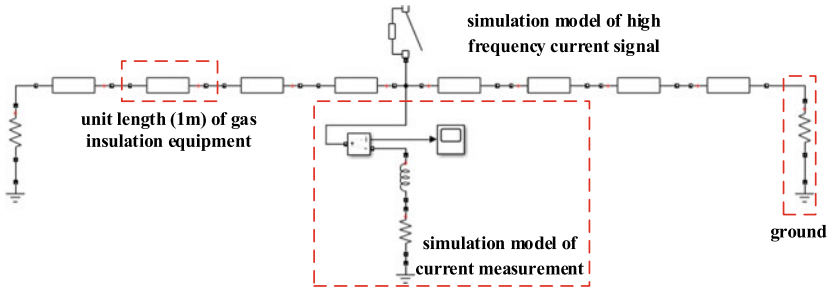
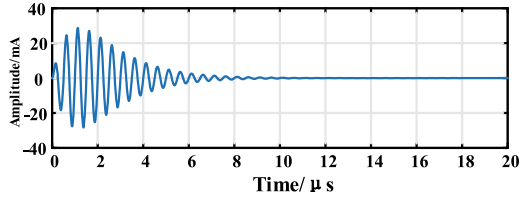


Fig. 4 Simulation circuit to study the effect of distance on propagation characteristics

$$i(t) = A(e^{-1.3t/\tau} - e^{-2.2t/\tau}) \sin(2\pi ft) \tag{4}$$

where A is the amplitude of high-frequency current signal, τ is attenuation coefficient, f is oscillation frequency. The simulation model of high-frequency current signal built by MATLAB/Simulink is shown in Fig. 2.

By adjusting the values of constant1 - constant5, the final expression of the current signal is $i(t) = 0.15(e^{-6.5 \times 10^5 t} - e^{-1.1 \times 10^6 t}) \sin(2 \times 10^6 \pi t)$. Figure 3 shows the simulation waveform of high-frequency current signal. It can be seen from Fig. 4 that the width of the current signal is about 100 ns and the amplitude is 28.64 mA. It has a similar frequency and amplitude to PD signal and is capable of simulating high-frequency currents.

3.2 Simulation Model of Gasinsulated Equipment

Since the resistance, inductance and capacitance of gas insulation equipment are not concentrated in one point, distributed parameter circuit module is selected for simulation. In this paper, Bergeron distribution parameter module in MATLAB/Simulink is used to simulate the gas-insulation equipment.

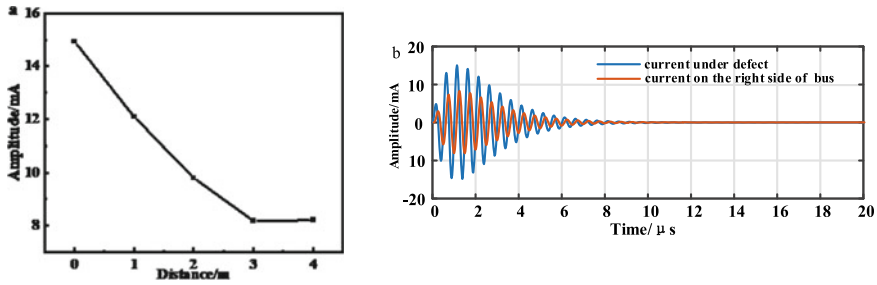


Fig. 5 Diagram of current amplitude (a) and waveforms (b) variation with position

4 Simulation Results

4.1 Effect of Distance on High-Frequency Current Propagation

Figure 4 shows the simulation circuit to study the effect of distance on propagation characteristics. As can be seen from the figure, the simulation circuit includes simulation model of high-frequency current signal (as shown in Fig. 2.), unit length (1 m) of gas insulation equipment, ground and model of current measurement. In the simulation, the effect of distance on propagation characteristics can be studied by changing the position of current measurement point.

Figure 5 (a) is the diagram of current variation with distance. From the figure, with the increase of distance, the amplitude of high-frequency current gradually decreases, but presents a nonlinear attenuation law. The rate of current decay changes from high to low, and the longer the distance, the slower the decay. Figure 5 (b) is the current waveforms at different positions. It can be seen from the figure that the closer the measuring point is to the discharge point, the greater the high-frequency current amplitude is. From the measuring point under the discharge point to the right side of the bus, the current amplitude decays by 45%. It can also be seen from Fig. 5 (b). The further the distance, the shorter the current duration.

4.2 Effect of Frequency on High-Frequency Current Propagation

The simulation circuit of high-frequency current propagation is shown in Fig. 6, which is basically the same as Fig. 6. The frequency of the simulated current signal is adjusted by changing constant 5. In the simulation, the measuring point is always located at the right side of the bus.

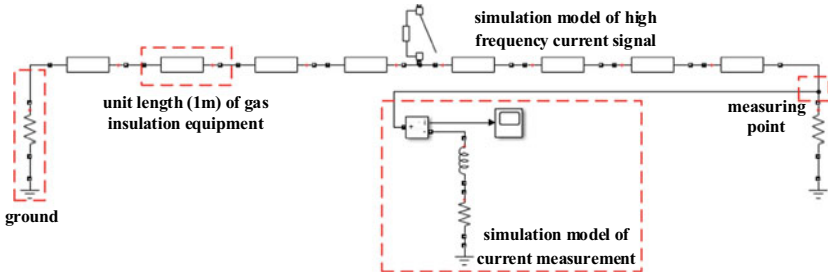


Fig. 6 Simulation circuit to study the effect of frequency on propagation characteristics

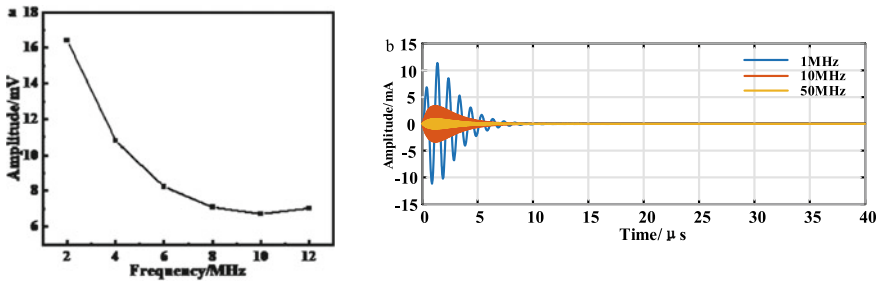


Fig. 7 Diagram of current amplitude and waveforms variation with frequency

Figure 7(a) is the diagram of current variation with frequency. As can be seen from the figure, the current amplitude shows a nonlinear decreasing trend with the increase of frequency. When the frequency increases from 2 to 12 MHz, the amplitude of the current decreases by about 57%.

Figure 7(b) is the current waveforms at different frequency. As can be seen from the figure, the current amplitude shows a nonlinear decreasing trend with the increase of frequency. When the frequency increases from 2 to 12 MHz, the amplitude of the current decreases by about 57%. From the current waveform, the higher the frequency, the shorter the current duration. When the frequency is 1 MHz, the current duration is more than 100 ns, while when the frequency is 50 MHz, the current signal duration is about 70 ns.

4.3 Effect of Discharge Position High-Frequency Current Propagation

Figure 8 is the simulation circuit to study the effect of discharge position on propagation characteristics, where the triangle marks the position of discharge point. The position of one discharge point is selected each time for simulation and the current at other positions of the line is measured.

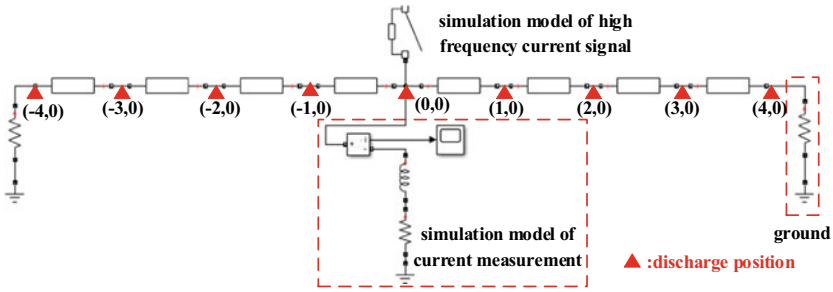


Fig. 8 Simulation circuit to study the effect of discharge position on propagation characteristics

Figure 9 is the diagram of current variation with discharge position, where (a) is the current transmission situation of the discharge point on the right side of the pipeline and (b) is the current transmission situation of the discharge point on the left side of the pipeline. As can be seen from the figure, when the discharge point is located at the end of the bus, the current variation trend increases first and then decreases. The amplitude of current is maximum at the discharge point, and gradually decreases nonlinearly to both sides. When the discharge point is located at the end of the bus, the current shows a single change law, rising or falling all the time. The attenuation rate of the current amplitude is the same as that in Sect. 4.1, and gradually slows down with the increase of the propagation distance.

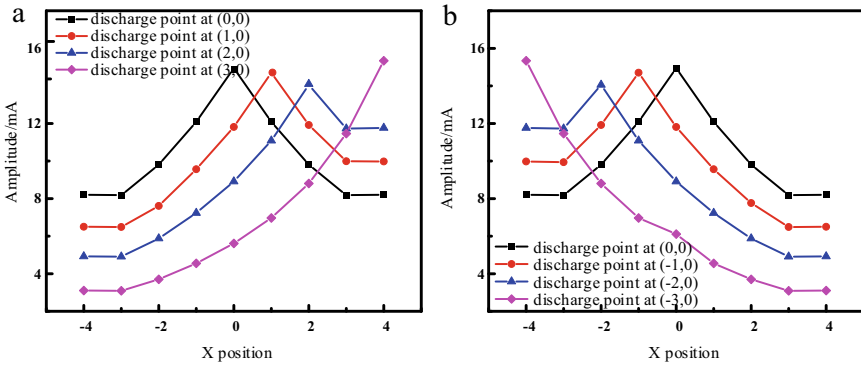


Fig. 9 Diagram of current variation with discharge position (a) discharge position from (0,0) to (4,0) (b) discharge position from (0,0) to (-4,0)

5 Conclusion

In this paper, the equivalent circuit of gas insulation equipment was established, the distribution parameters were calculated, and the simulation model of high frequency current and gas insulation equipment was built in MATLAB/Simulink, and the influence of distance, frequency and discharge position on the high-frequency current propagation characteristics was studied. The results show that the amplitude and duration of the high-frequency current decrease nonlinearly with the increase of distance. As the frequency rises, the high frequency current decay rate becomes slower and the duration becomes shorter. When the position of the discharge point changes, the maximum value of the discharge amplitude is located at the discharge point, and decreases to both sides, and the decay rate slows down gradually.

Acknowledgements This research is supported by the Science and Technology Program of the State Grid **Jiangsu Electric Power Company under Grant J2021049**.

References

1. Hermann, K., Felix, G., Tomasz, M., Karsten, J.: Technical aspects of gas insulated transmission lines and application of new insulating gases. *IEEE Trans. Dielectr. Electr. Insul.* **25**(4), 1448–1453 (2018)
2. Koch, H.: *Gas Insulated Transmission Lines(GIL)*, pp. 33–38. Wiley-IEEE Press, Chichester (2012)
3. Chen, G., Tu, Y., Wang, C., Li, C.: Environment-friendly insulating gases for HVDC gas insulated transmission lines. *J. Power Energy Syst.* **7**(3), 510–529 (2021)
4. Li, J., Han, X., Liu, Z., Li, Y.: Review on partial discharge measurement technology of electrical equipment. *High Voltage Eng.* **41**(8), 2583–2601 (2015). (in Chinese)
5. Yang, X., Liu, W., Gao, W., Yong, W.: Comparison of pd detection methods for power transformers - their sensitivity and characteristics in time and frequency domain. *IEEE Tran. Dielectr. Electr. Insul.* **23**(5), 2925–2932 (2016)
6. Zou, Y., Zhou, Q., Liu, M., Tang, Z., Zhang, D.: Research on quantitative evaluation on anti-electromagnetic interference capability of ultra high frequency partial discharge detection instrument. *Trans. China Electrotech. Soc.* **35**(10), 2275–2282 (2020). (in Chinese)
7. Ilkhechi, H.D., Samimi, M.H.: Applications of the acoustic method in partial discharge measurement: a review. *IEEE Trans. Dielectr. Electr. Insul.* **28**(1), 42–51 (2021)
8. Jiang, J., Chen, J., Li, J., Zhang, C.: Propagation and localisation of partial discharge in transformer bushing based on ultra-high frequency technique. *High Voltage* **6**(4), 684–692 (2021)
9. Meng, X., Song, H., Dai, J., Luo, L., Jiang, X.: Severity evaluation of UHF signals of partial discharge in GIS based on semantic analysis. *IEEE Trans. Power Delivery* **37**(3), 1456–1464 (2021)
10. Alvarez, F., Garnacho, F., Ortego, J., et al.: Application of HFCT and UHF sensors in on-line partial discharge measurements for insulation diagnosis of high voltage equipment. *Sensors* **15**(4), 7360–7387 (2015)

Research on the Motion Behavior and Discharge Characteristics of Spherical Metal Particles in DC GIS



Hu Qiu, Yahui Sun, Chuanxian Luo, Jing Zhang, Hao Wen, Ziqiu Luo, and Kang Wang

Abstract Free metal particles are a common cause of insulation failure in Gas Insulated Switchgear (GIS). The motion and abnormal discharge of metal particles are more severe under High Voltage Direct Current (HVDC). To study the motion behavior and discharge characteristics of spherical metal particles in DC GIS, this paper established a simulation model of two-dimensional spherical metal particle motion based on kinetic analysis, and analyzed the force and motion characteristics of metal particles in the coaxial cylindrical electrode structure. Meanwhile, a detection platform for the motion and discharge characteristics of metal particles was built, and the partial discharge pulse current signal and the motion trajectory of the particles under different conditions were recorded and observed. The research results show that: when the particles take off, the comparison of the magnitude of coulomb force, gas resistance, and gravity determines the motion of the particle. The motion of particles and the intensity of partial discharge are proportional to the applied voltage and particle size. In addition, the motion of multiple particles is more high-frequency and disordered than that of a single particle, which is more prone to discharge phenomenon and causes greater damage to the insulation inside the GIS.

Keywords GIS · Spherical metal particles · Motion behavior · Discharge characteristics

H. Qiu · C. Luo · J. Zhang · H. Wen · Z. Luo
Nanjing NARI Group Corporation (State Grid Electric Power Research Institute),
Nanjing 211106, China

Wuhan NARI Limited Liability Company of State Grid Electric Power Research Institute,
Wuhan 430074, China

Y. Sun
Ultra High Voltage Branch Company of State Grid Fujian Electric Power Co., Ltd.,
Fuzhou 350013, China

K. Wang (✉)
New Energy and Power Grid Equipment Safety Monitoring Hubei Engineering Research Center,
Hubei University of Technology, Wuhan 430000, China
e-mail: 1061259649@qq.com

1 Introduction

GIS have gained wide application in the field of high-voltage power transmission because of its advantages in less land occupied, environmental performance, and insulation performance [1–4]. Due to factors such as collision operations during assembly, mechanical vibrations during transportation and debris shedding caused by electrical discharges, the problem of particle contamination within the GIS cavity is unavoidable [5–7]. Compared to AC electric fields, free particles are more likely to jump when subjected to unipolar electric field forces under DC voltage. When metal particles move freely, they may induce electric field distortions that significantly reduce the withstand voltage of the equipment and even lead to insulation accidents [8, 9]. Therefore, it is important to study the behavior and discharge characteristics of metal particles in GIS under DC voltage in order to master the mechanism of insulation failure caused by particles in GIS, and then develop the metal particle suppression structure.

In the exploration of the motion behavior and discharge characteristics of metal particles, scholars have investigated the effect of the size of GIS foreign particles and the externally applied voltage on the particle take-off voltage, and the relationship between the particle flight time and the take-off height based on numerical simulation [10, 11]. Scholars often use the wedge-shaped plate electrode model and the coaxial cylindrical electrode model to simulate the insulating structure inside the GIS to study the motion behavior of free metal particles. Among them, factors such as the applied voltage, the initial position of the particles, the electrode material, the electrode tilt angle, and the randomness of collision reflection in the wedge-shaped plate electrode all affect the motion state and trajectory of the particles. In the coaxial cylindrical electrode, the resonant frequency of the particles is negatively correlated with the particle radius, SF₆ ratio, and insulating gas pressure; the particle activity is positively correlated with the random reflection angle and voltage amplitude, while there exists a maximum value with the change of particle radius [12–14]. In recent years, for the study of the discharge characteristics of free metal particles, the metal particles are often applied to the surface of real insulators. And the partial discharge is monitored by the pulse current method and the UHF method. The results show that the discharge development goes through three stages, and the danger level of metal particles can be effectively determined by the partial discharge characteristics [15, 16].

On the one hand, the motion behavior of free metal particles in GIS is closely related to the partial discharge and breakdown caused by the equipment, and the correlation needs to be further researched. On the other hand, no systematic conclusion has been formed for the motion behavior and discharge characteristics of metal particles in DC GIS. Therefore, based on the existing research foundation, this paper built an electro-mechanical transient coupled finite element calculation model of metal particle motion by using the kinetic analysis method and carried out the simulation of the motion trajectory and the analysis of the motion characteristics of the metal

particles. And combined with tests to detect the motion and partial discharge characteristics of spherical metal particles under the same structure. On this basis, the influencing factors and correlations of their motion behavior and discharge characteristics are analyzed to provide a reference for the design of DC GIS.

2 The Analysis of Force and Charging Mechanism of Particles

Referring to the GIS pipeline structure, the force model of particles under the coaxial cylindrical electrode is built as shown in Fig. 1. In which the outer radius of the conductor is R_1 and the inner radius of the shell is R_2 . A DC voltage U_{dc} is applied to the conductor and the shell is grounded.

Spherical metal particles with radius a (aluminum particles are used in this paper) are located inside the GIS cavity and are mainly subjected to coulomb force, electric field gradient force, gravity, buoyancy, and gas resistance. The main forces of particles in the DC GIS coaxial cylindrical electrode are shown in Table 1.

In the table, r is the distance of the particle from the GIS axis. ρ_{Al} is the density of aluminum particles; ρ_{gas} is the density of the gas; g is the gravitational acceleration.

Fig. 1 Force model of metal particles

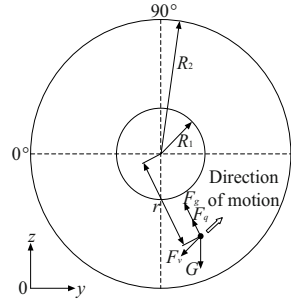


Table 1 The main forces on metal particle

Type of force	Force direction	Force magnitude
Gravity + Buoyancy	$-r$	$G = \frac{4}{3}\pi a^3(\rho_{Al} - \rho_{gas})g$
Coulomb force	$-r (q < 0)$	$F_{q-} = \frac{2k\pi^3 a^2 \epsilon_0 \epsilon_r}{3r R_2} (U_{dc} / \ln \frac{R_2}{R_1})^2$
	$+r (q > 0)$	$F_{q+} = \frac{2k\pi^3 a^2 \epsilon_0 \epsilon_r}{3r R_1} (U_{dc} / \ln \frac{R_2}{R_1})^2$
Electric field gradient force	$-r$	$F_g = 4\pi \epsilon_0 \epsilon_r \frac{a^3}{r^3} (U_{dc} / \ln \frac{R_2}{R_1})^2$
Gas resistance	$-v$	$F_v = \left(\frac{24}{Re} + \frac{6}{1+\sqrt{Re}} + 0.4 \right) \pi a^2 \frac{\rho_{gas} v^2}{2}$

ϵ_0 represents the vacuum permittivity, $\epsilon_0 = 8.85 \times 10^{-12}$ F/m; ϵ_r is the relative permittivity of the insulating gas. k is the correction factor due to the mirror image charge. When the micro discharge is ignored, $k = 0.832$ when the particle is on the electrode surface or near the homopolar electrode, and $k = 1$ in other cases [17, 18]. The gas density involved in this paper is about 2–30 kg/m³, and the particle radius a is in the range of 0.05–2 mm, so the Reynolds number $Re \geq 5$ can be estimated. For large Reynolds number spherical bypass resistance, the empirical formula is usually used to calculate [19].

3 Simulation of Metal Particle Motion in Coaxial Cylindrical Electrodes

Combined with the actual possible conditions inside the GIS cavity, simulation and experimental studies were conducted on the motion behavior of the particles. Based on the force model of metal particles established above, the radial motion of metal particles in a two-dimensional coaxial cylindrical electrode is simulated.

According to the relevant parameters of the existing equivalently scaled-down GIS test platform, the radius of high-voltage conductor $R_1 = 20$ mm, and the inner radius of the grounded shell is $R_2 = 60$ mm. The motion behavior of aluminum spherical metal particles with a diameter of $d = 1$ mm is simulated, and a DC voltage of 50 kV is applied to the high-voltage conductor. The insulating gas in the cavity is pure SF₆, and the gas pressure is 0.4 MPa. The force and motion behavior of the particle can be simulated as shown in Fig. 2.

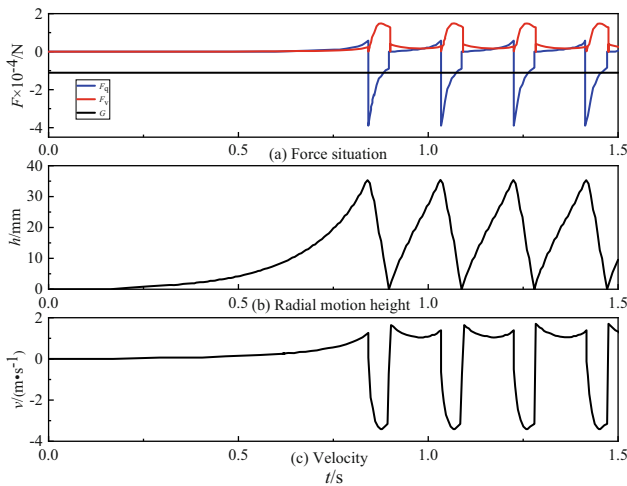


Fig. 2 The force and motion of spherical metal particle

From Fig. 2, the motion of the particle in the cavity can be seen as follows.

1. After the lifting voltage is reached, the spherical particle starts to jump under the combined effect of coulomb force, electric field gradient force, and gravity. In the initial stage of the beating, because the coulomb force on the particle is slightly greater than the gravity, the particle will experience a long-term acceleration process and slowly move towards the conductor.
2. In process of the particle approaching the conductor, its charge remains unchanged. However, as the particle gets closer and closer to the guide rod, the electric field strength of the particle at the location gradually increases, and the coulomb force on it increases, and the particle gradually accelerates until it collides with the conductor.
3. After the particle collides with the conductor, the speed becomes 0.553 times the original, and the charge of the particle increases from negative charge to a larger magnitude of positive charge. The coulomb force changes direction and increases greatly, so the particle accelerates toward the shell.
4. In the process of moving to the grounded shell, the coulomb force on the particle gradually decreases, and as the speed increases, the gas resistance gradually increases, the particle accelerates more and more slowly, until the collision with the shell, the speed and become 0.553 times before. Meanwhile, the charge of the particle be-comes negative and the charge decreases, the coulomb force decreases, resulting in the coulomb force on the particle is less than the combined force of gravity and gas resistance, and the particle speed will be reduced.
5. As the particle approaches the conductor again, the coulomb force gradually increases and the particle accelerates again towards the conductor until it collides with the conductor.

The metal particles maintain a “conductor-shell-conductor” resonant motion mode between the conductor and the shell. Considering the reciprocating motion of the particles between the conductor and the shell as a motion cycle, the average time of one motion cycle of the metal particles in Fig. 2. is $T = 0.1916$ s, and its resonant frequency is about $f = 5.22$ Hz.

4 Experimental Analysis of Metal Particle Motion Behavior and Discharge Characteristics

4.1 Test Platform

In this paper, a DC GIS metal particle motion and discharge characteristics detection platform is built, as shown in Fig. 3. It includes a HVDC power supply, a closed coaxial cylindrical electrode system, a partial discharge signal acquisition system, and a particle motion behavior capture system to simultaneously acquire and store the partial discharge signal and motion behavior of the particles.

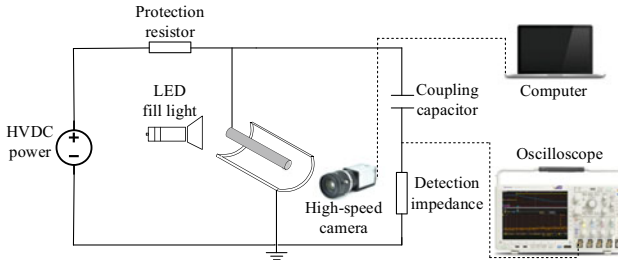


Fig. 3 Platform of DC GIS metal particle motion and discharge characteristics testing

Fig. 4 Enclosed coaxial cylindrical electrode simulation chamber



To simulate the motion and discharge characteristics of metal particles in the GIS cavity, a closed coaxial cylindrical scaled-down electrode model is designed and built in this paper. And its size corresponds to the simulation model, as shown in the Fig. 4.

4.2 Motion Behavior and Discharge Characteristics of Single Particles

In this paper, spherical particles of four diameters were tested. The same particles under the same environment and conditions, the motion mode and partial discharge signal are basically the same. Take the spherical particle with diameter $d = 2$ mm under the condition of gas pressure $p = 0.4$ MPa as an example. When the particle is stationary in the cavity, the detected partial discharge pulse signal is small, but when the DC voltage rises to 48.6 kV, the particle starts to lift and jump. Once the particle is lifted, it immediately performs repeated beating through the coaxial cylindrical cavity for resonant motion, which is consistent with the simulation analysis. A large partial discharge pulse signal was detected when particle was jumping. Figure 5 shows the variation of partial discharge pulse signal with the applied voltage when the test voltage is gradually increased for the particle. The motion behavior of a single spherical particle observed by the high-speed camera is shown in Fig. 6.

During the collision of the particles with the shell, the partial discharge pulses show repetitive cluster discharge, and the discharge quantity is mainly below 500

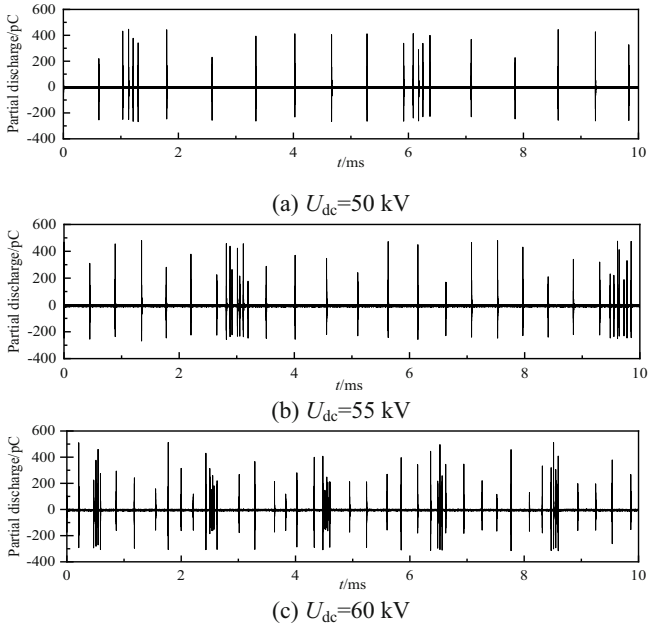


Fig. 5 Pulses of partial discharge when particle bounces up and down ($d = 2 \text{ mm}$; $p = 0.4 \text{ MPa}$)

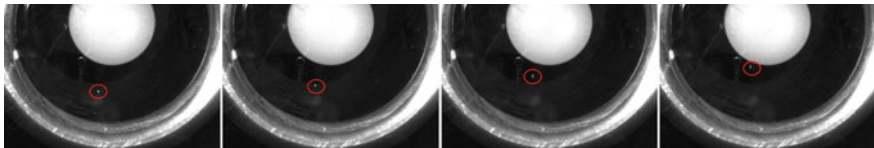


Fig. 6 Motion behavior of spherical metal particles

pC, where the discharge time interval between adjacent pulses with larger amplitude is larger than that between adjacent pulses with smaller amplitude.

The resonant frequencies of spherical metal particles under different voltages were counted through the particle motion video captured by the high-speed camera. And the resonant frequencies were used to characterize the activity of metal particles under DC voltage. The statistical results are shown in Table 2.

Table 2 Comparison of resonant frequencies of particle motion ($d = 2 \text{ mm}$)

Voltage amplitude/kV	Test results/kV	Simulation results/kV
50	4.69	4.72
55	5.21	5.16
60	5.94	6.02

Table 3 Partial discharge signal statistics for multiple particle motion ($U_{dc} = 55 \text{ kV}$)

Number of particles	1	2	3
Q_{av}/pC	136.96	167.32	188.21
$\Delta t/\text{ms}$	0.196	0.155	0.142

From Table 3, it can be seen that the resonant frequency test results and simulation results of metal particles at different voltages are consistent. As the voltage increases, the resonant frequency of the particles increases, and the motion of the particles becomes more active. Meanwhile, the relationship between the changes of partial discharge pulse signals at different voltages shows that as the applied voltage increases, the resonant frequency of particle increases, the collision between particle and electrode is more frequent, and the quantity of partial discharge caused by it increases, and the discharge frequency increases.

4.3 Effect of Particle Size

To investigate the effect of different metal particle sizes on their partial discharges, the average partial discharge quantity Q_{av} and the average partial discharge time interval Δt of four spherical particles with different diameters in the test were statistically calculated. The results are shown in Fig. 7.

From Fig. 7, it can be seen that at the same voltage, the average partial discharge Q_{av} increases with the increase of particle diameter d , and the average partial discharge increases significantly with the increase of voltage U_{dc} . The average partial discharge time interval Δt is within 0.10–0.35 ms and decreases with the increase of particle diameter d and the increase of voltage U_{dc} . Therefore, with the increase of particle size and voltage, the degree of partial discharge caused by particles becomes more severe, and the average partial discharge amount and discharge

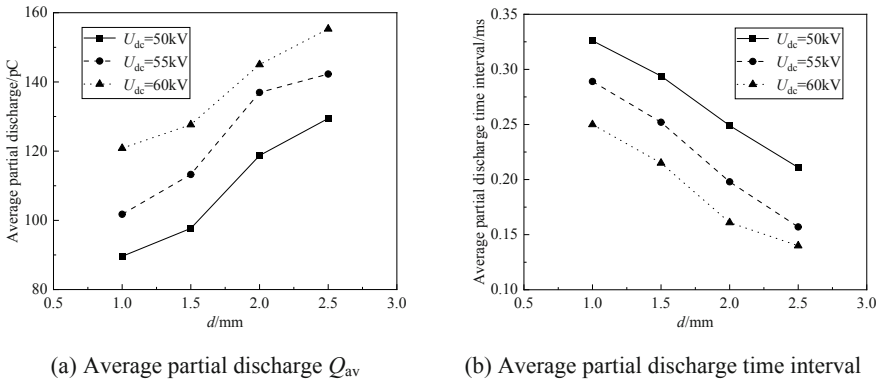


Fig. 7 Average partial discharge Q_{av} and Δt with different particle diameters ($p = 0.4 \text{ MPa}$)

frequency increase accordingly. It shows that the movement and discharge of large-sized particles inside the GIS cavity can have a greater impact on its insulation performance.

4.4 Effect of Different Numbers of Particles

In practical engineering, metal particle contaminants inside the GIS cavity are often present in more than one place simultaneously. In the paper, the motion behavior and partial discharge characteristics of different numbers of particles are investigated experimentally. Under the condition of gas pressure $p = 0.4$ MPa, two and three spherical particles with diameter $d = 2$ mm were placed in the GIS simulation cavity respectively.

In the test, it was found that with the increase in the number of particles, the initial discharge voltage changed additionally. The initial discharge voltage of a single particle is 48.6 kV, that of two particles is 46.2 kV, and that of three particles is 43.5 kV. At the same time, the particles moved horizontally when the initial discharge was detected. The reason for this phenomenon is that different particles in the same electric field environment will sense the same polarity of charge. Due to the repulsive force, two particles that are close to each other will bounce away, resulting in a horizontal motion, leading to a change in partial charge density, and making it easier for partial discharge to occur.

Under the test voltage $U_{dc} = 55$ kV, multiple particles in the cavity are beating continuously. After statistical analysis of the discharge signals, the average partial discharge quantity Q_{av} of the particles and the average partial discharge time interval Δt are shown in Table 3.

In Table 3, as the number of particles moving at the same time increases, the average partial discharge of particles increases. This indicates that the interaction between particles makes multiple particles more susceptible to induced charging causing irregular, high-frequency collisions and motion, which promotes the increase in the degree of partial discharge. The decrease of average partial discharge time interval is partly due to the simultaneous discharge of multiple particles, which improves the discharge frequency, but does not show a corresponding multiple increase with the increase of the number of particles. It shows that the discharge of multiple particles is not a simple superposition of individual particles, but their joint existence has an effect on the discharge and motion characteristics of the particles.

5 Conclusion

1. Under the effect of DC voltage, the metal particles are subjected to electric field force and move directly toward the conductor, and then carry out the resonant motion mode of “conductor-shell-conductor”.

2. During particle motion, The voltage amplitude and the size of the particles both will have an effect on the motion behavior and the discharge characteristics of the particles. As voltage increases, particles are moving more intensely, the resonance frequency increases, the degree of discharge is more intense, the particle motion becomes more intense, and the average partial discharge quantity and the discharge frequency increase. The particle size is positively correlated with the average partial discharge caused by its motion and negatively correlated with the partial discharge time interval.
3. Compared to individual metal particles, due to the high frequency and disorderly movement of multiple particles through the electric field and frequent charge exchange, the initial discharge voltage of multiple particles is lower, the average partial discharge time interval is reduced, and the average partial discharge volume is larger. Therefore, the aggregated discharge caused by multiple particles will cause greater damage to the internal insulation system of GIS.

Acknowledgements This work is supported by Science and Technology Project of SGCC (5500-202147110A-0-0-00).

References

1. Fu, Z., Cheng, D., Ma, J., Zhang, Q.: Investigation of research about discharge characteristics of GIS under combined voltage of DC and impulse. *High Volt. Apparatus* **56**(07), 94–102 (2020). (in Chinese)
2. Zhang, L., Lin, C., Li, C., et al.: Gas–solid interface charge characterisation techniques for HVDC GIS/GIL insulators. *High Volt.* **5**(2), 95–109 (2020)
3. Iwabuchi, H., Matsuoka, S., Kumada, A., et al.: Influence of tiny metal particles on charge accumulation phenomena of GIS model spacer in high-pressure SF₆ gas. *IEEE Trans. Dielectr. Electr. Insul.* **20**(5), 1895–1901 (2013)
4. Ma, H., Wang, L.X., Dai, F.: Motion behavior and discharge characteristics of metal particles in GIL. *Electr. Mach. Control* **26**(03), 49–58 (2022). (in Chinese)
5. Cookson, A.H.: Compressed gas insulated transmission systems: the present and the future. In: *Proceedings of the International Symposium on Gaseous Dielectrics*, pp. 286–313 (1978)
6. Zhao, K., Ma, J., Gao, S., et al.: Research on the movement and partial discharge characteristic of free metal particles in GIS. In: *2021 IEEE 4th International Conference on Renewable Energy and Power Engineering (REPE)*, pp. 76–80. IEEE (2021)
7. CIGRE WG 15.03: Effects of particles on GIS insulation and the evaluation of relevant diagnostic tools. CIGRE, Report, 15-103 (1994)
8. Zhang, L., Lu, S., Li, C., Wang, H., Tang, Z.: Motor behavior and hazard of spherical and linear particle in gas insulated switchgear. *Trans. China Electrotechnical Soc.* **34**(20), 4217–4225 (2019). (in Chinese)
9. Asano, K., Hishinuma, R., Yatsuzuka, Y.: Bipolar DC corona discharge from a floating filamentary metal particle. *IEEE Trans. Ind. Appl.* **38**(1), 57–63 (2002)
10. Ma, J., Zhang, Q., Wu, Z., et al.: Breakdown characteristics of particle-contaminated HVDC GIL under superimposed voltage of DC and impulse. *IEEE Trans. Dielectr. Electr. Insul.* **25**(4), 1439–1447 (2018)
11. Ma, F., Niu, B., Zhang, T., Tian, Y., Cao, W.: Study on movement process of foreign metal particles in GIS at high voltage. *High Volt. Apparatus* **57**(11), 35–41 (2021). (in Chinese)

12. Jia, J., Tao, F., Yang, L., Zhang, Q.: Motion analysis of spherical free conducting particle in non-uniform electric field of GIS under DC voltage. *Proc. CSEE* (08), 106–111 (2006). (in Chinese)
13. Jia, J., Zhang, Q., Shi, X., Yang, L.: Motion of conducting particle near PTFE spacer under AC voltage. *Trans. China Electrotechnical Soc.* (05), 7–11 (2008). (in Chinese)
14. Wang, J., Li, Q., Li, B., et al.: Motion analysis of spherical metal particle in AC gas-insulated lines: random effects and resistance of the SF₆/N₂ mixture. *IEEE Trans. Dielectr. Electr. Insul.* **23**(5), 2617–2625 (2016)
15. Qi, B., Li, C., Hao, Z., et al.: Surface discharge initiated by immobilized metallic particles attached to gas insulated substation insulators: process and features. *IEEE Trans. Dielectr. Electr. Insul.* **18**(3), 792–800 (2011)
16. Wang, J., Wang, Z., Ni, X., et al.: Experimental studies on the motion and discharge behavior of free conducting wire particle in DC GIL. *J. Electr. Eng. Technol.* **12**(2), 858–864 (2017)
17. Sakai, K., Tsuru, S., Abella, D.L., et al.: Conducting particle motion and particle-initiated breakdown in dc electric field between diverging conducting plates in atmospheric air. *IEEE Trans. Dielectr. Electr. Insul.* **6**(1), 122–130 (1999)
18. Sun, J., Chen, W., Li, Z., Yan, X., Yang, P., Liu, H.: Charge estimation and impact analysis of moving metal particle under DC electric field. *High Volt. Eng.* **44**(03), 779–786 (2018). (in Chinese)
19. Jia, Y., Ji, S., Lyu, L.: Motion characteristic of metal particles in GIL under DC voltage. *Electr. Power Eng. Technol.* **39**(06), 124–131 (2020). (in Chinese)

A Comparison Study of Nonlinear Solvers in Transient Circuit Analysis Involving Power Diodes



Ming Chen, Xiaoping Sun, Yanmei Zhang, He Chen, Pengcheng Zhu, and Jiawei Wang

Abstract The power diode is one of the most widely adopted devices in power electronics, thus intensive efforts has been made to reveal the underlying mechanism of its complex nonlinear behavior and develop reliable modeling and simulation methods. Existing circuit analysis tools often adopt implicit time integration methods such as the well-known backward Euler method, thus are faced with the solutions to nonlinear algebraic equations arising from time discretization. for large systems involving thousands of diodes and other semiconductor devices, e.g., the high voltage direct current (HVDC) transmission systems, the computational overheads can be prohibitive. In this manuscript, we focus on sorting out the most efficient nonlinear solver for tackling the nonlinearity of a single diode. Both Newton-type and fixed-point solvers are tested. Numerical results indicate that Newton-type solvers are more robust, while fixed-point solvers may be more efficient under small time-step size. This conclusion should shed light on the choice of sub-solvers in decomposition-like algorithms for transient analysis of practical large-scale power electronics.

Keywords Fixed-point method · Jacobian-free Newton-Krylov methods · Power diodes · Transient analysis

M. Chen

Ultra High Voltage Transmission Company of China Southern Power Grid Co., Ltd.,
Guangzhou 510663, China

X. Sun · Y. Zhang · H. Chen

Xi'an Xidian Power System Co., Ltd., Xi'an 710118, China

X. Sun · P. Zhu · J. Wang (✉)

School of Electrical Engineering, Xi'an Jiaotong University, Xi'an 710049, China
e-mail: jwwang@xjtu.edu.cn

© Beijing Paiké Culture Commu. Co., Ltd. 2023

X. Dong et al. (eds.), *The proceedings of the 10th Frontier Academic Forum of Electrical Engineering (FAFEE2022)*, Lecture Notes in Electrical Engineering 1054, https://doi.org/10.1007/978-981-99-3408-9_54

1 Introduction

The power diode [1] may be one of the most widely adopted devices in power electronics, thus intensive efforts has been made to reveal the underlying mechanism of the complex nonlinear behavior of the diodes and develop reliable modeling methods. Existing models of power diodes can be roughly divided into system-level models and device-level models. System-level models, which approximate the diodes' behavior by multi-value resistors and ideal switches, are favorable for low computational overheads, while the accuracy is not satisfying for many scenarios, e.g., loss calculation and electromagnetic interference (EMI) evaluation [2]. Device-level models, either behavior-based or physics-based, take into account many physical phenomena, including emitter recombination, mobile charge carriers in depletion layer, and carrier multiplication, exhibit much more precise transient behavior than those of the system-level models.

However, popular circuit simulation tools, e.g., PSPICE, Matlab Simulink, and ANSYS Simplorer, often adopt implicit time integration methods, among which the backward Euler (BE) method may be the most common choice, are faced with the solutions to nonlinear algebraic equations arising from time discretization. For small problems involving only a few diodes, the dimensions of the nonlinear systems are limited, and the computational overheads are not a big issue. On the contrary, for large systems, e.g., the high voltage direct current (HVDC) transmission systems [3], thousands of diodes and other semiconductor devices are involved. The resultant dimensions of the nonlinear equations can be huge and bring up prohibitive computational costs.

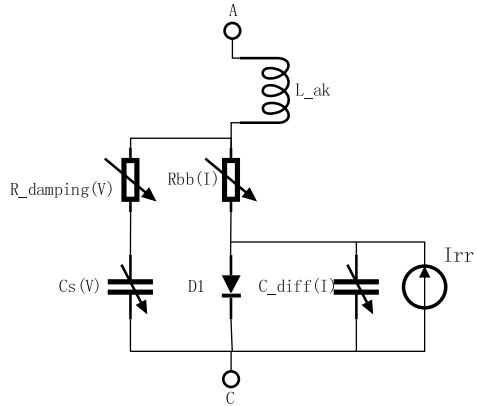
Therefore, for large-scale transient analysis, decomposition-like techniques, including the latency insertion method (LIM) [4] and transmission-line links [5], are often used to decouple and analyze the whole system in a divide-and-conquer manner. In these techniques, the sub-solvers that can efficiently resolve the nonlinearity of a single component are essential for overall efficiency. Thus, in this manuscript, we focus on sorting out the most efficient nonlinear solver for tackling the nonlinearity of a single diode. Most existing nonlinear solvers fall into fixed-point methods or Newton methods. In this work, both types of nonlinear solvers are tested on a behavior-based diode model integrated in ANSYS Simplorer and comparison regarding convergence and efficiency are carried out.

2 Formulations

2.1 Behavior-Based Model of Diodes

The adopted model [6–8], which is a behavior-based dynamic model of power diodes integrated in ANSYS Simplorer, is presented in Fig. 1. The diode core of this model is described as

Fig. 1 Behavior-based dynamic model of diodes in ANSYS Simplorer



$$V_F = \frac{kT}{q} \ln\left(\frac{I_F}{I_S} + 1\right) + I_F \cdot R_B(I_F) \tag{1}$$

$$R_B(I_F) = \frac{R_B^0}{\sqrt{1 + I_D/I_{NOM}}} \tag{2}$$

where $k = 1.380649 \times 10^{-23}$ J/K is Boltzmann constant, $q = 1.602177 \times 10^{-19}$ C the elementary charge, T the temperature in Kelvin, and I_S the saturation current.

In addition to the static behavior modelled by the diode core, charging and discharging of junction and diffusion capacitance are taken into account by introducing voltage-dependent capacitances. There is a distinction between the evaluation of depletion and enhancement capacitance behavior, but the curves keep differentiable at the transition from one region to the other. The transition happens when the effective junction voltage

$$V_{PN} = V_C - VSHIFT_JNCT \tag{3}$$

crosses 0 V. The voltage-dependent capacitances are given by the following piecewise function

$$C_S(V_{PN}) = \begin{cases} C_0 \cdot [2 - e^{-\frac{V_N}{V_{diff}}}], & V_{PN} \geq 0 \\ C_0 \cdot \left(\delta - \frac{1-\delta}{(1-\frac{V_{PN}}{V_{diff}})^\alpha}\right), & V_{PN} < 0 \end{cases} \tag{4}$$

where

$$V_N = \frac{V_{diff}}{(1 - \delta) \cdot \alpha} \tag{5}$$

It's worth noting that to avoid possible oscillations, we involve a damping resistor $R_{DAMP} = DAMPING \cdot \sqrt{L/C}$, which is related to parasitic inductances as well as the internal capacitance.

The reverse recovery behavior is described by a controlled current source, i.e., I_{rr} in Fig. 1. The reverse recovery waveform and related shape parameters are presented in Fig. 2. The piecewise analytical formulations of the reverse recovery current are

$$I_{rr}(t) = \begin{cases} \frac{I_{rr \max}}{\exp(\frac{t}{TAU}) - 1} [\exp(\frac{t}{TAU}) - 1] & [0, t_B] \\ I_{rr \max} \sin(\omega_1 t + \varphi_1) & [t_B, t_S] \\ I_{rr \max} \cos(\omega_2 t + \varphi_2) & [t_S, t_C] \\ \frac{(R_3 - R_2) I_{rr \max}}{SF_2 \cdot t_S} t + I_{rr \max} \left(R_2 - \frac{R_3 - R_2}{SF_2 \cdot t_S} t_C \right) & [t_C, t_C + SF_2 \cdot t_S] \\ a(t - t_{end})^2 & [t_C + SF_2 \cdot t_S, t_{end}] \end{cases} \quad (6)$$

where the unknown coefficients are calculated as

$$\begin{cases} t_B = TAU \cdot \ln(R_1(\exp(\frac{t_S}{TAU}) - 1) + 1) \\ \omega_1 = \frac{\arcsin(R_1) - \frac{\pi}{2}}{t_B - t_S} \\ \varphi_1 = \frac{\pi}{2} - \frac{\arcsin(R_1) - \frac{\pi}{2}}{t_B - t_S} t_S \\ t_C = t_S(1 + SF_1) \\ \omega_2 = \frac{\arccos(R_2)}{SF_1 \cdot t_S} \\ \varphi_2 = -\frac{\arccos(R_2)}{SF_1} \\ t_{end} = t_C + SF_2 \cdot t_S - \frac{2R_3 \cdot SF_2 \cdot t_S}{R_3 - R_2} \\ a = \frac{R_3 \cdot I_{rr \max}}{(t_C + SF_2 \cdot t_S - t_{end})^2} \end{cases} \quad (7)$$

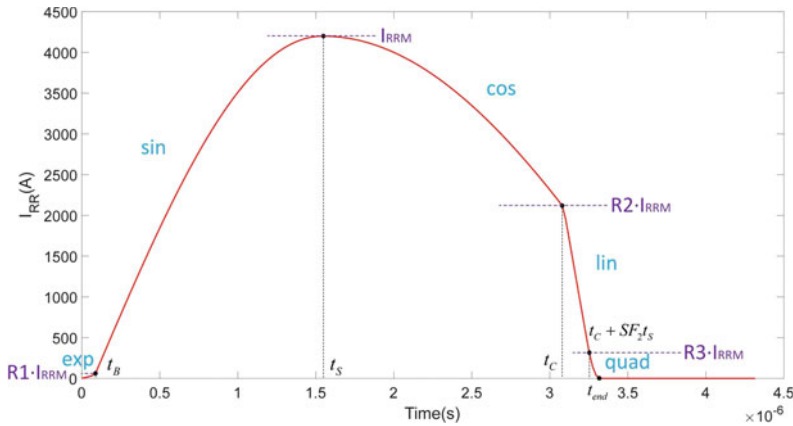


Fig. 2 Reverse recovery waveform and shape parameters

The unknown parameters in the above equations and figures can all be extracted by inputting the data from the manufacturer’s datasheet into the modelling tool integrated in ANSYS Simplorer.

2.2 Time Discretization of a Reference Problem

The test model, which is the reference problem considered in our context, is depicted in Fig. 3. The governing equations of this model are

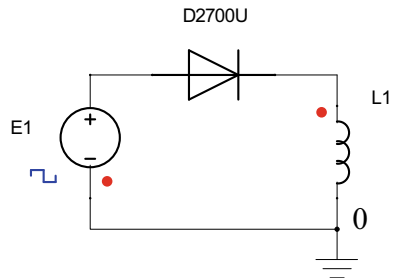
$$\begin{cases} \frac{dV_{ai}}{dt} = \frac{1}{R_{bb}C_{diff}} [V_{am} - V_{ai} - R_{bb}(I_F - I_{rr})] \\ \frac{dI_T}{dt} = \frac{1}{L_{ak}} (V_a - V_{am}) \\ \frac{du_{cs}}{dt} = \frac{1}{R_{damping} \cdot C_S} (V_{am} - u_{cs}) \end{cases} \tag{8}$$

where the intermediate variables

$$\begin{cases} V_{am} = \left(I_T - \frac{V_{am} - u_{cs}}{R_{damping}} \right) R_{bb} + V_{ai} \\ I_F = I_S \left[\exp\left(\frac{qV_{ai}}{kT} \right) - 1 \right] \\ R_{bb} = \frac{R_{B0}}{\sqrt{\frac{I_F}{I_{NOM}} + 1}} \\ R_{damping} = DAMPING \sqrt{\frac{L_{ak}}{C_S}} \\ C_{diff} = TAU \frac{I_F + I_S}{M_0 \cdot \frac{kT}{q}} \\ C_S^{n+1} = \begin{cases} C_0 \cdot [2 - e^{-\frac{V_{PN}}{V_{diff}}}], & V_{PN} \geq 0 \\ C_0 \cdot \left(\delta - \frac{1-\delta}{(1-\frac{V_{PN}}{V_{diff}})^\alpha} \right), & V_{PN} < 0 \end{cases} \end{cases} \tag{9}$$

The differential-algebraic equations (DAEs) given by Eqs. (8) and (9) are discretized by the widely adopted backward Euler (BE) scheme, which is unconditionally stable and can suppress unphysical oscillations of the numerical solutions. The resultant discretized DAEs are

Fig. 3 The reference model



$$\left\{ \begin{aligned}
 &V_{ai}^{n+1} \left(\frac{1}{\Delta t} + \frac{1}{R_{bb}^{n+1} C_{diff}^{n+1}} \right) - V_{ai}^n \left(\frac{1}{\Delta t} \right) - \frac{1}{R_{bb}^{n+1} C_{diff}^{n+1}} [V_{am}^{n+1} - R_{bb}^{n+1} (I_F^{n+1} - I_{rr}^{n+1})] = 0 \\
 &I_T^{n+1} \left(\frac{1}{\Delta t} \right) - I_T^n \left(\frac{1}{\Delta t} \right) - \frac{1}{L_{ak}} (V_a^{n+1} - V_{am}^{n+1}) = 0 \\
 &u_{C_S}^{n+1} \left(\frac{1}{\Delta t} + \frac{1}{R_{damping}^{n+1} C_S^{n+1}} \right) - u_{C_S}^n \left(\frac{1}{\Delta t} \right) - V_{am}^{n+1} \left(\frac{1}{R_{damping}^{n+1} C_S^{n+1}} \right) = 0 \\
 &V_{am}^{n+1} = \frac{R_{damping}^{n+1}}{R_{damping}^{n+1} + R_{bb}^{n+1}} \left[V_{ai}^{n+1} + R_{bb}^{n+1} \left(I_T^{n+1} + \frac{u_{C_S}^{n+1}}{R_{damping}^{n+1}} \right) \right] \\
 &V_a^{n+1} = \frac{1}{L_{ak} + L_1} (E_1^{n+1} L_{ak} + V_{am}^{n+1} L_1) \\
 &I_F^{n+1} = IS \left[\exp \left(\frac{q}{kT} V_{ai}^{n+1} \right) - 1 \right] \\
 &R_{bb}^{n+1} = \frac{R_{B0}}{\sqrt{1 + \frac{I_F^{n+1}}{I_{NOM}}}} \\
 &R_{damping}^{n+1} = DAMPING \sqrt{\frac{L_{ak}}{C_S^{n+1}}} \\
 &C_{diff}^{n+1} = TAU \frac{I_F^{n+1} + IS}{M_0 \cdot \frac{kT}{q}} \\
 &C_S^{n+1} = \begin{cases} C_0 \cdot [2 - e^{-\frac{V_{ai}^{n+1}}{V_{diff}}}], & V_{ai}^{n+1} \geq 0 \\ C_0 \cdot (\delta - \frac{1-\delta}{(1 - \frac{V_{ai}^{n+1}}{V_{diff}})^\alpha}), & V_{ai}^{n+1} < 0 \end{cases}
 \end{aligned} \right. \tag{10}$$

where the superscripts represent the time levels of the variables. In each time advance, the implicit nonlinear system described by Eqs. (10) needs to be solved by a proper solver. The choice of the nonlinear solver is our focus hereinafter.

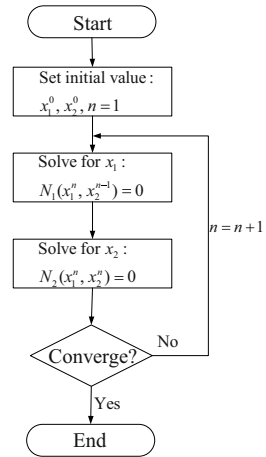
2.3 Fixed-Point and Newton-Type Nonlinear Solvers

Firstly, for each time advance we reformulate Eqs. (10) as $\mathbf{F}(\mathbf{x}) = \mathbf{0}$, where $\mathbf{x} = [V_{ai}, I_T, u_{C_S}, \dots, C_S]^T$ is a column vector holding all unknown variables.

Existing nonlinear solvers can be divided into fixed-point solvers and Newton-type solvers. Many well-known relaxation-based methods, including Jacobi method, Gauss-Seidel method, and successive-over-relaxation (SOR) method, belong to fixed-point solvers. In our context, we divide the unknowns into $\mathbf{x}_1 = [V_{ai}, I_T, u_{C_S}]^T$ and $\mathbf{x}_2 = [V_{am}, I_F, \dots, C_S]^T$, namely, unknowns explicitly involved in time derivatives are attributed to \mathbf{x}_1 . The flowchart of the fixed-point method is presented by Fig. 4.

As for Newton-type methods, among which Newton-Raphson (NR) method may be the most famous representative, the essence is to linearize the nonlinear systems and convert the task into a series of linear equations named Newton correction equations, the coefficient matrices of which are the Jacobian matrices of the nonlinear systems at current solutions. These methods usually require explicit evaluation and storage of the Jacobian matrices, which are very costly. Therefore, in this work a new variant of NR method, named the Jacobian-free Newton-Krylov (JFNK) method, is

Fig. 4 Flowchart of the relaxation-based fixed-point method [9]



chosen. JFNK method is a nested algorithm consisting of the Inexact Newton (IN) method for the solution of nonlinear equations, and Krylov subspace methods for solving the Newton correction equations. By using the finite difference technique, the matrix-vector products required for Krylov iterations are approximated without forming and storing Jacobian matrices. The readers can refer to [10] for detailed implementations.

3 Numerical Results and Discussions

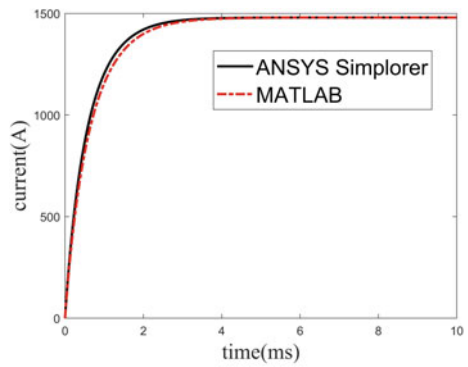
In this section, the proposed nonlinear solvers are tested on the reference problem. The type of diodes considered here is Infineon D2700U45X122. Firstly, the curves and data from the datasheet are inputted into the device characterization tool integrated in ANSYS Simplorer to extract necessary parameters in the previous equations. The results are given in Table 1, and the simulated transient current and voltage are depicted in Fig. 5.

The diode model and nonlinear solvers are implemented with MATLAB codes. For validation of our implementation, the turn-on process of the diode is analyzed. The total simulation time is 10 ms and the time-step size of MATLAB codes is 0.01 ms. The performance comparison of the nonlinear solvers is shown in Table 2. It's observed that the fixed-point method is obvious faster the JFNK method. Although the average iteration of JFNK method is less than that of the fixed-point method, for each iteration JFNK method demands two evaluations of nonlinear function $F(x)$, which may be the main reason of its lower efficiency. However, for a small portion of the time steps, both methods fail to converge to the desired error tolerance $1E-6$ within 100 iterations, which is the predefined maximum number of iterations for each time advance. In this sense, JFNK method is a more robust solver since it fails for fewer time advances.

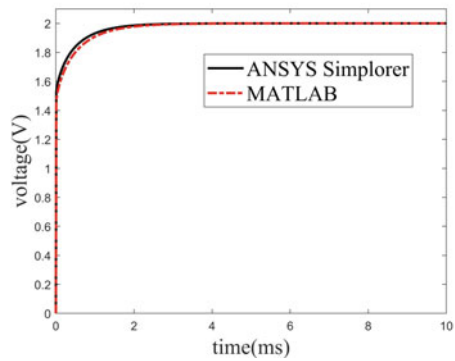
Table 1 Model parameters extracted using ANSYS Simplorer

Parameter	Explanation	Unit	Value
I_s	Saturation current	A	1.406
M_0	Ideality factor	1	1.188
RB_0	Bulk resistance	Ω	$7.796E-4$
C_0	Zero voltage junction capacitance	F	$1E-7$
V_{diff}	Diffusion voltage	V	0.5
α	Capacity exponent	1	0.5
δ	Capacity minimum factor	1	$4.089E-4$
TAU	Effective lifetime	s	$5.358E-7$
DAMPING	Relative damping factor	1	2.924
L_{ak}	Stray inductance	H	$2E-7$
I_{NOM}	Nominal current	A	2700

Fig. 5 Transient waveforms of the diode during the turn-on process



(a) Diode current during the turn-on process.



(b) Diode voltage during the turn-on process.

Table 2 Performance comparison of the solvers

Indicator	Value	
	JFNK	Fixed-point method
Execution time (s)	47	32
Evaluation of $\mathbf{F}(\mathbf{x})$	40,512	21,984
Number of failed time steps	23	30

When the time-step size is increased to 0.05 ms, it's a totally different story. Fixed-point method fails in most time steps and leads to incorrect waveforms. This is because the convergence of fixed-point methods is pretty sensitive to initial values, and larger time-step size induces more significant difference between current and new-time solution. For comparison, JFNK method fails in 98 time advances yet the waveforms are still acceptable. Nevertheless, the total number of the evaluations of $\mathbf{F}(\mathbf{x})$ increased to 62,298 mainly because it takes much more iterations for the inner Krylov solver to converge. Therefore, increased time-step size results in lower efficiency and of course worse accuracy.

4 Conclusions

In this manuscript, a modeling approach requiring merely the manufacturer's datasheet is adopted for transient modeling of power diodes. Then we test two types of nonlinear solvers for resolving the nonlinearity of the diodes. Two conclusions are drawn from the numerical results. Firstly, Newton-type methods are more robust methods, yet they may be less efficient under small time-step size due to the costs for dealing with the Jacobian matrices of the nonlinear systems, either explicitly or implicitly. Secondly, deliberate choice of time-step size is crucial for successful implementations of both types of nonlinear solvers.

Acknowledgements This research is sponsored by the National Natural Science Foundation of Shaanxi Province under Grant 2022JQ-484, and the state key laboratory of electrical insulation and power equipment, Xi'an Jiaotong University under grant EIPE21302.

References

1. Yuan, L., Meng, Q., Zhao, W., et al.: Study of the switching characteristic of power diode in the high power inverter. *Power Electron.* **50**(9), 106–108 (2016). (in Chinese)
2. Jia, S., Zhao, Z., Shi, B., et al.: Numerical modeling and analysis of electromagnetic interference in power electronics systems. *Trans. China Electrotechnical Soc.* **36**(11), 2383–2393 (2021). (in Chinese)

3. Oliveira, R., Yazdani, A.: A modular multilevel converter with DC fault handling capability and enhanced efficiency for HVDC system applications. *IEEE Trans. Power Electron.* **33**(1), 11–22 (2018)
4. Benigni, A., Monti, A., Dougal, A.: Latency-based approach to the simulation of large power electronics systems. *IEEE Trans. Power Electron.* **29**(6), 3201–3213 (2014)
5. Hui, S., Fung, K.: Fast decoupled simulation of large power electronic systems using new two-port companion link models. *IEEE Trans. Power Electron.* **12**(3), 462–473 (1997)
6. Zhu, R., Lin, N., Dinavashi, V., et al.: An accurate and fast method for conducted EMI modeling and simulation of MMC-based HVDC converter station. *IEEE Trans. Power Electron.* **35**(5), 4689–4701 (2020)
7. Lin, N., Zhu, R., Dinavashi, V.: Hierarchical device-level modular multilevel converter modeling for parallel and heterogeneous transient simulation of HVDC systems. *IEEE Open J. Power Electron.* **1**, 312–321 (2020)
8. Zhu, R., Huang, Z., Dinavashi, V.: A universal wideband device-level parallel simulation method and conducted EMI analysis for more electric aircraft microgrid. *IEEE J. Emerg. Sel. Top. Ind. Electron.* **1**(2), 162–171 (2020)
9. Wang, J., Chen, F., Ma, X.: A hybrid indirect-direct coupling method for strongly coupled nonlinear magnetic problems. *IEEE Trans. Magn.* **53**(8), 7207611 (2017)
10. Knoll, D., Keyes, D.: Jacobian-free Newton-Krylov methods: a survey of approaches and applications. *J. Comput. Phys.* **193**(2), 357–397 (2004)

Application of VMD-Based Electromagnetic Railgun Launch Current Feature Extraction in the Measurement of Muzzle-Leaving Time



Yi Chen, Jie Yan, Kai Huang, Weisheng Ye, Juxiang Li, Yi Wang, Sui Wang,
and Chengdong Liu

Abstract The muzzle-leaving time of projectile is an important index to evaluate the launching performance of electromagnetic railgun. The traditional testing technology is difficult to be applied in the harsh electromagnetic emission environment, and cannot guarantee the accuracy of testing. In order to get the key parameter of muzzle-leaving time of projectile quickly, simply and accurately, this paper proposes a feature extraction method of electromagnetic railgun launch current based on VMD (Variational Mode Decomposition), which is used to extract the muzzle-leaving time of projectile. Firstly, the characteristics of the launch current of the electromagnetic railgun are analyzed, and the relationship between the motion of the projectile in the bore and the launch current is obtained. Secondly, the VMD algorithm is proposed to decompose the emission current signal into multiple modal components, and extract the muzzle-leaving time of projectile according to the current change characteristics. Finally, the effectiveness of the algorithm is verified by launching experiments, and the accuracy is calculated based on the test results of muzzle voltage. The results show that the proposed method can easily measure the muzzle-leaving time of projectile with high accuracy, and has good engineering operability and application value. It lays a foundation for improving the shooting accuracy of electromagnetic railgun.

Keywords electromagnetic railgun · muzzle-leaving time of projectile · launch current · Variational Mode Decomposition · muzzle voltage

Y. Chen (✉) · J. Yan · K. Huang · W. Ye · J. Li · Y. Wang · S. Wang · C. Liu
Northwest Institute of Mechanical and Electrical Engineering, Xianyang 712000, China
e-mail: 1042385812@qq.com

© Beijing Paiké Culture Commu. Co., Ltd. 2023
X. Dong et al. (eds.), *The proceedings of the 10th Frontier Academic Forum of
Electrical Engineering (FAFEE2022)*, Lecture Notes in Electrical Engineering 1054,
https://doi.org/10.1007/978-981-99-3408-9_55

1 Introduction

Electromagnetic railgun is a new concept weapon of kinetic energy distraction. With many advantages such as high initial velocity, high accuracy, strong controllability and good concealment, it has become one of the important weapons in the field of national defense [1, 2]. The high precision launch control capability of the electromagnetic railgun is its significant advantage. Which is mainly reflected in that the muzzle-leaving state of projectile can be accurately controlled. In order to improve the damage probability, the shooting mode of multi tube synchronous firing is usually adopted. The multi-barrel volley puts forward higher requirements for the muzzle-leaving state of projectile. Therefore, it is necessary to accurately measure the muzzle-leaving state of projectile, so as to provide data support for subsequent design, and further improve the shooting accuracy [3, 4].

The velocity and time of the projectile exit the muzzle are two important evaluation indexes of the muzzle-leaving state of projectile. At present, most of the research focuses on the muzzle-leaving velocity of projectile. Li et al. [5] used B probe and laser to test the projectile velocity and compared the measurement accuracy. Chang et al. [6] established a simulation model, by adjusting the pulse power supply parameters to achieve accurate and controllable muzzle-leaving velocity of projectile. Zhang et al. [7] studied the influence of projectile initial velocity on hit probability under different shooting modes.

The muzzle-leaving time of projectile is an important indicator of the launch consistency, and it is also of great significance to the analysis of key technologies such as launch mechanism and in bore movement. The harsh electromagnetic environment of electromagnetic railgun makes it difficult to measure muzzle-leaving time of projectile. At present, there are few related research literatures on the time of electromagnetic railgun projectiles leaving the muzzle, and most of them focus on the test of traditional artillery. The projectile's muzzle-leaving time of traditional artillery is usually obtained by instrument measurement. The commonly used test methods include high-speed photography, recoil displacement method, target wire on-off method, photoelectric method and so on [8].

High-speed photography obtains the specific time by analyzing the image data of the projectile exit from the muzzle. The recoil displacement method determines the muzzle time through the recoil force change curve of the gun. The target wire on-off method is to arrange a copper wire flowing through the direct current at the muzzle, and judge the muzzle-leaving time of projectile by detecting the on-off of the copper wire. The photoelectric method detects the time through the photoelectric sensor arranged at the muzzle. Because of the simple measurement principle and easy implementation, the target wire on-off method and photoelectric method have been widely used in the traditional artillery testing field. However, they are vulnerable to external interference and difficult to obtain accurate time.

The strong emission current during the launch of the electromagnetic railgun will generate huge heat. At the muzzle, impurities such as aluminum filings are often ejected and strong arc discharges are generated. The harsh launch environment

greatly reduces the accuracy of the above test methods and even makes them fail. Therefore, it is difficult to directly apply the traditional testing method to the muzzle-leaving time of projectile, and the accuracy is poor. Therefore, because of the poor accuracy of the traditional testing methods, it is difficult to directly apply them to the muzzle-leaving time of projectile.

Based on the launch mechanism and mature testing technology of electromagnetic railgun, this paper proposes a testing and analysis method. Based on the armature-rail contact state contained in the launch current signal, the method decomposes the launch current signal by VMD, and then extracts the muzzle-leaving time of projectile according to the current change characteristics. Finally, the feasibility of the method is verified by the launch test.

2 Launch Current Analysis

During the launch of electromagnetic railgun, the desired launch current is generated by setting the discharge sequence of the pulse power supply. The electromagnetic force generated by the launching current drives the projectile to accelerate continuously, making it fly out of the muzzle at high speed. The movement process of the projectile is closely related to the discharge current waveform of the pulse power supply.

2.1 Circuit Principle of Pulse Power Supply

The pulse power supply is composed of multi-module parallel networking. Each module works in RLC or RL discharge mode during discharge. Due to the difference of discharge time, the whole pulse forming network has three working states [9].

At the beginning of power supply discharge, all modules are in RLC discharge state. According to the nodal voltage method, the current is shown in Formula (1), where C_i is the capacitance, R_{i1} is the resistance, L_{i1} is the inductance, $u_{i1}(0_-)$ is the voltage at both ends of R_{i1} , $i_{i1}(0_-)$ is the current flowing through R_{i1} , and the total number of modules is N .

$$\begin{aligned}
 I_1(s) &= \frac{U_{i1}}{R_L} \\
 &= \frac{\sum_{i=1}^N \frac{1}{sC_i + R_{i1} + s(L_{i1} + L_{i3})} \times [\frac{u_{i1}(0_-)}{s} + (L_{i1} + L_{i3})i_{i1}(0_-)]}{1 + R_L \times \sum_{i=1}^N \frac{1}{sC_i + R_{i1} + s(L_{i1} + L_{i3})}}
 \end{aligned} \tag{1}$$

$$\begin{aligned}
 I_2(s) &= \frac{U_{n2}}{R_L} \\
 &= \frac{\sum_{i=1}^M \frac{(L_{i2}+L_{i3})i_{i2}(0_-)}{R_{i2}+s(L_{i2}+L_{i3})} + \sum_{i=M+1}^N \frac{\frac{u_{i2}(0_-)}{s} + (L_{i1}+L_{i3})i_{i2}(0_-)}{\frac{1}{sC_i} + R_{i1}+s(L_{i1}+L_{i3})}}{1 + \sum_{i=1}^M \frac{R_L}{R_{i2}+s(L_{i2}+L_{i3})} + \sum_{i=M+1}^N \frac{R_L}{\frac{1}{sC_i} + R_{i1}+s(L_{i1}+L_{i3})}}
 \end{aligned} \quad (2)$$

In the middle of discharge, the capacitor voltage of some modules becomes 0, and the pulse power module is in the mixed state of RLC discharge and RL discharge. At this time, the launch current is shown in Formula (2), where M represents the number of modules in RL discharge.

When the capacitor voltage of all modules drops to 0, all modules are in RL discharge state, and the launch current is shown in Formula (3).

$$I_2(s) = \frac{U_{n3}}{R_L} = \frac{\sum_{i=1}^M \frac{(L_{i2}+L_{i3})i_{i3}(0_-)}{R_{i2}+s(L_{i2}+L_{i3})}}{1 + \sum_{i=1}^M \frac{R_L}{R_{i2}+s(L_{i2}+L_{i3})}} \quad (3)$$

From Formulas (1) to (3), it can be seen that the launch current of the electromagnetic railgun is closely related to the electrical parameters of the pulse power supply and the launcher [10].

2.2 Launch Current and Armature-Rail Contact State

During the launching process, the changes of the launcher's electrical parameters are mainly affected by the armature-rail contact state. In different launch stages, there is a corresponding relationship between the armature-rail contact state and the launch current. An example of the launch current waveform is shown in Fig. 1. According to the characteristics of electromagnetic emission, the current waveform is divided into four stages, which are current rising phase, current flat-topped phase, current decay phase and current ablation phase.

Current rising phase: The launch current rises rapidly from 0 to the peak current, and the armature gradually overcomes the friction and begins to accelerate. At this time, the armature-rail contact state is fixed electrical contact and low-speed sliding electrical contact.

Current flat-topped phase: The current is almost constant, the armature accelerates forward with constant acceleration, and the velocity and displacement of the projectile increase rapidly. At this time, it is a sliding electrical contact.

Current decay phase: The current gradually decreases from the peak value until the projectile flies out of the muzzle. The current value at the muzzle is usually 20–90% of the peak value, and this stage is a sliding electrical contact.

Current ablation phase: After the projectile leaves the muzzle, the emission current breaks through the air, arc discharge formed between rail and armature. As the

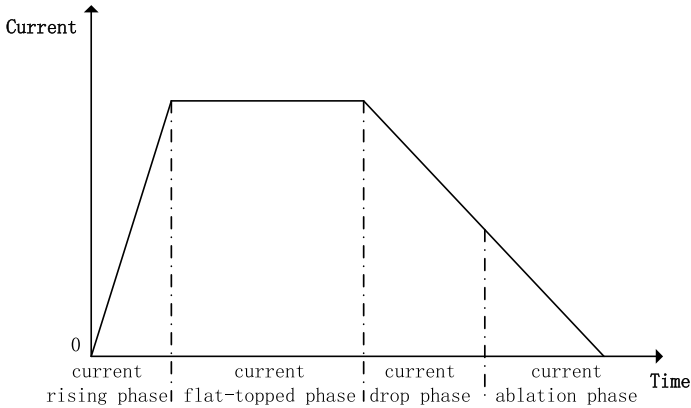


Fig. 1 Example diagram of launch current waveform

projectile moves away from the muzzle, the launch current is gradually consumed in the form of arc discharge. The contact mode between armature and rail changes from close contact to arc contact, the contact resistance increases sharply, and the launch current also changes suddenly [11].

From the above analysis, it can be seen that the launch current waveform will have a sudden change in the current decay phase, and the mutation point is the moment when the projectile flies out of the muzzle. This mutation point is difficult to visually determine, and further analysis and processing of current signals are required. In this paper, the VMD algorithm is used to decompose the mode and extract the characteristics of the launch current, so as to obtain a more accurate muzzle-leaving time of projectile.

3 VMD Algorithm

VMD is an adaptive signal processing algorithm with wide application and strong stability. It determines the bandwidth and center frequency of each component by solving the constructed constrained variational model, so as to realize the effective decomposition of the signal [12]. In the processing of the launch current signal, according to the frequency domain characteristics of the current, the signal components with different frequencies and bandwidths can be effectively decomposed. VMD algorithm can be divided into two parts: construction and solution of variational problems.

3.1 Variational Mode Construction

First, the number of modes is set to K , and the original signal $f(k)$ can be decomposed into K modal components $u_k(t)$ with center frequency $\omega_n (n = 1, 2, \dots, K)$, as shown in formulas (4) and (5), where $A_k(t)$ is the envelope and $\phi_k(t)$ is the phase.

$$f(t) = u_1(t) + u_2(t) + \dots + u_k(t) \quad (4)$$

$$u_k(t) = A_k(t) \cos(\phi_k(t)) \quad (5)$$

The unilateral spectrum of the modal component is calculated by Hilbert transform. where $\delta(t)$ is the impulse function.

$$\delta(t) + \frac{j}{\pi t} * u_k(t) \quad (6)$$

The spectrum of the modal variables is then moved to a fundamental frequency band centered at the center frequency.

$$[\delta(t) + \frac{j}{\pi t} * u_k(t)] \times e^{-jw_k t} \quad (7)$$

Then the square of the gradient-norm of formula (7) is calculated to obtain the bandwidth of the modal component, and the constrained optimization equation is obtained as shown in formula (8). The formula contains a target and a constraint condition. The target is to minimize the sum of the center frequency bandwidth, and the constraint condition is that the sum of the modal components is equal to the original signal.

$$\left\{ \begin{array}{l} \min_{\{u_k\}, \{w_k\}} \left\{ \sum_k \|\partial_t [\delta(t) + \frac{j}{\pi t} * u_k(t)] \times e^{-jw_k t}\|_2^2 \right\} \\ s.t. \sum_k u_k(t) = f \end{array} \right. \quad (8)$$

3.2 Solution of Variational Problems

VMD transforms the signal decomposition into a variational model, and its solution is equivalent to finding the optimal solution of the constrained variational model. For the above problems, the Lagrangian function is added to transform the constraint problem into non-constraint, as shown in formula (9), where α is the quadratic penalty factor and $\lambda(t)$ is the Lagrangian operator.

$$L(\{u_k\}, \{w_k\}, \lambda) = \alpha \sum_{k=1}^K \|\partial t[\delta(t) + \frac{j}{\pi t} * u_k(t)] \times e^{-jw_k t}\|_2^2 + \|f(t) - \sum_{k=1}^K u_k(t)\|_2^2 + \left\langle \lambda(t), f(t) - \sum_{k=1}^K u_k(t) \right\rangle \tag{9}$$

Then u_k, w_k, λ are updated according to the alternating direction multiplier algorithm, and the iterative update formula is shown in Formula (10)–(12).

$$\hat{u}_k^{n+1}(\omega) = \frac{\hat{f}(\omega) - \sum_{i \neq k}^K \hat{u}_i^n(\omega) + \frac{\hat{\lambda}^n(\omega)}{2}}{1 + 2\alpha(\omega - \omega_k^n)^2} \tag{10}$$

$$w_k^{n+1}(\omega) = \frac{\int_0^\infty \omega |\hat{u}_k^{n+1}(\omega)|^2 d\omega}{\int_0^\infty |\hat{u}_k^{n+1}(\omega)|^2 d\omega} \tag{11}$$

$$\hat{\lambda}^{n+1}(\omega) = \hat{\lambda}^{n+1}(\omega) + \tau \left(\hat{f}(\omega) - \sum_{k=1}^K u_k^{n+1}(\omega) \right) \tag{12}$$

When the conditions of Formula (13) are met, the iteration is stopped, the VMD decomposition is completed, and K modal functions are output, where ε represents the convergence accuracy.

$$\sum_k \frac{\|u_k^{n+1} - u_k^n\|_2^2}{\|u_k^n\|_2^2} < \varepsilon \tag{13}$$

The specific algorithm steps of muzzle-leaving time extraction based on the launch current signal are as follows:

- Step 1: read the launch current signal sample;
- Step 2: determine the VMD modal number K and other parameters;
- Step 3: decompose the samples of the launch current signal to obtain the decomposition set of the launch current signal;
- Step 4: According to the signal component with the most obvious characteristics, determine the launch current mutation turning point, namely the muzzle-leaving time of projectile.

4 Test and Data Analysis

In this paper, the above method is verified by launching test of electromagnetic railgun. The Rogowski coil is used to measure the launch current, the muzzle voltage is measured by the high-voltage differential probe, and the sensor signal is connected to the data-acquisition instrument. The pre-triggering time of the acquisition signal is 1330 μ s. The parameters of the launch system are randomly adjusted, and a total of 4 tests are carried out. The test parameters are shown in Table 1. The emission current waveform of the first test is shown in Fig. 2.

The VMD algorithm is used to decompose the launch current signal in Fig. 3 and extract the muzzle-leaving time of projectile. After comparing the decomposition effect of each parameter of VMD algorithm, determine the number of modes $K = 4$ and penalty factor $\alpha = 200,000$.

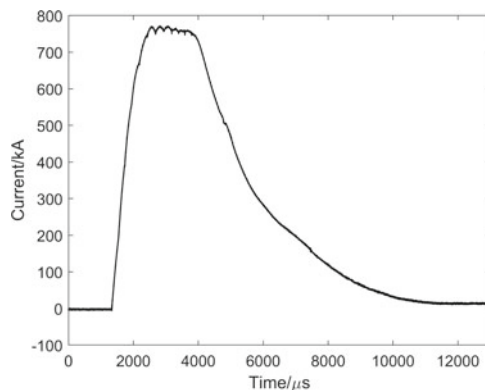
The VMD algorithm is used to decompose the launch current signal in Fig. 3 and extract the muzzle-leaving time of projectile. After comparing the decomposition effect of each parameter of VMD algorithm, determine the number of modes $K = 4$ and penalty factor $\alpha = 200,000$.

The decomposition results are shown in Fig. 3. The signal component 1–3 is the effective launch current signal with increasing frequency, and the signal component 4 is the high frequency noise collected by the system. In the signal component 3, the fluctuation trend of the launch current can be clearly seen, so that the muzzle-leaving time of projectile can be obviously extracted. At the point marked in Fig. 3(c), as the contact resistance changes abruptly, the launch current also changes dramatically.

Table 1 Launch system parameters

Test Times	1	2	3	4
Launcher Length/mm	4000			
Projectile Weight/g	152	100	81	53
Charging Voltage/V	4000	4200	2600	2300

Fig. 2 Launch current waveform



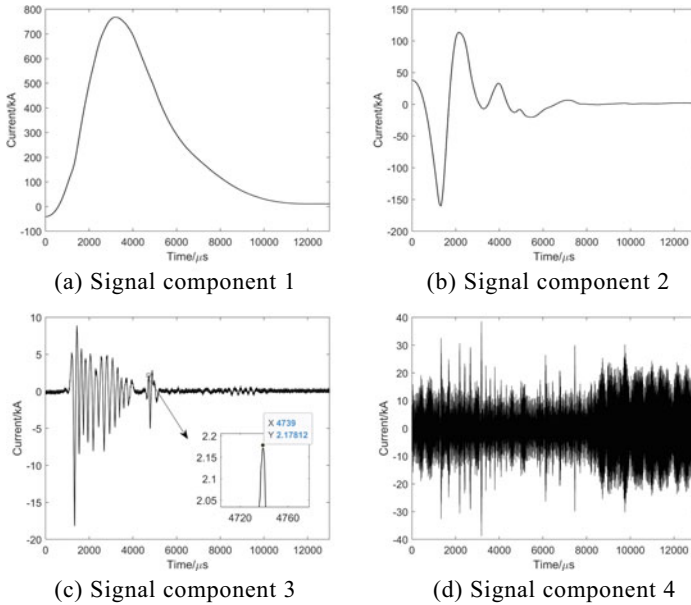


Fig. 3 VMD decomposition of modal components

After subtracting the pre-sampling time, the muzzle-leaving time of projectile is 3409 μ s.

In addition, the muzzle voltage can also directly reflect the armature-rail contact state during the launch process. The muzzle voltage waveform is shown in Fig. 4. At the beginning of the launch process, the muzzle voltage shows a negative value because the reverse induced electromotive force is greater than the positive voltage. As the forward voltage gradually increases and the reverse induced electromotive force gradually decreases, the waveform gradually rises to the forward direction. Due to the discharge timing of the pulse power supply, the waveform shows a trend of gradual increase in sawtooth shape. When the projectile flies out of the muzzle, the contact resistance increases sharply, and the muzzle voltage (armature-rail contact voltage) increases suddenly. Therefore, the above calculation results can be compared and verified by the muzzle voltage signal. It can be seen in Fig. 5 that the muzzle voltage changes sharply at 4711 μ s (3381 μ s after discharge), and this moment is the muzzle-leaving time of projectile.

Finally, the test accuracy is calculated based on the test results of the muzzle voltage. The calculation formula is shown in Formula (14), where t_v is the muzzle-leaving time obtained by the muzzle voltage, and t_l is the muzzle-leaving time obtained by the launch current.

$$\alpha = \frac{|t_v - t_l|}{t_v} \times 100\% \tag{14}$$

Fig. 4 Muzzle voltage waveform

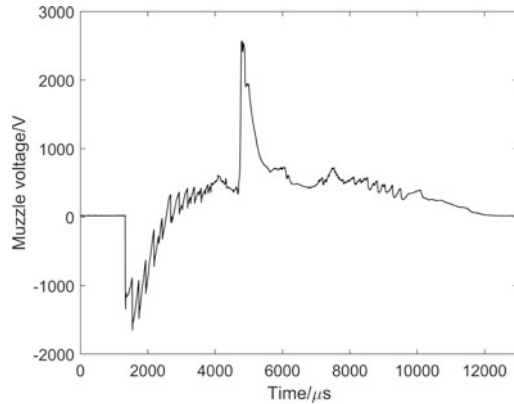


Table 2 Test result of muzzle-leaving time

Test Times	Test Method		
	Muzzle Voltage/ μ s	Launch Current/ μ s	Relative Accuracy/%
1	3381	3409	0.83
2	2193	2206	0.59
3	3778	3809	0.82
4	3374	3401	0.80

The results of the four tests are shown in Table 2. It can be seen from the table that this method achieves high test accuracy, with an average relative accuracy of 0.76%.

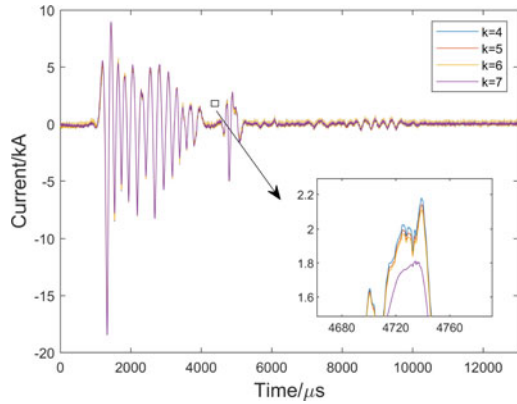
5 Discussion

In VMD algorithm, the number of modes K and penalty factor α are the key factors that affect the VMD decomposition effect. They are also important parameters to accurately extract the muzzle-leaving time of projectile.

The accuracy of mode number selection affects the effect of launch current decomposition. If the value of K is too small, it will occur under-decomposition phenomenon and cannot obtain effective information. When the value of K is too large and the number of decomposed modes increases, the over-decomposition phenomenon occurs. In addition, the number of VMD decomposition is proportional to the computation time of the algorithm.

In this paper, the modal number K is selected as 3, 4, 5, 6, 7. The other parameters are general empirical values. By comparing the extraction effects of different mode numbers on the muzzle-leaving time of projectile, the optimal parameters are determined. When $K = 3$, the algorithm is in an under-decomposition state, and the

Fig. 5 Comparison of modal components with different K values

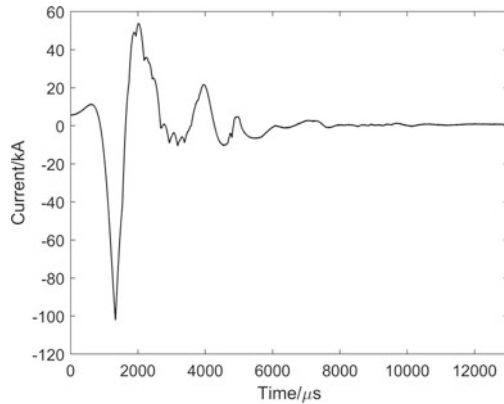


change trend of launch current is not obvious. There are still some frequency components that are not completely decomposed. It is impossible to accurately identify the mutation point of launch current. When $K = 4, 5, 6, 7$, the muzzle-leaving time point can be determined in the third modal component. The decomposition results of the third modal component obtained by different K values are shown in Fig. 5. It can be seen from the figure that when $K = 4$, the characteristics of launch current and time are the most obvious. With the increase of K value, the launch current signal is over decomposed. The mutation point of muzzle-leaving time is gradually smooth, which makes it difficult to find the characteristic point. In addition, the calculation time cost of the algorithm is greatly increased.

The value of penalty factor α will affect the bandwidth of each signal component. With the increase of α , the bandwidth decreases gradually. If α is too small, the frequency component of the original signal cannot be completely decomposed. If α is too large, the number of iterations to obtain the optimal decomposition effect will increase. And a large number of mode aliases will occur.

On the premise that $K = 4$ is determined, the value of α is 50000, 100,000, 200,000, 500,000 and 1,000,000 respectively, and the optimal value is determined by comparing the decomposition effects under different values of α . When $\alpha \leq 100,000$, modal aliasing occurs and effective frequency signal cannot be decomposed. Example of modal component when $\alpha = 50,000$ is shown in Fig. 6. When $\alpha \geq 200,000$, the effective frequency component can be obtained, and the muzzle-leaving time can be easily determined. When $\alpha = 20,000$, the modes are completely separated and the number of iterations is minimum. The decomposition effect and time cost are optimal.

Fig. 6 Modal component 3 waveform at $\alpha = 50,000$



6 Conclusion

Because of the terrible launch environment at the muzzle of the electromagnetic railgun, the traditional test methods are difficult to apply to the measurement of the projectile's muzzle-leaving time. Aiming at the characteristics and launch environment of electromagnetic railgun, according to the mutation point of launch current caused by the armature-rail contact characteristics, this paper proposes a feature extraction method of launch current based on VMD, which can quickly and intuitively find the time when the projectile leaves the muzzle in the appropriate decomposition mode, and verifies the proposed method through experiments. The test results show that the change of armature-rail contact state can be intuitively reflected in the launch current. VMD algorithm can effectively decompose the launch current signal and extract the characteristics of current changes at the moment when the projectile exits the muzzle. The method has satisfactory accuracy by comparing with the muzzle voltage test results.

In addition, the method of measuring launch current through Rogowski coil has been widely utilized in the field of electromagnetic launch. It has the significant advantages of easy operation, simple, convenient and high reliability. Compared with other testing methods, this method has higher engineering application value, and lays a foundation for improving the firing accuracy of electromagnetic railgun.

References

1. Li, S., Cao, R., Zhou, Y., et al.: Performance analysis of electromagnetic railgun launch system based on multiple experimental data. *IEEE Trans. Plasma sci.* **47**(1), 524–534 (2018)
2. Ma, W., Lu, J.: Electromagnetic launch technology. *J. Natl. Univ. Defense Technol.* **38**(6), 1–5 (2016). (in Chinese)
3. Karagoz, M., Civil, A., Yildirim, B., et al.: ASELSAN electromagnetic launch laboratory: first shot. *IEEE Trans. Plasma Sci.* **48**, 802–807 (2020)

4. Nab, M.: Brief history of the EML symposia: 1980–2018. *IEEE Trans. Plasma Sci.* **47**(5), 2136–2142 (2019)
5. Li, J., Cao, B., Fan, Z., Guo, W., Chen, Y.: Research on speed measurement by B-probe and precision based on laser method. *Trans. China Electrotechnical Soc.* **35**(S2), 327–332 (2020). (in Chinese)
6. Chang, X., Yu, X., Liu, X.: A velocity-controlling triggering strategy of capacitive pulsed power supply electromagnetic railgun system. *Trans. China Electrotechnical Soc.* **33**(10), 2261–2267 (2018). (in Chinese)
7. Zhang, Z., Wang, T., Guo, H., Wang, Y.: Antiaircraft firing strategy of electromagnetic railgun with adjustable muzzle velocity of projectile. *Acta Armamentarii* **42**(02), 430–437 (2021). (in Chinese)
8. Feng, M., Lan, G., Cheng, R.: Research on the measurement method of gun muzzle velocity. *Electron. Technol. Softw. Eng.* (24), 58–60 (2021). (in Chinese)
9. Xiong, S., Lu, J., Zheng, Y., Zeng, D.: Modeling and analysis of discharge of pulsed power supply for electromagnetic launch. *J. Natl. Univ. Defense Technol.* **41**(04), 53–59 (2019). (in Chinese)
10. Ruan, J., Chen, L., Xia, S., Wang, Z., Li, L.: A review of current distribution in electromagnetic railguns. *Trans. China Electrotechnical Soc.* **35**(21), 4423–4431 (2020). (in Chinese)
11. Zhu, C., Wang, J., Ma, F., Ni, Y., Tang, B., Li, B.: Analysis of sliding electric contact characteristics of series-augmented railgun based on breech voltage. *Acta Armamentarii* **41**(07), 1280–1287 (2020). (in Chinese)
12. Dragomiretskiy, K., Zosso, D.: Variational mode decomposition. *IEEE Trans. Sig. Process.* **62**(3), 531–544 (2014)

K-Means Based Multi-dimensional Charging Behavior Profiling Technique



Bin Zhu, Yulan Li, Zhi Li, Tingting Xu, Huicai Wang, Dong Yan ,
and Chongyang Luo

Abstract With the full-scale construction of electric vehicle charging facilities, the back-end management data of charging users have been seen in the beginning. To this end, this paper performs data cleaning and standardization based on charging user data in Banan District, Chongqing, in China and fuses RFM model to perform multidimensional K-means clustering analysis on user characteristic data grouping and derives a typical profile of user charging behavior. The results of the cluster analysis based on charging duration show that charging users with charging duration between 1200 and 5000 s have obvious characteristics; the results of the cluster analysis based on SOC show the mileage anxiety behavior of some charging users; the results of the cluster analysis based on RFM show that a small number of users have high usage residual charging behavior and regular charging residual behavior.

B. Zhu · Z. Li · T. Xu · H. Wang
State Grid Chongqing Electric Power Company Marketing Service Center (Metering Center),
Chongqing 400023, China
e-mail: 13098681679@163.com

Z. Li
e-mail: nanhuananmu@163.com

T. Xu
e-mail: 825328370@qq.com

H. Wang
e-mail: badmin101@163.com

Y. Li
Chongqing Electronic Engineering Vocational College, Chongqing 401331, China
e-mail: 153033107@qq.com

D. Yan (✉) · C. Luo
Chongqing University of Posts and Telecommunications School of Automation/Industrial Internet
School, Chongqing 400065, China
e-mail: yandong@cqupt.edu.cn

C. Luo
e-mail: somefoodluo@qq.com

The research results provide data base support for distribution network planning and management schemes and marketing strategies.

Keywords Electric Vehicle Charging · Clustering Analysis · K-means · User Profiling · RFM Model

1 Introduction

With the growth of the scale of new energy vehicles and the continuous expansion of charging station/pile construction, massive, multi-dimensional and structured operation data have been generated. In this regard, mining the potential value of user charging behavior data has become a new research hotspot for scholars at home and abroad.

The literature [1] analyzed and described the spatio-temporal behavior of electric vehicle users from the dimension of charging user behavior habits by analyzing the limited rational psychology of car users in choosing travel mode, travel path and departure moment. The literature [2, 3] conducted K-means-based clustering of electric vehicle user data in the dimensions of single-pile charging frequency, single-pile charging power, average charging power, average charging duration and power consumption time, and constructed five categories of typical user characteristics. The literature [4] implemented the fuzzy mean clustering algorithm (FCM) based on objective function for the average speed, average absolute acceleration and idle time ratio of vehicles to accurately analyze the traffic conditions of electric vehicle networks. The literature [5] analyzed users' mobile terminals, gender and age distribution, spending power and payment habits, and explored charging behavior patterns and charging load distribution based on weekly, seasonal and hourly time dimensions. The literature [6] used the K-means clustering method to output user characteristic labels in four dimensions: speed preference, driving style, time preference and proficiency. The literature [7] analyzes car user driving data by a hybrid algorithm of DBSCAN clustering and K-means clustering, which in turn predicts the user's place of residence. The literature [8] used text mining methods such as sentiment analysis, word frequency statistics and semantic network graphs to mine the sentiment features of online reviews of new energy vehicle users. The literature [9] conducted K-mean clustering analysis from the spatial, temporal and frequency characteristics of shared car users' trips to mine the typical travel patterns. The literature [10] considers the association between the travel charging behavior of vehicle user groups and the spatial and temporal characteristics of cities, and implements user charging demand prediction based on a decision tree model. The literature [11, 12] builds an energy consumption analysis model to optimize user charging cost based on historical driving data. The literature [13, 14] studied the influence law of user vehicle location, user charging mode preference and driving style on battery aging based on the statistical analysis method of big data.

In summary, mining the potential value of charging vehicle operation data is conducive to improving enterprise benefits and user interests. In order to further explore the user profile of new energy vehicles, this paper takes the actual charging behavior data of users in Banan District, Chongqing as the basis, pre-processes the data such as cleaning and standardization, and performs multi-dimensional clustering analysis of users from the original data features and high-dimensional data features respectively to derive the charging behavior user profile, which provides data basis and technical support for the marketing strategy of distribution network planning and management.

2 User Charging Behavior Data Analysis

This paper collects data on charging user behavior in Banan District, Chongqing, China. These data contain charging duration, SOC, user ID, user order time and electric capacity per charge. First, the non-normal data are cleaned, then the data are constructed twice, the data are clustered from different dimensions, and finally the user profile analysis is performed.

2.1 Abnormal Data Cleaning

The abnormal data in the back-end can have a great impact on the analysis results, solid this paper cleaned 224,005 EV user behavior data from August 2021 to July 2022 in Banan District, deleted 26,002 abnormal values, duplicate values and blank values, and got 198,003 valid data after cleaning.

2.2 Feature Selection

The user feature data is divided into raw features and high-dimensional features. Raw features are unprocessed data features, including the duration of each charge, SOC, user charge capacity, etc. High-dimensional features are the results of data after calculation and statistics. The following high-dimensional features are constructed.

The number of days between the last charge of the user in the data statistics and the end time of the statistics:

$$R = T_{now} - T_{rec} \quad (1)$$

where T_{now} is the statistical cut-off time of the data, T_{rec} indicates the most recent charging time.

Frequency of user charging during the time of data statistics:

$$F = \sum_{i=1}^q p_q \quad (2)$$

where p_q is the number of charges on the q -th day of the user during the data validity time.

User charging capacity:

$$E_{total} = \sum_{i=1}^q E_q \quad (3)$$

where E_q is the charging capacity of the user on the q -th day of the data validity time.

The raw data is organized and transformed into high-dimensional data characterized marked by a unique user ID, which is easy to mine more user characteristics and values.

2.3 Data Standardization

In this paper, the maximum-minimum normalization method is used to normalize the data, which is calculated as follows. The formula requires the calculation of the maximum value X_{max} and the minimum value X_{min} for all input data X .

$$X_{normal} = \frac{X - X_{min}}{X_{max} - X_{min}} \quad (4)$$

Standardization ensures that all data are within a reasonable interval, so that data of different magnitudes do not have a wide range of outliers in space, which not only accelerates the convergence speed of clustering but also makes the clustering results more reliable.

3 Multi-dimensional User Profiling Technology

3.1 RFM Model

RFM model (Recency-Frequency-Monetary Model) is an important tool and instrument to measure customer value and customer profitability [14].

In the user charging behavior data, the new RFM model with E_{total} instead of Monetary can reflect the relationship between charging load and user category more intuitively. In addition, the RFM model requires data to have IDs. Therefore, in this paper, after cleaning the data without IDs, 19,099 RFM data with user IDs were obtained.

3.2 K-Means Clustering

In this paper, the K-means method is used to cluster the data. This is a distance-based clustering method and when it clusters it is an iterative process. Its calculation steps are as follows:

- (1) Input n-dimensional data points, and randomly select K points as the initial clustering centers of the sample set.
- (2) Calculate the Euclidean distance between each data point and the cluster center, and assign them to the cluster center with the shortest distance.
- (3) Update the clustering centers and use the center of mass of all data points in each class as the new clustering center.
- (4) Determine whether the error between the new clustering centers and the previously outputted clustering center values converges, and if it converges, output the result; if it does not, skip to step 2 and continue to the next step.

The formula for calculating the Euclidean distance in the k-means clustering algorithm is as follows:

$$d_{(x,y)} = \sqrt{\sum_{i=1}^n (x_i - y_i)^2} \tag{5}$$

In this paper, the Silhouette Coefficient method is used to measure the clustering K metric. The K corresponding to the highest value of Silhouette Coefficient is chosen as the best clustering number.

3.3 Analysis of Clustering Results

In this paper, based on PyCharm development environment, we use k-means algorithm to cluster the charging duration, start SOC and end SOC, and RFM data in turn, and derive the clustering results, which can reflect the characteristics and composition of local users according to the clustering results.

Characteristic Analysis of Charging Duration. The clustering results of charging hours are shown in Table 1, and the cluster distribution is shown in Fig. 1.

Table 1 Charging duration feature clustering results

User Category	Number of Clusters	Clustering Center (second)
1	3834	10,665.45
2	95,066	3857.71
3	98,841	1672.36

Fig. 1 Clustered distribution of charging duration histogram

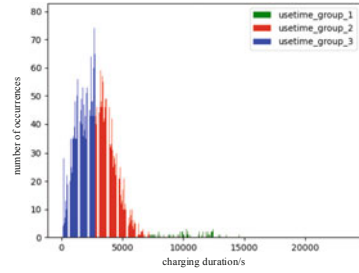


Table 2 SOC feature clustering results

User Category	Number of Clusters	Clustering Center	
		Start SOC (%)	End SOC (%)
1	26,098	37.6	93.21
2	28,142	0.96	75.17
3	116,491	0.49	97.7
4	11,241	68.36	94.9
5	14,769	5.33	45.5

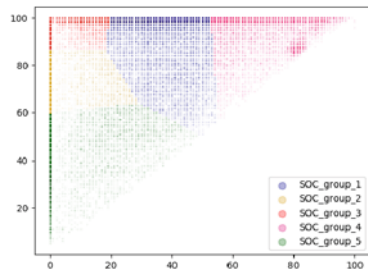
In Fig. 1, it can be seen that the number of users with charging time between 1200 and 5000 s is high, and the data shows a positive distribution, while the number of users with more than two hours is a small percentage.

Combining the data in Table 1 with the raw data, it is possible to classify the users' charging duration into three categories, i.e., the first category - long time charging, the second category - general charging, and the third category - short time charging. The clustering results show that the users of long time charging account for a relatively small.

SOC Feature Analysis. The results of clustering the SOC data are shown in Table 2, and the distribution of clusters is shown in Fig. 2.

From the scatter plot distribution in Fig. 2, it can be seen that the SOC feature points of users are aggregated, mainly gathered in the edge side of the plot.

Fig. 2 Scatterplot of SOC feature clustering distribution



Combined with the clustering results in Table 2, users can be divided into the following categories:

Charging type 1: Mild mileage anxiety. This type of user tends to choose to fully charge when there is still about 35% of power left.

Charging type 2–3: Regular users with the highest percentage, whose charging choice is generally: full charge when the power is depleted.

Charging type 4: Heavy mileage anxiety. The percentage is low. This type of user chooses to fully charge the car when it is less than half charged, and the data shows that this type of person basically does not have the habit of charging for a long time.

Charging type 5: Economical users, instead of replenishing the battery when it is very low, charge it to about 45% and have more precise control over the power level, which also results in relatively low electricity prices.

RFM Feature Analysis. The results obtained by RFM clustering are shown in Table 3, and the cluster distribution results are shown in Fig. 3.

Based on the analysis in Table 3, the users can be classified into the following types:

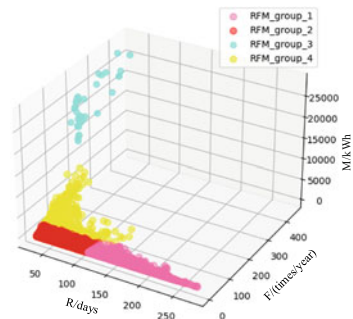
User type 1–2: casual customer type. The highest proportion, this type of users are not charged in time, and the frequency of charging in the region is very low every year, indicating that they leave after a short stay in the region, and the possibility of charging in the region again is very low.

User type 3: High usage residential users, the number of such users is very small. This type of user uses the vehicle very frequently, has been active in the area for a

Table 3 RFM feature clustering results

User Category	Number of Clusters	Clustering Center		
		R (days)	F (times/year)	M (kWh)
1	6086	162.38	2.35	57.9
2	12,218	61.49	4.14	99.3
3	39	30.54	242.79	21,343.19
4	757	40.06	69.78	5185.14

Fig. 3 Scatterplot of RFM feature clustering distribution



long time, is still active in the area, and is more likely to be a commercial vehicle user.

User type 4: Residential users who recharge regularly. The difference in R-values is small and the F- and M-values are relatively low compared to the high usage residential type users. Combining the raw data shows that these users have regular charging habits in the region.

4 Conclusion

In this paper, a multidimensional cluster analysis is conducted for the actual electric vehicle station user data in Banan District, Chongqing, and the following conclusions and recommendations are obtained:

- (1) A clustering implementation scheme for charging user profiles is proposed. For charging stations, one- and two-dimensional clustering is performed from the original data features for charging time and SOC feature pins, respectively; for data with ID information, clustering is performed from the high-dimensional features combined with RFM model to derive typical feature user categories.
- (2) In terms of charging choice, a few users have charging plans, the vast majority of users choose to charge when the power is close to zero, the charging time is short, and a considerable number of users have mileage anxiety. Companies still need to improve charging speed and improve the layout of charging facilities, so that users can have electricity to charge in some relatively remote areas and alleviate mileage anxiety.
- (3) Based on the clustering results, three categories of charging time and four categories of charging behavior can be derived. Among these three categories of users, resident users account for a minority and the vast majority are temporary users, which indicates that enterprises can push tariff package plans to resident users in a targeted manner.

Acknowledgements This research is supported by State Grid Chongqing Electric Power Company Science and Technology Project (522000220004) and Research on Key Technologies and Device Development of Orderly Charging of Electric Vehicle Charging Pile based on Multidimensional Data Perception.

References

1. Wu, F.Z., Yang, J., Lin, Y.J., Xu, J., Sun, Y.Z.: Spatio-temporal behavior characteristics of electric vehicles considering users' finite rationality. *J. Electr. Eng. Technol.* **35**(07), 1563–1574 (2020). (in Chinese)
2. Lu, W., Li, J.B., Peng, X., Cao, W.B., He, C.S.: User profile technology of electric vehicle charging stations in Jiading area. *Power Energy* **40**(02), 176–180 (2019). (in Chinese)

3. Wang, Y., et al.: The analysis of electrical vehicles charging behavior based on charging big data. In: 2019 IEEE 4th International Conference on Cloud Computing and Big Data Analysis (ICCCBDA), pp. 63–67 (2019)
4. Lv, Z., Qiao, L., Cai, K., Wang, Q.: Big data analysis technology for electric vehicle networks in smart cities. *IEEE Trans. Intell. Transp. Syst.* **22**(3), 1807–1816 (2021)
5. Liu, J., Zou, D., Chen, Y., Chu, Z.: Analysis of electric vehicle charging facilities operation data. In: 2020 IEEE 5th International Conference on Intelligent Transportation Engineering (ICITE), pp. 422–426 (2020)
6. Li, Z.H., Zhai, J., Diao, G.T., Li, X.G., Wu, J.: Research on the application of electric vehicle user driving behavior profile based on vehicle network data. *Sci. Technol. Wind* (18), 61–64 (2022). (in Chinese)
7. Cheng, D., Zhang, L., Zhao, S., Li, F., Wang, X.Y., Huang, Z.P.: Prediction of new energy vehicle users' residence based on clustering algorithm. *Pract. Autom. Technol.* **46**(10), 11–13 (2021). (in Chinese)
8. Yu, F.: Sentiment analysis of new energy car users based on text mining. *Logist. Eng. Manag.* **44**(01), 137–140 (2022). (in Chinese)
9. Tong, D., Zhou, X.C., Gong, R.X.: A study of car-sharing travel patterns in Shanghai based on big data. *Adv. Geosci.* **40**(12), 2035–2047 (2021). (in Chinese)
10. Sheng, Y.J., Guo, Q.L., Liu, M.J., Lan, J., Zeng, H.T., Wang, F.: Multi-source data fusion for user charging behavior analysis and charging facility planning practice. *Power Syst. Customization* **46**(12), 151–162 (2022). (in Chinese)
11. Bozorgi, A.M., Farasat, M., Mahmoud, A.: A time and energy efficient routing algorithm for electric vehicles based on historical driving data. *IEEE Trans. Intell. Veh.* **2**(4), 308–320 (2017)
12. Cui, D., Wang, Z., Zhang, Z., Liu, P., Wang, S., Dorrell, D.G.: Driving event recognition of battery electric taxi based on big data analysis. *IEEE Trans. Intell. Transp. Syst.* **23**(7), 9200–9209 (2022)
13. Liang, H.Q., He, H.W., Dai, K.W., Pang, B.: Analysis of the impact of electric vehicle user behavior on battery aging based on big data. *Autom. Eng.* **44**(08), 1212–1288 (2022). (in Chinese)
14. Long, B.T.: Research on customer value stratification based on improved RFM model. *J. Xichang Coll. (Nat. Sci. Ed.)* **36**(01), 52–57 (2022). (in Chinese)

Turn-to-Turn Overvoltage Test Technology for Dry-Type Smoothing Reactor



Qingsong Liu, Jiajie Huang, and Chenlei Liu

Abstract The dry-type smoothing reactor is one of the main devices of UHVDC transmission projects. However, the related insulation test is still less than perfect. The turn-to-turn over-voltage test for dry-type reactors has been gradually carried out in recent years and has been recognized by many standards, but at present it is mostly applied for small reactors of 35 kV or below. In this paper, the design of turn-to-turn insulation test for dry-type smoothing reactor is developed, and a high-frequency oscillation circuit is built. Simulations were performed using PSCAD to explore the effectiveness of the turn-to-turn overvoltage test method. The simulation results confirm the feasibility of using high-frequency attenuated oscillation waves for the turn-to-turn insulation overvoltage test of dry-type smoothing reactors.

Keywords UHV dry-type smoothing reactor · Turn-to-turn over-voltage test · The high-frequency oscillation test

1 Introduction

To solve the problem of uneven distribution of energy centres and power load centres in China, ultra-high voltage power transmission technology has emerged. As one of the important equipment in the UHV DC transmission project, dry-type smoothing reactor plays the role of suppressing transient overcurrent and reducing harmonic current in the DC system, and has many advantages such as reliable insulation, light weight, easy to use and maintain, etc. It is widely used in the UHV DC transmission project. The safe and stable operation of dry-type smoothing reactor contributes to the operational reliability of the UHV DC transmission system [1, 2].

Q. Liu · J. Huang

Maintenance Test Center of China Southern Power Grid EHV Transmission Company, Guangzhou 510663, China

C. Liu (✉)

School of Electrical Engineering, Shandong University, Jinan 250061, China

e-mail: liu_cl@sdu.edu.cn

© Beijing Paiké Culture Commu. Co., Ltd. 2023

X. Dong et al. (eds.), *The proceedings of the 10th Frontier Academic Forum of Electrical Engineering (FAFEE2022)*, Lecture Notes in Electrical Engineering 1054, https://doi.org/10.1007/978-981-99-3408-9_57

665

With the extensive use of dry-type smoothing reactor, damage to them occurs from time to time. According to relevant data, the majority of interturn short-circuit insulation faults in reactors originate from part damage to insulation of the coil. It in turn causes the coil to become damp, partial discharges to be enhanced and local overheating. And eventually the coil insulation is completely destroyed. According to statistics, interturn short-circuit faults account for more than 70% of the total number of reactor faults [3]. At the same time turn-to-turn insulation of the dry-type air-core reactor is subjected to overvoltage such as residual voltage of the lightning arrester, switching overvoltage, uneven distribution of the power frequency voltage caused by extreme conditions [4]. At the beginning of a turn-to-turn short circuit, the relevant electrical quantities do not change significantly and the existing fault detection methods can not reflect the true equipment condition; when the electrical quantities are obvious enough, the reactor is already on fire and it is too late for the circuit breaker to act [5]. It is therefore particularly important to strengthen turn-to-turn insulation detection during manufacture and operation and to develop a reliable and sensitive turn-to-turn short-circuit detection technique that can quickly, accurately and sensitively respond to the actual operating condition of the reactor.

For the dry-type air-core reactor of 35 kV voltage class and below, the international standard IEC 60076-6-2007, the newly implemented national standard GB 1094.6-2011, the industry standard JB/T 5346-1998 and the State Grid Corporation The “Technical Standard for Dry Reactors of 10–66 kV” allows the turn-to-turn overvoltage test to be used instead of the induction voltage test and lightning shock test. The switching overvoltage of reactors has high amplitude, high oscillation frequency (cut-off overvoltage is at the level of several tens of kHz, and re-ignition overvoltage can be up to MHz) and large voltage change rate, etc. [7, 8]. The standard stipulate that turn-to-turn overvoltage test uses a charging capacitor to directly discharge the dry-type air-core reactor at high density for several times, creating a high frequency pulse oscillation voltage on the reactor, with each multi-cycle oscillation waveform more favorable to detect turn-to-turn faults [9]. At present, numerous experts and scholars have already carried out research on overvoltage studies and high frequency oscillation tests with small reactance. However, there is currently less research into the insulation design and testing requirements of the ultra-high voltage dry-type smoothing reactor with higher through-current and higher insulation requirements, and they generally use the medium frequency oscillation test to detection the insulation of smoothing reactor.

This paper investigates the turn-to-turn overvoltage test circuit for UHV dry-type smoothing reactors based on the standard impulse oscillation turn-to-turn overvoltage test method, correctly selects the test parameters and verifies the effectiveness of this method for the detection of turn-to-turn short-circuit faults in dry-type smoothing reactors.

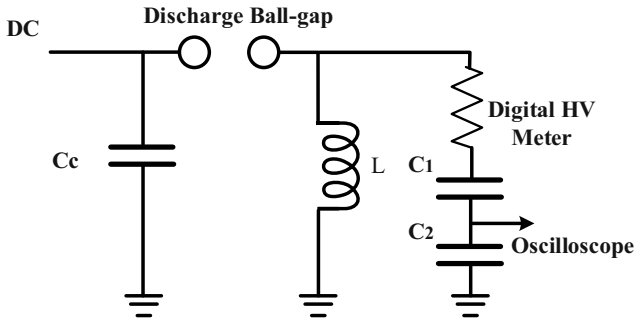


Fig. 1 Exponential decay oscillation voltage principle circuit recommended by the standard

2 Basic Principle

2.1 Standard Recommended Dry Reactor Turn-to-Turn Overvoltage Test Circuits

IEC Std. 60076 recommends a turn-to-turn insulation test for dry-type air-core reactor, and the exponentially decaying oscillating voltage generator for the turn-to-turn insulation overvoltage test is shown in Fig. 1. The damped oscillation frequency is required to be around 100 kHz in each industrial frequency cycle, with no less than 6000 consecutive shocks to the test reactor, then the capacitor needs to be repeatedly charged and to discharge to the test reactor through the ball gap [10–13].

The core idea of the circuit is to charge the capacitor and discharge to the reactor by a natural breakdown of the ball gap switch, then the voltage applied to the reactor is a high frequency exponential decay oscillation waveform of the same overvoltage waveform that appears on the reactor during the reactor switching process. The IEC standard specifies 7200 charges and discharges (7200 overvoltage waveforms) in 1 min. The IEC uses a frequency of 60 Hz and China uses a frequency of 50 Hz, so the GB standard stipulates that 3000 charges and discharges (3000 overvoltage waveforms) are completed in 1 min time and that the initial voltage amplitude of each discharge (the first voltage peak of the exponential decay oscillation voltage) is stable. As the resonant frequency of the turn-to-turn overvoltage is determined by the capacitance of the device and the inductance of the test piece, the frequency is not fixed and typically oscillation frequency at 100 kHz and below.

2.2 High Frequency Decay Oscillation Voltage Test Circuit

As shown in the Fig. 2, resistance voltage divider is used to measure the DC charging voltage value of the main capacitor CC and the capacitive voltage divider is used to

measure the exponentially decaying oscillating voltage at the output of the device. Both have large impedance values and the presence of both is ignored when analyzing the voltage-current relationship of the circuit. The circuit operation is described as follows. The ball gap switch is controlled to conduct once per frequency voltage cycle, that is to say, the main capacitor discharges the inductor once per frequency power cycle, just to meet the standard requirement of 3000 discharges per minute. In the negative half of the output voltage of the test transformer, the test transformer charges the main capacitor via the protective resistor, the damping resistor and the inductor coil. Compared to the impedance of the capacitor, the impedance of the protection resistor, damping resistor and inductor coil can be neglected, so the main capacitor is charged with the peak voltage of the test transformer with a negative peak potential on the left pole plate and zero potential on the right pole plate. During the positive half of the test transformer output voltage, the components on the left side of the ball gap switch are open-circuited. At this point the trigger signal is given and the ball gap switch is discharged on, ignoring the voltage drop across the damping resistor, the potential of the left pole plate of the main capacitor is forced to zero. As the energy stored on the capacitor cannot change abruptly, the potential of the right pole plate of the main capacitor jumps to a positive peak and the main capacitor discharges the inductor coil via the damping resistor (the capacitance is so small that it can be ignored). The energy is then converted between the electric field energy of the main capacitor and the magnetic field energy of the inductor coil until it is all absorbed by the damping resistor and the loop resistance, resulting in an exponentially decaying oscillating voltage across the inductor coil and the model specimen connected in parallel with it.

a. Charging circuit analysis

Analysis of the test principle shows that when the test transformer output voltage is in the negative half of the cycle, the ball gap switch is open and the principle circuit works in the charging state. The components involved in the operation include the regulator, test transformer, protection resistor, damping resistor, mains capacitor and inductor coil. The impedance of the inductor coil under DC can be ignored, so the amplitude of the voltage charged on the main capacitor depends on the test transformer output voltage, the protection resistor, and the

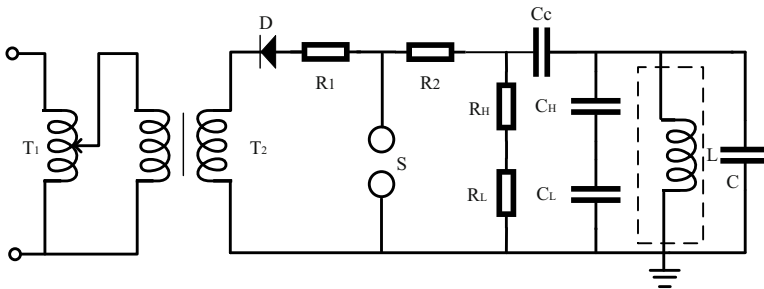


Fig. 2 High-frequency oscillation voltage test circuit

Table 1 Parameters of UHV dry-type smoothing reactor

Parameters	Values
Rated inductance/mH	75
Rated DC current/A	5000
Rated DC system voltage/kV	1100
Short-time (0.2 s) current/kA	40
Insulation material grade	F
Operating impulse withstand voltage/kV	1050

damping resistor. The reactor parameters for an UHV DC transmission project are shown in Table 1.

In this paper, the high frequency oscillation test voltage value is based on the switching impulse value of the UHV dry-type smoothing reactor, i.e., the high frequency oscillation test voltage is 1050 kV [14] and the protection resistance value is 40 k Ω .

b. Discharge circuit analysis

In order to make the damping resistor absorb all the electric field energy in the main capacitor (arc extinguished in the ball gap switch) and make the recovery time of the air insulation between the ball gap be long enough to ensure the controllability of the ball gap switch, the trigger moment of the ball gap breakdown is chosen at the moment when the output voltage of the test transformer changes from negative to positive over zero.

The ball gap discharge channel resistance is R_0 . The damping resistor R_2 and the reactor equivalent resistance R_L make up the discharge circuit resistance R . The initial charging voltage of the main capacitor is U_{C0} . And when the circuit oscillates, the oscillation circuit equation is as follow:

$$LC \frac{d^2 U_C}{dt^2} + RC \frac{dU_C}{dt} + U_C = 0 \quad (1)$$

Therefore,

$$U_C = \frac{\omega_0}{\omega} U_{c0} e^{-\delta t} \sin(\omega t + \beta) \quad (2)$$

ω_0 is the intrinsic frequency, δ is the attenuation factor, ω is the actual oscillation frequency, β is the initial phase.

$$i = C \frac{dU_C}{dt} = C \frac{\omega_0}{\omega} U_{c0} e^{-\delta t} (-\delta \sin(\omega t + \beta) + \omega \cos(\omega t + \beta)) \\ = -\frac{U_{c0}}{\omega L} e^{-\delta t} \sin(\omega t) \quad (3)$$

$$U_L = L \frac{di}{dt} = \frac{\omega_0}{\omega} U_{c0} e^{-\delta t} \sin(\omega t - \beta) \quad (4)$$

When the attenuation factor δ is sufficiently small, $\omega = \omega_0$. At this point, the voltage across the reactor and the frequency of oscillation are approximated as

$$f = \frac{\omega}{2\pi} = \frac{1}{2\pi\sqrt{LC_c}} \quad (5)$$

It can be seen that the voltage applied to the inductor coil is an exponentially decaying oscillating voltage and the oscillation frequency oscillation is only related to the main capacitor and the inductor coil. Based on the experimental frequency of 100 kHz and an inductance value of 75 mH, according to the (5), it can be calculated that the charging capacitance $C_c \approx 3.37e-2$ nF, and the damping resistance is set to 5 k Ω to meet the decay time.

3 Simulation Verification

The above circuit principle is simulated and analyzed using software called PSCAD to carry out a simulation study of turn-to-turn fault discrimination for an inductor of 75 mH. Studies have shown that the presence of short-circuiting turns in a dry-type air-core reactor will cause the presence of short-circuiting coils in the reactor, which reduces the number of effective turns and then result in a reduction in the overall reactor inductance. At the same time, the induction electromotive force will be generated in the short-circuit turns, and the circulating current caused by the induction electromotive force will have a demagnetising effect on the reactor, resulting in a reduction in inductance. The circulating current in the short-circuit turns will also increase the overall losses in the reactor.

3.1 Principle of High Frequency Decay Oscillation Test

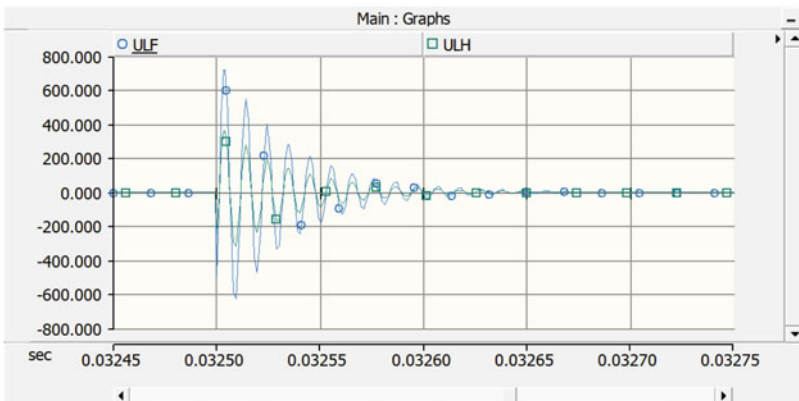
A pulse capacitor is used to discharge the smoothing reactor by adjusting the ball gap, creating a high-frequency oscillating voltage with an oscillation frequency of approximately 100 kHz on the UHV dry-type smoothing reactor. The capacitor charging voltage polarity is negative and the high frequency oscillation test sequence is as follows.

- 1) 1 negative half voltage
- 2) 3 negative full voltage
- 3) 1 negative half voltage

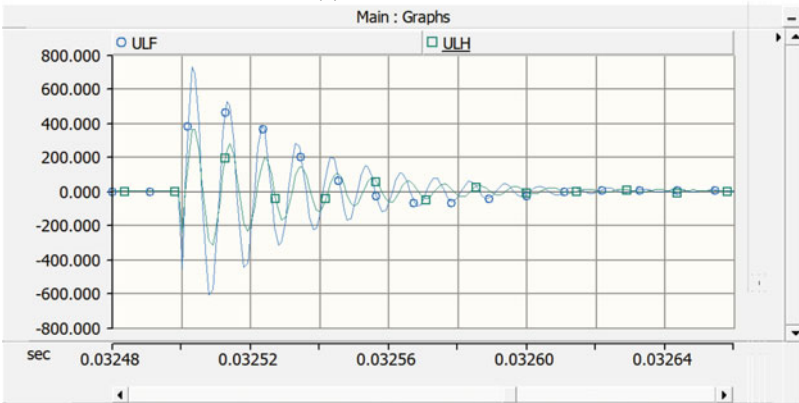
On the premise of completing the standard requirement for the intermediate frequency oscillation test sequence, a half-voltage test is added at the end to observe the frequency of the half-voltage waveform and to check whether the last intermediate frequency oscillation full voltage test caused damage to the reactor winding.

3.2 Analysis of Simulation Results

As can be seen from the Fig. 3, when a dry-type smoothing reactor has a short circuit between turns, the inductance value changes by 4.5%, at which point the oscillation frequency changes by 2.1% and the decay rate is significantly faster. From the results of the waveform, after several cycles of oscillation, the change in oscillation frequency causes a gradual increase in the difference in the waveform over the zero point, then we can detect a short circuit fault between the turns of the reactor through waveform comparison. The more oscillation periods there are, the more pronounced the differences in waveforms.



(a) Normal state



(b) Fault state

Fig. 3 High-frequency oscillation waveform, ULF means full-voltage oscillation waveform and ULH means half-voltage oscillation waveform

4 Conclusion

Through detailed analysis of the high frequency decaying oscillation test circuit and the simulation of the reactor with short-circuit faults, it is confirmed that the designed circuit can detect turn-to-turn short-circuit faults by waveform comparison, and that the higher the number of oscillation waveform periods, the more obvious the effect.

The use of high-frequency decaying oscillation waves is necessary and feasible for the implementation of turn-to-turn overvoltage test of UHV smoothing reactors. Taking the test method and circuit into account, it is feasible from a technical point of view as well as from a safety point of view and is capable of realising on-site partial discharge detection tests for high-voltage parallel reactors.

Acknowledgements Project Supported by the China Southern Power Grid Open Fund for Joint Laboratory of DC Transmission Equipment and Submarine Cables Safe Operation (CGYKJXM20200228).

References

1. Gong, S.Y., Li, T.T., Gao, C., et al.: Harmonic magnetic field analysis based on UHVDC smoothing reactor. In: 2019 IEEE 2nd International Conference on Automation, Electronics and Electrical Engineering (AUTEEE), United State, pp. 627–634. IEEE (2019)
2. Le, J., Wang, C., Luo, H.W., et al.: Study of the conducted electromagnetic interference in the converter station of an UHVDC transmission system. *Prog. Electromagnet. Res. B* **76**(1), 37–57 (2017)
3. Chen, W.T., Wu, T.B., Dolkun, D.: Application of ground penetrating radar to fault analysis in construction of grounding device. In: Proceedings of SPIE, vol. 11930, International Conference on Mechanical Engineering, Measurement Control, and Instrumentation, China, 119301T. SPIE (2021)
4. Zhou, X., Tian, T., Li, X.G., et al.: Study on insulation defect discharge features of dry-type reactor based on audible acoustic. *AIP Adv.* **12**(2), 025210 (2022)
5. Almerda, M.L., Peres, L.M., Santos, G.: Air-core dry-type shunt reactor protection based on an alternative current alpha plane. *IET Gener. Transm. Distrib.* **15**(1), 34–44 (2021)
6. Liao, M.F., Cheng, X., Zhai, Y.F.: Simulation and experiment on impulse oscillating turn-to-turn insulation test system of dry-type air core reactor. *High Volt. Eng.* **37**(6), 1343–1348 (2011). (in Chinese)
7. Xu, L.F., Lin, Y.F., Wang, Y.H., et al.: Impulse oscillator circuit of turn-to-turn over-voltage test for air-core reactor. *J. Harbin Univ. Sci. Technol.* **16**(6), 42–45 (2011). (in Chinese)
8. Do, C.B.W., Lopes, A., Filho, J.P.: Improving the failure detection in the lightning impulse test of low inductance air core reactors. In: 1999 Eleventh International Symposium on High Voltage Engineering, United Kingdom, pp. 217–221. IET (1999)
9. Wang, Y.H., Jiang, J., Wang, T.Y.: Breakdown characteristics of reactor interturn insulation under AC superimposed pulse oscillation voltage. In: 2018 12th International Conference on the Properties and Applications of Dielectric Materials (ICPADM), United States, pp. 262–265. IEEE (2018)
10. IEC 60076-6: Power transformers-Part 6: reactors (2007)
11. GB 1094.6: Power transformers-Part 6: reactors (2011)
12. IEEE Std C57.16: IEEE standard requirements, terminology, and test code for dry-type air-core series-connected reactors (1996)

13. IEEE Std C57.21: IEEE standard requirements, terminology, and test code for shunt reactors rated over 500 kVA (2008)
14. Wu, Y.K., Guo, X.F., Yao, S.L., et al.: Study on distribution of impulse voltage between two UHVDC smoothing reactor. *Electr. Equipment* **8**(3), 20–23 (2007). (in Chinese)

Research on Target User Optimal Complex Path Technology for Regional Fault Scenario



Jianyi Cai , Zhiwei Chen, and Yuxin Lin

Abstract Target users of the power grid, including important, focused, sensitive, and power supply users, exert a significant influence on social development and the public environment. Given their crucial role in power supply reliability, they are key objects of power grid dispatching. Currently, there are technical means, such as large-area fault restoration of the main network and self-healing of the distribution network, that can automatically isolate fault areas of the power grid and recover non-fault areas. While most studies focus on load maximization recovery and economic considerations, there is a lack of research on accurate and reliable power restoration technologies that address the needs of these key support users. Moreover, the existing methodologies are limited by the bottleneck bottleneck in achieving the complete power grid model and user data. Thus, in the event of a large-area power outage, it may not be feasible to provide target users with an optimal power restoration path, resulting in power grid risk events and significant social impacts. And developing a complex algorithm specifically for the above scenarios is not practical. This paper proposes a method that utilizes both conventional and unconventional power restoration techniques to achieve optimal complex power restoration path and programmatic restoration for target users after a power outage. The feasibility of the proposed algorithm is verified through testing, and it is demonstrated that this algorithm can enhance the capabilities of fault perception and rapid restoration of target users.

Keywords Regional Fault · Optimal Path · Target Users · Quick Power Recovery

J. Cai (✉) · Z. Chen · Y. Lin
Shantou Power Supply Bureau of Guangdong Power Grid Co. Ltd., Shantou 515000, China
e-mail: 834157892@qq.com

© Beijing Paiké Culture Commu. Co., Ltd. 2023
X. Dong et al. (eds.), *The proceedings of the 10th Frontier Academic Forum of Electrical Engineering (FAFEE2022)*, Lecture Notes in Electrical Engineering 1054, https://doi.org/10.1007/978-981-99-3408-9_58

1 Introduction

Target users in the power grid, such as important users, key attention users, sensitive users, and guaranteed power supply users, have a certain impact on social development and the public environment. When these target users experience power outages or are unable to restore power in time, it will result in power grid risk events, seriously affecting the safe operation of the power grid and having a significant impact on society. Therefore, subject to the above technical bottlenecks, when a large-scale power outage occurs in the main network [1], the automation system cannot provide accurate complex power restoration paths and strategies [2, 3]. Nowadays the technical solutions comprise power restoration technology for main network faults and power outages, as well as fault self-healing technology for the distribution network [4]. While most researches adopt heuristic search [5], expert system and mathematical optimization algorithm as solution, which can basically achieve fault area isolation and power restoration in non-fault areas [6], the non convergence of some solutions affects its accuracy [7]. However, in case of large-scale power outage of the main network, there is little research on reliable power restoration technology for target users. The existing power supply restoration technology for power grids [8] based on user preferences mainly focuses on the maximization of restoration of power supply areas and consideration of economic benefits, but it neglects the fact that target users, due to their social impact, should be given priority in power restoration. Secondly, the current technology is primarily constrained by the fact that the main network and distribution network employ distinct dispatch automation systems, resulting in inflexible integration of graphics and models between the main network and distribution network, thus leading to inadequate optimization and precision of the complex power restoration path for target users [9].

In the scenario of regional power failure, this paper proposes a method for power restoration of target users based on the topology search and contact data acquisition technology of the distribution network operation control system (OCS), considering both conventional and unconventional situations. By eliminating non-target users and screening paths based on the load rate, this method enables the distribution network OCS to find optimal complex power restoration path and automatically restore power through the program after the target user experiences power outages, thereby enhancing the speed and efficiency of target user power restoration.

2 Data Characteristics

2.1 Establish Target User Data Characteristics

The distribution OCS automatically obtains user data of the target users from the distribution network operation management system (OMS). Then the distribution network OCS compares the equipment ID of the target user with the equipment

records in the distribution network OCS database. If it is successful matched, the equipment will be marked as the target user in the database.

2.2 Establish Relationship with Bus Line Group

To establish the correlation relationship between 10 kV lines connected to the same 10 kV bus on the distribution network OCS, different sections of the bus and their 10 kV disconnecting switches are assigned with unique numbers. 10 kV disconnecting switch can be represented as $X_n(N_i)$ and other representations are as follows:

$$\left\{ \begin{array}{l} X \in \text{The name of the substation} \\ n \in \text{The serial number of 10 kV bus, } n \geq 1 \\ Xn(N_i) = \{N_i | N_{i+1} - N_i = 1, i \geq 1, N_1 = 1\} \end{array} \right. \quad (1)$$

2.3 Establish Regional Fault Characteristics

The main network OCS and the distribution network OCS have their respective power grid models, and the boundary point of the two models is the 10 kV station-side feeder switch in the substation, which can be used as a connection. The main network OCS uses the key messages (10 kV bus outage messages) obtained from monitoring in the substation and the telemetry data (current value drops to 0) of the 10 kV station-side feeder switch as regional fault features. When a large-scale power outage occurs in the power grid, the main network OCS transmits the fault features to the distribution network OCS. Based on the established bus-line group relationship, all 10 kV lines in the distribution network OCS can obtain the corresponding bus outage message from the main network OCS. If the target user’s line group located by the distribution network OCS is consistent with the outage line group, the optimal path analysis for power restoration of the target user will be activated.

3 Analysis of Power Restoration Path

3.1 Conventional Power Restoration Path

Based on the identification technology of “master station topology and open loop point sign” of distribution network OCS [10], the dispatcher can adjust the operation mode in real time, and automatically obtain the contact data of the loop network

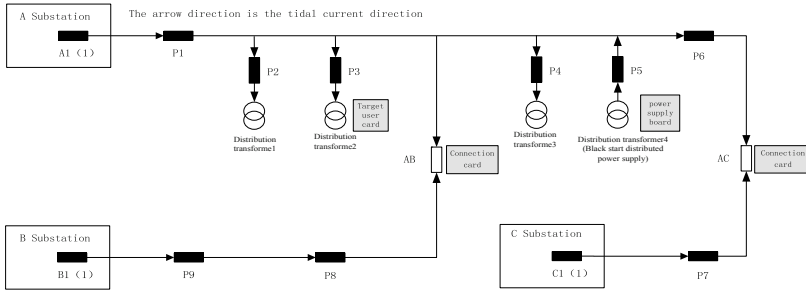


Fig. 1 Ring network in distribution network

line after placing the “contact” sign at the open loop point position. The distribution network OCS starts topology extension search from “Connection” card and “Target user” card and obtains corresponding data. Take the ring network power flow diagram in Fig. 1 as an example.

(1) Starting from the “Connection” card, search for solutions in the direction of the two sides of the line till the power source switch, so as to obtain the connection path and connection relationship. (2) Search for solutions topologically from the “Target user” card towards the power source direction until reaching the “Connection” board, so as to obtain the main and standby power supply paths of the target user and obtain the corresponding data, including the power switch, real-time voltage, real-time current and current limit value of each path. Thus, four conventional power restoration paths are obtained, as shown in Fig. 2, including one main power and three standby power supply paths.

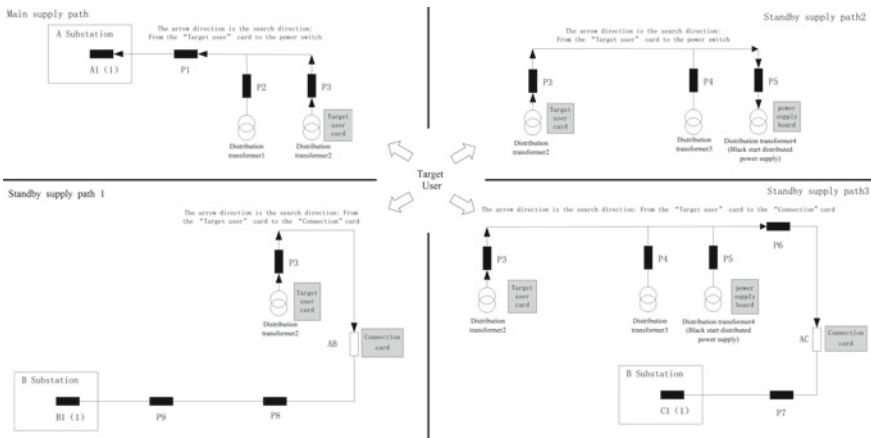
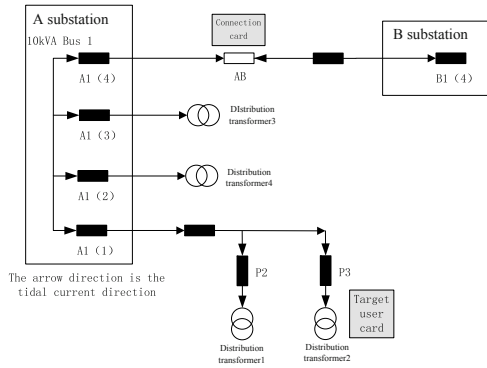


Fig. 2 One main supply path and three standby supply paths, among them, the distribution transformer 4 is an islanding startup power supply

Fig. 3 The distribution lines are supplied by the same 10 kV bus



3.2 Unconventional Power Restoration Path

Aside from the conventional power restoration paths for target users mentioned above, unconventional paths can also be utilized to restore power to the target users, as shown in Fig. 3.

As the unconventional path involves the 10 kV bus, which is not included in the distribution network OCS, the topology search cannot be completed entirely. Therefore, the models of the main network OCS and the distribution network OCS will be connected in the manner as in Sect. 1.2.

According to the line-group relationship, When the target user supplied by the distribution transformer 2 on A1(1) experiences a power outage and there is no tie on this line or no current in the power supply on the opposite side of the tie, the distribution network OCS obtains the restoration path from other lines in the same combination. For example, after AB tie switch is closed, B1 (1) supplies A1 (4), and A1 (4) can be used as the reverse power supply to supply A1 (1) and restore power to the target user.

3.3 Analysis of Optimal Power Restoration Path

The optimal power restoration path analysis logic can be defined as followings: If it is determined that the target user’s line has a tie switch and the power supply on the other side of the tie switch is operational, the “conventional power restoration path” logic will be used. Otherwise, if it is determined that the line has no tie switch or there is no current on the power supply on the other side of the tie switch, the “unconventional power restoration path” logic will be used.

3.3.1 Analysis of Conventional Power Restoration Path

The power restoration path for the target user is obtained as Sect. 3.1. If there is only one path obtained, the optimal power restoration path is obtained after “eliminating non target users”. If there are multiple paths (as shown in Fig. 2), the distribution network OCS executes the logic criteria of “minimum load rate screening” and “non target user elimination” to obtain the power restoration path. This is done to reduce the overload probability of the line, the probability of abnormal faults in the line after power restoration, and to improve the reliability and accuracy of power restoration for the target user.

(1) Minimum load rate filtering

According to the formula of line load rate:

$$f = I_{\text{Real time}}/I_{\text{Current limit}} \times 100\% \quad (2)$$

Assume that the real-time current of the power switch on the opposite side of each tie switch is $I_1, I_2 \dots I_n$ ($n \geq 1$) (the current value is collected by the main station in real time), and the current limit value is $I_{1L}, I_{2L}, \dots I_{nL}$ ($n \geq 1$) (the current limit value has been stored into the OCS database of the distribution network). According to formula (2), the load rate of the power supply line on the opposite side after power transfer is f , the minimum value is:

$$\min(f) = \frac{I_n}{I_{nL}} \times 100\%, (n \geq 1) \quad (3)$$

From formula (3), the minimum load rate ring network group can be located.

(2) Elimination of non target users

For non target users, the OCS of the distribution network chooses the ring network group with the minimum load rate and locates trunk switch and tie switch in this group through searching. Likewise, the trunk line segment where the target user is located is also identified through the search. The master station simulates to turn off the power supply switch and turn on the tie switch so that the trunk line segment where the simulation target user is located is powered by the tie switch. Then the end switch of the trunk line segment can be located through the power supply path, and the distribution network OCS simulates to turn off this switch. Thus, the power supply range of the tie switch can be identified. Finally, identify the non target users within the range (taking the distribution transformer without the “power protection” card as the criterion) and search for the superior switch of the non target user. Through backward simulation, the operation steps are as follows: turn off the switch of non target users → turn off the switch at the end of trunk line segment → turn off the switch of power supply → turn on the tie switch.

3.3.2 Analysis of Unconventional Power Restoration Path

According to the line grouping relationship obtained from Sect. 2.2, the 10 kV line groups on the same bus can be determined. Then, by conducting topological analysis on the 10 kV lines, the line groups with bus tie switches connecting to each other and having current on the other side of the switches can be screened out. Similarly to Sect. 3.3.1, the analysis is as follows:

(1) Minimum load rate filtering

Assume that the power supply current of each screened reverse power supply line is I_{in} ($i \geq 1$), and the power supply current of the opposite side of the tie point of each reverse power supply line is I_{inL} ($i \geq 1, n \geq 1$), and its current limit value is in limit. According to formula (2), the load rate f_{in} of the opposite side line after reverse power supply can be obtained, the minimum value is:

$$\min(f_{in}) = \frac{I_i + I_{in}}{I_{inL}} \times 100\%, (i \geq 1, n \geq 1) \tag{4}$$

From formula (4), the minimum load rate ring network group can be located.

(2) Elimination of non target users

Similarly to Sect. 2.3.1 (2), the distribution network OCS locates the reverse power supply line group with the minimum load rate. Because reverse power supply is involved, it is not necessary to disconnect the power supply switch during simulation. The operation steps for excluding non target users are as follows: turn off the switch of non target users → turn off the switch at the end of the trunk node section → turn on the tie switch.

4 Example

Take Fig. 1 as an example to test the feasibility of the conventional optimal power restoration path. Set the target distribution transformer as distribution transformer 2, with a capacity of 1000 kVA and a real-time current of 83 A at the 10 kV side. Figure 2 shows the conventional main power restoration path. The master station identifies three standby power restoration paths for conventional power restoration through topology, as shown in Fig. 2. Relevant data are shown in Table 1. At 10:00:30, the bus of substation experience a power outage, the voltage of line A1 (1) decreased from 10 to 0 kV, and the current of line A1 (1) decreased from 283 to 0 A.

According to the conventional power restoration logic and formula (3), load rate of standby path 1, path 2 and path 3: $f_1 \approx 16.73\%$, $f_2 \approx 103.75\%$, $f_3 \approx 24.01\%$, and thus $\min(f) = f_1$ and standby path 1 is the optimal power restoration path. The distribution network OCS locates the standby restoration path 1. The topology search shows that the trunk switch nodes are A1 (1), P1, AB, P8, P9 and B1 (1), the tie switch node is ab, and the trunk line segment of the distribution transformer 2

Table 1 Grid data before fault 1

Power supply path	Power switch	Voltage	Current	Current limit
Main supply path	A1(1)	10 kV	283 A	508 A
Standby supply path 1	B1(1)	10 kV	85 A	508 A
Standby supply path 2	P5	10 kV	12 A	80 A
Standby supply path 3	C1(1)	10 kV	122 A	508 A

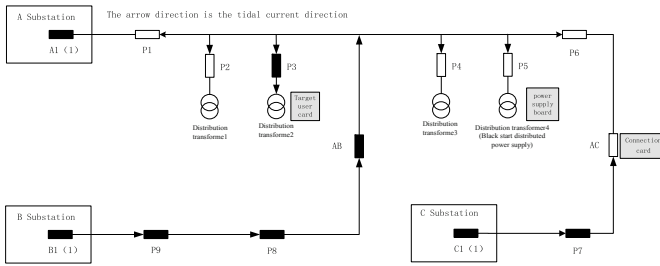


Fig. 4 Conventional optimal complex power restoration path

of the target user is P1-P6. The distribution network OCS simulates to turn off the power supply switch A1 (1) and the tie switch AB to locate the power supply range of the tie switch ab. The end switches of the trunk line segment of the distribution transformer 2 are P1 and P6 and the non target users in this range are distribution transformer 1, 3 and 4 while their superior switches as P2, P4 and P5.

According to the operation steps in 2.3.1 (2), the programmed operation: turn off P2 → turn off P4 → turn off P5 → turn off P1 → turn off P6 → turn off A1 (1) → turn on AB, as shown in Fig. 4.

The current curve is shown in Fig. 5(a). The telemetry current value of distribution transformer 2 gradually rises at 10:01:50, and returns to the original level at about 10:02:30. The telemetry current value of B1 (1) switch also rises synchronously because it bears the load of distribution transformer 2. The whole action process is about 1.22 min.

To verify the effect of standby power restoration path 2 and 3, a experiment that set the OCS to directly locate the optimal standby power supply path without filtering the minimum load rate is conducted, as shown in Fig. 2.

When the OCS identifies the standby power restoration path 3, the programmed operation steps are as follows: turn off P2 → turn off P4 → turn off P5 → turn off P1 → turn off A (1) → turn on AC to restore the power of distribution transformer 3. As shown in Fig. 5(b), the B current curve of standby power restoration path 1 and the C current curve of standby power restoration path 3 are compared. Under the current limiting value of 508 A, the B current margin (340 A) is greater than the C current margin (303 A), indicating that the standby restoration path 1 are better.

When the OCS identifies the standby power restoration path 2, the programmed operation steps are as follows: turn off P2 → turn off P4 → turn off P1 → turn off

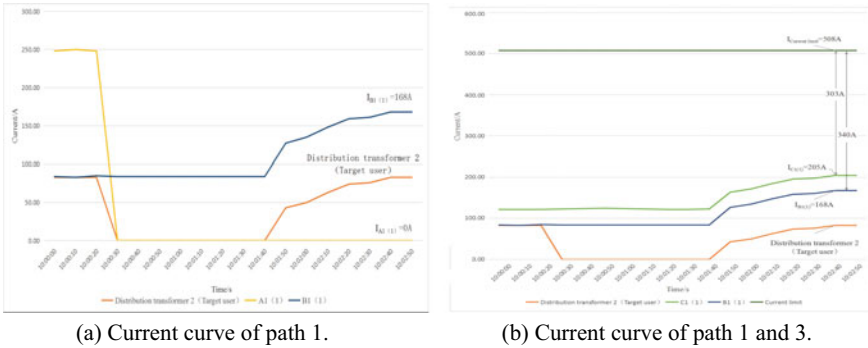


Fig. 5 Compared with the standby supply path 1 and path 3 of current curve and margin



Fig. 6 Current curve of standby supply path 2

P6 → turn off A (1) → black start of power restoration of distribution transformer 4. The current curve is shown in the Fig. 6.

The limited load available from the power supply causes a decrease in the grid frequency as the current of distribution transformer 2 increases. Ultimately, the power supply of distribution transformer 4 trips due to the activation of “low frequency load shedding protection”, resulting in the current of distribution transformer 2 dropping to 0 A. Hence, standby supply path 1 is the optimal power recovery path.

5 Conclusion

In this paper, a technical approach for conventional and unconventional power restoration of target users is proposed to achieve the optimal complex power restoration path and programmed operation following a power outage. It offers intelligent

auxiliary decision-making for optimal power restoration for dispatching and further enhances the fault perception and power supply reliability of target users.

References

1. Lv, Z., Chen, Y., Chen, J., et al.: Study on scenario construction method of large area blackout event for power security. *J. Shanghai Univ. Electr. Power* (2), 185–190 (2021). (in Chinese)
2. Xu, Y., Liu, C., Schneider, K.P., et al.: Microgrids for service restoration to critical load in a resilient distribution system. *IEEE Trans. Smart Grid* **9**(1), 426–437 (2018)
3. Atwa, Y.M., El-Saadany, E.F.: Reliability evaluation for distribution system with renewable distributed generation during islanded mode of operation. *IEEE Trans. Power Syst.* **24**(2), 572–581 (2009)
4. Chen, H., Cong, Q., Jiang, T., et al.: Distribution systems restoration with multi-energy synergy. *Trans. China Electrotechnical Soc.* **37**(3), 610–622 (2022). (in Chinese)
5. Wang, G., Li, X., Song, B., et al.: Load transfer control method of distribution network based on deep reinforcement learning. *Electr. Power Autom.* (7), 253–260 (2022). (in Chinese)
6. Caldon, R., Stocco, A., Turri, R.: Feasible of adaptive intentional islanding operation of electric utility systems with distributed generation. *Electr. Power Syst. Res.* **78**(12), 2017–2023 (2008)
7. Chen, B., Ye, Z., Chen, C., et al.: Toward a MILP modeling framework for distribution system restoration. *IEEE Trans. Power Syst.* **34**(3), 1749–1760 (2019)
8. Jia, L., Jiang, X.: User preference-based multi-objective service restoration in distribution network. *Proc. CSU-EPSCA* (12), 117–124 (2021). (in Chinese)
9. López, J.C., Franco, J.F., Rider, M.J., et al.: Optimal restoration/maintenance switching sequence of unbalanced three-phase distribution systems. *IEEE Trans. Smart Grid* **9**(6), 6058–6068 (2019)
10. Cai, J., Yang, W., Lin, Y., et al.: Research on automatic identification method of distribution network open-loop points based on DMS. *Electr. Eng.* **6**, 74–76 (2020). (in Chinese)

A Novel Design Method of Motor Speed Controller Based on Convex Optimization



Yiwei Tang , Xin Sun, Meng Zhang, and Xi Xiao

Abstract Speed fluctuation of the motor servo system is related to the disturbance torque and the speed feedback noise; thus, the motor speed controller often faces with trade-off between the disturbance suppression ability and the noise tolerance ability. Existing studies lack quantitative analysis of the performance boundary of motor speed controllers. This paper proposes a novel motor speed controller design method based on convex optimization. First, the mathematical model of the motor speed control system is established, and numerical indexes are selected to represent the disturbance suppression ability and the noise tolerance ability; Second, the parameterization method of two classic controllers, namely the Proportional-Integral controller, and the Disturbance-Observation-Based controller, are introduced, and their performance boundaries are calculated respectively; Third, general linear controllers are parameterized and searching the optimal linear controller is simplified to a finite-dimensional convex optimization problem, after which the performance boundary of general linear controllers is obtained. A simulation model is established to compare different controllers. The results show that the controller based on convex optimization can enhance the disturbance suppression ability without losing the noise tolerance ability.

Keywords Servo system · Controller design · Convex optimization

Y. Tang (✉) · X. Sun · X. Xiao
Department of Electrical Engineering, Tsinghua University, Beijing 100084, China
e-mail: tangyw18@mails.tsinghua.edu.cn

X. Sun
e-mail: x-sun13@tsinghua.org.cn

X. Xiao
e-mail: xiao_xi@tsinghua.edu.cn

M. Zhang
Beijing Institute of Control Engineering, Beijing 100190, China
e-mail: 4655574@qq.com

1 Introduction

Motor servo systems can accurately control the position and orientation of mechanical components. They are the core of automation equipment and is widely used in many fields such as machinery manufacturing, packaging, textile, plastic production, and medical equipment [1–3]. The speed mode is an important operating mode of the motor servo system, where the motor rotates according to a given speed command. Motor servo systems face with complex working conditions, where disturbance torque and speed feedback noise causes speed fluctuation. It is desirable to reduce the speed fluctuation as much as possible and hence prudent motor speed controller design is needed.

The motor speed controller should provide the motor servo system decent disturbance suppression and noise tolerance ability. Proportional-Integral (PI) controller is the most classic motor speed controller. It has a simple structure and easy implementation, and is widely used in industrial fields. Many scholars have made various improvements in terms of design methods and parameter setting methods for PI controllers. Reference [4] leverages the attenuation law of tracking error to guide controller design; reference [5] designs a composite PI controller based on the state equation, reference [6–8] uses particle swarm optimization to tune PI parameters, while in reference [9, 10], the genetic algorithm is used to tune the PI parameters; In reference [11], the PI controller is combined with a fuzzy controller. Another type of classic motor speed controller is the Disturbance-Observation-Based (DOB) controller, whose basic idea is to deploy an observer to estimate the unknown disturbance torque using the known control effort and system output. The estimated disturbance torque is then compensated to obtain better control effect. Reference [12] combines DOB controller and two-degree-of-freedom PI controller. Reference [13] designs multiple observers based on traditional DOB controller and gives switching strategies. Reference [14] designs a linear nonlinear hybrid DOB controller. Reference [15] applies the neural network in the observer to reduce the observation burden. In addition, scholars have also applied methods such as internal model control, sliding mode control, and model predictive control to motor speed control [16–18].

Most of the existing researches have noticed the trade-off between the disturbance suppression ability and the noise tolerance ability, and have made beneficial improvements in one aspect. However, for the quantitative analysis of the performance boundary, the existing research is still lacking. This paper proposes a design method of motor speed controller based on convex optimization and illustrates the pareto optimality of general linear controllers. Numerical indexes are first selected to represent the disturbance suppression and noise tolerance ability; Parameterization methods of the two classic linear controllers, PI and DOB controllers, are then introduced, with which the performance boundaries are obtained; Parameterization method and performance boundaries of general linear controllers are then provided. Simulation models are designed and verified.

2 Basics of Speed Controller Design

2.1 Basic Mathematic Model of Speed Control System

According to Newton's second law in the rotational form, the dynamic equation of motor servo system is written as

$$J\dot{\omega} + B\omega = T_d - T_l, \quad (1)$$

where ω is the motor speed; J is the moment of inertia of the system; B is the damping coefficient; T_d is the driving torque; T_l is the disturbance torque. Write (1) in operator form, we get

$$\omega = \frac{1}{B + s_0 J} (T_d - T_l), \quad (2)$$

where s_0 is the differential operator.

By adjusting the gain and time scale, (2) can be normalized and a first-order linear system is then yielded,

$$y_0 = P(s)(u - d), \quad (3)$$

$$P(s) = \frac{1}{1 + s}, \quad (4)$$

where $P(s)$ is the transfer function of the normalized speed control system, s is the normalized differential operator; y_0 is the normalized motor speed, serving as the system output; u is the normalized driving torque, serving as the control effort; d is the normalized disturbance torque, serving as the input disturbance.

Considering the measurement noise of the system output, the feedback control law should be expressed as

$$y = y_0 + n, \quad (5)$$

$$u = -C(s)y, \quad (6)$$

where y is the measurement of the system output; n is the measurement noise; $C(s)$ is the transfer function of the feedback controller.

When physically implementing the designed feedback controller, it should be de-normalized first, that is by letting

$$T_d = -C\left(\frac{J}{B}s_0\right)(B\omega). \quad (7)$$

2.2 Selection of Controller Index

By combining Eqs. (3) to (6), we obtain the closed-loop transfer function from the input disturbance to the system output

$$H_{yd}(s) = \frac{P(s)}{1 + P(s)C(s)}, \quad (8)$$

and the closed-loop transfer function from the measurement noise to the control effort

$$H_{un}(s) = \frac{-C(s)}{1 + P(s)C(s)}. \quad (9)$$

Controller design is the balance between the disturbance suppression ability and the noise tolerance ability. When the controller design is too aggressive (such as bandwidth being too high or gain too large), the disturbance suppression ability will be great, but the control effort will be significantly affected by noise which often causes saturation and oscillation; On the hand, if the controller design is too conservative, the noise tolerance ability will be good at the cost of poor disturbance suppression ability. The benefit of closed-loop feedback control is not fully exerted in such cases.

In order to select the appropriate index to represent the disturbance suppression ability and noise tolerance ability, the disturbance and noise model should be analyzed first. For the motor speed control system, the disturbance torque comes from harmonic torque, cogging torque, nonlinear friction torque, load torque, etc. Its components are complex, and the specific value is difficult to predict. It is usually aggregated and treated as a uniform disturbance. Consider the unit step response from the input disturbance d to the system output y , denoted as $e_{yd}(t)$, let the integration of squared speed fluctuation

$$\phi_1 := \int_0^{+\infty} e_{yd}^2(t) dt \quad (10)$$

be a characterization of disturbance suppression ability [19]. The smaller ϕ_1 is, the smaller the impact of the input disturbance d on the system output y will be, which means the disturbance suppression ability of the closed-loop system gets stronger. By Parseval's theorem,

$$\phi_1 = \frac{1}{2\pi} \left(\int_{-\infty}^{+\infty} \left| \frac{H_{yd}(j\omega)}{j\omega} \right|^2 d\omega \right)^{1/2} = \|WH_{yd}\|_2, \quad (11)$$

where W is the weight function

$$W(s) = \frac{1}{s}. \quad (12)$$

The noise n is the speed feedback error, which is the result of position measurement error and quantization error after differencing and low-pass filtering. Let

$$\phi_2 := \sup_{\|n\|_2 \leq 1} \|u\|_2 = \sup_{\omega} |H_{un}(j\omega)| = \|H_{un}\|_{\infty} \quad (13)$$

be a characterization of noise tolerance [20]. Smaller ϕ_2 indicates stronger noise tolerance ability of the closed-loop system.

3 Design and Analysis of Classic Speed Controllers

3.1 PI Controller

Parametrization of PI Controller. The PI controller is widely used in production practice. It has the transfer function form of

$$C_{PI}(s) = K_{PI} \frac{1 + sT_{PI}}{sT_{PI}}. \quad (14)$$

where K_{PI} is the gain of PI controller and T_{PI} is the time constant of PI controller. Let

$$K_{PI} = 2\xi\eta - 1, \quad T_{PI} = (2\xi\eta - 1)/\eta^2, \quad (15)$$

then the characteristic polynomial of the closed-loop system is

$$s^2 + 2\xi\eta s + \eta^2. \quad (16)$$

Here ξ represents the damping ratio; η represents the bandwidth. By adjusting ξ and η , the poles of the closed-loop system can be adjusted, thereby affecting performance of the closed-loop system.

PI Controller Performance Analysis. Substituting (4), (14) and (15) into (8) and (9), we get

$$H_{yd} = \frac{(2\xi\eta - 1)s + \eta^2}{s^2 + 2\xi\eta s + \eta^2}, \quad (17)$$

$$H_{un} = -\frac{((2\xi\eta - 1)s + \eta^2)(s + 1)}{s^2 + 2\xi\eta s + \eta^2}, \quad (18)$$

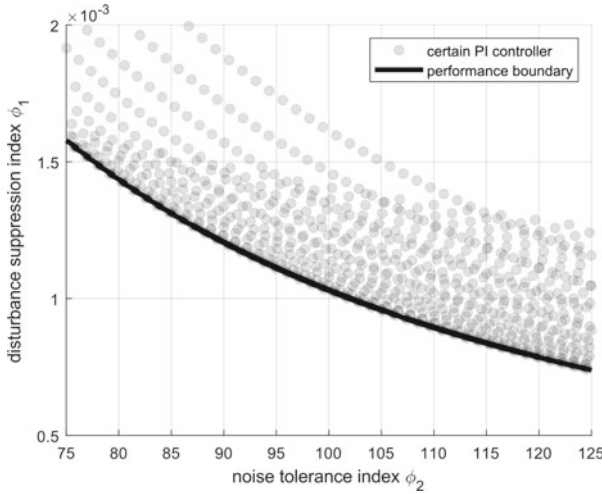


Fig. 1 Performance indexes of closed loop system using PI controller

By substitute (17) and (18) into (11) and (13) respectively, the disturbance suppression ability index ϕ_1 and noise tolerance ability index ϕ_2 can be calculated under different choices of ξ and η . Overall, as ξ increases or η decreases, the disturbance suppression ability of the closed-loop feedback system becomes stronger and the noise tolerance ability becomes weaker. The scatter diagram of the two performance indexes is shown in Fig. 1. Recall that smaller index means better corresponding performance. The thick solid line represents the Pareto boundary of PI controllers, where enhancement of disturbance suppression ability must be at the expense of weakening the noise tolerance ability, and vice versa. On the other hand, for sub-optimal PI controllers represented by the upper right shaded area, the disturbance suppression and noise tolerance ability can be both improved by parameter tuning. Lower left area of the thick solid line represents performance indexes beyond PI controllers' range. This is due to the structural limitation of PI controllers and cannot be surpassed by parameter tuning.

3.2 DOB Controller

Parametrization of DOB Controller. Combine linear friction and disturbance d into a term called total disturbance f ,

$$f := -(y_0 + d). \tag{19}$$

Now the normalized motor speed control system can be described as

$$\dot{y}_0 = u + f. \tag{20}$$

Assuming that the p -th order derivative of the full disturbance f with respect to time is constant, the extended state equation of the normalized motor speed control system is established,

$$\begin{bmatrix} \dot{x}_1 \\ \dot{x}_2 \\ \vdots \\ \dot{x}_p \\ \dot{x}_{p+1} \end{bmatrix} = \begin{bmatrix} 0 & 1 & 0 & \cdots & 0 \\ 0 & 0 & 1 & \cdots & 0 \\ \vdots & \vdots & \vdots & \ddots & \vdots \\ 0 & 0 & 0 & \cdots & 1 \\ 0 & 0 & 0 & \cdots & 0 \end{bmatrix} \begin{bmatrix} x_1 \\ x_2 \\ \vdots \\ x_p \\ x_{p+1} \end{bmatrix} + \begin{bmatrix} u \\ 0 \\ \vdots \\ 0 \\ 0 \end{bmatrix} + \begin{bmatrix} 0 \\ 0 \\ \vdots \\ 0 \\ f^{(p)} \end{bmatrix}. \tag{21}$$

Let the observer state equation be

$$\begin{bmatrix} \dot{z}_1 \\ \dot{z}_2 \\ \vdots \\ \dot{z}_p \\ \dot{z}_{p+1} \end{bmatrix} = \begin{bmatrix} 0 & 1 & 0 & \cdots & 0 \\ 0 & 0 & 1 & \cdots & 0 \\ \vdots & \vdots & \vdots & \ddots & \vdots \\ 0 & 0 & 0 & \cdots & 1 \\ 0 & 0 & 0 & \cdots & 0 \end{bmatrix} \begin{bmatrix} z_1 \\ z_2 \\ \vdots \\ z_p \\ z_{p+1} \end{bmatrix} + \begin{bmatrix} u \\ 0 \\ \vdots \\ 0 \\ 0 \end{bmatrix} - \begin{bmatrix} \beta_1 \\ \beta_2 \\ \vdots \\ \beta_p \\ \beta_{p+1} \end{bmatrix} (x_1 - z_1), \tag{22}$$

then the observer error equation is

$$\begin{bmatrix} \dot{d}_1 \\ \dot{d}_2 \\ \vdots \\ \dot{d}_p \\ \dot{d}_{p+1} \end{bmatrix} = \begin{bmatrix} -\beta_1 & 1 & 0 & \cdots & 0 \\ -\beta_2 & 0 & 1 & \cdots & 0 \\ \vdots & \vdots & \vdots & \ddots & \vdots \\ -\beta_p & 0 & 0 & \cdots & 1 \\ -\beta_{p+1} & 0 & 0 & \cdots & 0 \end{bmatrix} \begin{bmatrix} d_1 \\ d_2 \\ \vdots \\ d_p \\ d_{p+1} \end{bmatrix} - \begin{bmatrix} 0 \\ 0 \\ \vdots \\ 0 \\ f^{(p)} \end{bmatrix}, \tag{23}$$

where $d_i = z_i - x_i, i = 1, 2 \dots p + 1$. The closed-loop characteristic polynomial of the observer is

$$s^{p+1} + \beta_1 s^p + \cdots + \beta_{p+1}. \tag{24}$$

Choose

$$\beta_i = \frac{(p + 1)!}{i!(p + 1 - i)!} \omega_0^i, \quad i = 1, 2, \dots, p + 1, \tag{25}$$

then all the observer poles are located at $-\omega_0$. Define the observer bandwidth as the minimum distance between the characteristic polynomial roots and the imaginary axis. It can be proved that the configuration shown in (25) maximizes the observer bandwidth under the constraint that $\beta_i \leq \omega_0^{k+1}$. Combine (21) to (23) and we get the

transfer function from f to z_2

$$G_{z_2f} = 1 - \frac{s^{p+1} + \beta_1 s^p}{s^{p+1} + \beta_1 s^p + \dots + \beta_{p+1}} = 1 - \frac{s^{p+1} + \beta_1 s^p}{(s + \omega_0)^{p+1}}. \quad (26)$$

When $s \ll \omega_0$, $G_{z_2f} \approx 1$, and (20) can be approximated as

$$\dot{y}_0 = u + f \approx u + z_2. \quad (27)$$

Let

$$u = -z_2 - ky = -z_2 - k(y_0 + n) \quad (28)$$

to complete the DOB controller design.

Combining (21), (22), (25), and (28) leads to the transfer function of the controller

$$C_{DOBC}(s) = \frac{(s + \omega_0)^{p+1}(s + k)}{s^{p+1} + p\omega_0 s^p} - s, \quad (29)$$

where p , ω_0 , and k represent the order, the bandwidth and the gain of the controller, respectively. Note that the DOB controller degenerates into a proportional controller and a PI controller when p equals to 0 (that is, assuming that the full disturbance f is constant) and 1 (that is, assuming the first-order derivative of the full disturbance f with respect to time is constant), respectively. The following analysis hence only consider cases where the order is greater than 1.

DOB Controller Performance Analysis. By choosing certain order p , bandwidth ω_0 and gain k , and substituting (4) and (29) into (8), (9), (11) and (13), we can calculate the disturbance suppression ability index ϕ_1 and the noise tolerance indicators ϕ_2 . Overall, with the increase of ω_0 and k , the disturbance suppression ability gets stronger and the noise tolerance ability becomes weaker; increasing the order p can increase the H_{yd} slope in the low frequency band and hence improve the low frequency disturbance suppression ability, without affecting the noise tolerance ability much. The performance indexes scatter diagram is shown in Fig. 2.

4 Speed Controller Design Based on Convex Optimization

4.1 Parametrization of General Linear Controllers

For a general linear controller, denote its transfer function as $C(s)$, define

$$Q(s) = \frac{-C(s)}{1 + P(s)C(s)} \quad (30)$$

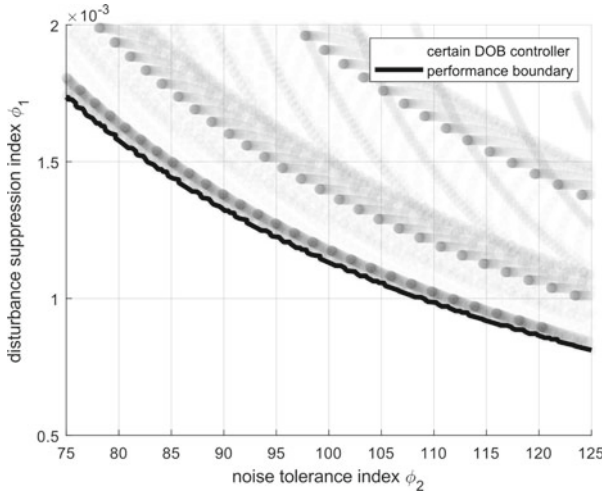


Fig. 2 Performance indexes of closed loop system using disturbance-observer-based controller

to be the tuning transfer function. Obviously, $C(s)$ can be uniquely determined by $Q(s)$.

Substituting (30) into (8) and (9), we get

$$\begin{aligned} H_{yd}(s) &= P(s) + P(s)Q(s)P(s), \\ H_{un}(s) &= Q(s). \end{aligned} \tag{31}$$

To obtain the performance bounds of general linear controllers, we need to consider the constrained optimization problem

$$\min_{\phi_2(Q) \leq \phi_2^*} \phi_1(Q), \tag{32}$$

that is to say, to solve the optimal disturbance suppression ability index value under the constraint that the noise tolerance ability value being not great than a certain threshold.

(32) takes Q as the optimization variable and belongs to infinite-dimensional optimization problems. When solving numerically, Ritz approximation can be used, that is, to expand Q according to some basis functions:

$$Q = \sum_{i=0}^N q_i H_i, \tag{33}$$

where N is the expansion order; q_i are the expansion coefficients; H_i are the expansion basis functions.

Substituting (33) into (32), we can obtain the finite-dimensional optimization problem

$$\min_{\phi_2(q) \leq \phi_2^*} \phi_1(q), \tag{34}$$

where

$$q = [q_0 \ q_1 \ \dots \ q_N]^T, \phi_1(q) = \|W H_{yd}(q)\|_2, \phi_2(q) = \|H_{un}(q)\|_\infty. \tag{35}$$

Choose the basis functions as such

$$H_0(s) = 1, H_i(s) = \frac{s}{(1 + s/\omega_0)^i}, i = 1, 2, \dots N. \tag{36}$$

where ω_0 is the bandwidth parameter. When N tends to infinity, the solution of the finite-dimensional optimization problem shown in (34) converges to the solution of the infinite-dimensional optimization problem shown in (32). Numeric experiment will show that the converging speed is sufficiently fast, therefore only a dozen or so terms are needed.

Considering the robustness of the system, $C(s)$ is required to include an integral stage, namely let

$$\lim_{s \rightarrow 0} C(s) = +\infty. \tag{37}$$

Thus

$$\lim_{s \rightarrow 0} Q(s) = -1. \tag{38}$$

Combining (33) and (36), we have

$$q_0 = -1, \tag{39}$$

then

$$Q = -1 + \sum_{i=1}^N q_i \frac{s}{(1 + s)^i}. \tag{40}$$

(40) is a parameterization of general linear controllers satisfying the robustness requirement. Specifically, $C(s)$ can be uniquely determined by (40) and (30) after the expansion term N and the bandwidth parameter ω_0 are selected, and a set of scalar expansion coefficient q_i are designed.

The stability of $C(s)$ is briefly explained now. Note first that $C(s)$ makes the closed-loop system transfer function

$$W(s)H_{yd}(s) = \frac{1}{s} \frac{P(s)}{1 + P(s)C(s)} \tag{41}$$

and

$$H_{un}(s) = -\frac{C(s)}{1 + P(s)C(s)} \tag{42}$$

stable, so $1 + P(s)C(s)$ has no unstable zeros and $C(s)$ has no unstable poles, that is, $C(s)$ is stable.

4.2 Design Process of Linear Speed Controller

(40) gives the parameterization scheme of general linear controllers, and makes the optimization problem shown in (34) a convex one. The detailed explanation is as follows:

First, the two-norm and infinite-norm of transfer functions satisfy that

$$\|H\|_2 - \|H^*\|_2 \geq g_{H^*}(H - H^*), g_{H^*}(\Delta H) := \frac{\int_{-\infty}^{\infty} \text{Re}(H^*(-j\omega)\Delta H(j\omega))d\omega}{2\pi \|H^*\|_2}, \tag{43}$$

$$\|H\|_{\infty} - \|H^*\|_{\infty} \geq \rho_{H^*}(H - H^*), \rho_{H^*}(\Delta H) := \frac{\text{Re}(H^*(-j\omega^*)\Delta H(j\omega^*))}{\|H^*\|_{\infty}}. \tag{44}$$

where $\text{Re}(\cdot)$ represents the real part, ω^* satisfies that $|H^*(j\omega^*)| = \|H^*\|_{\infty}$; g and ρ are linear functionals defined on the transfer function space. (43) is a corollary of the Cauchy-Schwartz inequality, while (44) can be quickly verified by the scaling method. (43) and (44) show that the two-norm and infinite-norm are convex functionals of the transfer function, and the subgradient is given by the linear functional g and ρ respectively.

Secondly, we know that H_{yd} and H_{un} are affine with respect to Q from (31); we know that Q is affine with respect to q from (40), so ϕ_1 and ϕ_2 are convex functions of q , and (34) gives a convex optimization problem.

Finally, the subgradients of ϕ_1 and ϕ_2 with respect to q are easily derived from (43) and (44)

$$\begin{aligned}
 \phi_1(q) - \phi_1(q^*) &= \|WH_{yd}(q)\|_2 - \|WH_{yd}(q^*)\|_2 \\
 &\geq g_{WH_{yd}(q^*)} \left((q - q^*)^T WP\vec{H}P \right) \\
 &= (q - q^*)^T g_{WH_{yd}(q^*)} \left(WP\vec{H}P \right), \\
 \phi_2(q) - \phi_2(q^*) &= \|H_{un}(q)\|_\infty - \|H_{un}(q^*)\|_\infty \\
 &\geq g_{H_{un}(q^*)} \left((q - q^*)^T \vec{H} \right) \\
 &= (q - q^*)^T g_{H_{un}(q^*)} \left(\vec{H} \right).
 \end{aligned}
 \tag{45}$$

where $\vec{H} = [H_1 \ H_2 \ \dots \ H_N]^T$, $g_{H_{yd}(q^*)}$ and $\rho_{H_{un}(q^*)}$ operate element-wise. (45) and (46) imply that the subgradients of the functions ϕ_1 and ϕ_2 defined at the point $q^* \in \mathbb{R}^N$ are respectively

$$\tilde{g} = g_{H_{yd}(q^*)} \left(P\vec{H}P \right)
 \tag{46}$$

and

$$\tilde{\rho} = \rho_{H_{un}(q^*)} \left(\vec{H} \right)
 \tag{47}$$

The finite-dimensional convex optimization problem shown in (34) can be effectively solved using the ellipsoid method. The specific steps are as follows.

Step 1. Initialize the feasible point q_0 , the ellipsoid matrix A_0 , set k to 0, and set the current optimal value $\hat{\phi}_{1,k} = \phi_{1,0}$;

Step 2. If $\phi_2(q_k) \leq \phi_2^*$, calculate \tilde{g}_k , let

$$\begin{aligned}
 \hat{\phi}_{1,k} &\leftarrow \min \left\{ \hat{\phi}_{1,k}, \phi_{1,k} \right\} \\
 \alpha &= \frac{\phi_{1,k} - \hat{\phi}_{1,k}}{\sqrt{\tilde{g}_k^T A_k \tilde{g}_k}} \\
 q_{k+1} &= q_k - \frac{1+N\alpha}{N+1} \frac{A_k \tilde{g}_k}{\sqrt{\tilde{g}_k^T A_k \tilde{g}_k}} \\
 A_{k+1} &= \frac{N^2(1-\alpha^2)}{N^2-1} \left(A_k - \frac{2(1+N\alpha)}{(N+1)(1+\alpha)} \frac{A_k \tilde{g}_k \tilde{g}_k^T A_k}{\tilde{g}_k^T A_k \tilde{g}_k} \right) \\
 k &\leftarrow k + 1 \\
 \text{Otherwise calculate } \tilde{\rho}_k, \text{ let} \\
 \alpha &= \frac{\phi_{2,k} - \phi_2^*}{\sqrt{\tilde{\rho}_k^T A_k \tilde{\rho}_k}} \\
 q_{k+1} &= q_k - \frac{1+N\alpha}{N+1} \frac{A_k \tilde{\rho}_k}{\sqrt{\tilde{\rho}_k^T A_k \tilde{\rho}_k}} \\
 A_{k+1} &= \frac{N^2(1-\alpha^2)}{N^2-1} \left(A_k - \frac{2(1+N\alpha)}{(N+1)(1+\alpha)} \frac{A_k \tilde{\rho}_k \tilde{\rho}_k^T A_k}{\tilde{\rho}_k^T A_k \tilde{\rho}_k} \right) \\
 k &\leftarrow k + 1
 \end{aligned}$$

Step 3. If $\phi_2(q_k) \leq \phi_2^* + \varepsilon_2$ and $\sqrt{\tilde{g}_k^T A_k \tilde{g}_k} \leq \varepsilon_1$, then skip to Step 4, otherwise skip to Step 2

Step 4. Output q_k as the minimum point, $\hat{\phi}_{1,k}$ as the minimum value.

In the above steps, the subscript k represents the k -th iteration cycle, and ε_1 and ε_2 are precision parameters.

After obtaining the expansion coefficients $q^* = q_k$ that minimizes ϕ_1 within the accuracy range, a linear controller can be determined using (40) and formula (30). The linear controller designed in such a way may have a high order. A balance truncation can be performed to obtain a linear controller with similar performance but a lower order, and Convex-Optimization-Based controller (COB controller) is obtained.

4.3 Performance Analysis of COB controller

Solve the convex optimization problem shown in (34) and we get the performance boundary of COB controllers, as shown in Fig. 3. The expansion order N used are 10, 20, and 30, respectively and the bandwidth parameter ω_0 equals to 70.

It can be seen that for the speed feedback control system, the performance boundary of COB controllers is better than that of the PI controllers and DOB controllers, which means the application of COB controller can enhance the disturbance suppression ability without losing the noise tolerance ability. Within a certain range, increasing the expanded order can push the performance boundary to be more optimal, but when N is sufficiently large, the performance boundary will tend to the limit, and increasing N will no longer have a significant impact on the results.

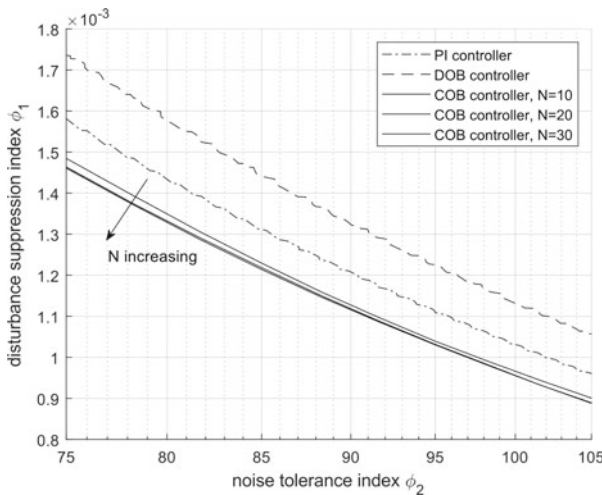


Fig. 3 Comparison among performance boundaries of different controllers

5 Simulation Verification

To benchmark a typical motor speed control system, a simulation model with the diagram shown in Fig. 4 is constructed. The measurement error comes from the geometric tolerance and the installation error, which is treated as white noise. It is then superimposed on the real position, and the result serves as the input of the position encoder. The position encoder produces sampled outputs periodically, and the rotational speed feedback value is obtained after differencing and filtering. The parameters of the simulation model are listed in Table 1, while the difference filter adopts the difference-by-difference method with a window length of 10.

The noise tolerance ability index is chosen as 100. Under this condition, the optimal PI controller has parameters $\xi = 0.6914$ and $\eta = 69.94$, and the obtained disturbance suppression ability index is 1.03×10^{-3} ; the optimal DOB controller has an order of 2, bandwidth of 54.81, and gain of 40.85, and the obtained disturbance suppression ability index is 1.13×10^{-3} . In the COB controller design process, let the expansion order N be 20, and the bandwidth parameter ω_0 be 70. After balanced truncation, a fourth-order controller can be obtained, whose transfer function is shown in (48), the obtained disturbance suppression ability index is 0.91×10^{-3} , and the noise tolerance ability index is 104.6.

$$\frac{122.1s^4 + 4.67 \times 10^{10}s^3 + 3.158 \times 10^{12}s^2 + 6.971 \times 10^{12}s + 3.671 \times 10^{12}}{s^4 + 4.892 \times 10^8s^3 + 1.154 \times 10^9s^2 + 4.687 \times 10^8s - 0.1831} \tag{48}$$

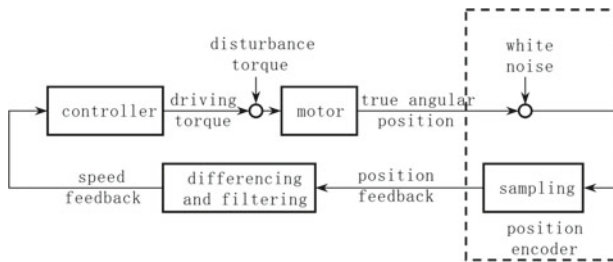


Fig. 4 Simulation model diagram

Table 1 Simulation model parameters

Parameter	Value	unit
Moment of inertia	1×10^{-3}	$\text{kg} \cdot \text{m}^2$
Damping coefficient	1×10^{-3}	$\text{Nm} \cdot \text{s} \cdot \text{rad}^{-1}$
Standard deviation of position error	9.70×10^{-5}	rad
Sampling resolution	6.28×10^{-4}	rad
Sampling period	100	μs

In the simulation model, the operating speed is set to 200 rad/s, and a step disturbance torque of 1Nm is applied. When different controllers are used, the control effort and the motor speed waveform before and after the disturbance step are shown in Fig. 5 and Fig. 6, respectively, the performance indexes obtained are shown in Table 2.

The control effort standard deviation indicates the fluctuation of the control effort in the steady state, which is related to the noise tolerance of the closed-loop system. The smaller this value is, the stronger the noise tolerance ability will be. The control effort maximum, the speed drop, the speed overshoot, and the integration of squared speed error are all related to the disturbance suppression ability of the closed-loop

Fig. 5 Control effort before and after disturbance step change

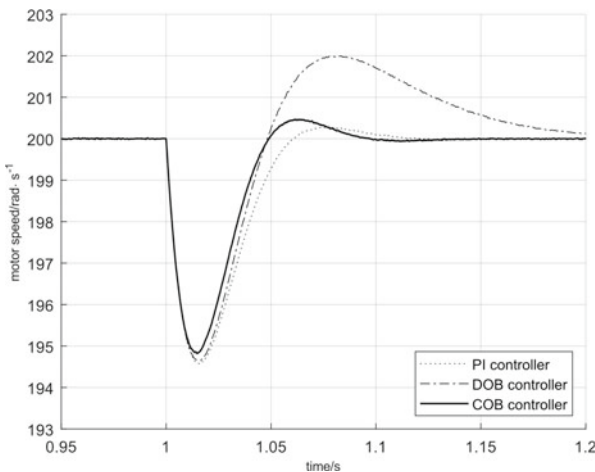
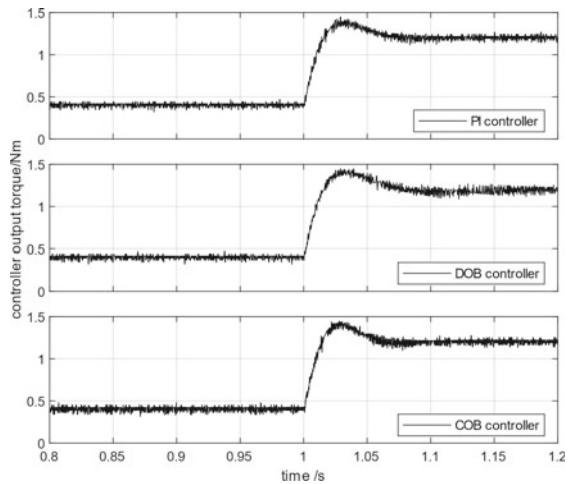


Fig. 6 Motor speed before and after disturbance step change

Table 2 Performance indexes obtained by different controllers in the simulation model

Parameter	PI	DOB	COB
Control effort standard deviation	0.0232	0.0231	0.0234
Control effort maximum	1.4501	1.4489	1.4474
Speed drop	5.4298	5.3527	5.1790
Speed overshoot	0.2812	1.9979	0.4681
Integration of squared speed error	0.6942	0.8451	0.5514

system. Smaller value means stronger disturbance suppression ability. The comparison shows that compared with the PI controller and DOB controller, the controller based on convex optimization has smaller disturbance step speed drop and square integral value of speed error while keeping the standard deviation of the steady-state output of the controller close. Overall, the controller based on convex optimization enhances the disturbance suppression ability without losing the noise tolerance ability.

6 Conclusion

This paper proposes a design method of motor speed controller based on convex optimization. Firstly, the mathematical model of the speed control system is established, and after normalization, the noise tolerance and disturbance suppression ability indexes expressed by the norm of transfer functions are introduced; the Proportional-Integral controller and the Disturbance-Observer-Based controller are analyzed and their parametric design method and performance boundary are quantitatively explained. Secondly, a parametric method is proposed for the general linear controller, which simplifies the motor speed controller design problem into an easy-to-handle convex optimization problem in finite-dimensional space; The performance boundary of the general linear controller is quantitatively given by the numerical method. Finally, a simulation model is designed for the typical motor speed servo system, and the performance indexes using different controllers are compared. The results show that the controller based on convex optimization acquires a stronger disturbance suppression ability without losing the noise tolerance ability.

Acknowledgements This work is supported by National Key Research and Development Program of China (Grant No. 2020YFE0205400) and Natural Science Foundation of China (Grant No. 51977008 and No. U1806224).

References

1. Cai, X.: Research on vector control of PMSM and its key parameters setting method. Dissertation, North China University of Technology (2021). (in Chinese)
2. Ji, X.: Research on control technology of permanent magnet synchronous motor without speed sensor. Dissertation, North China University of Technology (2021). (in Chinese)
3. Feng, K.: The research on flux weakening control of permanent magnet synchronous motor based on active disturbance rejection technology. Dissertation, Dalian University of Technology (2021). (in Chinese)
4. Fu, H.: Research on the PI controller strategy for speedloop of permanent magnetic synchronous motor. Dissertation, Nanjing University of Aeronautics and Astronautics (2017). (in Chinese)
5. Cui, Y., Zuo, Y., Gui, L., Zhu, X., Zeng, F.: Current control of permanent magnet servo motor based on compound PI controller. *Electr. Mach. Control Appl.* **23**(04), 105–110 (2019). (in Chinese)
6. Fan, X.: Simulation research of brushless DC motor PI automatic setting based on PSO. *J. Taiyuan Univ. (Nat. Sci. Ed.)* **40**(03), 45–50 (2022). (in Chinese)
7. Luo, R., You, M., Lin, J.: Simulation research of brushless DC motor PI automatic setting based on PSO. *Control Eng. China* **27**(05), 884–890 (2020). (in Chinese)
8. Quan, L., Wang, J., Cui, H., Wang, Z.: Vector control of induction motor based on particle swarm optimization PI and sliding mode observer. *Control Eng. China* **23**(05), 629–635 (2016). (in Chinese)
9. Pragati, A., Ganthia, B.P., Panigrahi, B.P.: Genetic algorithm optimized direct torque control of mathematically modeled induction motor drive using PI and sliding mode controller. In: *Recent Advances in Power Electronics and Drives*, pp. 351–366. Springer (2021)
10. Cao, F.: PID controller optimized by genetic algorithm for direct-drive servo system. *Neural Comput. Appl.* **32**, 23–30 (2020)
11. Liu, S.: Research and implementation of PMSM fuzzy PI control system based on ZYNQ. Dissertation, Harbin University of Science and Technology (2020). (in Chinese)
12. Zhang, H., Li, J., Xiong, J., Yin, J., Li, X.: Control strategy for permanent magnet synchronous motor with 2-DOF PI control based on ESO. *Electr. Mach. Control Appl.* **48**(05), 40–45 (2021). (in Chinese)
13. Zhu, S., Huang, W., Zhao, Y., Lin, X., Dong, D., Jiang, W., Zhao, Y., Wu, X.: Robust speed control of electrical drives with reduced ripple using adaptive switching high-order extended state observer. *IEEE Trans. Power Electron.* **37**, 2009–2020 (2021)
14. Hao, Z.: Research on key technologies of permanent magnet synchronous motor drive system based on active disturbance rejection control. Dissertation, Jilin University (2022). (in Chinese)
15. Li, Y.: Research on high performance permanent magnet synchronous motor control system based on optimized ADRC. Dissertation, Yangtze University (2021). (in Chinese)
16. Okoro, I., Enwerem, C.: Model-based speed control of a DC motor using a combined control scheme. In: *2019 IEEE PES/IAS PowerAfrica*, pp. 1–6. IEEE (2019)
17. Rakhonde, S., Kulkarni, V.: Sliding mode controller (SMC) governed speed control of DC motor. In: *2018 3rd IEEE International Conference on Recent Trends in Electronics, Information & Communication Technology (RTEICT)*, pp. 1657–1662. IEEE (2018)
18. Fan, Z., Li, S.: Model predictive control method based on permanent magnet synchronous motor speed regulation system. In: *Proceedings of the 31st Chinese Control Conference*, pp. 4412–4417. IEEE (2012)
19. Hanwate, S., Hote, Y.V., Saxena, S.: Adaptive policy for load frequency control. *IEEE Trans. Power Syst.* **33**, 1142–1144 (2017)
20. He, T., Zhu, G.G., Chen, X.: A two-step LMI scheme for $H_2 - H_\infty$ control design. In: *2020 American Control Conference (ACC)*, pp. 1545–1550. IEEE (2020)

Fire Extinguishing Effect of Reignition Inhibitor on Lithium Iron Phosphate Storage Battery Module



Mingjie Zhang, Kai Yang, Jialiang Liu, Yilin Lai, Hao Liu, Hao Chen, Maosong Fan, and Mengmeng Geng

Abstract After fire extinguishing, there will be smoke generation, reignition, and the uncontrolled heat spread of lithium-ion batteries. Given this situation, the fire-extinguishing effect of heptafluoropropane combined with reignition inhibitors on lithium iron phosphate batteries used for energy storage and the amount of reignition inhibitors are analyzed in this paper. The experimental results show that the reignition inhibitor with high thermal stability can exist in liquid form for a long time to achieve long-time cooling of the battery. Therefore, it can effectively inhibit the internal thermal runaway reaction of the battery and then impede the battery's reignition and thermal runaway spread after the fire. The dosage test of reignition inhibitor show that the cooling effect of full submerged method is better than the half submerged method. In addition, the fully submerged method can absorb various particles, and electrolyte vapors brought out by combustion smoke, reduce the amount and concentration of smoke injection, and reduce the harm of smoke after thermal uncontrol of the battery.

Keywords Lithium iron phosphate battery · Thermal runaway · Heptafluoropropane · RH-01 reignition inhibitor · Thermal runaway spread

1 Introduction

The rapid promotion of lithium-ion batteries leads to frequent fire and explosion accidents for the thermal runaway essentially [1, 2]. A large amount of heat and fume gas will be generated in the thermal runaway process, causing combustion and even explosion due to electric sparks and other external disturbances [3, 4].

For the fire protection of lithium-ion batteries, conventional extinguishants such as carbon dioxide, dry powder, and foam extinguishants have little effect on lithium-ion battery fires as they will often re-burn within a short time after the extinction of their

M. Zhang · K. Yang (✉) · J. Liu · Y. Lai · H. Liu · H. Chen · M. Fan · M. Geng
State Key Laboratory of Operation and Control of Renewable Energy & Storage Systems, China
Electric Power Research Institute, Beijing 100192, China
e-mail: ykbit@126.com

naked fires. Currently, heptafluoropropane extinguishant is mainly used for lithium-ion battery fire under the principle of chemical suppression and isolation of oxygen [5, 6], where heptafluoropropane decomposes at high temperatures to generate free radicals that can react with O₂, H, and other free radicals in the flame to interrupt the chain reaction of the combustion process to achieve fire extinguishing [7–9]. Gas extinguishant such as heptafluoropropane has now been widely used in energy storage power stations and battery rooms in substations. Still, it cannot efficiently lower the temperature for a long time, leading to the risk of battery re-burning and the spread of thermal runaway [10].

Regarding the inhibition of battery re-burning, the Project Team found that a liquid organic fluoride liquid with a high boiling point and thermal stability (named RH-01 re-burning inhibitor) can be used to inhibit the temperature rise of the battery effectively. Taking the tri-parallel module composed of square lithium iron phosphate battery commonly used in the energy storage field as the research object, the heptafluoropropane gas extinguishant, and RH-01 re-burning inhibitor (abbreviated as “RH-01”) as the fire protection method for thermal runaway batteries, the fire extinguishing effect of the tri-parallel module before and after the introduction of RH-01 was analyzed in this paper, accompanied with the exploration on the influence of the amount of RH-01 on the fire extinguishing effect.

2 Experimental Sample and Method

2.1 Experimental Sample

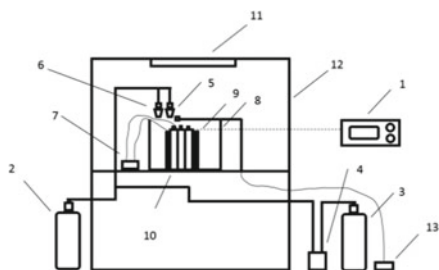
The square 60 Ah LiFePO₄ battery of a company was selected for the experiment. The battery was charged to 100% SOC before the experiment.

RH-01 re-burning inhibitor is a fluorinated liquid with C, O, and F as the main constituent elements, of which the relevant physical parameters were shown in Table 1.

Table 1 Physical Parameters of RH-01

Characteristic name	Molecular formula	Properties and state	Density	Dynamic viscosity	Volatility	Corrosiveness (to metal)	Decomposition temperature	Specific heat capacity
Characteristic value	(C ₃ F ₆ O) _n n = 10–60	Colorless and odorless transparent liquid	1.91 g/mL	10–250 mm ² /s	No volatility	No corrosion	>350 °C	0.99 kJ/kg·K

Fig. 1 Experimental platform



2.2 Experimental Device

The structure of the lithium-ion battery extinguishment experiment platform was shown in Fig. 1 (1-Data acquisition device; 2-Heptafluoropropane fire extinguishing device; 3-RH-01 fire extinguishing device; 4-Gear pump; 5-Gas extinguishant nozzle; 6-Liquid extinguishant nozzle; 7-Electric heating device; 8-Battery box; 9-Plywood; 10-Cell module; 11-Top exhaust device; 12-Experimental platform box; 13-Electric ignition device), on which the thermal runaway of a lithium-ion battery can be triggered by electric heating, and assist in igniting the battery and test its re-combustion through the electric ignition device, with the two sets of pipeline systems injecting heptafluoropropane gas extinguishant and RH-01 respectively. Meanwhile, the data acquisition device and the high-definition camera device collect the temperature and voltage data of the battery and the image data during the thermal runaway process.

2.3 Experimental Method

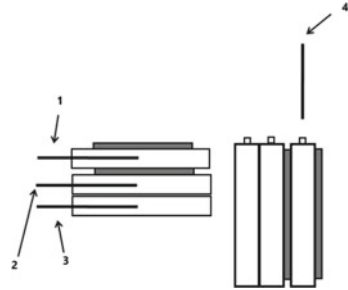
Nine square lithium iron phosphate batteries of the same model at full charge state (SOC = 100%) were selected in this experiment, and three parallel connection modules were formed in groups of three batteries, numbered LFP-1a, LFP-1b, LFP-1c, LFP-2a, LFP-2b, LFP-2c, LFP-3a, LFP-3b, and LFP-3c respectively. The heating method was used to trigger the thermal runaway of the battery. When the voltage dropped to 3 V, the heptafluoropropane was injected, and RH-01 was injected after 2 min. A control experiment was designed to study the impact of RH-01 dosage on the extinguishment effect of the lithium iron phosphate storage battery module. The experimental settings were shown in Table 2.

Two 500 w heating plates were set on both sides of the battery to be heated in the experiment, and k-type thermocouples were used for temperature measurement. The specific temperature measuring points layout was shown in Fig. 2 (bottom of No. 1-1 battery; bottom of No. 2-2 battery; bottom of No. 3-3 battery; and 10 cm above the safety valve of No. 4-1 battery).

Table 2 Experimental Content

	Heptafluoropropane consumption (Kg)	RH-01 consumption (L)
Experiment 1	1.5	0
Experiment 2	1.5	19
Experiment 3	1.5	9.5

Fig. 2 Thermocouple position arrangements



3 Results and Discussion

3.1 Analysis of Battery Burning Phenomenon

During the whole experiment, the main phenomena of the burning and extinguishment process of the battery module 1, which only used heptafluoropropane gas extinguishant to extinguish the fire, the battery module 2, which used RH-01 to flood the safety valve of the battery for extinguishment after injecting heptafluoropropane gas, and the battery module 3, which used RH-01 to immerse half of the battery for extinguishment after injecting heptafluoropropane gas, as well as the re-burning and thermal runaway spread after extinguishment were shown in Fig. 3, Fig. 4, and Fig. 5.

When the selected voltage of the extinguishment node was reduced to 3 V, the battery’s fire at this node had significantly increased compared with the initial burning stage. At the same time, it was judged that the battery had appeared to thermal runaway according to the temperature rise rate of the battery. At the moment of

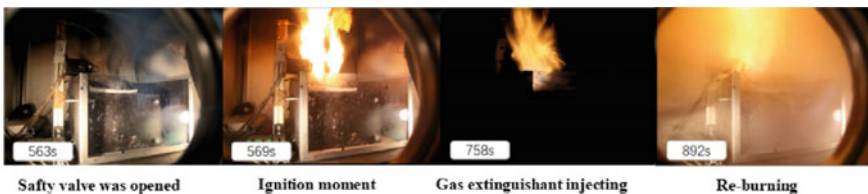


Fig. 3 The battery module is extinguished by heptafluoropropane

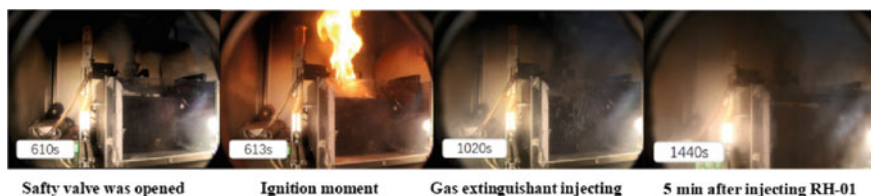


Fig. 4 RH-01 does not pass the battery safety valve to extinguish the fire

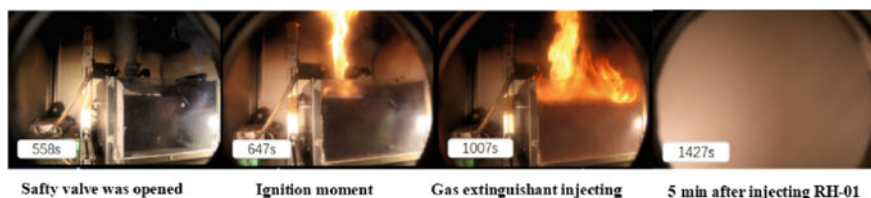


Fig. 5 Battery half-immersed model of RH-01 extinguishes a battery module fire

injecting the gas extinguishant, the open fire was successfully extinguished within 3 s in three experiments, which indicated that the heptafluoropropane extinguishant had a good effect on extinguishing the open fire.

However, it can be seen from Fig. 3 that the battery produced a large amount of fume gas after the open fire was extinguished. After the open fire was extinguished for 2 min, the electric ignition was turned on again, and the reburning happened. Then, LFP-1b deflagrated after 1139 s of heating, and a thermal runaway spread occurred in the battery module.

In Experiment 2, RH-01 was used to flood the safety valve of the battery; in Experiment 3, RH-01 was used to flood half of the battery, and there was no reburning and thermal runaway spread in both experiments. The difference was that the fume gas in the two experiments began dissipating within 5 and 12 min after injecting RH-01. From the above experimental phenomena, it can be seen that the RH-01 can effectively inhibit the re-burning and thermal runaway spread of the thermal runaway battery. The analysis indicated that the role of RH-01 is mainly manifested in three aspects:

① RH-01 is an organic solvent that can dissolve EC, DEC, and other organic electrolytes when it floods the safety valve of the battery. Therefore, it can be observed that the fume gas generated after extinguishing the thermal runaway battery was effectively inhibited in Experiment 2.

② RH-01 has a specific viscosity and a particular obstruction and adsorption effect on the outward injected gas and particles injected with the gas, which can effectively reduce the amount and concentration of fume gas injection.

③ RH-01 has a specific cooling capacity, which can effectively absorb the heat of the internal reaction of the thermal runaway battery. By reducing the internal temperature rise of the battery, the thermal runaway reaction of the battery can be

inhibited to inhibit the re-burning and spread of the thermal runaway battery from the origin.

The mass and voltage changes of each battery after the burning and extinguishment test were shown in Table 3. According to the mass data of the battery after the thermal runaway, LFP-1a had a complete thermal runaway and released all energy in Experiment 1. LFP-1b had a thermal runaway but did not react completely, and LFP-1c did not have a thermal runaway, indicating that the energy transferred from LFP-1a to LFP-1b had been weakened by heptafluoropropane extinguishant.

Thermal runaway happened to only the first battery in Experiments 2 and 3, but the battery mass loss was different, with 0.26 and 0.29 kg, respectively. There were two aspects included in the reasons: First, concerning the reignition inhibitor RH-01, the chemical reaction rate inside the battery was effectively inhibited by cooling down. Second, in Experiment 2, the battery mass was increased by a small amount of RH-01 entering the battery.

According to the extinguishment phenomenon, the extinguishment effect of heptafluoropropane was evident, and the open flame was successfully extinguished within 3 s. As shown in Figs. 6, 7 and 8(a) the flame temperature above the safety valve of the battery dropped from about 7007 °C to below 1007 °C at the moment of heptafluoropropane injection. Still, the properties of heptafluoropropane led to its rapid vaporization, and the battery could not be cooled continuously. Therefore, the thermal runaway reaction inside the battery continued to be carried out, and it could be seen from the figure that the temperature of the battery itself was still rising. In Experiment 1, re-ignition occurred after starting the electric ignition, with the temperature of the secondary burning flame reaching 529.7 °C. At 1,139 s, heat spread occurred, and the LFP-1b valve was broken. Deflagration occurred, and finally, the voltage of both batteries dropped to 0 V.

Through temperature monitoring, in Experiment 2, it was found that the temperature measuring point above the battery did not fluctuate significantly after RH-01 injection, indicating that there was no high-temperature flue gas injected from the safety valve. On the contrary, in Experiment 3, the temperature measuring point above the battery showed a relatively noticeable fluctuation, ranging from 79.7 to

Table 3 Experimental Content

	LFP-1a	LFP-1b	LFP-1c	LFP-2a	LFP-2b	LFP-2c	LFP-3a	LFP-3b	LFP-3c
Mass after the experiment (kg)	1.50	1.73	1.85	1.59	1.84	1.85	1.56	1.85	1.85
Loss mass (kg)	0.35	0.12	0	0.26	0.01	0	0.29	0	0
Voltage after the experiment (V)	0	0	3.31	0	3.30	3.32	0	3.33	3.32

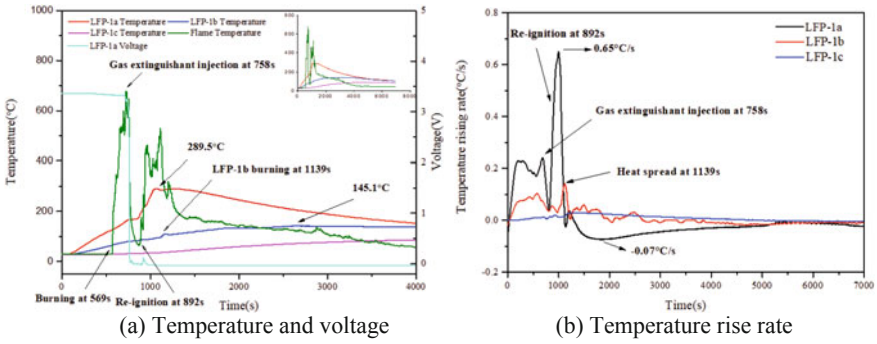


Fig. 6 Experiment 1 temperature and voltage change

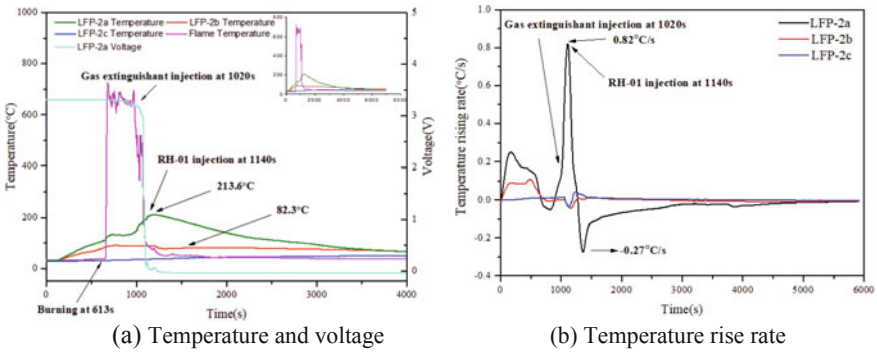


Fig. 7 Experiment 2 Temperature and Voltage Change

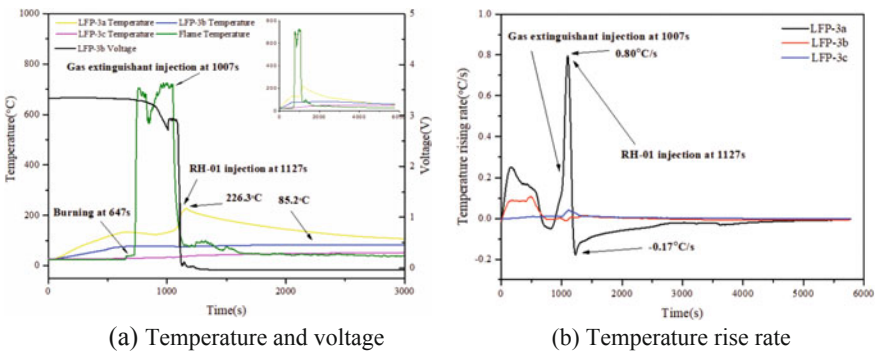


Fig. 8 Experiment 3 temperature and voltage change

97.7 °C. It is confirmed that RH-01t can inhibit the flue gas generation after flooding the battery safety valve.

After heptafluoropropane injection, the temperature of the battery body continued to rise. Injected RH-01 after 2 min, the highest temperature that the battery can reach was significantly reduced, and the temperature rise of the LFP-b battery in Experiments 2 and 3 was effectively inhibited, indicating that RH-01 can inhibit heat conduction and further heat spreading between batteries.

Under the effect of RH-01, the maximum cooling rate of the battery in Experiments 2 and 3 were 0.27 and 0.17°C/s, respectively, both of which indicate that RH-01 has an apparent cooling effect on the battery, and the cooling effect under the total flooding mode is better.

In conclusion, heptafluoropropane can effectively extinguish the open flame during the extinguishment. Still, it cannot restrain the temperature rise inside the battery and the generation of significant smoke, and it is easy to reignite the battery and thermal runaway propagation. This suggests that heptafluoropropane extinguishant is still of substantial potential safety hazard after battery extinguishment. RH-01 performs well at cooling. It can effectively inhibit the re-ignition of the battery and thermal runaway propagation, significantly restraining smoke generation under total flooding mode. Therefore, total flooding mode should be adopted when a reburning inhibitor is used.

4 Conclusion

1. Regarding fire appearing in lithium-iron phosphate energy storage battery modules, heptafluoropropane gas extinguishant can effectively extinguish the open flame. But, it cannot continuously and effectively cool batteries or isolate the oxygen around batteries subject to thermal runaway, which is prone to reignite the battery and trigger thermal runaway propagation of batteries inside the module.
2. RH-01 can effectively reduce the body temperature of batteries subject to thermal runaway and adjacent batteries, inhibit the internal reaction of batteries subject to thermal runaway, and prevent reignition and thermal runaway propagation of batteries.
3. Regarding the application amount of RH-01 liquid extinguishment, compared to semi-flooding mode, full flooding mode is of better cooling effect, and it can absorb a variety of particulate matters and electrolyte vapor brought out with the combustion smoke, reducing the amount and concentration of smoke injection.

References

1. Feng, X.N., Ren, D.S., He, X.M., et al.: Mitigating thermal runaway of lithium-ion batteries. *Joule* **4**(4), 743–770 (2020)
2. Wang, Z., Li, G.H., Liu, Y.: Research on current situation of fire safety and fire prevention countermeasures in energy storage power station. *China Fire* **5**, 62–65 (2021). (in Chinese)
3. Qi, P.Y., Zhang, M.J., Jiang, D., et al.: Combustion characteristics of lithium–iron–phosphate batteries with different combustion states. *eTransportation* **11**, 100148 (2022)
4. Chen, T.Y., Gao, S., Feng, X.N., et al.: Recent progress on thermal runaway propagation of lithium-ion battery. *Energy Storage Sci. Technol.* **7**(06), 1030–1039 (2018). (in Chinese)
5. Li, Y., Yu, D.X., Zhang, S.Y., et al.: Experimental Study on extinguishment of typical lithium-ion batteries. *J. Saf. Environ.* **15**(6), 120–125(2015). (in Chinese)
6. Liu, Y.J., Duan, Q.L., Li, K., et al.: Experimental study on fire extinguishing of large-capacity lithium-ion batteries by various fire extinguishing agents. *Energy Storage Sci. Technol.* **7**(06), 1105–1112 (2018). (in Chinese)
7. Meng, X D., Yang, K., Zhang, M.J., et al.: Experimental study on combustion behavior and fire extinguishing of lithium iron phosphate battery. *J. Energy Storage* **30**(2), 101532 (2020)
8. Zhang, M.J., Yang, K., Zhang, J., et al.: Fire extinguishing effect of heptafluoropropane on lithium iron phosphate energy storage battery. *Fire Sci. Technol.* **39**(5), 649–652 (2020). (in Chinese)
9. Peterson, S.D., Francisco, J.S.: Theoretical study of the thermal decomposition pathways of 2-H Heptafluoropropane. *J. Phys. Chem. A* **106**(13), 3106–3113 (2002)
10. Wang, Q.S., Shao, G.Z., Duan, Q.L., et al.: The efficiency of Heptafluoropropane fire extinguishing agent on suppressing the lithium titanate battery fire. *Fire Technol.* **52**(2), 1–10 (2016)

A Power Decoupling Strategy for Three-Phase Inverter Based on Mid-Leg Fundamental-Frequency Common-Mode Voltage Injection Under Unbalanced Conditions



Rui Zhang, Lan Xiao, Zhiquan Deng, and Xin Cao

Abstract Three-phase inverter is widely used in the fields of new energy grid-connected and power distribution, but it has the problem of double-frequency power pulsation when it is connected to unbalanced power grid. The double-frequency power pulsation will affect the lifetime and efficiency of the system. In this paper, a power decoupling strategy based on mid-leg common-mode voltage injection is proposed to suppress the double-frequency power pulsation, which connects the midpoint of the input split capacitor with the common point of the output filter capacitor, by controlling the fundamental-frequency common-mode voltage component in the midpoint voltage of the three-phase bridge, the double-frequency power can be decoupled. The advantage of this method is that the double frequency pulse power can be absorbed without additional components, and the pulse power of other frequencies is not introduced. Another feature of this method is that, compared with the differential decoupling method, the Output filter capacitor can be fully used and the voltage stress on Output filter capacitor can be reduced effectively.

Keywords unbalanced grid · Suppression of power pulsation · common-mode injection · power decoupling

R. Zhang (✉) · L. Xiao · Z. Deng · X. Cao
School of Automation, Nanjing University of Aeronautics and Astronautics, Nanjing 211100, China

e-mail: ankrearden@163.com

L. Xiao

e-mail: xiaolan@nuaa.edu.cn

Z. Deng

e-mail: dzq@nuaa.edu.cn

X. Cao

e-mail: caoxin@nuaa.edu.cn

© Beijing Paiké Culture Commu. Co., Ltd. 2023

X. Dong et al. (eds.), *The proceedings of the 10th Frontier Academic Forum of Electrical Engineering (FAFEE2022)*, Lecture Notes in Electrical Engineering 1054, https://doi.org/10.1007/978-981-99-3408-9_61

1 Introduction

Three-phase inverter is widely used in power grid-connected system. However, there are all kinds of disturbances in the power grid. Among them, the negative sequence component of the voltage in the unbalanced state is a typical disturbance [1], which can lead to the output of the double-frequency pulsation, the pulsating power's reflection on input terminal makes it hard for the photovoltaic system to operate at the optimal power point when using the photovoltaic system as power source. Or requires the instantaneous output power of the battery to increase and causes the battery to heat up when using the battery as power source. Therefore, it is necessary to suppress power pulsation's affection on power source. This operation is called power decoupling. The common method used in engineering applications is to connect large electrolytic capacitors in parallel on the DC side. Although this passive decoupling approach is easy to perform, the electrolytic capacitors have the disadvantages of large volume, short life and low reliability. In order to get rid of large electrolytic capacitors, many active decoupling methods have been proposed, by controlling the active device in a proper way, the dc-side double-frequency power pulsation can be absorbed by the energy storage device instead of the power source. Generally, the decoupling topology consists of two parts: The decoupling unit and the original converter, according to the multiplexing of the decoupling unit and the original converter, the active decoupling circuit can be divided into switch-multiplexed decoupling circuit and independent decoupling circuit. The independent decoupling circuit works independently with the original converter, and more active devices are needed in comparison with multiplexed decoupling circuit, so the economy and reliability of the converter is lowered. The multiplexed decoupling circuit needs to work in cooperation with the original converter, so the control strategy is relatively complex.

For the independent decoupling circuit, the decoupling method of single-phase inverter can be used directly: In [2], an active decoupling circuit is designed, which is composed of Buck-Boost converter and energy storage capacitor. In [3], a parallel connection of an independent six-switch power decoupling circuit is used at the AC side. [4, 5] use the third port parallel independent power decoupling unit, which can reduce the value of decoupling capacitance. [6, 7] use a H Bridge Structure and a Capacitor as an independent decoupling unit in the system.

For the switch-multiplexed decoupling scheme, an improved three-phase inverter topology is proposed in [8]. In this way, no there are DC voltage bias on output filter capacitors, the voltage stress of the filter capacitor is high. In addition, a quadruple-frequency pulsating power is generated. A four-leg modified converter and a three-leg split-capacitor converter are proposed in [9]. This method can realize the power decoupling by controlling the power on the added capacitor, but the cost and complexity of the system increases. And a much higher DC voltage is required in this way, which increases the voltage stress of the switch and increases the cost of the system.

Aiming at the disadvantages of existing active decoupling methods, a decoupling method based on mid-leg fundamental-frequency common-mode voltage injection is

proposed in this paper. This method can make the most of the output filter capacitors. In this paper, current stress and voltage stress of the switch before and after decoupling are analysed, and the accuracy and correctness of the theory are verified by simulation.

2 Methods

Figure 1 is the improved three-phase inverter topology with fundamental-frequency common-mode voltage injection. The power pulsation required to compensate the pulse power is generated by fundamental-frequency current flowing through the red dotted path in improved topology instead of second order harmonic current flowing through the black dotted path in unimproved topology.

After injecting a fundamental-frequency common-mode voltage, the output filter capacitor voltage is shown (1). Among them, u_{cfa} , u_{cfb} , u_{cfc} are the corresponding filter capacitor voltages, A is the root mean square value of common-mode voltage on output filter capacitor u_{comp} and φ is its initial phase.

$$\begin{cases} u_{cfa} = \sqrt{2}U_+ \sin(\omega_0 t + \Phi_{U+}) + \sqrt{2}U_- \sin(\omega_0 t + \Phi_{U-}) + u_{comp} \\ u_{cfb} = \sqrt{2}U_+ \sin(\omega_0 t - 2\pi/3 + \Phi_{U+}) + \sqrt{2}U_- \sin(\omega_0 t + 2\pi/3 + \Phi_{U-}) + u_{comp} \\ u_{cfc} = \sqrt{2}U_+ \sin(\omega_0 t + 2\pi/3 + \Phi_{U+}) + \sqrt{2}U_- \sin(\omega_0 t - 2\pi/3 + \Phi_{U-}) + u_{comp} \\ u_{comp} = \sqrt{2}A \sin(\omega t + \varphi) \end{cases} \quad (1)$$

The total instantaneous power of the output filter capacitor $p_{2\omega}$ can be derived from Formula (1), which is shown as:

$$p_{2\omega} = (3C_f + \frac{9C_f^2}{2C_n})\omega A^2 \sin(2\omega t + 2\varphi) \quad (2)$$

when the double-frequency harmonic pulse power on the capacitor and the output pulse power are equal, power decoupling is achieved.

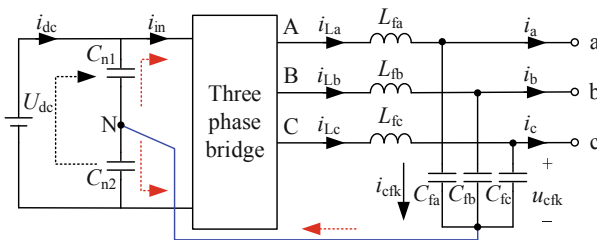


Fig. 1 Improved three-phase inverter topology

After injecting common-mode voltage, the minimum DC source voltage to meet the circuit operation will increase, so the voltage stress of the switch will increase. For comparing the voltage and current stress before and after decoupling, VI and CI is defined as:

$$\begin{cases} VI = \max[\frac{U_p}{U_{stress}}] \\ CI = \max[\frac{I_p}{I_{stress}}] \end{cases} \quad (k = a, b, c) \tag{3}$$

U_p and I_p are voltage stress and current stress of inverter switches with power decoupling, respectively. U_{stress} and I_{stress} are voltage stress and current stress of inverter switches without power decoupling, respectively.

α is shown in formula (4), U_- and U_+ represent the root mean square value of negative-sequence and the positive-sequence component of grid voltage. According to the national standard, the imbalance ‘ α ’ should not exceed 4%.

$$\alpha = \frac{U_-}{U_+} \times 100\% \tag{4}$$

Taking the fluctuation of the root mean square value of the voltage of phase A as an example, when the voltage of phase a falls by 11.5% or rises by 12.5%, the voltage imbalance will reach a critical 4%. According to this, a simulation model can be established, which is shown in Table 1.

Simulation is carried out according to the parameters in Table 1. As shown in Fig. 2, the relationship between the values of VI and CI and the imbalance is obtained. The positive and negative horizontal coordinates indicate the rise and fall of A-phase voltage. According to the diagram, if the inverter can satisfy the decoupling

Table 1 Simulation model parameters

parameters	symbol	value
Switching frequency	f_s	10 kHz
Output frequency	f_n	50 Hz
Filter inductor	L_{fa}, L_{fb}, L_{fc}	2 mH
Filter capacitor	C_{fa}, C_{fb}, C_{fc}	50 μ F
Grid side inductor	L	1 mH
Split capacitor	C_{n1}, C_{n2}	50 μ F
Output voltage	u_a, u_b, u_c	110 V
Rating power	P_o	1 kW
imbalance	α	4%
Voltage of phase A	e_a	97.35– 123.75 V
Voltage of phase B	e_b	110 V
Voltage of phase C	e_c	110 V

Fig. 2 The relative value of voltage and current stress of the improved topology switch

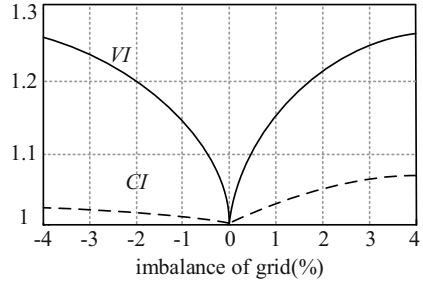
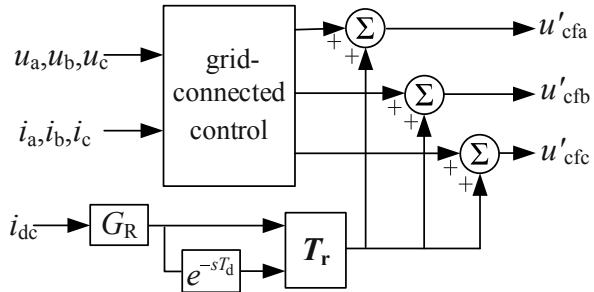


Fig. 3 Control Block diagram of improved three-phase inverter



requirement, the input voltage of the inverter needs to increase to 126.6% of the three-phase in equilibrium state, and the current stress of the inverter switch needs to increase to 106.8%.

3 Control Strategy and simulation verification

As shown in Fig. 3, the control strategy should consist of two parts: grid-connected control and double-frequency pulse power suppression control.

At present, grid-connected control has the control methods of instantaneous active-reactive power control, average active-reactive power control, instantaneously controlled positive-sequence, balance positive-sequence control and so on [10, 11]. The balance positive sequence control can ensure the sinusoidal balance of the output current, so this kind control method is adopted.

For the double-frequency pulse power suppression control. Because the purpose of control is eliminating the second order harmonic component of i_{dc} , so the resonant controller G_R shown in Formula (5) can be used to obtain the common-mode voltage needed to inject into min-leg. The resonant angular frequency ω_n is $2\pi f_n$ and k_n is set to be 25. The output of the resonant controller contains only the second harmonic component. According to this idea, this paper adopts the control strategy as shown in the Fig. 3, in which T_d is a quarter of cycles of second order harmonic. T_r is shown in Formula (6), the function is converting second harmonic signal into fundamental-frequency component signal. $u'_{cfa}, u'_{cfb}, u'_{cfc}$ is three-phase modulated wave.

$$G_R(s) = \frac{2k_n s}{s^2 + \omega_n^2} \quad (5)$$

$$T_r = \begin{bmatrix} \cos \omega t & \sin \omega t \\ -\sin \omega t & \cos \omega t \end{bmatrix} \quad (6)$$

In order to verify the effect of the proposed power decoupling method, the parameters in Table 1 are used for simulation verification. The key waveform diagram and the FFT analysis spectrum diagram of i_{dc} obtained by simulation are shown in Fig. 4, from top to bottom are grid voltage, output current, output filter capacitor voltage, i_{dc} after decoupling and before decoupling, FFT analysis spectrum diagram of i_{dc} . The voltage waveform corresponding to the maximum voltage stress of the output filter capacitor is shown in Fig. 4(b), which is 46% lower than the proposed method in [9] It is shown from the graph that the second harmonic of i_{dc} is eliminated after decoupling, indicating that the second harmonic pulse power can be totally absorbed by the output filter capacitor and the split capacitor..

Therefore, through the analysis and simulation verification, this power decoupling method has the following advantages:

1. The second harmonic pulse power on DC source can be well suppressed by optimizing the control strategy without adding additional components. And the other high-frequency components in i_{dc} can be significantly reduced.
2. Compared with the existing power decoupling method which connects the common point of the output filter capacitor to the negative terminal of the DC input bus, this method can reduce the voltage stress of the output filter capacitor, and make the most of output filter capacitor.

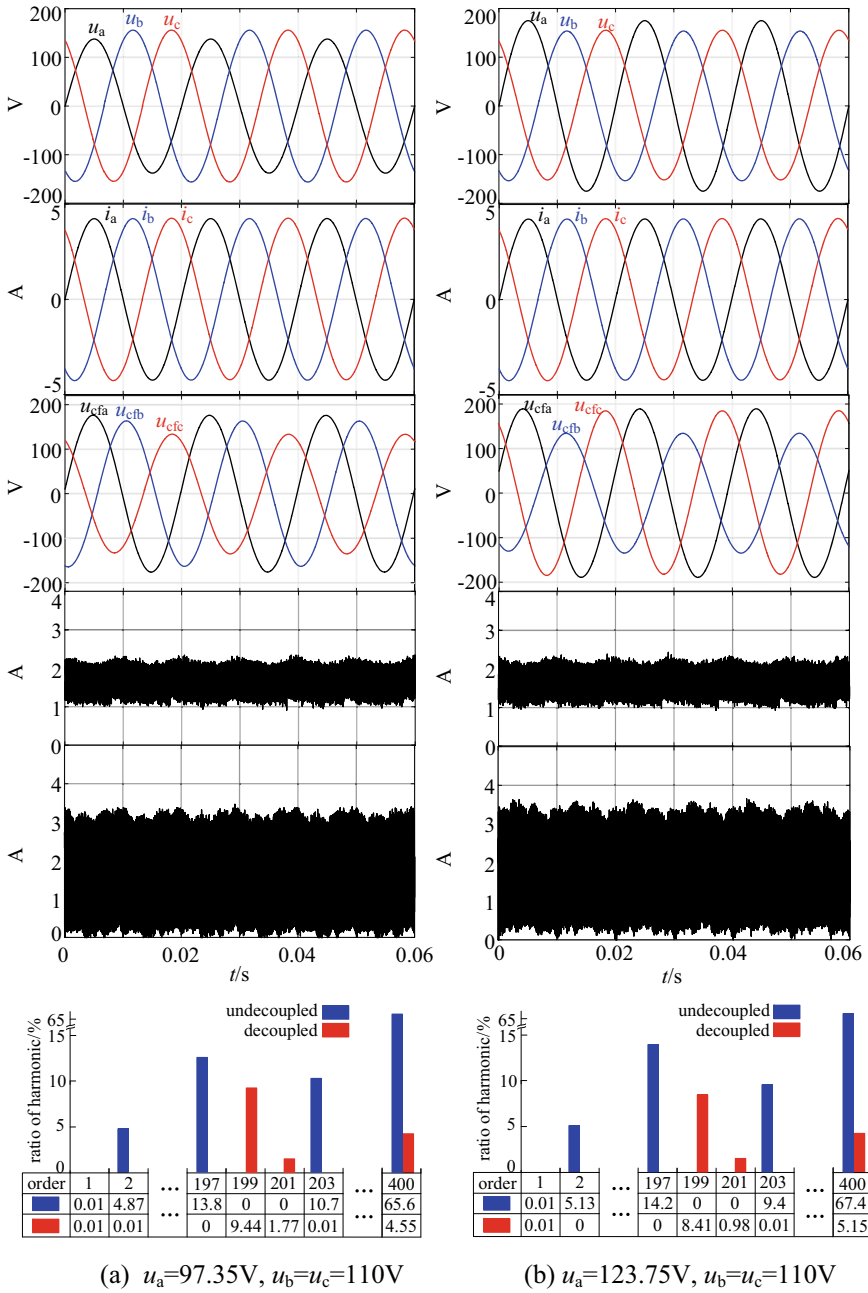


Fig. 4 Improved topology key waveform with 4% unbalance

4 Conclusion

This paper presents a power decoupling method for three-phase grid-connected inverter under unbalanced voltage conditions, without increasing the hardware complexity of the system, the second harmonic ripple current, which is supposed to flow through the DC source, is converted into the fundamental-frequency component current by establishing a new path, the power decoupling of the input terminal is realized. The topology is analyzed, discussed and verified by simulation. The results show that the proposed topology and control method can effectively suppress the double-frequency pulsating power on the DC source without introducing other high-frequency components.

Acknowledgment This research is supported by National Natural Science Foundation of China under Grant 52,177,049.

References

1. Kumar, C., Mishra, M.K., Mekhilef, S.: A new voltage control strategy to improve performance of DSTATCOM in electric grid. *Trans. China Electrotech. Soc.* **4**(4), 8 (2020)
2. Serban, I., Marinescu, C.: Active power decoupling circuit for a single-phase battery energy storage system dedicated to autonomous microgrids. In: *IEEE International Symposium on Industrial Electronics*. IEEE (2010)
3. Wen, C., Bangyin, L., Shanxu, D.: An active low-frequency ripple control method based on the virtual capacitor concept for BIPV systems. *IEEE Trans. Power Electr.* **29**(4), 1733–1745 (2014)
4. Hanlei, T., Yiwen, X., Maolin, C.: A single-stage non-bridge Virtual three-port rectifier with power decoupling capability. *Trans. China Electrotech. Soc.* **37**(08), 2006–2017 (2022) (in Chinese)
5. Song, Z., Liu, M.: Modeling of modular multi-port wireless power DC-DC converter and its multi-directional power flow decoupling control strategy. *Trans. China Electrotech. Soc.* **37**(24), 6262–6271 (2022) (in Chinese)
6. Liu, W., Wang, K., Chung, H. S. -H.: Modeling and design of series voltage compensator for reduction of DC-link capacitance in grid-tie solar inverter. *IEEE Trans. Power Electr.* **30**(5), 2534–2548 (2015)
7. Fan, Q., Lu, Y., Bi, K.: Power balance decoupling control strategy for two-phase staggered three-level bidirectional DC/DC converter based on frequency doubling sampling. *Trans. China Electrotech. Soc.* **37**(14), 3654–3664 (2022) (in Chinese)
8. Tang, J., Zhou, Z., Xin, S., Huang, Loh, P.C.: An Improved three-phase voltage source converter with high-performance operation under unbalanced conditions. *IEEE Access* **6**, 15908–15918 (2018)
9. Zhou, J.: Study on active power decoupling of three-phase grid-connected converter under unbalanced operating conditions. Beijing Jiaotong University, (2019) (in Chinese)
10. Blaabjerg, F., Teodorescu, R., Liserre, M.: Overview of control and grid synchronization for distributed power generation systems. In: *IEEE Trans. Indust. Electr.* **53**, 1398–1409 (2006)
11. Pei, X., Zhou, W., Kang, Y.: Analysis and calculation of dc-link current and voltage ripples for three-phase inverter with unbalanced load. *IEEE Trans. Power Electr.* **30**(10), 5401–5412 (2015)

Terminal Sliding Mode Control of Permanent Magnet Motor Considering Saturation Effect



Longfei Zhu, Jiani Liu, and Xueyan Han

Abstract The ideal linear permanent magnet motor does not consider the saturation effect leading to inductance and chain-related nonlinear parameter error problems. A new permanent magnet motor model based on discrete cross-direct axis current characteristic analysis and online identification of the magnetic chain table is proposed, and an improved non-singular fast terminal sliding mode control strategy is designed to control the simulation. Firstly, considering the uncertainty of motor parameters, the motor parameter regimes of the nonlinear permanent magnet motor model with different dq -axis currents considering the saturation effect are developed. Secondly, the non-singular fast terminal sliding mode control module is applied to the speed loop to improve the switching function to reduce the system jitter and improve the speed dynamic response performance of the system. Finally, the proposed model control method is compared with the conventional ideal model control method in simulation experiments, and the results show that the improved non-singular fast terminal sliding mode control proposed in this paper has fast dynamic response and high robustness under different speed and load torque conditions.

Keywords Saturation effects · Magnetic link form online recognition · Non-singular fast terminal slider · Switching functions

1 Introduction

As a system power source, permanent magnet synchronous motor has the advantages of high mechanical efficiency, high power factor, and high output power, and is used in more and more high-performance applications with considerable development prospects [1].

L. Zhu · J. Liu (✉) · X. Han

The National Engineering Research Center for Rare Earth Permanent Magnet Machines, Shenyang University of Technology, Shenyang 110870, China
e-mail: jiani980604@163.com

© Beijing Paiké Culture Commu. Co., Ltd. 2023

X. Dong et al. (eds.), *The proceedings of the 10th Frontier Academic Forum of Electrical Engineering (FAFEE2022)*, Lecture Notes in Electrical Engineering 1054, https://doi.org/10.1007/978-981-99-3408-9_62

721

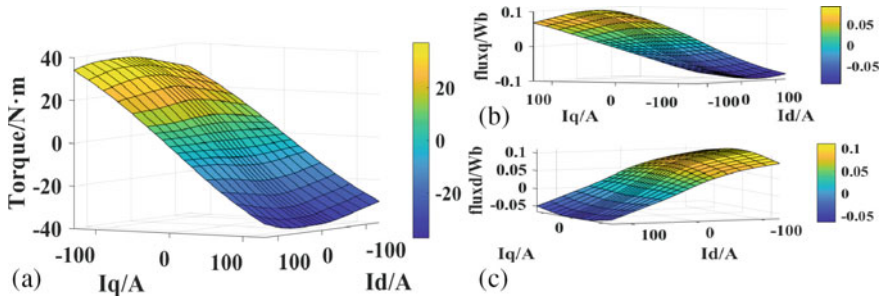


Fig. 1 *DQ*-axis magnetic chain **a**, **b** and torque characteristic curve **c**

However, in places where permanent magnet motors are required to have high saturation capacity, such as in high overload intelligent robots, they are bound to cause a higher degree of saturation of their own magnetic circuits than conventional motors [2]. The characteristic curves of magnetic chain and torque with current change during the operation of servo motors for robots (see Fig. 1), it is easy to see that the permanent magnet motors operate under high overload conditions with a greater degree of saturation, nonlinearity and other problems.

Therefore, an accurate model of permanent magnet motor considering saturation effect is established, and a suitable intelligent control strategy is proposed to improve the shortcomings of traditional control, achieve better control accuracy and dynamic performance, give full play to the high performance of permanent magnet motor, apply to automation and intelligent occasions, and improve production efficiency.

2 Methods

2.1 Analysis of Nonlinear Effects of Permanent Magnet Motors

The nonlinearity of permanent magnet motor mainly comes from the nonlinearity of its ferromagnetic material and magnetic circuit under the action of *dq*-axis current, and the inductance parameters *Ld* and *Lq* are nonlinear functions of *dq*-axis current.

The magnetic permeability varies nonlinearly with the current, and the magnetic chain is derived from the permeability, i.e., the magnetic chain of the permanent magnet ψ_f is a nonlinear function of the current.

In addition, the total magnetic chain consists of two parts: the chain generated by the stator current and the chain generated by the permanent magnets.

$$\psi(t) = \psi_s(t) + \psi_f(t) \tag{1}$$

where ψ_i is the magnetic chain generated by the stator current.

The current generates a magnetic chain that can be expressed by the inductance parameter, whose total magnetic chain is the following matrix:

$$\begin{aligned} \Psi_{i,dq} &= \begin{pmatrix} \psi_{i,d} \\ \psi_{i,q} \end{pmatrix} = L_{dq} i_{dq} \\ &= \begin{pmatrix} L_{dd} & L_{dq} \\ L_{qd} & L_{qq} \end{pmatrix} \begin{pmatrix} i_d \\ i_q \end{pmatrix} \end{aligned} \tag{2}$$

where: L_{dd}, L_{qq} are the dq -axis self-inductance of the three-phase winding; L_{dq}, L_{qd} are the dq -axis mutual inductance of the three-phase winding; $\Psi_{i,dq}$ is the current generation magnetic chain.

There are various nonlinear factors in the generation of magnetic chains by permanent magnets, whose permanent magnet rotor magnetic fields are distorted with different amplitudes and directions depending on the external state. The distribution of the non-sinusoidal rotor magnetic field in the air gap can be written in the form of Fourier series of the magnetic chain generated by the permanent magnets in the three-phase winding.

$$\begin{aligned} \psi_{f,d}(t) &= \psi_{f1} + [(\psi_{f5} + \psi_{f7}) \cos(6\theta_e)] \\ &+ [(\psi_{f11} + \psi_{f13}) \cos(12\theta_e)] + \dots \\ &= \psi_{f1} + \sum_{k=1}^{\infty} \{(\psi_{f,6k-1} + \psi_{f,6k+1}) \cos(6k\theta_e)\} \end{aligned} \tag{3}$$

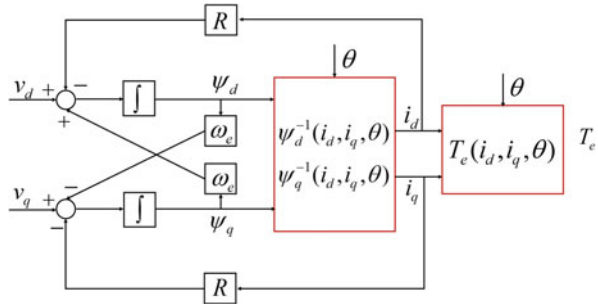
$$\begin{aligned} \psi_{f,q}(t) &= [(-\psi_{f5} + \psi_{f7}) \sin(6\theta_e)] \\ &+ [(-\psi_{f11} + \psi_{f13}) \sin(12\theta_e)] + \dots \\ &= \sum_{k=1}^{\infty} \{(-\psi_{f,6k-1} + \psi_{f,6k+1}) \sin(6k\theta_e)\} \end{aligned} \tag{4}$$

2.2 Consider the Mathematical Model of Nonlinear Permanent Magnet Motor

The voltage equation is obtained from the magnetic chain equation as follows.

$$\begin{cases} u_d(t) = Ri_d + \left(\frac{d\psi_{i,d}}{dt} - \omega_e \psi_{i,q} \right) + \left(\frac{d\psi_{f,d}}{dt} - \omega_e \psi_{f,q} \right) \\ u_q(t) = Ri_q + \left(\frac{d\psi_{i,q}}{dt} + \omega_e \psi_{i,d} \right) + \left(\frac{d\psi_{f,q}}{dt} + \omega_e \psi_{f,d} \right) \end{cases} \tag{5}$$

Fig. 2 Consider the saturated permanent magnet motor model



By the law of conservation of energy, the torque equation can be deduced as follows.

$$T_e = \underbrace{\frac{3}{2}p(\psi_d i_q - \psi_q i_d)}_{T_{dq}} + \underbrace{\frac{3}{2}p \left(\frac{\partial \psi_d}{\partial \theta_e} i_d + \frac{\partial \psi_q}{\partial \theta_e} i_q \right)}_{T_{ch}} - \underbrace{p \frac{\partial W_f(i_{dq}, \theta_e)}{\partial \theta_e}}_{T_f} \tag{6}$$

where T_{dq} is the average torque, and the magnetic chain is a nonlinear term: T_{ch} , T_f are the torque pulsations caused by space harmonics and magnetic energy variations, respectively.

A model of a permanent magnet motor considering the effect of saturation is established (see Fig. 2).

In order to derive the above nonlinear functional relationship, a finite element model of the permanent magnet motor in saturation operation is established, and the $\psi_d^{-1}(i_d, i_q, \theta)$ and $\psi_q^{-1}(i_d, i_q, \theta)$ curves are recorded under different cross-axis currents, and a Look-up Table (LUT) based on the axial magnetic chain is constructed for off-line access.

3 Designing Improved Terminal Slide Controllers

For the permanent magnet synchronous motor control problem, a non-singular fast terminal sliding mode control method is used with the aim of overcoming the singularity of the terminal sliding mode control and achieving global convergence of the state variables, improving the convergence speed while ensuring its robust performance to the internal inductance parameter regression [4].

Assuming no external disturbances and parameter changes, the dynamic model of PMSM is expressed as:

$$\begin{aligned}
\dot{\omega}_r(t) &= \frac{n_p K_t}{J} i_q(t) - \frac{B}{J} \omega_r(t) \\
&= \frac{n_p K_t}{J} i_q^*(t) - \frac{B}{J} \omega_r(t) + \frac{n_p K_t}{J} (i_q(t) - i_q^*(t)) \\
&= a i_q^*(t) + b \omega_r(t) + c(t)
\end{aligned} \tag{7}$$

where K_t is Torque constants; J is Rotational inertia; B is the damping factor; T_L is the load torque; ψ_r is the permanent magnet chain; $a = n_p K_t / J$; $b = -B / J$; $c(t) = a(i_q - i_q^*)$.

If load torque disturbances or parameter changes disturb the system, the PM motor dynamic model can incorporate variable parameters, and its equation is modified as:

$$\begin{aligned}
\dot{\omega}_r(t) &= (a + \Delta a) i_q^*(t) + (b + \Delta b) \omega_r(t) + c(t) - T_L \\
&= a i_q^*(t) + b \omega_r(t) + d(t)
\end{aligned} \tag{8}$$

where $d(t)$ is Focused interference, defined as

$$d(t) = \Delta a i_q^*(t) + \Delta b \omega_r(t) + c(t) - T_L \tag{9}$$

where the concentration disturbance is a bounded function, designed $|d(t)| < \eta_0$ is the system concentration disturbance maximum and η_0 is a constant greater than zero.

Defining the sliding die surface.

$$s = z + k_1 z^\lambda + k_2 \dot{z}^{p/q} \tag{10}$$

where z is the state variable, $k_1, k_2 > 0$, p and q are positive odd numbers and satisfy $1 < p/q < 2$ and $\lambda > p/q$.

Under vector control of $i_q^* = 0$, the input to the speed controller is the speed error for tracking the reference given value of ω_{ref} and requires strong immunity to load changes, while the output quantity is the q -axial current i_q . Now assume that the electric angular velocity reference is ω_{ref} and the electric angular velocity is ω_r , then the velocity error is defined as

$$e = \omega_{ref} - \omega_r \tag{11}$$

Rewriting Eq. (10) and deriving it gives:

$$\dot{s} = \dot{e} + k_1 \lambda |e|^{\lambda-1} \cdot \dot{e} + k_2 \frac{p}{q} |\dot{e}|^{(p/q-1)} \cdot (-a i_q^* + b \dot{e}) \tag{12}$$

Letting $\dot{s} = 0$ yields the equivalent control law of the system as follows.

$$\dot{u}_{eq} = \dot{i}_q^* = \frac{1}{a} \left[\frac{1}{k_2} \frac{q}{p} (\dot{e}^{[2-p/q]} + k_1 \lambda |e|^{\lambda-1} \dot{e}^{[2-p/q]}) + b \dot{e} \right] \tag{13}$$

In order to solve the jittering problem when close to the sliding die surface, the switching function is improved, the sign function in the convergence law is processed for continuity, and the improved switching function λ_n is designed as:

$$\lambda_n = - \begin{cases} \text{sgn}(s), & |s| > \phi(s) \\ \phi(s), & |s| \leq \phi(s) \end{cases} \tag{14}$$

$$\phi(s) = |\tanh(s)|^\gamma \tag{15}$$

where: γ is a constant and $\gamma \in (0 \ 1)$.

Proof: define the Lyapunuv function $V_1 = 1/2s^T s$, then

$$\dot{V}_1 = s^T \dot{s} = s^T \begin{bmatrix} \dot{e} + k_1 \lambda |e|^{\lambda-1} \dot{e} + \\ k_2 \frac{p}{q} |\dot{e}|^{(p/q-1)} \cdot (-a i_q^* - b \dot{\omega}_r - d) \end{bmatrix} \tag{16}$$

Substituting Eq. (16) yields.

$$\begin{aligned} \dot{V}_1 &= s^T \cdot k_2 \frac{p}{q} |\dot{e}|^{(p/q-1)} \cdot [\eta_0 - (\eta_0 + \varepsilon) \lambda_n] \\ &\leq k_2 \frac{p}{q} |\dot{e}|^{(p/q-1)} \cdot (\eta_0 - \eta_0 - \varepsilon) \end{aligned} \tag{17}$$

Since $1 < p/q < 2$, so $V_1 \dot{\leq} 0$. With Lyapunov’s theorem it is known that the permanent magnet motor system is asymptotically stable.

Figure 3 below shows the simulation block diagram of the improved non-singular fast terminal sliding mode control of a high-saturation permanent magnet servomotor.

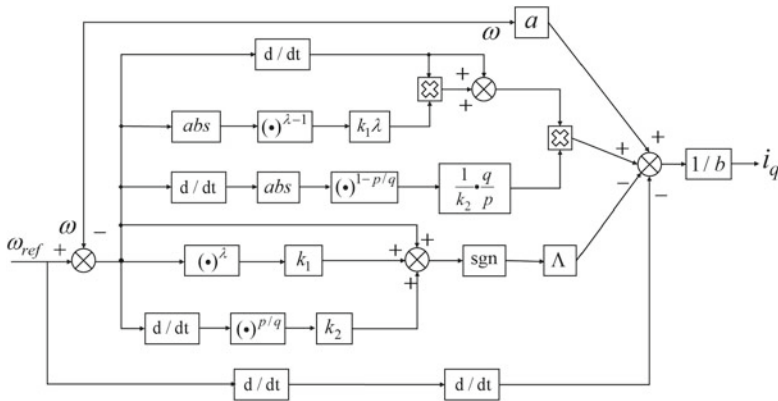


Fig. 3 Non-singular fast terminal sliding mode control

4 Simulation Analysis

To verify the effectiveness of the method, the motor speed control system is simulated using the improved control method and the conventional PI method respectively for comparison. MATLAB simulation is used to examine the speed response curve of the designed permanent magnet motor system and the anti-disturbance performance.

The output performance of the prototype was simulated in rated operation, short-time high overload operation and short-time high speed operation conditions, and the results were as follows.

Rated Operating. Simulation results under rated conditions show that the dynamic response speed of the control method proposed in this paper is 65% higher than that of PI control, with almost no overshoot and strong robustness when disturbed, and the control effect is obvious (see Fig. 4).

Short-time High Overload & Maximum Speed After the motor is started, the At $t = 0.02\text{ s}$ add Short-time maximum torque T_{max} , the results show that the model proposed in this paper model has strong robustness and fast dynamic response. The simulation results are excellent. Simulation of the motor model at the maximum speed operating condition shows that the improved control model The response speed $t = 0.01\text{ s}$ reaches the given speed compared to the PI model response speed faster and without overshoot (see Fig. 5).

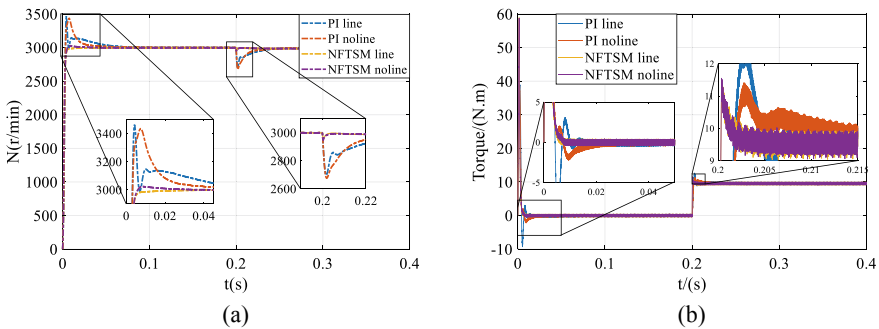


Fig. 4 Motor speed **a** and torque **b** waveform curves under rated operation

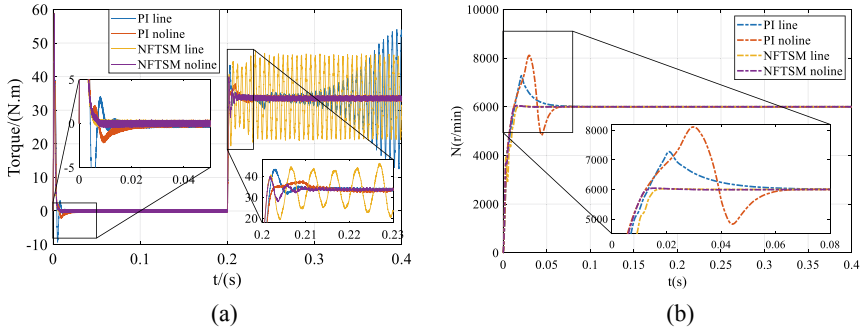


Fig. 5 Motor torque **a** and speed **b** waveform curves

5 Conclusion

In this paper, a nonlinear permanent magnet motor model with online identification of magnetic chain and torque parameters considering saturation effect is proposed, and an improved non-singular fast terminal sliding mode control strategy is designed to control it. The correctness and validity of the proposed model are verified by Matlab/Simulink simulation. The simulation results show that the proposed improved non-singular fast terminal sliding mode control strategy can effectively improve the dynamic response performance of the PM motor in the presence of overload conditions and achieve zero overshoot and strong robustness.

Acknowledgements The research was supported by National Natural Science Foundation of China (51307111), Liaoning Doctoral Research Start-up Fund (2020-BS-143), and Liaoning Department of Education Young Science and Technology Talent Breeding Program (LQGD2020006).

References

1. Zhang, L., Wang, S., Bai, J.: Fast-super-twisting sliding mode speed loop control of permanent magnet synchronous motor based on SVM-DTC:LETTER. *IEICE Electr. Exp.* **18**(1) (2021)
2. Wu, D.: Research on nonlinear modeling of permanent magnet synchronous motor. Southeast University (2018). (in Chinese)
3. Thieli, S.G., Abílio, G.H., Rodrigo, P.V.: Discrete-time sliding mode control based on disturbance observer applied to current control of permanent magnet synchronous motor. *IET Power Electr.* **14**(4) (2021)
4. Štumbergerb, B., et al.: Evaluation of saturation andcross-magnetization effects in interior permanent magnet synchronous motor. *IEEE Trans. Indust. Appl.* **39**(5), 1264–1271 (2003)
5. Fu, D., Zhao, X.: Adaptive nonsingular fast terminal sliding mode control for permanent magnet linear synchronous motor. *Trans. China Electrotech. Soc.* **35**(4), 717–723 (2023). (in Chinese)
6. Daly, J.M., Wang, D.W.L.: Output feedback sliding mode control in the presence of unknown disturbances. *Syst. Control Lett.* **58**(3) (2008)

7. Wei, J., Lu, Z., Avery, R.I.: Output-feedback sliding mode control for permanent magnet synchronous motor servo system subject to unmatched disturbances. *Math. Probl. Eng.* **2021** (2021)
8. Zhang, M., Xiao, F., Shao, R., Deng, Z., Su, H.-S.: Robust fault detection for permanent-magnet synchronous motor via adaptive sliding-mode observer. *Math. Probl. Eng.* **2020** (2020)
9. Li, W., Liu, J.: Sensorless optimization method for built-in permanent magnet synchronous motor considering magnetic circuit saturation and cross-coupling effect. *Trans. China Electrotech. Soc.* **35**(21), 4465–4474 (2020). (in Chinese)
10. Zhicheng, W., Jianjun, M.: Research on control system of permanent magnet synchronous motor based on high-order sliding mode method. *Manuf. Automat.* **43**(01), 8–11 (2021). (in Chinese)
11. Xia, P., Deng, Y., Wang, Z., Li, H., Betti, M.: Speed Adaptive sliding mode control with an extended state observer for permanent magnet synchronous motor. *Math. Probl. Eng.* **2018** (2018)

An Equivalent Transformer Capacitance Model Analysis Method for CM Noise Conduction



Kaining Fu , Zhiyong Qiu , Qiang Zhang , and Hanchao Zeng 

Abstract The parasitic capacitance of the transformer is the critical coupling path for common-mode (CM) noise conduction. The voltage pulsation assigned on winding terminals of transformers caused by switch on and off process of semiconductors switches is the main CM noise sources to conduct CM noise. In order to analyze the CM transmission characteristic of the transformer, this paper proposed a two-capacitor transformer winding capacitance model for CM noise analysis in flyback converter. Based on this model, the CM noise conduction characteristics in flyback transformer under different circuit configurations in secondary side are analyzed, respectively. For verifying the effectiveness of the proposed model, insertion loss was introduced to evaluate the CM characteristics of the designed PCB planar transformer. Finally, the experiment results prove the effectiveness of the proposed transformer winding model.

Keywords Common-mode (CM) Noise · Transformer model · Flyback · Capacitance

1 Introduction

Electromagnetic compatibility (EMC) is the key way to guarantee the safe and reliable operation of power electronic system. With the breakthrough of the technical bottleneck of the wide band gap (WBG) devices, such as SiC and GaN, the switching frequency of the switched mode power supply (SMPS) is also increased to above megahertz, which significantly reduces the size of the passive devices in the power converter and effectively improves the power density of the whole converter [1]. Then, the electromagnetic interference (EMI) caused by high switching frequency and compact layout becomes more and more serious [2]. In particular, the high switching frequency pushes the high-order harmonic component of the noise source

K. Fu (✉) · Z. Qiu · Q. Zhang · H. Zeng
Xiamen University of Technology, XiaMen, Fujian, China
e-mail: 18606939490@163.com

© Beijing Paiké Culture Commu. Co., Ltd. 2023
X. Dong et al. (eds.), *The proceedings of the 10th Frontier Academic Forum of Electrical Engineering (FAFEE2022)*, Lecture Notes in Electrical Engineering 1054, https://doi.org/10.1007/978-981-99-3408-9_63

to a higher frequency range. This seriously deteriorates the electromagnetic noise spectrum of SMPS in the higher frequency band of conducted electromagnetic interference (10–30 MHz) and even in the frequency band of radiation interference (30 MHz–1 GHz) [3]. The conducted EMI can be divided into CM noise and differential mode (DM) noise according to its noise propagation path. The generation mechanism and suppression method of DM noise are relatively simple, while the CM noise is relatively hard to be addressed due to its generation mechanism and complicated propagation paths. Distributed capacitance is the key coupling path for CM noise conduction [4]. Due to its complex parasitic parameter effect, the study of generation mechanism and suppression method of the CM noise has become a research hotspot in the EMC design of power converters. Developing an accurate, simple, and having actual physical parameters transformer CM noise model, is very critical for the analysis of EMI characters in isolated power converters.

Flyback converter is widely used as power adapter such as phone chargers and laptop chargers due to its simple structure and low cost. Figure 1 describes the conducted CM characteristics of flyback converters. In Fig. 1, there are two CM noise propagation paths. The first is the parasitic capacitance between primary MOSEFT and ground. The secondary is the interwinding capacitance of transformers. Power adapter used for mobile chargers is with only two wires (L and N). For this circuit configuration, the secondary ground of the designed flyback converter is floating. The parasitic capacitance C_{sg} between SG and the ground is used as the CM transmission impedance of the conduction path. Using Y-cap to bypass CM noise is also an effective way to eliminated the CM noise flowing through transformer at the cost of causing leakage current [5].

Transformer not only has functions in isolation and voltage transform but also has other function in CM EMI filtering [6–9]. Analyzing the CM noise conduction mechanism in transformer coupling path is very significant to build transformer winding capacitance model, which is beneficial to further analyze the high frequency

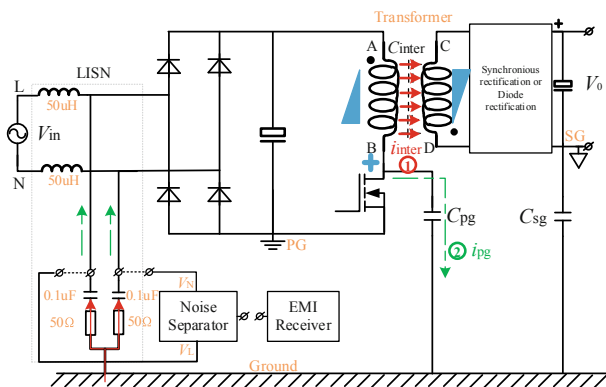


Fig. 1 Conduction EMI measurement and the CM noise conduction path of Flyback converter

CM noise characteristic and adopt proper noise cancelation methods to achieve noise attenuation.

2 Transformer Winding capacitance Model

Figure 2(a) shows the conducted CM model of the transformer consisting of six-capacitance [10], i.e., C_{AB} , C_{AC} , C_{AD} , C_{BD} , C_{CD} , and C_{BC} . The parasitic capacitance C_{AB} and C_{CD} paralleling with primary and secondary windings are not regarded as CM conduction paths. They can be removed in the CM noise analysis.

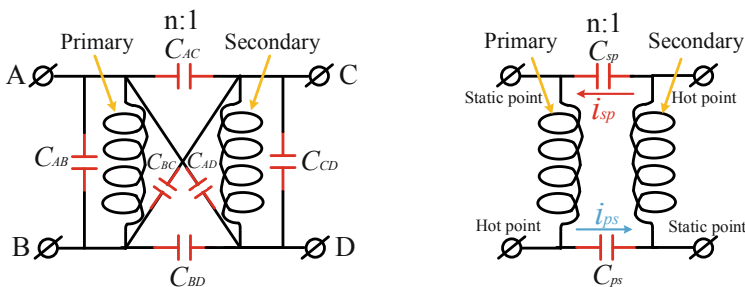
The displacement current flowing through the parasitic capacitance of the transformer can be calculated by:

$$\begin{aligned}
 i_{Trans} &= C_{AC} \frac{d(V_A - V_C)}{dt} + C_{BD} \frac{d(V_B - V_D)}{dt} \\
 &\quad + C_{BC} \frac{d(V_B - V_C)}{dt} + C_{AD} \frac{d(V_A - V_D)}{dt} \\
 &= (C_{AC} + C_{AD}) \frac{dV_A}{dt} + (C_{BD} + C_{BC}) \frac{dV_B}{dt} \\
 &\quad - (C_{BC} + C_{AC}) \frac{dV_C}{dt} - (C_{BD} + C_{AD}) \frac{dV_D}{dt}
 \end{aligned} \tag{1}$$

where point A and C are called voltage hot points connecting to the drain of the MOSFET, points B and D are called voltage static points connecting to the ground terminals of DC bus capacitor for flyback converter.

Because point B and D are static point, their potential are equal to the ground potential ($dv/dt = 0$). Then, the expression of (1) can be simplified as (2):

$$i_{Trans} = (C_{AC} + C_{AD}) \frac{dV_A}{dt} - (C_{BC} + C_{AC}) \frac{dV_C}{dt} \tag{2}$$



(a) Transformer winding six-capacitor model (b) Transformer winding two-capacitor model

Fig. 2 Transformer winding model

where the displacement current i_{Trans} will flow through the parasitic capacitance C_{AC} , C_{AD} , C_{BC} and C_{AC} to conduct CM noise. In order to do further simplification, the expression of the CM noise in (2) can be equivalent as in (3).

$$i_{Trans} = C_{ps} \frac{dV_A}{dt} - C_{sp} \frac{dV_C}{dt} \quad (3)$$

The function of $C_{AC} + C_{AD}$ is represented by a lumped capacitance called as C_{ps} . Similarly, using the lumped capacitance C_{sp} can represent the function of $C_{BC} + C_{AC}$.

As shown in Fig. 2(b), the voltage pulsation generated by dV_A/dt and dV_C/dt will be assigned on C_{ps} and C_{sp} to form CM noise i_{ps} and i_{sp} , respectively. It should be noted that the location of C_{ps} and C_{sp} are between voltage hot point and static point, representing the CM noise in primary or secondary side, flowing from voltage hot point to static point. Usually, i_{ps} is far larger than i_{sp} , because voltage pulsation dV_A/dt is far larger than dV_C/dt . Then, the total CM noise flowing through transformer is in the same direction with i_{ps} .

In order to eliminate the CM noise, it can be done in view of increasing C_{sp} . Then, the CM noise i_{sp} can also be increased. It is possible to make a balance between i_{ps} and i_{sp} and the CM noise can be effectively suppressed. There is a certain assumption that the phases of two CM noise sources are antiphase with each other. Otherwise, it is impossible to make a balance between i_{ps} and i_{sp} .

3 Transformer EMI Character with Different Topology

For Flyback converter, the secondary side using diode to rectify is commonly used topology due to its easy implement and low cost. Most of the scholars focus on the EMI characteristic of this topology, and many noise cancelation methods and noise balance methods are successively proposed to solve the EMI problems. In Fig. 3(a), the phase of secondary CM noise source is antiphase compared with that of primary CM noise source. Figure 3(b) shows the equivalent CM noise circuit. It can easily find that i_{sp} can cancel i_{ps} and i_{pg} , which means that reasonable transformer winding design can achieve CM noise reduction. When the flyback converter is with two-wire, the part of CM noise i_{pg} can be reasonable ignored due to too tiny of C_{pg} . Then, the main task should be focused on how to balance i_{ps} and i_{sp} .

In order to minimize the switching losses in the secondary side, the synchronous rectification technology is proposed and the power loss can be reduced. For lowering cost and easy design of gate driving, MOSFET in the secondary is in the low potential side instead of high potential side. However, this action can make a huge change for conductive CM noise characteristic. To further investigate the CM characteristic under this kind of circuit topology, Fig. 4(a) and (b) show the CM noise conduction paths. In Fig. 4(b), it can find that the location of secondary switch has changed, which lead to the phase of U_{DS2} to be inverted compared with that shown in Fig. 3(b),

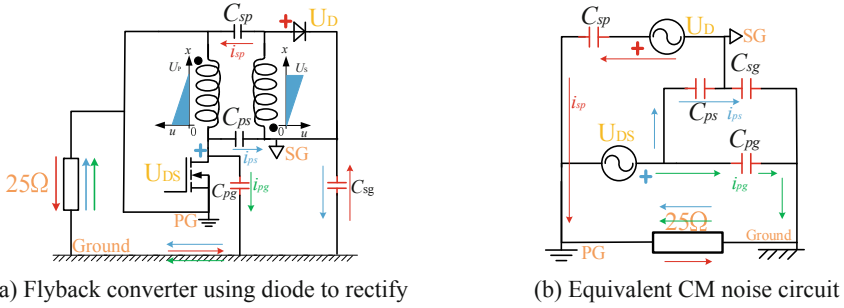


Fig. 3 CM noise conduction paths under diode rectification

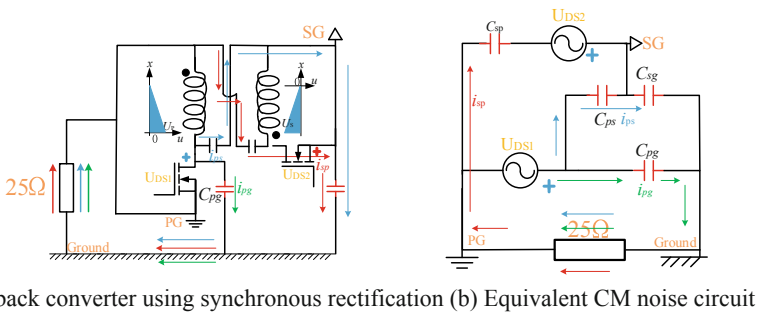


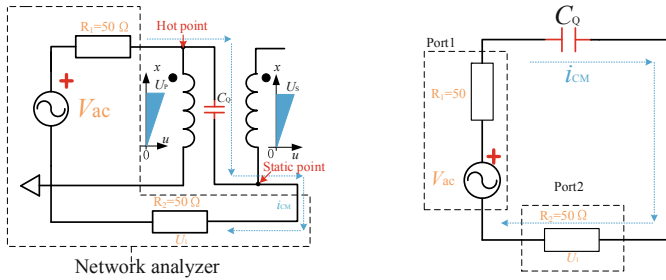
Fig. 4 CM noise conduction paths under synchronous rectification

i.e., the CM current i_{ps} and i_{sp} are in the same direction. So increasing i_{sp} can only worsen EMI problem instead of improving. That means the transformer with synchronous topology cannot attenuate CM noise by achieving the electric potential balance between the adjacent windings.

To further reveal the internal reason, the winding potential is also drawn in Fig. 4(a). It can find that the location of the secondary switch alters the potential of the secondary winding. The potential in primary winding is antiphase with the potential in secondary winding. Any way to adjust the winding arrangement cannot achieve CM noise attenuation. For the transformer under this kind of circuit configuration, antiphase CM noise sources should be created to achieve CM noise cancellation.

4 Experimental Verification

Based on the insertion loss (IL) method, the CM noise suppression characteristic of transformer is conducted network analyzer, and the dynamic CM capacitance C_Q of the transformer is obtained by normalization. The measurement method of C_Q is shown in Fig. 5(a), and Fig. 5(b) shows the corresponding equivalent circuit model.



(a) CM noise circuit of flyback converter (b) Equivalent CM noise circuit

Fig. 5 Measurement method of C_Q

In Fig. 5(b), the CM behavior of the transformer is represented by capacitance C_Q . The CM noise flows through C_Q from primary side to secondary side and cause voltage drop U_1 in resistor R_2 . Hence, C_Q can represent the CM characteristic of transformers.

The dynamic CM capacitance C_Q can be measured according to the following expression.

$$C_Q = \frac{1}{2\pi f \sqrt{10^{\frac{40-S_{21}(\text{dB})}{10}} - 10^4}} \tag{4}$$

where S_{21} parameter at a certain frequency is measured by network analyzer.

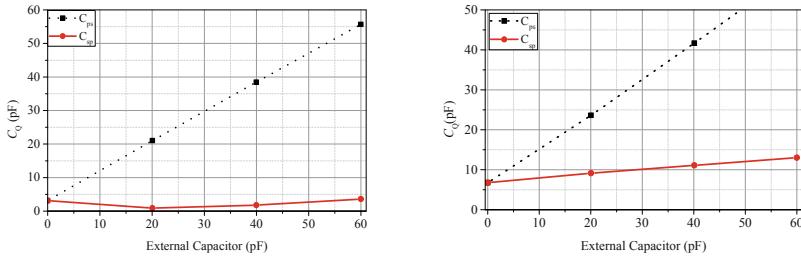
In this section, a flyback transformer is used to check the effectiveness of the proposed transformer capacitance model. The structure parameters of the designed PCB planar transformer are:

Transformer: EID22.5/12.3; Core material: PC95; Turn number: $N_P = 26$, $N_S = 3$; Winding arrangement: PSP.

As has been analyzed in section II, the CM noise i_{ps} and i_{sp} is determined by its voltage pulsation and the lumped parasitic capacitance. The flyback converter is usually used for lower voltage output. It means that the voltage pulsation in primary side is larger than that in secondary side. In order to cancel the CM noise, the value of the equivalent CM capacitance C_{ps} and C_{sp} can be adjusted, which can be achieved by the designed of transformer or paralleling an external capacitor between the transformer terminals.

For better and clear understanding, the external capacitors are used to manually adjust the lumped capacitance C_{ps} and C_{sp} . The sum of CM noise is the result of i_{ps} - i_{sp} , and it can be represented by the dynamic CM capacitance C_Q . The measurement results under two circuit configurations are shown in Fig. 6(a) and (b), respectively.

In Fig. 6(a), adding an external capacitor on the location of C_{ps} can increase i_{ps} ($i_{ps} = V_p \cdot C_{ps}$). Similarly, i_{sp} can be increased by adding an external capacitor on the location of C_{sp} ($i_{sp} = V_s \cdot C_{sp}$). As a matter of fact, V_p is far larger than V_s , adding an external capacitor on the location of C_{ps} will cause more CM current in



(a) Variation tendency of C_Q with secondary diode MOSFET (b) Variation tendency of C_Q with secondary diode MOSFET

Fig. 6 Variation tendency of C_Q

the transformer coupling path compared with that adding the same external capacitor on the location of C_{sp} . The CM noise sources V_p and V_s are anti-phased, and the CM noise can be cancelled by creating a balance between C_{ps} and C_{sp} . For further lowering the CM noise, the external capacitor should be parallel on the location of C_{sp} , and the CM noise will first decrease to zero and then increase. When the condition of $V_p \cdot C_{ps} = V_s \cdot C_{sp}$ is met, zero CM noise will be achieved.

In Fig. 6(b), adjusting C_{ps} and C_{sp} can only increase C_Q , that means the CM current i_{ps} and i_{sp} are in the same phase, and the CM current in transformer coupling path is increased. i_{ps} and i_{sp} cannot be canceled with each other. This situation is totally different from that shown in Fig. 6(a), which conforms well with the previous analysis mentioned in section III. Therefore, for Flyback transformer with synchronous technology, some of the CM noise attenuation methods may not be applied to reduce CM noise anymore. Because V_p and V_s are in the same direction, and it is impossible to achieve noise cancellation just by adjusting the value of C_{ps} and C_{sp} .

5 Conclusions

The proposed two-capacitor transformer CM model is very suitable and easy to analyze the CM current characteristics of transformers and it also points out that the CM cancellation characteristic is determined by the noise source. For the same transformer under different topologies, it can exhibit totally different the CM cancellation effect. Based on the proposed model, the CM noise conduction mechanism and its corresponding noise cancellation method in capacitive coupling frequency range can be investigated in detail. For higher frequency range, the proposed model should be extended to consider the effect of inductive coupling.

Acknowledgements This work was supported by the Education and Scientific Research Project for Young and Middle-aged Teachers in Fujian Province [Grant Number: JAT210342], Research Start-up Fund of Xiamen University of Technology [Grant Number: YKJ22021R], and Natural Science Foundation of Fujian Province [Grant Number: 2022J011257 and 2022J01126].

References

1. Parvez, M., Pereira, A.T., Ertugrul, N., Weste, D. Abbott, N.H.E., Al-Sarawi, S.F.: Wide Bandgap DC–DC converter topologies for power applications. *Proc. IEEE* **109**(7), 1253–1275 (2021)
2. Yao, J., Wang, S., Luo, Z.: Near field coupling's impact on radiated EMI and mitigation techniques for power converters in automotive applications. In: 2020 IEEE Energy Conversion Congress and Exposition (ECCE), pp. 5882–5889 (2020)
3. Yao, J., Ma, Z., Lai, Y., Wang, S.: A survey of modeling and reduction techniques of radiated emi in power electronics. In: 2021 IEEE International Joint EMC/SI/PI and EMC Europe Symposium, Raleigh, NC, USA, pp. 1081–1086 (2021)
4. Amin, A., Choi, S.: A Review on recent characterization effort of CM EMI in power electronics system with emerging wide band gap switch. In: 2019 IEEE Electric Ship Technologies Symposium (ESTS), Washington, DC, USA, pp. 241–248 (2019)
5. Y. Bai, X. Yang, D. Zhang, X. Li, W. Chen and W. Hu.: Conducted EMI mitigation schemes in isolated switching-mode power supply without the need of a Y-capacitor. In: *IEEE Transactions on Power Electronics*, vol. 32, no. 4, pp. 2687–2703 (2017).
6. Qingbin Chen, Wei Chen, Qingliang Song and Z. Yongfa.: An evaluation method of transformer behaviors on common-mode conduction noise in SMPS. In: 2011 IEEE Ninth International Conference on Power Electronics and Drive Systems, Singapore, pp. 782–786 (2011).
7. Chen, H., Liu, G.: Determination of the width of shielding foil in sandwiched winding transformer for minimizing common mode EMI of Flyback converters. *IEEE Trans. Electromag. Compat.* **62**(2), 639–642 (2020)
8. Saket, M.A., Ordonez, M., Shafiei, N.: Planar transformers with near-zero common-mode noise for Flyback and forward converters. *IEEE Trans. Power Electr.* **33**(2), 1554–1571 (2018)
9. Fu, K., Chen, W.: High side Flyback circuit configuration for CM noise cancellation. *J. Power Electr* **20**, 1306–1315(2020)
10. Duerbaum, T., Sauerlaender, G.: Energy based capacitance model for magnetic devices. In: APEC 2001. Sixteenth Annual IEEE Applied Power Electronics Conference and Exposition (Cat. No. 01CH37181), Anaheim, CA, USA, vol. 1, pp. 109–115 (2001)

Virtual Screening of New High Voltage Insulating Gases as Potential Candidates for SF₆ Replacement



Xiaodian Li, Dongwei Sun, Yongyan Zhou, Xiaopeng Fan, Li Li, Nian Tang, Zhuanglei Zou, and Gaokeng Xiao

Abstract A virtual screening protocol was developed to screen a massive ZINC database for potential candidates for sulfur hexafluoride (SF₆) replacement as insulating gases via estimation of boiling points, dielectric strengths (DS), filtering of some other relevant properties and then Global Warming Potential (GWP) index. Firstly, we calculated the boiling points of about 1200 million compounds, which is a subset of ZINC database with the molecular weights less than 250. 1329 compounds with their calculated boiling points below 70 °C were obtained. Next, we calculated the DS of the compounds using quantum mechanical methods and 1248 compounds with their DS values above 0.8 remained. Further filtering was applied to exclude those compounds with formal charges, polar hydrogens, metal elements, and elements such as chloride, bromine, boron, silicon and tin. At last, 41 compounds resulted from the virtual screening as potential candidates for SF₆ replacement. Among these compounds, 14 were reported in literature as insulating gases with their experimental DS values between 0.8 and 2.4. The rest had the potential to be novel insulating gases. After establishing the validity of our virtual screening protocol, we further calculated the GWP values of the screened compounds and recommended potential SF₆ replacements with high DS, low boiling points and low GWP values. In summary, a virtual screening protocol was developed in this study. It is able to enrich existing insulating gases and is likely to be useful to find novel SF₆ replacement candidates.

Keywords SF₆ · gas insulation · dielectric breakdown

X. Li · D. Sun (✉) · Y. Zhou · X. Fan · L. Li · N. Tang · Z. Zou
Electric Power Research Institute of Guangdong Power Grid Co. Ltd., Guangzhou 510080, China
e-mail: sundw91@163.com

G. Xiao
Guangzhou Molcalx Information and Technology Ltd., Longkou Science and Technology
Mansion, 34 Longkou East Road, Unit No. 2002Tianhe, Guangzhou 510630, China
e-mail: gkxiao@molcalx.com

© Beijing Paiké Culture Commu. Co., Ltd. 2023
X. Dong et al. (eds.), *The proceedings of the 10th Frontier Academic Forum of Electrical Engineering (FAFEE2022)*, Lecture Notes in Electrical Engineering 1054,
https://doi.org/10.1007/978-981-99-3408-9_64

1 Introduction

Sulfur hexafluoride (SF_6) is widely used in the electric power industry as insulating gases because it is chemically inert and nontoxic with a high dielectric strength and a low boiling point. It was estimated that more than 10,000 tons of SF_6 are produced every year and more than 8,000 tons are used in the electric power industry [1]. It was pointed out in the 2007 Inter-governmental Panel on Climate Change (IPCC) report that the concentration of SF_6 in the atmosphere has been increased steadily in accordance with the increasing usage of SF_6 [2]. Although it is an excellent electrical insulator, SF_6 is a potent greenhouse gas with a long atmospheric lifetime. Its Global Warming Potential (GWP) was estimated to be 23,000 times of CO_2 and will have a great impact on global warming. The only effective way to reduce the atmospheric concentration of this long-lived gas is to reduce its emissions. It has therefore been included in the Kyoto Protocol as one of the greenhouse gases [3]. The usage of SF_6 have been limited and steadily reduced over the past decade. Considerable efforts have been made to search for its replacement.

The characteristics that the SF_6 replacements must possess are chemical stability, low toxicity, low flammability, low GWP, high dielectric strength (DS), and suitable boiling point ranges for high voltage applications. It would be time consuming and very costly to test these properties of many compounds by performing individual experiments. In light of such difficulties, an alternative method is to use computational techniques to predict the properties first, then test selected compounds experimentally [4]. Previously, in order to find new classes of refrigerants with low GWP values, along with low to moderate flammability and suitable thermodynamic characteristics, Kazakov et al. developed new computational methods to narrow down to 1,234 candidates by applying environmental and safety criteria to the PubChem database of over 56,000 compounds [5]. Based on this work, Rabie et al. went one step further by systematically screening those chemical compounds obtained by Kazakov et al. for their suitability as high voltage insulating gases on the basis of the predictions of their dielectric strength, boiling points and other properties [6]. 141 compounds were enriched as potential candidates for SF_6 replacement. Such studies demonstrated the power of virtual screening and motivated us to develop our own virtual screening method.

In this study, we performed virtual screening on the subset of the ZINC database with the molecular weights less than 250 (about 12 million molecules in total) by filtering their calculated boiling points, calculated dielectric strengths, other relevant properties and GWP index. The virtual screening protocol is as follows: Firstly, the boiling points of the compounds were calculated by a machine-learning method and the compounds with the boiling points below 70 °C were kept. Secondly, the dielectric strengths of the remaining compounds were calculated by density functional theory (DFT) and the compounds with their dielectric strength values above 0.8 were kept. Lastly, the compounds with chlorine or bromine elements, which are previously known to be harmful to ozone, along with unstable structures and C-H bond were filtered. The results showed that our method was able to enrich existing

known insulating gases with high dielectric strengths and low boiling points. After establishing the validity of our virtual screening protocol, we further calculated the GWP values of the screened compounds and recommended potential SF₆ replacements with high DS, low boiling points and low GWP values. The virtual screening protocol is simple, fast, and easy to apply. It is likely to be a useful tool in the search for SF₆ replacement gases.

2 Methods

2.1 Estimation of Boiling Points

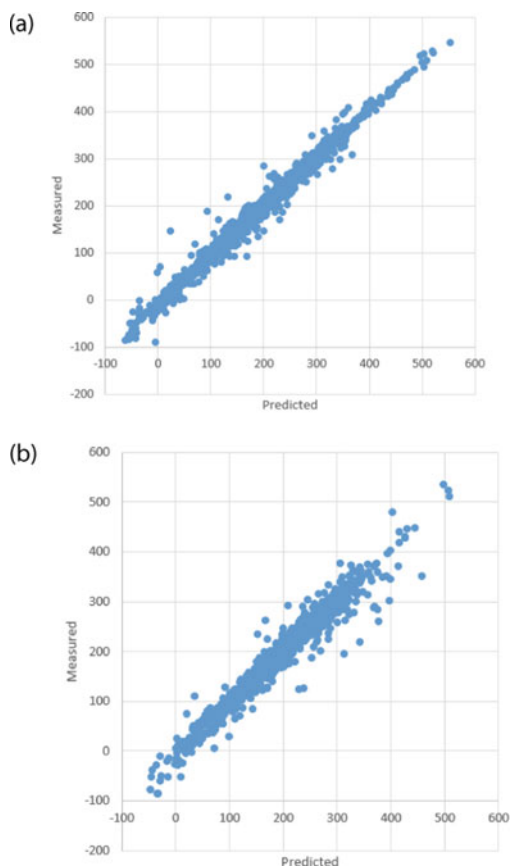
The estimation of boiling points was performed based on the well-established machine-learning method [7]. The experimentally measured boiling points of structurally diverse sets of environmental chemicals were taken from the EPA EPI Suite Data [8]. The boiling points of 4074 compounds were used as the training set and 1358 were used as the test set. The estimation model was built by the DNN deep-learning method within the framework of TensorFlow [9, 10] with the Morgan molecular fingerprints [11] calculated by RDKit 2017 [12] and molecular weights as the descriptor. The correlation coefficients (R^2) of the training set and the test set were found to be 0.985 and 0.955, respectively. The root mean squared deviations (RMSD) between the experimental and predicted values of the training set and test set were 9.05 and 18.28 °C, respectively. The maximum and minimum residuals of the training set were -124.91 and 74.82 °C, respectively. Those of the test set were -91.93 and -124.41 °C, respectively. The training and test datasets were available in Table 1. The scatter plots of the experimental data versus the estimated values for both the training set and the test set were shown in Fig. 1.

Next, the subset of the ZINC12 database [13, 14] with the molecular weights less than 250 (11,918,365 compounds) were estimated for their boiling points by the method described above. 1329 compounds with their boiling points below 70 °C were chosen for the estimation of their dielectric strengths in the next step.

Table 1 Confusion matrix

Class	Prediction			SUM
	1	2	3	
1	88	1	1	90
2	2	47	0	49
3	0	0	64	64
SUM	90	48	65	203

Fig. 1 The scatter plots of the measured and predicted boiling points for **a** the training set **b** the test set



2.2 Estimation of Dielectric Strength

The estimation of dielectric strength was based on DFT calculations as follows [15]. Firstly, the geometry optimization and frequency analyses were performed to confirm the convergence to the optimal structure at the ground state. Then the descriptors such as electronegativity (χ), polarizability (α) were calculated. All these calculations were done at APFD/6–311 + G(2dp) level using Gaussian 16 package [16]. The electronegativity χ was calculated according to Koopmans' theorem:

$$\chi = -\frac{E_{HOMO} + E_{LUMO}}{2} \quad (1)$$

APFD/6–311 + G(2dp)-based GIPF descriptors such as molecular surfaces (A), electrostatic balance parameter (ν), total variance of the surface electrostatic potential (σ_{tot}^2), local polarity of molecule (Π) were calculated using Multiwfn package (Version 3.4.1). A model was obtained when applying the above descriptors on the

Table 2 Accuracy statistics

Class	1	2	3
TPR	0.978	0.959	1
FPR	0.018	0.006	0.008
TNR	0.982	0.994	0.992
FNR	0.022	0.041	0
Precision	0.978	0.979	0.985
Sensitivity	0.978	0.959	1
Specificity	0.982	0.994	0.993
F-measure	0.978	0.969	0.992

dataset containing 42 compounds with their relative dielectric strength experimental determined.

$$DS = 0.00002736A^2 + 0.06949\alpha\chi + 0.0457\nu\sigma_{tot}^2 - 0.07247 + 0.3163 \quad (1)$$

The correlation coefficient was 0.9705 and the RMSD was 0.117, comparable to other methods for the same dataset reported in literature [15].

We then applied the model to the 1329 compounds from the previous step (see Table 2). The compounds with their DS values below 0.8 were filtered out. It resulted in 1248 compounds for the next step (see Table 3).

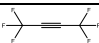
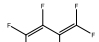
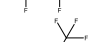
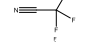
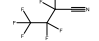
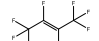
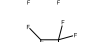
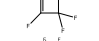
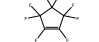
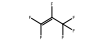

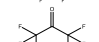

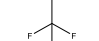
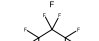

2.3 Filtering of Other Relevant Properties

In this final step of our virtual screening protocol, we further applied several filtering criteria as follows. We filtered out charged compounds because the SF₆ replacement candidates should not be charged for insulating gases. Compounds containing elements such as B, Si, Fe, Sn are considered unstable therefore they were filtered out. The elemental composition of the remaining compounds was only C, H, O, N, S. Compounds with some unstable functional groups such as O-O, N-F, O-F, carboxylic acid ester, amide, acyl halide were also filtered out. At last, only compounds without C-H were kept because they have the best chance to be SF₆ replacements. It resulted in 41 compounds. Their chemical structures, estimated boiling points and dielectric strengths are listed in Table 4.

2.4 Estimation of GWP

To analyze the resulting compounds from our virtual screening, their GWP values were further evaluated. GWP was introduced in the first IPCC Assessment Report

Table 3 Compounds with their relative DS above 0.8

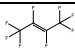
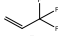
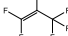
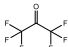
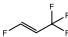
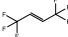
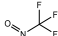
ID	Structure	BP Predicted	BP (Lit)	DS Pre-dicted	DS(Lit)
ZINC000001845819		-2.15	-24.6 [19]	1.32	1.71 [20]
ZINC000001845828		8.62	6-7 [21]	1.15	1.20 [15]
ZINC000001847433		2.64	-35 [22]	1.81	2.00 [15]
ZINC000001847489		8.68	2-5 [23]	2.22	2.40 [15]
ZINC000002004073		3.33	1.2 [24]	1.38	1.70 [20]
ZINC000002031388		4.76	5-6 [25]	1.03	1.70 [20]
ZINC000002034765		45.25	27 [26]	1.46	2.20 [20]
ZINC000002041032		-37.52	-29 [27]	0.91	0.94 [15]
ZINC000002041042		1.98	-5.9 [28]	1.24	1.50 [15]
ZINC000004262093		-24.16	-28 [29]	1.73	1.03 [20]
ZINC000005019026		-41.42	-64 [30]	1.51	1.50 [15]
ZINC000008214651		-43.54	-39 [31]	1.22	0.98 [20]
ZINC000039256939		10.54	23.5 [17]	2.12	2.20 [15]
ZINC000056897668		-0.05	-2 [32]	1.61	1.36 [20]
ZINC000095671149		19.04	0.6 [33]	1.44	1.89 [20]
ZINC000095676839		23.17	-85 [34]	0.93	0.72 [35]

as a simple metric for comparison of potential greenhouse gases in terms of their impacts on the climate system. IPCC defined GWP as the ratio of radiative forcing (RF) due to a pulse release of 1 kg of trace compound integrated over a chosen time horizon (TH) to that of the reference gas, CO₂:

$$\text{GWP} = \frac{\int_0^{\text{TH}} \text{RF} dt}{\int_0^{\text{TH}} \text{RF}_{\text{CO}_2} dt} \quad (3)$$

In this study, GWP was computed for the time horizon of 100 years, which is the value most commonly used in the policy framework.

Table 4 Compounds with reported DS values

ZINC ID	Structure	Dielectric Strength
ZINC00002004073		1.12 [38], 1.7 [39]
ZINC00002031461		0.80 [15]
ZINC00002041032		0.94 [15]
ZINC00004262093		1.03 [39]
ZINC000064370167		0.93 [40]
ZINC000064370165		2.20 [40]
ZINC000095676839		0.72 [41][42]

Potential SF₆ replacements should have comparable or even lower GWP than SF₆. In order to obtain compounds with diverse chemical structures, the constraint for GWP was set to GWP < 1000, instead of GWP < 200 as in Rabie's study [6]. The reason for the high GWP constraint was that the GWP of Novec 4710 marketed by 3 M company is 2100 [17], indicating that higher GWP values could be tolerated in the development of insulating gases. In this study, we used the 202 compounds in IPCC (2013) plus Novec 4710 as the training set. They were divided into three classes based on their GWP values:

Class 1 : GWP ≤ 200

Class 2 : 200 < GWP ≤ 1000

Class 3 : 1000 < GWP

We selected PM7 semiempirical method implemented in Gaussian 16 to compute the energies of highest occupied molecular orbital (HOMO) and lowest unoccupied molecular orbital (LUMO) of the compounds in the training set. Then a random forest classification (RF) model was built via the Weka 3.7 implemented in KNIME (Version 3.5). Classification accuracy reports the percentage of data points correctly classified and is defined as:

$$\text{classification accuracy} = \frac{C}{N} \times 100\% \quad (4)$$

where C is the number of data points correctly classified and N is the total number of data points.

Cohen's kappa (κ) measures the agreement between two raters who each classify N items into C mutually exclusive categories [18]. For a given classification prediction, we used the statistical measures such as classification accuracy, true positive rate (TPR), false positive rate (FPT), true negative rate (TNR), false negative rate (FNR), F-measure and Cohen's kappa (κ):

TPR is defined as

$$\text{TPR} = \frac{\text{TP}}{\text{TP} + \text{FN}} \quad (5)$$

FPT is defined as

$$\text{FPR} = \frac{\text{FP}}{\text{TP} + \text{TN}} \quad (6)$$

TNR is defined as

$$\text{TNR} = \frac{\text{TN}}{\text{TN} + \text{FP}} \quad (7)$$

FNR is defined as

$$\text{FNR} = \frac{\text{FN}}{\text{TP} + \text{FN}} \quad (8)$$

Precision is defined as

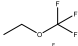
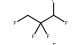
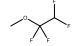
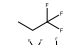
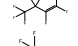
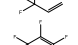
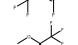
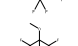
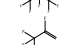
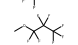
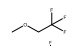
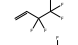
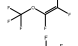
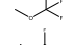
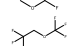
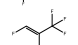
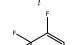
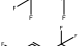
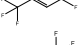
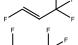
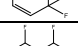
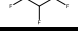

$$\text{Precision} = \frac{\text{TP}}{\text{TP} + \text{FP}} \quad (9)$$

F-measure is the harmonic mean between the recall and precision and is defined as.

$$\text{F - measure} = \frac{2 \times \text{Precision} \times \text{Recall}}{\text{Precision} + \text{Recall}} \quad (10)$$

The major statistical measures were summarized confusion matrix (Table 1) and accuracy statistics (Table 2). In this study, 199 out of 203 compounds were classified correctly with an overall classification accuracy of 98.03%. And Cohen's kappa (κ) of class prediction was 0.969. It was shown that our GWP classification model has a significant classifying prediction performance. The dataset used to build the classification model, the descriptors and the predicted results were listed in Table 5.

Table 5 Compounds with reported GWP values

ZINC ID	Formula (IPCC 2013)	Structure	GWP
ZINC000001845822	CF ₃ OCH ₂ CH ₃		29
ZINC000001845835	CH ₂ FCF ₂ CHF ₂		716
ZINC000001847428	CH ₃ OCF ₂ CHF ₂		301
ZINC000001847439	CH ₃ CH ₂ CF ₃		76
ZINC000001847513	CF ₃ CF ₂ CF=CF ₂		<1
ZINC000002031461	CF ₃ CH=CH ₂		<1
ZINC000002041032	CF ₃ CF=CF ₂		<1
ZINC000002242932	CF ₃ CF ₂ OCH ₃		654
ZINC000002379320	(CF ₃) ₂ CFOCH ₃		363
ZINC000002379349	CF ₃ CF=CH ₂		<1
ZINC000002379384	CH ₃ OCF ₂ CF ₂ CF ₃		530
ZINC000002560087	CF ₃ CH ₂ OCH ₃		1
ZINC000002584257	C ₂ F ₅ CH=CH ₂		<1
ZINC000004290222	CF ₃ OCF=CF ₂		<1
ZINC000005701046	CH ₃ OCF ₃		523
ZINC000008698363	CH ₃ OCHF ₂		144
ZINC000014611418	CF ₃ CH ₂ OCF ₃		979
ZINC000063146256	CF ₃ CF=CHF (Z)		<1
ZINC000063148507	CF ₃ CF=CHF (E)		<1
ZINC000064370165	CF ₃ CH=CHCF ₃ (Z)		2
ZINC000064370167	CF ₃ CH=CHF (E)		<1
ZINC000064370173	CF ₃ CH=CHF (Z)		<1
ZINC000080440236	CHF ₂ CHFCHF ₂		235

3 Results and Discussion

3.1 *The Virtual Screening Protocol Is Able to Enrich Compounds with High Dielectric Strengths and Low Boiling Points*

Among the final 41 compounds from the virtual screening in Sect. 2.3, there were 16 compounds with their DS reported in the literature (see Table 3). Except for compound ZINC000095676839 whose experimental DS value of 0.72 therefore should have been excluded, all compounds had their experimental values above 0.8. It suggested that our virtual screening protocol was able to enrich compounds with high dielectric strengths. In terms of boiling points, except for compound ZINC000002034765, all the compounds had their experimental boiling points lower than 30 °C. It indicated that our virtual screening protocol was able to enrich compounds with high dielectric strengths and low boiling points at the same time. The boiling point constraint of 70 °C was set by taking into consideration that there could be significant uncertainties in the calculations of boiling points and a high boiling point constraint could include relevant compounds as many as possible. Based on Table 3, it suggested that the boiling point constraint could be possibly set to a lower value for future virtual screenings.

Quantitative analysis of the predicted properties and their experimental values could further help us evaluate the accuracy of our calculations. As shown in Table 3, the predicted BP value of compound ZINC000095676839 was 27.17 °C while the experimental value was – 85 °C. The deviation was seemingly very big, up to 108 °C. However, it was still within the maximal deviation of our built model. Moreover, if this compound was excluded, the correlation coefficient was 0.7197 for the remaining 15 compounds. The Pearson correlation and the Spearman Rank Correlation were 0.848 and 0.875, respectively, indicative of strong correlation between the predicted values and the experimental data. As for the electric strength, compounds ZINC000002031388, ZINC000002034765 and ZINC000004262093 had the largest deviations of 0.67, 0.74, and 0.70, respectively. If they were excluded, the correlation coefficient was 0.796, and the Pearson Correlation and the Spearman Rank Correlation were 0.852 and 0.856, respectively, also indicative of strong correlation between the predicted values and the experimental data.

3.2 *The Virtual Screening Protocol is Able to Enrich Compounds with Diverse Structures*

There are six different types of structures for the final 14 compounds, as shown in Table 4.

The alkanes have a long atmospheric lifetime and high GPW therefore they are not suitable for SF₆ replacement [36, 37]. The alkenes are more interesting because they have a relatively short atmospheric lifetime and high dielectric strengths. For instance, perfluoroethene (ZINC000002004073) has a very low boiling point of 1.2 °C but excellent insulation capability (dielectric strength of 1.7). ABB Company has filed a patent for this compound (WO2017162578). Perfluorocyclobutene has shown similar performance with the boiling point of 5 °C and the same dielectric strength of 1.7. The boiling point of perfluoropropene is only -23 °C but its dielectric strength is about the same as SF₆. Owing to the very low boiling point, it is expected to be useful at areas of high latitude as an insulating gas [36]. Perfluoro-2-butylene (ZINC000001845819) has high dielectric strength of 1.71 and low boiling point of -24.6 °C. It was expected to be a good candidate for SF₆ replacement [36].

Four nitrile compounds have survived our virtual screening protocol, which is a great demonstration of the strength of our method because nitriles have been known to be good insulating gases and some of them have been commercialized. Mitsubishi Inc. was granted patents (US4547316) for use of perfluoronitriles such as perfluoroacetonitrile, perfluoropropionitrile, perfluorobutyronitrile and perfluoropentanenitrile as insulating gases in electric equipment. Based on these results, heptafluoroisobutyronitrile was commercialized by Alstom (Trade name Novec 4710) as a lower GWP alternative to sulfur hexafluoride (SF₆).

One perfluoroketone was in the final list of the virtual screening results. Such compounds also have high dielectric strengths and low boiling points as perfluoronitriles. Novec 5110 as an example in this kind has been commercialized. There are few scientific reports about perfluoroepoxides as insulating gases. However, they were included in the patent (US20130292614) filed by 3 M company.

3.3 Optimization of the Virtual Screening

Evidently, the net charges of the compound should be zero as insulating gases. Therefore, compounds with non-zero formal charges should be filtered out. The results from the previous section confirmed that it was possible to enrich compounds with known high DS values when the filtering criteria were set to be boiling points ≤ 30 °C and DS ≥ 0.8 . Therefore, we have adjusted our virtual screening protocol to the same criteria. Previously, compounds containing hydrogen were filtered out, which resulted in only 41 compounds. To increase the number of the hits, the filtering criteria were modified to retain the compounds with the element of hydrogen. Lastly, we hope that the compounds have low GWP values, therefore, compounds with GWP values lower than 1000 were selected by applying GWP classification model. The flowchart for the modified virtual screening is shown in Fig. 2. In the end, 170 compounds were screened out from our refined virtual screening protocol (see Table 6).

We obtained 170 compounds from our virtual screening protocol, including 7 known insulating gases (see Table 4). For these 7 compounds, there are perfluoro-compounds as well as compounds with C-H bonds. In the meantime, among the 170

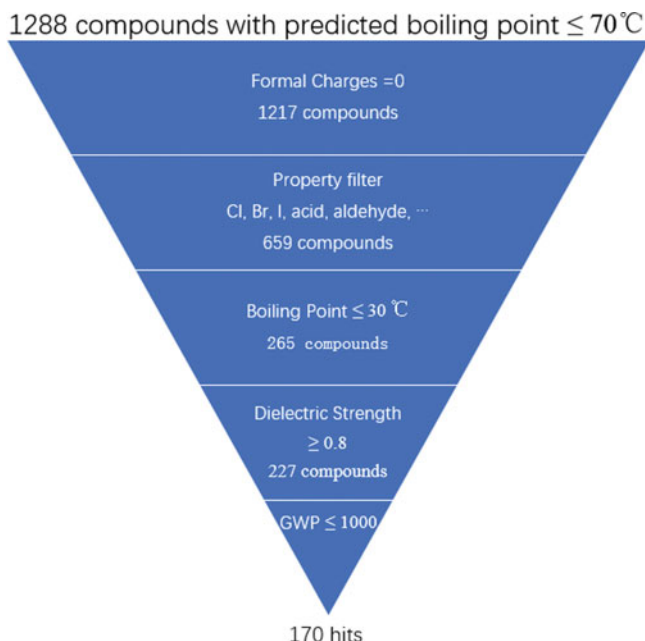


Fig. 2 Refined virtual screening protocol

compounds, there are 23 known compounds (see Table 5) with GWP values lower than 1000. It showed that our GWP prediction model was able to enrich compounds with low GWP values. 4 of them (see Table 7) have their reported DS values greater than 0.8. These 4 compounds had very low boiling points as well as low GWP values. All these suggested that our virtual screening protocol have the ability of enriching compounds with high DS values, low boiling point and low GWP values. Other compounds which have not been reported in literature yet have the potential to be possible SF_6 replacements.

When the GWP values were used as filtering criterion, nitrile compounds were filtered out due to their large predicted GWP values (>1000). Therefore, nitrile compounds were not included in the final compounds. Meanwhile, when building the prediction model, only one nitrile compound (NOVEC 4710) was included in the training set and its GWP value was as large as 2100. Because some commercial insulating gases are nitrile compounds and they do have rather large GWP values, it suggested that nitrile compounds should be treated separately to increase the possibility of finding novel insulating gases.

4 Conclusion

In this study, we performed virtual screening on the subset of the ZINC database with the molecular weights less than 250 by filtering their boiling points, dielectric strengths, GWP values as well as other relevant properties for SF₆ replacements. The results showed that our method is able to enrich insulation gases with high dielectric strengths, low boiling points and low GWP. It is simple, fast, and easy to apply. It is likely to be a useful tool in the search for SF₆ replacement gases.

Acknowledgements The authors thank Dr. Bin Lin from Shenyang Pharmaceutical University for helpful discussion and advice during the preparation of the manuscript. The current work is supported by the science and technology project of China Southern Power Grid (No. GDKJXM20170043).

References

1. Dervos, C.T., Vassiliou, P.: Sulfur hexafluoride (SF₆): global environmental effects and toxic byproduct formation. *J. Air Waste Manage. Assoc.* **50**, 37–141 (2000)
2. Solomon, S., Qin, D., Manning, M., Marquis, M., Averyt, K., Tignor, M., Miller, H.L., Chen, Z.: IPCC, 2007: Climate Change 2007 The Physical Science Basis, Contribution Of Working Group I to the Fourth Assessment Report of the Intergovernmental Panel on Climate Change. Cambridge University Press, Cambridge (2007)
3. United Nations Kyoto protocol to the United Nations framework Kyoto protocol to the United Nations framework. *Rev. Eur. Community Int. Environ. Law* **7**, 214–217 (1998)
4. Shoichet, B.K.: Virtual screening of chemical libraries. *Nature* **432**, 862–865 (2004)
5. Kazakov, A., McLinden, M.O., Frenkel, A.: Computational design of new refrigerant fluids based on environmental, safety, and thermodynamic characteristics. *Ind. Eng. Chem. Res.* **51**, 12537–12548 (2012)
6. Rabie, M., Frank, C.: Computational screening of new high voltage insulation gases with low global warming potential. *IEEE Trans. Dielectr. Electr. Insul.* **22**, 296–302 (2015)
7. Zang, Q., Mansouri, K., Williams, A.J., Judson, R.S., Allen, D.G., Casey, W.M., Kleinstreuer, N.C.: In silico prediction of physicochemical properties of environmental chemicals using molecular fingerprints and machine learning. *J. Chem. Inf. Model* **57**, 36–49 (2017)
8. EPI Suite Data. <http://esc.syrres.com/interkow/EPISuiteData.htm>. Accessed 21 May 2018
9. Abadi, M., et al.: TensorFlow: large-scale machine learning on heterogeneous systems. Software available from tensorflow.org
10. Abadi, M., et al.: TensorFlow: a system for large-scale machine learning. In: 12th USENIX Symposium on Operating Systems Design and Implementation (OSDI 2016), pp. 265–284(2016)
11. Landrum G Fingerprints in the RDKit. RDKit UGM (2012)
12. Greg L RDKit: Open-source cheminformatics (2017)
13. Irwin, J.J.: Shoichet BK ZINC - a free database of commercially available compounds for virtual screening. *J. Chem. Inf. Model* **45**, 177–182 (2005)
14. Irwin, J.J., Sterling, T., Mysinger, M.M., Bolstad, E.S., Coleman, R.: A free tool to discover chemistry for biology. *J. Chem. Inf. Model* **52**, 1757–1768 (2012)
15. Yu, X., Hou, H., Wang, B.: Prediction on dielectric strength and boiling point of gaseous molecules for replacement of SF₆. *J. Comput. Chem.* **38**, 721–729 (2017)
16. Frisch, M.J., et al.: Gaussian 16 Revision B.01 (2016)

17. 3M Novec 4710 Insulating Gas. <http://multimedia.3m.com/mws/media/1132124O/3m-novec-4710-insulating-gas.pdf>. Accessed 7 June 2018
18. Cohen, J.: A coefficient of agreement for nominal scales. *Educ. Psychol. Meas.* **20**, 37–46 (1960)
19. CAS Number: 692-50-2. <http://www.synquestlabs.com>. Accessed 7 June 2018
20. Rabie, M., Dahl, D., Donald, S.M.A., Reiher, M.: Franck C predictors for gases of high electrical strength. *IEEE Trans. Dielectr. Electr. Insul.* **20**, 856–863 (2013)
21. CAS Number: 685-63-2. <http://www.synquestlabs.com>. Accessed 7 June 2018
22. CAS Number: 422-04-8. <http://www.synquestlabs.com>. Accessed 7 June 2018
23. CAS Number: 375-00-8. <http://www.synquestlabs.com>. Accessed 7 June 2018
24. CAS Number: 360-89-4. <http://www.synquestlabs.com>. Accessed 7 June 2018
25. CAS Number: 697-11-0. <http://www.synquestlabs.com>. Accessed 7 June 2018
26. CAS Number: 559-40-0. <http://www.apolloscientific.co.uk>. Accessed 7 June 2018
27. CAS Number: 116-15-4. <http://www.apolloscientific.co.uk>. Accessed 7 June 2018
28. CAS Number: 115-25-3. <http://www.apolloscientific.co.uk>. Accessed 7 June 2018
29. CAS Number: 684-16-2. <http://www.apolloscientific.co.uk>. Accessed 7 June 2018
30. CAS Number: 353-85-5. <http://www.synquestlabs.com>. Accessed 7 June 2018
31. CAS Number: 76-19-7. <http://www.synquestlabs.com>. Accessed 7 June 2018
32. CAS Number: 355-25-9. <http://www.synquestlabs.com>. Accessed 7 June 2018
33. CAS Number: 773-14-8. <http://www.synquestlabs.com>. Accessed 7 June 2018
34. CAS Number: 334-99-6. <http://www.synquestlabs.com>. Accessed 7 June 2018
35. Meurice, N., Sandre, E., Aslanides, A.: Vercauteren DP Simple theoretical estimation of the dielectric strength of gases. *IEEE Trans. Dielectr. Electr. Insul.* **11**, 946–948 (2004)
36. Xiao, D.: Development prospect of gas insulation based on environmental protection. *High Volt. Eng.* **42**, 1035–1046 (2016)
37. Zhou, W., Zheng, Y., Yang, S., Qin, Z., Wang, B.: Research progress and trend of SF₆ alternative with environment friendly insulation gas. *Gaoya Dianqi/High Volt. Appar.* **52**, 8–14 (2016)
38. Vijh, A.K.: Electric strength and molecular properties of gaseous dielectrics. *IEEE Trans. Electr. Insul.* **EI-12**, 313–315 (1977)
39. Rabie, M., Franck, C.M.: Predicting the electric strength of proposed SF₆ replacement gases by means of density functional theory. In: *International Symposium on High Voltage Engineering*, pp. 1381–1386 (2013)
40. Beroual, A., Haddad, A.: Recent advances in the quest for a new insulation gas with a low impact on the environment to replace sulfur hexafluoride (SF₆) gas in high-voltage power network applications. *Energies* **10**, 1216 (2017)
41. Jiao, J., Xiao, D., Zhao, X., Deng, Y.: Analysis of the molecules structure and vertical electron affinity of organic gas impact on electric strength. *Plasma Sci. Technol.* **18**, 554–559 (2016)
42. Zhao, H., Li, X., Lin, H.: Insulation characteristics of c-C₄F₈-N₂ and CF₃I-N₂ mixtures as possible substitutes for SF₆. *IEEE Trans. Power Deliv.* **32**, 254–262 (2017)
43. CAS Number: 677-21-4. <http://www.synquestlabs.com>. Accessed 7 June 2018
44. Huang, J., Mendoza, B., Daniel, J.S., Nielsen, C.J., Rotstajn, L., Wild, O.: Anthropogenic and natural radiative forcing. In: *Climate Change 2013: The Physical Science Basis*, pp. 659–740 (2013)
45. CAS Number: 66711-86-2. <http://www.synquestlabs.com>. Accessed 7 June 2018
46. CAS Number: 29118-24-9. <http://www.synquestlabs.com>. Accessed 7 June 2018. LNCS Homepage. <http://www.springer.com/lncs>, Accessed 21 Nov 2016

Prediction of Global Warming Potential of Insulating Gases Using Random Forest Classifiers



Dongwei Sun, Yongyan Zhou, Xiaopeng Fan, Li Li, Nian Tang, Zhuanglei Zou, and Gaokeng Xiao

Abstract Greenhouse effects caused by insulating gases with high global warming potential (GWP) pose a severe threat to the environment therefore searching for their alternatives is imperative. In this study, random forest classifiers were utilized to build a classification model for prediction of global warming potential of insulating gases using random forest classifiers. The accuracy and the predictive power of the model were thoroughly evaluated.

Keywords gas insulation · SF₆ · modeling · environmental radiation effects

1 Introduction

Hydrofluorocarbons (HFCs) and sulfur hexafluoride (SF₆) are gases with severe greenhouse effects. The former is widely used as refrigerants while the latter is widely used as an electrical insulating gas. Concerns about climate change have prompted people to seek alternatives with low global warming potential (GWP) [1, 2]. Hydrofluoroethers (HFE) and hydrofluoroolefins (HFOs) as unsaturated HFCs are potential alternatives for HFC-based refrigerants [3] and the insulating gas SF₆ [4]. Due to the presence of double bonds in the compounds of HFOs, the reaction rate with atmospheric hydroxyl radical (OH) is high. Therefore, HFOs have a much lower atmospheric lifetime than the currently used HFC-based refrigerants and the insulating gas SF₆, therefore much lower GWP as well.

GWP was introduced as a simple metric to measure the impact of a particular substance in the atmosphere in the first Intergovernmental Panel on Climate Change

D. Sun (✉) · Y. Zhou · X. Fan · L. Li · N. Tang · Z. Zou

Electric Power Research Institute of Guangdong Power Grid Co. Ltd., Guangzhou 510080, China
e-mail: sundw91@163.com

G. Xiao

Guangzhou Molcalx Information and Technology Ltd., 34 Longkou East Road, Unit No. 2002, Longkou Science and Technology Mansion, Tianhe District, Guangzhou 510630, China
e-mail: gkxiao@molcalx.com

© Beijing Paiké Culture Commu. Co., Ltd. 2023

X. Dong et al. (eds.), *The proceedings of the 10th Frontier Academic Forum of Electrical Engineering (FAFEE2022)*, Lecture Notes in Electrical Engineering 1054, https://doi.org/10.1007/978-981-99-3408-9_65

753

(IPCC) Assessment Report. The IPCC Fourth Assessment Report (IPCC2007 AR4) [5] defines an index, based upon radiative properties of well mixed greenhouse gases, measuring the radiative forcing of a unit mass of a given well mixed greenhouse gas (i) in today's atmosphere integrated over a chosen time horizon, relative to that of carbon dioxide:

$$GWP_i = \frac{\int_0^{TH} RF_i(t)dt}{\int_0^{TH} RF_r(t)dt} = \frac{\int_0^{TH} a_i[C_i(t)]dt}{\int_0^{TH} a_r[C_r(t)]dt} \quad (1)$$

where TH is the time horizon, RF_i is the global mean radiative forcing capacity (RF) of component i , a_i is the RF per unit mass increase in atmospheric abundance of component i , $[C_i(t)]$ is the time-dependent abundance of i , and the corresponding quantities for the reference gas (r) in the denominator. The atmospheric lifetime τ is used to describe the time-dependent abundance of chemicals:

where TH is the time horizon, RF_i is the global mean radiative forcing capacity (RF) of component i , a_i is the RF per unit mass increase in atmospheric abundance of component i , $[C_i(t)]$ is the time-dependent abundance of i , and the corresponding quantities for the reference gas (r) in the denominator. The atmospheric lifetime τ is used to describe the time-dependent abundance of chemicals:

$$C_i(t) = C_i(t=0)e^{-t/\tau_i} \quad (2)$$

where $C_i(t=0)$ is the initial concentration of component i , and its concentration decreases exponentially.

The atmospheric lifetime τ depends on the reaction rate constants of component i with OH, expressed by the reaction rate constant relative to methyl chloroform and the atmospheric lifetime:

$$\tau_i = \tau_{\text{CH}_3\text{CCl}_3} \frac{k_{\text{CH}_3\text{CCl}_3}(277\text{K})}{k_i(277\text{K})} \quad (3)$$

where $k_{\text{CH}_3\text{CCl}_3}(277\text{K})$ and $k_i(277\text{K})$ are the reaction rate constants of methyl chloroform and component i with OH at 277 K, respectively.

The reference compound a_r is given by IPCC2007 AR4, so the GWP index of compound i over a given time span depends on its radiative forcing efficiency (RE) and atmospheric lifetime τ . Although there have been many separate reports of radiation forcing efficiency predictions [6–8] and atmospheric OH response rate predictions [9–12], it was not until 2012 that Kazakov et al. first reported the combination of the two directly for GWP predictions [3]. In that report, the GWP prediction was performed in three steps: (a) using the semi-empirical quantum mechanics method PM6 to calculate the infrared spectrum of a compound then predict the radiative forcing efficiency of the compound; (b) predicting the reaction rate of the compound using a modified hydroxyl radical reaction rate prediction model and estimating its atmospheric lifetime; (c) calculating the radiation efficiency and atmospheric life

into the Eq. (1) to obtain GWP_{100} (the GWP value when TH = 100 years). Using this method, it was shown that there was a clear correlation between the predicted GWP_{100} and the experimental data reported in the literature.

In order to cope with the threat from global warming, a framework agreement signed by various governments specified that the GWP_{100} of future emissions of chemical substances should be less than 200 [13]. The European Union has begun to implement the standard for refrigerants used in vehicles, ships and other means of transportations. In light of this, it is of utmost importance to develop refrigerants and insulating gases with their $GWP_{100} \leq 200$. Toward this goal, Kazakov et al. set the filtering criteria as $GWP_{100} \leq 200$ in their study [3]. However, it is possible to lower the GWP_{100} value by mixing a gas with a relatively high GWP_{100} value with another gas with a low GWP_{100} value. For example, the GWP_{100} of 3 M's insulating gas NOVEC 4710 is 2300 [15], far higher than 200. In order to balance both the use of single gas and mixed gas and to increase the chances of discovering potentially low GWP_{100} gases, we set the filtering criteria for GWP_{100} values to ≤ 1000 in this study.

The main purpose of this study is to describe a method for predicting gas molecule GWP_{100} using a random forest classification model with a prediction accuracy of over 95%. To the best of our knowledge, this is the first method to directly classify and predict the compound GWP_{100} with the highest accuracy. In order to facilitate the reader to reproduce the results of this article, the GWPclass online prediction server was set up and it is available at <http://sf6.molcalx.com.cn>. At this server, the GWP_{100} of a compound can be classified and predicted by drawing its chemical structure and providing its HOMO and LUMO energy values from density functional theory (DFT) calculations.

2 Methods

2.1 Compiling of the Dataset

More than 200 structurally diverse compounds were collected in Chapter 8 of the IPCC 2013 report [16], including their GWP_{100} values, radiation efficiency and atmospheric lifetime. They were selected as training data sets to establish a random forest classification model if the following selection criteria were met: 1) only elements such as H, C, N, O, S, F, Cl, Br and I are present; 2) at least 4 atoms per molecule; 3) The spin multiplicity is 1; 4) The time span HT of the GWP calculation is 100 years. In addition to the IPCC 2013 report, data reported by Kazakov et al. [3] and NOVEC 4710 data [15] from 3 M were also included. The compounds were represented by Daylight SMILES. Redundant structures were removed. Then they were categorized as follows: a compound with $GWP_{100} < 1000$ was labeled as Class 1; a compound with $GWP_{100} > 1000$ was labeled as Class 2.

2.2 Calculations of the Descriptors

Machine learning methods use features, such as descriptors, to characterize molecules of interest. In this study, compounds were characterized by four descriptors: the energy of the frontier molecular orbitals HOMO and LUMO (E_{HOMO} and E_{LUMO}), the number of carbon-hydrogen bonds (nBCH), and the number of unsaturated bonds containing C atoms (double bonds and triple bonds) (nCdt). E_{HOMO} and E_{LUMO} were calculated using the Gaussian 16 (Rev B.01) [17] at the level of APFD/6-311 + G(2d,p) and the energy unit was Hartree; nBCH and nCdt were calculated using RDKit (Version 2017.9.03) [18]. E_{HOMO} and E_{LUMO} were chosen as descriptors because they are related to the reactivity of compounds, and it was reported that E_{HOMO} is directly correlated with the reaction rate of atmospheric OH reaction [19]. nBCH is also related to the atmospheric OH reaction rate therefore it is listed as one of the main reaction modes in Atkinson's atmospheric OH reaction rate prediction method [9–11]. In the method of predicting the atmospheric OH reaction rate by Thomas et al. [12], nBCH is also used as one of the descriptors. It is well known that HFO refrigerants containing carbon-carbon double bonds have lower GWP than HFC-based refrigerants, and the reactions between compounds with carbon-carbon double bonds or triple bonds and atmospheric OH are also the main reactions in the prediction method of atmospheric OH reaction rate developed by Atkinson [9–11]. Therefore, nCdt was chosen as a descriptor for GWP prediction as well.

2.3 Random Forest Classification

Random forest is an integrated learning model that outputs the final predicted value by training multiple decision trees separately and finally combining the results of all decision trees via voting or averaging. Compared to decision trees, random forests are randomized in two ways. On the one hand, the training dataset is selected at random. The same size of data is extracted from the original data set then it is returned. By doing so, the constructed data set will partially overlap but will not contain all of the original data. The random forest uses the constructed data set to train the decision tree, and outputs the final results by combing all the results from the decision tree of the subdataset. For example, the voting model is used for the classification model, and the regression model is used to average the output. On the other hand, the features are selected at random. Not all the features are used during the split process of each decision tree. A feature set is formed from random selection. Use this feature set to select the best features and then split. The addition of the randomness makes the decision tree not necessarily select the global optimal feature for splitting, and the generated decision tree is a relatively weak decision tree.

Random forests are an algorithm that performs very well in many aspects and are widely used. Studies have shown that in the hundreds of data sets in different fields, compared to support vector machines, Bayesian classifiers, etc., random forests excel

on average [20]. Recently, Tao et al. used random forest classifiers for large-scale ligand-based virtual screening studies and the results showed that it performed well in the tests of several drug targets [21]. Therefore, we decided to apply this method for the prediction and classification of GWP_{100} .

There are many implementations of random forest algorithm. In this study, we used the random forest classifier in Python's scikit-learn machine learning library (Version 0.19.1) and optimized the parameters using the GridSearchCV module to obtain the final model.

2.4 Performance of the Model

The random forest model has about 33% of its data that is not used for training each tree because of its randomness, so the out of bag (OOB) cross-validation method of random forest can be used to examine the performance of the model. Specifically, the OOB error is used to examine the overall performance of the model. In addition, the performance of the random forest model can also be characterized by the Confusion Matrix, and be further evaluated using statistical indicators such as classification accuracy, true positive rate (TPR), false positive rate (FPR), true negative rate (TNR), false negative rate (FNR), precision and F-Measure etc. They are defined as follows (Eqs. 4–10):

$$\text{Classification accuracy} = \frac{C}{N} \times 100\% \quad (4)$$

where C is the number of data points that are classified correctly and N is the total number of data points.

$$TPR = \frac{TP}{TP + FN} \times 100\% \quad (5)$$

$$FPR = \frac{FP}{TP + FN} \times 100\% \quad (6)$$

$$TNR = \frac{TN}{TN + FP} \times 100\% \quad (7)$$

$$FNR = \frac{FN}{TP + FN} \times 100\% \quad (8)$$

$$\text{Precision} = \frac{TP}{TP + FP} \times 100\% \quad (9)$$

$$F - \text{measure} = \frac{2 \times \text{Precision} \times \text{Recall}}{\text{Precision} + \text{Recall}} \times 100\% \quad (10)$$

3 Results and Discussion

3.1 Datasets

A total of 203 non-redundant compounds were obtained, of which 199 were from Chapter 8 of IPCC 2013 Report [16], 3 from the study by Kazakov et al. [3], and one from 3 M Company's Novec 4710 brochure [15]. The data set was randomly divided into a training set and a testing set, where the training set contained 141 compounds and the testing set contained 62 compounds. The name of the compound, the SMILES code, the GWP₁₀₀ value reported in the literature, the classification label, and the division of the training and testing sets are given in the Supporting Information.

3.2 Calculations of the Descriptors

The form is generated during the electronic submission process. The compounds were processed by RDKit to calculate nBCH and nCdt. 3D structures were generated for Gaussian 16 to perform geometry optimization at the APFD/6-311 + G(2d,p) level. Convergences were confirmed by frequency calculations that there were no imaginary frequencies. The input files, E_{HOMO}, E_{LUMO}, nBCH and nCdt of all compounds are available in the Supporting Information.

3.3 Training and Verification of the Model

The descriptors were not directly used to train the model. Instead, the training set was normalized first by the preprocessing module of scikit-learn. The testing set was also normalized in the same way. 141 compounds in the training set were used for model training by the random forest classification method. The grid parameter search method of GridSearchCV module was used to perform fivefold cross-validation hyperparameter tuning. The three parameters are the number of decision trees. (n_estimators), decision tree maximum depth (max_depth) and decision leaf node minimum sample number (min_samples_leaf). The three optimized hyperparameters (see Table 1) are used to train the final model.

Table 1 Hyperparameter tuning

Hyperparameter	Value
n_estimators	20
Max_depth	4
Min_samples_leaf	1

Fig. 1 Confusion matrix for the train set (a) and the testing set (b)



The out-of-bagging error of the model is 7%, indicating that the model has good prediction accuracy. In order to further evaluate the model's prediction accuracy and generalization ability for new data, the model was validated against a testing set. The model's predicted performance for the training set and testing set is summarized in the confusion matrix of Fig. 1.

The predicted performance indicators of the model TPR, TNR, FPR, FNR, Precision, F-measure and accuracy are calculated according to the confusion matrix in Fig. 1. The results are shown in Table 2. It was found that the compounds in Class 1 of the training set has higher prediction accuracy than those in Class 2, which is 98.96 and 91.11%, respectively. For the testing set, the accuracy is predicted to be 93.33% for Class 1 and 100% for Class 2, respectively. There are 5 compounds in the prediction set and 3 compounds in the testing set which were predicted less accurately, but the model is basically consistent with the overall accuracy of the training set, the testing set and ensemble data, which are 96.45, 95.16 and 96.06%, respectively. It indicated that the model has good precision and generalization ability. Compared with Kazakov's GWP prediction model, the performance of the random forest model is better, the accuracy of the two is 87.2 and 96%, respectively, but the calculations were simpler and more convenient for the RF model.

Table 2 Main performance indicators of the FR model

Class	Training set		Testing set		Overall	
	Class 1	Class 2	Class 1	Class 2	Class 1	Class 2
TPR	95.96	97.62	100.00	85.00	97.16	93.55
TNR	97.62	95.96	85.00	100.00	93.55	97.16
FPR	2.38	4.04	15.00	0.00	6.45	2.84
FNR	4.04	2.38	0.00	15.00	2.84	6.45
Precision	98.96	91.11	93.33	100.00	97.16	93.55
F-Measure	97.44	94.25	96.55	91.89	97.16	93.55
Accuracy	96.45		95.16		96.06	

3.4 Analysis of Structure-GWP Relationship

The random forest evaluates the importance of features by examining whether the prediction error of the model is lowered when the order of the features is changed [23]. If the order of a feature is changed and the prediction error is unchanged, it indicates that the feature is not important for the model prediction; conversely, if the order of a feature is changed and the prediction error is increased, it suggests that the feature is important for the model prediction. Therefore, the feature importance score can be used to evaluate the relationship between the compound structural features (descriptors) and GWP_{100} . The importance of the four descriptors is ranked from high to low: $E_{HOMO} > nBCH > E_{LUMO} > nCdt$ (see Fig. 2).

Among them, E_{HOMO} had the highest score, reaching 0.543. This suggested that E_{HOMO} was the decisive factor in GWP_{100} prediction. This can also be seen from the scatter plot of E_{HOMO} vs GWP_{100} (Fig. 3): as E_{HOMO} increases, GWP_{100} decreases dramatically. The two lowest chemical substances in E_{HOMO} are carbon tetrafluoride and sulfur hexafluoride (-0.461 , -0.455 Hartree), and their GWP_{100} is 6630 and 23,500, respectively. Sulfur hexafluoride is the compound with the largest GWP_{100} in the data set.

According to Eqs. (1–3), GWP_{100} depends on the radiation efficiency of a compound and its atmospheric lifetime (τ), which in turn depends on its reaction rate constant with atmospheric OH. Bartolotti's results [19] showed that the reaction rate constant of atmospheric OH is linearly correlated to the E_{HOMO} calculated by density functional theory (DFT). E_{HOMO} can be used to predict the atmospheric OH reaction rate constant of HFC and HFE compounds (Eq. 11):

$$\log K_{OH} = \alpha + \beta E_{HOMO}^{DFT} \quad (11)$$

The larger the E_{HOMO} , the larger the atmospheric OH reaction rate constant, the smaller the GWP_{100} value. Therefore, E_{HOMO} affects the GWP_{100} of the compound by the atmospheric OH reaction rate constant. This is also consistent with Kazakov's

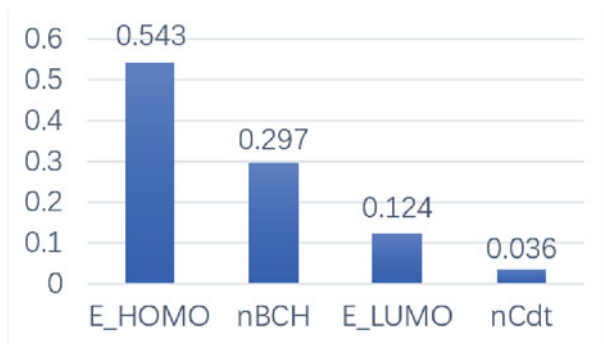


Fig. 2 Feature importance score

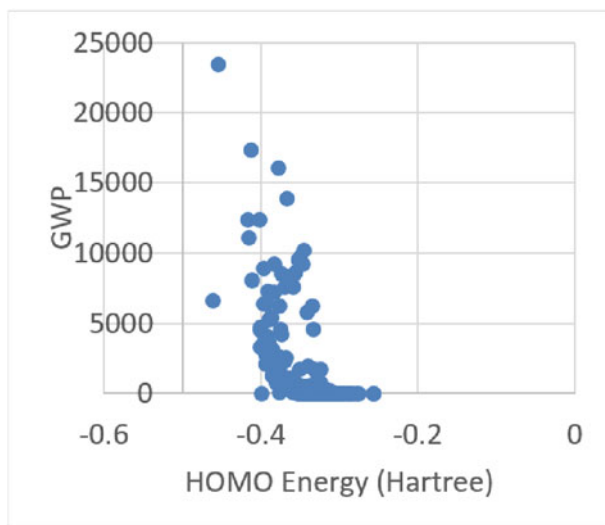


Fig. 3 Scatter plot of E_{HOMO} vs GWP_{100}

study [3], which reduces the need for GWP_{100} to rely on an increase in the rate constant of the atmospheric OH reaction to obtain, rather than alter, the radiative forcing efficiency of the compound.

We believe that E_{LUMO} affects the GWP_{100} value of the compound indirectly through electronegativity, therefore it is reflected in the random forest model as a lower feature importance score. From the relationship between electronegativity and GWP_{100} (see Fig. 4), it can be seen that the higher the electronegativity, the larger the GWP_{100} is. The electronegativity (χ) can be calculated by E_{HOMO} and E_{LUMO} according to Eq. (12):

$$\chi = -\frac{E_{HOMO} + E_{LUMO}}{2} \quad (12)$$

Because E_{LUMO} needs to influence GWP_{100} together with E_{HOMO} as shown in Eq. (12), it is reflected in the lower feature importance score. In addition, of the 203 compounds in the data set, SF_6 is the one with the greatest electronegativity and is one of the compounds with the largest GWP_{100} (see the Supporting Information). This further illustrates the need to take into account both the electronegativity of the compound and the GWP_{100} in the search for SF_6 replacement gases.

In the atmospheric OH reaction rate prediction method developed by Atkinson [9–11], the reaction is divided into four types: 1) the reaction of H atom replaced from CH or OH bond; 2) addition between the atmospheric OH and carbon–carbon double bonds and triple bonds; 3) addition between the atmospheric OH and aromatic rings; 4) reaction between the atmospheric OH and S, N, P. Atkinson’s method can fit 90% of the 500 reaction rate constants. In our feature importance analysis, the

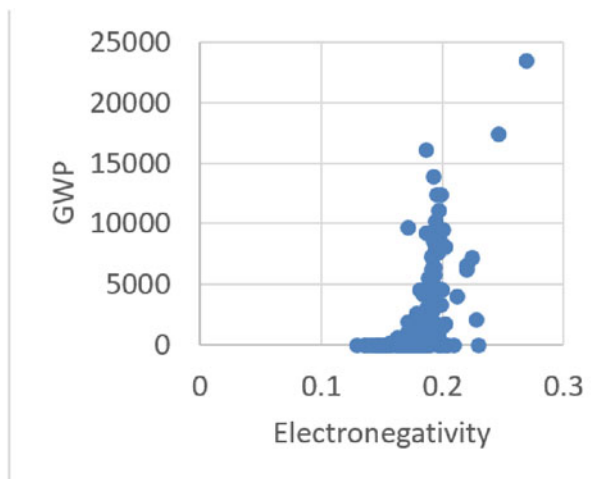


Fig. 4 Scatter plot of GWP vs electronegativity

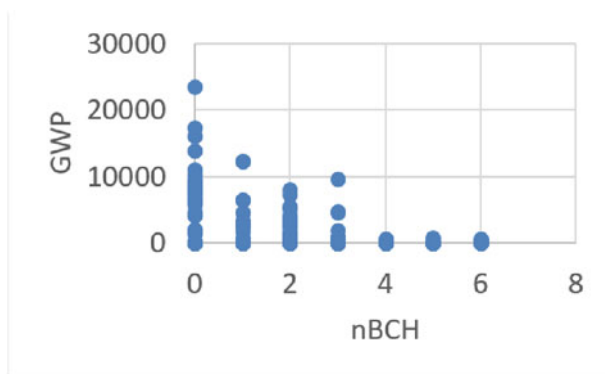


Fig. 5 GWP vs nBCH

feature importance of nBCH is 0.297, which is another important factor in the random forest model that affects GWP_{100} . As can be seen from Fig. 5, as the nCBH of the compound increases, the GWP_{100} also shows a decreasing trend. This is consistent with Atkinson's atmospheric OH reaction rate prediction model: increasing nCBH is beneficial for compounds to react with atmospheric OH, therefore lowering GWP_{100} .

Additions between the atmospheric OH and carbon-carbon double bonds and triple bonds are one of the types considered by Atkinson's atmospheric OH reaction rate prediction method, which is consistent with what we observed in the data set (see the Supporting Information): In addition to Novec 4710, All compounds with non-zero nCdt are compounds with low GWP_{100} values. This phenomenon did not seem in agreement with the low feature importance of nCdt (0.036). However, it is consistent

with the high feature importance of E_{HOMO} and E_{LUMO} compared to $n\text{Cdt}$. According to previous analysis, low E_{HOMO} and high electronegativity are favorable factors for high GWP_{100} values, while NOVEC 4710 is a low E_{HOMO} , highly electronegative compound. Its E_{HOMO} is -0.39458 Hartree and one of 30 compounds with the lowest E_{HOMO} , among which only one compound has a GWP_{100} of less than 1000. At the same time, NOVEC 4710 has an electronegativity of 0.227385 Hartree, which is one of the four compounds with the highest electronegativity in the dataset. While E_{HOMO} is much more important than $n\text{Cdt}$, Novec 4710 has a GWP_{100} greater than 1000, which is an exception to the low GWP_{100} rules for carbon-containing unsaturated bond compounds.

Of the total 203 compounds, there were 8 compounds predicted to the least accurate, with 5 for the training set and 3 for the testing set, respectively. Among them, the most surprising example is nitrous oxide and PFPME. Nitrous oxide has a higher E_{HOMO} , but it is predicted to be > 1000 ; while PFPME with similar E_{HOMO} is predicted to be < 1000 . The possible reason is that the descriptors of choice for the present model is not complete and one or more descriptors are still needed. It also shows that there is room for improvement for the current methodology. Such work is under way in the laboratory and results will be reported in due course.

4 Conclusions

In this study, a random forest classification model was built for the classification prediction of GWP_{100} of 203 compounds with known GWP_{100} . The model obtained was first evaluated with an out of pocket error rate (OOB error) of 7%. In addition, true positive rate (TPR), false positive rate (FPT), true negative rate (TNR), false negative rate (FNR), prediction, F-measure and other indicators were also used to evaluate the model. The overall prediction accuracy of the training set, testing set and complete set data is over 95%. The results showed that the model has excellent classification prediction accuracy and good generalization ability.

Moreover, the structure-GWP analysis of four descriptors was performed by using the characteristic importance of random forests. The importance of these factors to GWP_{100} is: $E_{\text{HOMO}} > n\text{BCH} > E_{\text{LUMO}} > n\text{Cdt}$. In general, improving E_{HOMO} is beneficial to lowering GWP_{100} value, and vice versa; E_{LUMO} together with E_{HOMO} may affect GWP_{100} through electronegativity, reducing electronegativity is beneficial to reducing GWP_{100} ; increasing carbon number is beneficial to reducing GWP_{100} , and vice versa; Increasing the number of carbon-free unsaturated bonds is beneficial for lowering GWP_{100} , but is less important. All of these conclusions, consistent with previous researchers' conclusions, can be used to guide the design of low GWP_{100} compounds. The GWP_{100} prediction model can explain about 96% of the data. However, there are 8 compounds (4%) predicted to be less accurate, and the model has room for further improvement. Research is in progress in this direction in our laboratory.

Acknowledgements The authors thank Dr. Bin Lin from Shenyang Pharmaceutical University for helpful discussion and advice during the preparation of the manuscript. The current work is supported by the science and technology project of China Southern Power Grid (No. GDKJXM20170043).

Availability of Data and Materials All the datasets used in this study can be downloaded free of charge at this link: <https://github.com/gkxiao/GAS>.

Competing interests. The authors declare that they have no competing interests.

Abbreviations

DS	Dielectric strengths
GWP	Global warming potential
SF ₆	Sulfur hexafluoride
IPCC	Inter-governmental Panel on Climate Change
DFT	Density functional theory
RMSD	Root mean squared deviation
RF	Radiative forcing
TH	Time horizon
HOMO	Highest occupied molecular orbital
LUMO	Lowest unoccupied molecular orbital
TPR	True positive rate
FPT	False positive rate
TNR	True negative rate
FNR	False negative rate

References

1. Velders, G.J.M., et al.: Preserving montreal protocol climate benefits by limiting HFCs. *Science* **335**, 922–923 (2012)
2. Beroual, A., Haddad, A.: Recent advances in the quest for a new insulation gas with a low impact on the environment to replace sulfur hexafluoride (SF₆) gas in high-voltage power network applications. *Energies* **10**, 1216 (2017)
3. Kazakov, A., McLinden, M.O., Frenkel, M.: Computational design of new refrigerant fluids based on environmental, safety, and thermodynamic characteristics. *Ind. Eng. Chem. Res.* **51**, 12537–12548 (2012)
4. Rabie, M., Franck, C.: Computational screening of new high voltage insulation gases with low global warming potential. *IEEE Trans. Dielectr. Electr. Insul.* **22**, 296–302 (2015)
5. Intergovernmental Panel on Climate Change Summary for Policymakers, In *Climate Change 2013 – The Physical Science Basis: Working Group I Contribution to the Fifth Assessment Report of the Intergovernmental Panel on Climate Change*, Cambridge: Cambridge University Press, pp. 1–30 (2014).

6. Papasavva, S., Tai, S., Illinger, K.H., Kenny, J.E.: Infrared radiative forcing of CFC substitutes and their atmospheric reaction products. *J. Geophys. Res. Atmos.* **102**, 13643–13650 (1997)
7. Blowers, P., Moline, D.M., Tetrault, K.F., Wheeler, R.R., Tuchawena, S.L.: Prediction of radiative forcing values for hydrofluoroethers using density functional theory methods. *J. Geophys. Res.* **112**, D15108 (2007)
8. Bravo, I., Aranda, A., Hurley, M.D., Marston, G., Nutt, D.R., Shine, K.P., Smith, K., Wallington, T.J.: Infrared absorption spectra, radiative efficiencies, and global warming potentials of perfluorocarbons: comparison between experiment and theory. *J. Geophys. Res. Atmos.* **115**, 1–12 (2010)
9. Atkinson, R.: Kinetics and mechanisms of the gas-phase reactions of the hydroxyl radical with organic compounds under atmospheric conditions. *Chem. Rev.* **86**, 69–201 (1986)
10. Kwok, E.S.C., Atkinson, R.: Estimation of hydroxyl radical reaction rate constants for gas-phase organic compounds using a structure-reactivity relationship: an update. *Atmos. Environ.* **29**, 1685–1695 (1995)
11. Atkinson, R.: A structure-activity relationship for the estimation of rate constants for the gas-phase reactions of OH radicals with organic compounds. *Int. J. Chem. Kinet.* **19**, 799–828 (1987)
12. Allison, T.C.: Application of an artificial neural network to the prediction of OH radical reaction rate constants for evaluating global warming potential. *J. Phys. Chem. B* **120**, 1854–1863 (2016)
13. Mascarelli, A.L.: A bright future for the montreal protocol. *Environ. Sci. Technol.* **44**, 1518–1520 (2010)
14. Directive 2006/40/EC of the European Parliament and of the Council of 17 May 2006 relating to emissions from air-conditioning systems in motor vehicles and amending Council Directive 70/156/EEC. <https://www.eea.europa.eu/policy-documents/directive-2006-40-ec>. Accessed 11 Nov 2019
15. 3M Novoc 4710 Insulating Gas. <http://multimedia.3m.com/mws/media/1132124O/3m-novoc-4710-insulating-gas.pdf>. Accessed 11 Nov 2019
16. Intergovernmental panel on climate change anthropogenic and natural radiative forcing. In: *Climate Change 2013 – The Physical Science Basis: Working Group I Contribution to the Fifth Assessment Report of the Intergovernmental Panel on Climate Change*, Cambridge: Cambridge University Press. pp. 659–740 (2014)
17. Frisch, M.J., et al.: *Gaussian 16 Revision B.01* (2016)
18. Greg, L.: *RDKit: Open-source cheminformatics* (2017)
19. Bartolotti, L.J., Edney, E.O.: Investigation of the correlation between the energy of the highest occupied molecular orbital (HOMO) and the logarithm of the OH rate constant of hydrofluorocarbons and hydrofluoroethers. *Int. J. Chem. Kinet.* **26**, 913–920 (1994)
20. Fernández-Delgado, M., Cernadas, E., Barro, S., Amorim, D., Fern, M., Cernadas, E.: Do we need hundreds of classifiers to solve real world classification problems? *J. Mach. Learn. Res.* **15**, 3133–3181 (2014)
21. Xiao, T., Qi, X., Chen, Y., Jiang, Y.: Development of ligand-based big data deep neural network models for virtual screening of large compound libraries. *Mol. Inform.* **37**, 1800031 (2018)
22. Pedregosa, F., et al.: Scikit-learn: machine learning in python. *J. Mach. Learn. Res.* **12**, 2825–2830 (2011)
23. Breiman, L.: Random forests. *Mach. Learn.* **45**, 5–32 (2001)

Analysis of an Internal Fault of Main Transformer



Zhou Xiu, Bai Jin, Ni Hui, Tian Tian, Chen Lei, Luo Yan, Sun Shangpeng, and Zhang Heng

Abstract In recent years, with a large number of photovoltaic and other new energy connected to the grid, higher requirements have been put forward for the safety and stability of the power grid. The on-load tap changer of the main transformer plays a vital role. According to the light gas alarm and heavy gas trip of the main transformer body caused by the gear adjustment, this paper first carried out the on-site inspection of the main transformer body, especially the gear indication, and then judged the fault position through the oil chromatogram data and electrical test of the body and the oil chamber of the change-over switch. The fault position and cause was determined through the on-site core lifting and internal oil discharge inspection, and the treatment suggestions and measures of the same type of on load tap changer are given.

Keywords Main transformer · on-load tap changer · fault analysis

1 Introduction

In recent years, with the accelerating pace of power grid construction, there are still cases where photovoltaic and other new energy sources are connected to a single main transformer in southern Ningxia, which puts forward higher requirements for the safe and reliable operation of the main transformer [1–3]. There have been too many main transformer or converter faults caused by tap-changers, bushing and other components, which not only seriously affected the safe and stable operation of the power grid, but even caused damage to personnel and equipment [4–7]. With the continuous development of photovoltaics in Ningxia Power Grid speeding up, put forward higher requirements for the stability of the power grid, and the impact of voltage fluctuation is one of them [8]. The number of actions of the on-load tap-changer on the high-voltage side of the transformer is becoming more and more frequent, but due to the complex structure of the on-load tap-changer itself, there are electrical and mechanical connections, and there are main contacts, main on–off

Z. Xiu · B. Jin (✉) · N. Hui · T. Tian · C. Lei · L. Yan · S. Shangpeng · Z. Heng
State Grid Ningxia Electric Power Research Institute, Yinchuan 750001, China

© Beijing Paiké Culture Commu. Co., Ltd. 2023
X. Dong et al. (eds.), *The proceedings of the 10th Frontier Academic Forum of Electrical Engineering (FAFEE2022)*, Lecture Notes in Electrical Engineering 1054, https://doi.org/10.1007/978-981-99-3408-9_66

contacts, and even-odd changeover contacts [9–12]. When the on-load tap-changer fails due to the composition of precision components such as head and transition resistance. In a 110 kV substation in the southern part of Ningxia, the 35 kV busbar voltage was too high and crossed the line. The busbar voltage was within the normal range. The operator adjusted the position of the on-load tap-changer on the high-voltage side of the main transformer to meet 35 kV. Safe operation of kV busbars. Today, the author takes the light gas alarm of the main transformer body caused by the failure of the on-load tap-changer of a 110 kV main transformer and the heavy gas trip of the oil room of the diverter switch as an example. According to the on-site inspection, oil chromatography analysis, electrical test and return to the factory inspection in-depth analysis of the cause of the failure, and put forward targeted opinions and preventive control measures.

2 Defect Description

On August 7, 2022, the No. 1 main transformer of a 110 kV substation had an on-load voltage regulation and heavy gas protection outlet, causing the three-side circuit breaker to trip, and the 35 kV I bus and 10 kV I bus lost voltage. At the same time, a light gas alarm signal appeared on the main transformer body, and the test personnel were immediately organized to sample the on-load tap-changer oil chamber and body oil and conduct oil chromatography analysis. The chromatographic data of the on-load tap-changer oil chamber and body oil were abnormal. It is characterized by “102 arc discharge”, indicating that there is an abnormality in the gas chamber of the transformer on-load tap-changer and the inside of the body. At the same time, manually adjust the tap changer gear to gear 3 on site, the No. 1 main transformer winding together with the bushing insulation resistance, dielectric loss and DC resistance test data are qualified, the high-voltage side to low-voltage side winding ratio is abnormal (compared with the second gear), indicating that the transformer winding and the on-load tap-changer are abnormal.

3 Equipment Information and Protection Action

3.1 Equipment Information

The transformer model is SSZ11-50,000/110, the date of manufacture is October 2014, and the date of operation is January 2017. The model of the on-load tap-changer is VKM-III500Y/72.5B-10193W, the date of manufacture is September 2014, the operation date is January 2017, the rated voltage is 794 V, the rated current is 291.6A, and the transition resistance is 2 Ω .

Fig. 1 Gear indication

3.2 Protective Action

On August 7, 2022, the main transformer protection device panel of a 110 kV substation acted. At 8:13:48.46 ms, the pressure regulation upshift selection was dispatched, and the main variable pressure regulation and heavy gas export action was at 8:13:53.224 ms. At 8:13:53. Tang transformer 501 circuit breaker, 301 circuit breaker, 101 circuit breaker tripped, and the main transformer body light gas alarm action at 8:14:6 s and 233 ms.

4 On-Site Inspection and Test

4.1 On-Site Inspection

Check the tap changer, the gear position indication is shown in Fig. 1. The operation counter value is 2957 times, the long pointer points to the 2nd gear, and the short pointer points to 16/33 (the handle rotates 33 turns, the gear is adjusted to 1 gear, and the current rotation is 16 turns, and the tap changer is not in place). According to the number of turns of the handle and the action sequence table of the contacts, confirm that the gear adjustment is in the action stage of the tap selector, and the changeover switch is not in action.

4.2 Oil Chromatography Test

Oil chromatography test was carried out on the tap-changer and the insulating oil of the body. The acetylene content in the oil chamber of the tap-changer was 167 $\mu\text{L/L}$, and the acetylene content in the body oil was 48 $\mu\text{L/L}$. The specific data are shown

Table 1 Oil chromatographic test data $\mu\text{L/L}$

Sampling location	H2	CH4	C2H6	C2H4	C2H2
Tap changer	214	133	50	297	167
noumenon	100	29	38	3	48

in Table 1. The three ratio codes are all 102. It is characterized by arc discharge characteristics, indicating that there is arc discharge in the tap changer and the main body.

4.3 Electrical Test

Manually adjust the tap changer gear to gear 3 on site, the No. 1 main transformer winding and the bushing insulation resistance, DC resistance, and dielectric loss test data are all qualified, and the high-voltage side to low-voltage side winding ratio is abnormal (consistent with the 2nd gear), indicating that the tap changer and body winding may be abnormal.

5 Toggle Switch Inspection Power Failure Test

During the inspection of the tap changer hanging core, 4 abnormalities were found. One is that the connecting line of the main on-off contact K4 of the switch V2 is disconnected. The other is that there are ablation marks on the surface of the static contact of V2 and the corresponding static contact of the insulating cylinder wall, as shown in Fig. 2. The third is that there is ablation of the V-phase odd-even conversion contacts, as shown in Fig. 3; the fourth is there are discharge traces on the surface of the disconnected terminal and the conductive rod of the V2 contact, as shown in Fig. 4. It means that a discharge fault occurs inside the changeover switch, which leads to the ablation of the static contact, the V2 odd-even changeover contact, and the conductive rod, resulting in abnormal oil chromatography in the oil chamber of the tap changer.

6 Internal Inspection of Oil Discharge and Disassembly Inspection Disposal of Power Failure

During the internal inspection of the transformer oil discharge, it was found that the switch and selector bolts (6 in total) were not fastened in place, and the spring washer was not flattened. The V1 lead has ablation traces, as shown in Fig. 5. The

Fig. 2 Metallographic sampling position of V2 outgoing static contact

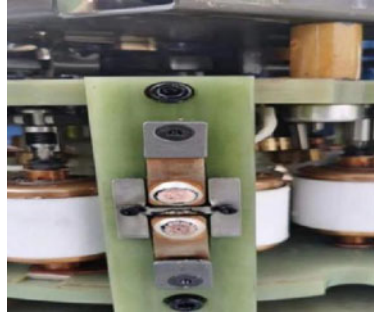


Fig. 3 Static contact corresponding to V2



Fig. 4 Single and even number conversion contact ablation



insulation of the W1 lead wire is damaged, and it is in contact with the drive gear at the bottom of the barrel, as shown in Fig. 6. In the process of returning to the factory for dismantling inspection, it was found that the insulation of the V1 lead was completely damaged and the copper wire was exposed, and the bottom of the tap changer insulation cylinder and the drive gear at the bottom of the cylinder were burnt, as shown in Fig. 7. The manufacturer's process control is not strict, and the bolts and gaskets are not checked after the changeover switch and tap selector are assembled. However, the transmission gear at the bottom of the cylinder and the

Fig. 5 Connecting bolts of change-over switch and selector are not fastened in place



neutral point are equipotential, once the V1 lead wire is damaged and contacts with the transmission gear at the bottom of the cylinder, an inter-pole short circuit will be formed, and the short-circuit large current will burn the bottom of the insulating cylinder and the transmission gear.

Fig. 6 Ablation of V1 lead



Fig. 7 Ablation of insulating cylinder bottom and gear



7 Failure Cause Analysis

7.1 Short-Circuit Current Calculation

The on-load tap-changer 2 taps are short-circuited to 1 tap, and the operating current of the high-voltage side of the transformer is 137 A when the transformer is running from the fault recorder. When the high-voltage side is the power input and a short circuit occurs between the voltage regulator taps, the short-circuit impedance under this condition is obtained by using the finite element simulation software to be 79%, then the short circuit multiple of the voltage regulator short-circuit winding when all energy is applied to the high-regulation winding system for:

$$n = \frac{100}{Z_k} = \frac{100}{79} = 1.2658$$

According to the magnetic potential balance:

$$I_1(W_1 + W_2) = I_2 W_2$$

Among them, W_1 is the total number of turns, $W_1 = 472$ turns, W_2 is the number of single tap turns, and $W_2 = 6$ turns. The short-circuit current can be obtained as:

$$I_2 = \frac{I_1(W_1 + W_2)}{W_2} = \frac{137(472 + 6)}{6} = 10914A$$

Then when a short-circuit fault occurs between the taps of the voltage regulating winding, the short-circuit current at the connection position of the voltage regulating winding contact is:

$$I_4 = n \times I_2 = 10.914 \times 1.2658 = 13.81kA$$

The short circuit diagram is shown in Fig. 8, R_1 is the main contact branch resistance, the field measured value is $65 \mu\Omega$, R_2 is the main on-off contact branch resistance, and the field measured value is $3000 \mu\Omega$.

At the instant of the fault, a current of 13.81 kA flows through the short circuit. The current through the main on-off contact K4 vacuum tube connection line is approximately:

$$I_3 = I_2 \frac{R_1}{R_1 + R_2} = 276A$$

Fig. 8 Schematic diagram of short circuit mechanism

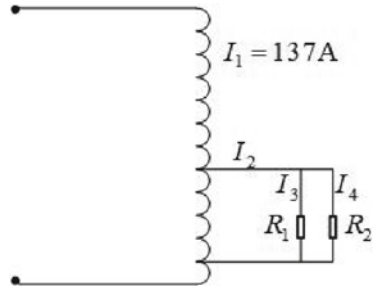
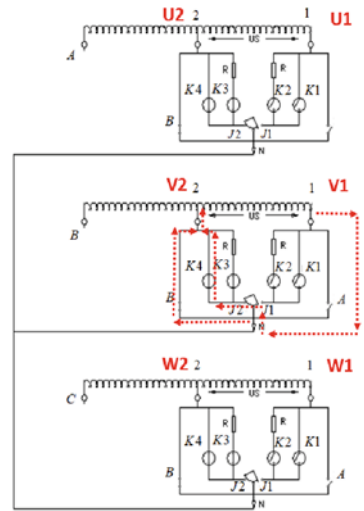


Fig. 9 Schematic diagram of short circuit path



7.2 Failure Cause Analysis

The lead wire is in contact with the transmission gear at the bottom of the insulating cylinder, and the gear rotates and wears the lead wire wrapped with insulating crepe paper during gear shifting, so that the lead wire insulation layer is damaged. On August 7th, during the gear shifting operation of the transformer, the degree of wear reached the critical value of insulation, resulting in the breakdown of the insulation of the V1 wire and the bottom gear (neutral point) and the formation of an arc. The arc ablated the bottom gear and caused gas to be generated, causing the main body has a light gas alarm, and the main transformer oil chromatography has arc discharge characteristics. The V1 lead and the three-phase neutral point form a short circuit, and the short-circuit path is: singular lead wire (V1) → neutral point lead wire → double commutation contact (J2) → double vacuum tube (K4) → double main on-off. The vacuum tube is connected to form an inter-stage short circuit, which causes the connection between the vacuum tube and the V2 lead-out contact to burn out, the V2 lead-out contact is ablated, the V-phase odd-even conversion contacts have

discharge traces, and at the same time, a large amount of gas is generated, which causes the switch to perform heavy gas protection (Fig. 9).

8 Conclusions

- (1) The fault is that the lead wire of the disassembled selector is in contact with the transmission gear at the bottom of the insulating cylinder. When the gear rotates, the lead wire is wrapped with insulating crepe paper, which causes the insulation layer of the lead wire to be damaged, resulting in a short circuit between the stages of the on-load tap-changer. Therefore, the manufacturer should have clear regulations and review work for the assembly and inspection of this part of the process to prevent the occurrence of this fault and ensure the safe and reliable operation of the main transformer.
- (2) Complete the replacement plan and on-site inspection rules for the same type of tap-changer cores, clarify the construction period and internal inspection points, replace the cores of 5 main transformer tap-changers of the same type, and evaluate the tap-changer cores.
- (3) Before the tap-changer of this type is treated, the voltage regulation of the same type of on-load tap-changer is prohibited. If the abnormal oil chromatography is found, the operation should be stopped in time. According to the power failure maintenance plan of the same type of hidden transformer, the hidden danger control work should be completed as soon as possible.

References

1. Xiu, Z., et al.: Comparative analysis of short-circuit mechanical properties of transformer windings under different models. *High Volt. Electr. Appar.* **58**(01), 148–154 (2022). (in Chinese)
2. Xiu, Z., Tian, T., Yan, L., et al.: Cause analysis and treatment of 330 kV main transformer abnormality. *Transformer* **57**(7), 86–87 (2020). (in Chinese)
3. Xiu, Z., et al.: Research on transformer partial discharge pattern recognition based on deep learning. *High Volt. Electr. Appar.* **55**(12), 98–105 (2019). (in Chinese)
4. Renjing, F., et al.: Strategy design and transient analysis of ITER PPEN transformer on-load tap changer during converter operation. *J. Fusion Energy* **37**(6) (2018)
5. Liang, G., Wang, L., Gao, F., Liu, X.: A new maximum step voltage calculation method of on-load tap-changer for symmetrical two-core phase-shifting transformer. *IEEE Trans. Power Deliv.* **33**(6) (2018)
6. Duan, R., Wang, F.: Fault diagnosis of on-load tap-changer in converter transformer based on time-frequency vibration analysis. *IEEE Trans. Indust. Electr.* **63**(6) (2016)
7. Accessory power supply allows transformer load tap changers to be easily tested. *Transmis. Distrib. World*(2015)
8. Xiu, Z., et al.: Health assessment model of power transformer considering historical conditions. *High Volt. Electr. Appar.* **58**(02), 70–76 (2021). (in Chinese)

9. Yang,R., Zhang, D., Li, Z., Yang, K., Mo, S., Li, L.: Mechanical fault diagnostics of power transformer on-load tap changers using dynamic time warping. *IEEE Trans. Instrum. Measur.* **68**(9) (2019)
10. Gu, L., Shi, C., Wu, Y., Xuefeng, B., Li, P.: Research on test of key parameters of on-load tap-changer in transformer. *IOP Conf. Ser. Earth Environ. Sci.* **300**(4) (2019)
11. Seo, J.,Ma, H., Saha, T.K.: A joint vibration and arcing measurement system for online condition monitoring of onload tap changer of the power transformer. *IEEE Trans. Power Deliv.* **32**(2) (2017)
12. Ruochen, D., Fenghua, W., Lidan, Z., Gang, Y.: Detection of mechanical states of on-load tap changers for converter transformers using narrowband noise-assisted multivariate empirical mode decomposition algorithms. *Trans. China Electrotech. Soc.* **32**(10), 182–189 (2017)

Smooth Wind Power Fluctuation Based on Sliding Average and Low Pass Filtering



Xingwu Fu and Yarui Hu

Abstract Due to the inherent characteristics of uncertainty and mutation of wind energy, direct grid connection is very easy to cause power quality damage, and even lead to the paralysis of the entire power system when the fluctuation range is extreme. Based on this, the wind farm is equipped with hybrid energy storage system (HESS) to suppress wind power fluctuation. First, the moving average filter is used to smooth the original wind power fluctuation, and the power fluctuation range is calculated according to the grid connected standard to obtain the grid connected power and the hybrid energy storage system stabilized power. Then, according to the characteristics of the energy storage device, select the appropriate handover frequency based on the amplitude frequency characteristics of the energy storage signal, use low pass filtering (LPF) to suppress the power component higher than the handover frequency by super capacitor energy storage, and suppress the power component lower than the handover frequency by battery energy storage, and select different filter time constants to analyze the output of the hybrid energy storage system, Compared with other algorithms, the optimal power allocation command is obtained. The results verify the effectiveness and rationality of the proposed method.

Keywords Power system · HESS · Moving average filtering · LPF

1 Introduction

With the gradual depletion of non-renewable energy, energy security and the contradiction between supply and demand are becoming more and more serious. Wind energy has attracted wide attention due to its pollution-free and sustainable utilization

X. Fu · Y. Hu (✉)

School of Electrical and Control Engineering, Liaoning University of Engineering and Technology, Huludao 125105, China

e-mail: yaruihu@lntu.edu.cn

X. Fu

e-mail: xingwufu@lntu.edu.cn

© Beijing Paiké Culture Commu. Co., Ltd. 2023

X. Dong et al. (eds.), *The proceedings of the 10th Frontier Academic Forum of Electrical Engineering (FAFEE2022)*, Lecture Notes in Electrical Engineering 1054, https://doi.org/10.1007/978-981-99-3408-9_67

777

[1]. However, the inherent volatility and intermittency of wind power can deteriorate power quality, resulting in undesired voltage and power fluctuations. The configuration of energy storage system is an effective means to reduce the output fluctuation of wind farm and improve the stability of power system. Energy storage types mainly include power storage and energy storage [2]. Compared with energy-type energy storage, power-type energy storage, such as super-capacitor and superconducting magnetic energy storage, has high power density, low energy density, more cycles, long service life and fast response speed. Energy-type energy storage has low power density, high energy density, but fewer cycles, short service life and slow response speed, such as battery energy storage. The function of single energy storage is limited and it is difficult to achieve the desired calming effect. HESS combines energy storage and power storage, making it have the advantages of two energy storage devices at the same time.

There has been a lot of research on reducing wind power fluctuation and improving grid-connected capacity. Literature [3] uses HESS bidirectional DC/DC converter and DC/AC converter control methods to smooth random wind power fluctuations. Literature [4] introduces a new method based on HESS of adiabatic compressed air energy storage system and flywheel energy storage system to suppress wind power fluctuation and improve wind power penetration. In literature [5], lead carbon cells were used to suppress photovoltaic power fluctuations, and the effectiveness of the proposed control strategy was proved by comparison with the moving average method. In literature [6], batteries and super-capacitors are used to suppress the power fluctuation of distributed energy, which can effectively reduce the depth and frequency of battery charging and discharging compared with the energy storage of a single battery. Literature [7] proposes an energy storage system power optimization distribution method based on zero-phase low-pass filtering. The above research has a good calming effect on wind power fluctuation. However, when the energy storage power signal is allocated, the amplitude-frequency characteristics of the signal are not analyzed, which is easy to cause the signal aliasing phenomenon due to the unreasonable selection of the handover frequency, and the lack of testing and comparison of the suppression effect.

Aiming at the above research problems, the method of smoothing wind power fluctuation is studied and improved. Firstly, the sliding average algorithm is used to smooth the original wind power fluctuations, and the grid-connected power and the hybrid energy storage system's calming power are obtained. Then, by using the amplitude-frequency characteristics of energy storage signals, the appropriate dividing frequency is selected, and the low-pass filter is used to separate the hybrid energy storage system into energy-type energy storage reference power and power-type energy storage reference power. Different filtering time constants are selected to analyze the charge–discharge power of the energy storage device, and the optimal power distribution instructions are obtained to make the system run efficiently and stabilities.

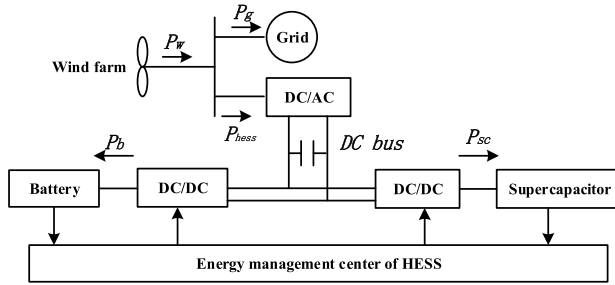


Fig. 1 Structural diagram of air storage combined system

2 Sliding Average Wind Power Decomposition

2.1 Structure of Combined Wind-Storage System

Figure 1 shows the structure of the combined wind-storage system. In this system, P_w stands for the original wind farm output power, P_g stands for the power absorbed into the grid after being suppressed, and P_{hess} stands for the HESS suppressed power. The battery and the ultra-capacitor are connected to the DC bus through their respective DC/DC converters, and then connected to the power grid through a unified DC/AC converter. The energy management center of the hybrid energy storage system provides their own charge–discharge reference power P_b and P_{sc} according to the monitoring of the charge–discharge state of the energy storage device.

Regardless of the energy loss of the system, according to the flow direction of the output power in Fig. 1, the relationship is as follows:

$$P_w = P_g + P_{hess} \tag{1}$$

$$P_{hess} = P_b + P_{sc} \tag{2}$$

where $P_b > 0$ and $P_{sc} > 0$ respectively indicate that the battery and super-capacitor are in charging state. $P_b < 0$ and $P_{sc} < 0$ respectively indicate that the battery and the ultra-capacitor are discharged.

2.2 Moving Average Algorithm

The sliding average filtering method is also known as recursive average filtering method. Its principle is: sampling a set of data stored in time series. When a new data is acquired, the earliest collected data will be discarded, and then the arithmetic average of a fixed amount of data including the new data will be calculated [8].

And so on, each time you take a sample, you calculate a new average. Taking the 24 h historical output power sampling data of a wind farm as an example, the sliding average filtering was carried out on it, and the sampling interval was 1 min. A total of 1440 points were collected. Select a fixed sliding filter length window and represent it by N . From time t_0 , N power values are collected, the arithmetic average of all the power values is calculated, and then a data is slid backwards. At time t_1 , the power value at time t_0 is discarded to ensure the data size of the sliding window remains unchanged, and the arithmetic average value is calculated. And so on, until it slides to t_{1440} , the calculation is over and the average filtering of wind power is realized. This process can be expressed as follows:

$$y(t) = \frac{1}{N} \sum_{i=t-N}^t P(i) \tag{3}$$

where $y(t)$ represents the power value obtained after filtering, $P(i)$ represents the power value at every moment before filtering, and N represents the length window of sliding filtering. The selection of N has a direct impact on the calming effect. The large selection has a significant smoothing effect, but the energy storage system needs to be equipped with a large capacity, which is not conducive to the economy of the system. If the selection is small and the calming effect is not sufficient, it will lead to high volatility and fail to meet the grid connection standard of volatility.

According to the regulations and standards of wind power grid-connection [9], for wind farms with a total installed capacity of 30–150 MW, the limit of active power variation capacity within 1 min is 1/10 of the total installed capacity. The limit of active power variation capacity within 10 min is 1/3 of the total installed capacity. Taking a wind farm with a total installed capacity of 30 MW as an example, the target power of wind power at time t after being flattened is $P_{des}(t)$, and its allowable fluctuation range within 1 and 10 min is as follows:

(1) Fluctuation range of 1 min:

$$\begin{cases} P_{des1}^{\min}(t) = \max_{t=i} P_{des}(t) - \frac{1}{10}E \\ P_{des1}^{\max}(t) = \min_{t=i} P_{des}(t) + \frac{1}{10}E \end{cases} \tag{4}$$

(2) Fluctuation range of 10 min:

$$\begin{cases} P_{des10}^{\min}(t) = \max_{t=j} P_{des}(t) - \frac{1}{3}E \\ P_{des10}^{\max}(t) = \min_{t=j} P_{des}(t) + \frac{1}{3}E \end{cases} \tag{5}$$

where $i = 1, 2, \dots, 60$; $j = 1, 2, \dots, 600$. Based on the above formula, the allowable fluctuation range of wind power within 1 and 10 min can be obtained as follows:

$$P_{des1}^{\min}(t) \leq P_{des}(t) \leq P_{des1}^{\max}(t) \tag{6}$$

$$P_{des10}^{\min}(t) \leq P_{des}(t) \leq P_{des10}^{\max}(t) \tag{7}$$

In order to verify the calming effect, the change rate of wind power is introduced as the evaluation index of the calming effect, and the calculation formula is as follows:

$$\Delta \tilde{P}_w = \frac{\max_{t \in (t, t+\Delta t)} P_w(t) - \min_{t \in (t, t+\Delta t)} P_w(t)}{E} \tag{8}$$

3 HESS Power Distribution Based on Low-Pass Filtering

3.1 LPF Structure

The typical first-order low-pass filter topology is as follows (Fig. 2):

The transfer function of the low-pass filtering can be expressed as:

$$H(s) = \frac{1}{1 + sT} \tag{9}$$

where T is the filtering time constant, which is discretized and obtained

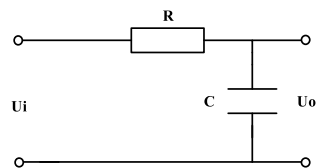
$$u_o(t) = \frac{T_c}{T + T_c} u_i(t) + (1 - \frac{T_c}{T + T_c}) u_o(t - 1) \tag{10}$$

then $s = \frac{1-z^{-1}}{T_c}$, T_c is the sampling period.

Make $\alpha = \frac{T_c}{T+T_c}$, expressed as filter coefficients, the low pass filter is expressed as the mathematical model

$$u_o(t) = \alpha u_i(t) + (1 - \alpha) u_o(t - 1) \tag{11}$$

Fig. 2 Topology of first-order low-pass filter



3.2 Power Distribution Based on LPF

In the hybrid energy storage system, the cycle life of energy storage such as battery is short and the response speed is slow. In order to prolong its service life, continuous charge and discharge action should not be carried out, which is suitable for suppressing low-frequency fluctuation power. As a power-type energy storage system, super-capacitors have fast response speed, millisecond time, and can carry out rapid cyclic charge and discharge, which is suitable for suppressing high-frequency fluctuating power in wind power fluctuations [10, 11]. Therefore, the boundary frequency of the two should be properly selected according to their energy storage characteristics, and the target power value P_{hess} should be low-pass filtering. Then, the power distribution of the hybrid energy storage system has the following relations:

$$P_b(t) = \alpha P_{hess}(t) + (1 - \alpha) P_b(t - 1) \quad (12)$$

$$P_{sc}(t) = P_{hess}(t) - P_b(t) \quad (13)$$

The cut-off frequency of the low-pass filter is expressed as:

$$f_c = \frac{\alpha}{2\pi T_c(1 - \alpha)} = \frac{1}{2\pi T} \quad (14)$$

It can be seen that the cutoff frequency is inversely proportional to the filtering time constant, and the selection of filtering time constant directly affects the output of energy storage. According to the application scenario of wind farm power fluctuation, different filtering time constants are selected for example analysis.

4 Analysis of Numerical Examples

4.1 Amplitude Frequency Characteristic

Fourier transform was used to decompose the power signal of HESS, and the amplitude-frequency characteristics of the power signal were obtained, as shown in Fig. 3.

As can be seen from Fig. 3, the frequency range is about $0 - 8.5 \times 10^{-3}$ Hz, and the frequency band of $0 - 10^{-3}$ Hz belongs to the power signal concentration area. Therefore, 10^{-3} Hz can be used as the reference handover frequency of HESS. The power component higher than the handover frequency is compensated by the super-capacitor energy storage, while the power component lower than the handover frequency is compensated by the battery energy storage.

Fig. 3 Amplitude frequency characteristics of hybrid energy storage power

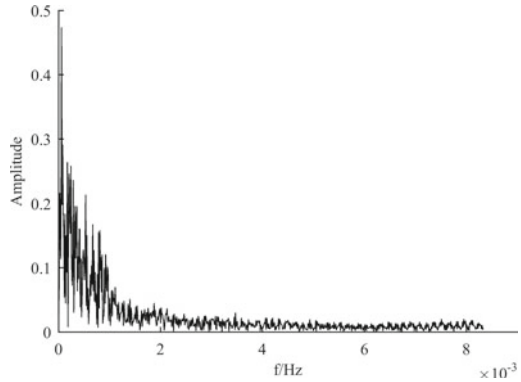
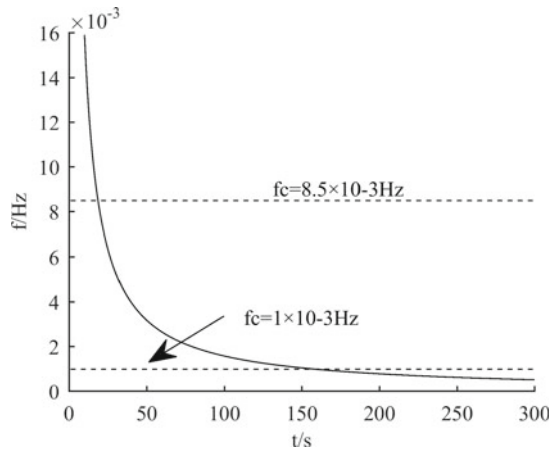


Fig. 4 Relationship between cutoff frequency and filtering time constant



The relationship between cutoff frequency and filtering time constant can be obtained from Eq. (14), as shown in Fig. 4. Note that when the filtering time constant is 160, f_c is 0.001 Hz; The power signal in this frequency band is relatively concentrated. When the filtering time constant is 20 and the f_c is 0.0085 Hz, almost all power signals are contained in this frequency band. In order to verify the power distribution effect of $T = 160$ s, the charging and discharging power of the energy storage device is analyzed with $T = 20$ s and $T = 160$ s, respectively.

4.2 Analysis of the Results of Inhibition

The original power fluctuation of wind power is smoothed by the sliding average algorithm, N is 15, then compared with the grid-connected power suppressed by the wavelet packet decomposition algorithm. Figure 5 and Fig. 6 show the output power

Fig. 5 Comparison of power fluctuation before and after stabilization

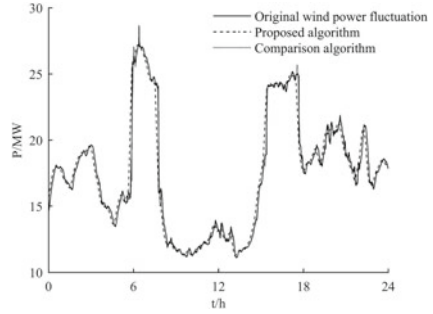
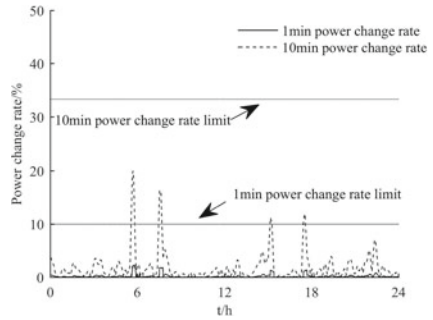


Fig. 6 Power change rate at 1 and 10 min



fluctuation diagram before and after the wind farm is suppressed, and the power change rate of grid-connected power within 1 and 10 min respectively.

As can be seen from Fig. 5, before leveling, the output power of wind power has strong mutability with obvious sharp points. After leveling, the grid-connected power curve becomes smooth. Although both algorithms achieve wind power fluctuation stabilization, relatively speaking, the former algorithm has better stabilization effect when wind power has obvious fluctuation. For example, when $t = 8$ h, the output power of the comparison algorithm is 3.91 MW, while that of the proposed algorithm is 6.58 MW, and the amplitude of fluctuation is greatly reduced. In addition, it can be seen from Fig. 6 that the limit of power change rate within 1 min is 10%, and the fluctuation range is reduced within 5% after smoothing. The fluctuation limit of the power change rate within 10 min is 33%, and the fluctuation rate cannot exceed 20% after smoothing. Table 1 shows the comparison of active power changes in 1 and 10 min before and after suppression.

As can be seen from Table 1, the power fluctuation within 1 min before suppression is 7.954 MW, and the power variation after suppression is 0.699 MW, which is 0.54 MW less than the comparison algorithm. After the power fluctuation within 10 min is suppressed, the comparison algorithm decreases to 8.528 MW, and the proposed algorithm decreases to 6.002 MW, which meets the requirement of active power variation of wind power grid-connected, and has obvious effect on improving wind power output fluctuation.

4.3 HESS Power Distribution

By comparing the energy storage output from wavelet packet decomposition with the energy storage output combined with the proposed sliding average and low-pass filtering, the charge–discharge power of the battery and the ultra-capacitor is shown in Fig. 7(a), (b) and (c) respectively.

When T is set to 20 s, the cut-off frequency is set at 0.0085 Hz, which contains most of the fluctuation components of energy storage, which are all suppressed by the battery, while the super capacitor is less suppressed, which conforms to the power distribution mode of hybrid energy storage in Fig. 7(a). When T is set at 160 s, the cutoff frequency is set at 0.001 Hz. The fluctuation component higher than 0.001 Hz is responded by the super-capacitor, and the fluctuation component lower than 0.001 Hz is responded by the battery. As can be seen from Fig. 7(b) and (c), when the wavelet packet decomposition algorithm is applied, the battery is frequently charged and discharged, and the maximum output power reaches 6.88 MW, which is not conducive to its service life. When the sliding average algorithm is combined with low-pass filtering, the battery cycles are significantly reduced, the output power is relatively gentle, and the maximum output power is 4.24 MW, which reduces the depth of charge and discharge of the battery and the capacity of the energy storage device. Therefore, the proposed method is more reasonable for the power distribution of the hybrid energy storage system and makes the service cycle of the hybrid energy storage device longer.

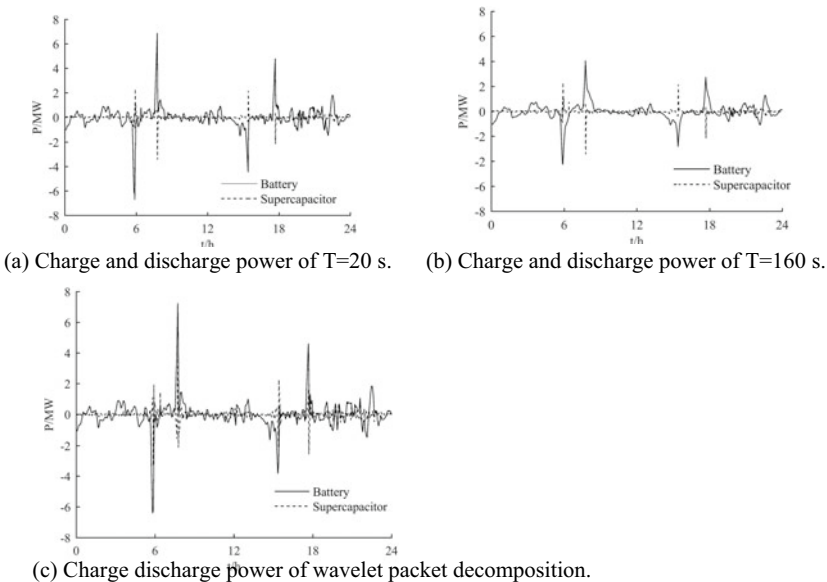


Fig. 7 Comparison of charge and discharge power between battery and super-capacitor

Table 1 1 and 10 min changes in active power before and after stabilization

	Time	Proposed algorithm	Comparison algorithm
Active power change before stabilization(MW)	1 min	7.954	7.954
	10 min	9.935	9.935
Active power change after stabilization(MW)	1 min	0.699	1.239
	10 min	6.002	8.528

5 Conclusions

A hybrid energy storage system is used to optimize active power output for wind power fluctuation and intermittent problems. The original wind power was obtained by using the sliding average algorithm to obtain grid-connected power and hybrid energy storage calming power. After the calming power, the fluctuation range of the power change rate was reduced within 5% within 1 min. The fluctuation limit of power variation rate within 10 min is less than 20%, and good calming effect is obtained. At the same time, the cut-off frequency point of the mixed energy storage power signal is set, and the high-frequency and low-frequency components of the signal are separated by low-pass filtering. According to the different characteristics of the energy storage device, the high-frequency signal is absorbed by the power type energy storage, and the low-frequency signal is absorbed by the energy type energy storage, and the power distribution mode is compared with the wavelet packet decomposition. With the wavelet packet decomposition algorithm, the battery needs to carry out frequent charge and discharge, and the maximum output power reaches 6.88 MW. With the power distribution by the proposed algorithm, the number of battery cycles is significantly reduced, and the maximum output power is 4.24 MW. In other words, the charge and discharge process of the battery is improved, and the capacity of the energy storage device is reduced. It has certain reference value for calming wind power fluctuation.

Acknowledgements This work was funded by the National Natural Science Foundation of China (No. 51674136).

References

1. Sun, Z.L., Chen, J., Yan, Y.L., et al.: Dual reactor self-circulation coordinated control based on hybrid energy storage to stabilize wind power fluctuation. *J. Solar Energy* **42**(04), 125–132 (2021). (in Chinese)
2. Cheng, L., Zhang, F.H.: Wavelet transform method for stabilizing power fluctuation in hybrid energy storage system. *Power Autom. Equip.* **41**(03), 100–104+128 (2021). (in Chinese)
3. Kong, L., Li, L., Wei, G., et al.: Techno-economic analysis of hydrogen energy for renewable energy power smoothing. *Int. J. Hydrogen Energy* **46**(3), 2847–2861 (2021)

4. Zhang, Y., Xu, Y., Guo, H., et al.: A hybrid energy storage system with optimized operating strategy for mitigating wind power fluctuations. *Renew. Energy* **125**(02), 121–132 (2018)
5. Lin, D., Zhao, B., Li, P., et al.: Real-time fluctuation smoothing method for photovoltaic power station using lead carbon battery. *Power Syst. Technol.* **42**(5), 1518–1525 (2018)
6. Ning, Y., Wei, L., et al.: Capacity allocation method in active distribution network based on hybrid energy storage. *Trans. China Electrotech. Soc.* **32**(19), 180–186 (2017)
7. Tang, J., Xiong, B., Huang, Y., et al.: Optimal configuration of energy storage system based on frequency hierarchical control in ship power system with solar photovoltaic plant. *J. Eng.* **2017**(13), 1511–1514 (2017)
8. Chen, Y., Zhang, Y., Xie, J.F.: Adaptive moving average and wavelet packet decomposition to suppress wind power fluctuation. *Control. Eng.* **28**(07), 1281–1288 (2021). (in Chinese)
9. Li, C.P., Yan, B., Li, J.H., et al.: Optimization strategy of hybrid energy storage to stabilize wind power fluctuation based on genetic algorithm. *Jilin Electr. Power* **49**(04), 6–10 (2021). (in Chinese)
10. Ding, M., Wu, J.: A novel control strategy of hybrid energy storage system for wind power smoothing. *Electr. Power Compon. Syst.* **45**(12), 1265–1274 (2017)
11. Zhu, Y., Qin, L.K., Yan, Q.C., et al.: Joint frequency modulation strategy of wind storage considering frequency response process and optimal configuration method of energy storage system. *Power Automat. Equip.* **41**(10), 28–35 (2021). (in Chinese)

Research on Repetition Frequency Pulse Current Source Based on Solid State Switching Technology



Xin Huang, Taixun Fang, Qiwen Zhou, Lei Zhang, Hui Chen,
and Xingxing Huangfu

Abstract Based on solid state switching technology and capacitor energy storage, a pulsed power current source with repetition frequency function is designed and developed. Using the thyristors with high di/dt and large peak current as a solid state switching device, a pulsed power current source with repetition frequency function is designed and implemented. FPGA control mode is adopted to realize the nano seconds level periodic triggering precision, and the triggering consistency of the control unit is good, with the maximum error less than 6 ns. A prototype was manufactured and the tests were carried out. The results of single pulse and repetition frequency tests showed that the pulse peak current of single series thyristor can reach 158 kA, the repetition rate can reach 1 Hz, and the period dispersion is less than 0.000025%, and the peak dispersion is less than 3%. The results show that the repetition frequency power current source based on solid state switch has the advantages of high current, high di/dt and repetition frequency triggering, and the cycle triggering precision is good, the control method is convenient, and the high and low voltage isolation is safe and reliable, so it has a certain popularization prospect.

Keywords Pulsed power current · Source repetition frequency · Solid state switch

1 Introduction

Pulse power technology is an emerging field of technology that stores energy over a relatively long period of time, compresses it quickly, converts it, and then effectively releases it to the load [1]. Pulse power technology mainly includes the following two aspects:

Energy storage: capacitor energy storage, inductive energy storage, mechanical energy storage, chemical energy storage and other ways in [2].

X. Huang (✉) · T. Fang · Q. Zhou · L. Zhang · H. Chen · X. Huangfu
NR Electrical Ltd Co., Nanjing 211110, Jiangsu, China
e-mail: huangx.nr@foxmail.com

© Beijing Paiké Culture Commu. Co., Ltd. 2023
X. Dong et al. (eds.), *The proceedings of the 10th Frontier Academic Forum of Electrical Engineering (FAFEE2022)*, Lecture Notes in Electrical Engineering 1054, https://doi.org/10.1007/978-981-99-3408-9_68

Switching technology: switch circuit, large capacity, small inherent inductance, small discharge delay and small dispersion. [3, 4] introduce the common switching equipment such as a gap switch, break switch, magnetic switch and solid state switch.

Test technology: measuring the parameters of the device, such as voltage and current. Generally the resistance voltage divider, capacitance voltage divider and other equipment measure voltage, and the Roche coil, shunt or other equipment measure current.

Applications of pulse power technology include: Controlled nuclear fusion and plasma physics research [5], emerging strong laser [6], nuclear explosion laboratory simulation, high power microwave, electromagnetic gun [7, 8] and agriculture[9, 10] etc. The pulse technology is widely used in high-tech fields and national defense construction. Many applications require pulsed power supply to run at repeated frequency, which puts forward higher requirements for switching technology.

Solid state switch has the advantage of small volume, high repetition rate, long life, high reliability, suitable for high repetition rate operation. To achieve the high voltage, high current technical index, it is required to solve many technical problems.

The research in this paper is mainly pulse power source with repetition frequency function based on capacitor energy storage mode and solid-state switching technology, which can generate micro seconds level and more than 100 kA peak current, and has the advantages of low sensing value, low discreteness, long life and high reliability.

2 Working Principle

The circuit of pulse power current source based on capacitive energy storage technology is shown in Fig. 1.

The equation of capacitor discharge circuit is as follows:

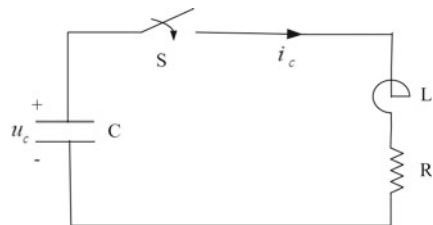
$$LC \frac{d^2 u_c}{dt^2} + RC \frac{du_c}{dt} + u_c = 0 \quad (1)$$

where the initial condition, $I(0) = 0, U_C(0) = U_0$.

There are three discharging type with different capacitor and resistor parameters.

Underdamping is the oscillation attenuation discharge process, when $R < 2\sqrt{L/C}$.

Fig. 1 Capacitor discharge circuit



Critical damping is the oscillation non-attenuation discharge process, when $R = 2\sqrt{L/C}$.

Overdamping is the non-oscillation attenuation discharge process, when $R > 2\sqrt{L/C}$.

Due to the small internal resistance of capacitive pulse power supply, so that the circuit meets the underdamping condition, is the discharge process of oscillation attenuation, the circuit type current is:

$$i(t) = \frac{U_0}{\omega L} e^{-\frac{R}{2L}t} \sin \omega t \tag{2}$$

The first peak value and arrival time are respectively:

$$i_{(m)} = U_0 \sqrt{C/L} e^{(-\frac{\alpha}{\sqrt{1-\alpha^2}})} \tan^{-1}(\sqrt{1-\alpha^2}/\alpha) \tag{3}$$

$$t_{(m)} = \frac{\sqrt{LC}}{\sqrt{1-\alpha^2}} \tan^{-1}(\sqrt{1-\alpha^2}/\alpha) \tag{4}$$

where, $\alpha = \frac{R}{2} \sqrt{C/L}$.

The maximum steepness of the circuit discharge pulse current is $t = 0$, and the maximum value is:

$$\left(\frac{di}{dt}\right)_m = \left(\frac{di}{dt}\right)_{t=0} = \frac{U_0}{L} \tag{5}$$

According to the above analysis, the peak current, the time to reach the peak, and the size of di/dt are related to the $L/C/R$ in the circuit and the initial charging voltage U_0 .

Capacitance parameters in the circuit are mainly determined by discharge capacitance, inductance parameters are mainly composed of load inductance and stray inductance in the loop, and resistance is mainly load resistance.

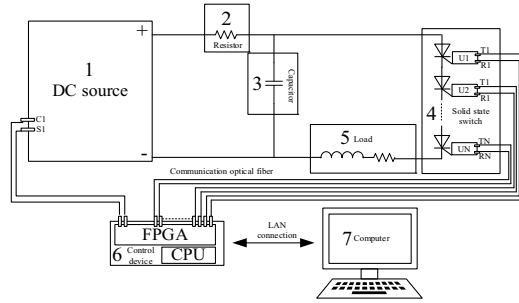
If the current steepness is to be increased, it is necessary to reduce the loop inductance and increase the charging voltage at the same time. The discharge current can be increased by increasing the capacitance, reducing the inductance, increasing the charging voltage.

3 Control System Design

In order to realize controllable repetition frequency pulse discharge function, a pulse power supply and its control system based on solid state switch and capacitor energy storage are designed (Fig. 2).

Pulse current source mainly includes the following parts:

Fig. 2 Pulse current source circuit and control system



DC source: It has the ability of fast charging energy storage capacitor and is controlled by the control device to start and stop.

Resistor: Used to limit charging current.

Capacitor: the main energy storage element of pulse current source, low speed energy storage and high-speed discharge.

Solid state switch: A switching device composed of semiconductor devices in series and parallel, which can be controlled by a control device and can withstand large di/dt and peak current. Generally, series and parallel thyristors (valve bank) that can withstand large current and high di/dt are used. Solid-state switches can also include diodes in reverse parallel.

Load: The equivalent impedance of the load varies according to the application situation, but the resistance and inductance load are mainly used.

Control device: The control system can receive the control target set by the man-machine interface, such as trigger times, trigger cycle, start, end and other commands. At the same time, the control device needs to communicate with the valve bank, receive the valve bank internal working state returned by the valve bank, and issue the valve bank opening instruction.

Computer: the user's operating platform to issue control commands to the control device, and has the function of issuing automatic trigger command, manual trigger command, manual charging command, etc.

In order to improve the trigger accuracy and reduce the trigger cycle dispersion, the automatic trigger function based on FPGA is designed.

The control device obtains the required discharge times and trigger interval through the man-machine interface (current peak and rise time are determined by loop parameters and charging voltage, so only trigger interval is set here). After receiving the trigger instruction from the man-machine interface, the automatic trigger starts immediately. The timing interval is generated by FPGA. When each timing interval is reached, it immediately sends a trigger signal to the solid-state switch, which starts to switch after receiving the instruction and discharge the energy storage capacitor to the load. After the end of a discharge cycle, the solid-state switch is turned off, and the control device starts the charging power again to charge the energy storage capacitor. After the completion of charging, the timing interval of

FPGA is reached, and the opening instruction is issued again to start a new discharge process until the discharge times meet the expected requirements.

The charging power supply needs to receive the start and stop instructions of the control device. After starting, the charging power supply needs to be able to charge quickly and complete the charging before the trigger interval arrives, otherwise it will lead to insufficient charging voltage and lower discharge current than expected. Due to current limiting resistance, the charging power supply will not be damaged.

If the charging power supply has the command of setting the charging voltage, the automatic triggering function of the control device can be realized.

The user input the required peak current through the man-machine interface, and the control device will calculate the required charging voltage through Formula (3). According to the calculation result, the charging voltage of the charging power supply is set, and then the automatic discharge process can be entered after the user sends the discharge instruction, and the function of automatic triggering can be completed.

4 Prototype Design and Test

In order to verify the actual effect of pulse power source based on solid state switch, a prototype pulse current source is designed. The prototype components and parameters are as follows:

Charging power supply: 6 kV DC power supply, which can communicate with the control device through optical fiber.

Solid state switch: 6-stage thyristor in series, maximum peak current 20 kA, repetition frequency triggering frequency set at 10 Hz. Each thyristor has a control unit connected with the control device through optical fiber, which can send and receive trigger and monitoring state instructions and realize high voltage isolation at the same time to ensure safety. The inductance of a single valve is less than 250 nH, and that of multiple valves in parallel is less than 100 nH.

Control device: Developed based on UAPC platform developed by NR Electric, it is composed of CPU board, DSP board and power board. The DSP board is integrated with FPGA module, and the main automatic triggering logic is designed in this board. Program processing cycle <100 us, FPGA trigger accuracy is ns level. A dynamic pressure equalization triggering mode with adaptive adjustment is designed to ensure the consistency of valve group triggering.

Energy storage capacitor: metal film capacitor, stainless steel shell, good explosion-proof performance, high energy storage density, capacitance value of 150 uF, stray inductance <40 nH.

The photo of prototype is shown as below (Fig. 3):

Fig. 3 Pulse current source prototype



Fig. 4 Valve bank trigger conformance test

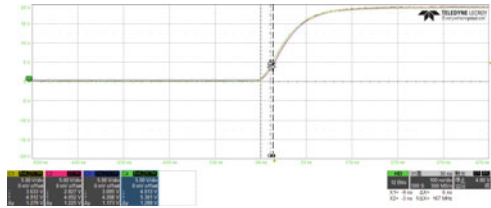


Fig. 5 Pulse current source test platform



4.1 Valve Bank Trigger Conformance Test

The solid state switch is connected by multi-stage thyristor in series. First, the consistency of triggering the solid state switch by the control system is tested, and the test results is shown the difference time of 4 test thyristor is less than 6 ns in Fig. 4.

4.2 Repetition Frequency Test

Building the pulse discharge system, as shown in the figure below (Fig. 5):

Table 1 Re-frequency pulse current test

Item	Result
Max pulse current	158 kA
Re-frequency pulse current	100 kA(1 Hz)
Peak dispersion	3‰
Periodic dispersion	0.000025‰

Note: The discreteness calculation method is to record multiple trigger data and calculate the ratio of variance to the mean value

The test platform uses a fast switch to control the start and stop of pulse power supply, uses current limiting resistance to protect the charging power supply and energy storage capacitor, and uses Roche coil to test the current, 1A/0.05 mV; The voltage is measured by an isolated high voltage probe: 1000 V/1 V. The control device is connected with the solid state switch by optical fiber, and the charging power is also communicated by optical fiber.

The test results are as follows (Table 1):

The solid state switch adopts single series thyristor, which can reach 158 kA peak current, and the two series in parallel can reach more than 300 kA.

The repetition frequency test finished the 1 Hz/100 kA test. Due to the limitation of charging power source, the test of higher trigger frequency and current has not been carried out.

The peak dispersion is mainly controlled by the voltage stability of the charging power supply. After adjustment, it should be within 3‰.

The consistency of cycle triggering is very good, which can be controlled at 0.000025‰, which can meet the requirements of most applications with repeated frequency.

5 Conclusion

Through the research of capacitive pulse power supply based on solid state switch type, design and manufacture a high current and high di/dt pulse current source which can realize repetition frequency trigger. The trigger consistency, cycle trigger accuracy, peak trigger accuracy and maximum peak current all meet the design requirements and have the prospect of practical application. The disadvantage lies in the charging power supply. It is necessary to improve the charging speed and voltage stability of the charging power supply, which can further improve the repetition frequency rate and peak current of the pulse current source and reduce the peak dispersion.

References

1. Han, M., Zou, X.B., Zhang, G.X.: *Technical Basis of Pulse Power*, 1st edn. Tsinghua University Press, Beijing (2010). (in Chinese)
2. Zhou, Z.S.: *Research on Characteristics of High Power Semiconductor Devices in Capacitive Energy Storage Pulse Power Source*, 1st edn. Nanjing University of Science and Technology, Nanjing (2010). (in Chinese)
3. Tsz, T., Chase, W., Matthew, K., Stephen, B.: SiC GTOs thyristor for long term reliability on pulsed power application test. In: *IEE Pulsed Power Conference 2021*, pp.1–4. IEEE, Denver (2021)
4. Mi, Y., Chen, J., Xu, N., Dai, J.: High frequency nanosecond pulse generator based on modular multilevel converter structure with auxiliary charging branch. *Trans. China Electrotechn. Soc.* **36**(2), 435–444 (2021). (in Chinese)
5. Hu, Y., Bao, J., Zhu, J.J., Zhu, C.Y., Cen, Z.N.: The finite difference time domain simulation of the distribution of irreversible electroporation ablation area in liver tissue by nanosecond electrical pulse. *Trans. China Electrotechn. Soc.* **36**(18), 3841–3850 (2021). (in Chinese)
6. Zhou, J.L., Shen, A., He, J.J.: Research on a high power and high repetition frequency pulsed laser power source. *Electron. Design Eng.* **30**(6), 151–155 (2022). (in Chinese)
7. Zhang, S.C.: Progress and prospect of civil pulse power source. *High Voltage Techno.* **35**(3), 618–631 (2009). (in Chinese)
8. Loeffler, M., Neumann, J.: Pulsed power from a German perspective. In: *IEE Pulsed Power Conference 2001*, pp.1–11. IET, London (2001)
9. Chinari, O., Kengo, N., Wang, D.Y., Mikiya, M., Ritsuo, T., Yoichi, I., Rieko, K., Takayuki, N., Kenji, N., Takayasu, N., Takao, N.: Inactivation of anisakis larva using pulsed power technology and quality evaluation of horse mackerel meat treated with pulsed power. *Fish. Sci.* **88**, 337–344 (2022)
10. Koichi, T., Katsuyuki, T., Nobuya, H., Wang, D.Y., Takayuki, O.: Pulsed power applications for agriculture and food. *Rev. Modern Plasma Phys.* **5**(12), 1–12 (2021)

Monitoring Method of Power Data Asset Operation Platform Based on Visualization Technology



Yingwei Liang  and Zewu Peng 

Abstract In the power data asset operation platform, it will be affected by the data edge distribution, data correlation and data drift value. The monitoring ARL value changes greatly and the monitoring performance becomes worse. Therefore, a monitoring method of power data asset operation platform based on visualization technology is proposed. The parallel coordinate visualization method in visualization technology is adopted to visualize the data of power data asset operation platform through five steps: preprocessing data, rearranging dimensions, clustering, modifying dimension labels and interactive technology; Determine the relationship between data samples and observations, use control chart technology, give the likelihood function of control chart monitoring platform data, construct platform monitoring control chart statistics, and monitor the power data asset operation platform according to the control chart function and control line calculation function. The experimental results show that its ARL value changes little, and is basically not affected by data edge distribution, data correlation and data drift, so it has better monitoring performance.

Keywords Visualization technology · Power data · Data assets · Asset operation · Operation platform · Platform monitoring

1 Introduction

As an inevitable trend for power development, the digitization of power information generates power data known as an important part of data resources [1, 2]. Therefore, electric utilities investigate and process power data by studying its power data asset operation (PDAO) platform for integration, while generate analysis results of power system operation for users to quickly and accurately understand the power system operation, ensuring the power system operation with countermeasures according to the data analysis results [3]. However, the PDAO platform keep growing with

Y. Liang (✉) · Z. Peng
Guangdong Power Grid Co., Ltd., Guangzhou 510000, China
e-mail: liang_yingwei@163.com

© Beijing Paiké Culture Commu. Co., Ltd. 2023
X. Dong et al. (eds.), *The proceedings of the 10th Frontier Academic Forum of Electrical Engineering (FAFEE2022)*, Lecture Notes in Electrical Engineering 1054, https://doi.org/10.1007/978-981-99-3408-9_69

complexity, high frequency of change, and diversification of user needs, more “dirty data” such as errors, redundancy and ambiguity emerged, interrupting the operation of power data assets in platform operation [4]. Therefore, it is necessary to study the monitoring technology of the PDAO platform, identify and clean up the “dirty data” timely.

Many domestic and international organizations are researching monitoring methods of PDAO platform in terms of adaptive control charts, cumulative sum (CUSUM) control charts, Shewhart control charts, Hotelling’s T^2 , X^2 control charts, MNP, hybrid models, unsupervised learning methods, k control charts [5]. As in Ref. [6], researchers took traffic video big data as the research object, designing monitoring parallel algorithms with Hadoop to detect abnormality in the video data to monitor traffic video data. As in Ref. [7], with high-dimensional nonlinear contour data as the research object, researchers process data to reduce dimension with LLE algorithm, before applying the SVDD algorithm to monitor the contour data extraction in real time. However, there is still problem of drastic changes in the ARL value of the platform monitoring during the monitoring of PDAO platform, reducing the monitoring performance of the monitoring method.

To this end, a monitoring method of the platform based on visualization technology is proposed.

2 A Monitoring Method of Power Data Asset Operation Platform Based on Visualization Technology

2.1 Visualizing Operation Platform Data Based on Visualization Technology

In this study, the parallel coordinate visualization method is adopted to visualizing data for PDAO platform. The specific process is as follows:

1. Data preprocessing: Use Z-score for standard preprocessing of platform data with the function in the following equation:

$$X' = \frac{X - \bar{X}}{\sigma} \quad (1)$$

In Eq. (1), X' denotes the platform data after standard preprocessing; X denotes the platform dataset; \bar{X} denotes the mean of X ; and σ denotes the variance of X [8].

2. Dimensional rearrangement: It is mainly to determine the dimensional relationship between data in the dataset. For this purpose, there are three steps, namely first dimension selection, dimensional correlation calculation and dimensional rearrangement according to the process as follows:

- 1) First dimension selection. The platform data are decomposed according to the platform data after standard pre-processing, as shown in Eq. (1), selecting the first dimension in the data by singular value decomposition, calculated as follows:

$$F = RHU^T \tag{2}$$

In Eq. (2), F denotes singular values, and arbitrary matrices as well; T denotes right singular vector; R is left singular matrix; H is singular composition matrix; U is right singular matrix.

- 2) Calculate dimension correlation. Based on the first dimension selected in Eq. (2), data correlation is calculated to rank the optimal data dimension. Due to the certain linear data relationship, the correlation coefficient is used to calculate the data correlation, as shown in the following equation:

$$r = \frac{\sum_{i,j=1}^n (x_j - \bar{X})(x_i - \bar{X})}{\sqrt{\sum_{j=1}^n (x_j - \bar{X})^2} \sqrt{\sum_{i=1}^n (x_i - \bar{X})^2}} \tag{3}$$

In Eq. (3), x_j denotes the j th data in X ; x_i denotes the i th data in X ; n denotes the number of data in the dataset; and r denotes the data correlation with a threshold value of $[-1, 1]$ [9]. As the formula shown in Eq. (3), x_j is positively correlated with x_i when $R > 0$; conversely, it is negatively correlated.

- 3) Rearrange dimensions. Adopt the formula shown in Eq. (3) to calculate the data correlation in X in pairs and form a $m * m$ -dimensional similarity matrix R :

$$R = \begin{pmatrix} r_{11} & \dots & r_{1m} \\ \vdots & \ddots & \vdots \\ r_{m1} & \dots & r_{mm} \end{pmatrix} \tag{4}$$

In Eq. (4), the values of $r_{11} \dots r_{mm}$ and $r_{1m} \dots r_{m1}$ denoted dimensional contribution, are calculated from Eq. (2); the values other than $r_{11} \dots r_{mm}$ and $r_{1m} \dots r_{m1}$ as the absolute values of r , denote dimensional similarity.

In Eq. (4), the matrix is symmetric, and for this reason, the larger on between $r_{11} \dots r_{mm}$ and $r_{1m} \dots r_{m1}$ is selected as the first data dimension, and then select the correlation coefficient mostly correlated with the first dimension as the second dimension of the rearranged dimension. Based on

this process, all data dimensions are identified and sorted in descending order to complete the dimensional rearrangement of the data.

3. Data clustering: mainly for mining data information. To this end, cluster the platform data with K-means clustering method by the following clustering process:

- 1) From the rearranged data, N th data vectors \vec{x}_N are randomly selected as the initial clustering center O of data clustering;
- 2) The Euclidean distance d between \vec{x}_N and O is calculated as follows:

$$d = \sqrt{\sum_{i=1}^n (x_{1i} - x_{2i})^2} \quad (5)$$

In Eq. (5), $x_{1i} \neq x_{2i}$ denotes the two data vectors in m dimensions [10].

- 3) \vec{x}_N is assigned to the corresponding category with the minimum d according to the calculation result of Eq. (5);
 - 4) Reselect clustering centers;
 - 5) Repeat steps 2) and 3) until $\operatorname{argmin} \sum_{j=i}^N \sum_{x_j \in X} \|x_j - \bar{X}\|$ is satisfied, with argmin indicates that the minimum value function is taken. Output data clustering results.
4. Modifying dimension labels: After processing the above three steps, display the correlation of data dimensions by dimensional similarity size and name labels.
 5. Interactive technology: In order to realize the interaction between users and data, use scaling interactive technology to scale data information and realize interactive data visualization.

2.2 Monitoring Power Data Asset Operation Platform

Adopt visualized platform data by the technology described the previous subsection, monitor the power data asset operation platform with the control chart techniques. To this end, it is assumed that the visualization data sample of the power data asset operation platform collected at the j th moment is $\{(x_i, y_{ij}), i = 1, 2, \dots, n\}$, where x_i denotes the i th platform visualization data sample; y_{ij} denotes the observation of x_i collected at the j th moment. When the data sample process is under control, y_{ij} and x_i have the following relationship:

$$y_{ij} = a_0 + a_1 x_i + \varepsilon_{ij} \quad (6)$$

In Eq. (6), a_0, a_1 denote the controllable parameters of the control chart; ε_{ij} denotes the standard normal random variable [11]. Get the likelihood function of the control chart monitoring platform according to the relation shown in Eq. (6):

$$\begin{aligned} \gamma(Ln, kn) = & -2(\gamma_{max}^{(0)} - \gamma_{max}^{(1)}) = \sum_{j=L+1}^k \sum_{i=1}^n \left[\frac{y_{ij} - a_0 - a_1x}{\sigma^2} \right]^2 \\ & - (k - L)n \left[1n \left(\frac{\sigma_{(k-L)n}^2}{\sigma^2} \right) + 1 \right] \end{aligned} \tag{7}$$

In Eq. (7), k denotes the number of data visualization samples collected from the platform, $L \in k$ denotes the L group of samples, $\gamma_{max}^{(0)}$ denotes the maximum value of the log-likelihood function in the controllable state of the control chart, and $\gamma_{max}^{(1)}$ denotes the value of the pairwise maximum likelihood function corresponding to the data variation point.

According to the likelihood function shown in Eq. (7), the maximum likelihood function value $\gamma_{max,k}$ for the sample of k groups of data is defined as:

$$\gamma_{max,k} = \max_{0 \leq L < k} \gamma(Ln, kn) \tag{8}$$

The platform monitoring control chart statistic $G(Ln, kn)$ developed with the maximum likelihood function shown in Eq. (8), is shown in the following equation:

$$G(Ln, kn) = \max[0, \eta \cdot \gamma(Ln, kn) + (1 - \eta)\bar{X}((t - 1)n, kn)] \tag{9}$$

In Eq. (9), η denotes the smooth parameter; $\gamma'(Ln, kn)$ denotes the normalized likelihood function. According to the control chart statistic shown in Eq. (9), the obtained expression for the control chart function is:

$$G_{max}(kn) = \max_{0 \leq x \leq 1} G(Ln, kn) \tag{10}$$

Given the false alarm rate λ of the control chart, the control line calculation function for the control chart determined based on the control chart $G_{max}(kn)$ is:

$$\begin{cases} \gamma[G_{max}(kn) > I_k(\lambda) | G_{max}(Mn) \leq I_M(\lambda), 1 \leq M < k] = \lambda & \text{for } k > 1 \\ \gamma[G_{max}(n) > I_1(\lambda)] \end{cases} \tag{11}$$

In Eq. (11), I_k denotes the control line; M denotes the number of sample data.

According to the calculation process of Eqs. (9)–(11) above, after monitoring the platform data samples, calculate the $G_{max}(kn)$ value and the sizes of $G_{max}(kn)$ value, compare the I_k value. If $G_{max}(kn) \leq I_k$, the platform data assets are in normal operation and the platform data continues to be monitored; if $G_{max}(kn) > I_k$ the platform data assets operation is judged to be in trouble and the first problem alert is issued, thus realizing the monitoring of the power data assets operation platform.

3 Simulation Experiment

Select the MSTM control chart-based monitoring method and the Hotelling’s T²-based monitoring method as the comparison methods for this experiment, with the power data asset operation platform data as the object of this experimental study to verify the monitoring method of the PDAO platform based on visualization technology of this study on the bootstrap simulation platform.

3.1 Experimental Data

The experimental data selected from the PDAO platform for this experiment are shown in Fig. 1.

Based on the experimental data shown in Fig. 1, the monitoring alarm signal is set to start when the mean value of the platform data drifts. Its drift criterion is shown in the following equation:

$$\begin{cases} \bar{x}_i = \frac{1}{n} \sum_1^n x_j \\ \sigma = \frac{1}{n-1} \sum_1^n (x_i - \bar{x}_i)(x_i - \bar{x}_i)' \\ B = (x_i - \bar{x}_i)' \sigma^{-1} (x_i - \bar{x}_i) > f \end{cases} \tag{12}$$

In Eq. (12), *B* denotes the alarm signal given by the method.

$X = \{x_1, x_2, \dots, x_i, \dots\}$ denotes the experimental dataset shown in Fig. 1; x_i denotes the experimental dataset of class *i*; \bar{x}_i denotes the mean of the data in the experimental data set of class *i*; σ denotes the covariance matrix; *f* denotes the monitoring curve of the method; n_i denotes the number of data in the experimental dataset of class *i*; $x_j \in x_i$ denotes the *j* th data in the experimental dataset of class *i*.

According to the generation conditions of data alarm signals shown in Eq. (12), alarm signals are designed for each of the three monitoring methods to monitor the experimental data shown in Fig. 1.

3.2 Experimental Indicators

The experiment selects the ARL average run length as the comparison index of the monitoring effect under the three methods, which is mainly to indicate the controlled average chain length of the process generated during the monitoring of data by such three methods. Its calculation formula is shown in the following equation:

$$A = \frac{1}{p} \tag{13}$$

In the Eq. (12), A denotes the controlled average chain length of the monitoring process; p denotes the probability of the first monitoring alarm error during the monitoring of experimental data by the three monitoring methods.

Based on Eq. (12), the larger the value of A , the longer the monitoring method used to monitor the platform data, the better its monitoring effect. Since the smaller the p value shown in Eq. (12), the smaller the monitoring loss, the significance level of the p value was set to 0.005 in this experiment, and the initial value of the A value was 410 chains.

3.3 Experimental Environment

The experimental data shown in Fig. 1 were monitored by the three groups of methods selected for this experiment, and the correlation degree of the data was classified as moderate correlation degree and strong correlation degree, with values taken as 0.5 and 0.8, respectively. The two experimental environments are designed as follows:

Simulation environment 1: For the controlled data, it exhibits an edge distribution expectation value of 1, showing an edge distribution state. Therefore, the drift value size of the experimental data was set to (0,0), (0,1), (0,1.5), (0,2), (0,4), (0,5), and (0,5.5) for the simulation according to the data drift calculation formula shown in Eq. (12).

Simulation environment 2: For the controlled data, it exhibits an edge distribution expectation value of 2, showing two edge distribution states. Based on Eq. (12), the drift value size of the experimental data was set to (0,0), (1,1), (1.5,1.5), (2,2), (4,4), (5,5), and (5.5,5.5) for the simulated experiments.

In the above two experimental environments, three methods were used to monitor data of two correlation degrees, and 10,000 random simulations were executed on the bootstrap simulation platform by R language.

Power data asset operation platform					
Time	Voltage/V	Current /A	Active power/W	Current power	Power factor
10:30:00	525.00	1.12	587.50	37468.5	0.9
10:35:00	685.00	1.26	865.00	32896.5	0.9
10:40:00	65.00	1.17	762.50	43326	0.9
10:45:00	58.00	1.08	625.00	42874.9	0.9
10:50:00	52.00	1.06	552.00	45445.8	0.9
10:55:00	525.70	1.12	588.60	39578.7	0.9
11:00:00	685.90	1.26	866.40	34197.9	0.9
11:05:00	650.80	1.17	763.80	41890	0.9
11:10:00	580.40	1.08	625.90	48228.2	0.9
11:15:00	520.80	1.06	553.10	52313.3	0.9
11:20:00	244.20	51.30	1222.20	45398.1	0.9
11:25:00	242.90	42.20	8540.50	52152	0.9
11:30:00	274.00	33.70	5943.40	47688	0.9
11:35:00	243.30	7.20	1158.70	51492.8	0.9
11:40:00	243.20	1.30	156.80	44673.8	0.9
11:45:00	241.10	168.10	39696	40528.9	0.9

Fig. 1 Experimental data

3.4 Comparison of Monitoring Effects

3.4.1 Simulation Environment 1

In simulated environment 1, when the data correlation coefficient is 0.5, the monitoring effect of the platform data shown in Fig. 1 monitored by the three monitoring methods is shown in Table 1.

As seen in Table 1, the ARL values of the research method are 0.15 chains and 0.81 chains higher compared to the two comparison methods selected for this experiment without drift value for the data shown in Fig. 1. The difference is insignificant.

However, when the data drift value is greater than 5, the difference between the ARL values of the research method compared to the ARL values of the two comparison methods selected for this experiment has reached 30 and keep increasing. Thus, with a data correlation coefficient of 0.5, the research method still has a superior monitoring effect for ARL values if the platform data has drift values greater than 5.

When the data correlation coefficient is 0.8, the monitoring effect of the platform data shown in Fig. 1 monitored by the three monitoring methods is shown in Table 2.

Table 1 Comparison table of the monitoring effect when the correlation coefficient is 0.5 (chain)

Data drift value	Research method	Monitoring method based on MSTM control chart	Monitoring method based on Hotelling's T^2
(0.0)	399.02	398.87	398.21
(0.5.5)	388.58	278.27	299.12
(0.5)	390.57	321.85	357.85
(0.4)	391.91	357.62	369.91
(0.2)	394.67	393.38	392.26
(0.1.5)	396.88	395.41	396.64
(0.1)	397.46	395.69	396.67

Table 2 Comparison table of the monitoring effect when the correlation coefficient is 0.8(chain)

Data drift value	Research method	Monitoring method based on MSTM control chart	Monitoring method based on Hotelling's T^2
(0.0)	402.42	401.27	400.92
(0.5.5)	390.49	318.42	313.09
(0.5)	390.91	341.66	316.72
(0.4)	391.13	353.53	351.19
(0.2)	397.91	391.32	396.86
(0.1.5)	397.96	391.51	397.00
(0.1)	397.99	391.80	397.18

As seen in Table 2, there is no drift value data when the value of data correlation coefficient is 0.8. In contrast, the ARL value increases significantly without drift value data when the data correlation coefficient is 0.5. Moreover, when the data drift value is greater than 5, the ARL values of the three methods at 0.8 are generally higher than the ARL values at 0.5, with the research method being the most significant. As a result, the higher the degree of data correlation, the better the monitoring performance of the monitoring method.

In addition, the research method has a watershed data drift value of 3 for strongly correlated platform data under simulated environment 1 conditions. For drift values greater than 3, the difference in ARL values by the research method compared to those by the MSTM control chart-based monitoring method and the Hotelling’s T^2 -based monitoring method reaches more than 50 chains; for drift values less than 3, the difference is only between [1, 2]. As a result, the higher the degree of data correlation, the better the research method monitoring platform effect.

3.4.2 Simulation Environment 2

In simulated environment 2, when the data correlation coefficient is 0.5, the monitoring effect of the platform data shown in Fig. 1 monitored by the three monitoring methods is shown in Table 3.

As seen in Table 3, when the value of the data correlation coefficient is 0.5, the ARL values by the research method in the environment 2 condition are extremely close to those under the environment 1 conditions and are not affected by the marginal distribution of the data. For drift values greater than 5, the difference in ARL values under the environment 2 and the environment 1 conditions by the research method compared to those by the MSTM control chart-based monitoring method and the Hotelling’s T^2 -based monitoring method reaches more than 20 chains; when the platform is monitored by the research method, the results are affected by the edge distribution of the platform data.

Table 3 Comparison table of the monitoring effect when the correlation coefficient is 0.5 (chain)

Data drift value	Research method	Monitoring method based on MSTM control chart	Monitoring method based on Hotelling’s T^2
(0.0)	399.02	398.87	398.21
(5.5, 5.5)	388.16	314.67	329.12
(5.5)	392.14	344.76	345.24
(4.4)	393.79	369.77	374.72
(2.2)	396.45	395.55	393.63
(1.5, 1.5)	397.88	396.75	396.22
(1.1)	398.00	397.06	396.449

Table 4 Comparison table of the monitoring effect when the correlation coefficient is 0.8 (chain)

Data drift value	Research method	Monitoring method based on MSTM control chart	Monitoring method based on Hotelling's T^2
(0.0)	402.42	401.27	400.92
(5.5, 5.5)	388.70	297.83	270.81
(5.5)	391.79	324.87	296.17
(4.4)	393.66	327.97	349.74
(2.2)	396.39	389.50	387.29
(1.5, 1.5)	396.77	394.96	393.50
(1.1)	396.99	395.34	394.48

To further verify the effect of data edge distribution on the monitoring effect, the monitoring effect of the platform data shown in Fig. 1 monitored by the three monitoring methods is shown in Table 4 when the data correlation coefficient is 0.8.

As seen from Table 4, when the data correlation coefficient is 0.8, the ARL values for monitoring strongly correlated data by the MSTM control chart-based monitoring method and Hotelling's T^2 -based monitoring method are, in turn, smaller than those for moderately correlated data, which are different from those for environment 1. Therefore, the MSTM control chart-based monitoring method and Hotelling's T^2 -based monitoring method T^2 -based monitoring methods are more influenced by the data edge distribution. The ARL values for monitoring strongly correlated data under the research method differ very little from the ARL values at environment 1 and are not affected by the data edge distribution. It proves that platform monitoring by the research method is not affected by the distribution of the platform data.

Combining the above two sets of experimental results, it showed that monitoring the PDAO platform data by the research method is basically unaffected by data edge distribution, data correlation and data drift values, and has superior control performance.

4 Conclusion

Extracting data from the visualized the PDAO platform will enable visualized monitoring of the platform through graph control technology. It is experimentally verified that this research method is mostly unaffected by data edge distribution, data correlation and data drift values, enhancing the control performance of the operation platform.

However, this research can't monitor of small drift data properly in the platform. In the future research, it is also necessary to study in depth the monitoring techniques for small drift data in the platform, and further improve the monitoring methods for small drift data in the platform.

References

1. Ge, F., Wang, J.: The design and implementation of urban water data operation platform. *Water Wastewater Eng.* **56**(1), 367–370 (2020). (in Chinese)
2. Xiang, D., Zhou, R., Huang, Z., et al.: Study on key technologies of electricity market trading platform based on hybrid cloud computing platform. *J. Shandong Agric. Univ. (Nat. Sci. Edn.)* **52**(4), 704–708 (2021). (in Chinese)
3. Li, F.: Anomaly detection based on deep support vector data description under surveillance scenarios. *Infrared Laser Eng.* **50**(9), 372–378 (2021). (in Chinese)
4. Huang, L., Zhuang, W., Long, S., et al.: Research and application of data monitoring technologies on electricity trading platform. *Power Syst. Technol.* **45**(8), 3200–3206 (2021). (in Chinese)
5. Rui, D.: Monitoring and evaluation technology for high resolution processing of seismic data. *Lithol. Reserv.* **32**(1), 94–101 (2020). (in Chinese)
6. Li, X.: Big video monitoring scheme of traffic video based on Hadoop. *Chin. J. Liquid Cryst. Displays* **35**(11), 1204–1209 (2020). (in Chinese)
7. Liu, Y., Liang, X., Zhao, Z., et al.: A real-time monitoring method for high-dimensional nonlinear contour data based on LLE-SVDD. *Statist. Dec.* **36**(19), 20–24 (2020). (in Chinese)
8. Chu, J., Cao, M., Zhao, L., et al.: Bibliometrics and visualization analysis of EwE model based on CiteSpace. *Chin. J. Appl. Ecol.* **32**(2), 763–770 (2021). (in Chinese)
9. Xue, B.: Nurbol. Research on visual analysis method based of multi-view collaboration on network traffic data. *J. Chin. Comput. Syst.* **41**(9), 1893–1897 (2020). (in Chinese)
10. Qiong, Z., Wang, Y., Tu, C., et al.: Color computing in data visualization. *J. Comput. Aided Des. Comput. Graph.* **32**(10), 1549–1559 (2020). (in Chinese)
11. Feng, X., Yang, Q., Shi, L., et al.: Critical memory data access monitor based on dynamic strategy learning. *J. Comput. Res. Develop.* **56**(7), 1470–1487 (2019). (in Chinese)

Primary Frequency Modulation Study of Receiver System with High Proportion Power Electronic Power Supplies



Zexiang Zhu, Chao Fu, Junfeng Qi, Zhuo Liu, and Fei Tang

Abstract New energy, DC and other power electronic power supplies are connected to the grid through converters, weakening the equivalent inertia of the system and reducing the frequency regulation capacity, leading to the prominent problem of primary frequency regulation of the receiving-end grid. In this paper, we analyze the main contradictions of the frequency impact of high proportion power electronic power supplies on the receiving system by focusing on the control mode of power electronic power supplies. By constructing the frequency response model, the frequency response characteristics of the system and the principles followed when the power electronic power supply is involved in primary frequency regulation are analyzed. Finally, a four-machine, two-zone system containing wind power, photovoltaic, energy storage and DC is built by BPA to verify the effect of different control strategies of power electronic power supply on the primary frequency regulation of the system.

Keywords Power electronic power supply · Frequency response · Receiving-end grid · Primary frequency modulation

Z. Zhu · C. Fu

CSG Electric Power Research Institute, China Southern Power Grid, Guang Zhou 510663, China
e-mail: zhuzx@csg.cn

C. Fu

e-mail: fuchao@csg.cn

J. Qi (✉) · Z. Liu · F. Tang

School of Electrical Engineering and Automation, Wuhan University, Wuhan 430072, China
e-mail: qijunfeng@whu.edu.cn

Z. Liu

e-mail: 2018302070205@whu.edu.cn

F. Tang

e-mail: tangfei@whu.edu.cn

© Beijing Paiké Culture Commu. Co., Ltd. 2023

X. Dong et al. (eds.), *The proceedings of the 10th Frontier Academic Forum of Electrical Engineering (FAFEE2022)*, Lecture Notes in Electrical Engineering 1054, https://doi.org/10.1007/978-981-99-3408-9_70

1 Introduction

According to the government's goal of carbon peak in 2030 and carbon neutrality in 2060, the power electronic power system is gradually formed [1]. This weakens the system equivalent inertia, reduces the capacity for active reserve frequency regulation, and deteriorates the system frequency immunity and stability characteristics [2]. Large-scale blackouts due to frequency problems occurred in developed countries such as Australia and the United Kingdom [3, 4]. The problem of power electronic power supply involved in frequency modulation to suppress system frequency disturbance has become a hot research issue nowadays [5].

The main system frequency safety and stability indicators are the rate of change of frequency (RoCoF), the maximum frequency offset, and the steady-state frequency deviation [6]. The traditional power system frequency safety and stability issues are mainly determined by the synchronous generator, and the frequency regulation capability of the synchronous generator determines whether the three indicators of frequency cross the boundary. The large scale of DC feed-in to a typical receiver system and the high penetration of wind power and photovoltaic lead to the equivalent replacement of large scale synchronous generating units, which weakens the frequency regulation capability of synchronous generating units.

The power electronic power supply is connected to the grid through the inverter and the output characteristics are controlled by the power command, which does not satisfy the rotor equation of motion of the synchronous generator [5–7]. Reference [7–9] pointed out that wind power, PV, and DC transmission control systems use P and Q decoupling control, which leads to decoupling the output power from the system frequency, i.e., it does not participate in the system frequency response.

In the reference [10], control methods for power electronic power supply participation in primary frequency regulation are reviewed from the control perspective. Reference [11] considers the new energy FM(frequency modulation) control strategy as well as the effect of penetration rate and establishes the SFR model consistent with the system containing high percentage of power electronic power supply. The FM parameters required to maintain the system frequency safety and stability are calculated by the frequency domain function. Reference [12] proposed indexes to measure the frequency response capability of power electronic power supplies, mainly including the system frequency recovery speed index and the safety stability index of the power supply. It was pointed out that the positive response of new energy units represented by wind turbines to system frequency changes can suppress the maximum change in frequency (RoCoF_{\max}), but it can lead to serious frequency secondary dips problems. Reference [13, 14] points out that DC system operation in the reduced load state can participate in frequency regulation through virtual-droop control, but the economic losses due to DC reduced load operation and those due to emergency faults are yet to be measured. The zoning effect of the DC system leads to the decoupling of the frequency at the sending and receiving ends of the system, but when the DC participates in the frequency response at the receiving end, the DC sending end also generates a power disturbance of the corresponding magnitude. Therefore, the

operating state of the system at the sending end also affects the frequency response capability at the receiving end of the system.

In summary, the power electronic power supply involved in frequency regulation becomes a trend, but the power electronic power supply involved in frequency response has different power sources. Over-response can lead to the subsequent phenomenon of secondary frequency drop. Reference [15, 16] effectively suppressed the frequency secondary drop phenomenon by combining energy storage with wind turbines to participate in frequency regulation, which provides a research reference for future power electronic power sources to participate in frequency regulation with the aid of energy storage.

So this paper firstly analyzes the influencing factors of power electronic power supply grid connection from power electronic power supply control strategy and gets the dominant problem contradiction by sensitivity analysis. Secondly, we study the control method of power electronic power supply involved in frequency response to improve the system frequency stability. Then analyze the possible subsequent frequency disturbance problems in the frequency regulation process. The control method of using energy storage assisted participation in frequency regulation improves the power electronic power supply's own stability as well as avoids the phenomenon of subsequent frequency secondary disturbance of the system. Finally, a four-machine, two-zone model with DC system built by BPA is simulated and verified.

2 Receiving-End Grid Frequency Security Issues

This section analyzes the main influencing factors that cause the frequency stability decrease of the receiving power system in terms of the control strategy of the power electronic power supply and the installed capacity.

2.1 Basic Control Strategies for Power Electronics Power Supplies

Wind turbines, such as DFIG exist rotating devices, are connected to the grid through back-to-back dual PWM converters, and the rotor frequency is decoupled from the system frequency by fast phase-locked control of the rotor-side inverter phase-locked loop.

The DC transmission system asynchronizes the AC system into an AC-DC-AC hybrid system through the rectifier-inverter station at the sender-receiver side to realize the frequency decoupling of the grid at the sender-receiver side. The control targets of the converter at the sending and receiving ends are DC transmission current

I and DC voltage U respectively, which determines the decoupling of transmission active power P from the frequency at the sending and receiving ends.

The PV power system is connected to the grid through the inverter, and its control strategy is similar to the DFIG grid-side inverter and the DC receiver-side inverter control strategy.

So from the point of view of the receiving-end grid, ignoring the internal control links of power electronics, when the frequency problem-led safety and stability problems occur (i.e., not triggering other protective actions of new energy sources such as: low unit voltage, high penetration does not pass), the power electronic power supply behaves externally as a constant power source, or negative impedance mode. Therefore, the external inertia and regulation coefficient are zero.

2.2 Equivalent FM Parameters of the Receiving-End Grid

To maintain the system source-load balance, a large amount of power electronic power supplies connected to the grid at the receiving end will replace the thermal power unit output. Define the ratio of grid-connected capacity to total installed capacity of the system as the penetration rate α of power electronic power supply in the receiving grid:

$$\alpha = \frac{\sum_{j=1}^m S_j}{\sum_{i=1}^n S_i + \sum_{j=1}^m S_j} \quad (1)$$

where n is the number of synchronous units and m is the number of power electronic power units, including wind turbines, feed-in DC and PV units.

The equivalent inertia time constant H_{eq} and the modulation factor R_{eq} of the receiver grid can also be obtained as:

$$\begin{cases} H_{eq} = \frac{\sum_{i=1}^n S_i H_i}{\sum_{i=1}^n S_i + \sum_{j=1}^m S_j} = (1 - \alpha)H \\ \frac{1}{R_{eq}} = \frac{\sum_{i=1}^n S_i \frac{1}{R_i}}{\sum_{i=1}^n S_i + \sum_{j=1}^m S_j} = (1 - \alpha) \frac{1}{R} \end{cases} \quad (2)$$

where, H and R are the inertia time constant, load modulation coefficients of the synchronous unit, respectively.

So the frequency response model of the receiving power system can be obtained as follows:

In the figure, $\Delta P_d(s)$ is the system disturbance power, $\Delta P_G(s)$ is the FM response power, and $\Delta w(s)$ is the system frequency variation. D is the system load damping factor, and K_m , F_H , and T_R are the external equivalent control parameters of the synchronous unit, respectively.

2.3 Identification of Dominant Factors for Frequency Stability of the Receiving-End Grid

According to the frequency response model of the receiving power system shown in Fig. 1, the frequency deviation expression can be obtained as follows.

$$\Delta\omega(s) = \frac{\Delta P_d(s)R(1 + T_R s)}{R(1 + T_R s)(2(1 - \alpha)Hs + D) + (1 - \alpha)K_m(1 + F_H T_R s)} \quad (3)$$

Using Laplace’s initial value theorem and final value theorem, the maximum frequency rate of change of the system, $RoCoF_{max}$, and the frequency steady-state deviation, Δf_s , can be obtained as follows.

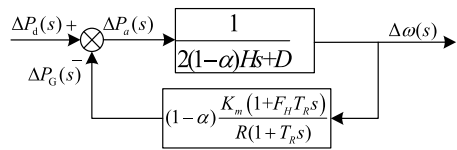
$$RoCoF_{max} = f_N \lim_{s \rightarrow \infty} s \Delta\omega(s) = f_N \frac{1}{1 - \alpha} \cdot \frac{\Delta P_d}{2H} \quad (4)$$

$$\Delta f_s = f_N \lim_{s \rightarrow 0^+} s \Delta\omega(s) = f_N \frac{\Delta P_d}{D + (1 - \alpha) \frac{K_m}{R}} \quad (5)$$

According to Eq. (4), the main influencing factor of $RoCoF_{max}$ is the power electronic power supply penetration rate α . There are more influencing factors of Δf_s in Eq. (5). which can be identified by using the method of sensitivity analysis. The parameters of the system low-order frequency response model are referred to the reference [10]. The results of the sensitivity analysis are shown in the following table (Table 1).

According to the sensitivity analysis, it can be obtained that the main contradiction of the frequency safety of the receiver system of the high proportion power electronic power supply is the disturbance power ΔP_d and permeability α leading to $RoCoF_{max}$ and Δf_s not meeting the frequency safety and stability requirements. The permeability α weakens the system frequency immunity as well as recovery capability by affecting the system equivalent inertia time constant H_{eq} and the equivalent FM modulation coefficient R_{eq} .

Fig. 1 Receiver system frequency response model



3 Power Electronic Power Supply Involved in FM

3.1 Wind Turbine Participation in Frequency Regulation

There are rotating devices in wind turbines, which release rotor rotational kinetic energy during emergency power disturbance, sacrificing rotor speed to provide short-time power support to the system, playing a virtual inertia and virtual sagging support effect of synchronous-like units.

$$\begin{cases} P_{wind} = P_{MPPT} + \Delta P \\ \Delta P = -K_{df} \frac{d\Delta f}{dt} + K_d \Delta f \end{cases} \quad (6)$$

where P_{wind} is the wind turbine power command, P_{MPPT} is the wind turbine power command in normal operating condition, K_{df} is the virtual inertia coefficient, and K_d is the virtual sag coefficient.

The supportable average power at the safe speed of the wind turbine is:

$$\overline{P}_w = \frac{1}{2} \frac{J(w_{r1}^2 - w_{r2}^2)}{T_s} \quad (7)$$

where J is the rotor rotational inertia of the fan, T_s is the fan participation in the frequency response time, w_{r1} , w_{r2} are the rotor speed before and after the fan participation in frequency regulation, respectively.

The wind turbine load shedding standby control sacrifices the economic operation of the system in the normal state and can provide higher support capacity. As shown in Fig. 2, the blade tip speed ratio λ_1 corresponds to w_{r1} under MPPT state, when there is a maximum wind energy utilization coefficient C_{Pmax} , and λ_3 corresponds to w_{r2} under reduced load $d_1\%$, when it corresponds to reduced load wind energy utilization coefficient C_{P_del} . so w_{r2} is obviously larger than w_{r1} , which can provide more power support according to Eq. (7).

Fig. 2 Variation of wind energy utilization coefficient with leaf tip speed ratio

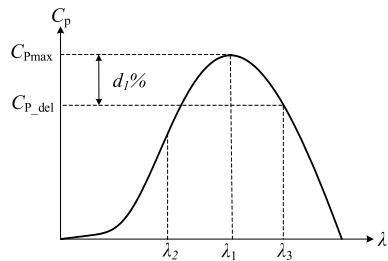
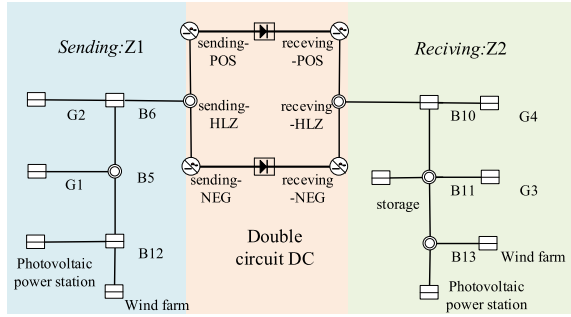


Fig. 3 Four machine-two zero model in BPA



3.2 DC Participation in FM

As described in Sect. 2.1, the DC system is connected to the grid at the receiving end through an inverter, so the virtual frequency regulation strategy applying Eq. (6) can establish the coupling between the DC delivered power and the two AC asynchronous system configuration frequencies. And the DC capacity is several times the capacity of a single wind farm, so the power support capacity is stronger.

Compared to wind turbines, DC has no rotating energy storage elements and no speed protection module, which also determines that frequency regulation can only be performed through load-shedding standby. When the DC is operating at $d_2\%$ load shedding, the DC power response is

$$\begin{cases} P_{HVDC} = P_0 \cdot (1 - d_2\%) + \Delta P \\ \Delta P = \frac{K_p}{1 + T_H s} \Delta f \end{cases} \quad (8)$$

where P_0 is the DC rated power, K_p is the DC FM virtual sag factor, and T_H is the time constant.

The PV plant does not have a rotating energy storage element and participates in a frequency response strategy similar to that of the DC system, which is not repeated here.

3.3 Energy Storage Assisted Participation in Frequency Regulation

When the wind turbine rotates from a frequency lower than or close to the minimum safety threshold, the speed recovery strategy will be activated, which is equivalent to the occurrence of power secondary disturbance.

DC participation in the receiving-end grid frequency regulation, the power of the sending-end grid will also occur corresponding power disturbance problems, so the

actual frequency regulation capacity of the sending-end grid will also determine the effect of the receiving-end grid frequency regulation.

When DC participation in frequency regulation capacity is limited by the frequency regulation capacity of the sending-end grid, the fan starts the speed recovery strategy, the receiver system of high proportion power electronic power supply will have a serious frequency secondary drop phenomenon.

Multi-type energy storage is connected to the grid through the inverter, and the working state is affected by its own SOC.

$$P_{ESS} = \begin{cases} \frac{K_{ESS}}{1 + T_{ESS}s} \Delta f & 20\% < \text{SOC} < 80\% \\ 0 & \text{else} \end{cases} \quad (9)$$

The frequency modulation factor K_{ESS} as well as the time constant T_{ESS} of the energy storage system are shown in Table 2. Multiple types of energy storage respond to different time scales as well as operating costs, and can respond to different phases of the system frequency considering economic factors.

The power electronic power supply replaces the synchronous generator set, although it weakens the system equivalent inertia time constant and the regulation coefficient, but its power electronics fast frequency tracking capability can effectively improve the frequency response capability.

Table 1 Sensitivity parameter calculation table

Parameter variables	Sensitivity	Order of magnitude	Degree
Damping factor D	$-fN \frac{\Delta P_d}{[D+(1-\alpha)K_m/R]^2}$	10^{-2}	Small
Speed governor R	$fN \frac{(1-\alpha)K_m \Delta P_d / R^2}{[D+(1-\alpha)K_m/R]^2}$	10^0	Normal
Power Factor K_m	$-fN \frac{(1-\alpha)\Delta P_d / R}{[D+(1-\alpha)K_m/R]^2}$	10^{-1}	Smaller
Power disturBance ΔP_d	$fN \frac{1}{D+(1-\alpha)K_m/R}$	10^1	Very big
Penetration rate α	$fN \frac{K_m \Delta P_d / R}{[D+(1-\alpha)K_m/R]^2}$	10^1	Big

Table 2 Multi-type energy storage parameters

Parameters	SMES	SCES	FES	EES
K_{ESS}	6	5	4	2
T_{ESS}/s	0.26	0.3	0.35	0.5
Rated power/MW	10	30	20	10
capacity/MWh	30	0.5	5	40
SOC limits/%	20–80			

4 Case Study

In order to verify the relationship between the frequency of the receiving end system and the permeability and power disturbance of the high duty power electronic power supply analyzed in this paper, and the effectiveness of the power electronic power supply participating in frequency modulation, this paper builds a four machine nine node system simulation model through BPA. The area Z1 transmits power to Z2 through DC, which is a typical sending end system and a receiving end system. The output of wind power and PV in Z1 accounts for 30%, and that of wind power, DC and PV in Z2 accounts for 50%. At the same time, Z2 is connected to the energy storage power station (Fig. 3).

Set the following three simulation cases:

1. Wind power, DC power and photovoltaic power do not participate in frequency modulation. Under different power electronic power supply penetration rates, the same power disturbance event occurs in the receiving end system, and the frequency response effect of the transmitting and receiving end systems is different;
2. When the power electronic power supply participates in frequency modulation, the frequency response effect of the receiving end system under different power disturbance events;
3. Research on energy storage assisting in frequency modulation and suppressing secondary drop of system frequency.

4.1 Case 1

The frequency change curve of the transmitter receiver system when 0.5, 0.8 and 1.1 pu power disturbances occur in the receiver system is shown in Fig. 4a. Due to the partition effect of the DC system, after the system frequency of the receiving end is unstable, the frequency disturbance of the sending end system is within 0.05 Hz, and the frequency of the sending end and the receiving end is divided asynchronously.

When no additional frequency modulation control is added, the DC transmission power disturbance caused by frequency disturbance is within 5 MW, which is caused by the phase-locked loop disturbance caused by the voltage fluctuation at the DC feeding point, as shown in Fig. 4b. It is precisely because of the drop in DC power that the frequency at the sending end fluctuates, as shown by the dashed line in Fig. 4a. However, the frequency of the sending end system is not affected by the accident disturbance of the receiving end system when there is no serious accident disturbance such as commutation failure in the DC.

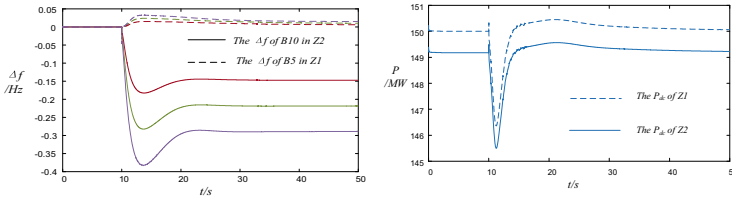


Fig. 4 a. Case 1 frequency variation diagram under different power disturbances. b. Case 1 DC output variation diagram

4.2 Case 2

When power electronic power sources such as DC and wind power participate in frequency modulation, power disturbances of 0.5 and 1.1 pu will occur in the receiver system. The system frequency of the transmitter receiver system is shown in Fig. 5a. When DC participates in the frequency response of the receiving end system, the additional transmission power is equivalent to the power shortage of the transmitting end system, as shown in Fig. 5b. Therefore, when the power disturbance is 0.5 pu, compared with case 1, the frequency of the sending end system fluctuates greatly, but it is within the stability threshold of 0.15 Hz. When the disturbance amplitude reaches 1.1pu, the steady-state frequency deviation of the sending end system approaches 0.2 Hz, and the frequency safety and stability margin decreases. At the same time, affected by the rated DC capacity (175 MW), the lowest frequency of the receiving end system and the steady-state frequency deviation are close to the instability sideline. Therefore, at this time, only relying on DC and other power electronic power supplies to participate in frequency modulation may cause subsequent serious frequency secondary accidents.

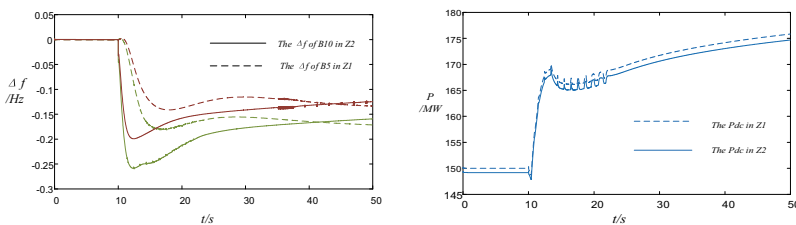


Fig. 5 a. Case 2 frequency variation diagram under different power disturbances. b. Case 2 DC output variation diagram

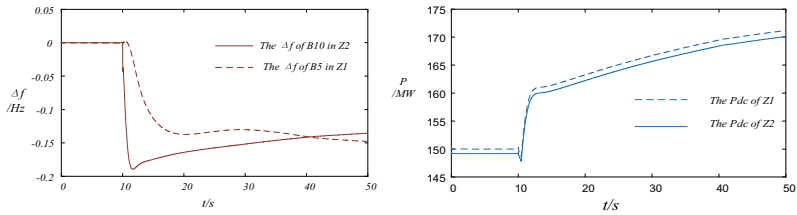
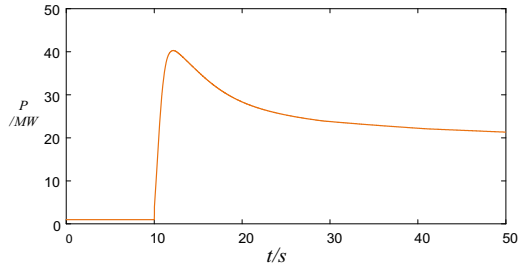


Fig. 6 a. Frequency change diagram of case3. b. Case 3 DC output variation diagram

Fig. 7 Case 3 energy storage output change diagram



4.3 Case 3

In case 2, when the accident disturbance of the receiving end system is large, it may cause the frequency instability of the transmitting and receiving end system. At this time, energy storage is introduced to participate in auxiliary frequency modulation. When there is a 1.1 pu power shortage in the system, the frequency change of the transmitter receiver system is shown in Fig. 6a. Compared with cases 1 and 2, the introduction of energy storage improves the lowest point of system frequency and the steady-state frequency margin.

The maximum output power of DC shall be kept below the rated power as shown in Fig. 6b. Compared with case 2, it is equivalent to energy storage to make up for DC output deficiency in time, as shown in Fig. 7.

5 Conclusion

The equivalent inertia and the equivalent adjustment coefficient of the receiving end system of the high duty electronic power supply decrease, which leads to the reduction of the primary frequency response ability. Aiming at the control strategy of power electronic power supply, this paper considers the frequency security and stability of

the sending and receiving end, analyzes the frequency stability of the receiving end system and the solutions. The main research conclusions are as follows:

1. The main contradiction of frequency safety is disturbance power ΔP_d and permeability α , resulting in rocof_{\max} and Δf_S does not meet the frequency safety and stability requirements.
2. When the power electronic power supply participates in frequency modulation, it is affected by the frequency stability of the sending end system and the power upper limit of the power electronic power supply such as DC, and there is a risk of serious secondary frequency disturbance in the later period of the frequency response of the receiving end system;
3. Reasonable setting of energy storage and frequency modulation capacity will improve the safety and stability margin of system frequency on the basis of ensuring the safe operation of DC and other power electronic power supplies.

Acknowledgements This research was supported by State Key Laboratory of HVDC, Electric Power Research Institute, China Southern Power Grid (grand number SKLHVDC-2021-KF-04).

References

1. Hansen, K., Breyer, C., Lund, H.: Status and perspectives on 100% renewable energy systems. *Energy* **175**, 471–480 (2019)
2. Delkhosh, H., Seifi, H.: Power system frequency security index considering all aspects of frequency profile. *IEEE Trans. Power Syst.* **36**(2), 1656–1659 (2021)
3. Australian Energy Market Commission. Mechanisms to enhance resilience in the power system—review of the South Australian black system event. Sydney South NSW: Australian Energy Market Commission (2019)
4. Appendices to the technical report on the events of 9 August 2019. <https://www.nationalgrid.co.uk/document/152351/download>
5. Tan, B., Zhao, J., Netto, M., Krishnan, V., Terzija, V., Zhang, Y.: Power system inertia estimation: review of methods and the impacts of converter-interfaced generations. *Int. J. Electric. Power Energy Syst.* **134** (2022)
6. Qi, J., Tang, F., Xie, J., Li, X.: Effect of DFIG under droop control on center migration of out-of-step oscillation. In: 2021 IEEE 5th Conference on Energy Internet and Energy System Integration (EI2), pp. 2970–2974 (2021)
7. Bidadfar, A., Saborío-Romano, O., Sakamuri, J.N., Cutululis, N.A., Akhmatov, V., Sørensen, P.E.: On feasibility of autonomous frequency-support provision from offshore HVDC grids. *IEEE Trans. Power Deliv.* **35**(6), 2711–2721 (2020)
8. Yoo, J.I., Kang, Y.C., Muljadi, E., Kim, K.-H., Park, J.-W.: Frequency stability support of a DFIG to improve the settling frequency. *IEEE Access* **8**, 22473–22482 (2020)
9. Wu, Z., et al.: State-of-the-art review on frequency response of wind power plants in power systems. *J. Mod. Power Syst. Clean Energy* **6**(1), 1–16 (2018)
10. Qi, J., Tang, F., Xie, J., Li, X., Wei, X., Liu, Z.: Research on frequency response modeling and frequency modulation parameters of the power system highly penetrated by wind power. *Sustainability* **14**, 7798 (2022)
11. Li, H., Wang, J., Du, Z., Zhao, F., Liang, H., Zhou, B.: Frequency control framework of power system with high wind penetration considering demand response and energy storage. *J. Eng.* **2017**, 1153–1158 (2017)

12. Shi, Q., Li, F., Cui, H.: Analytical method to aggregate multi-machine sfr model with applications in power system dynamic studies. *IEEE Trans. Power Syst.* **33**(6), 6355–6367 (2018)
13. Ambia, M.N., Meng, K., Xiao, W., Al-Durra, A., Dong, Z.Y.: adaptive droop control of multi-terminal HVDC network for frequency regulation and power sharing. *IEEE Trans. Power Syst.* **36**(1), 566–578 (2021)
14. Rouzbehi, K., Zhang, W., Ignacio Candela, J., Luna, A., Rodriguez, P.: Unified reference controller for flexible primary control and inertia sharing in multi-terminal voltage source converter-HVDC grids. *IET Gener. Transm. Distrib.* **11**, 750–758 (2017)
15. Sanchez, F., Cayenne, J., Gonzalez-Longatt, F., Rueda, J.L.: Controller to enable the enhanced frequency response services from a multi-electrical energy storage system. *IET Gener. Transm. Distrib.* **13**, 258–265 (2019)
16. Frew, B., et al.: Impact of operating reserve rules on electricity prices with high penetrations of renewable energy. *Energy Policy* **156** (2021)

IGBT Module Status Monitoring Method Based on High-Speed Peak Holding



Xiaoming Zhu, Jie Chen, Hui Wang, Xuefei Li, Jinpeng Li, Ruichang Qiu, and Zhigang Liu

Abstract A new IGBT module bond wires condition monitoring method is proposed, which realizes the condition monitoring of IGBT module bond wires aging in off-state. The method defines the collector-emitter peak voltage (V_{CEp}) when the IGBT module is turned on as the health indicator, so as to judge the aging state of the bond wires of the IGBT module. Based on theoretical analysis, the changes of gate loop stray inductance and inter-electrode capacitance caused by bond wires cracking and shedding will affect the peak collector-emitter voltage during the turn-on process. In order to eliminate the influence of DC voltage, load current, junction temperature and other factors during the measurement process, the measurement process is carried out in the shutdown state of the inverter system. In addition, a special high-speed peak voltage hold circuit is designed to realize the peak detection of the collector-emitter peak voltage, and the high-speed peak voltage hold circuit is analyzed. The results show that the circuit can effectively identify and maintain

X. Zhu · J. Chen (✉) · J. Li · R. Qiu · Z. Liu
School of Electrical Engineering, Beijing Jiaotong University, Beijing 100044, China
e-mail: jiechenu@bjtu.edu.cn

X. Zhu
e-mail: 20117038@bjtu.edu.cn

J. Li
e-mail: 21121438@bjtu.edu.cn

R. Qiu
e-mail: rchqiuu@bjtu.edu.cn

Z. Liu
e-mail: zhgliu@bjtu.edu.cn

Z. Liu
Rail Transit Electrical Engineering Technology Research Center, Beijing 100044, China

H. Wang
Institute of Space Launch Technology, Beijing 100048, China

X. Li
CRRC Changchun Railway Vehicles Co., Ltd., Changchun 130062, China

the peak value, has reliable performance and fast response speed, and has important guiding significance for the realization of the state monitoring of IGBT modules.

Keywords IGBT · Condition monitoring · Collector-emitter peak voltage · High-speed peak hold

1 Introduction

IGBT (Insulated Gate Bipolar Transistor) is widely used in power electronic systems, wind power, photovoltaic power, automotive industry, etc. [1, 2]. The reliability of IGBT affects the safe of power electronic system. However, despite the efforts of major manufacturers to improve the reliability of IGBT, IGBT failure accidents still emerge in an endless stream. According to relevant questionnaire survey, 31% of respondents believe that semiconductor power devices, including IGBT, are the most prone to failure in field applications [3]. Among various IGBT fault types, bond wires fault is one of the most common faults [4, 5]. It is that IGBT has a multi-hierarchical structure and each layer is composed of different materials [6]. IGBT bond wires condition monitoring is the focus of this paper.

Domestic and foreign experts and scholars have carried out a lot of research on IGBT failure mechanism and health indicators, and have made a lot of achievements. It is proposed to use IGBT turn-on gate voltage overshoot to monitor the state of bond wires [7]. In addition, it has been proposed to use the duration of grid charge to monitor the bond wires fatigue of multi-chip IGBT modules in the off-state [8]. The most commonly used health indicator is the collector-emitter on-state voltage drop $V_{CE,on}$. The team of Professor Stig of Aalborg University in Denmark found that $V_{CE,on}$ tended to rise with the aging of IGBT [9]. Generally, $V_{CE,on}$ is the result of the coupling of aging, junction temperature, current and other factors, and cannot be used as the state indicator of the bond wires. In engineering application, the peak collector-emitter voltage V_{CEp} in off-state is proposed as the health indicator. Firstly, V_{CEp} is easy to measure and changes obviously with IGBT aging. Secondly, the influence of temperature, bus voltage and other factors can be excluded in off-state measurement. Finally, The measurement process does not need to disassemble the IGBT, which is convenient for engineering implementation.

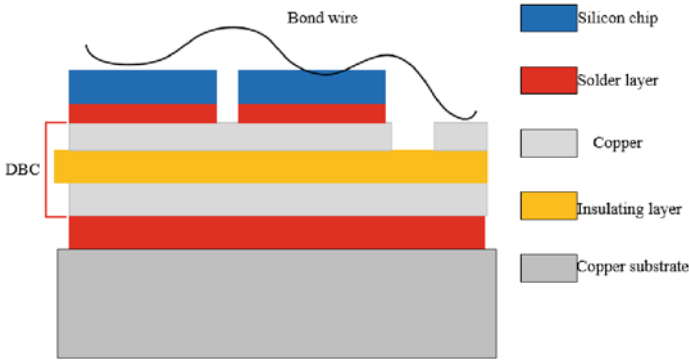


Fig. 1 Sectional drawing of IGBT module

2 Health Indicator

2.1 Failure Mechanism

IGBT is the main device to realize electric energy conversion in the power electronic system, works in the frequent switching mode, the switching loss and on-state loss in the whole process will be transferred in the form of heat, resulting in temperature fluctuations in the whole module. Figure 1 shows the internal structure of the IGBT module.

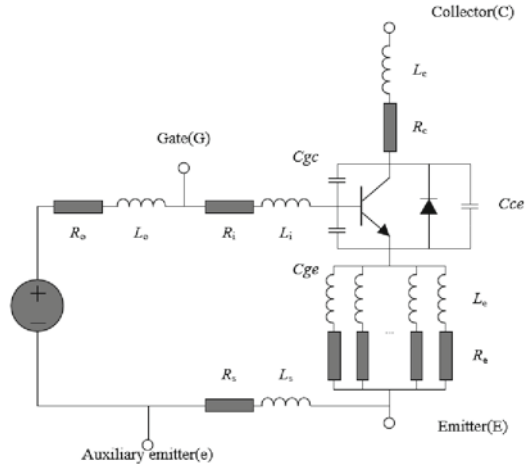
In the process of heat transfer from the semiconductor chip to the heat sink from top to bottom, there are significant differences in coefficients of thermal expansion (CTE) among the materials of each layer, the deformation mechanical stress of each layer caused by the same heat is different. In different application scenarios, the long-term accumulation of environmental factors such as vibration, external high and low temperature and humidity will also lead to fatigue of each layer of materials, which specifically shows irreversible damage such as crack growth, internal cavity and metallization reconstruction. These two factors lead to IGBT module aging during long-term application process.

2.2 Internal Parasitic Parameters of the IGBT Module

The parasitic parameters of IGBT module mainly include equivalent resistance, parasitic inductance and electrode capacitance. Figure 2 shows the gate equivalent circuit diagram of IGBT module.

R_o and L_o are the resistance and inductance of the outer pole loop, R_i and L_i are the resistance and inductance of the inner pole loop, R_e and L_e are the equivalent resistance and inductance of the emitter bond wires, R_s and L_s are the equivalent

Fig. 2 Internal equivalent circuit diagram of IGBT



resistance and inductance of the auxiliary emitter, R_c and L_c are the equivalent resistance and inductance of the collector. C_{gc} is gate-collector capacitance; C_{ge} is the gate-emitter capacitance; C_{ce} is the collector - emitter capacitance.

[10] proposed that the equivalent inductance and equivalent resistance of bond wires are related to the quantity and size. In the aging process of IGBT module, the cracking or shedding of bond wires reduces the number of parallel connections of bond wires, and the equivalent activated area of gate, emitter and collector decreases, leading to the change of parasitic parameters, which leads to the increase of the on-voltage peak. In this paper, V_{CEp} is selected as the health indicator of bond wire lift-off.

3 Voltage Peak Detection Circuit

The peak conduction voltage frequency reaches megahertz, which is difficult for conventional AD converter circuit to meet the requirements. Therefore, it is necessary to design the corresponding high speed peak holding circuit, which lays the foundation for the engineering realization of IGBT condition monitoring.

The schematic diagram of the peak-holding circuit designed in this paper is shown in Fig. 3. The circuit consists of amplitude discrimination, memory capacitor, drain circuit and buffer circuit. The components of the circuit are shown in Table 1.

The amplitude discrimination circuit needs to realize the voltage amplitude comparison of input signals at different times, which is commonly realized by operational amplifiers or comparators. The propagation delay time of TLV3501 is 4.5 ns and the input bias current is 0.01 nA, which can meet most design requirements. The reverse leakage current of a JFET is much smaller than that of a diode or transistor. The source and drain of a JFET are directly connected and used as a diode. Memory

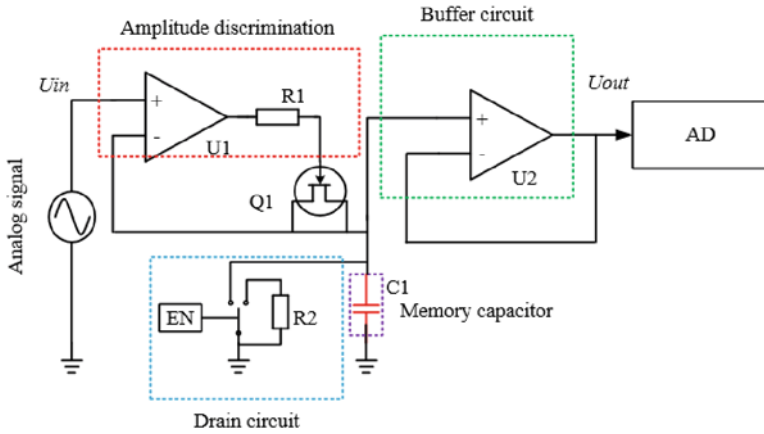


Fig. 3 Schematic diagram of peak detection circuit

Table 1 Components and related parameters of peak detection circuit

Device	Name	Type
U1	High speed comparator	TLV3501
U2	Electrometer operational amplifier	OPA128
R1	Resistor	SMD
R2	Resistor	SMD
C1	Memory capacitor	Polystyrene
Q1	JFET	2N4117A

capacitor selected polystyrene capacitor, compared with other materials, polystyrene capacitor has high insulation resistance, negative temperature coefficient, low leakage current.

The drain circuit ensures that the capacitor charge is zero between the initial state of the capacitor and the next peak. The buffer circuit reduces the effect of AD sampling circuit on capacitance charge. The voltage maintained by the memory capacitor needs to be read and converted by the post-stage AD sampling circuit. Due to the post-stage circuit will lead to capacitor charge loss, the OPA128 electrometer operational amplifier is adopted as the input/output buffer. The input bias current of the operational amplifier is very low, and the maximum input bias current of the OPA128 is only 75 fA. This ensures that the memory capacitor will not discharge on the later circuit.

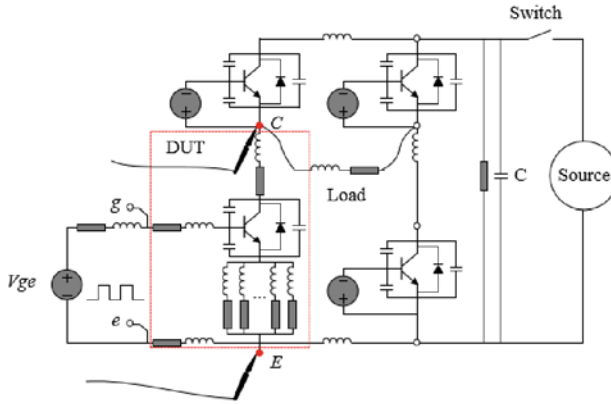


Fig. 4 Schematic diagram of the proposed condition monitoring scheme

4 Experimental Validation and Results Comparison

4.1 Condition Monitoring Program

In this paper, V_{CEp} is selected as the health indicator of bond wire lift-off. Figure 4 shows a schematic diagram of the condition monitoring scheme. In this paper, the H-bridge topology is selected for analysis. In fact, the analysis idea of H-bridge topology is also applicable to other topological forms. First, the main voltage is cut off, and the temperature of the module is waited long enough to reach a uniform and stable state. Then, the switch on command is issued to the IGBT device under test (DUT), and the V_{CE} at both ends of the DUT is measured simultaneously. Although the measurement is made with the main circuit off, there are voltage spikes at the ends of the collector and emitter when the gate voltage is applied due to the presence of parasitic parameters.

4.2 Experimental Platform

In order to verify the effectiveness of V_{CEp} as a health indicator of the aging state of IGBT bond wires, the H-bridge experimental platform was built according to the schematic diagram shown in Fig. 4, as shown in Fig. 5.

The DC side capacitance is $0.47 \mu\text{F}$ and the load inductance is $8 \mu\text{H}$. The measured device is an Infineon FF300R12KS4 half-bridge module. The experiment requires two modules. In order to reduce the error, two devices from the same batch are selected. The oscilloscope model is DLM2024, and the sampling frequency is set at 2.5 GS/s . The data in this paper is collected by oscilloscope and then processed by MATLAB.

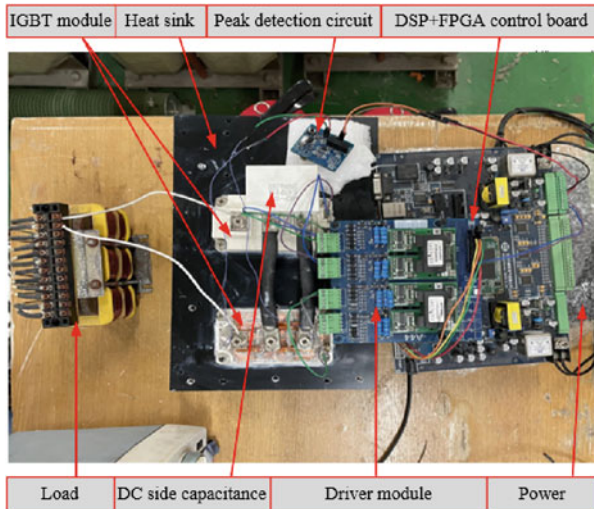


Fig. 5 Experimental platform

2SC0435T2A0 is used as the driving core in the gate drive circuit board, and the corresponding peripheral circuit is designed according to the data manual. The control board adopts DSP+FPGA as the core architecture, and integrates the AD sampling chip, Ethernet communication chip, power chip and FLASH memory chip, etc., which can meet the control requirements, send out the gate drive signal, and also supply power to the gate drive board.

4.3 Experimental Results

The number of bond wires was continuously reduced by manual cutting, and then the output of the V_{CEp} and the peak sampling circuit were measured separately. Figure 6 shows the sampling results.

The results show that V_{CEp} increases gradually with the decreasing number of bond wires, and V_{CEp} can reflect the aging state of IGBT bond wires. The output voltage of the peak detection circuit and the voltage amplitude after $3.2 \mu s$ gradually increase with the gradual increase of V_{CEp} , and the mean V_{CE} difference is 5–10 mV with the increase of the number of cut bond wires. It can be seen that the peak holding circuit can effectively follow the V_{CEp} and realize the condition monitoring of IGBT bond wire lift-off.

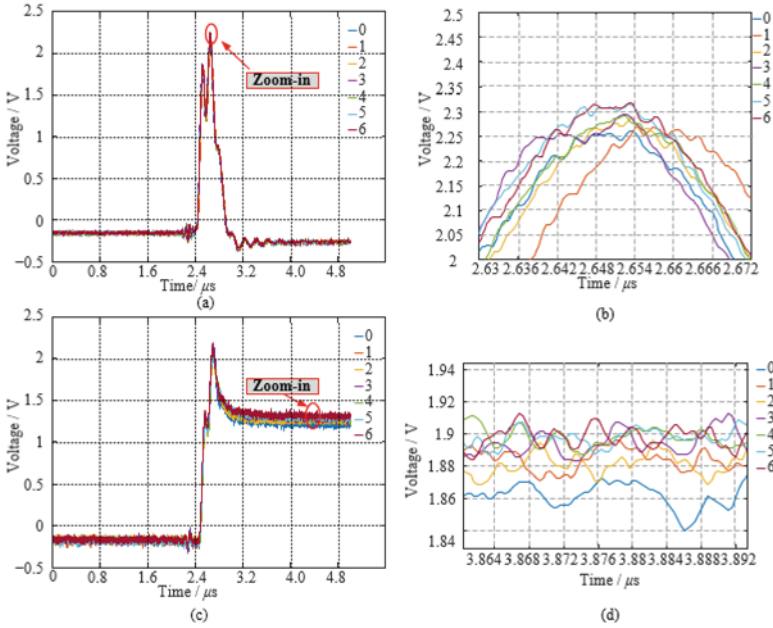


Fig. 6 Experimental waveforms of V_{CE} and peak detection under different bond wires aging. (a) the waveforms of V_{CE} ; (b) zoom-in figure of V_{CE} ; (c) the waveforms of peak detection; (d) zoom-in figure of peak detection

5 Conclusion

This paper presents a new method for monitoring the aging state of IGBT module bond wires. The peak collector-emitter voltage V_{CEp} during switching is selected as the health indicator, and the corresponding high speed voltage peak holding circuit is designed, which can realize the following of V_{CEp} under off-state. This method does not need to remove the IGBT module. Taking the H-bridge topology as an example, the current flow direction in the circuit under off-state, the principle of V_{CEp} generation and the relationship between V_{CEp} and the aging state of the bond wires are analyzed. According to the high frequency characteristic of V_{CEp} , the correlative peak voltage detection circuit is designed to realize the detection of V_{CEp} . The experimental results show that the peak detection circuit has reliable performance, fast response speed, and can effectively screen V_{CEp} . The method proposed in this paper provides an effective scheme for the application of IGBT module condition monitoring in engineering.

References

1. Wang, H., Liserre, M., et al.: Toward reliable power electronics: challenges, design tools, and opportunities. *Indust. Electron. Magaz. IEEE* **7**(2), 17–26 (2013)
2. Choi, U.M., Jrgensen, S., Blaabjerg, F.: Advanced accelerated power cycling test for reliability investigation of power device modules. *IEEE Trans. Power Electron.* **31**(12), 8371–8386 (2016)
3. Yang, S., Bryant, A., Mawby, P., et al.: An industry-based survey of reliability in power electronic converters. *IEEE Trans. Ind. Appl.* **47**(3), 1441–1451 (2011)
4. Wei, K., Du, M., Xie, L., et al.: Study of bonding wire failure effects on external measurable signals of IGBT module. *IEEE Trans. Device Mater. Reliab.* **14**(1), 83–89 (2014)
5. Zhang, J., Zhang, L., Cheng, Y.: Review of the lifetime evaluation for the IGBT module. *Trans. China Electrotechn. Soc.* **36**(12), 2560–2575 (2021)
6. Choi, U.M., Blaabjerg, F., Jørgensen, S., et al. Reliability improvement of power converters by means of condition monitoring of IGBT modules. *IEEE Trans. Power Electron.* 7990–7997 (2017)
7. Yang, Y., Zhang, P.: A novel bond wire fault detection method for IGBT Modules based on Turn-on Gate Voltage Overshoot. *IEEE Trans. Power Electron.* (99), 7501–7512 (2021)
8. Wang, K., Zhou, L., Sun, P., et al.: Monitoring bond wires fatigue of multichip IGBT module using time duration of the gate charge. *IEEE Trans. Power Electron.* (99), 888–897 (2021)
9. Pedersen, K.B., Kristensen, P.K., Pedersen, K., et al.: VCE as early indicator of IGBT module failure mode. *IEEE International Reliability Physics Symposium. Fa 1.1–1.6* (2017)
10. Mandeya, R., Chen, C., Pickert, V., et al.: Gate-emitter pre-threshold voltage as a health sensitive parameter for IGBT chip failure monitoring in high voltage multichip IGBT power modules. *IEEE Trans. Power Electron.* 9158–9169 (2018)

An Abnormal Power Consumption Identification Method Considering User Psychology



Xiaoyi Xiong, Jinyu Wu, Zijie Rong, Pengwei He, Na Dong, Xiaoyong Jiang, Xuan He, and Yannan Ji

Abstract Abnormal power consumption detection is the key to pinpointing electricity theft events. However, affected by the diversity of users' power consumption behaviors and unidentified causes of various abnormal power consumption load curves, present methods have relatively high false positive rate. Therefore, this paper proposes a method to cause deification of abnormal power consumption based on user psychology. Firstly, abnormal power consumption behavior is divided into malicious and non-malicious abnormal power consumption behavior according to users' psychology. Secondly, considering that the load curve is decomposed into several parts following the behavior types, the Chi-square goodness of fit test based detection method is investigated to extract characteristics of power consumption events. And then, characteristics matching of user behavior is applied to identify the causes of different abnormal load curves. Finally, simulating analysis is carried out to validate the authenticity. The results show that the proposed method can effectively identify two types of abnormal power consumption behaviors and supply a reference for practical engineering.

Keywords Abnormal power consumption detection · Electricity theft · Cause identification · User psychology · User behavior

1 Introduction

Recently, power supply companies have applied big data processing and analysis technology to mine deeply massive electric energy metering data stored in the user's power data acquisition system [1, 2]. Meanwhile, such abnormal power consumption behavior as electricity theft is the main cause of non-technical losses (NTL) in power system, and has already caused great economic losses to power supply companies [3,

X. Xiong (✉) · J. Wu · Z. Rong · P. He · N. Dong · X. Jiang · X. He · Y. Ji
State Grid Sichuan Electric Power Company Chengdu Power Supply Company, Chengdu 610000, China
e-mail: cdgdjgzclass1@163.com

© Beijing Paiké Culture Commu. Co., Ltd. 2023
X. Dong et al. (eds.), *The proceedings of the 10th Frontier Academic Forum of Electrical Engineering (FAFEE2022)*, Lecture Notes in Electrical Engineering 1054, https://doi.org/10.1007/978-981-99-3408-9_72

833

4]. Therefore, it's necessary to carry on research about abnormal power consumption detection (especially capturing electricity theft events) by advanced application of electric energy metering data.

With the development of smart grid and big data technology, the detection of abnormal power consumption at this stage is mainly based on more intelligent data-driven methods [5–7]. The data-driven based abnormal power consumption detection can be roughly divided into two main researches, machine learning model based abnormal detection and network topology based correlation analysis. In [5], a novel convolutional neural networks (CNN) model based electricity theft detection method is proposed to address the problem of the poor accuracy of electricity theft detection. A framework for combining the maximum information coefficient (MIC) and the clustering technique by fast search and find of density peaks (CFSFDP), is proposed to detect various types of electricity theft events in [6]. In [7], the problem of electricity theft pinpointing is formulated as a time-series correlation analysis problem and two coefficients are defined to evaluate the suspicion level of a user's reported energy consumption pattern.

The abnormal power consumption detection methods above can effectively identify users' abnormal load curves and capture the electricity theft events to save the economic losses of the power supply company. However, the methods ignore the diverse power consumption behavior information contained in the abnormal load curves and lead to high false positive rate.

Therefore, this paper proposes a method of abnormal power consumption identification based on user psychology. Firstly, abnormal power consumption behavior is divided into malicious and non-malicious abnormal power consumption behavior according to user psychology. Secondly, considering that the load curve is decomposed into several parts following the behavior types, the Chi-square goodness of fit (χ^2 GOF) test based detection method is investigated to extract characteristic of power consumption events. And then, characteristic matching of user's behavior is applied to identify the causes of different abnormal load curves. Finally, simulating analysis is carried out to validate the authenticity based on the metering data of the actual resident of a power grid in Southwest China. The results show that the proposed method can effectively identify two types of abnormal power consumption behaviors and supply a reference for practical engineering.

2 Patterns of Abnormal Power Consumption Behavior

2.1 *Malicious Abnormal Power Consumption Behavior*

Considering the user psychology, we defines the users' illegal power consumption behaviors for their own interests, such as changing the power consumption category without authorization, exceeding the planned power consumption index without authorization, and electricity theft by tampering with the metering data through

Fig. 1 Example of typical patterns of FDI

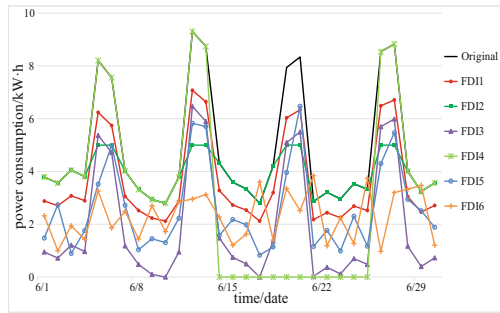


Table 1 Typical patterns of FDI

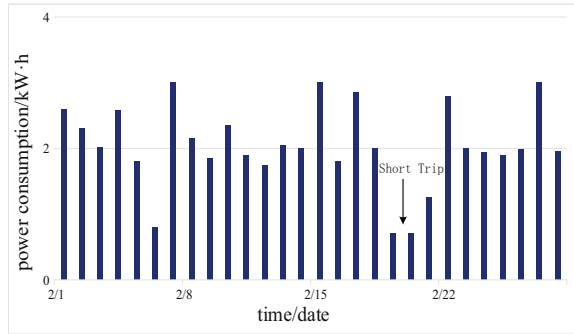
Types	Modification	Scope of application
FDI1	$\tilde{x}_t = \alpha x_t$	Where $0.2 < \alpha < 0.8$ is randomly generated
FDI2	$\tilde{x}_t = \begin{cases} x_t, & x_t \leq \gamma \\ \gamma, & x_t > \gamma \end{cases}$	Where $0 \leq \gamma \leq \max x$ is randomly defined
FDI3	$\tilde{x}_t = \max\{0, x_t - \gamma\}$	Where $0 \leq \gamma \leq \max x$ is randomly defined
FDI4	$\tilde{x}_t = f(t) \cdot x_t$	Where $f(t) \begin{cases} 0, & t_1 < t < t_2 \\ 1, & t \leq t_1 \cup t \geq t_2 \end{cases}$, t_1 and t_2 are randomly defined
FDI5	$\tilde{x}_t = \alpha_t x_t$,	Where $0.2 < \alpha_t < 0.8$ is randomly generated
FDI6	$\tilde{x}_t = \alpha_t \bar{x}$	Where $0.2 < \alpha_t < 0.8$ is randomly generated, \bar{x} is the average consumption of the load curve

various means as malicious abnormal power consumption behavior. Among them, in practice, electricity theft is a typical type of malicious abnormal power consumption behavior [8, 9]. At this stage, some criminals with high scientific quality have developed the method of electricity theft by digital attack. This method is similar to hacker attack, that is, it uses mathematically programming to carry out network attack, and directly tampers with the metering data by means of false data injection (FDI) [10]. The means of electricity theft based on FDI is an important research direction of the current electricity theft detection. The following Table 1 gives 6 typical patterns of FDI. The example of typical patterns of FDI is shown in Fig. 1. where x_t is the original load curve, \tilde{x}_t is the tampered load curve by FDI.

2.2 Non-Malicious Abnormal Power Consumption Behavior

In contrast to malicious abnormal power consumption behavior, we define the user’s power consumption behavior reflected by the abnormal load curves caused by many

Fig. 2 Power consumption of a household



reasons, such as the change of user's power consumption habits and non-malicious abnormal power consumption behavior. The load curves generated by users' non-malicious abnormal power consumption behavior is detected as abnormal power consumption behavior under the present methods because the characteristics are contrary to the ones of typical load curve generated by user's normal power consumption behavior. However, different from malicious abnormal power consumption behaviors such as electricity theft, it is not the user's power consumption psychology out of fraud but belongs to the user's honest psychology as the normal power consumption behavior. For example, it shows the load data of a family in the United States collected by researchers at the Pacific Northeast National Laboratory (PNNL) (see Fig. 2). It can be found that the power consumption in the 19th and 20th days is obviously low, that is, the measurement data of the two days are abnormal. The reason why the power consumption in the two days is at a low level is that the user has carried out short trip [11]. However, present abnormal power consumption detection methods cannot identify the causes and may be easily confused with users' malicious and non-malicious abnormal power consumption behaviors.

3 Cause Identification Method of Abnormal Power Consumption

3.1 Power Consumption Event Detection Based on X2GOF Test

Based on the load curve, the power consumption events generated by the user's power consumption behavior are detected. Event detection is to capture the switching time of electric equipment, that is, the start time when power consumption behavior appears. Load curve is of typical time series, so that it can be regarded as a change point detection problem.

χ^2 GOF test is selected as the power consumption event detection method in this paper, which is a hypothesis test method using Chi-square statistics. The principle of the method is: assuming that the data of two adjacent observation windows have the same distribution characteristics, a test hypothesis H_0 is proposed. The process of the method is as follows:

First, select the size of the observation window. The setting of the window size follows the guidelines below:

$$n_0 < n < n_1 \tag{1}$$

where n_0 is the minimum value of the observation window size, and its calculation formula can be obtained from reference [12] as shown in the following formula (2). n_1 is the maximum value of the observation window, which is determined by the maximum duration of the equipment.

$$n_0 = \left(\frac{z_{\alpha/2} \sigma_p}{E} \right)^2 \tag{2}$$

where $z_{\alpha/2}$ is the upper quantile of the standard normal distribution, and σ_p is the standard deviation. E is the allowable deviation of the detected power consumption event, and its value is set according to the condition of each household electric equipment, for example, $E = 50$ W.

After the observation window size is selected, χ^2 GOF test statistics are calculated as follows:

$$l_{GOF} = \sum_{i=1}^n \left(\frac{x_{now_i} - x_{pre_i}}{x_{pre_i}} \right)^2 \tag{3}$$

where x_{now_i} is the i -th sample value of the current observation window, x_{pre_i} is the i -th sample value of the previous observation window, and n is the window length obtained from Eq. (1).

Finally, the hypothesis test is carried out based on the obtained test statistic l_{GOF} :

$$\begin{cases} l_{GOF} > \chi_{\alpha, n-1}^2 & \text{refuse } H_0 \\ l_{GOF} < \chi_{\alpha, n-1}^2 & \text{obey } H_0 \end{cases} \tag{4}$$

where α is the confidence level and generally taken as 0.05, and $n-1$ is the degree of freedom which depends on the window size n .

If the null hypothesis H_0 is rejected in the calculated value l_{GOF} , it indicates that a power consumption event has occurred in the current detection window.

3.2 Characteristics Extraction of Power Consumption Events

After the event detection, the power consumption event set $R = [r_1, r_2, \dots, r_m]$ generated by the user's power consumption behavior can be obtained. For the constituent elements of the power consumption event set R , that is, the detected power consumption events r_1, r_2, \dots, r_m can be further divided into a single power consumption event set $S = [s_1, s_2, \dots, s_o]$ and a composite power consumption event set $T = [t_1, t_2, \dots, t_{m-o}]$ according to the composition of the power consumption equipment. Now consider characteristics extraction for power consumption events, that is, complete the electrical characteristics description of power consumption equipment.

Considering that the current load data can be collected and applied at the minute-level, the steady-state characteristics, including active power P and reactive power Q , are selected as the characteristic quantities to describe power consumption events.

$$\Delta P = \frac{1}{n} \sum_t^{t+n} |P(i) - P(i - n)| \quad (5)$$

$$\Delta Q = \frac{1}{n} \sum_t^{t+n} |Q(i) - Q(i - n)| \quad (6)$$

where n is the window length, $P(i)$ and $Q(i)$ are separately the active power and the reactive power at time i .

Through the processing of Eqs. (5) and (6), the characteristics extraction of the single power consumption event set S can be directly completed. However, for the composite power consumption event set T , this paper adopts bottom-up recursive search to extract the characteristics of power consumption equipment.

Considering the electrical characteristics of the load, the load curve can be regarded as the total power signal formed by the superposition of the power signals of all electric equipment:

$$P_{sum}(t) = \sum_{i=1}^n P_i(t) + A(t) \quad (7)$$

For each element in the composite power consumption event set T , after the time series signal in Eq. (7) is processed by Eq. (5), each element can be regarded as the characteristic superposition of each single power consumption equipment, as shown in Eq. (8):

$$t_{\Delta P} = \sum_{i=1}^n \Delta P_i + \Delta A \quad (8)$$

where $t_{\Delta P}$ is the characteristics value of element t , and ΔP_i is the active power of the i -th load, ΔQ_i similarly. ΔA is the noise characteristics after the treatment of Eq. (7).

Through the analysis of Eq. (8), the elements in the single power consumption event set S can be fully combined based on the recursive method, and the elements in the composite power consumption event T can be matched from bottom to top, so as to determine the working information of the electric equipment of the composite power consumption event.

3.3 Cause Identification of Abnormal Power Consumption Behavior Based on Characteristic Matching

After the characteristics extraction of the electric equipment in the power consumption event, based on the idea that the electricity theft data cannot reflect the working state information of the real electric equipment, and the load data generated by the non-malicious abnormal power consumption behavior is still the real data, this paper proposes the characteristics matching method to identify the causes of two different abnormal power consumption behaviors. Since the purpose of characteristics matching in this paper is to distinguish the nature of two abnormal power consumption behaviors, the research only needs to focus on the success of the characteristics matching process, without specifying the specific load type and working state. Therefore, Density-Based Spatial Clustering of Applications with Noise (DBSCAN) method is selected to realize this process.

The main idea of the algorithm is to find a high-density sample set in the space, and then use the low-density region to divide it into several clusters. Then, the density connectivity between different clusters is used to find new clusters of arbitrary shape that can be included in the range of clusters, until they cannot meet the requirements of forming new clusters. The specific flow of the algorithm is detailed in reference [13], which will not be repeated in this paper.

4 Case Study

4.1 Identification Results of Malicious Abnormal Power Consumption Behavior

In this section, the method proposed in this paper is used to verify the identification of users' malicious abnormal power consumption behavior. A total of 200 pieces of load curves were randomly selected from the working day of the resident within 10 months as the data to be tested. The ratio of the training set to the test set was 7:3, that is, the training set includes 140 pieces of data, and the test set contains 60 pieces of data. Based on 6 kinds of FDI patterns, electricity theft data is constructed for 40 pieces of data in the test set. Since the proposed method is to perceive the power consumption events generated by users' power consumption behavior, 200

Fig. 3 Characteristics matching results of power consumption information

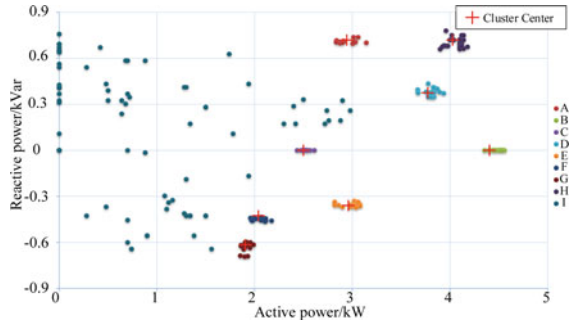


Table 2 Identification result of malicious abnormal power consumption behavior

Types	Actual electricity theft	Detected as electricity theft	Accuracy/%
FDI1	25	21	84
FDI2	25	19	76
FDI3	25	22	88
FDI4	25	25	99.9
FDI5	25	24	96
FDI6	25	25	99.9

detected power consumption events are selected for example analysis. Among them, 25 power theft incidents were selected from the six FDI modes respectively.

The power consumption modes A-H shown in Fig. 3 respectively represent 10 typical working states of the household electrical equipment, and the cluster centers under each mode can be obtained through the training set. The outliers are power consumption characteristics matching failure events, which are suspected to be caused by the user’s electricity theft behavior.

Further verification is carried out on them, and the results are shown in Table 2. It can be seen that the accuracy of the method proposed in this paper to judge the malicious abnormal power consumption behavior of users can reach a high level.

4.2 Identification Results of Non-Malicious Abnormal Power Consumption Behavior

The method proposed in this paper is used to verify the identification of users’ non-malicious abnormal power consumption behavior. A total of 180 load curves are selected from the daily load data of the resident for a half year as the data to be tested. The ratio of training set to test set is 7:3, that is, the training set includes 126 pieces of data, and the test set contains 54 pieces of data. The identification results are shown in Table 3.

Table 3 Identification result of non-malicious abnormal power consumption behavior

Types	Data	Correct detection	Accuracy
Normal power consumption behavior	25	12	99.9%
Non-malicious Abnormal Power Consumption Behavior	25	38	90.5%

The test set includes all rest days of the half year. Since the task of this section is to judge whether the user’s non-malicious abnormal power consumption behavior is misjudged as malicious abnormal power consumption behavior, the observation window is selected as one day. That is, 54 daily load curves of the test set are analyzed. If two or more power consumption events fail to match the power consumption characteristics on a certain day, it is considered that the detection is wrong.

4.3 Mixed Discrimination Results

The method proposed in this paper (method 1) is used to verify the cause distinguishing of the two above abnormal power consumption behaviors. The data set to be tested is the combination of the first two sections. Two existing abnormal power consumption detection methods, abnormal detection based on machine learning model (method 2) and correlation analysis based on network topology (method 3), are selected as comparison algorithms. The identification results are shown in Table 4.

It can be seen from Table 4 that the accuracy of the method proposed in this paper to identify normal power consumption behavior, malicious abnormal power consumption behavior and non-malicious abnormal power consumption behavior is 99.9, 90.5 and 90.7% respectively, which are higher than the other two methods. This is because the method proposed in this paper can notice the active perception of users’ power consumption behavior through the identification of the working conditions of electric equipment. The example results show that the proposed method can identify the causes of two different types of abnormal power consumption behavior.

Table 4 Algorithm accuracy comparison results

Types	Data	Method1	Method2	Method3
Normal power consumption behavior	12	75%	91.7%	99.9%
Non-malicious Abnormal Power Consumption Behavior	42	28.6%	78.6%	90.5%
Malicious Abnormal Power Consumption Behavior	150	77.3%	85.3%	90.7%

5 Conclusion

In order to solve the problems that present methods have relatively high false positive rate, this paper proposes an abnormal power consumption identification method considering user psychology. Based on the user's power consumption psychology, the abnormal power consumption behavior is divided into malicious and non-malicious abnormal power consumption behavior. Through the authenticity test of load data under power consumption events, the two different abnormal power consumption behaviors can be identified. Based on the measured data, the effectiveness of the proposed method is verified, which can meet the needs of engineering practice.

References

1. Wang, Y., Chen, Q., Hong, T., et al.: Review of smart meter data analytics: applications, methodologies, and challenges. *IEEE Trans. Smart Grid* **10**(3), 3125–3148 (2019)
2. Wang, Y., Chen, Q., Gan, D., et al.: Deep learning-based socio-demographic information identification from smart meter data. *IEEE Trans. Smart Grid* **10**(3), 2593–2602 (2019)
3. Guerrero, J.I., Monedero, I., Biscarri, F., et al.: Non-technical losses reduction by improving the inspections accuracy in a power utility. *IEEE Trans. Power Syst.* **33**(1), 1209–1218 (2018)
4. Glauner, P., Meira, J.A., Valtchev, P., et al.: The challenge of non-technical loss detection using artificial intelligence: a survey. *Int. J. Comput. Intell. Syst.* **10**(1), 760–775 (2017)
5. Zheng, Z., Yang, Y., Niu, X., et al.: Wide and deep convolutional neural networks for electricity-theft detection to secure smart grids. *IEEE Trans. Industr. Inf.* **14**(4), 1606–1615 (2018)
6. Zheng, K., Chen, Q., Wang, Y., et al.: A novel combined data-driven approach for electricity theft detection. *IEEE Trans. Industr. Inf.* **15**(3), 1809–1819 (2019)
7. Biswas, P.P., Cai, H., Zhou, B., et al.: Electricity theft pinpointing through correlation analysis of master and individual meter readings. *IEEE Trans. Smart Grid* **11**(4), 3031–3042 (2020)
8. Yan, Z., Wen, H.: Performance analysis of electricity theft detection for the smart grid: an overview. *IEEE Trans. Instrum. Meas.* **71**, 1–28 (2022)
9. Sahoo, S., Nikovski, D., Muso, T., et al.: Electricity theft detection using smart meter data. In: 2015 IEEE Power & Energy Society Innovative Smart Grid Technologies Conference (ISGT), pp. 1–5 (2015)
10. He, Y., Mendis, G.J., Jin, W.: Real-time detection of false data injection attacks in smart grid: a deep learning-based intelligent mechanism. *IEEE Trans. Smart Grid* **8**(5), 2505–2516 (2017)
11. Ning, L., Du, P., Guo, X., et al.: Smart meter data analysis. In: Transmission and Distribution Conference and Exposition (T&D), 2012 IEEE PES, pp. 1–6 (2012)
12. Jin, Y., Tebekaemi, E., Berges, M., et al.: Robust adaptive event detection in non-intrusive load monitoring for energy aware smart facilities. In: 2011 IEEE International Conference on Acoustics, Speech and Signal Processing (ICASSP), pp. 4340–4343 (2011)
13. Ester, M., Kriegel, H.P., Sander, J., Xu, X.: A density-based algorithm for discovering clusters in large spatial databases with noise. *KDD* **96**, 226–231 (1996)

Bearing Fault Diagnosis Using 1D-CNN Combined with Multi-Dimensional Input and Self-Attention Mechanism



Lanlan Fang, Zicheng Liu, Dong Jiang, and Ronghai Qu

Abstract To achieve intelligent and effective fault diagnosis of motor bearings, a machine-learning-based approach is proposed in the paper. 1D-CNNs are adopted to extract the features and a softmax classifier is used to distinguish the faults. However, given that there are many kinds of faults in the complex system, and there is coupling between fault signals, the reliability of fault diagnosis based on single-dimension data is limited, therefore we take the current signals and vibration signals of the motor as the input simultaneously. What's more, to achieve further improvement in fault diagnosis accuracy fault diagnosis and reduce computational effort, a self-attention layer is introduced after feature extraction to selectively strengthen the valid information of the features. Subsequently, the performance of the approach is demonstrated on the bearing dataset of KAt-DataCenter. Finally, the effectiveness of multi-dimension input and the superiority of the self-attention mechanism are verified through comparative experiments.

Keywords Bearing Fault Diagnosis · Multi-dimension input · Self-attention mechanism

L. Fang (✉)

China-EU Institute for Clean and Renewable Energy, Huazhong University of Science and Technology, Wuhan 430074, China
e-mail: m202071294@hust.edu.cn

Z. Liu · D. Jiang · R. Qu

School of Electrical and Electronic Engineering, Huazhong University of Science and Technology, Wuhan 430074, China
e-mail: liuzc@hust.edu.cn

D. Jiang

e-mail: jiangd@hust.edu.cn

R. Qu

e-mail: ronghaiqu@hust.edu.cn

© Beijing Paiké Culture Commu. Co., Ltd. 2023

X. Dong et al. (eds.), *The proceedings of the 10th Frontier Academic Forum of Electrical Engineering (FAFEE2022)*, Lecture Notes in Electrical Engineering 1054, https://doi.org/10.1007/978-981-99-3408-9_73

1 Introduction

As the key facility for electromechanical energy conversion, motors play an increasingly important role in various industries and sectors of modern society. Timely and accurate fault diagnosis (FD) is essential to ensure the safe and reliable operation of motors. And the bearing is the indispensable part of the motor, which is prone to failure under a harsh working environment and alternating load [1]. According to statistics, bearing failures account for approximately 40% of motor failures [2]. Therefore, this paper will focus on bearing faults of motors and explore a feasible and effective method for FD.

Most of the traditional bearing FD methods extract features manually from time domain, frequency domain, or time–frequency domain signals and identify faults by comparing them with fixed thresholds, and they usually achieve better results only in a specific system, under a specific load and a specific fault level, and are less likely to meet FD needs in multiple operating scenarios [3]. However, with the development of information technology, models of machine learning are also applied to the field of FD, which can automatically learn effective fault information from data to achieve FD, greatly facilitating the process of FD and expanding the scope of application.

In the early stage, the machine-learning-based methods usually extract features artificially from the original data, and then feed them into the model for FD. For example, reference [4] used time-domain statistical features of the vibration signals to depict the bearing health conditions, artificial neural networks (ANNs) and the support vector machine (SVM) were employed to distinguish faults of bearings; G.F. Bin et al. in reference [5] utilized wavelet packets decomposition combined with empirical mode decomposition for feature extraction and the backpropagation (BP) neural network for classification; Bing Li et al. in reference [6] applied generalized S transform and two-dimensional non-negative matrix factorization to extract the time–frequency representation of the vibration signals, then the K nearest neighbor classifier (KNNC), the naive bayes classifier (NBC) and SVM were employed to evaluate the performance. The above approaches still require hand-crafted features. Nevertheless, feature engineering is an art. Features may not be consistent under different load conditions and different fault levels. Therefore, the rationality of hand-crafted features needs to be verified, and meanwhile, the process requires prior knowledge and the applicability of the designed features is also limited.

Nowadays, with the development of deep learning technology, fault features can be automatically learned from large amounts of raw data with the help of the powerful nonlinear expression ability of the network, which is more generalized and intelligent. For instance, [7] proposed a DNN-based intelligent method that is able to adaptively extract and fuse multi-dimensional features for rolling bearing fault diagnosis; one-dimensional convolutional neural networks (1-D CNNs) were adopted to automatically extract the fault features [8]; reference [9] proposed a conversion method converting signals into two-dimensional (2-D) images and then extracted the features of the 2-D images to eliminate the effect of handcrafted features; reference [10] designed enhanced sparse filtering network to work directly on raw vibration

signals with environmental noise to acquire the characteristics, and then fed the features to a softmax classifier to distinguish the faults.

However, most of the above deep learning models are based on single-dimensional data. Considering that there may be multiple signal representations in the system after the fault occurs, e.g., when the motor bearing fails, the vibration signals, current signals, and speed signal of the motor will be “abnormal”, and what’s more, given that there are many kinds of faults in the actual complex system, and there is coupling between fault signals, the reliability of FD based on single-dimension data is limited, thus, in order to further improve the effectiveness of FD, this paper proposes a bearing FD model based on multi-dimensional data. Given that the characteristics of vibration signals and current signals are the most prominent in bearing FD, this paper will combine current signals and vibration signals for FD.

Recently, due to the ability of selectively strengthening valid information and parallel working, self-attention mechanism has attracted extensive attention and has been widely used in natural language processing (NLP), computer vision (CV), text classification, and even FD [11].

Reference [12] adopted the multi-head attention mechanism to optimize the CNN structure for the bearing FD and achieve good performance. A self-attentive CNN was also proposed to diagnose the faulty wafers [13]. Also, in reference [14], a novel time–frequency Transformer based on self-attention mechanism is designed to diagnose the faults of rolling bearings and the superiority of the model was verified through experiments. Hence, to select the effective information from the multi-dimensional data more efficiently, this paper considers introducing self-attention into the FD method of bearings.

In conclusion, inspired by the above research, this paper proposes a self-attention-based 1D-CNN for bearing FD based on multi-dimension input. The 1D-CNNs are utilized to automatically extract the characteristics from the current signals and vibration signals. And then the self-attention mechanism works to emphasize valid information. Lastly, a softmax classifier is adopted to distinguish the faults. The proposed method has been tested on the bearing dataset of KAt-DataCenter [15]. Moreover, the effectiveness of multi-dimension input and the superiority of the self-attention mechanism are verified through comparative experiments.

The structure of the rest of the paper is as follows. Section 2 introduces the model and related knowledge. The description of the bearing dataset and the parameters of the model are detailed in Sect. 3. And results of the experiment and comparative analysis are presented in Sect. 4. Finally, in Sect. 5, a conclusion is derived.

2 Proposed Method

The proposed method consists of three basic steps. Firstly, the 1D-CNNs are utilized to automatically extract the characteristics from the current signals and vibration signals. Secondly, the self-attention mechanism selectively emphasizes valid information. And thirdly, a softmax classifier is adopted to distinguish the faults.

2.1 1D-CNN and Self-Attention

CNN is one of the representative algorithms of deep learning. And it's usually applied in the field of image recognition and CV. 1D-CNN is one of the CNNs and the input of 1D-CNN is usually a one-dimensional or two-dimensional array, the convolution kernel slides in one direction only, and is widely used in the field of time series data processing. The details of CNN can be found in [9]. In this work, 1D-CNNs are adopted to extract features from the current signals and vibration signals. The basic working principle of 1D-CNN is shown in Fig. 1, the calculation process is shown below.

$$f_k = g((W_k \cdot x) + b_k) \tag{1}$$

where f_k denotes the result of the k th convolution kernel, $g(\cdot)$ is the activation function, W_k and b_k are the weight and bias matrix of the k th convolution kernel respectively, x represents the input signal. 1D-CNN uses the convolution kernel to slide along the direction of time dimension, weights the elements in the time window, and then extracts features through non-linear transformation of the activation function.

Self-attention mechanism is first proposed in [11] for the purpose of exploring the correlation between different sections of the input. And subsequently it has been applied to NLP, CV, speech processing, and many other areas, and has achieved good results. Actually, the essence of self-attention is to implement a weighted sum of the input, with the weights being increased where attention is needed, so as to achieve the purpose of focusing on effective information. In this work, the features extracted from 1D-CNNs are fed to the self-attention layer, to selectively strengthen the useful information to improve the precision and efficiency of the bearing FD. The structure

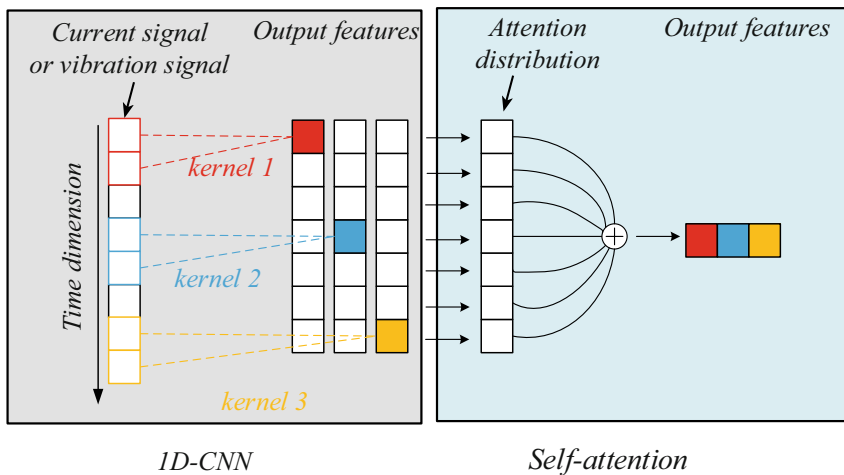


Fig. 1 The working process of 1D-CNN and self-attention layer

is also shown in Fig. 1 and the details of the calculation process are described as follows.

The input of the self-attention layer is $X = (f_1, f_2, \dots, f_k)^T, f_k \in R^{m \times 1}, (1 \leq k \leq K)$, and the first step is to calculate the attention distribution. Here we adopt a two-layer neural network to calculate the attention distribution $W = (w^1, w^2, \dots, w^m), (W \in R^{1 \times m})$ as described in (2) [13].

$$W = (w^1, w^2, \dots, w^m) = \text{soft max}(v_2^T \tanh(V_1 X)) \tag{2}$$

where $V_1 \in R^{S \times K}$ and $v_2 \in R^S$ are the matrix and vector, respectively, which are the model parameters learned by backpropagation.

Next, the output of the self-attention layer can be calculated as shown in (3) [13].

$$Y = (y_1, y_2, \dots, y_k), y_k = W f_k \tag{3}$$

where Y is the output and W is the attention distribution.

2.2 Proposed Method

Combining 1D-CNN and self-attention mechanism, this paper designs a deep-learning model for motor bearing FD, the structure is presented in Fig. 2, which mainly consists of four parts, convolution layer, self-attention layer, feature concatenation, and softmax classifier. The inputs of the model consist of the three-phase current signals of m consecutive time steps $I = \{i_A, i_B, i_C\}, (i_p \in R^{m \times 1}, p = A, B, C)$ and the vibration signal $a \in R^{m \times 1}$. Considering the difference in amplitude between the vibration and current signals, if they are directly concatenated and fed into the same network, there will be a problem of information loss. Hence, the original signals are considered to be sent to the 1D convolution layers separately in this paper, and for each signal, we can extract features from multiple angles with different convolution kernels. And then the features of each signal $F = \{f_1 \dots f_K\}, f_i \in R^{m-L+1}$ (K and L are the number and length of the kernels respectively) are accessed. And after that, the features are fed to the self-attention network to selectively highlight the effective information. After that, feature concatenation is carried out, the features derived from vibration signals and current signals are stitched into a column vector. Lastly, a softmax classifier is applied to distinguish the faults. The details of the calculations are described in Sect. 2.1, which will not be repeated anymore.

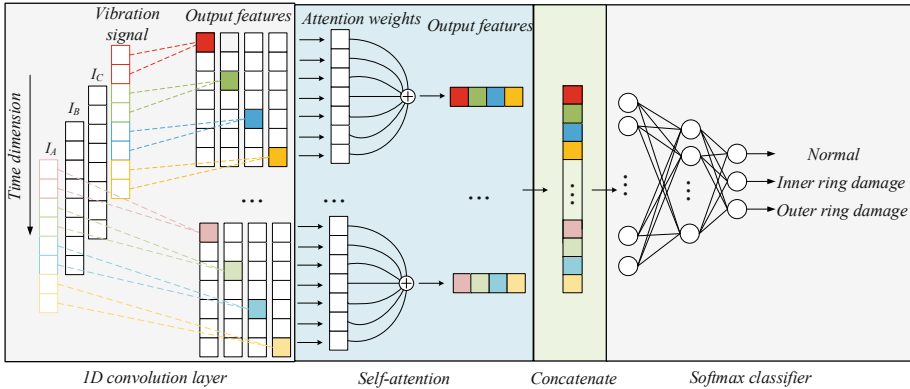


Fig. 2 Schematic diagram of the proposed method

3 Dataset Description and Parameters Setting

3.1 Dataset Description

The dataset used in this paper is from the KAt-DataCenter of the Chair of Design and Drive Technology, Paderborn University, Germany [15]. The data are measured on a three-phase PMSM test rig, which includes three fault conditions, normal condition, inner ring damage, and outer ring damage. For each condition, the multi-dimensional data under different load and rotational speed conditions, such as current, vibration, torque and speed, are collected. What's more, the dataset covers the damage of different causes and levels of faults. For instance, for inner ring damage, the dataset includes the data under the “fatigue: pitting” and “plastic deform: indentations”, and also includes the data under single damage and repetitive damage, which is more authentic and representative.

In this paper, the current and vibration data with the real damages are used for bearing FD. The sampling frequency of these data is 64 kHz and the duration is 4 s. To save computational resources, in this study, the dataset is down-sampled at an appropriate frequency $f = 16$ kHz and the input length of the model is set to 1 s. Besides, the data of bearings are divided into a training set, a validation set and a test set in the proportion of 6:2:2.

3.2 Parameters Setting

The approach proposed in this paper has some parameters to be tuned, which are detailed in Table 1.

Table 1 The parameters setting of the model

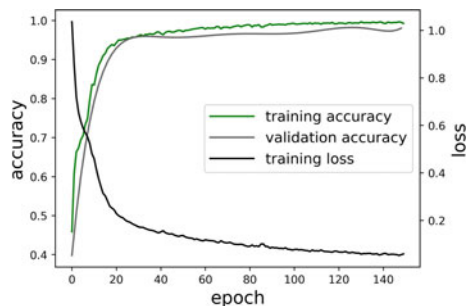
Model parameters			Training parameters	
1D convolution layer	Number of the kernel	4	Weight	Random normal
	Stride of the kernel	200	Optimizer	Adam
	Time window of the kernel	100	Learning rate	1e-3
Self-attention layer	S	15	Epochs	150
Softmax classifier	Number of the hidden neurons	20	-	-

4 Experimental Results and Comparison Analysis

The three-phase current and vibration data from the above dataset are used to diagnose the failure of the motor bearings. The results of the experiment are shown in Fig. 3. From Fig. 3, we can see that after nearly 80 iterations, the accuracy reaches 99% on the training set, 98% on the validation set, and the value of the loss curve drops to about 0.06. Finally, the test set is used to further examine the effectiveness of the method, and the accuracy can reach as high as 98%. All the above results prove that the proposed method in the paper can achieve accurate and useful bearing FD and has good generalization ability.

Moreover, to demonstrate the effectiveness of multi-dimension input and the superiority of the self-attention mechanism, two more comparative experiments are performed. The first one is to only take the vibration signal as the input and the structure of the model is identical to the method proposed in the paper. The second one is that the input is still the multi-dimension data including current and vibration signals, whereas, the self-attention layer in the model is cancelled. In addition, given that multi-dimension input can not only influence the accuracy of FD, but also increase the amount of calculation and the complexity of the model, resulting in a decrease in the convergence speed of the model, in order to more comprehensively measure the performance of the method proposed in the article, we also compare the complexity of the models, which is measured here by the number of trainable

Fig. 3 The curve of accuracy and loss of the proposed method



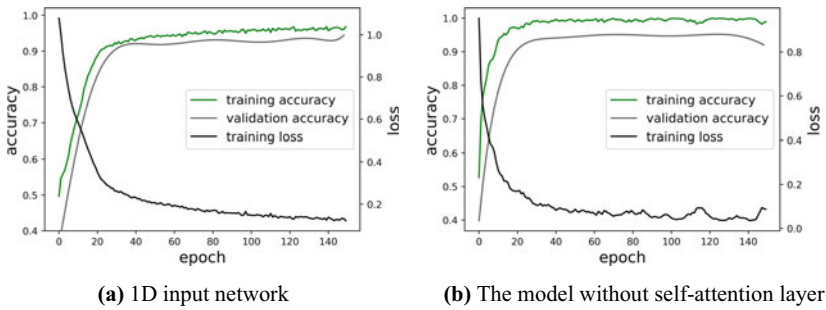


Fig. 4 The curve of accuracy and loss of the methods

parameters. The results of the experiments are shown in Fig. 4 and the comparison results are shown in Table 2. As can be seen from Table 2.

- (1) Compared with one dimension data input method, the method with the multi-dimension input has more trainable parameters, but the accuracy is improved, especially in the validation set and test set, the accuracy is improved by 5%;
- (2) For the model without self-attention layer, the accuracy on the training set reaches 99%, but the accuracy on the validation set and the test set is only 95%, which is 3% lower than the method proposed in the paper. Besides, as the self-attention layer is not added to the model, the features are fed directly to the softmax classifier without discrimination and selection, leading to a sharp increase in the input dimension of the classifier, and further resulting in the fact that the trainable parameters in this model are far more than in the proposed model.

To sum up, the model with multi-dimension input and self-attention mechanism can achieve accurate bearing FD and has good generalization ability, although the complexity of the model has increased to a certain extent.

Table 2 Comparison results of three methods

Method	Accuracy on training set	Accuracy on validation set	Accuracy on test set	Number of trainable parameters
Proposed method	99%	98%	98%	3959
1D input network	96.6%	93%	92.5%	1052
The model without self-attention layer	99%	95%	95%	54,211

5 Conclusion

This paper presents a machine-learning-based method for FD of motor bearings. The proposed method combines the multi-dimension input and self-attention mechanism, and can achieve an accuracy of 98% on the bearing dataset of KAT-DataCenter. Through comparative experiments, it's verified that multi-dimensional input contains more fault representations and the self-attention mechanism can selectively strengthen the useful information of the extracted features, both of which improve the accuracy effectively. However, the calculation amount of the model is also increased due to the multi-dimension input and there's still a long way from online diagnosis. But beyond that, it can provide a reference for fault prediction to achieve preventive maintenance, which is even more significant for the stable operation of the system.

References

1. Yang, G., Zong, M., Dengyun, S., et al.: 2MNet: Multi-sensor and multi-scale model toward accurate fault diagnosis of rolling bearing. *Reliabil. Eng. Syst. Safety* **216**, 108017 (2021)
2. Lau, E.C.C., Ngan, H.W.: Detection of motor bearing outer raceway defect by wavelet packet transformed motor current signature analysis. *IEEE Trans. Instrument. Measure.* **59**(10), 2683–2690 (2010)
3. He, M., He, D.: A deep learning based approach for bearing fault diagnosis. *IEEE Trans. Ind. Appl.* **53**(3), 3057–3065 (2017)
4. Samanta, B., Nataraj, C.: Use of particle swarm optimization for machinery fault detection. *Eng. Appl. Artif. Intell.* **22**(2), 308–316 (2009)
5. Bin, G.F.: Early fault diagnosis of rotating machinery based on wavelet packets—empirical mode decomposition feature extraction and neural network. *Mech. Syst. Sign. Process.* **16** (2012)
6. Li, B.: Feature extraction for rolling element bearing fault diagnosis utilizing generalized S transform and two-dimensional non-negative matrix factorization. *J. Sound Vibrat.* **12** (2011)
7. Zhou, F., Zhang, Z., Chen, D.: Bearing fault diagnosis based on DNN using multi-scale feature fusion. In: 2020 35th Youth Academic Annual Conference of Chinese Association of Automation (YAC), pp. 150–155. Zhanjiang, China (2020)
8. Zhang, X., Han, P., Xu, L., et al.: Research on bearing fault diagnosis of wind turbine gearbox based on 1DCNN-PSO-SVM. *IEEE Access* **8**, 192248–192258 (2020)
9. Wen, L., Li, X., Gao, L., et al.: A new convolutional neural network-based data-driven fault diagnosis method. *IEEE Trans. Indust. Electron.* **65**(7), 5990–5998 (2018)
10. Zhang, Z.: Enhanced sparse filtering with strong noise adaptability and its application on rotating machinery fault diagnosis. *Neurocomputing* **398**, 31–44 (2020)
11. Vaswani, A., Shazeer, N., Parmar, N., et al.: Attention Is All You Need. In: arXiv: 1706.03762 [cs.CL] (2017)
12. Wang, H., Xu, J., Yan, R., et al.: Intelligent bearing fault diagnosis using multi-head attention-based CNN. *Procedia Manufac.* **49**, 112–118 (2020)
13. Kim, E., Cho, S., Lee, B., et al.: Fault detection and diagnosis using self-attentive convolutional neural networks for variable-length sensor data in semiconductor manufacturing. *IEEE Trans. Semiconduct. Manufac.* **32**(3), 302–309 (2019)
14. Ding, Y., Jia, M., Miao, Q., et al.: A novel time–frequency Transformer based on self–attention mechanism and its application in fault diagnosis of rolling bearings. *Mech. Syst. Signal Process.* **168**, 112–118 (2022)

15. Christian, L., James, K., Zimmer, et al.: Condition monitoring of bearing damage in electromechanical drive systems by using motor current signals of electric motors: a benchmark data set for data-driven classification. In: European Conference of The Prognostics and Health Management Society, Bilbao, Spain (2016)

Interfacial Breakdown Voltage and Morphology of Cable Accessories Considering Different Interface States and Temperatures



Kai Wu, Tianfeng Zhang, Shaolei Wu, Yu Feng, and Yunxiao Zhang

Abstract The cable joint interface is highly susceptible to discharge along the face, which becomes the weakest link in power cable systems. In this paper, the effects of different interface roughness, pressure and temperature on the AC breakdown voltage at the silicone rubber/polyethylene double-layer dielectric interface are investigated, and the interface discharge channels after breakdown are analyzed. The results show that the interface breakdown voltage at room temperature is related to the interface gap size. The larger the gap size, the lower the interface breakdown voltage, and the larger the interface charging area. With the increase of temperature, the interfacial breakdown voltage decreases initially. However, with temperature further increasing, the breakdown voltage does not decrease significantly. In addition, the carbonized area shows a trend of first increasing and then decreasing with the increase of temperature. The interface state and temperature of cable accessories have a significant impact on the interface breakdown characteristics, which should be paid attention to during cable operation and maintenance.

Keywords Interface · Cable accessories · Silicone rubber · Breakdown voltage · Carbonized area

1 Introduction

At present, power cables are widely used for the transmission of electric energy [1], while cable joints, one important part of high-voltage cable transmission lines, are very problematic. The breakdown between the cable body and the accessory interface, which is prone to discharge along the face, is the weakest point in the entire cable

K. Wu · S. Wu · Y. Feng
Electric Power Research Institute, Anhui Electric Power Company of State Grid, Hefei, China

T. Zhang · Y. Zhang (✉)
College of Electrical Engineering and Automation, Fuzhou University, Fuzhou, Fujian, China
e-mail: zhangyxthu@163.com

system [2–4]. According to statistics, about 70% of failures are caused by faulty cable accessories [5]. The inherent problem of cable joints is due to the composite interface composed of different materials. Different from the breakdown of the surface of a single dielectric insulator, the breakdown of the composite dielectric interface is not only related to the insulation properties of the dielectric material, but the contact state of the composite interface. The interface gap filler are important factors that affect the breakdown voltage of the interface [6, 7].

Currently, Emre Kantar and Dimitrios Panagiotopoulos have conducted some studies on the effects of interfacial roughness, interfacial pressure, material elastic modulus and composite media filler on the interfacial breakdown strength of two-layer dielectrics, and the results show that the interfacial AC breakdown voltage increases with increasing interfacial pressure, and that the smaller the elastic modulus, the more significant the effect of interfacial pressure. It is also found that using the insulating oil to fill the interfacial cavity is also beneficial to increase the interfacial breakdown voltage [7–9]. However, the actual cable operates in the state of multi-physics coupling, and there is still a lack of research on the interface breakdown characteristics of cable accessories considering the combined effect of temperature, pressure and electric field. which leads to a lack of clarity on the failure mechanism of interfacial insulation under multi-physics.

Therefore, in this paper, silicone rubber (SIR) and polyethylene (PE) materials, which are used as insulation materials for cable accessories, are selected to build a multi-physical field interface breakdown test platform. The effects of different interface roughness, different interface pressure and different temperature on the breakdown voltage of SIR/PE under AC voltage are investigated. The interface after breakdown is photographed and the microscopic characteristics of the interface breakdown pattern under different conditions are analyzed. Based on this, the influence process of SIR/PE interface breakdown under multi-physics fields is analyzed and discussed.

2 Experiment

2.1 Materials and Specimens

In this article, we use PE sheets from Wanhe Plastic Insulation Materials, which are cut to a length and width of 40 mm×40 mm and a thickness of 10 mm, as samples for testing. The PE samples are then sanded with #80, #400, #600, #1000 and #2000 grit sandpaper and cleaned with anhydrous ethanol to produce five different roughness.

Liquid SIR from Zhonglan Chenguang is used as the raw material to prepare block samples of 2 mm thickness. Firstly, the two phases of SIR are selected in a ratio of 1:1, and then put it into a magnetic stirrer to mix for more than 20 min; Next, the finished mixed raw material is put into a vacuum drying oven for 10 min to remove the air bubbles in the material; Finally, the raw material is injected into the mold and

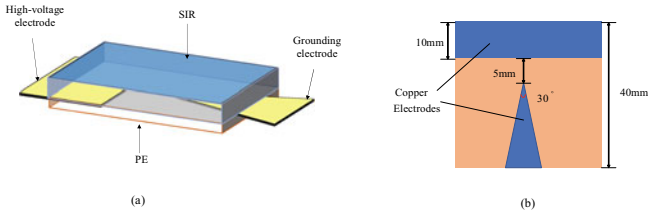


Fig. 1 **a** SIR/PE interface specimen arrangement. **b** Interfacial electrode arrangement

vulcanized using a plate vulcanizer at 165°C and 5 MPa. The length and width of sample is 40 mm×40 mm and the thickness is 20 mm.

Fig.1(a) and Fig.1(b) show the specimen and interfacial electrode arrangement for the SIR/PE bilayer media interface, respectively. A copper foil with thickness of 5 mm is used as the interfacial electrode.

2.2 Interface Breakdown Test

Figure 2(b) shows the interface breakdown test platform under AC voltage, which consists of AC high voltage power supply, voltage regulator, AC resistive capacitance divider, protective resistor and breakdown platform, etc. The test area mainly includes the SIR/PE interface specimen, the oven and the interface pressure application device shown in Fig. 2(a).

The experiments for both the interface roughness and interface pressure groups are carried out at a temperature of 25 °C and a humidity of 70%. Breakdown experiments are carried out using short and rapid pressurization with a ramping rate of 0.5 kV/s. Five sets of breakdown tests are carried out for different variable groups. The average value of the five groups of breakdown voltages is taken as the breakdown voltage of the SIR/PE interface under that variable. After breakdown, the PE and SIR interface are placed under a optical microscope to photograph the breakdown channel.

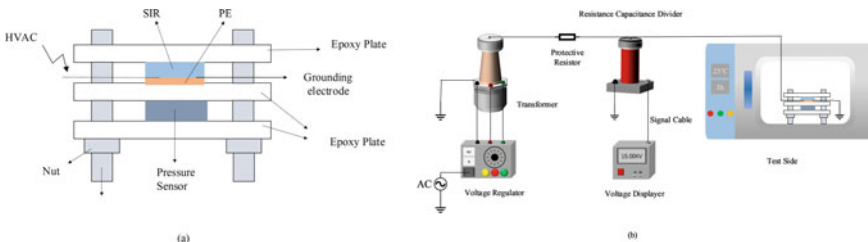


Fig. 2 **a** Interfacial pressure application device and sample arrangement. **b** Interface AC breakdown test rig

3 Results and Discussions

3.1 Interfacial Breakdown Tests at Different Roughness

Figure 3 shows the interfacial breakdown voltage of five different roughness levels at 0.1 MPa interface pressure. The results show that the breakdown voltage of the double-layer dielectric interface is significantly influenced by the roughness of the interface, and that the smoother the interface, the higher the breakdown voltage of the interface. In addition, as the unpolished PE samples inevitably have some surface defects such as scratches and micro-grooves during the preparation process, the interface is not as smooth as the PE interface polished by fine 2000-grit sandpaper, and therefore the breakdown voltage is lower.

Figure 4 shows a schematic diagram of the contact between the PE and SIR interface. In fact, when the rough surface is in contact, it is the highest micro-convex body on the surface that makes contact first, so the contact between the two media interfaces can be considered as contact between irregular micro-convex bodies on a rough surface and the sum of the contact surface areas of the micro-convex bodies on the interface is defined as the true contact area of the two media interfaces [6].

The surface of the PE samples is smoother after sanding with the higher grit sandpaper, while the surface of the samples is rougher after sanding with the lower grit sandpaper. It can be seen from Fig. 4(a) that the micro-convexities on the surface of PE sanded with 80-grit sandpaper are highly randomly distributed, that the true contact area between PE and SIR is small, and that the interfacial gaps are small in number but large in size. The gas in the gap is an important factor affecting the interfacial breakdown, and it is known from Paschen's law that the larger the size of the gas gap, the lower the breakdown field strength [7], so the interfacial breakdown

Fig. 3 Interfacial breakdown voltage at different roughness

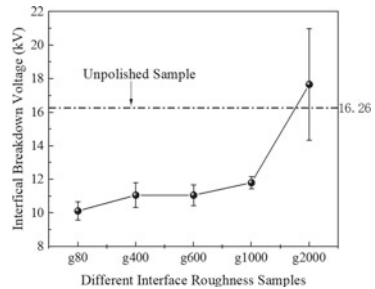
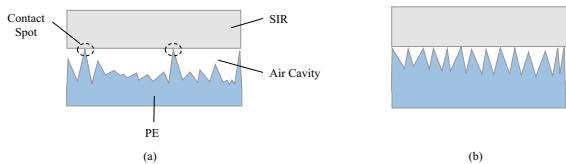


Fig. 4 Schematic diagram of SIR/PE contact: **a** SiR/PEg80, **b** SiR/PEg2000



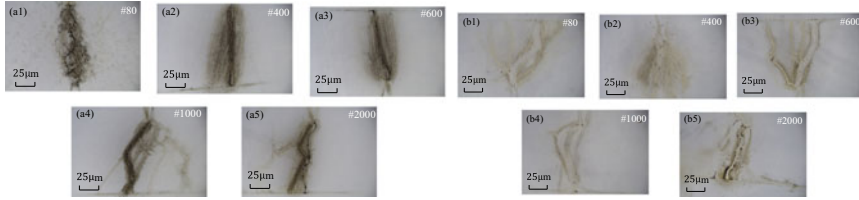


Fig. 5 Interfacial patterns after breakdown of PE and SIR for different roughness: **a1-a5** PE interface; **b1-b5** SIR interface

voltage of specimen SIR /PEg80 is the lowest. The surface of the PE plate polished with 2000-grit sandpaper is smooth, and it can be seen from Fig. 4(b) that the height index of the micro-convex body on the PE surface is relatively regular, that the real contact area between PE and SIR is larger, that the number of interfacial gaps is small in size, and that the total gap volume is small, therefore the breakdown voltage is large.

Figure 5(a) and Fig. 5(b) show the patterns of the PE and SIR interfaces after breakdown at different roughness levels, respectively. The brownish-yellow and slightly black parts of the patterns are the carbonized areas. It can be clearly seen that the carbon traces in the carbonized areas are mainly left on the PE surface, while there are no obvious traces in the SIR. Therefore, this paper focuses on the analysis of the PE interface pattern after the breakdown.

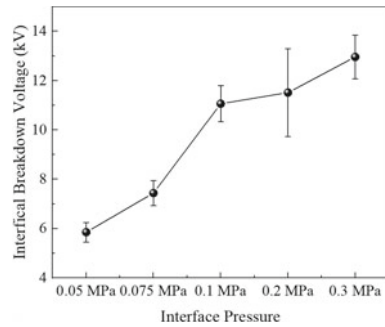
As the interface voltage rises, the gas in the gap is the first to be broken through and the discharge phenomenon occurs. As the discharge proceeds, the molecular chains with lower bonding energy on the PE surface are gradually broken and carbon particles randomly appear at the interface. As the voltage continues to rise, the carbonization becomes more and more severe and the carbon particles at the interface gradually associate, eventually interconnecting and short-circuiting the interface electrodes, resulting in a complete failure of the interface insulation [10]

Furthermore, it can be noticed from Fig. 5(a) that the carbonized area decreases as the smoothness of the interface increases. This is because the size of the carbonized region is correlated with the randomness of the discharge. The smoother the interface and the smaller the overall size of the gap between the interface of PE and SIR, the lower the randomness of the discharge. From the initial discharge to the interface breakdown, all the discharge paths are almost at the same position, and the interface at the same position is repeatedly destroyed, resulting in a concentration of places where carbonization occurs, i.e., a smaller carbonized region.

3.2 Interfacial Breakdown Tests at Different Pressures

Figure 6 shows the breakdown voltage of the interface SIR/PEg400 at 0.05 MPa, 0.075 MPa, 0.01 MPa, 0.2 MPa and 0.3 MPa, respectively. The breakdown voltage

Fig. 6 Breakdown voltage at the PEG400/SIR interface at different pressures



at the interface is as low as 5.82 kV at 0.05 MPa. With the increase of pressure, the interface breakdown voltage shows an upward trend.

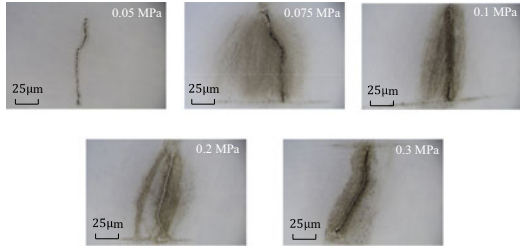
When the interface pressure is small, there is a large number of gaps in the composite interface, and the dielectric constant of the gas in the gaps is much smaller than that of PE or SIR, so the distribution of the interface electric field is extremely uneven, and the interface is more likely to discharge. When the interface pressure is increased, the gap in the interface is filled with soft SIR, so the interface gap becomes smaller. At this time, the interface electric field distribution is more uniform, so the discharge is less likely to occur. Therefore, increasing the interfacial pressure is beneficial to the insulating properties of the interface [11]

Figure 7 shows the patterns of the PE interface after breakdown at different pressures. In the breakdown test, with the increase of voltage, although the defect distribution on the interface is complex, it is still small overall. Due to the large gap of the composite interface, the time interval from the initial discharge to the breakdown is short, so the interface carbonization phenomenon is not serious. It can be seen from Fig. 7 that the carbon trace pattern after breakdown has no obvious carbonized area. When the interface pressure increases to 0.075 MPa, with the gradual increase of voltage, the molecular chains inside the PE are broken to produce carbon particles. And at this time, due to the obvious time interval between the generation of the initial discharge and the breakdown, the carbon particles on the interface are gradually associated, and the obvious carbonization phenomenon occurs. After that, with the increase of the interface pressure, the interface carbonized area gradually decreases. The gap decreases with the increase of pressure, so the randomness of the interfacial discharge becomes weaker, and therefore the interfacial carbonized area decreases.

3.3 Breakdown Tests at Different Temperatures

In this test, the SIR/PEG400 samples are selected and tested at a pressure of 0.1 MPa for five sets of breakdown voltages at different temperatures, as shown in Fig. 8. The breakdown voltage at the interface is significantly highest at room temperature

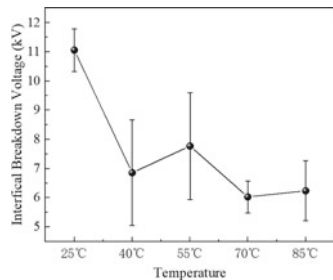
Fig. 7 Interface pattern after PE breakdown at different roughness



25 °C. When the temperature is raised, the carrier velocity of the material interface increases, which makes the interface breakdown rate faster, so there is a significant drop in breakdown voltage at a temperature of 40 °C. However, as the temperature further increases, the breakdown voltage does not decrease significantly. This is because the higher the temperature is, the softer the surface of the material becomes. The melting point of PE is 85°C-110°C, and SIR can still work stably at 180°C, so the surfaces of PE and SIR become softer at high temperatures. However, since the experimental temperature is close to the melting point of PE, the surface of PE becomes softer at high temperatures. Under certain pressure, the real contact surface of PE becomes softer at high temperatures. Under certain pressure, the real contact surface of the interface between PE and SIR increases, and the gap between the interfaces decreases, so the breakdown voltage does not significantly decrease.

Figure 9 shows the interfacial patterns after PE breakdown at different temperatures. The carbonized area of the interface becomes larger first, which is because the thermal ionization of the gas in the interfacial gap is more intense at higher temperature, resulting in more intense interfacial discharge and serious molecular chain breakage at the PE interface, so the carbonized area of the interface becomes larger. As the temperature further rises, the interfacial contact area rises and the gap size decreases due to the softening of the material, so the number of gas molecules in the gap decreases, which reduces the chance of interfacial discharge and the ability to damage the interface, therefore the interfacial carbonized area decreases.

Fig. 8 Interfacial breakdown voltage of SIR / PEG400 at different temperatures



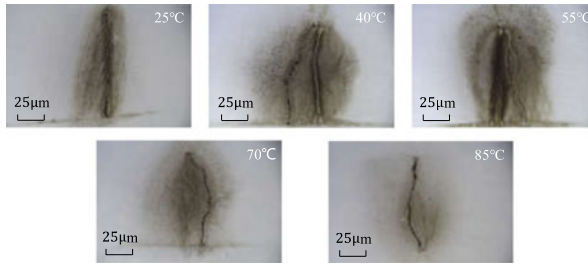


Fig. 9 Interface pattern after PE breakdown at different temperatures

4 Conclusion

In this paper, the breakdown voltage and morphology of SIR/PE interfaces have been investigated at AC voltage considering different interface roughness, pressure and temperature. The detailed results are shown as follows:

- (1). The carbonized areas of the SIR/PE double layer dielectric interface after breakdown and the carbon traces left by the discharge channels remain mainly on the surface of the PE sheet.
- (2). As the smoothness of the PE interface increases, the breakdown voltage of the interface will be larger, and the carbonized area of the interface will be smaller.; with the increase of the interface pressure, the breakdown voltage of the double-layer dielectric interface will be higher, and the carbonized area of the PE interface will be smaller.
- (3). The breakdown voltage of the SIR/PE media interface shows an overall decreasing trend with increasing temperature. With the increase of temperature, the material becomes softer, and the real contact area of PE / SIR increases under a certain pressure, so the breakdown voltage at the interface does not drop significantly. In addition, the PE interfacial carbonized area will show a trend of increasing first and then decreasing with the increase of temperature.

References

1. Zhang, Y., Zhou, Y., Zhu, X., et al.: Electrical tree evolution of BN sheet/epoxy resin composites at high voltage frequencies. *IEEE Transactions on Dielectrics and Electrical Insulation* (2022)
2. Hu, S., Zhang, Y., Shao, Q., et al.: Comprehensive performance comparisons of polypropylene-based HVDC cable insulating materials adopting different modification technical route. In: *Proceedings of the CSEE* **42**(4), 1243- 1252 (2022, in Chinese)
3. Settembre, A., Candela, R., Cavallini, A., et al.: Pre-breakdown leakage current of tangential dielectric interfaces with different coupling pressures. In: *2022 IEEE 4th International Conference on Dielectrics (ICD)*, pp. 688–691. IEEE (2022)

4. Yu, S., Ying, L., Rui, L., et al.: Effect of surface smoothness on electrical tree characteristics at XLPE-SiR interface. In: 2019 2nd International Conference on Electrical Materials and Power Equipment (ICEMPE), pp. 150–153. IEEE (2019)
5. Chang, L., Baojun, H., Mingli, F., et al.: Influence of mechanical stress on the operation reliability of silicone rubber high voltage cable accessories. *High Voltage Eng.* **44**(2), 518–526 (2018, in Chinese)
6. Bin, Z., Zhi Dong, J., Hao, H., et al.: Relationship between the interfacial ramped DC breakdown voltage and the morphology of the XLPE/SiR interface. *IEEE Trans. Dielectr. Electr. Insul.* **26**(3), 689–697 (2019)
7. Kantar, E., Panagiotopoulos, D., Ildstad, E., et al.: Factors influencing the tangential AC breakdown strength of solid-solid interfaces. *IEEE Trans. Dielectr. Electr. Insul.* **23**(3), 1778–1788 (2016)
8. Kantar, E., Mauseth, F., Ildstad, E., et al.: Longitudinal AC breakdown voltage of XLPE-XLPE interfaces considering surface roughness and pressure. *IEEE Trans. Dielectr. Electr. Insul.* **24**(5), 3047–3054 (2017)
9. Kantar, E., Mauseth, F., Ildstad, E., et al.: Effect of pressure and elastic modulus on tangential breakdown strength of solid-solid interfaces. *IEEE Electrical Insulation Conference*, pp. 431–435. IEEE (2016)
10. Du, B.X., Zhu, X.H., Gu, L., et al.: Effect of surface smoothness on tracking mechanism in XLPE-Si-rubber interfaces. *IEEE Trans. Dielectrics and Electrical Insulation* **18**(1), 176–181 (2011)
11. Du, B.X., Liang, G., et al.: Effects of interfacial pressure on tracking failure between XLPE and silicon rubber. *IEEE Trans. Dielectrics and Electrical Insulation* **17**(6), 1922–1930 (2010)

Research on Critical Breakdown Distance of 110 kV/220 kV AC Transmission Lines with Trees Approaching



Kai Yang, Hong Wu, Shitao Liu, Jinpeng Hao, Yumeng Zeng, Haochen Zhang, Yu Wang, and Yeqiang Deng

Abstract In order to reduce the trip fault of transmission lines, it is necessary to study the electric field distribution law and critical breakdown distance when trees are close to conductors. In this paper, the canopy arcing experiments under 110 kV and 220 kV AC transmission lines are carried out, and the critical breakdown distance between trees and wires under corresponding voltage levels is obtained. Use COMSOL Multiphysics finite element software to build three-dimensional models of trees under 110 kV and 220 kV transmission lines. The initial field strength of streamer is taken as the standard of breakdown gap. The simulation results of the critical tree-wire breakdown distance under the corresponding voltage level are obtained. By comparing with the experimental results, the accuracy of the simulation method to calculate the critical breakdown distance is verified. According to the simulation and experimental results, the distance between 110 and 220 kV conductors and trees should be greater than 12 cm and 48 cm respectively to avoid the occurrence of the arcing fault.

Keywords AC transmission Lines · Gap Breakdown · Electric Field Distribution · COMSOL Multiphysics

K. Yang (✉) · H. Wu · J. Hao
State Grid Ningxia Electric Power Research Institute, Yinchuan, China
e-mail: m13871581126@163.com

S. Liu
State Grid Ningxia Electric Power Co. Ltd, Yinchuan, China

Y. Zeng · H. Zhang · Y. Wang · Y. Deng
School of Electrical Engineering and Automation, Wuhan University, Wuhan, China
e-mail: yuwang@whu.edu.cn

Y. Deng
e-mail: dengyeqiang@whu.edu.cn

1 Introduction

The contradiction and conflict between transmission lines and trees is an unavoidable problem in the process of power grid construction, management, operation and maintenance. The excessive growth of trees in high voltage transmission corridors can easily cause line tripping, which will seriously threaten the safe operation of overhead transmission lines. There have been many power grid blackouts caused by trees at home and abroad [1, 2].

In recent years, the solution to the ‘tree-wire contradiction’ caused by the transmission line passing through the forest area has developed rapidly from the traditional regular manual inspection to the current monitoring and prevention [3–6]. Trees are rich in high conductivity water, and the curvature radius of the top edge is small, with a sharp tip. When the tree is close to the transmission line, the electric field distortion at the top of the tree will form a discharge phenomenon after exceeding the critical breakdown field strength. When determining the minimum clearance distance between overhead transmission lines and trees, the maximum overvoltage gap is often used as a reference standard [7]. In recent years, the relevant standards and research in China have also begun to use the electric field effect as a criterion when determining the minimum clearance distance between overhead transmission lines and trees.

At present, most of the relevant research is about the change of the synthetic electric field when the trees are close to the UHVDC transmission line [8–11]. There are few studies on the safety distance when there are trees under the AC transmission line. With the development of satellite remote sensing and other technologies, the measurement of tree height can achieve higher accuracy. Studying the critical breakdown tree-wire distance makes the relevant early warning of tree-wire problem more perfect and distinguish different levels of early warning.

In this paper, the flashover experiments of trees under 110 kV and 220 kV conductors are carried out, and the tree-wire breakdown distance under the corresponding voltage level is obtained. The COMSOL Multiphysics finite element simulation software is used to build a model when there are trees under the wire. The minimum safety tree-wire distance is determined according to the surface field strength of trees. It has certain engineering guiding significance for the operation safety of transmission lines and the management of trees in the corridor.

2 Experimental Method

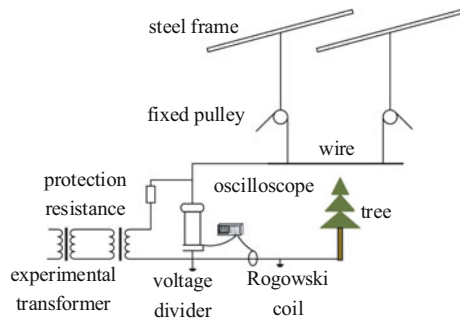
2.1 *The Method of the Experiment*

The experiment in this paper is completed in the high voltage test hall. The test circuit is shown in Fig. 1. The experimental transformer is connected to the simulated conductor of the steel pipe in series with a protection resistance. The voltage on

the conductor is raised to 110 kV and 220 kV by the test transformer. The tree is placed under the wire, and the tree is grounded through the wire. The current value is connected to the oscilloscope using the Rogowski coil, and the voltage value is connected to the oscilloscope through the voltage divider.

The test site is arranged as shown in Fig. 2. The tree is placed under the wire, and the vertical distance between the wire and the tree is continuously adjusted by pulling the rope. The test transformer continuously raises the voltage by means of a point boost until the tree line gap breaks down, and the oscilloscope records the voltage and current values of the breakdown. Each distance to do five breakdown experiments, take the average breakdown voltage at this distance, constantly adjust the distance, until the breakdown voltage to the desired voltage level. The critical breakdown distance of 110 kV and 220 kV can be determined by many experiments. The critical breakdown distance of 110 kV is 12 cm, and the critical breakdown distance of 220 kV is 27 cm. The arc is shown in Fig. 3.

Fig. 1 Experimental circuit



(a) 110kV test site

(b) 220kV test site

Fig. 2 Experiment site layout (a) 110 kV test site (b) 220 kV test site

Fig. 3 Arc at gap breakdown



(a) 110kV breakdown arc (b) 220kV breakdown arc

3 Simulation Study on Adjacent Trees Under AC Transmission Line

3.1 Electrostatic Field Simulation

In this paper, COMSOL Multiphysics finite element simulation software is selected to simulate transmission lines and trees. Based on the electrostatic field theory, Poisson equation is used to describe the electric field of transmission lines:

$$\nabla^2\varphi = -\rho/\varepsilon \quad (1)$$

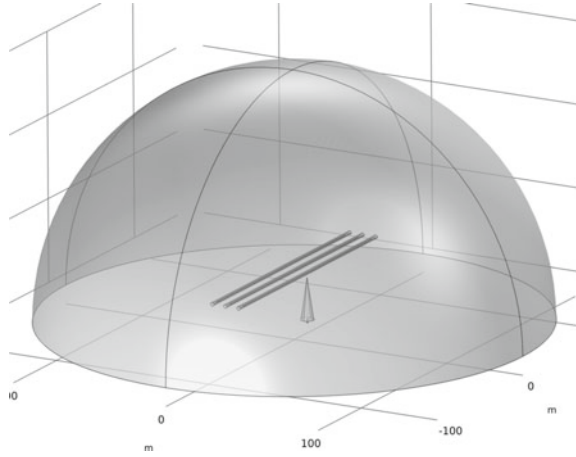
In Eq. (1), ∇ is the Hamiltonian operator, which is used to represent the partial derivatives vector sum of a physical quantity in the three coordinate directions of x , y and z ; φ is the potential of any point in space, unit V; ρ is the space charge density, unit C/m³; ε is the relative dielectric constant, unit F/m.

Power system overhead high voltage transmission lines generally adopt three-phase three-wire system. The phases of A, B, and C three-phase conductors are selected as 0° , -120° , and 120° , respectively. The boundary of the calculation domain is set to zero charge, and the ground potential $V = 0$. Trees are regarded as good grounding conductors. Three-phase wire corresponding set surface potential, such as A phase wire:

$$U_A = U_1 * e^{i*a} \quad (2)$$

In the formula, U_1 is the amplitude, a is the phase angle. The diagram of the constructed geometric model is shown in Fig. 4.

Fig. 4 Diagram of the model



3.2 Simulation Verification

Criterion of Streamer Initial Field Strength

The gap between trees and transmission lines is a non-uniform field, and the discharge belongs to long air gap discharge. The streamer is the initial performance of long air gap breakdown. In this paper, the typical streamer inception criteria of rod-plane gap in extremely inhomogeneous field proposed in Reference [12] is used:

$$E_{i-impulse} = 22.8(1 + \frac{1}{\sqrt[3]{R}} + \frac{0.22R + 0.08}{R^2} \sqrt{\frac{dU}{dt}}) \tag{3}$$

Under the action of AC power frequency voltage, formula (4) can be simplified as:

$$E_{i-impulse} = 22.8(1 + \frac{1}{\sqrt[3]{R}}) \tag{4}$$

In the formula, $E_{i-impulse}$ is the streamer initial field strength, and the unit is kV/cm. R is determined by the shape of the crown top. In this paper, the conical crown is regarded as an electrode, and the radius is taken as the radius of the top ball. The initial field strength of streamer can be calculated by substituting Eq. (6).

According to the radius value of the top of the experimental tree, the radius of the top sphere is determined. The crown radius of the breakdown experiment at 220 kV voltage level is $R = 4$ cm, and the initial field strength of the streamer is 37.16 kV/cm. The crown radius of the breakdown experiment at the 110 kV voltage level is $R = 1$ cm, and the initial field strength of the streamer is 45.6 kV/cm.

Table 1 Comparison of simulation and experimental results

Voltage level	Initial streamer field strength	Simulation value of breakdown distance	Experimental value of breakdown distance
110 kV	45.6 kV/cm	10 cm	12 cm
220 kV	37.16 kV/cm	24 cm	27 cm

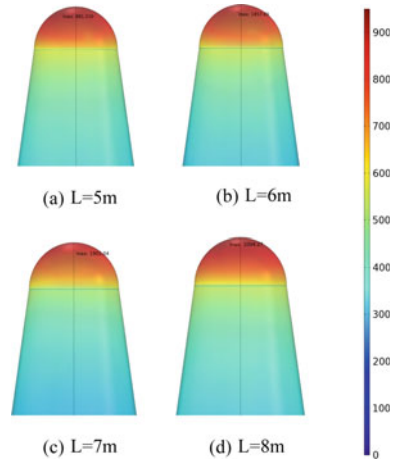
Comparison of Experimental Results

In this paper, the 220 kV and 110 kV voltage level transmission lines are simulated by electrostatic field. The height of the tree is adjusted by keeping the tree directly below the edge phase conductor. When the maximum field strength on the crown surface reaches the initial field strength of the streamer, the tree-wire vertical distance is the critical breakdown distance. In the 220 kV voltage level line model, when the tree-wire distance is 24 cm, the maximum field strength on the tree crown surface is 37.16 kV/cm, which is close to the initial field strength of the streamer. In the 110 kV voltage level line model, when the tree-wire distance are 10 cm and 9 cm, the maximum field strength on the tree crown surface are 44.09 kV/cm and 46.82 kV/cm, respectively. The comparison results are shown in Tab. 1. The simulation results are close to the experimental results, which can verify the accuracy of this simulation method to calculate the critical breakdown distance between tree lines.

3.3 Analysis of Simulation Results

The cone crown has a great influence on the distortion of the spatial electric field. Taking the 220 kV model as an example, the wire spacing is 6.5 m. Keep the height of the tree unchanged, and study the influence of different horizontal positions of the tree on the spatial electric field distribution by changing the horizontal position. When the horizontal position of the tree is 5 m, 6 m, 7 m and 8 m from the center, the maximum values of the field strength on the surface are 881.21 kV/m, 1 857.69 kV/m, 1901.04 kV/m and 1004.27 kV/m, respectively. It can be seen that when the tree is gradually close to the edge conductor, the field strength value of the crown surface gradually increases, and the crown tip gradually moves away from the edge conductor, and the maximum surface electric field strength also decreases. The electric field distribution on the crown surface is shown in Fig. 5. And the maximum field strength on the tree crown surface is 3606.63 kV/m, which is the largest right below the edge phase conductor.

Fig. 5 Side view of electric field distribution on tree surface at different horizontal distances



3.4 Determination of Safe Distance Between Trees and Wires

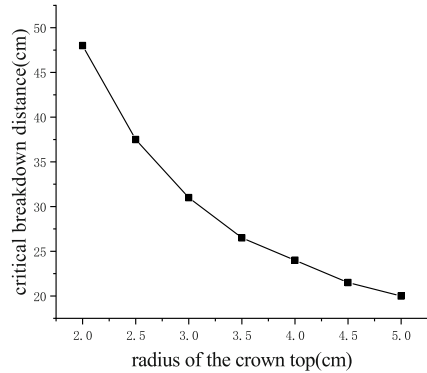
When studying the safety distance between the line and the tree, the maximum probability of discharge under normal conditions is considered as the minimum safety standard, and the critical situation is the most serious when the side phase voltage is at the positive peak [13]. Therefore, phase A of side conductor is set at positive peak value in the simulation. Keep the tree below the A-phase conductor and adjust the height of the tree.

When the radius of top of the canopy changes, the initial field strength of the streamer change. Considering the influence of the structure and tip of the actual tree on the simulation results, the top radius is 2 cm to 5 cm, and the critical breakdown distances corresponding to different radii are calculated respectively. The simulation results of the 220 kV model are shown in the following table. The relationship between the critical breakdown distance and the radius of the top of the canopy can be obtained from the data in Table 2, as shown in Fig. 6.

Table 2. 220 kV model simulation calculation results

Radius of the Crown Top	Initial streamer field strength	Maximum field strength at critical height	Critical breakdown distance
2 cm	40.98 kV/cm	40.89 kV/cm	48 cm
2.5 cm	39.59 kV/cm	39.54 kV/cm	37.5 cm
3 cm	38.61 kV/cm	38.46 kV/cm	31 cm
3.5 cm	37.81 kV/cm	37.81 kV/cm	26.5 cm
4 cm	37.16 kV/cm	36.70 kV/cm	24 cm
4.5 cm	36.61 kV/cm	36.57 kV/cm	21.5 cm
5 cm	36.13 kV/cm	36.06 kV/cm	20 cm

Fig. 6 The relationship between the critical breakdown distance and the radius of the top of the canopy



The smaller the radius value of the top of the canopy, the greater the critical breakdown distance. In the simulation of the 110 kV model, when the radius is 1 cm, the critical breakdown distance is 0.1 m, which is less than the experimental value. The critical breakdown distance should be a larger value between the simulation value and the experimental value, which is 0.12 m. For 220 kV transmission lines, the maximum critical breakdown distance is 0.48 m.

4 Conclusion

- 1) The simulated canopy breakdown gap experiments under 110 kV and 220 kV AC transmission lines were carried out. The tree-wire breakdown distance under the corresponding voltage level was determined by continuously adjusting the distance between the wire and the tree to record the voltage value at breakdown. At 110 kV voltage level, the air gap is broken down when the tree is 12 cm away from the wire, and the critical breakdown distance at 220 kV voltage level is 27 cm. The simulation results are close to the experimental results, which can verify the accuracy of the simulation method.
- 2) The simulation results show that the smaller the radius of the top of the canopy, that is, the sharper the top of the tree, the greater the critical breakdown distance. According to the experimental results and simulation results, the critical breakdown distance of 110 kV transmission line is 12 cm, and that of 220 kV transmission line is 48 cm. In order to avoid the fault, the tree-wire distance should be greater than the critical breakdown distance.

Acknowledgements This work is supported by Key R&D project of Ningxia Hui Autonomous Region(2021BDE931027); Science and technology project of State Grid Ningxia Electric Power Co. Ltd(5229DK2004P).

References

1. Xu, Z.: Research on Protection Method of UHVDC Transmission Line. Shanghai Dianji University, Shanghai, China (2021). (in Chinese)
2. Maruvada, P.S.: Electric field and ion current environment of HVDC transmission lines: comparison of calculations and measurements. *IEEE Trans. Power Delivery* **27**(1), 401–410 (2012)
3. Liu, H., Wu, J., Chen, H., et al.: Research on the prediction of hidden trouble of distribution lines. *Power Safety Technol.* **23**(6), 47–50 (2021). (in Chinese)
4. Zhou, Y., Wang, R., Xie, Y., et al.: Tree height growth rhythm of fast-growing ultra-high trees under overhead line. *J. Central South Univ. Forestry & Technol.* **36**(2), 75–78 (2016). (in Chinese)
5. Liu, W., Zhang, T., Hu, Z., et al.: A Transmission line monitoring device based on ultrasonic and wireless networking technologies. *Automation of Electric Power Syst.* **37**(10), 97–103 (2013). (in Chinese)
6. Johnson, G.B., Clairmont, B.A.: Measurements of AC and DC field and corona effects in a hybrid corridor. In: *Proceedings of the American Power Conference*, April 24 – 26, Chicago, USA (1988)
7. DL/T 436–2021. Code for design of 110 kV/750 kv overhead transmission line. Beijing, China: China Planning Press (2010)
8. Wang, D.: Research on Ion Flow Field Characteristics of HVDC Transmission Lines Adjacent to Complex Objects. North China Electric Power University, Beijing, China (2019). (in Chinese)
9. Li, X., Cui, X., Zhen, Y., et al.: The ionized fields and the ion current on a human model under 800 kV HVDC transmission lines. *IEEE Trans. Power Delivery*, **27**(4), 2141–2149 (2012)
10. Fang, X.: Analysis of Distribution Characteristics and Influencing Factors on Ion Flow Field of HVDC Transmission Lines. Northeast Electric Power University, Jilin, China (2020). (in Chinese)
11. Maruvada, P.S.: Influence of wind on the electric field and ion current environment of HVDC transmission lines. *IEEE Trans. Power Delivery*, **29**(6) (2014)
12. Geng, Y., Zhuang, C., Zeng, R., et al.: Streamer inception characteristics under positive lightning impulse voltage. *Proceedings of the CSEE* **32**(19), 148–153+198 (2012, in Chinese)
13. Zhao, H., Huang, S.: Study on electric field variation characteristics and critical breakdown distance of 110k V transmission line near trees. *Comput. Digital Eng.* **48**(08), 2057–2063 (2020). (in Chinese)

An Optimization Design Method of Multi-chip Parallel Power Module Based on Machine Learning



Jianing Wang, Yaodong Huang, Fuchen Wu, and Shaolin Yu

Abstract As an important component in power electronic energy conversion system, power semiconductor module layout and its multi-objective optimization are considered to be the key steps to achieve excellent performance of silicon carbide. Low parasitic parameters, low junction temperature, high power density and high reliability are the key design elements of multi-chip parallel silicon carbide power module. The existing traditional design methods largely rely on the experience of trial and error, the design cycle is long and the cost is high. This paper proposes a multi-objective optimization design method of power module based on artificial neural network ANN and deep reinforcement learning (DRL). Firstly, ANN and FEM are used to solve the problem that the self-inductance and mutual inductance of power module and the thermal coupling between multi-chips are difficult to be represented by mathematical formulas. At the same time, deep reinforcement learning (DRL) and the training results of artificial neural network (ANN) are used for multi-objective optimization of three optimization objectives: parasitic inductance, junction temperature and power density. Based on this method, a 1200 V/300 A half bridge power module with three parallel chips is optimally designed. This power module has good parasitic inductance, junction temperature and power density. This design method has certain guiding significance for the packaging design of silicon carbide multi chip parallel power modules.

Keywords Power Module · Artificial Neural Network · Deep Reinforcement Learning · Multi-objective Optimization Design

J. Wang · Y. Huang (✉) · F. Wu · S. Yu
School of Electrical Engineering, Hefei University of Technology, Hefei 230009, China
e-mail: hyd.1999@qq.com

© Beijing Paiké Culture Commu. Co., Ltd. 2023
X. Dong et al. (eds.), *The proceedings of the 10th Frontier Academic Forum of Electrical Engineering (FAFEE2022)*, Lecture Notes in Electrical Engineering 1054,
https://doi.org/10.1007/978-981-99-3408-9_76

1 Introduction

With the rapid development of new energy power generation, electric vehicles, high-speed rail and other electrified transportation fields, the requirements for power modules are getting higher and higher. Silicon carbide power module has been widely used for its advantages of high switching speed and low loss [1]. In the field of medium and large power applications, the capacity of power modules has been put forward a higher and higher demand. In the large capacity power modules, more and more chips need to be connected in parallel. However, most of the existing package design schemes are inherited from the silicon (Si)-based module packaging technology, which is difficult to play the characteristics of silicon carbide devices [2]. In order to meet the increasingly stringent operating conditions, the power module should meet the requirements of low parasitic inductance, low junction temperature, high power density, and high reliability. Compared with the single-sided heat dissipation power module, the double-sided cooling multi chip parallel power module has higher power density and lower parasitic parameters. In recent years, in order to further improve the efficiency, power density and reliability of vehicle motor controllers, the application of double-sided heat dissipation power modules in electric vehicles has received more and more attention [3].

However, when the layout of the power module is not correct, there are certain differences in the parasitic parameters of the parallel chip branches and the degree of thermal coupling between the chips. The above reasons will cause serious current sharing problems at the moment when the power module is on and off, and lead to different aging problems during the use of the power module. For some commercial multi-chip power modules, articles [4] and [5] have proved that the current overshoot gap is more than twice due to the difference of parasitic parameters, and the different junction temperature distribution of the chip has different effects on the aging of the chip.

At present, there has been extensive research on multi-chip parallel connection and junction temperature. Articles [6] proposed a copper clamp method to reduce the parasitic inductance caused by the bonding wire, so as to balance the current sharing effect of parallel chips. Articles [7] proposed a staggered plane packaging method, which effectively reduced the parasitic inductance and junction temperature of the module by using the principles of mutual inductance and double-sided heat dissipation. Reference [8] proposed an automatic placement software for power modules, which uses NSGA algorithm and Randomization algorithm to carry out multi-objective optimization. Articles [9] proposed a double-sided power module based on silver sintering technology, which effectively reduces the junction temperature of double-sided power module by using silver sintering technology. Articles [10] proposed a full bridge power module with highly integrated PCB embedded, which effectively reduced the parasitic inductance of the power module. However,

there are still some problems in the multi-objective optimization design of dual sided heat dissipation power modules:

1. Although the traditional design method can improve the performance of the double-sided heat dissipation power module, to a large extent, it depends on experience trial and repeated tests. The whole design process has a long cycle, high cost and low competitiveness. In addition, the traditional design methods focus on reducing the parasitic parameters of the package, ignoring the thermal performance.
2. In the complex power module structure, the self-inductance and thermal coupling between multiple chips of the power module are difficult to be characterized by mathematical formulas.
3. At present, most of the mainstream multi-objective optimization algorithms are NSGA algorithms. Although the genetic algorithm has been proved to be suitable for multi-objective optimization scenarios, the NSGA algorithm cannot accurately obtain the weight ratio of each optimization objective and its corresponding optimal solution.

Aiming at the current design problem of double-sided heat dissipation power module, this paper proposes an optimization design method of power module based on machine learning. First, a power module with low parasitic inductance and low junction temperature is designed by using the theory of laminated terminals and equivalent heat transfer area. Then, parametric scanning simulation and ANN training are carried out for the designed power module. Finally, DRL and ANN are used for parasitic inductance and junction temperature, three optimization objectives of power density are used for multi-objective optimization.

2 Layout of Double Side Cooling Power Module Based on Laminated Terminal and Equivalent Heat Transfer Area

2.1 Laminated Terminal and Equivalent Heat Transfer Area

The laminated terminals can not only reduce the area of the converter circuit, but also use the principle of mutual inductance cancellation, as shown in Fig. 1 (a), to achieve the low parasitic inductance design of the power module. The rectangular conductor placed in the upper and lower layers in Fig. 1 (a) represents the upper and lower terminals of the power module, and the corresponding parasitic inductance model is shown in Fig. 1 (b).

The loop inductance can be roughly calculated by Eq. (1):

$$L_{eq} = L_1 + L_2 - 2M_{12} \quad (1)$$

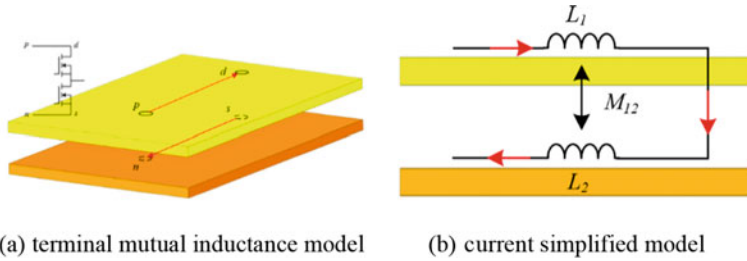


Fig. 1 Schematic diagram of laminated terminal

L_1 and L_2 are upper and lower terminals, and M_{12} represents mutual inductance between them. Due to the counteraction of mutual inductance M_{12} , the total parasitic inductance decreases.

The double side cooling module is usually of the 10 layer structure shown in Fig. 2 (a), which has good thermal conductivity, electrical insulation and other advantages. According to the electrothermal analogy, the thermal characteristics of the power module can be represented by the thermal network model. As shown in Fig. 2 (b), the current source, resistance and ground potential in the thermal network model are respectively equivalent to the heat source power consumption, thermal resistance and ambient temperature in the thermal system.

The SiC power module will generate power loss during operation, which will cause the chip temperature to rise. The module is internally encapsulated with silicon gel, so the heat generated by the chip is mainly transferred through the bottom plate of the upper and lower DBCs in the form of thermal convection. When the heat is diffused from the upper substrate or the lower substrate, thermal diffusion will occur. The thermal diffusion path is shown in Fig. 2 (a). When the chip spacing is close, the thermal coupling effect between chips is strong. Under the same power consumption conditions, the temperature difference is higher. According to the definition of thermal resistance, it can be seen that:

$$R_{th} = \frac{\delta}{\lambda A} = \frac{\Delta T}{P} \tag{2}$$

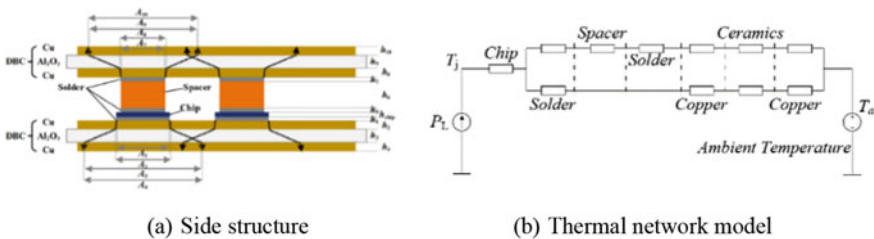


Fig. 2 Schematic Diagram of side structure and thermal network model

In Eq. (2), R_{th} is the thin layer thermal resistance, δ is the thickness of thin layer, λ is the thermal conductivity of the material, A is the equivalent heat transfer area, ΔT is the temperature difference between two sides of the object, and P is the heat transfer power.

In the above formula, the equivalent heat transfer area is mainly determined by the thermal diffusion angle of the material. For the thermal diffusion angle, there is a fixed value of 45° , which is commonly used at present. The arc tangent of the ratio of the current layer thermal conductivity to the lower layer thermal conductivity is calculated or the Fourier series method is used to analyze the thermal diffusion angle, and most of the thermal diffusion angles are models of single-sided heat dissipation modules. Therefore, the finite element method (FEM) is used to obtain a series of heat flow densities on the vertical path of the chip center and draw the change curve. Because the upper and lower thermal resistances of the two-sided water-cooled heat dissipation module are different, the heat transfer heat flow densities of the solder layer and the lower solder layer on the chip need to be simulated by Finite Element Method to calculate the power consumption of heat dissipation through the upper and lower DBC, and finally determine the size of the heat diffusion angle.

According to the thermal diffusion angle theory and the thermal coupling principle, determine a more appropriate chip landing position on the DBC, and determine the landing position of the stack terminal according to the demand for parallel current sharing between multiple chips.

2.2 Overall Structure of Power Module

According to the existing chip power level, EPM3-1200-0017D1 silicon carbide chip is selected as the parallel chip of the packaging module. The current carrying capacity of a single chip is weak, only 134 A, and multiple chips need to be connected in parallel to meet the power demand of the vehicle module. In order to ensure 100 KW power output, the form of three chips in parallel is selected. This design can meet the application requirements of most vehicle modules. The equivalent circuit diagram of the packaging module is shown in Fig. 3(a). The packaging module is a half bridge module composed of three silicon carbide (SiC) chips in parallel on each of the upper and lower bridge arms. The overall structure of the half bridge module is shown in Fig. 3(b).

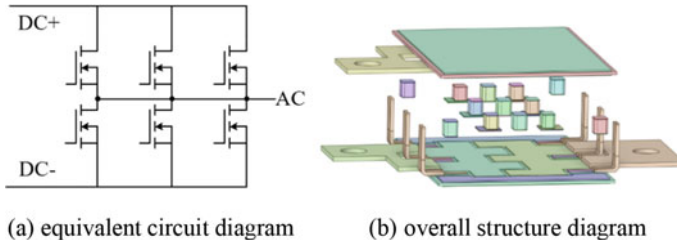


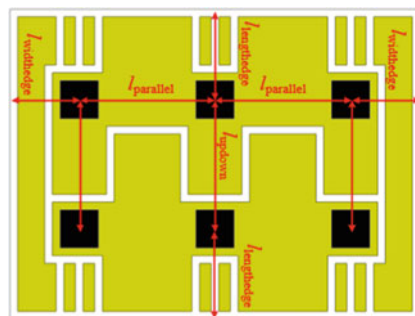
Fig. 3 Overall structure of power module

3 Modeling of Parasitic Inductance, Thermal Resistance and Power Density

According to the power module structure in the first section, this section will model the parasitic inductance, thermal resistance and power density of the power module. Its main dimensions on the plane are shown in Fig. 4. $l_{parallel}$ is the distance between parallel chips on the same bridge arm, l_{updown} is the distance between upper and lower bridge arm chips, $l_{lengthedge}$ is the distance between the chip and the length of the module, and $l_{widwedge}$ is the distance between the chip and the width of the module.

Artificial Neural Network (ANN) can be regarded as a general function approximator, which can be set with arbitrary precision and approximate the relationship between input and output data [11]. ANN is a new algorithm, which is similar to the biological brain. A group of signal processing units (artificial neurons) receive, process and transmit information from neurons. The weights between neurons are obtained by training parameters. The ANN is trained through the provided data set, so as to achieve the effect of approximating the relationship between input and output data [12]. In the power module design, if multiple groups of design parameters and performance indicators are obtained and the relationship between parameters is obtained by training ANN, the simulation results corresponding to different data can be obtained at the fastest speed.

Fig. 4 Main dimensions of power module



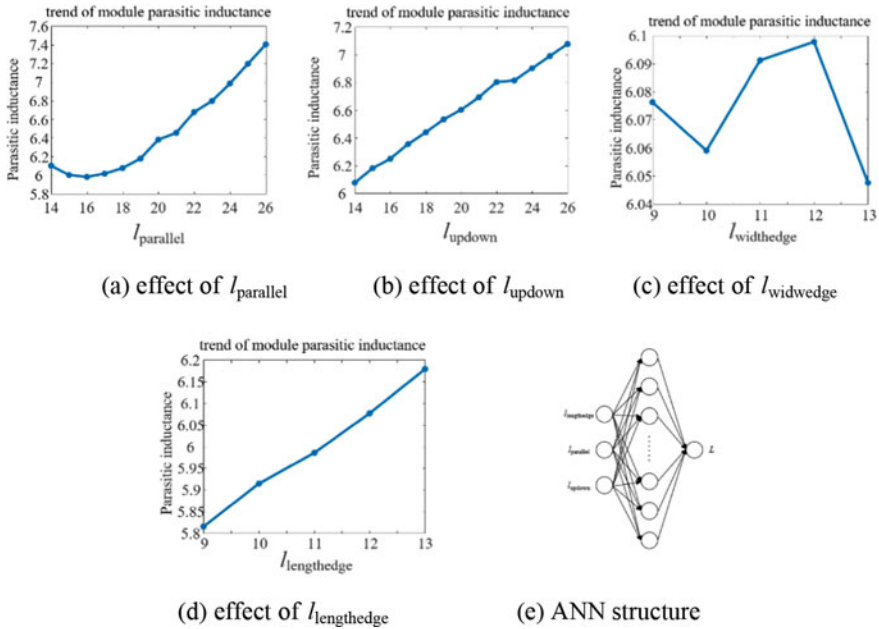


Fig. 5 Influence of variables on inductance and ANN structure

3.1 Model of Parasitic Inductance

This part further explores the influence of each variable on the parasitic inductance. Parametric simulation is carried out for four variables. The influence of each variable on the parasitic inductance is shown in Fig. 5(a) (b) (c) (d). It can be seen from the change trend that $l_{widwedge}$ has little influence on the parasitic inductance, and the remaining variables $l_{parallel}$, l_{updown} , and $l_{lengthedge}$ have great influence on the parasitic inductance.

Therefore, $l_{parallel}$, l_{updown} , and $l_{lengthedge}$ are ANN input variables, and the parasitic inductance L is the output variable. With $l_{parallel}$, l_{updown} , and $l_{lengthedge}$ as independent variables, a total of 845 groups of data were obtained through the parametric scanning simulation through the Q3D finite element simulation software, and neural network training was conducted for the parasitic inductance data set using the artificial neural network. The structure of the parasitic inductance ANN is shown in Fig. 5(e).

3.2 Model of Junction Temperature

This part further explores the impact of each variable on the junction temperature. Parametric simulation is carried out for four variables. The impact of each variable

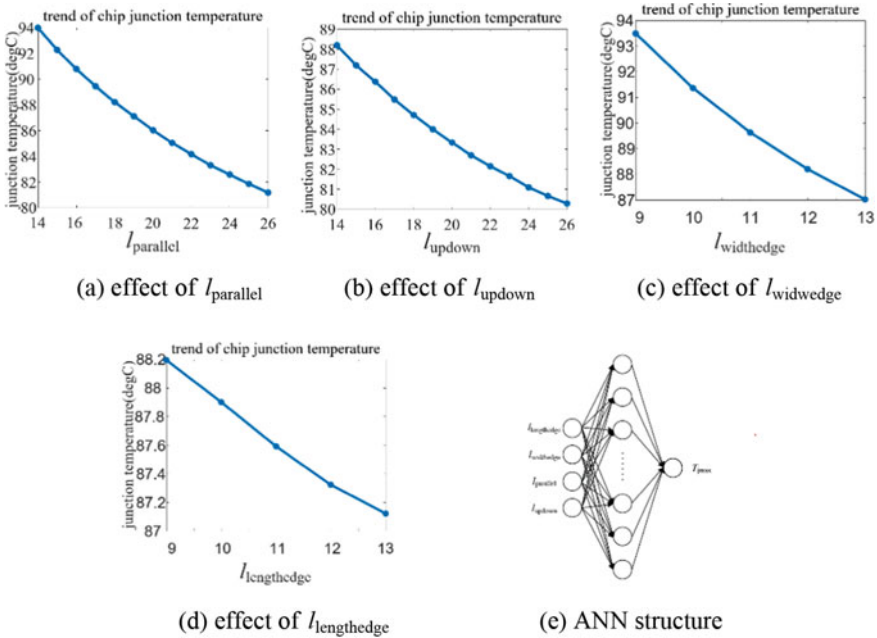


Fig. 6 Influence of variables on junction temperature and ANN structure

on the junction temperature is shown in Fig. 6 (a) (b) (c) (d). From the change trend, it can be seen that $l_{lengthedge}$, $l_{widthedge}$, $l_{parallel}$, and l_{updown} have a greater impact on the parasitic inductance. Therefore, $l_{lengthedge}$, $l_{widthedge}$, $l_{parallel}$, and l_{updown} are the ANN input variables, and the highest junction temperature T_{jmax} of the module is the output variable.

Through COMSOL finite element simulation software, 4225 groups of data were obtained through electrothermal coupling parametric scanning simulation, and neural network training was conducted for junction temperature data set using artificial neural network. The structure of ANN of parasitic inductor is shown in Fig. 6(e).

3.3 Model of Power Density

The power density can be directly calculated by the formula. The specific calculation formula is shown in Formula (3), where h is the module height, U is the rated voltage, and I is the rated current.

$$Power\ Density = \frac{U \times I}{((2l_{parallel} + 2l_{widthedge}) \times (l_{updown} + 2l_{lengthedge}) \times h)} \quad (3)$$

4 Power Module Optimization Design

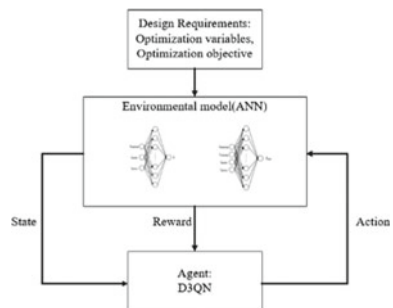
4.1 Principle of D3QN Deep Reinforcement Learning

In recent years, power electronic automation design can quickly realize the optimal design of power electronic converters through computers, which has attracted extensive attention of researchers [13, 14]. At present, meta heuristic algorithms such as genetic algorithm, particle swarm optimization algorithm and ant colony algorithm are mostly used in power electronic automation design to achieve optimal design of power electronic system [15]. In order to overcome the optimization time consuming problem caused by the change of design requirements in meta heuristic algorithm, the artificial intelligence optimization algorithm based on machine learning has been developed rapidly because it can quickly respond to the change of design requirements to provide optimal decisions, and has been initially applied in the field of electric energy. This paper establishes a flexible optimization mechanism through the D3QN algorithm in DRL. This optimization mechanism can optimize the size of power modules. The optimization design framework is shown in Fig. 7.

Dueling Double Deep Q Network algorithm (D3QN) consists of two neural networks, one as a real-time training network and the other as an output network. First, under the state S_t at time t , the action A_t is obtained through the strategy network, which is input into the power module environment, and the reward R_t at this time and the next state S_{t+1} are obtained. Then, the state transition sequence (S_t, A_t, R_t, S_{t+1}) is stored in the experience playback pool. Finally, N groups of data are randomly selected according to the small batch sampling strategy to train the neural network, where the actions are ϵ_greedy policy. The real-time training network parameters are updated through the strategy gradient, and the calculation formula is shown in Eq. (4). The agent scores actions during interaction, so the reward R is set as shown in Eq. (5):

$$y_t = r_{t+1} + \gamma q(S_{t+1}, \operatorname{argmax}_a q(S_{t+1}, a; \omega_e); \omega_i) \tag{4}$$

Fig. 7 Optimization design framework



$$R = 5^{(3 - (k_1 \times L^2 + k_2 \times T^2 + k_3 \times Powerdensity^2))} \tag{5}$$

4.2 D3QN Training Results

Before formal training, the key parameters of the algorithm need to be set, as shown in Table 1, and the specific training process of D3QN is shown in Table 2.

Figure 8 shows the average reward convergence diagram of D3QN algorithm training process. It can be seen from Fig. 8 that the average cumulative reward is relatively small in the early stage of training, because the agent immediately executes actions in the early exploration stage, interacts with the environment and collects experience data, the network parameters start to update, the agent gradually learns the optimization strategy of the optimal size, the average cumulative reward gradually increases and converges, and after the training process. The optimal size can be obtained. When the weight ratio $K_1 : K_2 : K_3 = 1 : 1 : 1$, the optimal size is shown in Table 3.

Table 1 Variable range

variable	value
$l_{parallel}$ (mm)	14–26
l_{updown} (mm)	14–26
$l_{lengthedge}$ (mm)	9–13
$l_{widthedge}$ (mm)	9–13

Table 2 Training process

Algorithm: D3QN algorithm
Input: determine the state space and action space, initialize the neural network parameters, and determine the experience playback pool
1: For each training round:for episode = 1,2,...,M:
2: Get Initial State S_1
3: For each step in the training round:for t = 1,2,...,T:
4: Get the action according to the current strategy;
5: The environment model executes actions to obtain rewards and the next state;
6: Save the state transition sequence to the experience playback pool;
7: Randomly select N groups of data from the experience playback pool;
8: Update the neural network once;
9: End of single training round
10: Update the strategy network every five training rounds
11: End of M training rounds

Fig. 8 Training reward convergence graph

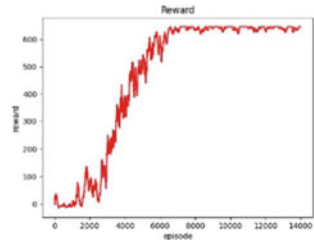


Table 3 Optimum size

variable	value
$l_{parallel}$ (mm)	17.6
l_{updown} (mm)	16.9
$l_{lengthedge}$ (mm)	10.8
$l_{widthedge}$ (mm)	9

5 Simulation Verification

5.1 Simulation and Verification of Parasitic Inductance

The module is a half bridge circuit, and the topology is shown in Fig. 3. In the above module, the entire module has three paths, and each branch is coupled with each other. The parasitic inductance of the entire circuit will be simulated based on Q3D. The simulation result is an inductance matrix containing self-inductance and mutual inductance. The effective inductance of each branch needs to be obtained after decoupling. First, the parasitic inductance from DC + to DC- is simulated. The simulation diagram is shown in Fig. 9. According to the Q3D simulation results, the overall parasitic inductance from DC + to DC - is 6.14 nH.

Fig. 9 Parasitic inductance simulation

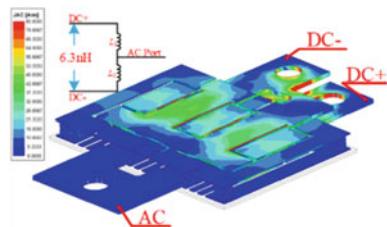
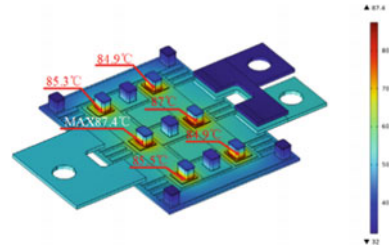


Fig. 10 Temperature field simulation



5.2 Simulation and Verification of Temperature Field

Generally, the farther the chip spacing is, the smaller the thermal coupling between chips is. When the equivalent heat transfer areas cross, there is a thermal coupling relationship. When the DBC area size is fixed, the chip distribution should be as uniform as possible. After comparison, it is found that under the same DBC size, the chips are arranged in six shapes, which can not only reduce the temperature coupling, but also take into account the current sharing and the overall parasitic inductance of the module.

Based on COMSOL simulation software, the module conduction current is set to 210A, the heat dissipation boundary condition is located on the upper and lower surfaces of the power module, and the thermal convection coefficient is set to 5000. The DBC material is set to copper (Cu) and aluminum oxide (AlN), the gasket material is molybdenum (Mo), the chip material attribute is set to silicon carbide (SiC), and the solder layer is silver sintered (Ag). The temperature field simulation results are shown in Fig. 10 below, the maximum junction temperature of the module is 87.4 °C.

6 Conclusion

In this paper, a half bridge power module is initially constructed by using the equivalent heat transfer area, laminated terminals and other theories, and a multi-objective optimization design method of power module based on artificial neural network (ANN) and deep reinforcement learning (DRL) is proposed. Finally, Q3D is used for parasitic inductance simulation design verification, which proves that this power module has extremely low parasitic inductance; COMSOL is used to verify the electrothermal coupling simulation design, which proves that this power module has a good heat dissipation effect.

References

1. Huang, A.Q.: Power semiconductor devices for smart grid and renewable energy systems. In: Proceedings of the IEEE, **105**(11), 2019–2047
2. Bęczkowski, S., Jørgensen, A.B., Li, H., Uhrenfeldt, C., Dai, X., Munk-Nielsen, S.: Switching current imbalance mitigation in power modules with parallel connected SiC MOSFETs. In: 2017 19th European Conference on Power Electronics and Applications (EPE'17 ECCE Europe), p. 18 (2017)
3. Zeng, Z., Ou, K., Wang, L., Yu, Y.: Reliability-oriented automated design of double-sided cooling power module: a thermo-mechanical-coordinated and multi-objective-oriented optimization methodology. In: IEEE Transactions on Device and Materials Reliability **20**(3), 584–595
4. Wu, R., Smirnova, L., Wang, H., Iannuzzo, F., Blaabjerg, F.: Comprehensive investigation on current imbalance among parallel chips inside MW-scale IGBT power modules. In: 2015 9th International Conference on Power Electronics and ECCE Asia (ICPE-ECCE Asia), pp. 850–856 (2015)
5. Zhong, Y., Meng, J., Ning, P., Zhang, D., Wen, X.: Comprehensive comparative analysis of two types of commonly-used layouts of IGBT packages. In: 2014 17th International Conference on Electrical Machines and Systems (ICEMS), pp. 1952–1956 (2014)
6. Wang, L., et al.: Cu clip-bonding method with optimized source inductance for current balancing in multichip SiC MOSFET power module. In: IEEE Transactions on Power Electronics **37**(7), 7952–7964
7. Yang, F., et al.: Interleaved planar packaging method of multichip SiC power module for thermal and electrical performance improvement. In: IEEE Transactions on Power Electronics **37**(2), 1615–1629
8. Al Razi, I., Le, Q., Evans, T.M., Mukherjee, S., Mantooh, H.A., Peng, Y.: PowerSynth design automation flow for hierarchical and heterogeneous 2.5-D multichip power modules. In: IEEE Transactions on Power Electronics **36**(8), 8919–8933
9. Ding, C., Liu, H., Ngo, K.D.T., Burgos, R., Lu, G.-Q.: A double-side cooled SiC MOSFET power module with sintered-silver interposers: I-design, simulation, fabrication, and performance characterization. In: IEEE Transactions on Power Electronics **36**(10), 11672–11680
10. Li, B., Yang, X., Wang, K., Zhu, H., Wang, L., Chen, W.: A compact double-sided cooling 650V/30A GaN power module with low parasitic parameters. In: IEEE Transactions on Power Electronics **37**(1), 426–439
11. Dragičević, T., Wheeler, P., Blaabjerg, F.: Artificial intelligence aided automated design for reliability of power electronic systems. In: IEEE Transactions on Power Electronics **34**(8), 7161–7171
12. Guillod, T., Papamanolis, P., Kolar, J.W.: Artificial neural network (ANN) based fast and accurate inductor modeling and design. In: IEEE Open Journal of Power Electronics, **1**, 284–299
13. Busquets-monge, S., et al.: Power converter design optimization. In: IEEE Industry Applications Magazine **10**(1), 32–38
14. Evans, P.L., Castellazzi, A., Johnson, C.M.: Design tools for rapid multidomain virtual prototyping of power electronic systems. In: IEEE Transactions on Power Electronics **31**(3), 2443–2455
15. De León-Aldaco, S.E., Calleja, H., Aguayo Alquicira, J.: Metaheuristic optimization methods applied to power converters: a review. In: IEEE Transactions on Power Electronics **30**(12), 6791–6803

Low-Cost Modular Multilevel Converter Topology and Its Fault Control Strategy for Offshore Wind Power



Shuangfei Yang, Man Chen, Yongqi Li, Yuebin Zhou, Zhenkai Hu, Wenming Gong, and Yue Wu

Abstract Modular multilevel converter (MMC) used for offshore wind power transmission has become a major technical trend. Voltage drop of power grid will lead to limited power transmission, and dissipation device should be installed to meet the requirements of fault ride through. Considering the high cost of building the dissipation device separately for offshore wind power transmission system, the CSM topology is proposed in this paper, in which the chopper circuit and submodule of the onshore MMC are designed integrated to reduce the investment cost. The corresponding fault control strategy is proposed to match the asymmetric structure of CSM converter. In order to further reduce the design requirements of converter, the cooperative control strategy of the wind farm and CSM converter is adopted, which makes full use of the low voltage ride through ability of the full power wind turbine to consume part of the generated power, and greatly reduces the energy consumption of the converter during the fault ride through period. A system simulation model of 600 MW wind power transmission is built, and the integrated CSM converter topology and its control strategy are analyzed and verified.

Keywords Offshore Wind Power · CSM Converter · Voltage Ride Through · Circulating Control · Cooperative Control Strategy

1 Introduction

AC transmission of offshore wind power requires a large amount of dynamic reactive power compensation, while DC transmission does not have reactive power problems and the transmission distance is not limited [1]. With the development of modular

S. Yang (✉) · Y. Zhou · W. Gong · Y. Wu
Electric Power Research Institute, China Southern Power Grid Co., Ltd., Guangzhou, Guangdong, China
e-mail: yangsf@csg.cn

M. Chen · Y. Li · Z. Hu
CSG PGC Power Storage Research Institute, Guangzhou, Guangdong, China

© Beijing Paiké Culture Commu. Co., Ltd. 2023
X. Dong et al. (eds.), *The proceedings of the 10th Frontier Academic Forum of Electrical Engineering (FAFEE2022)*, Lecture Notes in Electrical Engineering 1054, https://doi.org/10.1007/978-981-99-3408-9_77

multilevel converter (MMC) technology, DC transmission based on MMC topology has become an effective way to achieve far-reaching offshore wind power transmission [2], and researchers have carried out a lot of research on MMC topologies and faults [3, 4]. The MMC based high-voltage direct-current (MMC-HVDC) transmission system of offshore wind power adopts cable transmission, and the line fault rate is low and most of them are permanent faults. Therefore, the fault ride through problem of AC collection line and DC transmission line cannot be considered, and it mainly needs to solve the fault ride through problem of onshore AC power grid. When voltage drop occurs, the power output of the MMC-HVDC system is limited. If the wind farm continues to generate electricity, energy dissipation devices need to be set to consume excess electric energy.

Common electrical faults of MMC have been summarized in [5], and a thorough and comprehensive review of the existing online fault diagnostic methods has been conducted. Considering the operating principle of AC energy dissipation device, an active energy control strategy [6] of converter based on AC / DC current dual control technology is proposed. DC chopper circuit is installed on high-voltage DC line [7], although the working principle of this kind of scheme is simple, it is technically difficult to connect IGBTs in series, and improper design may lead to breakdown of IGBTs in series. [8] proposes a modular DC side energy dissipation circuit, which avoids the series IGBT structure and improves the feasibility. However, under normal conditions, voltage balance control needs to be used to constantly switch submodules, which will cause additional losses. [9] sets the energy dissipation device at the AC collection point of the wind farm, and onshore converter needs to switch to the constant DC current control mode to trigger the dissipation device to consume energy.

For the wind farm composed of constant speed and doubly fed wind turbines, since the generator is directly coupled with the centralized power grid, the frequency up and the voltage down methods can be used to control the converter at the wind farm side, limit the power generated by the wind turbines to realize fault ride through [10, 11]. For full power wind turbines, the method of reducing the collection voltage of the wind farm [12] to limit the generated power has been proposed, but it has no detailed analysis. [13] has proposed to use communication to limit the power of the wind farm to reduce the unloading energy of the DC chopper, and the communication delay is considered in the analysis.

Considering that the space and load of the offshore converter station platform are limited, and it is not convenient and uneconomical to set the dissipation device at the wind farm side. Therefore, this paper proposes a novel topology, in which the energy dissipation device and the onshore converter are designed in an integrated structure to simplify the circuit structure and reduce the system cost, and the corresponding fault control strategy to adapt to this asymmetric configuration is designed. In addition, the cooperative control strategy of MMC-HVDC and the wind farm is proposed and analyzed to further reduce the energy dissipation requirements, then the proposed topology and control strategies are proved and analyzed by the simulation model. Finally, this paper draws a conclusion at the end.

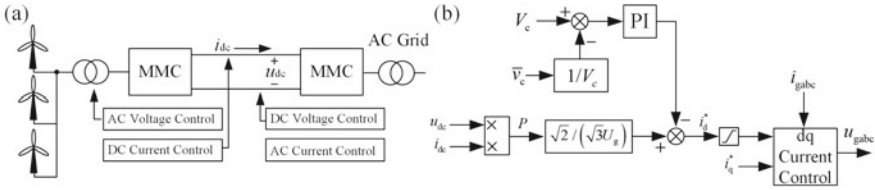


Fig. 1 Offshore wind power transmission system (a) System structure and basic control, (b) Current control of onshore converter.

2 Integrated Design and Control of CSM Converter

2.1 Offshore Wind Power Transmission System

The system structure of offshore wind power transmitted through MMC-HVDC is shown in Fig. 1(a). The offshore converter controls the AC collection grid voltage and DC output current, and the onshore converter controls DC voltage and AC current. The current control of onshore converter is shown in Fig. 1(b). The active current reference signal is jointly determined by the DC power calculation value and the capacitor voltage feedforward of the submodule. Through the feedback of the average capacitor voltage, the internal energy stability of converter can be dynamically maintained, and the impact of losses can be eliminated.

When the grid voltage drops, the AC output power will decrease rapidly while the DC input power will not change, resulting in a rapid increase of capacitor voltage of the converter submodules on the grid side, and the capacitor voltage feedforward control will make the given signal of active current reach the limit value quickly. If the excess power is not consumed in time, the overvoltage fault of the submodule will be triggered, and the fault can be detected and triggered in a variety of ways: 1. Detect the voltage amplitude of the power grid, 2. Detect the limiting link of the given signal of the grid connected active current, and 3. Detect the capacitor voltage of the sub-module. In this paper, the unloading control of the DC chopper circuit is triggered by the current limiting link.

2.2 Integrated Design of DC Chopper Circuit and Converter

The low-cost modular multilevel converter topology is shown in Fig. 2, which is applied to the onshore converter. A DC chopper circuit is added to submodules of phase A and phase B to form the CSM (Submodule with Chopper) phases, the conventional phase C is bridge arm with half bridge submodules, and the modular multilevel converter with CSM phases is called CSM converter in this paper.

Assuming that the unloading power of the system is P_S , the average power P_R of each energy dissipation resistor is as follows:

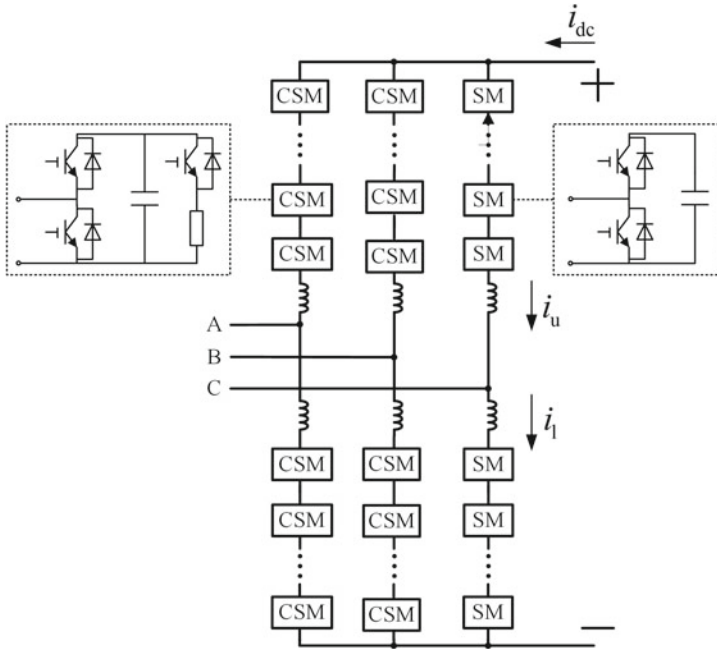


Fig. 2 Modular multilevel converter with CSM phases.

$$P_R = \frac{P_S}{2N} \tag{1}$$

where N is the number of submodules in each phase. Then the maximum resistance of the energy dissipation resistance is as follows:

$$R_{CSM} = \frac{2N V_c^2}{P_S} \tag{2}$$

where V_c is the rated voltage of the submodule capacitor. Choosing a smaller energy dissipation resistor can increase the dynamic regulation ability of the chopper circuit, but it will increase the current stress of the chopper IGBT. If a three-phase symmetrical voltage drop fault occurs in the power grid, the direct current of CSM phases during fault crossing is as follows:

$$i_{dcS} = \frac{P_S}{V_{dc}} + \frac{P}{3V_{dc}} \eta\% \tag{3}$$

where V_{dc} is the converter DC voltage, P is the rated system power, $\eta\%$ is the percentage of power that can still be sent during voltage drop period. Therefore, a large P_S will make the current of bridge arms to be much higher than the rated value

during the fault period, causing to select a half bridge IGBT with a higher rated current, so reducing P_S is of great significance for reducing the cost of the converter.

The chopper circuit of CSM directly consumes the energy of submodule, and its control is related to the capacitor voltage ripple of submodule. The expression of capacitor voltage ripple [14] is as follows:

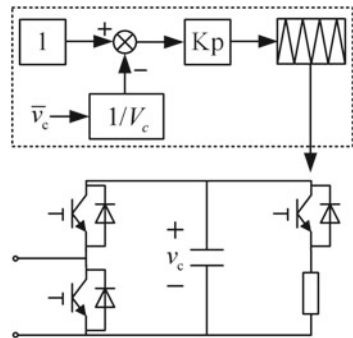
$$V_{\text{cpp}} = \frac{2S}{3m\omega V_c C N} \left(1 - \left(\frac{m \cos \varphi}{2} \right)^2 \right)^{\frac{1}{2}} \tag{4}$$

where V_{cpp} is peak to peak value of the capacitor voltage ripple, m is the modulation ratio, S is the apparent power, ω is the angular frequency, and C is the capacitance of the submodule. Capacitor voltage ripple is related to modulation ratio and apparent power. During low voltage ride through period, the modulation ratio of converter will decrease significantly. If the apparent power decreases in an equal proportion, the capacitor voltage ripple amplitude value will not change. However, it is generally necessary to inject a certain reactive current into the grid, so the voltage ripple amplitude value will be significantly higher than the rated value. The chopper circuit is a pure energy consumption device, if the chopper circuit is frequently triggered due to large capacitor voltage fluctuations, it will lead to excessive energy consumption of the bridge arm, causing the capacitor voltage to be lower than the rated value.

Figure 3 shows the control block diagram of the DC chopper. Since the fundamental frequency fluctuations in the capacitor voltages of the upper and lower bridge arms are complementary, feedback control using the average value of the capacitor voltages of the upper and lower bridge arms can eliminate the influence of the fundamental frequency ripple. On the other hand, using a proportional regulator for differential regulation can also avoid excessive energy consumption.

Compared with the independent modular DC dissipation device, the circuit structure of CSM is more simplified, the submodules have achieved voltage equalization in the normal operation state, and the chopper circuit is in the locked state, which will not cause additional losses. In addition, the energy of submodules can be directly consumed at the valve control layer, which can achieve better dynamic control effect.

Fig. 3 Chopper control of CSM.



2.3 Converter Circulating Control

In order to suppress the double frequency circulating component, it is generally necessary to add circulating suppression function to MMC control. A conventional circulation control method [15] is shown in Fig. 4. When the grid voltage is three-phase symmetrical, the internal circulating current component is obtained by subtracting 1/3 of the DC current component from the common mode current component. A double frequency proportional resonance controller is used to control the circulating current in a closed-loop. The circulating current control voltage is superimposed on the bridge arm modulation voltage to suppress the circulating current. The resonant controller can eliminate the double frequency circulating current component, and because of the existence of the proportional link, the harmonic circulating current of each frequency can be suppressed. However, for MMC equipped with CSM, if the above control method is still adopted, the CSM phases can only consume at most 2/3 of the DC input power during fault period, and the remaining phase will quickly occur sub-module over-voltage fault. Therefore, it is necessary to design corresponding circulating current control to introduce the excess power into the CSM phases.

Considering that asymmetric voltage drop may also occur in power grid, and the active output capacity of each phase of the converter may be different during fault period, so the DC current given signal of the conventional bridge arm should be determined according to the corresponding output power at the AC side. The improved circulating current control is shown in Fig. 5, where the DC current given signal of phase C is mainly calculated from the single-phase instantaneous power. Since the single-phase instantaneous power contains large double frequency fluctuations, the double frequency band stop filter is used for filtering, and the feedforward control of the capacitor voltage of the submodule is added to enhance the ability to dynamically stabilize the capacitor voltage of the submodule. The DC current given signals of the CSM phases are obtained by subtracting the DC current given signal of the conventional phase from the DC input current.

For normal operation, since the grid voltage is three-phase symmetrical, the AC output power is three-phase symmetrical, and the AC power and DC power is balanced, so the control strategy in Fig. 5 is equivalent to that in Fig. 4. When a power grid fault occurs, the improved control strategy can automatically introduce

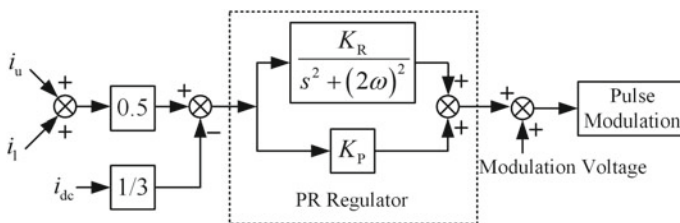


Fig. 4 Conventional circulating control of MMC.

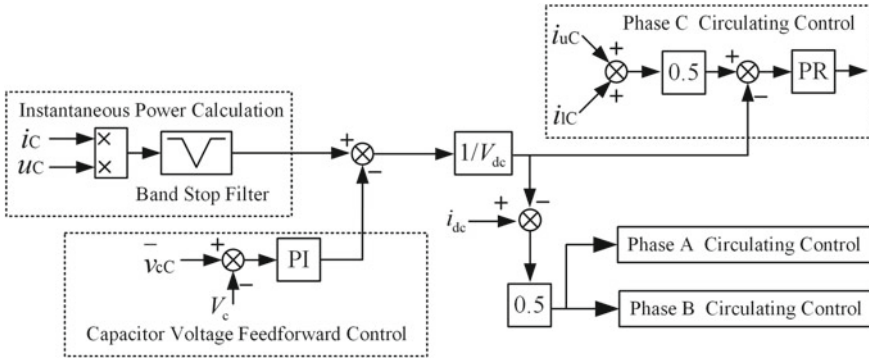


Fig. 5 Improved circulating current control of MMC with CSM phases.

excess power into the CSM bridge arms according to the output power state of the bridge arm without switching the control mode.

3 Cooperative Control of CSM Converter and Wind Farm

The low voltage ride through standard of wind turbines in China is shown in Fig. 6(a), which requires that wind turbines can operate at 90% of rated voltage for a long time, and operate continuously for 625 ms when the voltage drops to 20%, and inject reactive current into the power grid during the voltage drop period. The required injected reactive current is as follows:

$$I_T \geq 1.5 \times (0.9 - U_T) I_n \quad (0.2 \leq U_T \leq 0.9) \tag{5}$$

where I_n is the rated current of the wind turbine, U_T is the voltage unit value of the wind farm's common coupling point. Full power wind power converters are widely used for offshore wind power, and DC chopper circuit is generally installed at the DC bus of the wind turbines converter. When the output power is limited due to fault at the AC side, the voltage of the DC bus rises, and the DC chopper circuit is triggered to consume excess power by the voltage protection. Since the wind turbine generator is completely isolated from the grid, the grid connected current is completely controlled by the grid side wind turbine converter, so full power wind turbines have better low voltage ride through capability.

If the power generation of the wind farm is not limited during fault period, the CSM system needs to consume a large amount of electric energy in a short time, which puts forward strict requirements for the DC chopper circuit design of the CSM converter. Therefore, it is necessary to reduce the energy consumption requirements of the system by using the existing low voltage ride through capability of the wind turbines. During the low voltage ride through period, the offshore converter can

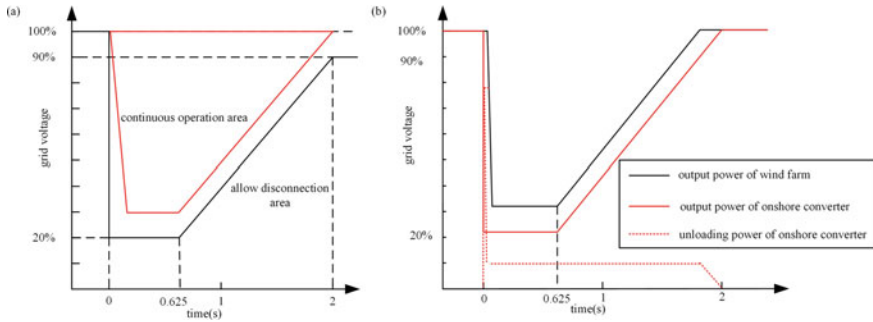


Fig. 6 Power curves during low voltage ride through period (a) for full power wind turbine, (b) for wind farm and onshore converter cooperative control.

control the wind farm’s collection voltage according to the red curve in Fig. 6(a), and the distribution of unloading power between the wind farm and the converter can be changed by setting the voltage sag depth. Since the collection voltage of the wind farm is controlled by the offshore converter, the low voltage crossing operation area of the wind turbine generator is reduced, and the voltage change rate is controlled, which reduces the risk of the wind turbine off the grid.

It is assumed that the grid voltage drops to the maximum, the collection voltage of the wind farm drops to 30% of the rated voltage with a certain slope, and the active current of the wind turbine and converter operate at 1.1 times of overload. When the collection voltage drops to 90% of the rated voltage, the DC chopper circuit of the wind turbine starts to work, and the power curve shown in Fig. 6(b) can be obtained. At the lowest point of the voltage, the wind farm and onshore converter retain 33% and 22% of the active power transmission capacity respectively. Since the voltage control of the collection grid lags behind the voltage drop of the power grid, there will be a short power impact of onshore converter in the initial state of fault, but then the power of the DC chopper circuit will be constant at 11% of the rated power of the system, thus the total energy consumption can be reduced significantly.

4 Simulation Analysis

A simulation model of 600 MW wind power transmission system is built. The DC transmission voltage is 320 kV, the modulation ratio is 0.9, the capacitance of the submodule is 30mf, the rated voltage of the submodule is 2 kV, the CSM chopper resistance is 2 Ω, and the wind farm adopts a single machine aggregation model.

Figure 7 shows the simulation results of fault ride through without cooperative control when fault occurs at $t = 2$ s. The AC voltage waveform of CSM converter is shown in Fig. 7(b). The grid voltage drops to 0.2p.u. and recovers to 0.9p.u. after two seconds, and the active current of the CSM converter operates at 1.1 times overload. The collection grid voltage of the wind farm is stable without limiting

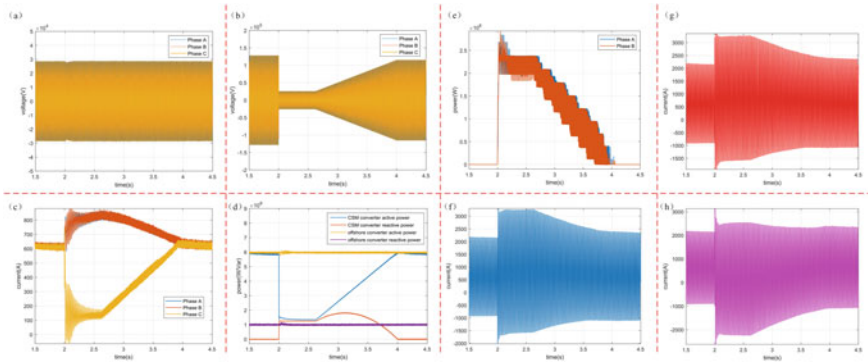


Fig. 7 Simulation results without cooperative control (a) Collection grid voltage, (b) CSM converter voltage, (c) Three-phase DC current components of CSM converter, (d) Active power and reactive power of converters, (e) Dissipation power of CSM converter, (f), (g), (h) Bridge arm current of Phase A, Phase B, Phase C in CSM converter.

the power generation of wind farm, as shown in Fig. 7(a). Figure 7(d) shows the generated power of the wind farm is still 600 MW because of the stable voltage. After fault occurs, the surplus power of the transmission system is consumed by the CSM converter, and because the power of the DC chopper circuit is discontinuous, Fig. 7(e) shows the result after resistance power filtering. When the fault occurs, according to the proposed current control strategy, due to the drop of output power of phase C, the DC current given signal of the bridge arm rapidly decreases, and most of the DC current is introduced into the CSM phases, the results of Fig. 7(c) and Fig. 7(f)-Fig. 7(h) verify the effectiveness of this control strategy. There is a peak current at the moment of fault, and the high-frequency harmonic circulation increases, the circulation controller quickly makes the internal current to a stable state.

According to the simulation results, the residual DC current is almost evenly introduced into phase A and phase B, and the maximum current of the half bridge IGBT of the CSM bridge arm is increased about 50% compared with the rated working state. If the CSM is configured in only one phase of the onshore converter, the maximum current in the configured CSM bridge arm will nearly double, which means that the half bridge IGBT of the CSM bridge arm needs to have a short-time overload operation capacity close to one time of the rated current, so the proposed topology is also conducive to the balance of bridge arm current during the low voltage fault period.

Figure 8 shows the simulation results of fault ride through with cooperative control. The CSM converter control remains unchanged in Fig. 8(b). In Fig. 8(a), the collection voltage of the wind farm drops to 0.3p.u. with a slope of 0.01p.u. per millisecond, and recovers to the rated value after two seconds. During fault period, the wind turbine operates at 1.1 times overload. The dissipated active power is shown in Fig. 8(e), compared with Fig. 7(e), the total energy consumption of the DC chopper

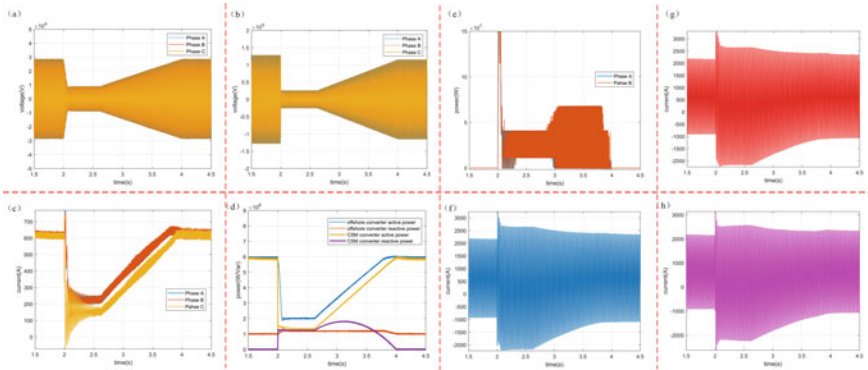


Fig. 8 Simulation results with cooperative control (a) Collection grid voltage, (b) CSM converter voltage, (c) Three-phase DC current components of CSM converter, (d) Active power and reactive power of converters, (e) Dissipation power of CSM converter, (f), (g), (h) Bridge arm current of Phase A, Phase B, Phase C in CSM converter.

resistor is greatly reduced, which reduces the design requirements of the chopper circuit, and this is also demonstrated by the DC current in Fig. 8(c) compared with Fig. 7(c).

In Fig. 8(f)-Fig. 8(h), the peak current of bridge arm is still 50% higher than the rated working state at the moment of fault, but the current stress of phase A and phase B are only slightly higher than that of phase C at other times. Considering that IGBTs generally have the peak current conduction capacity of twice the nominal current, after adopting the cooperative control strategy, the half bridge IGBTs of the MMC on the grid side can be uniformly selected to avoid cost increase.

5 Conclusion

The DC chopper circuit and submodule are designed together in two phases of the onshore CSM converter for offshore wind power transmission system. Compared with the independent modular dissipation device, the circuit of CSM converter is more simplified and economical. During AC fault ride through period, residual DC current is introduced into CSM bridge arms for dissipation through circulating current control. If the power generation of the wind farm is not limited during the fault ride through period, because of the high unloading energy, the half bridge IGBTs of the CSM bridge arms need to have a short-time overload operation capacity of nearly twice the rated current. In this paper, the average power and total energy consumption of the chopper circuit are greatly reduced by using the proposed cooperative control strategy, and the half bridge IGBTs of the CSM bridge arms can be uniformly selected with other bridge arm, further reducing the hardware investment cost.

References

1. Liu, G., Fan, M.M., Wang, P.Y., et al.: Study on reactive power compensation strategies for long distance submarine cables considering electrothermal coordination. *J. Marine Sci. Eng.* **9**(1), 90 (2021)
2. Li, X., Yao, L., Cheng, F., Mao, B., et al.: Economic Analysis of Multi-type DC System Topologies for Offshore Wind Power Transmission. *J. Global Energy Interconnection* **4**(5), 2096–5125 (2021). (in Chinese)
3. Cai, X., Yang, R., et al.: Review on offshore wind power integration via DC transmission. *Automation of Electric Power Syst.* **45**(21), 222 (2021). (in Chinese)
4. Chen, Y., Pan, S., Huang, M., Zhu, Z., Liu, Y., Zha, X.: MMC-MTDC transmission system with partially hybrid branches. *China Electrotechnical Society Trans. Electrical Machines Syst.* **5**(2), 124–132 (2021)
5. He, J., Yang, Q., et al.: On-line fault diagnosis and fault-tolerant operation of modular multilevel converters-a comprehensive review. *China Electrotechnical Society Trans. Electrical Machines and Syst.* **4**(4), 360–372 (2020)
6. Zhang, H., Xiang, W., Zhou, M., Wen, J.: Cooperative strategy of active energy control and ac energy dissipation device in offshore wind power MMC-HVDC system. *Proceedings of the CSEE* **42**(12), 4319–4330 (2022). (in Chinese)
7. Dong, X., Zhang, J., Wang, F., et al.: AC and DC fault ride-through technology for wind power integration via VSC-HVDC overhead lines. *Automation of Electric Power Syst.* **40**(18), 48–55 (2016). (in Chinese)
8. Li, Q., Song, Q., Liu, W., Rao, H., et al.: A coordinated control strategy for fault ride-through of wind farm integration based on VSC-HVDC. *Power System Technol.* **38**(07), 1739–1745 (2014). (in Chinese)
9. Cao, S., Xiang, W., Yao, L., et al.: AC and DC fault ride-through strategies for wind power integration via hybrid MMC-HVDC. *Automation of Electric Power Syst.* **42**(07), 37–43+49 (2018)
10. Wang, Y., Fu, Y., Su, X., et al.: Fault ride-through control strategy of wind farm integrated with VSC-HVDC. *Trans. China Electrotechnical Society* **28**(12), 150–159 (2013). (in Chinese)
11. Li, X., Song, Q., Liu, W., et al.: Impact of fault ride-through methods on wind power generators in a VSC-HVDC system. *Automation of Electric Power Syst.* **39**(11), 31–36+125 (2015). (in Chinese)
12. Jing, Y., Li, R., Xu, L., et al.: Enhanced AC voltage and frequency control of offshore MMC station for wind farm connection. *IET Renew. Power Gener.* **12**(15), 1771–1777 (2018)
13. Nanou, S., Papathanassiou, S.: Evaluation of a communication-based fault ride-through scheme for offshore wind farms connected through high-voltage DC links based on voltage source converter. *IET Renew. Power Gener.* **9**(8), 882–891 (2015)
14. Debnath, S., Qin, J., Bahrani, B., et al.: Operation, control, and applications of the modular multilevel converter: a review. *IEEE Trans. Power Electron.* **30**(1), 37–53 (2015)
15. Li, Z., Wang, P., Chu, Z., et al.: An inner current suppressing method for modular multilevel converters. *IEEE Trans. Power Electron.* **28**(11), 4873–4879 (2013)

Simulation Study on Thermal Effect of Multistage PIN Limiter



Mingxuan Gao, Yang Zhang, Lishan Zhao, and Jun Zhang

Abstract The thermal effect and damage mechanism of multistage PIN limiters under high-power microwave (HPM) signals are analyzed in this paper. The simulation model of a double-stage PIN limiter is built based on the circuit-field co-simulation method, and the temperature changes of the first and second-stage diodes during the injection of the HPM signals are studied by using this model. It is concluded that the burning point is in the I-region. The point where the damage happened first is close to the P-region of the first-stage PIN diode. The temperature change of the second stage PIN diode is relatively small during the whole burning-out process, which will not cause damage. Finally, the temperature change and damage mechanism during the burning process are analyzed by combining the physical images of the temperature field, electric field, and current density.

Keywords Multistage limiter · PIN Diode · Thermal effect

1 Introduction

As an important device to protect the electronic system from the damage of high-power signals, the PIN limiter has been widely used in the fields of radar and communication. However, the PIN limiter itself can also be damaged when the signal power

M. Gao · Y. Zhang (✉) · L. Zhao
College of Advanced Interdisciplinary Studies, National University of Defense Technology,
Changsha, China
e-mail: zhangyang21f@nudt.edu.cn

M. Gao
e-mail: gaomx20@nudt.edu.cn

L. Zhao
e-mail: lishanzhao@nudt.edu.cn

J. Zhang
College of Science, National University of Defense Technology, Changsha, China
e-mail: zhangjun@nudt.edu.cn

is large enough, resulting in the disconnection of the transmission link. The limiting function of the PIN limiter is mainly realized by the PIN diode and the burning out of the PIN diode is also an important reason for the limiter failure [1]. According to the ways of PIN diode cascade, PIN limiters can be classified into single-stage limiters and multi-stage limiters. Compared with a single-stage limiter, a multi-stage limiter can withstand higher power while ensuring the threshold and sensitivity to the signal. However, currently, research on the damaging effect of PIN limiters mainly focuses on the single-stage limiter, rather than multi-stage limiter.

The research on the damage effect of semiconductor devices is usually based on simulation or experimental methods. Compared with experimental methods, simulation can obtain the physical image of the device during the damage process more directly. The models used in the simulation mainly include the equivalent circuit model and the physical model. The simulation speed of the equivalent circuit model is very fast, but this method involves more complex parameter extraction steps [2, 3]. Reference [4, 5] studies the transient response and temperature response of PIN limiter and PIN diode based on an equivalent circuit model. Reference [6] studies the damage effect of LNA under HPM and reference [7, 8] discusses the damage effect of the transistor under high power microwave, both of them are carried out based on the multi-physical field model.

At present, many studies have been carried out on the thermal effect of a single PIN diode or single-stage limiter, but the thermal effect of a multi-stage limiter under the action of microwave signals is still less. In this paper, a multi-physics field simulation model of a double-stage limiter is built based on the hybrid simulation method of finite element and circuit. The temperature change characteristics and damage mechanism of a double-stage limiter under a HPM signal are studied by using this model.

2 Model of the PIN Diode and PIN Limiter

The simulation circuit of the double-stage limiter is shown in Fig. 1, where S1 is the signal source, and R1 represents its internal resistance, which is $50\ \Omega$. L1, L2, and L4, L5 represent the connecting line equivalent inductance of the PIN diode, with the value of $0.3\ \text{nH}$. L3 is the DC inductance, with the value of $50\ \text{nH}$. R2 represents the load impedance, which is $50\ \Omega$. The above devices are represented by the SPICE model in the simulation. D1 and D2 are different PIN diodes, of which D1 has a greater I-region thickness and is used as the coarse stage in the multistage limiter, and D2 has a smaller I-region thickness, which is used as the clean-up stage in the multistage limiter. In order to study the damage mechanism of the diodes in the limiter under the HPM signal, the diodes are modeled by the finite element method.

The models of PIN diodes D1 and D2 are shown in the left and right figures in Fig. 2, respectively. The P-region thickness of D1 and D2 is $2\ \mu\text{m}$, and the N-region thickness of D1 and D2 is $124\ \mu\text{m}$. The I-region thickness of D1 and D2 is $7\ \mu\text{m}$.

Fig. 1 Circuit structure of the limiter

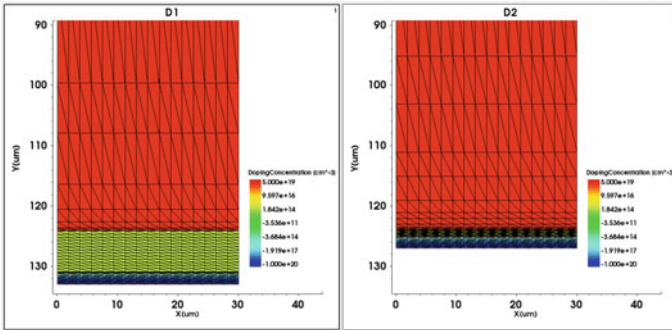
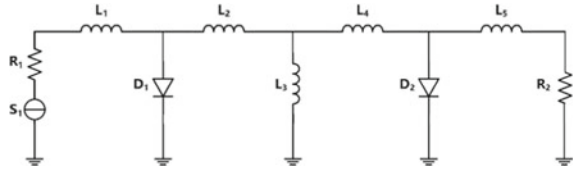


Fig. 2 Models of PIN diodes D1 and D2 (local)

and 1 μm , respectively. The effective area of both diodes is 0.09mm^2 , and the P-region is a Gaussian doped layer. The peak concentration is 10^{20} cm^{-3} . The doping concentration of N-region and I-region is $5 \times 10^{19}\text{ cm}^{-3}$ and $2.5 \times 10^{14}\text{ cm}^{-3}$, respectively.

3 Physical Model

3.1 Mobility Model

To better describe the carrier mobility, we have introduced different mobility sub-models, and the total mobility is calculated according to Matthiessen’s law on the basis of varying mobility sub-models:

$$\frac{1}{\mu} = \frac{1}{\mu_1} + \frac{1}{\mu_2} + \dots \tag{1}$$

Mobility Degradation Effect Induced by Doping

In order to fit the more extensive temperature range in this simulation better, we use the UniBo model to describe the mobility degradation effect induced by doping [9]. The mobility is expressed as:

$$\mu_{dop}(T) = \mu_0(T) + \frac{\mu_L(T) - \mu_0(T)}{1 + \left(\frac{N_D}{C_{r1}(T)}\right)^\alpha + \left(\frac{N_A}{C_{r2}(T)}\right)^\beta} - \frac{\mu_1(T)}{1 + \left(\frac{N_D}{C_{s1}(T)} + \frac{N_A}{C_{s2}(T)}\right)^{-2}} \quad (2)$$

In which $\mu_L(T) = \mu_{\max} \left(\frac{T}{300K}\right)^{-\gamma + c\left(\frac{T}{300K}\right)}$, $\mu_0(T) = \frac{\mu_{0d}N_D + \mu_{0a}N_A}{N_D + N_A}$, $\mu_1(T) = \frac{\mu_{1d}N_D + \mu_{1a}N_A}{N_D + N_A}$.

Carrier-Carrier Scattering

Here we describe the effect of carrier concentration changes on mobility using the Conwell-Weiskopf model as follows [10]:

$$\mu_{eh} = \frac{D(T/300K)^{3/2}}{\sqrt{np}} \left[\ln \left(1 + F \left(\frac{T}{300K} \right)^2 (pn)^{-1/3} \right) \right]^{-1} \quad (3)$$

Mobility Saturation Effect

We use the Canali model to calculate the mobility under high fields:

$$\mu(F) = \frac{(\alpha + 1)\mu_{low}}{\alpha + \left[1 + \left(\frac{(\alpha+1)\mu_{low}F_{hfs}}{v_{sat}} \right)^\beta \right]^{1/\beta}} \quad (4)$$

For the silicon-based devices we use, there is: $v_{sat} = v_{sat,0} \left(\frac{300K}{T}\right)^{v_{sat,exp}}$, $\beta = \beta_0 \left(\frac{T}{300K}\right)^{\beta_{exp}}$.

3.2 Recombination Model

SRH Recombination

SRH recombination usually refers to the recombination process through deep defect energy levels in the band gap. The recombination model is expressed as follows:

$$R_{net}^{SRH} = \frac{np - n_{i,eff}^2}{\tau_p(n + n_1) + \tau_n(p + p_1)} \quad (5)$$

Auger Recombination

Auger recombination is essential in regions with high carrier concentrations. Since both P and N regions are heavily doped for the PIN diode, it is necessary to describe this process. The rate of auger recombination can be expressed as follows:

$$R^{Auger} = (C_n n + C_p p)(np - n_{i,eff}^2) \quad (6)$$

Avalanche Model

The Avalanche generation model is introduced in this simulation, and the avalanche multiplication generation rate can be expressed as:

$$G^{Avalanche} = \alpha_n n v_n + \alpha_p p v_p \quad (7)$$

Considering the extensive temperature range involved in the simulation, the UniBo collision ionization model is used here to describe the ionization coefficients according to which [11]:

$$\alpha(F_{ave}, T) = \frac{F_{ave}}{a(T) + b(T) \exp\left[\frac{d(T)}{F_{ave} + c(T)}\right]} \quad (8)$$

3.3 Thermodynamic Model

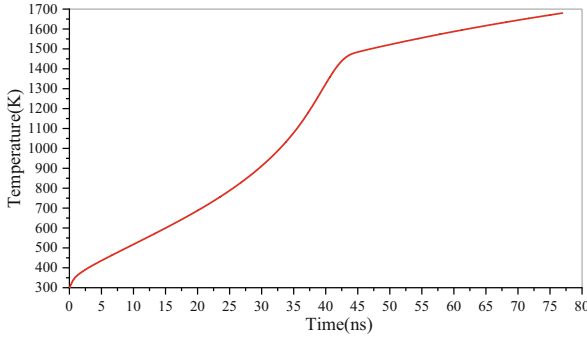
By introducing the thermodynamic model, the temperature in a PIN diode can be calculated by the following equations:

$$\begin{aligned} \frac{\partial}{\partial t}(c_L T) - \nabla \cdot (\kappa \nabla T) = & -\nabla \cdot \left[(P_n T + \Phi_n) \vec{J}_n + (P_p T + \Phi_p) \vec{J}_p \right] \\ & - \frac{1}{q} \left(E_C + \frac{3}{2} kT \right) (\nabla \cdot \vec{J}_n - q R_{net,n}) - \frac{1}{q} \left(-E_V + \frac{3}{2} kT \right) (-\nabla \cdot \vec{J}_p - q R_{net,p}) \\ & + \hbar \omega G^{opt} \end{aligned} \quad (9)$$

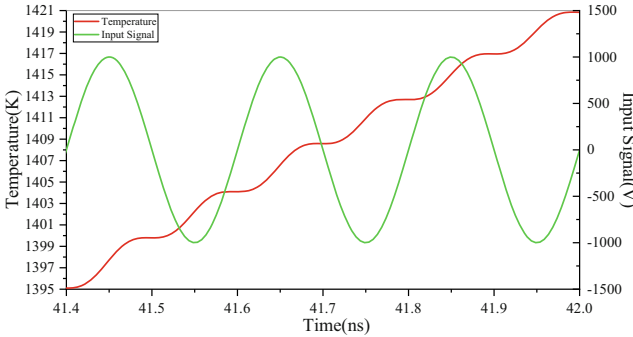
4 Results and Discussions

In the limiter simulation circuit shown in Fig.two1, the output of signal source S1 is a microwave signal with a frequency of 5 GHz and an amplitude of 1000 V.

Unlike a single-stage limiter, combining two PIN diodes with different I-region thicknesses in a double-stage limiter enables the limiter to withstand a larger injection power while ensuring that the limiter has an appropriate threshold level. The temperature change curve of PIN diode D1 during the burning out process under microwave signal is shown in Fig. 3(a), and part of the temperature change curve and corresponding input signal waveform is shown in Fig. 3(b):



(a) Temperature change of the first-stage PIN diode D1 during burning out

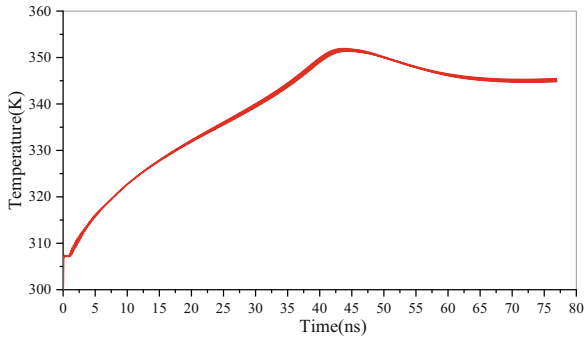


(b) Part of the temperature change curve and corresponding input signal waveform

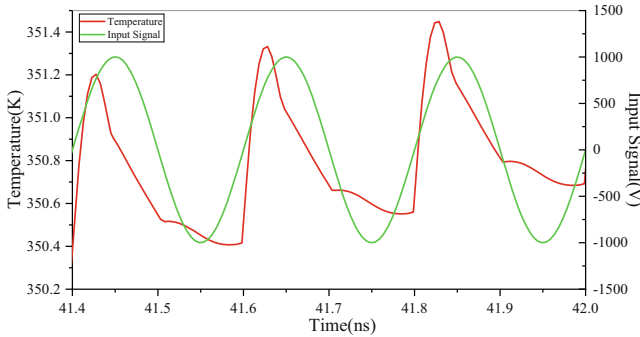
Fig. 3 Temperature change of the first stage PIN diode during the burning out process of the limiter

As shown in Fig. 3(a), the temperature of the first-stage PIN diode rises continuously during the action of the microwave signal. When the temperature of the first-stage PIN diode increases to a specific temperature (about 1450 K), the temperature rise slows down significantly, and the maximum temperature inside the PIN diode is close to the burning-out temperature at this time, which is about 1680 K. For the whole burning-out process, the time taken to rise from 1450 to 1680 K accounts for 44.2% of the total burning-out time, while the rising temperature only accounts for 13.7% of the total rising temperature.

The I-region thickness of the second-stage PIN diode D2 is small. The use of D2 can ensure the limiter has an appropriate threshold level. The temperature change of the second-stage PIN diode D2 during the burning-out process is simulated, and the result is shown in Fig. 4(a). Take part of the temperature change of D2 and the corresponding input signal waveform as shown in Fig. 4(b):



(a) Temperature change of the second-stage PIN diode D2 during burning out



(b) Part of the temperature change curve and corresponding input signal waveform

Fig. 4 Temperature change of the second stage PIN diode during the burning out of the limiter

It can be seen that the maximum temperature change of D2 during the injection of the microwave signal is different from that of D1. The temperature of the second PIN diode D2 increases first and then decreases during the injection of the microwave signal. The turning point of D2's temperature from rising to falling occurs at about 43 ns, which is also the time point when the temperature of D1 reaches 1450 K, and the temperature-increasing speed begins to slow down significantly. From Fig. 4(b), it can be seen that for the limiter studied in this paper, the internal maximum temperature of the second-stage PIN diode D2 increases only during the rise of positive and negative half-cycle signal, while there is an apparent cooling process in other periods. But for the whole burning-out process of the limiter, the maximum temperature that the second-stage diode D2 can reach is only 352 K, which is not enough for the damage of it. The burning-out position of the second-stage limiter under the action of the microwave signal is the first-stage PIN diode.

Figure 5 shows the internal temperature distribution during the burning-out process of the first-stage PIN diode D1. The time points we selected are 5.05 ns, 20.05 ns, 35.05 ns, 60.05 ns, and 75.05 ns. All of them correspond to the wave crest of the microwave signal input to the limiter. From Fig. 5, it can be seen that the heating location is mainly in the I-region, and as the signal continues, the heat mainly diffuses to the N-region.

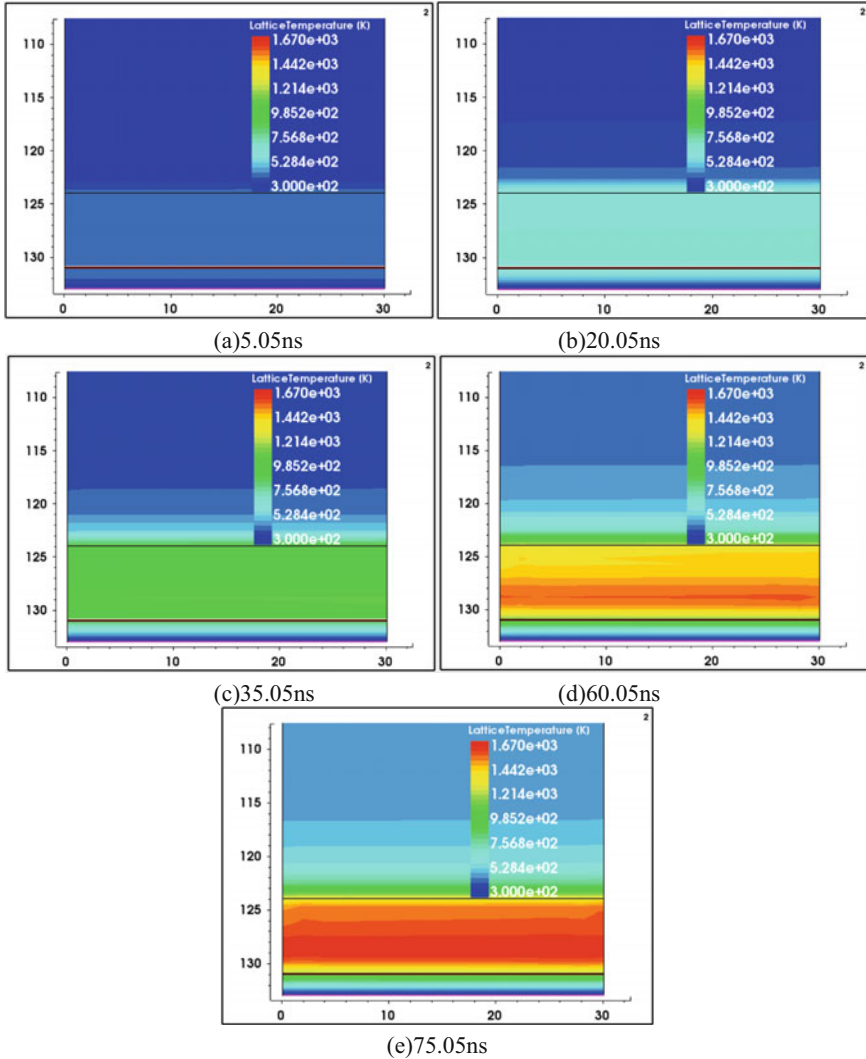


Fig. 5 Internal temperature distribution of the first stage PIN diode during the burning out of the limiter

Temperature distribution inside the first-stage PIN diode D1 at 35 ns, 35.05 ns, 35.1 ns, 35.15 ns, and 35.2 ns are shown in Fig. 6, and these five points correspond to the zero cross point, wave crest, zero cross point, wave trough, and zero cross point respectively in a microwave signal cycle. It can be seen that the main hot spot of the first-stage PIN diode is located in the I-region, which is about 2 μm away from the PN junction. In a single signal cycle, the temperature of the main hot spot continues to rise, and the location of the main hot spot does not change significantly.

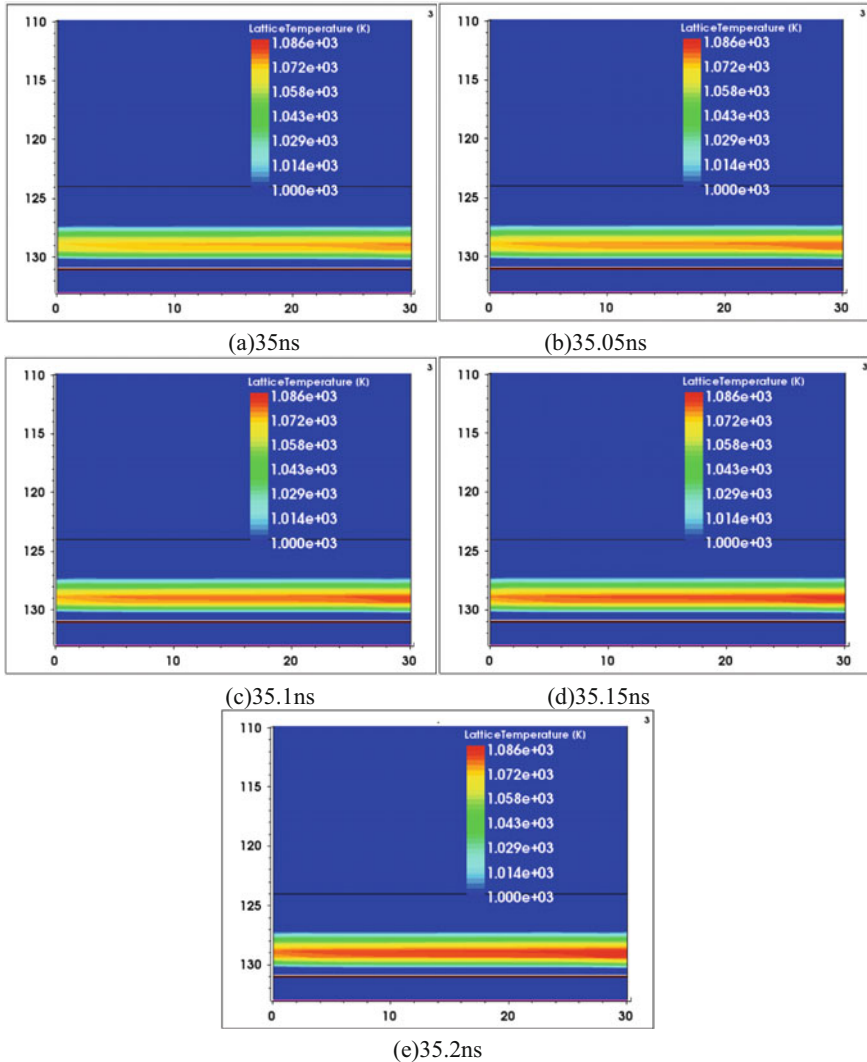


Fig. 6 Temperature distribution inside the first stage PIN diode in a single microwave period

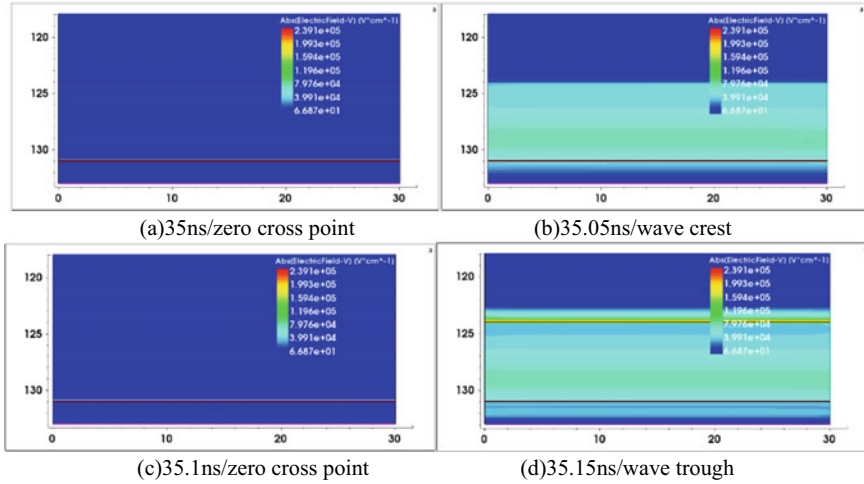


Fig. 7 Electric field distribution inside the first stage PIN diode in a single microwave period

Figure 7 shows the change in the internal electric field intensity distribution of the first-stage PIN diode D1 in a microwave signal period. It can be seen that the electric field intensity at zero cross point (35 ns and 35.1 ns) is relatively low in this signal period, and the corresponding electric field intensity at wave trough (35.15 ns) is the largest, and the extreme value of the electric field intensity appears in a minimal area at the boundary of N and I regions at this time. However, for the positive and negative half cycle of the signal, the electric field intensity in the I-region near the P-region is relatively large, and the distribution range is also much wider.

Figure 8 shows the current density change at the corresponding time of this signal cycle. It can be seen that the current density at the zero cross point of the signal is relatively small, the current density corresponding to the signal wave crest and the signal wave through is significant, and there is always a considerable current density inside the device throughout the whole signal cycle.

The reason for the temperature rise of PIN diode under the action of microwave signal is its internal power dissipation, which can be expressed as:

$$Q = J \times E \tag{10}$$

It can be seen that the current density and electric field determine the internal temperature of PIN diode. The temperature change and temperature distribution inside the PIN diode can be explained by combining the dissipation power density with the electric field and current density distribution shown in Fig. 7 and Fig. 8: Because the electric field intensity and current density near the zero cross point of the signal are relatively small, and because the device itself radiates heat, the temperature rising speed of D1 near the zero cross point of the signal is slower, and the higher the instantaneous absolute value of the signal in a single cycle, the faster the temperature

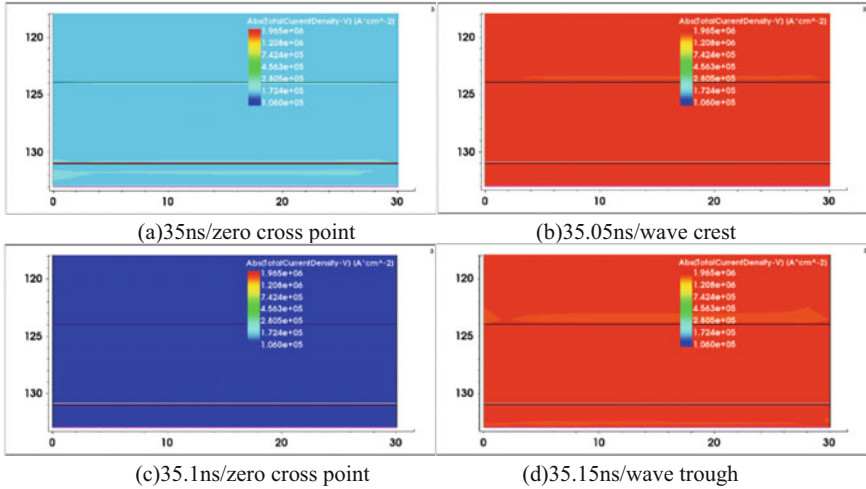


Fig. 8 Current density distribution inside the first stage PIN diode in a single microwave period

rise; because the electric field intensity in the I-region is relatively large and has a specific distribution range near the boundary of P-region, this location is where the highest temperature occurs inside the device and where the first PIN diode D1 is burned out.

5 Conclusion

In this paper, the thermal effect of the double-stage limiter under a microwave signal is studied, and the limiter model based on the hybrid simulation method of the circuit and finite element is established. A suitable physical model is adopted for the device to describe its internal physical process accurately. The temperature change of the two PIN diodes in the limiter during the burning-out process of the limiter is obtained through simulation, and the intuitive physical image of the burning process and the internal burning-out position of the first-stage PIN diode is obtained. At the same time, the conclusion that the temperature change of the second-stage PIN diode is small during the whole burning-out process of the limiter is given. The images of the temperature field, electric field, and current density distribution of the PIN diode at different times during the burning-out process are obtained, and the reasons for the change of the highest temperature position and the speed of temperature rise are explained.

Acknowledgements This work is supported by Science and Technology Innovation Program of Hunan Province(2021RC2065) and Scientific Research Plan of NUDT(ZK22-42).

References

1. Bera, S.C., Bharadhwaj, P.S.: Insight into PIN diode behavior leads to improved control circuit. *IEEE Trans. Circ. Syst. II, Analog Digital Sig. Process.* **52**(1), 1–4 (2005)
2. Wang, M., Liang, Z., Xiong, M., Qu, S., Hu, S., He, X.: Analysis of PiN diode reverse recovery based on the field-circuit couple modeling. In: 2019 IEEE Energy Conversion Congress and Exposition (ECCE), pp. 399–403 (2019)
3. Li, X., Luo, Y., Duan, Y., Huang, Y., Liu, B.: A lumped-charge model for high-power PT-p-i-n diode with a buffer layer. *IEEE J. Emerg. Sel. Top. Power Electron.* **7**(1), 52–61 (2019)
4. Yuan, Y., Chen, Z., Ma, H., Qin, F.: High power microwave effect of PIN limiter induced by single pulse. *High Power Laser and Particle Beams* **32**(6), 57–62 (2020). (in Chinese)
5. Hanini, W., Ayadi, M.: Electro thermal modeling of the power diode using Pspice. *Microelectron. Reliab.* **86**, 82–91 (2018). <https://doi.org/10.1016/j.microrel.2018.05.008>
6. Li, F., et al.: Study on high power microwave nonlinear effects and degradation characteristics of C-band low noise amplifier. *Microelectron. Reliab.* **128**, 114427 (2022). <https://doi.org/10.1016/j.microrel.2021.114427>
7. Li, H., Chai, C.-C., Liu, Y.-Q., Han, Wu., Yang, Y.-T.: Damage effects and mechanism of the silicon NPN monolithic composite transistor induced by high-power microwaves. *Chin. Phys. B* **27**(8), 088502 (2018). <https://doi.org/10.1088/1674-1056/27/8/088502>
8. Xi, X.-W., Chai, C.-C., Liu, Y., Yang, Y.-T., Fan, Q.-Y., Shi, C.-L.: Analysis of the damage threshold of the GaAs pseudomorphic high electron mobility transistor induced by the electromagnetic pulse. *Chin. Phys. B* **25**(8), 088504 (2016). <https://doi.org/10.1088/1674-1056/25/8/088504>
9. Reggiani, S., et al.: Electron and hole mobility in silicon at large operating temperatures - Part I: Bulk mobility. *IEEE Trans. Electron Devices* **49**(3), 490–499 (2002). <https://doi.org/10.1109/16.987121>
10. Canali, C., Majni, G., Minder, R., Ottaviani, G.: Electron and hole drift velocity measurements in silicon and their empirical relation to electric field and temperature. *IEEE Trans. Electron Devices* **22**(11), 1045–1047 (1975)
11. Vecchi, M.C., Rudan, M.: Modeling electron and hole transport with full-band structure effects by means of the spherical-harmonics expansion of the BTE. *IEEE Trans. Electron Devices* **45**(1), 230–238 (1998). <https://doi.org/10.1109/16.658836>

Hybrid Energy Storage System with Doubly Fed Flywheel and Coordination Control Strategy



Chenyu Wu, Zhengxiang Song, Junyue Wang, Kun Yang, Qiuyao Xiao, Weiquan Wang, and WenChao Liu

Abstract Doubly fed flywheel has fast charging and discharging response speed and long cycle life. It can form a hybrid energy storage system with lithium batteries, complement each other's advantages, and jointly suppress the fluctuation of new energy generation. This paper studies the structure and coordination control strategy of hybrid energy storage system with doubly fed flywheel and battery. Firstly, the simulation model of AC hybrid energy storage microgrid is built, and a coordinated control strategies of hybrid energy storage system is proposed and simulated for grid connected operation mode and isolated island operation mode. In this strategy, the power response delay of lithium battery is considered and the integrated inertia control is introduced. The research results show that after the microgrid is introduced into the doubly fed flywheel energy storage system, the doubly fed flywheel energy storage can effectively reduce the power fluctuation of the connection point under the grid connected operation mode. And it can effectively reduce the power impact of the battery at the moment of power shortage, slow down the aging of the battery and prolong the service life, reduce the frequency fluctuation of the microgrid, slow down the frequency deterioration, and improve the stability of the microgrid operation under the isolated island operation mode.

Keywords Doubly fed flywheel · lithium battery · hybrid energy storage system · control strategy

1 Introduction

With the advancement of “double carbon” process, the proportion of micro-sources such as wind power and photovoltaic in the power system is gradually increasing, resulting in the decrease of inertia characteristics of the power system [1], and the

C. Wu · Z. Song (✉) · J. Wang · K. Yang · Q. Xiao · W. Wang · W. Liu
State Key Laboratory of Electrical Insulation and Power Equipment, Xi'an Jiaotong University,
Xi'an 710049, China
e-mail: 1427996243@qq.com

© Beijing Paiké Culture Commu. Co., Ltd. 2023
X. Dong et al. (eds.), *The proceedings of the 10th Frontier Academic Forum of Electrical Engineering (FAFEE2022)*, Lecture Notes in Electrical Engineering 1054, https://doi.org/10.1007/978-981-99-3408-9_79

existing thermal power units in the system alone are gradually unable to support the power system to accept a high proportion of volatile new energy. Flexible energy storage resources have the advantage of fast and accurate response, which can quickly smooth out the random disturbance of new energy, assist system frequency regulation, increase system inertia, and solve the contradiction between supply and demand of grid frequency regulation capacity under the new energy penetration rate.

The flywheel uses a doubly-fed induction motor as the drive motor, and is therefore called a doubly-fed flywheel, as shown in Fig. 1. Traditional flywheel energy storage uses permanent magnet motor as the driving motor, full power converter and a large amount of non-ferrous and rare metal requirements, which greatly increases the investment cost. The double-fed grid-connected method itself has the advantage of small capacity converter, plus the breakthrough progress of gearbox torque power density technology in recent years, which makes the double-fed flywheel significantly more advantageous than permanent magnet flywheel in terms of large capacity.

Doubly-fed flywheel is a short-time energy storage system with 50 ms or even lower response time, million charge/discharge cycle life, suitable for high frequency charging and discharging, and can be organically combined with lithium battery to achieve complementary advantages for new energy frequency regulation and ensure stable and reliable operation of microgrid.

The literature [2] investigated the power allocation strategy between battery and permanent magnet flywheel energy storage at long time scales based on wind power fluctuation data with a sampling interval of 5 min, and the simulation verified that the proposed strategy can effectively reduce the number of frequent battery switching and help prolong the service life of hybrid energy storage. In the literature [3], based on the dynamic frequency model of power system, the optimal frequency control strategy of hybrid energy storage system consisting of battery and flywheel energy storage under different scenarios was studied, which significantly improves the frequency safety stability of the system. In the literature [4–6], a frequency regulation model of a hybrid energy storage auxiliary generator set containing flywheel and battery was constructed, and the power optimization allocation strategy was studied to reduce the system frequency fluctuation, solve the unit wear and reverse frequency regulation problem, and guarantee the safe and economic operation of the unit. The current research on hybrid energy storage of flywheel and battery mainly studies the optimal scheduling and power distribution strategy of hybrid energy storage upper layer from

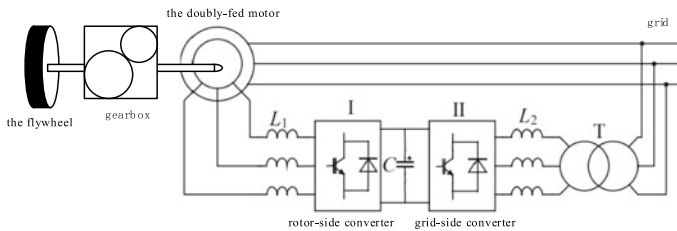


Fig. 1 Composition of doubly fed flywheel energy storage system

a longer time scale, while ignoring the battery response delay problem and short-time high current impact problem in a short time scale. The error power caused by the power response delay of the battery will affect the dynamic performance and power quality in the microgrid steady state [7], and the short-time high-current shock will accelerate the battery aging and shorten its service life.

Most of the research objects of flywheel energy storage in hybrid energy storage are mainly permanent magnet flywheel, while less research is done on doubly-fed flywheel. In literature [8], the theoretical analysis of the stator-rotor side power relationship and working principle of doubly-fed flywheel was carried out. In literature [9], the control strategy of variable frequency start-up and stable operation was studied. In literature [10], the simulation verified that doubly-fed flywheel is beneficial to improve the transient stability of the system. The current research on doubly-fed flywheel focuses on the ontology control strategy and ontology engineering application research, but does not focus on its cooperation with the battery to give full play to the advantages of power-based energy storage and make up for the defect of less energy.

This paper firstly establishes a microgrid model with double-fed flywheel and lithium battery hybrid energy storage, and discusses its topology and equivalent model of each part. Then the coordinated control strategy of double-fed flywheel and lithium battery hybrid energy storage is studied under the premise of considering the power response delay of lithium battery. Finally, two grid-connected operation schemes and four islanding operation schemes are simulated and compared to verify the effectiveness of the adopted strategy.

2 Double-Fed Flywheel and Lithium Battery Hybrid Energy Storage Microgrid

This paper designs an AC microgrid with a hybrid energy storage system of doubly-fed flywheel and lithium battery, and the system structure is shown in Fig. 2. The AC microgrid consists of a photovoltaic system, a lithium battery energy storage system, a doubly-fed flywheel energy storage system and an AC/DC load. The lithium battery is connected to the AC bus through the energy storage converter, and the control strategy block diagram is shown in Fig. 2(b). In the isolated operation of microgrid, the energy storage converter adopts sagging control strategy. During grid-connected operation, the energy storage converter adopts the PQ control strategy of d axis phasing. The rotor side converter of double-fed flywheel adopts stator flux vector control, as shown in Fig. 2(c). The grid side converter adopts DC constant voltage control, as shown in Fig. 2(d).

The energy demand of AC and DC loads in the microgrid mainly comes from the PV battery and lithium battery, and the doubly-fed flywheel mainly suppresses the shock load and high frequency disturbance in the microgrid.

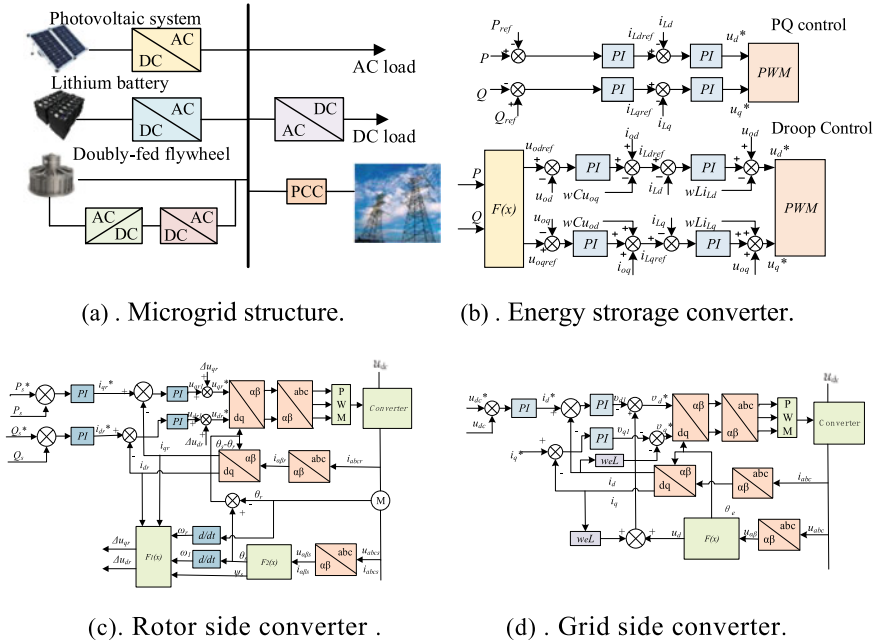


Fig. 2 Microgrid structure and control strategy

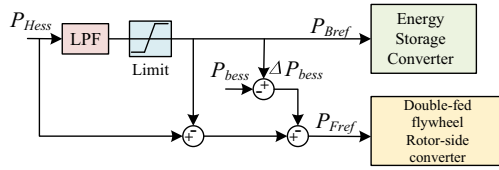
3 Hybrid Energy Storage Coordinated Control Strategy

3.1 Coordinated Control Strategy for Grid-Connected Operation of Hybrid Energy Storage

The PV hybrid energy storage microgrid is connected to the grid through the point of common coupling (PCC) for grid-connected operation, where the grid provides voltage support to the microgrid.

The grid connection mode can be divided into free grid connection mode and dispatching grid connection mode, and this paper mainly considers the dispatching grid connection mode, which means that the microgrid PCC power is controlled by the higher-level dispatching agency. Under normal conditions, the PV unit runs in the maximum power tracking mode, the Li-ion battery and the doubly-fed flywheel both run in the PQ power source mode, and the hybrid energy storage system is mainly used to compensate the power difference between the PV output, the load and the PCC scheduling command. Let the PV output power be P_{PV} , the PCC scheduling command power reference value be P_{PCC} , the load demand power be P_{Load} , and the hybrid energy storage needs to level off the power reference value be P_{Hess} , the following relationship exists when the microgrid is operating stably.

Fig. 3 Grid connected operation control block diagram of hybrid energy storage



$$P_{PV} + P_{Hess} = P_{PCC} + P_{Load} \tag{1}$$

Among them, P_{PV} and P_{Hess} use the power supply convention with positive output; P_{PCC} and P_{Load} use the load convention with positive input.

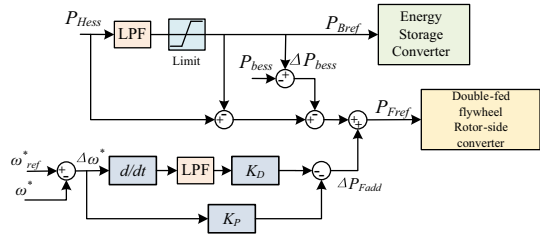
Considering that the power response time of battery storage is about 500 ms, when the microgrid only uses a single battery storage as the power shortage compensation power source, the transient power shortage caused by the power response delay will be borne by the large grid as a constant voltage source. As the total number of PV installations in the system increases, coupled with the uncertainty of sudden changes in lighting conditions and cloud cover, the magnitude of transient power deficits to be borne by the grid will become larger and more frequent. Due to the high power density of doubly-fed flywheel and the response speed of less than 50 ms, it can be used to compensate the power shortage during the above transient process. Therefore, according to the output characteristics of the doubly-fed flywheel, a hybrid energy storage control strategy considering the power response delay of the lithium battery is proposed, and its control structure block diagram is shown in Fig. 3.

3.2 Hybrid Energy Storage Control Strategy for Islanding Operation

But the conductor system is a nonlinear geometrical construction. As a result, the inherent frequency of the system will change with the vibration amplitude changes. Because the loads are applied at fixed time intervals, the motion state of the excitation point is uncertain when the excitation force is applied in each period. Therefore, the system cannot maintain a stable vibration state, and the vibration amplitude of the transmission line decreases continuously after 140 s. Thus, the time intervals of the excitation force should be adjusted adaptively according to the wire vibration state. The key is to find change of wire vibration characteristics caused by excitation wave.

The PV hybrid energy storage microgrid islanding operation mode requires maintaining the power balance relationship between PV power, hybrid energy storage and load, which in turn ensures the AC bus voltage and frequency stability. In this paper, the master-slave control mode is adopted, and the lithium battery adopts droop control to provide voltage and frequency support for other power sources and loads in the microgrid. Under normal conditions, the PV unit operates in the maximum power

Fig. 4 Island operation control block diagram of hybrid energy storage



tracking mode, and the hybrid energy storage system is mainly used to compensate the power deficit between PV output and load demand, which is obtained from Eq. (1), by setting the P_{PCC} to zero.

$$P_{Hess} = P_{Load} - P_{PV} \tag{2}$$

In a single energy storage system, the lithium battery, as the only voltage source in the microgrid, needs to respond quickly to the system power shortage in order to stabilize the power fluctuation in the microgrid. When faced with a sudden increase in the shock load in the microgrid or a sudden drop in PV power due to cloud cover, the lithium battery has to bear the shock power shortage in order to maintain the microgrid voltage frequency stability, which accelerates the battery aging and affects the cycle life. In order to reduce the transient power shocks borne by the battery, a doubly-fed flywheel energy storage system with integrated inertia control is introduced, whose control structure block diagram is shown in Fig. 4.

The input reference power of lithium battery droop control is the same as that of grid-connected operation during islanding operation, and the input reference power value of the converter on the doubly-fed flywheel machine side adds the integrated inertia control additional power ΔP_{Fadd} to the grid-connected power reference value.

$$\Delta P_{Fadd} = -K_P \Delta\omega^* - K_D \frac{d\Delta\omega^*}{dt} \tag{3}$$

where, K_P and K_D are the proportional and differential coefficients of integrated inertia control, respectively, ω_{ref}^* is the rated angular frequency of the system; ω^* is the actual angular frequency $\Delta\omega^*$ is the deviation of the angular frequency of the system. (The superscript * represents the standardized value).

A doubly-fed flywheel integrated inertia control strategy is introduced to add an additional portion of additional power to the original high-speed response to simulate the primary frequency regulation characteristics and inertia response characteristics of a conventional synchronous generator set. Considering that the allowable speed range of conventional thermal power units is only 0.95–1, which provides about 9.75% of the rotor kinetic energy. For doubly-fed flywheel energy storage, there is a large operating control of rotor speed during normal operation, which can run from a sub-synchronous turndown rate of 0.5 to a super-synchronous turndown rate of 1.5, that is, the doubly-fed flywheel can provide 75% of the kinetic energy of the flywheel

rotor. Therefore, the inertia support capacity of the doubly-fed flywheel is about 7 times higher than that of a conventional thermal power unit of the same capacity.

4 Hybrid Energy Storage System Simulation

In order to verify the hybrid energy storage coordinated control strategy based on the doubly-fed flywheel and lithium battery proposed in this paper, the hybrid energy storage microgrid model shown in Fig. 2(a) is built based on Matlab/Simulink simulation platform. The rated power of the PV system is 50 kW, and the MPPT control method is used. The battery is 50 kW/20kWh and the parameters of the double-fed flywheel are 100 kW/10kWh. The large grid model is rated at 380 V and rated frequency 50 Hz in. The simulated load is modeled with two sets of throwable loads.

4.1 Analysis of Grid-Connected Operation

Grid-connected operation parameters: assume the initial state light intensity is 500 W/m², the system load is 30 kW, and the dispatch command at the PCC point is 10 kW; the time intensity increases abruptly to 800 W/m² at 1 s; the dispatch command at the grid connection point decreases from 10 to 2 kW at 2 s; the load increases abruptly to 50 kW at 3 s; the time intensity decreases abruptly to 600 W/m² at 4 s, and the simulation time of grid-connected operation is 5 s. The AC microgrid operation under 2 different grid connection schemes is compared. In this paper, the response delay of the battery is 500 ms, and the response delay of the doubly-fed flywheel energy storage is 50 ms.

Scheme A: the internal power fluctuation of the microgrid is smoothed by the lithium battery only, and the power deficit is directly used as the reference value of the active power of the lithium battery.

Scheme B: The hybrid energy storage composed of battery and doubly-fed flywheel energy storage suppresses the internal power fluctuation of the microgrid together according to the hybrid energy storage control strategy that considers the power response delay of the lithium battery proposed in Subsect. 3.1.

The power allocation principle of hybrid energy storage system in microgrid is generally as follows: low frequency fluctuation power component (0.01–0.1 Hz) is smoothed by energy-based energy storage lithium battery, high frequency fluctuation power component (>0.1 Hz) is absorbed by power-based energy storage doubly-fed flywheel.

Since the Matlab online simulation time is limited, this paper shrinks the time by 10 times in order to shorten the simulation time, so a low-pass filter with a cutoff frequency of 1 Hz is selected for hybrid energy storage power distribution in this paper.

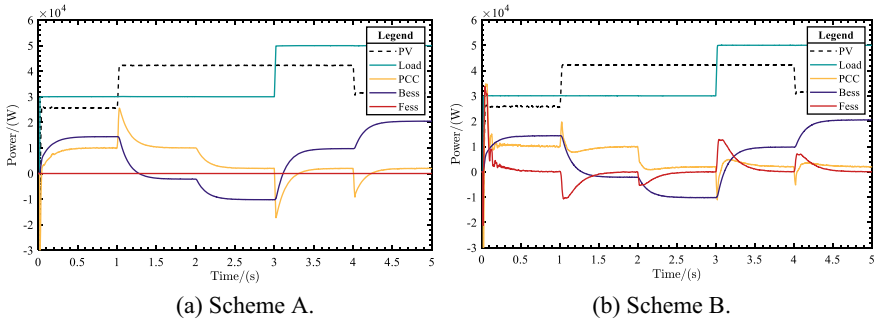


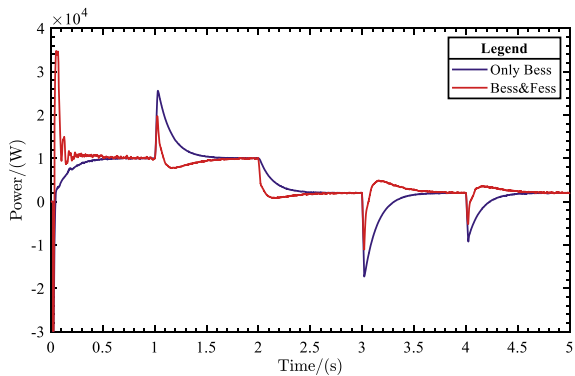
Fig. 5 Output curve of each module of microgrid under scheme A&B

Figure 5 shows the power output curves of each module of the microgrid under two scenarios of Scheme A and Scheme B. Where PV is PV, Load is load, PCC is grid-connected power, Bess is battery energy storage, and Fess is flywheel energy storage.

Figure 6 compares the power fluctuations of the parallel network under the two schemes. It can be seen that after the introduction of doubly-fed flywheel energy storage, since the uncompensated power of lithium battery power response delay can be provided by doubly-fed flywheel, the duration of transient impact power disturbance at the grid connection point is shortened from 500 to 50 ms, and the duration of dispatch command tracking error is shortened by 90%, which will improve the grid connection revenue of PV power plant to some extent. At the same time, the PCC tracking dispatching command error magnitude is reduced by about 37.5%, which reduces the large grid rotating reserve capacity and equivalently improves the large grid inertia characteristics.

By simulating the sudden increase and decrease of PV output and load, it can be seen that the introduction of doubly-fed flywheel energy storage can greatly solve the battery response delay problem, thus reducing the fluctuation of grid-connected

Fig. 6 Power fluctuation in parallel node under scheme A & B



electric power, speeding up the recovery of power balance, and strictly tracking the grid-connected scheduling plan.

4.2 Islanding Operation Analysis

The parameters of islanding operation are set as follows: the initial state light intensity is assumed to be 500W/m^2 and the system load is 30 kW ; at 1 s , the light intensity suddenly increases to 800W/m^2 ; at 2 s , the load increases by 20 kW and the total load is 50 kW ; at 3 s , the light intensity suddenly decreases to 700W/m^2 ; at 4 s , the load decreases by 20 kW and the simulation duration of islanding operation is 5 s . The simulation compares four different islanding scenarios of AC micro In this paper, the response delay of the battery is 500 ms , and the response delay of the double-fed flywheel energy storage is 50 ms .

Scheme I: the internal power fluctuation of the microgrid is only suppressed by the lithium battery, and the power deficit is directly used as the active power reference value of the lithium battery droop controller.

Scheme II: the internal power fluctuation of the microgrid is suppressed by the hybrid energy storage, but the double-fed flywheel energy storage does not introduce integrated inertia control, i.e., $K_P = 0$ and $K_D = 0$.

Scheme III: the hybrid energy storage jointly suppresses the internal power fluctuation of the microgrid, and the doubly-fed flywheel energy storage introduces integrated inertia control, but K_P is set to 0 and $K_D = 10 \times 10^5$, that is, the doubly-fed flywheel only participates in inertia support and not in primary frequency regulation.

Scheme IV: the hybrid energy storage together suppresses the internal power fluctuation of microgrid, and the double-fed flywheel storage introduces integrated inertia control, and $K_P = 20 \times 10^5$, $K_D = 10 \times 10^5$, that is, the double-fed flywheel participates in both primary frequency regulation and inertia.

Figure 7 gives the power output curves of each module of the microgrid under four different islanding scenarios. It can be seen that the power output of Li-ion battery and double-fed flywheel energy storage has obvious changes under different schemes. In the initial stage, the power deficit between PV and load is provided by the energy storage system, which is only compensated by the lithium battery in scheme I. In schemes II, III and IV, the hybrid energy storage is used to compensate together, and the power output characteristics of the hybrid energy storage are different due to the different settings of the integrated inertia control parameters. When the load increases suddenly in 1 s , there is a step power shortage in the system, and the lithium battery takes up the instantaneous step power growth in Scheme I. The doubly-fed flywheel assists the lithium battery to take up the instantaneous power step in Scheme II, III and IV, so as to reduce the inrush current borne by the lithium battery. Similarly, sudden drop in light intensity, sudden drop in load, and sudden increase in light intensity occur sequentially at 2 s , 3 s and 4 s , and the lithium battery switches from discharging operation state to charging operation state, and the doubly-fed flywheel switches frequently between charging and discharging. Compared with

Scheme II, the flywheel response power in Scheme III increases the flywheel inertia response auxiliary power, thus reducing the instantaneous response power of the lithium battery.

Figure 8 and Fig. 9 compare the lithium battery power output curve and the microgrid frequency dynamic response curve under the four islanding operation scenarios, respectively. Because the battery is used as the main source of the microgrid when the microgrid is islanded, it needs to provide power support passively to maintain the microgrid frequency stability when power fluctuations occur within the microgrid. At 1 s, the lithium battery in Scheme I suffers about 20.94 kW instantaneous power shock, and the lithium batteries in Scheme II, III and IV suffer about 14.66 kW instantaneous power shock. It can be seen that the introduction of the double-fed flywheel reduces the instantaneous shock power amplitude of the lithium battery by 30%, thus reducing the impact of accelerated aging by the inrush current to a certain extent and prolonging the service life of the lithium battery. Comparing Scheme II and III, it can be seen that the proportional coefficient in the integrated inertia control of doubly-fed flywheel can slow down the rate of microgrid frequency deterioration, thus reducing the frequency fluctuation during microgrid disturbance and improving the stability of microgrid islanding operation. The differential coefficient can reduce the frequency fluctuation and slow down the power change rate of lithium battery

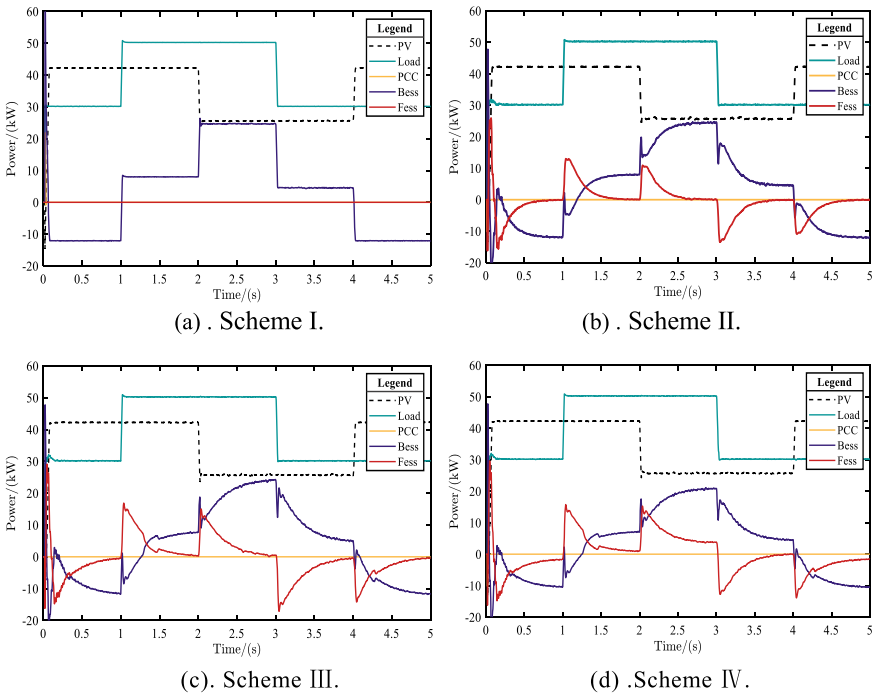


Fig. 7 Output curve of each module of microgrid under four schemes

by allowing the doubly-fed flywheel to increase the auxiliary inertia support power, thus reducing the number of frequent switching of lithium battery and improving the cycle life of lithium battery. Comparing with schemes III and IV, the introduction of the proportionality factor increases the steady-state output of the doubly-fed flywheel when there is a deviation in the microgrid frequency, and the higher the deviation in frequency, the higher the output. The increase of the steady-state output of the doubly-fed flywheel reduces the frequency fluctuation range from 49.73 to 50.13 Hz in Scheme III and 49.78 to 50.11 Hz in Scheme IV. The frequency fluctuation range of Scheme IV is reduced by about 17.5% compared with that of Scheme III.

Through the above analysis, it can be found that the high-speed response doubly-fed flywheel effectively reduces the transient shock power amplitude borne by the battery, while the integrated inertia control parameters do not have a significant effect on reducing the shock amplitude. In the integrated inertia control, the differential and proportional coefficients simulate the generator inertia characteristics and primary frequency regulation characteristics respectively, which can effectively slow

Fig. 8 Battery output curves under four different scenarios

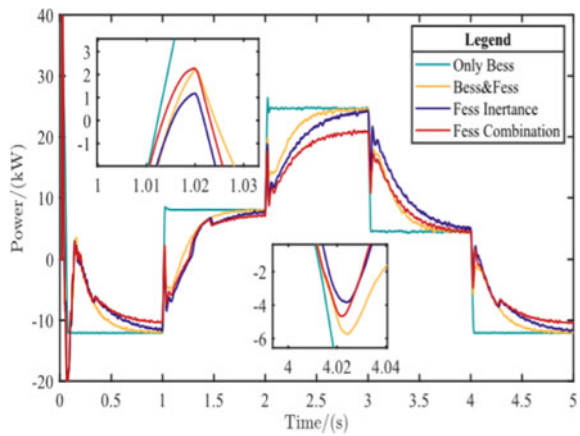
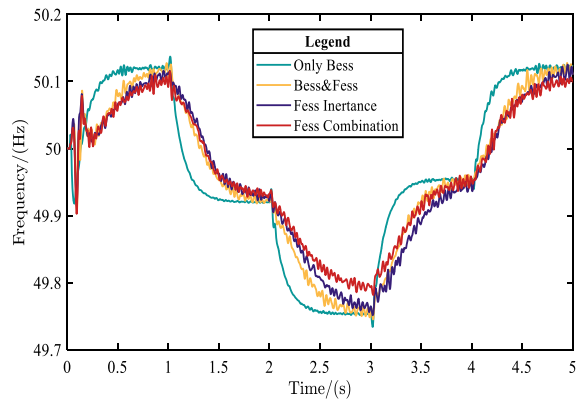


Fig. 9 Frequency dynamic response curves of microgrid in four different scenarios



down the microgrid frequency deterioration rate, reduce the frequency fluctuation range, and enhance the microgrid inertia characteristics, thus improving the microgrid islanding operation stability.

5 Conclusion

The introduction of doubly-fed flywheel energy storage system in microgrid can effectively enhance the microgrid inertia and thus improve the frequency stability, whether in grid-connected or islanded operation.

Under the grid-connected operation mode, the introduction of doubly-fed flywheel energy storage and comprehensive consideration of lithium battery power response delay error can effectively reduce the power fluctuation of grid-connected network caused by response delay, speed up the microgrid to restore power balance, strictly track the scheduling plan, and reduce the stability problem caused by microgrid uncertainty to the large grid.

In the island operation mode, the battery and the doubly-fed flywheel energy storage jointly suppress the power fluctuation inside the microgrid, and the doubly-fed flywheel energy storage participates in both primary frequency regulation and inertia support of the system with the best operation effect. In this control mode, the doubly-fed flywheel energy storage can effectively reduce the power shock that the battery needs to bear at the moment of power shortage of the microgrid, slow down the battery aging and prolong the service life, and reduce the frequency fluctuation of the microgrid, slow down the frequency deterioration and improve the operational stability of the microgrid.

The simulation results show that the power fluctuation of grid-connected network under the hybrid energy storage control scheme is reduced by 37.5% compared with that of single Li-ion battery storage during grid-connected operation, and the instantaneous impact power amplitude of Li-ion battery under the hybrid energy storage control scheme is reduced by 30% compared with that of single Li-ion battery storage during islanding operation, and the frequency fluctuation range of microgrid is reduced by 17.5%, which achieves the expected effect. In addition, the hybrid energy storage based on double-fed flywheel and lithium battery can also be applied to wind power microgrid, which has a promising application.

Acknowledgements Supported by State Key Laboratory of Electrical Insulation and Power Equipment (EIPE22304).

References

1. Kumar, S., Saxena, A., Shankar, R., Ranjan, M.: Enhanced grid frequency stabilization with renewable energy and virtual inertia support. In: 2022 2nd International Conference on Emerging Frontiers in Electrical and Electronic Technologies (ICEFEET), Patna, India, pp. 1–5 (2022)
2. Chi, Y., Zhao, Z., Xu, H., et al.: Control strategy of flywheel and battery hybrid energy storage in wind power system. *J. Shenyang Inst. Eng. (Nat. Sci.)* **222**, **18**(1), 12–19. (in Chinese)
3. Zheng, H., Zhao, Z., Liu, S., et al.: Modelling and control of hybrid energy storage system with fast frequency response in new power system. *Electr. Power Constr.* **222**, **43**(8), 13–21. (in Chinese)
4. Miyoshi, H., et al.: Study on suppressing variation of storage battery power in micro grid using flywheel. In: 2015 IEEE International Telecommunications Energy Conference (INTELEC), Osaka, Japan, pp. 1–5 (2015). <https://doi.org/10.1109/INTLEC.2015.7572297>
5. Han, J., Xue, F., Liang, S., et al.: Hybrid energy storage system assisted frequency modulation simulation of the coal-fired unit under fuzzy control optimization. *Energy Storage Sci. Technol.* **11**(7), 2188–2196 (2022). (in Chinese)
6. Wu, H., Li, H., Li, C., et al.: Research on primary frequency control strategy of nuclear power unit assisted by hybrid energy storage. *Shandong Electr. Power* **49**(3), 14–19 (2022). (in Chinese)
7. Yang, Y., Zhu, L.: Control strategy of microgrid super capacitor hybrid energy storage system. *J. Guangxi Norm. Univ. (Nat. Sci. Ed.)* **39**(2), 71–80 (2021). (in Chinese)
8. Chen, Z., Zou, X., Duan, S., et al.: Research on excitation control system of multi-functional flexible power conditioner. *Przegląd Elektrotechniczny* **87**(4), 172–175 (2011). (in Chinese)
9. Chen, Z., Li, D., Zou, X., et al.: Research on stable operation control method of flywheel energy storage system driven by doubly fed machine. *J. Electr. Power Sci. Technol.* **36**(1), 177–184 (2021). (in Chinese)
10. Li, G., Cheng, S., Wen, J., Pan, Y.: Power system stability enhancement by the flexible power conditioner. *Proc. CSEE* (23), 1–6 (2006). (in Chinese)

Multi-scenario Safe Operation Method of Energy Storage System for Cascade Utilization of Retired Power Batteries



Yan Wu, Peigen Tian, Xi Xiao, Yuan Cao, and Lu Yu

Abstract A multi-scenario safe operation method of the retired power battery cascade utilization energy storage system is proposed, and the method establishes a safe operation model of the retired power battery cascade utilization. The rate of rise is a constraint. Aiming at the problem that particle swarm optimization is easy to fall into local optimum, an adaptive weight-simulated annealing-particle swarm optimization algorithm (AW-SA-PSO) is proposed. According to the safety requirements in different operating scenarios, the method designs the maximum risk constraints in different operating scenarios, and uses the safety model to solve the operating margins of the energy storage state of charge and temperature rise rate in different scenarios. It can perform energy scheduling and temperature control according to the margin, so as to ensure the safety of system operation. This paper uses the NASA battery data set, and designs different operating scenarios for power generation side energy storage and user side energy storage for verification. The safe operation of the power battery energy storage system provides a solution. It is conducive to further promoting the large-scale promotion and construction of the system for the cascade utilization of energy storage of retired power batteries. Finally, the improved particle swarm optimization algorithm is used to solve the risk factor model of the retired battery energy storage system. The simulation results fully prove the superiority of the algorithm, and obtain the constraint condition margin of the risk factor in different scenarios.

Keywords State of charge · Temperature rise rate · Retired power batteries · Particle swarm optimization · Scene optimization

Y. Wu · Y. Cao

School of Electrical and Control Engineering, Liaoning Technical University, Huludao 123000, China

P. Tian (✉) · X. Xiao

Department of Electrical Engineering and Applied Electronics Technology, Tsinghua University, Beijing 100084, China

e-mail: tianbacon@mail.tsinghua.edu.cn

L. Yu

Xi'an Xianyang International Airport Co., Ltd., Xi'an 710086, China

© Beijing Paiké Culture Commu. Co., Ltd. 2023

X. Dong et al. (eds.), *The proceedings of the 10th Frontier Academic Forum of Electrical Engineering (FAFEE2022)*, Lecture Notes in Electrical Engineering 1054, https://doi.org/10.1007/978-981-99-3408-9_80

925

1 Introduction

The cascade utilization of Decommissioned power battery Energy storage system (DE) is a key part of realizing the national strategy of “carbon peaking and carbon neutrality” and building a new power system with new energy as the main body [1]. However, compared with the traditional energy storage systems that use brand new batteries as energy storage elements, the performance of retired power batteries has been attenuated to a certain extent by the use of new energy vehicles, so the safety issues when they are applied to large-scale energy storage systems are more prominent [2].

In order to improve the safety of echelon battery energy storage system, the method of pre-screening and clustering is mainly used to screen batteries at this stage [3, 4], but the screening workload is huge, and excessive screening will reduce the utilization rate of echelon batteries. Therefore, in order to ensure the safety of DE during operation, the reference [5, 6] specifies the safety margin of the energy storage system by setting the upper and lower limits of the SOC of the echelon battery, so as to improve the operating life of the entire energy storage system, but it only considers the SOC and Other reasons that may induce safety accidents are ignored, the evaluation factors are single, and important safety factors such as the temperature and remaining life of decommissioned batteries are not considered [7]. Reference [8] proposes the risk factor of DE, which fully considers the characteristics of important safety factors such as the temperature and remaining service life of decommissioned batteries, and defines the risk factor by taking the RUL, SOC and temperature rise rate of the echelon battery as the evaluation factors. And established an evaluation model. Therefore, according to the risk factor evaluation model, the optimal operation scheduling strategy of DB in multiple scenarios is given, which has far-reaching significance for the full echelon utilization of retired power batteries and the safe operation of DB.

Particle swarm optimization algorithm is a global optimization evolutionary algorithm based on swarm intelligence. In recent years, PSO algorithm has been widely used in function optimization, neural network training, combinatorial optimization, pattern recognition, power system optimization and other fields. The PSO algorithm has the characteristics of simple principle, easy implementation, and easy integration with other algorithms, but there are also problems such as local convergence. The literature [9] proposes an inertia weight adjustment strategy given the idea of fuzzy reasoning, but does not consider the adjustment of the two acceleration coefficients, which play an equally important role in determining the particle's position at the next moment. Reference [10] adjusts the composition of the comprehensive index by changing the index weight value of the improved Delphi method, and then uses the particle swarm calculation method of chaotic mutation to obtain the optimal configuration plan, but the method of determining the weight of this method has human factors and cannot be objective. reflect the real optimal solution.

In summary, this paper proposes an improved particle swarm optimization algorithm, which combines the adaptive weight algorithm and the principle of simulated annealing, and then obtains a new adaptive weight-simulated annealing-particle swarm optimization algorithm (AW-SA-PSO). Before each population update, the algorithm first calculates the fitness value of its parent population particles, and changes the inertia weight adaptively by comparing the relationship between each parent particle and the population fitness mean value, and then uses the simulated annealing algorithm to adjust the fitness value. After adjustment, the fitness of the particles is corrected to determine whether the new position is accepted, thereby avoiding blind adjustment of algorithm parameters and balancing the algorithm’s global search and local search capabilities. Finally, the improved particle swarm algorithm is used to simulate and solve the risk coefficient of DE in different scenarios, and the corresponding evaluation index margins are obtained.

2 Optimal Configuration Mathematical Model

2.1 Objective Function

The risk factor indicates that in unit time, by considering RUL, SOC and T_r , it characterizes the comprehensive risk of the echelon battery. Using the comprehensive risk score to score the risk of the echelon battery can overcome the difficulty of monitoring the safety evaluation indicators in the actual operation of the energy storage system, and is more conducive to engineering applications and large-scale promotion of energy storage systems [11]. The expression of the formula for the risk factor is as follows:

$$P_i = -\frac{1}{n} \times \ln\left(\begin{bmatrix} \alpha \\ \beta \end{bmatrix} o \begin{bmatrix} w_A \\ w_K \end{bmatrix} \cdot \begin{bmatrix} P_{RUL} \\ P_{SOC} \\ P_{\Delta T} \end{bmatrix}\right) \tag{1}$$

In the formula, P_i is the risk score of the i echelon battery in the energy storage system. The risk score can characterize the comprehensive safety of a single echelon battery in an energy storage system. n is the number of evaluation indicators. α and β are the adjustment coefficients of the subjective and objective weighting algorithm, w_A and w_K are the weights calculated by the subjective and objective weighting algorithm respectively, o is the Hadamard product of the matrix, \cdot is the quantity product of the matrix, P_{RUL} , P_{SOC} and $P_{\Delta T}$ are the normalized values of RUL, SOC and T_r of the echelon battery, respectively.

The SOC and T_r models of retired power batteries are shown in formula (2):

$$\begin{cases} U_{bj} = \sum_{j=1}^G (U_{bj_0} - \alpha_{bj} \frac{E_{bj}}{E_{bj} - \int i_{bj} dt} + (U_{bj_max} - U_{bj_e}) e^{-\frac{3}{E_{bj_e}} \int i_{bj} dt}) \\ \alpha_{bj} = \sum_{j=1}^G (U_{bj_max} - U_{bj_last} - 1 + (U_{bj_last} - U_{bj_e}) e^{-\frac{3}{E_{bj_e}} E_{bj_last}}) \cdot \frac{E_{bj} - U_{bj_last}}{E_{bj}} \\ S_{bj} = \sum_{j=1}^G (1 - \frac{\int i_{bj} dt}{3600 U_{bj}}) \times 100\%, \Delta T_i = \frac{T_i - T_{i-1}}{t_i - t_{i-1}} \end{cases} \quad (2)$$

In the formula, α_{bj} is the amplitude within the exponential region of the single battery j ; G is the number of single batteries in the energy storage unit; i_{bj} is the current value of charging and discharging; U_{bj_max} is the full-charge voltage amplitude; U_{bj_e} is the index Regional voltage limit value; U_{bj_last} is the nominal regional voltage limit value, U_{bj_0} is the standard value of charging voltage; E_{bj_e} is the exponential regional capacity limit value; E_{bj_last} is the nominal regional capacity limit value, S_{bj} is the SOC of the lithium battery b_j , ΔT_i is the i -th The T_r at the second sampling time, t_i , t_{i-1} is the time at the i -th and $i-1$ th sampling time, and T_i , T_{i-1} is the temperature at the i -th and $i-1$ st sampling time.

2.2 Constraint Function

During the operation of DE, the state variables and control variables need to be constrained, as follows:

$$\begin{cases} U_{min} \leq U \leq U_{max} \\ I_{min} \leq I \leq I_{max} \\ SOC_{min} \leq SOC \leq SOC_{max} \\ T_{min} \leq T \leq T_{max} \\ RUL_{min} \leq RUL \leq RUL_{max} \\ N_{min} \leq N \leq N_{max} \end{cases} \quad (3)$$

In the formula, I , U are the current and voltage during the charging and discharging process, SOC is the value of the retired power battery in the EB operating state, RUL is the value of the battery cell, N is the number of series-parallel nodes, U_{min} , U_{max} , I_{min} , I_{max} , SOC_{min} , SOC_{max} , T_{min} , T_{max} , RUL_{min} , RUL_{max} , N_{min} , N_{max} are the corresponding minimum and maximum value.

3 Improved Particle Swarm Optimization Algorithm

3.1 Standard Particle Swarm Optimization and Simulated Annealing

The basic principle of the PSO algorithm is that each particle in the group continuously adjusts its speed and position in the search space according to formula (4) and (5) until the convergence termination condition is met.

$$v_{id}(k+1) = \omega v_{id}(k) + c_1 r_1 (p_{id}(k) - x_{id}(k)) + c_2 r_2 (p_{gd}(k) - x_{id}(k)) \quad (4)$$

$$x_{id}(k+1) = x_{id}(k) + v_{id}(k+1) \quad (5)$$

In the formula, $v_{id}(k)$ is the velocity of particle i in the d -th dimension in the k -th iteration; $x_{id}(k)$ is the position of particle i in the d -th dimension in the k -th iteration; ω is the inertia weight; c_1 c_2 are Acceleration coefficient or learning factor; $p_{id}(k)$ is the position of the individual extreme point of particle i in the d -th dimension in the k -th iteration; $p_{gd}(k)$ is the global d -dimension of the entire particle swarm in the k -th iteration. The position of the extreme point; r_1 and r_2 are random numbers with independent uniform distribution in the interval $[0, 1]$.

The Simulated Annealing (SA) algorithm is a global optimization algorithm. Its basic idea is to simulate the process of solid annealing and improve the traditional Monte Carlo sampling by using the Metropolis importance sampling criterion of formula (6). Computational efficiency, such as and controlling algorithm progress through a set of cooling schedules [12].

$$p = \begin{cases} 1, & E(n+1) < E(n) \\ \exp(-\frac{E(n+1)-E(n)}{T}), & E(n+1) \geq E(n) \end{cases} \quad (6)$$

In the formula, p is the reception probability, and $E(n)$ is the system energy.

3.2 Improved Particle Swarm Optimization Algorithm

The improved adaptive weight-simulated annealing-particle swarm optimization algorithm (AW-SA-PSO) first considers the fitness of the overall particle, and establishes a new weight self-update function based on particle fitness. The difference between the degree and the average fitness is used to determine the weight value used in the next position update, and then the particle fitness is corrected according to the simulated annealing algorithm. Ensure a two-way balance of efficiency and precision.

The process of improving the algorithm is as follows:

- (1) Calculate the fitness mean of all the current particles f_v .
- (2) Update and multiply the particles, and count the particles whose fitness is greater than or less than f_v in the new generation of particles.
- (3) Update the speed weight, and assign different target weight values to the particles whose fitness is greater than, less than f_v , and between f_{v1} and f_{v2} , respectively. The improved iterative formula is:

$$v_i = \omega_i \cdot v_i + c_{1t} \cdot rand \cdot (pbest_i - x_i) + c_{2t} \cdot rand \cdot (pbest_i - x_i) \quad (7)$$

$$\omega_t = \omega_{min} + \frac{(\omega_{max} - \omega_{min}) \cdot (gen - t)}{gen} \quad (8)$$

$$\omega_i = \begin{cases} \omega_{max} \cdot \alpha, & f_i > f_{v1} \\ (\omega_t - \frac{(\omega_t - \omega_{min})(f_{v1} - f_i)}{f_{v1} - f_{v2}}) \cdot \alpha, & f_{v2} \leq f_i \leq f_{v1} \\ \omega_{min} \cdot \alpha, & f_i < f_{v2} \end{cases} \quad (9)$$

In the formula, $c_{1t} = 2.5 + (0.5 - 2.5) \times t/gen$, $c_{2t} = 2.5 + (0.5 - 2.5) \times t/gen$, $x_i = x_i + v_i$, ω_{max} , ω_{min} are the index for judging the diversity of the population, and it is determined by itself according to the needs of solving the model.

- (4) According to the simulated annealing algorithm, the fitness of particles is corrected, and the correction formula is:

$$F' = \exp(T_0 \times p^k \times F) \quad (10)$$

In the formula, F' is the fitness value, F is the objective function value of the individual; k is the evolution function, T_0 is the initial temperature of simulated annealing, generally taking the value of the same order of magnitude as the objective function; p is the attenuation coefficient, generally taking slightly less than 1 number of. In this way, in the initial stage of the algorithm, p^k is larger, which is conducive to the diversity of particles; with the evolution of the algorithm, the number of iterations of the algorithm gradually increases, and the particle fitness value gradually decreases, which is beneficial for the algorithm to converge to the global optimum.

- (5) The acceptance probability that the particle has the original position $x_{id}(k)$ to become the new position $x'_{id}(k)$ after the adaptive weight adjustment is determined by the Metropolis criterion in the simulated return, and the formula is:

$$p = \begin{cases} 1, & F'_{new} < F'_{old} \\ \exp(-\frac{F'_{new} - F'_{old}}{T(k)}), & F'_{new} \geq F'_{old} \end{cases} \quad (11)$$

In the formula, F'_{new} and F'_{old} are the fitness of the new position and the original position after the adaptive weight adjustment, and $T(k)$ is the temperature of the k th

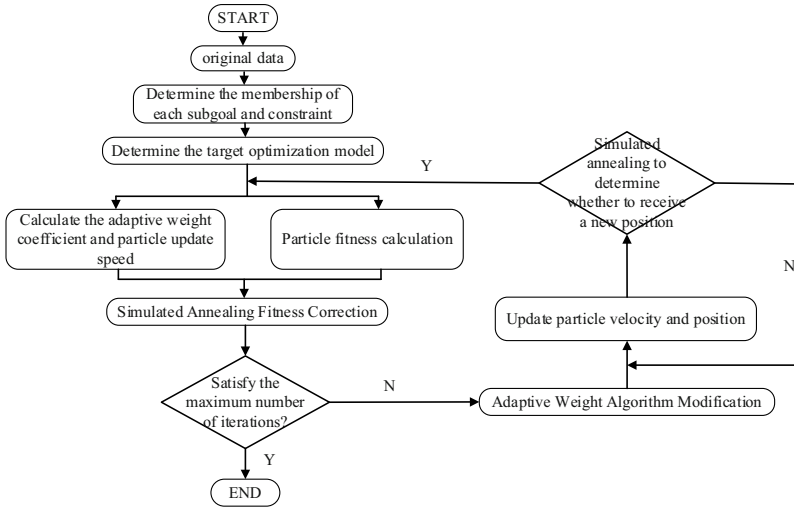


Fig. 1 AW-SA-PSO algorithm flow chart

generation of the PSO algorithm. When the cooling method of the classical simulated annealing algorithm is used, $T(k)$ adopts the following formula:

$$T(k) = \frac{T_0}{\lg(1 + k)} \tag{12}$$

If the fitness value of the new position after adjustment is smaller than the fitness value of the original position, indicating that the new position is better than the original position, the acceptance probability of the new position is 1, and the fitness value of the new position is compared with the individual extreme value $P_{id}(k)$ and the global extreme value. The fitness values of the value $P_{gd}(k)$ are compared respectively. If it is still small, $P_{id}(k)$ and $P_{gd}(k)$ are also updated. Otherwise, the original position of the particle is kept and the next iteration is continued until the optimal solution is obtained.

The flowchart of the algorithm is shown in Fig. 1.

4 Case Analysis

4.1 Battery Data Source

The National Aeronautics and Space Administration (NASA) dataset [13] is derived from the prognostics center of excellence (PCoE) at Ames Research Center, numbered B05, B06, B07, and B18. The battery data set is the aging data of 18,650

lithium battery with graphite anode and $\text{LiNiCo}_0.15\text{Al}_0.05\text{O}_2$ cathode, and the nominal capacity is 2 Ah. In the aging experiment, the four groups of batteries were charged with a constant current of 1.5 A until the battery voltage reached 4.2 V, and then the constant voltage continued to charge until the current charging current dropped to 20 mA, and then a constant current of 2 A was applied to discharge until the four groups. The voltage of the battery was dropped to 2.7 V, 2.5 V, 2.2 V and 2.5 V, respectively. The experiment was carried out at room temperature of 24 °C, and the experiment was terminated when the rated capacity of the battery dropped by 30%.

The data set provides the capacity decay data and the corresponding charge and discharge voltage and current data when the battery capacity drops from 100 to 70%. Since the capacity of the cascade battery has dropped to 80% when it is applied to the energy storage system [14], this paper intercepts the decay data when the capacity drops from 80 to 70% to characterize the experimental data of the cascade battery during the operation of the energy storage system. Follow-up safety assessment of energy storage systems.

4.2 Scene Selection and Simulation Analysis

According to the different risks and the risks of retired power batteries, two scenarios on the power generation side and the user side are defined. Considering the safety and economy comprehensively, improving the utilization rate of SOC and maintaining the risk factor of the energy storage system should be lower than 0.45. Considering the optimal safety, the risk factor of the entire energy storage system should be reduced, the use range of SOC should be shortened, and the risk factor of the pillow energy storage system should be lower than 0.40.

The initial parameters of the AW-SA-PSO algorithm are selected as follows: population size $N = 30$; initial inertia weight $\omega = 0.6$; acceleration coefficient $c_1 = c_2 = 2.0$; the maximum number of iterations is 100 as the algorithm termination condition; the initial temperature T_0 of simulated annealing = 200; decay coefficient $p = 0.95$ for simulated annealing. In the standard PSO algorithm, the inertia weight changes from a maximum of 0.9 to a minimum of 0.4 according to a linear decreasing strategy, and the remaining parameters are the same as the AW-SA-PSO algorithm.

Figure 2 shows the comparison results of DE optimization of the AW-SA-PSO algorithm based on the NASA data set B0005 battery when the user-side energy storage environment is used. The SOC and temperature rise rate margins after the DE optimization are shown in Table 1. Show. It can be seen that after the optimization of the improved AW-SA-PSO algorithm, the maximum risk factor index increased from 0.341 to 0.412, and the optimized SOC and temperature rise rate margins increased from 51.7–77.7% and 0.009–0.015 °C/s increased to 41.6–81.4% and 0.005–0.019 °C/s. From Fig. 3(a)–(c), the change curves of the risk coefficient, SOC and temperature rise rate with the number of iterations can be seen more

intuitively, the optimization effect of the improved algorithm is due to the PSO algorithm.

From Fig. 3(a)–(c), the change curves of the risk coefficient, SOC and temperature rise rate with the number of iterations can be seen more intuitively, the optimization effect of the improved algorithm is due to the PSO algorithm.

Figure 4 compares the operation curve of the hazard coefficient after using the AW-SA-PSO algorithm to optimize the algorithm and the use of the traditional maintaining charge-discharge process 15–85. It can be seen intuitively from the figure that

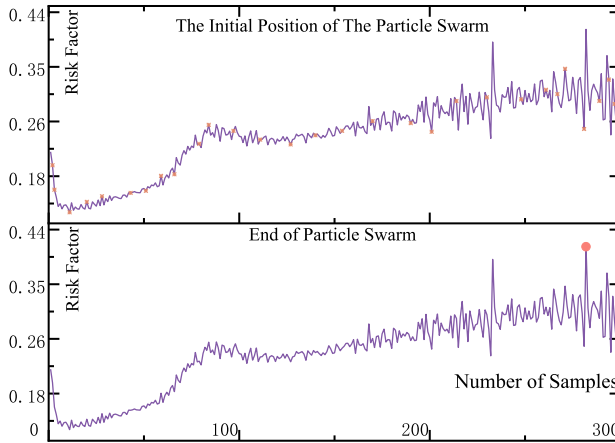


Fig. 2 Comparison before and after the improved particle swarm optimization algorithm

Table 1 Table captions should be placed above the tables

Project name	Initial state	PSO	AW-SA-PSO
Risk factor	0.216	0.341	0.412
SOCmax	77.7%	77.7%	81.4%
SOCmin	59.3%	51.7%	41.6%
T _r max	0.022 °C/s	0.015 °C/s	0.019 °C/s
T _r min	0.040 °C/s	0.009 °C/s	0.005 °C/s

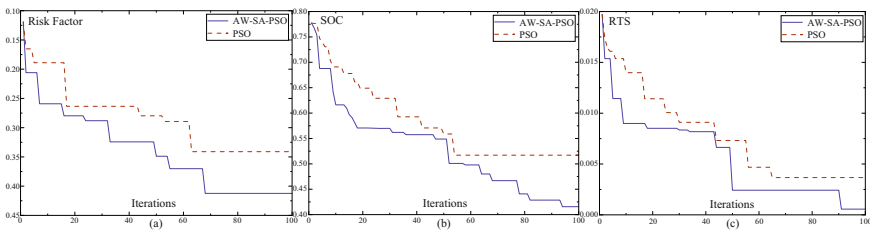


Fig. 3 Variation curve of the number of iterations of traditional and improved PSO

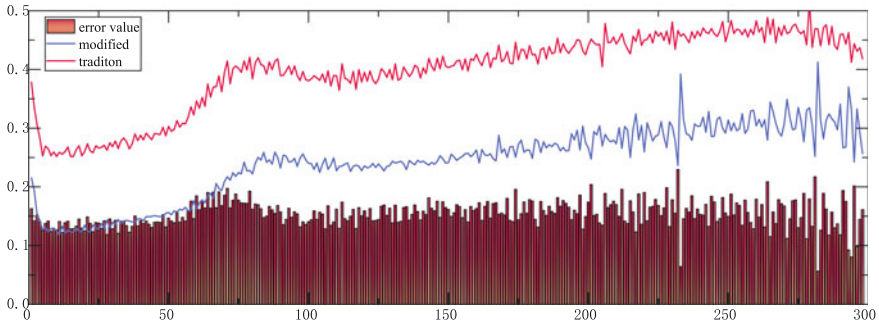


Fig. 4 Influence of traditional and improved PSO energy scheduling on risk factor

the SOC margin optimized by the AW-SA-PSO algorithm can well ensure that the risk factor of DE is always lower than the set value during the operation process, which is more secure and can It provides a reference margin for energy scheduling when the DE is connected to other power systems, so as to ensure the safe operation of the DE. It is further explained that the characteristics displayed by the improved PSO algorithm are more suitable for decommissioning power battery energy storage systems in different scenarios. Safe operation provides the solution.

5 Conclusion

This paper researches and proposes a multi-scenario safe operation method of the energy storage system for the cascade utilization of retired power batteries, and establishes a safe operation model for the cascade utilization of retired power batteries and the rate of temperature rise are constraints. Aiming at the problem that particle swarm optimization is easy to fall into local optimum, an AW-SA-PSO algorithm is proposed. The algorithm corrects the fitness of the particles after adjusting the adaptive weight parameters and the simulated annealing algorithm, and judges whether the new position is accepted in the form of probability. Finally, according to the safety requirements in different operating scenarios, the maximum risk constraints on the user side and the power generation side in different operating scenarios are designed, and the energy storage state of charge and temperature rise rate margin for safe operation in the two scenarios are obtained through the safety model., the energy storage system can perform energy scheduling and temperature control according to the margin during operation, so as to ensure the safety of the system operation. The calculation example results show the effectiveness of the method and the superiority of the algorithm, and provide solutions for the safe operation of retired power battery energy storage systems in different application scenarios. It is conducive to further promoting the large-scale promotion and construction of the system for the cascade utilization of energy storage of retired power batteries.

Acknowledgements This work was supported by the S&T Major Project of Inner Mongolia Autonomous Region in China (2020ZD0018).

References

1. Li, J., Li, Y., Lv, C., et al.: Key technology and research status of cascaded utilization in decommissioned power battery. *Autom. Electr. Power Syst.* **44**(13), 172–183 (2022)
2. Huang, J., Li, J., Li, Z., et al.: A state of health rapid assessment method for decommissioned lithium-ion batteries. *Power Syst. Prot. Control* **49**(12), 25–32 (2022)
3. Li, J., Li, Y., Lv, C., et al.: Key technology of retired batteries' screening and clustering under target of carbon neutrality. *Power Syst. Technol.* **46**(2), 429–441 (2022)
4. Yu, L., Zhang, H., Tian, P., et al.: A battery safety evaluation method for reuse of retired power battery in energy storage system. *Acta Energetica Solaris Sinica* **43**(5), 447–453 (2022)
5. Yu, L., Zhang, H., Tian, P., et al.: Multi-level on-line safety assessment of reconfigurable energy storage system using secondary batteries risk warning positioning method. *Acta Energetica Solaris Sinica* **43**(5), 462–467 (2022)
6. Xiao, X., Tian, P., Yu, L., et al.: Status and prospect of safety studies of cascade power battery energy storage system. *J. Electr. Eng.* **1**, 208–224 (2022)
7. Ning, Y., Zuo, X., Wei, L., et al.: Economic dispatch application of power system with energy storage systems. *IEEE Trans. Appl. Supercond.* **26**(7), 1–5 (2016)
8. Cao, Y., Wu, Y., Tian, P., et al.: Risk assessment of echelon utilization retired power battery energy storage system. In: *International Conference on Energy Storage and Intelligent Vehicles* (2022)
9. Li, X., Zhu, Q.: Application of improved particle swarm optimization algorithm to multi-objective reactive power optimization. *Trans. China Electrotech. Soc.* **25**(7), 137–143 (2010)
10. Meng, J., Li, X., Ding, X.: Optimal allocation of distributed generation based on improved adaptive weight multi-objective particle swarm optimization. *J. Electr. Power Sci. Technol.* **35**(2), 55–60 (2020)
11. Liu, J., Wang, H.: Radar resource allocation method based on improved multi-objective particle swarm optimization algorithm. *J. CAEIT* **17**(6), 550–556 (2022)
12. He, L., Lv, H., Li, J., et al.: Research on optimal scheduling of microgrid energy based on sa_afa. *Acta Energetica Solaris Sinica* **41**(9), 36–43 (2020)
13. Liu, D., Zhou, J., Liao, H., et al.: A health indicator extraction and optimization framework for lithium-ion battery degradation modeling and prognostics. *IEEE Trans. Syst. Man Cybern. Syst.* **45**(6), 915–928 (2015)
14. Liu, Y.Q., Li, S., Zhang, L., et al.: Characteristics and application prospects of second use batteries for energy storage. *Sci. Technol. Manag. Res.* **37**(1), 59–65 (2017)

Research on Characteristics of Submersible Motor Under Fault Condition Based on Electromagnetic-Thermal Coupling



Tianle Li, Baichuan Xu, Yahui Zhang, Yi Wang, Yixiao Luo , and Kai Yang 

Abstract Submersible motors are prone to failure during production, which can result in operation interruption and serious economic losses. It is very important to use the collected data effectively to evaluate the state of the motor system, so as to avoid faults. However, the actually collected data of submersible motors are often very complex, which make it difficult to accurately identify faults. In this paper, three most common fault types of submersible motors are selected for research, including rotor broken bar fault, air gap eccentric fault and turn-to-turn short circuit fault. Based on the finite element method, the electromagnetic thermal coupling field simulation is carried out to obtain the electromagnetic, thermal and mechanical signals of motor under fault conditions, the fault features are extracted, and then the influence of different fault degrees on the motor temperature field is studied. The above research lays a foundation for accurate fault diagnosis of submersible motor.

Keywords Submersible motor · Finite element analysis · Characteristic signal · Fault diagnosis

T. Li · B. Xu · Y. Zhang · Y. Wang · Y. Luo · K. Yang (✉)
School of Electrical and Electronic Engineering, Huazhong University of Science and Technology, Wuhan 430071, China
e-mail: yk@hust.edu.cn

T. Li
e-mail: litl14@hust.edu.cn

B. Xu
e-mail: xubaichuan@hust.edu.cn

Y. Zhang
e-mail: zhangyahui@hust.edu.cn

Y. Wang
e-mail: m202171941@hust.edu.cn

Y. Luo
e-mail: luoyx@hust.edu.cn

1 Introduction

As a key component of offshore platform, offshore electric submersible pump plays a vital role in oilfield production. Electric submersible pump is composed of submersible motor, power cable, multistage centrifugal pump, oil-gas separator, safety valve, transformer and other components, Relying on the rotary pressurization of multi-stage impeller in multi-stage centrifugal pump to realize the pressurization and acceleration of channel liquid, it has the characteristics of large displacement, high head, simple operation, convenient management and easy installation. It is widely used in oilfield production [1].

Through the investigation of the actual fault data of offshore platforms, in the electric submersible pump system, the submersible motor is the equipment with the most faults. Generally, once the electric submersible pump breaks down, it needs workover operation and high maintenance cost, which not only brings heavy economic burden to oil-field enterprises, but also affects the normal production of the oilfield [2]. Therefore, it is necessary to conduct indepth research on the fault diagnosis technology of submersible motor, and apply new methods and technologies to the fault diagnosis of submersible motor, so as to ensure the better work of electric submersible pump and create better economic benefits for enterprises.

Most submersible motors use three-phase squirrel cage induction motors [3]. In this paper, the rotor bar breaking, air gap eccentricity and inter turn short circuit faults of submersible motors are selected as the research objects fault diagnosis method of mechanical multi-source information fusion.

For a long time, motor fault diagnosis methods based on signal monitoring have been research hotspots. The signals used by scholars include current, voltage, temperature, vibration, and so on. The underlying fact is that all motor systems will generate electrical and thermal signals during their work. The electrical and thermal signals obtained from the motor contain a lot of information about the working state of the motor [4]. For example, the current and voltage of a normal motor are three-phase symmetrical. When the temperature reaches the steady state, the temperature is within the allowable range of the insulation level, and the temperature field is more evenly distributed. However, there are new current harmonic content in the faulty motor, and local high temperature or Low temperature. The change of the electrical signal spectrum can be used to identify the fault state of the motor, and the change of the temperature signal can be used to estimate the extent of the fault development. The latest advances in artificial intelligence and the availability of low-cost current and temperature sensors allow researchers to use a wealth of monitoring data to study effective motor fault diagnosis methods. A diagnosis method based on current residual of current signal is proposed [5]. Through machine learning model, fault diagnosis and location are carried out simultaneously, simplifying the diagnosis process. Zhenli Xu et al. [6] proposed an infrared thermal image few-shot learning method based on CAPNet. This method is used to diagnose the faults of induction motors and has good performance. Wei Xu et al. [7] proposed an improved slight fault diagnosis strategy for induction motor. The additional even and triple

harmonics, caused by the faulty asymmetric structure, are taken into account. The diagnosis accuracy for the induction motor under the slight fault situation is enhanced. Taner Goktas et al. [8] proposed an evaluation and classification method of double bar breakages through three-axes vibration sensor in induction motors, and higher reliability of broken bar fault detection is realized. Peng Chen et al. [9] studied the harmonics of air-gap magnetic field of induction motors with stator turn-to-turn fault, and the relevant fault characteristics are obtained through analysis and experiments. Kai-Jung Shih et al. [10] proposed a method to realize turn-to-turn short circuit fault diagnosis of permanent magnet synchronous motor by machine learning. The diagnostic accuracy of support vector machine and convolutional neural network is compared. It is found that both methods can achieve high accuracy, but the support vector machine method requires a small amount of data. Bilal Djamel Eddine Cherif et al. [11] proposed a machine-learning-based diagnosis method of an inverter-fed induction Motor. By processing the current signal, the open circuit fault of the switch in the two-level three-phase voltage source inverter fed induction motor is detected and automatically monitored.

In this paper, a finite element analysis method based on electromagnetic thermal coupling is proposed. Obtaining accurate fault characteristic signals is helpful for accurate fault identification of submersible motors. The severity of the fault can be further evaluated by temperature field analysis.

2 Multi-field Coupling Analysis

2.1 Electromagnetic Signal Acquisition

This paper proposes an electromagnetic thermal mechanical multi field coupling analysis method to obtain the characteristic signals of the submersible motor under different working conditions, so as to provide data reference for accurate identification of various types of faults.

The fracture of rotor bar is one of the main faults of the motor, accounting for about 10% of the fault causes. It is mainly caused by the uneven stress on each part of the bar under complex working conditions. When the motor rotor bar breaks or the end ring breaks, the current characteristic component ($\pm 2ksf$) will appear on both sides of the main frequency of the stator current due to the change of the magnetic field, and its amplitude has a positive relationship with the number of broken bars. The following characteristic frequencies will appear in the corresponding stator current:

$$f_{1z} = (1 \pm 2ks)f \quad (1)$$

where f is the grid frequency and s is the motor slip.

The air gap eccentricity of the motor can be divided into two basic situations: one is static eccentricity, the designated rotor is not concentric, and the rotor takes

its own geometric axis as the rotating axis; The other is dynamic eccentricity. The designated rotor is not concentric, but the rotor takes the geometric axis of the stator as the rotating axis. Other complex eccentricities are the combination of these two basic types. Based on the traditional methods of magnetomotive force and magnetic guided wave, some scholars have obtained the current components of some specific frequencies in the stator winding when there is air gap eccentricity in the motor, and verified by experiments. The frequency components related to eccentricity can be expressed as:

$$f_h = \left[(kR \pm n_d) \frac{1-s}{p} \pm v \right] f \quad (2)$$

where: f is the fundamental frequency of power supply; R is the number of rotor slots; s is the slip rate; p is the polar logarithm; k is any integer; v is the harmonic order of power supply ($v = 1, 2, 3 \dots$); n_d is the eccentricity order, $n_d = 0$, in static eccentricity, $n_d = 1, 2, 3$ in dynamic eccentricity.

After long-time operation of the motor, the internal turn to turn insulation may be damaged due to the impact, aging, overheating, electromagnetic force and other stress effects, so that the winding will be subject to a large short circuit current, which will increase the local temperature at the short circuit, further damage the surrounding insulation, and cause a large range of winding turn to turn short circuit faults. At this time, the stator current waveform is distorted, and the following fault characteristic harmonic components appear:

$$f_z = \left| \frac{n}{p}(1-s) \pm m \right| f \quad (3)$$

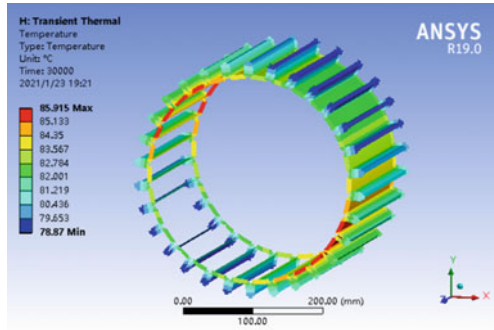
where $n = 1, 2, 3$; $m = 1, 3, 5, \dots$ p is the number of motor poles; F is the fundamental frequency of power supply.

The waveform of radial electromagnetic force at a certain point in the air gap of the motor is obtained by the field calculator. By integrating the radial electromagnetic stress along the circumferential direction, the unbalanced magnetic pull on the rotor can be obtained. The spectrum characteristics of the above two forces can also be used to diagnose the faults of submersible motors.

2.2 Thermal Signal Acquisition

Through the electromagnetic field finite element simulation, the average iron loss, copper loss and mechanical loss of the submersible motor under different working conditions are obtained, and the thermal field analysis module is introduced as the heat source to solve its temperature distribution. The obtained temperature field is used as the external excitation in the stress field analysis, and the thermal stress distribution is finally obtained by simulation analysis.

Fig. 1 Temperature field distribution of submersible motor casing under normal conditions



Firstly, the temperature field of the submersible motor under normal conditions is analyzed, which can be used as a reference for the subsequent analysis of various abnormal conditions. According to the actual working environment of the submersible motor, considering the special structure of the hollow rotating shaft of the submersible motor, the heat dissipation boundary conditions in the motor are reasonably designed, the air gap is quasi-static treated, and is equivalent to a static flowing solid. The equivalent thermal conductivity is given after calculating and comparing the Reynolds number and the critical Reynolds number formula. Through calculation, the air gap Reynolds number of the motor model used in the study is 92.416826, which is less than the critical Reynolds number 379.85. Therefore, the gas is laminar flow, and the thermal conductivity of the gas is taken as 0.0305038 w/mK. Since the temperature sensor is usually placed on the surface of the submersible motor casing, the temperature field distribution on the surface of the motor casing is analyzed. The average temperature of the casing is 82.205 °C, as shown in Fig. 1. The measured temperature of the submersible motor is 80.691 °C, and the temperature error is 1.876%, which proves which proves the high accuracy of the analysis model.

3 Instance Verification

The finite element simulation model of submersible motor is established in ANSYS Maxwell. The motor model used in this analysis is shown in Fig. 2, its main dimensions are shown in Table 1.

The broken bar fault is simulated by setting the conductivity of the squirrel cage guide bar to 0, the winding partial short circuit is set to simulate the inter turn short circuit fault, and the air gap eccentricity fault is simulated by giving the displacement of the rotating shaft center relative to the stator center. The current, radial electromagnetic force and unbalanced electromagnetic force waveforms of electric submersible pump under normal, overload and main fault conditions (including rotor broken bar, air gap eccentricity and stator turn to turn short circuit) are obtained, and the spectrum

Fig. 2 Simulation model of the motor

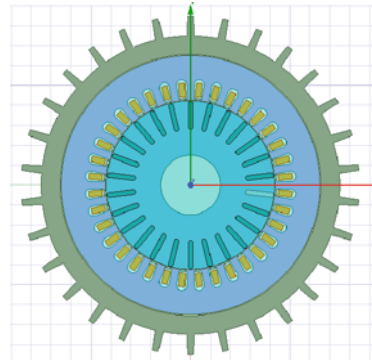


Table 1 Motor main sizes

Parameter	Value
Polar pairs	1
Phase number	3
Stator and rotor slot fit	36/26
Outer diameter of stator/mm	175
Stator inner diameter/mm	120
Outer diameter of squirrel cage rotor/mm	119.4
Inner diameter of squirrel cage rotor/mm	38
Rated speed/(R/min)	2900
Rated slip	0.0333
Rated voltage/V	380
Rated power/kW	11

analysis is carried out to extract the fault frequency component. The spectrum characteristics of stator current, radial electromagnetic force and unbalanced magnetic pull under different working conditions are shown in Figs. 2, 3 and 4.

Each fault will increase the harmonic distortion rate of stator current, and the stator current distortion is the most serious when the rotor bar breaks. The characteristic frequency component of stator current under fault condition can be used as the basis for motor fault identification and diagnosis. The main components of the radial electromagnetic stress spectrum of the motor are the DC component and the second harmonic fundamental wave (100 Hz); Turn-to-turn short circuit fault will lead to a large increase in the DC component and the second harmonic component of radial electromagnetic stress. Broken bars and eccentric faults will lead to an increase in the characteristic frequency of radial electromagnetic stress fault. Unbalanced magnetic pull reflects the degree of instability of the motor. It is found that the characteristic

Fig. 3 Spectrum characteristics of stator current under different working conditions

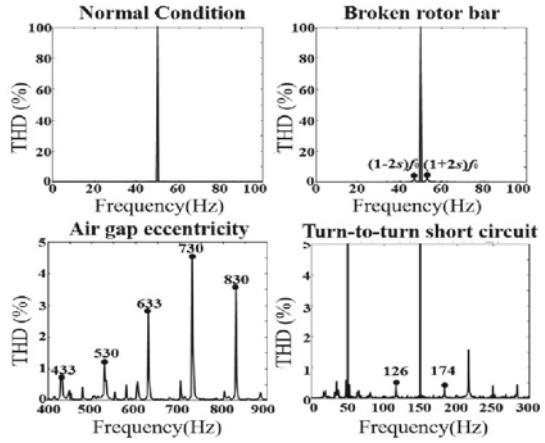
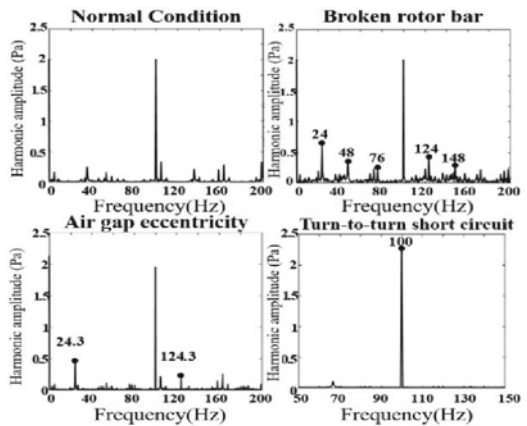


Fig. 4 Spectrum characteristics of radial electromagnetic force under different working conditions



frequency of unbalanced magnetic pull is obvious only when the air gap eccentricity fault occurs.

According to the electromagnetic thermal coupling finite element simulation, the temperature distribution of the motor is shown in Fig. 6.

Fig. 5 Spectrum characteristics of unbalanced magnetic pull under different working conditions

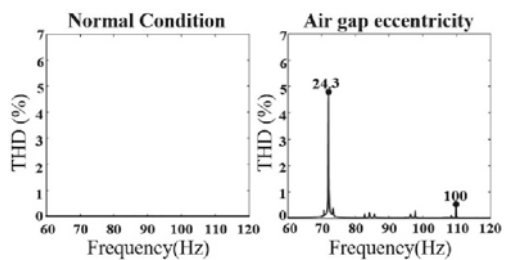
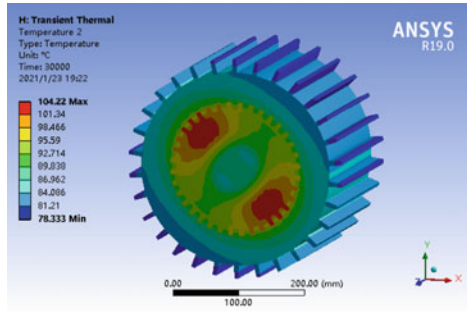


Fig. 6 Distribution of internal temperature field of submersible motor under normal working conditions



Similarly, the temperature field distribution of the motor under different degrees of fault can be obtained, as shown in Tables 2, 3 and 4.

Where condition 1 is dynamic eccentricity 0.1 mm, static eccentricity 0.4 mm, condition 2 is dynamic eccentricity 0.2 mm, static eccentricity 0.4 mm.

It is found that the characteristic frequency of stator current in Fig. 2 is completely consistent with the calculation results of Eqs. 1, 2 and 3. The characteristic frequencies of radial electromagnetic force and unbalanced magnetic pull of the motor under different working conditions were obtained. According to the temperature data given in the table, the severity of various faults can be estimated.

Table 2 Average temperature data of rotor broken bar

Parts	Temperature of 2 broken bars (°C)	Temperature of 4 broken bars (°C)
Motor	93.34	95.13
Stator	92.15	93.82
Rotor	97.77	99.90
Winding	99.34	101.49
Bars	99.10	101.23
Insulation	96.27	98.21

Table 3 Average temperature data of air-gap eccentric faults

Parts	Temperature of air-gap eccentric condition 1 (°C)	Temperature of air-gap eccentric condition 2 (°C)
Motor	91.68	91.99
Stator	90.67	90.99
Rotor	96.27	96.50
Winding	98.35	98.62
Bars	97.91	98.15
Insulation	95.54	95.83

Table 4 Average temperature data of turn-to-turn short circuit faults

Parts	Temperature of 25% turn-to-turn short circuit fault (°C)	Temperature of 50% turn-to-turn short circuit fault (°C)
Motor	101.73	115.06
Stator	99.84	112.81
Rotor	111.51	126.67
Winding	120.15	137.05
Bars	115.22	131.07
Insulation	112.30	127.58

4 Conclusion

In this paper, the electromagnetic and thermal characteristics of submersible motor under various fault conditions are studied. Firstly, the finite element model of submersible motor is constructed. Through electromagnetic field calculation, the fault characteristics of stator current, radial electromagnetic force and unbalanced magnetic pull are analyzed. The electromagnetic loss is used as the heat source, and the temperature distribution of the motor is obtained through coupling analysis. Compared with traditional analytical methods, the proposed method can obtain more accurate fault signals. After verification, stator current, radial electromagnetic force and unbalanced magnetic pull can be used to identify fault types, and the temperature can be used to evaluate the state of fault.

References

1. Zhao, F.: Research status and development trend of fault diagnosis technology for electric submersible pump. *China Pet. Mach.* **39**(01), 80–84 (2011). (in Chinese)
2. Sunal, C.E., Velisavljevic, V., et al.: Review of machine learning based fault detection for centrifugal pump induction motors. *IEEE Access* **10**, 71344–71355 (2022)
3. Miljković, D.: Brief review of motor current signature analysis. *CrSNDT J.* **5**, 14–26 (2015)
4. Atta, M.E.E.-D., Gilany, M.I., et al.: Broken bar fault detection and diagnosis techniques for induction motors and drives: state of the art. *IEEE Access* **10**, 88504–88526 (2022)
5. Zhang, Z., Tao, X., et al.: A hybrid diagnosis method for inverter open-circuit faults in PMSM drives. *China Electrotech. Soc. Trans. Electr. Mach. Syst.* **4**(3), 180–189 (2020)
6. Xu, Z., Pang, B., et al.: An infrared thermal image few-shot learning method based on CAPNet and its application to induction motor fault diagnosis. *IEEE Sens. J.* **22**(16), 16440–16450 (2022)
7. Xu, W., Luo, D., et al.: Improved slight fault diagnosis strategy for induction motor considering even and triple harmonics. *IEEE Trans. Ind. Appl.* **58**(4), 4436–4449 (2022)
8. Goktas, T.: Evaluation and classification of double bar breakages through three-axes vibration sensor in induction motors. *IEEE Sens. J.* **22**(13), 13602–13611 (2022)
9. Chen, P., Xie, Y.: Harmonics analysis of air-gap magnetic field of induction motors with stator inter-turn fault. *IEEE Trans. Magn.* **58**(7), 1–9 (2022)

10. Shih, K.-J., Hsieh, M.-F., et al.: Machine learning for inter-turn short-circuit fault diagnosis in permanent magnet synchronous motors. *IEEE Trans. Magn.* **58**(8), 1–7 (2022)
11. Cherif, B.D.E., Chouai, M., et al.: Machine-learning-based diagnosis of an inverter-fed induction motor. *IEEE Lat. Am. Trans.* **20**(6), 901–911 (2022)

Data-Driven Dynamic Modeling Methods for Offshore Wind Turbine Generators



Xinhu Ding and Haidong Chen

Abstract Accurate model is the basis of analyzing the operation characteristics of wind power system. To solve the difficulty of determining the wind turbine generator's (WTG's) parameters due to the lack of measurement information under severe disturbances, an intelligent modelling method for doubly-fed induction generator (DFIG)-based WTGs is proposed by training BP neural network with small disturbance response data. Firstly, the data-driven modelling principle is introduced based on the BP neural network. Secondly, the power spectrum characteristic data of response signal is extracted based on a simulation system with a DFIG wind farm integrated into an infinite system. Thirdly, the key parameters are attained based on the power spectrum sensitivity. Finally, the BP neural network are used to construct the nonlinear mapping between the power spectrum of response signal and model parameters, and model parameters are identified based on trained neural network. The error of BP neural network based dynamic model is analyzed, which shows that the feasibility of data-driven modelling method for WTGs.

Keywords DFIG WTG · Parameter identification · Power spectrum characteristics · Identifiability analysis · BP neural network

1 Introduction

China is rich in offshore wind power resources. By the end of 2021, China's cumulative installed capacity of offshore wind power was about 25GW. However, large-scale wind power grid connection brings new challenges to the safety and stability simulation analysis of power system [1–3], We need to build an accurate wind turbine model. Due to the complex operating environment of offshore wind turbines, the inconvenient detection and maintenance, and the serious lack of measurement data

X. Ding (✉) · H. Chen
College of Energy and Electrical Engineering, Hohai University, Nanjing 210098, China
e-mail: 373977391@qq.com

© Beijing Paiké Culture Commu. Co., Ltd. 2023
X. Dong et al. (eds.), *The proceedings of the 10th Frontier Academic Forum of Electrical Engineering (FAFEE2022)*, Lecture Notes in Electrical Engineering 1054, https://doi.org/10.1007/978-981-99-3408-9_82

947

under large disturbance, it is particularly important to study the modeling method based on random small disturbance response data under normal operation state.

Power system modeling includes two categories: mechanism modeling and non-mechanism modeling. At present, mechanism modeling method is often used for wind turbine model research. For example, The adaptability of the general model of wind turbines is analyzed and further studied in literature [4–6]. Literature [7] proposed a non-mechanism modeling method for wind power plants based on transfer function. Literature [8] proposed a VSC equivalent modeling method based on model and data hybrid drive, and literature [9] proposed a dynamic load modeling method based on long short-term memory neural network. However, the current data-driven wind turbine modeling research is rarely reported.

At present, status monitoring and parameter identification based on random small disturbance data under normal operation is an important means to identify whether the offshore wind turbine is in normal operation and obtain model parameters. In this paper, a data-driven offshore wind turbine dynamic modeling strategy is proposed. Firstly, according to the system response data under turbulence excitation, analyze the nonlinear mapping relationship between the response signal power spectrum and the wind turbine model parameters; further according to the historical big data, construct the BP neural network model between the wind turbine model parameters under turbulent wind speed and the rotor speed response, and finally verify the feasibility of BP neural network modeling.

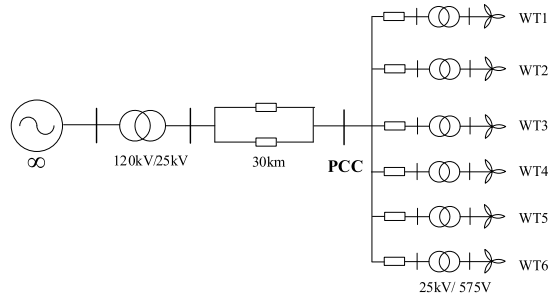
2 Mathematical Model and Its Dynamic Characteristics of Wind Turbine

2.1 *Response Characteristics of Wind Turbines Under Turbulent Wind Speed Excitation*

This paper takes the doubly-fed wind turbines in offshore wind turbines as an example to discuss the data-driven modeling method. The modeling of direct-drive wind turbines is similar, which will not be further described. The structure of the doubly-fed wind turbine connected to the infinite system is shown in Fig. 1.

The simulation system shown in Fig. 1 is set up based on the MATLAB/Simulink simulation platform. The wind farm is composed of 6 double-fed wind turbines with a rated power of 1.5 MW, with a unit network connection voltage of 575 V, boosted to 25 kV through a transformer with a capacity of 6×1.75 MVA, boosted to 120 kV by a 30 km high voltage transmission line and boost transformer, and finally connected to an infinite power supply. The wind turbine model adopts the average model (DFIG Average Model) in the Simulink simulation platform.

Fig. 1 OMIB system with DFIG interconnection



2.2 Response Characteristics of Wind Turbines Under Turbulent Wind Speed Excitation

Linearized model can be used for wind turbine under random small disturbance excitation To describe its dynamic behavior [10]. Let the linear equation be as follows:

$$\begin{cases} \Delta \dot{x} = A\Delta x + B\Delta u \\ \Delta y = C\Delta x \end{cases} \quad (1)$$

where, Δu is the input vector, corresponding to the turbulent wind speed; Δx is the state variable of the wind turbine; A, B and C are the coefficients of the model; and Δy is the output vector.

The following relationship between inputs and output exists [11]:

$$H(s) = \frac{\Delta y(s)}{\Delta u(s)} = \sum_{i=1}^n \frac{R_i}{s - \lambda_i} \quad (2)$$

where, λ is the eigenvalue of the matrix A, R_i is the constant coefficient of the corresponding characteristic root; n is the model order.

From the frequency domain perspective, its input and output satisfy the following relationships:

$$S_{YY}(\omega) = H(j\omega) \cdot S_{XX}(\omega) \cdot H(j\omega)^T \quad (3)$$

where, $S_{XX}(\omega)$ and $S_{YY}(\omega)$ represent the power spectrum of input and output signals, respectively, and T indicates conjugate transposing.

The Kaimal power spectrum simulation of turbulent wind speed was selected as the system excitation. Since the turbulent wind speed excitation belongs to small perturbation excitation, $S_{XX}(\omega)$ is a constant diagonal matrix when the turbulent wind velocity is white noise. Therefore, according to Eq. 3, when the input signal is random white noise, $S_{YY}(\omega)$ and the system parameters A, B and C have a nonlinear mapping relationship, and the system parameters themselves correspond to the model

parameters of the doubly-fed fan model. Therefore, when the output variable of wind turbine under random incentive can be measured and the data is sufficient, the neural network model of input signal and output variables can be built according to the historical data (BP network). On this basis, the intelligent identification of parameters can be further combined with the actual operation state of wind turbine.

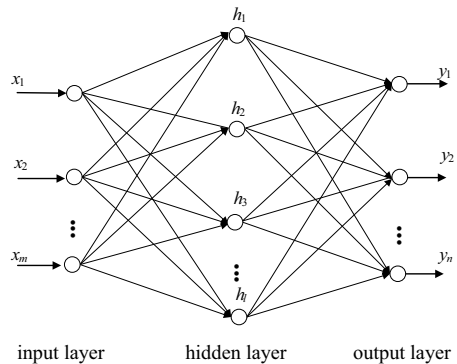
3 Data-Driven Offshore Wind Turbine Modeling Process

3.1 BP Neural Network

BP (Back Propagation) neural network is a multi-layer feedforward network trained by error back-propagation, which builds an adaptive dynamic nonlinear system by simulating a biological neural network and deals with various complex signal problems.

Generally, the BP neural network includes three layers of input layer, hidden layer and output layer. The data processing of each layer is realized through the neurons. After processing, the neurons will output the operation results to the next layer. Figure 2 shows a schematic representation of the structure of the individual neurons. The training of BP network uses the back propagation algorithm to continuously improve the weight and threshold of each layer of the network. Finally, based on the gradient descent method, the set of weights and threshold with the smallest network error are found, so as to establish the mapping relationship.

Fig. 2 Back propagation neural network



3.2 Wind Turbine Data Feature Extraction

The training data set includes wind turbine, model parameters, and the response of wind turbine under turbulent wind speed excitation under the corresponding model parameters.

Considering that the fan response signal cannot be directly used as an input to the neural network, this paper proposes to extract the features of the response signal, including the significant periods of the power spectrum of the response signal and the 6 frequency domain indicators serve as the input amount of the neural network, which can better reflect the frequency domain characteristics of the signal. The specific extraction process is as follows.

Significant Period of the Response Signal Power Spectrum

To extract the data features of the response signal, significant periods of the spectrum of the test signal power were selected. When calculating the standard spectrum size, the signal power spectrum should be compared. The white noise standard power spectrum under the threshold is calculated first, and the period when the response signal power spectrum is greater than the standard power spectrum is the significant period.

Frequency Domain Index of the Response Signal Power Spectrum

Six commonly used, frequency domain indicators are used to characterize the power spectrum of the response signal, respectively: mean frequency (AVG), Center of gravity frequency (FC), Mean-square frequency (MSF), Frequency variance (VF), Mean-square-root frequency (RMSF) and frequency standard deviation (RVF), as defined as follows:

$$\begin{cases} AVG = \int_0^{+\infty} s(f)df/f \\ FC = \int_0^{+\infty} f s(f)df / \int_0^{+\infty} s(f)df \\ MSF = \int_0^{+\infty} f^2 s(f)df / \int_0^{+\infty} s(f)df \\ VF = \int_0^{+\infty} (f - FC)^2 s(f)df / \int_0^{+\infty} s(f)df \\ RMSF = \sqrt{MSF} \\ RVF = \sqrt{VF} \end{cases} \quad (4)$$

where, f is the frequency; $s(f)$ is the power spectrum of the signal.

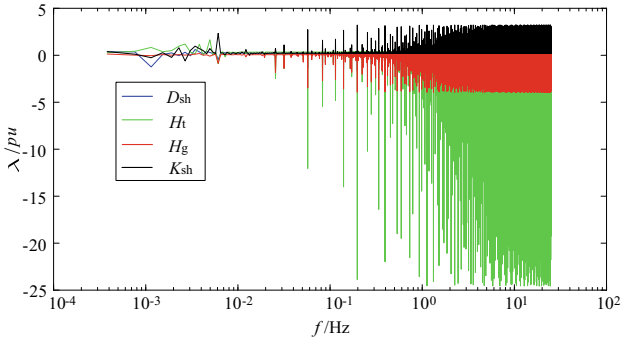


Fig. 3 PSD Sensitivity curves of parameters in drive system

4 Example and Analysis

4.1 Key Parameters of Wind Turbine

Take the system in Fig. 1 as an example, the driving system adopts a two-mass model, and the parameters to be identified are the inertia constant of the generator (T_g), the inertia time constant of the wind turbine (T_t), the stiffness coefficient of the shafting (K_{sh}) and the damping coefficient (D_{sh}).

The 5-min turbulent wind speed is taken as the input of the wind turbine, and the rotor speed response signal is obtained by simulation. The parameter value is simulated to obtain the output signal power spectrum under different parameters, and the power spectrum sensitivity of each parameter is calculated as shown in Fig. 3. It is seen that the parameter H_g and K_{sh} compared with D_{sh} more recognizable;

4.2 Neural Network Input and Output Data

Taking the system shown in Fig. 1 as an example, the rotor speed response curve is obtained by simulation, and the selected frequency is 50 Hz. The significant period test results of the rotor speed power spectrum with a significant period calculated are shown in Fig. 4. The power spectrum estimation curve beyond the standard spectrum part is the significant period region, which shows that the data period is significant around 1500.

The frequency domain index value of the rotor speed response signal power spectrum is calculated according to Eq. 4. The results are shown in Table 1.

Fig. 4 Significant periodic test chart of power spectrum of rotor speed

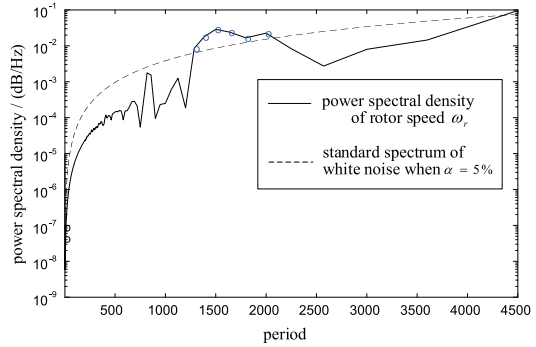


Table 1 Frequency domain indexes of rotor speed power spectrum

Metric	Value	Metric	Value
AVG	0.199	VF	40.545
FC ($\times 10^{-5}$)	1.709	RMSF	0.009
MSF ($\times 10^{-5}$)	7.889	RVF	6.367

4.3 Model Training

This paper randomly changes the parameters of the doubly fed wind turbine transmission system 2000 times and obtains the speed response power spectrum of the rotor of the doubly fed wind turbine under the corresponding parameters. The characteristic data (significant period and 6 frequency domain indicators) of the speed response power spectrum under these 2000 simulations are taken as input, and the model parameters of the corresponding doubly-fed wind turbine are taken as output, together as the modeling data set. The proportion of data for such training, validation, and testing was 70, 15, and 15%, respectively. Model structure is selected to construct a 3-layer BP neural network, in which, the number of hidden layer neurons is 50. The training parameters are set as: the minimum error is 0.05, the training times are 400 times, the learning efficiency is 0.02, the display frequency is 25, that is, the training is 25 times displayed once, and the minimum performance gradient is the default value of 10^{-6} , The maximum number of confirmation failures is 6. Figure 5 shows the performance evaluation indexes of the BP neural network. In addition, the mean-squared error of the parameter prediction is defined as:

$$MSE = \sum_{j=1}^n \left(\frac{\hat{\theta}_j - \theta_j}{\theta_j} \right)^2 / n_s \tag{5}$$

where, θ is the true value, $\hat{\theta}$ is the predicted value, n_s is the number of samples.

Figure 5 shows the performance diagram of BP neural network, including training, verification, testing and synthesis set. The abscissa is the target value, and the ordinate

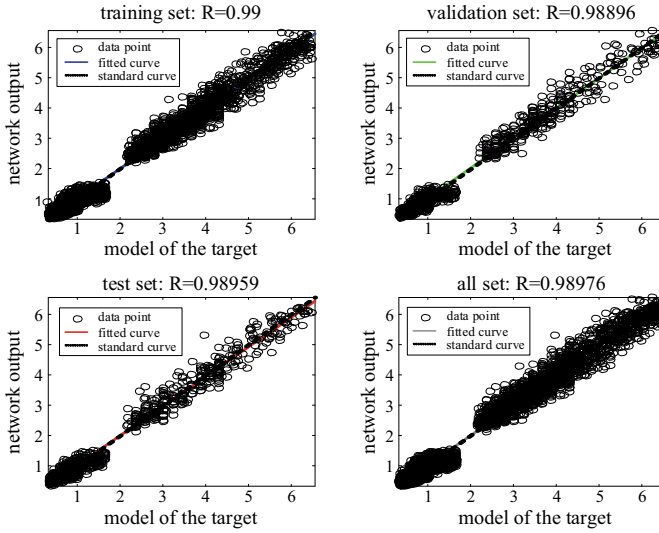


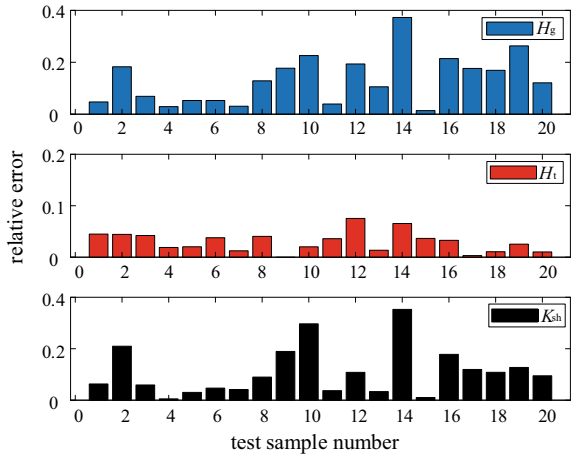
Fig. 5 Performance evaluation of BP neural network

is the predicted value of the neural network. As can be seen in the figure: the closer the data point is to the diagonal, that is, the closer the R is to 1, the better the fit of the neural network is. The training results all have R values of 0.98+, indicating that the neural network has a good fit.

4.4 Precision Analysis

In order to analyze the modeling accuracy of the BP neural network, the parameters of the doubly-fed wind turbine transmission system were randomly changed 20 times as the test sample sequence. Ten simulations and the BP neural network parameters were predicted for each set of parameter values, and the obtained results were averaged with a further small prediction error. Parameter prediction is carried out based on trained BP neural network and the relative error of the 20 sets of predicted results with the true values about 3 parameters H_g , H_t and K_{sh} is shown in Fig. 6. According to Eq. 5, the mean square error MSE of the 3 parameters is 0.02629, 0.00125 and 0.02052, respectively, which shows that the prediction result of BP neural network is close to the actual value, which shows the feasibility of the proposed method.

Fig. 6 Relative error of parameter prediction based on BP neural network



5 Conclusion

In view of the problems of difficult operation and maintenance and testing of offshore wind turbines, this paper puts forward the strategy of using the artificial intelligence method for data modeling based on the small disturbance response data under the turbulent wind speed excitation.

The paper firstly analyzes the dynamic characteristics of wind power system under small disturbance, and analyzes the feasibility of data modeling of wind turbine response data based on the relationship of output response characteristics and unit dynamics. At the same time, the frequency sensitivity method is proposed to study the key parameters of wind turbine, pointing out that the greater the sensitivity, the easier to identify the parameters. Results were found for the parameter H_t , the largest frequency sensitivity, so the parameter is easier to identify.

According to the response signal and the power spectrum, the significance period of the power spectrum and the six frequency domain statistical indicators are proposed as the input of the neural network, and the key parameters are taken as the output. The historical dataset is divided into the training set, the validation set and the test set in some proportion, and the BP neural network is trained, and the final model is obtained according to the convergence rules. Based on the test samples, the data were parameter identified, and finally the parameter identification error was analyzed to verify the feasibility of the proposed method.

Acknowledgements Project supported by the National Natural Science Foundation of China (No. 52077061).

References

1. Chi, Y., Tang, B., Hu, J.: Overview of mechanism and mitigation measures on multi-frequency oscillation caused by large-scale integration of wind power. *CSEE J. Power Energy Syst.* **5**(4), 433–443 (2019)
2. Qiu, J., Lin, S.: Analysis on the development status of offshore wind power and the impact of large-scale access on power grid. *Electrotech. Electr.* **12**, 74–76 (2019). (in Chinese)
3. Chi, Y., Liang, W., Zhang, Z., et al.: An overview on key technologies regarding power transmission and grid integration of large scale offshore wind power. *Proc. Chin. Soc. Electr. Eng.* **36**(14), 3758–3771 (2016). (in Chinese)
4. Chen, W., Wang, L., Tan, L., et al.: Recent progress of developing WECC generic models of wind turbine generators/plants for dynamic simulation. *Proc. CSEE* **37**(3), 738–750 (2017). (in Chinese)
5. Zhang, L., Zhu, L., Chen, N., et al.: Review on generic model for wind power generation. *Autom. Electr. Power Syst.* **40**(12), 207–215 (2016). (in Chinese)
6. Zi, P., Zhou, X., Tian, F., et al.: Electromechanical Transient modeling of wind turbines based on doubly-fed induction generator. *Proc. CSEE* **35**(5), 1106–1114 (2015). (in Chinese)
7. Wu, F., Qian, J., Ju, P.: Transfer function based equivalent modeling method for wind farm. *J. Mod. Power Syst. Clean Energy* **7**(3), 549–557 (2019). (in Chinese)
8. Chen, J., Wang, H.: A model-data hybrid driven method of VSC equivalent modeling of a permanent magnetic synchronous generator. *Power Syst. Prot. Control* **49**(2), 10–17 (2021). (in Chinese)
9. Chao, Z., Wang, S., Liu, Y., et al.: A novel equivalent model of active distribution networks based on LSTM. *IEEE Trans. Neural Netw. Learn. Syst.* **30**(9), 2611–2624 (2019)
10. Pan, X., Ju, P., Wu, F., et al.: Parameter estimation of drive system in a fixed-speed wind turbine by utilising turbulence excitations. *IET Gener. Transm. Distrib.* **7**(7), 665–673 (2013)
11. Liu, G., Venkatasubramanian, V.: Oscillation monitoring from ambient PMU measurements by frequency domain decomposition. In: *International Symposium on Circuits and Systems*, Seattle, pp. 2821–2824. IEEE (2008)

Electric Bicycle Charging Load Identification Technology Based on Non-intrusive Load Monitoring



Ke Wu, Gan Zhou, and Feifei Zhu

Abstract In recent years, fire accidents caused by illegal charging of electric bicycles have occurred frequently. According to reports, about 80% of the fires caused by electric bicycles occur during the charging process. For this reason, the property and fire departments often need to manually detect the illegal charging behavior of users on the spot, but there are problems such as low efficiency and low user cooperation. Therefore, the application of NILM technology to the efficient detection of illegal charging of electric bicycles has great practical feasibility. In order to identify whether there is illegal charging of electric bicycles, This paper proposes a charging load identification technology for electric bicycles based on non-intrusive load monitoring. For transient and steady state characteristics, the method of event detection, time-sharing algorithm and dual-state tracking and confirmation of charging start and stop is used to improve the identification accuracy. In the experiments conducted in real user scenarios, the identification accuracy exceeds 91.2%. The method has high identification accuracy and certain rapidity.

Keywords Non-intrusive load monitoring · Electric bicycle load · Event detection · Feature extraction

1 Introduction

The number of electric bicycles in China exceeds 300 million, and the problem of fire accidents caused by charging electric bicycles at home has become increasingly prominent [1]. Although the government departments have issued regulations prohibiting electric bicycles from charging at home, there are still some e-bikes owners who are lucky enough to charge by pushing carts into the home or carrying

K. Wu (✉) · G. Zhou
School of Electrical Engineering, Southeast University, Nanjing 210096, China
e-mail: 642583295@qq.com

F. Zhu
College of Engineering and Applied Sciences, Nanjing University, Nanjing 210096, China

© Beijing Paiké Culture Commu. Co., Ltd. 2023
X. Dong et al. (eds.), *The proceedings of the 10th Frontier Academic Forum of Electrical Engineering (FAFEE2022)*, Lecture Notes in Electrical Engineering 1054, https://doi.org/10.1007/978-981-99-3408-9_83

batteries into the house. It is impossible to find out in time by the traditional method of property personnel inspection, and there are potential safety hazards.

At present, the feature extraction of non-intrusive load monitoring mainly focuses on two aspects: physical feature extraction and space-time feature extraction [2].

Chang et al. used learning vector quantization and back propagation to select features. In Chang et al.'s work, equipment power was used as a label, in which no noise was added. Five different types of equipment are turned on and off in a random mode to simulate an example close to the real world to realize load identification [3].

Man and others are the first researchers to study industrial and commercial load identification. In their work, they studied the use of different harmonics to determine the variable speed drive. With a sampling rate of 8 MHz, they calculated the phase-locked short-time Fourier transform of the current waveform. They use the fifth and seventh harmonics to identify variable speed drives. In order to optimize the decomposition results, they removed the harmonics from the rest of the signal to identify the industrial and commercial load [4].

Batra et al. focus on the difference between load identification in residential and commercial environments. In the work of Batra et al., they used NILMTK for energy decomposition in a university campus in Delhi, India. The collected data has been downsampled to 601 Hz. For a university campus with a large amount of energy consumption, there may be a variety of devices to change the power state, which violates the normal assumption of NILM. The type of load consists of variable speed drives, not steady state loads. The temporal dependence in commercial buildings is quite different from that in residential buildings. Multiple devices can be started at the same time with source dependency, which violates the assumption once. In this work, they found it difficult to classify elevators because it depends on the number of people and the number of floors of elevators. Batra et al. have shown how difficult it is to use NILM in commercial buildings due to multiple power changes at the same time. They pointed out that using EMI method can provide better results, but it requires using a higher sampling rate to collect data [5].

For the research of load clustering algorithm, Jungsuk Kwac and others put forward an adaptive K-means algorithm, and realized the clustering analysis of user load [6]. Mutan et al. put forward a new clustering method, which uses iterative self-organizing data-analysis technique algorithm I (SODATA) to cluster, and considers the influence of seasonal temperature difference on load change [7]. Luan proposed a self-adapting a two-stage event detection method [8]. Existing methods for identifying continuously variable loads require large training datasets [9].

2 Identification Method of Charging Load of Non-intrusive Electric Bicycle

2.1 Overview of Methods

The load identification technology of e-bike based on non-intrusive method mainly includes capturing the suspected charging state of e-bike based on frequency spectrum characteristics and tracking the confirmed charging state of e-bike based on the whole charging process. Firstly, the users who meet the charging characteristics of electric bicycles are monitored in real time, and the incoming current and voltage data of customers are read. Through fuzzy matching, when the frequency spectrum characteristics of the electric bicycle are consistent with the charging process, the electric bicycle is identified as a ‘suspected charging’ electric bicycle. Track users who have ‘suspected charging’ behavior for a long time to determine whether there are false positives in the ‘suspected charging’ status, and improve the identification accuracy.

2.2 Analysis of Charging Principle and Feature Selection of Electric Bicycle

The essence of electric bicycle charger is a single-phase AC/DC power supply with the ability to control voltage and current output [10]. Its basic circuit schematic diagram is shown in Fig. 1.

Electric bicycle charging is mainly divided into three stages: ‘constant current-constant voltage-trickle’, as shown in Fig. 2, and its main working features are:

1. Constant current stage: the charging active and reactive power are high, the output is stable, the waveform distortion is serious, and it contains large harmonic components, the voltage gradually rises from the switching-in moment, and the current basically remains unchanged.

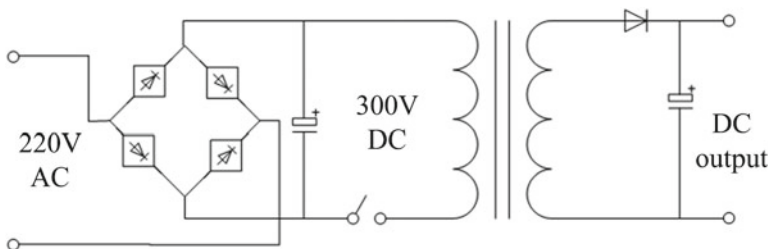


Fig. 1 The schematic diagram of the electric bicycle charging circuit

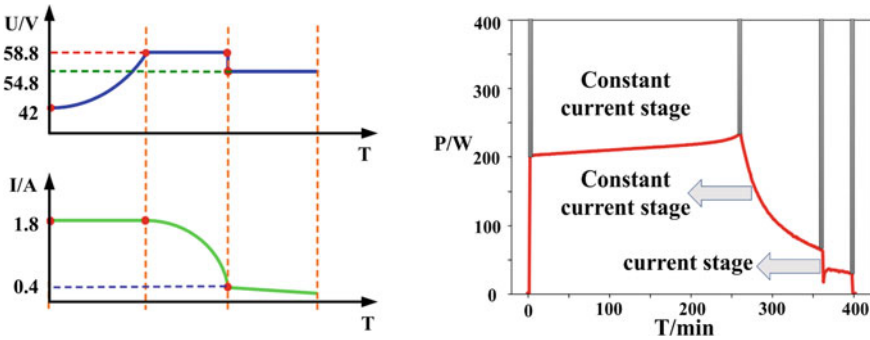


Fig. 2 Electric bicycle charging process

2. Constant voltage stage: charging active and reactive power gradually attenuates with time, and the waveform distortion is serious, but the degree of distortion will change with time, the voltage is constant and the current gradually decreases, the constant current and constant voltage stages last for about 8–10 h [11].
3. Trickle stage: The active and reactive power of charging are very small, only about 20 W and 10 Var, the voltage drops slightly, and the current drops slowly, lasting about 3 h.

There are rectification and chopping links in the circuit schematic diagram of e-bikes charger, and a large number of odd harmonics exist in its output current.

Select a brand of electric bicycle to carry out current harmonic analysis, the electric bicycle charging current is a stable sharp angle wave with obvious characteristics. By using the fast Fourier decomposition algorithm, the harmonic ratio can be obtained as shown in Fig. 3.

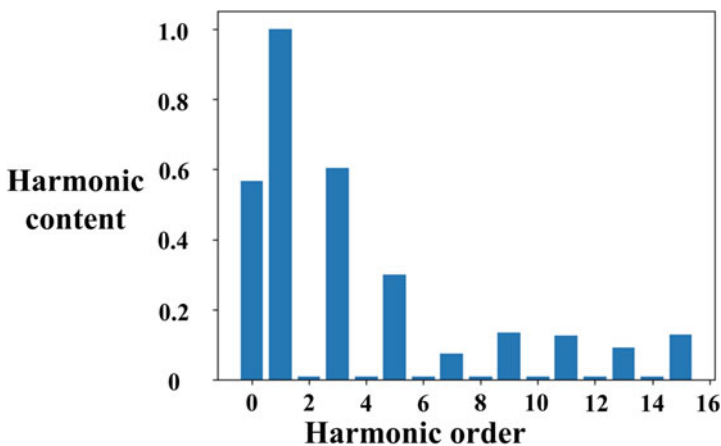


Fig. 3 The proportion of harmonics of each order of a certain brand of electric bicycles

The above measured results are consistent with theoretical analysis, that is, the DC component and odd component are high, and the third and fifth harmonics can account for 60% and 25% respectively. Therefore, the active and reactive power of DC component combined with the third and fifth harmonics is a typical characteristic parameter for charging identification of electric bicycles.

2.3 Grab the Charging Status of Electric Bicycles Based on Spectrum Characteristics

The flow chart of electric bicycle charging state capture based on spectrum characteristics is shown in Fig. 5, and the specific steps are as follows:

The data of electric bicycle is collected, and the charging current, voltage, active power, reactive power and other data of electric bicycle are obtained through the wave recording device. For N electric bicycle data samples, the variance and mean of steady-state active power increment are calculated.

$$\mu = \frac{\sum_{i=1}^N \Delta P_i}{N} \tag{1}$$

$$\sigma^2 = \frac{\sum_{i=1}^N (\Delta P_i - \mu)^2}{N} \tag{2}$$

Define the power threshold P_{Th} And variance σ , average value μ . The relation function of is:

$$P_{Th} = f(\mu, \sigma) = \ln \sigma \cdot \mu + C \tag{3}$$

where C is a constant, which is determined by the power fluctuation value of other electrical appliances in steady state. The threshold value is modified to improve the identification rate of electric bicycles when multiple electrical appliances are superimposed. In the actual scene, the threshold of active power takes the upper limit of 400 W and the lower limit of 50 W.

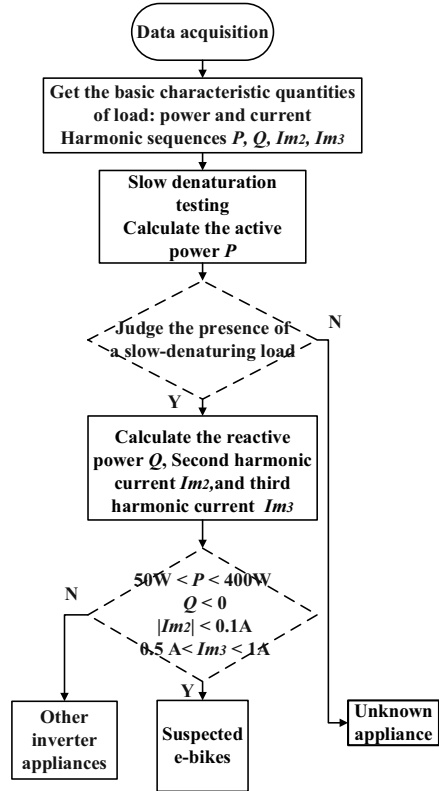
Because the collected current is a discrete value, fast Fourier transform is used to calculate the charging current. The amplitude of each current component can be obtained by FFT analysis.

$$F_i = f_{FFT}(i) \tag{4}$$

$$f_i(k) = (k - 1) f_s / N_s \tag{5}$$

$$I_k = \left(\frac{50kN_s}{f_s} + 1 \right) \cdot F_i \tag{6}$$

Fig. 4 Flow chart of electric bicycle charging state capture based on spectral features



where f_{FFT} Calculate the function for FFT, i is current sequence for FFT transformation, F_i is the length after transformation. N_s is the amplitude sequence, f_s is the sampling frequency, $f_i(k)$ is the actual frequency sequence.

2.4 Tracking the ‘Confirmed Charging’ Status of Electric Bicycle Based on the Whole Charging Process

After capturing the charging state of the electric bicycle based on the spectrum characteristics, the identification judgment result is tracked and identified in the cloud. The flow chart is shown in Fig. 4, and the specific steps are as follows:

- Step1.** Start the tail tracking process after receiving the information of charging on the e-bikes.
- Step2.** After charging starts by default, it is a steady charging period. Start to determine the charging stage, with 5 min as a window.

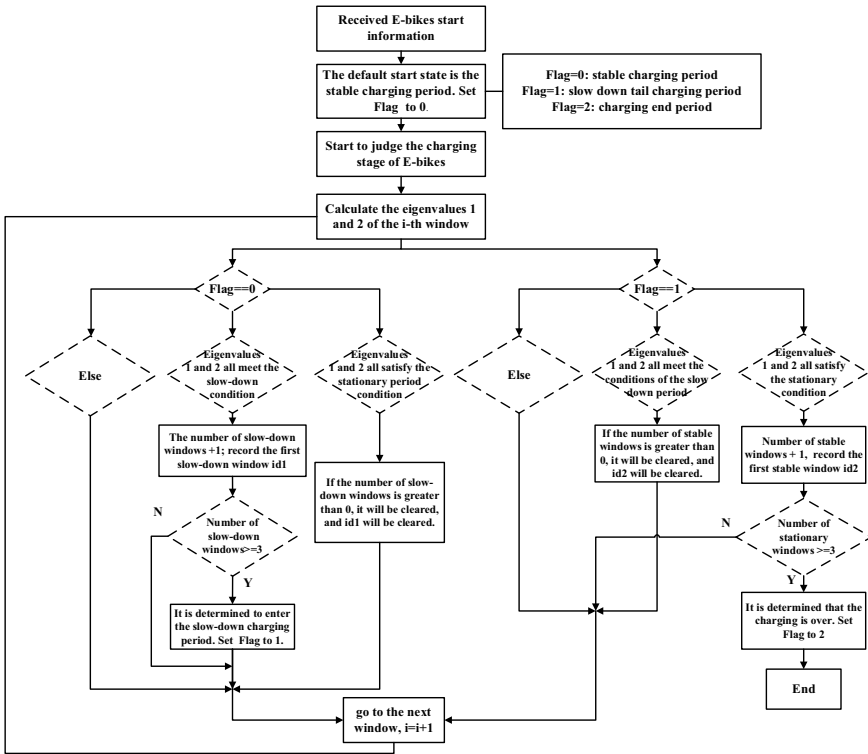


Fig. 5 Tracking the ‘confirmed charging’ status of electric bicycles based on the entire charging process

Step3. In the steady charging period, if the accumulated three windows meet the slow-down condition, it is judged that the slow-down period is entered, and if a slow-down window appears before the accumulated three windows, the number of slow-down windows is cleared;

Step4. Entering the charging slow-down period, if the accumulated three windows meet the gentle conditions, it is judged that the charging end period is entered, and if there is a slow-down window before the accumulated three stable windows, the number of gentle windows is cleared;

Step5. After entering the charging end period, consider this charging end, and end the tail tracking process.

3 Experimental Analysis

In order to verify the accuracy of the algorithm, five different brands with high market share were selected, and each brand had two different battery capacities, and a total of 10 electric bicycles were used as samples for the experimental test.

Select 10 electric bicycles with battery gears of high, medium and low power respectively (high power: 75–100%, medium power: 25–75%, low power: 0–25%), and conduct repeated tests of electric bicycle charging identification under single working condition (Table 1).

According to the experimental results, it can be seen that:

1. The identification result is related to the battery power state. Therefore, the missing report of electric vehicle charging load identification is mainly when the battery is charged with high power. The analysis reason is that the battery is close to full power, in trickle charging, and there is no state switching during charging, so the missing report occurs. When the battery is charged with medium or low power, the reporting accuracy rate is 100%.
2. The identification result has no obvious relationship with the brand, battery capacity and battery type of electric bicycle. The test covers different brands and models of electric bicycles, and the battery types cover lithium batteries and lead-acid batteries with different capacities. The identification results have no obvious relationship with the above factors.
3. ‘Suspected charging’ is reported in real time, and the average reporting time of ‘confirmed charging’ is 61.8 min, but the accuracy rate is higher than that of ‘suspected charging’. According to the spectrum characteristics, the algorithm captures the real-time report of ‘suspected charging’ electric bicycle, and switches and refreshes the tracking charging state to ‘confirmed charging’ to improve the accuracy. The accuracy rate is high, but it takes a certain time, and there will be a false report when the battery is high.

Table 1 Electric bicycle charging identification test results

Battery level	Accuracy of reporting suspected charging (real-time) (%)	Accuracy of reporting confirmed charging (%)	Average reporting time/min
High	99.0	93.0	42.8
Medium	100	100	62.9
Low	100	100	75.6

4 Conclusion

The potential safety hazards caused by illegal charging of electric bicycles have attracted more and more attention from the society. In this paper, the charging load identification methods of non-intrusive electric bicycles are studied, and a non-intrusive online charging load identification method based on spectrum characteristics at the edge and a ‘confirmed charging’ state identification method based on tracking the whole charging process in the cloud are proposed. Five different brands with high market share are selected for experimental tests. The experimental results show that this method has high identification accuracy and certain rapidity, and has a broad application prospect in the fields of illegal charging inspection of electric bicycles.

References

1. Wang, T.: Electric bicycle fire cause analysis and 7 key points of fire investigation technology. *Fire Prot. Today* **4**(11), 32–33 (2019). (in Chinese)
2. Yu, X.: Smart grids: a cyber–physical systems perspective. *Proc. IEEE* **104**(5), 1058–1070 (2016)
3. Chang, H.H., Yang, H.T.: Load identification in neural networks for a non-intrusive monitoring of industrial electrical loads. In: *International Conference on Computer Supported Cooperative Work in Design*, pp. 664–674. Springer, Heidelberg (2007)
4. Laughman, C.: Power signature analysis. *IEEE Power Energy. Mag.* **1**(2), 56–63 (2003)
5. Batra, N., Kelly, J.: NILMTK: an open source toolkit for non-intrusive load monitoring. In: *5th International Conference on Future Energy Systems*, pp. 265–276 (2014)
6. Kwac, J.: Household energy consumption segmentation using hourly data. *IEEE Trans. Smart Grid* **5**(1), 420–430 (2014)
7. Mutanen, A.: Customer classification and load profiling method for distribution systems. *IEEE Trans. Power Deliv.* **26**(3), 1755–1763 (2011)
8. Luan, W.: An adaptive two-stage load event detection method for nonintrusive load monitoring. *IEEE Trans. Instrum. Meas.* **71**, 1–14 (2021)
9. Reinhardt, A., Bouchur, M.: On the impact of the sequence length on sequence-to-sequence and sequence-to-point learning for NILM. In: *5th International Workshop on Non-Intrusive Load Monitoring*, pp. 75–78 (2020)
10. Shi, Y.: Non-intrusive charging identification method for electric bicycles based on feature selection and incremental learning. *Autom. Electr. Power Syst.* **45**(7), 87–94 (2021). (in Chinese)
11. Wang, L.: Refined analysis of user behaviour based on non-intrusive load monitoring. *Proc. CSU-EPSA* **33**(4), 102–107 (2021). (in Chinese)

An Approach to Approximate Evaluation of Shielding Effectiveness of Double-Cavity Structure with an Aperture Array Using BLT Equation



Xin Zhang, Zhangpeng Zhou, Zonglin Wang, Hai Jin, and Kejian Chen

Abstract A shielding cavity can effectively avoid the influence of electromagnetic interference (EMI) on intelligent weak current equipment. In actual engineering, taking into account ventilation and heat dissipation, the shielding cavity usually has multiple apertures. By the characteristics of the double cavity structure with an aperture array, this paper presents an effective shielding effectiveness estimation approach. From the equivalent circuit of the model, a signal flow diagram based on the electromagnetic topology theory is established. The BLT (Baum-Liu-Tesche) equation is then obtained from the signal flow diagram. The computational model of the shielding effect of the plane-wave double-cavity structure under external radiation is deduced. To verify the accuracy of the analytical model, the computational results are compared with the previously published hybrid analytical model and CST numerical simulations, and all three methods are in good agreement. The approach can be used by researchers to estimate shielding effectiveness when designing cavity structures.

Keywords Double-cavity structure · Shielding effectiveness · BLT equation

1 Introduction

Electronic devices, such as breakers and isolator switches in power systems, often need to consider heat dissipation, external power supply, data transmission, and other factors. In consequence, the shielding cavity has a complex opening structure, which

X. Zhang · Z. Zhou · Z. Wang

Gansu Electric Power Extra High Voltage Company of State Grid, Lanzhou 730050, China

H. Jin (✉) · K. Chen

College of Electric Engineering and Information Engineering, Lanzhou University of Technology, Lanzhou 730050, China

e-mail: jinhai@lut.edu.cn

© Beijing Paiké Culture Commu. Co., Ltd. 2023

X. Dong et al. (eds.), *The proceedings of the 10th Frontier Academic Forum of Electrical Engineering (FAFEE2022)*, Lecture Notes in Electrical Engineering 1054, https://doi.org/10.1007/978-981-99-3408-9_84

967

reduces the shielding efficiency. At the same time also greatly increases the difficulty of shielding efficiency analysis [1, 2]. To quantify the shielding effect of shielding measures, shielding effectiveness (SE) has been defined internationally as an important indicator to evaluate shielding measures' electromagnetic interference (EMI) protection capability. In reality, the structure of the shielding cavity is not limited to a single open cavity, but more of a dual-cavity structure with an array of apertures and a multi-cavity structure. The shielding effectiveness of shielding cavities can be measured experimentally, but the experiments often require shielding chambers, microwave darkrooms, and other experimental sites with expensive instruments and equipment, which are costly and less reproducible [3–5]. Therefore, it is of great theoretical and engineering importance to study the efficient calculation method of shielding effectiveness of shielding cavity.

The methods of estimating the SE of the shielding cavity consist of numerical simulation and analytical methods. Although numerical methods allow accurate modeling of complex models, they consume a large amount of computer memory and processor computation time, especially when the computational results are accurate, and often require re-modeling when changing the model parameters. For instance, numerical computational methods such as the method of moments (MoM) based on Maxwell's equations [6], Mesh-Free method [7], finite-difference time-domain (FDTD) method [8], transmission-line matrix method [9] are subject to these problems. In contrast to numerical simulation methods, the key of analytical calculations is to establish the mathematical expression of the model, which usually requires reasonable simplifications and assumptions about the problem to obtain approximate results.

Compared with numerical simulation, the analytical calculation method is faster, takes fewer resources, and has a clear physical meaning, which is more suitable for the regular study of important parameters that affect the calculation results. Analytical methods are limited to simple structures, but a reasonable analytical computational approach can still lead to desirable results. The equivalent circuit model based on waveguide and transmission line theory was first proposed by Robinson et al. [10]. In this model, the front panel of a metal shielded cavity with a rectangular opening is equated to a coplanar transmission line shorted at both ends. The rest of the rectangular metal shielded cavity is considered as a waveguide shorted at the ends except for one surface containing the openings. Since then, a series of extended equivalent circuit methods have been proposed based on Robinson's analytical model. J. R. Solinc et al. derived the shielding effectiveness formula from the electromagnetic field perspective based on the Bethe small-aperture coupling theory, but the solution process is complicated [11]. F.A. Pod et al. derived the cavity and opening based on the continuity of the electric field at the opening coupling coefficient, corrected the impedance at the opening and calculated the lateral migration of the opening toward the center of the cavity surface [12]. Based on the electromagnetic topology theory and BLT equation, the shielding efficiency of a rectangular cavity with an inner dielectric plate irradiated by plane waves was investigated in reference [13], and the effects of the thickness, material, and location of the dielectric plate on the shielding effect were analyzed in detail, but only a single cavity with rectangular

aperture was calculated. A hybrid analytical model has been proposed to estimate the shielding effectiveness of a two-cavity structure with an array of apertures [14], but its computational accuracy is not sufficient. Reference [15] further extended the hybrid analytical model by considering a central aperture array, an eccentric aperture array, a higher-order mode, and a multi-cavity structure, respectively.

The purpose of this paper is to obtain a new and accurate analytical method to estimate the shielding effect based on the BLT equation, following the previously published hybrid analytical model [14]. It is found to be in good agreement with the hybrid analytical model and the CST numerical simulation. Moreover, the accuracy of this paper in the TE₁₀ model is higher than that of the reference [14]. Compared with the CST numerical method, the present analytical model not only occupies less memory but also has high computational efficiency, which can provide an accurate and fast estimation method for engineers and technicians to study such problems.

2 Theoretical Analysis

2.1 The Equivalent Circuit Model

The computational model and equivalent circuit in this study are shown in Fig. 1. It is assumed that the cavity size with wall thickness t is $a \times b \times c$, the aperture array size is $l \times w$, the number of apertures in length and height are M and N , d is the aperture diameter, d_v and d_h are the distance between vertical and horizontal apertures respectively. P_0 represents the external monitor point and the inner monitor point is P , which is located in the center of the model.

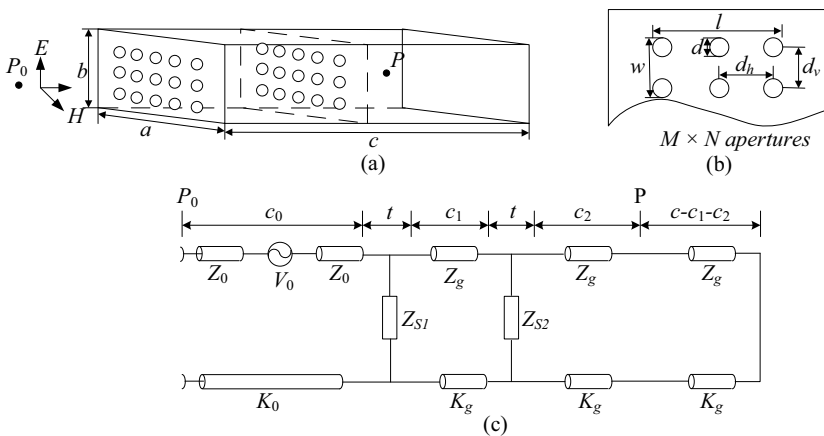


Fig. 1 Dual-cavity structure (a) calculation model; (b) aperture array diagram; (c) equivalent circuit diagram

As shown in Fig. 1 (c), the voltage source V_0 represents the incident electromagnetic wave, whose wave impedance and spread constant in free-space are Z_0 and K_0 , respectively. P_0 and P are the observation points of external and inner with the cavity respectively. The distance from external monitor point P_0 to the front wall of the outer cavity is c_0 . c_1 is the length of the external cavity, and the distance between the internal observation point P and the anterior wall of the internal cavity is c_2 . The distance from P to the end of the cavity is $c - c_1 - c_2$. For TE_{mn} mode, the characteristic impedance and spread constant of the waveguide are $Z_{gmn} = Z_0/\sqrt{1 - (m\lambda/2a)^2 - (n\lambda/2b)^2}$, $K_{gmn} = K_0/\sqrt{1 - (m\lambda/2a)^2 - (n\lambda/2b)^2}$, respectively. Here, only TE_{10} is taken into consideration for simplification.

For a vertically incident plane wave, the small aperture in the infinitely thin metal plate corresponds to an inductive receptor parallel to the transmission line of the TEM mode. Supposing that without resistive losses and $d < d_h$, $d < d_v$, $d_h \ll \lambda$, $d_v \ll \lambda$, the normalized parallel admittance of the structure shown in Fig. 1 (b) is [14]:

$$\frac{Y_{ap}}{Y_0} = -j \frac{3d_v d_h \lambda_0}{\pi d^3} + j \frac{288}{\pi \lambda_0 d^2} \left[\sum_{m=0}^{\infty} \sum_{n=0}^{\infty} \left(\frac{\epsilon_n^2}{d_v^2} + \frac{\epsilon_n m^2}{d_h^2} \right) J_1^2(x) \right] \tag{1}$$

Thus, the impedance of an aperture array in an infinitely thin metal plate can be represented by $Z_{ap} = 1/Y_{ap}$. As illustrated in Fig. 1 (b), the impedance of the aperture array in a finite cavity is:

$$Z_s = Z_{ap} \frac{l \times w}{a \times b} \tag{2}$$

Therefore, the impedance of the external and inner aperture array can be obtained respectively:

$$Z_{s1} = Z_{ap} \frac{l_1 \times w_1}{a \times b} \tag{3}$$

$$Z_{s2} = Z_{ap} \frac{l_2 \times w_2}{a \times b} \tag{4}$$

2.2 Calculation Method of Shielding Effectiveness

The signal flow graph of Fig. 1(c) is given in Fig. 2. The node J_1 is an external monitor point of the cavity and the W_s is the plane wave. The nodes J_2 and J_3 represent the plane of the outer and the inner aperture array respectively. The node J_4 is an internal observation point, and the node J_5 is the end of the cavity. The signal flow graph consists of four transmission tubes ($T_1 \dots T_4$), where tube T_1 is the propagation of

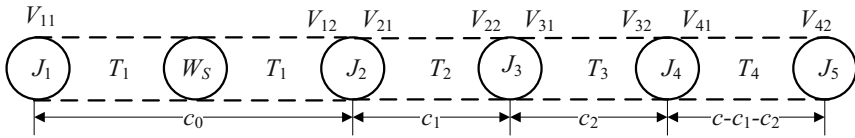


Fig. 2 The signal flow graph

the wave in free-space, $T_2 \dots T_4$ are wave propagation in rectangular waveguide. V_{j1} and V_{j2} are the voltage at both ends of the tube.

The BLT equation corresponding to the voltage of each node can be obtained from Fig. 2:

$$V = (U + \rho)(\Gamma - \rho)^{-1}S \tag{5}$$

In Eq. (5), U is a unit matrix of 8×8 ; V and S are the voltage vector and excitation source vector arranged by the order of nodes; ρ and Γ represent the scattering matrix and the propagation matrix arranged by order of node and order of tube, respectively.

The voltage vector V can be expressed by the order of nodes:

$$V[V_{11} \ V_{12} \ V_{21} \ V_{22} \ V_{31} \ V_{32} \ V_{41} \ V_{42}]^T \tag{6}$$

The excitation vector S can be expressed by the order of nodes:

$$S[V_0 \ 0 \ 0 \ 0 \ 0 \ 0 \ 0 \ 0]^T \tag{7}$$

where, V_0 is the source signal generated by W_s in T_1 , $V_0 = I$.

The scattering matrix ρ is expressed as:

$$\rho = \text{diag}(\rho_1, \rho_2, \rho_3, \rho_4, \rho_5) \tag{8}$$

where the reflection coefficients of the J_1 and J_5 are expressed as $\rho_1 = 0$ and $\rho_5 = -1$, respectively. The scattering matrix of the node J_i ($i = 2, \dots, 4$) is:

$$\left\{ \begin{array}{l} \rho_2 = \begin{bmatrix} \frac{Y_0 - Y_g - Y_{ZS1}}{Y_0 + Y_g + Y_{ZS1}} & \frac{2Y_g}{Y_0 + Y_g + Y_{ZS1}} \\ \frac{2Y_0}{Y_0 + Y_g + Y_{ZS1}} & \frac{Y_g - Y_0 - Y_{ZS1}}{Y_0 + Y_g + Y_{ZS1}} \end{bmatrix} \\ \rho_3 = \begin{bmatrix} \frac{-Z_{S2}}{2Y_g + Y_{ZS2}} & \frac{2Y_g}{2Y_g + Y_{ZS2}} \\ \frac{2Y_g}{2Y_g + Y_{ZS2}} & \frac{-Z_{S2}}{2Y_g + Y_{ZS2}} \end{bmatrix} \\ \rho_4 = \begin{bmatrix} 0 & 1 \\ 1 & 0 \end{bmatrix} \end{array} \right.$$

where Y_0 and Y_g are the admittance of free-space and air waveguide, while Y_{zs1} and Y_{zs2} are the admittance of outer cavity and inner cavity aperture array respectively.

The propagation matrix Γ is expressed as:

$$\Gamma = \text{diag}(\Gamma_1, \Gamma_2, \Gamma_3, \Gamma_4) \tag{9}$$

where the propagation matrices of the four sections of the channel are as follows:

$$\left\{ \begin{array}{l} \Gamma_1 = \begin{bmatrix} 0 & e^{jK_0 c_0} \\ e^{jK_0 c_0} & 0 \end{bmatrix} \\ \Gamma_2 = \begin{bmatrix} 0 & e^{jK_g c_1} \\ e^{jK_g c_1} & 0 \end{bmatrix} \\ \Gamma_3 = \begin{bmatrix} 0 & e^{jK_g c_2} \\ e^{jK_g c_2} & 0 \end{bmatrix} \\ \Gamma_4 = \begin{bmatrix} 0 & e^{jK_g(c-c_1-c_2)} \\ e^{jK_g(c-c_1-c_2)} & 0 \end{bmatrix} \end{array} \right.$$

By substituting Eqs. (6) and (9) into Eq. (5), the voltage of each node will be solved, where the voltage of J_4 (observation point P) can be expressed as:

$$V_P = V_{32} + V_{41} \tag{10}$$

When there is no shielding cavity, the voltage at point P is $V_{P0} = V_0/2$, so the electric shielding effectiveness of point P can be obtained as:

$$SE_e = -20 \lg \left| \frac{V_P}{V_{P0}} \right| = -20 \lg \left| \frac{2V_P}{V_0} \right| \tag{11}$$

3 Model Validation and Discussion

In the calculation, the external dimension size of the shielding cavity is 300 mm × 120 mm × 100 mm, the internal dimension size is 300 mm × 120 mm × 200 mm, and the wall thickness $t = 1$ mm. Other specific parameters are given in Table 1. To verify the effectiveness of the analytical model established in this paper, four sets of cases are provided to calculate the electric SE of the model. The monitor point P is located in the center of the established model. The frequency range of simulation is 0–1.6 GHz for most scenarios.

In Fig. 3 (a), the BLT algorithm in this paper, the hybrid algorithm in reference [14] and the CST were respectively used to calculate the electric shielding efficiency of the model parameters provided by case 1. In this case, the number of aperture arrays in both the inner and outer cavities is 5×3 . The monitor point is located in the center plane of the dual-cavity structure. As can be seen from Fig. 3 (a), the calculation results of the three methods are consistent in the range of frequency domain under consideration, while the accuracy of the BLT algorithm of this article is higher than that of reference [14] in the frequency range below 1 GHz, which because of the reflected electromagnetic energy is in account. In fact, when the propagation of electromagnetic waves encounters obstacles, a part of electromagnetic energy is reflected, which cannot be calculated by the method of reference [14]. When BLT algorithm is used to calculate the SE of cavity, the propagation constant can well reflect the propagation of electromagnetic wave in the cavity, resulting in high accuracy of SE. By comparing these three methods, the correctness of the BLT algorithm in this paper can be proved. Therefore, the BLT algorithm proposed can effectively estimate the SE of the porous dual-cavity model, where the TE_{10} mode is dominant.

Compared with case 1, case 2 and case 3 changed the diameter of the apertures and the number of apertures in the outer cavity respectively. The calculated results are shown in Fig. 3 (b) and Fig. 3 (c). It is obvious that SE increases and decreases respectively, but their resonance points do not shift. Therefore, it indicates that the cavity resonant frequency cannot be changed by the change of the diameter and number of apertures without changing the dimension size of the cavity. The calculation results in Fig. 3 (d) clearly show that the resonant frequency has changed, and the main reason is that the dimension size of the outer cavity has been increased in case 4. Meanwhile, the SE is about 10 dB higher than that of

Table 1 Parameters for the validity of the analytical model

Cases	c_1 (mm)	c_2 (mm)	M_1	N_1	M_2	N_2	d (mm)	d_v (mm)	d_h (mm)
1	100	50	5	3	5	3	10	20	20
2	100	50	5	3	5	3	5	10	10
3	100	50	10	6	5	3	10	20	20
4	150	50	5	3	5	3	10	20	20

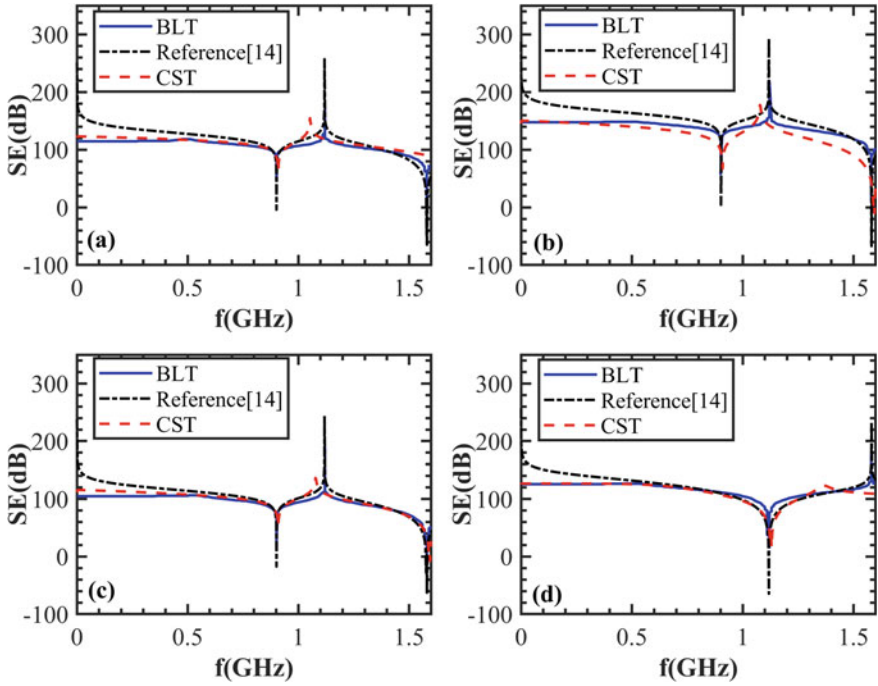


Fig. 3 SE of the three methods for (a) case 1, (b) case 2, (c) case 3, (d) case 4

case 1. However, it is noteworthy that although increasing the length of cavity is beneficial to improve the SE, the increased size should be reasonably considered to avoid resonance position, which has important guiding significance for engineering application. Besides, from Fig. 3 (a) to Fig. 3 (d), there is a common characteristic that SE reaches the minimum or even negative value at the resonant frequency. In this case, the shielding cavity not only has no shielding effect but also increases the electric field in the cavity. This is due to the formation of standing wave resonance in the cavity, which increases the electric field amplitude of the observation point in the cavity, leading to the minimum value of its SE. Then the frequency of the incident electromagnetic wave gradually increases. When the frequency is greater than the resonant frequency of the cavity, the electric field amplitude at the monitor point decreases correspondingly with the disappearance of the standing wave in the cavity, and the SE gradually increases at last. Until the minimum value occurs again at the next resonant frequency, which is the reason why SE has multiple minimal values, even negative values. However, it can be seen obviously from Fig. 3 that when the frequencies are greater than the first resonant frequency of the cavity, the consistency between the analytical model calculation results and CST simulation results decreases. Several reasons can be given to illustrate this point. On the one hand, the reason is that the cavity and the aperture array are treated equivalently in the analytical method. On the other hand, the main reason is that

the analytical method is derived from TE_{10} mode, but different modes correspond to different impedance or admittance, thus, the analytical method without considering the influence of multi-mode as CST.

4 Conclusion

In this paper, according to the characteristics of electromagnetic waves under external radiation, based on electromagnetic topology theory and BLT equation, a new analytical approach is established to estimate the shielding effectiveness of dual-cavity. Four sets of simulations were carried out to consider the effect of cavity diameter, number of apertures and cavity size on the shielding effect. In addition, the analytical model established in this paper was compared with the hybrid model of reference [14] and CST simulation software, and all three methods were in excellent agreement. The results of the study indicate that the number of aperture arrays and the size of the cavity should be reasonably considered in the design of the shielding cavity according to the actual application. At the same time, the installation of electronic devices and the layout of the circuit should be considered to avoid the location of high electric field strength so as to achieve the best shielding capacity of the shielding cavity.

Acknowledgements This work is supported by Natural Science Foundation of Gansu Province No. 21JR7RA237.

References

1. Chen, K., Ma, Z., Jin, H., Zhang, X., Zhou, Q., Liu, Z.: Analysis of radiated interference of 10kV intelligent distribution switch. In: 2020 IEEE International Conference on High Voltage Engineering and Application (ICHVE), pp. 1–4. IEEE (2020)
2. Pradhan, S.S., Unnikrishnan, L., Mohanty, S., Nayak, S.K.: Thermally conducting polymer composites with EMI shielding: a review. *J. Electron. Mater.* **49**(3), 1749–1764 (2020)
3. Peng, M., Qin, F.: Clarification of basic concepts for electromagnetic interference shielding effectiveness. *J. Appl. Phys.* **130**(22), 225108 (2021)
4. Bai, W., Ning, F., Yang, X., Jiao, C., Chen, L.: Low frequency magnetic shielding effectiveness of a conducting plate with periodic apertures. *IEEE Trans. Electromagn. Compat.* **63**(1), 30–37 (2020)
5. Olyslager, F., Laermans, E., De Zutter, D., Criel, S., De Smedt, R., Lietaert, N., De Clercq, A.: Numerical and experimental study of the shielding effectiveness of a metallic enclosure. *IEEE Trans. Electromagn. Compat.* **41**(3), 202–213 (1999)
6. Nobakhti, M., Dehkhoda, P., Tavakoli, A.: Improved modal method of moments technique to compensate the effect of wall dimension in shielding effectiveness evaluation. *IET Sci. Meas. Technol.* **8**(1), 17–22 (2014)
7. Mohammadi, E., Dehkhoda, P., Tavakoli, A., Honarbakhsh, B.: Shielding effectiveness analysis of large enclosures by domain decomposition mesh-free method. *IEEE Trans. Electromagn. Compat.* **59**(5), 1441–1448 (2017)

8. Kuo, C.-W., Kuo, C.-M.: Finite-difference time-domain analysis of the shielding effectiveness of metallic enclosures with apertures using a novel subgridding algorithm. *IEEE Trans. Electromagn. Compat.* **58**(5), 1595–1601 (2016)
9. Nie, B.-L., Du, P.-A., Yu, Y.-T., Shi, Z.: Study of the shielding properties of enclosures with apertures at higher frequencies using the transmission-line modeling method. *IEEE Trans. Electromagn. Compat.* **53**(1), 73–81 (2010)
10. Robinson, M.P., Turner, J., Thomas, D.W., Dawson, J., Ganley, M., Marvin, A., Porter, S., Benson, T., Christopoulos, C.: Shielding effectiveness of a rectangular enclosure with a rectangular aperture. *Electron. Lett.* **32**(17), 1559–1560 (1996)
11. Solin, J.R.: Formula for the field excited in a rectangular cavity with an aperture and lossy walls. *IEEE Trans. Electromagn. Compat.* **57**(2), 203–209 (2014)
12. Po'ad, F.A., Jenu, M.Z.M., Christopoulos, C., Thomas, D.: Estimation of electric and magnetic shielding effectiveness of a metallic enclosure with apertures. In: 2006 International RF and Microwave Conference, pp. 291–295. IEEE (2006)
13. Hao, J., Jiang, L., Fan, J., Gong, Y.: Electromagnetic topology model for the shielding effectiveness of an apertured enclosure with a lossy dielectric layer. *Diangong Jishu Xuebao/Trans. China Electrotech. Soc.* **32**(9), 101–111 (2017)
14. Jin, H., Zhang, H., Ma, Y., Chen, K., Sun, X.: An analytical hybrid model for the shielding effectiveness evaluation of a dual-cavity structure with an aperture array. *Prog. Electromagn. Res. Lett.* **91**, 109–116 (2020)
15. Shen, W., Wang, S., Li, W., Jin, H., Zhang, H.: An extended hybrid analytical model for shielding effectiveness prediction of multi-cavity structure with numerous apertures. *Prog. Electromagn. Res. M.* **96**, 181–190 (2020)

Power System Multi-oscillation Center Cut Sets Identification Method Based on Algebraic Graph Theory



YanQiang Shi, Jing Li, Zhiyong Qiu, Haoyin Ding, Zhenyao Li,
and Deqiang Gan

Abstract The valid identification of the oscillation center is a key step to implementing emergency control after experiencing a large disturbance. This paper first uses the structural properties of the network based on algebraic graph theory to decompose the voltage vector of any node into the potential component and the load component, revealing the mechanism of the oscillation center. Then an optimization model of the static topology grouping of the power grid is formulated, the mathematical basis of the power grid oscillation center is provided and a multi-oscillation center cut sets identification method is proposed. Lastly, the four-machine two-zone system, IEEE 39 bus system, and practical power grid examples further verify the validity of the proposed method.

Keywords Oscillation center · Identification method · Algebraic graph theory

1 Introduction

A reliable supply of electric power is essential for the modern society, whereas the ongoing complex power network structure and the growing demand pose a challenge to the stability and reliability of power system [1]. Distinguished from traditional power supply mode with simple network, modern power system is featured with large capacity generators, long distance transmission, regional interconnection such that the issue of rotor-angle become a major engineering problem, threatening the stability

Y. Shi · Z. Qiu · H. Ding
East China Branch, State Grid Company of China, Shanghai 200120, China
e-mail: shiyuanqiang111@126.com

J. Li · Z. Li · D. Gan (✉)
School of Electrical Engineering, Zhejiang University, Hangzhou 310027, China
e-mail: dgan@zju.edu.cn

J. Li
e-mail: eelijing@zju.edu.cn

of power system [2]. The effective identification of oscillation center is key step to implement emergency control after experiencing large disturbance [3].

The oscillation center of a power system is usually regarded as the point where the voltage drop is the most severe due to the swing of the generator power angle in a certain oscillation mode [4]. The existing oscillation center identification theory includes model analysis method and clustering graph method [5].

- 1) Model analysis method. GAO Peng et al. [6] use the vector method to give the exact position function of the oscillation center in the two-machine system, and further analyzes the drift characteristics of the oscillation center; Y. Q. Xiao et al. [7] adopt the different voltage frequencies on both sides of the tie line of the equivalent machine. The corresponding oscillation center section was captured, based on the equivalent three-machine system, Y. Q. Xiao et al. [8] deduce the oscillation center expression of the multi-machine system, and give the location of multi-oscillation center of the power grid. Most of the above methods are based on quantitative analysis of equivalent systems, and then the results are extended to multi-machine systems. Whether they can continue to maintain effectiveness in complex multi-machine power supply scenarios still needs further discussion;
- 2) Clustering graph theory. Quiros Tortos J et al. [9] use the spectral clustering method to delineate the isolated section of the grid to prevent cascading failures. This method can quickly give the grid section cut set based on the response data; ZHANG Songtao et al. [10] use the electrical distance characteristics to model the power grid. The network is formed into a graph network, and the label propagation algorithm in the network community detection theory is used to carry out the identification of the weak section of the power grid. NI Xiangping et al. [11] use the complex network community structure theory and uses the graph theory properties of the power grid to construct the weighted Laplacian matrix of the power grid. LIN Jikeng et al. [12] attributed the problem of the active decoupling section identification of the power grid to the optimal equilibrium segmentation problem of the graph, and then gave the grid decoupling section by solving the optimization model. All in all, the clustering graph method usually attributes the oscillation center to the identification of weak nodes or sections of the power grid, and conducts research through graph theory or clustering methods. Due to the lack of necessary theoretical analysis, its practical level still needs to be further advanced.

Inspired by the method of clustering graph and model analysis method, this paper, combining the natural Laplacian property of the power grid with algebraic graph theory, propose a method to identify power system multi-oscillation center cut sets. Different from the previous methods, a more rigorous mathematical foundation of the power grid oscillation center is provided. The four-machine two-zone system, IEEE39 bus system further verify the validity of the theoretical analysis and the proposed method.

2 Multi-oscillation Center Identification Method

2.1 Fundamental Theory of Algebraic Graph

Given a finite set \mathcal{I}_n , let $|\mathcal{I}_n|$ be its cardinality, and define for $n \in \mathbb{N}$ the set $\mathcal{I}_n = \{1, \dots, n\}$. Given a two dimensions matrix $\{A_{ij}\}$ with $i, j \in \mathcal{I}_n$, let $\mathbf{A} \in \mathbb{C}^{n \times n}$ denotes associated matrix and A^T the transposed matrix. We use the following notation from reference [13] for submatrices for two non-empty index set $\alpha, \beta \subseteq \mathcal{I}_n$, let $\mathbf{A}[\alpha, \beta]$ be the submatrices of \mathbf{A} gained by rows indexed by α and columns indexed by β , hence $\mathbf{A}(\alpha, \beta) = \mathbf{A}[\mathcal{I}_n \setminus \alpha, \mathcal{I}_n \setminus \beta]$, $\mathbf{A}[\alpha, \beta] = \mathbf{A}[\alpha, \mathcal{I}_n \setminus \beta]$, $\mathbf{A}(\alpha, \beta) = \mathbf{A}[\mathcal{I}_n \setminus \alpha, \beta]$, and we introduce the following theorem:

Theorem 1 [13]: (*Structure Properties of Kron Reduction*): For Graph $\mathcal{G} := (\mathbf{N}, \mathcal{E}, \mathbf{A})$, Let $\mathbf{Y} \in \mathbf{R}^{n \times n}$ be a symmetric irreducible loopy Laplacian and $\alpha \subseteq \mathbf{N}$ ($|\alpha| \geq 2$) be a proper set. The Kron-reduced matrix \mathbf{Y}_{red} is calculated as follows:

$$\begin{aligned} \mathbf{Y}_{red} = & \mathbf{Y}_{aug} \setminus \mathbf{Y}_{aug}(\alpha, \alpha) \triangleq \mathbf{Y}_{aug}[\alpha, \alpha] \\ & - \mathbf{Y}_{aug}[\alpha, \alpha] \mathbf{Y}_{aug}(\alpha, \alpha)^{-1} \mathbf{Y}_{aug}(\alpha, \alpha) \end{aligned} \quad (1)$$

The following statements hold for \mathbf{Y}_{red} :

- i) Existence: The Kron-reduced matrix \mathbf{Y}_{red} is well defined.
- ii) Closure properties: \mathbf{Y}_{aug} is a symmetric loopy, strictly loopy, or loop-less Laplacian matrix, respectively, the \mathbf{Y}_{red} is a symmetric loopy, strictly loopy, or loop-less Laplacian matrix, respectively.

Remark: The above theorem points out that the structure properties will hold after Kron reduction, i.e. \mathbf{Y}_{red} and \mathbf{Y}_{aug} share the same matrix properties.

Theorem 2 [14]: (*Courant Fischer Theorem*): Let $\mathbf{A} \in \mathbf{M}_n$ be Hermitian and let $\lambda_1 \leq \lambda_2 \leq \dots \leq \lambda_n$ be its algebraically ordered eigenvalues. Let $k \in \{1, \dots, n\}$ and let S denote a subspace of \mathbf{C}^n . The

$$\lambda_k = \max_{\{S: \dim S = n - k + 1\}} \min_{\{x: 0 \neq x \in S\}} \frac{x^* \mathbf{A} x}{x^* x} \quad (2)$$

Remark: The Courant Fischer theorem tell us the Rayleigh problem, i.e. $x^* \mathbf{A} x / x^* x$, will get its minimum λ_k when x equal the k -th eigenvector \mathbf{u}_k corresponding λ_k .

Lemma 1 [15]: (*row characteristic of \mathbf{F}_{LG}*): Consider current balance equation $\mathbf{I} = \mathbf{Y}\mathbf{U}$, where \mathbf{I} 、 \mathbf{U} are the bus injected current and nodal voltage, the admittance matrix can be decomposed into four submatrix as following:

$$\mathbf{Y}_1 = \begin{bmatrix} \mathbf{Y}_{GG} & \mathbf{Y}_{GL} \\ \mathbf{Y}_{LG} & \mathbf{Y}_{LL} \end{bmatrix} \quad (3)$$

Then the composite matrix $\mathbf{F}_{LG} = -\mathbf{Y}_{LL}^{-1}\mathbf{Y}_{LG}$ has the following properties:

- 1) \mathbf{F}_{LG} is approximately a full real number matrix;
- 2) The row sum of \mathbf{F}_{LG} is close to one.

Next, we will introduce the Nodal domain theorem, which illustrates the connection between nodes group and the sign pattern of eigenvector.

Definition (Nodal domain): D is a nodal domain of function $f : D \rightarrow \mathbb{R}$ if it is a maximal subset of V subject to the two conditions:

- i) D is connected;
- ii) if $x, y \in D$ then $f(x)f(y) > 0$

Theorem 3 [16]: (Nodal domain theorem): Let L be a generalized Laplacian of a connected graph on $\mathcal{G} = (\mathbf{N}, \mathcal{E}, \mathbf{A})$ with n vertices. Then a nodal domain D_k associated with the k -th eigenvalue is defined as a maximal connected subgraph as:

$$i, j \in D_k \Leftrightarrow u_k(i)u_k(j) \geq 0 \tag{4}$$

where \mathbf{u}_k is the eigenvector corresponding to the k -th eigenvalue λ_k of L , and let $NND(\mathbf{u}_k)$ denote the number of nodal domains of eigenvector \mathbf{u}_k with multiplicity m_k $NND(\mathbf{u}_k)$ is bounded as:

$$NND(\mathbf{u}_k) \leq k + m_k - 1 \tag{5}$$

Remark: The nodal domain theorem tells us the connection between nodes clustering and the eigenvector’s sign of Laplacian matrix of graph, which corresponding to the cut sets of power system multi-oscillator centers.

2.2 Mathematical Graph Model of Power System

The mathematical model of power system includes differential equations and algebraic equations of network, then the power system can be deemed as DAE equations as follows:

$$\begin{cases} \dot{\mathbf{X}} = \mathbf{f}(\mathbf{X}, \mathbf{V}) \\ \mathbf{YV} = \mathbf{I}(\mathbf{X}, \mathbf{V}) \end{cases} \tag{6}$$

where $\mathbf{f}(\mathbf{f} : \mathbb{R}^{2m+n} \mapsto \mathbb{R}^{2m})$ are the generator’s swing equations, \mathbf{x} is state variables, i.e. $\delta, \omega, \mathbf{V} \in \mathbb{C}^{n \times n}, \mathbf{I} \in \mathbb{C}^{n \times n}$ is, respectively, the grid voltage and the injection current, $\mathbf{Y} \in \mathbb{C}^{n \times n}$ is the power network admittance matrix. Specifically, we can

model the power system as a graph from the perspective of the network equations, and all nodes in the power grid can be encoded as follows:

- 1) $\mathbf{I} = \{1, 2, \dots, m\}$ represents a set of generator internal nodes;
- 2) $\mathbf{G} = \{m + 1, m + 2, \dots, 2m\}$ represents a set of generator terminal nodes;
- 3) $\mathbf{L} = \{2m + 1, 2m + 2, \dots, 2m + n\}$ represents a set of load nodes;

Moreover, the adjacency matrix of the power network can be defined as follows:

$$\mathbf{A} = \begin{cases} a_{ii} = j\omega C_i & (i, i) \in \mathcal{E} \\ a_{ij} = G_{ij} + jB_{ij} & (i, j) \in \mathcal{E} \end{cases} \quad (7)$$

where \mathcal{E} is the edge set of all branch, C_i is the charging capacitor at node i , and $G_{ij} + jB_{ij}$ is line admittance between node i and node j . Thus, a power system can be described by the graphs notation:

$$\mathcal{G} := (\mathbf{N}, \varepsilon, \mathbf{A}), \mathbf{N} = \mathbf{I} \cup \mathbf{G} \cup \mathbf{L}, \varepsilon \subseteq \mathbf{N} \times \mathbf{N} \ominus \quad (8)$$

Suppose all loads and generators in a power system are represented by passive impedances and second-order model, then the current balance equation describing graph \mathcal{G} is as followed:

$$\begin{bmatrix} \mathbf{Y}_d & -\mathbf{Y}_d & \mathbf{0} \\ -\mathbf{Y}_d & \mathbf{Y}_{GG} + \mathbf{Y}_d & \mathbf{Y}_{GL} \\ \mathbf{0} & \mathbf{Y}_{LG} & \mathbf{Y}_{LL} \end{bmatrix} \begin{bmatrix} \mathbf{V}_I \\ \mathbf{V}_G \\ \mathbf{V}_L \end{bmatrix} = \begin{bmatrix} \mathbf{I}_G \\ \mathbf{0} \\ \bar{\mathbf{S}}_L / \bar{\mathbf{V}}_L \end{bmatrix} \quad (9)$$

where $\mathbf{Y}_d = \text{diag}(y_{d1}, \dots, y_{dm}) \in \mathbb{C}^{m \times m}$ is the diagonal transient reactance matrix, $\mathbf{Y}_{GG}, \mathbf{Y}_{GL}, \mathbf{Y}_{GL}, \mathbf{Y}_{GL}$ are the four sub-blocks of \mathbf{Y} matrix, $\mathbf{V}_I = \mathbf{E}'_q e^{j\delta}$ is the internal potential Voltage of generator, $\mathbf{V}_G, \mathbf{V}_L$ is, respectively, generator terminal voltage and load voltage, $\bar{\mathbf{S}}_L$ represents the node injected power at load bus, the symbol./ represents the dot division between elements.

Using theorem 1, i.e. Kron reduction, let $\alpha = \mathbf{I} \cup \mathbf{L}$ and eliminate the generator terminal nodes, Eq. (1) can be written as follows:

$$\begin{bmatrix} \mathbf{Y}_d - \mathbf{Y}_d \bar{\mathbf{Y}}_{GG}^{-1} \mathbf{Y}_d & \mathbf{Y}_d \bar{\mathbf{Y}}_{GG}^{-1} \mathbf{Y}_{GL} \\ \mathbf{Y}_{LG} \bar{\mathbf{Y}}_{GG}^{-1} \mathbf{Y}_d & \mathbf{Y}_{LL} - \mathbf{Y}_{LG} \bar{\mathbf{Y}}_{GG}^{-1} \mathbf{Y}_{GL} \end{bmatrix} \begin{bmatrix} \mathbf{V}_I \\ \mathbf{V}_L \end{bmatrix} = \begin{bmatrix} \mathbf{I}_G \\ \bar{\mathbf{S}}_L / \bar{\mathbf{V}}_L \end{bmatrix} \quad (10)$$

where $\bar{\mathbf{Y}}_{GG} = \mathbf{Y}_{GG} + \mathbf{Y}_d$. The expressions for calculating \mathbf{V}_L with respect to influence of source potential and load demand are as follows:

$$\begin{aligned}
 \mathbf{V}_L &= -\underbrace{(\mathbf{Y}_{LL} - \mathbf{Y}_{LG}\mathbf{Y}'_{GG}\mathbf{Y}_{GL})^{-1}\mathbf{Y}_{LG}\mathbf{Y}'_{GG}\mathbf{Y}_d}_{\mathbf{F}_{LG}}\mathbf{V}_G + \underbrace{(\mathbf{Y}_{LL} - \mathbf{Y}_{LG}\mathbf{Y}'_{GG}\mathbf{Y}_{GL})^{-1}\bar{\mathbf{S}}_L}_{\mathbf{Z}_{LL}}/\bar{\mathbf{V}} \\
 &= \underbrace{\mathbf{F}_{LG}\mathbf{E}'_q e^{j\delta}}_{\mathbf{V}_\delta} + \underbrace{\mathbf{Z}_{LL}(\bar{\mathbf{S}}_L/\bar{\mathbf{V}}_L)}_{\mathbf{V}_{SL}} = \mathbf{V}_\delta + \mathbf{V}_{SL}
 \end{aligned}
 \tag{11}$$

where \mathbf{V}_L can be decomposed into two parts: potential component and load component. Meantime, according to lemma 1, we know that \mathbf{F}_{LG} complies with two properties: 1) \mathbf{F}_{LG} is approximately a full real number matrix; 2) The row sum of \mathbf{F}_{LG} is close to one.

In the transient process of power system, generators that are closely coupled in electrical sense tend to swing together in groups during disturbances, i.e. coherency phenomenon, which will make the potential $E'_q e^{j\delta_i}$ behave a grouping characteristic. The voltage of some nodes will fall into zero constructed by the product of generator potential and weight coefficient of row value of \mathbf{F}_{LG} , and that is, oscillation center of power system. Thus, we can explore the oscillation center cut set from the perspective of potential component.

2.3 Power System Multi-oscillation Center Identification

Consider the potential component \mathbf{V}_δ , which is the key factor determining the oscillation center cut set of power system. Thus, we can omit the load component, that is, all loads \mathbf{S}_L are set to zero. Then the network equation will be described by:

$$\begin{bmatrix} \mathbf{Y}_d & -\mathbf{Y}_d & \mathbf{0} \\ -\mathbf{Y}_d & \mathbf{Y}_{GG} + \mathbf{Y}_d & \mathbf{Y}_{GL} \\ \mathbf{0} & \mathbf{Y}_{LG} & \mathbf{Y}_{LL} \end{bmatrix} \begin{bmatrix} \mathbf{V}_I \\ \mathbf{V}_G \\ \mathbf{V}_L \end{bmatrix} = \begin{bmatrix} \mathbf{I}_G \\ \mathbf{0} \\ \mathbf{0} \end{bmatrix}
 \tag{12}$$

where $\mathbf{Y}_L = \text{diag}(y_{L1}, \dots, y_{Ln})$, Let $\alpha = \mathbf{I}$, and all of nodes except internal potential node is eliminated using Kron reduction theorem. The formula is satisfied as following:

$$\mathbf{Y}'_{red}\mathbf{V}_I = \mathbf{I}_G
 \tag{13}$$

where $\mathbf{Y}'_{red} = \mathbf{Y}_d - \mathbf{Y}_d(\tilde{\mathbf{Y}}_{GG}^{-1} + \tilde{\mathbf{Y}}_{GG}^{-1}\mathbf{Y}_{GL}\Delta^{-1}\mathbf{Y}_{LG}\tilde{\mathbf{Y}}_{GG}^{-1})\mathbf{Y}_d$, and $\Delta = \mathbf{Y}_{LL} - \mathbf{Y}_{LG}\tilde{\mathbf{Y}}_{GG}^{-1}\mathbf{Y}_{GL}$, $\tilde{\mathbf{Y}}_{GG} = \mathbf{Y}_{GG} + \mathbf{Y}_d$.

Let $\mathcal{G}' := (\mathbf{I}, \mathcal{E}'_{red}, \mathbf{A}'_{red})$ be the graph induced by \mathbf{Y}'_{red} , we know that \mathcal{G}' is a graph again from theorem 1 such that the reduced network admittance matrix \mathbf{Y}'_{red} satisfies Laplacian properties approximately. The matrix \mathbf{Y}'_{red} can be rewritten into the follow form by spectral decomposition.

$$\mathbf{Y}'_{red} = \lambda_1 \mathbf{u}_1 \mathbf{v}_1^* + \lambda_2 \mathbf{u}_2 \mathbf{v}_2^* + \dots + \lambda_m \mathbf{u}_m \mathbf{v}_m^* \quad (14)$$

We can obtain the following inequality by arranging the eigenvalue of \mathbf{Y}'_{red} :

$$0 \approx \lambda_{\min} = \lambda_1 < \lambda_2 < \dots < \lambda_m = \lambda_{\max} \quad (15)$$

The problem of identification of cut set of oscillation center can be reiterated by algebraic graph language: consider a graph $\mathcal{G}' := (\mathbf{I}, \mathcal{E}'_{red}, \mathbf{A}'_{red})$, try to find set $\mathcal{V}_1, \mathcal{V}_2$ such that $\mathcal{V}_1 \cup \mathcal{V}_2 = \mathbf{I}$, $\mathcal{V}_1 \cap \mathcal{V}_2 = \emptyset$ and $\mathcal{V}_1, \mathcal{V}_2 \neq \emptyset$, and subject to:

$$\min J(\mathcal{V}_1, \mathcal{V}_2) = \sum_{i \in \mathcal{V}_1, j \in \mathcal{V}_2} a'_{ij} \quad (16)$$

The optimization problem of Eq. (1) cannot be solved directly due to the NP-hardness property. We can define an index set $\mathbf{x} \in \{1, -1\}^n$ such that $i \in \mathcal{V}_1$ if $x_i = 1$ or $i \in \mathcal{V}_2$ if $x_i = -1$, then the optimization problem can be write into Laplacian potential form as follow:

$$\min J(\mathbf{x}) = \frac{1}{8} \sum_{i,j \in 1}^n a'_{ij} (x_i - x_j)^2 \quad (17)$$

The above formula is equivalent to the following form duo to the Laplacian property of \mathbf{A}'_{red} .

$$\min_{\mathbf{x} \in \{1, -1\}^n, \mathbf{x} \neq \pm \mathbf{1}} J(\mathbf{x}) = \frac{1}{4} \mathbf{x}^T \mathbf{Y}' \mathbf{x} \quad (18)$$

We can convert the continuous form into discrete form using slack technique:

$$\min_{\mathbf{y} \in \mathbb{R}^n, \|\mathbf{y}\|_2 = 1, \mathbf{y} \perp \mathbf{1}} J(\mathbf{y}) = \frac{1}{4} \mathbf{y}^T \mathbf{Y}' \mathbf{y} \quad (19)$$

Then theorem 2 points out that the solution of Eq. (19) is:

$$J = \lambda_2, \mathbf{y} = \mathbf{u}_2 \quad (20)$$

According to Theorem 3, we can find group of generator by using the sign pattern of \mathbf{u}_2 , which is called Fiedler vector by the community of complex network generally. Moreover, we can find another cut set of oscillation center if we consider the different unstable mode, then the following optimization model is established:

$$\min_{\mathbf{y} \in \mathbb{R}^n, \|\mathbf{y}\|_2 = 1, \mathbf{y} \perp \mathbf{1}, \mathbf{y} \perp \mathbf{u}_2} J(\mathbf{y}) = \frac{1}{4} \mathbf{y}^T \mathbf{Y}' \mathbf{y} \quad (21)$$

we can observe that the solution of Eq. (1) is by using theorem 2 again:

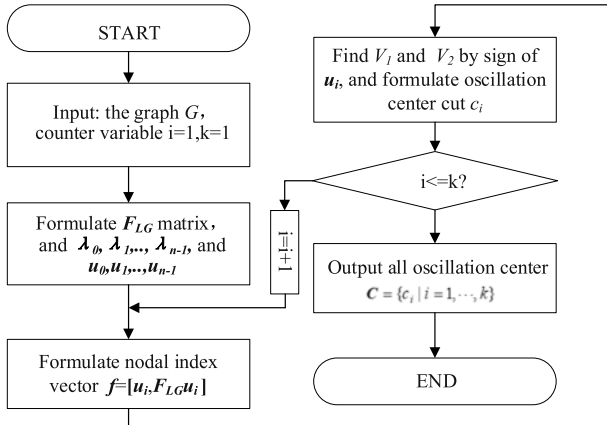


Fig. 1 Flow chart of the algorithm to identify oscillation center cut

$$J = \lambda_3, \mathbf{y} = \mathbf{u}_3 \tag{22}$$

In conclude, the algorithm to identify the cut set of oscillation center we proposed is described in Fig. 1.

3 Numerical Examples

3.1 Four Machines Two Areas System Case

Taking the four machines two areas system as an example, there are 4 equivalent synchronous generators and three equivalent loads in this system as Fig. 2 shows.

Firstly, we will investigate the oscillation center of the system by setting a three phases fault on bus 8 and the fault is cleared after 0.12 s, then the response of angle and voltage dynamic is showed as followed :

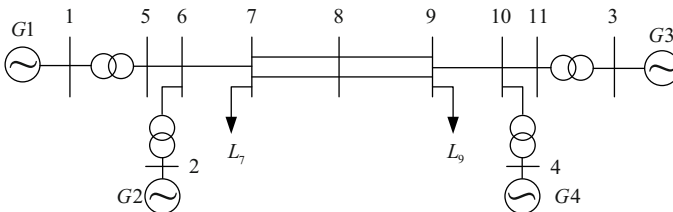


Fig. 2 Four machines two areas system

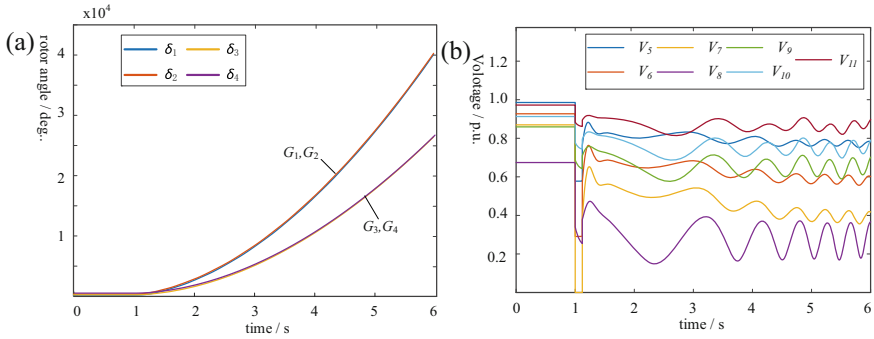
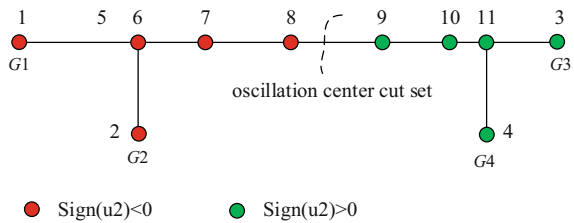


Fig. 3 Generator responses; a) angle responses b) voltage responses

Fig. 4 Oscillation center cut



From the left side of Fig. 5, we can see that generators are divided into two groups and the minimum voltage over all network is bus 8, constituting the oscillation center. Furthermore, we calculate the second eigenvector u_2 of Y_{red} , and the index vector $[u_2, F_{LG}u_2]$ is showed as following:

Then the distribution of sign pattern of $[u_2, F_{LG}u_2]$ over all network node is showed as Fig. 4, we can see that the all nodes is divided into two groups depending its sign pattern, and the oscillation center cut set is nearing the node 8, which is consistent with the time domain simulation showed in Fig. 3, thus those result demonstrates the validity of proposed method.

3.2 IEEE39 Bus New England System

The IEEE39 bus test system have 10 equivalent synchronous generators and 18 equivalent loads in the system, of which the generator adopts the classical second-order model and the load adopts the constant impedance model.

We set a three-phase short circuit fault at bus 16, and the system loses synchronism after the fault is cleared at 0.72 s. We found that generators are divided into two groups, and then multiple groups of the generators with angle instability occur after the fault time is extended. The response of rotor angles is showed as followed:

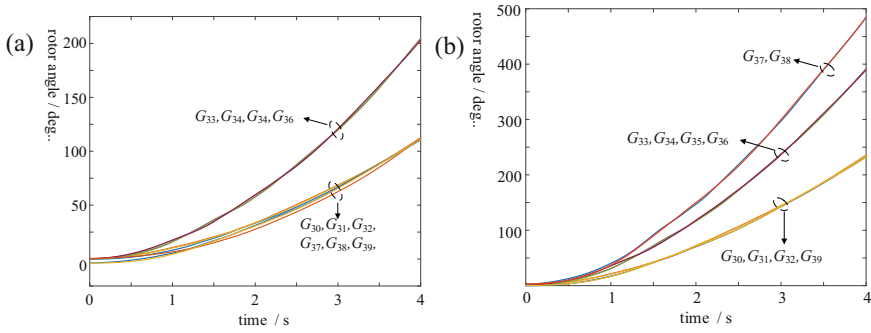


Fig. 5 Angle Rotor angle response; (a) angle instability with two groups generators, (b) angle instability with three groups generators

Using the algorithm proposed in the paper, we calculate the eigenvector corresponding to the second small eigenvalue, as shown in the following table.

The partition of all generators corresponding to second eigenvector u_2 is $\mathcal{V}_1 = \{ G_{30}, G_{31}, G_{32}, G_{37}, G_{38}, G_{39} \}, \mathcal{V}_2 = \{ G_{33}, G_{34}, G_{35}, G_{36} \}$, similarly, the partition corresponding to eigenvector u_3 is $\mathcal{V}_1 = \{ G_{33}, G_{34}, G_{35}, G_{36} \}, \mathcal{V}_2 = \{ G_{30}, G_{31}, G_{32}, G_{39} \}, \mathcal{V}_3 = \{ G_{37}, G_{38} \}$, and then the oscillation center cuts are identified by the algorithm proposed as Fig. 6 below shows.

We can see that the generator group divided by oscillation center cut I and II is corresponded with the time domain simulation showed in Fig. 5. For example, the generator is divided into two group by oscillation center cut I, respectively, \mathcal{V}_1 and \mathcal{V}_2 , which corresponds to the angle dynamic depicted in left side of Fig. 5, thus those result demonstrates the validity of proposed method.

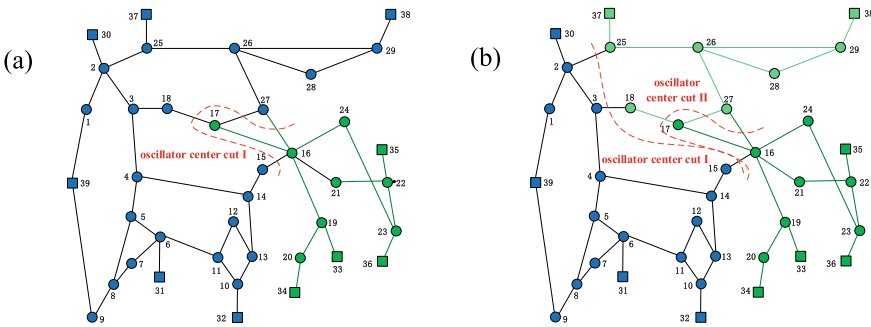


Fig. 6 a Oscillation center cut set I, b Oscillation center cut set II,

Table 1 Element of index vector $[u_2, F_{LG}u_2]$

u_2	$F_{LG}u_2$
-0.5609, -0.4757, 0.5168, 0.4383	-0.3417, -0.2898, -0.2514, -0.0100, 0.2316, 0.2670, 0.3149

Table 2 Element of index vector $[u_2, F_{LG}u_2]$

eigenvalue	eigenvector
$\lambda_2 = 7.5203$	$u_2 = [-0.1532, -0.1627, -0.0746, 0.2968, 0.3218, 0.3716, 0.4822, -0.2908, -0.5137, -0.1837]$
$\lambda_3 = 8.0104$	$u_3 = [-0.0221, 0.6066, 0.3278, -0.0876, -0.0959, -0.1182, -0.1594, -0.0467, -0.6451, 0.2224]$

4 Conclusion

This paper focuses on the identification power system multi-oscillation center cut sets by algebraic graph theory. There are three contributions. Firstly, voltage vector of the network is decomposed into the potential component and the load component by investigating the structural properties of the network, and the mechanism of oscillation center is revealed by potential component. Second, an optimization model for generator grouping is formulated, which provides solid mathematical foundation of power system multi-oscillation center. Finally, a multi-oscillation center cut sets identification method is proposed and algorithm to find multi-oscillation center cut sets is designed. The four-machine two-zone system, IEEE39 bus system further verify the validity of the proposed method.

Acknowledgements This research was funded by the Science and Technology Project of State Grid (SGTYHT/20-JS-221).

References

1. Alvarez-Alvarado, M.S., Donaldson, D.L., Recalde, A.A., et al.: Power system reliability and maintenance evolution: a critical review and future perspectives. *IEEE Access* **10**, 51922–51950 (2022)
2. Rezaei, J., Golshan, M.E.H., Alhelou, H.H.: Impacts of integration of very large-scale photovoltaic power plants on rotor angle and frequency stability of power system. *IET Renew. Power Gener.* **16**(11), 2384–2401 (2022)
3. Hu, Y., Wang, X.R., Huang, T., et al.: An optimal frequency control method of asynchronous power grid considering multi-HVDC emergency power support. *IEEE Access* **10**, 78011–78021 (2022)
4. Liu, F., Fang, Y., Wu, X., et al.: Instantaneous frequency characteristics and oscillation center location method for out of step oscillation. *Proc. CSEE* **36**(04), 986–992 (2016). (in Chinese)

5. Ahangar, A.R.H., Gharehpetian, G.B., Baghaee, H.R.: A review on intentional controlled islanding in smart power systems and generalized framework for ICI in microgrids. *Int. J. Electr. Power Energy Syst.* **118** (2018)
6. Gao, P., Wang, J., Zhou, W., et al.: Study on oscillation center. In: Proceedings of the CSU-EPSC (02), 48–53 (2018). (in Chinese)
7. Yu, Q.Y., Sun, G.H., Chen, S.L., et al.: Research on application of oscillation location and control in large-scale power grid, pp. 246–250 (2016)
8. Xiao, Y.Q., Qian, W., Ni, H.P., et al.: Oscillation center migration law in multi-frequency out-of-step oscillation scenario, pp. 1635–1638 (2017)
9. Quiros-Tortos, J., Sanchez-Garcia, R., Brodzki, J., et al.: Constrained spectral clustering-based methodology for intentional controlled islanding of large-scale power systems. *IET Gener. Transm. Distrib.* **9**(1), 31–42 (2015)
10. Zhang, S., Zhang, D., Li, Z., et al.: Fast location method for controlled splitting sections of power grid based on label propagation algorithm. *Power Syst. Technol.* <https://doi.org/10.13335/j.1000-3673.pst.2021.1161>. (in Chinese)
11. Xiangping, N.I., Shengwei, M.E.I.: Coherency-based dynamic equivalence algorithm with community structure of complex network theory. *Autom. Electr. Power Syst.* **07**, 10–14 (2008). (in Chinese)
12. Lin, J., Li, S., Wu, P., et al.: Model and algorithm for the optimal controlled partitioning of power systems. *Proc. CSEE* **32**(13), 86–94+195. (in Chinese)
13. Dorfler, F., Bullo, F.: Kron reduction of graphs with applications to electrical networks. *IEEE Trans. Circ. Syst. I-Regul. Papers* **60**(1), 150–163 (2013)
14. Horn, R.A.: *Matrix Analysis*. Cambridge University Press (2012)
15. Dassios, I.K., Cuffe, P., Keane, A.: Visualizing voltage relationships using the unity row summation and real valued properties of the F-LG matrix. *Electr. Power Syst. Res.* **140**, 611–618 (2016)
16. Biyikoglu, T., Hordijk, W., Leydold, J., et al.: Graph Laplacians, nodal domains, and hyperplane arrangements. *Linear Algebra Appl.* **390**, 155–174, Oct 1 (2004)

Research on the Adsorption Performance of β -Ga₂O₃ on C₂H₄ Gas in Transformer Oil



Zhou Zemin, Wang Jialin, Pang Jianyou, Zhou Xiong, Huang Qianxiu, Shao Chen , and Guo Yuzheng 

Abstract C₂H₄ is an essential characteristic gas in the oil of oil-immersed power transformers used to assess the occurrence of faults. Its online monitoring provides an effective reflection of the transformer's operating conditions in real time. To address the problem that conventional gas sensors are not responsive to characteristic gases, this paper uses an ultra-wide bandgap semiconductor material (β -Ga₂O₃) as a gas sensor to detect the fault characteristic gas C₂H₄. The structural and electronic properties of β -Ga₂O₃ have been investigated by means of first principles calculations, and its gas-sensitive mechanism and adsorption properties have been analyzed. Firstly, the optimal adsorption position of C₂H₄ gas on the β -Ga₂O₃ surface was determined by structural optimization; secondly, the adsorption behavior of C₂H₄ gas on the β -Ga₂O₃ surface was obtained by further analysis of the charge density difference, adsorption energy, electronic density of states, band structure and work function of the adsorption model. The results show that when C₂H₄ gas is adsorbed on the surface of β -Ga₂O₃, new surface states appear in the electronic density of states and band structure near the valence band maximum and conduction band minimum, which facilitates the carrier transfer between the valence and conduction bands. Also acting

Z. Zemin · P. Jianyou · Z. Xiong · H. Qianxiu
Guilin Power Supply Bureau of CSG Guanxi Power Grid, Guilin, Guanxi, China
e-mail: 187180251@qq.com

P. Jianyou
e-mail: 2466051467@qq.com

Z. Xiong
e-mail: 23749445@qq.com

W. Jialin
CSG Guanxi Power Grid, Nanning, Guanxi, China
e-mail: 276580661@qq.com

S. Chen · G. Yuzheng (✉)
School of Electrical Engineering and Automation, Wuhan University, Wuhan 430072, China
e-mail: yguo@whu.edu.cn

S. Chen
e-mail: cshaol@whu.edu.cn

as an electron acceptor, β -Ga₂O₃ attracts electrons from the C₂H₄ gas molecule with a strong adsorption effect. The paper explores the potential of applying β -Ga₂O₃ materials to the detection of dissolved gases in typical transformer oils, provides a theoretical basis for gas-sensitive adsorption, and demonstrates that β -Ga₂O₃ has excellent gas-sensitive properties for C₂H₄ gas.

Keywords Absorption · Transformer oil · Ga₂O₃ · C₂H₄ · first-principles

1 Introduction

Transformers play a key role in the stability and reliability of the power grid. Among all types of transformers, the oil-immersed power transformer is one of the most widely used equipment [1–3]. In the long-term operation of the transformer, the transformer oil pyrolysis due to high temperature or partial discharge is a significant problem. The pyrolysis decomposition products include methane (CH₄), ethane (C₂H₆), ethylene (C₂H₄), acetylene (C₂H₂) and other gases [4, 5]. In order to ensure a stable operation of the transformer and improve the safety and reliability of the power system, effective monitoring of the status of the transformer and on-time troubleshooting must be assured [6]. The analysis found that the type of transformer failure is directly related to the composition of the mixed gas dissolved in the transformer oil which can be affected by factors such as high temperature and partial discharge. Currently, dissolved gas analysis (DGA) has been widely used as a technique to efficiently monitor the operating status of transformer equipment [7]. C₂H₄ is one of the characteristic gases whose concentration can accurately characterize the real-time condition of the transformer. At present, the main method to effectively and reliably detect C₂H₄ is the by using gas sensor [8, 9]. So far, a lot of work have reported different gas sensors based on different material structures [10]. Among them, semiconductor sensors are becoming a key research content in monitoring fault characteristic gases in transformer oil due to their significant advantages of low cost and ease of synthesis.

Jin et al. [11] has proposed a doped SnO₂ based sensor, and reported a better detection performance with doping. Gao et al. [12] showed that the ZnO sensor has a strong adsorption capability. Wang et al. [13] discussed the gas adsorption performance of doped MoS₂, and showed that doped MoS₂ has stronger detection performance. Zhou et al. [14] discussed the detection performance of Pt-doped tungsten WSe₂, and the calculation results showed that Pt-doped WSe₂ has a good application prospect for on-line monitoring of fault characteristic gases in transformer oil.

Gallium oxide (Ga₂O₃) is currently one of the most well concerned ultra-wide bandgap semiconductor materials, and its experimental band gap is about 4.8 eV. So far, Ga₂O₃ has 5 main crystal structures, among which the β phase is most stable. High-quality β -Ga₂O₃ thin films can be obtained by various methods such as laser molecular beam epitaxy, pulsed laser deposition, and radio frequency magnetron sputtering. Like other oxide semiconductors, β -Ga₂O₃ thin films have different

conductivity in gases with different components after heating up. Thus, the potential of β -Ga₂O₃ in the field of gas sensing has long attracted lots of research attention. Fleischer et al. [15] proved that β -Ga₂O₃ can be used as a stable oxygen-sensitive material. In addition, β -Ga₂O₃ itself has good chemical and thermal stability properties, which makes the material have greater potential in gas sensing.

Our work propose to use the ultra-wide bandgap semiconductor material (β -Ga₂O₃) as a gas sensor to detect the fault characteristic gas C₂H₄. By using the first-principle calculation method, the adsorption sites of C₂H₄ gas molecules on the β -Ga₂O₃ crystal surface were studied. Then we study the geometry and electronic structure of the adsorption system to obtain the adsorption of gas molecules on β -Ga₂O₃, and it was proved that β -Ga₂O₃ has an application potential in DGA as a gas sensor.

2 Modeling and Calculation Method

In this paper, Abinit software was used to perform first-principle calculations on the gas adsorption process of C₂H₄ [16]. The exchange correlation between electrons is described by the generalized gradient approximation (GGA) of Perdew-Burke-Ernzerhof (PBE) through density functional theory [17]. The interaction between ions and valence electrons is described by projection and plane wave method [18]. To avoid the exchange–correlation effect of the surface model, a vacuum layer thickness of 15 Å was added the the structure. The plane wave cutoff energy is set to 520 eV, the Brillouin zone is sampled using a $5 \times 5 \times 1$ Monkhorst–Pack k-point grid. The energy convergence value is set to 1×10^{-5} eV/atom, and the maximum stress is set to within 0.01 eV/Å. We performed modified calculations of the band structure using the hybrid functional (HSE06) to match the experimental bandgap [19]. The DFT-D correction was adjusted using the Grimme method to improve the accuracy of the adsorption energy calculation [20].

The adsorption energy E_{ads} of the gas adsorption process is given by:

$$E_{abs} = E_{(C_2H_4/\beta-Ga_2O_3)} - E_{(C_2H_4)} - E_{(\beta-Ga_2O_3)} \quad (1)$$

where $E_{(C_2H_4/\beta-Ga_2O_3)}$, $E_{(C_2H_4)}$, $E_{(\beta-Ga_2O_3)}$ are the total energy after adsorption, the energy of C₂H₄ and the energy of β -Ga₂O₃, respectively.

In addition, the charge density difference $\Delta\rho$ can be obtained as follow:

$$\rho = \rho_{(C_2H_4/\beta-Ga_2O_3)} - \rho_{(C_2H_4)} - \rho_{(\beta-Ga_2O_3)} \quad (2)$$

where $\rho_{(C_2H_4/\beta-Ga_2O_3)}$ is the charge density of the system after adsorption of C₂H₄ on the surface of β -Ga₂O₃. $\rho_{(\beta-Ga_2O_3)}$ is the charge density of the surface of β -Ga₂O₃ before adsorption of C₂H₄. $\rho_{(C_2H_4)}$ is the charge density of C₂H₄ before adsorption.

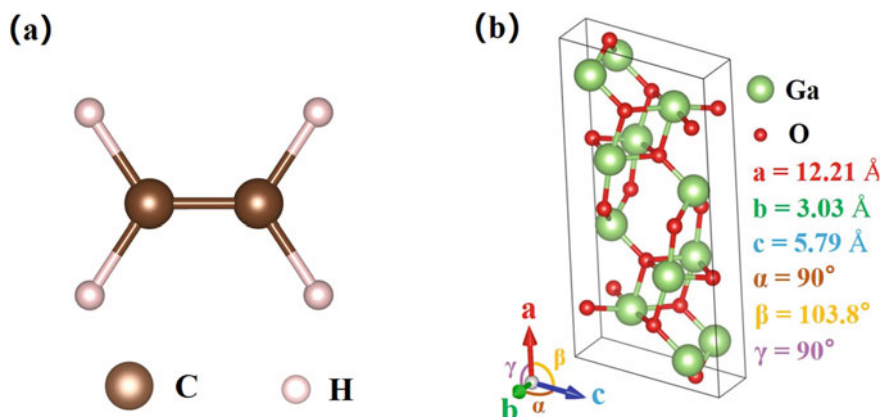


Fig. 1 Optimized C_2H_4 and Ga_2O_3 atomic structure

3 C_2H_4 Gas Molecule and β - Ga_2O_3 Structure

Before establishing the adsorption model, we performed a precise structural optimization on the crystal structure of C_2H_4 gas molecules and β - Ga_2O_3 , in order to obtain lattice constants consistent with the experimental results. The optimized geometry and lattice constants of C_2H_4 and β - Ga_2O_3 are shown in Fig. 1.

As shown in Fig. 1(a), the molecular structure of C_2H_4 is a linear structure. The C-C bond length is 1.21 Å, and the C-H bond is 1.07 Å. As can be seen from Fig. 1(b), the lattice parameters of β - Ga_2O_3 are $a = 12.21$ Å, $b = 3.03$ Å, $c = 5.79$ Å, $\alpha = \gamma = 90^\circ$, $\beta = 103.8^\circ$, which are consistent with the experimental work [21]. Each unit cell contains four Ga_2O_3 molecular formula units. The Ga atoms in each β - Ga_2O_3 unit cell are mainly composed of tetrahedral coordination (Ga_1 , four O atoms around each Ga) and octahedral coordination (Ga_2 ; eight O atoms around each Ga). In β - Ga_2O_3 , the ratio of these two Ga atoms is 1:1. There are three coordination modes of O atom, in which the O_1 is bonded with two Ga_2 and one Ga_1 atom; the O_2 atom is bonded with three Ga_2 atoms and one Ga_1 atom; the O_3 atom is bonded with two Ga_1 atoms and one Ga_2 atom. The anion close-packed structure of β - Ga_2O_3 makes it easy to form O ion vacancies, resulting in an n-type semiconductor characteristic.

4 Adsorption Analysis of C_2H_4 Gas on β - Ga_2O_3 Surface

We choose 2D β - Ga_2O_3 crystal as the gas adsorption surface. The most stable adsorption structure system of C_2H_4 on the surface of β - Ga_2O_3 is shown in Fig. 2. It can be seen from the figure that the adsorption distance between C_2H_4 molecule and β - Ga_2O_3 is 2.75 Å. It can be judged by the calculation of the adsorption energy that the adsorption energy is -0.22 eV, where the negative sign indicates that the adsorption

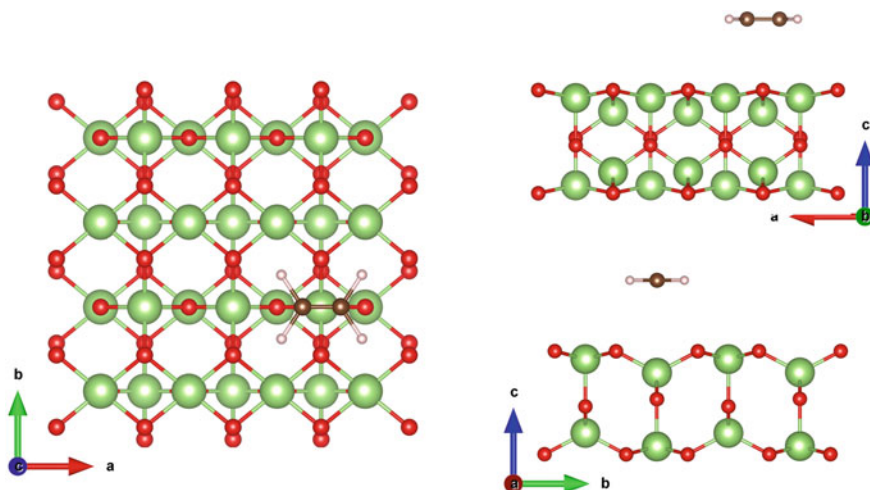


Fig. 2 Adsorption model of C₂H₄ on β -Ga₂O₃

process is an exothermic process, which proves that the surface of β -Ga₂O₃ has a strong adsorption of C₂H₄ gas molecules.

As shown in Fig. 3, from the charge density difference we found that the C₂H₄ gas transferred electrons to the β -Ga₂O₃ surface due to the adsorption reaction. C₂H₄ gas molecules act as electron donors, and the transferred electrons mainly surround the O atoms on the surface of β -Ga₂O₃, that is, the characteristics of strong electron acceptors. According to the above charge transfer phenomenon, C₂H₄ gas molecules have strong adsorption on the surface of β -Ga₂O₃.

Figure 4 and Fig. 5 show the total density of states (TDOS) and energy band structure diagrams of β -Ga₂O₃ before and after adsorption. Firstly, the bandgap value of β -Ga₂O₃ obtained by hybrid functional is 4.41 eV, which is consistent with the experimental value. Secondly, the TDOS diagram shows that the overall model after adsorption shifts to the left, and the energy required for electrons to transfer from the top region of the valence band to the bottom of the conduction band decreases. At the same time, the band gap of the model after adsorption is 3.65 eV. Comparing the energy band structure before and after adsorption of C₂H₄ molecules on the β -Ga₂O₃ crystal plane, the band gap of the β -Ga₂O₃ is 17% smaller than that before adsorption. From the charge density difference in Fig. 3, it can be seen that when C₂H₄ is adsorbed on the β -Ga₂O₃ crystal plane, electron transfer occurs, thereby reducing the band gap after adsorption. This shows that the conductivity of the model after adsorption increases, and when β -Ga₂O₃ is used as a gas sensor for C₂H₄, the resistance decreases.

Figure 6 shows the work function of C₂H₄ gas molecules before and after adsorption on the surface of β -Ga₂O₃, and the work function before adsorption is 7.92 eV. After adsorption, due to the charge transfer between the adatoms and the adsorption surface, the surface dipole moment changes, and the work function after adsorption

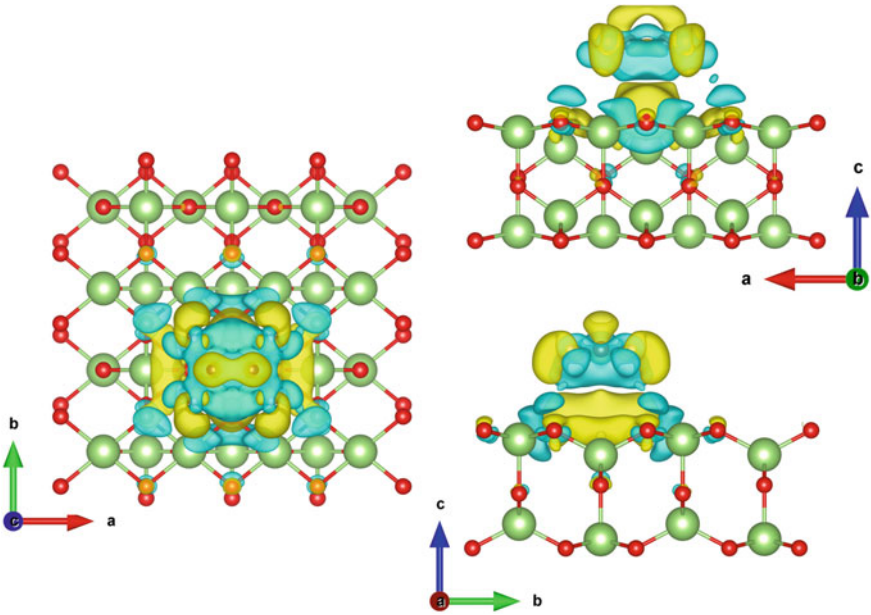
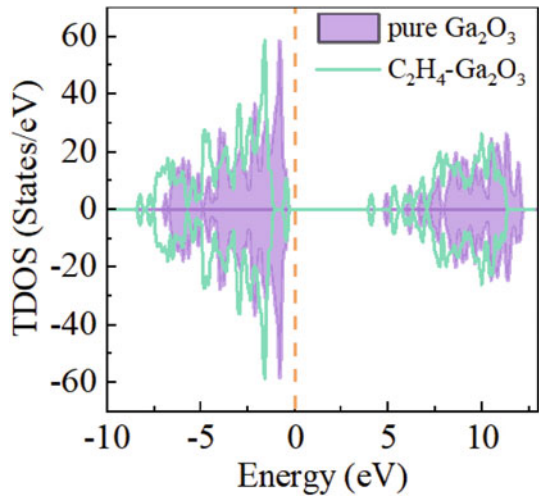


Fig. 3 Charge Density Difference of C_2H_4 on the surface of $\beta\text{-Ga}_2O_3$

Fig. 4 Electronic density of states of pure Ga_2O_3 and $C_2H_4\text{-Ga}_2O_3$



becomes 8.75 eV, an increase of 0.83 eV. The significant change of work function shows that $\beta\text{-Ga}_2O_3$ has the potential to be a work function gas sensor.

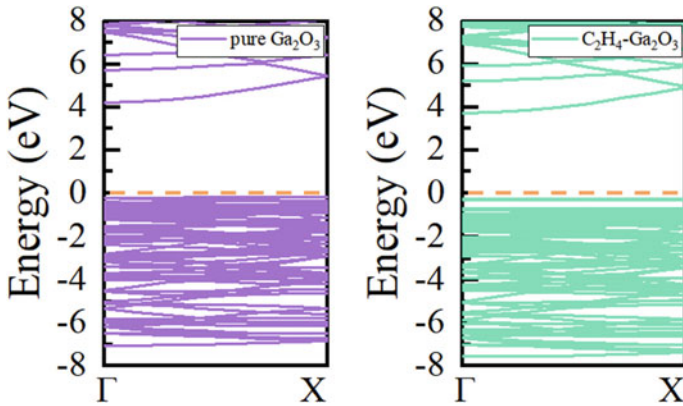
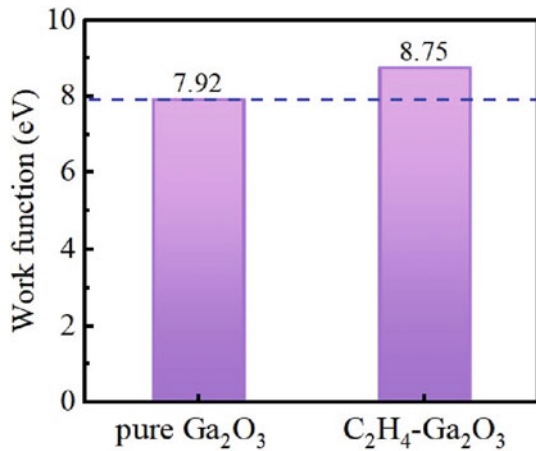


Fig. 5 Band structure of pure Ga₂O₃ and C₂H₄-Ga₂O₃

Fig. 6 Work function of C₂H₄ before and after adsorption



5 Conclusion

Through first-principle calculations, this work uses Abinit software to theoretically explore the detection performance of the fault characteristic gas C₂H₄ in transformer oil on the β -Ga₂O₃ crystal surface, and proves the application potential of β -Ga₂O₃ in gas sensors. The electronic behavior of β -Ga₂O₃ before and after C₂H₄ adsorption was determined according to the analysis of charge transfer, electronic density of states and energy band structure. During the adsorption process, β -Ga₂O₃ strongly adsorbs C₂H₄ gas, and C₂H₄ gas transfers electrons to β -Ga₂O₃, which leads to a decrease in the forbidden band width, that is, a decrease in resistivity. The discussion of the detection performance of β -Ga₂O₃ in this paper provides theoretical guidance for further experimental research.

References

1. Dong, X.X., Zhang, C., Ruan, J.J., et al.: Research and practices of dynamic thermal rating for oil-immersed power transformer. *High Volt. Eng.* **47**(6), 1959–1968 (2021)
2. Zhang, Y.Z., Sun, X., Tan, S., et al.: Adsorption characteristic of Rh-doped MoSe₂ monolayer towards H₂ and C₂H₂ for DGA in transformer oil based on DFT method. *Appl. Surf. Sci.* **487**, 930–937 (2019)
3. Gui, Y.G., Chen, Y., Zhang, X.X., et al.: Adsorption properties of Pd doped GaNNTs nanotubes to transformer oil dissolved C₂H₄ Gas. *High Volt. Eng.* **48**(4), 1462–1470 (2022)
4. Wang, X.C.: Research on optimization and improvement of analyzing acetylene content in transformer oil. *Transformer* **55**(7), 70–72 (2018)
5. Zhang, X.X., Cui, H., Zhang, J., et al.: Adsorption characteristic of Pd-4 cluster carbon nanotube towards transformer oil dissolved components: a simulation. *Appl. Surf. Sci.* **419**, 802–810 (2017)
6. De Faria Jr. H., Costa, J.G.S., Olivas, J.L.M.: A review of monitoring methods for predictive maintenance of electric power transformers based on dissolved gas analysis. *Renew. Sustain. Energy Rev.* **46**, 201–209 (2015)
7. Bakar, N.A., Abu-Siada, A., Islam, S.: A review of dissolved gas analysis measurement and interpretation techniques. *IEEE Electr. Insul. Mag.* **30**(3), 39–49 (2014)
8. Tang, S.R., Chen, W.G., Xu, L.N., et al.: Study on C₂H₂ detection characteristics of Ag-doped ZnO nanoparticle gas sensor. *China J. Sci. Instrum.* **37**(1), 15–23 (2016)
9. Wu, G.N., Yuan, H.M., Gao, B., et al.: Fault diagnosis of power transformer based on feature evaluation and kernel principal component analysis. *High Volt. Eng.* **43**(8), 2533–2540 (2017)
10. Hong, C.X., Zhou, Q., Zhang, Q.Y., et al.: Fabrication and sensing properties of ZnO based gas sensors to methane. *China J. Senors Actuat.* **30**(5), 645–649 (2017)
11. Jin, L.F., Chen, W.G., Tang, S.R., et al.: Metal-doped SnO₂ based H₂ /C₂H₂ Gas sensor array and its detection characteristics. *China J. Sci. Instrum.* **40**(5), 144–152 (2019)
12. Gao, T.Y., Chen, W.G., Gan, H.L., et al.: Investigation on C₂H₂ detection characteristics of gas sensor with various hierarchical ZnO nanostructures. *China J. Sci. Instrum.* **36**(3), 523–529 (2015)
13. Wang, J.X., Zhou, Q., Gui, Y.G., et al.: Adsorption properties of the C₂H₂ characteristic gas in oil by doped MoS₂. *High Volt. Eng.* **46**(6), 1962–1969 (2020)
14. Zhou, Q., Chen, Z.W., Zhang, S.L., et al.: Adsorption analysis of dissolved gas in oil based on density functional theory. *Electr. Power Eng. Technol.* **40**(1), 155–161 (2021)
15. Fleischer, M., Meixner, H.: Gallium oxide thin films: a new material for high-temperature oxygen sensors. *Sens. Actuators B Chem.* **4**(3–4), 437–441 (1991)
16. Gonze, X., Amadon, B., Antonius, G., et al.: The Abinit project: Impact, environment and recent developments. *Comput. Phys. Commun.* **248**, 107042 (2020)
17. Perdew, J.P., Burke, K., Ernzerhof, M.: Generalized gradient approximation made simple. *Phys. Rev. Lett.* **77**(18), 3865–3868 (1996)
18. Blöchl, P.E.: Projector augmented-wave method. *Phys. Rev. B* **50**(24), 17953–17979 (1994)
19. Heyd, J., Scuseria, G.E., Ernzerhof, M.: Erratum: Hybrid functionals based on a screened Coulomb potential. *J. Chem. Phys.* **118**, 8207 (2003). *J. Chem. Phys.* **124**(21), 219906 (2006)
20. Grimme, S.: Semiempirical GGA-type density functional constructed with a long-range dispersion correction. *J. Comput. Chem.* **27**(15), 1787–1799 (2006)
21. Peelaers, H., Van de Walle, C.G.: Brillouin zone and band structure of β -Ga₂O₃. *Status Solidi B* **252**(4), 828–832 (2015)

Research on Growth Characteristics of Water Tree in XLPE



Hong Yang, Xiaokai Meng, Zhumao Lu, and Wei Wang

Abstract Water trees are one of the important reasons for the deterioration of XLPE insulation. How to quickly cultivate a water tree in XLPE that is consistent with the actual cable has always been a concern. The accelerated water tree aging was performed on cross-linked polyethylene samples using a 10 kHz high-frequency high-voltage power supply. Different induction conditions were set for comparison, and the growth characteristics of water trees were observed, the aspect ratio and fractal dimension of water trees were counted. The research results show that in water tree cultivation, if the water does not fully enter the defect, there will be bubbles at the tip, forming a local high field area and inducing the formation of an electric tree. To induce the formation of water trees, moisture must be full of defects. Up to 10 kHz, increasing the voltage frequency will not change the morphology of the water tree, but will accelerate the growth of the water tree. Under the action of high-frequency voltage, the water tree grows in a fan shape from the knife edge to the outside, and the growth rate of the water tree is nonlinear. The fractal dimension of the water tree does not change with the growth of the water tree. From the induction to the penetration, the fractal dimension of the water tree remains unchanged, with an average value of about 1.85.

Keywords Water tree · XLPE · High frequency · Growth

1 Introduction

Some medium and low voltage XLPE cables run in a high humidity environment for a long time, which may easily lead to the formation of water trees and lead to cable accidents [1]. Accelerated water tree aging culture in the laboratory is an

H. Yang · X. Meng · Z. Lu
State Grid Shanxi Electric Power Research Institute, Taiyuan, China

W. Wang (✉)
North China Electric Power University, Beijing, China
e-mail: ww790324@163.com

© Beijing Paiké Culture Commu. Co., Ltd. 2023
X. Dong et al. (eds.), *The proceedings of the 10th Frontier Academic Forum of Electrical Engineering (FAFEE2022)*, Lecture Notes in Electrical Engineering 1054, https://doi.org/10.1007/978-981-99-3408-9_87

important means of water tree research [2, 3]. In the current study, different levels and frequencies of applied voltages lead to different growth characteristics of water trees [4, 5]. J. Sletbak [6] accelerated water tree aging for XLPE cables with different voltage levels, and found that when the applied voltage was increased from 50 Hz to 5 kHz, the water tree induction time became shorter and the growth rate became faster; Peter werelius et al. [7] used Power frequency voltage accelerates the aging of water trees, and found that as the aging time of water trees increases, the dielectric properties of XLPE also change; Sverre Hvidsten [8] and others found that different applied voltages will produce water trees with different morphologies, long and sparse. Water trees and dense and non-penetrating water trees; Zhou Kai [9] and others found that there were significant differences in the size and morphology of water trees in cross-linked polyethylene materials under four rectified voltages with different polar frequencies of 400 Hz.

At present, most of the researches focus on the effects of cable water tree aging and water tree aging characteristics. There are few studies on the water tree aging process, and the research on the aging rate and morphological characteristics of water trees.

In this paper, the water jet electrode method was used to accelerate the aging of the XLPE material under the condition of a high-frequency high-voltage power supply of 10 kHz and 5.5 kV, and the length of the water tree was calculated by continuous observation of the water tree. Through the continuous observation of water trees, the aspect ratio and fractal dimension of water trees were counted, and the growth characteristics of water trees were studied.

2 Sample Preparation and Test Methods

2.1 Sample Preparation

Select 8.7/10 kV XLPE cable to make the sample. Strip the cable outer jacket, copper shield, inner and outer semiconductor layers. The cross-linked polyethylene insulating layer was taken out, and a rectangular sample of 50 mm × 50 mm × 4.7 mm was made by a mold, and an area with a central diameter of 20 mm was taken as the accelerated water tree aging area. The experiment adopts the water jet electrode method, and the blade is pressed into the interior along the direction perpendicular to the surface of the sample. As shown in Fig. 1, three knife edges are formed on the surface of the sample, the length of the knife edge is 3 mm, and the insulation thickness is 2.5 mm. Defects of cross-linked polyethylene.

Fig. 1 XLPE sample schematic

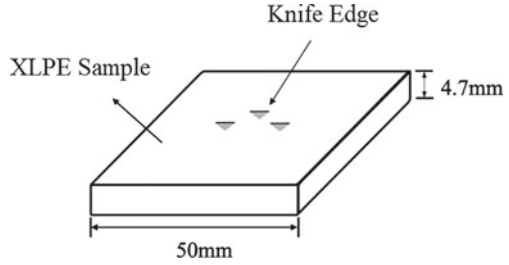


Fig. 2 Water tree aging experiment platform



2.2 Test Methods

The accelerated water tree aging test was carried out on the XLPE flake samples using the cup-shaped experimental tank recommended by the IEC/TS 61,956 standard, and an appropriate amount of 1 mol/L sodium chloride solution was added to the experimental tank. The power supply applied a high frequency voltage of 10 kHz and an effective value of 5.5 kV for water tree aging. The temperature of the aging experiment is room temperature 23–25 °C, and the experiment is carried out in an atmospheric pressure environment. The appearance of the experimental platform is shown in Fig. 2.

3 Results and Analysis

3.1 Observation and Statistics of Water Tree Samples

A piece of cross-linked polyethylene sample was taken every other day. Cut the sample with a thickness of about 200 m in the vertical direction of the knife edge, soak it in methylene blue at 90 °C for 4 h, and wipe it with a dust-free cloth after it is fully dyed, and then place it under a microscope to observe the growth of water branches., and measure the length and lateral width of the water tree growing in the direction of the knife edge. Take 2 values at each knife edge, and observe and count 6 values for each test sample. The length and width of the water tree were measured

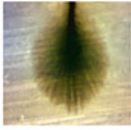
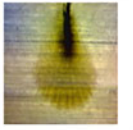
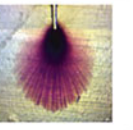
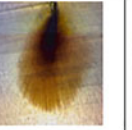
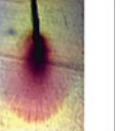





Water tree					
Aging time	1 day	2 days	3 days	4 days	5 days
Length (mm)	0.42-0.8	1.06-1.39	1.28-1.49	1.27-1.74	1.39-1.66
Width (mm)	0.21-0.51	0.46-0.65	0.65-0.76	0.58-0.84	0.88-1.24
Water tree					
Aging time	6 days	7 days	8 days	9 days	10 days
Length (mm)	1.51-1.85	1.67-1.90	1.76-2.09	1.76-1.97	1.88-2.12
Width (mm)	0.64-1.03	0.87-1.18	0.56-0.62	0.63-0.94	0.7-0.95

Fig. 3 Statistics on the length and width of water tree in different aging time

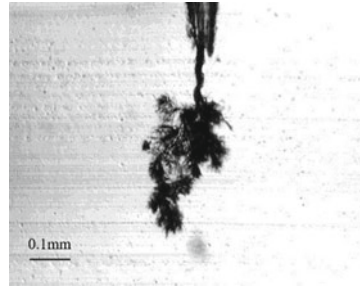
using the software provided with the microscope. The statistical results are shown in Fig. 3.

From the perspective of length, the growth length of water tree shows a parabolic relationship with time. The initial stage of water tree growth (1–3 days) grows rapidly, and the length increases with the increase of aging time. However, the growth of water trees slowed down after 3 days of aging. From the perspective of width, in the early stage of aging, the width of water tree increased with time, but in the middle stage of aging, there was no obvious relationship between the width of water tree and time.

3.2 Conditions for the Formation of Water Trees

Since some scholars have different cultivation conditions for water trees, and they have reached a unified conclusion about the formation conditions of water trees, under the aforementioned experimental conditions, this paper made a set of comparative experiments, and one of the two groups of experimental tanks was pumped. Vacuum treatment, one is not taken, under the condition of no vacuum, because of the surface tension of water, the water fails to enter the defect, so that there are air bubbles at the tip of the defect. The experimental tank was vacuumed, and the defect was filled with sodium chloride solution. The samples were aged separately under the same external application conditions. The experimental results showed that in the presence of air

Fig. 4 Bubble-induced electrical tree



bubbles at the tip, no water tree was induced for up to 20 days. If the test voltage is increased, the cross-linked polyethylene samples will directly induce the formation of electrical trees, as shown in Fig. 4. The samples that have been vacuumed can basically successfully induce water trees. Through the simulation calculation of the electric field distribution of the needle tip, it is found that when there is an $r = 2 \mu\text{m}$ bubble at the tip, the maximum field strength at the tip is about 6 times that without bubbles. It can be seen that if the experiment needs to induce the formation of water trees, it needs to exist in the presence of water and electric field at the same time, and the intensity of the electric field cannot be too high, otherwise the formation of electric trees will be induced. Therefore, we especially suggest that it is very important to get sufficient water into the defect interior in cultivating water trees.

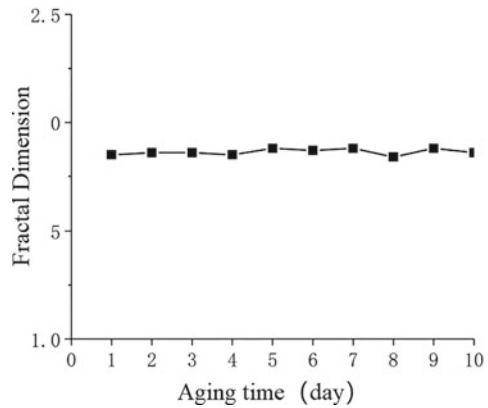
3.3 *The Effect of Voltage Frequency on the Growth of Water Trees*

Since this experiment uses a higher frequency, there is currently no basis for research on whether the increase in frequency will affect the change of water tree morphology. Therefore, this paper compares the 10 kHz situation with other scholars' 400 Hz and 3 kHz water tree morphology characteristics. The morphological characteristics of the water tree are shown in Table 1.

Table 1 Morphological characteristics of water tree under different frequencies

Frequency	Aging time	Length/Width (mm)
400 Hz	20 days	0.275/0.249
3 kHz	7 days	0.35/0.288
10 kHz	3 days	1.42/0.7

Fig. 5 Fractal dimension of water tree



3.4 Water Tree Fractal Dimension

After converting the water tree image into a binarized image, the box-counting dimension method [10] is used to conduct fractal dimension statistics on the water tree induced by the water jet electrode every day. The calculation method is as follows:

$$Dim_B F = \lim_{\delta \rightarrow 0} ((\log N_\delta(F)) / -\log \delta) \quad (1)$$

In the formula: F is the non-empty bounded subset of R^n , and $N_\delta(F)$ is the minimum number v of the set whose diameter is at most δ that can cover F .

The results (see in Fig. 5) show that the fractal dimension of water trees maintained at about 1.85 for 10 days of waterjet electrode culture. By referring to the literature [11], it is known that the fractal dimension of water trees is basically maintained at about 1.85.

This shows that the use of 10 kHz voltage for water tree cultivation can improve the growth rate of water trees without changing the morphology of water trees, so it can improve the efficiency more efficiently.

4 Conclusion

In water tree cultivation, if the water does not fully enter the defect, there will be bubbles at the tip, forming a local high field area and inducing the formation of an electric tree. To induce the formation of water trees, moisture must be full of defects.

Up to 10 kHz, increasing the voltage frequency will not change the morphology of the water tree, but will accelerate the growth of the water tree.

Under the action of high-frequency voltage, the water tree grows in a fan shape from the knife edge to the outside, and the growth rate of the water tree is nonlinear.

The fractal dimension of the water tree does not change with the growth of the water tree. From the induction to the penetration, the fractal dimension of the water tree remains unchanged, with an average value of about 1.85.

This shows that the use of 10 kHz voltage for water tree cultivation can improve the growth rate of water trees without changing the morphology of water trees, so it can improve the efficiency more efficiently.

Acknowledgements This work was supported by the science and technology project of State Grid Shanxi electric power company under Grant 52053020000V.

References

1. Li, J., Zhao, X., Yin, G., Li, S., Zhao, J., Ouyang, B.: The effect of accelerated water tree ageing on the properties of XLPE cable insulation. *IEEE Trans. Dielectr. Electr. Insul.* **18**(5), 1562–1569 (2011)
2. Thomas, A.J., Saha, T.K.: Statistical analysis of diagnostic indicators during an accelerated ageing experiment for XLPE cable specimens. *IEEE Trans. Dielectr. Electr. Insul.* **19**(1), 274–282 (2012)
3. Karakelle, M., Phillips, P.J.: The influence of structure on water treeing in crosslinked polyethylene: tree morphology and the influence of organic contaminants. *IEEE Trans. Electr. Insul.* **24**(6), 1101–1108 (1989)
4. R. Patsch and J. Jung: Water trees in cables: generation and detection. *IEE Proc. Sci. Meas. Technol.* **146**(5), 253–259 (1999)
5. Bulinski, A.T., Bamji, S.S., Densley, R.J.: The effects of frequency and temperature on water tree degradation of miniature XLPE cables. *IEEE Trans. Electr. Insul.* **EI-21**(4), 645–650 (1986)
6. Sletbak, J., Botne, A.: A study of inception and growth of water trees and electrochemical trees in polyethylene and cross linked polyethylene insulations. *IEEE Trans. Electr. Insul.* **EI-12**(6), 383–389 (1977)
7. Werelius, P., Tharning, P., Eriksson, R., Holmgren, B., Gafvert, U.: Dielectric spectroscopy for diagnosis of water tree deterioration in XLPE cables. *IEEE Trans. Dielectr. Electr. Insul.* **8**(1), 27–42 (2001)
8. Hvidsten, S., Faremo, H., Benjaminsen, J.T., Ildstad, E.: Non-destructive diagnostic testing of service aged MV XLPE cables. In: Conference Record of the 2000 IEEE International Symposium on Electrical Insulation (Cat. No. 00CH37075), Anaheim, CA, USA, pp. 137–140 (2000). <https://doi.org/10.1109/ELINSL.2000.845476>
9. Zhou, K., Yang, M., Tao, W., Yang, D., Huang, M.: Water tree growth characteristics of cross-linked polyethylene power cable under single-polarity DC voltage. *High Voltage Eng.* **41**(04), 1075–1083 (2015). (in Chinese)
10. Li, Y., Sun, H., Xu, M.: Box-counting method and its application to the detection of fog using GMS-5 weather satellite data. *Bull. Sci. Technol.* (01), 29–31 (2003). (in Chinese)
11. Lanca, M.C., Marat-Mendes, J.N., Dissado, L.A.: The fractal analysis of water trees: an estimate of the fractal dimension. *IEEE Trans. Dielectr. Electr. Insul.* **8**(5), 838–844 (2001)

Pitch Angle Control of Wind Generation System Based on Wind Speed Prediction



Xia You, Bo Zhou, Youren Wang, Xiang'an You, Qingxi Zeng,
and Honghao Guo

Abstract For limitation of mechanical and electrical load, wind power generator system (WPGS) should keep constant power while running above nominal wind speed. Since hysteresis characteristic of pitch actuator, output power exists a big fluctuation when wind speed changes. This paper combines feed forward control based on wind speed prediction with single neural PID control to realize constant power control when wind speed is above rated value. BP neural network optimized by Genetic Algorithm is used to predict wind speed of next step, then the compensation value of feed forward pitch angle is given in advance according to predicted wind speed, thus compensate time-delay of pitch angle actuator. Simulation results show that with the produced constant power control strategy based on wind speed prediction, the output power of WTGS shows smaller fluctuation, thus can reduce mechanical load and prolong the service life of WTGS.

Keywords Wind speed prediction · Constant power control · BP neural network · Genetic Algorithm

X. You (✉) · B. Zhou · Y. Wang · Q. Zeng
College of Automation Engineering, Nanjing University of Aeronautics and Astronautics,
Nanjing 211100, China
e-mail: youxiajy@nuaa.edu.cn

B. Zhou
e-mail: zhoubo@nuaa.edu.cn

Y. Wang
e-mail: wangyrac@nuaa.edu.cn

Q. Zeng
e-mail: jslyzqx@nuaa.edu.cn

X. You
Beijing Spacecrafts Limited Company, Beijing 100094, China

H. Guo
College of Automation, Nanjing University of Posts and Telecommunications, Nanjing 210023,
China
e-mail: ghh@njupt.edu.cn

© Beijing Paiké Culture Commu. Co., Ltd. 2023

X. Dong et al. (eds.), *The proceedings of the 10th Frontier Academic Forum of Electrical Engineering (FAFEE2022)*, Lecture Notes in Electrical Engineering 1054, https://doi.org/10.1007/978-981-99-3408-9_88

1005

1 Introduction

When wind turbine operates above rated wind speed, due to the limitation of mechanical and electrical loads, the pitch angle must be adjusted in time, so as to adjust the aerodynamic torque of the wind turbine and make the wind turbine output constant power. Because most of the pitch mechanism has time delay, the adjustment of pitch angle often lags behind the change of the wind speed, resulting in large fluctuations of the output power, thus the drive system bears a larger load. At present, the common methods of constant power control include PID control, neural network control, sliding mode control, etc. They are all feedback control methods based on deviation. The controller will start to adjust only when the output power deviates from the given power [1–5]. Literature [6] uses Newton–Raphson algorithm to estimate effective wind speed according to real-time power, and gives appropriate feedforward pitch angle according to estimated wind speed, which improves the effect of constant power control. But the above method does not compensate for the delay of the pitch angle adjustment mechanism. This paper proposes a pitch angle control strategy based on the combination of predictive wind speed feedforward and single neuron PID control to compensate time-delay of pitch angle adjustment mechanism [7–9].

2 Mathematical Model of Variable Pitch WPGS

2.1 Wind Turbine Model

From the aerodynamics of the wind turbine, the expressions of the mechanical power P_m and aerodynamic torque T_m captured by the wind turbine are as follows:

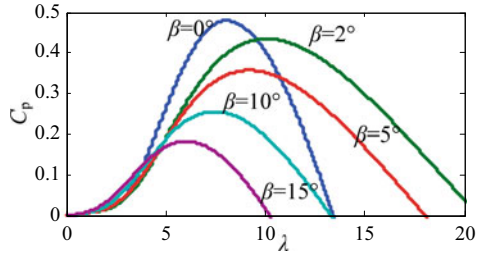
$$P_m = \frac{1}{2} \rho S C_p(\beta, \lambda) v^3 \quad (1)$$

$$T_m = P_m / \omega \quad (2)$$

where ρ is air density, S is the swept area of wind wheel, β is pitch angle, λ is tip speed ratio, v is wind speed, ω is rotation speed of wind turbine.

The power coefficient curve of C_p is shown in Fig. 1. It can be seen that C_p can be changed by adjusting pitch angle β . The output power P_m also changes accordingly.

Fig. 1 Power coefficient curve



2.2 Transmission System Model

The transmission model of the direct-drive WPGS can be obtained from the mechanical Eq. (3).

$$T_m - T_e = B\omega + J \frac{d\omega}{dt} \tag{3}$$

where, T_m is the output torque of the wind turbine, T_e is the generator resistance torque, B is the friction coefficient, and J is the moment of inertia.

2.3 Model of Double Salient Electro-Magnetic Generator

Double salient electro-magnetic generator (DSEG) is a new type of brushless generator with the advantages of simple structure, flexible control, high reliability, low cost and low starting torque. According to literature [10], we can build the Model of DSEG. The output voltage and torque will change with the variation of excitation current. Power signal feedback method is used to adjust the electromagnetic torque of DSEG by controlling the excitation current at low wind speed, so as to realize maximum power point tracking (MPPT) control at low wind speed.

2.4 Pitch Angle Actuator Model

Most of the pitch actuators of large wind turbines are of crank-slider structure. The electro-hydraulic proportional valve is used to control the servo hydraulic cylinder system. The system equation is:

$$\frac{d\beta}{dt} = \frac{1}{T_\beta}(\beta_r - \beta) \tag{4}$$

Taking the time-delay characteristics of the hydraulic drive system into account, the transfer function of pitch actuator can be obtained:

$$\frac{\beta(s)}{\beta_r(s)} = \frac{1}{T_\beta s + 1} e^{-\tau s} \quad (5)$$

where, β is the output pitch angle, β_r is the reference pitch angle output by the constant power controller, T_β is the time constant of the inertia link, and τ is the time delay of the hydraulic transmission system.

3 Wind Speed Prediction Based on Genetic BP Neural Network

3.1 Principle of Genetic Algorithm

Genetic algorithm is a parallel random search optimization method. When genetic algorithm is used for optimization, the parameters to be optimized are coded into individuals by binary or real number coding method, and then the individuals are screened according to fitness function and through selection, crossover and mutation operations. The individuals with good fitness are retained, and the individuals with poor fitness are eliminated. The new population is superior to the previous generation. The iteration is repeated until the maximum evolution algebra or the specific fitness value is reached, and the optimal individual is obtained.

3.2 Introduction to BP Neural Network

BP neural network is a multilayer feedforward neural network. BP neural network is composed of input layer, one or more hidden layers and output layer. In the forward transmission of signals, the input signals are processed layer by layer from the input layer to the hidden layer until the output layer. The neuron state of each layer only affects the neuron state of the next layer. If output cannot reach the expected output, the error will be back-propagated, and the weight and threshold will be changed.

3.3 Genetic BP Neural Network Prediction Flow

The Genetic BP neural network prediction includes four parts: the determination of BP neural network structure, the optimization of initial weights and thresholds, the training of BP neural network, and BP neural network prediction.

- 1) Structure determination of BP neural network. The structure of BP neural network is determined according to the number of input and output parameters. The wind speed at the next moment is predicted according to the historical wind speed at the first three points. Therefore, BP neural network has three input parameters and one output parameter. The number of nodes in the hidden layer can be selected as 5 according to experience. The structure of BP neural network can be set as 3-5-1, with $3 \times 5 + 5 \times 1 = 20$ weights and $5 + 1 = 6$ thresholds. The real number encoding method is adopted, and the individual encoding length is $20 + 6 = 26$.
- 2) Genetic algorithm optimization. Genetic algorithm is used to optimize the initial weight and threshold of BP neural network, so that the optimized BP neural network can better predict the function output. The elements of genetic algorithm to optimize BP neural network include population initialization, fitness function determination, selection operation, crossover operation and mutation operation. Through genetic algorithm optimization, individuals with the highest fitness are found, and the initial weights and thresholds of BP neural network to be trained are determined.
- 3) BP neural network training. The following steps are included:
 - Step 1: input and output data normalization.
 - Step 2: Calculate hidden layer output.
 - Step 3: Calculate output layer output.
 - Step 4: Error calculation.
 - Step 5: Update weights and thresholds.
 - Step 6: Judge whether the algorithm iteration is over. If not, return to Step 2.
- 4) BP neural network prediction. Input the test data into the trained BP neural network, use BP neural network to predict the corresponding output, and compare the actual output with the theoretical output to show the prediction error.

4 Pitch Control Based on Predictive Wind Speed Feedforward

4.1 Pitch Angle Controller

The pitch compensation control based on predictive wind speed feedforward is introduced. The system combines predictive pitch angle control with single neuron PID control to control the change of pitch angle. The block diagram of pitch angle

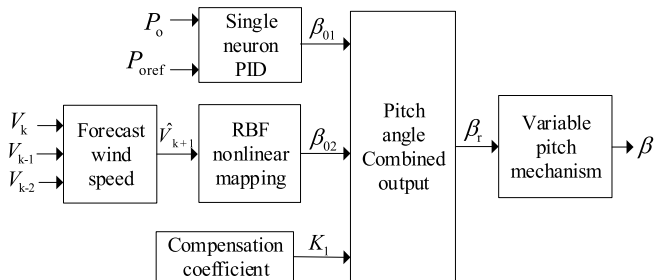


Fig. 2 Block diagram of pitch angle controller based on predictive wind speed feedforward

controller is shown in Fig. 2. When the wind speed change is predicted, the feed-forward controller will give the compensation amount β_{02} in advance. To avoid overshoot of pitch angle, the pitch angle β_{01} output by PID control is multiplied by a smaller coefficient K_1 when wind speed changes. After the wind speed is stable, the output of PID control is output normally, thus effectively avoiding overshoot of pitch angle.

4.2 Modeling of Nonlinear Relationship Between Pitch Angle and Wind Speed

There is a nonlinear relationship between the pitch angle and the wind speed. In order to obtain the feedforward compensation amount, take the wind speed $V = [9 \ 10 \ 11 \ 12 \ 13 \ 14 \ 15 \ 16]$ and obtain the desired pitch angle compensation amount $\beta_{02} = [10^{-5} \ 1.2 \ 4.25 \ 10 \ 14.5 \ 17.86 \ 20.7 \ 23.13]$ of corresponding wind speed through simulation. RBF neural network is used to establish the nonlinear mapping of wind speed and compensation angle, so that the compensation amount of pitch angle can be given in real time according to predicted wind speed.

5 Simulation Study and Results Analysis

Taking the wind speed data of a wind farm in Jiangsu as an example, the genetic BP neural network is used to predict wind speed. The wind speed of first 600 s is taken as training data, and the last 100 s is taken as prediction data. First, the initial weight and threshold of the BP neural network are optimized by genetic algorithm, and then the BP neural network is trained by the training data, Finally, the trained BP neural network is used to predict wind speed. The solid line in Fig. 3 is the predicted wind speed, and the dotted line is the actual wind speed. It can be seen that the predicted wind speed curve almost coincides with the actual wind speed curve.

Fig. 3 Predicted wind speed and actual wind speed

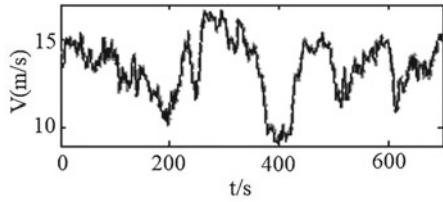


Fig. 4 Response curve of measured wind speed feedforward under step wind speed

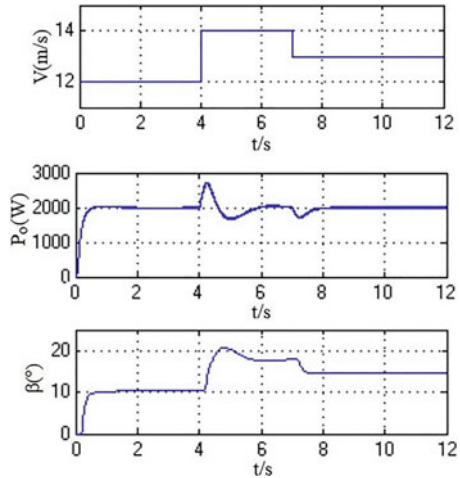


Figure 4 and Fig. 5 respectively simulate the response under step wind speed. It can be seen that: 1) In predicted wind speed feedforward control mode, the pitch angle starts to adjust at the moment of wind speed jump without delay, the output power fluctuation is smaller. 2) When the wind speed increases, the pitch angle increases to ensure constant power output.

Figure 6 and Fig. 7 respectively simulate the response under random wind speed. It can be seen that after initial state, output power fluctuation of predicted wind speed feedforward control is smaller, and the control effect is better.

Fig. 5 Response curve of predicted wind speed feedforward under step wind speed

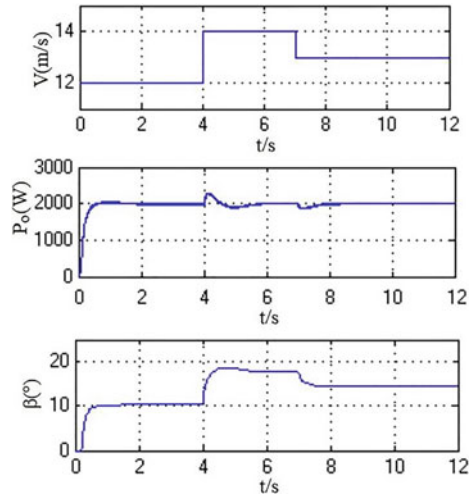


Fig. 6 Response curve of measured wind speed feedforward under random wind speed

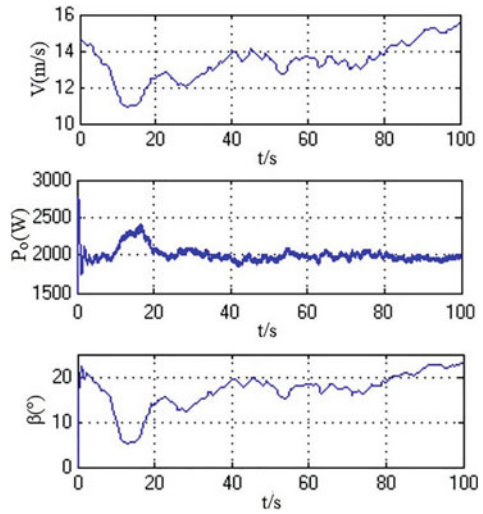
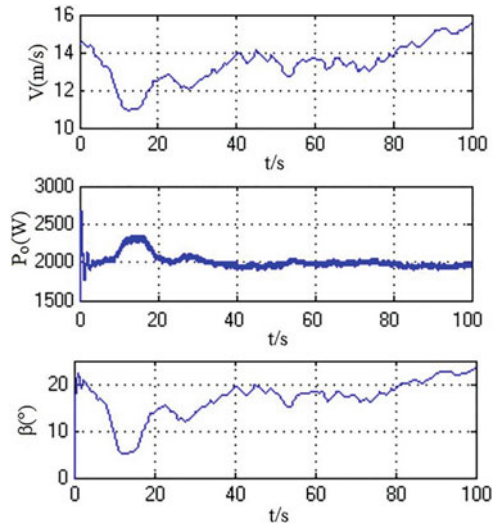


Fig. 7 Response curve of predicted wind speed feedforward under random wind speed



6 Conclusions

This paper proposes a pitch angle control method based on wind speed prediction feedforward. It uses genetic algorithm optimized BP neural network to predict wind speed, and obtains the corresponding pitch angle feedforward compensation based on RBF neural network according to the predicted wind speed. The simulation shows that the control effect using predicted wind speed feedforward is better than measured wind speed feedforward method. The output power of the former is more stable.

Acknowledgements This research was funded by NUAA special project of graduate education and teaching reform (2023YJXGG-B04), NUAA cultivation project of graduate education and teaching reform (ZDH-YJSJG202205), NUAA research project of graduate education and teaching reform (2021YJXGG08), NUAA special project of three aspects of education, National Basic Research Program of China (2007CB210302), and Basic Scientific Research Expenses of NUAA (NS2012089). The authors gratefully acknowledge all the people who contribute to this work.

References

1. Qiao, Y., Hao, S., Hao, W., Shang, Y., Wang, H., Sun, Z.: Maximum power tracking and constant power control of wind turbine based on integral sliding mode control. *J. Suzhou Univ. Sci. Technol. (Nat. Sci. Ed.)* **38**(2), 61–67 (2021). (in Chinese)
2. Su, X., Zhu, L., Jin, S., Zhang, F., Sun, D.: Research on direct power control for brushless doubly-fed wind power generator with a novel hybrid rotor. *Trans. China Electrotech. Soc.* **35**(3), 494–501 (2020). (in Chinese)

3. Zhou, Z., Wang, C., Guo, L., Xu, W., et al.: Output power curtailment control of variable-speed variable-pitch wind turbine generator at all wind speed regions. *Proc. CSEE* **35**(08), 1837–1844 (2015). (in Chinese)
4. Xiao, X., Wang, H., Wu, Y., Zhang, Y., et al.: Coaxial dual motor with master-slave structure model-predictive direct torque control speed sensorless control strategy based on double sliding mode estimation. *Trans. China Electrotech. Soc.* **36**(5), 1014–1026 (2021). (in Chinese)
5. Iqbal, A., Singh, G.K.: PSO based controlled six-phase grid connected induction generator for wind energy generation. *China Electrotech. Soc. Trans. Electr. Mach. Syst.* **5**(1), 41–49 (2021)
6. He, Y., Huang, S., Du, J., et al.: Variable pitch control of wind turbine based on feed forward. *Power Syst. Prot. Control* **40**(3), 15–20 (2012). (in Chinese)
7. Sizhao, L., Di, Z., Kai, L., Siqi, L.: A distributed feedforward control method for power electronic transformers. *China Electrotech. Soc. Trans. Electr. Mach. Syst.* **4**(4), 319–328 (2020)
8. Li, Y., Zhang, Z., Li, K., Zhang, P., Gao, F.: Predictive current control for voltage source inverters considering dead-time effect. *China Electrotech. Soc. Trans. Electr. Mach. Syst.* **4**(1), 35–42 (2020)
9. Dan, H., Zeng, P., Xiong, W., Wen, M., Su, M., Rivera, M.: Model predictive control-based direct torque control for matrix converter-fed induction motor with reduced torque ripple. *China Electrotech. Soc. Trans. Electr. Mach. Syst.* **5**(2), 90–99 (2021)
10. You, X., Zhou, B., Zuo, G., Guo, H.: A novel algorithm for fast and adaptive maximum power point tracking of wind energy generation system. *Adv. Mater. Res.* **383–390**, 3633–3638 (2012)

An Experiment on the Characteristics of Sturgeon Perceiving and Avoiding Current Fields in Water



Nan Liu, Ke Zhong, Yunfan Ye, Jiahao Chen, Bo Tan, Huiwu Wang, and Hailiang Lu

Abstract Single-ground HVDC transmission line and auxiliary anode in impressed current cathodic protection will inject DC current to the ground and likely impact the actions of fish in the surrounding waters. Two rod electrodes were utilized to inject DC current into the water and simulate an inhomogeneous current field. Sturgeon was chosen as the experimental species. On the aquarium, a wireless camera was installed to record video of the fish's behavior. A three-dimensional tracking algorithm was developed to quantify the response of sturgeon samples subjected to various voltages and to examine their trajectory and velocity. The trajectories of fish in varied DC current fields were recorded by varying the DC power source's output voltage. Findings indicate that sturgeon can detect the water's current and would turn at a particular current density. By statistically analyzing the current intensity at the turning places, the turning and bearing threshold was determined to be 0.5172 A/m^2 .

N. Liu · K. Zhong · Y. Ye · H. Wang · H. Lu (✉)
School of Electrical Engineering and Automation, Wuhan University, Wuhan 430072, China
e-mail: luhailiang@whu.edu.cn

N. Liu
e-mail: liunan@whu.edu.cn

K. Zhong
e-mail: zhongke@whu.edu.cn

Y. Ye
e-mail: yeyunfan@whu.edu.cn

H. Wang
e-mail: wanghuiwu@whu.edu.cn

J. Chen
Guangzhou Power Supply Bureau of Guangdong Power Grid Company, Ltd., Guangzhou 510630, China

B. Tan
Wuhan Branch of China Electric Power Research Institute, Wuhan 430072, China
e-mail: tanbo@springer.com

Keywords Inhomogeneous current field · Three-dimensional tracking program · Fish behavior · Current density

1 Introduction

HVDC is frequently utilized in China given to its various advantages. Yet, during the single-ground operation of HVDC, rated current will be injected straight to the ground, and the impressed current cathodic protection's auxiliary anode will also produce ground entry current. The conductivity of water is greater than that of soil, therefore once there is water adjacent to the entry site, the current will likely influence the behavior of aquatic organisms, particularly fish.

Previous researchers have built up a variety of platforms to study the influence of electromagnetic fields on fish behavior, obtaining positive results [1]. The scholar Prel has investigated the critical value of electric field intensity Irritation to many fish, utilizing a fishing net to confine the fish between electrode plates and control the plate's movement to amplify the electric field, and recording the critical value of electric field when the fish reacts visibly to the change in field intensity [2]. Yang Quanwei and his colleagues have used dipole electric field to test the fish's avoidance reaction, utilizing frame-by-frame method to record the fish's action of pause, turning back, and by-passing and the corresponding electric field strength, and determining the critical value of electric field when sturgeon of various months exhibit avoidance behavior [3].

With the development of electric fishing technology in the 1960s, researchers from all nations undertook studies on electric fishing. The scholar Privolnev observed that fish enter a paralyzed state when stimulated by a particular current density in the water, and he estimated the right voltage for electric fishing equipment [4]. Cai Houcai and his colleagues observed the behavior of fish in a direct current electric field, recording the fish's respiratory interruption rate, rate of side-fall, and balance full recovery time after power failure in varying electric field intensities, thereby establishing a correlation between electric field intensity and a variety of stimulating behaviors of fish [5].

In fish research, fish are anesthetized for manipulation when vaccinations, blood samples, and anatomies are required. The scholar Feng Guang-peng and his colleagues used to electrically anesthetize fish with varying voltages, recording their behavioral characteristics and serum biochemical index at various times after electrical anesthesia, thereby determining the practical utility of electroanesthesia [6]. David A. Sterritt and his colleagues administered electrical anesthesia to mature salmon. According to the data he collected, fish treated with electrical anesthesia had a significantly lower mortality rate than those treated with chemical anesthesia [7].

Relevant international standards can be found by searching for pertinent information: Per the CIGRE and IEC standards [8, 9], the limit of current density of an unprotected ocean ground pole is 6 to 10 A/m², based on the human body's safety

current, and the limit will be 40 to 50 A/m² after specific protective measures are taken. There are primarily the following limitations in the present research:

1. Using the observational method alone will result in an undue influence of subjective factors. Fish stimuli responses cannot be accurately measured. The precision is inadequate, and the rigor is absent.
2. In certain experiments, it is detrimental to fish. For instance, throughout the course of an experiment, experimental fish suffered paralysis, shock, breathing interruption, and floating, resulting in important data that harms fish and does not meet ecological and environmental protection standards.
3. The experimental environment's design cannot accurately simulate the actual project's current field.
4. Current worldwide critical value guidelines for current density are drawn from human safety standards and have a low reference value for fish studies.

For the aforementioned problems, it is possible to construct a platform for investigating the impact of electric current field on fish behavior in a comprehensive manner, based on a three-dimensional tracking program, describing fish's stimulating behavior objectively, conducting a systematic study of the effect of electric ground current on fish behavior without causing obvious harm to fish, and determining the relevant critical value. This experiment's results can inform the formulation and adjustment of applicable standards.

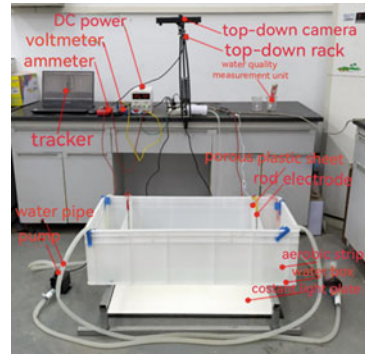
2 Experimental Program

2.1 *Experimental Platform and Experimental Process*

The experimental tank measures 70 cm 50 cm, and two stainless steel rod electrodes with a diameter of 6 mm are placed in the center of both sides of the tank to generate an asymmetrical current field. The electrodes of the rods are linked to the positive and negative terminals of the DC-regulated power supply, which is capable of providing a consistent output of 100 V voltage and 1A current. The experiment is designed to apply a maximum of 50 V of electricity. In accordance with the calculated circuit resistance values, the output of the power supply can meet the specifications. A wireless camera is mounted above the aquarium to record the behavior trajectory of fish. Figure 1 depicts the physical diagram constructed in accordance with the experimental platform design plan.

The three-month-old juvenile sturgeon utilized in the experiment was obtained from an aquatic market. The oxygen concentration was maintained for 15 days using an oxygenation pump and dechlorinated water. The water temperature was (28 ± 1) degrees Celsius, and the photoperiod lasted 12 h. Every sturgeon was fed once each day. The sturgeon were fasted for twenty-four hours before to the test. The testing technique was as follows: (the water level was 3.5 cm to ensure that the sturgeon

Fig. 1 Arrangement of the experimental platform



could swim freely and also to avoid strenuous movements in the vertical direction). Wait until the test fish becomes accustomed to the environment. After the test fish swam uniformly around the wall, the experiment was initiated and all researchers were instructed to remain silent so as not to influence the behavior of the sturgeon. As a control group, the camera recorded five minutes of natural swimming behavior prior to applying the voltage. Subsequently, DC voltages of 5 V, 10 V, 15 V, 20 V, 25 V, 30 V, 35 V, 40 V, and 45 V were applied to the electrodes, causing an unequal current field to form in the water. The camera recorded the swimming activity of the test fish for five minutes in an uneven current field. To allow the sturgeon to recuperate from the effects of electrical stimulation, a three-minute break was placed between test groups.

2.2 Selection of Experimental Fish

Important to the experimental design is the selection of test fish. Several varieties of fish are utilized in biological investigations. In this paper, we examine the correlation between the design of current fields and the behavioral responses of fish, and the electro-receptors of fish play a significant role in this correlation. In order to obtain relatively representative results, fish with electroreceptors should be selected when selecting fish, and sturgeon is the most common fish with electroreceptors in existing studies.

To conform to the experimental platform design and video tracking technology, the test fish species must meet the following criteria: 1. The test fish should be of moderate length to ensure that the experimental tank in the laboratory does not inhibit the fish's usual activity. 2. The test fish should be of moderate size to make breeding and experimenting easier. The test fish should have low water quality requirements and be less susceptible to water quality. The test species is more common and accessible.

Due to the length and size of mature fish with electroreceptors, it is difficult to conduct behavioral research under laboratory circumstances. A variety of electroreceptor-containing fish have been demonstrated [10], and sturgeon is the

species of electroreceptor-containing fish with the most individual experimental research; the sturgeon used in this study are 3-month-old hybrid sturgeon juveniles obtained by breeding.

2.3 Target Identification and Tracking Program Implementation

Mainstream target recognition techniques include the inter-frame difference-based method, the background difference-based method, and the optical flow equation-based method. In this experiment, motion target detection occurs predominantly against a static background (in the water tank), and since the background difference approach has a higher recognition rate against a static background, it is employed for programming.

At the initial phase, the background model is developed. The color information in the video captured by the camera is RGB three-channel information, which has a significant amount of data, a sluggish computing speed, and is susceptible to factors such as lighting. This experiment uses the approach of converting the color video acquired by the camera into a grayscale image, utilizing a weighted average algorithm to compute the grayscale value, as stated in the following equation, in order to reduce the number of calculations and increase computation speed.

$$I = 0.2989 \times r + 0.5890 \times g + 0.1140 \times b \quad (1)$$

where I is the gray value, r is the blue component, g is the green component, and b is the blue component. The weighting coefficients of each channel are obtained according to the different sensitivities of human eyes to different colors, and the coefficient ratio of the three channels is 3:6:1.

The statistical background model estimate method is used to determine the grayscale backdrop, and the average gray value R of each pixel point of the image over a period of time and the variance of gray value C throughout this period are computed. The pixels within this time interval are filtered under the following conditions:

$$|R(x, y) - B(x, y)| < C(x, y) \quad (2)$$

where $B(x, y)$ is the pixel gray value of the background image, $R(x, y)$ is the mean of the gray value of the pixel over time, and $C(x, y)$ is the variance of the gray value of the pixel over time.

The second phase involves frame-by-frame distinction. After establishing the grey background model, the images in the video can be greyed out frame by frame and then differenced from the grey background model. The difference method is then used to segment the target. The computation for the difference is provided in the following equation.

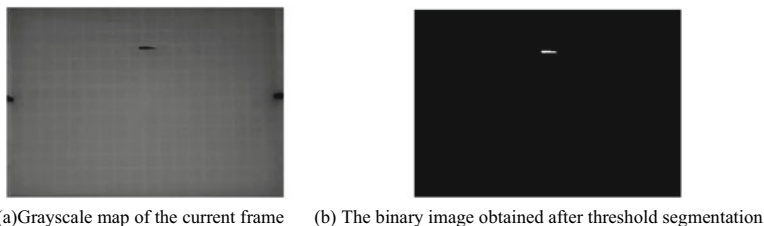


Fig. 2 Background Difference and Threshold Segmentation Objectives

$$D(x, y) = |N(x, y) - B(x, y)| \quad (3)$$

where $D(x, y)$ is the set of foreground image pixels obtained by differencing, that is the set of pixels of the identified target; $N(x, y)$ is the set of gray values of all pixels of the current frame image; $B(x, y)$ is the set of gray values of all pixel points of the background model.

Due to the slight change of illumination, there will still be a slight difference between the background pixels in the current frame and the background pixels in the background model. Therefore, in the current frame, the foreground pixel points are calculated to get a larger D value, while the background pixel points are calculated to get a smaller D value, and a threshold is needed to filter the pixel points to get the set of foreground (target) pixel points. The discriminant equation is:

$$F(x, y) = \begin{cases} 0, & D(x, y) < T \\ 1, & D(x, y) \geq T \end{cases} \quad (4)$$

where $F(x, y)$ is the set of pixels in the foreground (target); $D(x, y)$ is the set of pixels obtained by differencing the current frame and the background frame; T is the segmentation threshold, which can be calculated by the maximum interclass variance algorithm.

In the third phase, the segmentation threshold is chosen using the maximum inter-class variance technique. The maximum interclass variance technique iterates through all 0–255 grayscales, obtains two sets of pixels $C1$ and $C2$ when the threshold T is different grayscales, and calculates the inter-class variance between the two sets. When the interclass variance value produced is the maximum, the grayscale value is the segmentation threshold, at which time a stronger segmentation effect may be achieved and the target is separated (Fig. 2).

2.4 Calculation of Spatial Distribution of Current Density

Comprehensive calculation and analysis are required to further explain the change in swimming behavior of sturgeon in the current flow field. Using the finite element

approach, the spatial distribution of current density was computed. Conductivity of 0.03 S/m was utilized based on water quality tests, a 3D model was created based on the actual dimensions of the platform, and the steady state flow field was estimated. Current conservation equation is the model’s control equation:

$$\nabla \cdot \vec{J} = 0, \nabla \times \vec{E} = 0 \tag{5}$$

J is the current density vector, A/m²; E is the potential gradient vector, V/m. The conducting medium’s inherent relationship is:

$$\vec{J} = \gamma \vec{E} \tag{6}$$

γ is the electrical conductivity, S/m. The electrodes on both sides of the model obey the potential boundary condition:

$$\varphi_1 = U_1, \varphi_2 = 0 \tag{7}$$

The edges of the water tank obey the electrically insulated boundary conditions:

$$\vec{n} \cdot \vec{J} = 0 \tag{8}$$

Figure 3 displays the electric field intensity distribution and potential distribution of the aqueous section at a voltage of 10 V between the electrodes.

According to the calculations, the current density is very high close to the electrodes but quickly decreases further off. The middle region resembles a uniform current field since its wide area of current density is nearly constant. The current density is lowest in the tank’s corners.

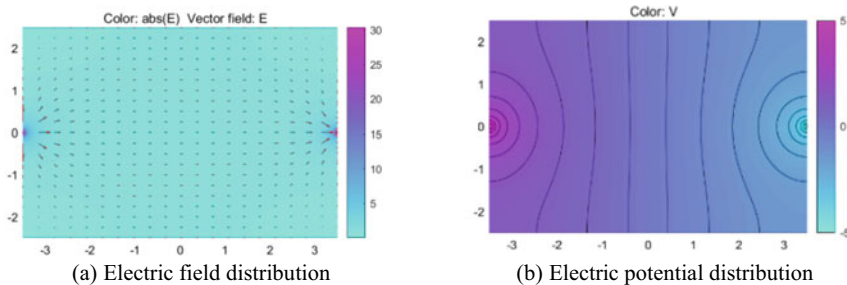


Fig. 3 Electric field distribution on cross section of water tank

3 Experimental Results

Four sturgeon samples (numbered 1–4) were utilized in the experiment. Video analysis of the control group and nine test groups with varying voltages revealed movement patterns in sturgeon; Fig. 4 displays the behavioural trajectory of sample 1. Sample 1’s running trajectories are exhibited in succession under a variety of voltage situations. Figure 5 illustrates the relationship between the instantaneous velocity of sample 1 and time variation. The instantaneous velocity of sample 1’s behavioural trajectory was calculated.

Sturgeons travel constantly around the tank’s edges under natural conditions and without power, as depicted in Fig. 4. When the applied voltage is between 5 and 25 V, it is possible to observe a change in the trajectory. When the voltage increases, the sturgeon continues to swim toward the electrode area, but alters its trajectory and accelerates as it approaches the tank’s edge.

Figure 5 demonstrates that the velocity profile exhibits numerous spikes, or transient fast swimming behaviours with shorter acceleration durations, as sturgeon swim faster as they approach the electrode when the applied voltage is between 5 and 35 V. When the applied voltage level exceeds 40 V, the velocity, in addition to the presence of short-time spikes, also has the same lower velocity trajectory points near

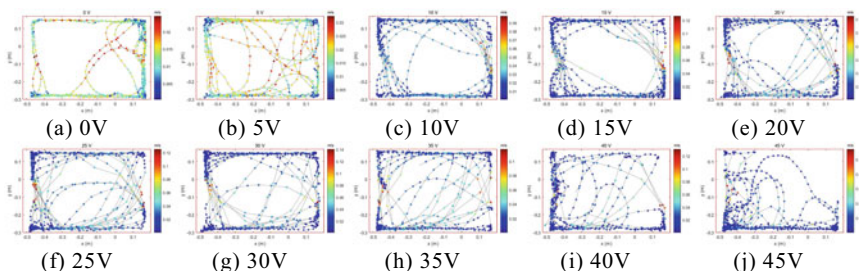


Fig. 4 Two-dimensional trajectory of sturgeon No.1 under different voltages

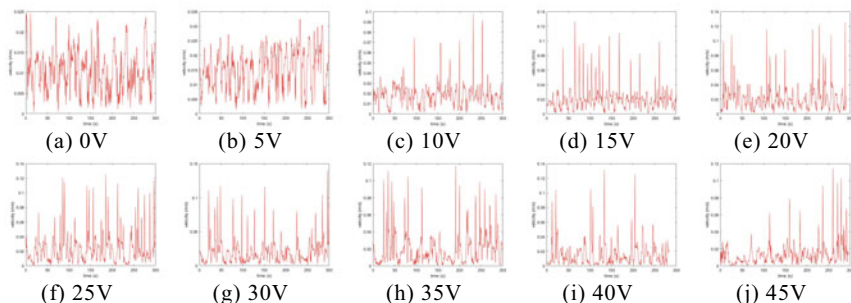


Fig. 5 Speed Chart of Sturgeon No.1 at Different Voltages

the electrode, because the voltage level is so high that the sturgeon samples in the vicinity of the electrode exhibit the short-time paralysis phenomenon and are unable to accelerate in time to swim away.

The findings indicated that the water circulation had a direct and considerable impact on the behaviour of fish. The current effect gradually increases as the current density increases. Yet, when the density of the current reaches a particular threshold, the impact on fish becomes more severe.

4 Discussion

A video target tracking program's ballistic results can only provide visual information for study. To demonstrate that the swimming behaviour of sturgeon has changed in the current setting, the trajectory data were statistically evaluated.

Through the above analysis, it was determined that the effect of a nonuniform flow field on the velocity of sturgeon is evident, and that the velocity increases greatly in the zone near the electrode. Thus, an analysis of the avoidance threshold was conducted based on the relationship between the current density and velocity at the trajectory point.

When the applied voltage was too high, velocity decrease points due to short-term paralysis appeared in the area near the electrode, and these trajectory points could not achieve good unity with the phenomenon of high current density causing the sturgeon to accelerate swimming away, so the experimental groups with smaller applied voltage were primarily considered when conducting the threshold analysis, which could eliminate the difficulty of phase superposition analysis. The first five experimental groups (5 V, 10 V, 15 V, 20 V, and 25 V) were subjected to threshold analysis.

Create a scatter plot illustrating the relationship between velocity and current density for each group of track points. The horizontal axis represents current density, while the vertical axis represents velocity. Each point along the trajectory correlates to a velocity and spatial current density. Use the minimum speed point of the big current density range as the dividing speed, and the maximum speed point of the small current density range as the dividing current density. Then, we may divide the zone of high current density that will not exhibit low velocity in the strictest meaning.

The trajectory points in the lower left region are mainly distributed in the left side, and there are very few scattered points near the current density dividing line; therefore, based on the principle that small probability events are impossible events, "low speed marching in the large current density region" is regarded as a small probability event, the statistical 5% small probability event is used as the threshold, and the 5% trajectory points with the largest current density are excluded. Figure 6 illustrates the outcome of threshold division. In the figure, the blue dashed line represents the speed dividing line and the current density dividing line, while the red dashed line represents the avoidance current density threshold line. The results are detailed in table 1.

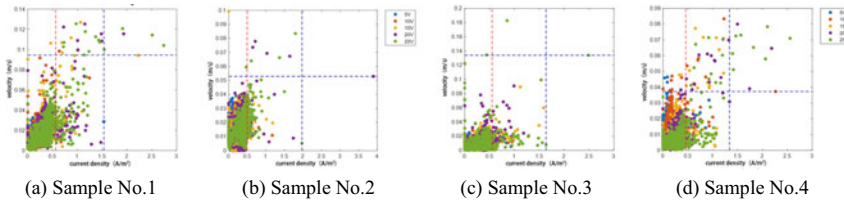


Fig. 6 Threshold Current Density Definition Results

Table 1 Calculation results of threshold current density

Sturgeon sample number	No.1	No.2	No.3	No.4
Dividing speed (m/s)	0.0941	0.0529	0.1341	0.0373
Dividing current density (A/m^2)	1.533	1.972	1.635	1.337
Threshold current density (A/m^2)	0.5641	0.4964	0.5517	0.4565
Average threshold current density (A/m^2)	0.5172			

5 Conclusion

- 1) Using a rod-shaped electrode to create a heterogeneous current field in the water, an experimental platform for examining the effect of heterogeneous current field on fish behaviour was constructed in order to determine if current field in water can influence fish behaviour. We use sturgeon as the experimental subject, administering 0–45 V voltage stepwise at either end of the electrode, observing fish behaviour trajectories at different voltages using a wireless camera to watch fish activity.
- 2) Using images captured by a wireless camera, we employ a three-dimensional tracking algorithm based on the background subtraction method to objectively describe fish behaviour trajectories at different voltages. The behaviour trajectories of fish subjected to various voltages were displayed, and their instantaneous velocities at various times were measured. It has been determined that both the swimming trajectory and swimming speed of fish are impacted by voltage differences.
- 3) When sturgeon reach places with a higher density of current, their initial wall swimming habit changes and they exhibit varying degrees of avoidance. By analyzing the position's current density, the critical current density for sturgeon to avoid in a non-uniform current field was determined to be $0.5172 A/m^2$. This information can serve as a guide for relevant engineering design, ensuring the building and operation of DC-grounded facilities.

References

1. Foroozandeh, E., Barjoei, P.D.: Fish behaviors in electromagnetic fields. *J. Mol. Biomark. Diagn.* **09**(1), 1000377 (2018)
2. Prel, E.T.: Effect of voltage gradient in an electrical field on threshold indices of fish response. *Acta Ichthyol. Piscat.* **21**(2), 37–44 (1991)
3. Yang, Q., Zhang, X., Guo, H., et al.: The avoiding response to dipole stimuli in juvenile sturgeon. *Acta Hydrobiol. Sin.* **40**(3), 6 (2016)
4. Priwalhuangfu, T.И., Zhong, Z.: Activity of fish in electric fields. *Chin. Fish.* (11), 30+29 (1960)
5. Cai, H., Lv, W., et al.: A preliminary study of crucian carp behaviour under the strong DC field. *Zhejiang Fish. Coll.* (4 issues), 282–286
6. Fen, G., Zhuang, P., et al.: Anaesthesia effects on behaviour and haematological biochemistry of juvenile *Acipenser schrenckii*. In: 77th Engineering Science and Technology Forum of Chinese Academy of Engineering Aquatic Science and Technology Forum (2008)
7. Sterritt, D.A., Elliott, S.T., Schmidt, A.E.: Electrical anesthesia for immobilizing adult coho salmon in freshwater. *North Am. J. Fish. Manag.* **14**(2), 453–456 (1996)
8. General Guidelines for HVDC Electrode Design, TB675. CIGRE (2017)
9. Design of earth electrode stations for high-voltage direct current (HVDC) links- General guidelines, IEC/TS 62344. Commission I E (2014)
10. He, D.: *Fish Behaviour*. Xiamen University Press (1998)

Research on Position Estimation Method of PMSM Based on SVPWM Control



Yu Ji, Zhe Chen, and Yue Hu

Abstract Most position estimation methods are based on back-EMF observer and high-frequency current injection. However, back-EMF observer is susceptible to current harmonics and function inaccurately when motor is under low-speed condition. Meanwhile, high-frequency current injection method is limited by switching frequency and its dynamic estimation performance still need to improve. This paper aims to improve the dynamic performance of rotor position estimation in the zero-low speed case of permanent magnet synchronous motors by analyzing the coupling between transient current and rotor position within one switching cycle and extracting rotor position information from the fundamental linear current variation within the effective voltage vector action time. Afterwards, a linear regression algorithm is adopted to fit the slope of the fundamental current for each voltage vector and the VHDL code of SVPWM module is obtained by MATLAB code generation and the rest codes by manual writing on Linux and FPGA open-source motor vector control platform to achieve high accuracy closed-loop control. Results show that low-speed and medium-speed position estimation error can be controlled within 5° under the control of proposed method and the convergence time can be reduced to 0.2 s. Thus, this research is positive to improve the accuracy of low-speed sensorless control and dynamic estimation performance.

Keywords Position estimation · Fundamental linear current · Code generation · FPGA · PMSM · SVPWM

Y. Ji (✉) · Y. Hu

Department of Electrical Engineering, School of Electronic Information and Electrical Engineering, Shanghai Jiao Tong University, Shanghai 200240, China
e-mail: 325108810@qq.com

Y. Ji · Z. Chen

Department of Electrical Engineering and Automation, College of Automation, Northwestern Polytechnical University, Xi'an 710000, China

© Beijing Paiké Culture Commu. Co., Ltd. 2023

X. Dong et al. (eds.), *The proceedings of the 10th Frontier Academic Forum of Electrical Engineering (FAFEE2022)*, Lecture Notes in Electrical Engineering 1054, https://doi.org/10.1007/978-981-99-3408-9_90

1027

1 Introduction

High-performance permanent magnet synchronous motor (PMSM) control systems require position sensors to detect rotor position in real time, but in complex electromagnetic environments and harsh operating conditions position sensors are susceptible to interference or even damage, endangering system safety. Thus, sensorless control has become a focus of motor control research. Recently, rotor current is widely used in PMSM sensorless control due to its extraordinary dynamic performance, and there has been a bunch of successful sensorless control system based on it. For example, Bui's team has presented one position estimation method by using the slope of the transient fundamental current under the action of the fundamental voltage vector in one PWM cycle [1]. The specific relationship between the fundamental current slope and the position is also obtained by using the artificial neural network slope identification instead of the least square method [2].

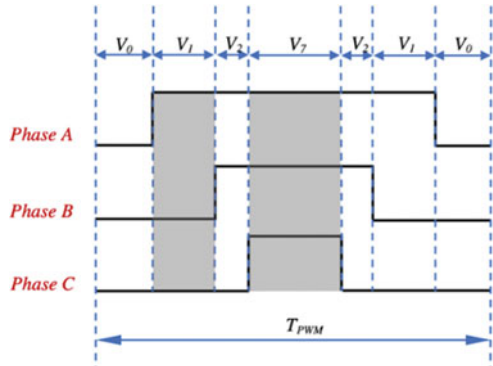
Undoubtedly, tons of calculation such us data acquisition, data processing and curve fitting will be involved in this current-position estimation method. When the motor is under high-speed condition, it is very likely that long calculation-time will lead to estimation deviation, affecting the performance of motor. To solve this problem, this paper selects the rotor current slope under the action of a specific voltage vector for position estimation based on SVPWM control. In other words, this method doesn't collect the whole section of current signal for position estimation, which greatly reduces the amount of calculation in position prediction, and solves the problem of position estimation delay at high motor speed.

On the choice of control chip, FPGA is widely favored for its rapidity and parallelism, while VHDL also has high flexibility and simplicity [5]. However, there are a lot of trigonometric operations and irrational number operations in SVPWM algorithm. Since FPGA can only realize fixed-point operation, when it comes to trigonometric function and radical operation, FPGA need to call the IP core to solve the problem, which makes it difficult to realize SVPWM algorithm. Many researches have simplified SVPWM algorithm by using new sector judgment method [3, 4] to make programming easier. This paper will build a complete Simulink SVPWM control model, and complete the VHDL project by using the combination of MATLAB code generation and manual writing. This method can avoid triangle operation and irrational number operation, reduce a large number of fixed-point operations, and ensure the high accuracy of the system.

2 Fundamental Current Model

In the three-phase coordinate system, the three-phase voltage Eq. of the motor and the self inductance of stator phase winding and mutual inductance Eq. (only phase A is given) is as follows [6]:

Fig. 1 Voltage vector distribution in one PWM cycle



$$\begin{aligned}
 V_A &= R_A i_A + L_{AA} \frac{di_A}{dt} + L_{AB} \frac{di_B}{dt} + L_{AC} \frac{di_C}{dt} + e_A \\
 L_{AA} &= L_\Sigma + L_\sigma + L_\Delta \cos(2\theta_e) \\
 L_{AB} &= -L_\Sigma/2 + L_\Delta \cos(2\theta_e - 2\pi/3)
 \end{aligned}
 \tag{1}$$

where V_A, V_B, V_C are stator voltage, i_A, i_B, i_C are stator current, R_A, R_B, R_C are stator resistance, e_A, e_B, e_C are stator back electromotive force (EMF), L_{AA}, L_{BB}, L_{CC} are self inductance of stator phase winding, L_{AB}, L_{BC}, L_{AC} refer to mutual inductance between stator phase windings, where $L_{AB} = L_{BA}, L_{AB} = L_{BA}, L_{AB} = L_{BA}, \theta_e$ is the electrical angle of the motor, L_Σ and L_Δ are the constant component and double frequency component of the main self inductance respectively, L_σ is the leakage inductance of motor stator phase winding.

Taking the voltage vector in the first sector as an example, as shown in Fig. 1. The current slope under the action of two vectors which are the effective voltage vector V_1 (100) in one PWM switching cycle and zero vector V_7 (111) respectively is selected for position estimation [1].

When V_1 (100) is valid, phase A is powered on, while phase B and C is not. The corresponding line voltage is as follows:

$$\begin{aligned}
 V_{AB} &= V_{DC} = \left(R_A i_A^{(1)} + L_{AA} \frac{di_A^{(1)}}{dt} + L_{AB} \frac{di_B^{(1)}}{dt} + L_{AC} \frac{di_C^{(1)}}{dt} + e_A^{(1)} \right) \\
 &\quad - \left(R_B i_B^{(1)} + L_{BA} \frac{di_A^{(1)}}{dt} + L_{BB} \frac{di_B^{(1)}}{dt} + L_{BC} \frac{di_C^{(1)}}{dt} + e_B^{(1)} \right) \\
 V_{BC} &= 0 = \left(R_B i_B^{(1)} + L_{BA} \frac{di_A^{(1)}}{dt} + L_{BB} \frac{di_B^{(1)}}{dt} + L_{BC} \frac{di_C^{(1)}}{dt} + e_B^{(1)} \right) \\
 &\quad - \left(R_C i_C^{(1)} + L_{CA} \frac{di_A^{(1)}}{dt} + L_{CB} \frac{di_B^{(1)}}{dt} + L_{CC} \frac{di_C^{(1)}}{dt} + e_C^{(1)} \right) \\
 V_{AC} &= V_{DC} = \left(R_A i_A^{(1)} + L_{AA} \frac{di_A^{(1)}}{dt} + L_{AB} \frac{di_B^{(1)}}{dt} + L_{AC} \frac{di_C^{(1)}}{dt} + e_A^{(1)} \right) \\
 &\quad - \left(R_C i_C^{(1)} + L_{CA} \frac{di_A^{(1)}}{dt} + L_{CB} \frac{di_B^{(1)}}{dt} + L_{CC} \frac{di_C^{(1)}}{dt} + e_C^{(1)} \right)
 \end{aligned}
 \tag{2}$$

Similarly, when V_7 is valid, phase A, B, C are all powered on. So, $V_{AB} = V_{BC} = V_{AC} = 0$, the corresponding line voltage is as follows:

$$\begin{aligned}
 V_{AB} = 0 &= \left(R_A i_A^{(7)} + L_{AA} \frac{di_A^{(7)}}{dt} + L_{AB} \frac{di_B^{(7)}}{dt} + L_{AC} \frac{di_C^{(7)}}{dt} + e_A^{(7)} \right) \\
 &- \left(R_B i_B^{(7)} + L_{BA} \frac{di_A^{(7)}}{dt} + L_{BB} \frac{di_B^{(7)}}{dt} + L_{BC} \frac{di_C^{(7)}}{dt} + e_B^{(7)} \right) \\
 V_{BC} = 0 &= \left(R_B i_B^{(7)} + L_{BA} \frac{di_A^{(7)}}{dt} + L_{BB} \frac{di_B^{(7)}}{dt} + L_{BC} \frac{di_C^{(7)}}{dt} + e_B^{(7)} \right) \\
 &- \left(R_C i_C^{(7)} + L_{CA} \frac{di_A^{(7)}}{dt} + L_{CB} \frac{di_B^{(7)}}{dt} + L_{CC} \frac{di_C^{(7)}}{dt} + e_C^{(7)} \right) \\
 V_{AC} = 0 &= \left(R_A i_A^{(7)} + L_{AA} \frac{di_A^{(7)}}{dt} + L_{AB} \frac{di_B^{(7)}}{dt} + L_{AC} \frac{di_C^{(7)}}{dt} + e_A^{(7)} \right) \\
 &- \left(R_C i_C^{(7)} + L_{CA} \frac{di_A^{(7)}}{dt} + L_{CB} \frac{di_B^{(7)}}{dt} + L_{CC} \frac{di_C^{(7)}}{dt} + e_C^{(7)} \right)
 \end{aligned} \tag{3}$$

Since the switching action is extremely fast, it can be assumed that the motor position and EMF will not change in one switching cycle. In Eq. 2 and Eq. 3, it can be obtained that $e_A^{(1)} = e_A^{(7)}$, $e_B^{(1)} = e_B^{(7)}$, $e_C^{(1)} = e_C^{(7)}$. At the same time, the voltage drop of the stator winding is far less than the bus voltage VDC, which can be ignored. Meanwhile, the stator windings adopt star connection mode, which means $i_A + i_B + i_C = 0$. Equation 4 can be obtained after derivation.

$$\left(\frac{di_A^{(1)}}{dt} - \frac{di_A^{(7)}}{dt} \right) + \left(\frac{di_B^{(1)}}{dt} - \frac{di_B^{(7)}}{dt} \right) + \left(\frac{di_C^{(1)}}{dt} - \frac{di_C^{(7)}}{dt} \right) = 0 \tag{4}$$

Subtract Eq. 3 from Eq. 2 and combine Eq. 4, finally we can get Eq. 5 as follows:

$$\begin{aligned}
 \frac{di_A^{(1)}}{dt} - \frac{di_A^{(7)}}{dt} &= \frac{1}{g} \left(2 - \frac{2L_\Delta}{L_\Sigma + \frac{2L_\sigma}{3}} \cos(2\theta_e) \right) \\
 \frac{di_B^{(1)}}{dt} - \frac{di_B^{(7)}}{dt} &= -\frac{1}{g} \left(1 + \frac{2L_\Delta}{L_\Sigma + \frac{2L_\sigma}{3}} \cos\left(2\theta_e - \frac{2\pi}{3}\right) \right) \\
 \frac{di_C^{(1)}}{dt} - \frac{di_C^{(7)}}{dt} &= -\frac{1}{g} \left(1 + \frac{2L_\Delta}{L_\Sigma + \frac{2L_\sigma}{3}} \cos\left(2\theta_e - \frac{4\pi}{3}\right) \right) \\
 g &= \frac{9}{2V_{DC}} \left(L_\Sigma + \frac{2L_\sigma}{3} \right) \left(1 - \left(\frac{2L_\Delta}{L_\Sigma + \frac{2L_\sigma}{3}} \right)^2 \right)
 \end{aligned} \tag{5}$$

Define three positional variables p_A , p_B , p_C and make it equal to the following equation:

$$\begin{aligned}
 p_A &= \frac{2L_\Delta}{L_\Sigma + \frac{2L_\sigma}{3}} \cos(2\theta_e) \\
 p_B &= \frac{2L_\Delta}{L_\Sigma + \frac{2L_\sigma}{3}} \cos\left(2\theta_e - \frac{2\pi}{3}\right) \\
 p_C &= \frac{2L_\Delta}{L_\Sigma + \frac{2L_\sigma}{3}} \cos\left(2\theta_e - \frac{4\pi}{3}\right)
 \end{aligned} \tag{6}$$

Substitute Eq. 6 into Eq. 5, finally we can obtain the relationship between the slope of the transient current and the position variables:

$$\begin{aligned}
 p_A &= 2 - g \left(\frac{di_A^{(1)}}{dt} - \frac{di_A^{(7)}}{dt} \right) \\
 p_B &= -1 - g \left(\frac{di_C^{(1)}}{dt} - \frac{di_C^{(7)}}{dt} \right) \\
 p_C &= -1 - g \left(\frac{di_B^{(1)}}{dt} - \frac{di_B^{(7)}}{dt} \right)
 \end{aligned}
 \tag{7}$$

It can be seen from the above derivation that in one PWM switching cycle, the three-phase position variables can be calculated using the slope of the transient rotor current under the action of the effective vector V1 and the zero vector V7, and the rotor position can be finally calculated. Similarly, the position information can also be estimated by using the current slope under the action of other effective vectors and zero vector V7. See Table 1 [1] for the specific results.

Taking the first sector as an example, as shown in Fig. 1, the transient current slope under the action of effective vector V1 and zero vector V7 is selected for position estimation in one PWM switching cycle. The specific formula corresponds to the second line of Table 1. Where $di_A^{(1)}/dt$ is the slope of phase A current under the action of voltage vector V1; $di_A^{(7)}/dt$ is the slope of phase A current under the action of voltage vector V7, and so on. The variable g can be regarded as unchanged in one PWM switching cycle, but when the voltage vector sector changes, the calculation formula of g will also change. The specific formula is shown in Table 2. In this way, by selecting the appropriate effective voltage vector and zero vector in a switching cycle, the corresponding position of the motor in the switching cycle can be quickly obtained.

Table 1 Position variables under different effective vectors

Vector	p_A	p_B	p_C
V_1, V_7	$2 - g \left(\frac{di_A^{(1)}}{dt} - \frac{di_A^{(7)}}{dt} \right)$	$-1 - g \left(\frac{di_C^{(1)}}{dt} - \frac{di_C^{(7)}}{dt} \right)$	$-1 - g \left(\frac{di_B^{(1)}}{dt} - \frac{di_B^{(7)}}{dt} \right)$
V_2, V_7	$-1 + g \left(\frac{di_B^{(2)}}{dt} - \frac{di_B^{(7)}}{dt} \right)$	$-1 + g \left(\frac{di_C^{(2)}}{dt} - \frac{di_C^{(7)}}{dt} \right)$	$2 + g \left(\frac{di_C^{(2)}}{dt} - \frac{di_C^{(7)}}{dt} \right)$
V_3, V_7	$-1 - g \left(\frac{di_C^{(3)}}{dt} - \frac{di_C^{(7)}}{dt} \right)$	$2 - g \left(\frac{di_B^{(3)}}{dt} - \frac{di_B^{(7)}}{dt} \right)$	$-1 - g \left(\frac{di_A^{(3)}}{dt} - \frac{di_A^{(7)}}{dt} \right)$
V_4, V_7	$2 + g \left(\frac{di_A^{(4)}}{dt} - \frac{di_A^{(7)}}{dt} \right)$	$-1 + g \left(\frac{di_C^{(4)}}{dt} - \frac{di_C^{(7)}}{dt} \right)$	$-1 + g \left(\frac{di_B^{(4)}}{dt} - \frac{di_B^{(7)}}{dt} \right)$
V_5, V_7	$-1 - g \left(\frac{di_B^{(5)}}{dt} - \frac{di_B^{(7)}}{dt} \right)$	$-1 - g \left(\frac{di_A^{(5)}}{dt} - \frac{di_A^{(7)}}{dt} \right)$	$2 - g \left(\frac{di_C^{(5)}}{dt} - \frac{di_C^{(7)}}{dt} \right)$
V_6, V_7	$-1 + g \left(\frac{di_C^{(6)}}{dt} - \frac{di_C^{(7)}}{dt} \right)$	$2 + g \left(\frac{di_B^{(6)}}{dt} - \frac{di_B^{(7)}}{dt} \right)$	$-1 + g \left(\frac{di_A^{(6)}}{dt} - \frac{di_A^{(7)}}{dt} \right)$

Table 2. g under different selected voltage vector

Vector	g	Vector	g
V_1, V_2	$\frac{3}{\left(\frac{di_A^{(1)}}{dt} - \frac{di_A^{(7)}}{dt}\right) + \left(\frac{di_B^{(2)}}{dt} - \frac{di_B^{(7)}}{dt}\right)}$	V_2, V_3	$\frac{3}{\left(\frac{di_A^{(2)}}{dt} - \frac{di_A^{(7)}}{dt}\right) + \left(\frac{di_B^{(3)}}{dt} - \frac{di_B^{(7)}}{dt}\right)}$
V_3, V_4	$\frac{-3}{\left(\frac{di_A^{(4)}}{dt} - \frac{di_A^{(7)}}{dt}\right) + \left(\frac{di_C^{(3)}}{dt} - \frac{di_C^{(7)}}{dt}\right)}$	V_4, V_5	$\frac{-3}{\left(\frac{di_A^{(4)}}{dt} - \frac{di_A^{(7)}}{dt}\right) + \left(\frac{di_B^{(5)}}{dt} - \frac{di_B^{(7)}}{dt}\right)}$
V_5, V_6	$\frac{-3}{\left(\frac{di_A^{(5)}}{dt} - \frac{di_A^{(7)}}{dt}\right) + \left(\frac{di_B^{(6)}}{dt} - \frac{di_B^{(7)}}{dt}\right)}$	V_6, V_1	$\frac{3}{\left(\frac{di_A^{(1)}}{dt} - \frac{di_A^{(7)}}{dt}\right) + \left(\frac{di_C^{(6)}}{dt} - \frac{di_C^{(7)}}{dt}\right)}$

The SVPWM closed-loop control model is built in Simulink. Theoretical analysis shows that the stronger the motor saliency, the better the experimental effect. In this model, $L_d = 0.011715H$, $L_q = 0.001715H$. At the same time, in order to increase the current amplitude, the load torque TL of the current can be increased. Set the simulation duration to 0.1 s to see more details of the transient current. After the simulation, the measured three-phase current, six channel PWM signals output by SVPWM module and the measured motor position signal are imported into the state space for data processing. Finally, by collecting the ABC three-phase current Ia, Ib, Ic corresponding to each voltage vector, and using linear regression, the current slope corresponding to each voltage vector is calculated. According to Table 1 and Table 2, the three-phase position variables of p_A, p_B, p_C can be calculated, and the rotor position can be finally estimated by Eq. 8.

$$\begin{aligned}
 p_\alpha &= \frac{(2p_A - p_B - p_C)}{3} = \frac{2L_\Delta}{L_\Sigma + \frac{2L_\sigma}{3}} \cos 2\theta_e \\
 p_\beta &= \frac{(p_B - p_C)}{\sqrt{3}} = -\frac{2L_\Delta}{L_\Sigma + \frac{2L_\sigma}{3}} \sin 2\theta_e
 \end{aligned}
 \tag{8}$$

This simulation model adopts seven segment SVPWM control. The instantaneous state of sector change is not considered. Obviously, there are at least four effective vectors in a sector, as shown in Fig. 2. In sector (2), there are two V1 and two V2. To reduce the error and simplify the calculation, the first effective vector is selected, that is, V1 and V2 marked in sector (2). At the same time, it can be seen from Table 1 that the position variables under the action of each effective vector can be estimated. To reduce the amount of calculation, the following modifications can be made:

When the voltage vector is in the first sector and the second sector, V1 is used for position estimation; When the voltage vector is in the third sector and the fourth sector, V3 is used for position estimation; When the voltage vector is in the fifth sector and the sixth sector, V5 is used for position estimation. Finally, code according to the above conditions for location estimation. Simplified calculation can effectively improve the real-time and rapidity of position estimation at high speed. However, when the motor is at low speed, due to the above algorithm, there is only one position estimation value in a PWM cycle causing low accuracy. In order to solve this problem, as shown in Fig. 3 this paper uses triangle fitting to fit the corresponding trigonometric

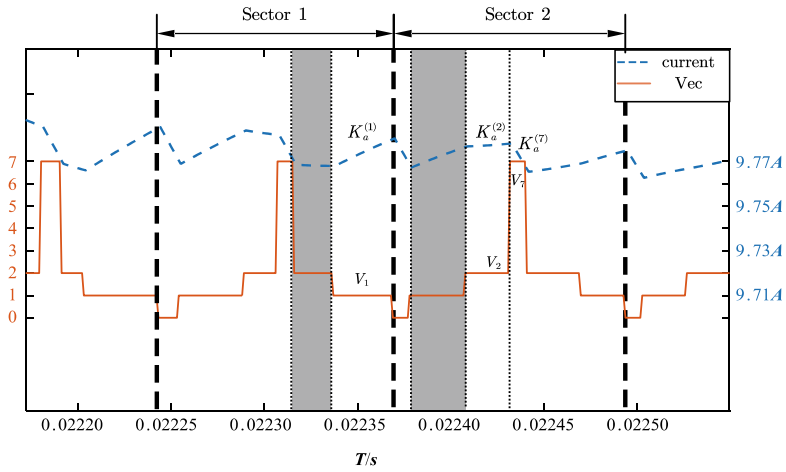
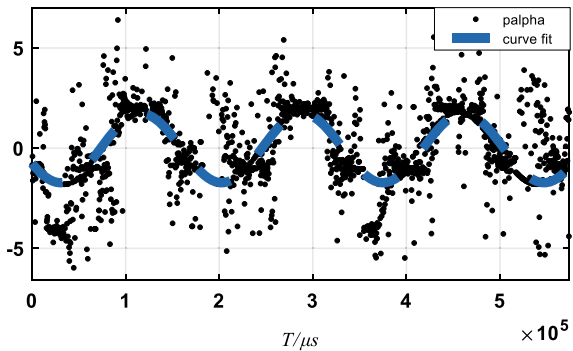


Fig. 2 Effective voltage vector selection

function curve in real time by using the numerical points of p_{alpha} and p_{beta} , which can make up for the position accuracy of under low-speed condition. At the same time, through triangle fitting, the data points with large or wrong errors of p_{alpha} and p_{beta} are eliminated to a certain extent, and the accuracy of position estimation is improved.

The experimental results are shown in Fig. 4. It can be found that the p_{alpha} and p_{beta} form a sinusoidal curve, but there are several error points in each cycle. After analysis, the error is mainly caused by the switching of voltage vector sectors. Since the switching time of voltage vector is very short, the rotor position of the motor can remain unchanged. Therefore, during sector switching, the values of p_{alpha} and p_{beta} at the previous time can be used to replace, which can eliminate error. Finally, through the phase-locked loop, the p_{alpha} and p_{beta} are converted into position signals θ_e (Fig. 5).

Fig. 3 Triangle curve fit



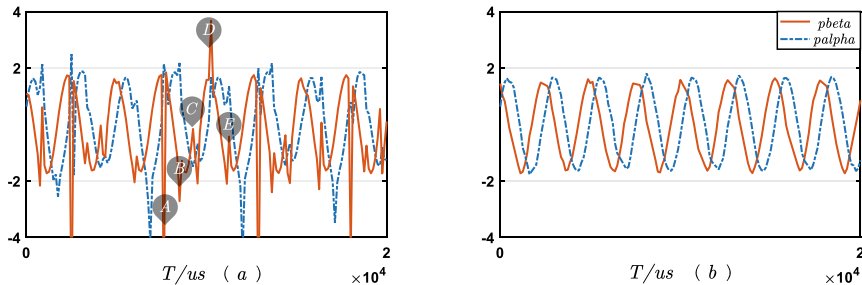


Fig. 4 Position variables and noise elimination

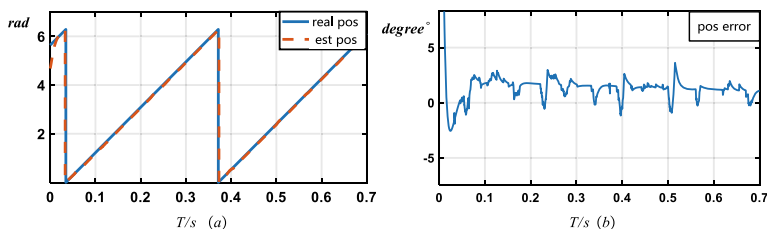


Fig. 5 Simulation experiment results

As shown in Fig. 6 (a), when the speed is under 170 r/min, the solid line in the figure represents the real motor position actually measured by the position sensor, and the dotted line is the position estimation signal. It can be seen that the coincidence between the two is good, and the position error can be controlled between -5° and 5° except in the initial stage. Therefore, the position information contained in the slope of the fundamental wave of the transient current has been verified.

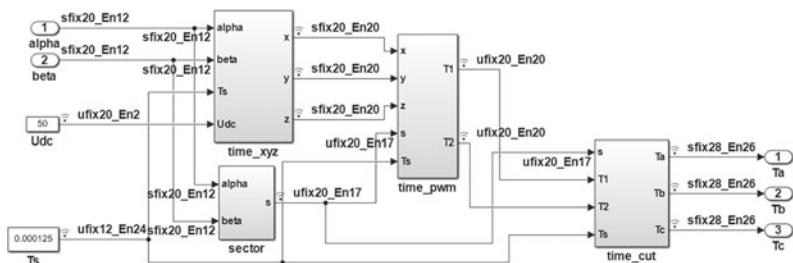


Fig. 6 Simulink fixed-point model of SVPWM module

3 Experimental Methods and Results

3.1 Code Generation

Although the readability of the code is improved by manually writing the VHDL code, the project amount is large. At the same time, when the data is basically added, subtracted, multiplied and divided, there is also a large number of fixed-point processes. In order to simplify the experimental process, MATLAB can be used to generate module code, and then the top-level file can be manually written for signal communication before the module. Using the hdlsetup function in MATLAB, the final SVPWM fixed-point model is shown in the following figure.

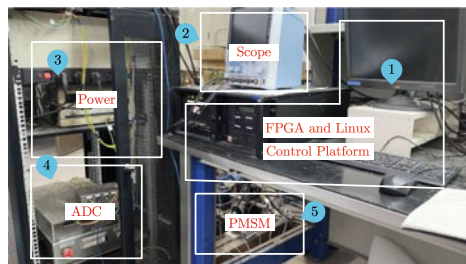
3.2 FPGA and Linux Control Platform

Experiment platform is shown in Fig. 7. The switching frequency of the system is set to 8 kHz. In order to better observe the common mode current and better fit the fundamental current slope, the sampling frequency should be as large as possible. In this experiment, the sampling frequency of the oscilloscope is set to 5 MHz, and the AB two-phase current is oversampled. At the same time, the signal of the sector where the voltage vector is located and the rotor position signal are collected through the DAC7716 to facilitate the verification of the relationship between the fundamental current slope and the common mode current amplitude and the rotor position.

Set the given speed to 220 r/min, DC load to 15 Ω , and measure the three-phase current IA, IB and IC of the motor. The phase current measured electrical angle and waveform is shown in Fig. 8. The estimated position waveform and position error are shown in Fig. 9.

At the same time, in order to verify the accuracy and rapidity of the position estimation when the motor under low-speed state condition and the feasibility of the improved algorithm at high motor speed. We set the given speed of the motor to 30 r/min and 24000 r/min, bring in the mechanical load, and collect the speed signal and estimated position error signal of the motor. The specific waveform is shown in

Fig. 7 FPGA and Linux Control Platform



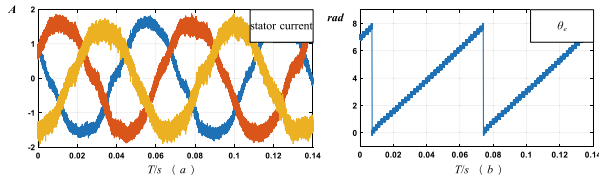


Fig. 8 Three-phase current and electrical angle

Fig. 9 Estimated position and estimation error (medium-speed)

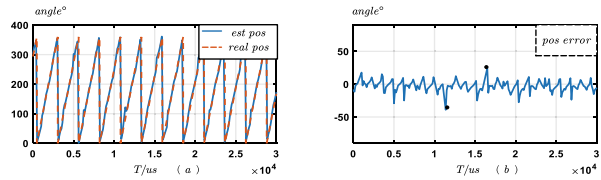


Fig. 10 (A). When the motor is under low-speed condition, the estimated position can successfully follow the actual position when the time is 0.156 s according to the position error waveform, and the error is controlled within 5° . The speed of the motor also reached the expected speed within 0.2 s, which successfully verified that when the motor was in the starting stage and low speed state, the position estimation using the rotor current had the advantages of rapidity, high dynamics and high accuracy. When the motor is at high speed, the estimated position can still follow the actual position, which successfully proves the feasibility of the improved algorithm. However, the position error is large, and a few estimated positions lag behind the actual position, which is shown as spike in the waveform.

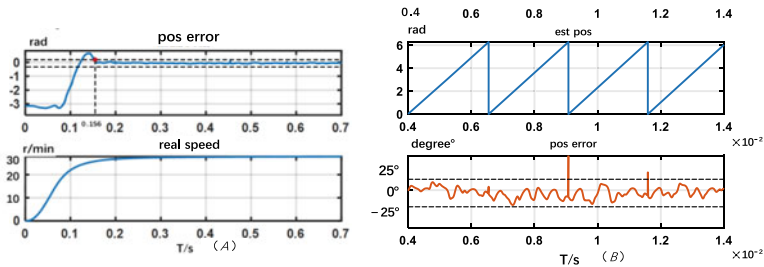


Fig. 10 30 r/min and 24000 r/min experiment results

4 Conclusion

By analyzing the coupling relationship between the transient current and the rotor position in one switching period under SVPWM control, this paper successfully uses the fundamental linear current in the effective voltage vector action time to estimate the position through simulation and experiment. This method has the advantages of fast speed and good dynamic performance. The experimental results show that the position error can be controlled within the range of 5° under medium and low speed conditions, which can meet the most actual motor control requirements and has reference value.

References

1. Bui, M.X., Guan, D., Xiao, D., et al.: A modified sensorless control scheme for interior permanent magnet synchronous motor over zero to rated speed range using current derivative measurements. *IEEE Trans. Ind. Electron.* **66**(1), 102–113 (2019)
2. Hind, D., Sumner, M., Gerada, C.: Use of an artificial neural network for current derivative estimation. In: *Conference EPE*, pp. 1–10 (2013)
3. Zhou, W., Wu, Z.: A simple and fast algorithm for voltage space vector pulse width modulation. *New Technol. Electr. Energy* **24**(2), 28–30 (2005)
4. Pu, Z., Huang, L., Wu, X.: Research on simplified algorithm of space vector control for three-phase PWM rectifier. *New Electr. Energy Technol.* **21**(2), 56–60 (2002)
5. Monmasson, E., Idkhajine, L., Naouar, M.W.: FPGA-based controllers. *IEEE Ind. Electron. Mag.* **5**(1), 14–26 (2011)
6. Chen, Z., Zhang, H., Luo, G.: FPGA based hybrid sensorless controller design for PMSM drive system. In: *ICEMS 2018 - 2018 21st International Conference on Electrical Machines and Systems, KIEE EMECS (KIEE Electrical Machinery and Energy Conversion Systems)*, pp. 1574–1579 (2018)

PMSM Vector Control System Based on NPC Three-Level Inverter and Fuzzy Control Algorithm



Pingjun Dai, Jinwu Gong, and Xiaoming Zha

Abstract In order to solve the problems of traditional vector control system, such as high stator current harmonic content, large torque ripple during stable operation and fixed control parameters of the controller, a three-level inverter and fuzzy proportional and integral controller are designed based on the analysis and establishment of the vector control model of PMSM. And a vector control system of PMSM based on fuzzy control strategy and three-level inverter is established. Finally, the harmonic of current is reduced and the parameters of speed loop controller are optimized online. The data of the simulation show that the system has wonderful control effect.

Keywords PMSM · NPC three level inverter · Fuzzy control algorithm · Vector control

1 Introduction

The traditional control strategy can not guarantee the favourable dynamic property. Different from the traditional control strategy, vector control is a control theory which focuses on both amplitude and phase of the current vector.

Two - level inverter is widely used in vector control system. However, it has the disadvantage of high harmonic content of output voltage. Compared with traditional inverters, inverters that have three levels can obtain better current and torque control effect.

In the process of system operation, PMSM speed will inevitably be disturbed by the outside world. By combining the fuzzy control algorithm with PI regulator and optimizing the control parameters of PI regulator online by fuzzy control algorithm, the system can better obey the given and resist disturbance.

P. Dai (✉) · J. Gong · X. Zha
School of Electrical Engineering and Automation, Wuhan University, Wuhan 430072, China
e-mail: 2022202070030@whu.edu.cn

© Beijing Paiké Culture Commu. Co., Ltd. 2023
X. Dong et al. (eds.), *The proceedings of the 10th Frontier Academic Forum of Electrical Engineering (FAFEE2022)*, Lecture Notes in Electrical Engineering 1054, https://doi.org/10.1007/978-981-99-3408-9_91

1039

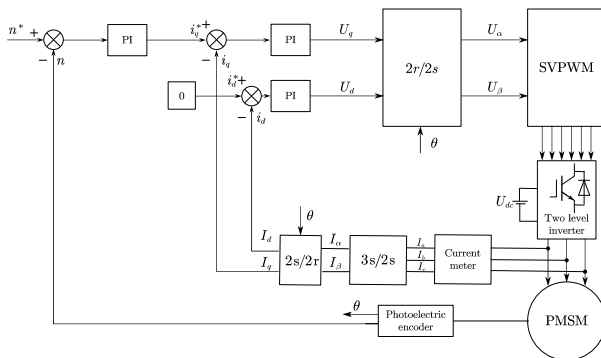


Fig. 1 SCH of PMSM vector control system

In order to work out the problems of vector control system which is traditional, a vector control system of PMSM based on fuzzy control strategy and three-level inverter is established. Finally, through the analysis of simulation data, the high performance of three-level inverter and fuzzy control algorithm is obtained.

2 Vector Control System of PMSM

In PMSM control theory, the traditional control strategy can not guarantee the good dynamic property. Different from the traditional control tactic, the vector control theory is a kind of control theory which focuses on both the quantitative value of the stator current vector and the phase position of the rotor magnetic field [1].

$$t_e = p_0 \psi_f \times i_s \tag{1}$$

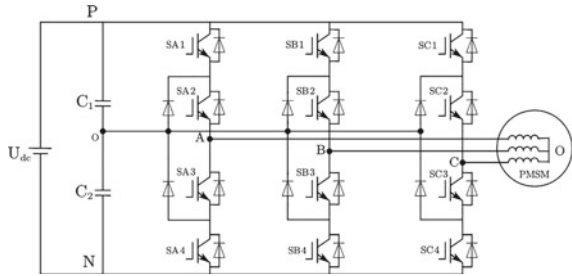
The expression of the torque vector shows that if you want to control the electromagnetic torque, you can control the quantitative value of the stator current vector and the phase position relative to the rotor flux vector in the DQ coordinate axis. This is the core content of vector control of three-phase PMSM. The SCH of PMSM vector control system is shown in the picture below [2] (Fig. 1).

3 NPC Three-Level Inverter

3.1 Main Circuit

The NPC type inverter which has three levels is mainly composed of 3 bridge arms. Its schematic is displayed in Fig. 2 [3].

Fig. 2 Topology of NPC three-level inverter



3.2 Working Status

The output voltage of each phase of inverter has 3 kinds, and, which are respectively defined as P, O and N.

Since the inverter has 3 bridge arms, each of which has three working states, there are a total of 27 basic voltage space vectors. Among the 27 kinds of basic voltage space vectors, there are 6 kinds of long vectors; 6 kinds of medium vectors; 12 kinds of short vectors; 3 kinds of zero vectors.

3.3 Implementation Steps of SVPWM Algorithm

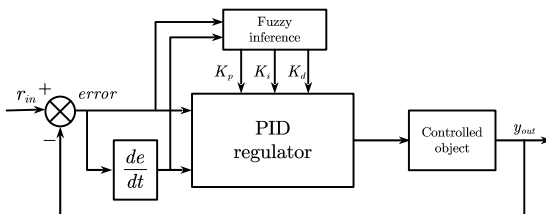
In order to generate a circular rotating magnetic field in the motor, the SVPWM tactic is employed in controlling the inverter. SVPWM control algorithm mainly includes four steps: coordinate transformation, sector and region judgment, basic voltage space vector action time calculation and basic voltage space vector action sequence planning [4].

4 Fuzzy Control Algorithm

In the process of system operation, PMSM speed will inevitably be disturbed by the outside world. For the sake of improving the anti-interference property of the system, PI regulator is introduced into the conventional system [5].

In this paper, fuzzy logic and PI regulator are combined, and the control parameters of PI regulator are optimized and adjusted online by fuzzy logic, so that the control system can better obey the given and resist disturbance.

Fig. 3 SCH of fuzzy PI regulator



The SCH of fuzzy proportional and integral regulator are displayed in Fig. 3 [6].

5 Simulation Study

For the sake of verifying the advantages of NPC three-level inverter and fuzzy self-tuning controller, this paper conducts a simulation study on surface insertion PMSM [7].

The parameters of the motor are selected as follows: stator resistance is 0.9 Ω, d-axis inductance of stator is 5 mH, q-axis inductance of stator is 12 mH, polar logarithm is 4, permanent magnet flux is 0.2Wb.

The research consists of two parts. The first part is: two kinds of inverters are used respectively in the vector control system of PMSM, and the control effect of the system is compared; The second part is to compare the effect of the PMSM vector control system speed loop using three-level inverter by using ordinary PI regulator and fuzzy PI self-tuning regulator respectively [8].

5.1 Comparison of Control Effect Between Two Kinds of Inverters

In the vector control system of PMSM, inverter which has 2 levels and inverter which has 3 levels are used to complete the simulation analysis of the system and the simulation results are obtained.

When two kinds of inverters are used, the output line voltage of the inverter is displayed in Fig. 4. The abscissa of the image represents time in seconds and the ordinate represents the voltage value in volts.

It is obvious to see that the inverter which has 3 levels can output the driving voltage of three levels, and its waveform is much closer to the sine wave, which greatly reduces the harmonic content.

When two kinds of inverters are used, the stator winding current curve and local amplification curve of PMSM are displayed in Fig. 5 and Fig. 6. The abscissa of the picture represents time in seconds and the ordinate represents the current value in amperes.

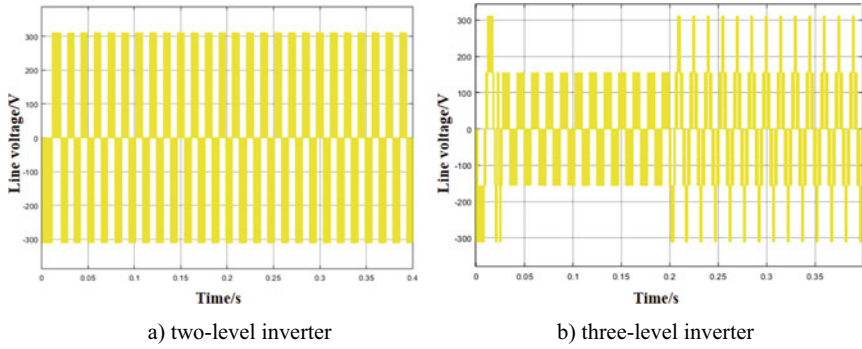


Fig. 4 Inverter output line voltage

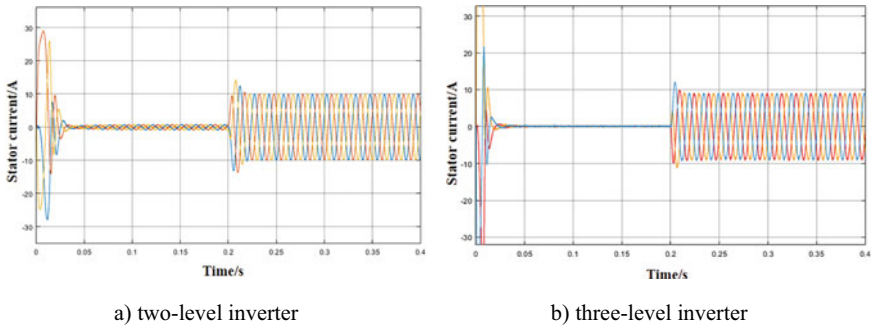


Fig. 5 Stator winding currents of PMSM

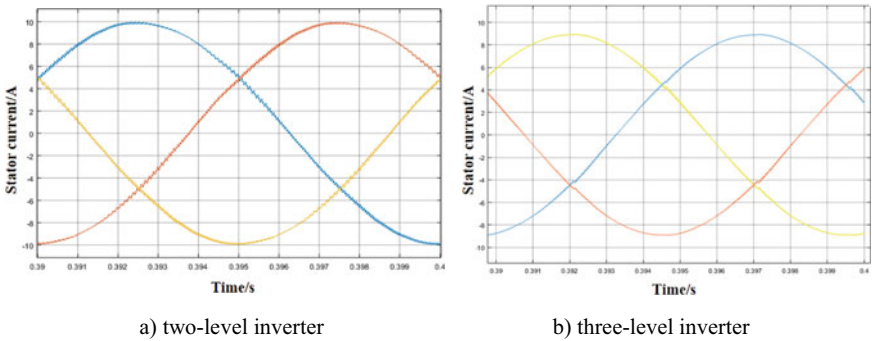


Fig. 6 Local magnification of PMSM stator winding current

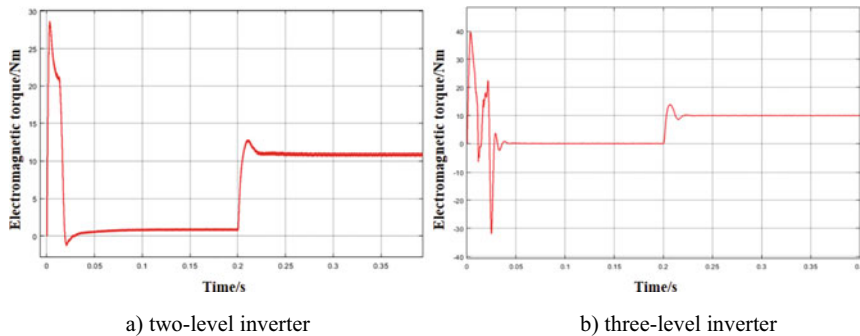


Fig. 7 PMSM electromagnetic torque

It is obvious to see that, compared with the two-level inverter, the stator current sinusoidal property of PMSM is better and the current curve is smoother when the inverter which has 3 levels is used.

It is apparent to see from the expression of electromagnetic torque that the stability of electromagnetic torque is determined by 2 parameters in the expression of electromagnetic torque when the motor runs in steady state. The rotor permanent magnet magnetic field is constant. Since the output current of the latter inverter has better sinusoidal property, it is obvious that the permanent magnet motor driven by the inverter which has 3 levels will obtain better torque characteristics.

When 2 kinds of inverters are used, the electromagnetic torque of PMSM is displayed in Fig. 7. Obviously, the electromagnetic torque of PMSM almost has no fluctuation in the steady operation when the latter inverter is used, and the stability is better [9].

When the two different inverters are respectively used, the analysis of PMSM stator current harmonic content is shown in Table 1. Fnd, H2, H3... and H10 respectively represent fundamental wave and each harmonic relative to the fundamental wave.

The results in the table are graphically displayed, and the resulting image is shown in Fig. 8. It should be noted that because the proportion of harmonics is small, it is difficult to compare the harmonic content if you want to display the column corresponding to the fundamental wave completely. Therefore, the bar chart shown in Fig. 8 is actually obtained after harmonic amplification. In fact, the column corresponding to the fundamental wave is much higher than that corresponding to the harmonic wave.

Compared with the two-level inverter, the content of current harmonics (especially low-frequency harmonics) of PMSM stator decreases significantly when three-level inverter is used. Obviously, the employment of inverter which has 3 levels greatly improves the sine degree of PMSM stator current.

Table 1 Comparison of current harmonic content

	2-level inverter	3-level inverter
Fnd	100%	100%
H2	0.26%	0.02%
H3	0.04%	0.02%
H4	0.26%	0.12%
H5	0.36%	0.34%
H6	0.02%	0.00%
H7	0.26%	0.31%
H8	0.04%	0.08%
H9	0.02%	0.01%
H10	0.07%	0.04%

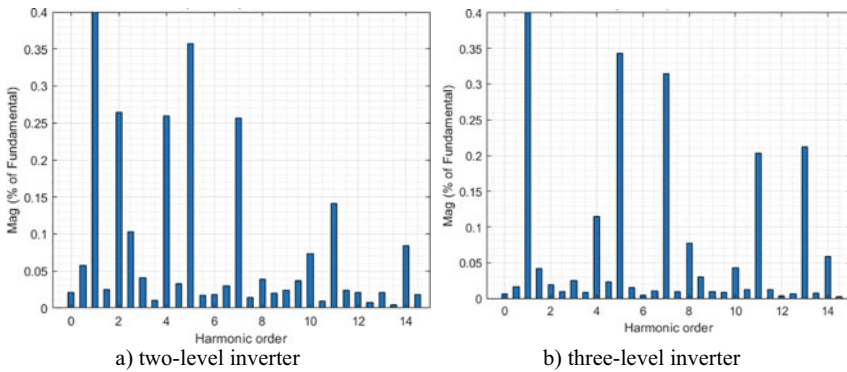


Fig. 8 Analysis of current harmonic content

By comparing the driving effect of the two kinds of inverters, it can be found that the inverter which has 3 levels can output voltage waveform which is much closer to the sinusoidal curve, the current harmonic content is lower, and the sinusoidal degree is better, which greatly improves the stability of the torque.

5.2 Online Optimization and Adjustment Effect of Speed Ring Control Parameters

As can be seen from the figure, when PI regulator is used, the maximum speed overshoot is 191 r/min and the adjustment time is 0.014 s during PMSM starting. When the system is disturbed at 0.2 s, the speed drops to 922 r/min at the lowest, and the change is 78 r/min.

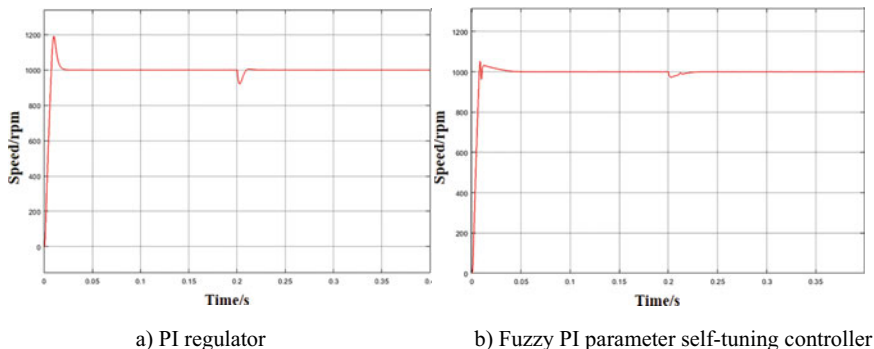


Fig. 9 Change curve of speed

When fuzzy PI regulator is used, the maximum speed overshoot is 52 r/min and the adjustment time is 0.008 s during PMSM starting. When the system is disturbed at 0.2 s, the speed drops to 972 r/min, and the change is 28 r/min [10].

Compared with PI controller, using fuzzy PI self-tuning controller, the maximum speed overshoot decreases by 72.8% and the adjustment time decreases by 42.9% during the motor starting process. When disturbed, the speed variation decreases by 64.1%. Obviously, the motor speed overshoot and regulation time are significantly reduced, and the system can better resist disturbance and obey the given [11] (Fig. 9).

6 Conclusion

In the PMSM vector control system, 2 kinds of inverters are used in this paper, and the simulation analysis is carried out respectively. When using three-level inverter, before and after adding adaptive fuzzy control algorithm, the simulation analysis is also operated.

Obviously, the inverter which has 3 levels can get better control effect. In addition, the adaptive fuzzy control algorithm can resize the control arguments of the speed loop according to the external disturbance, so that the control system can better resist the disturbance and obey the given, and obtain better speed control characteristics.

Through the fuzzy control tactic, the speed control effect of the motor is improved obviously, and the system can better resist the disturbance and obey the given.

By combining the inverter which has 3 levels based on SVPWM algorithm with fuzzy control algorithm and applying it to the vector control system of PMSM, the control ability of voltage, current, torque and speed of the system is greatly enhanced, and good control effect is obtained [12].

References

1. Wan, Y., Hu, H., Du, L., Jia, Z.: Research on three-level Inverter SVPWM applied to permanent magnet synchronous motor control. *Ship Electr. Technol.* **40**(8), 32–37. <https://doi.org/10.13632/j.m.eee.2020.08.010> (in Chinese)
2. Yan, G.: Research on servo control system of permanent magnet synchronous motor based on TMS320F2812. Huazhong University of Science and Technology (2007) (in Chinese)
3. Yang, E.: Application of three-level inverter in permanent Magnet Synchronous Motor Drive System. Chongqing University (2015) (in Chinese)
4. Shi, J., Ge, L., Li., C.: Simulation system of PMSM based on space vector pulse width modulation. *Mater. Sci. Eng.* **768**(2020), 42–49 (in Chinese)
5. Li, N., Chen, N., Ren, Z.: Based on the speed of the electromagnetic bearing control parameter self-tuning study. *J. Bear.* **29**(05), 6–9. <https://doi.org/10.19533/j.issn1000-3762.2017.05.003>. (in Chinese)
6. Zhongqiao, Z., Yanhong, Z.: Research on fuzzy adaptive PID control in active maglev system. *Manuf. Autom.* **35**(15), 19–22 (2013). (in Chinese)
7. Shama, R.K., Sanadhya, V., Behera, L.: Vector control of a permanent magnet synchronous motor. *IEEE India Conf.* **116**, 81–86 (2008)
8. Pillay, P.: Modeling simulation and analysis of permanent-magnet motor drives. *IEEE Trans. Indust. Appl.* **25**, 32–37 (2009)
9. Fujita, K.: New design and stability analysis of fuzzy proportional-derivative control systems. *IEEE Trans. Indust. Appl.* **28**, 864–872 (1992)
10. Bose, B.K.: Power electronics and motion control-technology status and recent trends. *IEEE Trans. IA* **29**, 902–909 (2013)
11. Dong, J., Zhang, Y., Li, Y.: Research on control method of permanent magnet synchronous motor based on fuzzy PI self-tuning. *Indust. Control Comput.* **35**(07), 161–162. (in Chinese)
12. Chen, Y., Zheng, B.: Based on fuzzy PI control of permanent magnet synchronous motor vector control performance study. *J. Foreign Electr. Measure. Technol.* **9**(7), 75–81. <https://doi.org/10.19652/j.carol.carroll.nki.femt.2203876>. (in Chinese)

An Optimized Fault-Tolerant Strategy Based on Uncoupled Zero-Sequence Voltage Injection for Cascaded Multilevel Converters



Ganlin Kong, Liming Shi, Fei Xu, Mingyuan Zhang, Jinhai Liu,
and Shijiong Zhou

Abstract For cascaded multilevel converters, the extensive use of power cells increases the possibility of failure and reduces system stability. When some cells fail and are bypassed, the neutral point drifting strategy is often applied to solve the problem of unbalanced output line voltage. However, this traditional strategy focuses on the feasibility of constructing an equilateral triangle of output line voltage, which is deeply affected by the phase with the most faults and causes the waste of healthy cells in other phases. In this paper, an optimized fault-tolerant strategy is proposed to improve the output line voltage. By decoupling the faults of each phase and injecting zero-sequence voltages pertinently, it can reduce the mutual influence between the phases, thereby making more use of the healthy cells and increasing the DC bus voltage utilization under multiple fault conditions. The correctness and superiority of the proposed strategy have been verified by the simulation results.

Keywords Fault tolerance · Zero-sequence voltage Injection · Cascaded multilevel converter · Cell fault

G. Kong · L. Shi (✉) · F. Xu · M. Zhang · J. Liu · S. Zhou
Key Laboratory of Power Electronics and Electric Drive, Institute of Electrical Engineering,
Chinese Academy of Sciences, Beijing 100190, China
e-mail: limings@mail.iee.ac.cn; shijiongz@mail.iee.ac.cn

G. Kong
e-mail: konggl@mail.iee.ac.cn

M. Zhang
e-mail: myzhang@mail.iee.ac.cn

J. Liu
e-mail: liujinhai@mail.iee.ac.cn

G. Kong · M. Zhang · J. Liu · S. Zhou
University of Chinese Academy of Sciences, Beijing 100049, China

© Beijing Paiké Culture Commu. Co., Ltd. 2023
X. Dong et al. (eds.), *The proceedings of the 10th Frontier Academic Forum of Electrical Engineering (FAFEE2022)*, Lecture Notes in Electrical Engineering 1054,
https://doi.org/10.1007/978-981-99-3408-9_92

1 Introduction

Through the series connection of power cells, the cascaded multilevel converter realizes high-voltage and high-power output while reducing the voltage stress on power devices [1]. It is commonly used in metallurgy, ship propulsion, and other fields requiring strict reliability. When failures occur, these systems need to reduce capacity and keep running instead of shutdown. With the improvement of voltage levels, the use of power switching devices increases and the fault probability becomes higher. Therefore, the fault-tolerant operation strategy of cascaded multilevel converters is an important research direction.

Figure 1 represents the topology of a cascaded $(2N + 1)$ level converter. There are N power cells in series per phase. And each cell consists of the three-phase full-wave rectifier bridge, DC bus capacitor, H-bridge inverter and the bypass switch as shown in Fig. 2. To achieve the fault-tolerant operation, one of the simplest methods is to set redundant cells. When cell failure occurs, the fault cells will be shorted by the bypass switches and replaced by the redundant cells.

In addition to the hardware redundancy method, the fault-tolerant operation is often realized through system reconfiguration. For a star-connected three-wire converter, after bypassing the fault cells, the voltage amplitude of the fault phase can be reduced by injecting zero-sequence voltage without affecting the balance of the output line voltage [2, 3]. The design of injected zero-sequence voltage is often based on the neutral point drifting strategy proposed by Siemens [4], which aims to calculate the phase-shifting angle when the output line voltage equilateral triangle is successfully constructed [5]. Although the obtained solution can meet the requirements of the phase voltage after failure, since this strategy lacks the function

Fig. 1 Topology of a cascaded $(2N + 1)$ level converter

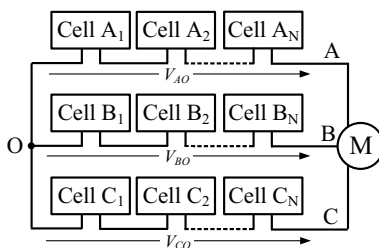
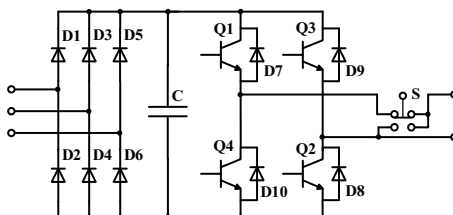


Fig. 2 Circuit of each power cell



of screening, it cannot select the one which maximizes the output line voltage from the many solutions that meet the fault conditions [6].

In this paper, an optimized fault-tolerant strategy based on uncoupled zero-sequence voltage injection for cascaded multilevel converters is proposed. Comparing with the traditional neutral point drifting strategy, the proposed strategy splits the total zero-sequence injection voltage into three independent components to suppress the phase voltage of each phase respectively, so that each phase voltage reaches the maximum value under the fault condition as much as possible. The amplitude of output line voltage is increased and the power loss is reduced effectively.

2 Optimized Fault-tolerant Strategy Based on Uncoupled Zero-Sequence Voltage Injection

For a three-phase star connected cascaded multilevel converter, set the number of series power cells in each phase N . Take the phase voltage amplitude at normal operation as the reference value and establish a per-unit model.

Set the number of fault cells in each phase M_A, M_B, M_C . So, after the fault occurs, the normalized value of output phase voltage amplitude A_{mp} is limited to:

$$\begin{cases} A_{mpA} = 1 - M_A/N \\ A_{mpB} = 1 - M_B/N \\ A_{mpC} = 1 - M_C/N \end{cases} \tag{1}$$

Taking phase A as an example, to make the output voltage amplitude of phase A less than A_{mpA} , zero-sequence voltage should be injected into the reference voltage. The target zero-sequence voltage in a period of $x \in (0, 2\pi)$ is:

$$u_{zeroA}^*(x) = \begin{cases} \cos(x + \varphi) - A_{mpA}, & x \in (-\varphi, \theta - \varphi) \cup (2\pi - \theta - \varphi, 2\pi - \varphi) \\ \cos(x + \varphi) + A_{mpA}, & x \in (\pi - \theta - \varphi, \pi + \theta - \varphi) \end{cases} \tag{2}$$

where φ is the initial phase angle, $\theta = \arccos(A_{mpA})$ is the minimum peak-reduction angle of phase A and $\theta \in (0, 0.5\pi)$.

Decompose (2) into Fourier series as shown in (3)

$$u_{zeroA}^*(x) = \frac{a_{0A}}{2} + \sum_{n=1}^{\infty} [a_{nA} \cos(nx) + b_{nA} \sin(nx)] \tag{3}$$

where the Fourier coefficients are:

$$\begin{cases} a_{0A} = \frac{2}{T} \int_{t_0}^{t_0+T} u_{zeroA}^*(x) dx \\ a_{nA} = \frac{2}{T} \int_{t_0}^{t_0+T} u_{zeroA}^*(x) \cos(nx) dx \\ b_{nA} = \frac{2}{T} \int_{t_0}^{t_0+T} u_{zeroA}^*(x) \sin(nx) dx \end{cases} \quad (4)$$

Substitute (2) into (4) to calculate the Fourier coefficients as shown in (5).

$$\begin{aligned} a_{0A} &= 0 \\ a_{nA} &= \begin{cases} 0, (n = 2k, k \in N_+) \\ \frac{\sin[(n+1)\theta - n\varphi] + \sin[(n+1)\theta + n\varphi]}{\sin(n\theta - n\varphi) + \sin(n\theta + n\varphi)} + \frac{\sin[(n-1)\theta - n\varphi] + \sin[(n-1)\theta + n\varphi]}{(n-1)\pi} \\ - \frac{2A_{mpA}[(n+1)\pi]}{2A_{mpA}[\sin(n\theta - n\varphi) + \sin(n\theta + n\varphi)]}, (n = 2k + 1, k \in N_+) \\ \frac{n\pi}{\sin(2\theta - \varphi) + \sin(2\theta + \varphi)} + \frac{2\theta \cos \varphi}{\pi} - \frac{2A_{mpA}[\sin(\theta - \varphi) + \sin(\theta + \varphi)]}{\pi}, (n = 1) \end{cases} \\ b_{nA} &= \begin{cases} 0, (n = 2k, k \in N_+) \\ \frac{\cos[(n+1)\theta - n\varphi] - \cos[(n+1)\theta + n\varphi]}{\cos(n\theta - n\varphi) - \cos(n\theta + n\varphi)} - \frac{\cos[(n-1)\theta - n\varphi] - \cos[(n-1)\theta + n\varphi]}{(n-1)\pi} \\ + \frac{2A_{mpA}[(n+1)\pi]}{2A_{mpA}[\cos(n\theta - n\varphi) - \cos(n\theta + n\varphi)]}, (n = 2k + 1, k \in N_+) \\ - \frac{n\pi}{\cos(2\theta - \varphi) - \cos(2\theta + \varphi)} + \frac{2A_{mpA}[\cos(\theta - \varphi) - \cos(\theta + \varphi)]}{\pi}, (n = 1) \end{cases} \end{aligned} \quad (5)$$

Take the superposition of the fundamental voltage and the third harmonic voltage in the Fourier series as the injected zero-sequence voltage. Let the initial phase angle $\varphi = 0$ and substitute it into (5). Then (6) is obtained as:

$$\begin{cases} a_{3A} = \frac{3 \sin(4\theta) + 6 \sin(2\theta) - 8A_{mpA} \sin(3\theta)}{6\pi} \\ b_{1A} = b_{2A} = b_{3A} = 0 \end{cases} \quad (6)$$

And the phase A fault component of the injected zero-sequence voltage is shown as:

$$u_{zeroA}(x) = a_{1A} \cos x + a_{3A} \cos(3x) \quad (7)$$

Similarly, the fault components of phase B and C of the injected zero-sequence voltage can be obtained as:

$$\begin{cases} u_{zeroB}(x) = a_{1B} \cos(x - 2\pi/3) + a_{3B} \cos[3(x - 2\pi/3)] \\ u_{zeroC}(x) = a_{1C} \cos(x + 2\pi/3) + a_{3C} \cos[3(x + 2\pi/3)] \end{cases} \quad (8)$$

So, the total injected zero-sequence voltage is the sum of decoupled three-phase components as shown in (9).

$$u_{zero}(x) = u_{zeroA}(x) + u_{zeroB}(x) + u_{zeroC}(x) \quad (9)$$

And the three-phase output voltages after injection are shown as (10).

$$\begin{cases} u_A(x) = \cos(x + \varphi) - u_{zero}(x) \\ u_B(x) = \cos(x + \varphi - 2\pi/3) - u_{zero}(x) \\ u_C(x) = \cos(x + \varphi + 2\pi/3) - u_{zero}(x) \end{cases} \quad (10)$$

3 Simulation Analysis

The effectiveness of the proposed strategy is proved in the simulation platform built in MATLAB/Simulink by comparing with the traditional neutral point drifting strategy.

Table 1 shows the 20 fault conditions with the number of cells in series per phase $N = 11$. And Fig. 3 gives the comparison of output line voltages applying the two strategies under different fault conditions when IPD (In-Phase Disposition)-SPWM (Sinusoidal Pulse Width Modulation) [7–11] is adopted.

Table 1 Fault conditions

Number	N_A, N_B, N_C	$(N_{ABC}/3N)/\%$	$U_{tra}/\%$	$U_{pro}/\%$
1	10,11,11	96.97	96.88	100.00
2	9,11,11	93.94	93.59	100.00
3	8,11,11	90.91	90.15	97.92
4	7,11,11	87.88	86.55	91.19
5	6,11,11	84.85	82.82	83.35
6	10,10,11	93.94	93.83	100.00
7	9,10,11	90.91	90.60	99.13
8	8,10,11	87.88	87.19	93.59
9	9,9,11	87.88	87.39	94.27
10	7,10,11	84.85	83.62	85.54
11	8,9,11	84.85	83.97	87.48
12	6,10,11	81.82	79.88	77.46
13	7,9,11	81.82	80.35	79.03
14	8,8,11	81.82	80.49	80.81
15	10,10,10	90.91	90.91	100.00
16	9,10,10	87.88	87.78	99.41
17	8,10,10	84.85	84.47	93.07
18	9,9,10	84.85	84.73	93.55
19	7,10,10	81.82	80.98	84.72
20	8,9,10	81.82	81.47	86.44

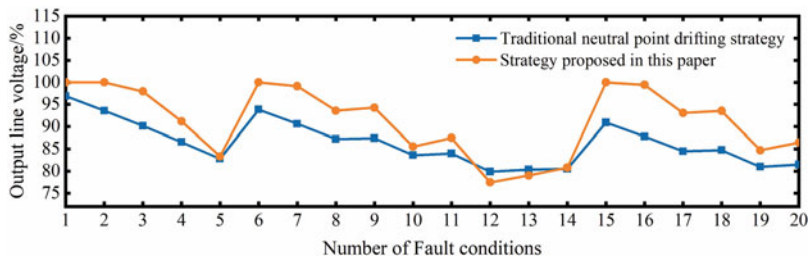


Fig. 3 Comparison of output line voltages

It can be seen from Fig. 3 that compared with the traditional neutral point drifting strategy, the zero-sequence injection strategy proposed in this paper can generally and significantly improve the output line voltage. Combined with Figs. 2, 3, it can be seen that the output line voltage can be increased by 4.96% on average and 11.63% at most by using the proposed strategy. Among all the 20 fault conditions, only under the two conditions of $(N_A, N_B, N_C) = (6, 10, 11)$ and $(N_A, N_B, N_C) = (7, 9, 11)$, the output line voltage of the proposed strategy is lower by 1–2%, which is quite slightly.

Figure 4 presents the comparison of output phase voltage and line voltage between the two strategies under the condition of $(N_A, N_B, N_C) = (9, 10, 10)$. When using the traditional neutral point drifting strategy, the output line voltage amplitude after fault is 87.78% of that before fault. And when using the proposed strategy, the output line voltage amplitude after fault is 99.41% of that before fault. That is to say, the output line voltage amplitude almost does not decrease, which reflects the obvious advantage of this strategy in improving the output line voltage amplitude.

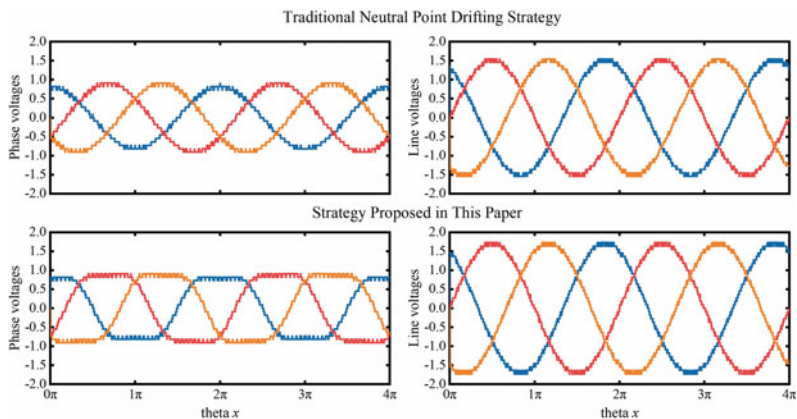


Fig. 4 Comparison of output line voltages under the condition of $(N_A, N_B, N_C) = (9, 10, 10)$

4 Conclusion

In this paper, an optimized fault-tolerant strategy based on uncoupled zero-sequence voltage injection for cascaded multilevel converters is proposed to improve the output line voltage after power cell failures. In this strategy, the injected zero-sequence voltage is divided into three-phase components without coupling. According to the different numbers of fault cells, the minimum peak-reduction angles of three phases are determined and the injected voltage components are designed separately. This strategy effectively suppresses the mutual interference between three-phase zero-sequence injection voltages in traditional strategy, so as to improve the output line voltage while maintaining the balance, improve DC bus voltage utilization, and improve the reliability of the converter system. Comparative simulation results demonstrate the correctness and the efficiency of the presented strategy.

References

1. Carnielutti, F., Pinheiro, H., Rech, C.: Generalized carrier-based modulation strategy for cascaded multilevel converters operating under fault conditions. *IEEE Trans. Industr. Electron.* **59**(2), 679–689 (2011)
2. Ni, Z., Abuelnaga, A.H., Narimani, M.: A new fault-tolerant technique based on non-symmetry selective harmonic elimination for cascaded h-bridge motor drives. *IEEE Trans. Industr. Electron.* **99**, 1–1 (2020)
3. Neyshabouri, Y., Iman-Eini, H.: A new fault-tolerant strategy for a cascaded h-bridge based STATCOM, *IEEE Trans. Industr. Electron.* **65**, 6436–6445 (2018)
4. Sharma, R., Das, A.: Postfault operation of cascaded H-bridge converter for equal power handling by the healthy cells. *IEEE Trans. Industr. Electron.* **99**, 1–1 (2020)
5. Rodriguez, J., Hammond, P.W., Pontt, J., et al: Operation of a medium-voltage drive under faulty conditions. *IEEE Trans. Industr. Electron.* **52**, 1080–1085 (2005)
6. Hammond, P.W.: Enhancing the reliability of modular medium-voltage drives. *IEEE Trans. Industr. Electron.* **49**(5), 948–954 (2002)
7. Xue, C., Shen, K., Ji, Y., et al.: Capacitor voltage balancing of modular multilevel converter. *Electr. Power Autom. Equip.* **34**(7), 27–31 (2014)
8. Sun, Y., Zhao, J., Ji, Z.: Control strategy of DC voltage balance and power equilibrium for grid-connected cascaded H-bridge converters. *Electr. Power Autom. Equip.* **34**(1), 5–60 (2014)
9. Wang, X., Zhang, X., Ruan, X.: Optimal SPWM control strategy and its power balance scheme for cascaded multilevel inverters. *Trans. China Electrotechn. Soc.* **24**(5), 92–99 (2009)
10. Wang, K., Feng, L., Li, G.: A novel carrier-based disposition PWM method with voltage balance for flying capacitor multilevel inverter. *Power Syst. Protect. Control* **42**(14), 8–13 (2014)
11. Wang, X., He, X., Deng, Y.: PWM methods with carrier overlapping characteristics in flying capacitor multilevel inverters. *Proc. CSEE* **27**(10), 98–102 (2007)

Wind Speed Estimation Based MPPT for WPGS



Xia You, Bo Zhou, Qingxi Zeng, Yajie Lin, and Honghao Guo

Abstract This paper proposes a maximum power point tracking (MPPT) method for variable speed wind power generation systems (WPGS) based on wind speed estimation. The proposed control algorithm has been effectively applied to WPGS based on doubly salient electromagnetic generator (DSEG). By adjusting the rotational speed of the generator, variable speed WPGS can obtain maximum wind power at different wind speeds. A nonlinear input output mapping based on back propagation (BP) neural network is used to approximate the relationship between output power, rotational speed, and wind speed. Based on this nonlinear mapping, wind speed can be estimated in real time based on measured WPGS output power and DSEG rotational speed. The estimated wind speed is then used to determine the optimal DSEG rotor speed command for MPPT. By adjusting the excitation current of the DSEG, the speed of the DSEG can be adjusted to its command value. The entire wind power generation system is modeled in Matlab/Simulink, and the simulation results verify the effectiveness of proposed MPPT method.

Keywords Maximum power point tracking (MPPT) · Wind power generation systems (WPGS) · Wind speed estimation · Double salient electromagnetic generator (DSEG) · Back propagation (BP) neural network

X. You (✉) · B. Zhou · Q. Zeng · Y. Lin

College of Automation Engineering, Nanjing University of Aeronautics and Astronautics, Nanjing 211100, China

e-mail: youxiajy@nuaa.edu.cn

B. Zhou

e-mail: zhoubo@nuaa.edu.cn

Q. Zeng

e-mail: jslyzqx@nuaa.edu.cn

Y. Lin

e-mail: linyj@nuaa.edu.cn

H. Guo

College of Automation, Nanjing University of Posts and Telecommunications, Nanjing 210023, China

© Beijing Paiké Culture Commu. Co., Ltd. 2023

X. Dong et al. (eds.), *The proceedings of the 10th Frontier Academic Forum of Electrical Engineering (FAFEE2022)*, Lecture Notes in Electrical Engineering 1054, https://doi.org/10.1007/978-981-99-3408-9_93

1057

1 Introduction

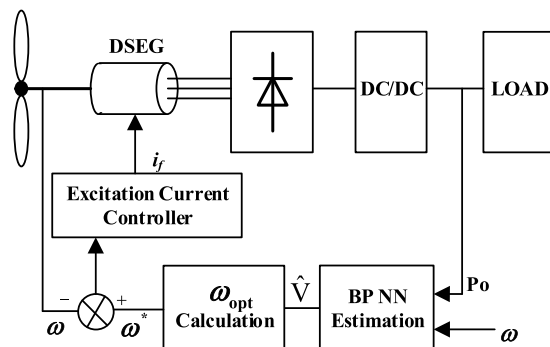
Compared to constant speed wind power generation systems, variable speed wind power generation systems are more effective. By adjusting the rotational speed of the generator, a variable speed wind turbine can capture the maximum wind power at different wind speeds. In order to achieve maximum wind power extraction, variable speed wind power systems often use anemometers to measure wind speed. These installed anemometers not only increase costs, but also reduce the reliability of the entire wind power generation system [1–3].

Recently, people have studied how to implement MPPT without measuring wind speed. In literature [4], the hill climbing search (HCS) method is used to search for the maximum power point (MPP) of a WPGS automatically. This method does not require wind speed information, but the HCS method may take a long time to gradually search for MPPs. If wind speed changes quickly, the WTGS cannot even reach MPP. In [5], Quincy Wang et al. first searched for MPPs using advanced HCS methods, and then recorded them as lookup tables for real-time application. However, to accurately locate WPGS to MPPs, this method requires a large amount of memory space and consumes too much time. This paper selects a BP neural network to estimate real-time wind speed, and then uses the predicted wind speed to determine the optimal rotational speed of wind power generation system. Simulation studies verify the effectiveness of proposed method.

2 DSEG Wind Power Generation System

The composition of the WPGS studied in this article is shown in Fig. 1. The wind turbine is directly connected to DSEG. The power generated by DSEG is first rectified and then supplied to the load through a DC/DC converter.

Fig. 1 Composition of studied DSEG wind power generation system



2.1 Wind Turbine Aerodynamic Model

The mechanical power P_m of a wind turbine is shown by the following equation:

$$P_m = \frac{1}{2} \rho S C_p v^3 \tag{1}$$

where, ρ is the air density (kg/m^3), and S is wind turbine sweeping area (m^2).

The power coefficient C_p is determined by the tip-speed ratio λ and pitch angle β as shown in Eq. (2).

$$C_p(\lambda_i, \beta) = 0.5176 \left(116 \frac{1}{\lambda_i} - 0.4\beta - 5 \right) e^{-21 \frac{1}{\lambda_i}} + 0.0068\lambda \tag{2}$$

where, $\frac{1}{\lambda_i} = \frac{1}{\lambda + 0.08\beta} - \frac{0.035}{\beta^3 + 1}$

The curve of C_p is shown in Fig. 2. From Fig. 2, we can conclude that when β is constant, wind turbine can capture maximum wind power at its optimal tip-speed ratio λ_{opt} .

The tip-speed ratio λ is defined as

$$\lambda = \frac{\omega R}{V} \tag{3}$$

where, R is wind turbine radius (m), V is wind speed (m/s), ω is wind turbine rotation speed (rad/s).

The power output characteristics of wind turbine are shown in Fig. 3. It can be seen that the optimal rotational speed ω_{opt} of a wind turbine is not the same under different wind speeds. Therefore, when wind speeds vary, the rotor speed ω of DSEG should be adjusted to its optimal value of current wind speed so as to realize MPPT.

Fig. 2 Power coefficient curve

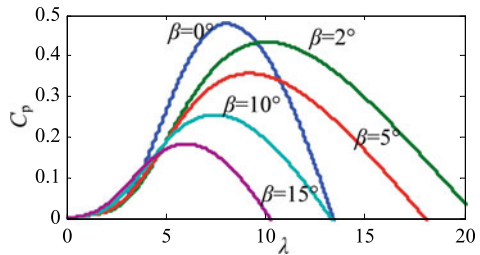
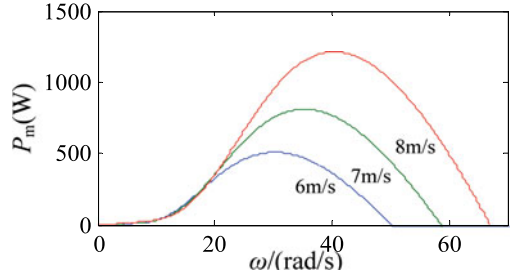


Fig. 3 Power output characteristics



2.2 Modeling of DSEG

DSEG is a new type of brushless generator with outstanding advantages such as simple structure, flexible control, high reliability, low cost, and low starting torque. The cross-section of the three-phase 24/16 structure DSEG studied is shown in Fig. 4. The stator and rotor of DSEG adopt salient structure. No windings are mounted on the rotor, and all excitation and armature windings are mounted on the stator.

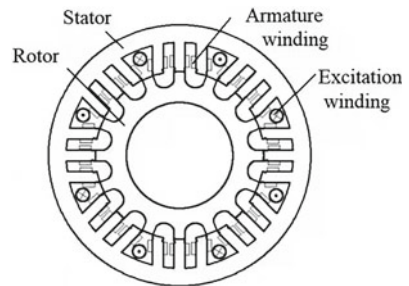
According to literature [6–8], the phase voltage u_p and excitation voltage u_f of DSEG can be described by following equations:

$$u_p = e_p - R_p i_p = -\frac{d\psi_p}{dt} - R_p i_p \tag{4}$$

$$u_f = -e_f + R_f i_f = \frac{d\psi_f}{dt} + R_f i_f \tag{5}$$

where, p represents phase A, B or C; i_p is phase current; R_p is the equivalent resistor of armature winding, ψ_p is phase magnetic linkage. i_f is excitation current; R_f is the equivalent resistor of excitation winding, ψ_f is magnetic linkage of excitation winding.

Fig. 4 Cross-section of 24/16 DSEG



The magnetic linkage of a DSEG can be described by the following equation:

$$\begin{bmatrix} \psi_a \\ \psi_b \\ \psi_c \\ \psi_f \end{bmatrix} = \begin{bmatrix} L_a & 0 & 0 & L_{af} \\ 0 & L_b & 0 & L_{bf} \\ 0 & 0 & L_c & L_{cf} \\ L_{af} & L_{bf} & L_{cf} & L_f \end{bmatrix} \begin{bmatrix} i_a \\ i_b \\ i_c \\ i_f \end{bmatrix} \quad (6)$$

where L_p is the self inductance of armature winding, and L_{pf} is the mutual inductance between the excitation winding and armature winding. Both L_p and L_{pf} of DSEG are nonlinear function of rotor position angle θ . The rotor position angle can be obtained by calculating the integral of rotor speed.

According to formulas (4) and (6), the phase voltage can be described as follows:

$$u_p = -\frac{d\psi_p}{dt} - R_p i_p = -\frac{d(L_p i_p + L_{pf} i_f)}{dt} - R_p i_p \quad (7)$$

The phase electromagnetic torque T_p of DSEG can be given by following equation:

$$T_p = \frac{1}{2} i_p^2 \frac{dL_p}{d\theta} + i_p i_f \frac{dL_{pf}}{d\theta} \quad (8)$$

If the full bridge rectifier is used, two of three phases will operate together in sequence. Take phase A and phase C working together as an example, the output voltage of DSEG after rectification is as follows:

$$u_o = u_a - u_c \quad (9)$$

The output torque T_e of DSEG is the sum of T_a and T_c , i.e.

$$T_e = T_a + T_c \quad (10)$$

From formulas (7) to (10), it can be seen that both the output voltage and torque change with the variation of i_p and i_f . Therefore, in order to provide a constant voltage to the load, a DC/DC converter is connected between the rectifier and the load. The excitation current is controlled to adjust T_e of DSEG.

2.3 Drive Train Dynamic

Because DSEG can operate at low speeds, the wind turbine is directly connected to the DSEG without using a gearbox. The shafting of a direct drive WPGS can be represented by a mass model. The rotor speed is determined by following equation:

$$J \frac{d\omega}{dt} = T_m - T_e - B\omega = \frac{P_m}{\omega} - T_e - B\omega \tag{11}$$

where, J is the total inertia constant of the WTG; T_m is the mechanical torque of wind turbine; and B is the friction coefficient.

3 BP NN Based Wind Speed Estimation

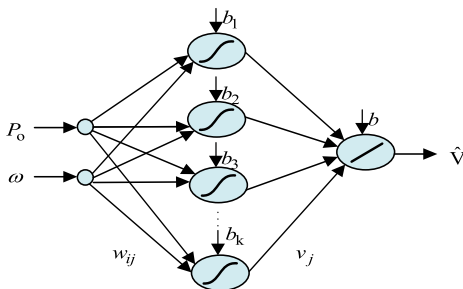
This paper uses a three-layer BP neural network to estimate wind speed in real time. By simulating wind turbine models at different wind speeds, we can obtain a training data set. Using output power P_o and rotational speed ω as two inputs and wind speed as an output, a BP neural network can be trained. The block diagram of BP neural network is shown in Fig. 5. The number of neurons in the hidden layer is assumed to be k . The transfer function of the hidden layer neuron adopts the hyperbolic tangent S-shaped function "tansig" defined in Formula (12). The output layer neurons use a linear transfer function. The overall mapping relationship between the input and output signals of the BP neural network is given by Formula (13).

$$\tan \operatorname{sig}(x) = \frac{2}{1 + e^{-2x}} - 1 \tag{12}$$

$$\hat{V} = b + \sum_{j=1}^k v_j \tan \operatorname{sig}(w_{1j}P_o + w_{2j}\omega + b_j) \tag{13}$$

In formula (13), b_j and b are the bias terms of the hidden layer and the output layer respectively; w_{1j} and w_{2j} are the weights between input and hidden layers; v_j are the weights between hidden layer and output layer.

Fig. 5 Block diagram of BP Neural Network



The trained BP NN can be generated as an NN module. The generated module is then embedded into the model of the wind power generation system to achieve real-time wind speed prediction.

4 MPPT Realization of Wind Power Generation System

Based on BP NN prediction, the wind speed can be estimated in real time. According to formula (3), the optimal rotor speed command is then determined by:

$$\omega^* = \frac{\lambda_{opt} \hat{V}}{R} \tag{14}$$

In order to achieve maximum power, a DSEG speed controller is designed by adjusting the excitation current. Figure 6 shows the topology of excitation circuit. When system operates normally, Q_2 is always on; the switching state of Q_1 is controlled by duty cycle generated in Fig. 7. When a fault occurs, Q_1 and Q_2 are closed simultaneously. Figure 7 shows the detailed control diagram of the excitation current regulator. The excitation current command gives the duty ratio of Q_1 through the excitation current hysteresis comparison control based on the error between the optimal speed and the actual speed.

Fig. 6 The topology of excitation circuit

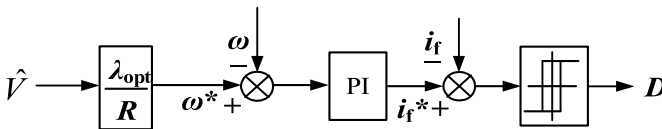
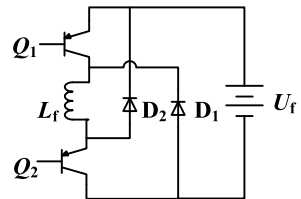


Fig. 7 The control diagram of excitation current

Fig. 8 Real wind speed and estimated value

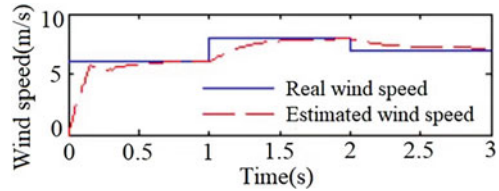
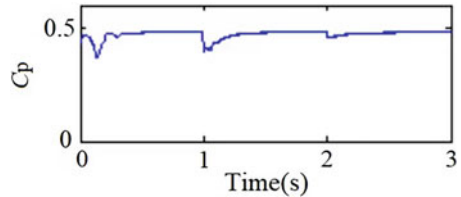


Fig. 9 Wind power coefficient



5 Simulation Study and Result Analysis

Simulation studies are conducted in Matlab/SimuLink to verify the effectiveness of proposed wind speed estimation algorithm [9, 10]. The main parameters of studied WPGS are as follows: (1) wind turbine: the blade radius is $R = 1.6$ m; the air density is $\rho = 1.225$ kg/m³; the optimal tip speed ratio $\lambda_{opt} = 8.1$; the maximum wind power coefficient $C_{pmax} = 0.48$. (2) DSEG: the rated power is 2 kW, the number of stator and rotor poles is 24/16, $R_p = 4 \Omega$, $L_{pmax}/L_{pmin} = 0.6H/0.06H$, $L_{pfmax}/L_{pfmin} = 0.3H/0.03H$, and the moment of inertia is $J = 0.2$ kg·m². The simulation results are shown in Fig. 8 and Fig. 9. From Fig. 8, we can see that the estimated wind speed tracks the (simulated) real wind speed with good accuracy. Based on the estimated wind speed, the wind power coefficient can reach a maximum value of 0.48, as shown in Fig. 9.

6 Conclusions

This paper proposes a new maximum wind power tracking algorithm for direct drive DSEG wind power generation systems. Based on the measured output power and rotor speed, the real-time wind speed is estimated using BP neural network. Then, the estimated wind speed is used to control the rotational speed of the DSEG to achieve MPPT. The simulation results of a 2 kW DSEG wind power generation system demonstrate the effectiveness of the proposed estimation method.

Acknowledgements This research was funded by NUAAs special project of graduate education and teaching reform (2023YJXGG-B04), NUAAs cultivation project of graduate education and teaching reform (ZDH-YJSJG202205), NUAAs research project of graduate education and teaching reform (2021YJXGG08), NUAAs special project of three aspects of education, National Basic


Research Program of China (2007CB210302), and Basic Scientific Research Expenses of NUAA (NS2012089). The authors gratefully acknowledge all the people who contribute to this work.

References

1. Chunyuan, B., Haiyang, X., Xiaoxia, L., Shangyue, L., Yulong, J.: Compensation strategy for commutation error of sensorless brushless DC motor wind power generation system based on speed change rate. *Trans. China Electrotech. Soc.* **36**(11), 2374–2382 (2021). (in Chinese)
2. Litong, X., Ming, C., Xinchu, W., et al.: Power signal feedback control of maximum power point tracking control for brushless doubly-fed wind power generation system considering loss. *Trans. China Electrotech. Soc.* **35**(3), 472–480 (2020). (in Chinese)
3. Xiao, X., Wang, H., Wu, Y., Zhang, Y., Zhou, Y., Li, J.: Coaxial dual motor with master-slave structure model-predictive direct torque control speed sensorless control strategy based on double sliding mode estimation. *Trans. China Electrotech. Soc.* **36**(5), 1014–1026 (2021). (in Chinese)
4. Muhammad Raza, K.S., Goto, H., Guo, H., Ichinokura, O.: A novel algorithm for fast and efficient maximum power point tracking of wind energy conversion systems. In: *ICEMS 2008*, pp. 1–6 (2008)
5. Wang, Q., Chang, L.: An intelligent maximum power extraction algorithm for inverter-based variable speed wind turbine systems. *IEEE Trans. Power Electron.* **19**(5), 1242–1249 (2004)
6. Zhang, L., Zhou, B., Cheng, F., Zuo, G.: A novel maximum power point tracking control method suitable for doubly salient electro-magnetic wind power generator system. In: *World Non-Grid-Connected Wind Power and Energy Conference*, pp. 1–6 (2009)
7. You, X., Zhou, B., Zuo, G., Guo, H.: A novel algorithm for fast and adaptive maximum power point tracking of wind energy generation system. *Adv. Mater. Res.* **383–390**, 3633–3638 (2012)
8. Ling, L., Yishan, M.: A novel nonlinear integral sliding mode control for maximum wind energy capture of doubly fed induction generators. *J. Xi'an Jiaotong Univ.* **54**(5), 95–101 (2020). (in Chinese)
9. Honghao, G., Bo, Z., Ying, L., Enli, X., Xia, Y.: Static and dynamic behaviour emulation of wind turbine based on load torque observation. *Proc. CSEE* **27**(33), 145–153 (2013). (in Chinese)
10. Xiaoying, S., Liancheng, Z., Shi, J., Fengge, Z., Dan, S.: Research on direct power control for brushless doubly-fed wind power generator with a novel hybrid rotor. *Trans. China Electrotech. Soc.* **35**(3), 494–501 (2020). (in Chinese)

A Simplified Prediction Method of Magnetic Field Radiation of High-power Power Electronic Equipment



Lei Zhang , GuiSheng Jie, Shan Gao, and ShengXian Ji

Abstract In the integrated power system (IPS) of ship platform, the conducted interference generated by high-power power electronic equipment will not only spread along the wire on the power grid, but also radiate to the surrounding space through the cable. With the increasingly strict electromagnetic compatibility standards, the magnetic field radiation generated by the high-power power electronic equipment has also been strictly limited. Predicting it can more effectively design the interference suppression measures and improve the electromagnetic compatibility (EMC) performance of equipment. First a basic cable radiation model is established based on the electromagnetic field theory. Then, the conducted interference estimation of power electronic equipment has been briefly introduced. Finally, a simplified prediction method of magnetic field radiation of high-power power electronic equipment according to the calculation results of conducted interference and cable radiation model is proposed. The effectiveness of this method is verified by experiments.

Keywords Power electronics · Magnetic field radiation · Electromagnetic compatibility (EMC) · Integrated power system (IPS)

1 Introduction

The integrated power system has been extended used in the new ships in recent years due to its high efficiency and flexibility. More and more high-power power electronic devices have been used in various ships. These devices have many advantages for power conversion, such as low noise, high efficiency, flexible layout, but due to their

L. Zhang · G. Jie (✉) · S. Gao · S. Ji

National Key Laboratory of Science and Technology on Vessel Integrated Power System, Naval University of Engineering, Wuhan 430033, Hubei, People's Republic of China

e-mail: zhenyujie@sina.com

L. Zhang

e-mail: zhangltx@sina.com

© Beijing Paiké Culture Commu. Co., Ltd. 2023

X. Dong et al. (eds.), *The proceedings of the 10th Frontier Academic Forum of Electrical Engineering (FAFEE2022)*, Lecture Notes in Electrical Engineering 1054, https://doi.org/10.1007/978-981-99-3408-9_94

1067

switching working mode, they will also bring some negative effects to the power mains, such as electromagnetic interference.

When high-power power electronic equipment works, the power electronics elements are continuously switched on and off. It inevitably produces a lot of interference in the power system. These interferences will not only be directly transmitted to the equipment connected to the power grid along the wire, but also be radiated to the sensitive equipment around the equipment through the power line.

Compared with the energy of working current in the power grid, the interference energy is small, but its frequency band is very wide and often cover the operation frequency of the sensitive system. If EMC is improperly designed, it will easily affect the normal operation of the sensitive system [1], especially for the narrow space of ships. To limit the harm of the interference, the current EMC standards have increasingly strict restrictions on such electromagnetic radiation [2]. Therefore, in addition to the suppression of conducted interference in the power mains, it is also necessary to predict the radiated interference of the equipment, so as to improve the EMC performance of the high-power power electronic devices.

For the prediction of conducted interference of power electronic equipment, there have been many in-depth studies [3–4], but for the prediction of radiated interference generated by such high-power power electronic equipment, relatively little research has been done. Cristina S has carried out research on near-field radiated interference of power electronic switching circuits. The research conclusion points out that the radiation generated by high-frequency conducted interference generated by switching tubes through connecting cables is the main source of near-field radiated interference of switching power supplies [5]. Some literatures have studied the radiation emission of cables, but most of them only put forward some suppression measures, lacking corresponding cable interference prediction models [6–8]. In addition, some research has also been carried out on the radiation of power electronic systems. These documents are mainly concentrated on the internal PCB board and far-field analysis of power electronic equipment, but there are few studies on the prediction and design of near-field electromagnetic radiation of the equipment itself [9–11].

Unlike the communication or radar system, there are no intentional transmitters and transmitting antennas in power electronic systems. It is little difficult to obtain the radiation source and the radiation antenna model directly in the power electronics equipment. However, the equivalent transmission source and antenna can be determined according to the energy distribution in the power electronics system.

The high-power equipment implements electric conversion in the cabinet and transmits energy to the system through long cables. The electromagnetic energy is inevitably leaked from the cables and cabinets since their shielding layers cannot achieve ideal shielding. The cabinet can be regarded as a transmitter because of the interference current generated during the power conversion in the cabinet, while the cables are regarded as antennas due to its high efficiency radiation.

In this paper, according to the electromagnetic field theory and several cable model, a simplified prediction method of magnetic field radiation of high-power power electronic equipment is proposed.

2 Basic Cable Magnetic Field Radiation Model

2.1 Basic Radiation Model

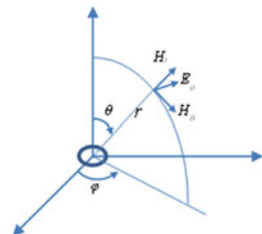
Electromagnetic radiation research usually needs to be analyzed according to antenna theory in the communication or radar system. In such systems, the frequency, power and antenna of the transmission source can be deduced from the working process of the system, so the parameters can be accurately calculated. However, in the power electronic system, these knowledges cannot be obtained directly from the system working process, but needs to be calculated and analyzed in advance. For example, the frequency of the radiation source in the power electronic system is usually not the working frequency of the system, but is related to the parasitic parameters in the system [12]. Thus, it is more difficult to make the radiation modeling of the power electronic system.

On the other hand, the research of radiation interference in power electronic systems is just to analyze the impact on the system environment, so its radiation model is not necessarily as accurate as in communication systems. Therefore, according to the working characteristics of power electronic equipment, the equipment can be simplified to obtain the equivalent radiation model of power electronic equipment.

Compared with the communication system, the interference frequency band in the power electronic equipment is relatively low, and only large-size components can play the role of transmitting antenna. Therefore, the long high-power cables in the system become the most effective transmitting antennas in the system. The cables between the equipment can be regarded as line antennas, while the cables constituting the loop in the system can be regarded as loop antennas. They can correspond to two kinds of ideal electromagnetic radiation models in antenna theory, electric dipole and magnetic dipole. In the electromagnetic field analysis, the basic magnetic field radiation unit is the current loop, as shown in Fig. 1.

When the distance r between the observation point and the current loop is far greater than the size of the current loop, the radiation field of the magnetic dipole is Eq. (1).

Fig. 1 Magnetic Dipole in Spherical Coordinate System



$$\begin{cases} H_r = \frac{I \cdot S \cdot \cos(\theta)}{2\pi \omega \varepsilon} \cdot \left[\frac{1}{r^3} + \frac{jk}{r^2} \right] \cdot e^{-jkr} \\ H_\theta = \frac{I \cdot S \cdot \sin(\theta)}{2\pi \omega \varepsilon} \cdot \left[\frac{1}{r^3} + \frac{jk}{r^2} - \frac{k}{r^2} \right] \cdot e^{-jkr} \\ E_\varphi = \frac{-j \cdot I \cdot S \cdot k \cdot \eta \cdot \sin(\theta)}{4\pi} \cdot \left[\frac{1}{r^2} + \frac{jk}{r} \right] \cdot e^{-jkr} \\ H_\varphi = E_r = E_\theta = 0 \end{cases} \quad (1)$$

Here, $k = 2\pi/\lambda$ is the phase shift constant, ε is the dielectric constant, $\eta = \sqrt{\mu/\varepsilon}$ is the wave impedance.

2.2 Radiation Model of Different Cables

In fact, any radiation circuit can be decomposed into several electric or magnetic dipoles, and the radiation field of each electric or magnetic dipole can be calculated separately. However, it is difficult to apply this method to power electronic equipment because there are too many current-carrying devices in the equipment, and their size, shape, layout, and carrying power of internal cables are different. Using this method to calculate will not only be very complex and time-consuming, but also difficult to understand the variation factor of interference. As the prediction of electromagnetic interference of the power electronics system, more attention is paid to the impact of the overall equipment on the external electromagnetic environment. Therefore, a simplified calculation method must be considered. Because the current flow direction of the equipment is determined, the complex circuit composed of all devices in the cabinet can be equivalent with a simplified current loop to obtain a simplified radiation source model. Therefore, the circuit inside the cabinet can be simplified as a wire pair or current loop in the prediction of electromagnetic environment. After considering the shielding effectiveness of the cabinet, the magnetic field radiation of high-power equipment can be predicted.

In this paper, the current-carrying cable is regarded as the basic unit of the electromagnetic radiation research of the integrated power system. The size and shape of the cable can be approximated according to the design situation, and the current on the cable can be obtained by conducting interference analysis. After the corresponding magnetic field emission model is established, the electromagnetic radiation of the equipment can be predicted.

For simplicity, the magnetic field radiation source in the system can be defined as three basic units as shown in Fig. 2:

- a) semi-infinite wire, simulating the input and output long cables of the equipment;
- b) Limited length conductor, simulating the cables in the equipment cabinet;
- c) Ring current, it can be used to simulate the current loop inside the equipment.

According to Biot-Savart law, it is easy to calculate the magnetic induction intensity of these models. When the current denoted as I , the magnetic induction intensity of these models at the distance r from the current source is as follows:

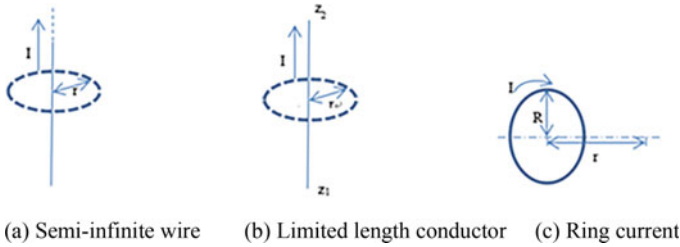


Fig. 2 Several Basic Models of Magnetic Field Radiation Calculation

a) semi - infinite wire: $B = \frac{\mu_0 I}{4\pi r}$ (2)

b) Limited length conductor, $B = \frac{\mu_0 I}{4\pi r} \left(\frac{z_2}{\sqrt{z_2^2 + r^2}} - \frac{z_1}{\sqrt{z_1^2 + r^2}} \right)$ (3)

c) Ring current, $B = \frac{\mu_0 I R^2}{2(R^2 + r^2)^{3/2}}$ (4)

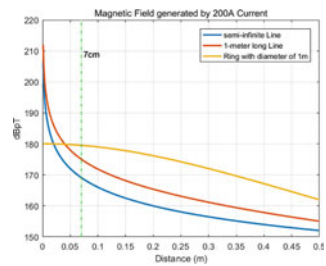
Here, μ_0 is the permeability in free space, $\mu_0 = 4\pi \times 10^{-7}$ (H/m).

According to Eqs. (2)–(4), the variation of magnetic induction intensity with distance r can be obtained. For example, when the current of the equipment is 200 A, the magnetic field of semi-infinite length, 1 m long wire and 1 m diameter circle at a distance of 1 mm to 0.5 m from the current source shown in Fig. 3.

It can be seen that without shielding, the magnetic field radiation values at 7 cm of the three models are 169, 175, 179 dBpT, which have exceeded the limit of 150 dBpT of MIL-STD-461G RE101. The calculation also shows that to meet the limit of RE101 without shielding, the equipment current should be within 100 A.

When high-power power electronic equipment works, the pulse current on the cable will become the source of magnetic field radiation, so it is necessary to calculate the electromagnetic radiation when considering interference.

Fig. 3 Magnetic Field Generated by Different Radiation Sources



3 Magnetic Field Prediction Considering Interference

From Eqs. (3) to (5), it can be seen that the magnetic induction intensity is only depend on the current, so when predicting the magnetic field generated by the interference current, it is important to predict the amplitude of the interference current. The current limit specified in the standard (such as MIL-STD-461G CE101, etc.) or the predicted value of conducted interference can be used to predict the magnetic field radiation of high-power equipment.

3.1 Prediction from the EMC Standard

Examples are as follows. If the switching frequency of a high-power equipments is 5.5 kHz, its switching frequency harmonics are 11 and 22 kHz, the DC working current is about 240 A, and the output AC current is about 120 A, then the allowable interference current of the equipment under each harmonic can be estimated using the limits of CE101 and CE102. The magnetic field at the switching frequency can be calculated and compared with the RE101 limit. CE102 gives the conduction voltage standard, which can be converted into current by subtracting 34 dB from 50-Ω standard impedance.

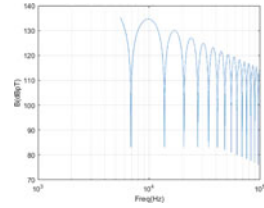
For DC and AC equipment, Table 1 shows the magnetic field calculation results of harmonic current at typical switching frequency under the condition that the interference current limit is met. Here, the magnetic field unit is dBpT.

It can be seen that even if the interference current of the equipment meets the CE101 limit, the magnetic field generated by the interference current far exceeds the RE101 limit. Therefore, attention must be paid to the shielding of these radiation sources. It also can be seen that the magnetic field radiation generated by the ring is the largest in the tables, so it is important to try to avoid the formation of large loops of current.

Table 1 Magnetic Field (dBpT) of the DC and AC Equipment

Frequency	5.5 kHz		11 kHz		22 kHz	
Equipment	DC	AC	DC	AC	DC	AC
Current limit	1A	1A	3.61 mA	3.22 mA	1.61 mA	1.43 mA
Semi-infinite wire	123.098	123.098	74.27	73.26	67.23	66.26
1 m long wire	129.03	129.03	80.21	79.19	73.17	72.20
1 m diameter circle	133.52	133.52	84.69	83.67	77.66	76.68
Magnetic field limit	91.35	91.35	85.08	85.08	78.81	78.81

Fig. 4 Magnetic Field Radiation Prediction from Conducted Current Calculation



3.2 Prediction from the Conducted Interference

The internal working current and voltage of the power electronic equipment are in a pulse state. These pulses are the source of power electronic equipment interference. When making interference prediction, the pulse can be simply regarded as a trapezoidal pulse train. The corresponding interference amplitude can be obtained by Fourier expansion of trapezoidal wave:

$$I(nf_s) = 2I_s D \frac{\sin(\pi n f_s \tau)}{\pi n f_s \tau} \cdot \frac{\sin(\pi n f_s t_r)}{\pi n f_s t_r} \tag{5}$$

Here, I_s is the working current, $\tau = DT$, D is the duty cycle of the pulse, T is the working cycle, $T = 1/f_s$, f_s is the switching frequency.

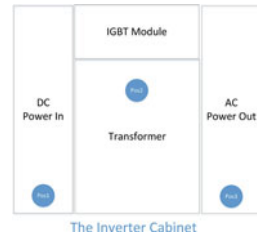
According above formulas, the magnetic field radiation generated by the high-power equipment in 3.1 can be calculated. The results are shown in Fig. 4.

4 Experiment

In order to verify the effectiveness of the prediction method, a high-power inverter is tested. The inverter composition and magnetic field radiation test layout are shown in Fig. 5. Figure 5 is the inverter composition diagram. The input voltage of the inverter is 440 V DC, the current is 230 A, the output voltage is three-phase 390 V, the current is 120 A. The cabinet can be divided into three rooms, the left is the DC input room, the middle is the power unit and transformer room, and the right is the AC output room; Different positions for magnetic field radiation test are also marked in the figure, and the test distance is set at 7 cm from the cabinet.

According to the previous analysis, when predicting the magnetic field radiation of the cabinet, the cables inside the cabinet need to be regarded as transmitting antennas, that is, the current loop inside the cabinet needs to be analyzed. According to the working principle of the inverter, the main current circuit inside the inverter is shown in Fig. 6. Because the AC output and DC input in the cabinet are composite buses, the circuit area is small, and the largest area of circuit loop is composed of transformers, as shown in Loop1–Loop6 in Fig. 6. There are three DC current loops and three AC current loops in the transformer room. According to the size of the

Fig. 5 The layout of the Inverter Cabinet



cabinet, It can be considered that the conductor is about 2 m long and the diameter of the current loop inside the cabinet is 1 m.

The cabinet, DC input terminal and AC output terminal are tested and calculated respectively. In order to better verify this method, the current value measured by conducted interference is used here. The comparison between calculation results and test results is shown in Fig. 7.

It can be seen that the predicted value is larger than the measured value, because the model simplifies the actual equipment and does not consider the influence of current phase difference on different lines.

In addition, the distance and direction from the interference source to the test point in the actual line are not ideal, but the calculation results can basically reflect the envelope of the equipment magnetic field radiation. The interference at 5.5 kHz is not obvious because the equipment uses dual design, and the equivalent switching frequency of the equipment is increased to 11 kHz. For the characteristic frequency

Fig. 6 The Current Loop in the inverter Cabinet

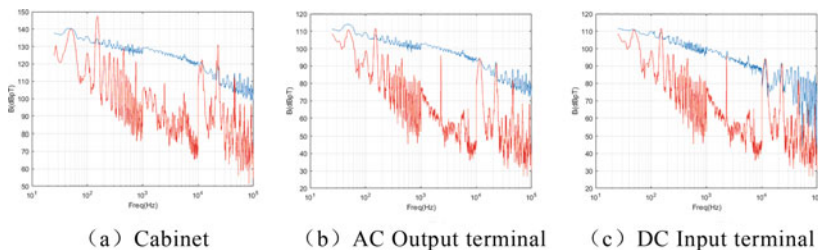
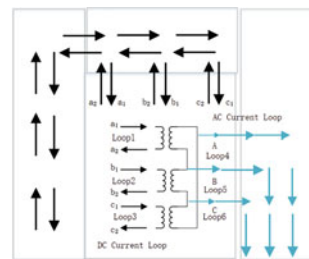


Fig. 7 The Measured and Predicted Results (Red –Measured, Blue–Predicted)

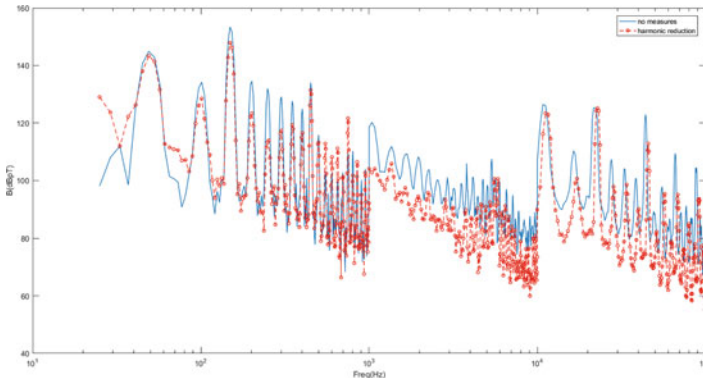


Fig. 8 The interference Reduction

points of 11 and 22 kHz, the predicted value is more accurate, which may be that the current of these two frequencies is mainly common-mode, and the principle of this prediction method is simple adding together, so it is more conducive to the calculation of common-mode current radiation.

Because its emission source is a current loop composed of harmonic current, there are two solutions to reduce the magnetic field radiation. First, reduce the harmonic current as much as possible. Second, reduce the area of current loop. Some measures has been taken to reduce the harmonic currents, the effect is with a change of about 3–5 dB, which is shown in Fig. 8.

At present, the inverter cabinet is too compact, and it is difficult to change the current loop size, the test effect of the measures is not obvious. It needs further research about how to take this way to more effectively to suppress this interference.

5 Conclusion

The conducted interference generated by high-power power electronic equipment with large current and high voltage will radiate interference into space through cables in the system. According to the basic magnetic dipole model, combined with the calculation of conducted interference of high-power power electronic equipment, the magnetic field radiation of high-power power electronic equipment has been researched, and the magnetic field radiation models of system cables are proposed. A simplified prediction magnetic radiation model of the high-power power electronic equipment is obtained and the effectiveness of the method is verified by experiment. The calculation results can also provide reference for the EMC design of equipment.

Acknowledgements This work is supported by Key Projects of Basic Strengthening of the Science and Technology Commission (2017JCJQZD0041001).

References

1. Meng, J., Zhang, L., Zhao, Z., et al.: Analysis, Measurement and Protection of the Electromagnetic Interference in New Vessel system. Publishing House of Electronics Industry, Beijing (2020). (in Chinese)
2. MIL-STD-461G Requirements for the control of electromagnetic interference characteristics of subsystems and equipment. Department of Defense (2015)
3. Huang, H., Tong, H., Wang, N., et al.: Analysis of the influence of IGBT segmented transient model with parasitic oscillation on electromagnetic interference prediction. *Trans. China Electrotech. Soc.* **36**(12), 2434–2445 (2021). (in Chinese)
4. Jin, M., Ma, W., Zhang, L., et al.: EMI evaluation of power converters considering IGBT switching transient modeling. *Proc. CSEE* **25**(20), 16–20 (2005). (in Chinese)
5. Cristina, S., Antonini, G., Orlandi, A.: Switched mode power supplies EMC analysis: near field modeling and experimental validation. In: *IEEE International Symposium on EMC, Piscataway*, IEEE, pp. 453–458 (1995)
6. Sheng, L., Yaming, G.: Study on EMC optimization of ship cable spacing. *J. Harbin Eng. Univ.* **29**(9), 938–943 (2008). (in Chinese)
7. Su, C., Hubing, T.H.: Calculating radiated emissions due to I/O line coupling on printed circuit boards using the imbalance difference method. *IEEE Trans. Electromagn. Compat.* **54**(1), 212–217 (2012)
8. Feng, X., Wang, B., Liu, H., et al.: Suppressing radiated noise of unshielded cable on the relay protection test signal source research. *Electr. Eng.* **21**(3), 44–51 (2020). (in Chinese)
9. Schneider, D., Beltle, M., Siegel, M., et al.: Radiated emissions of an electric drive system estimated on a bench using disturbance currents and transfer functions. *IEEE Trans. Electromagn. Compat.* **57**(3), 311–321 (2015)
10. Henglin, C., Tao, W., Limin, F., et al.: Determining far-field EMI from near-field coupling of a power converter. *IEEE Trans. Power Electron.* **29**(10), 5257–5264 (2014)
11. Laour, M., Tahmi, R., Vollaire, C.: Modeling and analysis of conducted and radiated emissions due to common mode current of a Buck converter. *IEEE Trans. Electromagn. Compat.* **59**(4), 1260–1267 (2017)
12. Zhang, K., Wang, S., Li, M., et al.: Method of electromagnetic radiation prediction and suppression based on capacitance parameter equivalence in power converter system. *Trans. China Electrotech Soc.* **36**(2), 235–247 (in Chinese)

Study on the Influence of Different Degrees of Deterioration of Oil-Paper Insulation on Partial Discharge Characteristics



Li Longfei, Wu Tianbo, Liu Lei, Wang Xin, Zhang Fei, Ge Zhijie, Zhang Shuobo, and Liu Hongshun

Abstract The experimental platform of partial discharge under AC/DC composite voltage is built, and the time–frequency characteristics, pulse waveform characteristics, spectrum characteristics, energy characteristics and entropy characteristics of partial discharge under different aging conditions and AC/DC working conditions are studied. It is found that with the increase of aging days, the dispersion of discharge decreases, the steepness of discharge waveform increases, the energy released by discharge increases, and the discharge becomes more intense. With the increase of DC content, the discharge decreases. When the aging time is the same, the discharge of extremely uneven field is more intense and the dispersion of discharge is smaller than that of slightly uneven field.

Keywords Partial discharge · oil-paper insulation · time–frequency characteristics · spectrogram characteristics

1 Introduction

Oil-paper insulation is the main form of internal insulation of converter transformer [1, 2], and partial discharge and charge accumulation are not only the main causes of oil-paper insulation aging and deterioration, but also the important signs and manifestations of insulation aging and deterioration [3–5]. Therefore, it is necessary

L. Longfei · W. Tianbo · L. Lei · Z. Fei · G. Zhijie · Z. Shuobo
State Grid Xinjiang Electric Power Research Institute, Urumqi 830011, China

W. Xin
DC Technology Center of State, Grid Corporation of China, Beijing 100053, China

L. Hongshun (✉)
Shandong Provincial Key Laboratory of UHV Transmission Technology and Equipment,
Jinan 250061, China
e-mail: lhs@sdu.edu.cn

to study the influence of different deterioration of oil-paper insulation on partial discharge.

Many researches on partial discharge in oil-paper insulation have been carried out. Chen Weigen [6] built a test platform for the development characteristics of air-gap discharge, extracted the discharge characteristic parameters, and divided the different development stages of discharge using system clustering. Based on the change of discharge characteristic parameters, a method of discharge development stage recognition based on cluster-wavelet neural network is proposed. Ling Yun has built a laboratory partial discharge test platform [7], and proposed a new characteristic quantity of average discharge energy per second, which can well characterize the change of discharge characteristics in different discharge stages during the discharge development process. At the same time, the discharge development process is divided based on the fuzzy C-means clustering method. Long Zhenze et al. made five size air gap discharge models [8], carried out accelerated degradation tests on defect models with two sizes of air gap, and introduced random forest algorithm and Adaboost algorithm into partial discharge fault diagnosis. Sun Zhenquan and others studied the partial discharge pulse of typical air-gap discharge model of oil-paper insulation under AC voltage, DC voltage, oscillating impulse voltage and lightning impulse voltage respectively [9].

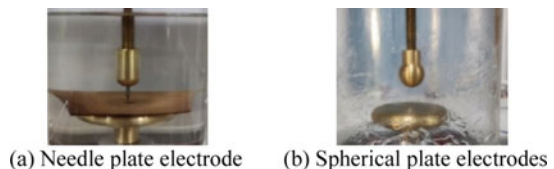
In this paper, the experimental platform of partial discharge under AC and DC combined voltage is built, and the time–frequency characteristics, pulse waveform characteristics, spectrum characteristics, energy characteristics and entropy characteristics of partial discharge in extremely non-uniform electric field and slightly non-uniform electric field under different working conditions and different aging conditions are studied.

2 Partial Discharge Test Platform

In this model, the radius of curvature of the needle electrode tip is $50\ \mu\text{m}$. The width of the oil gap and the thickness of the oil-immersed paperboard are $0.5\ \text{mm}$. The ball plate electrode is shown in Fig. 1(b). Spherical plate electrode is used to simulate the discharge under slightly uneven electric field.

The circuit diagram and physical diagram of the experimental platform are shown in Fig. 2(a) and (b) respectively. The DC isolation capacitor allows the AC and DC voltage to be superimposed through parallel phases, which is beneficial to protect

Fig. 1 Plate electrode



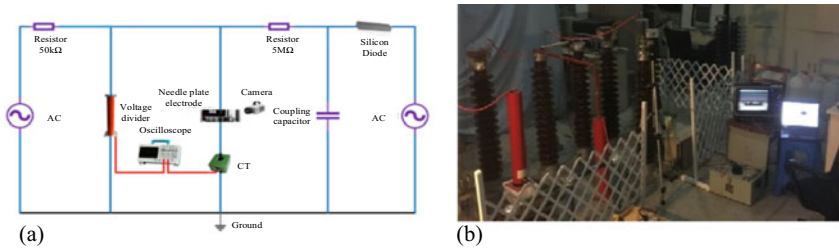


Fig. 2 Experimental platform under AC-DC composite voltage

the power supply. The DC high voltage is provided by the DC high voltage source combined by the corona free AC high voltage source and the rectifier circuit, while the AC high voltage is directly provided by the corona free AC high voltage source. The coupling capacitance required for rectification is 0.1 nF; The transmission cable connected to the oscilloscope adopts the terminal matching method, and its wave impedance is 50 Ω.

High-speed camera and oscilloscope are also used in the experimental circuit. The former is used to capture the shape of partial discharge, and the latter is used to record the pulse voltage waveform. The main parameters of these instruments are shown in Table 1. The high-speed camera should be triggered simultaneously with the oscilloscope after the delay correction. In the experimental circuit, partial discharge will also occur outside the needle plate electrode. In order to reduce this discharge phenomenon, various experimental devices should be connected with shielded wires. The shielded wire should be as long or bent as possible, and each contact should be wrapped with copper foil. The test circuit complies with IEC-60270, and the relevant tests shall be conducted in a normal temperature laboratory with noise less than 10 pC.

Table 1 Main parameters of partial discharge detection instrument.

Measuring instrument	Parameter	Value
High-speed camera	Maximum resolution	1696 × 1710
	Pixel size (μm × μm)	8 × 8
	Maximum frame rate (fps)	2.98 × 10 ⁵
	Exposure time (μs)	>3.4
Oscilloscope	Analog bandwidth (GHz)	1
	Sampling rate (GS/s)	5
	Sensitivity (mV)	1

3 Partial Discharge Test Platform

3.1 Partial Discharge Characteristics of Extremely Uneven Electric Field Under AC/DC 1:1 Working Condition Under Different Aging Conditions

(1) Time-frequency characteristic

The equivalent time spectrum diagram under AC/DC 1:1 voltage is shown in Fig. 3. With the increase of aging days, the equivalent frequency F_{eq} and the equivalent time T_{eq} both increase, indicating that the time domain range of the discharge pulse is wider, the rising edge is steeper, and the discharge is more intense.

(2) Pulse waveform characteristics

The partial discharge pulse at different aging stages is shown in Fig. 4. The positive partial discharge waveform is a single peak pulse, and the negative partial discharge waveform is an oscillating pulse, and also has a narrow pulse width, a fast rising and falling edge.

(3) Spectral characteristics

The characteristics of partial discharge spectrum of extremely uneven electric field under AC and DC 1:1 working conditions under different aging conditions are shown in Fig. 5. The spectrum shows asymmetric distribution under AC and

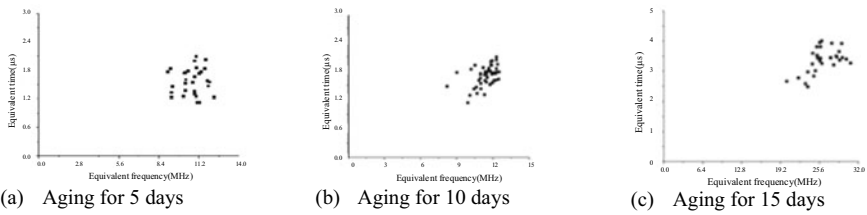


Fig. 3 Spectrogram characteristics of partial discharge of extremely uneven electric field under different aging conditions under 1:1 AC/DC conditions

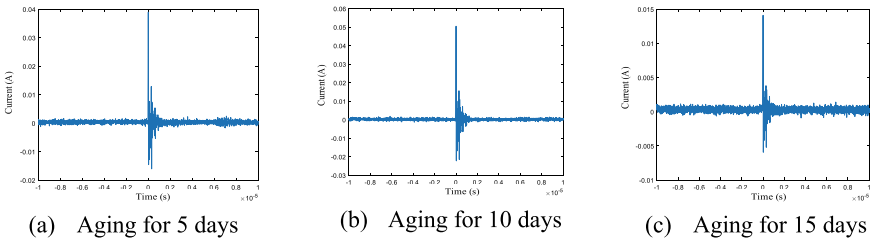


Fig. 4 Pulse waveform characteristics of extremely uneven electric field under different aging conditions under AC/DC 1:1 conditions

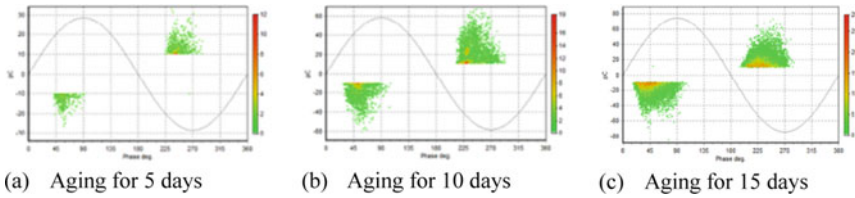


Fig. 5 Partial discharge spectrogram characteristics of extremely uneven electric field under different aging conditions under 1:1 AC/DC conditions

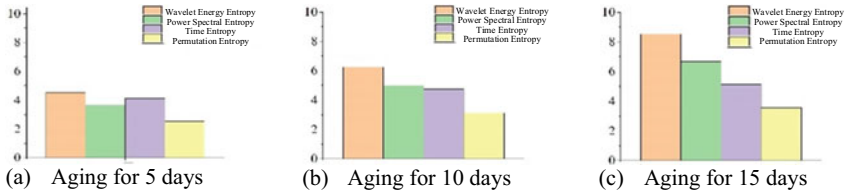


Fig. 6 Partial discharge entropy characteristics of extremely uneven electric field under different aging conditions under 1:1 AC/DC conditions

DC superposition, with dense positive half-cycle discharge and large discharge amplitude.

(4) Energy characteristic and entropy characteristic

The entropy characteristics of partial discharge under different aging conditions are shown in Fig. 6. With the increase of aging days, all kinds of information entropy values increase, while wavelet energy entropy and power spectrum entropy increase significantly, indicating that the energy released by discharge is larger and the discharge is more intense.

3.2 Partial Discharge Characteristics of Extremely Uneven Electric Field Under AC/DC 1:3 Working Condition Under Different Aging Conditions

(1) Time–frequency characteristic

The spectrum characteristics of partial discharge under different aging conditions under AC and DC 1:3 working conditions are shown in Fig. 7. With the increase of aging days, the spectrum distribution becomes more concentrated, indicating that the difference of partial discharge pulse waveform is small and the dispersion is low. The waveform steepness increases with the increase of frequency.

(2) Pulse waveform characteristics

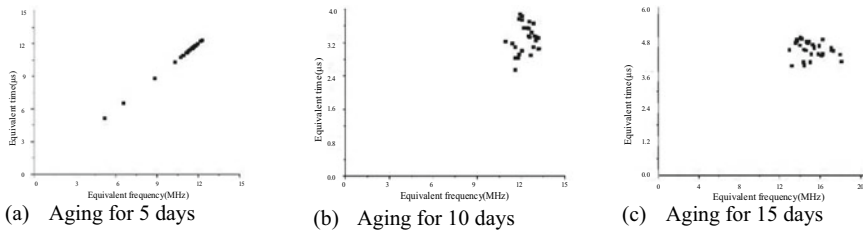


Fig. 7 Spectrogram characteristics of partial discharge of extremely uneven electric field under different aging conditions under 1:3 AC/DC conditions

The characteristics of partial discharge pulse waveform under different aging conditions are shown in Fig. 8. The aging stage has a great impact on the partial discharge pulse waveform of oil-paper insulation, but the DC component proportion and polarity only affect the parameters of F_{eq} , T_{eq} , T_u , T_h , etc.

(3) Spectral characteristics

The characteristics of partial discharge spectrum under different aging conditions are shown in Fig. 9. The dispersion of maximum discharge, average discharge and apparent discharge of negative partial discharge is always high, reflecting obvious polarity effect.

(4) Energy characteristic and entropy characteristic

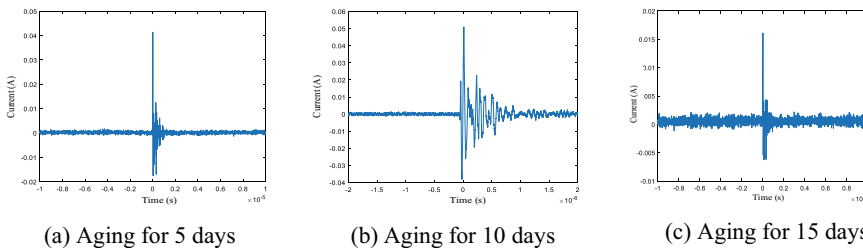


Fig. 8 Pulse waveform characteristics of extremely uneven electric field under different aging conditions under 1:3 AC/DC conditions

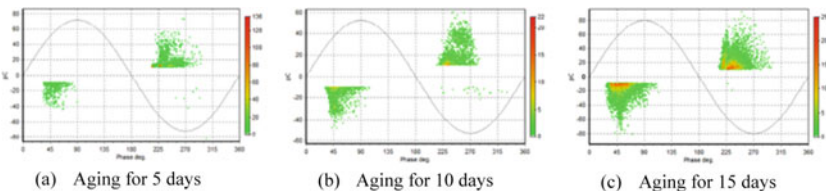


Fig. 9 Partial discharge spectrogram characteristics of extremely uneven electric field under AC/DC 1:3 operating conditions under different aging conditions

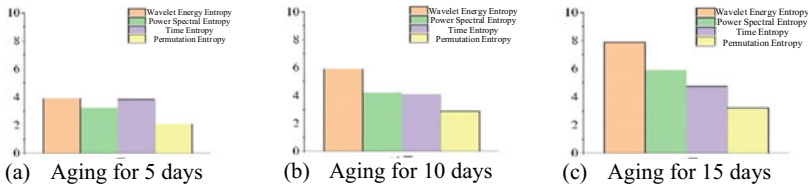


Fig. 10 Partial discharge entropy characteristics of extremely uneven electric field under ac/DC 1:3 operating conditions under different aging conditions

The partial discharge entropy characteristics of extremely uneven electric field under AC/DC 1:3 working condition are shown in Fig. 10, and the entropy value is reduced compared with that under AC/DC 1:1 working condition. With the increase of aging days, all kinds of entropy values increase, while the wavelet energy entropy and power spectrum entropy increase significantly, indicating that the energy released by the discharge is larger and the discharge is more intense.

Figure 11 shows the partial discharge pulse energy–discharge frequency distribution spectrum of 50 power–frequency oil–paper insulation samples at different aging stages. It can be seen from Fig. 11 that at the initial stage of aging (0–5 days), the partial discharge pulse energy of oil–paper insulation is small; The discharge pulse energy of new paper is less than 4 μ J. After aging for 24 and 72 h, the maximum partial discharge pulse energy is only 6%, although its partial discharge pulse energy is higher than that of new paper μ J. In the middle stage of aging (5–10 days), large energy discharge pulse began to appear, and the number of small energy discharge pulse also increased correspondingly; The maximum partial discharge pulse energy of oil–paper insulation after 5 days of aging reaches about 9 μ J. After aging for 10 days, its maximum pulse energy further increases to 10 μ J above indicates that the deterioration rate of oil–paper insulation is accelerated at this stage. At the end of aging (10–15 days), the number of small energy discharge pulses continued to increase, but the maximum partial discharge pulse energy showed a downward trend; After 10 days of aging, only a small amount of discharge pulse energy reaches 12 μ About J, when aging for 15 days, the maximum partial discharge pulse energy decreases to 10 μ J or so. It can be seen that with the increase of aging degree, the maximum partial discharge pulse energy of oil–paper insulation first increases and then decreases, but the number of small energy discharge pulses always keeps increasing.

3.3 Partial Discharge Characteristics of Slightly Uneven Electric Field Under AC/DC 1:1 Working Condition Under Different Aging Conditions

(1) Time–frequency characteristic

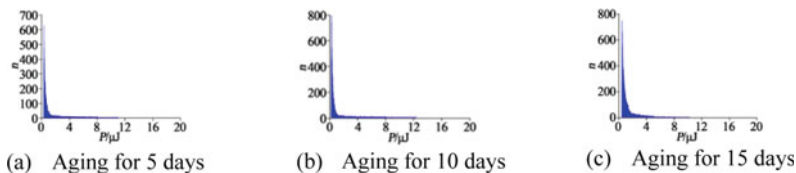


Fig. 11 Discharge pulse energy-discharge frequency distribution of oil-paper insulation at different aging stages

The equivalent time–frequency spectrum under AC/DC 1:1 voltage is shown in Fig. 12. The time–frequency spectrum changes from scattered to concentrated and scattered with the increase of aging days.

(2) Pulse waveform characteristics

The partial discharge pulse at different aging stages is shown in Fig. 13. The weak oscillation of the tail of the negative partial discharge pulse indicates that the main discharge is accompanied by weak reverse discharge and secondary discharge; The weak oscillation of the positive partial discharge pulse peak is different from that under the positive half cycle of AC. On the one hand, it contains white noise, and on the other hand, it is determined by the characteristics of DC partial discharge.

(3) Spectral characteristics

The spectral characteristics of different aging stages are shown in Fig. 14. In the case of AC and DC superimposed, the spectrum shows asymmetric distribution, and

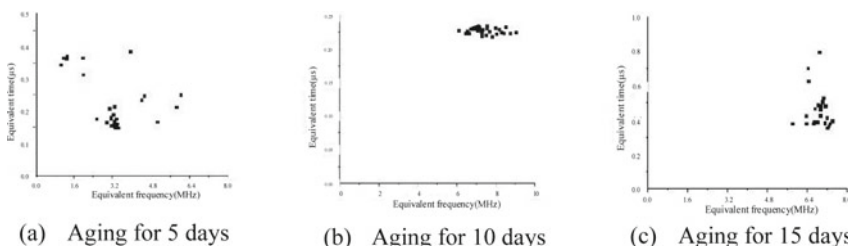


Fig. 12 Temporal spectrogram characteristics of slightly uneven electric field under different aging conditions under 1:1 AC/DC conditions

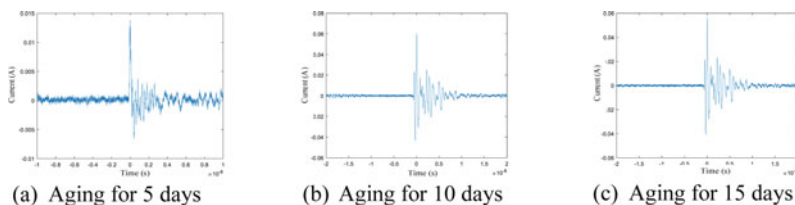


Fig. 13 Pulse waveform characteristics of slightly uneven electric field under different aging conditions under AC/DC 1:1 conditions

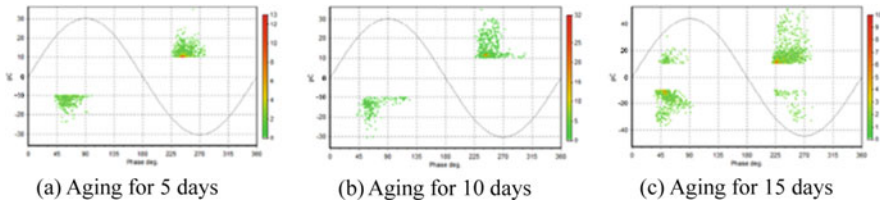


Fig. 14 Partial discharge spectrogram characteristics of slightly uneven electric field under AC/DC 1:1 operating conditions under different aging conditions

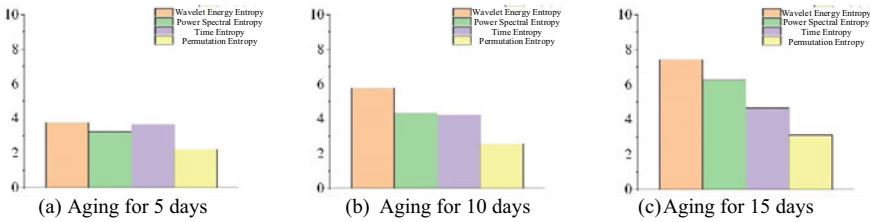


Fig. 15 Partial discharge entropy characteristics of slightly uneven electric field under AC/DC 1:1 conditions under different aging conditions

the dispersion of the maximum discharge, average discharge and apparent discharge of negative partial discharge is always high, reflecting the obvious polarity effect.

(4) Energy characteristic and entropy characteristic

The partial discharge entropy characteristics of different aging conditions on slightly uneven electric field under AC/DC 1:1 working condition are shown in Fig. 15. With the increase of aging days, the energy entropy and power spectrum entropy indicate that the discharge releases more energy and the discharge is more intense.

3.4 Partial Discharge Characteristics of Slightly Uneven Electric Field Under AC/DC 1:3 Working Condition Under Different Aging Conditions

(1) Time–frequency characteristic

The time–frequency characteristics of different aging stages are shown in Fig. 16. The equivalent frequency is increasing as a whole, indicating that the steepness of the rising edge of the waveform and the pulse bandwidth become larger. The spectrum changes from scattered to centralized, and finally becomes scattered.

(2) Pulse waveform characteristics

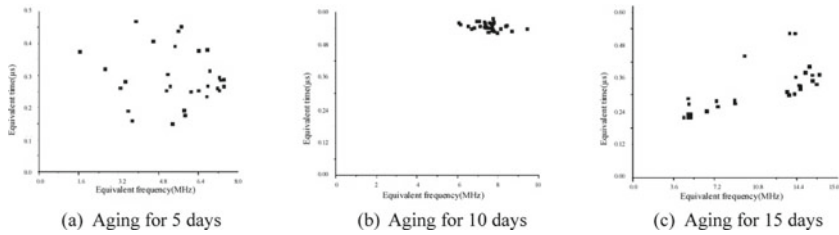


Fig. 16 Time-spectrum spectrogram characteristics of slightly uneven electric field under different aging conditions under 1:3 AC/DC conditions

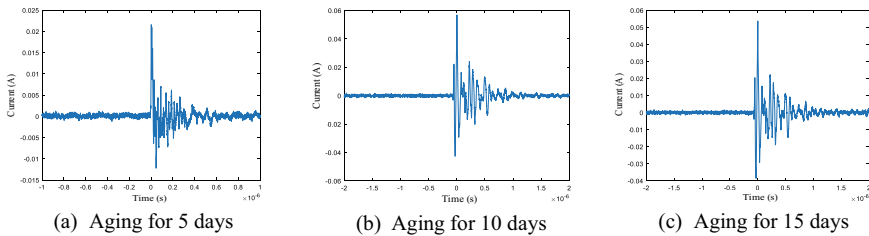


Fig. 17 Pulse waveform characteristics of slightly uneven electric field under different aging conditions under AC/DC 1:3 conditions

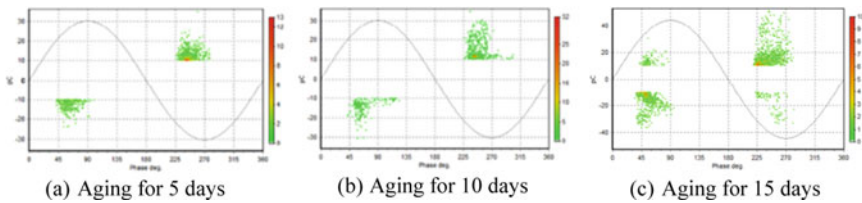


Fig. 18 Partial discharge spectrogram characteristics of slightly uneven electric field under different aging conditions of AC/DC 1:3

The partial discharge pulse at different aging stages is shown in Fig. 17. The positive partial discharge waveform is a single peak pulse, while the negative partial discharge waveform has a main peak and multiple secondary small peaks, and its pulse width is narrow, and its rising and falling edges are fast.

(3) Spectral characteristics

The characteristics of partial discharge spectrum of slightly uneven electric field under AC/DC 1:3 working conditions under different aging conditions are shown in Fig. 18. Compared with AC/DC 1:1, DC content increases and discharge decreases.

(4) Energy characteristic and entropy characteristic

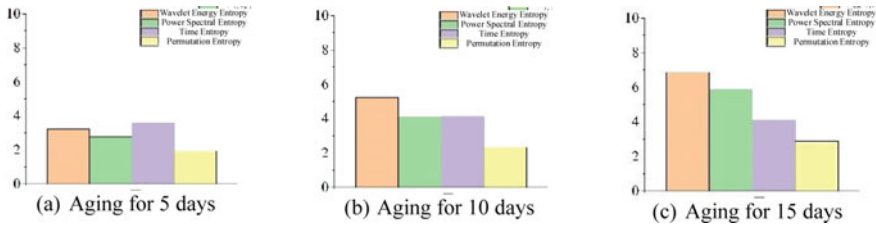


Fig. 19 Partial discharge entropy characteristics of slightly uneven electric field under AC/DC 1:3 operating conditions under different aging conditions

The partial discharge entropy characteristics of slightly uneven electric field under AC/DC 1:3 working conditions are shown in Fig. 19. With the increase of aging days, the entropy value increases and the discharge becomes more and more intense.

4 Conclusion

In this paper, the experimental platform of partial discharge under AC and DC combined voltage is built, and the time–frequency characteristics, pulse waveform characteristics, spectrum characteristics, energy characteristics and entropy characteristics of partial discharge under different aging conditions and AC and DC conditions are studied.

With the increase of aging days, the discharge dispersion decreases, the discharge waveform steepness increases, the discharge energy increases, and the discharge becomes more intense. The main discharge of negative partial discharge pulse is accompanied by weak reverse discharge and secondary discharge, and there is obvious polarity effect. With the increase of DC content, the discharge decreases. When the aging time is the same, the discharge of extremely uneven field is more intense and the dispersion of discharge is smaller than that of slightly uneven field.

References

1. Li, Q., Wang, L., Wang, P., et al.: A review on partial discharge and charge distribution characteristics of oil-paper insulation of converter transformer. *High Volt Technol.* **46**(08), 2815–2829 (2020)
2. Du, B., Jiang, J.: An overview of the influence of oil-paper insulation moisture on partial discharge behavior of converter transformer. *High Volt. Technol.* **47**(08), 2932–2945 (2021)
3. Li, Q., Li, S., Si, W., Wang, G., Wang, B., Liu, B.: Analysis of key problems in the evaluation of oil-paper insulation state of power transformer based on partial discharge. *High Volt. Technol.* **43**(08), 2558–2565 (2017)
4. Gao, S., Zhao, J., Qiao, H., Tian, Y., Wang, Y., Yin Yi: A review on partial discharge detection and characteristics of converter transformer. *Insulat. Mater.* **55**(07), 1–9 (2022)

5. Zhang, R., Zhang, Q., Zhou, J., Wang, S., Sun, Y., Wen, T.: Partial discharge characteristics and deterioration mechanisms of bubble-containing oil-impregnated paper. *IEEE Trans. Dielectr. Electr. Insul.* **29**(4), 1282–1289 (2022)
6. Chen, W., Ling, Y., Gan, D., Wei, C., Yue, Y.: Identification method of oil-paper insulated air gap discharge stage based on clustering-wavelet neural network. *Power Grid Technol.* **36**(07), 126–132 (2012)
7. Yun, L.: *The Characteristic Information Extraction of Air-Gap Discharge in Transformer Oil-Paper Insulation and Research on its Process Dividing*. Chongqing University, Chongqing (2012)
8. Long, Z.: *Characteristics and Development Stage Recognition of Air-gap Discharge within Oil-impregnated Paper Insulation Considering Effect of Cavity Size*. Chongqing University, Chongqing, China (2015)
9. Chunshe, X., Zhenquan, S., Xuefeng, Z., et al.: Experimental study on partial discharge characteristics of oil-paper insulated air gap model. *High Volt. Appar.* **02**, 34–41 (2012)

Power Grid State Assessment Method Based on RMT-PCA



Xinzhi Ye, Lei Shang, Xuzhu Dong, Chengxi Liu, and Ye Tian

Abstract With the establishment of WAMS (Wide Area Measurement System), the power grid has accumulated a lot of measurement data. This paper proposes a power grid state assessment method based on RMT – PCA (Random Matrix Theory - Principal Component Analysis) from the perspective of data-driven. The proposed RMT-PCA-based method can effectively identify abnormal events such as load change under the operation state of power grid by using existing measurement data of power grid. The case study is designed to verify the accuracy and effectiveness of the method proposed in this paper. At the same time, the method proposed in this paper can reduce the calculation time, compared with the commonly used MSR (Mean Spectral Radius) index.

Keywords Principal component analysis · Random matrix theory · State assessment

1 Introduction

With significant deployment of online monitoring devices in the power grid, a large amount of data is collected [1]. The traditional model method for power grid state assessment is difficult to cope with the expansion of power grid scale and the complexity of grid structure. Therefore, from the perspective of data-driven, it has become a research hotspot to analyze the real-time running state of power grid by using big data technology.

Random matrix theory (RMT) originated from the development and research of quantum physics [2] and has achieved good application effect in the field of finance [3] and communication [4]. In the field of power system, RMT has been used to

X. Ye · L. Shang (✉) · X. Dong · C. Liu
Wuhan University, Wuhan 430072, China
e-mail: 2021282070137@whu.edu.cn

Y. Tian
Electric Power Research Institute of Liaoning Electric Power Co., Ltd., Shenyang 110006, China

© Beijing Paiké Culture Commu. Co., Ltd. 2023
X. Dong et al. (eds.), *The proceedings of the 10th Frontier Academic Forum of Electrical Engineering (FAFEE2022)*, Lecture Notes in Electrical Engineering 1054, https://doi.org/10.1007/978-981-99-3408-9_96

1089

evaluate the operation state of power grid [5], analyze the stability [6], evaluate the equipment performance [7] and analyze the power consumption behavior [8]. Literature [9] use RMT for rolling bearing performance degradation assessment and proposes an evaluation method combining RMT and principal component analysis (PCA).

At present, the Marcenko-Pastur Law (M-P Law), Ring Law, mean spectral radius (MSR) and the corresponding entropy index in RMT are widely used in power system to evaluate the power grid operation state. This paper proposes an RMT-PCA-based power grid state assessment method, which only uses M-P Law in the random matrix to decompose and extract eigenvalues, and constructs a fusion feature index based on PCA algorithm to effectively represent the power grid operation state. By this way, the calculation time can be reduced.

2 Random Matrix Theory

The large amount of measurement data accumulated in the power grid is a typical spatio-temporal big data and traditional analysis tools can hardly meet the requirements of data processing accuracy in the big data environment by establishing assumptions and simplified models [10]. A matrix with independent and identically distributed random variables as elements is called a random matrix. The random matrix theory obtains the random degree of the actual data by statistical analysis of the energy spectrum and eigenstates of the complex system, and reveals the behavior characteristics of the overall correlation in the actual data [11]. In the field of mathematics, RMT requires that its matrix dimension tends to infinity, but in a matrix with moderate scale, for example, when the matrix dimension ranges from tens to hundreds of dimensions, it can also get quite accurate results [12]. Therefore, RMT can be used to solve the problems of power system.

2.1 M-P Law

M-P Law describes the asymptotic behavior of singular values of random matrices [10]. Let $X = \{x_{i,j}\}$ be a random matrix of $N \times T$ dimension, where the mean value $\mu(X) = 0$, variance $\sigma^2(X) < \infty$ and satisfy independent identically distributed. When N and T tend to infinity, their proportional coefficient $c = N / T \in (0,1]$. The corresponding sample covariance matrix S can be obtained and the empirical spectrum distribution (ESD) of S converges to the M-P Law, and the density function can be expressed as Eq. (1) [13].

$$f_{ESD}(\lambda_s) = \begin{cases} \frac{1}{2\pi\lambda c\sigma^2} \sqrt{(b-\lambda)(\lambda-a)}, & a \leq \lambda \leq b \\ 0, & \text{others} \end{cases} \quad (1)$$

where, $a = \sigma^2 (1 - \sqrt{c})^2$; $b = \sigma^2 (1 + \sqrt{c})^2$; λ is the characteristic value of S .

2.2 Ring Law

Suppose the elements of a random matrix X_n of $N \times T$ dimension meet the mean value $\mu (X_n) = 0$, variance $\sigma^2 (X_n) = 1$ after standardization, and the matrix is independent and identically distributed. Then, the singular value equivalent matrix of X_n is obtained by the unitary matrix U , so that its eigenvalues are mapped to the complex plane. The singular value equivalent matrix X_u can be obtained by singularity treatment according to Eq. (2).

$$X_u = U \sqrt{X_n X_n^H} \tag{2}$$

where, U is a Haar unitary matrix of $N \times N$ dimension, $X_u X_u^H \equiv X_n X_n^H$ and superscript H denotes conjugate transposition.

Meanwhile, L matrices can be selected to obtain L singular equivalent matrices from Eq. (2), and the matrix product Z can be obtained from Eq. (3).

$$Z = \prod_{i=1}^L X_{u,i} \tag{3}$$

Then, normalize the element z_i of matrix Z according to Eq. (4) to obtain the matrix \tilde{Z} .

$$\tilde{z}_i = \frac{z_i}{\sqrt{N} \sigma(z_i)} \tag{4}$$

The ESD of matrix \tilde{Z} obeys Ring law, and the probability density function can be expressed as Eq. (5) [14].

$$f_{RL}(\lambda) = \begin{cases} \frac{1}{\pi c L} |\lambda|^{2/L-2}, & (1 - c)^{L/2} \leq |\lambda| \leq 1 \\ 0, & \text{others} \end{cases} \tag{5}$$

where, λ is the eigenvalue of matrix \tilde{Z} , which will be distributed between a standard ring with an outer ring radius of 1 and an inner ring radius of $(1 - c)^{L/2}$ on the complex plane.

2.3 Mean Spectral Radius (MSR)

MSR is a commonly used linear eigenvalue statistic of random matrix, which is the distance between the eigenvalue of the matrix and the origin on the complex plane [9]. Combined with the relevant characteristics of Ring Law, MSR is defined as follows [15].

$$r_{MSR} = \frac{1}{N} \sum_{i=1}^N |\lambda_i|, i = 1, 2, \dots, N \quad (6)$$

where, r_{MSR} is the average spectral radius of the random matrix; λ_i is the eigenvalues of the matrix.

2.4 Construction of Power Grid State Matrix

A large number of phasor measurement units (PMUs) have been deployed in the power system, and the WAMS has been established. Each PMU monitors multiple state variables of each node. At each sample time t_i , the measurement data can form a column vector as follows.

$$x(t_i) = [x_1(t_i), x_2(t_i), \dots, x_N(t_i)]^T \quad (7)$$

With the increase of sample time, the measurement data form a data source matrix X of $N \times M$ dimension as follows.

$$X_{N \times M} = [x(t_1), \dots, x(t_i), \dots, x(t_M)] \quad (8)$$

The sliding time window technology is used to intercept a part of the data source matrix, and the window width is T , that is, while collecting the data at time t_i , the historical data with a length of $T-1$ before the time is fully used to form a random matrix as follows [10].

$$X_{N \times T} = [x(t_{i-T+1}), \dots, x(t_i)] \quad (9)$$

As shown in Fig. 1 (a), the power grid data such as node voltage and DG power can be selected as state variables, and the sample covariance matrix or singular value equivalent matrix is obtained through time window interception, standardization and other operations. Then the power grid operation state can be evaluated by combining the eigenvalue distribution of the matrix and the above theorem.

In addition, the augmented matrix method is used to augment the data of a certain state variable in the random matrix of power grid state [16], and the random matrix can better characterize the characteristics of the state variable by expanding a certain

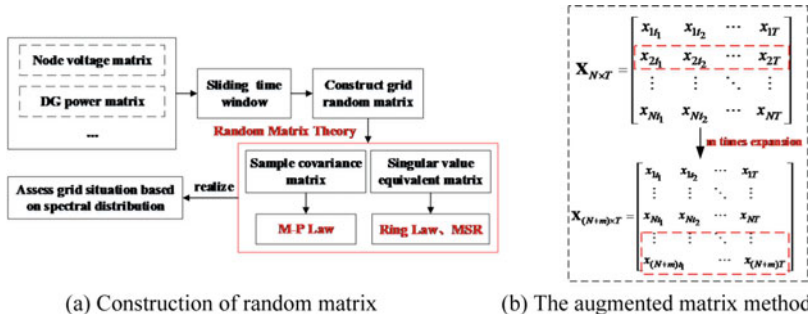


Fig. 1 Construction and application of power grid state random matrix

multiple. By successively augmenting the data of each node, combining the eigenvalue distribution of each augmented matrix and the above theorem, the identification and location of abnormal links are realized. The specific process is shown in Fig. 1 (b).

Figure 2 and Fig. 3 show the effect diagram of M-P Law, Ring Law and MSR in normal and abnormal conditions, respectively. It should be noted that the calculation amount of solving the singular value equivalent matrix is much higher than that of solving the sample covariance matrix. Among them, the MSR index is the most widely used in the state assessment of power grid, but it is generally extended from the Ring Law and needs to calculate the singular value equivalent matrix. Therefore, PCA is introduced in this paper to construct the fusion characteristic index based on the sample covariance matrix, which can intuitively evaluate the operation state of the power grid and reduce the calculation cost at the same time.

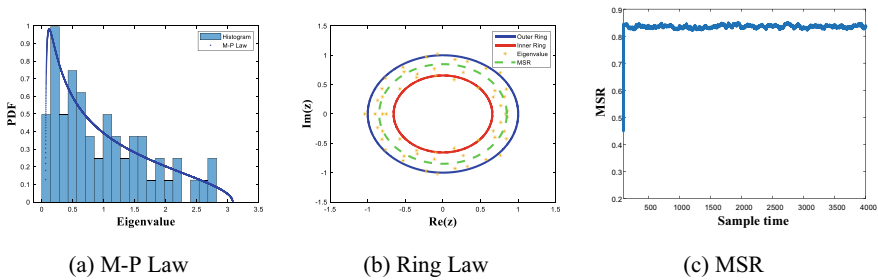


Fig. 2 Effect diagram of RMT under normal state of the power grid

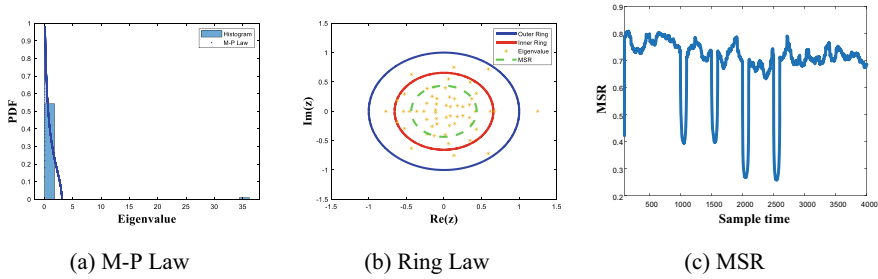


Fig. 3 Effect diagram of RMT under abnormal state of the power grid

Table 1 Feature index extraction based on sample covariance matrix

Feature index	Feature extraction	Feature index	Feature extraction
P1	Median(λ)	P4	Max(λ)-Min(λ)
P2	Max(λ)/Median(λ)	P5	Max(λ)/Mean(λ)
P3	Max(λ)-Median(λ)	P6	Max(λ)/Var(λ)

3 Power Grid State Assessment Based on RMT-PCA

According to the M-P Law, eigenvalues of the sample covariance matrix is distributed between $[a, b]$, and the probability distribution meets a certain standard form. As shown in Table 1, extracting the eigenvalues λ of the sample covariance matrix and construct the feature index vector $\mathbf{P}(t_i) = [P1(t_i), P2(t_i), \dots, P6(t_i)]^T$ at the sample time t_i . Then we can use feature index vectors at different sample times to form the feature index matrix $\mathbf{P} = [\mathbf{P}(t_1), \mathbf{P}(t_2), \dots, \mathbf{P}(t_n)]$. Compared with a single index, the feature index set can better represent the state changes of the power grid.

In order to realize the comprehensive utilization of information, PCA algorithm is used for principal component extraction and information fusion of multiple indicators [9]. PCA is a method to reduce the dimension of complex data sets to reveal the hidden information [17]. The specific steps of PCA are not introduced here.

4 Case Study

In order to verify the effectiveness of the proposed power grid state assessment method, this paper uses Matpower as the simulation tool and IEEE57 bus system as the simulation example. The mutation of load and continuous increase of load are taken as abnormal events for verification.

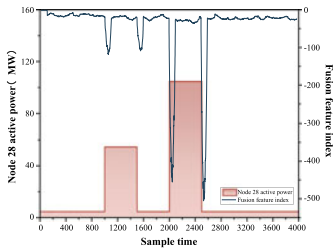
4.1 Case 1

Case 1 uses the modified IEEE57 bus system, in which node 15 and node 31 are connected to a certain size of distributed generation. Select the node voltage and distributed generation active power output as state variables, add white noise of appropriate size to the data so as to simulate the data collected by WAMS. At this time, $N = 59$, $T = 100$, $c = N/T \in (0,1]$, the RMT-PCA-based method is used to verify the occurrence of load mutation.

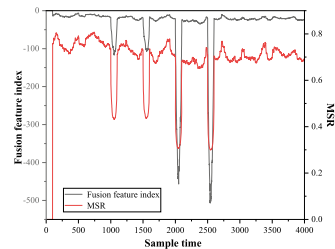
As shown in Fig. 4 (a), when $t = 1000$, the active power of node 28 suddenly increased by 50 MW. At this time, the fusion feature index fell rapidly, and then reached balance in the new state, and the fusion feature index rose. When $t = 1501$, the active power of node 28 returns to its original size. At this time, the fusion feature index drops rapidly, and then it reaches equilibrium again in the new state, and the fusion feature index rises again. Similarly, when $t = 2001$, the active power of node 28 suddenly increases by 100 MW. When $t = 2501$, the active power of node 28 returns to the original size. The fusion feature index also changes correspondingly and the range of change increases, indicating that the load mutation event is more serious and in line with the set situation.

In order to better prove the effectiveness of the fusion feature index, as shown in Fig. 4 (b), the fusion feature index is compared with the MSR index. It can be seen that the two show the same change trend.

In order to compare the calculation speed between different methods, the calculation time comparison test is carried out in the computer in the same environment (Configuration: AMD Ryzen 9 4900HS CPU and 16 GB RAM), and each event is repeated 50 times to eliminate the randomness in the test process. In Case 1, the average calculation time of the fusion feature index proposed in this paper is 4.40 s and the average calculation time of MSR is 14.42 s. Obviously, the fusion feature index proposed in this paper greatly shortens the calculation time.

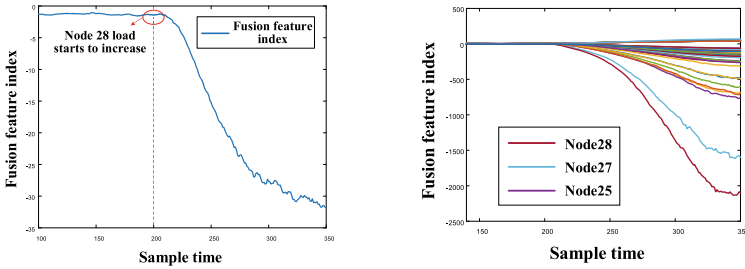


(a) Change of fusion feature index corresponding to load mutation



(b) Comparison of fusion feature index and MSR

Fig. 4 Fusion feature index from Case 1



(a) Fusion feature index from the system (b) Comparison of fusion feature indexes

Fig. 5 Fusion feature index from Case 2

4.2 Case 2

Case 2 uses the standard IEEE57 bus system, and sets the active power of node 28 to increase continuously from the 200th sample time. Then use the augmented matrix method to expand the data of each node, and the expansion multiple m is 63. At this time, $(N + m) = 120$, $T = 140$.

As shown in Fig. 5 (a), when $t = 200$, the active power of node 28 gradually increases, and the fusion feature index slowly drops. Then use the augmented matrix method to enlarge the data of each node 63 times in turn, and observe the changes of the index. As shown in the Fig. 5 (b), the indexes obtained from every node augmentation matrix all fall in response to the active power growth. Among them, the drop of node 28 is the most obvious, so it can be judged that node 28 is an abnormal link.

5 Conclusion

In this paper, a method of power grid state assessment based on RMT-PCA is proposed. From the perspective of data-driven, the relevant data of the power grid is collected to form the state matrix, and constructs a fusion feature index based on RMT and PCA to effectively represent the changes of power grid operation state and realize the identification of abnormal links. Compared with the commonly used MSR method, the method proposed in this paper takes less computing time.

Acknowledgements This work was funded by State Grid Corporation of China Headquarters Management of Science and Technology Project (5400-202128154A-0-0-00).

References

1. Shi, X., Qiu, R., Ling, Z., et al.: Spatio-temporal correlation analysis of online monitoring data for anomaly detection and location in distribution networks. *IEEE Trans. Smart Grid* **11**(2), 995–1006 (2020)
2. Brody, T.A., Flores, J., French, J.B., et al.: Random-matrix physics: spectrum and strength fluctuations. *Rev. Mod. Phys.* **53**(3), 385–479 (1981)
3. Drozd, S., Kwapien, J., Osiewicz, P.: Empirics versus RMT in financial cross-correlations. *arXiv.org, Quantitative Finance Papers* 38 (2007)
4. Lin, C., Zheng, L., Zhang, W., et al.: WSN abnormal node location algorithm based on random matrix theory. *Comput. Eng.* **46**(01), 157–163 (2020). (in Chinese)
5. Li, Z., Zhang, Z., Gu, J.: Power grid state analysis and disturbance location method based on random matrix theory. *Autom. Electr. Power Syst.* **42**(12), 93–99, 126 (2018). (in Chinese)
6. Liu, W., Zhang, D., Wang, X., et al.: Transient stability analysis of power system based on stochastic matrix theory. *Proc. CSEE* **36**(18), 4854–4863+5109 (2016). (in Chinese)
7. Yan, Y., Sheng, G., Wang, H., et al.: Key performance evaluation method of power transmission and transformation equipment based on high-dimensional random matrix big data analysis model. *Proc. CSEE* **36**(02), 435–445 (2016). (in Chinese)
8. Wu, L., Zhang, Y., Chen, W., et al.: Electric behavior characterization method based on clustering and random matrix theory. *J. Lanzhou Univ. Technol.* **47**(05), 70–75 (2021). (in Chinese)
9. Zhu, W., Luo, M., Ni, G., et al.: An evaluation method for rolling bearing performance degradation combining random matrix theory and principal component analysis. *J. Xian Jiaotong Univ.* **55**(02), 55–63 (2021). (in Chinese)
10. Wang, B., Wang, J., Liu, D., et al.: Power grid weak point evaluation method based on high-dimensional random matrix theory. *Proc. CSEE* 2019 **39**(6), 1682–1691 (1864). (in Chinese)
11. Xu, S.: *Random Matrix Theory Analysis of Complex Networks*. China University of Mining and Technology (2014). (in Chinese)
12. Wu, J., Ota, K., Dong, M., et al.: Big data analysis based security situational awareness for smart grid. *IEEE Trans. Big Data* **4**(3), 408–417 (2018)
13. Marčenko, V., Pastur, L.: Distribution of eigenvalues for some sets of random matrices. *Math. USSR-Sbornik* **1**(4), 457–483 (1967)
14. Chen, X., Gong, Q., Ren, Z., et al.: Identification of abnormal state of UHVDC power grid based on random matrix theory. *Eng. J. Wuhan Univ.* 2020, 53(03): 232–240. (in Chinese)
15. Wang, B., Wang, H., Zhu, D., et al.: Weak point identification method of integrated energy system based on unified power flow big data. *Autom. Electr. Power Syst.* **46**(07), 85–93 (2022). (in Chinese)
16. Wu, Q., Zhang, D., Liu, D., et al.: Power grid static stability situation assessment method based on random matrix theory. *Proc. CSEE* **36**(20), 5414–5420, 5717 (2016). (in Chinese)
17. Jonathon, S.: A tutorial on principal component analysis. *arXiv preprint* [arXiv:1404.1100](https://arxiv.org/abs/1404.1100) (2014)

Simulation of the Leakage Magnetic Field Under Inter-turn Short Circuit in the Transformer



Meng Huang, Bo Qi, Wei Zheng, Mao Ji, Haomin Lv, Wenbing Zhu,
and Jian Wang

Abstract Whether the operation state of the transformer is healthy has always been the top priority. If the inter-turn short circuit occurs in the transformer winding, it will seriously endanger the safe and stable operation of the transformer and affect the safety of the power system. When the inter-turn short circuit of the transformer winding occurs, the distribution of the leakage magnetic field inside the transformer will change drastically. Therefore, this paper selects the appropriate position inside the transformer to install the leakage magnetic field sensor, and monitors the distribution of the leakage magnetic field inside the transformer to determine whether the transformer has inter-turn short circuit and the occurrence of inter-turn short circuit. It is of great significance to propose an online monitoring method of transformer health based on the change of internal leakage magnetic field of transformer. In this paper, the finite element method is used to simulate the three-winding transformer model. The leakage magnetic field distribution of the transformer under normal operation and the leakage magnetic field distribution under different inter-turn short circuit conditions are simulated and compared and summarized. The simulation results of this paper show that the distribution of the leakage magnetic field of the transformer is different in the case of different inter-turn short circuit faults, but the same rule is that the leakage magnetic field of the winding accessory changes more violently in the case of inter-turn short circuit fault, and the maximum change of the leakage magnetic field can reach 1.1 T. On the basis of simulation calculation, this paper proposes to arrange five sensors, the position is selected at the end of the winding and outside the low-voltage winding. The on-line monitoring of the operating state of the transformer and the occurrence of inter-turn short-circuit fault are determined, which provides a basis for the on-line monitoring method of the operating health status of the transformer based on the leakage magnetic field.

M. Huang (✉) · B. Qi · W. Zheng · M. Ji · H. Lv
North China Electric Power University, Beijing, China
e-mail: huang_m2011@163.com

W. Zhu · J. Wang
State Grid Shandong Electric Power Company, Electric Power Research Institute, Shandong
Jinan, China

Keywords leakage magnetic field · sensor placement method · transformer · inter-turn short circuit

1 Introduction

Power transformer is the core equipment in power conversion, and it is also the key equipment that affects the power quality of users. Their safe and stable operation is crucial to the stability and safety of the power system [1, 2]. Use the ITSC instead of inter-turn short circuit in this article. Use the LMF to represent for leakage magnetic field. According to the existing data, the main cause of power transformer failure is ITSC. Therefore, In order to ensure the user 's power quality and the healthy operation of the transformer, In the aspect of transformer health monitoring, the most important thing is to monitor and identify the ITSC timely and effectively. At present, there is a lack of fast and effective on-line monitoring method for ITSC in engineering, which cannot judge the health status of transformer in time, and limits the safe and stable operation of transformer to a certain extent.

For ITSC faults, there are mainly off-line detection methods such as voltage-to-current ratio method and online monitoring methods such as dissolved gas analysis [3–5]. However, in the voltage-to-current ratio method, the defective part in the minor ITSC accounts for a relatively low percentage of the whole winding, resulting in an insignificant difference in the ratio, which makes it difficult for the method to carry out effective detection. The dissolved gas analysis has defects such as complicated and time-consuming procedures, and it cannot locate the location of the inter-turn short circuit. Previous studies [6] have shown that transformer ITSC can lead to changes in the distribution of LMF. The key step is to study the distribution characteristics of the transformer LMF corresponding to the ITSC in different situations and the optimal selection of the installation position of the LMF sensor in the transformer. The paper [7] calculated the distribution characteristics of the LMF in the height direction of the transformer under different degrees of ITSC, but only the LMF of two fixed paths was analyzed, and the spatial distribution law of the LMF was less studied. The paper [8] calculated the distribution characteristics of transformer LMF under winding deformation and ITSC, but it did not analyze the spatial distribution characteristics of LMF when ITSC occurred at different locations. Therefore, it is of great significance to analyze the LMF distribution of transformers under different ITSC so as to guide the installation of LMF sensors.

In this paper, considering the symmetry of the transformer, the finite element software is used to simulate the 110 kV three winding power transformer. Based on the finite element simulation model, the LMF distribution under normal conditions and different ITSC conditions is simulated and calculated, and the results are compared to obtain the variation law of LMF distribution and fault conditions. The optimized arrangement method of LMF sensor is proposed to make up for the lack of actual installation of transformer LMF sensor in engineering, which provides a feasible

Table 1 Parameters of transformer

Quantity	Detail
Capacity	250 kVA
Voltage of HV/ MV/ LV winding	110/35/10.5 kV
Number of turns of HV/ MV/ LV winding	623/198/103
Core radius	300 mm
High-voltage winding radius	481.5–558.0 mm
Middle-voltage winding radius	388.5–449.5 mm
Low-voltage winding radius	315.0–369.5 mm

method for online monitoring of transformer health status and detecting the actual installation of LMF sensor in ITSC.

2 Modeling of Transformer

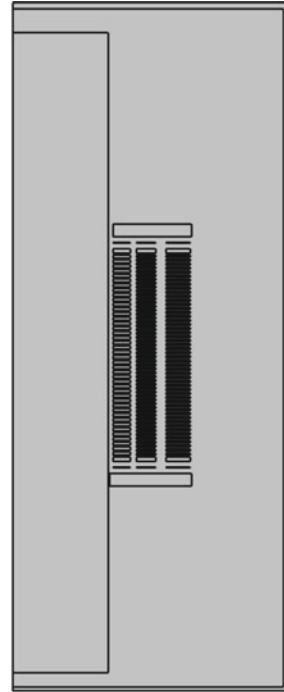
In this paper, the finite element method is used to analyze the variation of LMF during different ITSC, and a 110 kV oil-immersed three-phase three-winding transformer is used as the object of study. On the basis of the transformer simulation model, considering the three-phase symmetrical characteristics of the transformer, this paper only analyzes one phase. At the same time, due to the small influence of the eddy current effect of the core and winding, it is ignored and solved by static analysis. Table 1 is the main technical parameters of transformer.

Figure 1 is a two-dimensional axisymmetric model of power transformer, where the left side of the model is axisymmetric boundary, and the upper side, lower side and right side of the model, are set as the second boundary condition. In this model, the core material is 30QG105 silicon steel sheet, the tank wall material is Q235 steel, while the relative permeability of all other materials is set to 1.

3 Analysis of LMF Distribution Under Different Winding Deformations

This paper simulate and analyze the LMF of the transformer under two conditions, normal operation and ITSC. In order to simulate the normal operation state of power transformer in simulation calculation, the winding current value on the three-phase power transformer model shown in Fig. 1 is directly set to the rated current value.

In this paper, the simulation calculation principle of ITSC is to apply short circuit current to the ITSC of power transformer winding under the condition of normal operation of power transformer [9]. According to the existing data statistics, when the ITSC occurs in the power transformer, the short-circuit current increases sharply,

Fig. 1 Transformer model.

which is 15–23 times of the current under the normal operation of the transformer [7]. In this paper, the current of the transformer in the case of ITSC is 20 times the normal working current.

Due to the symmetry of the transformer model, this paper also considers the symmetry when simulating the power transformer model. Therefore, the location of the ITSC only needs to select the middle and upper parts of the power transformer winding. According to the simulation results, the distribution law of the LMF when the ITSC occurs in the symmetrical part of the power transformer winding can be obtained by symmetry.

Figure 2 shows the distribution law of LMF in the whole transformer during normal operation of power transformer. It can be seen from Fig. 2 that the LMF near the winding changes greatly under normal operation. Therefore, this paper chooses the area near the winding to study the change of LMF caused by the ITSC.

3.1 Analysis of ITSC with Different Degrees

Figure 3 shows the variation law of the LMF in the winding area under the condition of 2.5% and 5% ITSC in the upper part of the transformer. For the same location of ITSC, the distribution of the variation of the LMF is similar as the severity of

Fig. 2 The distribution of LMF in normal condition

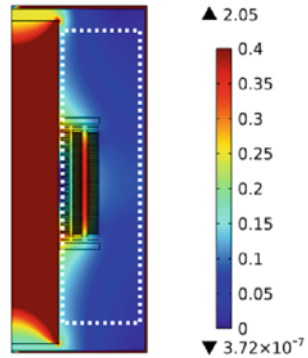
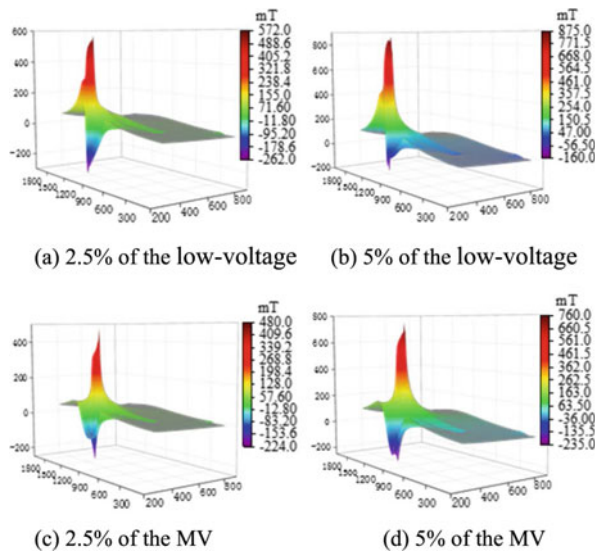


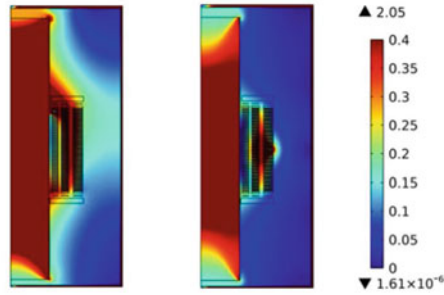
Fig. 3 The variation law of LMF when ITSC with different degrees occurs in upper of winding



the ITSC increases, but the maximum variation of the LMF shows an increasing trend. The maximum variation of LMF is 572 mT when a 2.5% ITSC occurs in the low-voltage winding, and 875 mT when a 5% ITSC occurs. In order to obtain the variation of LMF of transformer under severe conditions, the degree of ITSC is taken as 5% in the later analysis.

3.2 ITSC

Due to the symmetry of the transformer model, when the ITSC occurs at the middle height position, the distribution of the LMF is also symmetrical, and when the ITSC



(a) Upper of the low-voltage winding (b) Middle of the high-voltage winding

Fig. 4 The distribution law of LMF when ITSC occurs in different position

occurs at the non-middle height position of the winding, the symmetry of the LMF distribution is seriously damaged. As shown in Fig. 4, this illustrates the distribution of LMF when ITSC occurs at the middle height of the high-voltage winding and the non-middle height of the low-voltage winding.

Figures 4 and 5 show the variation of the LMF inside the transformer when 5% ITSC occurs at different positions of the winding. When ITSC occurs in the upper part of the asymmetric position of the low-voltage winding, the maximum variation of LMF is 875 mT and the minimum variation is -160 mT, and they are all near the short circuit coil. While when it occurs in the middle part, the overall LMF in the winding area becomes larger, and the maximum variation of the LMF reaches 1100 mT, and the LMF increases by 5 mT at the location with the smallest variation of the LMF. When the ITSC occurs in the middle-voltage winding, the maximum variation of LMF is smaller than that in the low-voltage winding, only 760 mT, and in the area between the short-circuiting coil and the core, the LMF becomes smaller compared with the normal working condition, but in the rest of the locations away from the short-circuiting coil, the LMF generally becomes larger. Compared with the case where the ITSC occurs in the low-voltage winding and the medium-voltage winding, when the ITSC occurs in the high-voltage winding, the maximum change of LMF is smaller, only 652 mT. Another significant difference between the ITSC occurring in the high voltage winding and the ITSC occurring in the medium voltage winding and the low voltage winding is that the LMF near the ITSC coil is larger, and the LMF at other locations is generally smaller.

4 Analysis and Sensor Layout

In order to determine the sensor installation location, the variation of the LMF on the specific path needs to be analyzed. Taking into account the difficulty of installation and the distance from the faulty coil, the variation of the LMF on the two paths on the

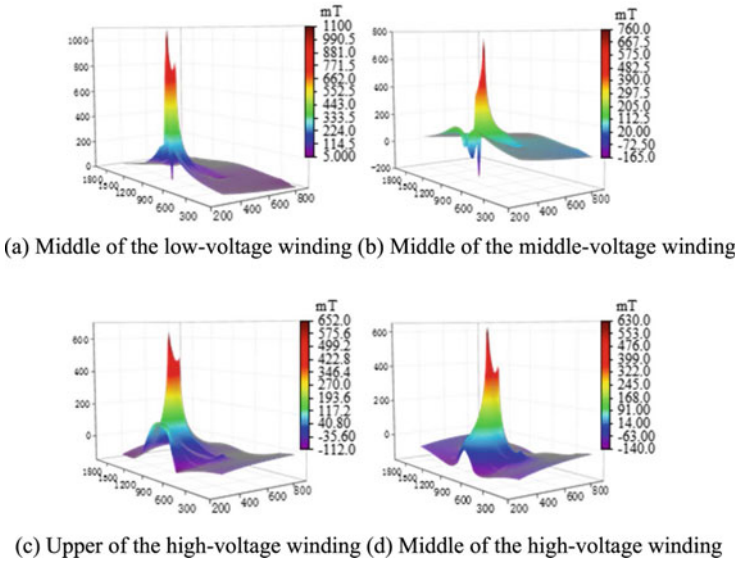


Fig. 5 The variation of LMF when ITSC occurs in different position

outside of the low-voltage winding and the inside of the winding end insulation was selected for analysis, as shown in Figs. 6 and 7. When an ITSC occurs, the variation of LMF on the outside of the low-voltage winding has significant characteristics, up to 700 mT. For the LMF on the inside of the winding end insulation, even if ITSC occurs in the symmetrical position of transformer winding, the change of LMF is still obvious, up to 100 mT.

As shown in Fig. 6, when different ITSC occur, there is a significant difference in the variation of the LMF on the outer path of the low-voltage winding, which is helpful to distinguish the ITSC, but when an ITSC occurs, the high temperature may damage the sensors installed on the outside of the low-voltage winding, so the number of sensors installed here needs to be minimized.

Fig. 6 The variation of LMF on the outside of the low-voltage winding under different ITSC

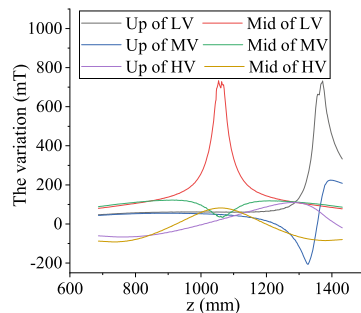
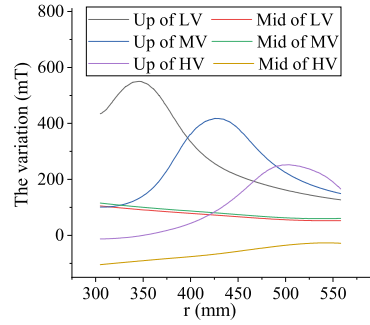


Fig. 7 The variation of LMF on the inside of the winding end insulation under different ITSC



It can be seen from Fig. 7 that when the ITSC occurs at the same position of the low-voltage winding and the middle-voltage winding, that is, it occurs in the symmetrical position of the winding, the variation law of the LMF is similar, which is not conducive to distinguishing the two types of ITSC, but here it is easy to install sensors. Therefore, combining the advantages and disadvantages of outside the low-voltage winding and inside the winding end insulation, a total of five sensors are chosen to be installed at these locations for ITSC online monitoring. The schematic diagram of the sensor installation locations is shown in Fig. 8.

When different ITSC occur at different positions, the variation of the LMF at the sensor position is shown in Table 2. The analysis of the data in the table shows that when the ITSC occurs under different conditions, the LMF changes monitored by the sensors at different positions are different. For example, when the ITSC occurs in the middle of the middle-voltage winding and the middle of the low-voltage winding in the same case, although the variation of the LMF at sensor positions 1, 2, 4 and 5 is similar, the variation of the LMF at sensor position 3 is significantly different, which is 699.24 mT and 38.31 mT, respectively. When a ITSC occurs in the high-voltage winding, at least three sensor positions have a negative variation in the LMF. These are favorable for ITSC online monitoring.

Fig. 8 Sensor placement

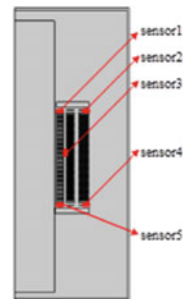


Table 2 Variation of LMF at the sensor during ITSC (unit: mT)

Type	sensor1	sensor2	sensor3	sensor4	sensor5
LV upper	46,536	126.83	60.82	31.62	60.6
LV middle	101.88	52.66	699.24	53.49	104.91
MV upper	102.31	149.03	48.26	29.38	56.31
MV middle	111.74	60.31	38.31	61.31	114.78
HV upper	-11.78	165.83	22.9	-28.54	-77.87
HV middle	-101.23	-28.3	81.72	-26.36	-110.95

5 Conclusion

1. The variation of the LMF has different characteristics when ITSC occurs. The variation law of the LMF of the high-voltage winding is different from that of the middle-voltage and low-voltage windings. When the ITSC occurs in the high-voltage winding, the LMF is very large near the short circuit coil, and the other positions are generally small, which is completely different from the ITSC of the middle-voltage and low-voltage windings.
2. When the ITSC occurs inside the transformer, the position selection of the sensor is the most important. The LMF will change significantly at the inner side of the winding end insulation and the outer side of the low-voltage winding. Installing sensors at these two positions can effectively monitor the health status of the transformer and prevent the occurrence of the ITSC.

Acknowledgements This research was funded by the Science and Technology Project of SGCC (No. 5206002000D6, Research on key technologies of leakage magnetic field and stress field sensing for power transformer transparency).

References

1. Yong, L., Fan, Y., Fan, Z., et al.: Study on sweep frequency impedance to detect winding deformation within power transformer. *Proc. CSEE* **35**(17), 4505–4516 (2015)
2. Zhang, H., et al.: Dynamic deformation analysis of power transformer windings in short-circuit fault by FEM. *IEEE Trans. Appl. Supercond.* **24**(3), 1–4 (2014)
3. Xiong, X., et al.: A protection method of transformer inter-turn short circuit based on the variation of current ratio. *Power Syst. Protect. Control.* **41**(9), 112–115 (2013)
4. Mosinski, F., Piotrowski, T.: New statistical methods for evaluation of DGA data. *IEEE Trans. Dielect. Elect. Insul.* **10**(2), 260–265 (2003)
5. Qi, B., Wang, Y., Zhang, P., Li, C., Wang, H.: A novel deep recurrent belief network model for trend prediction of transformer DGA data. *IEEE Access* **7**, 80069–80078 (2019). <https://doi.org/10.1109/ACCESS.2019.2923063>
6. Haghjoo, F., Mostafaei, M., Mohammadi, H.: A new leakage flux based technique for turn-to-turn fault protection and faulty region identification in transformers. *IEEE Trans. Power Delivery* **33**(2), 671–679 (2018)

7. Pan, C., et al.: Study on electromagnetic characteristics of interturn short circuit of single-phase transformer. *High Volt. Eng.* **46**(5), 1839–1856 (2020)
8. Ouyang, X., Zhou, Q., et al.: Analysis on the magnetic flux leakage distribution in the transformer under different winding deformation and typical working condition. In: 2020 IEEE International Conference on High Voltage Engineering and Application (ICHVE) (2020)
9. Zhang, B., et al.: Analysis of physical characteristics of power transformer windings under inter-turn short circuit fault. *High Volt. Eng.* **47**(6), 2177–2185 (2021)

Sag Monitoring of Transmission Line Based on Motion Sensor



Zhang Huiquan, Jiang Zelong, Ma Haoyu, Bi Ran, Pan Shi, He Jinliang, and Hu Jun

Abstract In recent years, with the continuous increase of domestic electricity demand, the scale of power grid is expanding, and there is more and more power grid construction and equipment maintenance work under complex terrain conditions. However, transmission lines are difficult to patrol and maintain due to their large dispersion, long distance, and easy to be affected by natural disasters such as gale, rainstorm and blizzard. Wind deflection flashover, wire dancing, wire icing and other disasters of high-voltage transmission lines occur from time to time. Lots of disaster conditions are related to transmission line mechanical parameters such as wire sag. The motion sensor, as a measurement device for motion characteristics such as acceleration and inclination, has a broad application prospect with its small size, high accuracy, easy installation, and controllable cost. This paper focuses on the role played by motion sensors in online monitoring of transmission lines, and conducts research on solution of transmission line sag and sensor installation strategies. The paper selects the suspended chain line model for further analysis, and the data generated by the sensors under the condition of wind deflection are used to solve the arc sag parameters of the transmission line model. Adjustments of the algorithm and strategy according to the simulation results are conducted so as to reduce the solution error.

Keywords Motion Sensor · Transmission Line · Catenary Model · Sag Monitoring

1 Introduction

In recent years, with the growth of economy and the increase of electricity demand, the electric power industry develops rapidly in our country. The scale of the power system is increasing, and the transmission lines are constantly extending. As the lines

Z. Huiquan (✉) · J. Zelong · M. Haoyu · B. Ran · P. Shi · H. Jinliang · H. Jun
Department of Electrical Engineering, Tsinghua University, Beijing 100084, China
e-mail: zhq22@mails.tsinghua.edu.cn

© Beijing Paike Culture Commu. Co., Ltd. 2023
X. Dong et al. (eds.), *The proceedings of the 10th Frontier Academic Forum of Electrical Engineering (FAFEE2022)*, Lecture Notes in Electrical Engineering 1054, https://doi.org/10.1007/978-981-99-3408-9_98

1109

used in high-voltage transmission corridors are mostly bare lines, the overhead lines are exposed to the air and affected by environmental factors such as wind, rain and lightning strikes, and its failure is often inevitable. According to statistics, in 2013, the State Grid's power transmission lines had a total of 1311 trips, with a trip rate of 0.175 times per 100 km every year. Among these incidents, the 110 kV AC-DC transmission lines had 239 trips in total, among which 65 trips were caused by wind bias and other reasons, accounting for 27.2% of the total number of trips [1]. Once the transmission line fails, it may cause great loss to the power system.

In addition to lightning strikes, transmission line faults caused by natural factors mainly include those caused by strong wind, snow and ice, which lead to changes in transmission line mechanical structure and insulation distance, including arcs falling, wind deflection, ice covering, dancing and interaction of various factors, etc. The above faults are often accompanied by the variation of overhead transmission wire sag. Therefore, real-time monitoring of overhead line sag is of great significance for fault monitoring and early warning of transmission lines. By monitoring the sag parameters of transmission lines, the fault caused by various natural factors such as ice covering can be further deduced, so as to improve the observability of transmission line state and ensure the safe operation of transmission lines.

A variety of sag detection methods have been proposed such as manual inspection, sensor-based sag monitoring, application of image processing technology, wire positioning based on positioning system, microwave ranging and so on. Manual inspection has poor real-time performance and low measurement efficiency, and it is very difficult to monitor in complex geographical environment. The sensors that can be used for sag monitoring include temperature sensor, stress sensor, dip sensor [2] and magnetic sensor. The temperature sensing method uses the property of thermal expansion and cold contraction of wire to establish the relationship between wire temperature and length, and then calculates the arc length. However, this approach cannot eliminate the influence of climate causes and uneven temperature distribution. The stress sensor and the dip sensor need to be installed between the tower and the insulator, which is not practical for the installed transmission lines and difficult to be widely applied in practice. The magnetic sensing method can estimate traverse sag and wind deflection from magnetic field distribution by installing magnetic field sensors at positions such as poles and towers [3, 4]. However, it is difficult to calculate the magnetic field in practical application, and the magnetic field distribution in simulation and calculation model is often very different from that in practice. In addition, a camera can be installed on the UAV or pole tower to calculate the traverse sag [5–7] by image processing technology. However, when the visibility is low, the optical monitoring system is difficult to realize the monitoring function. Wire positioning based on positioning system can obtain multi-point position information of transmission lines based on DGPS differential positioning technology, and then calculate the sag size [8]. By installing a millimeter wave transmitter, receiver and incident angle sensor on the transmission line, the microwave ranging method can reverse the arc through the change of signal receiving power and incident angle [9]. However, fog, rain, snow and other weather may cause the MMW power attenuation in the transmission process, thus affecting the accuracy of calculation. Other

sag monitoring methods, such as using power line inspection robot [10] or analyzing power-line carrier signal behavior [11], were also proposed in recent years. However, most of them have application difficulties to some extent.

Motion sensor is a device that can convert motion features such as speed and acceleration into electrical signals. With advantages of convenient installation, low cost and high precision, it is suitable for sag monitoring. Meanwhile, as the measured data directly reflect the real motion state of the transmission line, motion sensor has a certain advantage in data processing and state identification. It can be combined with intelligent equipment for multi-point installation of transmission lines to realize non-invasive monitoring of overhead line motion status.

This paper presents a monitoring method of transmission line sag parameters based on motion sensor. Firstly, the catenary model of transmission line is selected as the basis of this paper. Under the wind deflection condition, the simulation data of the sensor is obtained by using the line parameters and appropriate external conditions, and the important parameters of the transmission line are restored by selecting different combinations of the number of sensors combined with the sensor errors. Further, the reduction errors of line parameters are analyzed, and appropriate strategies and algorithms are considered to reduce the errors. By increasing the number of sensors, the randomness of sensor measurement data can be weakened and the measurement accuracy can be increased. The best placement strategy of sensor position can be obtained by changing the position of sensor and making comparative analysis.

2 Modeling and Parameter Solving of Transmission Lines

2.1 Catenary Model of Transmission Lines

The schematic diagram of the overhead power line is shown in Fig. 1. Where, A and B are suspension points, C is the midpoint of AB connection, and O is the lowest point of traverse sag. h is the arc of the line, that is, the length of OC; l is the span of the line, that is, the length of AB.

Catenary model is a physical model commonly used to solve power transmission lines in engineering applications. It refers to a soft, non-extendable chain with uniform distribution of thickness and mass at both ends, which has a curved shape only under the action of gravity. Under appropriate coordinate system conditions, a very simple catenary equation can be obtained.

The force analysis diagram of catenary is shown in Fig. 2. O for catenary, P for online at any point, the tangent P with horizontal plane angle for θ ; The tension of the line at O is in the horizontal direction, denoted as H; the tension of the line at B is in the tangential direction, denoted as T; then the force analysis of the whole OP section can be obtained that, in the horizontal and vertical directions, there is:

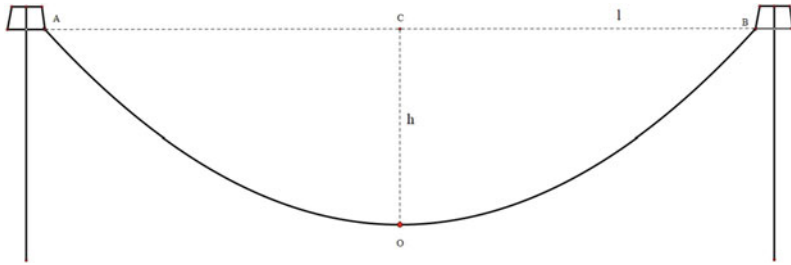
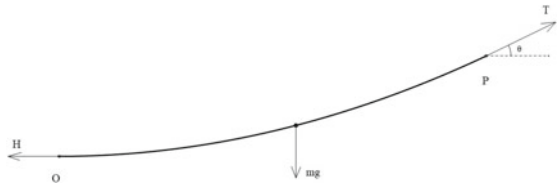


Fig. 1 Schematic diagram of overhead power lines.

Fig. 2 Force analysis of catenary



$$\begin{cases} H = T \cdot \cos\theta \\ mg = T \cdot \sin\theta \end{cases} \tag{1}$$

By substituting the dip angle of point P, combined with Eq. 1, we can obtain Eq. 2.

$$\frac{dy}{dx} = \tan\theta = \frac{mg}{H} \tag{2}$$

Based on the assumption that the wire is flexible and non-extendable, the linear density and length of the wire before and after suspension remain unchanged. Set the linear density of the wire for σ , OP wires for s long, there is:

$$s = \frac{m}{\sigma} = \frac{dy}{dx} \cdot \frac{H}{\sigma g} \tag{3}$$

It can be obtained by analyzing and integrating the element at point P that:

$$s = \int_0^{x_p} ds = \int_0^{x_p} \sqrt{1 + \frac{dy^2}{dx^2}} \cdot dx \tag{4}$$

Set $p = dy/dx$. United Eq. 4 with Eq. 5 that:

$$p = \frac{\sigma g}{H} \int_0^{x_p} \sqrt{1 + \frac{dy^2}{dx^2}} \cdot dx$$

$$\frac{dp}{\sqrt{1+p^2}} = \frac{\sigma g}{H} dx \tag{5}$$

As $g(x) = \sinh^{-1}(x)$:

$$\varphi(x) = \sinh^{-1}(p) = \frac{\sigma g}{H} x + C_1$$

$$\sinh(\varphi(x)) = p = \frac{dy}{dx} = \sinh\left(\frac{\sigma g}{H} x + C_1\right)$$

$$y = \frac{H}{\sigma g} \cosh\left(\frac{\sigma g}{H} x + C_1\right) + C_2 \tag{6}$$

Set $a = H/\sigma g$ and adjust the position of the coordinate system to eliminate constant C_1 and C_2 , we get catenary equation that:

$$y = a \cosh\left(\frac{x}{a}\right) \tag{7}$$

The physical meaning of a is the distance from the origin of the frame to the lowest point of the arc. In the transmission line model under catenary assumption, the static characteristics of the transmission line can be fully described only by determining the value of parameter a , so as to obtain the arc and other parameters of the transmission line.

2.2 Algorithm for Transmission Line Parameter Solving

For a section of transmission line between two towers, the information we can obtain is the span of the transmission wire and the acceleration data collected by the motion sensor installed on the wire.

Under the condition of windage, assuming that the wind effect on transmission line perpendicular to the conductor, as shown in Fig. 3. Under the action of wind, the sensor will generate motion data of each point position due to the overall deviation of catenary motion. As shown in Fig. 4, motion sensors are placed at two points M and N. m_1 and m_2 are the distances from point M to OC and AB, respectively. n_1 and n_2 are the distances from point N to OC and AB respectively. l is the span of the transmission wire and a_1, a_2 are accelerations of M, N.

From geometrical relationship and catenary equation we get that:

$$\begin{cases} m_2 = y_A - y_M \\ n_2 = y_A - y_N \\ h = y_A - y_O \end{cases} \tag{8}$$

Fig. 3 Wind action direction

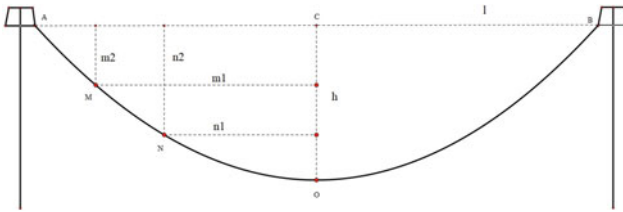
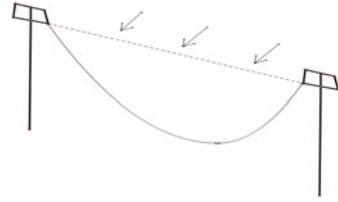


Fig. 4 Sensor location

$$\begin{cases} y_A = a \cosh\left(\frac{x_A}{a}\right) = a \cosh\left(\frac{l}{2a}\right) \\ y_N = a \cosh\left(\frac{x_N}{a}\right) = a \cosh\left(\frac{n_1}{a}\right) \\ y_M = a \cosh\left(\frac{x_M}{a}\right) = a \cosh\left(\frac{m_1}{a}\right) \\ y_O = a \cosh\left(\frac{x_O}{a}\right) = a \end{cases} \quad (9)$$

Considering the influence of windage, the ratio of horizontal acceleration perpendicular to the axis of the wire at points M and N is proportional to the ratio of arcs at this point, i.e.

$$\frac{a_1}{a_2} = \frac{m_1}{n_2} \quad (10)$$

Sag h can be obtained by solving Eq. 8 ~ Eq. 10.

2.3 The Influence of Sensor Error

There will be measurement errors inevitably in the actual measurement, which will introduce solving errors to the parameter solving algorithm above. The error of the sensor consists of two parts.

Part of it is percentage error δ_1 , which means that when the sensor is used for data measurement, the size of the measurement error has a certain percentage relationship with the size to be measured. Meanwhile, for the measurement of the same numerical result, the error follows the principle of normal distribution. Percentage error can be expressed as:

$$\delta_1 = p \cdot r * n_{cdf} \tag{11}$$

In which r is the percentage and n_{cdf} is one observed value of normal distribution.

The other part is the fixed error δ_2 , or “zero drift,” which refers to what the sensor reads when not measuring or measuring a zero-value object. Before the sensor is installed and used, it usually needs to be zeroed out. However, due to the limited zeroed ability or the long-time use of the sensor, there will be a certain amount of fixed error of the sensor.

Take these errors into consideration, the measured acceleration will be expressed as:

$$\begin{cases} \hat{a}_1 = a_1 + \delta_{11} + \delta_{12} \\ \hat{a}_2 = a_2 + \delta_{21} + \delta_{22} \end{cases} \tag{12}$$

Assume that $(\delta_1)r = 0.1\%$, $\delta_2 = 10^{-3}$. Examples including transmission lines of different specifications as shown in Table 1 are designed to verify the above models.

Figure 5 shows the variation of solving error with sensor percentage error and fixed error. Solving results shows that for transmission lines with different parameters, the smaller the sag ratio is, the more the sensor error will affect the solution process.

This conclusion is beneficial to on-line monitoring of transmission lines to some extent. On the line with large sag ratio, the line is more susceptible to the influence of snow and wind due to the relatively large sag, and the error of the solution results

Table 1 Four transmission line parameters.

	Sag	Span	Catenary parameter a	Sag ratio
Line 1	2.04	70	300	0.028
Line 2	10.03	200	500	0.05
Line 3	15.56	500	2000	0.03
Line 4	25.02	1000	5000	0.025

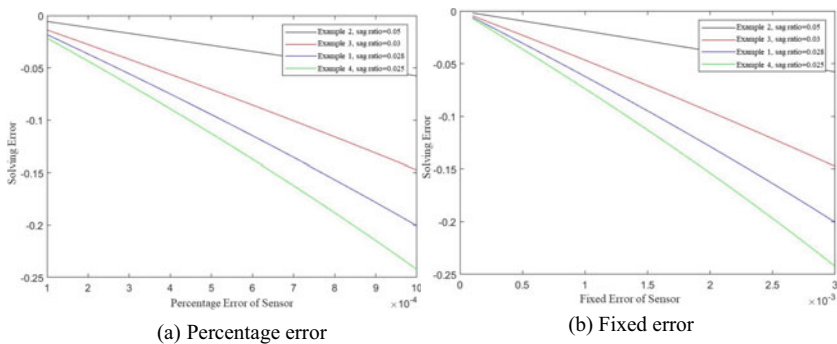


Fig. 5 Variation of solving error with sensor percentage error and fixed error

of the line using sensor combined with catenary model is relatively small, which is more conducive to the realization of monitoring. On lines with small vertical span, although the error of the solution results is large, the line has a large tension, and is more resistant to the interference of natural factors such as external wind, so the demand for online monitoring is relatively small. Therefore, this method can be used as far as possible on the lines with large vertical span, which can improve the accuracy and reduce the redundancy monitoring.

3 Solving Error Optimization

In this section, solving error is analyzed under the condition of a certain sensor accuracy, and some reasonable means are adopted to improve the algorithm and reduce the solving error.

3.1 *Effect of the Number of Sensors*

The aforementioned algorithm uses the measured data of sensors at two different positions on the transmission line, and then the data is substituted into the equations for solving. In this case, the coefficient matrix of the system is full rank, so there is only one set of solutions. In a practical application scenario, more sensors can be placed at different locations on the transmission line. On the one hand, the redundancy of sensors increases the reliability of online monitoring of transmission lines, that is, the damage of a single sensor device or abnormal data does not affect the online monitoring performance of transmission lines, and the redundant sensors that work properly can be used to replace the damaged sensors to complete the measurement work. On the other hand, the increase in the number of sensors means the increase in the number of measurement samples. According to the statistical principle, the increase in the number of samples will weaken the randomness of the solution results of line parameters, that is, solving error will be reduced to some extent. Increasing the number of sensors is also a feasible method to improve the on-line monitoring ability under the condition that the measurement accuracy of sensors is certain.

When the number of sensors is increased to 3, the position of sensors are shown in Fig. 6. The equations to be solved become:

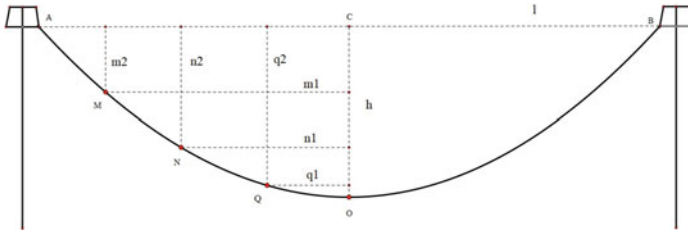


Fig. 6 Sensors placed on overhead line

$$\left\{ \begin{array}{l}
 m_2 = y_A - y_M \\
 n_2 = y_A - y_N \\
 q_2 = y_A - y_Q \\
 y_A = a \cosh\left(\frac{x_A}{a}\right) = a \cosh\left(\frac{l}{2a}\right) \\
 y_M = a \cosh\left(\frac{x_M}{a}\right) = a \cosh\left(\frac{m_1}{a}\right) \\
 y_N = a \cosh\left(\frac{x_N}{a}\right) = a \cosh\left(\frac{n_1}{a}\right) \\
 y_Q = a \cosh\left(\frac{x_Q}{a}\right) = a \cosh\left(\frac{q_1}{a}\right) \\
 y_O = a \cosh\left(\frac{x_O}{a}\right) = a \\
 \frac{a_1}{a_2} = \frac{m_1}{n_2} \\
 \frac{a_1}{a_3} = \frac{m_1}{q_2} \\
 h = y_A - y_O = a \cosh\left(\frac{l}{2a}\right) - a
 \end{array} \right. \quad (13)$$

The introduction of data at point Q adds 3 independent equations to the original system of equations, but only 2 unknown numbers are introduced, so the data at point Q is redundant. In order to make better use of the redundant data and reduce the solving error, the equations need to be adjusted further.

It can be obtained from the above equations that:

$$\frac{a_1}{a_2} = \frac{\cosh\left(\frac{l}{2a}\right) - \cosh\left(\frac{m_1}{a}\right)}{\cosh\left(\frac{l}{2a}\right) - \cosh\left(\frac{n_1}{a}\right)} \quad (14)$$

$$\frac{a_2}{a_3} = \frac{\cosh\left(\frac{l}{2a}\right) - \cosh\left(\frac{n_1}{a}\right)}{\cosh\left(\frac{l}{2a}\right) - \cosh\left(\frac{q_1}{a}\right)} \quad (15)$$

$$\frac{a_3}{a_1} = \frac{\cosh\left(\frac{l}{2a}\right) - \cosh\left(\frac{q_1}{a}\right)}{\cosh\left(\frac{l}{2a}\right) - \cosh\left(\frac{m_1}{a}\right)} \quad (16)$$

Due to the influence of historical data or the difference of instrument specifications, if the sensor at a certain point has a high degree of trust or high accuracy, for example, the sensor at Q is a high-precision sensor, we can add Eq. 15 and Eq. 16 that:

Table 2 Comparison of statistical characteristics of the three methods

Statistical item	Method a	Method b	Method c
Mean value	9.9157	9.8918	9.9173
Variance	0.7952	0.7453	0.4919

$$\frac{a_1}{a_3} + \frac{a_2}{a_3} = \frac{\cosh(\frac{l}{2a}) - \cosh(\frac{m_1}{a})}{\cosh(\frac{l}{2a}) - \cosh(\frac{q_1}{a})} + \frac{\cosh(\frac{l}{2a}) - \cosh(\frac{n_1}{a})}{\cosh(\frac{l}{2a}) - \cosh(\frac{q_1}{a})} \tag{17}$$

The above argument is verified below. Motion sensors are placed at point M, N and Q, and the sensor at point Q has higher accuracy. At present, three ways are adopted to solve the arc of transmission lines under the wind deflection condition:

- a. Data of M and Q is used combined with Eq. 16.
- b. Data of N and Q is used combined with Eq. 15.
- c. Data of M, N and Q is used combined with Eq. 17

100 groups of random samples were used for testing, and the statistical characteristics of the data under the three schemes were compared in Table 2. It was found that the variance of the results of method c. was significantly smaller than that in the other two methods when the mean values were not different, which indicated that the solution results of t method c. had the best convergence and the smallest deviation range, so it could obtain higher solution accuracy. The above analysis is proved to be correct.

3.2 Sensor Placement Strategy

In actual installation, the position of the sensor may be deviated, resulting in a certain deviation between the solution result of the model output and the actual parameters of the line. At the same time, because the slope and other parameters at different positions of the line are different, the error of the sensor itself may have different effects on the solution of the model equations at different positions. This section analyzes the sensitivity of solving results to changes in the horizontal coordinate of the sensor, determines the installation strategy of the sensor on the line and selects the most appropriate installation point when there is objective sensor position deviation and sensor error.

3.2.1 Sensor Position Sensitivity Analysis

As shown in Fig. 7, two sensors are placed on the wire. Fixed sensor 1 position at $x = 90$, adjust the position of the sensor 2 and an installation error Δx is added to the abscissa. Set $\Delta x = 0.01$, solving result of sag h is shown in Fig. 8(a).

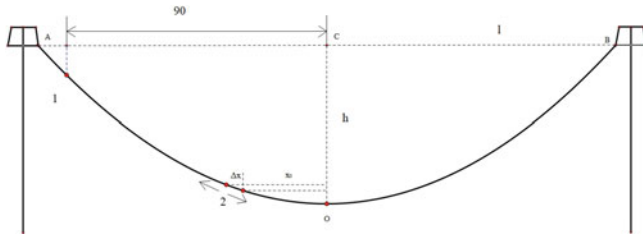


Fig. 7 Sensor position sensitivity analysis

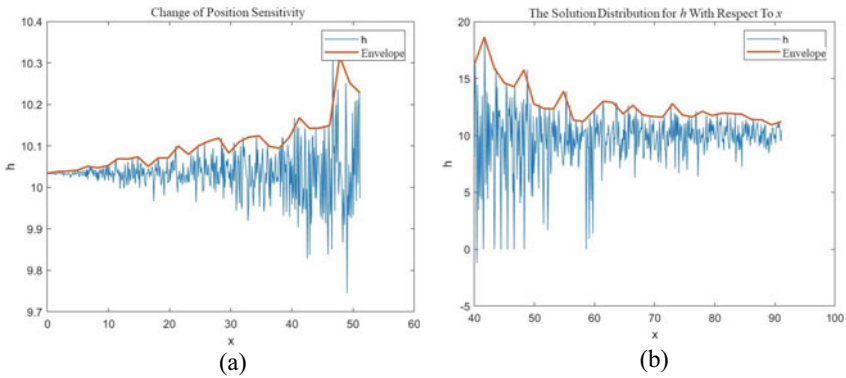


Fig. 8 Influence of sensor position on solution deviation

The fluctuate of h due to the normal distribution that sensor error follows. As can be seen from the curve on the envelope, within the scope of the abscissa in $(0, 50)$, when x increases, solve deviation increases. At the same time, within the scope of the abscissa in $(0, 10)$, the envelope is relatively flat, solving deviation is relatively small. When the abscissa is in the range of $(0, 10)$, the envelope is relatively steep. Therefore, it is more appropriate to place sensor 2 at the abscissa in range of $(0, 10)$.

3.2.2 The Influence of Sensor Error

Sensor error is divided into percentage error and fixed error. When the measurement value is large, the percentage error is dominant in the whole error term. When the measurement value is small, on the contrary, the fixed error may have a greater effect on the error term. At the measuring point of the sensor near both ends of the line, the measurement value is small and the influence of fixed error is great because of the small acceleration at the point. In the center of the line, due to the larger sag and acceleration, the sensor there has a larger measurement value, so the percentage error has a great influence.

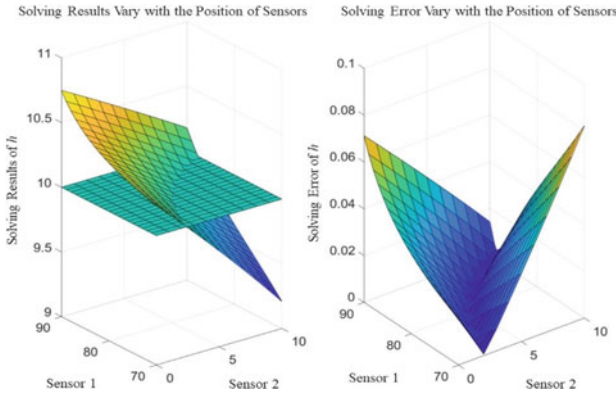


Fig. 9 Influence of sensor position on solution deviation under given sensor error condition

Set the position of sensor 2 at $x = 0$, adjust the position of sensor 1 only consider the effect of sensor error, analysis how solving result changes as the change of abscissa of sensor 1. solving results are shown in Fig. 8(b). As can be seen from the curve on the envelope, within the scope of the abscissa in (40, 90), when x increases, solving deviation reduces. At the same time, within the scope of the abscissa in (40, 60), the envelope is relatively steep. When the abscissa is in the range of (60, 90), the envelope is relatively smooth. Therefore, it is appropriate for the abscissa of the sensor to be in the range of (60, 90), as the sensor error has little influence on the solution results.

In order to weaken randomness, fix the percentage error of the sensor, adjust the position of sensor 1 and sensor 2, analyze the appropriate placement strategy of the two sensors. The results are shown in Fig. 9. The left is the change of solving result as sensor position changes and the plan with $h_0 = 10$. The right is the change of solving error as sensor position changes. We can find that, near the $x = 0$ and $x = 90$, surface gradient is relatively slow, the results are more likely to achieve higher precision.

It can be seen from the above analysis results that if sensor 1 is placed near the lowest point of the arc and sensor 2 is placed near the suspension points at both ends of the line, solving deviation caused by measuring errors of sensors is small.

In fact, in the catenary model, the slope is relatively smooth near the bottom of transmission line, so the installation position error has little impact. Near the suspension point, the line acceleration is small and the sensor measurement value is small. When the line acceleration is used as the numerator in the ratio of acceleration, the influence caused by the sensor error is diluted by a larger denominator, so the influence is small compared with other positions.

4 Conclusions

In this paper, a model of transmission line parameter solving monitoring based on motion sensor is proposed to meet the requirements of online monitoring of transmission lines. Based on catenary model, the algorithm of transmission line sag parameters is studied, and the sensor error is modeled in detail, and the applicability of the model is verified according to the sensor error. Under this model, the solution results of lines with larger spans are more accurate.

In addition, in this paper, influence on the solving result due to positions and amounts of sensors is analyzed. Under the condition that the sensor error is certain, the number of sensors installed in the same section of wire is increased to 3, and the sensors are installed near the suspension points at both ends of the line and near the lowest sag point, which can effectively reduce the solving error and improve the accuracy of the sag solving model.

Acknowledgements This work was funded by State Grid Corporation of China (No. 5500-201999527A-0-0-00).

References

1. Liang, Z.: Statistical analysis of transmission line fault tripping in state grid corporation of China in 2011–2013. *East China Elect. Power* **42**, 2265–2269 (2014). (in Chinese)
2. Yin, W., Huang, L.: Researches on transmission line icing monitoring based on motion angle sensors and different types of power tower. *Power Syst. Big Data* **23**, 14–20 (2020). (In Chinese)
3. Khawaja, A.H., Huang, Q.: Estimating sag and wind-induced motion of overhead power lines with current and magnetic-flux density measurements. *IEEE Trans. Instrum. Meas.* **66**(5), 897–909 (2017)
4. Khawaja, A.H., Huang, Q., Li, J., Zhang, Z.: Estimation of current and sag in overhead power transmission lines with optimized magnetic field sensor array placement. *IEEE Trans. Magn.* **53**(5), 1–10 (2017). <https://doi.org/10.1109/TMAG.2017.2657490>
5. Golinelli, E., Ogliari, G.M., Bartalesi, D.: New optical system for online, real time sag monitoring of high voltage overhead lines. In: 2021 AEIT International Annual Conference (AEIT), Milan, Italy, pp. 1–5 (2021)
6. Golinelli, E., Ogliari, G.M., Bartalesi, D., Perini, U.: Prototype design and preliminary tests for on line, real time sag monitoring of high voltage overhead lines. In: 2020 Italian Conference on Optics and Photonics (ICOP), Parma, Italy, pp. 1–4 (2020)
7. Hao, B., Cai, Y., Zhu, C.: Research on method of wire sag measurement based on RTK UAV photogrammetry. *Northeast Elect. Power Technol.* **43**, 28–31 (2022). (In Chinese)
8. Komaragiri, S.S., Mahajan, S.M.: A sag monitoring device based on a cluster of code based GPS receivers. In: 2009 IEEE Power & Energy Society General Meeting, Calgary, AB, Canada, pp. 1–7 (2009)
9. Mahin, A.U., Hossain, M.F., Islam, S.N., Munasinghe, K.S., Jamalipour, A.: Millimeter wave based real-time sag measurement and monitoring system of overhead transmission lines in a smart grid. *IEEE Access* **8**, 100754–100767 (2020)
10. de Villiers, W., Cloete, J.H., Wedepohl, L.M., Burger, A.: Real-time sag monitoring system for high-voltage overhead transmission lines based on power-line carrier signal behavior. *IEEE Trans. Power Deliv.* **23**(1), 389–395 (2008)
11. Zengin, A.T., Erdemir, G., Akinci, T.C., Seker, S.: Measurement of power line sagging using sensor data of a power line inspection robot. *IEEE Access* **8**, 99198–99204 (2020)

Inversion of Transmission Line Icing State Based on Sag Monitoring



Zhang Huiquan, Jiang Zelong, Jiang Hong, Zhang Huajie, Zhao Mengshi, He Jinliang, and Hu Jun

Abstract China is one of the countries in the world where transmission lines are heavily iced. In recent years, along with the rapid development of Chinese electric power construction, ultra-high voltage and ultra-high voltage transmission line is put into operation. With the growth of transmission line distance, large areas of ice accidents occur all over the country due to complex environmental characteristics. With the development of sensing technology, the monitoring conditions for the mechanical characteristics of wire such as dance, sag and vibration are increasingly perfect. In this paper, the catenary model of the transmission line is supplemented and modified, and the elastic catenary model is proposed. Based on the iterative algorithm, the algorithm of inverting the ice-covering condition of transmission lines is studied based on the sag monitoring results of transmission lines.

Keywords Sag Monitoring · Transmission Line · Catenary Model · Icing Detection

1 Introduction

With the rapid expansion of power grid, the large area of ice damage accidents occur frequently. In 2008, a wide range of snow and rain in southern China caused 1,252 110–500 kV lines with 7,377 towers toppled and 3,092 towers damaged, resulting in huge safety accidents and economic losses. In Northwest China, ice accumulation of transmission lines also causes adverse impact on power grid safety [1]. Ice covering of transmission lines can cause a sharp decrease in mechanical and electrical performance. Overloading leads to broken strands or broken lines or tower collapse, damages the performance of fittings and insulators, results in insulator ice

Z. Huiquan (✉) · J. Zelong · H. Jinliang · H. Jun
Department of Electrical Engineering, Tsinghua University, Beijing 100084, China
e-mail: zhq22@mails.tsinghua.edu.cn

J. Hong · Z. Huajie · Z. Mengshi
Jiaxing Power Supply Company, Zhejiang Electric Power Corporation, Jiaxing 314033, China

© Beijing Paiké Culture Commu. Co., Ltd. 2023
X. Dong et al. (eds.), *The proceedings of the 10th Frontier Academic Forum of Electrical Engineering (FAFEE2022)*, Lecture Notes in Electrical Engineering 1054, https://doi.org/10.1007/978-981-99-3408-9_99

1123

flash. When the line is covered with uneven ice, it is easy to cause damage and deformation of tower head. Uneven deicing jumper of wire leads to a decrease in the safety distance between phase and ground, resulting in ground short circuit fault.

In the decades of power grid development, manual line inspection used to be the main method for line monitoring and maintenance. Although problems of power lines can be found and marked or solved on the spot, the inspection frequency and efficiency are low, and real-time monitoring cannot be realized on the basis of consuming a lot of human and material resources. At present, for the early warning and protection of transmission line ice covering, the methods that have been proposed include optical sensor [2–4], image processing [5], positioning device [6], mechanical sensor [7, 8] and capacitance measurement [9]. These online monitoring methods are proposed to alarm the factors that may cause failure. Self-ice-melting conductors are also used for on-line icing protection [10].

The mechanical state of transmission lines can be monitored by proper monitoring methods. This paper presents a method of inversion of transmission line ice-covered states based on sag monitoring. In this paper, the catenary model of transmission line is selected as the research basis, and it is improved and expanded. Adding an elastic factor to the line enables the line to undergo elastic deformation when the weight changes, such as when the ice is covered, thus changing the size of the sag. Through the iterative algorithm, the linear density of the line can be deduced from the line sag parameters obtained by the on-line monitoring means, so as to invert the ice covering condition of the outlet line.

2 Modeling of Transmission Lines

2.1 Catenary Model of Transmission Lines

The schematic diagram of the overhead power line is shown in Fig. 1. Where, A and B are suspension points, C is the midpoint of AB connection, and O is the lowest point of traverse sag. h is the arc of the line, that is, the length of OC; l is the span of the line, that is, the length of AB.

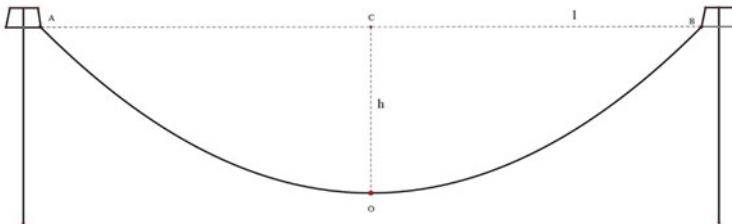


Fig. 1 Schematic diagram of overhead power lines

Catenary model is a physical model commonly used to solve power transmission lines in engineering applications. It refers to a soft, non-extendable chain with uniform distribution of thickness and mass at both ends, which has a curved shape only under the action of gravity. Suppose the linear density of the wire is σ , the horizontal tension on the lowest point of the catenary is denoted as H , and the acceleration of gravity is denoted as g , then the catenary equation is shown in Eq. 1, where $a = H/\sigma g$.

$$y = a \cosh\left(\frac{x}{a}\right) \tag{1}$$

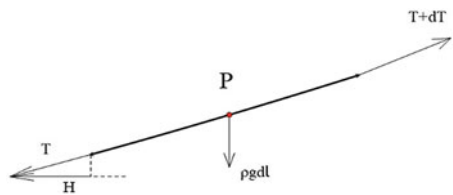
2.2 Elastic Catenary Model

The basic assumption of catenary model is that the line is soft and cannot be extended. That is, in the flexible line model, the length of the line does not change with the change of the line tension, that is, the line length has nothing to do with the stretching or load increase. But for a stretch of elastic and weight cannot be ignored, the tension caused by the dead weight will make it elastic deformation, that is, its length in the natural flat state and suspension length will have a certain gap. At the same time, when the load of the line increases, such as under the condition of ice covering, the dead weight of the line increases, so the length of the line will also change. Under the premise of constant span, the sag of the line will also increase. In order to simulate the changing process and monitor the ice-covered state of the line online, it is necessary to introduce the elastic line model to analyze the transmission line [11].

The force analysis of the micro unit near the point P of the line is carried out as shown in Fig. 2. Under the natural state of flat, set the cross-sectional area of the line as A_0 , linear density as ρ_0 . Under the natural state of suspension, set the cross-sectional area as A , linear density as ρ . H is the component of T in the horizontal direction. Balanced by forces in the vertical direction, there is:

$$H \frac{d^2y}{dx^2} = \rho g \sqrt{1 + \left(\frac{dy}{dx}\right)^2} \tag{2}$$

Fig. 2 Force analysis of P point element



Set the axial elastic modulus of the transmission line as E . According to Hooke's theorem, it can be obtained by assuming that the mass of the suspended front and rear lines remains unchanged that:

$$\rho = \frac{\rho_0}{1 + \frac{T}{EA_0}} \tag{3}$$

It can be obtained by Eq. 2 and Eq. 3 that:

$$Hy'' = \rho g \frac{\sqrt{1 + (y')^2}}{1 + \frac{T}{EA_0}} \tag{4}$$

On the basis of the foregoing derivation, the following parameter transformations are considered:

$$\begin{cases} \epsilon = \frac{H}{EA_0} \\ a = \frac{H}{\rho_0 g} \\ \frac{dx}{dy} = \sinh(u) \end{cases} \tag{5}$$

It can be obtained by applying the above transformation to Eq. 4 that:

$$\begin{aligned} \cosh(u)du &= \frac{\frac{\cosh(u)}{a}}{1 + \epsilon \cosh(u)} dx \\ a(1 + \epsilon \cosh(u))du &= dx \\ x &= a(u + \epsilon \sinh(u)) + C_1 \end{aligned} \tag{6}$$

Similarly, it can be obtained that:

$$y = a \left(\cosh(u) + \frac{1}{2} \epsilon \cosh^2(u) \right) + C_2 \tag{7}$$

Adjust the position of the coordinate system to eliminate constant C_1 and C_2 , the elastic catenary can be obtained:

$$\begin{cases} x = a(u + \epsilon \sinh(u)) \\ y = a \left(\cosh(u) + \frac{1}{2} \epsilon \cosh^2(u) \right) \end{cases} \tag{8}$$

Fig. 3 Schematic diagram of flexible and elastic lines

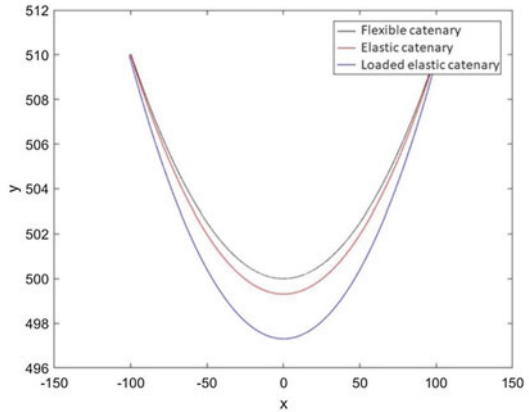


Figure 3 is a schematic diagram reflecting the flexible catenary and the elastic catenary at the same span. Among the three curves, the highest one is the flexible catenary. The second highest is the elastic catenary. There is a small elastic deformation, and the sag is increased. The lowest is the case after the line is weighted (such as icing). As a result of the weight, the line deformation increases and the line elongation causes the sag to increase further.

For the flexible line model, the line weight and load do not affect the change of sag, while the weight gain of the line can be deduced from the change of sag in the elastic line model. Therefore, the necessity of introducing the elastic catenary model can be analyzed.

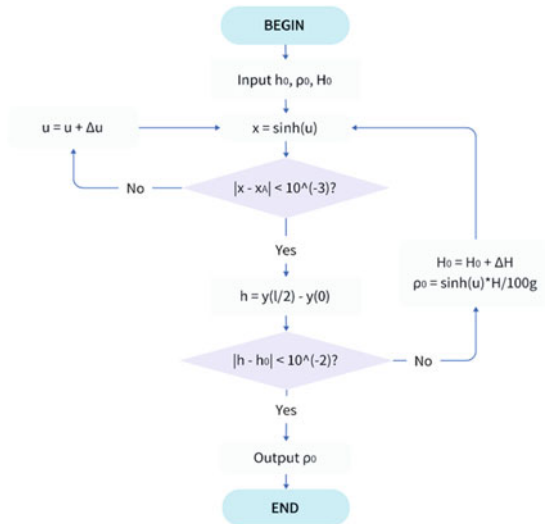
3 Icing Detection

Under the elastic catenary model, if the linear density of the line changes, for example, the line is aggravated by ice covering, then the shape of the transmission line will change due to the elastic deformation of the line, and the sag will also increase. The more the line is aggravated, the larger the sag will be. In other words, if the sag of the line is observed to have significant changes according to the measurement data, then the ice covering condition of the line can also be inferred from the results of the arc changes.

With ice covering, line density of the transmission line ρ is related to sag h . h meets:

$$h = y_A - y_O \tag{9}$$

Fig. 4 Iterative algorithm



In the elastic catenary parameters equation model, according to Eq. 8, under the condition of given ρ and H , y_A and y_O can be inferred from parameters u . As the abscissa of point A and point O is known, u_A, u_O can be inferred from x_A, x_O , then y_A and y_O can be inferred, from which we can get sag h .

It is difficult to express parameters u by x, y respectively, so it's necessary to get u from x with the method of numerical iterative, then we are able to work out parameter y .

Using the given initial conditions ρ and H we can work out the sag value h by iteration. If the deviation with the given sag value h_0 is allowable, we can consider the initial condition is reasonable. If there is greater difference between h and h_0 , we need to modify the initial conditions to make h to be near h_0 . If the above process is repeated continuously until $h \approx h_0$, the iteration is stopped and the modified initial condition is considered reasonable. This iterative algorithm is shown in Fig. 4.

The typical parameter of 110 kV lines is used to test the above analysis and algorithm. We can know that transmission line conductor elastic modulus $E = 74$ Gpa, cross-sectional area $A_0 = 277.75$ mm², span $L = 200$ m, horizontal component of tensile force $H = 5000$ N, $\rho_0 = 1$ kg/m. Using the above algorithm to solve linear density of the wire as sag h changes in range of 10–20 m. The results are shown in Fig. 5(a). From the point of view of numerical solution, it can be seen that in a certain range, with the increase of sag, the wire density also increases. From the angle of causality, the length of the wire increases and the sag increases as the line weight increases and the line density increases. The numerical solution is actually a process of inversely deducing line density from sag. Figure 5(b) shows the correlation between sag and icing density.

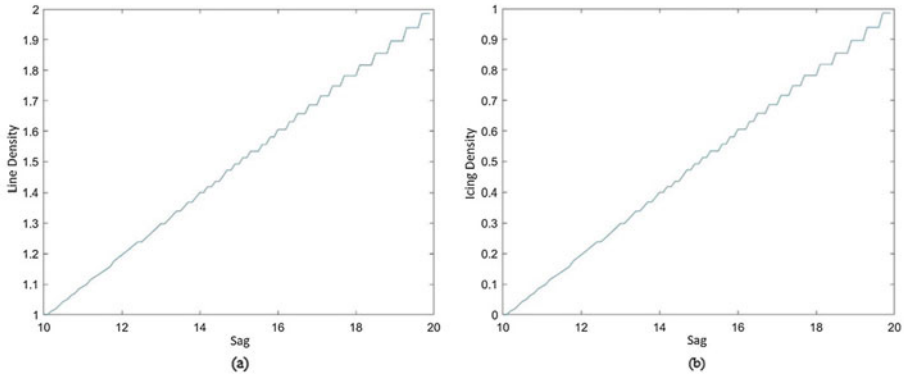


Fig. 5 The correspondence between sag, line density and icing density

In addition, the large step ripple appears in the curve when the sag is large, which is caused by the larger judgment condition of convergence of the above algorithm. The ripple can be eliminated by modifying the convergence condition to make the curve smoother. However, it is followed by an increase of calculation amount. If the data set is large enough, the balance between calculation speed and calculation accuracy should be balanced to maximize the overall efficiency of online monitoring.

4 Conclusions

Based on the monitoring results of transmission line arcs, this paper designs an algorithm to invert the ice-covering state of transmission lines from sag. The elastic catenary model is proposed based on the improvement of the catenary model. The elastic modulus is introduced into the mechanical characteristics of the flexible catenary model, so that the changes of the length and sag of the transmission line under the influence of weight load can be reflected in the model. Furthermore, based on the elastic catenary model, a Newton-like method is adopted to obtain the correlation curve of line sag value and line density by numerical iteration. After the sag is detected by the existing monitoring methods, the sag is input into the iterative solution process as a known quantity to obtain the monitoring value of the line density, and then the ice-covering condition of the line can be predicted according to the changes of the line density, thus realizing the ice-covering state inversion of the transmission line.

Acknowledgements This work was funded by State Grid Corporation of China (No. SGTYHT/19-JS-215).

References

1. Zhuang, W.L., Zhang, L., Yang, Y.: Research on ice accumulation of transmission lines in Xinjiang. In: 2022 Power System and Green Energy Conference (PSGEC), Shanghai, China, pp. 1012–1015 (2022)
2. Deng, Y., Liu, T., Liu, S.: Application of optical sensing technology in on-line monitoring of transmission lines. *Res. Appl. Power Commun. Technol.* **7**, 216–222 (2019). (in Chinese)
3. Wang, M., Li, L., Zhou, D.: Overview of studies on application of distributed optical fiber sensing technology in online monitoring of transmission lines. *Power Syst. Technol.* **45**, 3591–3600 (2020). (in Chinese)
4. Barat, A., Guo, Q., Fan, F., Guo, X., Zhang, Q.: Analysis and design of transmission line icing monitoring system based on optical fiber sensing. In: 2022 IEEE 10th Joint International Information Technology and Artificial Intelligence Conference (ITAIC), Chongqing, China, pp. 1846–1849 (2022)
5. Xu, H., Peng, S., Mao, Y.: Transmission line ice thickness detection based on image processing. In: Shaanxi Electric Power, vol.45, pp. 32–35, May 2017. (in Chinese)
6. Zhang, W.: Research on DGPS Based Real-time Monitoring System for Deformation of Electric Power Transmission Line. Xidian University (2014). (in Chinese)
7. Yang, J.: Research on Wire Icing Monitoring Based on FBG Tension and Dip Sensing. Kunming University of Science and Technology (2019). (in Chinese)
8. Chang, H.: Prediction and Experimental Study on Ice Thickness of Overhead Transmission Line Based on Dynamic Tension and Angle. Chongqing University (2013). (in Chinese)
9. Huan, H., Wang, Y., Mao, X., Zeng, H., Niu, W.: Experimental study on icing monitoring method based on capacitance measurement for transmission lines. In: 2022 IEEE International Conference on High Voltage Engineering and Applications (ICHVE), Chongqing, China, pp. 1–4 (2022)
10. Li, B., Mo, S., Tan, Y., Zhu, S., Huang, Q., Zhu, Y.: Real-time on-line anti-icing and ice-melting power calculation method for transmission lines based on self-ice-melting conductors. In: 2019 IEEE 3rd Conference on Energy Internet and Energy System Integration (EI2), Changsha, China, pp. 2439–2442 (2019)
11. Fan, H.: The parameter transformation method for elastic catenary equation and its application in engineering. *Mech. Eng.* **32**, 32–34+15 (2010). (in Chinese)

Overvoltage Distribution Characteristics of Long Distance Gas Insulated Transmission Lines



Qishen Lv, Gen Li, Zhiren Tian, Guoxing Wu, Shu Xu, Lin Zhang, and Yu Zheng

Abstract When gas insulated transmission line (GIL) is applied to long-distance transmission in urban underground pipe gallery, it will generate overvoltage due to capacity rise effect, which may threaten the insulation safety of equipment. However, at present, there is little research on voltage distribution along long-distance GIL. In this paper, the transmission line distributed parameter model is used to establish the voltage distribution calculation model along GIL, and the voltage distribution characteristics along GIL at different distances and voltage levels are calculated by taking typical transmission voltage levels as examples. The results show that the maximum value of GIL no-load line overvoltage occurs at $1/4$ of the electromagnetic wavelength on the line from the head end of the line, and the line voltage increases with the distance when it is within $1/4$ of the wavelength from the head end of GIL line. Through the analysis of overvoltage distribution of GIL lines with typical length, it is found that within 20 km, the increase rate of GIL end overvoltage is lower than 0.03% compared with that of the head end, and the influence of GIL line end overvoltage can be ignored. Considering 1.1 times of insulation withstand capacity, for 800 kV GIL line, the impact of Overvoltage on GIL equipment insulation can only be considered when its length reaches about 410 km. The results of this paper have reference significance for overvoltage protection and insulation test of long-distance GIL lines.

Keywords Gas insulated transmission line · Distributed voltage · Capacity rise effect · Overvoltage · Transmission line model

Q. Lv · Z. Tian · G. Wu · S. Xu · L. Zhang
Shenzhen Power Supply Company, Shenzhen 518048, China

G. Li (✉) · Y. Zheng
School of Electrical Engineering and Automation, Wuhan University, Wuhan 430072, China
e-mail: leagren@whu.edu.cn

© Beijing Paiké Culture Commu. Co., Ltd. 2023
X. Dong et al. (eds.), *The proceedings of the 10th Frontier Academic Forum of Electrical Engineering (FAFEE2022)*, Lecture Notes in Electrical Engineering 1054, https://doi.org/10.1007/978-981-99-3408-9_100

1131

1 Introduction

GIL (gas insulated metal-enclosed transmission line) is an important part of power transmission system [1–3]. GIL is a high voltage and high current power transmission equipment with metal shell and conductor arranged coaxial, using SF₆ or SF₆/N₂ mixed gas as insulation medium. Compared with overhead lines and cables, GIL equipment has large transmission capacity, low unit loss, strong environmental friendliness, high operation reliability, and less land area. It is widely used in power transmission of large hydropower stations and nuclear power stations, as well as complex transmission channels such as river crossing and mountain crossing [4–6]. Due to the capacity rise effect, the voltage at the end of no-load long distance GIL line will be higher than the voltage at the head end. In the case of operation, maintenance, overhaul test, etc., overvoltage at GIL end will affect the safety of equipment and personnel [7, 8].

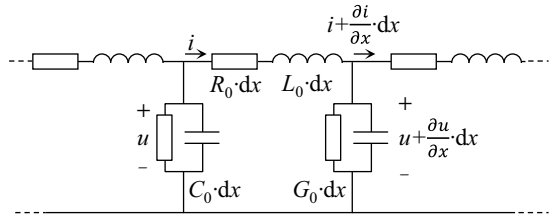
Reference [9] accurately measured the transient voltage generated by insulation breakdown during voltage test and operation of GIL by using the ultra-broadband transient voltage monitoring system installed in 1100 kV Sutong GIL integrated pipe gallery project. Accurately assess insulation hazards of transient voltage to GIL. Reference [10] proposed an accurate fault location method of GIL based on transient voltage monitoring, which was applied in the 1100 kV Sutong GIL integrated pipeline corridor project. In this method, broadband voltage sensing based on capacitive voltage division can realize rapid and accurate location of insulation breakdown fault of GIL, and the location error is less than 5 m. At present, most researches focus on the transient voltage test of GIL, but lack the theoretical analysis of the distributed voltage of long distance GIL lines.

In this paper, the calculation model of GIL line's electrical parameters is established by the transmission line equation. The calculation method of voltage along GIL line is given through theoretical deduction. The voltage characteristics of line distribution are analyzed by typical GIL structure. Considering the distributed voltage characteristics of each GIL structure, the warning value of line length considering terminal overvoltage is given.

2 Theoretical Model

The electrical parameters along the GIL line can be described by a transmission line model, as shown in Fig. 1. In the figure, R_0 is the resistance per unit length of the GIL high voltage conductor in Ω/m ; L_0 is the inductance per unit length of the GIL high voltage conductor in H/m ; G_0 is the conductance per unit length of the GIL gas insulation in S/m ; C_0 is the capacitance per unit length of the GIL gas insulation in F/m . The model does not take into account the GIL metal shell to ground conductance and capacitance to ground. The model treats each structure of the GIL

Fig. 1 Schematic diagram of the designed galloping test system



as a homogeneous material and does not take into account the bending deformation of the GIL.

For the instantaneous voltage $u(z, t)$ at moment t from the first z on the high voltage conductor and the instantaneous current $i(z, t)$ at that point satisfy the set of partial differential equations shown in Eq. (1), which is mapped from the time domain to the complex frequency domain to obtain Eq. (2), where U is the voltage phase of the high voltage conductor; I is the current phase, ω is the angular velocity of the system in rad/s, and j is the imaginary unit [11].

$$\begin{cases} -\frac{\partial u}{\partial x} = R_0 i + L_0 \frac{\partial i}{\partial t} \\ -\frac{\partial i}{\partial x} = G_0 u + C_0 \frac{\partial u}{\partial t} \end{cases} \quad (1)$$

$$\begin{cases} -\frac{d\dot{U}}{dx} = (R_0 + j\omega L_0)\dot{I} \\ -\frac{d\dot{I}}{dx} = (G_0 + j\omega C_0)\dot{U} \end{cases} \quad (2)$$

Equation (3) is the general solution of (2), where V^+ is the coefficient to be determined and its value is determined by the boundary conditions, γ is the propagation coefficient, calculated by Eq. (4), Γ is the reflection coefficient, calculated by Eq. (5), for no-load conditions, $\Gamma = 1$, Z_0 is the characteristic impedance, calculated by Eq. (6); Z_L is the load impedance in Ω ; and l is the GIL length in m.

$$\begin{cases} \dot{U}(z) = V^+ e^{-\gamma z} [1 + \Gamma e^{-2\gamma(l-z)}] \\ \dot{I}(z) = \frac{V^+}{Z_0} e^{-\gamma z} [1 - \Gamma e^{-2\gamma(l-z)}] \end{cases} \quad (3)$$

$$\gamma = \sqrt{(R_0 + j\omega L_0)(G_0 + j\omega C_0)} \quad (4)$$

$$\Gamma = \frac{Z_L - Z_0}{Z_L + Z_0} \quad (5)$$

$$Z_0 = \sqrt{\frac{R_0 + j\omega L_0}{G_0 + j\omega C_0}} \quad (6)$$

Substituting the boundary condition Eq. (7) into Eq. (3), the voltage along the GIL is obtained as shown in Eq. (8), where, V_S is the first end voltage in V. The line electromagnetic wave wavelength λ is calculated by Eq. (9), where Im denotes the

imaginary part of the complex number extraction operation.

$$\begin{cases} \dot{U}(0) = V_S \\ \dot{U}(l) = Z_L \dot{I}(l) \end{cases} \tag{7}$$

$$\dot{U}(z) = \frac{1 + \Gamma e^{-2\gamma(l-z)}}{1 - \Gamma e^{-2\gamma l}} V_S e^{-\gamma z} \tag{8}$$

$$\lambda = \frac{2\pi}{\text{Im}[\gamma]} \tag{9}$$

3 Voltage Analysis Along the Long Distance GIL

The structural differences between GIL circuits of different voltage levels are mainly determined by the internal aluminium conductor and the inner and outer diameter of the housing. Typical GIL equivalent circuit parameters are shown in Table 1. The long distance GIL voltage oscillation wavelength can be calculated from Eq. (9). The voltage oscillation wavelength along the GIL at a rated voltage of 800 kV is 5.99×10^6 m. At a voltage of 1105 kV at 1/4 wavelength, the voltage deviation amounts to 37.5%, which can pose a serious threat to the equipment insulation (Fig. 2).

Table 1 data can be substituted into Eq. (8) to obtain the voltage distribution along the GIL at different rated voltages. Taking a 20 km GIL line as an example, the voltage distribution along the line in the case of an open circuit at the end is shown in Figs. 3, 4 and 5.

The GIL end voltages at 145 kV, 362 kV and 800 kV rated voltages are all increased to some extent compared to the first end voltage due to the capacitive rise effect. The further away from the head end, the higher the voltage rise. Define the voltage deviation V as the proportion of the distributed voltage to the first end voltage lift, as shown in Eq. (10). The voltage deviation at the end of the GIL at 145 kV, 362 kV and 800 kV rated voltage is 0.0228%, 0.0224% and 0.0221% respectively, as shown in Fig. 6.

$$\Delta V = \left| \frac{\dot{U}(z) - V_S}{V_S} \right| \tag{10}$$

Table 1 GIL parameters at different rated voltage

Rated voltage (kV)	145	362	800
R_0 ($10^{-6} \cdot \Omega/m$)	18	13	10
L_0 ($10^{-6} \cdot H/m$)	0.187	0.210	0.247
G_0 ($10^{-15} \cdot S/m$)	15	12	10
C_0 ($10^{-12} \cdot F/m$)	59	53	45

Fig. 2 Voltage distribution along the GIL line

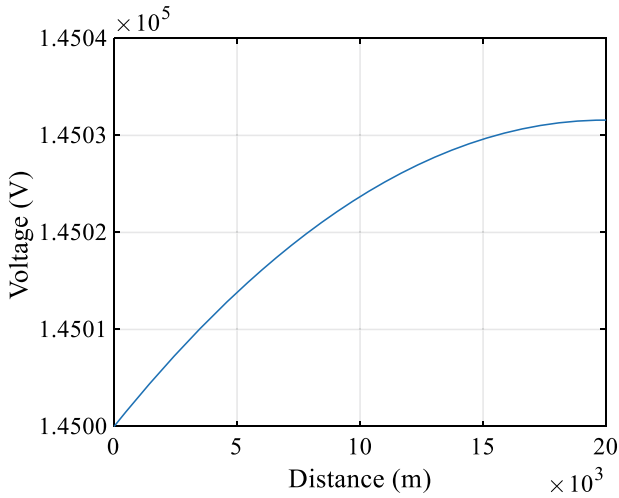
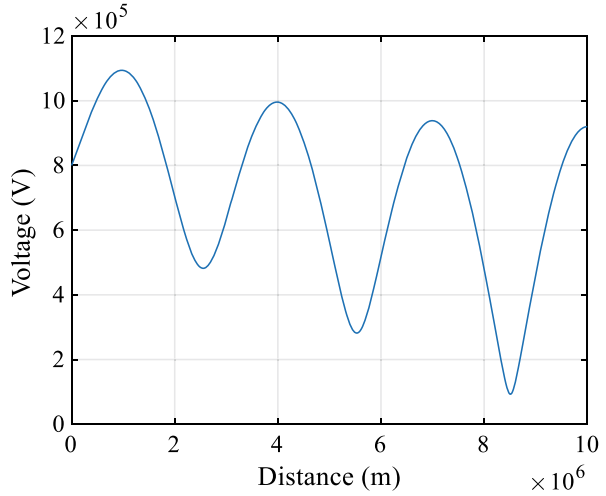


Fig. 3 Voltage distribution along the 145 kV GIL line

The end voltage is set at 1.1 times the first end voltage as a warning value and the line length is 405 km, 407 km and 410 km when the GIL end voltage reaches the warning value at 145 kV, 362 kV and 800 kV rated voltage respectively. it is therefore recommended to consider the effect of end overvoltage when the line length reaches 400 km.

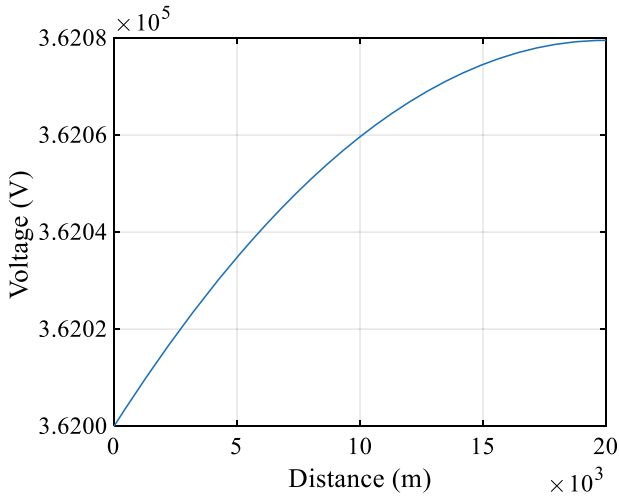


Fig. 4 Voltage distribution along the 362 kV GIL line

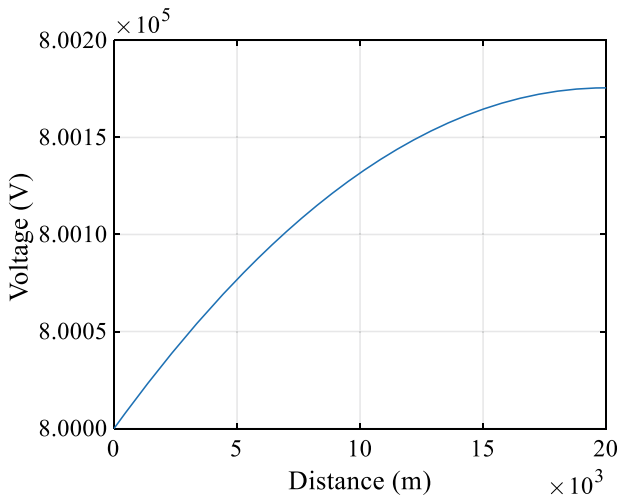


Fig. 5 Voltage distribution along the 800 kV GIL line

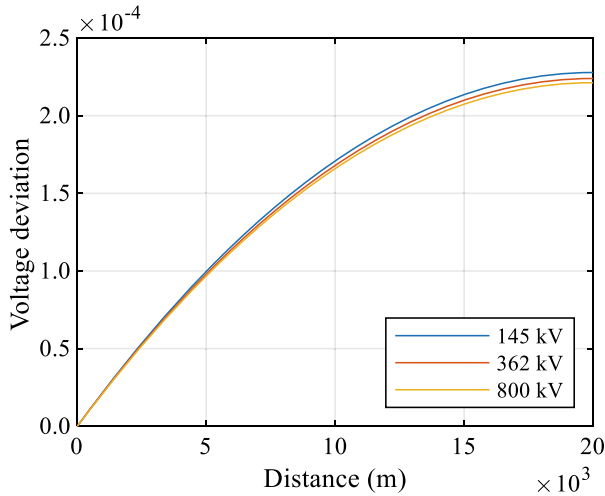


Fig. 6 Voltage deviation along the GIL line at different rated voltage

4 Conclusions

In this paper, the following conclusions are drawn from calculations of the voltages along long GIL.

- 1) The voltage rise at the end of the GIL for line lengths of 20 km at rated voltages of 145 kV, 362 kV and 800 kV is 0.0228%, 0.0224% and 0.0221% respectively, and the impact of voltage fluctuations along the GIL at this length class is more limited.
- 2) When the GIL line lengths are rated at 145 kV, 362 kV and 800 kV for 405 km, 407 km and 410 km respectively, the line end voltage is 1.1 times the first end voltage. It is recommended to consider the effect of terminal overvoltage when the line length reaches 400 km.

Acknowledgements This work is supported by Science and Technology Project of China Southern Power Grid Co., Ltd. Research on Key Technologies of long distance and high reliability GIL transmission line in urban power grid. (090000KK52210175).

References

1. Kuroyanagi, Y., Toya, A., Hayashi, T., et al.: Construction of 8000 A class 275 kV gas insulated transmission line. *IEEE Trans. Power Deliv.* **5**(1), 14–20 (1990)
2. Quanrong, R., Xiaoping, X.: *Research and Practice on Engineering Design of Gas-Insulated Metal-Enclosed Power Transmission Lines*, pp. 1–2. China Water Conservancy and Hydropower Press, Beijing (2011)

3. Memita, N., Suzuki, T., Itaka, K., et al.: Development and installation of 275 kV SF₆ gas-insulated transmission line. *IEEE Trans. Power Appar. Syst.* **103**(4), 691–698 (1984)
4. Sabot, A.: Insulation go-ordination procedure for 420 kV gas insulated lines (GIL). In: 1999 Eleventh International Symposium on the High Voltage Engineering. London, UK: IET, pp. 1–10 (1999)
5. Chen, X., Hu, Y., Xin, Y., et al.: Prospect of high voltage long distance compressed-air insulated transmission lines. *High Voltage Eng.* **35**(12), 3137–3142 (2009). (in Chinese)
6. Hillers, T.: Gas insulated transmission lines(GIL): ready for the real world. In: Power Engineering Society Winter Meeting, pp. 575–579. IEEE Singapore (2000)
7. Lu, J., Cao, W., Zhou, Z.: The structural design of 550 kV GIL bus. *Electr. Eng.* **16**(9), 59–63 (2015). (in Chinese)
8. Bo, Q., Zhang, G., Li, C., et al.: Research status and prospect of gas-insulated metal enclosed transmission line. *High Voltage Eng.* **41**(5), 1466–1473 (2015). (in Chinese)
9. Ding, D., Han, X., Wang, N., et al.: Time and frequency domain characteristics of transient voltage excited by insulation breakdown in UHV GIL. *Power Syst. Technol.* **44**(6), 8 (2021) (in Chinese)
10. Ding, D., Han, X., Wang, N., et al.: Fault location method and engineering application in UHV GIL based on transient voltage monitoring. *High Volt. Eng.* **47**(3), 1092–1099 (2021). (in Chinese)
11. Paul, C.R.: Analysis of Multiconductor Transmission Lines. IEEE (2007). <https://doi.org/10.1109/9780470547212>

500 KV GIL Fault Location Based on Single Terminal Transient Monitoring in Field Takeover Test



Lin Zhang, Junqiang Gong, Zhiyi Luo, Fan Zhang, Jian Cheng, Gen Li, and Yu Zheng

Abstract In this study, the fault location method in 500 kV gas insulated transmission line (GIL) based on single terminal transient voltage and current monitoring was proposed. The measurement bandwidth of the transient voltage and current sensing system is 2.1 Hz ~ 230 MHz and 100 MHz ~ 500 MHz respectively. The time and frequency domain feature of transient voltage and current generated by GIL breakdown is analyzed. It is found that when insulation breakdown occurs in the 500 kV GIL, the first change steepness of the transient voltage is less than 60 ns. A typical traveling wave process is formed when the transient voltage spreads between the break point and bushing. The accurate position of the fault point can be calculated based on the time when the transient traveling wave reached the measuring points and the propagation speed of traveling wave. According to the results of disintegration verification, the fault position is determined. The results show that the positioning error based on transient voltage is less than 2 m, the error based on transient current is approximately 5 m.

Keywords 500 kV GIL · Field test · Fault location · Transient voltage · Transient current

1 Introduction

500 kV gas insulated transmission line (GIL) is widely used in substations and large hydropower stations. Post insulators are widely applied in 500 kV GIL. Because the surface electric field control of post insulator is difficult and the manufacture process is more complicated, the fault rate is high under the combined action of electrical

L. Zhang · J. Gong · Z. Luo · F. Zhang · J. Cheng
Shenzhen Power Supply Company, Shenzhen 518048, China

G. Li (✉) · Y. Zheng
School of Electrical Engineering and Automation, Wuhan University, Wuhan 430072, China
e-mail: leagren@whu.edu.cn

and mechanical composite stress. In the takeover test and operation, it is necessary to accurately locate the fault [1–3].

It is unfeasible to directly use the traditional gas decomposition components detection method to determine the fault chamber because of the large number of gas chambers in long-distance GIL. Therefore, it is essential to research the fast and accurate location method for GIL [4, 5]. Research on fault location method of transmission lines focuses on the overhead line and cable has been extensively conducted [6, 7]. The location error is approximately 500 m, which is difficult to meet the needs of fault location in long GIL from the perspective of engineering [8–10]. If the fault location technique based on ultrasonic is applied to GIL, a lot of sensors need to be arranged. It is also impracticable due to the large cost and huge operation and maintenance burden [11–13].

Hence, a monitoring system based on ultra-wideband transient voltage and current sensing is proposed in this study, which can monitor the transient voltage and current generated by insulation breakdown inside the GIL. Then, the time and frequency domain characteristics of transient voltage and current are analyzed. Moreover, the transient voltage traveling process in GIL is revealed, which provides support for accurate fault location of GIL. The proposed method and the established system are applied in field, and the positioning error meets the requirements of field application.

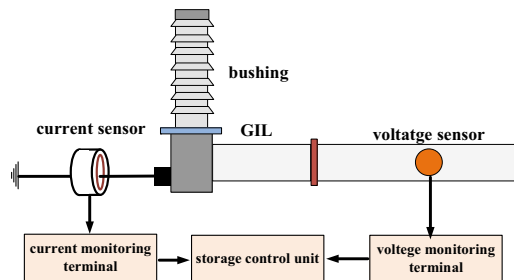
2 Construction of Transient Monitoring System

Transient voltage and current measurement points are set at the port of the GIL bushings, as shown in Fig. 1. The monitoring system consist of three parts: voltage and current sensor, voltage and current monitoring terminal, and storage control unit.

2.1 Voltage and Current Sensor

The wideband monitoring method of GIS transient voltage based on capacitive voltage sensing technology is presented in this paper. The voltage sensor based on the

Fig. 1 Structure diagram of the transient current and voltage monitoring system



capacitive voltage divider principle is mainly composed of the handhole cover plate, the sensing electrode and the insulating film as shown in Fig. 2. The diameter of the sensing electrode is 100 mm, and the thickness of the insulating film (Teflon film) between the electrode and the hand hole cover plate is 100 μm . The high-voltage arm capacitance formed by the sensing electrode and GIS high-voltage bus is 0.001 pF level, and the low-voltage arm capacitance formed by the sensing electrode and GIS handhole cover form is nF level. The frequency response bandwidth of the voltage sensor is calibrated using the standard measurement system. The results show that the measurement bandwidth of the transient voltage sensing system is 2.1 Hz ~ 230 MHz. The voltage sensor is set approximately 3 m away from the bottom end of the bushing.

Ultra-high frequency (UHF) transient current sensor adopts the principle of penetrating UHF electromagnetic coupling and is installed at the grounding bar of GIL enclosure near the bushing. The transient current sensor is installed in an open caliper type, which is convenient and fast. The UHF transient current sensor is made of amorphous ferromagnetic material, which can better sense the transient current signal within the frequency band of 100 MHz ~ 500 MHz. The average equivalent impedance is greater than 15 Ω as shown in Fig. 3. The inner diameter opening of UHF transient current sensor shall not be less than 60 mm. The sensor is connected to the monitoring terminal through a high-frequency coaxial cable.

Fig. 2 Structure of the voltage sensor

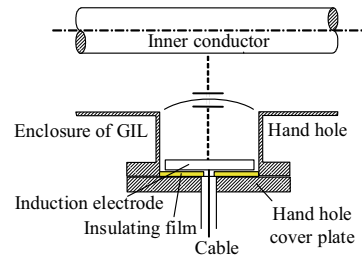
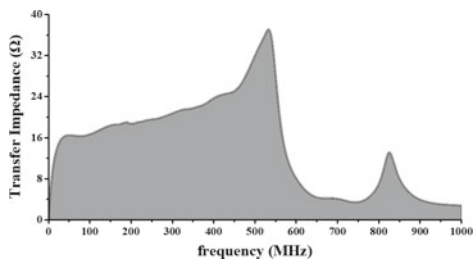


Fig. 3 Transfer characteristic of UHFCT



2.2 Voltage and Current Monitoring Terminal

In order to realize the wideband measurement of transient voltage, it is necessary to expand the high-frequency and low-frequency characteristics of the monitoring system simultaneously. Hence, a conversion circuit is employed to improve the high frequency and low frequency characteristics of the system. The high input impedance if the conversion circuit ($G\Omega$ level) can significantly expand the low cut-off frequency of the monitoring system, and the low output impedance ($<0.1 \Omega$) can help to improve the high-frequency characteristics of the system.

In order to reduce the measurement error of high frequency transient current, a filter unit is introduced, and the frequency band is 100 MHz ~ 500 MHz.

The monitoring terminal contains a high-speed data acquisition unit with a sampling rate of 1 GS/s, an analog bandwidth of 500 MHz, and a storage depth of 2 GB. All units are placed in a metal shielding box fixed on the flange outside the sensor, and a special designed isolation transformer is used to suppress the interference of ground potential rise.

2.3 Storage Control Unit

The storage control unit includes optical switch, control host (server) and other equipment. The monitoring terminal is connected to the optical switch through optical fiber, and the optical switch is connected to the storage control unit through network cable. The transient voltage and current signals are sent to the storage control unit. Then, the data is stored and analyzed by the storage control unit. The feature time is automatically calculated, and the fault location is quickly determined combining with the transient voltage propagation speed.

3 Transient Voltage and Current Waveform Analysis

In the withstand voltage test process of a 500 kV 1 km GIL, when the test voltage rises to 740 kV, insulation breakdown occurs inside the GIL. The transient voltage and current waveforms excited by insulation breakdown are analyzed in depth, and the time domain and frequency domain characteristics are investigated. Moreover, the transient voltage and current are used for fault location in GIL.

3.1 Transient Voltage Waveform Analysis

During the withstand voltage process, the transient voltage waveform recorded at the bushing end by the transient monitoring system within 200 ms excited by insulation breakdown of GIL is shown in Fig. 4. In case of insulation breakdown, the test voltage rapidly drops to 0 after a short period of oscillation, and the duration is very short. After the arc inside the GIL is extinguished, if the power supply of the test system is not cut off, a power-frequency voltage of approximately 120 kV can be established on the GIL.

As shown in Fig. 5, the transient voltage lasts approximately 400 μ s, which is far less than the transient voltage duration caused by the flashover of the insulator in the withstand test. The breakdown may be caused by the breakdown of SF₆ gap. The transient voltage lasts for nearly 80 square wave periods, and the amplitude decreases linearly. The transient voltage wave head generated during insulation breakdown in 500 kV GIL is shown in Fig. 6. The square half wave period of the voltage is 2.36 μ s, and the voltage wave head decreases from 980 kV to -1200 kV. It has experienced about 60 ns, and the half wave abrupt change time is about 30 ns. Because the insulation distance of SF₆ gap in 500 kV GIL is shorter and the time required for breakdown is shorter than that of 1000 kV GIL, the half wave abrupt change time of the new wave head of transient voltage is also shorter than that of 1000 kV GIL. Since the transient voltage traveling wave propagates to the end of the bushing at time t_1 , the bellows connected to the end of the bushing has a large inductance. Under the action of transient voltage, creepage occurs on the inner surface of the bellows, and a new transient voltage appears, which is superimposed with the transient voltage generated by the previous fault, resulting in short-time oscillation at the first falling edge of the voltage traveling wave and distortion to the subsequent voltage traveling wave.

Fig. 4 Voltage variation process when the insulation breakdown

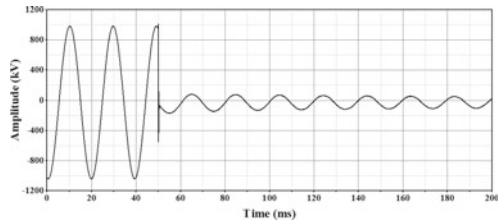


Fig. 5 Transient voltage when the insulation breakdown in 500 kV GIL

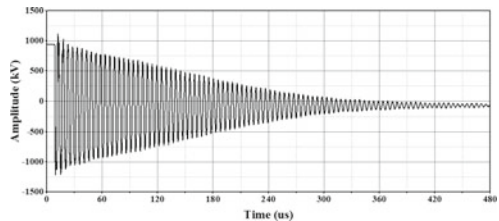
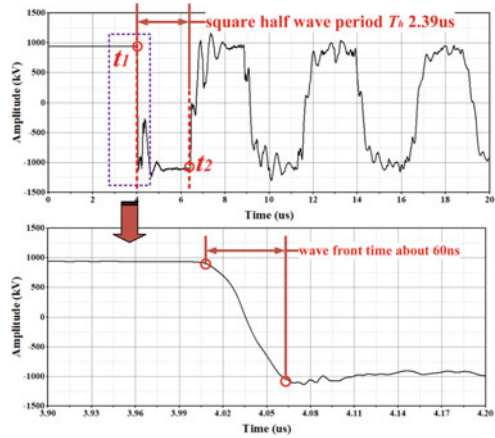


Fig. 6 Transient voltage when the insulation breakdown in 500 kV GIL during voltage withstand test



The transient voltage in Fig. 6 is subjected to FFT transformation, and the frequency distribution characteristics are shown in Fig. 7. The maximum value is taken as the reference value, and the spectral components are normalized. The main frequency components of the transient voltage measured at the bushing are all lower than 1 MHz. The main characteristic frequency of transient voltage is 200 kHz, and there are obvious component distributions near 600 kHz and 1 MHz. The period corresponding to the main characteristic frequency of the transient voltage is approximately 2 times the square half wave period, which is 4 times the time required for the transient voltage to propagate from the fault point to the bushing.

In Fig. 6, the moment t_1 and t_2 can be determined, and the duration (T_h) between t_1 and t_2 is approximately 2.39 μs. The propagation speed v of transient voltage in the 500 kV GIL can be theoretically calculated to be 292.4 m/μs based on the equivalent capacitance (35.72 pF/m) and equivalent inductance (0.31 μH/m) of the GIL. Then, the distance (L) between the fault point and the bushing can be calculated as follows:

$$L = \frac{T_h \times v}{2} = 349.4(\text{m}) \tag{1}$$

Fig. 7 Time frequency distribution of transient voltage

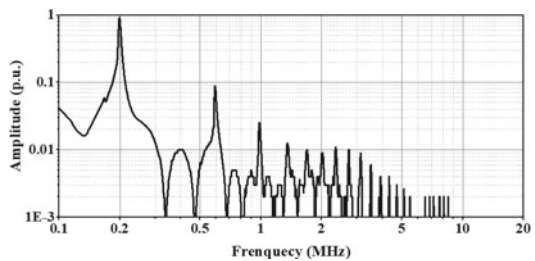


Fig. 8 Transient current when the insulation breakdown in 500 kV GIL

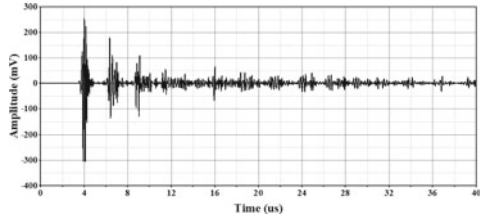
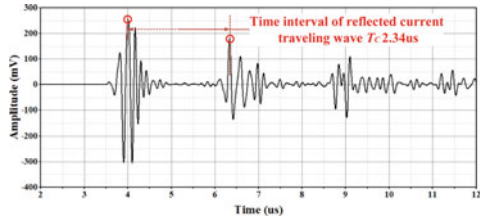


Fig. 9 Waveform head of transient current



3.2 Transient Current Waveform Analysis

Figures 8 and 9 show the transient current measured at the grounding of GIL enclosure near the bushing during the internal insulation breakdown of 500 kV GIL

The UHF transient current lasts for nearly 20 us, the current amplitude decays rapidly, and the first four transient current events are relatively clear. The time interval T_C between the first and second transient current events can be obtained to be about 2.34 us by taking the time of the maximum peak point of the positive polarity of the current as the arrival time of the transient current. The distance L between the fault point and the bushing is calculated according to the single end positioning algorithm as follows:

$$L = \frac{T_C \times v}{2} = 342.1(m) \tag{2}$$

3.3 Field Verification

After the insulation breakdown during the withstand test of GIL, the gas return was conducted in the positioning area, and the fault area was determined. the fault was determined to be about 347.5 m away from the bushing. Obvious discharge trace were found on the inwall and the high voltage conductor in the fault area as shown in Fig. 10, which may be due to the metal particles left near the inwall, or the protrusions of the high voltage conductor because of poor polishing. Under the severe voltage of 740 kV, the SF₆ gap breakdown occurred. The single terminal location error based on the transient voltage waveform traveling wave is 1.9 m, and the error of the

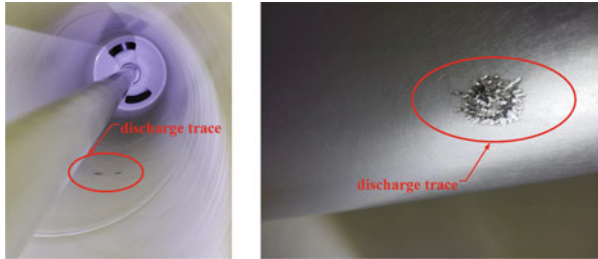


Fig. 10 Discharge trace in GIL

high frequency component of the current wave is 5.4 m, The positioning error of current traveling wave is larger than that of voltage traveling wave, but it also meets engineering requirement.

4 Conclusion

- 1) The duration of transient voltage excited by SF₆ gap breakdown in 500 kV GIL during withstand test is short about 400 us. However, the wave front time is short about 60 ns, which is far lower than 120 ns in 1100 kV GIL. It can be seen that the lower the voltage level of GIL, the smaller the insulation distance of SF₆, the shorter the arc distance during breakdown, and the faster the breakdown time. However, the attenuation of transient voltage by different voltage levels of GIL has no obvious difference.
- 2) Wideband voltage sensing at the end of the bushing is applied to realize accurate positioning of single terminal the fault in 500 kV GIL based on the signal terminal location method, with a positioning accuracy of less than 2 m.
- 3) The transient current excited by the insulation breakdown of GIL can be sensed at the grounding of GIL enclosure near the bushing. The single terminal location of GIL fault can also be realized through the characteristic time of the transient current. However, the location error based on the transient current part is slightly larger than voltage, but it can still meet the field demand.

Acknowledgements This work is supported by Science and Technology Project of China Southern Power Grid Co., Ltd. Research on Key Technologies of long distance and high reliability GIL transmission line in urban power grid (090000KK52210175). Thanks to the efforts of Prof. Dengwei Ding of Tsinghua University.

References

1. Kuroyanagi, Y., Toya, A., Hayashi, T., et al.: Construction of 8000A class 275 kV gas insulated transmission line. *IEEE Trans. Power Deliv.* **5**(1), 14–20 (1990)
2. Chen, X., Hu, Y., Xin, Y., et al.: Prospect of high voltage long distance compressed-air insulated transmission lines. *High Volt. Eng.* **35**(12), 3137–3142 (2009). (in Chinese)
3. Hillers, T.: Gas insulated transmission lines (GIL): ready for the real world. In: *Power Engineering Society Winter Meeting*, pp. 575–579. IEEE, Singapore (2000)
4. Koch, H.: *Gas Insulated Transmission Lines (GIL)*, pp. 33–38. Wiley-IEEE Press, Chichester (2012)
5. Benato, R., Mario, C.D., Koch, H.: High-capability applications of long gas-insulated lines in structures. *IEEE Trans. Power Deliv.* **22**(1), 619–626 (2007)
6. Memita, N., Suzuki, T., Itaka, K., et al.: Development and installation of 275 kV SF6 gas-insulated transmission line. *IEEE Trans. Power Appar. Syst.* **103**(4), 691–698 (1984)
7. Sabot, A.: Insulation go-ordination procedure for 420 kV gas insulated lines (GIL). In: *1999 Eleventh International Symposium on the High Voltage Engineering*, pp. 1–10. IET, London, UK (1999)
8. Koch, H., Schuette, A.: Gas insulated transmission lines for high power transmission over long distances. *Elect. Power Syst. Res.* **44**(1), 69–74 (1998)
9. Schaefer, M.T., Lamb, D.W., Bradbury, R.: A comparison of two ranging approaches in an active, optical plant canopy sensor. In: *Sensors Applications Symposium (SAS)*, pp. 253–257. IEEE, Queenstown, New Zealand (2014)
10. Nishibori, K., Nishibori, K.: Measurements of inclination angle and distance of curved mirror using LED light sources. In: *IECON 2012–38th Annual Conference on IEEE Industrial Electronics Society*, pp. 2601–2606. IEEE, Montreal, Canada (2012)
11. Jiao, C., Ding, D., Liu, W., He, L., Zhang, Z., Yu, M.: Construction of transient voltage UWB on-line monitoring system in UHV GIL based on capacitive voltage division. In: *2020 IEEE International Conference on High Voltage Engineering and Application (ICHVE)*, pp. 1–4 (2020)
12. Wang, Y., Ding, D., Zhu, L., Mo, W., Fan, W., Zhang, Z.: Fault accurate location method in UHV GIL based on transient voltage travelling wave. In: *2020 International Conference on Sensing, Measurement & Data Analytics in the era of Artificial Intelligence (ICSMD)*, pp. 170–173 (2020)
13. Mao, L., et al.: Research on Single-terminal Fault Location Method Based on CWT Cumulative Coefficient of Traveling Wave for GIL. In: *2021 IEEE International Conference on Energy Internet (ICEI)*, pp. 236–239 (2021)

Channel Path Simulation and Channel Loss Calculation of 5G Substation



Yifeng Li, Xingfa Liu, Bo Tang, Chenlin Cai, Longbin Zhang,
and Yushan Yao

Abstract Due to the complexity of the spatial layout of metal equipment in the substation, the traditional geometric modeling method cannot accurately calculate the 5G channel loss in the substation. Due to the short wavelength of the 5G signal, it can be seen as ray propagation. Therefore, this paper introduces the basic idea of ray tracing algorithm. Based on the geometric optics theory of ray propagation, the reflection point and diffraction point are determined by using the spatial geometric characteristics of signal reflection and diffraction, and the effective channel path of 5G signal in substation is traced. Then, the energy loss caused by the reflection and diffraction of the signal is calculated by the electromagnetic reflection theory and the consistent diffraction theory. Combined with the relationship between the free space loss and the electric field change of the 5G signal on the transceiver path, the solution method of the 5G channel loss in the substation is derived.

Keywords 5G channel · Ray tracing algorithm · Geometrical Optics Theory · Electromagnetic reflection · Free space loss

1 Introduction

Due to the high-speed propagation characteristics of 5G networks, wireless sensing devices in substations have begun to gradually adopt 5G technology. However, high-frequency 5G signals are easily affected by the placement of wireless sensing equipment in substations, resulting in a large amount of channel path loss. When the channel path loss value is greater than the receiving sensitivity of the wireless sensing

Y. Li · B. Tang · C. Cai · L. Zhang · Y. Yao
College of Electrical Engineering and New Energy China Three Gorges University Yichang,
Yichang, China

X. Liu (✉)
China Electric Power Reseinducedh Institute State Grid Corporation of China, Wuhan 430000,
China
e-mail: 2585437587@qq.com

© Beijing Paike Culture Commu. Co., Ltd. 2023
X. Dong et al. (eds.), *The proceedings of the 10th Frontier Academic Forum of Electrical Engineering (FAFEE2022)*, Lecture Notes in Electrical Engineering 1054,
https://doi.org/10.1007/978-981-99-3408-9_102

1149

device [1], the wireless sensing device will not be able to transmit the monitoring data of the substation operation, affecting the operation safety of the substation [2]. In order to find the optimal location of wireless sensing equipment, a calculation method suitable for 5G channel path loss in substations is urgently needed to provide guidance for the layout of wireless sensing equipment in substations.

Regarding the calculation of 5G channel path loss, the 3GPP38.901 protocol gives its formula [3]. However, this formula only considers the influence of communication distance and signal frequency on the channel path loss. In the context of practical applications, multiple factors such as the height of the receiving/transmitting antenna, obstacle density, and material will affect the channel loss, so the formula has a large error. [4]. For this reason, the literature [5] proposes a method of fitting and solving the channel path loss according to the field measured data, however, this method can only characterize the specific channel loss characteristics of a given scene and lacks universal applicability.

For this reason, considering that the propagation of 5G signals is very similar to light propagation, this paper applies the ray tracing algorithm to 5G in substations based on the geometric optics theory and consistent diffraction theory of ray propagation, combined with the complex layout of various metal power equipment in substations Signal path simulation, proposed a tracing algorithm suitable for the effective 5G channel path in the substation, and realized the solution of the 5G channel loss in the substation.

2 Ideas for Solving 5G Channel Loss in Substations

In order to accurately calculate the channel path loss of each point in the substation, it is necessary to determine the changes caused by each metal device in the substation to the direct, reflected and diffracted channel paths of the 5G signal.

The distribution of 5G channel paths in the substation is shown in Fig. 3. As can be seen from Fig. 3, when the 5G signal sent by the 5G antenna encounters the shielding of the metal equipment in the substation during the propagation process, multiple reflections or diffractions will occur on the surface or tip of each metal equipment until it is received by the wireless sensing device. Therefore, if each specific signal propagation path can be traced, the accurate solution of the 5G channel loss in the substation can be carried out (Fig. 1).

To this end, the basic idea of ray tracing algorithm can be used. Through the geometric relationship of signal reflection and diffraction, combined with the spatial layout of each metal equipment in the power station and the position of the 5G signal transceiver, the reflection point and diffraction on the metal equipment can be determined in turn. The specific signal propagation path can be obtained by connecting each reflection point and diffraction point. On this basis, through the coupling relationship between the field strength amplitude and the channel loss, the field strength generated on each channel path traced by the vector superposition can be used to calculate the 5G channel loss at any point in the substation.

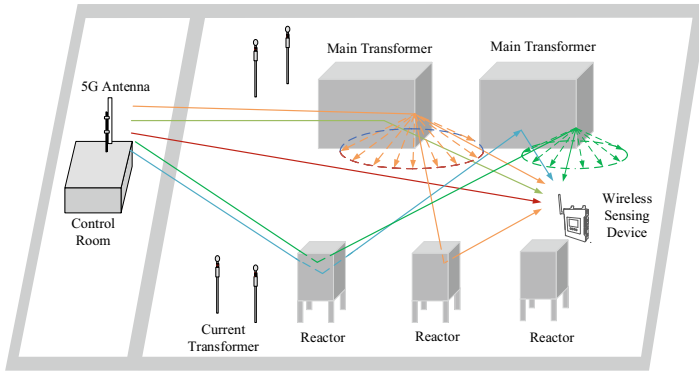


Fig. 1 Schematic diagram of the distribution of 5G channel paths in the substation

3 Calculation of 5G Channel Loss in Substation

3.1 Tracing of 5G Channels in Substations

Although the overall distribution of 5G channels in a substation is relatively complex, for any point in space, since the point where the 5G signal originates has been determined, the total number of channels experienced by the 5G signal when it reaches this point must be limited. Considering that the energy of the 5G signal propagated through the third reflection path or the second diffraction path is weak, it is an invalid channel, so this paper only considers the direct path, the first reflection path, the first diffraction path, the first reflection diffraction path, the first Diffraction reflection path, secondary reflection path for tracing.

After determining the effective channel type for tracing, it is necessary to conduct an intersection test on all metal walls and edge lines existing between the signal sending and receiving points to determine whether the channel is valid. Because the direct radiation path and the primary reflection path can be regarded as special cases among the other channel types, they are relatively simple. Therefore, only the secondary reflection path, the primary reflection diffraction path, and the primary diffraction reflection path are analyzed.

First, a schematic diagram of a 5G signal being received by a wireless sensing device through the secondary reflection path is shown in Fig. 2. The Cartesian space coordinate system is established with the launch point as the origin, and the space coordinate information of all equipment in the substation space is known. It is possible to set the point coordinates on the outer surface (excluding edges) of all metal equipment in the substation to form a set A. The point coordinates on any surface of the device constitute a subset of the set A, then:

$$A = \{A_1, A_2, A_3 \cdots \cdots A_n\} \tag{1}$$

Fig. 2 Anti-diffraction tracing diagram of 5G channel 2 in the substation

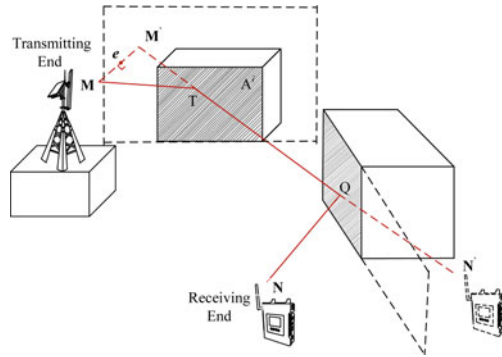
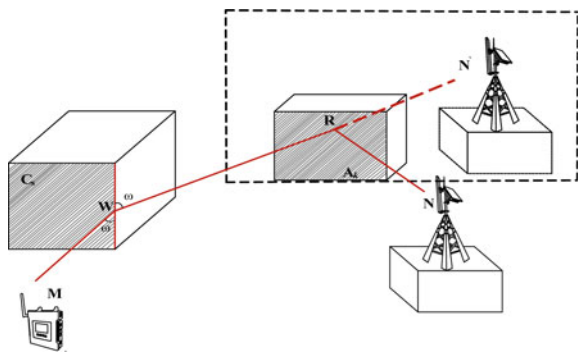


Fig. 3 Schematic diagram of primary diffraction and primary emission



Among them, n is the total number of planes of metal equipment in the substation.

The coordinates of the 5G signal transmitting point and receiving point are set to $M(x_1, y_1, z_1)$ and $N(x_2, y_2, z_2)$ in turn. take any two subset faces A_i and A_j of set A ($1 \leq i, j \leq n, i \neq j$), the mirror point of M about A_i plane is denoted as $M'(x'_1, y'_2, z'_3)$, The mirror point of N on the A_j plane is denoted as $N'(x'_2, y'_2, z'_3)$, All point coordinates on line segment $M'N'$ form set B . When line segment $M'N'$ has intersections $T(k_1, k_2, k_3)$ and $Q(t_1, t_2, t_3)$ with two planes A_i and A_j , It can be determined that the secondary reflection path exists. At the same time, in order to ensure that the signal is not blocked by the rest of the equipment in the substation when it is reflected on the two planes where A_i and A_j are located, line segment $M'N'$ should not intersect the other planes. So the mathematical expression for the intersection test is:

$$\begin{cases} B \cap A_i = T, B \cap A_j = Q \\ B \cap \text{CuP}\{A_i, A_j\} = \emptyset \end{cases} \quad (2)$$

After the reflective surface is determined, a vertical line is drawn to the A_i plane through the M point, and the coordinates of the vertical point can be obtained by combining the space analytical equation of the vertical line and the A_i plane. Then,

according to the characteristics of the line segment $M'N'$ in the vertical point e, the coordinates of M' can be obtained indirectly. In this way, let the equation of the reflection plane A_i be $ax + by + cz + d = 0$, then the solution formula of the coordinates of the mirror point M' is:

$$\begin{cases} ak_1 + bk_2 + ck_3 + d = 0 \\ \frac{1}{a'}(k_1 - x_1) = \frac{1}{b'}(k_2 - y_1) = \frac{1}{c'}(k_3 - z_1) \\ x' = 2k_1 - x_1, y' = 2k_2 - y_1, z' = 2k_3 - z_1 \end{cases} \quad (3)$$

According to this method, the coordinates of mirror point $N'(x'_2, y'_2, z'_3)$ can be determined in the same way. Then write two-point equations for the two mirror points, and solve them simultaneously with the equations of the two reflecting surfaces to obtain the intersection coordinates $T(k_1, k_2, k_3)$ and $Q(t_1, t_2, t_3)$. Therefore, according to the principle of mirror symmetry, the solution of the length of the secondary reflection radius can be simplified to the solution of the distance between the two mirror points. Then in the triangle with the receiving/transmitting point and the mirror point as vertices, the incident angle and the reflection angle can be obtained by using the law of cosines. In this way, the spatial information of the secondary reflection path is completely determined.

Secondly, the schematic diagram of the 5G signal propagating through the primary reflection diffraction path and being received by the wireless sensing device is shown in Fig. 3. At this time, it may be assumed that the points on the line segment where the edges of all metal equipment in the substation form a set C, and the points on any edge form a subset of the set C, then:

$$C = \{C_1, C_2, C_3 \cdots \cdots C_m\} \quad (4)$$

Among them, m is the total number of edges that the metal equipment in the substation has.

Take a subset $A_k (1 \leq k \leq n)$ of set A and a subset $C_s (1 \leq s \leq n)$ of set C arbitrarily, as the mirror point $N'(x'_2, y'_2, z'_3)$ of the signal receiving point $N(x_2, y_2, z_2)$ about the plane A_k , and at the same time take the set C_s . The coordinates of the two end points are $F(x_3, y_3, z_3)$ and $E(x_4, y_4, z_4)$, and it is assumed that there is a diffraction point $W(x_5, y_5, z_5)$ on the set C_s . According to Koller's principle, the angles δ and ω between the diffracted ray and the incident ray and the edge where the diffraction point is located are equal:

$$\frac{\vec{WE} \cdot \vec{WN'}}{|\vec{WE}||\vec{WN'}|} = \frac{\vec{WM} \cdot \vec{WF}}{|\vec{WM}||\vec{WF}|} \quad (5)$$

In order to ensure that the signal can be diffracted and reflected successively on edge C_s and plane A_k without being obstructed by other equipment in the substation, the combination D of the point where line segment PN' is located only has common elements with set C_s and set A_k respectively:

After determining the coordinates of the diffraction point $W(x_5, y_5, z_5)$, the intersection of the line segment WN' and the reflection surface A_k can be obtained to obtain the coordinate value of the reflection point $R(x_6, y_6, z_6)$. Finally, according to the spatial coordinates of the receiving/transmitting point and the reflection point, and using the mirror relationship and the cosine theorem in the same way, the spatial parameters such as the channel length and the inverse/diffraction angle can be obtained. The solution process of the first-order diffraction reflection path is similar to this, so it is not repeated here.

3.2 Calculation of 5G Channel Loss in Substations

After determining the 5G channel path in the substation, based on the free space loss, combined with the electromagnetic reflection theory and the consistent diffraction theory to determine the loss of the signal when the signal propagates through reflection and diffraction, the loss at any point in the substation can be calculated. 5G channel loss situation.

When the transmitting power of the 5G signal in the substation is PF and the receiving power is PS, the path loss calculation formula of the channel is:

$$P_{LS} = 10 \lg \frac{P_F}{P_S} \quad (6)$$

According to the Friis transmission theorem, when the wireless signal propagates in a straight line within the line-of-sight range, the signal power received by the receiving antenna is:

$$P_S = P_F G_S G_F \left(\frac{\lambda}{4\pi d} \right)^2 \quad (7)$$

In the formula: G_F and G_S are the gains of the transmitting antenna and the receiving antenna respectively; d is the distance between the signal sending and receiving points; λ is the signal wavelength, and the free space loss can be obtained by substituting formula (7) into formula (6).

For the calculation of the loss on the reflection and diffraction paths, since the power is proportional to the square of the field strength, the calculation formula of the channel path loss can be converted into:

$$P_{LS} = 20 \lg \left| \frac{E_F}{E_S} \right| \quad (8)$$

In the formula, E_F is the field strength of the transmitting point, and E_S is the field strength of the receiving point. Therefore, the corresponding power loss can be

obtained indirectly according to the change of the field strength after the signal propagates through the reflection path and the diffraction path. In this way, the problem is transformed into solving the magnitude of the combined field strength E_F at the receiving point.

After determining the relationship between the field strength generated by the reflected signal and the diffracted signal and the direct field strength, the total field strength E_S at any point in the substation can be obtained:

$$E_s = E_0 + \sum_{i=1}^{T-1} \left(F_{d1}^{k1} F_{d2}^{k2} V_d^{k3} E_0 \frac{L_Z}{L_d} \exp(-j \Delta \omega_i) \right) \tag{9}$$

Since the field strength is proportional to the square of the power, the path loss of the 5G signal in the final substation can be determined according to the ratio of the transmit and receive power when propagating in a straight line in free space:

If the transmitting and receiving antennas of the signals in the 5G substation are regarded as the same ideal antenna, the above formula can be simplified as:

$$P_{LS} = 10 \lg \left(\left(\frac{4\pi d}{\lambda} \right)^2 \times \frac{1}{G_S G_F} \times \left| \frac{E_s}{E_0} \right|^2 \right) \tag{10}$$

According to the above calculation method of the 5G channel loss in the substation based on the ray tracing algorithm, the channel path loss value at any point in the substation space can be obtained.

4 Conclusion

In conclusion, it is proposed to use the ray tracing algorithm to solve the 5G channel loss in the substation and make up for the shortcomings of the previous algorithm. This paper is based on the basic idea of ray tracing algorithm for studying light propagation, and based on geometric optics theory, using the spatial geometric characteristics of signal reflection and diffraction to trace the effective channel path of 5G signal in the substation, by calculating the 5G signal in the substation The free space loss in the transceiver path and the energy loss in reflection and diffraction can solve the 5G channel loss in the substation with dense metal equipment.

Acknowledgements This work was supported by the Project supported by Science & technology project of SGCC (5217L021000X).

References

1. Qiu, Y., Wu, L., Chen, J., Bian, Q., Jin, S.: Research on relay protection based on 5G communication technology. *Power System Protection and Control* **49**(07), 31–38 (2021). (in Chinese)
2. Chen, H., Xu, S., Li, Z., Jin, Z., Wan, X.: A new fast comprehensive protection scheme of an active distribution network considering the abnormal operating conditions of 5G communication. *Power Syst. Protect. Control* **49**(15), 159–168 (2021). (in Chinese)
3. Huang, Y., Li, B., He, Y.: Channel analysis of wireless monitoring system in digital substation. *Transducer Microsyst. Technol.* **38**(06), 42–45 (2019). (in Chinese)
4. He, Y., Xu, Y.: Modeling and analysis of vehicle communication channels in geometrical scattering environment. *J. Electron. Measure. Instrum.* **32**(09), 80–87 (2018). (in Chinese)
5. Guo, M.: Geometry-based stochastic model for three-dimensional UAV channel. *Appl. Res. Comput.* **38**(12), 1001–3695 (2021). (in Chinese)
6. Wei, T., Wang, W., Chen, J., Wang, W., Feng, W.: Environmental information-aided maritwireless channel measurement and modelling. *J. Tsinghua Univ. (Sci. Technol.)* **61**(09), 1002–1007(2021). (in Chinese)
7. Dai, T., Zhao, Y., Zhang, J., Zhang, X.: Signal propagation characteristics of wireless sensor networks in forestry environmental monitoring. *J. Fujian Agric. Forestry Univ. (Nat. Sci. Edn.)* **49**(02), 199–205 (2020). (in Chinese)
8. Liu, L., Zhang, J., Fan, Y., Fan, Y., Yu, L., Zhang, J.: *J. Commun.* **42**(02), 134–153 (2021). (in Chinese)
9. Yee, C.F., Isa, M.M., Al-Hadi, A.A., et al.: Techniques of impedance matching for minimal PCB channel loss at 40 GBPS signal transmission. *Circuit World* **45**(03), 132–140 (2019)
10. Riviello, D.G., Di Stasio, F., Tuninato, R.: Performance analysis of multi-user MIMO schemes under realistic 3GPP 3-D channel model for 5G mmWave cellular networks. *Electronics* **11**(03), 130–130 (2022)
11. Liao, S.-K., Yong, H.-L., Liu, C., et al.: Long-distance free-space quantum key distribution in daylight towards inter-satellite communication. *Nat. Photonics* **11**(08), 509–513 (2017)
12. Pokhrel, S.R., Panda, M., Vu, H.L., et al.: TCP performance over Wi-Fi: joint impact of buffer and channel losses. *IEEE Trans. Mob. Comput.* **15**(05), 1279–1291 (2016)

5G Antenna Distribution in Substations Considering Electromagnetic Interference Factors



Xingfa Liu, Bo Tang, Can Zhang, Daokun Qi, Yushan Yao, and Yifeng Li

Abstract In order to reduce the electromagnetic interference caused by the introduction of the 5G base station antenna into the substation to the sensitive equipment in the station, and to optimize the 5G signal at each monitoring device in the station, a method for 5G base station antenna placement in the substation based on the multi-objective particle swarm algorithm is proposed, namely, The radio frequency field strength at the sensitive equipment of the substation cannot exceed the specified electromagnetic compatibility immunity limit as the constraint condition, and the Pareto optimal solution of the signal received by the monitoring equipment in the station is used as the objective function. Find the most suitable base station antenna layout. Taking the 500 kV Guandu substation as an example, according to its actual internal space layout, four antenna layout installation schemes are obtained by using the algorithm in this paper, which can make the radio frequency field strength at all sensitive equipment in the station lower than the 10 V/m immunity limit, and at the same time It can also increase the average signal of each monitoring equipment in the station by 3.77, 6.37, 4.34 and 4.58 dB respectively, and the variance of the monitoring equipment signal is reduced by 15.07, 12.64, 14.62 and 14.78% respectively. It can improve the signal strength at the monitoring equipment to a certain extent, and can also reduce the dispersion of the signals at the monitoring equipment in the station,

X. Liu

State Grid Electric Power Research Institute, Wuhan 430074, China
e-mail: liuxingfa@epri.sgcc.com.cn

B. Tang · C. Zhang · Y. Yao (✉) · Y. Li

College of Electronic Engineering and New Energy, Three Gorges University, Hubei 443002, Yichang, China
e-mail: 1663681954@qq.com

B. Tang

e-mail: tangboemail@sina.com

D. Qi

State Grid Henan Eco-nomic Research Institute, Zhengzhou 450052, China

B. Tang

Hubei Provincial Engineering Technology Research Center for Power Transmission Line, Hu-bei 443002, Yichang, China

© Beijing Paike Culture Commu. Co., Ltd. 2023

X. Dong et al. (eds.), *The proceedings of the 10th Frontier Academic Forum of Electrical Engineering (FAFEE2022)*, Lecture Notes in Electrical Engineering 1054, https://doi.org/10.1007/978-981-99-3408-9_103

1157

so that the signal coverage at the monitoring equipment is more stable, which can be used for the actual project. 5G base station antenna layout in substations Provide some reference.

Keywords Multi-objective optimization · Particle swarm optimization · Pareto optimal solution · Electromagnetic compatibility

1 Introduction

In order to improve the transmission rate of monitoring data in substations, some domestic substations have started to adopt 5G communication technology [1]. Compared with traditional 3G or 4G base station antennas, 5G base station antenna adopts large-scale MIMO (multi-in and multi-out system) technology, with greater transmitting power, more concentrated beam, and more intense electromagnetic radiation of [2]. This for the electromagnetic environment is already complex substation, has undoubtedly added a new high frequency strong electromagnetic field source. In this case, if the 5G base station antenna is not properly arranged properly, it will bring serious electromagnetic compatibility problems to the substation.

The existing literature generally uses multi-objective particle swarm optimization (MOPSO) algorithm by constructing corresponding constraints and objective functions, and genetic algorithm (GA) [7-12]. For example, [7] used GA to calculate the layout of vehicle radar antenna, and literature [8] studied the layout of ground monitoring antenna using the improved NSGAN-algorithm. According to the literature [9], it used MOPSO algorithm to study the antenna layout of the upper ship, and achieved good layout results. Considering that the metal environment of the upper layer of the ship is basically similar to the internal metal environment of the substation. Therefore, the optimal layout location of the 5G base station antenna in the substation can also be calculated according to this method.

This paper takes the Pareto optimal solution of signals received by in-station monitoring equipment, and points points the 5G base station antenna in the substation based on MOPSO algorithm, which provides some reference for the subsequent study of substation base station antenna distribution problem.

2 Layout Requirements of 5G Base Station Antennas in Substations

At According to the conclusions of the existing research on the electromagnetic environment of the substation [14], the space of the electrical equipment of the substation can be roughly divided into three areas of the strong electromagnetic environment, the protected area and the outside of the substation as shown in Fig. 1.

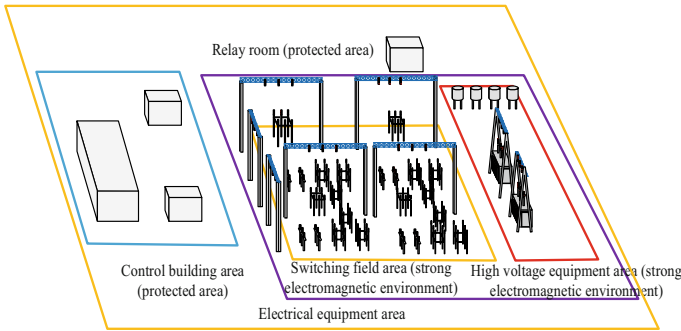


Fig. 1 Regional division of the electromagnetic environment of the substation

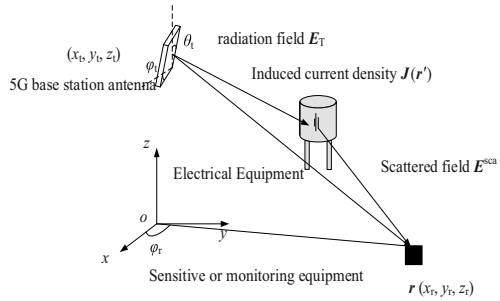
For the 5G base station antenna, the protected area of the substation is the internal working area such as the control building and the relay room in the station. The sensitive equipment in this area has usually taken special shielding measures, plus wall blocking. Therefore, the 5G signal that the region may suffer is very weak. For the electrical equipment area of the substation, because the area is directly exposed to the radiation of the base station antenna and the lack of corresponding shielding measures for high-frequency radiofrequency radiation, the sensitive equipment here is extremely vulnerable to interference by 5G high-frequency electromagnetic waves. Therefore, when the 5G base station antenna is planted in the substation, it is necessary to mainly consider the RF radiation resistance of sensitive equipment in the electrical equipment area.

3 Substation 5G Base Station Antenna Layout

3.1 Mathematical Model Derivation of Field Strength of 5G Base Station Antenna

When the base station antenna is deployed, the 5G radio frequency signal or electric field received by sensitive equipment and monitoring equipment in the electrical equipment area of the substation is divided into two parts, one from the direct radiation of the 5G base station antenna, and the other from the scattering of the nearby metal equipment on the radiation field of the 5G base station antenna, as shown in Fig. 2. Among them, (x_t, y_t, z_t) is the point position of the 5G base station antenna in the layout area, xoy is the three-dimensional right-angle coordinate system in the substation space, θ_t and φ_t are the pitch angle of the 5G base station antenna and the angle between the reflector plate and the x-axis respectively, and $r(x_r, y_r, z_r)$ is the sensitive settings in the substation.

Fig. 2 Schematic diagram of 5G signal radiation exposure of sensitive equipment or monitoring equipment in substation



Prepare or monitor the location of the equipment. The radiation field $E_{T(r)}$ of the 5G base station antenna affected by monitoring equipment and sensitive equipment can be calculated by the following formula:

$$E_T(r) = C \frac{e^{-jkr}}{R} \sum_{m=0}^{N_x-1} \sum_{n=0}^{N_y-1} I_{mn} e^{jk(md_x \cos \theta + nd_y \sin \theta) \sin(\phi_r - \phi_t)} \tag{1}$$

In the formula, k is the number of electromagnetic wave waves emitted by the 5G base station antenna; R is the distance from the base station antenna to sensitive equipment or monitoring equipment, C is the antenna unit factor; I_{mn} is the excitation current of the m -line and n th column oscillators in the array antenna; d_x and d_y are the row and column spacing between array antenna oscillators respectively; $N_x N_y$ is the total number of rows and arrays of 5G base station antennas respectively; ϕ_r is the angle of the connection and x -axis of sensitive equipment or monitoring equipment and coordinate origins.

For the scattering field $E_{sca(r)}$ of sensitive equipment and monitoring equipment in the station, the electric field integral equation can be calculated, that is:

$$E^{sca}(r) = j\omega\mu \int_S G(r, r') J(r') dS' - \frac{1}{j\omega\epsilon} \nabla \int_S G(r, r') \nabla J(r') dS' \tag{2}$$

In the equation, $J(r)$ is the induction current on the surface of the nearby metal device, ω is the incident wave angular frequency, μ is the permeability, ϵ is the dielectric constant, S is the surface integral domain of the metal device, and $G(r; r')$ is the Green function.

This paper uses the large element-physics optic (LE-PO) method to adopt the large-scale element physical optics three. The angular basis function $A_{n(r)}$ discretises the sensing current on the surface of the scatterer:

$$J(r) = \sum_{n=1}^N \gamma_n \Lambda_n(r) \tag{3}$$

In the equation: γ_n is an unknown coefficient.

After substitution (6) into the formula (5), according to the triangular product method, the scattering field size of the monitoring equipment or sensitive equipment at the substation r can be solved. Then the total radio frequency electric field of the sensitive equipment or monitoring equipment at the r is:

$$E(r) = E^{sca}(r) + E^{inc}(r) \tag{4}$$

During the deployment of the base station antenna, the RF electric field $E_{(r)}$ of the equipment terminal and monitoring equipment at the known point r is actually a function about the distance from the base station antenna to the equipment terminal, the antenna elevation angle θ , and the angle between the reflector plate and the x-axis. From the perspective of the base station antenna, the function $E(x_t, y_t, z_t, \theta_t, \phi_t)$ can also be used to represent the field strength of sensitive equipment during the antenna layout.

According to the analysis of Sect. 2.1, if the radio frequency anti-disturbance of the substation is 10 V/m stipulated in the national standard, as the RF field strength limit at the sensitive equipment in the substation when the antenna is routed, there are constraints:

$$s.t. E_i(x_t, y_t, z_t, \theta_t, \phi_t) \leq 10 \tag{5}$$

In the formula: P_j is the signal strength in dBm at the $j(j = 1, 2, \dots, J)$ monitoring equipment in the substation, which satisfies:

$$P_j = E_j + G - AF - 107 - K \tag{6}$$

In the formula: E_j is the strong and small radio frequency field at the monitoring equipment $j(j = 1, 2, \dots, J)$ in the substation, in $\text{dB}\mu\text{V/m}$; G is the antenna gain in dBi; AF is the antenna coefficient in dB/m; K is the bandwidth factor in dB.

3.2 Selection of 5G Base Station Antenna Optimization Layout Under MOPSO Algorithm

This paper introduces the Pareto optimal solution concept as the 5G base station antenna layout optimization judgment index, and make $A = (x_t, y_t, z_t, \theta_t, \phi_t)$ to define the Pareto solver, 5G base station antenna layout point:

Definition 1. Pareto Domination: Assuming that A_1 and A_2 are two sets of feasible solutions during the deployment of the 5G base station antenna in the substation, A_1 disposable A_2 is called A_2 , if A_1 and A_2 meet the following relationships:

$$\begin{cases} P_i(A_1) \geq P_i(A_2), \forall i \in 1, 2, \dots, I \\ P_i(A_1) > P_i(A_2), \forall i \in 1, 2, \dots, I \end{cases} \quad (7)$$

Definition 2. Pareto non-dominant solution: Assume that A is a set of feasible solutions during the deployment of the 5G base station antenna of substations, and there is no other de-dominance A .

Definition 3. Pareto optimal solution set: a set of all Pareto non-dominant solutions.

Then, the defined Pareto optimal solution concept is introduced into the MOPSO algorithm, using the idea of the best of the best, using the Pareto optimal solution set to guide particle groups to the overall optimal solution set, and then select the optimal solution from the optimal solution set, this paper using MOPSO algorithm for substation 5G base station antenna layout selection flow diagram, as shown in Fig. 4.

4 Application of the Algorithm

4.1 Instance Application

Taking the ground in the southwest location of Henan 500 kV Guandu Substation as an example, According to the specific situation within the station, the MOPSO algorithm is used to redistribute the 5G base station antenna in the station area 1,2,3 and 4. The 5G base station antenna layout height is set between 8 and 15 m, the base station antenna inclination θ_t is between 0° and 45° , the reflection plate and the x-axis clip angle φ_t is between 0° and 360° , and the algorithm has 200 iterations. The overall convergence of the 5G base station antenna is shown in Fig. 4.

As can be seen from Fig. 3, under the deployment scheme of the four 5G base station antennas, the electromagnetic radiation exposure of sensitive equipment can be reduced to the specified 10 V/m anti-disturbance limit.

As can be seen from Table 1, the layout scheme calculated in this paper is 3.77, 6.37, 4.34, 4.58 dB, and the variance of the monitoring equipment under the four methods is higher than the original layout point in the station. It decreased by 15.7, 12.64, 14.62 and 14.78% respectively. This shows that using the Pareto optimal solution of the signal received by the monitoring equipment in the station as the objective function, it can not only improve the signal strength at the monitoring equipment to a certain extent, but also reduce the discreteness of the signal at the monitoring equipment in the station, making the signal coverage more stable at the monitoring equipment.

Fig. 3 Flowchart of this substation 5G base station antenna layout selection flowchart

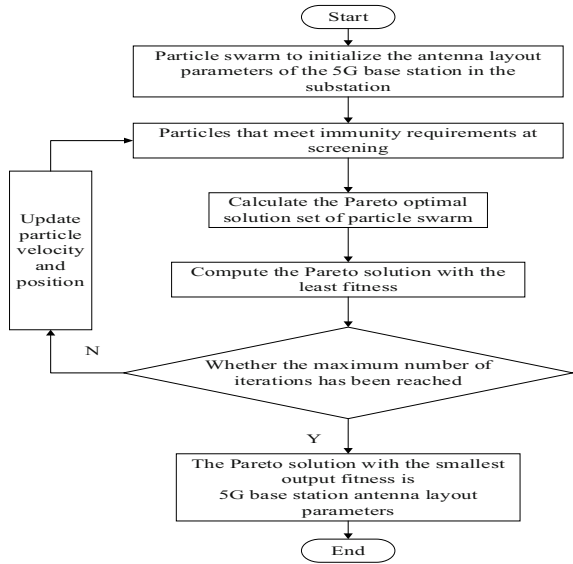
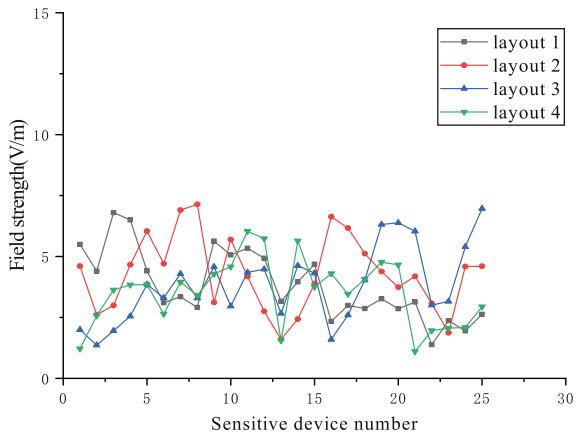


Fig. 4 In this paper, the radio frequency field is strong at the various sensitive equipment



5 Conclusion

In this paper, the MOPSO algorithm is used to carry out 5G base station antenna layout at Henan 500 kV Guandu Substation. The results show that this method can meet the RF anti-disturbance requirements of sensitive equipment in the station and ensure the signal stability of the monitoring equipment. Therefore, it can provide a certain 5G base station antenna layout reference for engineers in the station.

Table 1. The signal (dBm) size of the monitoring equipment under the layout scheme in this paper

layout number	1	2	3	4	original layout
1	-47.17	-59.92	-58.64	-51.33	-46.87
2	-53.21	-53.22	-56.42	-49.35	-57.29
3	-54.32	-48.37	-56.17	-53.67	-53.77
4	-57.11	-53.85	-55.23	-50.89	-59.93
5	-56.82	-47.61	-58.48	-55.17	-60.11
6	-57.73	-54.25	-55.94	-54.42	-60.22
Average signal size	-55.14	-52.54	-54.57	-54.33	-58.91
Signal variance	9.54	11.97	9.99	9.83	24.61

In the actual project, it is also necessary for the construction personnel to choose the layout area of the 5G base station antenna according to the layout of the internal equipment, buildings, etc. of the substation, so that the algorithm can be used to get a better layout solution.

Acknowledgements This work was supported by the Project Science & technology project of SGCC (5217L021000X).

References

1. Mulin, X.S.: Research and application of intelligent inspection technology of substation electrical equipment based on 5G. *Power Inf. Commun. Technol.* **19**(12), 109–116 (2021). (In Chinese)
2. Germany technology and the china academy of information and communications technology (CAICT) have joined hands to accelerate the 5G base station performance test organized by the IMT-2020 (5G) Promotion Group. *J. Electron. Measure. Instrum.* **34**(01), 200 (2020). (In Chinese)
3. Wang, Z., Hu, Y., Meng, S., et al.: Research on location selection method of 5G base station in substation considering radiation disturbance and conduction disturbance. In: 2022 International Conference on Computer Communication and Informatics (ICCCI), pp. 1–8 (2022)
4. Li F., Tang, B., Qi, D., Liu, X., Kuang, Y., Xie, H.: Electromagnetic interference of 5G base station antennas on secondary equipment in substations. *Southern Power Grid Technol.* **15**(10), 111–117 (2021). (In Chinese)
5. National electromagnetic compatibility standardization technical committee. GB/Z 17799.6-2017, General Standard for Electromagnetic Compatibility, Disturbance Resistance in Power Plant and Substation Environments. Beijing: China Standard Publishing House (2016). (In Chinese)
6. Ma Haijie, A.: Electromagnetic Harassment Analysis of Power Communication Equipment in Substation. China Electric Power Publishing House, Beijing (2015). (In Chinese)
7. Le, Z., Wei, W., Xuetian, W.: Optimization method of vehicle-mounted radar antenna array layout based on genetic algorithm. *Microw. J.* **34**(S1), 155–158 (2018). (In Chinese)

8. Du Wenzhan, Y., Zhiyong, Y., Haibin, J.: Research on improving the NSGA-II algorithm and monitoring antenna deployment optimization. *J. Xi'an Univ. Electron. Sci. Technol.* **48**(05), 239–248 (2021). (In Chinese)
9. Qilong, Z., Shaochang, C.: Application of multi-objective optimization algorithm in ship antenna layout. *Ship Sci. Technol.* **36**(09), 132–135 (2014). (In Chinese)
10. Yongbin, Z.S., Li, D., Shi, Y., Jiang, W.: The optimal particle initial value estimation method based on array Taylor weight. *Electron. Measure. Technol.* **44**(06), 70–75 (2021). (In Chinese)
11. Jinwen, S., Xingang, Z., Zhengxin, S., Ying, Z.: Optimization design of high performance assignment antenna based on genetic algorithm. *Microw. J.* **35**(03), 16–19 (2019). (In Chinese)
12. Qianli, F.: CFC-PSO optimization of aeroengine pipeline layout considering L-shaped bracket clamp constraints. *Foreign Electron. Measure. Technol.* **40**(03), 130–136 (2021). (In Chinese)
13. Amber. Study on electromagnetic compatibility of wireless sensors in substations. North China Electric Power University (Beijing) (2017). (In Chinese)
14. National Electromagnetic Compatibility Standardization Technical Committee. GBZ 17799.6-2017 Electromagnetic Compatibility General Standard Disturbance Resistance in Power Plant and Substation Environment. China Standard Publishing House, Beijing (2017). (In Chinese)

A New Distributed Intelligent Distribution Ring Main Unit Based on System on Chip Design



Jiawen Chen, Chao Cai, Yang Lei, Gaohai Wang, Changsheng Sun, and Si Yang

Abstract In order to solve the problems such as insufficient perception ability of distribution equipment, low level of intelligence, and difficulty in accessing distribution automation system, this paper proposes a new distributed intelligent distribution ring network cabinet based on system on chip design. This equipment adopts distributed DTU design mode to make primary and secondary equipment deeply integrated, improve the equipment structure and improve its reliability; At the same time, the automatic mapping system of single line diagram of distribution network is used to reduce the pressure of data processing and calculation of the entire network of the original mapping system, and improve the mapping efficiency of the system; In addition, the self-describing model of distributed distribution terminals is established based on IEC61850 standard, which realizes plug and play of distributed distribution terminals and improves the intelligence and reliability of the ring network cabinet; Finally, a highly reliable intelligent sensing monitoring system for power distribution equipment integrating temperature and partial discharge is adopted to improve its fault detection capability.

Keywords Distribution ring network cabinet · System-on-Chip · Graph-auto-making Program · Self-describing model · Plug-and-play

J. Chen (✉) · C. Cai
State Grid Hubei Electric Power Co., Ltd., Wuhan 430077, China
e-mail: 6052079@qq.com

Y. Lei
Electric Power Research Institute, State Grid Hubei Electric Power Co., Ltd., Wuhan 430077, China

G. Wang · C. Sun · S. Yang
Dong Fang Electronics Co., Ltd., Yantai 264000, China

© Beijing Paiké Culture Commu. Co., Ltd. 2023
X. Dong et al. (eds.), *The proceedings of the 10th Frontier Academic Forum of Electrical Engineering (FAFEE2022)*, Lecture Notes in Electrical Engineering 1054, https://doi.org/10.1007/978-981-99-3408-9_104

1 Introduction

With the development of smart grid, new requirements are put forward for the reliability of distribution equipment and on-line monitoring perception and interconnection of equipment status. In the power distribution equipment, the distribution ring cage plays an important role in the power distribution and power supply for the users in the whole power system [1–4]. At present, SF₆ ring network cabinets are mainly used in China, and solid insulation ring network cabinets have been gradually used. At present, there are many problems in ring network cabinets, such as low level of automation and informatization, low stability of equipment operation, and poor environment for equipment replacement and maintenance.

Distribution Terminal Unit (DTU) is one of the most important units in the distribution ring network cabinet. Its function, technology and reliability directly affect the stability of distribution and power supply [5, 6]. To solve many defects in the traditional ring network cabinet, it is necessary to simplify the structure between its internal modules, therefore, it is particularly important to conduct in-depth research on the distribution terminal [7–9]. The traditional distribution terminal needs to manually configure the point table, which greatly increases the cost and difficulty of the operation and maintenance of the distribution network, the internal functional components of the distribution terminal are too complicated, and some functions are repeated with the functions of other units in the ring network cabinet, and the cooperation between the functional modules is not optimized.

In recent years, in order to reduce the cost of distribution terminal configuration and maintenance, and further make the ring main unit more intelligent and reliable, it is very important to realize the information self-description and plug and play function of distributed DTU to meet the above functions [10, 11]. Relevant research has proposed a holographic perception intelligent fusion ring network cabinet, which has holographic perception and edge computing capabilities, and can meet the plug and play, topology automatic analysis and upload functions of different terminals [12–14]. The ring network cabinet adopts distributed DTU, which is different from the traditional centralized DTU, the distributed DTU is composed of a common unit and several bay units. Reference [15] proposed the information interaction mechanism of distributed generation in distribution network based on IEC61850 standard, which improved the effectiveness of grid-connected operation of distributed generation but did not give the method of establishing a perfect distribution terminal model. At present, there are few studies on distributed DTU self-description and plug-and-play technology.

In order to improve the reliability and information degree of the ring network cabinet, the comprehensive perception and intelligent application of the ring network cabinet equipment status are realized, in this paper, a new type of distributed intelligent distribution ring network cabinet based on System-on-Chip (SoC) design is proposed, it supports protection control, measurement, state acquisition and other functions, it has a variety of communication modes, and can form a set of integrated intelligent switch cabinet with various switch cabinets in the existing ring

network cabinet, it has the characteristics of intelligence, miniaturization, integration, multi-function and various communication modes.

2 Key Technologies Research

To cope with the high reliability of the complete set of ring network cabinets, we adopted the principle of redesign, adopted the principle of distributed station terminals, and re-studied the distributed intelligent distribution terminals based on the idea of chip system.

2.1 *Intelligent Power Distribution Terminal Based on System on Chip (SoC)*

The intelligent ring network cabinet based on the chip system includes two parts: the interval unit and the common unit. The interval unit is responsible for the remote measurement acquisition and remote signal data acquisition of the interval switch, and realizes the state monitoring, fault judgment and intelligent distributed function of the switch of the interval module; the public unit is responsible for the three remote data collection of all the interval units in the intelligent ring network cabinet, the collection unit data of various intelligent sensors in the intelligent ring network cabinet, the data interaction with the master station and the remote control command of the master station to each interval unit.

The common unit is realized by the main control board + interface board. The main control board of the common unit completes the function realization of the main processing network port, SPI, IIC, UART and other resources, the assembly diagram is shown in Fig. 1 (a). The design of the spacer unit is realized by liquid crystal board, main control board and interface board. LCD panel to complete the LCD display and buttons, the main control board completes sampling, network port, SPI, I2C, remote control output and other functions. Figure 1 (b) is the assembly diagram.

2.2 *Automatic Mapping Method of Single Line Diagram of Distribution Network*

In this paper, a single-line diagram automatic mapping system of distribution network is proposed, which generates the segmented line equipment information and topology relationship information of distribution network at the source end through distributed thinking, and actively triggers the automatic update of the whole network topology

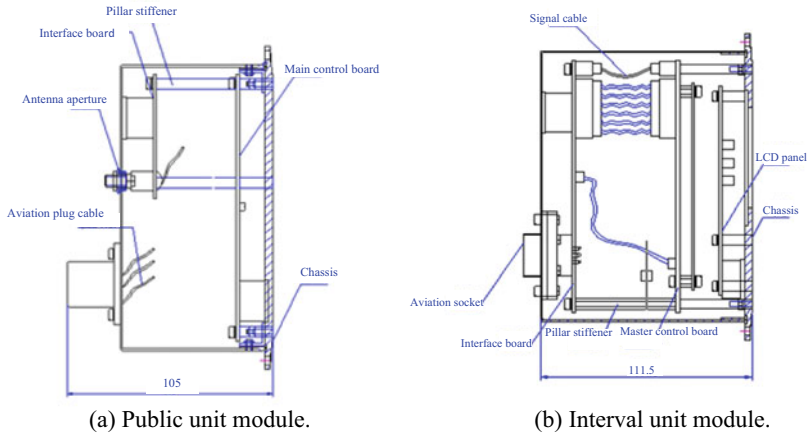


Fig. 1 Assembly diagram of intelligent ring-network cabinet

graph. The system consists of a plurality of distribution terminals distributed on each section of the distribution network line as acquisition components and a distribution network model processing center deployed on the side of the distribution network master station.

Figure 2 is the logic diagram of the graph model management and analysis module, in which the distribution terminal is used to store the topology model files of each line in a distributed manner. The distribution master station system module is used to obtain and save the topology model files of each line. The model conversion module is used to generate the model file sent by multiple terminals according to the line. The graph-mode conversion module is used to convert the line topology model into a single line diagram of the distribution network.

The distribution network diagram and model processing centre automatically generates the incoming and outgoing line interval of the ring-network cabinet according to the interval number by acquiring the equipment information and topology relationship of the components collected by the distribution terminal, analysis the equipment information to obtain the physical parameters of the equipment, analysis the topology relationship to obtain the electrical connection relationship of

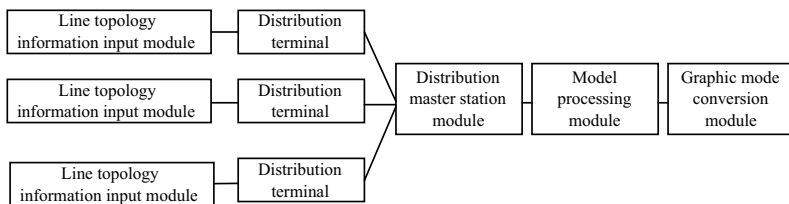


Fig. 2 Logic diagram of graph model management and parsing module

the equipment, automatically builds the model to generate the equipment resource asset information such as the circuit breaker in the interval, and automatically updates the line model and single line diagram locally, After verification, it will be synchronized to the distribution master station and backfilled to the PMS system.

2.3 Research on Self-description and Plug-and-Play Technology

Considering that the traditional distribution network lacks the self-description ability, it is difficult to realize the plug and play of distribution automation. This paper establishes a self-description information model of distributed distribution terminals based on IEC61850 standard, designs the communication architecture of distributed distribution terminals and master stations based on MQTT protocol, and realizes the plug and play of distributed distribution terminals.

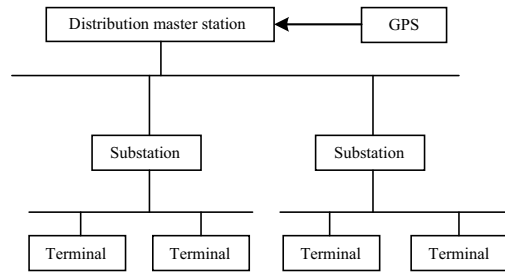
2.3.1 Research on Self-description Model of Distribution Equipment

In order to make the terminal equipment in the distribution network have the function of self-description and plug and play, it is necessary to introduce the model method and data exchange method of IEC61850 standard into the distribution network, establish a unified information model of distribution automation terminal, and describe the data model and service model of terminal equipment in SCL language, so that the control centre or other equipment can identify and obtain its functional services.

IEC 61,850 standard has three characteristics, which are hierarchical information model, data self-description and object-oriented model method, separation of service and mapping. In order to realize the exchange of data in the information type of distribution automation terminal, it is necessary to select the information exchange model suitable for distribution network data transmission in the standard, in order to realize the plug and play function of distribution terminal, this paper mainly studies the file transmission model, time synchronization model and registration model.

- 1) File transfer model: the distribution automation terminal stores self-description files, the master station to obtain terminal model, the file transfer model can be used.
- 2) As shown in Fig. 3, the time signal of the distribution master station system comes from the global positioning system GPS clock, and the sub-station receives the time synchronization signal of the master station to calibrate the time of the distribution automation terminal.
- 3) Registration model: After the distribution automation terminal is powered on, to realize the plug and play of the terminal, a registration model can be used.

Fig. 3 Real object diagram of ring cage operation state perception



2.3.2 Plug and Play Technology of Distribution Equipment

The realization of the plug and play function of the distribution automation terminal, the whole closed-loop management of the automatic access, operation and exit of the distribution automation terminal equipment can effectively reduce the workload brought by the access and debugging. The plug-and-play function is an automatic access system for the terminal side after power-on. For the control centre, it is to automatically identify the installed terminal and detect its operating status, the automatic identification is that when a new power-on terminal is connected, the control centre establishes a connection with the terminal and obtains its self-description model and automatically updates the operating status and parameters of the terminal.

2.4 Intelligent Sensing Technology of High Reliability Distribution Equipment

The paper adopts a new fault monitoring technology that uses sensor temperature measurement and ultrasound to determine fault types. The technology uses MEMS microphone to collect the ultrasonic signal generated by partial discharge and uses the temperature measuring probe to collect the temperature of the device under test. After amplification and hardware filtering, the signal is restored by ADC sampling. According to the sensor temperature measurement and ultrasonic determination of the fault type, the partial discharge diagnosis is carried out, and the intelligent sensor monitoring system of high reliability distribution equipment with temperature and partial discharge integration is constructed.

The temperature and partial discharge integrated sensor fault monitoring system designed and developed in this paper has the following functions:

- 1) Partial discharge diagnostic function: MEMS microphone is used to collect ultrasonic signals generated by partial discharge, and partial discharge diagnosis is carried out according to the signals.
- 2) Temperature measurement function: The temperature probe is used to collect the temperature of the device under test, and the acquisition frequency can be adjusted by the temperature rise.

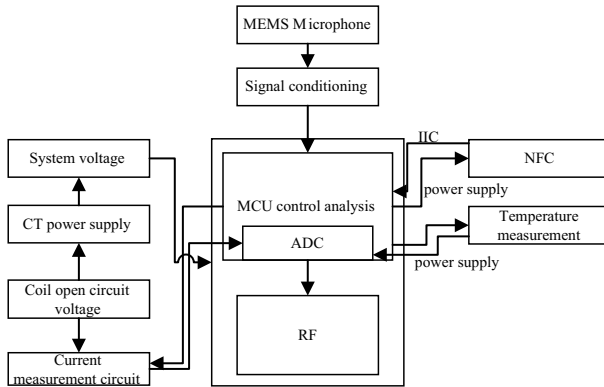


Fig. 4 Hardware Design Block Diagram

- 3) Current measurement: Use coil open-circuit voltage to measure the current.
- 4) NFC function: NFC sensor with identity recognition function is designed to read and write sensor installation position information.
- 5) Wireless communication: 2.4G wireless communication is used to upload status information.
- 6) Passive CT power

The hardware design diagram is shown in Fig. 4. The MEMS microphone collects the change of ultrasonic signal generated during partial discharge, and its output amplifies the weak voltage signal after signal conditioning, the MCU chip (STM321432KBU6) analysis and restores the signal, and performs partial discharge diagnosis according to the signal, at the same time, the temperature of the equipment is measured, the current of the transmission line is measured, the NFC records the sensor address information, and the results are sent out wirelessly.

3 Application Effect and Advantages

In this paper, a high reliability distributed intelligent distribution terminal holographic sensing ring network cabinet has been developed. It has been applied in many places, and the application effect is good, compared with the traditional distribution ring network cabinet, it has the following technical advantages:

- 1) One is the fully enclosed design, second, standardized double-ended prefabrication, the structure of the design is shown in Fig. 5 (a).
- 2) The distributed DTU design mode is adopted to reduce the overall volume of the ring cage by about 25%, the structure of the design is shown in Fig. 5 (b).
- 3) The intelligent distributed feeder automation (FA) based on DTU peer-to-peer communication is used to locate the fault quickly when the fault occurs.

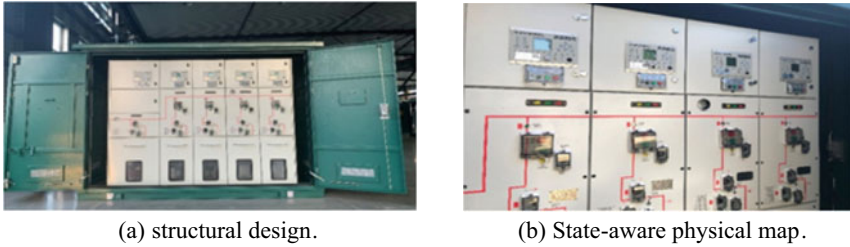


Fig. 5 Intelligent distribution terminal holographic perception ring network cabinet

- 4) The pilot company use the graph model center sharing service and graph model data, which effectively solves the problem of the company's graph model data penetration, improves the system mapping efficiency, reduces the original mapping system, the work efficiency is improved by 80%. Through data governance, the basic data quality of the distribution network stock of the pilot company reached 98.3%, which effectively improved the data quality of the distribution network model.

4 Conclusions

In this paper, a new type of distributed intelligent distribution ring network cabinet is developed, the main conclusions are as follows:

- 1) An acquisition controller structure design suitable for a variety of switch cabinets is developed, including the analysis and research of SoC bus architecture, hardware and software co-design, chip synthesis/timing analysis/verification and other technologies.
- 2) Through the distributed idea, the segmented line equipment information and topology relationship information of the distribution network are generated at the source end, and a single-line diagram automatic mapping system of the distribution network that actively triggers the automatic update of the whole network topology is designed.
- 3) Based on IEC 61,850 standard, the self-description model technology, plug and play technology and MQTT-based communication protocol technology of distribution equipment studied, and the self-description model establishment and plug and play function of distribution equipment are realized.
- 4) Using MEMS microphone to collect ultrasonic signals generated by partial discharge, combined with temperature signals, a new composite partial discharge fault monitoring technology is proposed, and a fault monitoring system with temperature and partial discharge integrated sensing is designed.

References

1. Shaoshi, L., Zhuding, W., Haiyan, Z., et al.: Discussion on lean planning and management improvement strategies for first-class distribution networks. *Power Syst. Prot. Control* **49**(03), 165–176 (2021). (in Chinese)
2. Al-Masri, E., Raj Kalyanam, K., Batts, J.: Investigating messaging protocols for the Internet of Things (IoT). *IEEE Access* **8**, 94880–94911 (2020)
3. Boya, Q.I.N., Dong, L.I.U.: Research progresses and prospects on analysis and control of cyber-physical system for power grid. *Proc. CSEE* **40**(18), 5816–5827 (2020). (in Chinese)
4. Zhengyou, H.E., Bo, L.I., Kai, L.I.A.O., et al.: Key Technologies for protection and control of novel urban power grids. *Proc. CSEE* **40**(19), 6193–6207 (2020). (in Chinese)
5. Yanchun, X.U., Xiaoming, L.I.U., Zhenhua, L.I., et al.: Influence of PMU quasi-real-time data on robust estimation of active distribution network. *Electr. Power Autom. Equipment* **40**(10), 15–22 (2020). (in Chinese)
6. Alvarez-Herauld, M.C., Labonne, A., Touré, S., et al.: An original smart-grids test bed to teach feeder automation functions in a distribution grid. *IEEE Trans. Power Syst.* **33**(1), 373–385 (2018)
7. Haoyong, C., Xiaojuan, W., Zhihao, L., et al.: Distributed sensing and cooperative estimation/detection of ubiquitous power internet of things. *Prot. Control Mod. Power Syst.* **4**(1), 1–8 (2019)
8. Huo, C., Mu, D., Wang, Y.: Research and application of a new edge computing DTU device. In: *IEEE 2nd International Conference on Big Data, Artificial Intelligence and Internet of Things Engineering (ICBAIE)*, pp. 1010–1014 (2021)
9. Yin, X., Jinghan, H., Ying, W., et al.: A review on distribution system restoration for resilience enhancement. *Proc. CSEE* **34**(16), 3416–3429 (2019). (in Chinese)
10. Lei, H., Singh, C., Sprintson, A.: Reliability modeling and analysis of IEC 61850 based substation protection systems. *IEEE Trans. Smart Grid* **5**(5), 2194–2202 (2014)
11. Han, G., Xu, B.: Suonan, J.: IEC 61850-based feeder terminal unit modeling and mapping to IEC 60870-5-104. *IEEE Trans. Power Delivery* **27**(4), 2046–2053 (2012)
12. Rining, W., Yi, W., Haoming, W., et al.: Topology identification method for a distribution network area based on the characteristic signal of a smart terminal unit. *Power Syst. Prot. Control* **49**(6), 83–89 (2021). (in Chinese)
13. Zhang, N., Ma, G., Guan, Y., et al.: Panoramic information perception and intelligent grid. *Proc. CSEE* **41**(4), 1274–1283+1535 (2021). (in Chinese)
14. Liu, Y., Ouyang, H., Li, G., et al.: Common information model design for integrated marketing and distribution terminal device based on IEC-CIM. *Smart Power* **47**(02), 75–81 (2019). (in Chinese)
15. Jing, X., Qi, Y., Yu, L., et al.: Research on plug and play information interaction mechanism of distributed generators. *Distrib. Utilization* **36**(10), 52–60 (2019). (in Chinese)

Research on Small Current Grounding Fault of Distributed Small Hydropower with Different Permeability when Connected to the Grid



Jiawen Chen, Chao Cai, Fan Yang, Lin Liu, Changsheng Sun, and Si Yang

Abstract The grounding fault of distribution network is the main cause of power failure on the user side. In distributed power access and distribution network, the characteristics of distributed small hydropower with different permeability in short circuit fault are different from traditional faults. To study the treatment measures of small current grounding fault, this paper analyzes different permeability and contact resistance of the distributed energy access to 10 kV distribution line, put forward the fault characteristic signal acquisition and processing technology, the research is suitable for the terminal optimization and proximal small hydropower grid maintenance technology, the use of RTDS simulation platform for fault analysis, the changes of frequency and voltage are obtained to provide reference for the research of grid connection of distributed small hydropower.

Keywords Distributed generation · Small hydropower · Permeability

1 Introduction

In recent years, distributed generator (DG), which has the function of peak cutting and load balancing, has been widely used. Distributed power generation such as small hydropower and photovoltaic in the distribution network not only increases the standby capacity of the grid [1–3], but also makes the power production closer

J. Chen (✉) · C. Cai
State Grid Hubei Electric Power Co., Ltd., Wuhan 430077, China
e-mail: 6052079@qq.com

F. Yang
Electric Power Research Institute, State Grid Hubei Electric Power Co., Ltd., Wuhan 430077, China

L. Liu · C. Sun · S. Yang
Dong Fang Electronics Co., Ltd., Yantai 264000, China

© Beijing Paiké Culture Commu. Co., Ltd. 2023
X. Dong et al. (eds.), *The proceedings of the 10th Frontier Academic Forum of Electrical Engineering (FAFEE2022)*, Lecture Notes in Electrical Engineering 1054, https://doi.org/10.1007/978-981-99-3408-9_105

1177

to the load and reduces the loss in power transmission. However, when the short-circuit fault occurs in the distribution network, the distributed power supply will also provide short-circuit current, which can help increase or decrease the short-circuit current, and may cause the original protection device to fault or refuse to operate [4–6].

Based on the theoretical analysis of the principle and characteristics of short circuit fault of small hydropower in distribution network, this paper proposes the optimization technology of feeder automation terminal suitable for this system. Then, based on the 10 kV distribution line, the RTDS (Real time digital simulation system) simulation is carried out to verify the low current grounding fault of small hydropower under different permeability and different transition resistance. Finally, the treatment measures of low current grounding fault are summarized. It provides reference for design optimization and operation and maintenance management of distributed small hydropower.

2 Research Methods

2.1 Fault Analysis Under Distributed Small Hydropower

As shown in Fig. 1, one or more small hydroelectric power sources are connected to the 10 kV line 1. If the power generated by small hydroelectric power is equal to the load of the line, once a ground fault occurs, the small current line selection device in the substation will trigger the trip of the outgoing circuit breaker CB1. Because of the existence of distributed energy DG, the line still has power after trip. The segment switch cannot perform the original logical action for fault isolation [7–9].

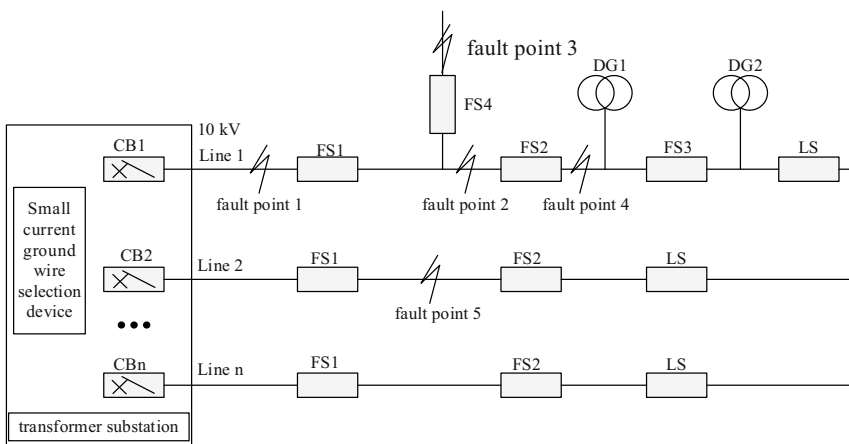


Fig. 1 Feeder automation after distributed energy access

For the low-current grounding system, the existing feeder automation method is to make a judgment by docking the ground line with the low-current grounding line selection device, and trigger the tripping of substation outgoing circuit breaker from large to small according to the probability of fault occurrence. After the setting time, the feeder automation switch on the line will be electrocuted step by step. When it is close to the ground fault point, When the three-phase five-column voltage transformer detects zero sequence voltage (and is greater than the fixed value) before installation and switch, the switch will automatically open and lock within the set time (2.5 s), so as to realize the automatic positioning and isolation of ground fault. However, it cannot automatically handle the ground fault.

In view of above problems, it is necessary to study influence of distributed power access with different permeability on the original fault handling technology [10].

The permeability of this article refers to the permeability of small water electricity, and the permeability of the distributed power generation and the real-time total demand power of the distributed power supply are used by W_{DG} and W_n respectively.

Permeability is calculated as follows:

$$\eta = \frac{W_{DG}}{W_n} \times 100\% \quad (1)$$

When the big power grid trips, all the load on the line is provided by small hydropower, which can be considered in two cases:

1) Low permeability of small hydropower.

Large power grid tripping will appear a large number of active power gap, in addition to the general small hydropower for economic benefits will multiple active power, basically no reactive power, so without a large power grid, system reactive power will also appear gaps, voltage will drop, the greater the gap, the faster the rate of decline, until the collapse of the system.

2) Small hydropower has higher permeability.

When the large power grid trips, if the permeability is high or even over 100%, the active power of the system will be excessive. If the small hydropower cannot be quickly adjusted, the system voltage will rise, affecting the safety of users' electricity consumption. In this case, the small hydropower can be quickly cut out according to the characteristics of overvoltage and over-frequency to prevent damage to users' electrical appliances [11].

2.2 Fault Feature Collection and Processing

Taking a certain distribution network as an example, there are a large number of small hydropower in the distribution network. Generally, the small water and electricity power connected to the grid through a 10 kV line is not large, and the permeability of the line is inconsistent. During the field investigation, the equipment in several small water power plants are all old, basically have no isolated island operation ability,

Table 1 Table of two section protection Settings

Physical quantity	Frequency/Hz	Frequency/Hz	Voltage/V	Voltage/V
Data range	<47	47–49.5	<50% U_n	50%–85% U_n
Data range	>55	50.5–55	>135% U_n	110%–135% U_n
Delay tripping/s	0.2	1	0.2	1

and the ability to respond to load changes is poor. All of them are manually adjusted or cannot be adjusted. Based on the above situation, a fault collection scheme is proposed.

1) Fault recording function.

In case of conditions that need to trigger the recording, such as voltage sag and current mutation, the recording function can be started in time to record the characteristic information of abnormal moments. When the condition of triggering RMS recording function is reached, the changes of current RMS can be recorded in time. This function records the voltage and current value according to the configuration, records the density of 10ms a point, and records the duration of 5s.

When small hydropower works in PQ mode, it does not have the ability of rapid frequency and voltage regulation. Therefore, when the system's active power and reactive power are unbalanced, voltage and frequency fluctuations will be caused. When the system active power is insufficient ($\eta < 100\%$) will cause frequency decline, active power redundancy ($\eta > 100\%$) frequency will rise; When the reactive power of the system is low, the voltage drops; when the reactive power is redundant, the voltage rises.

Therefore, this paper proposes to adopt two-stage protection for voltage and frequency problems, with U_n as the rated reference voltage, as shown in Table 1.

At the same time, it should have the loss of voltage trip, the load side has the power prohibition closing, automatic call closing, zero voltage protection and other functions, to ensure that the fault can be moved, and only allow the power side call closing, prohibit the reverse power supply of small hydropower.

2.3 Feeder Automation Terminal Optimization and Near End Design

Terminals are an important link in distribution network, of which feeder terminal unit (FTU) and backup power supply are the key components.

For rain prevention, the design of the FTU outer box requires that it can be sealed against water. The bottom of the box should be designed with a rain proof skirt to prevent heavy rain from entering the cable. The top of the box should be designed as an inclined plane to prevent water droplets from dripping directly onto the equipment.

The varistor is installed at the FTU voltage sampling entrance to prevent over-voltage, and an isolated voltage transformer is used to ensure that the voltage entering the system does not damage the AD loop. The FTU remote loop is connected with the auxiliary contact of the switching mechanism. The remote power supply selects the high isolation voltage and voltage isolation power supply to protect the system from lightning strikes.

In this paper, the technical solution of standby power supply is battery online monitoring system + battery monitoring data management software. And the monitoring software is configured so that the data can be read and displayed remotely in the main station system of the distribution network.

In addition, for the near-end design, this paper focuses on the key technologies of near-end security, aiming at realizing authorized maintenance. The scheme is to design a four-layer defense system for near-end security.

- Layer 1: Authorization at the primary site layer
- Layer 2: Local maintenance tool authentication
- Layer 3: User identity authentication
- Layer 4: Terminal maintenance authentication

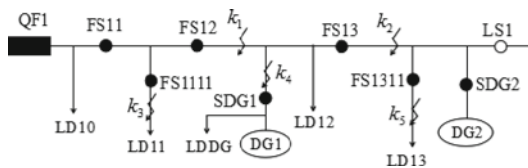
Through the above four layers of authentication protection, can effectively occur illegal access. Bluetooth is used as the communication channel of near field maintenance, the signal coverage is small, the data is authenticated by AES encryption algorithm, and the frequency hopping mode of communication is adopted to effectively prevent illegal eavesdropping.

3 RTDS Simulation Verification

In this paper, the verification environment of feeder automation scheme for distributed energy access is built by using RTDS, and the de-routing function of feeder terminal of complete equipment and the feeder automation scheme are verified.

Figure 2 is the test topology diagram, the test fault type in this experiment is single-phase grounding fault, which is divided into two test processes and four test results. Where the permeability is 150% (high permeability) and 30% (low permeability) in the case of single-phase grounding fault. When a ground fault occurs, the ground resistance is 200 Ω and 2 kΩ.

Fig.2 Electrical topology of the test



3.1 Ground Fault Test Under Different Permeability

The test environment is ungrounded system, and the test fault point is located in K1. Test parameters are set: small hydropower capacity 1 MW, power factor target 0.8, reactive power 0.5MVar, load reactive power 0.4Mvar, PQ control mode; The detection switches were located at SDG1 and FS11 respectively. The 10 kV transformer has a capacity of 20 MW. The exit switch trips 4 s after the ground fault occurs, and overlaps another 6 s.

The test system consists of four loads, with power of 0.25 MW, 0.5 MW, 0.5 MW and 0.25 MW respectively. The permeability in this test was 150% and 30%, respectively. CB1, FSDG1, FS11 trip in sequence; After CB1 outlet coincides for 6 s, FS11 segment switch will delay the call closing. Due to grounding fault, zero voltage mutation is detected and tripping again and locking is completed, thus achieving fault isolation.

As shown in Fig. 3 (a), after CB exit is switched off, the voltage of DG is detected by the connecting point to drop slowly. When the low voltage limit and time are reached, the connecting point switch trips.

As shown in Fig. 3 (b). After CB outlet trip, due to high permeability and excess active power, the frequency will rise. When the high frequency limit and time are reached, the parallel dot switch will also trip. The controller recorded the RMS recording and the frequency gradually increased from 51.41 Hz to 53.14 Hz as the U_{ab} decreased. Here's what happens when permeability is 30%.

As shown in Fig. 4 (b) CB outlet trip, due to low permeability, active power shortage, will cause the frequency drop.

The simulation results show that after outlet trip, the frequency of the system will decrease due to insufficient active power (30% permeability), and increase due to

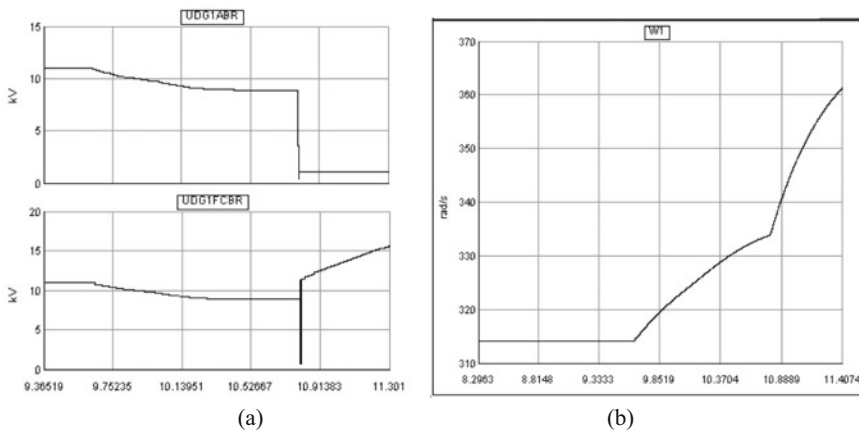


Fig. 3 Voltage waveform and frequency change at DG with 150% permeability

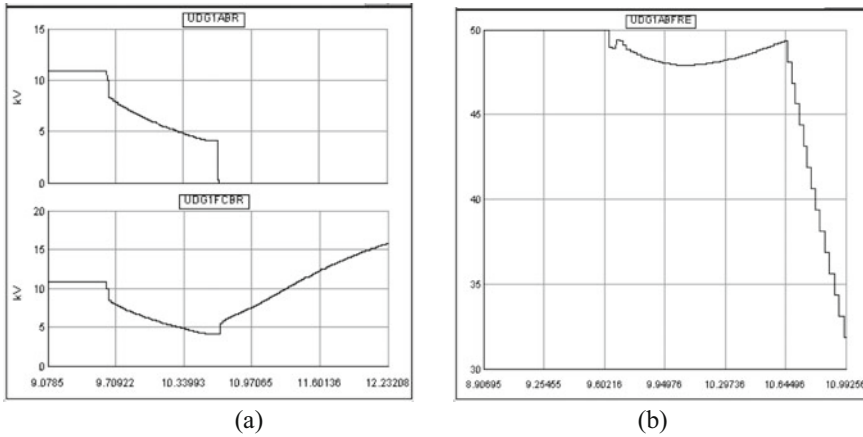


Fig. 4 Voltage and frequency change at DG when 30% permeability

excessive active power (150% permeability). And when the system reactive power is insufficient, the voltage drops; Without too much power, the voltage rises.

3.2 Ground Fault Test of Different Transition Resistors

The test environment is an ungrounded system, the test failure point is located in K1, and the permeability is fixed at 50%. Test parameters are set, small hydropower capacity 1 MW, power factor target 0.8, reactive power 0.5MVar, load reactive power 0.4Mvar, PQ control mode; The detection switches were located at SDG1 and FS11 respectively. 10 kV transformer capacity of 20 MW. The outlet switch trips 4 s after the ground fault occurs, and then coincides with another 6 s. 200Ω and 2kΩ contact resistors were set respectively for simulation (Fig. 5).

The following are the simulation results with a transition resistance of 2kΩ, aiming to reflect the current, voltage and frequency characteristics of different transition resistors. The voltage waveform, frequency change, zero sequence voltage and zero sequence current change waveform at DG can be visually observed on the simulation platform (Fig. 6).

The simulation results show that when ground fault occurs, if the outlet does not trip, the voltage frequency of the junction point of small hydropower station does not change.

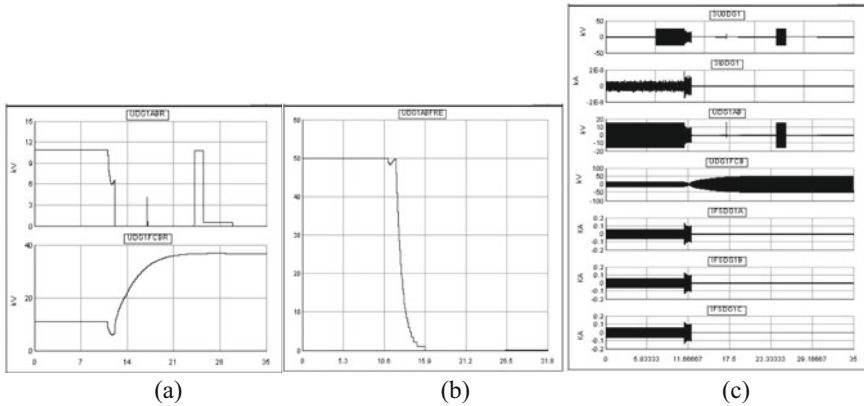


Fig. 5 Transition resistance, frequency change and zero-sequence voltage at DG under 200Ω

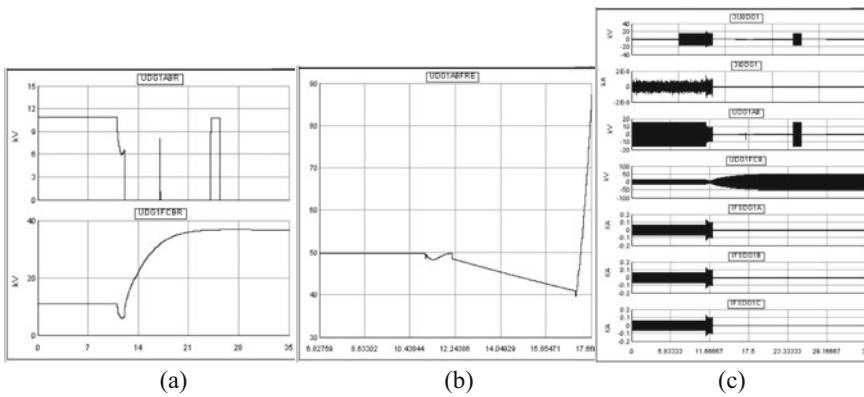


Fig. 6 Voltage waveform frequency change and zero-sequence voltage at DG under 2kΩ

4 Conclusions

Based on the distributed small hydropower distribution system, this paper analyzes the small current grounding fault. Through the collected data and simulation analysis, the short circuit under the permeability of 30% and 150% and the transition resistance of 200Ω and 2kΩ is compared, and the following conclusions are drawn:

For small hydropower grid-connected systems, two-stage voltage and frequency protection should be configured. The design of FTU outer box should pay attention to rain and lightning protection, and a four-layer defense system should be developed to cope with the near-end security design.

Once ground short circuit fault occurs in distributed small hydropower grid-connected system, high permeability configuration will cause frequency increase,

low permeability will cause frequency decrease, and zero sequence voltage and zero sequence current caused by different transition resistors are different.

References

1. Fan, X., Yongjun, X., Kanjun, Z., et al.: Research on network protection principle of distribution network with new energy access. *Trans. China Electr. Soc.* **34**(S2), 709–719 (2019). (in Chinese)
2. Yao, H., HuangQiang, L., et al.: Research on Load forecasting of power grid with small water based on residual correction. *Electr. Measur. Technol.* **45**(06), 50–58 (2022). (in Chinese)
3. Qunmin, Y., Jia, W., et al.: Review on voltage reactive power optimization control of distribution network with small hydropower. *Power Capacitor React. Power Compensation* **43**(01), 1–11 (2022). (in Chinese)
4. Yingliang, L., et al.: Calculation of short-circuit current in high permeability active distribution network. *Southern Power Syst. Technol.* **15**(07), 61–66 (2021). (in Chinese)
5. Zhen, S., Hao, X., Hongzhi, Z., et al.: Phase selection method of single-phase earth fault based on Earth fault ratio for unbalanced distribution network. *Power Syst. Protect. Control* **50**(12), 108–116 (2022). (in Chinese)
6. Yuanbo, Y., Xiang, C., et al.: Research on fast phase selection method for single-phase ground fault in distribution network. *Power Syst. Protect. Control* **49**(03), 96–103 (2021). (in Chinese)
7. Wang, P., Zhang, Z., Lee, W.J., et al.: Robustness Improvement on PMU based dynamic equivalent modeling of distributed small hydropower generator stacks. *IEEE Trans. Power Syst.* **99**, 1–1 (2020)
8. Zhang, L., Pang, M., Bahaj, A., et al.: Small hydropower development in China: Growing challenges and transition strategy. *Renew. Sustain. Energy Rev.* **11053**, 137 (2021)
9. Wang, X., Chen, L., Chen, Q., et al.: Model and analysis of integrating wind and PV power in remote and core areas with small hydropower and pumped hydropower storage. *Energies* **11**(12), (2018)
10. Di, W., Chao, C., Liwu, G., et al.: Comprehensive evaluation of distribution station state of high permeability distributed power supply. *Rural Electr.* **424**(09), 5–8 (2022). (in Chinese)
11. Jinhai, Y., Jiahui, W., Haiyun, W., et al.: Dynamic security domain analysis of multiple new energy power system under different permeability. *Electr. Power Constr.* **43**(04), 58–68 (2022). (in Chinese)

Research Progress of New Multi-functional Transformer



Yu Dong, Feiyang Zhou, Yifan Wang, Lingyun Gu, Shingzhe Wang, and Yan Wu

Abstract The new multi-functional transformer can transform voltage, provide isolation, compensate reactive power and stabilize voltage. It is expected to solve the prominent problem of large power flow and voltage fluctuation caused by the large number of distributed new energy connected to the power grid in the new power system. This paper mainly introduces the power electronic transformer, Hybrid distribution transformer and magnetic control transformer are three new multi-functional transformers, and the research progress of the three transformers is reviewed in detail from the perspective of basic principle, topology and control strategy. Finally, the possible difficulties in their further development and the development trend are summarized.

Keywords Multifunctional transformer · New power system · Reactive power compensation · Voltage stabilization

1 Introduction

The future power system will be a new type of power system dominated by clean energy with strong volatility, but strong volatility is not conducive to the stable operation of the power system, which will lead to large voltage fluctuations and large changes in reactive power demand [1, 2]; In addition, the lines and loads of the distribution network have also changed greatly compared with the past - cable transmission lines have been applied on a large scale, and will generate more capacitive reactive power than overhead lines; The electric vehicle charging pile on the load side will also need more reactive power support [3].

Y. Dong · Y. Wang (✉)

School of Electrical Engineering and Automation, Wuhan University, Wuhan 430072, China
e-mail: 1286628332@qq.com

F. Zhou · L. Gu · S. Wang · Y. Wu

Beijing Key Laboratory of Distribution Transformer Energy-Saving Technology (China Electric Power Research Institute), Beijing 100192, China

© Beijing Paiké Culture Commu. Co., Ltd. 2023

X. Dong et al. (eds.), *The proceedings of the 10th Frontier Academic Forum of Electrical Engineering (FAFEE2022)*, Lecture Notes in Electrical Engineering 1054, https://doi.org/10.1007/978-981-99-3408-9_106

1187

The traditional reactive power stabilization scheme mainly uses external capacitors and reactors for reactive power stabilization. However, the external capacitors and reactors cover a large area and are not suitable for urban distribution networks with limited space. Therefore, the existing technical means cannot cope with the problems related to voltage and reactive power after the new power system is fully popularized.

New type multi-functional transformer generally refers to a transformer with one or more functions such as frequency conversion, voltage stabilization, reactive power compensation, power flow control and harmonic treatment in addition to the voltage transformation and isolation functions of traditional transformer. Research teams have conducted research on a new multi-functional transformer with reactive power compensation and voltage stabilization capability, which has great potential to solve problems. This paper summarizes the research progress of its principle, topology and control strategy.

2 Power Electronic Transformer

2.1 Working Principle

Power electronic transformer (PET) is a new type of multi-functional transformer with reactive power compensation, phase adjustment and harmonic control functions.

The topology of pet can be divided into single-stage topology, double-stage topology and multi-stage topology according to the number of times the power is rectified or inverted. The more the number of stages, the more flexible the power conversion of pet will be and the larger the adjustment range will be. However, the more the number of stages, the more the number of power electronic devices will be, and the reliability of pet will be lower and lower. Document [4] proposes AC/AC single-stage pet as shown in Fig. 1 on the basis of early power electronic transformers. It does not include a DC link, and only converts electrical energy from high frequency to high frequency, and then from high frequency to power frequency. Therefore, it can only realize the conversion of voltage and current amplitude and frequency, and can not change the phase, that is, it can not output reactive power.

Figure 2 shows a typical AC/DC/AC two-stage pet topology, which adds a DC link to AC/AC pet, so that the transformer can change the phase of voltage and current, and has the ability to output reactive power. However, this topology has high requirements for high-voltage and high-power semiconductor devices, and can not meet the requirements of large-scale applications in terms of manufacturing process and cost. MMC pet, cascaded H-bridge pet and other multi-stage pet divide the high voltage borne by the transformer into multiple power electronic devices, reducing the withstand voltage requirements of a single power electronic device, but the cost will also be greatly increased [5, 6].

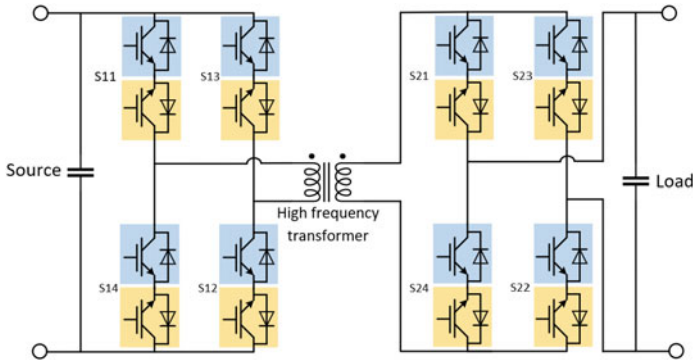


Fig. 1 AC/AC type pet topology

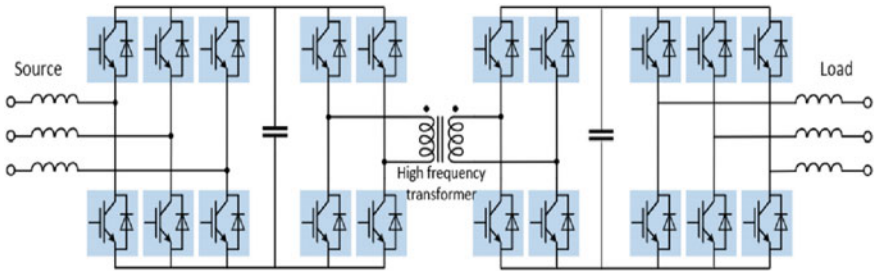


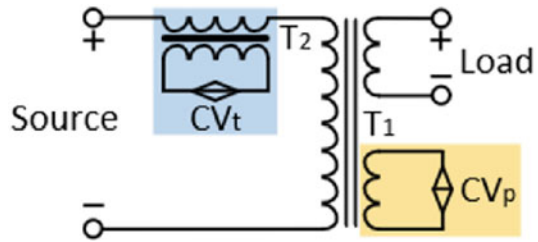
Fig. 2 AC/DC/AC type pet topology

2.2 Control Strategy

The control of PET is mainly divided into three parts, namely, the control of input stage, isolation stage and output stage. The control objective of the pet input stage is to rectify the power frequency voltage on the primary side into a stable DC voltage. Document [7] proposes a new lc-mpdpc control strategy for PWM rectifier, which realizes synchronous control of active power and reactive power, has less harmonic current and low power ripple than the traditional one, and has good stability and fast dynamic response.

The isolation stage of PET connects the input stage and the output stage, and the most widely used control method is the phase-shift control method. Document [8] proposes a DC voltage balancing strategy for pet isolation stage, adjusting the phase shift angle of H-bridge units to control active power. Document [9] proposes a phase-to-phase voltage balance control strategy based on negative sequence voltage injection, simplifying the calculation of negative sequence voltage and requiring only a single current inner loop control. This solves the problem of phase-to-phase voltage imbalance and in phase voltage imbalance in power electronic transformers.

Fig. 3 Equivalent circuit diagram of HDT



Literature [10, 11] also achieved good results by using resonance technology to design the soft switch of power electronic transformer.

The output stage control of PET requires the output voltage of the secondary side to be stable. Literature [12] has studied the strategy of controlling multiple modules, especially when energy is input. Specifically, keep the voltage of the main inverter unchanged and the current of the secondary inverter unchanged. The master–slave control model is established, which greatly improves the voltage stability at the output side of the power electronic transformer and reduces the voltage distortion rate at the output end.

3 Hybrid Distribution Transformer

3.1 Working Principle

Hybrid distribution transformer (HDT) is a new multi-functional transformer that converts part of its capacity through power electronic devices, so it has the dual advantages of traditional transformer and power electronic technology [13]. HDT can usually be combined by traditional transformer and UPQC, DVR, APF and other power compensation equipment, but at present, scholars have studied more about the combination of HDT and AC/DC/AC converter [5] (Fig. 3).

HDT realizes the functions of compensation and voltage stabilization, reactive power compensation and harmonic treatment by controlling CV_p and CV_t [14, 15].

3.2 Control Strategy

Hybrid transformer has good voltage and current control functions, and its control objectives include output side voltage control, input side current control and power control. In order to realize high controllability of hybrid transformer, its control strategy is very important.

Reference [16] proposed a fuzzy control based control strategy for HDT DC bus voltage. By adding a fuzzy controller to the PI controller, the mathematical model

is established, and the control equations of HDT current and voltage are derived, which effectively improves the transient and steady-state performance of the DC bus voltage control system. In reference [15], a robust model predictive control strategy is proposed for the model uncertainty caused by the fluctuation error of line parameters. By converting the uncertainty fluctuation range in the predictive model into the maximum and minimum value problem, it is applied to adjust the reactive power dynamic optimization of HDT in and, making its adjustment smoother and improving the robustness of the control algorithm.

4 Magnetic Control Transformer

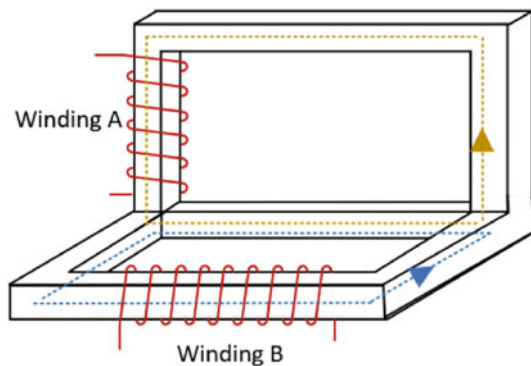
Magnetically controlled transformer is a new multi-functional transformer that does not rely on power electronic equipment for power conversion, but realizes reactive power compensation, harmonic processing, stable point voltage and other functions through electromagnetic principle, which is different from the above three new multi-functional transformers. The following will introduce various magnetic control transformers from the aspects of working principle and topology.

4.1 Magnetically Integrated Transformer

The magnetic integrated transformer decouples each winding so that the magnetic flux generated by them does not affect each other. As shown in Fig. 4, winding a and winding B have separate magnetic flux loops respectively, and the two loops are arranged at 90° in space, thus realizing the orthogonal decoupling of the two windings.

However, orthogonal decoupling will increase the iron core of the transformer and also increase the cost. Therefore, in practical applications, the winding method

Fig. 4 Schematic diagram of orthogonal decoupling of windings A and B



of orthogonal decoupling is often less used, while the method of non-orthogonal decoupling is widely used. Literature [17] also designed a new transformer based on this method, which combines linear reactor with transformer and has good reactive power compensation and harmonic filtering function.

4.2 Magnetic Saturation Transformer

The magnetic saturation transformer has an iron core with a smaller cross-sectional area than the normal iron core, which is called a small magnetic valve. Because the area of the small magnetic valve is smaller than that of the normal iron core, it is easier to saturate. Therefore, by adding some DC magnetic flux to the magnetic valve, the small magnetic valve can reach the magnetic saturation state. Achieving saturation means that the core works at the high point of the B-H curve. At this time, the excitation reactance of the transformer decreases sharply, so the magnetic saturation transformer can achieve the purpose of controlling voltage or outputting reactive power.

At present, the magnetically saturated transformer has only single-phase topology. The single-phase is a three-column or four-column topology. Only three single-phase magnetically saturated transformers can be used in the three-phase system, which will greatly increase the floor area of the magnetically saturated transformer. Therefore, under the premise of not affecting the working performance of the magnetic saturation transformer, how to compact the magnetic saturation transformer is an urgent problem to be solved.

4.3 Magnetic Material Type Transformer

The magnetic material transformer is a new type of multi-function transformer, which uses a new type of composite magnetic material as a part of the magnetic core. Literature [18] uses composite materials to make the transformer have multiple functions. The specific principle is to change the working point of the B-H curve of the composite materials to adjust the magnitude of the excitation reactance, so as to control the voltage and reactive power. However, it is difficult to prepare nanocomposite magnetic materials on a large scale.

In addition, the magnetic material type transformer, like the magnetic saturation type transformer, currently only has single-phase topology mechanism, and the use of three single-phase magnetic material type transformers also has the problems of large floor space and high cost.

5 Conclusions

The research of many new types of multi-functional transformers has achieved certain theoretical and practical results, but it is still at the stage of theoretical research on the whole, and there is still a certain distance from the actual large-scale application. Based on the principle, topology and control strategy of the development of a variety of new multi-functional transformers, the following conclusions can be reached:

- 1) Power electronic transformers are very suitable for use in new power systems, but they cannot be used in large-scale applications in new power systems in the short term. Therefore, substitutes are needed to fill the gap [19].
- 2) Both kinds of new multi-function transformers have broad prospects, but still need to solve the problems of cost control, reliability and harmonic. In particular, the topology of three-phase transformer needs to be solved urgently, which will be the key factor for the large-scale promotion of magnetic control transformer.

Acknowledgements This research was funded by Supported by Open Fund of Beijing Key Laboratory of Distribution Transformer Energy-Saving Technology (China Electric Power Research Institute), grant number PDR51202102015.

References

1. Ma, Z., Zhang, H., Zhao, H., Wang, M., Sun, Y., Sun, K.: New mission and challenge of power distribution and consumption system under dual-carbon target. *Proc. CSEE* **42**(19), 6931–6945 (2022). (in Chinese)
2. Zhang, Z., Kang, Z.: Challenges and prospects for constructing the new-type power system towards a carbon neutrality future. *Proc. CSEE* **42**(08), 2806–2819 (2022). (in Chinese)
3. Fu, Y., Meng, X., Su, X., Mi, Y., Tian, S.: Coordinated charging control of PEV considering inverter's reactive power support and three phase switching in unbalanced active distribution networks. *Electr. Power Autom. Equipment* **40**(12), 1–12 (2020). (in Chinese)
4. Kang, M., Enjeti, P., Pitel, I.: Analysis and design of electronic transformers for electric power distribution system. *IEEE Trans. Power Electron.* **14**(6), 1133–1141 (1997)
5. Liang, D., Liu, Y., Kou, P., Cai, S., Zhou, K., Zhang, M.: Analysis of development trend for intelligent distribution transformer. *Autom. Electr. Power Syst.* **44**(07), 1–14 (2020). (in Chinese)
6. Wang, H., Luan, J.: Summary of power electronic evolution of transformer and its influence on voltage stability. *Power Syst. Prot. Control* **48**(16), 171–187 (2020). (in Chinese)
7. Li, H., Lin, M., Yin, M., Ai, J., Ai, W.: Three-vector-based low-complexity model predictive direct power control strategy for PWM rectifier without voltage sensors. *IEEE J. Emerg. Sel. Topics Power Electron.* **7**(1), 240–251 (2018)
8. Tian, J., et al.: Individual DC voltage balance control for cascaded H-bridge electronic power transformer with separated DC-Link topology. In *IEEE Access* **7**, 38558–38567 (2019)
9. Zhang, H., Wang, M.: Voltage balance control strategy for a cascaded H-bridge converter-based power electronic transformer. *Mod. Electr. Power* **37**(01), 98–103 (2020). (in Chinese)
10. Wu, J., Li, Y., Sun, X., Liu, F.: A new dual-bridge series resonant DC–DC converter with dual tank. *IEEE Trans. Power Electron.* **33**(5), 3884–3897 (2017)

11. Yang, Y., Pei, W., Deng, W., Zhang, S.: Benefit analysis of using multi-port and multi-function power electronic transformer connecting hybrid AC/DC power grids. *J. Eng.* **2019**(16), 1076–1080 (2019)
12. Gu, J., Liu, S., Liu, C., Liu, X., Li, S., Zhao, Z.: The output power quality improvement strategy for power electronic transformer. *Control Eng. China* **27**(07), 1274–1280 (2020). (in Chinese)
13. Yang, B., Zhao, J., Ji, Z., Wang, J., Liu, K.: Overview of hybrid transformer technologies. *Electr. Power Autom. Equipment* **40**(02), 205–213+1–3 (2020). (in Chinese)
14. Burkard, J., Biela, J.: Evaluation of topologies and optimal design of a hybrid distribution transformer. In: 2015 17th European Conference on Power Electronics and Applications (EPE'15 ECCE-Europe), pp. 1–10. Geneva, Switzerland (2015)
15. Gao, R., Kou, P., Liang, D., Liu, Y., Wu, Z.: Robust model predictive control for the voltage regulation in active distribution networks with hybrid distribution transformers. *Proc. CSEE* **40**(07), 2081–2090+2388 (2020). (in Chinese)
16. Li, D., Liang, D., Gao, Y., Zhang, M., Zhang, L.: A control strategy based on fuzzy logic control for hybrid distribution transformer. *Trans. China Electrotechnical Soc.* **36**(S2), 696–703+722 (2021). (in Chinese)
17. Liao, W.: The linear filtering reactor integrated in the transformer research based on the non-orthogonal decoupling theory. Doctor, Hunan University (2015). (in Chinese)
18. Chen, Z.: Study on multi-function transformer with adjustable magnetic state based on nano-materials. Doctor, Shenyang University of Technology (2017). (in Chinese)
19. She, X., Huang, A., Lukic, S., Baran, M.: On integration of solid-state transformer with zonal DC Microgrid. *IEEE Trans. Smart Grid* **3**(2), 975–985 (2012)

Potential Development and Planning Method of Industrial Load Regulation



Chaoliang Wang, Wei Liu, Jiangming Zhang, and Hanqing Liu

Abstract High energy consumption industrial load has the potential to participate in power grid regulation and control. Fully developing the adjustable capacity of industrial load plays a key role in the safe and stable operation of new power system and new energy consumption. This paper also considers the planning and operation problems of industrial load participating in power grid regulation and control, and proposes a two-level optimization model for industrial load development planning. The inner optimization problem is responsible for solving the operation problem of industrial load, mainly for the operation plan of industrial load and thermal power unit considering new energy sources, and the outer optimization problem is responsible for solving the planning problem of industrial load, mainly for the development layout of industrial load. Finally, genetic algorithm is used to solve the model, and IEEE 10 machine 39 bus system is used to verify the effectiveness of the method proposed in this paper, which provides a reference for large-scale development of industrial load under the new power system.

Keywords Industrial load · Bilevel programming · Ancillary services · Investment benefit

1 Introduction

Due to the multiple security problems caused by the high proportion of new energy grid connection, the characteristic structure of each link of the new power system "source network load storage" will change [1]. In view of the system operation risk that may be caused by intermittent and uncertain output of new energy power supply, the power system needs to have the real-time control capability for a large number of flexible resources [2].

C. Wang · W. Liu (✉) · J. Zhang · H. Liu
State Grid Zhejiang Electric Power Co., Ltd., Marketing Service Center, Hangzhou 311100, China
e-mail: 827836282@qq.com

© Beijing Paiké Culture Commu. Co., Ltd. 2023
X. Dong et al. (eds.), *The proceedings of the 10th Frontier Academic Forum of Electrical Engineering (FAFEE2022)*, Lecture Notes in Electrical Engineering 1054, https://doi.org/10.1007/978-981-99-3408-9_107

Important production equipment (such as electrolytic cell, submerged arc furnace and reduction furnace) in a variety of high energy consumption industrial loads have similar energy storage characteristics [3, 4]. By installing additional control terminals, they can participate in the frequency and peak regulation of the power grid in a short time, which plays an important role in the safe and stable operation of the power grid under the new power system and the consumption of new energy [5]. At present, the research on industrial load participating in power grid regulation focuses on the control strategy, while the research on how to effectively tap its adjustable potential and carry out large-scale development is less.

At present, many literatures have studied the planning method of energy storage system: Literature [6] proposed a comprehensive optimization model for planning and operation to improve the access capacity of wind power based on the two-level decision-making problem, and solved it through a heuristic algorithm; Literature [7] proposed the time series voltage sensitivity index under the new power system, and deeply studied the optimal location and configuration of energy storage system from the perspective of voltage improvement; Reference [8] proposed a location and capacity determination method for energy storage system taking into account the uncertainty of wind power, and used Benders decomposition algorithm to reduce the computational burden; Literature [9] uses the subgradient cutting method to solve the double-layer model to optimize the location and size of the energy storage system, and ensures the profitability of the energy storage investment through the constraint of the rate of return on investment.

2 Potential Development Method of Industrial Load Regulation

Due to the weak real-time interaction between the current power grid and industrial enterprises, the power regulation instructions of the power grid cannot be directly issued to industrial enterprises. In order to develop the real-time adjustability of industrial load, it is necessary to install additional control terminal equipment for electrical equipment suitable for real-time power regulation in industrial enterprises. The terminal equipment needs to have two functions of local regulation and remote regulation: local mode means that the terminal control equipment can receive the frequency signal from the power grid frequency acquisition device, calculate the power to be adjusted by the load adjustable capacity in real time, and issue control commands to the load power control device after processing, which is applicable to the load participating in the primary frequency modulation of the power grid; Remote mode refers to that the terminal control equipment can calculate the load adjustable capacity at the current moment online and report it to the control master station. The control master station sends the regulating signal to the terminal control equipment according to the demand for frequency modulation and peak shaving, and then the

terminal control equipment sends the control command to the load power control device.

The installation of additional terminal control equipment requires a certain amount of financial support. Because its installation purpose is to ensure the security and stability of the power grid, this part of funds should be paid by the power grid. What industrial loads should be selected in a certain area for the development of regulation capacity, and whether all industrial loads can be developed to achieve the optimal economic performance is a problem that needs to be studied.

3 Industrial Load Planning Method

3.1 Inner Layer Optimization

The inner layer optimization is mainly the real-time control cost of the power grid and industrial load, including the coal cost of the generator, the penalty cost of abandoning wind and light, and the loss cost caused by the passive power regulation of industrial load. The control cost is divided into upward regulation cost and downward regulation cost. The downward regulation cost is mainly the economic loss caused by the decline of output, and the upward regulation cost is the economic loss caused by the decline of production efficiency. The specific formula is as follows:

$$\min C_{in} = C_{gen} + C_{pun} + C_{control} \tag{1}$$

$$C_{gen} = \sum_{i=1}^{N_g} \sum_{t=1}^T (a_i P_{g,i,t}^2 + b_i P_{g,i,t} + c_i) \tag{2}$$

$$C_{pun} = \sum_{j=1}^{N_w} \sum_{t=1}^T \eta_w (P'_{w,j,t} - P_{w,j,t}) \cdot \Delta t + \sum_{k=1}^{N_s} \sum_{t=1}^T \eta_s (P'_{s,j,t} - P_{s,j,t}) \cdot \Delta t \tag{3}$$

$$C_{control} = \sum_{i=1}^{N_l} \sum_{t=1}^T |C_I \times \Delta P_{l,i,t} \times \Delta t| \tag{4}$$

$$C_I = \begin{cases} (F_p - F_c)/C_E, \Delta P_{l,i,t} < 0 \\ \{F_p - [F_c \times (1 - \alpha) + F_c \times \alpha/\eta]\}/(C_E/\eta), \Delta P_{l,i,t} > 0 \\ 0, \Delta P_{l,i,t} = 0 \end{cases} \tag{5}$$

wherein, C_{in} represents the total cost of the real-time system, C_{gen} refers to the coal cost of the generator unit, C_{pun} refers to the penalty cost of abandoning wind and light, and $C_{control}$ refers to the control cost. The cost of coal-fired power generation is expressed in the form of a quadratic function of the unit output., a_i 、 b_i and

c_i are cost coefficients respectively, $P_{g,i,t}$ representing the real-time output of the generator set and N_g the number of generators in the system. The penalty cost of wind and photovoltaic power abandonment is expressed in the form of a linear function of output, η_w and η_s are respectively the grid price of wind power and photovoltaic power, $P'_{w,j,t}$ and $P'_{s,j,t}$ are respectively the maximum output power of wind power and photovoltaic power in a typical day, $P_{w,j,t}$ and $P_{s,j,t}$ are respectively the actual average output power of wind power and photovoltaic power in a period after considering the phenomenon of wind and photovoltaic power abandonment, N_w and N_s the number of wind turbines and photovoltaic stations in the system. $\Delta P_{l,i,t}$ is the regulating power of the i th industrial load in the period, and Δt is the regulating duration; C_I is the unit control cost coefficient, F_p represents the selling price per unit load (yuan/ton), F_c the production cost per unit load (yuan/ton), C_E the power consumption per unit output (kWh/ton), α the percentage of power consumption cost in the production cost of industrial enterprises, and η the power production efficiency.

The above objective functions have certain constraints:

$$\sum P_{g,i,t} + \sum P_{new,j,t} = \sum P_{L,t} + \sum \Delta P_{load,l,t} \quad (6)$$

Equation (6) represents the power balance constraint, that is, the total real-time output of thermal power unit and wind turbine is equal to the total active power of the real-time load of the system. The thermal power unit in the system has the following constraints:

$$r_{i,down} \leq P_{g,i,t} - P_{g,i,t-1} \leq r_{i,up} \quad (7)$$

$$P_{g,min} \leq P_{g,i,t} \leq P_{g,max} \quad (8)$$

$$t_{g,i,last\ min} \leq t_{g,i,last} \quad (9)$$

Equation (7), Eq. (8) and Eq. (10) respectively represent the climbing constraint, upper and lower output limit constraint and start stop time constraint of thermal power units. Wind power and photovoltaic in the system have the following constraints:

$$0 \leq P_{new,j,t} \leq P'_{new,j,t} \quad (10)$$

Equation (10) represents the upper and lower limit constraints of wind power and photovoltaic output. The industrial load in the system has the following constraints:

$$\Delta T_{l,down\ max} \leq \Delta P_{load,l} \cdot \Delta t / cm \leq \Delta T_{l,up\ max} \quad (11)$$

$$\Delta P_{load,l,down\ max} \leq \Delta P_{load,l,t} \leq \Delta P_{load,l,up\ max} \quad (12)$$

Because heat storage equipment is required in most industrial loads, its temperature needs to meet the safety production requirements. Equation (11) refers to the production temperature constraint of industrial loads. It can be seen from literature [10] that the temperature of heat storage load is related to its integrated electric quantity. Equation (12) represents the upper and lower limit constraints of industrial load adjustable capacity. In addition, there are constraints on industrial load power distribution, that is, when multiple industrial loads participate in grid regulation at the same time, the regulated power is proportional to its rated capacity.

3.2 Outer Layer Optimization

After the adjustment power of industrial load in each period of typical day is determined by the internal optimization, the final total system cost can be obtained by substituting the output plan into the external optimization model:

$$\min C_{grid} = C_{gen} + C_{pun} + C_{ploss} + \sum C_{l,invest} + \sum C_{Eb,l} \tag{13}$$

$$C_{l,invest} = F_{ncu,l} + F_{line,l}D_{line,l} + F_{MP} \tag{14}$$

$$C_{ploss} = \eta_{loss} \left(\sum_i U_i \sum_{j \in i} U_j G_{ij} \cos \theta_{ij} \right) \tag{15}$$

$$C_{Eb,l} = C_{Eb1,l} + C_{Eb2,l} \tag{16}$$

$$C_{Eb1,l} = \begin{cases} (\Delta P_{load,l,up \max} - \Delta P_{load,l,down \max}) \times R_2, & \Delta P_{load,l,t} \neq 0 \\ 0, & \Delta P_{load,l,t} = 0 \end{cases} \tag{17}$$

$$C_{Eb2,l} = \begin{cases} \Delta P_{load,l,t} \times \Delta t \times m_1 \times (24 \times R_5), & \Delta P_{load,l,t} > 0 \\ |\Delta P_{load,l,t}| \times \Delta t \times m_2 \times (2 \times 24 \times R_5), & \Delta P_{load,l,t} < 0 \end{cases} \tag{18}$$

wherein, C_{grid} represents the total cost of the power grid, C_{ploss} represents the system network loss, $\sum C_{l,invest}$ represents the investment cost of additional terminal control equipment, and $\sum C_{Eb,l}$ represents the auxiliary service compensation fees that the power grid needs to pay for industrial loads.

Peak regulation compensation income is divided into regulation reserve capacity compensation and peak regulation auxiliary service compensation. Regulation reserve capacity compensation refers to the cumulative supply compensation cost of its adjustable capacity during the period when industrial load participates in grid regulation, $C_{Eb1,l}$ represents regulation reserve capacity compensation, $\Delta P_{l,up \max}$ represents upward regulation capacity, and $\Delta P_{l,down \max}$ represents downward regulation capacity. R_2 is the compensation standard for the regulation capacity of grid

connected main body AGC (yuan/MWh); The compensation standards for peak shaving and valley filling response in peak shaving auxiliary service compensation are different, $\Delta P_{load,i,t}$ represents the actual adjustment amount of peak shaving and R_5 represents the compensation standard for deep peak shaving (yuan/MWh).

4 Industrial Load Development Planning Process

In this paper, genetic algorithm is selected to solve the industrial load development planning in the distribution network. The method flow is as follows:

1. Sort the industrial enterprises that can install additional terminal equipment in the distribution network, and generate a row matrix composed of random 0–1 variables. For example $X = [0, 0, 1, \dots, 0]$, the number of columns in the matrix is the number of industrial loads that can be developed. Each column X corresponds to the sorted industrial loads. 0 means no development, 1 means development, and each different represents a development plan. Randomly generate M initial individual combinations to become the initial population;
2. Conduct internal optimization based on the predicted output of wind power and photovoltaic on typical days to determine the output plan of thermal power units and the power regulation plan of industrial loads;
3. Substitute the output plan into the distribution network for power flow calculation. If it can be solved, the total system operation cost under this development plan will be finally obtained;
4. Select, cross and vary the population of the development plan to form the next generation of the development plan population;
5. Judge whether it has converged or reached the maximum number of iterations, jump out of the cycle and output the final results, and determine the optimal development plan.

5 Example Analysis

In this paper, three types of typical adjustable industrial loads: electrolytic aluminum, steel and polysilicon enterprises are used to analyze the development planning of participating in power grid regulation. The specific index data of three types of industrial enterprises are shown in Table 1.

The simulation system topology adopts IEEE standard 10 machine 39 node system, and 12 industrial enterprises are set at different nodes. The specific data required for its development are shown in Table 2, where Type 1 represents electrolytic aluminum, Type 2 represents submerged arc furnace, and Type 3 represents polycrystalline silicon.

Table 1 Index data of three types of industrial enterprises

Load type	Electrolytic aluminium	Submerged arc furnace	polysilicon
Production cost (yuan/ton)	12,500	3830	65,000
Selling price (yuan/ton)	14,300	4000	78,000
Power cost (yuan/kWh)	0.400	0.429	0.450
Power consumption (kWh/t)	14,000	2800	50,000
Electric energy production efficiency	50%	50%	50%
Downward adjustment cost (yuan/kWh)	0.1290	0.0607	0.260
Upward adjustment cost (yuan/kWh)	0.136	0.184	0.095

Table 2 Industrial load investment development data

Industrial load No	Type	node	Rated capacity/100 MW	Distance between equipment and substation/ km
1	1	3	4.1	3
2	1	4	4.0.1	2
3	2	15	0.76	3.5
4	2	25	0.76	1.5
5	3	18	1.22	1.5
6	3	16	1.22	2
7	1	28	4.1	2.5
8	2	8	0.76	3.5
9	3	16	1.22	3
10	1	15	4.1	3.5
11	2	21	0.76	2.5
12	3	22	1.22	2

Thermal power units are set at nodes 30, 31, 34, 36, 37 and 39, photovoltaic stations are set at nodes 32, and wind farms are set at nodes 33, 35 and 38. Finally, the total system cost for 10 years is calculated, and the optimal development plan is obtained through genetic algorithm. The row matrix consisting of 0–1 variables is $X = [1, 0, 1, 1, 0, 1, 0, 1, 1, 1, 1, 1]$. Table 3 shows the calculation results of industrial load in the system without development, full development and optimal development plan.

Table 3 Costing Results

Load type	Not developed at all	Full development	Optimal plan
Total operating cost	25,573,000	1,823,000	19,889,000
Load control cost	0	111,747	76,793
Network loss cost	7,877,500	7,876,700	7,876,800
Compensation expenses	0	6,311,159	3,961,081
Investment cost	0	9,600,000	7,200,000
Total system cost	10,035,087,621	9,701,424,703	9,502,226,400

To sum up, the total system cost of the industrial load optimal development plan is less than the total system cost after the industrial load is fully developed. The main influencing factors are the compensation cost of auxiliary services and the investment cost of additional control terminal equipment. The total cost of the system after the industrial load is fully developed is less than the total cost of the system that is not fully developed, and the main influencing factor is the total cost of the operation phase.

6 Conclusion

The main work of this paper is to comprehensively consider the planning and operation problems of industrial load participating in power grid regulation, propose a two-level optimization model for industrial load development planning, and solve the model using genetic algorithm. Finally, IEEE10 machine 39 bus system is used to verify the effectiveness of the method proposed in this paper, which proves that the development of the adjustable potential of the power grid for industrial load should select the appropriate load for development, rather than all development, under the principle of economy. The method proposed in this paper can provide an important reference for the large-scale installation of industrial load control terminal equipment oriented to grid interaction response and the development of the adjustable potential of industrial load.

Acknowledgements This research is supported by Program of Research and demonstration application of key technologies for large-scale adjustable load resource assessment, planning and operation, and optimal regulation (Grant 2021ZK52).

References

1. Zhuo, Z., Zhang, N., Xie, X., et al.: Key technologies and development challenges of high proportion renewable energy power system. *Autom. Elect. Power Syst.* **45**(9), 171–191 (2021). (in Chinese)
2. Wei, H., Zhuo, Z., Zhang, N., et al.: Analysis on optimization and influencing factors of carbon peak and carbon neutral transformation path of China's power system. *Autom. Elect. Power Syst.* 1–13 [2022–09–04]. (in Chinese)
3. Liao, S.: Research on frequency control method of high energy consumption load participating in high permeability isolated wind power grid. Wuhan University, Wuhan (2016). (in Chinese)
4. Tu, X., Xu, J., Liao, S., et al.: Energy consumption behavior analysis and power characteristic modeling of steel industry load considering process control. *Autom. Elect. Power Syst.* **42**(02), 114–120 (2018). (in Chinese)
5. Pan, C., Fan, G., Wang, J., et al.: Low carbon optimization of integrated electric heating energy system involving flexible resources [J/OL]. *Trans. China Electrotechn. Soc.* 1–14 [2022–09–26]. <https://doi.org/10.19595/j.cnki.1000-6753.tces.211725>. (in Chinese)
6. Zheng, L., Hu, W., Lu, Q., et al.: Comprehensive optimization model for planning and operation of energy storage system to improve wind power access. *Proc. CSEE* **34**(16), 2533–2543 (2014). (in Chinese)
7. Li, Z., Chen, S., Fu, Y., et al.: Optimal allocation of energy storage in active distribution network based on time series voltage sensitivity. *Proc. CSEE.* **37**(16), 4630–4640+4888 (2017). (in Chinese)
8. Xu, B., et al.: Scalable planning for energy storage in energy and reserve markets. *IEEE Power Energy Soc. Gener. Meet. (PESGM)* **2018**, 1–1 (2018)
9. Xiong, P., Singh, C.: Optimal planning of storage in power systems integrated with wind power generation. *IEEE Trans. Sustain. Energy* **7**(1), 232–240 (2016)
10. Nikoli, D., Negnevitsky, M., de Groot, M., et al.: Fast demand response as an enabling technology for high renewable energy penetration in isolated power systems. In: *IEEE PES General Meeting*, July 27–31, 2014, Washington DC, USA (2014)

Diagnosis Method for Inter-Turn Short Circuit in Winding Based on Feature Extraction of Traveling Wave



Haipeng Zhao, Mengjiao Xue, Chu Li, Jianpan Lyu, Liming Huang, Hongyue Men, E Yiyang, and Min Peng

Abstract Aiming at the problem that the early inter-turn short circuit fault of the dry-type air-core reactor is not easy to detect, this paper proposes a method to detect the inter-turn short-circuit fault by using the characteristic value extracted from the traveling wave waveform. Firstly, by inputting a signal at the head of the dry-type reactor winding to obtain the traveling wave reflection response signal at the head and end of the winding. Then, based on the response signal, the characteristic waveform is built and the characteristic value is extracted, and the characteristic quantity is used as the judgment basis for the fault diagnosis of inter-turn short circuit. Finally, the diagnosis method proposed in this paper is verified by conducting an inter-turn short circuit fault diagnosis experiment on an outdoor dry-type reactor. Experimental results show that the variation of characteristic value is consistent with the simulation results, so the method proposed in this paper can be applied to the diagnosis of inter-turn short circuit faults in different structures of reactors.

Keywords Dry-type Air-core Reactor · Winding Fault · Feature Extraction · Traveling Wave Theory · Fault Diagnosis

1 Introduction

The dry-type air-core reactor is widely used in different voltage levels from 6 to 1000 kV and is an important piece of equipment in converter stations and substations [1, 2]. According to electric power department statistics, inter-turn short circuit

H. Zhao · M. Xue · C. Li · J. Lyu · L. Huang · H. Men · M. Peng
State Grid Xinjiang Electric Power Co., Ltd. EHV Branch Company, Ürümqi 830002, China

E. Yiyang (✉)
Hubei Engineering Research Center for Safety Monitoring of New Energy and Power Grid Equipment, Hubei University of Technology, Wuhan 430068, China
e-mail: 704797476@qq.com

Xiangyang Industrial Institute of Hubei University of Technology, Xiangyang 441100, China

fault is the main reason for equipment fault of the dry-type air-core reactor, which accounts for more than 70%. When the dry-type air-core reactor is working, the huge circulating current formed by the inter-turn short circuit will make the local temperature rise sharply [3], which will accelerate the insulation failure and induce damage to the reactor leading to a fire. Therefore, timely detection of winding inter-turn short circuit faults is of great practical importance to the maintenance of dry-type air-core reactors.

When the conductor insulation is faulty, the distributed parameters of the conductor will change, accordingly, the refraction and reflection propagation process of the traveling wave signal along the conductor will change [4]. The traveling wave method is to use propagation characteristics of the traveling wave signal in the winding to determine the state and location of defects, and the method has been used in some areas such as cable fault location [5, 6]. In recent years, some scholars have also applied the traveling wave method to the diagnosis of transformer inter-turn short circuit defects and achieved some results [7]. Reactors are coil-type devices like transformers, theoretically, the traveling wave method is also applicable to reactors.

This paper investigates the application of traveling wave theory in the diagnosis of inter-turn short circuit of the reactor. Firstly, the propagation process of traveling wave in winding is analyzed theoretically. Then, a distributed-parameter model of reactor combined is built with multi-conductor transmission line theory. Finally, the effect of an inter-turn short circuit on the response signal at the head and end of the reactor is analyzed after signal injection. On this basis, this paper proposes to construct feature waveforms by integrating the response signal and extracting eigenvalues, and analyzing the influence law of the number of fault turns and position on the eigenvalues.

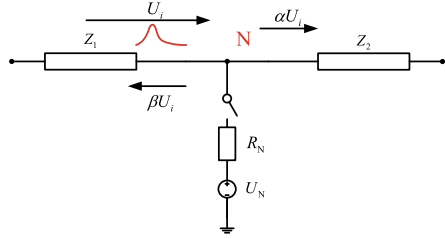
2 Mathematical Model of Dry Reactor Winding Wave Process

2.1 Refraction and Reflection of Traveling Waves

Reflection and refraction are the basic characteristics of traveling waves propagating along conductors. When the wave propagates along the transmission line, it can be divided into forward and reverse waves. When the forward wave propagates along the transmission line, refraction and reflection will occur at node where the wave impedance changes abruptly, in which the reflected wave propagates backward as a reverse wave, and the refracted wave continues to propagate forward as a new forward wave. The refraction and reflection of the traveling wave at the fault point are usually analyzed by Peterson law [8]. Figure 1 is a schematic diagram of the refraction and reflection after the traveling wave propagates to the fault point.

Where Z_1 , Z_2 – the wave impedance of the line before and after the fault point N, R_N – transition resistance at fault point, U_N – equivalent power supply at fault point,

Fig. 1 Peterson Law Equivalent Circuit



U_i – incident wave, α – refractive coefficient, β – reflection coefficient. According to Peterson’s Law:

$$\alpha = \frac{2Z_2}{Z_1 + Z_2} \tag{1}$$

$$\beta = \frac{Z_2 - Z_1}{Z_1 + Z_2} \tag{2}$$

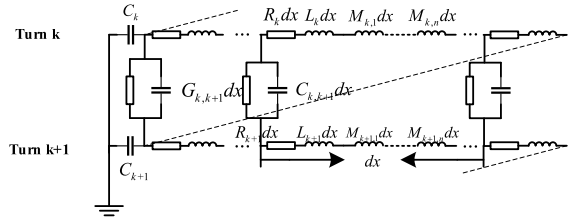
2.2 MTL Model of Dry-Type Air-Core Reactor Winding

Firstly, considering the average diameter of the coil is much larger than the radial width of the winding, thus the effect of bending the wire turns can be ignored. Secondly, the average turn length of the coil is longer than the cross-sectional size of the coil, so the delay of the voltage wave propagation along the axial and radial directions can be ignored. Thirdly, each turn of the coil can be viewed as a uniform transmission line of approximately equal length arranged laterally. Through the above analysis, the wave transmission process in the reactor winding can be analyzed with the help of the multiconductor transmission line theory [9, 10]. Figure 2 shows the schematic diagram of the parasitic parameters equivalent circuit model of the dry-type air-core reactor. Where R_k - equivalent resistance per unit length of the k-turn wire, L_k - equivalent self-inductance per unit length of the k-turn wire, C_k - equivalent capacitance to ground per unit length of the k-turn wire, $M_{k,k+1}$ - mutual inductance between the k-turn wire and the k + 1-turn wire, $C_{k,k+1}$ - inter-turn capacitance between the k-turn wire and the k + 1-turn wire.

3 Simulation Model Construction

The calculation of distributed parameters is the basis for the construction of the MTL model. The parameters required by the winding MTL model include unit resistance, self-inductance, inter-turn mutual inductance, inter-turn capacitance, capacitance to

Fig. 2 Distributed parameters equivalent circuit model of reactor windings



ground, etc. [11]. Although can use analytical methods or empirical formulas to calculate the above parameters, the above methods are obtained based on a series of equivalent simplifications, and large errors may occur when calculating the distributed parameter matrix of the reactor. For the sake of accuracy, this paper uses finite element analysis to calculate the parameter matrix required by the MTL model [12].

Considering the symmetry of the reactor structure, the winding model can be equivalent to a two-dimensional axisymmetric model. This paper refers to the structure and size of the CKGKL-16.7/10-1W outdoor dry-type air-core reactor, and the established simulation model is shown in Fig. 3. The model size setting parameters are shown in Table 1.

Considering that the capacitance is less affected by the frequency, use the energy method to obtain the capacitance to ground and mutual capacitance matrix of each conductor under the electrostatic field, and convert it into a potential coefficient matrix of unit length [13]. As for solving the inductance and resistance matrices, it is necessary to consider the high-frequency skin effect. According to relevant research [14], in the case of high frequency, the influence of the increase of frequency on the inductance is no longer obvious, so this paper selects 1 and 20 MHz as the

Fig. 3 Winding finite element analysis model

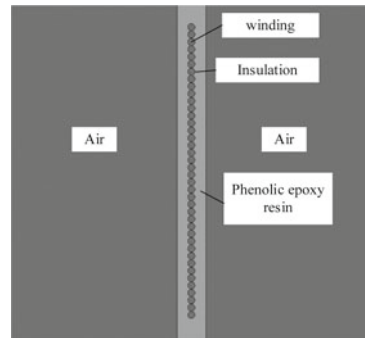


Table 1 Size parameters

Turns	Conductor radius	Winding inner radius	Winding height
40	1.2 mm	343 mm	410 mm

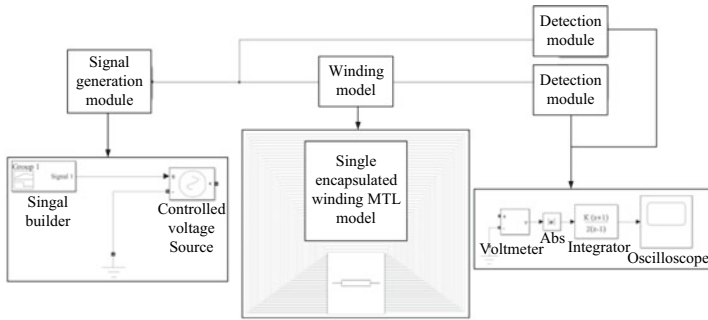


Fig. 4 Simulation circuit of inter-turn short circuit fault of reactor

solution environment and uses voltammetry to extract the inductance and resistance parameters [15].

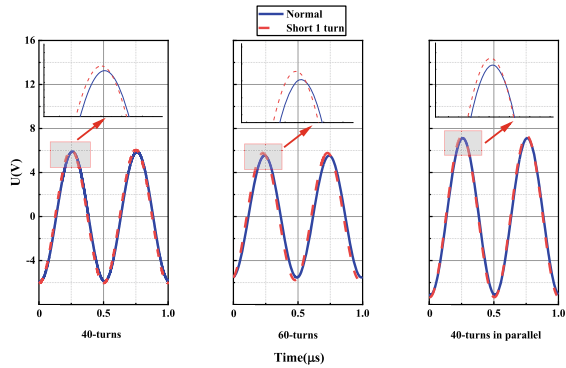
This paper uses the distributed parameter line module in Matlab/Simulink software and the calculated distributed parameters to build the MTL model of the dry-type air-core reactor winding [16], as shown in Fig. 4. In this model, inter-turn short circuit faults are simulated by shorting the terminals corresponding to different turns.

4 Simulation

4.1 Sine Wave

Using the established simulation model and the distribution parameters obtained in the 1 MHz environment, the simulation calculations are carried out for the windings in the condition of a normal working state and the one-turn short circuit fault at the head. A 10 V sinusoidal voltage signal with a frequency of 1 MHz is injected at the head of the model, and the response signal detected at the end is shown in the figure below. As the number of short-circuit turns increases, the equivalent reactance value of the reactor decreases [17], thereby reducing the blocking effect of the reactor on AC, and it is the reason for the increase in the amplitude of the response signal in the simulation results. To investigate the influence of the coil structure, simulation calculations were carried out under the condition of three groups of 40-turn windings in parallel and 60-turn single windings. According to the calculation results, the changing trend of the response signal is the same as that of the 40-turn single winding (Fig. 5).

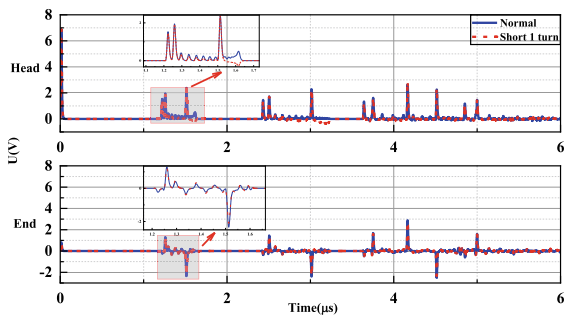
Fig. 5 Response signal waveform comparison



4.2 Pulse Signal

Using the distribution parameters obtained in the 20 MHz environment, a pulse signal with an amplitude of 7 V and pulse width of 50 ns is injected at the head of the winding model, and the response signal is extracted at the head and end of the model respectively. The response signal waveform is shown in Fig. 6. Considering that when the number of short-circuit turns is few, the slight difference between the wave peaks may also be misjudged by on-site interference in actual detection, so the characteristic waveform is constructed by integrating the absolute value of the waveform to highlight the difference in the detection results under different insulation states. Also, same as above, to investigate the influence of the coil structure, simulation calculations were carried out under the condition of three groups of 40-turn windings in parallel and 60-turn single windings. The characteristic waveforms in the three cases are shown in the figure below. It can be seen from Fig. 6 that the echo signals obtained at the head and the end show a certain interval. Corresponding to the integral stable interval in Fig. 7, the characteristic waveform generally presents a step-up trend, and the interval between the sum of the integral rising interval and the stable interval of each step is the same.

Fig. 6 Waveform comparison



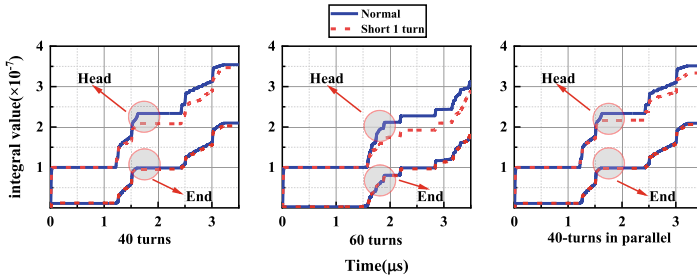


Fig. 7 Characteristic waveforms

Comparing the simulation calculation results under three conditions, it is found that the variation law of the characteristic waveform under different structures is similar to 40 turns. Therefore, the following article focuses on analyzing the influence of inter-turn short circuits on the characteristic waveform based on a 40-turns structure.

4.3 Eigenvalue Construction

Based on the characteristics of the amplitude change of the AC response signal and the step change of the pulse characteristic waveform in the simulation, this paper proposes the characteristic values E_1 , E_2 , and E_3 to continue to study the inter-turn short-circuit fault of the dry-type air-core reactor. Among them, E_2 and E_3 are further divided into head eigenvalues (E_{2-h} , E_{3-h}) and end eigenvalues (E_{2-e} , E_{3-e}).

$$E_1 = \frac{U_h}{U_e} \tag{3}$$

$$E_2 = \frac{S_2}{S_1} \tag{4}$$

$$E_3 = \frac{S_3}{S_1} \tag{5}$$

where, U_h - the amplitude of the AC injected at the head, U_e - amplitude of the response signal at the end, S_1 - the first step value of the head and end characteristic waveforms, S_2 - the second step value of the head and end characteristic waveforms, S_3 - the third step value of the head and end characteristic waveforms. Since E_1 mainly reflects the change of the winding reactance value, the research on E_1 only focuses on the number of short-circuit turns. The research on E_2 and E_3 focuses on the location of the short circuit and the number of short-circuit turns. With the change

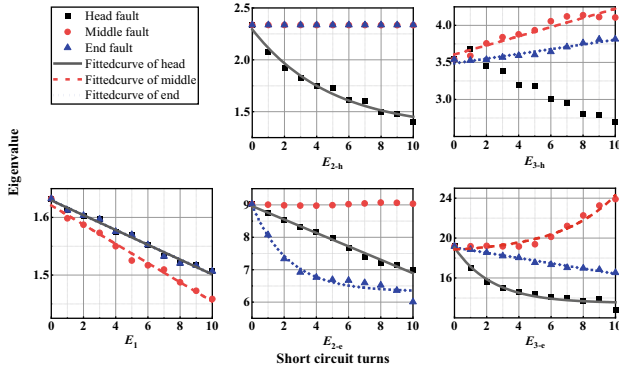


Fig. 8 Variation of eigenvalues with different short-circuit positions and severity

of the short-circuit position and the number of short-circuit turns, the changes of E_1 , E_2 , and E_3 are shown in Fig. 8.

The above five eigenvalues vary with the position and severity of the inter-turn short circuit, and the variation rules of the five eigenvalues can be seen in Table 2. Therefore, the different inter-turn short circuit faults can be comprehensively diagnosed with the help of the above five eigenvalue variation rules. First, use E_1 to predict the fault, and then use E_2 and E_3 to diagnose the severity and position of the short-circuit fault.

Observing the trend of eigenvalues changing with the number of short-circuit turns in the figure, it is found that the changing trend of eigenvalues conforms to a certain law. The fitting analysis of the eigenvalues shows that there is a linear or exponential relationship between the number of short-circuit turns, and $R^2 > 9.5$. The specific fitting function can be seen in Table 2. Using the same method, the waveform eigenvalues of 60-turn single-winding and 40-turn 3-winding structures under different winding insulation states are calculated, and some calculation results are shown in Fig. 8. The calculation results show that the change law of the five eigenvalues in the above case is consistent with that of the 40-turn single winding,

Table 2 Variation of eigenvalues of different inter-turn insulation states

	Head fault	Middle fault	End fault
E_1	$y = 1.6207 - 0.0166 * x \downarrow$	$y = 1.6296 - 0.0128 * x \downarrow$	$y = 1.6208 - 0.0165 * x \downarrow$
E_{2-h}	$y = 0.9645 * e^{-\frac{x}{4.8179}} + 1.3294 \downarrow$	/	/
E_{3-h}	/	$y = 3.6070 + 0.0617 * x \uparrow$	$y = 3.4872 + 0.0319 * x \uparrow$
E_{2-e}	$y = 8.9641 - 0.2071 * x \downarrow$	/	$y = 2.6815 * e^{-\frac{x}{2.2375}} + 6.3270 \downarrow$
E_{3-e}	$y = 5.5680 * e^{-\frac{x}{2.3760}} + 13.4828 \downarrow$	$y = 0.3387 * e^{\frac{x}{3.5224}} + 18.5136 \uparrow$	$y = 19.0552 - 0.2633 * x \downarrow$

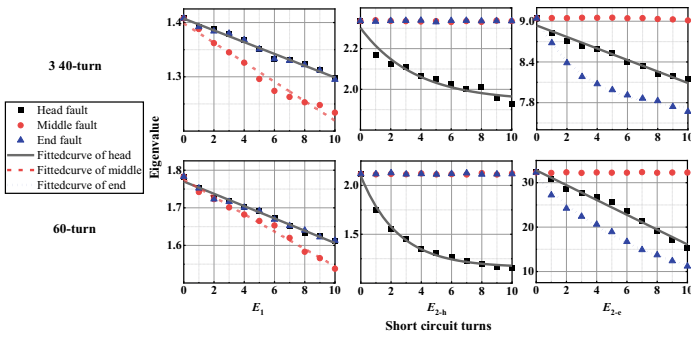


Fig. 9 Variation of eigenvalues for different winding structures

which further shows that the changing trend of the proposed eigenvalues can be used to diagnose the inter-turn short circuit of reactors with different structures (Fig. 9).

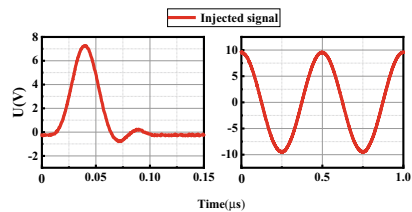
5 Experimental Verification

To verify the correctness of the diagnostic method proposed in this paper, a 100-turn winding was wound about the CKGKL-16.7/10-1W outdoor dry-type air-core reactor. In the case of short-circuiting 3 turns at the head, middle and end, the response signals were collected and the eigenvalues were calculated. The injected signal is shown in Fig. 10. The response signal and characteristic curve are shown in Fig. 11.

Because the pulse injected each time will be slightly different in the actual measurement, also, there will inevitably be external interference, which will lead to a small increase in an integral stable interval of the characteristic waveform. Therefore, the values of S_1 , S_2 , and S_3 are all taken as the median of the rising amplitudes in the stable interval. The solution results and changing trends are shown in Table 3.

It can be seen from Table 3 that the variation trend of the eigenvalues obtained in the experiment is consistent with the simulation results, which can preliminarily verify the feasibility and correctness of the method proposed in this paper.

Fig. 10 Injected pulse signal and sinusoidal signal



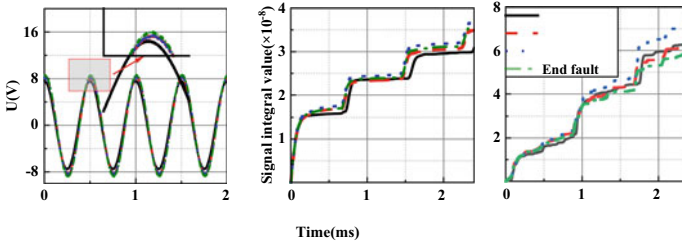


Fig. 11 Response signal and characteristic waveform

Table 3 Eigenvalues of short-circuit at different positions of the winding

	Normal	Head fault	Middle fault	End fault
E_1	1.28	1.21↓	1.15↓	1.21↓
E_{2-h}	1.51	1.40↓	/	/
E_{3-h}	1.86	/	2.00↑	1.92↑
E_{2-e}	2.69	2.21↓	/	2.36↓
E_{3-e}	3.93	3.12↓	4.16↑	3.37↓

6 Results

Based on the multi-conductor transmission line theory, this paper researches the application of the traveling wave method in the fault diagnosis of the inter-turn short circuit of dry-type air-core reactor:

1. Referring to the dry-type air-core reactor winding structure, the distributed parameters are calculated by finite element simulation, and the MTL distributed parameter simulation model of the winding structure is constructed.
2. The characteristic waveform is constructed by integrating the absolute value of the impulse response signal. Based on the sinusoidal response signal and pulse characteristic waveform, five eigenvalues are proposed for the diagnosis of inter-turn short-circuit faults, which improve the identifiability of inter-turn short-circuit faults.
3. E_1 is used for pre-judgment, and the changing trend of E_2 and E_3 is used to comprehensively diagnose the severity and position of inter-turn short-circuit faults. The comparison between the simulation and the experimental results shows that the above method can be applied to the inter-turn short circuit diagnosis of dry-type air-core reactors with different winding structures.

Acknowledgements This research is supported by Science and Technology Project of SGCC (Grant No. SGXJX00YJJS2200119).

References

1. Leitch, J.D.: Transactions of the American Institute of electrical engineers. *IEEE J. Mag.* **68**(1), 469–475 (1949)
2. Guo, Y., Xian, R., Leng, X., Hao, Y., Li, Z.: Study on fault characteristics of layer short circuit of dry-type air-core series reactor. *Mob. Inf. Syst.* **2022** (2022). ID: 5429807
3. Bi, D., Wang, X., Wang, W.: Measured impedance based shunt reactor protection against small inter-turn fault. *Autom. Electr. Power Syst.* **29**(3), 57–60 (2005). (in Chinese)
4. Li, M., Liu, J., Ma, N., Zhu, T., Zhou, W., Zhou, C.: A novel traveling-wave-based method improved by unsupervised learning for fault location of power cables via sheath current monitoring. *Sensor* **19**(9), 2083 (2019)
5. Wang, D., Hou, M., Guo, Y.: Travelling wave fault location of HVAC transmission line based on frequency-dependent characteristic. *IEEE Trans. Power Deliv.* **36**(6), 3496–3505 (2021)
6. Leite, E., Lopes, F., Costa, F., Neves, W.: Closed-form solution for traveling wave-based fault location on non-homogeneous lines. *IEEE Trans. Power Deliv.* **34**(3), 1138–1150 (2019)
7. Li, Z., Peng, M., Huang, Q., Wan, X., Liu, D.: Application of the traveling-wave reflection method in inter-turn short fault location for transformer. *Power Syst. Prot. Control* **44**(21), 84–89 (2016). (in Chinese)
8. Naidu, O., Pradhan, A.: A traveling wave-based fault location method using unsynchronized current measurements. *IEEE Trans. Power Deliv.* **34**(2), 505–513 (2019)
9. Liang, G., Zhu, X., Dong, H.: Simulation modeling of transformer windings at high frequencies. *High Volt. Eng.* **35**(2), 393–398 (2009). (in Chinese)
10. Ji, T., Tang, W., Wu, Q.: Detection of power transformer winding deformation and variation of measurement connections using a hybrid winding model. *Electr. Power Syst. Res.* **87**, 39–46 (2012)
11. Liu, X., Zheng, T., Huang, T.: Protection scheme based on the identification of equivalent leakage inductance against turn-to-turn fault of magnetically controlled shunt reactor. *Trans. China Electrotechnical Soc.* **35**(1), 134–145 (2020). (in Chinese)
12. Wang, P., Zhao, Y., Lü, F., Li, K., Ding, Y.: Distribution of electric field and structure optimisation on the surface of a +/- 1100 kV smoothing reactor. *IET Sci. Meas. Technol.* **13**(3), 441–446 (2019)
13. Yang, Y., Wang, Z.: Piecewise frequency-domain modeling of large power transformer windings for very fast transient overvoltage simulations. *Proc. CSEE* **30**(10), 66–71 (2010). (in Chinese)
14. Ruan, L., Zhao, C., Ruan, J., et al.: Calculation of distributed parameters of transformer winding based on the model of multi-conductor transmission line. *High Volt. Apparatus* **45**(4), 41–46 (2009). (in Chinese)
15. Popov, M., Van, S., Paap, G., et al.: Computation of very fast transient overvoltages in transformer windings. *IEEE Trans. Power Deliv.* **18**(4), 1268–1274 (2003)
16. Liu, D., Peng, M., Wan, X., et al.: Inter-turn short-circuit fault location for transformer winding based on traveling wave analysis. *Chin. J. Sci. Instrument* **36**(9), 2091–2096 (2015). (in Chinese)
17. Xian, R., Lu, Y., Chen, L., Geng, K., Wang, Y., Yin, B.: Fault characteristics of an inter-turn short circuit of a dry-type air-core series reactor. *Power Syst. Prot. Control* **49**(18), 10–16 (2021). (in Chinese)

Research on Output Characteristics of Vibrational Energy Harvesting Device Based on Double Crystal Piezoelectric Cantilever Beam Structure



Yuqing Sun, Zhiye Du, Mouyuan Chen, and Xinyi Huang

Abstract With the rapid development of social economy, the research and development of vibration energy, friction energy, electromagnetic energy and other micro energy harvesting devices have come into the public's vision and continue to deepen. In order to meet the requirements of miniaturization and passivity of the energy harvesting device, a dynamic energy harvesting device for double-crystal cantilever beam was designed based on the principle of piezoelectric effect. Through the COMSOL finite element software simulation calculation, the relationship between the output steady-state voltage of the cantilever beam device and the external load and vibration frequency was determined, the output voltage characteristics of the device was obtained, and the relationship between the output voltage of the energy extraction device and the amplitude of the vibration free end was obtained. A 50 Hz sinusoidal shaking table was used to measure the steady-state output voltage of the cantilever beam at different amplitudes, and the output efficiency and load capacity under different external resistance. Compared with the finite element simulation results under ideal conditions, the effectiveness of the model is verified. This is of great significance for further research and development of self-powered energy cells with vibration energy acquisition objects.

Keyword Double-crystal piezoelectric cantilever · Finite element simulation · Output steady-state voltage · External resistance value · Vibrational energy

1 Introduction

With the development of smart grid and various miniature low-power devices, the replacement of wireless sensors used in power system networks is difficult, costly and dangerous. The disadvantages of the traditional chemical battery such as short service life and repeated disassembly make it unable to meet the needs of modern power grid

Y. Sun (✉) · Z. Du · M. Chen · X. Huang

School of Electrical Engineering and Automation, Wuhan University, Wuhan 430072, China
e-mail: 1772476019@qq.com

© Beijing Paiké Culture Commu. Co., Ltd. 2023

X. Dong et al. (eds.), *The proceedings of the 10th Frontier Academic Forum of Electrical Engineering (FAFEE2022)*, Lecture Notes in Electrical Engineering 1054, https://doi.org/10.1007/978-981-99-3408-9_109

1217

construction. The collection of environmental energy such as solar energy, vibration energy and electromagnetic energy to replace the traditional chemical battery power supply has become a research hotspot in the direction of reserve energy. Therefore, it is a forward-looking and environment-friendly solution to apply the energy collection technology with the characteristics of “self-collection and self-use” to power the wireless sensor [1].

With the development of power monitoring sensors towards low power consumption and miniaturization, environmental spurious energy supply has become a new power supply approach. Taking the transformer in the current power network system as an example, there is a lot of vibration energy in the working environment of the transformer. It is an efficient way to collect the vibration energy in the working environment and use it in the wireless sensor of the transformer. Vibration energy collection technology includes piezoelectric, electrostatic, electromagnetic and composite, etc. Because of the advantages of simple structure, small size, no pollution, low-cost, high-energy density and so on, piezoelectric has gradually become the focus of energy research of micro electronic devices [2]. How to effectively utilize the positive piezoelectric effect of the piezoelectric vibrator to efficiently and sustainably convert the weak and unstable vibration mechanical energy into electric energy has become a key problem in the field of piezoelectric energy acquisition [3].

According to the existing research results, the main factors that affect the generating capacity of the piezoelectric vibration energy collector are: the structural parameters of the cantilever beam, the parameter plate of the piezoelectric oscillator, the piezoelectric resonant frequency, the amplitude of the external vibration source and the parameters of the fixed mass block at the free end of the cantilever beam.

Kan et al. [4] established a simulation and analysis model for the power generation capacity of single and double crystal piezoelectric beams, studied the influence laws of structure size, excitation mode and material properties on their power generation capacity, and concluded that the maximum power generation of double crystal beams was about twice that of single crystal beams. Sodano et al. [5] designed a double-crystal piezoelectric cantilever beam type vibration energy collector. By adjusting the structure size, the main frequency of the system is synchronized with the frequency of the external vibration source. Zhang et al. [6] explored the influence of different connection modes of double-crystal piezoelectric plates on the collector's power generation characteristics, internal resistance, output voltage and output power at different speeds of the motor, and concluded the optimal connection mode of double-crystal piezoelectric plates with two electrodes in parallel. Based on the distributed parameter model of the cantilever piezoelectric vibration energy collector, Tian [7] optimized the mass block length, electrode length, cantilever beam width and other parameters of the micro piezoelectric vibration energy collector, and analyzed the influence of the piezoelectric layer's Young's modulus and mechanical damping ratio on the optimization results. Kim et al. [8] proposed an electromechanical coupling model of a cantilever piezoelectric energy collector with proof mass, proving that mass is the key to moving device resonance to the optimal frequency point for collection, which is of great significance for optimizing device design for various applications and quantifying the performance of nonlinear (structural and

piezoelectric coupling) devices. Xie [9] studied the influence of changing the height of the center of mass on the natural frequency and output voltage of the system by changing the shape of the mass block. He found that when the mass of the mass block remained the same, with the increase of the height of the center of mass, the first-order natural frequency of the system would decrease while the power generation capacity would also increase. By changing the material of the piezoelectric plate, using flexible phosphor bronze as the supporting layer and thin PZT thick film as the piezoelectric layer, Tian [10] reduces the resonant frequency of the piezoelectric device and improves the durability of the piezoelectric device.

On this basis, the external load resistance, resonant frequency and vibration amplitude of the double-crystal piezoelectric cantilever are studied. Through experiments, the output voltage under different vibration amplitude with fixed excitation frequency, the output steady-state voltage and power under different external loads and the load capacity of the double-crystal piezoelectric cantilever beam device were investigated. Through simulation, the relationship between the output characteristics and the excitation frequency under fixed amplitude is explored.

2 Theoretical Research

2.1 Piezoelectric Effect

There are two modes of piezoelectric effect: positive piezoelectric effect and inverse piezoelectric effect. The double-crystal piezoelectric cantilever is developed based on the positive piezoelectric effect. The positive piezoelectric effect is a phenomenon in which the shape of an object changes to generate electrical polarization and convert mechanical energy into electrical energy. The inverse piezoelectric effect is the opposite of the positive piezoelectric effect, that is, electricity is applied to the surface of the piezoelectric material, resulting in the deformation of the piezoelectric material, and the conversion of electric energy into mechanical energy is realized. Positive piezoelectric effect and inverse piezoelectric effect exist at the same time. It is impossible to have a piezoelectric material with only positive piezoelectric effect or only inverse piezoelectric effect.

There are two working modes of piezoelectric effect: d33 and d31 [11]. The difference between these two working modes is that the force direction is perpendicular to the polarization direction in d31 mode, while the force direction is parallel to the polarization direction in d33 mode.

d31 mode is mostly used in cantilever beam device. In this paper, a double-crystal piezoelectric cantilever beam device which adopts d31 mode is simulated and tested, and the relationship between the output steady-state voltage and the external load resistance and the external excitation frequency is studied under the external vertical sine wave vibration excitation.

2.2 Theoretical Calculation of Double Crystal Piezoelectric Cantilever Beam

Double-crystal piezoelectric cantilever beam device is the cantilever beam fixed on system response to expand the amplitude, to drive the cantilever beam piezoelectric material deformation, thus generating electric energy, and then through the circuit to collect and store the energy for the use of low power devices.

The double-crystal piezoelectric cantilever beam device is composed of a cantilever beam support layer, a base, a double-layer PZT piezoelectric layer and a terminal mass block. Compared with the conventional single-crystal cantilever beam, the double-crystal piezoelectric plate has better voltage output and higher energy efficiency under the same external excitation. The double-crystal piezoelectric cantilever device designed in this paper is shown in Fig. 1.

In the double-crystal piezoelectric cantilever device, the PZT piezoelectric layers are connected in parallel, and each piezoelectric layer can be equivalent to the parallel connection of a controlled power supply and an internal capacitor.

According to Kirchhoff’s law, the circuit equation of the above configuration can be derived as follows:

According to Kirchhoff’s law, the circuit equation of the above configuration can be derived as follows:

$$C_{\bar{p}} \frac{dv_p(t)}{dt} + \frac{v_p(t)}{2R_1} - i_{\bar{p}}^p(t) = 0 \tag{1}$$

$$C_{\bar{p}} = \frac{\epsilon_{33}^s bL}{h_{\bar{p}}}, i_{\bar{p}}^p(t) = - \sum_{r=1}^{\infty} k_r \frac{d\eta_r^p(t)}{d(t)} \tag{2}$$

The relation of k_r is as follows:

$$k_r = e_{31} h_p b \int_0^L \frac{d^2 \varphi_r(x)}{dx^2} dx \tag{3}$$

Equation (3) is substituted into the ordinary differential equation with modal coordinates (1) as follows:

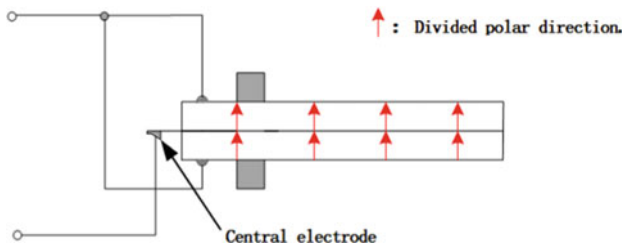


Fig. 1 Diagram of double-crystal piezoelectric cantilever device in parallel

$$\frac{d^2\eta_r^p(t)}{dt^2} + 2\zeta_r\omega_r \frac{d\eta_r^p}{dt} + W_r^2\eta_r^p(t) - \chi_r^p v_p = f_r(t) \tag{4}$$

The modal electromechanical coupling terms are:

$$X_r^p = \vartheta_p \frac{d\phi_r(x)}{dx} |_{x=L} \tag{5}$$

Based on the linear system hypothesis, it is assumed that the frequency of the device and the excitation frequency of the device are the same:

$$\eta_r^p(t) = H_r^p e^{j\omega t}, v_p(t) = V_p e^{j\omega t} \tag{6}$$

It can also be obtained from (2):

$$(\omega_r^2 - \omega^2 + j2\zeta_r\omega_r\omega)H_r^p - \chi_r^p V_p = F_r \tag{7}$$

$$\left(\frac{1}{2R_1} + j\omega C_{\bar{p}}\right)V_p + j\omega \sum_{r=1}^{\infty} k_r H_r^p = 0 \tag{8}$$

The steady-state voltage response can be obtained from [12]:

$$V_p(t) = \frac{\sum_{r=1}^{\infty} \frac{-j\omega k_r F_r}{\omega_r^2 - \omega^2 + j2\zeta_r\omega_r\omega}}{\frac{1}{2R_1} + j\omega C_{\bar{p}} + \sum_{r=1}^{\infty} \frac{j\omega k_r \chi_r^p}{\omega_r^2 - \omega^2 + j2\zeta_r\omega_r\omega}} \tag{9}$$

It can be concluded that the output steady-state voltage of the double-crystal piezoelectric cantilever is proportional to the external resistance R.

3 COMSOL Simulation of Steady-State Output Voltage

COMSOL finite element software was used to model and simulate the double-crystal piezoelectric cantilever device. Through the simulation, the output charge characteristic curve of the double-crystal piezoelectric cantilever device was explored when the free end of the double-crystal piezoelectric cantilever beam was fixed amplitude, and the excitation frequency was applied.

The model is shown in Fig. 2. In the stress field, the bottom of the base is fixed as the constraint, PZT-5H is selected as the piezoelectric material, the upper and lower ends of the device are grounded by PZT piezoelectric material, and the support layer in the middle of the double-crystal piezoelectric plate is used as the output charge end to give gravity to the whole device. The cantilever beam support is set to be 30 mm wide, 13 mm thick and 20 mm long, and the mass block is 30 mm wide,

2.1 mm thick and 10 mm long. The overall width of the cantilever beam is 30 mm thick, 0.6 mm thick and 80 mm long, and each of the three layers is 0.2 mm thick.

Taking the amplitude of the free end of the double-crystal piezoelectric cantilever as the starting point, different stress changes occur on the surface of the double-crystal piezoelectric cantilever under the action of external excitation. Figure 3 shows the vibration cloud image of the modeled cantilever beam under 50.1 Hz excitation.

The free end displacement was set as 4.8 mm to explore the relationship between output and excitation frequency. Figure 4 shows the ideal results obtained by simulation of the output voltage and output power of the double-crystal piezoelectric cantilever device with no load.

It can be seen from Fig. 4 that when the amplitude of the free end is determined, the output voltage and electric energy generated by the positive piezoelectric effect are positively correlated with the excitation frequency, and the output mechanical energy is also positively correlated with the excitation frequency due to the existence of the inverse piezoelectric effect, and the output curves of the mechanical energy and electric energy basically coincide.

Fig. 2 Simulation diagram of double-crystal piezoelectric device

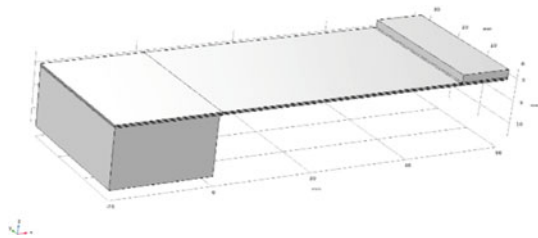
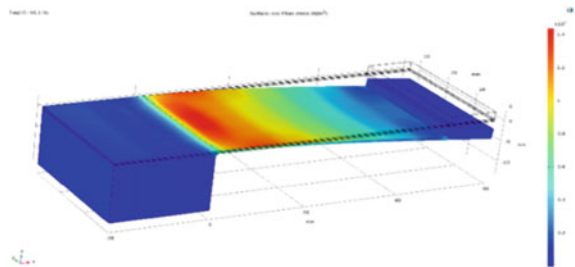


Fig. 3 Displacement nephogram of two-crystal piezoelectric device under external excitation



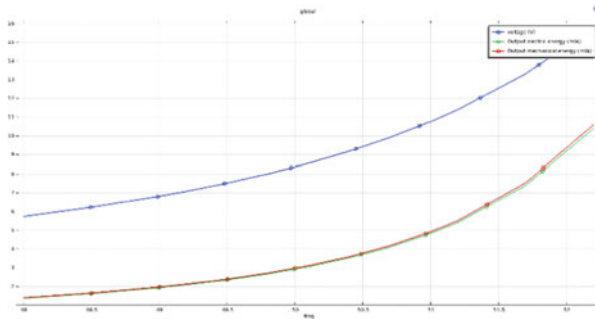


Fig. 4 Excitation and output curves of double-crystal piezoelectric cantilever device

4 Experimental Inquiry

In the case of the relationship between the double-crystal piezoelectric cantilever device and the external resistance value, the conclusion that the steady-state output voltage of the double-crystal piezoelectric cantilever device is proportional to the external resistance R is verified by experiments, and the load capacity of the double-crystal piezoelectric cantilever is tested.

A double-crystal piezoelectric arm was constructed with PZT-5H as the piezoelectric material and copper as the supporting layer, base and mass block. The double-crystal piezoelectric plate was combined with the structural steel base to form a double-crystal cantilever beam device, which was fixed on the sinusoidal vibration table with power frequency of 50 Hz. The relevant parameters of the shaking table were adjusted, the output amplitude of the shaking table was changed, and the open-circuit voltage of the double-crystal piezoelectric cantilever beam device was measured. Keep the amplitude unchanged, change the load resistance in series, make it vary within the range of 1–10 k Ω , use a multimeter to measure the output voltage and current of the device under different load resistance, and calculate the load power, measurement and calculation results are shown in Table 1 and 2.

Table 1 Device output voltage at different amplitudes

Amplitude	open circuit voltage
1.2 mm	3.21 V
2.4 mm	4.06 V
3.6 mm	5.38 V
4.8 mm	7.26 V
6.0 mm	18.6 V

Table 2 The output parameters of the device at 4.8 mm amplitude

Resistance	open circuit voltage	current	voltage	power
1 k Ω	7.26 V	0.516 mA	0.56 V	0.289 mW
2 k Ω	7.26 V	0.297 mA	1.00 V	0.297 mW
3 k Ω	7.26 V	0.215 mA	1.42 V	0.306 mW
4 k Ω	7.26 V	0.173 mA	1.83 V	0.317 mW
5 k Ω	7.26 V	0.150 mA	2.20 V	0.330 mW
6 k Ω	7.26 V	0.134 mA	2.55 V	0.344 mW
7 k Ω	7.26 V	0.125 mA	2.89 V	0.360 mW
8 k Ω	7.26 V	0.117 mA	3.24 V	0.378 mW
9 k Ω	7.26 V	0.110 mA	3.58 V	0.395 mW
10 k Ω	7.26 V	0.106 mA	3.92 V	0.415 mw

5 Conclusion

- (a) Based on the piezoelectric effect, this paper designs a double-crystal piezoelectric cantilever beam structure to collect vibration energy. Through the experiment, the output voltage, external resistance and vibration amplitude are obtained. At a fixed frequency, the output voltage increases with the increase of load and amplitude, and with the increase of resistance, the output steady-state voltage gradually approaches the open-circuit voltage. The output power also increases with the load.
- (b) At a fixed amplitude, the output voltage of the double-crystal piezoelectric device is positively correlated with the excitation frequency
- (c) The research results of the load capacity of the piezoelectric plate prove that the double-crystal piezoelectric cantilever beam device has good energy conversion capacity and stable load capacity, and can generate a higher output voltage under 50 Hz external vibration. As a vibration energy acquisition device, it can be applied to the online monitoring system of electric power equipment, and provide energy for the micro-online monitoring sensor of transformer, reactor and other types of equipment.

Acknowledgements This paper is supported by the Innovation Training Project for College Students of National Natural Science Foundation of China (51741728) (202210486053).

References

1. Tian, X.: Research and application of self-power supply based on rotary composite nano-generator. Chongqing University of Posts and Telecommunications, Chongqing (2021). (In Chinese)
2. Zhang, Z., Yang, R., Zheng, L., Hou, L.: Experimental study on double-crystal piezoelectric energy harvesting device of cantilever beam. *Sci. Technol. Eng.* **20**(35), 14518–14522 (2020). (In Chinese)
3. Wu, X., Fang, H., Lin, J., et al.: MEMS piezoelectric cantilever beam for vibration energy harvesting. *J. Funct. Mater. Dev.* **14**(2), 467–471 (2008). (In Chinese). <https://doi.org/10.3969/j.issn.1007-4252.2008.02.041>
4. Kan, J., Tang, K., Wang, S., et al.: Modeling and simulation analysis of piezoelectric cantilever beam power generation device. *Opt. Precis. Eng.* **16**(1), 71–75 (2008). (In Chinese). <https://doi.org/10.3321/j.issn:1004-924X.2008.01.013>
5. Beltrán-carbajal, F., Silva-Navarro, G.: Active vibration control in Duffing mechanical systems using dynamic vibration absorbers. *J. Sound Vibr.* **333**(14), 3019–3030 (2014). <https://doi.org/10.1016/j.jsv.2014.03.019>
6. Zhang, Z., Ni, C., Hou, L.: Power generation performance of double-crystal piezoelectric plates with different connections of cantilever beam. *Electron. Dev.* **41**(04), 893–897 (2018). (In Chinese)
7. Tian, X.: Research on micro piezoelectric vibration energy collector. Chongqing University, Chongqing (2020). (In Chinese)
8. Kim, M., Hoegen, M., Dugundji, J., et al.: Modeling and experimental verification of proof mass effects on vibration energy harvester performance. *Smart Mater. Struct.* **19**(4), 045023:1–045023:21 (2010). <https://doi.org/10.1088/0964-1726/19/4/045023>
9. Xie, Z.: Modeling and simulation of vibration energy collector for piezoelectric cantilever beam. *Agric. Equipment Veh. Eng.* **58**(12), 46–50 (2020). (In Chinese)
10. Tian, Y., Li, G., Yi, Z., et al.: A low-frequency MEMS piezoelectric energy harvester with a rectangular hole based on bulk PZT film. *J. Phys. Chem. Solids* **117**, 21–27 (2018). <https://doi.org/10.1016/j.jpcs.2018.02.024>
11. Roundy, S., Wright, P.K., Rabaey, J.: A study of low level vibrations as a power source for wireless sensor nodes. *Comput. Commun.* **26**(11), 1131–1144 (2003)
12. Huang, B.: Research on double-crystal cantilever piezoelectric MEMS vibration energy collector. Nanchang Institute of Engineering (2020). (In Chinese)

Numerical Study on Ultra-Low Specific Speed Pump as Turbine for Micro-hydropower System



Jiawei He, Peng Wang, Fanjie Deng, Wentao Sun, and Qiaorui Si

Abstract Micro-hydropower technology is of great significance to ensure the normal use of electricity by residents in remote mountainous areas. Pump as turbine (PAT) has a broad prospect in the field of micro-hydropower generation in remote rural areas because of its low cost and simple structure. Aiming at the problems of PAT, such as sudden drop of power under small flow rate and narrow efficient operation area, an ultra-low specific speed PAT with a specific speed only 16.52 is designed with the maximum power as the goal. The power characteristics and energy loss characteristics of ultra-low specific speed PAT are analyzed by means of experimental test and numerical simulation. The results show that the maximum power can reach 2 kW when the flow rate is 28 m³/h; The dynamic and static interference and the water impact loss at the outlet of impeller are the important factors that cause the energy loss of ultra-low specific speed PAT. In addition, the power of the PAT increases with the increase of speed and flow rate, and the maximum and minimum power of the impeller in a rotational cycle are closely related to the direction of water flow at the volute outlet and the impeller blade shape.

Keywords Pumped storage · Ultra-low specific speed PAT · Power output characteristics · Energy loss characteristics

J. He · P. Wang · F. Deng · W. Sun · Q. Si (✉)
National Research Center of Pumps, Jiangsu University, Zhenjiang 212013, China
e-mail: siqiaorui@ujs.edu.cn

P. Wang
Hefei Huasheng Pump and Valve Co., Ltd., Hefei 231100, China

Wenling Research Institute of Fluid Machinery, Jiangsu University, TaiZhou 317525, China

© Beijing Paiké Culture Commu. Co., Ltd. 2023
X. Dong et al. (eds.), *The proceedings of the 10th Frontier Academic Forum of Electrical Engineering (FAFEE2022)*, Lecture Notes in Electrical Engineering 1054, https://doi.org/10.1007/978-981-99-3408-9_110

1227

1 Introduction

PAT is the earliest research and development technology in the field of liquid pressure energy recovery, which is widely used in the recovery system of high pressure surplus energy in petrochemical, steel metallurgy and many other process industries [1]. At present, the PAT device mainly uses pump inversion as a PAT, which has simple structure, low price and low operation and maintenance cost [2]. With the development of micro-hydropower, the application scope of PAT is further broadened, especially in the field of micro-hydropower generation. The development cost of traditional PAT is high and the income is small, so PAT is favored in micro-hydropower generation [3–5]. At present, scholars mainly focus on the influence of various factors on the performance, performance optimization and internal flow characteristics of PAT.

Miao et al. [6] studied the energy conversion characteristics in the volute of a PAT, and found that the conversion between dynamic pressure energy and static pressure energy in the contraction section of the volute essentially depends on the reduction of the flow area, and the flow rate decreases in waves from the throat to the end of the volute. Zhang et al. [7] studied the influence of blade placement angle distribution law on the performance of PAT, and found that the efficiency of the impeller with concave distribution law is higher than other schemes, and the high efficiency area is wider. Huang et al. [8] applied the entropy production theory to the analysis of the internal flow field of the hydraulic turbine, and found that the entropy production theory can accurately locate the source of energy loss. Jiang et al. [9] optimized the PAT based on RBF-HDMR model and PSO algorithm, and the numerical simulation efficiency of the optimized PAT increased by 4.78%. Zhang et al. [10] found that the transient characteristics of PAT in the atypical start-up phase mainly come from the acceleration effect of the moment of inertia, rather than the flow inertia effect.

Although scholars have done a lot of research on PAT, and the related theory of PAT has developed rapidly, the problems such as narrow high efficiency area and sudden drop of power under small flow rate limit the application of PAT to micro hydropower. Therefore, an ultra-low specific speed hydraulic turbine with a specific speed of only 16.5 is designed, and its power characteristics and internal flow characteristics are analyzed theoretically with the help of experiments and ANSYS software.

2 Hydraulic Design of Ultra-Low Specific Speed PAT

Volute and impeller are the core components of PAT. In this design, hydraulic design is carried out based on flow equation and excellent model conversion. It is designed according to the design method of the pump, and then adjusted according to the characteristics of PAT working conditions [11].

Table 1 Design parameters of ultra-low specific speed PAT

Flow Rate	Maximum Recovery Head	Rotation Speed	Power	Pressure
28 m ³ /h	<90 m	1500 r · min ⁻¹	2.0 kW	4 Mpa

Table 2 Basic parameters of PAT

Design parameter	value
Impeller	
Outlet diameter D_1 (mm)	55
Inlet diameter D_2 (mm)	265
Inlet width b_2 (mm)	8
Inlet angle β_1 (°)	31
Outlet angle β_2 (°)	31
Number of blades Z	8
Volute	
Base circle direct D_3 (mm)	275
Inlet width b_3 (mm)	8
Suction diameter D_d (mm)	50
Diffusion tube height L (mm)	345

2.1 Main Geometric Parameters

According to the investigation, the design parameters are determined as shown in Table 1. After calculation, specific speed of PAT is 16.52, which is less than 30, and its hydraulic design is more difficult. It is an ultra-low specific speed PAT. The final main parameters of the impeller and volute are shown in Table 2. The specific speed n_s is defined as follows:

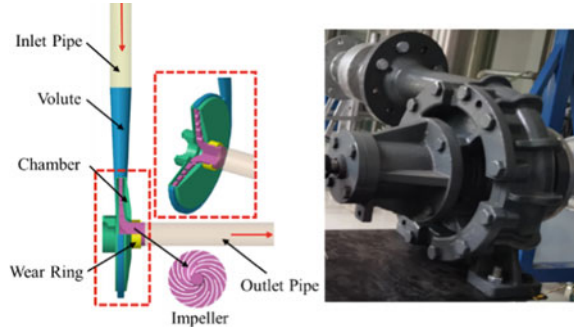
$$n_s = \frac{3.65n\sqrt{Q}}{H^{0.75}} \tag{1}$$

where n is the rotational speed, r · min⁻¹, Q is the flow rate of the PAT, m³/h, H is the recovery head of PAT, m.

3 Establishment of Three-Dimensional Model

CREO software was used to model ultra-low specific speed PAT, and a three-dimensional model of the whole flow domain including volute, impeller, chamber, and wear ring are established, and an inlet pipe and outlet pipe are established at the inlet of volute and the outlet of impeller respectively to ensure stable inlet and

Fig. 1 Three-dimensional model of PAT and hydraulic prototype



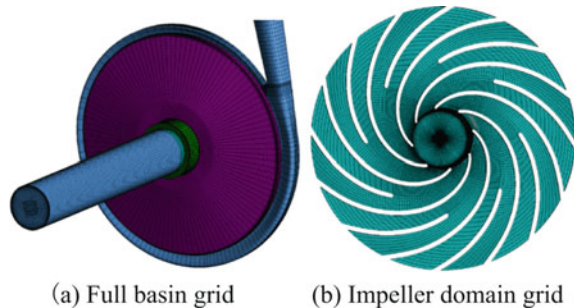
outlet flow patterns in numerical simulation. Three-dimensional model of PAT and hydraulic prototype are shown in Fig. 1.

4 Numerical Simulation

After modeling, the components are meshed in ANSYS ICEM. Computational domain grid is shown in Fig. 2. Since the number of meshes in the calculation domain has an important influence on the calculation results [12], this paper analyzes the grid independence of PAT under the design condition and design speed, and finds that when the number of meshes is greater than 4.1 million, the power of PAT is basically unchanged. So, 4.1 million meshes are used as the final mesh number.

Numerical simulation of ultra-low specific speed PAT using ANSYS CFX software. Multiple coordinate systems are adopted, and the dynamic and static interface is set to Frozen Rotor mode; The standard wall function is applied to the near wall, the solid wall adopts the non-slip boundary condition, the convergence residual standard is 10^{-4} , and the fluid medium is 25 °C water. Perform transient simulations using steady-state results as initial data. The time step of the transient simulation is about 3.4483×10^{-4} s [13], and the boundary conditions are set to pressure inlet and mass flow outlet.

Fig. 2 Computational domain grid



4.1 Turbulence Model and Control Equation

At present, the turbulence model based on the Reynolds time average Navier-Stokes equation is divided into Reynolds stress model and vortex viscosity model. The Reynolds stress model is too complex and requires a large number of differential equations to be solved and the solution calculation is huge, so the two-equation model RNG $k-\varepsilon$ turbulence model in the vortex viscosity model is selected, and the RNG $k-\varepsilon$ model can analyze the transients and streamline bending in the fluid well compared with the standard $k-\varepsilon$ model. In the RNG $k-\varepsilon$ model, the transport equations for turbulent kinetic energy k and turbulent dissipation rate ε are as follows:

$$\frac{\partial(\rho k)}{\partial t} + \frac{\partial(\rho k u_i)}{\partial x_i} = \frac{\partial}{\partial x_j} \left[\alpha_k \mu_{eff} \frac{\partial k}{\partial x_j} \right] + G_k + G_b - \rho \varepsilon - Y_M + S_k \quad (2)$$

$$\frac{\partial(\rho \varepsilon)}{\partial t} + \frac{\partial(\rho \varepsilon u_i)}{\partial x_i} = \frac{\partial}{\partial x_j} \left[\alpha_\varepsilon \mu_{eff} \frac{\partial \varepsilon}{\partial x_j} \right] + C_{1\varepsilon} \frac{\varepsilon}{k} (G_k + C_{3\varepsilon} G_b) - C_{2\varepsilon}^* \rho \frac{\varepsilon^2}{k} \quad (3)$$

where the model constants can be assigned as: $C_\mu = 0.09$, $C_\mu = 0.09$, $C_{1\varepsilon} = 1.44$, $C_{2\varepsilon} = 1.92$, $G_b = Y_M = S_k = S_\varepsilon = 0$.

4.2 Test Verification

In order to verify the accuracy of the numerical simulation and obtain the accurate performance parameters of the ultra-low specific speed PAT, a PAT test bench was built to test the ultra-low specific speed PAT, and the schematic diagram of the test bench is shown in Fig. 3. The power of ultra-low specific speed PAT is shown in the following equation

$$P = M \frac{2\pi n}{60} \quad (4)$$

where M is the torque output of the ultra-low specific speed PAT, $N \cdot m$; n is the rotational speed, $r \cdot \text{min}^{-1}$.

Ultra-low specific speed PAT converts liquid pressure energy into mechanical energy output, the damper consumes the energy generated by the turbine, the torque meter measures the speed and torque, and the pressure sensor measures the pressure at the inlet and outlet position of PAT. The measurement accuracy of electromagnetic flowmeter is 0.15%, the measurement accuracy of pressure transmitter is 0.25%, and the measurement accuracy of torque tester is 0.2%.

The external characteristics of ultra-low specific speed hydraulic turbine are manifested as output power, and the ultra-low specific speed PAT is tested. According to the test results, the output power of the PAT increases with the increase of flow rate. As shown in Fig. 4, under the design conditions, the output power of numerical

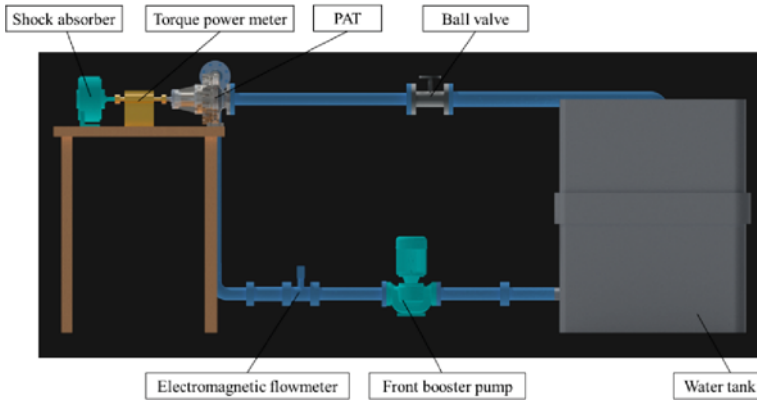
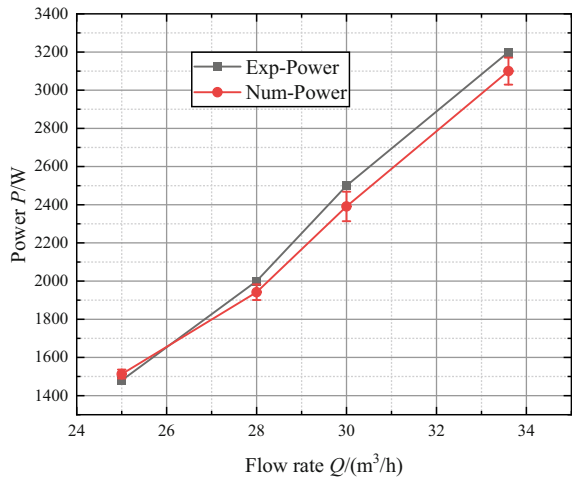


Fig. 3 Diagram of test bench testing

Fig. 4 Comparison of numerical simulation and experiment



simulation is 1.94kW, and the test output power is 2kW. The external characteristic simulation and test error is 3%, which meets the accuracy requirements of simulation [14].

4.3 Pressure Field

The pressure cloud diagram of different planes is shown in Fig. 5, from which it can be seen that the pressure gradually decreases from the inlet to the outlet, of which the pressure gradient is the largest in the impeller. On the one hand, the power output consumes part of the pressure energy, and on the other hand, due to the unstable

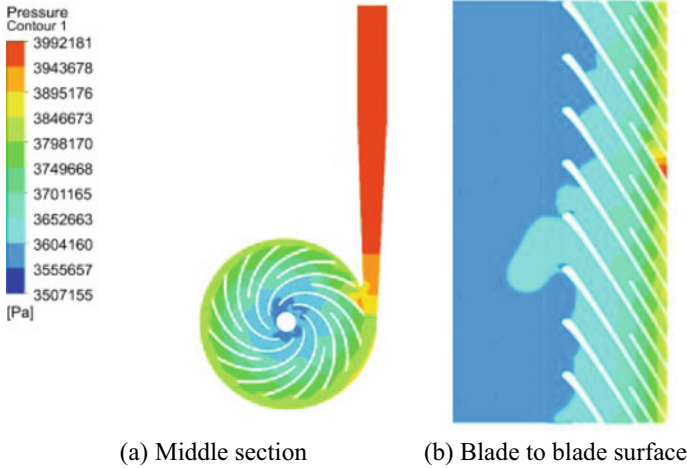


Fig. 5 Pressure nephogram under different planes

flow such as dynamic and static interference and water flow impact, the greater the pressure difference between the impeller inlet and outlet, the higher the power output.

It can be seen from the blade to blade to surface that the pressure distribution of the whole process is uniform, and only a local high-pressure area is generated at the diaphragm, which is due to the greatest influence of dynamic and static interference between the volute and the impeller, and the pressure energy loss here is also the largest.

4.4 Vortex Core Distribution

Figure 6 uses velocity to represent vortex nuclei distribution, which are mainly distributed in volute, chamber and impeller. Under the design condition, the distribution of vortex nuclei in the PAT is roughly regular, that is, the vortex core area gradually increases along the direction of water flow in the volute. In impeller, the vortex core distribution is the most complex, but the general trend is still that the vortex nucleus of the impeller channel near the volute is the most distributed, and the vortex core area along the flow direction increases and then decreases, and the distribution area of the vortex nucleus of the impeller closest to the volute is the largest, which is caused by the dynamic and static interference between the impeller and the volute. In addition, tailwater vortex zones are generated at the outlet of the impeller and the outlet pipe, mainly due to the water flow impact in each flow channel at the outlet of the impeller, forming a large number of whirlpools in impeller and outlet pipe.

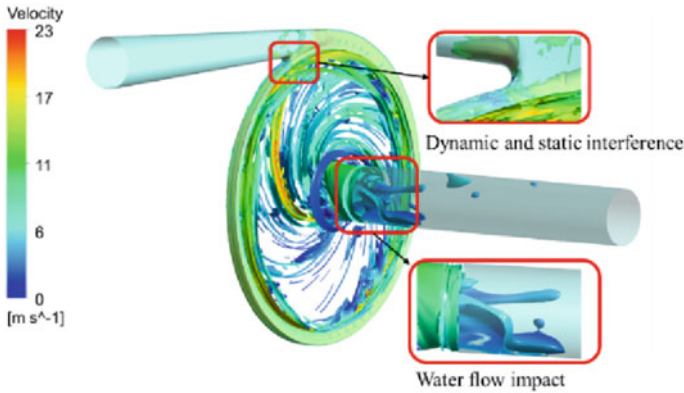
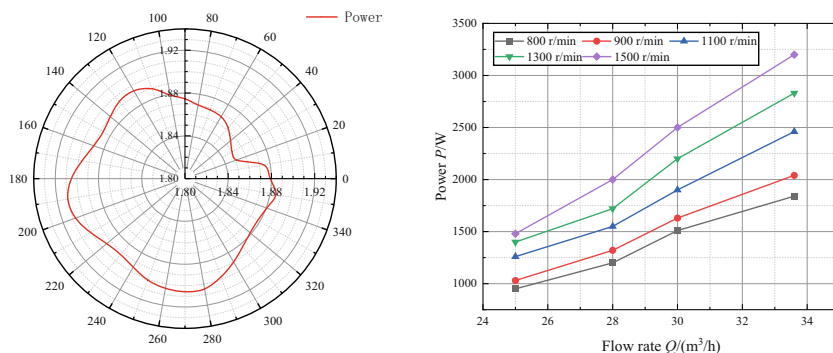


Fig. 6 Vortex core distribution of ultra-low specific speed PAT

4.5 Power Output Characteristics

In order to study the power capability of the impeller in one cycle, a rotational cycle was selected to explore the power characteristics of the ultra-low specific speed PAT. As shown in Fig. 7(a), there are maximum and minimum values for the power output over a rotation cycle. The maximum power output is 1.91 kW and the minimum output is 1.85 kW. The water flow acts on the impeller to achieve power output, and when the blade rotates to about 190°, the water flow direction of volute outlet is parallel to the blade normal, and the output power is maximum. When rotated to 20°, the direction of water flow at the outlet of the volute is perpendicular to the normal of the blade shape, in which case the power is minimal. It can be seen from Fig. 7(b) that the ultra-low specific speed PAT power of this design increases with the increase of flow rate and rotational speed, and can output large power at small flow, which solves the problem of insufficient output power of PAT under small flow.



(a) Power in one rotation cycle (b) Power at different flow rates and speeds

Fig. 7 Energy characteristics of ultra-low specific speed PAT

5 Conclusion

In this paper, the power energy loss characteristics of ultra-low specific speed PAT are analyzed by combining experimental test and numerical simulation, and the following conclusions are reached through research and analysis:

- (1) Through the comparative test and numerical simulation results, it can be seen that the error between experimental test and numerical simulation is within 3%, indicating that the numerical simulation method used this time can accurately predict the ultra-low specific speed PAT performance.
- (2) The dynamic and static interference between the impeller and the volute and the water flow impact loss at the outlet of the impeller are the main factors causing the loss of ultra-low specific speed PAT energy.
- (3) The output power of the ultra-low specific speed PAT increases with the increase of speed and flow, and the maximum and minimum power output of the impeller in a rotation cycle, and these value of output power is closely related to the direction of water flow at the outlet of the volute and the impeller blade type.

Acknowledgements This work was funded by National Key R&D Project (2020YFC1512400) and Jiangsu Province Carbon Peak Carbon Neutrality Science and Technology Innovation Special Fund (BE2022032-3).

References

1. Lin, T., Zhu, Z., Li, X., et al.: Review and prospect of centrifugal pump as turbine performance prediction. *J. Drainage Irrig. Mach. Eng.* **39**(06), 562–568 (2021)

2. Liu, M., Tan, L., Cao, S.I.: Performance prediction and geometry optimization for application of pump as turbine: a review. *Front. Energy Res.* **9** (2022)
3. Ali, K., Gustavo, M., Bruno, B.: Employing demand prediction in pump as turbine plant design regarding energy recovery enhancement. *Renewable Energy* **187**, 223–236 (2022)
4. Zhang, J., Adu, D., et al.: Pump as turbine for small-hydropower generation a solution to Africa's energy. *Int. J. Smart Grid Clean Energy* **8**(3), 361–366 (2019)
5. Morabito, A., Hendrick, P., et al.: Pump as turbine applied to micro energy storage and smart water grids: a case study. *Appl. Energy* **241**, 567–579 (2019)
6. Miao, S., Zhang, H., Shi, F., et al.: Study on energy conversion characteristics in volute of pump as turbine. *Fluid Dyn. Mater. Process.* **17**(1), 201–214 (2021)
7. Zhang, Z., Li, Y., et al.: Study on the influence of blade placement angle distribution on hydraulic turbine performance. *J. Hydroelectric Eng.* **40**(05), 125–134 (2021)
8. Huang, N., Li, Z., et al.: Application of entropy production theory in the analysis of flow field in pump as turbine. *Pet. Sci. Bull.* **5**(02), 269–276 (2020)
9. Jiang, B., Yang, J., Wang, X., et al.: Pump as turbine blade optimization based on RBF-HDMR model and PSO algorithm. *J. Mech. Eng.* **58**(12), 283–292 (2022)
10. Zhang, Y., Zhao, Y.: The atypical startup characteristics of a pump as turbine. *Energy Sci. Eng.* **10**(1), 132–144 (2021)
11. Guan, X.: *Modern Pump Theory and Design*. China Aerospace Press, Beijing (2011)
12. Sun, S., Dong, Y., Guo, P., et al.: Effect of diaphragm angle on two-phase flow characteristics of pump as turbine. *Chin. J. Hydrodyn.* **36**(03), 355–362 (2021)
13. Ji, L., Li, W., Shi, W., et al.: Energy characteristics of mixed-flow pump under different tip clearances based on entropy production analysis. *Energy* **199**, 117447–117462 (2020)
14. Lu, J., Chen, Q., Liu, X., et al.: Investigation on pressure fluctuations induced by flow instabilities in a centrifugal pump. *Ocean Eng.* **258**, 111805–111818 (2022)

The Research on Ablation Characteristics of Oil and Gas Pipeline Under Power Frequency Current



Chunjiu Wu, Jianwei Jin, Lei Guo, Hailiang Lu, Zhibing Huang, Bo Tan, and Wenqiang Yang

Abstract When the transmission line has a short circuit to ground at the tower, the power frequency short circuit current will flow into the ground through the grounding device, posing a threat to the buried pipeline around the grounding conductor. The ablation test platform of pipeline samples was built in the paper, the ablation test of pipeline under power frequency current was carried out when the current and arcing time were controlled respectively, and the ablation depth, ablation area, ablation volume and other parameters were measured. A time current factor consisting of current and arcing time is proposed to characterize ablation energy, and multivariate nonlinear regression analysis is conducted for the coefficient. The results show that the weight loss, volume and depth of ablation have obvious linear relationship with the corresponding time and current factors respectively, while the linear relationship between ablation area and temperature and the optimized time and current factors is weak, and the data shows obvious dispersion.

Keywords Lightning Strike · Power Frequency Current · Arc · Pipeline Ablation · Ablation Energy · Ablation Characteristics

1 Introduction

The insulator flashover may occur when lightning strikes overhead transmission lines. Generally, There is an ionization channel along the insulator surface when flashover occur, which is connected to the tower and grounding foundation to release lightning

C. Wu (✉) · J. Jin · Z. Huang · B. Tan · W. Yang
China Electric Power Research Institute Co., Ltd., Wuhan 430074, China
e-mail: wuchunjiu@epri.sgcc.com.cn

L. Guo
State Grid Henan Electric Power Research Institute, Zhengzhou 450052, China

H. Lu
Wuhan University, Wuhan 430072, China

© Beijing Paiké Culture Commu. Co., Ltd. 2023
X. Dong et al. (eds.), *The proceedings of the 10th Frontier Academic Forum of Electrical Engineering (FAFEE2022)*, Lecture Notes in Electrical Engineering 1054, https://doi.org/10.1007/978-981-99-3408-9_111

1237

current to the shallow soil near the tower grounding foundation. If the amplitude of lightning current is too large, the soil around the grounding conductor may be broken down, forming an arc in the soil, and the end point of the arc path may be the nearby buried pipeline [1]. There will be power frequency continuous current after the flashover current caused by lightning stroke, and the power frequency current at this time is consistent with the component of the short circuit current entering the ground passing through the tower in case of single-phase short circuit fault. If the most serious situation of duration is considered, it will often last for several or even dozens of power frequency cycles until the fault is removed through the circuit breaker [2]. If the pipeline is out of repair for a long time, the buried metal pipeline will be damage further and its service life is reduced, and even the whole pipeline is burned, which causes a serious accident and incalculable loss.

Zhong Wei [3] of the Chinese Academy of Engineering Physics made a detailed study on the distribution and statistical law of the splashed products on the electrode by using microscopic morphology observation. Radasky [4] studied the influence of power frequency arc on the impedance of the ground electrode, and analyzed the relationship between the propagation speed of the arc in the soil, the resistance per unit length of the arc and the current amplitude. Jiang Xiaofeng [5] of Northwest Nuclear Technology Research Institute designed and tested a three electrode switch based on tungsten nickel iron alloy, and the experiment shew that the switch had excellent performance. Wu Yi [6] of Xi'an Jiaotong University reported a method for real-time observation of electrode material splashing during DC arc ablation: a high-speed camera combined with a specific wavelength laser and a narrowband filter was used to capture and track the trajectory of droplet splashed from electrode ablation. Sonehara [7] studied the influence of several parameters on lightning pulse, and made some supplementary studies on the factors which depended on whether the arc can be reliably formed under the action of lightning current. Yao Xueling [8] of Xi'an Jiaotong University found that under the action of high pulse current, the surface of copper tungsten electrode appeared fish scale cracks. The formation and growth of cracks were caused by the existence of structural weaknesses such as tungsten matrix itself in copper tungsten alloy and pores formed during processing. Hu Jing et al. [9] conducted ablation tests on pipe slices and analyzed some influence parameters during pipe ablation. Zhang Yongmin [10] of Xi'an Jiaotong University studied the ablation resistance and life of electrodes with different surface types.

The simulation test platform for power frequency arc ablation of pipeline was built in the paper, the ablation test of power frequency arc on pipeline was carried out when the current amplitude and arcing time were controlled, and the ablation depth, ablation area, ablation volume and other parameters were measured to characterize the ablation degree. A time current factor consisting of current amplitude and arcing time was proposed to characterize ablation energy, and the quantitative relationship between ablation energy and ablation degree was analyzed.

2 Simulation Test Platform of Power Frequency Arc Ablation on Pipeline

The electrical wiring diagram of the test circuit is shown in Fig. 1. The test circuit is composed of four parts: (1) power supply: transformer can generate power frequency short circuit current, the test current was adjusted through adjustable reactor, and the duration of current was controlled through computer program; (2) measuring part: the ROGOWSKI coil is used to measure arc current; (3) arc striking part: it is composed of electrode and metal wire. After the circuit is connected, the metal arc striking wire will melt in a very short time under the action of large current and cause an arc between gaps; (4) test sample: the pipe slice is used as the ablation sample.

The test platform is shown in Fig. 2. The electrode material is carbon steel Q235, which is commonly used in the tower grounding device. The electrode was fixed on the lead out copper bar of the transformer through bolt structure and 21 mm diameter gasket, so as to ensure that the electrode would not have large displacement due to the influence of electrodynamic force during the test. Two round holes with the diameter of 12 mm were drilled on the bottom plate, the pipe slice was fixed on the bottom plate by means of bolts and gaskets with the diameter of 18 mm, and another copper bar was leaded back at the same time.

Fig. 1 Test circuit

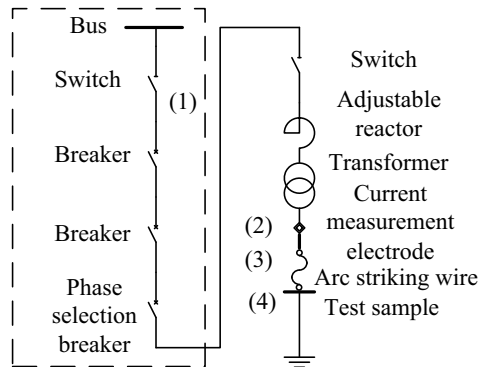


Fig. 2 Test platform

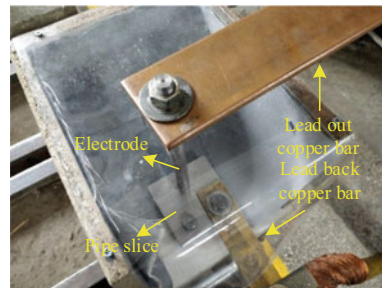


Fig. 3 Test phenomenon

As shown in Fig. 3, the arc burns and makes a crackle under the action of power frequency current. After the test circuit is cut off by the time relay, the arc is interrupted. Even if the set arcing time is short, there will still be severe sparks splashing. The gas heated by the metal particle spark expands under the action of high arc temperature, causing the air pressure difference inside and outside the test center. And it will spread near the test platform and pose a threat to the safety performance of surrounding equipment.

3 Analysis Method of Ablation Characteristics

In the process of ablation characteristic analysis, the parameters characterizing ablation degree include ablation depth, ablation area, ablation loss, ablation volume, and temperature, and the parameters for characterizing ablation energy include current and arcing time.

Theoretically, the influence of current duration on ablation parameters can be studied by controlling a single variable, such as changing the current duration when the current amplitude is unchanged. However, in actual tests, each current amplitude will have a deviation, which is not conducive to quantitative analysis. To solve this problem, the time current factor is proposed as a variable, and the relationships between ablation energy and each ablation amount are studied based on this variable. For the value of the factor, the current and arcing time is used as the power function weight, and a constant is added as a correction. The formula is as follows.

$$y = a + b x_1^c x_2^d \quad (1)$$

$$K = x_1^c x_2^d \quad (2)$$

$$y = a + bK \quad (3)$$

In the formula, a , b , c and d are controllable coefficients, y are dependent variables that need to be concerned, here are power frequency current amplitude and arcing

time, respectively, and K is the set time current factor. For different dependent variable y , the time current factor can be controlled by changing the coefficient to fit and analyze the change trend of ablation variable data.

In regression analysis, in order to characterize the fitting degree of the regression equation to the measured value, goodness of fit is introduced. Its statistic is R^2 , representing the ratio of the regression square sum ESS to the total square sum TSS.

$$R^2 = \frac{ESS}{TSS} = \frac{\sum_{i=1}^n (\hat{y}_i - \bar{y})^2}{\sum_{i=1}^n (y_i - \bar{y})^2} \tag{4}$$

In the formula, \hat{y}_i is the regression equation data, y_i is the measurement data, and \bar{y} is the average value of the measurement data. The value of R^2 is between 0 and 1. When it is closer to 1, it means that the fitting degree of the regression line to the measured value is better. On the contrary, when it is closer to 0, it means that the fitting degree is worse.

4 Relationship Between Time Current Factor and Ablation Parameter

4.1 Analysis of Ablation Depth and Ablation Loss

The data of 20 groups were obtained through the test, as shown in Table 1, in which the arcing time was controlled at about 0.3 s for 1 to 10 groups, and each ablation amount data increased with the increase of power frequency current, that is, the ablation amount was positively related to the power frequency current. The power frequency current of 11 to 20 groups is controlled at about 9kA, and each ablation amount data increases with the increase of arcing time, that is, the ablation amount is positively related to the length of arcing time.

By changing the values of c and d , the linear fitting with constant coefficients is discussed. The fitting results of ablation depth and ablation loss with time current factor at constant coefficient are shown in Table 2.

It can be seen from Table 2 that the goodness of fit of ablation depth and ablation loss with the time current coefficient is the highest under the condition of constant coefficient when coefficient is It. At the same time, it can be seen from the trend that R^2 increases first and then decreases that the optimal range of current amplitude and duration can be basically determined between 0 and 2.

The value of intercept a is controlled to be slightly greater than 0 for ablation depth. The value of slope b is controlled to be greater than 0 and less than 3 considering a certain margin. For ablation loss, it is also considered that $a = 0$ and $b > 0$, which

Table 1 Test results

Number	Current amplitude (kA)	Arcing time (s)	Ablation depth (mm)	Ablation depth (g)
1	8.62	0.332	4.00	19
2	8.97	0.294	5.75	23
3	9.18	0.335	4.00	14
4	9.19	0.325	5.13	17
5	9.17	0.318	6.00	34
6	9.06	0.322	4.29	28
7	9.37	0.290	2.71	9
8	9.14	0.313	3.85	18
9	11.95	0.323	4.33	25
10	14.67	0.297	7.16	38
11	9.08	0.315	5.60	34
12	9.25	0.296	3.30	8
13	9.20	0.330	3.54	20
14	9.38	0.250	2.71	9
15	9.07	0.313	3.81	14
16	9.10	0.483	7.42	33
17	9.04	0.511	8.97	46
8	9.36	0.201	4.00	20
19	9.19	0.207	4.00	26
20	9.06	0.422	6.95	27

Table 2 The fitting results of ablation depth and ablation loss with time current factor

	<i>a</i>	<i>b</i>	<i>c</i>	<i>d</i>	R^2
Ablation depth	2.22627	0.35412	1	0	0.1255
	1.47403	12.46974	0	1	0.48172
	0.77695	1.39527	1	1	0.72513
	2.77651	0.0793	2	1	0.57915
	3.46741	1.70206	1	2	0.64496
Ablation loss	2.61596	2.51278	1	0	0.14724
	1.22993	78.80196	0	1	0.47472
	-1.61785	8.538	1	1	0.68947
	9.73319	0.50093	2	1	0.56421
	13.56027	11.07518	1	2	0.65532

are consistent with the test. The value of intercept a is controlled to be around 0 considering the possible negative value. The value of slope b is controlled to be greater than 0 and less than 20 considering a certain margin. After improvement of regression analysis, the fitting results are shown in Table 3. The relationship between ablation depth, ablation loss and time current factor is shown in Fig. 4 and Fig. 5.

After considering the multivariate nonlinear regression analysis of the boundary, the goodness of fit of ablation depth and ablation loss increased slightly, R^2 was greater than 0.7, indicating that there was a certain degree of linear relationship under the set time current factor. If the range is not considered when analyzing the

Table 3 The fitting results of ablation depth and ablation loss after improvement of regression analysis

	a	b	c	d	R^2
Ablation depth	3.035e-09	1.913	0.864	0.909	0.7261
Ablation loss	8.479	3.005	1.429	1.387	0.7076
	0	6.691	1.085	1.021	0.7039

Fig. 4 The relationship between ablation depth and time current factor

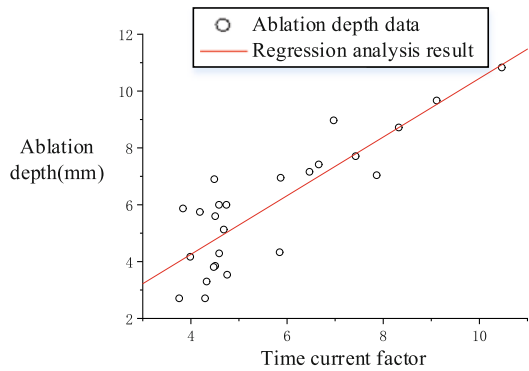
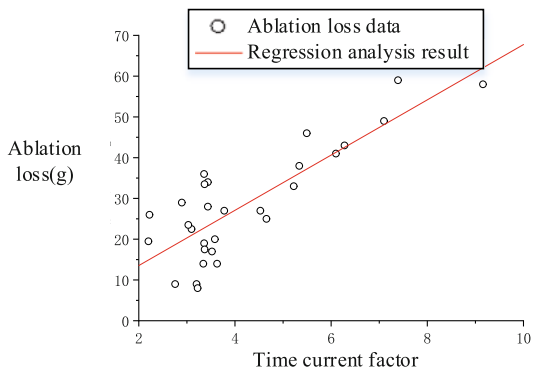


Fig. 5 The relationship between ablation loss and time current factor



ablation loss, obvious large intercept will appear in the regression analysis, which does not conform to the basic logic principle of the test, that is, when the current amplitude and time are close to zero, each ablation amount must be close to zero. It can be seen from the data that if the intercept a is considered to be close to 0, the goodness of fit will decrease slightly. The weight of current and arcing time is equivalent, and the influence weight of arcing time in ablation depth is slightly greater than that of current, while the opposite is true in ablation weight loss.

4.2 Analysis of Ablation Volume, Area and Temperature

Regression analysis was conducted on ablation volume, ablation area and temperature data, among which there were two temperature data acquisition points, those are, temperatures at 10 s and 20 s after the test. The intercept a is controlled near the origin and the slope b is more than zero. Multivariate nonlinear regression analysis is conducted for the dependent variable. Due to space limitation, the fitting results of regression analysis coefficients of ablation volume, area and temperature are given directly, as shown in Table 4. The relationship between ablation volume difference, ablation area and temperature data and time current factor is shown in Fig. 6, 7, 8 and 9.

For ablation volume, R^2 can be greater than 0.7 by changing the time and current factor after regression analysis, indicating that there is still a certain degree of linear relationship, and the weight of the arc time degree is obviously greater than that of current, which is different from the result of ablation loss. The possible reasons are as follows.

- (1) In the ablation process, some by-products are produced, and the electrode will melt partially and fall on the surface of the slice, resulting in that there is no strict positive correlation between the ablation loss and the ablation volume difference.

Table 4 The fitting results of ablation volume, area and temperature after improvement of regression analysis

	a	b	c	d	R^2
Ablation volume	1.984	1.213	1.142	1.504	0.7017
Ablation area	802.1	28.16	2	1.834	0.5989
	0	283.3	0.9663	0.6957	0.5652
Temperature at 10 s	258.2	2.135	2	2	0.5924
	0	198.5	0.2708	0.2298	0.5299
Temperature at 20 s	240.4	2.039	1.94	2	0.5215
	0	191.8	0.2387	0.207	0.471

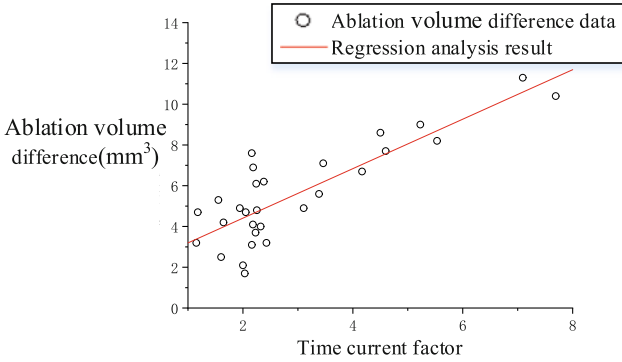


Fig. 6 The relationship between ablation volume difference and time current factor

Fig. 7 The relationship between ablation area and time current factor

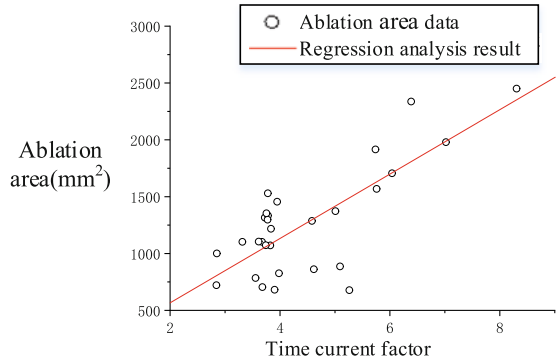
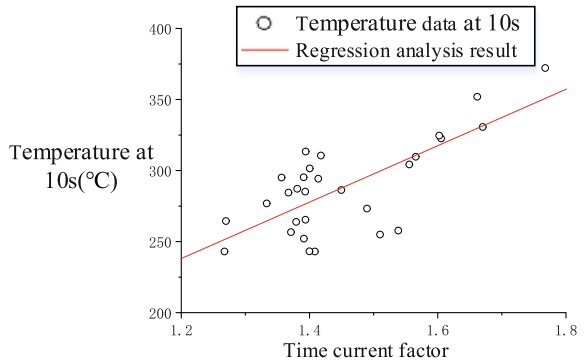
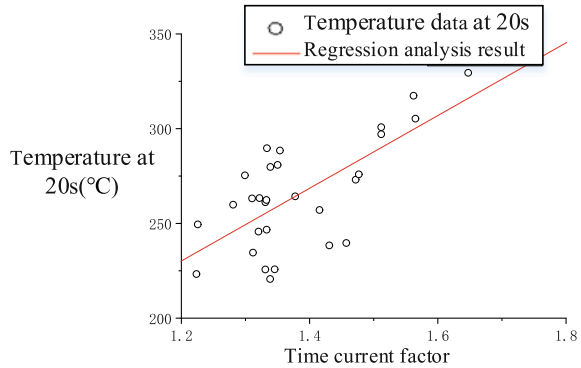


Fig. 8 The relationship between temperature at 10 s after the test and time current factor



(2) Due to the mentioned errors caused by the interference of external conditions during the measurement of volume difference, and considering the discreteness

Fig. 9 The relationship between temperature at 20 s after the test and time current factor



of test data, the current amplitude and time length weights obtained still have some room for improvement.

- (3) For ablation volume difference, there may be an arc burning time that has a more obvious impact on ablation volume difference than that of the power frequency current value under the set test platform conditions, which means to some extent that if the relatively smaller current can be maintained for a longer time, it can still cause more serious damage to the slice samples.

For ablation area and temperature, as in the analysis of ablation loss, if the intercept a is considered to be close to 0, the goodness of fit will decrease slightly. As far as the trend of temperature change is concerned, the temperature will show a downward trend between 10 and 20 s after the test. The temperature at 20 s will drop by about 10% compared with that at 10 s. The drop ratio is closely related to the initial temperature and air convection.

In the analysis of ablation area and temperature dependent variable, the data has obvious discreteness. Even through regression analysis, the relative linear relationship cannot be obtained. R^2 is still less than 0.6 after treatment. The power exponent weight of power frequency current is slightly greater than that of the arcing time, but the overall current amplitude and time have the same weight.

In addition, after regression analysis of the temperature after ablation test, the power exponent weights c and d of current amplitude and arcing time are far less than 1, ranging from 0.2 to 0.3. It shows that with the increase of current and arcing time, the rising trend of arc temperature is slower obviously.

5 Conclusion

A simulation test platform of power frequency arc ablation on pipeline was built in the paper, and the ablation test of power frequency arc on pipeline was carried out. The ablation depth, ablation area and ablation volume are used to characterize the ablation degree of the pipe slice, and a time current factor consisting of the current

amplitude and the arcing time is proposed to characterize the ablation energy. The following conclusions are drawn.

There is a linear relationship between ablation depth and ablation loss at a given time current factor. The weight of current and arcing time is equivalent, and the influence weight of arcing time on ablation depth is slightly greater than that of current, while the opposite is true in ablation loss.

There is a linear relationship between ablation volume and time current coefficient. The weight of arcing time is obviously greater than that of the current, which may be affected by by-products and measurement interference. It also indicates to some extent that relatively small current can still cause more serious damage to the pipeline sample if it can be maintained for a long time.

The linear relationship between ablation area, 10 s and 20 s temperature after test and time current coefficient is not obvious. With the increase of the current and the arcing time, the trend of arc temperature rising is obviously slow.

Acknowledgements This work is Supported by the science and technology project of the headquarters of State Grid Corporation of China “Research on the Impact and Protection of Large Regional Power Grid on the Safe Energy Transmission of Buried Metal Pipe Network” (52170219001D).

References

1. Sunde, E.D.: *Earth Conduction Effects*. Dover, New York (1968)
2. China National Standards Commission: *Code for design of overvoltage protection and insulation coordination for AC electrical installations*. China Planning Press, Beijing (2014). (in Chinese)
3. Zhong, W., Li, X., Yang, L., et al.: Splashing characteristics of microparticles from electrode erosion for copper, molybdenum, and tungsten-copper. *IEEE Trans. Plasma Sci.* **47**(2), 1387–1393 (2019)
4. Radasky, W.A., Gilbert, J.L.: The impact of high power current arcs on ground rod impedance. In: *19th International Zurich Symposium on Electromagnetic Compatibility*, Singapore. IEEE (2008)
5. Jiang, H., Jiang, X., Sun, F., et al.: Design and experiment analysis of a low inductance three-electrode field-distortion gas switch. *IEEE Trans. Plasma Sci.* **47**(8), 4114–4120 (2019)
6. Cui, Y., Niu, C., Wu, Y., et al.: Experimental study on the transformation of the W70Cu30 anode erosion mode in DC gaseous arcs-better insights into mechanisms of electrode erosion behavior using in situ diagnosis. *J. Phys. D Appl. Phys.* **52**(47), 474001 (2019)
7. Sonehara, T., Kusano, H., Tokuoka, N., et al.: Visualization of lightning impulse current discharge on CFRP laminate. In: *Lightning Protection*, Shanghai, pp. 835–839. IEEE (2014)
8. Han, R., Wu, J., Ouyang, J., et al.: A general framework for evaluating electrode erosion under repetitive high current, high energy transient arcs. *J. Phys. D Appl. Phys.* **52**(42), 425203 (2019)
9. Hu, J., Lan, L., Wen, X.-S.: Ablation test of power frequency arcs to buried metal pipes. *High Voltage Apparatus* **46**(02), 55–58 (2010). (in Chinese)
10. Wang, Y., Zhang, Y., Qiu, A., et al.: Ablation and breakdown characteristics of high current gas spark switch with different profiles. In: *2019 IEEE Pulsed Power and Plasma Science Conference*, USA, p. 71. IEEE (2019)

Lightweight Object Detection Algorithm Based on Grid Site Work Dress Code Detection Method



Kexin Li, Jing Wang, and Liang Qin

Abstract To realize the real-time and accurate detection of the dress code of the field operators of the power grid site, this paper uses the mobile deployment ball equipped with a lightweight object detection algorithm. Since the commonly used object detection algorithms are difficult to deploy on mobile devices, a lightweight object detection algorithm is proposed, which is consist of a lightweight convolutional neural network and an improved bi-direction feature pyramid network. Finally, a dataset of grid dress code detection is built, and the improved algorithm is experimentally validated on a mobile device equipped with artificial intelligence chips. The detection results show that the lightweight object detection algorithm used in this paper improves the real-time video detection speed by 22.00% to 15.50 FPS.

Keywords Lightweight Convolutional Neural Network · Improved Bi-direction Feature Pyramid Network · Dress Code Detection

1 Introduction

On March 18, 2021, the Global Energy Internet Development Cooperation proposed to build a modern energy system with clean energy production and electrification of energy consumption, emphasizing the construction of China's energy internet led by ultra-high voltage grid [1]. The future power grid shows a "double high" trend of high proportion of clean energy and high proportion of power electronics. The grid structure is becoming more complex, the operation maintenance, construction tasks are increasing. The safety risks and accident hazards are intertwined and superimposed, the security management is becoming more and more difficult, and the security and stability of the power system is facing huge challenges.

K. Li (✉)

State Grid Wuhan Electric Power Supply Company, Wuhan 430000, China
e-mail: 821156189@qq.com

J. Wang · L. Qin

School of Electrical and Automation, Wuhan University, Wuhan 430072, China

© Beijing Paiké Culture Commu. Co., Ltd. 2023

X. Dong et al. (eds.), *The proceedings of the 10th Frontier Academic Forum of Electrical Engineering (FAFEE2022)*, Lecture Notes in Electrical Engineering 1054, https://doi.org/10.1007/978-981-99-3408-9_112

1249

With complex personnel and extensive safety control points at power grid operation sites, personal and equipment accidents such as electrocution caused by irregular dress code are frequent [2]. The relevant electric power safety work procedures have made strict regulations on the safety requirements for operators to comply with at the work site, including clear requirements for the correct wearing of safety helmets and work clothes. The traditional power grid work site dress code detection is based on manual audit [3], and the person in charge of the work and safety guardian to the workforce for one-to-one or one-to-many control, it is difficult to achieve comprehensive and real-time safety control. Therefore, video monitoring of operators at the work site can effectively ensure and supervise the standard dress code of relevant operators, reducing the safety risks of operators.

Due to the need of real-time and accuracy of dress code detection for grid site operations, one-stage object detection algorithms are considered for detection [4–8]. However, due to the deep network level and large number of parameters of such algorithms, the requirements for hardware configuration are high and not suitable for deployment on mobile deployment spheres, so the algorithm needs lightweight processing. In this paper, a lightweight detection algorithm based on lightweight convolution neural network is proposed. The algorithm can enhance the detection accuracy by improving the backbone network and neck network of the algorithm without basically affecting the detection speed of the algorithm.

2 Object Detection Algorithm

2.1 *Process of Object Detection Algorithm*

Object detection algorithms based on deep learning includes the two-stage object detection algorithms and the one-stage object detection algorithms. The two-stage object detection algorithm generates a candidate region and uses convolutional neural networks to extract features. Then, a classifier is used to determine whether the objects in the candidate frame belong to the objects or the background, and finally uses non-maximal suppression to merge the candidate frames to obtain the output of the algorithm. However, the one-stage object detection algorithm directly uses convolutional neural networks for feature extraction and target frame regression, and finally merges the candidate frames by NMS to get the output of the object detection algorithm. Therefore, the detection speed of this kind object detection algorithm is generally faster.

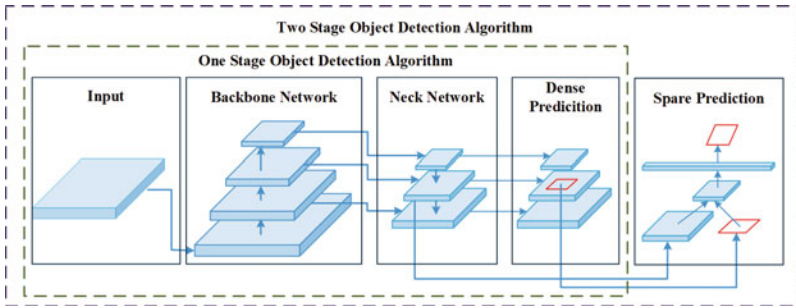


Fig. 1 Network structure of commonly object detection algorithm

2.2 Network Structure of Object Detection Algorithm

Presently, the object detection algorithm generally consists of an input network, a backbone network, a neck network and an output prediction network, as shown in Fig. 1.

The input of the algorithm is generally an image, patch or image pyramid. The backbone network is mainly used to extract the features of the input and generate feature maps, and this part of the network generally adopts VGG16, ResNet-50, CSPResNeXt50, CSPDarknet53 [9], etc. The neck network and the output prediction network are subsets of the backbone network to achieve further fusion and discrimination of features. The neck network is divided into additional network and feature fusion module, and the additional network generally adopts SPP, ASPP, RFB, SAM, etc. The feature fusion module generally adopts feature pyramid network FPN, PANet, BiFPN, etc. The output prediction networks are divided into dense predictions and sparse predictions.

3 Lightweight Object Detection Algorithm

In order to facilitate the deployment of object detection algorithm on mobile devices, this paper lightens the YOLOv4 algorithm by lightening the backbone network and neck network of the algorithm respectively. Figure 2 shows the network structure diagram of the lightweight object detection algorithm.

In this algorithm, the lightweight convolutional neural network stacked by the mobile inverted bottleneck convolution (MBConv) is used as the backbone network, which cut downs the burden of the algorithm and improves the detection speed of the algorithm. The improved feature pyramid network is also used as the neck network to construct bi-direction feature fusion paths. By repeating the bi-direction paths, the feature fusion ability of the algorithm is enhanced, thus improving the feature

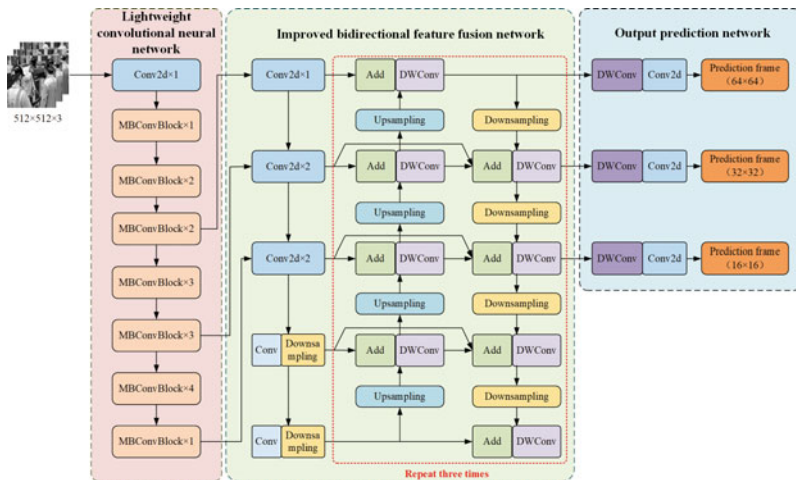


Fig. 2 Network schematic of lightweight object detection algorithm in this paper

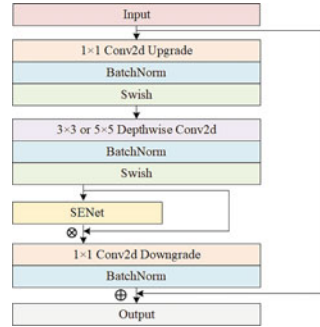
utilization rate. The output prediction network simultaneously predicts and regresses the class and location of the target.

3.1 Design of Backbone Network

Compared with regular convolution, depth-separable convolution can significantly cut down the amount of calculation and number of parameters while obtaining the same output result. So it is widely used in lightweight networks, which makes the networks lightweight. Therefore, depth-separable convolution is adopted in this paper to realize the lightweight design of the algorithm.

The bottleneck structure is a special residual structure that uses a 1×1 convolutional layer to raise and lower the dimension of the feature map, which allows for flexible network design and significant reduction in computation. Compared with the regular residual structure, the inverted residual structure has the following differences: (1) The input feature map is first up-dimensioned and then down-dimensioned. It is a dilation-convolution-compression process. (2) The regular 3×3 convolution is replaced by a depth-separable convolution. (3) The ReLU activation layer of the last convolutional layer is removed because the ReLU activation function tends to deactivate some neurons, while the high-dimensional ReLU can retain the complete information of the low-dimensional features while keeping the network nonlinear. This structure can improve the efficiency of memory usage. Therefore, this paper constructs a MBCConv based on the bottleneck structure and the inverted residual structure, and the structure of this convolutional block is shown in Fig. 3.

Fig. 3 Network schematic of MBConv



The input of MBConv block is divided into two paths. The left path passes through a regular convolution layer, a depth-separable convolution layer and a regular convolution layer in turn. Firstly, the input image passes through a 1×1 regular convolution layer to realize channel expansion, then it is sent to a 3×3 or 5×5 depth-separable convolution layer to extract features among different features, and at last it is put into a 1×1 regular convolution layer for dimensionality reduction. This is due to the efficiency of the feature extraction in high-dimensional space is higher. At the same time, this module also introduces the Squeeze and Excitation Network (SENet) after the depth-separable convolution layer to adjust the weight of each channel, thus enhancing the weight of important features and weakening the weight of unimportant features. However, it takes some time to add the attention mechanism, so the number of channels in the first regular convolution layer is reduced to 1/4, which can improve the detection accuracy without increasing the detection time. The right path is the residual edge, which directly connects the input and output, thus enhancing the gradient propagation of the network. The Swish activation function is used instead of ReLU in this structure, because it is smoother and faster.

To realize the lightweight algorithm, this paper constructs a lightweight convolutional neural network composed of the MBConv blocks as the backbone network of the object detection algorithm to cut down the computation and the parameters number of the algorithm. Figure 2 shows the backbone network structure. After the image is input into the network, the initial feature extraction is carried out through a regular convolutional layer, and then the efficient feature extraction is carried out through 16 MBConv blocks. In the end, the outputs of the fifth, eleventh and sixteenth MBConv block are adopted as the outputs of the backbone network and put into the neck network for further feature processing.

3.2 Design of Neck Network

After the initial feature extraction of the input image, it is necessary to further fuse features in the feature fusion layer to realize the full utilization of the features.

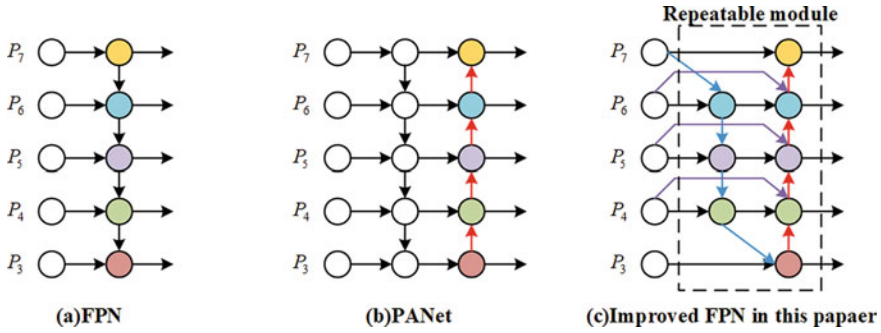


Fig. 4 Network structure of FPN, PANet and improved bi-direction feature pyramid network

Since the input features at different scales have different resolutions and contribute differently to the fused output features, simple fusion can easily lead to the loss of features. Therefore, feature pyramid networks can be introduced to realize the fusion of different size features.

The traditional feature pyramid network FPN fuses multi-scale features in a top-down path, as shown in Fig. 4(a). This feature fusion approach can pass the features from the top level to the bottom level, but the features at the bottom level cannot affect the top level, and the fusion of features is limited by the one-way feature flow, so the feature utilization is not high. Therefore, a bottom-up feature fusion path is proposed, and the structure is shown in Fig. 4(b). By adding another bottom-up feature fusion path after the initial path, the features from the bottom layer can be passed to the top layer, which improves the feature availability and thus achieves the effective fusion of features at different scales. However, this method only achieves bi-direction fusion of features once, and feature utilization is still not very high. If the bi-direction path is repeated many times, the volume of the network will rise significantly, which is not suitable for mobile device deployment [10]. Therefore, the number of repetitions of this bi-direction path is also worth studying.

Therefore, this paper constructs an improved bi-direction feature pyramid network, which has the following five characteristics. The structure is shown in Fig. 4(c).

- (1) In the improved bi-direction fusion path, depth-separable convolution is used instead of regular convolution, which significantly cut down the volume of the network.
- (2) Concatenate of features refers to the combination of feature channels, and the number of channels of feature map increases, but information volume in each channel remains unchanged. The addition of features represents the superposition of eigenvalues, and the number of channels in the feature graph remains unchanged, but information volume in each channel is increased. Therefore, the concatenate of features in the network can be changed to the addition of features, thus reducing the parameters of the network.

- (3) If the feature sizes of input and the output node of the original path are consistent, an extra edge can be introduced. In this way, more features can be integrated with less calculation cost.
- (4) If a node has only one input edge, it has no feature fusion and contributes little to feature fusion in different dimensions, so it can be deleted to lighten the network.
- (5) Reuse bi-direction paths for more advanced feature fusion.

Since the outputs of the backbone network are different sizes, the number of channels of all three effective feature layers needs to be adjusted to 64 by using the convolutional layer to allow the superposition of features. Then the 3rd effective feature layer is down-sampled twice and two effective feature layers with scales of (8, 8, 64) and (4, 4, 64) are obtained separately, which are used for further feature mix. The bi-direction path is then adopted for three times to upgrade the mix of features.

4 Dress Code Detection in Power Grid Site Operations

4.1 Dataset

In this paper, a dataset of the dress code detection for grid site operations is created, which contains 3,880 sample images from three professional job sites: transmission, substation and distribution. The dataset consists of four label categories: wearing helmet correctly (aqm), not wearing helmet correctly (wdaqm), wearing work clothes correctly (gzf), and not wearing work clothes correctly (wczgf). The dataset of grid site work dress code detection is divided into the training set, the validation set and the test set randomly during the experiment at the ratio of 8:1:1.

4.2 Hardware Environment

The algorithms are trained in the server, and download to a mobile arming sphere with artificial intelligence chip for testing. The real-time video stream used for the test is collected by a USB camera with a resolution of 1080p, which latency is about 200–300 ms. Table 1 shows the hardware configuration parameters used in this experiment.

Table 1 Hardware configuration parameters of server and mobile device

Equipment	Model	GPU	CPU
Server	ZFB2-U20G	Nvidia GeForce RTX 3090 GPU*2	Intel Xeon Platinum 8171 M CPU*2
Mobile arming sphere	NVIDIA Xavier NX	384-core NVIDIA Volta™ GPU 48 Tensor Cores	6-core NVIDIA Carmel ARM@v8.2 64-bit CPU

4.3 Experimental Evaluation Index

The evaluation metrics consist of the detection speed and the detection accuracy of the algorithm. The detection speed refers to the number of images that can be processed in one second, i.e., *FPS*.

The evaluation indexes of detection accuracy include precision (*P*), recall (*R*), average precision (AP) and mean average precision (mAP).

Precision rate refers to the ratio of the number of correctly predicted objects in this category to the number of predicted frames in this category, i.e., the accuracy rate. Recall rate represents the number of correctly predicted objects of that class as a percentage of all true labels of that class, i.e., the check-all rate. The average precision is the size of the area surrounded by Precision-Recall curve and horizontal and vertical coordinates. The m AP is the average of the AP values for each type of object.

4.4 Detection Results of Lightweight Object Detection Algorithm

This experiment compares the object detection algorithm proposed in this paper with commonly object detection algorithms in Table 2. Figure 5 shows the comparison of the detection effect images. All experiment algorithms did not use any algorithm optimization methods.

It can be seen from Table 2 that both the Faster R-CNN algorithm and the YOLOv4 have a higher detection accuracy on the mobile arming sphere equipped with artificial intelligence chip, but their detection speed cannot satisfy the demand for real-time detection (12.5 *FPS*). The YOLOv4-Tiny algorithm has a smaller volume and a higher detection speed, but the recall and AP of the algorithm are low and prone to missed detection, which cannot meet the accuracy requirements of field operation dress code detection.

The detection speed of the improved object detection algorithm is 15.50 *FPS* when performing power site operation dress code detection, which is 201.56% and 22.00% higher than the Faster R-CNN algorithm and the YOLOv4 algorithm. The improved

Table 2 Experimental results of various object detection algorithms based on the dataset in this paper

Algorithm	Layer	Parameter	AP/%				mAP/ %	Speed/ FPS
			aqm	wdaqm	gzf	wcgzf		
Faster R-CNN	185	28.37 M	93.68	83.14	92.89	90.54	90.06	5.14
YOLOv4	370	64.02 M	92.60	78.37	93.37	89.64	88.50	12.71
YOLOv4-Tiny	76	6.06 M	79.11	53.37	78.85	77.58	72.22	18.21
MobileNetV1-YOLOv4	245	12.75 M	83.43	61.60	86.39	83.18	78.65	16.64
MobileNetV2-YOLOv4	315	10.87 M	86.11	54.74	88.87	86.20	78.98	16.25
MobileNetV3-YOLOv4	368	11.79 M	85.90	54.73	88.55	85.28	78.59	16.29
Algorithm in this paper	390	12.67 M	90.48	67.57	90.47	86.18	83.67	15.50



Fig. 5 Comparison of detection effect images of various object detection algorithms in this experiment

lightweight algorithm only has 4.41 million parameters, which is 1.65 million less than that of YOLOv4-Tiny, so it is more fit in mobile deployment.

As for the detection accuracy of the algorithm, the improved lightweight object detection algorithm presents the highest detection accuracy among the lightweight YOLOv4 algorithms. It can be seen from Table 2, the AP of the classification with a small sample size like ‘not wearing helmet correctly’ is higher. As can be seen in Fig. 5, the YOLOv4-Tiny algorithm misses a ‘wearing work clothes correctly’. Also, the lightweight object detection algorithm in this paper obtains the best detection effect.

In summary, it can be seen that the improved lightweight object detection algorithm can significantly cut down the volume of the algorithm. At the same time, it has a faster speed on real-time video detection, to achieve the rapid and accurate detection of field operation dress code.

5 Conclusion

To realize the deployment of the grid dress code detection algorithm at the mobile deployment sphere, while taking into account both the detection speed and detection accuracy of the algorithm, a lightweight object detection algorithm is proposed. Firstly, a lightweight convolutional neural network which consists of depth-separable convolution and MBConv blocks is built. It can decrease the volume of the algorithm and upgrade the efficiency of the algorithm. Then, an improved bi-direction feature pyramid network is adopted, which can enhance the information availability of various semantic characteristics and heighten the extraction ability of small size characteristics. Finally, the improved algorithm is verified based on the dataset of the power grid dress code detection. And the results show that the volume of the lightweight object detection algorithm is greatly decrease and the detection speed of the algorithm is faster, which means that the improved algorithm can be used in the real-time accurate detection of the dress code detection of the field site.

References

1. Huang, Y.: Application of risk management in power security production management. *Power Secur. Technol.* **11**(02), 4–6 (2009). (in Chinese)
2. Yang, J., Wang, D., Xu, J.: Research on data-driven early warning of power production safety accident risk. *Power Syst. Big Data* **22**(04), 9–14 (2019). (in Chinese)
3. Wang, Y., Luo, Y., Pei, J.: Research on risk management and control mode of violation behavior in electric power enterprise. *J. Saf. Sci. Technol.* **14**(4), 173–180. (2018). (in Chinese)
4. Redmon, J., Divvala, S., Girshick, R.: You only look once: unified, real-time object detection. In: *Proceedings of the IEEE Conference on Computer Vision and Pattern Recognition*, pp. 779–788 (2016)
5. Redmon, J., Farhadi, A.: YOLO9000: better, faster, stronger. [arXiv:1612.08242v1](https://arxiv.org/abs/1612.08242v1) (2016)
6. Redmon, J., Farhadi, A.: Yolov3: an incremental improvement. [arXiv preprint arXiv:1804.02767](https://arxiv.org/abs/1804.02767) (2018)
7. Bochkovskiy, A., Wang, C.Y., Liao, H.Y.M.: Yolov4: optimal speed and accuracy of object detection. [arXiv preprint arXiv:2004.10934](https://arxiv.org/abs/2004.10934) (2020)
8. Liu, W., Anguelov, D., Erhan, D., et al.: SSD: single shot multibox detector. In: *European Conference on Computer Vision*, pp. 21–37 (2016)
9. Wang, C.Y., Liao, H., Yeh, I.H., et al.: CSPNet: a new backbone that can enhance learning capability of CNN. In: *IEEE Conference on Computer Vision and Pattern Recognition (CVPR)* (2019)
10. Zheng, Z., Wang, P., Ren, D., et al.: Enhancing Geometric Factors in Model Learning and Inference for Object Detection and Instance Segmentation (2020)

Application and Research of Digital Twin Technology in Distribution Transformer Area



Chang Wu, Li Kong, and Hanmin Jiang

Abstract At present, with the development of the distribution network, the low-voltage distribution network is widely distributed, with a large amount of access equipment and complex power supply and consumption. For a long time, it is difficult to obtain the real-time operation status of the low-voltage side of the distribution network, and the lack of active perception of the operation status of important equipment and the power consumption of users in the transformer area. In view of the shortcomings of the operation and maintenance management of the current transformer area, the digital twin intelligent distribution transformer area is constructed based on the digital twin technology and the construction of the distribution Internet of Things, so as to realize the all-round control of the distribution transformer area, improve the work efficiency of the operation and maintenance personnel, and improve the electricity experience of customers.

Keywords Digital twin · Distribution transformer area · Intelligent distribution transformer terminal · Power distribution Internet of Things · Lean operation and maintenance

1 Introduction

At present, on the low-voltage side of the distribution network, the low-voltage distribution network is widely distributed with a large amount of access equipment and the form of power supply is complex. For a long time, it is difficult to obtain the real-time operation status of the low-voltage side of the distribution network, and there is a lack of active perception of the operation status of important equipment and the power consumption of users [1, 2]. In the distribution side, transformers, switch contacts, comprehensive distribution boxes and other devices lack load and dynamic loop monitoring, there are certain safety risks, and the equipment life is

C. Wu (✉) · L. Kong · H. Jiang
State Grid Wuhan Dongxihu District Power Supply Company, Wuhan 430000, China
e-mail: wuchang_zju@163.com

© Beijing Paiké Culture Commu. Co., Ltd. 2023
X. Dong et al. (eds.), *The proceedings of the 10th Frontier Academic Forum of Electrical Engineering (FAFEE2022)*, Lecture Notes in Electrical Engineering 1054, https://doi.org/10.1007/978-981-99-3408-9_113

1259

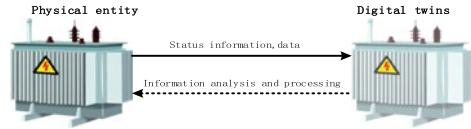
difficult to optimize. On the line side, it is difficult to effectively check and locate the line faults of the low-voltage distribution network, and the lack of intelligent means, the manual inspection workload is large, the efficiency is low, and the effect is limited [3]. In terms of users, the access of distributed electric energy, charging pile and other new energy affects the power quality and stable operation of low-voltage distribution network, and lack of effective monitoring means. The management of the transformer area relies too much on passive operational maintenance and rush repair, which is easy to bring poor electricity experience [4].

Digital twin technology provides a solution to these problems. Digital pairing is a virtual digital mapping based on the physical entities, it realizes the real-time perception of the distribution substation area in the actual space, monitors, diagnoses and predicts the operation status and guide its decision by returning instruction data to the entity or system. Through in the digital space modeling, simulation, deduction and manipulation, strengthen the end of the distribution network self perception and self iterative ability, promote the digital and intelligent transformation of the end of the grid.

At present, the application of digital twin is concentrated in aerospace, intelligent manufacturing, smart city, smart transportation, smart building and other fields, and also applied in smart energy such as Jining oil and gas pipeline, Langfang thermal power plant and other [5]. Literature [6] analyzed and studied the key technology of digital matching system of AC/DC distribution network. According to the characteristics of the power grid, Literature [7] expounded the operation mode, typical application and development prospect of the digital power grid. On the basis of smart grid and digital twin, Literature [8] introduced the meta-universe into the power system and put forward the concept of “meta-power”, and expounded its concept and characteristics. The research and application of digital pairing technology in the field of terminal distribution substation are relatively few. According to the development trend of the Internet of Things of distribution network, combined with the digital matching technology, the basic framework of digital matching of distribution substation area is expounded. With the intelligent distribution transformer terminal (IDT) as the edge computing core, the typical application of digital twin of the distribution transformer area is proposed to create the last “wisdom one kilometer” connecting the distribution network to the electricity customers.

2 The Concept of Digital Twin

Digital twin for the first time by professor Grieves in 2003 in the university of Michigan on the product full life cycle management course, when the concept is called “mirror space model” [9]. “Digital twin” the word in 2010 NASA technical report is formally mentioned, and is defined as “integrated physical quantity, multiple scale, multiple probability system or aircraft simulation process”. Digital twin is a virtual entity that creates physical entities in a digital way. With the help of historical data, real-time data and algorithm models, the technical means of simulating, verifying,

Fig. 1 Digital twin system

predicting and controlling through the whole life cycle process of physical entities is expounded in literature [10] (Fig. 1).

The digital twin system architecture can be divided into five layers: physical perception layer, data communication layer, model operation layer, system function layer and application display layer: [11].

Physical perception layer: it mainly includes physical entities equipped with advanced Internet of Things technology.

Data communication layer: mainly including high-precision data acquisition, high-speed data transmission, high-reliability data storage, which is the basis of digital twin.

Model operation layer: the use of big data, artificial intelligence and other advanced technologies for modeling and simulation, the calculation and analysis of the lower layer of data, and the support for the upper layer function, is the core of the digital twin.

System function layer: realize the state display, analysis and prediction, fault diagnosis and decision assistance of physical entities.

Application display layer: it outputs relevant information by visualizing 2D/3D model, GIS, topology, VR/AR and other technologies.

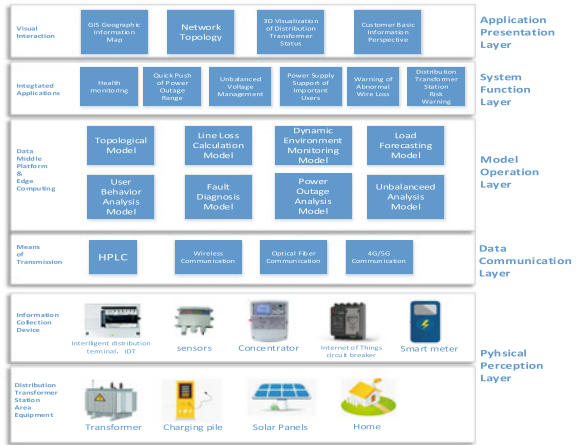
3 The Realization of Digital Twin in the Transformer Area

3.1 Digital Twin System Architecture of the Transformer Area

At present, the pace of digital transformation of power grid companies is accelerating, and the construction of digital achievements such as GIS transformer, enterprise data middle transformer, distribution network automation system, and mining system have been promoted. For example, the “Digital Power Grid Map” created by State Grid Wuhan Power Supply Company covers the operation data of 220 kV substations to 0.4 kV distribution transformers, and preliminarily realizes the mapping from the physical entity of the power grid to the digital virtual power grid. These digital construction achievements have laid a good foundation for the construction of the digital twin in the distribution transformer area.

From the structure of the digital twin described above. The transformers, low-voltage switches, smart meters and intelligent distribution terminals in the transformer distribution area constitute the physical sensing layer. The data acquisition,

Fig. 2 Digital twin system architecture of the distribution and transformer area

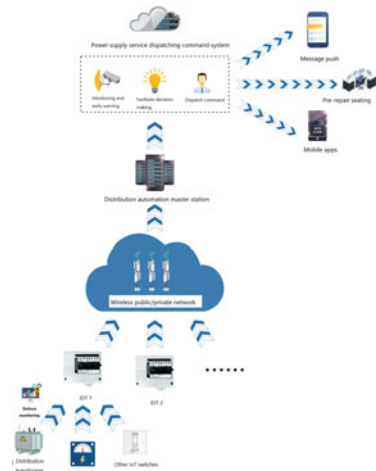


storage and transmission of intelligent transformer terminal, intelligent instrument and Internet of things switch constitute the data communication layer. The encapsulated edge computing model of the intelligent transformer terminal and various computing models in the data transformer constitute the model operation layer. The application group for transformer operation and maintenance management, user quality service, potential risk early warning and so on constitute the system function layer. Transformer area topology map, GIS geographic information map, three-dimensional model and related information interface constitute the application display layer. As shown in Fig. 2.

3.2 Technical Realization of Digital Twin Matching Transformer Area

Physical Perception and Data Interaction. The realization of the digital twin is based on the perception of the physical entity. IDT is the data acquisition and storage, connection management, equipment monitoring, terminal security access, data model unification, edge computing, remote maintenance and upgrade functions in the integration of the distribution network edge side equipment. It meets the requirements of basic operation information monitoring and analysis, power quality monitoring, demand side management, operation and maintenance control of low-voltage distribution network, and collaborative control of main station terminals. The IDT is remotely connected to the main station through ethernet or wireless network. The local network connects various service terminals and sensors to realize the communication convergence, edge computing and regional autonomy in the physical perception layer. As shown in Fig. 3.

Fig. 3 Contact diagram of digital twin transformer area and main network



On the side of the transformer, the low-voltage main switch, various parameter sensors of the transformer, concentrator and reactive power compensation device are connected to the intelligent transformer terminal through RS485 bus to realize the functions of moving ring monitoring and reactive power compensation in the transformer area.

On the side of the line, the low-voltage branch box is equipped with the intelligent terminal of the transformer and a supporting three-phase current transformer to realize the voltage and current monitoring, with the function of topology signal injection and identification, and is sent to the IDT through the HPLC module. The user is configured with the Internet of Things intelligent circuit breaker, with intelligent microswitch, which realizes the entry/exit line voltage, current monitoring and switch position monitoring functions. The intelligent circuit breaker sends the information to the Internet of Things communication unit through wireless or RS485 communication mode, and is connected to the IDT through the HPLC communication module. As shown in Fig. 4.

Digital Modeling and Model Update. The application implementation of the digital twin in the transformer is the visualization of the physical entity. The key technology is the digital modeling of physical equipment. Physical model, data model and hybrid model are the three main ways of conducting digital twin modeling. Physical model is based on physical structure, electromagnetism and thermodynamics; the data model is based on database and artificial intelligence algorithms such as deep learning and machine learning; the hybrid model is a combination of the first two. An important part of digital twin technology is the model update for physical entities and digital twin models. The collected data is compared with the output data of the virtual twin, and the optimal parameters are found iteratively to complete the update of the digital twin model. As shown in Fig. 5.

Fig. 4 Composition of physical sensing layer in digital twin transformer area

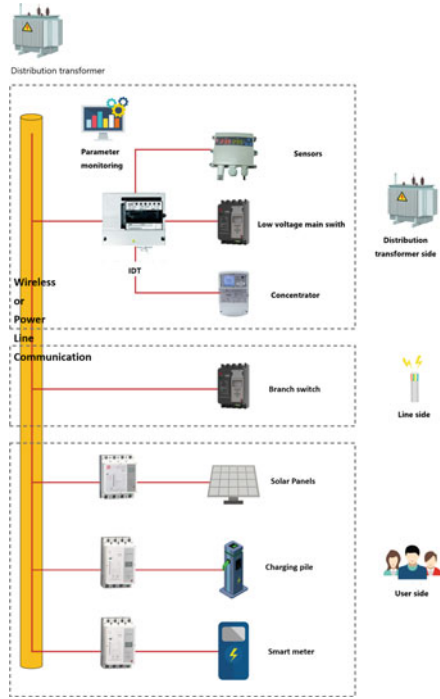
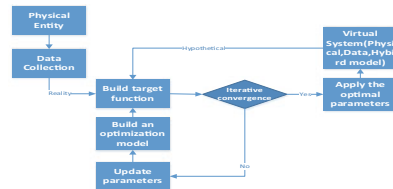


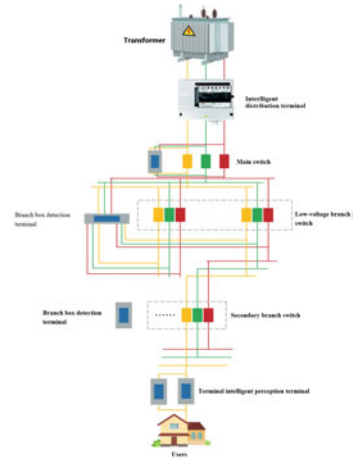
Fig. 5 Flowchart of digital twin models updates



4 Application of Digital Twin Function in the Transformer Area

The digital twin of the transformer area can collect the transformer status information, low voltage topology information, smart meter information and Internet of Things circuit breaker information in the area, and conduct comprehensive calculation, evaluate and locate the low voltage fault in the area, generate the emergency repair work order, and push it to the mobile terminal, service center and dispatching table. Realize the “visualization” of the end of the distribution network.

Fig. 6 Dynamic management of low voltage side topology



4.1 Dynamic Management of the Topology in the Low-Voltage Transformer Area

The basis of informatization and intelligence of distribution network lies in maintaining the topological relationship between equipments. The topological relationship of the power distribution Internet of Things is “station-line-transformer-user”. The “transformer-user” layer need to confirm relationship of “transformer-table box-user”. But the area data and topology structure are usually not in conformity with the actual, cause low voltage fault treatment all rely on team personnel experience, which may cause fault processing not timely.

Using the digital twin of the transformer area, through the communication signal between the HPLC communication module of the IDT and HPLC module of the intelligent meter at all levels, the identification of the station area, branch and subordination of the box table is realized. Realize the automatic identification and dynamic management of low-voltage topology (Fig. 6).

4.2 Fault Analysis and Accurate Positioning

Through the intelligent monitoring unit at the side of the meter box, the voltage cycle signal of the power line (i.e., whether the effective AC cycle is over zero) and the voltage amplitude are monitored in real time, and the power failure event information is uploaded to the IDT. According to the operation information, the IDT analyzes and uploads the power failure.

According to the evaluation result information uploaded form the IDT, the system carries out the fault location and automatically push the alarm to generate the power failure event record. Combined with the low-voltage topology relationship,

the system realizes the rapid positioning of the user range after power failure, and supports the rapid repair of power failure and the reliability analysis of power supply.

4.3 Line Loss Management

Line loss in transformer area is a common problem in distribution network. At present, only the distribution transformer area can be calculated and monitored as a whole. For the abnormal line loss, it often needs to spend a lot of time to determine the location of the abnormal line loss and the causes.

The digital twin of the transformer station area can accurately perceive all the equipment parameters and terminal information in the area, realize the segment calculation and accurate positioning of the line loss abnormality, realize the lean management of the line loss, and save a lot of human resources.

4.4 Comprehensive Treatment of the Three-Phase Imbalance

Due to the different power consumption habits, access equipment and equipment power of each user, the three-phase load of the transformer will fluctuate according to the users' behavior. At present, the main solution is for manual inter-phase load adjustment, which often depends on experience, and cannot accurately grasp the dynamic load distribution data of the transformer. The digital twin of the transformer can grasp the load distribution of the whole area, the all-weather time curve of the three-phase load and electricity consumption preference of the users in real time. According to the historical data, the optimization data is analyzed and calculated, and the optimal scheme of the alternating load adjustment is given to improve the three-phase imbalance in the transformer area.

5 Conclusion

By explaining the architecture and main application of the digital twin in the distribution station area, this paper makes the digital power grid further extend to the end of the distribution network, helps the digital transformation of the power grid, open up the last "one kilometer" at the end of the power supply, and makes the distribution network dispatching and power supply service command more efficient and accurate. Combined with the current work process of digital distribution network construction and digital twin construction in the distribution transformer area, there will be more technological breakthroughs and applications in the future. The future development direction and key work will mainly focus on the following aspects: the research and development of an efficient and accurate hybrid analysis and computing

model, the application of multi-dimensional sensors and the development of virtual reality/augmented reality.

References

1. He, W., Cheng, Y., Li, Y., Zhao, H., Zhang, R.: The research of index system of power supply service quality evaluation. *Power Demand Side Manag.* **19**(05), 41–44+51 (2017). (in Chinese)
2. Li, B., Li, Z., Ju, P.: An edge-cloud collaborative fault detection method for low-voltage distribution networks based on random matrix theory. *Proc. CSEE* **42**(01), 25–37 (2022). (in Chinese)
3. Erdiwansyah, M., Husin, H., Nasaruddin, M.Z., et al.: A critical review of the integration of renewable energy sources with various technologies. *Prot. Control Mod. Power Syst.* **6**(1), 37–54 (2021)
4. Liu, T., Yu, H., Yin, H., et al.: Research and application of digital twin technology in power grid development business. In: 2021 6th Asia Conference on Power and Electrical Engineering (ACPEE), pp. 383–387. IEEE (2021)
5. China Institute of Electronic Technology Standardization, Shugen Internet Technology Co., Ltd.: Digital Twin Application White Paper (2020). (in Chinese)
6. Tang, Q., Chen, B., Deng, W., Jiang, J.: Application research of digital twin technology in AC-DC distribution network. *Guangdong Electric Power* **33**(12), 118–124 (2020). (in Chinese)
7. Xiang, C., Zeng, S., Yan, P., Zhao, J., Jia, B.: Typical application and prospect of digital twin technology in power grid operation. *High Voltage Eng.* **47**(05), 1564–1575 (2021). (in Chinese)
8. Huang, C., Bu, S., Chen, Q., Li, X.: Meta-power: next-generation smart grid. *Power Gener. Technol.* **43**(02), 287–304 (2022). (in Chinese)
9. Grieves, M.: Product lifecycle management: the new paradigm for enterprises. *Int. J. Prod. Dev.* **2**(1/2), 71–84 (2005)
10. Jain, P., Poon, J., Singh, J.P., et al.: A digital twin approach for fault diagnosis in distributed photovoltaic systems. *IEEE Trans. Power Electron.* **35**(1), 940–956 (2019)
11. Tao, F., Zhang, M., Cheng, J., Qi, Q.: Digital twin workshop: a new paradigm for future workshop. *Comput. Integr. Manuf. Syst.* **23**(01), 1–9 (2017). (in Chinese)

Application of Intelligent High Voltage Switchgear



Qin Zou, Hao Lei, Xushu Ye, Xiting Dong, Kezhen Yang, and Jin Chen

Abstract In the background of modern distribution model, people put forward higher requirements for the power system, and the intelligent high-voltage switchgear in the modern distribution model of the intelligent distribution network link plays a crucial role. This paper focuses on the application of intelligent high voltage switchgear and compares the structure and function of traditional high voltage switchgear and intelligent high voltage switchgear. This paper briefly introduces the faults in the operation of the high voltage switchgear. In the design and application of monitoring system, mechanical characteristics detection system, video double confirmation system, electric grounding switch, electric chassis car were introduced and analyzed, and analyzed the advantages of intelligent high voltage switchgear in substation, operation and maintenance, safety and other fields of application, for reference.

Keywords High voltage switch complete equipment · Electrical design · Intelligent Chinese library classification number

1 Introduction

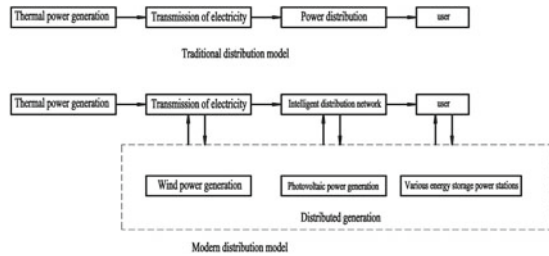
With the emergence of 5G, sensors, computers and other new technologies, as well as the development of alternative energy sources such as wind power generation, photovoltaic power generation and various energy storage stations (such as pumped energy storage, compressed air energy storage, flywheel energy storage, super capacitor, chemical battery energy storage, etc. [1]), energy can come from different places, and its coordination and control have become more advanced. Distribution models are also transitioning from traditional single-source to end-customer side distribution models to modern ones, as shown in Fig. 1.

Q. Zou · H. Lei · X. Ye · X. Dong · K. Yang (✉) · J. Chen
Wuhan OURUN Electric Equipment Co., Ltd., Wuhan 430000, China
e-mail: 544407864@qq.com

© Beijing Paiké Culture Commu. Co., Ltd. 2023
X. Dong et al. (eds.), *The proceedings of the 10th Frontier Academic Forum of Electrical Engineering (FAFEE2022)*, Lecture Notes in Electrical Engineering 1054, https://doi.org/10.1007/978-981-99-3408-9_114

1269

Fig. 1 Traditional distribution model and modern distribution model diagram



The modern distribution model in Fig. 1 is compared with the traditional distribution model. The power generation mode has changed from the traditional thermal power generation to the multi-source form of thermal power generation plus distributed power generation. The distribution network has changed from the traditional distribution mode to the intelligent digital distribution network. The intelligent high-voltage switchgear plays a vital role in the intelligent distribution network.

Intelligent high voltage switchgear, it is based on the modern Internet technology under the condition of a new type of electrical products, through the introduction of computer technology to it as the core of detection, protection, and with circuit breakers, sensors, electric ground cutter and other components, so that the functions of protection, control, communication and recording can be reliably applied through intelligent technology. This is also in line with the requirements of distribution network automation.

2 Traditional High Voltage Switchgear and Intelligent High Voltage Switchgear

2.1 Traditional High Voltage Switchgear

The traditional high voltage switch cabinet is mainly composed of isolation switch, earthing knife-switch, current transformer, surge arrester, vacuum circuit breaker, interlocking mechanism, live display, ammeter, signal indicator light, transfer switch, electromagnetic lock and cabinet body. The protection level of cabinet body is IP2X. It plays the role of power distribution and control in the three-phase AC 50 Hz indoor system. As shown in Fig. 2.

This traditional switch cabinet needs to be equipped with various analog pointer instruments and relays. It is difficult to realize more complex control logic. The operation mode is mainly manual operation and it is more complex. There are also safety risks such as entering the equipment electrified interval by mistake, unlocking by mistake, and operating by mistake, which brings great inconvenience to production, monitoring, and operation and maintenance.

Fig. 2 Traditional high voltage switchgear diagram



2.2 Intelligent High-Voltage Switch Cabinet

The intelligent high-voltage [2] switch cabinet is divided into four independent compartments: bus room, instrument room, circuit breaker room and cable room. The protection grade of the cabinet is IP4X, as shown in Fig. 3.

The intelligent high-voltage switch cabinet includes vacuum circuit breaker, electric earthing switch, video double confirmation host, camera, electric chassis, intelligent terminal, sensor and other components. Its metering, protection, control, communication and recording functions are safely and reliably applied through intelligent technology, digital display technology and other technologies, which is also consistent with the requirements of distribution network automation. As shown in Fig. 4.

Compared with the traditional high-voltage switch cabinet, the system design of intelligent switch cabinet uses computer technology as the core technology of monitoring, metering and protection. Transform the complex, error-prone and manned traditional operation process into data visualization, simplified operation process and remote control. For some scenarios where it is difficult for personnel to reach in a harsh environment, it can effectively avoid various safety risks and effectively



Fig. 3 Intelligent high voltage switchgear diagram

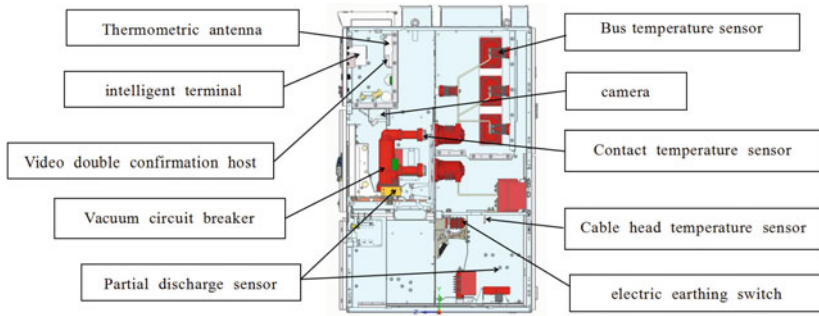


Fig. 4 Components of intelligent high voltage switchgear

Fig. 5 Accident diagram of high voltage switchgear



reduce equipment maintenance costs. So as to ensure the safe, intelligent, efficient and stable operation of the intelligent distribution network.

3 Failure in the Operation of High Voltage Switchgear

High-voltage switchgear will have insulation aging, mechanical failure, heating and other problems in long-term operation. If these faults are not repaired in time, they will often cause mis operation or refusal of operation of the switch, which will expand the fault. If the fault is serious, it will lead to a large area of power failure. When the heating fault accumulates the heat to a certain extent, it will cause the secondary side of the equipment or even the equipment itself to burn, and even the spread of the electrical fire to adjacent equipment leads to a large scale, causing great damage, as shown in Fig. 5.

Literature [3] lists the failure modes of high voltage switchgear, which mainly include rejection failure, mis operation failure, breaking and closing failure, insulation failure, external force and other failures. The key to solve the above problems lies in online state detection, timely discovery and timely treatment of faults. The intelligent high voltage switchgear can effectively discover and notify the operation and maintenance personnel to deal with the above faults in time.

4 Design and Application of Intelligent High Voltage Switchgear

Taking an intelligent high-voltage switchgear pilot project of Huayuan Electric as an example, this project adopts monitoring system, mechanical characteristics monitoring system, video double confirmation system, electric earth switch and electric chassis car, and its topological structure is shown in Fig. 6

4.1 Monitoring System

The monitoring content of the intelligent high-voltage switchgear includes partial discharge monitoring, ultrasonic wave, geoelectric wave and temperature sensor to collect corresponding data, and then transmit it to the intelligent data acquisition gateway through wired mode. The intelligent data acquisition gateway transmits the collected monitoring data to the monitoring center server through the optical network.

Contact Temperature Monitoring

Literature [4] has studied the temperature rise characteristics under typical contact faults, such as the fault at the junction of the incoming busbar of the switchgear, the plum contact fault and the circuit breaker contact fault, and has concluded that the overall temperature rise of the switchgear is increased and the temperature rise at the fault point is the highest when the contact fault occurs. These typical faults will cause overheating, which will accelerate insulation aging and lead to breakdown. It is the main failure mode of high-voltage switchgear.

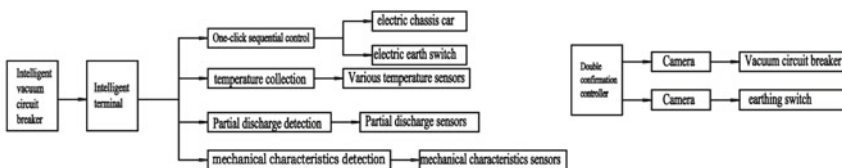
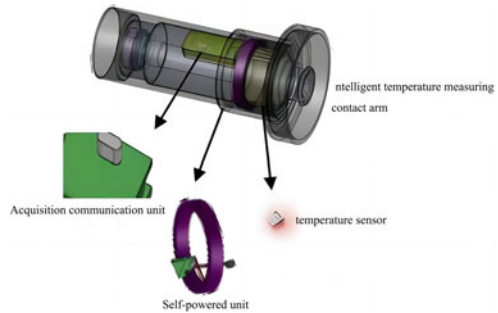


Fig. 6 Topological diagram of intelligent high voltage switchgear

Fig. 7 Structure diagram of the intelligent temperature measuring contact arm



The wireless temperature sensor of the intelligent high voltage switchgear is built into the vacuum circuit breaker to monitor the temperature change of the measuring point in real time to realize early fault prediction and alarm. When a fault occurs, it sends alarm information to quickly determine the location of the fault point and take safety measures according to the corresponding plan.

As shown in Fig. 7, the intelligent temperature measuring contact arm is composed of acquisition communication unit, self-powered unit and temperature sensor. The self-powered unit provides power for the acquisition communication unit and the temperature sensor. The acquisition and communication unit collects the temperature data generated by the temperature sensor in real time and sends the data wirelessly to the monitoring system. This sensor installation mode has the advantages of self-powered, maintenance-free, complete isolation of high and low potential, no electrical connection, flexible installation mode, etc. [5].

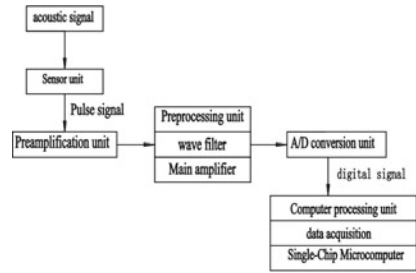
Partial Discharge Monitoring

The damage process of potential partial discharge is often slow and long-term. However, the characteristics of partial discharge can better confirm the insulation problem, so the insulation performance of the product can be objectively evaluated by comprehensive measurement of partial discharge characteristics.

For the intelligent high-voltage switchgear designed by our company, its partial discharge detection method adopts ultrasonic detection method. Ultrasonic method is a kind of mechanical vibration wave. From the perspective of energy, the process of partial discharge is the process of energy release, and electrical energy is released in the form of sound, light, heat and electromagnetic energy. The electrical breakdown occurs in the air gap. At this time, the discharge is completed in an instant and converted into heat energy. The air in the discharge center expands under the influence of heat energy, and its temperature is higher than the ambient temperature, and the sound wave is generated to spread outward; Because the area of partial discharge is relatively small, the local discharge sound source is the point sound source [6].

As shown in Fig. 8, when the sensor picks up the acoustic signal generated by partial discharge in the equipment, it converts the acoustic signal into electric pulse signal, which is amplified by the preamplifier unit and sent to the signal preprocessing unit. The signal preprocessing unit completes the filtering and further

Fig. 8 Schematic diagram of ultrasonic detection device



amplification of the electrical signal, and then converts the partial discharge acoustic analog signal into digital signal through the A/D conversion unit, It is transmitted to the computer and the digital signal is analyzed and processed by the processing software to determine the discharge mode and position [7].

4.2 Mechanical Characteristics Detection System

At present, when the circuit breaker on the high voltage switchgear is too fast, its action mechanism will bear greater mechanical stress and impact, resulting in the deformation of the mechanism parts and shortening the mechanical life of the circuit breaker; when the opening speed is too low, the arc extinguishing time will be increased, and the arc will cause metal melting on the surface of the contact, thus accelerating the electrical erosion of the circuit breaker contacts and reducing the service life of the circuit breaker [8] (Fig. 9).

The mechanical characteristic detection system sets standard mechanical characteristic parameters and corresponding mechanical characteristic error range parameters during installation. Compare the current mechanical characteristic parameters when the equipment is running. If the current mechanical characteristic parameters exceed the error range, it will be judged as abnormal. At the same time, when the circuit breaker acts, the system will generate a corresponding action report to display the parameters of the action, such as opening and closing time, speed, serial number, circuit breaker count, etc.

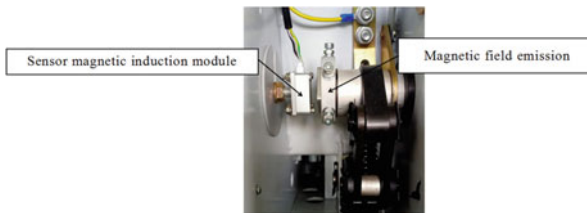
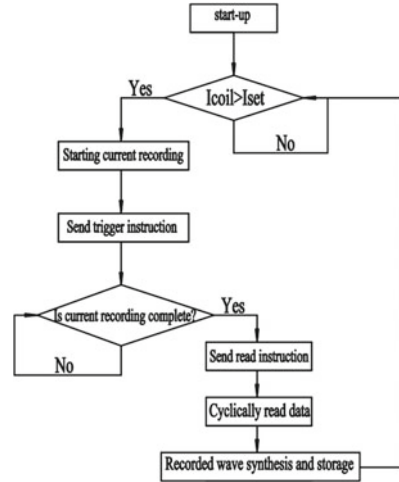


Fig. 9 Mechanical characteristics sensor installation diagram

Fig. 10 Flow chart of mechanical characteristics sensor



As shown in Fig. 10, the device can determine whether the circuit breaker acts by detecting whether there is current in the opening and closing coil current in real time. The current setting I_{set} can be set manually. After the opening and closing coil has current, the device sends the trigger command, the sensor starts to record the mechanical characteristic curve, and the device starts the current recording. After the current wave recording is completed, read the mechanical characteristic curve data for wave recording synthesis and storage [9].

4.3 Video Double Confirmation System

The video double confirmation system measures the displacement of the hand car through video, monitors the movement of the hand car throughout the whole process, intelligently analyzes the working position of the hand car, the test position, and the full stroke of the opening and closing of the hand car for video monitoring. According to the video status, it can be clearly seen the contact entering state when the hand car moves. During the inspection process, it can provide real-time video images of the intelligent high voltage switch cabinet (Fig. 11).

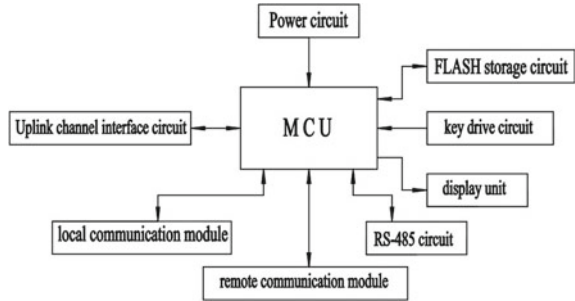
The double confirmation image processing host includes MCU module, power circuit, uplink channel interface circuit, FLASH storage circuit, key drive circuit, display unit, local communication module, remote communication module and RS-485 circuit.

As shown in Fig. 12, the MCU module is equipped with software to identify the algorithm of the corresponding color block within the range of HSV and the size range of the color block. The power circuit supplies power to the MCU module, the video signal output terminal of the MCU module is connected to the video signal input terminal of the display unit, and the key signal output terminal of the

Fig. 11 Actual position diagram of circuit breaker contact cabinet



Fig. 12 Schematic diagram of video double confirmation system



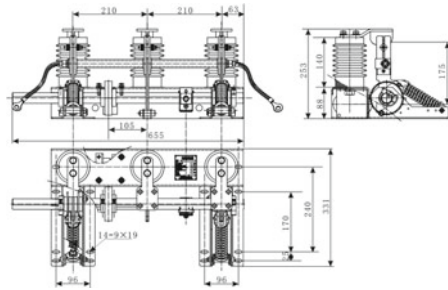
key drive circuit is connected to the key signal input terminal of the MCU module. The uplink channel interface circuit, FLASH storage circuit, local communication module, remote communication module and RS-485 circuit are connected to the communication port of MCU module. The double confirmation measurement camera is connected to the video signal of MCU module through 7RS-485 circuit. The upper computer is connected to MCU module through the remote communication module [10].

4.4 Electric Earth Switch

The electric earth switch does not change the opening and closing structure of the original earth switch body, but adds an electric operating device, which enables the switch to also conduct electric opening and closing operations, with local operation, remote operation and manual priority functions. Its structure is simple and its operation is safe and reliable.

The electric earth switch is composed of switch body, motor, clutch gear, transmission gear, valve electromagnet, energy storage spring, large shaft, etc. (Fig. 13).

Fig. 13 Structure diagram of electric earth switch



When closing is required, the positive transmission of the motor drives the clutch gear to rotate, thus driving the transmission gear and large shaft to rotate to the dead point of the energy storage spring, the position switch automatically switches the motor, and the earth switch quickly closes under the action of the energy storage spring.

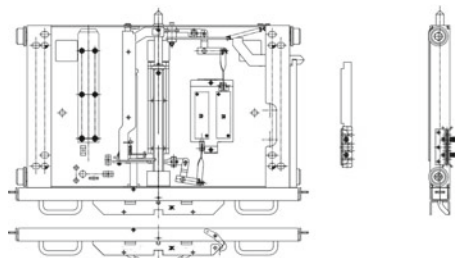
When opening is required, the motor reverses, drives the clutch gear, transmission gear and large shaft to move in reverse direction, the energy storage spring reaches the dead point, and the position switch switches again to realize opening operation [11].

4.5 Electric Earth Switch

The electric chassis car can not only operate the chassis car electrically, but also manually in the case of no power supply. It has local and remote operation functions. The electric chassis car is composed of chassis, lead screw, motor and other parts (Fig. 14).

When the motor is started, it drives the gear to rotate through the reducer, thus driving the screw to rotate. Under the action of the screw, the chassis car drives the circuit breaker to the working position until it reaches the working position. The normally closed contact of the auxiliary switch at the working position is switched

Fig. 14 Structure diagram of electric chassis car



to normally open contact, the motor is shut down, and the chassis car stops moving [12].

5 Conclusion

In recent years, as the demand for electricity has soared, the demand for power supply has become increasingly high. It is very important to ensure the security of intelligent distribution network, and the key node is prevention. High voltage switchgear as an important complete set of equipment in power system, ensure its stable and efficient operation, can have a direct and significant impact on the power supply quality of intelligent distribution. The following describes the advantages of intelligent high voltage switchgear in intelligent operation and maintenance.

5.1 *Advantages of Application in Intelligent Substation*

In the application environment of intelligent substation, the operation and maintenance of high-voltage switchgear has changed from manual patrol inspection to online monitoring, from fault repair to active repair, from post-repair to pre-warning, and from passive power failure to active operation and maintenance. The intelligent high-voltage switchgear has the functions of on-line real-time monitoring and remote control, which lays the technical foundation for intelligent substation to realize “feeder automation”, when the distribution network line fails, The distribution automation master station can conduct fault research and judgment by itself, perform fault isolation by fully automatic remote control, and quickly restore power supply to non-fault areas, thus reducing the time and scope of power failure, improving power supply reliability, and bringing social benefits.

5.2 *Advantages of Application in Equipment Operation and Maintenance*

The monitoring system, video double confirmation system and mechanical characteristic monitoring system configured for the intelligent high-voltage switchgear can provide a lot of convenience for the operation and maintenance management work, so that the operation and maintenance personnel can obtain extremely reliable auxiliary force in the equipment monitoring. Through real-time collection of uploaded video imaging and data, the alarm will be sent in time after the abnormal problem is detected, so as to ensure that the operation and maintenance personnel can find the abnormal information in time, According to the intelligent monitoring results, we

can quickly find the root cause of the problem, reduce its negative impact on power supply, improve the effectiveness of operation and maintenance management, and effectively reduce the occurrence rate of high-voltage switchgear failure.

5.3 Advantages of Application in Operation and Maintenance Security

Intelligent high-voltage switch cabinet is equipped with electric earth switch, electric chassis car, intelligent vacuum circuit breaker and other components. It is the basis for realizing the “remote control” function. It is precisely based on the realization of the “remote control” function that personnel can operate the high-voltage switchgear remotely, thus avoiding the impact of electric arc burns, electric current burns, skin metallization, explosion and other injuries caused by poor contact of the circuit breaker contacts during the opening and closing operation. The application of electric chassis vehicle can effectively prevent the operation and maintenance personnel from being hit and injured by objects caused by the overturning of handcart during the operation of handcart transfer and maintenance. Reduce the accident risk through remote operation and fully guarantee the personal safety of operation and maintenance personnel.

To sum up, the designers have continuously integrated new technologies and materials during the design and practice of high-voltage switchgear to accumulate technical experience. Constantly improve the operation efficiency and stability of the equipment, and lay a good foundation for the operation of the intelligent distribution network.

References

1. Koohi-Fayegh, S., Rosen, M.A.: A review of energy storage types, applications and recent developments. *J. Energy Storage* **27**(Feb), 101047.1–101047.23 (2020)
2. Jia, Y., Wu, X., Wang, J., Wang, B., Li, L.: Introduction of mechanical tests on intelligent high voltage switchgear. In: 9th IET International Conference on Advances in Power Systems Control, Operation and Management, Hong Kong, China, pp. 216–220. Curran Associates, Inc. (2013)
3. Zhou, S.: On-line monitoring and fault diagnosis of high-voltage switchgear. *Super Sci.* **22**, 64–65 (2020). (in Chinese)
4. Peng, T., Tang, B., Zhao, L., et al.: Study on temperature rise characteristics of medium voltage switchgear under typical contact fault. *High Voltage* **47**(12), 4331–4345 (2021). (in Chinese)
5. Lu, H., Yuan, Y.: Substation equipment temperature monitoring system design based on self-powered wireless temperature sensors. In: The 2014 2nd International Conference on Systems and Informatics (ICSAI 2014), Shanghai, China, pp. 209–214. IEEE (2014)
6. Shen, J., Lai, B., Xu, F.: Intelligent robot for ultrasonic discharge detection of high-voltage switchgear in substation. *Shandong Ind. Technol.* (6), 38–42 (2022). (in Chinese)

7. Xu, J.-J.: Research on online monitoring parameter identification and typical fault criteria of transformer equipment in southern Hebei power grid. *J. North China Electric Power Univ.* 1–63 (2015). (in Chinese)
8. Yang, F., et al.: Research on fault simulation of hydraulic spring circuit breaker in low temperature environment. In: 2022 IEEE International Conference on High Voltage Engineering and Applications (ICHVE), Chongqing, China, pp. 1–4. IEEE (2022)
9. Qingdao Yihe Electric Group Co. Ltd. The utility model relates to an integrated intelligent pre-inspection system for switchgear cabinet and apre- inspection method, ZL202011563216.0 (2020). (in Chinese)
10. Hunan Changgao Senyuan Electric Power Equipment Co. Ltd. The utility model relates to a smart switchgear video double confirmation device, ZL2020631935.0 (2020). (in Chinese)
11. Shanghai Baoling Chaoya Electric Appliance Co., Ltd. The utility model relates to electric earth switch device, ZL201220056831.7 (2012). (in Chinese)
12. State Grid Hunan Electric Power Co., Ltd. The utility model relates to a switchgear electric chassis car, ZL202010910757.X (2020). (in Chinese)

Research on Real-Time Data Acquisition of Flexible Distribution Network Based on SCU



Yi Yang

Abstract With the proposal of the dual-carbon goal, a higher proportion of new energy is widely connected to the smart grid, making the structure of the power system increasingly complex. In this context, timely and accurate power data acquisition directly affects the power quality and safe operation of equipment. In this paper, ETL technology is used for data acquisition and full management on the same standard in flexible distribution network, which realize real-time monitoring and control. After incorporating SVM method, the node voltage phase estimation model based on SCU is developed, the results show that the model can effectively improve the speed of information exchange, reduce network loss and reduce network loss rate in the process of network transmission. The combination of load forecasting and distribution network operation conditions can provide reference basis for power grid. The safety and reliability of distribution network are improved by processing real-time data with SVM module in LCA.

Keywords Flexible distribution network · Data acquisition · Node voltage

1 Introduction

The development of modern power market has put forward new requirements for power quality, and real-time data acquisition is the basis of realizing the safe and reliable work of power network [1, 2]. At present, most of the power enterprises in China use flexible monitoring tools to detect power quality, voltage stability and frequency [3]. However, the real-time data acquisition and communication technology is not widely used in industrial applications, and the real-time detection information cannot be timely transmitted to the power grid dispatch center [4].

The existing methods of data acquisition and transmission in the distribution network can not solve the problems of inaccurate data acquisition when the internal

Y. Yang (✉)

State Grid Hubei Electric Power Co, Ltd., Wuhan 430074, China

e-mail: 29169826@qq.com

© Beijing Paiké Culture Commu. Co., Ltd. 2023

X. Dong et al. (eds.), *The proceedings of the 10th Frontier Academic Forum of Electrical Engineering (FAFEE2022)*, Lecture Notes in Electrical Engineering 1054, https://doi.org/10.1007/978-981-99-3408-9_115

1283

equipment in the distribution network fails, users cannot know in time when the distribution network fails, and the system fails to work properly due to emergencies [5]. Meanwhile, traditional data acquisition methods can not accurately obtain information such as the voltage values of all load nodes on the line [6]. Therefore, based on the SGZ-CKE II T016 (DJBG), a set of real-time data acquisition scheme is designed in this paper for DSC/ASR system [7].

In order to meet the requirements of real-time data acquisition in flexible distribution network, a non-contact measurement method for synchronization and phase separation of three-phase power network is established, which enables real-time data acquisition of power network. Based on RS-485 bus technology, this method installs sensor devices directly in three-phase network and communicates through coaxial cable, which can effectively reduce errors caused by external factors in traditional measurement, avoid errors caused by human operation, and improve the coordination accuracy between distribution equipment, reduce system failure rate and maintenance costs. Based on RS-485 bus technology, real-time data acquisition of three-phase circuit can be achieved in the distribution network, and the information can be transmitted to PC through coaxial cable for centralized processing. The system structure is simple and the cost is low [6].

2 Theoretical Basis for Real-Time Data Acquisition in Flexible Distribution Network

2.1 Definition of Real-Time Data Acquisition in Flexible Distribution Network

Real-time data acquisition in flexible distribution network uses power metering to transmit real-time information generated on the network to remote monitoring stations in a variety of ways, so as to achieve fast and accurate monitoring of load, voltage and current values and other parameters.

In the traditional distribution network, real-time data acquisition uses the method of layer-by-layer acquisition and layer-by-layer transmission. With the development and application of power electronics technology, it is necessary to establish a real-time data acquisition and transmission mode that can provide a large number of fast and accurate data at the same time, and complete real-time monitoring and fault location through a variety of terminal devices [8] (Table 1).

For flexible distribution network, real-time data acquisition and network transmission have a large amount of information, so advanced real-time acquisition system is required to achieve fast and accurate monitoring of the parameters related to power measurement. It can combine power electronics technology, communication and computer technology to process the information transmitted by modern sensors devices.

Table 1 Table of Voltage-Current Meter

Instant value	Fixed-point freeze value	Interval value
Instant voltage/V	Continuous Cumulative Transfer Demand Power/W	Maximum Voltage/V
Instant Transfer Power/W	Cumulative demand transportation power/W	Minimum Voltage/V
Instant Receive Power/	Maximum demand transportation power/W	Receive Reactive Power/var·h
Requirement Repeat Number	Receive Reactive Power/var·h	Accumulated Voltage Measurement/V·h
Number of reversed times of the meter direction	Transfer reactive power/var·h	Transmission power/W·h
Number of blackouts	Receive power/W·h	
Number of Moves	Transmission power/W·h	

2.2 Factors Influencing Real-Time Data Acquisition in Flexible Distribution Network

- (1) External environment. Natural weather, temperature, humidity and so on will affect the accuracy of data acquisition, weather should be taken into account in daily maintenance, and the protection of the site environment to avoid human damage is necessary [4].
- (2) Internal factors. The structure of electric power equipment is complex, so it is unavoidable that faults or accidents will occur during operation. In addition, there are unpredictable problems in the power network itself, such as line aging, insulation layer damage and other device failures, which will affect data acquisition.
- (3) Fault factors of equipment, cable breakdown due to aging of line, damage of insulation layer or other reasons when adjusting cable voltage, and tripping due to faulty switching operation or short-circuit status of distribution substation, which will directly affect the accuracy and reliability of data acquisition.

3 Features of Flexible Distribution Network Based on SCU

3.1 Flexible Distribution Network Structure

The research object of this paper is the SVM-FT system, whose flexible distribution network structure is shown in Fig. 1. When a temporary power outage or other faults occur and the power supply signal cannot be transmitted to the dispatch center to restore power supply, the dispatch center will be notified to reconnect or transfer the load to maintain the stable operation of the power network and ensure the security of

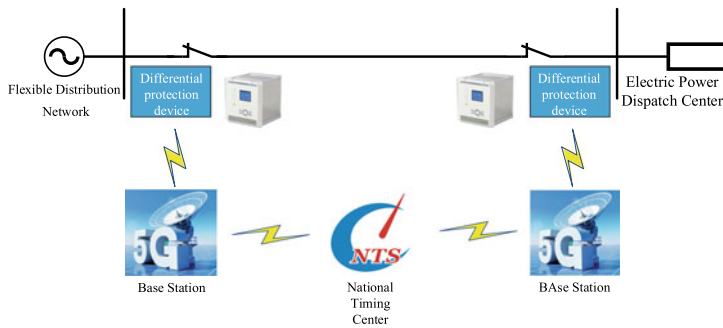


Fig. 1 Structural Diagram of Flexible Distribution Network

the whole system. All devices can be positioned by GPS Positioning System (TTSC) and RS-485 bus of monitoring [9].

3.2 Three-Phase Flexible Distribution Network Structure Based on SCU

Real-time data collection of distribution network refers to accurate and reliable measurement of various types of loads in the power system, and timely provision of this information to relevant managers, so as to achieve optimal configuration of power resources.

Flexible distribution network based on SCU can effectively improve power quality and service level. At present, most distribution networks in China use the power supply mode of double-feed structure. Real-time data acquisition should be connected to the bus of terminal equipment by two cables or the same main transformer circuit from different voltage levels. For single-phase load, single-phase double-feed structure is used because of its limited number of power supply loops, low power supply reliability and easy to fail in the actual operation process. For three-phase loads, data acquisition can be done through multiple transformers (Fig. 2).

3.3 Synchronous Data Acquisition Method for Flexible Distribution Network

There are many factors that affect real-time data acquisition. When the power transmission line fails or the equipment fails, the overload or overvoltage phenomena existing in the power network can not be obtained accurately in time [2]. The traditional on-site detection method is not only labor-intensive, but also can not collect

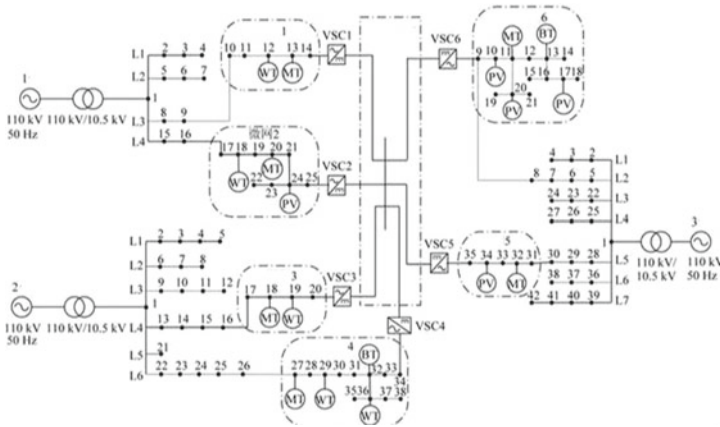


Fig. 2 Schematic Diagram of Flexible Distribution Network Based on SCU

information quickly and effectively, which is not conducive to the real-time data acquisition and monitoring of the operation status of distribution cables.

The platform consists of UPS power supply, generator protection control platform and remote detection station. UPS power supply is responsible for power supply to the control system of the protection device. The three-phase generator protection device is equipped with AVR system independently, and the voltage and current values are collected in real time [7]. These parameters are transferred to the switch of the power dispatch center through the switch, distribution network optical fiber in turn, and displayed on the board display [5].

The system mainly includes data acquisition module, drive motor module and display unit. First, in the aspect of data collection, real-time data acquisition is carried out for distribution network, and the data is saved as a complete model. Secondly, it receives the internal information from the devices through the sensor array and then transmits it to the PC terminal and display on the power network dispatch center. Finally, through the RS-485 bus and the computer connection, the data storage in the management system is achieved.

Data acquisition mainly consists of two parts: real-time measurement module and real-time display module. The system designed in this paper mainly uses the DSP-485 chip to store and transmit the required information in the distribution network. The JDK8001 radio frequency transceiver is used as a data measurement node unit to receive information from external devices and send it to the terminal display after processing. The real-time display module establishes the interface protocol with the upper computer, and communicates through the RS-485 bus. Parameters can be set as needed in the system. In the real-time display module, the collected information is processed and sent to the display through CDMA and GA chips [10] (Fig. 3).

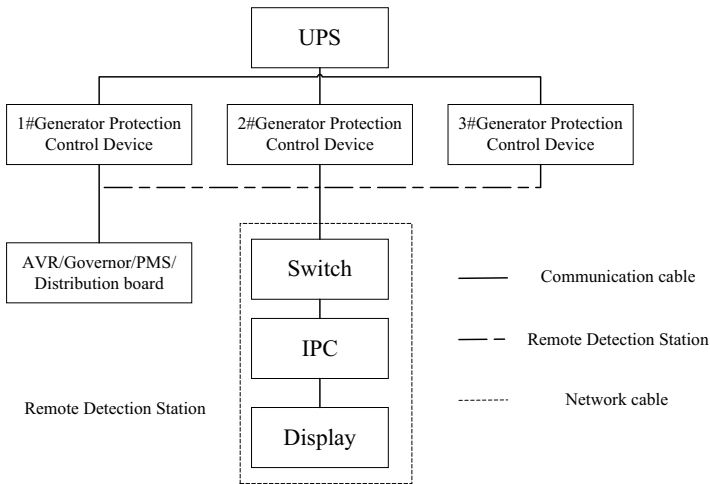


Fig. 3 Diagram of real-time data collection in flexible distribution network

4 Design of SCU Real-Time Data Acquisition System

4.1 Design Scheme of SCU Real-Time Data Acquisition System

This paper mainly focuses on the distribution management system to achieve the real-time data acquisition, so the plan should consider the design of a reasonable hardware structure and software configuration according to the actual situation, meanwhile, minimizing cost input should be taken into consideration when meeting current information requirements.

The system has three layers of architecture, the first layer is database management, the second layer is client, and the third layer is data management. This paper mainly focuses on the development and research of the background distribution management system, to realize the sharing and transmission function. Combining with the existing technical means, complete the relevant module design is required in the whole process. Data management is the main basis for daily maintenance and fault diagnosis of the system (Fig. 4).

4.2 Control of SCU Real-Time Data Acquisition System

In order to ensure the accuracy, stability and reliability of data acquisition, the corresponding control module is designed in the system, which can process the real-time data with the same input.

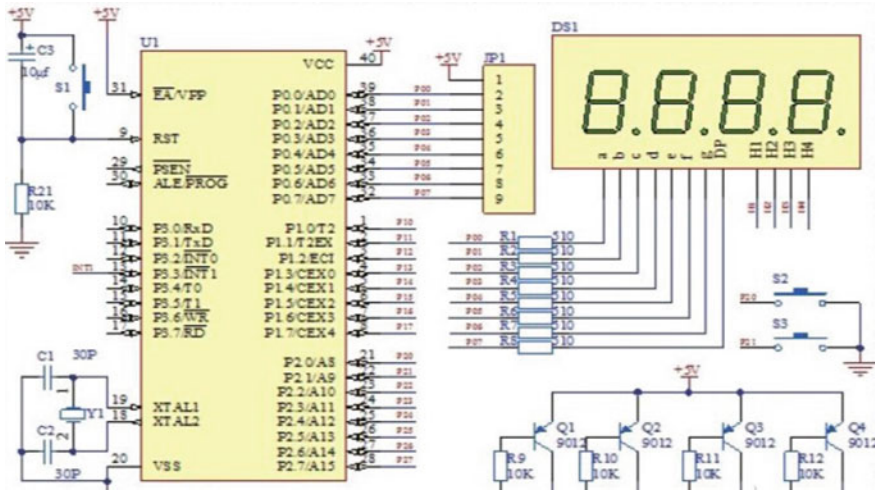


Fig. 4 Design Diagram of SCU Based Real-time Data Acquisition System

There is a correlation between the real-time information and the time difference. Using binocular vision technology, current signals collected from distribution network are monitored and converted to voltage values. The time delay error of the output and input values is measured at the same time. When the time delay of the sampling node is detected, the system will automatically generate corresponding time delay cancellation, and set a real-time clock in the system to monitor the status of the collection point.

The time difference of transmission is related to the corresponding output. Real-time data entry uses two calculation methods, reading current and voltage values of sampling nodes, converting them into digital signals and transporting them to the controller, to achieve the state conversion of real-time data acquisition points. In the whole system, the timer and the timer counter are two independent control units, which can switch between each other, or can be transmitted remotely by single-unit communication. Storage is used to store parameter information such as voltage value and phase difference between the sample node and the receiver.

5 Case Study of Real-Time Data Acquisition for Flexible Distribution Network Based on SCU

5.1 Application of Real-Time Data Acquisition

Real-time data acquisition is an important basis for power dispatch department to make decisions and control, and is also the premise to ensure the safe operation of distribution equipment, improve power supply reliability and power quality. At present, there are three main types of real-time data acquisition systems in the market, GPS, SIM and GPRS. There are problems in the application of the existing systems. Firstly, there is no universal installation of information collection devices in the distribution network, and the collection of information is not timely or comprehensive, which brings errors in working condition determination for the safe and stable operation of the power network. Secondly, there is no uniform standard, which results in the data not fully reflecting the real operating conditions. If a large number of device operation parameters are not transferred to the monitoring center in time for centralized processing and storage in the database, it may cause a lot of unnecessary losses.

5.2 Data Acquisition Strategy for Flexible Distribution Network

In real-time data acquisition, the most important thing is to realize real-time monitoring of the transmission process. Because of the influence of system structure, hardware environment and operation characteristics based on IEC standard design, non-rigid constraints are used to ensure the distribution network can operate safely and reliably, so corresponding measures must be taken to ensure real-time data storage and sharing.

Real-time acquisition strategy means that when monitoring real-time information, related data can be obtained by switching to a remote transmission terminal or switching to a distribution network. Real-time acquisition strategy refers to the acquisition of relevant information by switching to the sending terminal during data transmission. Remote monitoring means that when the system is in a failure state or in an unexpected situation, real-time data can be used to determine the operating conditions. Power network failure recovery strategy refers to the decision of data and corresponding measures taken by remote control devices when abnormal conditions such as short-circuit or break occur.

6 Conclusion

This paper presents a real-time data acquisition method for flexible distribution network based on SCU system, establishes the corresponding calculation model, and uses MATLAB to do column value and correlation analysis of the data. This method can be used to accurately determine the amount of information needed to put the distribution network into the flexible state, and the number of time-slice reports and update them in time. At the same time, it can also make an intuitive response to the income obtained under different types of loads to provide a more reliable and comprehensive quantitative basis for the power dispatch center. Using SVM technology to evaluate the operation benefit of distribution network, through a large amount of real-time data and corresponding model, more decision-making basis can be obtained according to different types of loads.

References

1. Li, P.: Optimal operation of soft open points in active distribution networks under three-phase unbalanced conditions. *IEEE Trans. Smart Grid* **10**(1), 380–391 (2018)
2. Li, Y., Xiao, J., Chen, C., Tan, Y., Cao, Y.: Service restoration model with mixed-integer second-order cone programming for distribution network with distributed generations. *IEEE Trans. Smart Grid* **10**(4), 4138–4150 (2018)
3. Zhang, L., Zhou, H., Ren, W., et al.: Urban distribution network monitoring system based on WebGIS development technology. *Electr. Technol.* **8**, 2 (2001). (in Chinese)
4. Zhao, M., Xu, G.: Research on transformer intelligent sensing data acquisition based on flexible strategy. *Comput. Appl.* **35**(11), 5 (2018). (in Chinese)
5. Meng, X., Sheng, W.: Design and construction of distribution network real-time data collection platform based on eDNA database. *Electric Power Constr.* **32**(3), 5 (2011). (in Chinese)
6. Fang, Y., Yang, B.: Research and design of real-time data acquisition system based on RTAI. *Comput. Inf.* **25**(4), 3 (2009). (in Chinese)
7. Wei, M., Wang, J., Wang, Z.: Real-time simulation of multi-terminal flexible DC distribution network based on RT-LAB. China Institute of Electrical Engineering (2015). (in Chinese)
8. Zeng, Q., Mu, D., Liu, H., Hu, W.: Research on real-time data acquisition system based on VxWorks. *Mechatronics* (11), 62–64. (in Chinese)
9. Fang, Y.: Research and Implementation of Real-time Data Acquisition System Based on RTAI. Southwest Jiaotong University. (in Chinese)
10. Wen, Q.: Research and application of data acquisition interface and real-time database based on DCS. Beijing University of Chemical Technology (2009). (in Chinese)

Deep Learning-Based Breakdown Voltage Prediction for Ball-to-Ball Discharge with an Air Gap Less Than 1.5 m



Changzhi Peng, Xuzhu Dong, Jiangjun Ruan, Yanpu Zhao, Bing Luo, Tingting Wang, and Shucan Cheng

Abstract The air gap breakdown voltage is an important physical quantity to consider when designing external insulation. The breakdown voltage is usually determined through extensive experimentation. In this study, we attempted to provide a novel approach for predicting air gap breakdown voltage. Using air gap break-down voltage data from 0.1 m to 1.5 m of ball to ball electrode, we calculated the electrical field and potential distribution between the air gap. Based on existing experimental data from various literature, we classified the experimental data as breakdown and withstand data. We proposed a neural network inspired by the computer vision method to study the electrostatic field characteristics based on labeled experimental data and initial conditions. The neural net predicts the breakdown voltage with an accuracy of more than 95% for air gaps ranging from 0.1 m to 1.5 m. Deep learning produces superior results when compared to traditional machine learning methods.

Keywords Breakdown Voltage · Deep Learning · Air Gap

1 Introduction

The air gap breakdown voltage is an important foundation for designing and optimizing external insulation in high-voltage power transmission projects [1, 2]. At the moment, theoretical research cannot completely determine the insulation strength of an air gap. As a result, only the air gap discharge test results can be used in the external insulation design of EHV/UHV power transmission and transformation projects. Over the last several decades, test data obtained by domestic and foreign

C. Peng · X. Dong (✉) · J. Ruan · Y. Zhao · S. Cheng
School of Electrical Engineering and Automation, Wuhan University, Wuhan 430072, China
e-mail: dongxz@whu.edu.com

B. Luo · T. Wang
Electric Power Research Institute, CSG, Guangzhou 210094, China

© Beijing Paiké Culture Commu. Co., Ltd. 2023
X. Dong et al. (eds.), *The proceedings of the 10th Frontier Academic Forum of Electrical Engineering (FAFEE2022)*, Lecture Notes in Electrical Engineering 1054, https://doi.org/10.1007/978-981-99-3408-9_116

1293

scholars through a large number of air gap discharge tests has provided strong support for the external insulation design of high-voltage power transmission and transformation projects [3, 4]. The worth of a large amount of experimental data has not been thoroughly investigated. It is critical to investigate the potential value of large amounts of experimental data and develop an AI model to predict the breakdown voltage.

Currently, air gap discharge voltage prediction methods primarily include simplified formula method, physical model, and artificial intelligence algorithm. In 1972, Mosch proposed a method for calculating the voltage–time characteristics of long rod-plane gaps under positive voltage [5]. In 1976, Carrara and Thione proposed a fitting formula for breakdown voltage based on the positive switching impulse discharge test results of the rod plate and wire plate gaps, assuming that the leader development speed was constant [6]. In 1989, Rizk derived the formula for calculating the continuous leader's starting voltage for gap structures such as rod plate, wire plate, rod-rod, wire rod, and so on with electrode curvature less than the critical radius [7]. In some small specific cases, these simplified methods can really show a good fitting effect. Because they are based on many assumptions, the prediction effect is poor when a specific condition change.

In addition to the simplified empirical formula, the second most popular method is to solve the physical model to obtain the breakdown voltage of the gap. The basic idea behind the physical model of the air gap discharge process is: establish mathematical models or criteria for each discharge stage in turn, and then simulate the entire discharge process by calculating the key physical parameters of each discharge stage [8]. The existing physical models of air gap discharge are primarily concerned with positive polarity. Corona initiation model, streamer development model, leader initiation model, continuous leader development model, and terminal jump model are the main simulation models for different discharge stages. Reather., (1964) developed the streamer inception formula based on Townsend theory [9]. The corona initiates when the number of electrons at the electrode head reaches 10^8 . Arevalo et al. (2012) of Sweden established a space charge calculation model based on Gauss theorem to simulate the streamer discharge process, which can consider the change of corona shape with the distribution of background electric field [10]. Diaz et al. (2016) created a physical model to predict the 50% breakdown voltage of long air gaps, which could be used to estimate electric fields, leader and streamer region propagation, and so on. In general, building an accurate physical model to describe the discharge process is difficult due to the complexity of the physical process of air discharge [11]. Furthermore, solving the physical model takes a long time, especially when the air gap is large.

Many researchers are interested in the machine learning method for predicting the breakdown voltage. Bourek et al. (2009) developed the dataset using the streamer inception criterion and the electrode curvature radius, gap distance, and applied voltage as the input of the fuzzy logic system to predict the breakdown voltage [12]. Ruiz et al. (2013) created a neural network model with 100 samples to construct the relationship between applied voltage and breakdown [13]. Qiu et al. (2016) proposed a machine learning method for breakdown voltages and corona inception voltages based on the electric field distribution characteristics and support vector machines [14]. Wang et al. (2019) used a support vector machine to create a standard operation impulse discharge voltage prediction model for the tower air gap [15, 16]. The 1000 kV wine glass tower edge phase air gap discharge voltage was predicted. The maximum error of the predicted value of the discharge voltage in the 4–8 m long gap is within 10% when compared to the discharge characteristic experimental results.

The traditional machine learning method could only study a small sample size and required manual extraction of feature quantity. The success of deep learning in various research fields, such as speech recognition and image recognition, demonstrates the benefits of deep learning for processing large amounts of data. In this study, we will use a convolutional neural network to study the electric field characteristics between air gaps and predict the breakdown voltage.

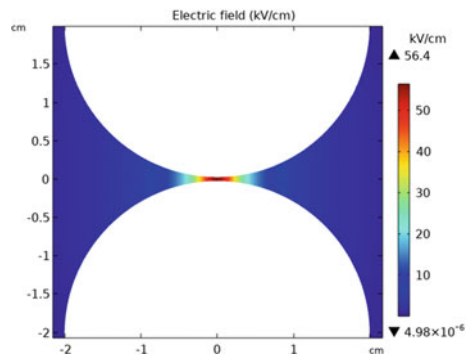
2 Data

The breakdown voltage data used in this study was obtained from the IEC 60,052(2002) [17]. As shown in the Table 1, the value given is a brief overview of the highest stable voltage level at which the air gap breakdown occurs. The sphere gap spacing ranges from 0.05 cm to 150 cm, and the sphere diameter ranges from 2 to 200 cm. The breakdown voltage ranges from 2.8 kV to 2250 kV. We generated breakdown samples and withstand samples based on the maximum breakdown voltage as the boundary for each given air gap distance and sphere diameter. Comsol is used to create the electrode structure, and the applied voltage is used as an input to the model to calculate the electrostatic field by finite element method. The electrostatic field was calculated using an air gap of 0.05 cm and a sphere radius of 2 cm, with an applied voltage of 2.8 kV, as shown in Fig. 1. The electric field between electrodes varies greatly depending on the air gap and electrode structure. We generated approximately 5000 samples for use as training data.

Table 1 Peak breakdown $U_{50\%}$ values (kV) for sphere air gap

Air gap(cm)	Sphere radius						
	2	5	6.25	10	12.5	...	200
0.30	11.2	11.2					
0.40	14.4	14.3	14.2				
0.50	17.4	17.4	17.2	16.8	16.8		
0.60	20.4	20.4	20.2	19.9	19.9		
0.70	23.2	23.4	23.2	23.0	23.0		
0.80	25.8	26.3	26.2	26.0	26.0		
0.90	28.3	29.2	29.1	28.9	28.9		
1.0	30.7	32.0	31.9	31.7	31.7		
...	...						
150							2350

Fig. 1 The electric field distribution characteristics under a voltage of 2.8 kV



3 Methodology

3.1 Convolutional Neural Network

A multilayer feedforward artificial neural network called a convolutional neural network (CNN) is mostly made up of pooling and convolution layers [18]. Convolutional layers are mostly utilized for feature extraction. Utilizing the one-dimensional and two-dimensional signals' local strongly correlated properties, it extracts the local features of the signals using the proper convolution kernel filtering.

In comparison to artificial feature extraction, the neural network can extract more distinct features through continuous learning of a large number of parameters. These local features are then extended to the overall features to produce the best feature extraction. Convolutional neural networks have grown in popularity as a study topic recently, especially in the disciplines of speech recognition, pedestrian detection, and image processing.

3.2 Neural Network Architecture Design

We attempt to design a convolutional neural network to study the characteristics of the electric field between air gaps in light of the excellent performance of two-dimensional convolution networks in image recognition and image understanding. The convolution layer is the most important layer in a convolution neural network. During testing, the convolution layers act as image filters, extracting features from images and calculating match feature points. Equation 1 depicts the operation mode of a convolutional layer.

$$O(i, j) = (K * I)(i, j) = \sum_m \sum_n I(i + m, j + n)K(m, n) \tag{1}$$

where O represents the convolutional layer’s output, K represents the convolutional kernel, and I represent the convolutional layer’s input.

The number of convolutional layers determines the performance of a neural network. In addition to the convolutional layer, there is an input layer, a pooling layer, and a fully connected layer. The input layer is the model’s first layer. The polling layer is responsible for retaining information from the convolutional layer. The fully connected layer is the model’s final layer, and it is responsible for converting the input into categories with labels. In this study, the air gap, sphere radius, and applied voltage are all inputs to the network model, in addition to the electric field. As a result, we created the deep learning model depicted in Fig. 2.

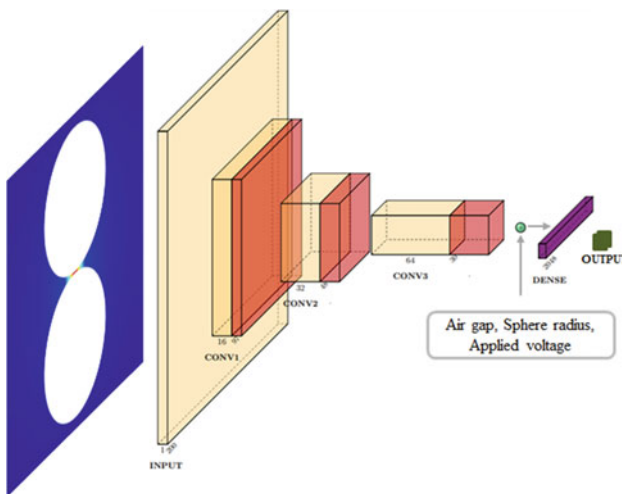


Fig. 2 Neural network structure for breakdown voltage prediction

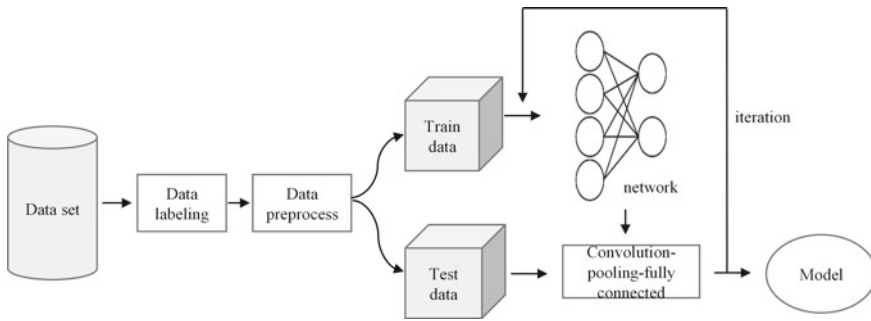


Fig. 3 Deep learning workflow

3.3 Workflow of Algorithm

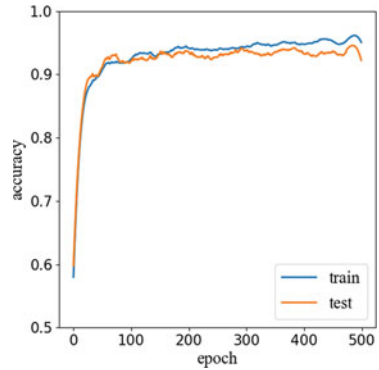
The workflow consists primarily of data labeling, preprocessing, network model training, and model testing. Figure 3 depicts the workflow. In machine learning, the data labeling process is used to identify the original data (pictures, text files, videos, etc.) and add one or more meaningful information tags to provide the following so that the machine learning model can learn from it. Our data in this study are labeled with breakdown and withstand. Data preprocessing in Machine Learning is an important step that helps improve data quality and promotes the extraction of meaningful insights from data. In this study, we use normalization to preprocess the raw data. The network model training is used to obtain appropriate weights for the network in order to achieve good training results. Finally, the test data is used to determine the network model's accuracy.

4 Results

To begin, 80% of the data set is chosen at random for training, while the remaining data is used for testing. We start with 500 iterations to determine the epochs of the model training. Figure 4 depicts the model's accuracy. It is discovered that when the number of iterations exceeds 200, the model's accuracy does not improve significantly. Furthermore, as training times increase, the model is likely to be trained over fit. When the training times exceed 400, the test accuracy suffers a slight decrease. As a result, in subsequent training, we used 200 iterations to compare network model performance with different convolutional layers.

Different model layers and structures will yield different experimental outcomes. This paper's model structure is based on the results of numerous experiments. Furthermore, we compared the effect of the number of convolutional layers on model accuracy. We trained the model using various convolutional layers. The training and testing results of models with various convolution layers are shown in Fig. 5. The

Fig. 4 Network model accuracy with an iteration of 500



performance of the 3-layer and 10-layer convolution models is compared using the 5-layer convolution model proposed in this paper as a baseline. After training these three models for 200 times, the classification accuracy of each model for test data can reach more than 95%. Based on our findings, a 5-layer neural network model is adequate for our training. As a result, we use a 5-layer neural network for our model.

Finally, using our trained network model and a sphere radius of 50 cm, we predicted the breakdown voltage for an air gap of 10 to 20 cm. Figure 6 displays the outcomes of the neural network and the experiment. The black solid line represents the predicted results, and the red prismatic represents the experimental findings. The breakdown voltage can be accurately predicted by the network model, it has been discovered.

Fig. 5 Training and test results of models with different convolutional layers

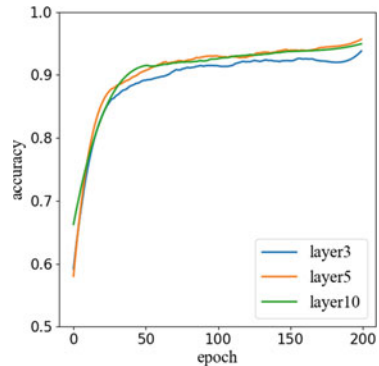
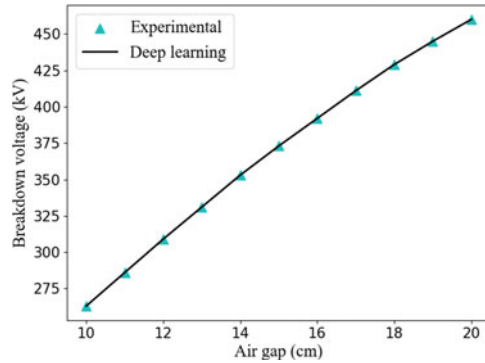


Fig. 6 Comparison of experimental results and predicted results



5 Conclusions

This study proposed a deep learning method for predicting the breakdown voltage of the sphere electrode with an air gap space less than 1.5 m. Based on the Comsol electric field and experimental data as input, the network model can achieve a breakdown voltage accuracy of more than 95%. Deep learning is more convenient than traditional machine learning methods because it does not require the extraction of features manually. The preliminary results of using deep learning by combining experimental and simulation results show that deep learning has the huge potential in insulation prediction and experimental data mining.

Acknowledgements This study was supported by the National Engineering Research Center of UHV Technology and New Electrical Equipment (2020-4201-21-000066). Data and additional information are available upon request from the corresponding author (dongxz@whu.edu.cn).

References

1. Shu, Y., Chen, W.: Research and application of UHV power transmission in China. *High voltage* **3**(1), 1–13 (2018)
2. Du, Z., Xiu, L., He, J., Cai, H., Li, E.: Computation of total electric field considering natural wind under high-altitude UHVDC transmission lines. *IEEE Trans. Magn.* **58**(9), 1–4 (2022). <https://doi.org/10.1109/TMAG.2022.3186483>
3. Huang, D., Shu, Y., Ruan, J., Yi, H.: Ultra high voltage transmission in China: developments, current status and future prospects. *Proc. IEEE* **97**(3), 555–583 (2009). <https://doi.org/10.1109/JPROC.2009.2013613>
4. Kim, N.-K., Lee, S.-H., Georghiou, G.E., Kim, D.-W., Kim, D.-H.: Accurate prediction method of breakdown voltage in air at atmospheric pressure. *J. Elect. Eng. Technol.* **7**(1), 97–102 (2012)
5. Mosch, W., Lemke, E., Larionov, V.P., Kolecizky, E.S.: An estimation of the voltage-time characteristic of long rod plane gaps in air at positive switching impulse voltages. In: *Proceedings of the 13th International Conference on Phenomena in Ionized Gases, Berlin, September 1977* (1977)

6. Carrara, G., Thione, L.: Switching surge strength of large air gaps: a physical approach. *IEEE Trans. Power Appar. Syst.* **95**(2), 512–524 (1976)
7. Rizk, F.A.M.: A model for switching impulse leader inception and breakdown of long air-gaps. *IEEE Trans. Power Deliv.* **4**(1), 596–606 (1989). <https://doi.org/10.1109/61.19251>
8. Chen, W., Rong, Z., He, H.: Research progress of long air gap discharges. *High Volt. Eng.* **39**(06), 1281–1295 (2013)
9. Reather, H.: *Electron Avalanches and Breakdown in Gases*. Butterworth, London (1964)
10. Arevalo, L., Cooray, V., Dong, W., Jacobson, B.: A new static calculation of the streamer region for long spark gaps. *J. Electrostat.* **70**(1), 15–19 (2012)
11. Diaz, O., Arevalo, L., Cooray, V.: Parameter variation in leader channel models used in long air gap discharge simulation. *Elect. Power Syst. Res.* **139**, 32–36 (2016)
12. Bourek, Y., Mokhnache, L., Said, N.N., Kattan, R.: Study of discharge in point-plane air interval using fuzzy logic. *J. Elect. Eng. Technol.* **4**(3), 410–417 (2009). <https://doi.org/10.5370/JEET.2009.4.3.410>
13. Ruiz, D., LloveraSegovia, P., Pomar, V., Quijano, A.: Analysis of breakdown process at U50 voltage for plane rod discharges by means of neural networks. *J. Electrostat.* **71**(3), 336–340 (2013)
14. Qiu, Z., Ruan, J., Huang, D., Ziheng, P., Shu, S.: A prediction method for breakdown voltage of typical air gaps based on electric field features and support vector machine. *IEEE Trans. Dielect. Elect. Insul.* **22**(4), 2125–2135 (2015). <https://doi.org/10.1109/TDEI.2015.004887>
15. Wang, X., Qiu, Z., Ruan, J., et al.: Air gap discharge voltage prediction of uhv cup tower outer phase under switching impulse. *High Volt. Eng.* **45**(05), 1413–1419 (2019)
16. Ruan, J., Zhang, Y., Zhang, Y., et al.: Numerical simulation research and applications of electromagnetic metaphysical field for electrical equipment. *High Volt. Eng.* **46**(03), 739–756 (2020)
17. IEC 60052:2002. Voltage measurement by means of standard air gaps
18. Ghorbanzadeh, O., Blaschke, T., Gholamnia, K., Meena, S., Tiede, D., Aryal, J.: Evaluation of different machine learning methods and deep-learning convolutional neural networks for landslide detection. *Rem. Sens.* **11**(2), 196 (2019). <https://doi.org/10.3390/rs11020196>

Remaining Useful Life Prediction Method of Lithium-Ion Batteries Based on Relevance Vector Machine



Qiancheng Tian , Haitao Chen, Shuai Ding, Lei Wang, Jun Huang, and Ziwei Yang

Abstract The wide popularity of lithium-ion batteries in the aerospace field accelerates the development of its remaining useful life (RUL) prediction. The RUL of lithium-ion batteries can be predicted by the relevance vector machine (RVM), but the prediction effect depends on the kernel function. Different kernel functions will get different prediction effects. In the SK (SK) RVM, since there is only one kernel function and the choice is subjective, the effect of RUL is common. This paper proposes a new RUL prediction method with multi-kernel (MK) RVM, which enhances the accuracy and credibility of the prediction. In order to give full play to the advantages of each kernel function, particle swarm optimization (PSO) is used to realize parameters self-optimization. Based on NASA's battery capacity degradation data set, carrying out the RUL prediction of SK and MK RVM.

Keywords RVM · PSO · Phase-space reconstruction · RUL

1 Introduction

With the popularization of lithium-ion batteries, more and more scholars pay attention to the RUL prediction. It is very difficult to get the battery mechanism model, the data on batteries are few and most of them are not available, so better prediction methods are needed for the RUL. Compared with only using the RVM method for the RUL prediction, more research work is carried out by combining RVM and other methods for prediction [9–15].

Currently, there are three main ways to predict the RUL of lithium-ion batteries, as shown in Fig. 1. The first category is the method used in the mechanism model. Fan [1] used a particle filter to establish an empirical model to describe the law

Q. Tian · H. Chen · S. Ding · L. Wang · J. Huang (✉) · Z. Yang
Shanghai Institute of Space Power-Sources, Shanghai 200245, China
e-mail: huju1981@163.com

State Key Laboratory of Space Power Sources, 200245 Shanghai, China

© Beijing Paiké Culture Commu. Co., Ltd. 2023
X. Dong et al. (eds.), *The proceedings of the 10th Frontier Academic Forum of Electrical Engineering (FAFEE2022)*, Lecture Notes in Electrical Engineering 1054, https://doi.org/10.1007/978-981-99-3408-9_117

1303

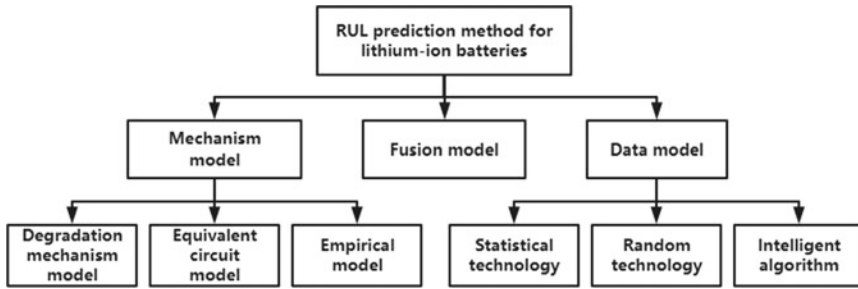


Fig. 1 Main RUL prediction methods of lithium-ion batteries

of capacity degradation and achieve RUL prediction. Wang [2] proposed a battery RUL estimation method using RVM and a 3-parameter degradation model. The final prediction accuracy depends on the accuracy of the parametric degradation model, and the prediction effect is not very ideal. The second category is the data-driven approach that uses historical data to predict RUL. Zhou [3] proposed an RUL prediction method based on the optimized incremental RVM model. The prediction effect has made much progress compared with the SVM. The third category is the fusion method composed of a variety of methods. Long [4] used a modified AR model and obtained better RUL prediction results. Zheng [5] made use of UKF and RVM for short-term prediction and gained more accurate RUL prediction results. Because SK RVM prediction is subjectively selective and singleness, some researchers began to carry out the RUL prediction of MK RVM.

Parameter and weight determination of kernel function is the key problem of MK RVM. Recently, a large number of parameter optimization methods have emerged to solve the problem of parameter self-optimization [6–8]. Due to the PSO algorithm, it is easier to implement, easier to understand, and faster to converge, this paper chooses PSO as the parameter optimization method of MK RVM.

2 RUL Prediction by SK RVM

2.1 RVM Algorithm

RVM is a very powerful tool for regression and prediction based on the Bayesian theory framework. It contains Markov, Bayesian, Autocorrelation criterion, and Maximum likelihood theory, which can obtain a sparse kernel function sum and solve regression and classification problems. RVM is better and more sparse than support vector machine (SVM), which makes them faster on the test set. RUL is a multi-step time series prediction, a relevance vector regression (RVR) problem in essence. It is very suitable to use RVM to predict the RUL of lithium-ion batteries.

The expression of RVR can be obtained:

$$c = \phi w + \varepsilon \tag{1}$$

Among them, c is the nonlinear model, w is the weight coefficient, Φ is the kernel function matrix, and ε is Gaussian noise which is independent and identically distributed.

The variance and output are:

$$\sigma^2(x) = (\beta^*)^{-1} + \phi(x)^T \sum \phi(x) \tag{2}$$

$$c = m^T \phi(x) \tag{3}$$

Among them, β^* is the hyperparameter that maximizes the marginal likelihood function, and m is the posterior mean.

The most basic and core part of the RVM is the training algorithm, which trains the data to get the training model. In the training process, the maximum likelihood function can excavate the data features from the training data and extract the data features for data prediction. Prior distribution can identify the level of data and the complexity of the system so that more useful data information can be obtained during training and the universality of data prediction can be improved.

The basic training method is the most basic and original training algorithm of RVM, which is characterized by simple steps and is easy to implement. The detailed process of the basic iterative training algorithm of the RVM is given below.

Step 1 (initialization): Initialize the hyperparameter and variance, set the number of hyperparameters, set the value of each hyperparameter to 0, and set the value of variance to 0.

Step 2 (calculation): Calculate the mean and variance of the posterior distribution.

Step 3 (update): In the process of iterative calculation, constantly update the hyperparameter and variance.

Step 4 (convergence judgment): Judge whether the convergence condition is reached. If not, continue to cycle Step 2 and Step 3 until the maximum number of cycles is reached or the gradient of the output result is less than the convergence condition. If the convergence condition is reached, the next step is run.

Step 5 (screening): Compare all hyperparameters with the set values of the maximum hyperparameter. If the value of the hyperparameter is greater than the set value of the maximum hyperparameter, the corresponding kernel function and its weight coefficient will be eliminated.

Step 6 (prediction): At the beginning of the prediction, the convergence parameter obtained in Step 4 is used to substitute the new sample into the model completed by training, so as to predict the value.

In the whole training process, Step 5 needs to set a reasonable maximum value of the super parameter. If the selected value of the super parameter is large, the number of correlation vectors will be reduced, which cannot fully reflect the characteristics and trends of the data and affect the accuracy of the prediction. If the super parameter selection value is small, the number of correlation vectors will increase. Although it can fully reflect the characteristics of the data, the increase in the calculation amount will greatly increase the training time, which will affect the speed of prediction.

2.2 Phase-Space Reconstruction

General time series mainly study the model in the time domain, but for chaotic time series, both the calculation of chaotic invariants and the establishment and prediction of the chaotic model is carried out in the so-called phase space. Therefore, phase-space reconstruction is a very important step in the processing of chaotic time series. The so-called chaotic sequence can be regarded as a set of observed values that change over time when a chaotic system is examined.

Variables in the system are the mutual influence between the phase-space reconstruction, the basic idea of RUL prediction is significant research on time series multi-step prediction. In Takens embedding theorem, the existence of embedding dimension D and delay time τ is only proved theoretically without specific expression. Moreover, time series in practical applications are finite sequences with noise, and appropriate values of embedding dimension and time delay must be selected according to the actual situation.

For phase space reconstruction of data, the key problem is how to choose the appropriate D and τ . In the actual working process of the lithium-ion battery, there is no constant D and τ , and the values of D and τ need to be determined according to the working condition. There are two kinds of methods for determining d and τ . One is the τ before d , such as the modified Cao method. The other is to determine D , τ simultaneously, such as the C-C method.

2.3 RUL Prediction Experimental Method of SK RVM

RUL prediction of SK RVM is mainly divided into three parts: phase-space reconstruction, RVM modeling, and iterative prediction.

The first step is to reconstruct the original data sequence with a certain dimension and delay to construct the model training data.

The second step is to train the reconstructed data of phase space and establish the RVM prediction model.

The third step is to use the RVM prediction model to iteratively predict the capacity. The prediction model framework of the SK RVM is shown in Fig. 2.

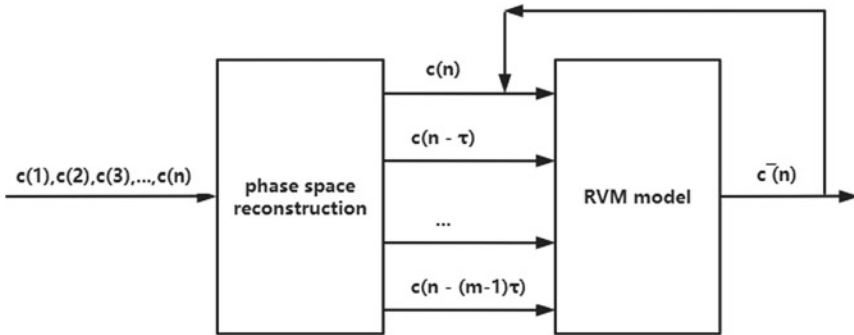


Fig. 2 Framework of the SK RVM

In the framework of the SK RVM model, $c(1), c(2), \dots, c(n)$ is the historical capacity data, $\bar{c}(n + 1)$ represents the predicted capacity data, τ , and m are in phase-space reconstruction, respectively. In this paper, $\tau = 1$, $m = 6$, and time window length 6 are selected to reconstruct capacity data.

3 RUL Prediction by PSO MK RVM

3.1 MK RVM Algorithm

MK RVM can have the advantage of multiple kernel functions at the same time. For example, it can reflect not only local trends but also global trends. For simplicity, this paper first uses the hyperparameter determination method of the SK function to build the RVM model of each SK function for training before combining kernel functions, so as to determine relatively good hyperparameters. On the basis of keeping the setting of single kernel hyperparameters unchanged, kernel functions are combined, focusing on optimizing the coefficient of a linear combination of kernel functions. The MK RVM model after optimization is compared with the SK RVM model constructed by different kernel functions.

The mathematical expression of the MK kernel function is as follows:

$$K_5(x, z) = w_1 K_1(x, z) + w_2 K_2(x, z) + w_3 K_3(x, z) + w_4 K_4(x, z) \quad (4)$$

Among them, w_1, w_2, w_3 and w_4 are the weight. k_1, k_2, k_3 , and k_4 are the Gaussian kernel, the Linear kernel, the Sigmoid kernel, and the Polynomial kernel respectively. The method to improve the prediction accuracy is to select the appropriate weight coefficient. Considering many situations, PSO is chosen to realize self-optimization of weight coefficients.

3.2 PSO Algorithm

The main idea of the PSO algorithm is information sharing, from the local optimum to the global optimum.

The particle's velocity v_i is updated:

$$v_i^d = wv_i^d + c_1r_1(p_i^d - x_i^d) + c_2r_2(p_g^d - x_i^d) \quad (4)$$

The particle's position x_i is updated:

$$x_i^d = x_i^d + \alpha v_i^d \quad (5)$$

Among them, $i = 1, 2, 3 \dots M$, $d = 1, 2, 3 \dots N$, r_1 and r_2 are random numbers, α is the constraint factor, w is inertia factor, p_i and p_g are the optimal values, c_1 and c_2 are acceleration constants.

3.3 RUL Prediction Experimental Method of MK RVM

Figure 3 is the flow chart of the MK RVM model. The calculation method of root mean square error (RMSE) is as follows:

$$RMSE = \sqrt{\frac{1}{n} \sum_{i=1}^n (x(i) - \bar{x}(i))^2} \quad (6)$$

Among them, $x(i)$ represents the actual capacity value, n is the capacity cycle number, and $\bar{x}(i)$ represents the capacity predicted result.

The RUL prediction of MK RVM is similar to that of the SK method. PSO can optimize the weight of functions on the capacity degradation data before the starting point of training, to construct the MK RVM model of particle swarm optimization.

4 Prediction Simulation

4.1 The Experimental Data

The lithium-ion battery data used in this article came from NASA's datasets. The dataset contains charge and discharge data for batteries 5, 6, 7 and 18. All four batteries have a rated charging capacity of 2Ah and a constant charging current. Select the battery capacity as the indicator of battery performance degradation. When the

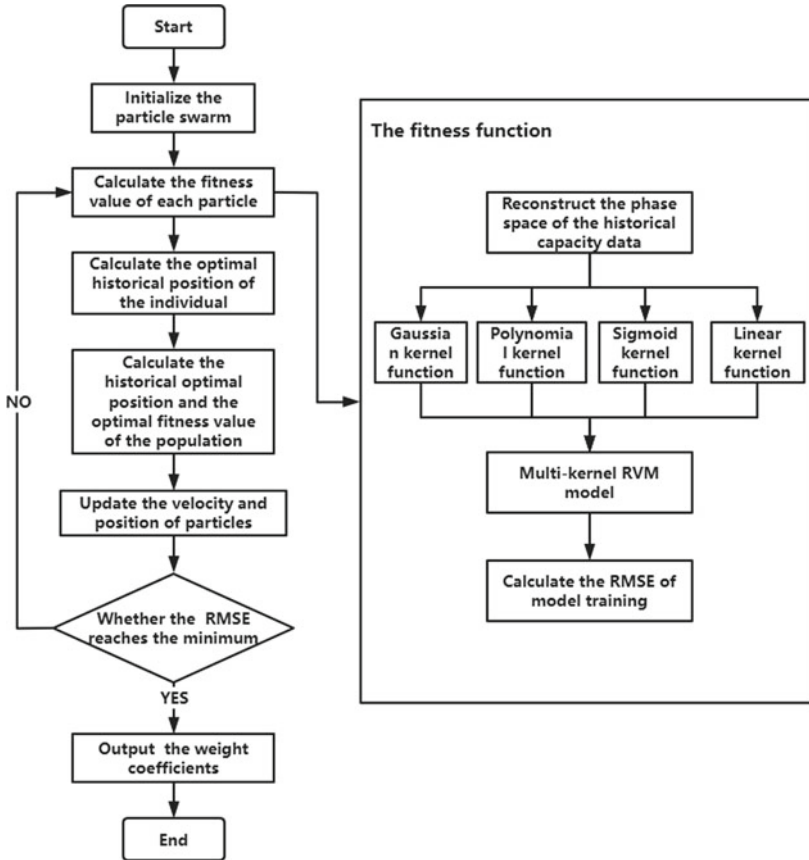


Fig. 3 Block diagram of MK RVM model

capacity degrades to 70%, the battery life is over. The battery capacity degradation curve is shown in Fig. 4.

4.2 Analysis of Experimental Results

Taking the No.6 battery as example, the expected starting point has a great influence on the prediction effect. The lifetime of the lithium-ion battery is predicted when SP is 40, 60, and 80 cycles. In order to reflect the predictive effect, this paper compares the results of SK and MK RVM. The prediction effects are shown in Table 1.

Among them, SP is the predicted starting point, EP is the predicted lifetime endpoint, RP is the remaining life of prediction, RE is the real error, MAE is the mean absolute error, and RA is the relative accuracy.

Fig. 4 Battery capacity degradation curve

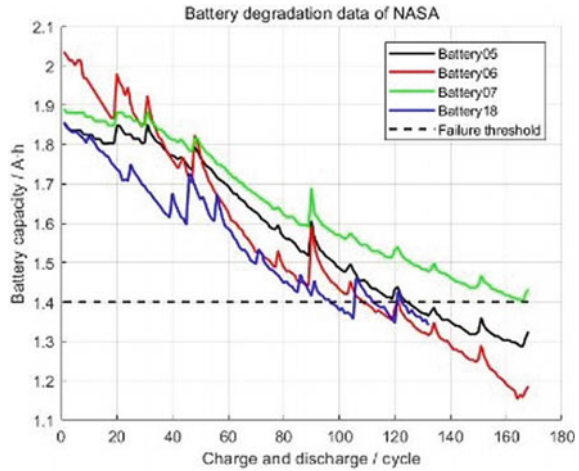


Table 1 Comparison of prediction results of MK and SK RVM

SP	algorithm	EP	RP	RE	MAE	RMSE	RA
40	SK	104	64	4	0.0417	0.0474	94.1%
	MK	110	70	2	0.0258	0.0351	97.1%
60	SK	102	42	6	0.0512	0.0560	87.5%
	MK	107	47	1	0.0234	0.0309	97.9%
80	SK	96	16	12	0.0854	0.0927	57.1%
	MK	102	22	6	0.0266	0.0348	78.6%

$$MAE = \frac{1}{n} \sum_{i=1}^n |x(i) - \bar{x}(i)| \tag{7}$$

In Table 1, no matter MAE or RMSE, the value of particle swarm optimization MK RVM is lower, and its prediction effect is better than that of SK RVM.

Focus on the comparison of the prediction effect when SP = 60. The solid red, dashed blue and solid black lines are the real value of capacity degradation data, the predicted value of capacity degradation data and the failure threshold respectively. The 3σ confidence interval is the light blue shaded area.

In Fig. 5, when the SP is 60, the EP is 102, the RP is 42, the true endpoint of life is 108, the true RUL is 48, and the 3σ confidence interval is [88,119], and the RA of prediction is 87.5%.

In Fig. 6, when the SP is 60, the EP is 107, the RP is 47, the true endpoint of life is 108, the true RUL is 48, and the 3σ confidence interval is [89,126], and the RA of prediction is 97.9%.

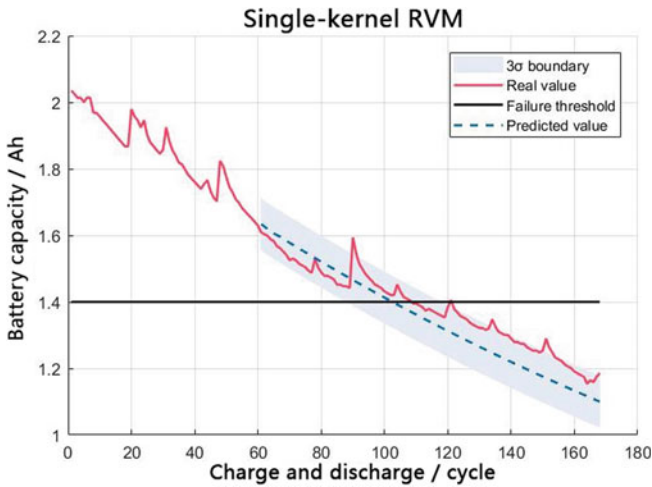


Fig. 5 SP = 60, SK RVM prediction

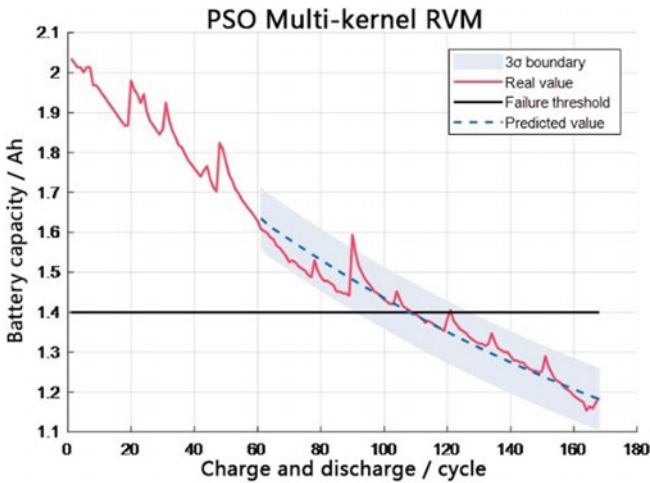


Fig. 6 SP = 60, MK RVM prediction

5 Conclusion

In this paper, an RUL prediction method of MK RVM based on PSO is proposed. MK can have the advantage of multiple kernel functions and reflect not only local trends but also global trends. To reduce the coupling between kernel functions, multiple kernel functions are combined linearly. The RMSE of the training set is taken as the fitness function of the PSO to realize the self-optimization of the weight coefficient of the MK function. MK prediction method has achieved better prediction results

than SK RVM. The PSO algorithm is one of the intelligent optimization algorithms. The fusion of an intelligent optimization algorithm and MK RVM can effectively improve prediction accuracy, which will also become the topic of my subsequent research.

References

1. Liming, F., Kunsheng, W., Cheng, Q.: Remaining useful life prediction of lithium battery based on physics of failure and particle filtering. *J. Ordnance Equip. Eng.* **41**(9), 171–175 (2020). (in Chinese)
2. Dong, W., Qiang, M., Michael, P.: Prognostics of lithium-ion batteries based on relevance vectors and a conditional three-parameter capacity degradation model. *J. Power Sour.* **239**, 253–264 (2013)
3. Zhou, J.: Research on Lithium-ion Battery Remaining Useful Life Estimation with Relevance Vector Machine. Harbin Institute of Technology, Harbin (2013). (in Chinese)
4. Long, B., Xian, W., Jiang, L., Liu, Z.: An improved autoregressive model by particle swarm optimization for prognostics of lithium-ion batteries. *Microelectron. Reliab.* **53**(6), 821–831 (2013)
5. Zheng, X., Fang, H.: An integrated unscented Kalman filter and relevance vector regression approach for lithium-ion battery remaining useful life and short-term capacity prediction. *Reliab. Eng. Syst. Saf.* **144**, 74–82 (2015)
6. Zhang, S., Pu, J., Si, Y., Sun, W.: Survey on application of ant colony algorithm in path planning of mobile robot. *Comput. Eng. Appl.* **56**(08), 10–19 (2020). (in Chinese)
7. Lin, W., Lv, S., Yu, Z.: Literature survey of fruit fly optimization algorithm. *Control Decis.* **32**(07), 1153–1162 (2017). (in Chinese)
8. Shaorong, H.: Survey of particle swarm optimization algorithm. *Comput. Eng. Des.* **30**(08), 1977–1980 (2009). (in Chinese)
9. Gao, K., Xu, J., Li, Z., Cai, Z., Jiang, D., Zeng, A.: A novel remaining useful life prediction method for capacity diving lithium-ion batteries. *ACS Omega* **7**(30), 26701–26714 (2022). <https://doi.org/10.1021/acsomega.2c03043>
10. Ansari, S., Ayob, A., Lipu, H., Hussain, A., Saad, H.Md.: Remaining useful life prediction for lithium-ion battery storage system: a comprehensive review of methods, key factors, issues and future outlook. *Energy Rep.* **8**, 12153–12185 (2022). <https://doi.org/10.1016/j.egy.2022.09.043>
11. Zraibi, B., Mansouri, M., Loukili, S.E.: Comparing deep learning methods to predict the remaining useful life of lithium-ion batteries. *Mater. Today Proc.* **62**(11), 6298–6304 (2022)
12. Wang, J., Zhang, S., Li, C., Wu, L., Wang, Y.: A data-driven method with mode decomposition mechanism for remaining useful life prediction of lithium-ion batteries. *IEEE Trans. Power Electron.* **37**(11), 13684–13695 (2022)
13. Zhang, H., Mo, Z., Wang, J., Miao, Q.: Nonlinear-drifted fractional Brownian motion with multiple hidden state variables for remaining useful life prediction of lithium-ion batteries. *IEEE Trans. Reliab.* **69**(2), 768–780 (2020)

14. Gou, B., Yan, X., Feng, X.: State-of-health estimation and remaining-useful-life prediction for lithium-ion battery using a hybrid data-driven method. *IEEE Trans. Veh. Technol.* **69**(10), 10854–10867 (2020). <https://doi.org/10.1109/TVT.2020.3014932>
15. Cai, S., Jun, H., Ma, S., Yang, Z., Wu, H.: Remaining useful life prediction method of EV power battery for DC fast charging condition. *Energy Rep.* **8**(13), 1003–1010 (2022)

Capacity Optimization of Haolebaoji-Ji'an Railway Freight Transportation



Kai Xu and Xiaoning Zhu

Abstract Under the guidance of national policies, China Railway tries to take advantages of Haolebaoji-Ji'an railway, one of the north-to-south heavy-haul railway in China, to carry out "freight increment" and "road to railway" target. Based on the analysis of Haolebaoji-Ji'an railway, this paper analyzes the influence on the transportation corridor capacity from three perspectives. First, the service area covered by traffic flow path is limited and the trains make a detour in some areas. Second, the capacity of the collection and distribution system cannot fit the demand of railway coal transportation. Third, the management of the empty wagon dispatching is still disorganized leading to the lack of empty wagon in some stations. According to the drawbacks, this paper proposes some strategies and suggestions for enhancing the transportation capacity.

Keywords Haolebaoji-ji'an Railway · Capacity Optimization · Traffic Flow Path · Collection and Distribution System · Empty Wagon Dispatching

1 Introduction

In China, coal production is mainly located in the northwest, while consumption is distributed in the east and south. Due to the unbalanced layout of resource and industry, the supply and demand of coal are separated geographically, resulting in the transportation situation of "Coal from the north to the south" and "Coal from the west to the east". As the main mode of coal transportation in China, railway has formed seven vertical and five horizontal transportation corridors. The seven vertical

K. Xu (✉) · X. Zhu

School of Traffic and Transportation, Beijing Jiaotong University, Beijing, China

e-mail: 21114031@bjtu.edu.cn

X. Zhu

e-mail: xnzhu@bjtu.edu.cn

© Beijing Paiké Culture Commu. Co., Ltd. 2023

X. Dong et al. (eds.), *The proceedings of the 10th Frontier Academic Forum of Electrical Engineering (FAFEE2022)*, Lecture Notes in Electrical Engineering 1054, https://doi.org/10.1007/978-981-99-3408-9_118

1315

corridors include Jiaozuo-Liuzhou Railway, Beijing-Kowloon Railway, Beijing-Guangzhou Railway, Baotou-Xi'an Railway, Haolebaoji-Ji'an Railway, Nanning-Kunming Railway, the part of Lanzhou-Chongqing Railway and Lanzhou-Xinjiang Railway in Xinjiang. The five horizontal corridors include northern corridor, middle corridor and southern corridor in "San Xi" area, Shanghai-Kunming Railway, the part of Xilinhaote-Wulahaote Railway and Bayanwula-Xinqiu Railway in Inner Mongolia. As a vital north-to-south heavy-haul railway, Haolebaoji-Ji'an Railway catches more and more attention with the growing freight volumes.

The researches mainly concentrate on the analysis of Haolebaoji-Ji'an Railway transportation organization and system, including how to reduce the cost and improve the capacity. Based on the transportation market of Haolebaoji-Ji'an Railway, Li analyzed the factors and challenges on constructing collection and distribution system. Then the strategies were proposed from four aspects: accelerating the construction of strategic loading sites along the line, building the coordinated system for multi-modal transportation, improving the yard distribution and facilities and building the fourth-party logistics platform, so as to promote further development of the collection and distribution system for Haolebaoji-Ji'an Railway [1]. Wu et al. analyzed the current situation of Haolebaoji-Ji'an Railway transportation capacity from the loading station and corridor capacity, rolling stock and unloading equipment, collection and distribution system, impact of restricted sections. In order to further release the transportation capacity, this research put forward some suggestions such as improving the construction of infrastructure, promoting disciplinary operation of freight transportation, focusing on the restricted section including Jingbian-Shenmu Railway and Xiangyangbei station [2]. Based on the analysis of Haolebaoji-Ji'an Railway attraction area and the coal freight market status, Dong and Fu proposed the influence of Haolebaoji-Ji'an Railway on China's coal freight market from the following three aspects: the existing layout of coastal coal transportation, the change in the coal transportation pattern, and the new trend of the coal transportation reform. As a result, Haolebaoji-Ji'an Railway has intensified competition in some regions. According to the statistics of China Energy Investment, this research studied on two main coal transportation modes including "sea-to-river" transportation and through railway transportation. Then this research analyzed the potential transfer of coal transportation volume of these two methods to Haolebaoji-Ji'an Railway [3].

At present, the researches about Haolebaoji-Ji'an Railway are just at the beginning. The specific optimization still need to refer to the existing researches about heavy-haul railway transportation. Bondin et al. established a nonlinear integer programming model based on the through traffic flow marshalling problem caused by high traffic density and inefficient transportation capacity to solve the optimal problem of the through traffic flow direction [4]. Marin et al. studied the interaction between traffic flow and train, also defined train operation frequency and the method of traffic flow path segmentation [5]. Zhang, based on the situation of Baotou-Shenmu Railway, established an optimization model for the multi-path traffic flow organization to calculate the optimized train operation plan [6]. Zhou analyzed the defects of the collection and distribution system of Datong-Qinhuangdao Railway, and put forward the plan of rebuilding and constructing the corridor to improve

the capacity [7]. Wang studied the collection channel and the construction of loading station based on Datong-Qinhuangdao Railway transportation organization mode, and proposes a suitable construction scheme for the collection system [8]. According to the background of German railway, Cordeau et al. regarded the empty wagon allocation problem as a job-shop scheduling problem and established a model with the goal of minimizing the dispatching cost of empty wagons [9]. Haghani [10] and Beaujon et al. [11] regards the empty wagon allocation problem as an inventory problem for each freight operation station to calculate the number of the empty wagons needed in the operation.

How to guarantee the utilization of corridor capacity has become the most important issue for Haolebaoji-Ji'an Railway. In this paper, we provide some specific suggestions on the optimization of Haolebaoji-Ji'an Railway transportation, on the basis of problem analysis. We divide the problem analysis into three parts. In Sect. 2, we focus on the traffic flow path. In Sect. 3, the collection and distribution system are studied. In Sect. 4, we concentrate on the dispatching of empty wagon. Section 5 provides strategies for the issues and Sect. 6 includes the paper.

2 Traffic Flow Path

Haolebaoji-Ji'an Railway originates from Haolebaojinan railway station in Ordos, Inner Mongolia and terminates at Ji'an station on the Beijing-Kowloon Railway, which passes through seven provinces and regions, including Inner Mongolia, Shanghai, Henan, Hubei, Hunan and Jiangxi. It is one of the Class I railway lines in Chinese national railway system and the possesses the total length of 1813.5 km. With the operation of Haolebaoji-Ji'an Railway, "San Xi" area and "Liang Hu Yi Jiang" area is directly connected by railway which result in more convenient coal supply. However, the problems in traffic flow path will lead to insufficient capacity. The main problems are as follows.

2.1 Limited Service Coverage

Based on the loading statistics in 2022, Haolebaoji-Ji'an Railway covered 15 railway bureaus and 22 provinces. The specific proportion of train destination is shown in the Table 1 below.

As shown in the table, the central regions in China, such as Hubei, Jiangxi, Hunan and Henan, is the main direction of Haolebaoji-Ji'an Railway transportation. The provinces surrounding the railway corridor, such as Anhui, Jiangsu, Chongqing and Sichuan, is the secondary direction. While some provinces far away from the line, such as Qinghai, Gansu, Jilin, Heilongjiang, Hainan and Tibet, have not been covered yet. Therefore, Haolebaoji-Ji'an Railway still has great potential in the coal transportation with further development through the optimization and adjustment of traffic flow path.

Table 1 Loading direction of Haolebaoji-Ji'an Railway in 2022

Index	Province	Percentage(%)	Index	Province	Percentage(%)
1	Hubei	38.51	12	Ningxia	0.54
2	Jiangxi	20.88	13	Shanxi	0.39
3	Hunan	14.84	14	Fujian	0.25
4	Henan	12	15	Yunnan	0.21
5	Anhui	2.88	16	Zhejiang	0.19
6	Jiangsu	2.32	17	Shaanxi	0.1
7	Chongqing	1.77	18	Guangdong	0.09
8	Sichuan	1.4	19	Hebei	0.02
9	Shandong	1.1	20	Shanghai	0.01
10	Guizhou	1.09	21	Liaoning	0.01
11	Guangxi	0.72	22	Xinjiang	0.005

2.2 Angular Wagon Flow

The connecting line between Baotou-Xi'an Railway and Haolebaoji-Ji'an Railway has a negative influence on the traffic flow path. If a train from Baotou-Xi'an Railway want to get to Haolebaoji-Ji'an Railway, it need go to Taiyuan-Zhongwei-Yinchuan Railway by transferring at Suide station first and then pass through Yangqiaopan station and Jingbiandong station. The whole traffic flow path produces a large number of detours and generates serious angular wagon flow problems.

(1) Repeated occupation of equipment.

The angular wagon flow means that the circuitous transportation exists which will occupy the up and down equipment respectively and have an impact on the transportation capacity. The more angular wagon flow in the traffic flow path, the more waste of railway station capacity.

(2) Affecting other traffic operations in the rail exchange yard.

Railway stations generally have lines dedicated to special operations in the rail exchange yard, such as filling the refrigerated truck with ice. The occupation of the rail exchange yard by the angular wagon flow will interfere with these operations and increase the dwell time of these vehicles at the station.

(3) Increasing the station transit time and reducing transport efficiency.

The operation procedures of adapting the angular wagon are as below: arrival, disintegration in the first system before the transition, aggregation before transition, transition, second disintegration, aggregation, grouping and departure. Therefore, the vehicle operation time is additional.

(4) Increasing transportation costs and consuming railway station adaptation capacity.

Angular wagon flow makes the shunting operation and dwell time increased which will bring substantial cost such as operation expenses, cargo detention fees and Infrastructure costs in railway stations. If there are many angular wagon flows, the economic losses in operation and engineering can be considerable.

3 Collection and Distribution System

The concept of "insisting on integrated planning and supporting the construction of the collection and distribution system" was proposed in the beginning of Haolebaoji-Ji'an Railway project. In fact, the construction of the collection and distribution system is obviously slower than the main line. The slow construction progress of the special railway lines and coal bases around the railway line leads to the lack of the capacity.

3.1 Inadequate Supply in Collection

The main coal supply for Haolebaoji-Ji'an Railway comes from "San Xi" area. Inner Mongolia has a coal production capacity over 70 million tons, but most of the volume is transported by water rather than railway. It is estimated that the coal supply will be about 20 million tons in 2021 and about 35 million tons in the long term. Coal supply in Shaanxi is more than 100 million tons. While due to the relatively slow construction of coal mines, the actual production capacity is limited. It is estimated that in 2021, Yulin will supply about 40 million tons of coal for transportation by Haolebaoji-Ji'an Railway, and about 60 million tons in the long term. The annual output of Shanxi coal is about 6 million tons, which is mainly for local sales at present. After connecting with Haolebaoji-Ji'an Railway in the future, it is estimated that the coal supply will be about 3 million tons.

Because Haolebaoji-Ji'an Railway is a new planned coal transportation corridor, there are a lot of disadvantages such as development condition, coal supply and transportation distance. The slow construction progress of infrastructure leads to the loss of originally planned coal supply. At present, the construction of the main line and connecting line is at normal process. While the construction progress of the collection station and special railway line is obviously lagging, which results in the lack of collection capacity. In summary, it is necessary to speed up the development of direct connection projects of coal sources to ensure the long-term coal transportation indicators.

3.2 Inadequate Capacity in Distribution

With the decline of the coal production capacity in “Liang Hu Yi Jiang” area, the coal consumption demand has gradually increased. The annual coal consumption in Hubei Province is about 120 million tons, with 115 million tons imported from other provinces, of which about 57 million tons are imported by railway. The annual coal consumption in Hunan Province is about 100 million tons, with 82 million tons imported from other provinces, of which about 33 million tons are imported by railway. The annual coal consumption of Jiangxi Province is about 82 million tons, with 78 million tons imported from other provinces, of which about 33.5 million tons are imported by railway.

The coal bases supporting the line are mostly in the stage of planning, design and construction because of the aspects such as land and environmental, resulting in the lack of capacity in the short term. As of 2020, only Hubeihuadianjiangling Electric Power Plant and Guodiantoufenyi Electric Power Plant have been opened in the distribution system. While the demand requires the coal to be transferred to other lines in order to get to the destination, the current capacity cannot satisfy the demand of “Liang Hu Yi Jiang” area. Restricted by the existing railway line capacity, Haolebaoji-Ji’an Railway cannot be utilized fully.

4 Empty Wagon Dispatching

In the process of railway transportation production, transportation organization must insist on the principle of “unloading-Wagon plan-loading” which means sending out loaded wagons and recycling empty wagons. Therefore, empty wagon is an important factor affecting transportation efficiency. Empty wagon dispatching involves the whole links of the transportation system including rolling stock, unloading equipment and so on.

The collection and distribution system of Haolebaoji-Ji’an Railway is relatively scattered which may bring challenges on transportation organization. At present, the empty wagon dispatching plan of Haolebaoji-Ji’an Railway is given by China State Railway Group. The empty wagons mainly come from Wuhan Bureau, Nanchang Bureau and Guangzhou Bureau to meet the demand of Taiyuan Bureau and Xi’an Bureau through some boundary stations such as Goulinnan, Yueyangbei and Xinyuxi. And Xi’an Bureau also offers some empty wagons to Hohhot Bureau. Without fixed train marshalling for empty wagons, the whole dispatching is filled with randomness which means the railway bureau can get the empty wagons in case of shortage without schedule. In another word, the unreasonable utilization of the empty wagon leads to the insufficient capacity.

And due to the inconsistent rolling stock model, there are all kinds of unloading equipment which may affect the unloading efficiency of the arrival station. Without the supporting of advanced equipment, just unloading by manual work or ordinary dumper will result in a backlog of the wagons at the station. For example, Jiangling Station use the single hook unloading dumper which can only unload one vehicle at a time in the initial stage. The low efficiency has a direct effect on the whole corridor capacity.

5 Capacity Optimization Strategy

In view of the above problems, this paper proposes the following constructive suggestions for the capacity optimization of Haolebaoji-Ji'an Railway freight transportation.

5.1 Traffic Flow Path Adjustment

(1) Expanding the scope of services

The premise of expanding the scope of services is to enhance the railway capacity. With the boom of the economic, railway freight transportation get the development opportunities. Haolebaoji-Ji'an Railway corridor can connect with Dongsheng-Wuhai Railway, Taiyuan-Zhongwei-Yinchuan Railway, Datong-Puzhou Railway, Lanzhou-Lianyungang Railway, Nanjing-Xi'an Railway, Jiaozuo-Liuzhou Railway, Beijing-Kowloon Railway, Shanghai-Kunming Railway, Beijing-Guangzhou Railway by the connecting line to cover the coal transportation network of "nine vertical and six horizontal".

And with the development of the connecting line, the traffic flow path will update. Haolebaoji-Ji'an Railway can get the coal from Shanggao-Xinyu Railway through Wushenqinan connecting line and Taolimiaoan connecting line. The traffic flow path is the coal mine in Ordos-Wushenqi station- Wushenqinan connecting line/Taolimiao station-Taolimiaoan connecting line-Haolebaoji-Ji'an Railway. The whole traffic flow path of Taiyuan-Zhongwei-Yinchuan connecting line is the coal mine in Ningxia- Taiyuan-Zhongwei-Yinchuan Railway-Yangqiaopan station-Jingbiandong connecting line-Haolebaoji-Ji'an Railway. And Baotou-Xi'an connecting line brings the coal mine in Shaanxi, Lanzhou-Lianyungang connecting line sends the coal from Haolebaoji-Ji'an Railway to the center and east of China, Zilin station connecting line connects Haolebaoji-Ji'an Railway and Jiaozuo-Liuzhou Railway.

(2) Optimization of angular wagon flow

First, choose a reasonable location for the railroad station. Yan'andong station, an intersection between Baotou-Xi'an Railway and Haolebaoji-Ji'an Railway, can be set up as a technical station to eliminate the angular wagon flow. And select the direction of the line into the station appropriately for the angular wagon flow is generated by

mismatching between railway line and station. When setting up the line, we should not only pay attention to the safety and the capacity of the receiving operation but also reduce the conflict with other operation. In summary, use the straight line to replace the angular wagon flow in the traffic flow path.

Meanwhile, it is effective to enhance the capacity by planning long-distance through transportation and making long-distance through train marshalling. The long-distance through train need fewer number of uncoupling and less cost. In another word, with the sufficient line conditions, the long-distance through transportation can reduce the number of angular wagon and remarshalling operation. When the capacity is not enough, diversion of operation to other auxiliary stations is quite useful. This method is suitable for large and scattered traffic flow and the direction of the diversion should minimize conflict as much as possible.

5.2 Collection and Distribution System Construction

(1) Push forward the construction progress of collection and distribution project.

Among the planned collection and distribution projects, less than half of the projects have been started, and only a few have been completed. As to the collection system, it is necessary to accelerate the process of constructing collection station and special railway line projects such as Nalinhe and Yanguangyingpanhao. Meanwhile, it is also important to focus on the construction of the connecting line between Haolebaoji-Ji'an Railway and other railway such as Baotou-Xi'an Railway and Xilinhaote-Wulanhaote Railway. And the focus of the distribution system is the construction situation of Huarong coal railway-water intermodal logistics base, Yueyang coal railway-water intermodal base and Xinyu coal storage base and other projects. By putting the project into operation, Haolebaoji-Ji'an Railway can establish the connection with the existing railway to increase the transportation direction and volume.

With the construction of collection and distribution project, building a unified information platform for railway, coal supply and demand becomes more and more important. The transparent collection and distribution information can promote trade development, reduce coordination cost, realize the seamless connection and improve the efficiency.

(2) Focus on logistics system construction

Traditional railway station is difficult to adapt to the development of modern logistics if not considering warehousing, packaging, processing, distribution facilities and information system. In order to develop railway logistics, railway freight yards should be professionalized, standardized, scaled and marketed. The logistics station is capable of handling coal transportation, storage and processing operations, while also providing personalized service for costumers, with loading and unloading, measuring, safety testing, information systems and other equipment.

And relying on the stations around the coal mining areas, the pressure of single coal source from Jingbian-Shenmu Railway can be relieved by constructing strategic cargo-loading spots such as Haizetan and Wushenqinan. In the region with rich coal resources and output capacity such as Taolimiao, Jingbian, Yan'an and Hancheng, the construction of the collection and transportation facilities can stimulate the coal market demand and adapt to the future development.

5.3 Empty Wagon Dispatching Strategy

(1) Make a scientific empty wagon dispatching plan

China Railway Group need to make a scientific and effective empty wagon dispatching plan for solving the problem of random adjustment. Before formulating the plan, it is necessary to consider the daily loading demand and the difference between the loading station on the line in order to calculate the number of empty wagons that should be sent back more accurately from the perspective of the whole corridor. Under the premise of guaranteeing the number of the empty wagon and the transportation distance, empty wagon dispatching can consider proximity principle which means sending the empty wagons to the demand area from the stations around the line first.

According to the unbalanced supply and demand, the empty wagon dispatching plan for Haolebaoji-Ji'an Railway can be based on the through empty wagon train and the empty and loaded wagon mixing composition train. The through empty wagon train can transport empty wagons quickly and in large quantity. The empty and loaded wagon mixing composition train need less assembly time and can also supplement some empty wagons.

(2) Reinforce the railway management

The railway bureaus operating the coal transportation network should divide the responsibilities clearly and exchange the relevant information fluently based on the existing management model. For example, the stations in the charge of Xi'an Bureau are mostly loading station, while the stations in the charge of Wuhan Bureau are mostly unloading station. Therefore, Xi'an Bureau need the empty wagons from Wuhan Bureau sufficiently and steadily.

(3) Improve infrastructure conditions

The capacity of the railway is determined by the restricted sections on the line which means some sub-lines may affect the capacity of the whole line. The cargo from Taiyuan-Zhongwei-Yinchuan Railway and Shanggao-Xinyu Railway account for about 40% of the collection volume and the cross-line cargo account for about 70% of the distribution volume. Therefore, the restricted sections of the other railway will still have an impact on the capacity of Haolebaoji-Ji'an Railway. It is necessary to improve the infrastructure conditions and upgrade the equipment. For example, building the double track railway, increasing the station track and use the same wagon model.

6 Conclusion

This paper discusses the issues of Haolebaoji-Ji'an Railway from three perspectives: traffic flow path, collection and distribution system, empty wagon dispatching. And then this paper analyzes the harm of each issue to the whole corridor. At last, some strategies and suggestions are put forward in order to optimize the freight transportation organization and enhance the corridor capacity for the further development.

References

1. Li, Z.: Current situation and strategies for the collection and distribution system of Haolebaoji-Ji'an coal railway. *Freight Logist.* **38**(10), 49–53 (2020). (in Chinese)
2. Wu, Q., Meng, K., Li, S., Li, D., Chen, G., Yang, J.: Countermeasures against elevating freight volume of Haolebaoji-Ji'an Railway. *Freight Transp. Organiz.* **39**(08), 06–11 (2021). (in Chinese)
3. Dong, D., Fu, T.: Analyzing the impact of opening of Haoji railway on coal freight market. *J. Transp. Eng. Inf.* **002**(020), 0145–0149 (2022). (in Chinese)
4. Bodin, L.D., Golden, A.D.: A model for the blocking of train. *Transp. Res. Part II: Mythol.* **14**(1), 115–120 (1980)
5. Marín, A., Salmerón, J.: Tactical design of rail freight networks. Part II: local search methods with statistical analysis. *Eur. J. Oper. Res.* **94**(1), 43–53 (1996). [https://doi.org/10.1016/0377-2217\(95\)00193-X](https://doi.org/10.1016/0377-2217(95)00193-X)
6. Zhang, S.: Study on the organization and optimization of baoshen railway traffic flow. Beijing Jiaotong University (2020). (in Chinese)
7. Xiaowen, Z.: The analysis and strategy of the collection and distribution corridor capacity of Datong-Qinghuangdao Railway. *Railway Econ. Res.* **01**, 35–37 (2005). (in Chinese)
8. Qiming, W.: Study on the construction of Datong-Qinghuangdao Railway collection and distribution system. *Taiyuan Railway Technol.* **02**, 8–11 (2009). (in Chinese)
9. Cordeau, J.F., Toth, P., Vigo, D.: A survey of optimization models for train routing and scheduling. *Transp. Sci.* **32**(4), 380–404 (1998)
10. Haghani, A.E.: Formulation and solution of a combined train routing and makeup, and empty car distribution model. *Transp. Res. Part B* **23**(6), 433–452 (1989)
11. Beaujon, G.J., Turnquist, M.A.: A model for fleet sizing and vehicle allocation. *Transp. Sci.* **25**(1), 19–45 (1991). <https://doi.org/10.1287/trsc.25.1.19>

Electric Field Simulation and Optimization of Environmentally Friendly ± 400 kV DC Wall Bushing



Xiaohui Duan, Sai Liu, Yinghui Chai, Shuai Du, Xian Cheng, and Xiangyuan Dong

Abstract SF₆ is still widely used as insulation medium for DC wall bushing, although it possesses strong greenhouse effect. C₄F₇N/CO₂ mixture gas has attracted attention as a potential SF₆ alternative gas. In this paper, the dielectric strength of the 4% ~ 6% C₄F₇N/CO₂ mixture gas is calculated. When the gas pressure is 0.6 MPa, the breakdown field strength is about 18.03 kV/mm under power frequency voltage and about 21.56 kV/mm under lightning impulse. Secondly, a 3-D model of the DC wall bushing is established, and the internal electric field distribution is simulated and calculated. The maximum field strength is 25.24 kV/mm at the end of the shield. Finally, the shield structure is optimized by BP neural network, the maximum value of the field strength is reduced by 7.9 kV/mm and the electric field nonuniformity coefficient is reduced to 3.2 after optimization. Based on the breakdown field strength, liquefaction temperature and other factors, the 4% ~ 6% C₄F₇N/CO₂ gas mixture at 0.6 MPa has the potential to be applied to ± 400 kV DC wall bushing.

Keywords ± 400 kV DC wall bushing · C₄F₇N/CO₂ mixture gas · Electric field optimization · BP neural network

X. Duan · Y. Chai · X. Dong
Technical Centre of PingGao Group Co., Ltd., Pingdingshan, Henan, China
e-mail: duanxiaohui81@163.com

Y. Chai
e-mail: 894767819@qq.com

X. Dong
e-mail: 49039973@qq.com

S. Liu · S. Du · X. Cheng (✉)
School of Electrical and Information Engineering, Zhengzhou University, Zhengzhou, China
e-mail: chengxian@zzu.edu.cn

S. Liu
e-mail: 576586958@qq.com

S. Du
e-mail: dushuai94@163.com

1 Introduction

China clearly puts forward that carbon emissions will reach the peak by 2030 and be carbon neutral by 2060, and the whole industry must strive to achieve. In HVDC transmission project, DC wall bushing is one of the most critical and important equipment, which is often called the "throat" of HVDC transmission project [1].

There have been many successful cases of researches on DC wall bushing in China. The ± 800 kV DC wall bushing developed by China XD Group and Xi'an Jiaotong University has passed the test. The bushing is capacitive bushing. China Electric Power Research Institute has successfully developed ± 1100 kV DC wall bushing, which has played an important pioneering role in China [2]. Pinggao Group has carried out research on key technologies of ultra-high voltage DC wall bushing and completed the development of ± 550 kV DC wall bushing [3]. However, SF₆ is widely used as insulating gas for the above bushings.

The DC breakdown characteristics of C₄F₇N are also widely concerned. Some researchers reported that SF₆ insulation performance is 30% higher than 7.8% C₄F₇N/CO₂ gas mixture at 0.4 MPa air pressure [4–7]. Others pointed out that under quasi-homogeneous electric field, the positive and negative DC breakdown field strength of C₄F₇N/CO₂ mixture increases with pressure [8]. The gas mixture has good insulation recovery performance. Under highly non-uniform electric field, the breakdown voltage of positive polarity decreases with the increase of pressure, which means C₄F₇N/CO₂ has obvious polarity effect [9–11].

At present, there is little research on the application of environmental protection gas in DC wall bushing. In this paper, the physical properties of C₄F₇N/CO₂ mixture gas were analyzed firstly, and the insulation strength threshold values under different mixing ratios and air pressures were obtained. Secondly, the structure of DC wall bushing is studied, its 3-D simulation model is established, and the electric field simulation analysis is carried out to obtain the overall electric field and voltage distribution inside the DC through wall bushing. Finally, according to the electric field simulation results, BP neural network is used to optimize the shield to obtain the optimal solution of the electric field distribution.

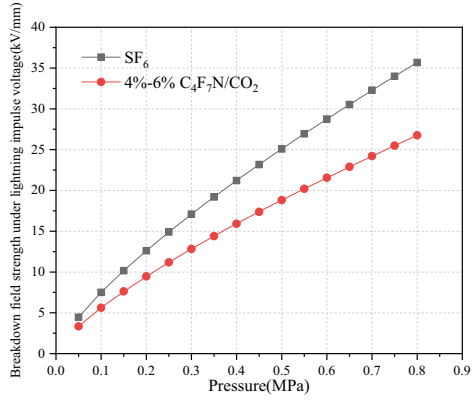
2 Characteristic Analysis of C₄F₇N/CO₂ Gas Mixture

2.1 Insulation Strength of C₄F₇N/CO₂ Gas Mixture

According to paper data, the conversion ratio of 4% ~ 6% C₄F₇N/CO₂ gas mixture to SF₆ under the same air pressure is 0.75. Taking lightning impulse voltage and power–frequency AC voltage as an example, the formulas of SF₆ power–frequency AC voltage and lightning impulse voltage is shown as follows:

$$E_{dt} = 65(10p)^{0.73} \text{ kV/cm} \quad (1)$$

Fig. 1 Breakdown field strength curve under lightning impulse voltage



$$E_{dt} = 75(10p)^{0.75} \text{ kV/cm} \tag{2}$$

where p is the absolute pressure of SF₆ and E_{dt} is the breakdown field strength.

According to the existing empirical formula of SF₆ insulation characteristics, the insulation characteristic curve of 4% ~ 6% C₄F₇N/CO₂ mixture gas is shown in Fig. 1.

Based on the empirical formulas and the curves in these figures, it can be concluded that the insulation breakdown field strength of 4% ~ 6% C₄F₇N/CO₂ mixture presents a slightly saturated trend with the increase of air pressure. The value of E_{dt} for a gas mixture of 4% ~ 6% C₄F₇N/CO₂ at gas pressure of 0.6 MPa is 18.03 kV/mm for power frequency voltage and 21.56 kV/mm for lightning impulse, as an example. It should be noted that the conclusion data obtained from formula (1) and formula (2) are the lower limit values obtained by integrating multiple groups of data. The result calculated by the formula is on the small side, which may lead to the problem of over-insulation during selection. The formula is only applicable to quasi-homogeneous electric field and has no practical reference effects for highly non-uniform electric field.

3 Calculation Model

The DC wall bushing consists of five main parts, including the hollow composite insulator, the through-wall cylinder, the shield, the central conductor and the grading ring, as shown in Fig. 2. Both sides of the through wall cylinder are respectively connected with indoor and outdoor hollow composite insulators, which are coaxial. The length of outdoor insulator is longer than that of indoor insulator. The shielding cover structure is set inside the cylinder, fixed on the inner wall of the through wall cylinder, and the two are directly connected. The through wall cylinder is embedded on the wall and directly connected with the earth to achieve zero potential. Therefore,

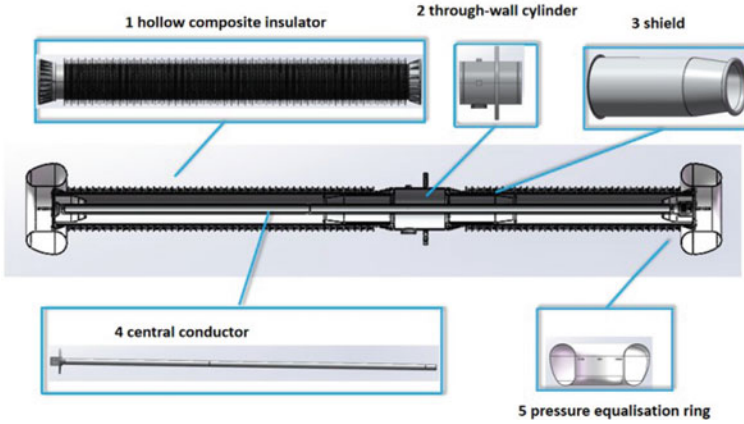


Fig. 2 3-D model of a DC wall bushing

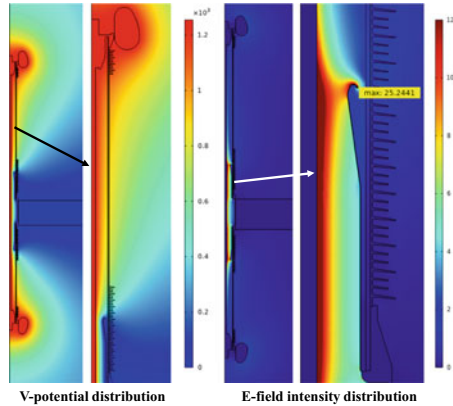
the overall shielding cover is also zero potential, which plays a role in shielding and optimizing the electric field. The central conductor is directly fixed with the grading ring and does not contact any other parts inside the bushing. The bushing is mainly protected by the inner insulating gas.

Table 1. lists the material parameters of the DC wall bushing, which is used for simulation. The bushing operation needs to be tested by various forms of voltage and current. To simplify the simulation process and check the validity, the most stringent lightning surge voltage of 1255 kV was selected as the applied voltage value.

Table 1 Material parameters of DC wall bushing

Material	relative dielectric constant	specific conductance(S/m)	Critical breakdown field strength(kV/mm)
Air	1.0005	-	3.0
SF ₆	1.002	-	≥ 6.5
Silicone rubber umbrella skirt	11.7	10 ⁻¹²	22
Epoxy glass tube	4.2	10 ⁻¹⁴	18
Metallic conductor	10 ¹⁰	5.81 × 10 ⁷	-
Wall	6	-	-

Fig. 3 Initial potential and field intensity distribution of ± 400 kV DC wall bushing



4 Analysis of Electric Field Simulation Results

4.1 Analysis of Electric Field and Potential Simulation Results

The calculated results are shown in Fig. 3. From the thermal diagram of potential, it can be seen that the central conductor and the grading ring at both ends are in the region with the highest potential and gradually diffuse to the middle. The potential distribution is shaped like a letter K. The distribution of electric field is relatively balanced, but the peak value is too high, and the maximum field intensity is within the arc region at the end of the shield, which is 25.2441 kV/mm. A large electric field is also formed on the outer surface of the arc at both ends, which is the weakness of the whole ± 400 kV DC wall bushing.

4.2 Analysis of Electric Field Nonuniformity

For the complex electric power equipment, the electric field nonuniformity inside the bushing is an important basis for selecting the environment-friendly internal insulating gas. The electric field nonuniformity coefficient f is introduced, and f represents the ratio of the maximum field intensity E_{max} to the average field intensity E_{avg} in the selected analysis area. The specific formula is as follows:

$$f = \frac{E_{max}}{E_{avg}} \tag{3}$$

In the formula, f is the coefficient of electric field nonuniformity, E_{max} is the maximum field intensity, and E_{avg} is the average field intensity.

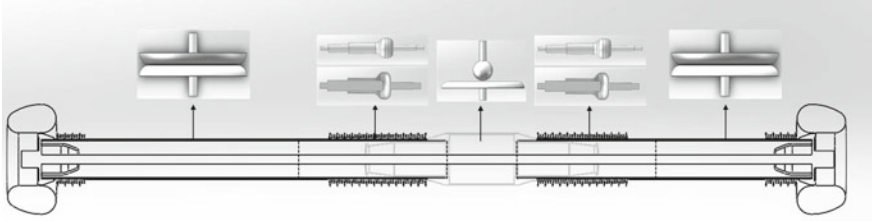


Fig. 4 Equivalent electrode structure of ± 400 kV DC wall bushing electric field nonuniformity

As shown in Fig. 4, the ± 400 kV DC wall bushing is divided into five regions. The middle area of the through-wall cylinder can be approximately equivalent to a spherical-plate electrode, which is a quasi-homogeneous electric field. The middle of the insulating tubes on both sides can be approximately equivalent to a plate-electrode, which is a uniform electric field. The shield cover is the area with the largest nonuniformity of the electric field of the whole bushing, with the maximum field strength of 25.2441 kV/mm, located at the arc end of the shield cover. The average field strength is 4.59 kV/mm, and the calculated electric field nonuniformity is 5.5, which is highly non-uniform electric field.

5 Optimization of Shield Structure

5.1 Parametric Design of Shield Structure

It can be seen from the above that there is a maximum field intensity at the arc at the end of the shield. In order to explore the law of structure of the two-section arc and the peak field intensity, parametric design of the arc is carried out. As shown in Fig. 5, the first segment of the arc is tangent to the line, with the outer radius set to r_2 and the termination angle set to θ_2 . The second segment of the small arc is initially angled tangent to the large arc, with the outer radius set to r_1 and the termination angle set to θ_1 . The absolute positions of the arcs at both ends can be determined by these four parameters, and the electric field relationship under different structures can be simulated by setting the combination of different parameters.

When $r_1 = 14$ mm and $r_2 = 58$ mm, θ_1 and θ_2 are set at different angles. Partial results are shown in Fig. 6. When $\theta_2 = 150^\circ$, the maximum electric field increases with θ_1 , and the strong electric field is distributed at the tip. When $\theta_2 = 120^\circ$, the strong electric field diffuses to the epoxy glass tube, which increases the internal field intensity of the glass tube. As can be seen, the arc parameters can significantly change the distribution of the surrounding electric field, which in turn affects the selection of environmentally friendly insulating gases, and it is necessary to find the optimum solution for the peak field strength.

Fig. 5 Setting of arc parameters of the shield

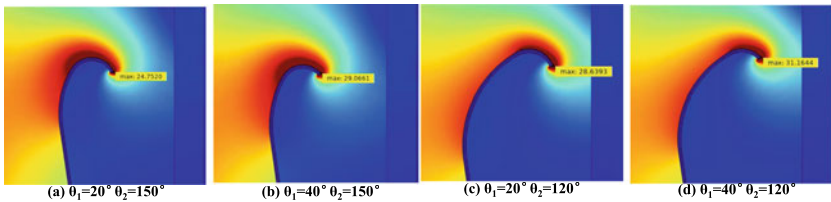
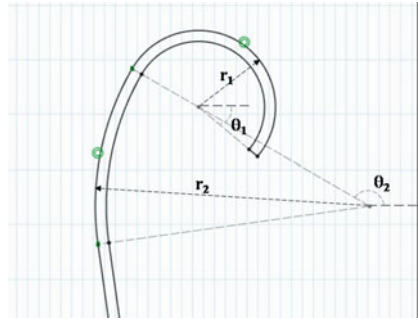


Fig. 6 Influence of partial structural parameters on electric field distribution

5.2 Optimization Method Based on BP Neural Network

There is a mapping F between the maximum value of the internal field strength of the ± 400 kV DC wall bushing and the structural parameters of the circular arc at the end of the shield.

$$E_{max} = F(r_1, r_2, \theta_1, \theta_2) \tag{4}$$

In the above formula, E_{max} is the maximum field intensity inside the bushing.

The objective of optimization is to obtain a set of values of r_1, r_2, θ_1 and θ_2 to minimize the target object E_{max} . Because this mapping relationship is multidimensional and non-linear, it is impossible to obtain the expression from a few simple sets of data. It is common practice to select the domain of definition of each variable and then compose all permutations of the variables and input them into the simulation software for computational solution. Although the process is clear and the method is simple, this enumeration method needs to consume a lot of computing power and time, because there are too many combinations of variables, it is impossible to find out the rule between variables and the objective function. Take this ± 400 kV DC wall bushing shielding optimization task as an example. When r_1, r_2, θ_1 and θ_2 values range from [12, 22], [58, 70], [-60, 60] and [120, 180] respectively, and the length step is 1 mm and the angle step is 2, a total of 270,413 sets of solutions need to be solved. Each set of simulation solutions takes 20 s, and a total of 1502 h are needed. Clearly this cost of calculation and time is huge and undesirable.

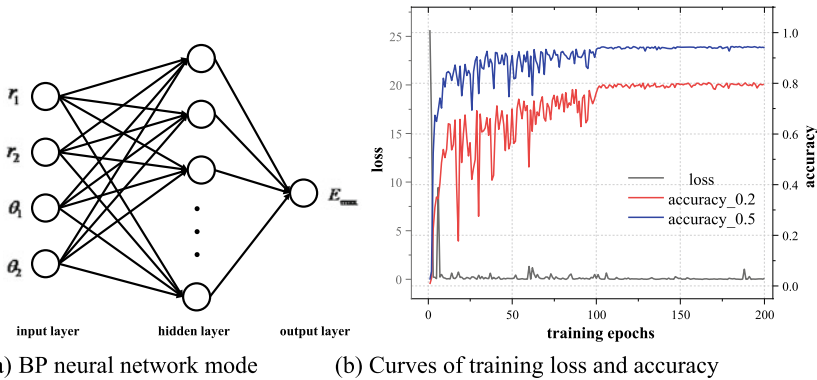


Fig. 7 BP neural network model and training loss and accuracy

5.3 Optimization Model and Result Analysis

In recent years, artificial intelligence has developed rapidly, and BP neural networks are widely used in the engineering field because of their powerful fitting and generalization capabilities. Figure 7(a) shows the established neural network model, which includes input layer, hidden layer and output layer. The input layer is the four variables of the shield, the hidden layer is designed with three layers and the number of neurons is 18, 40 and 40 respectively, only one layer is drawn in the figure for brevity, and the output layer is the maximum internal field strength.

After the design of the network and the pre-processing of the data, the training of the BP neural network is started. Adam was selected as the optimizer of network training, the initial learning rate was 0.01, and the number of training epochs was 200. After 100 training epochs, the learning rate was lowered to 0.001, and the loss function was selected as MSE (Mean Square Error). In this way, when the initial state is fitted with a larger learning rate, it is helpful to skip the local optimal solution and converge more quickly. In the later training period, it is helpful to find the optimal solution and improve the accuracy of the model by lowering the learning rate to a smaller one. To quantify the accuracy metrics of the model, the model prediction error of less than 0.2 kV/mm is defined as accuracy_0.2 and the model prediction error of less than 0.5 kV/mm is defined as accuracy_0.5. The loss and accuracy curves for the model training process are shown in Fig. 7(b).

As can be seen from Fig. 7, the loss decreased significantly in the first several rounds of training, and finally stabilized near zero. Accuracy_0.2 and Accuracy_0.5 showed an upward trend of fluctuation, and there was an obvious segmentation near the 100 epochs, because the learning rate Settings near the 100 epochs were different and the adjustment ranges of parameters were different. The best models after training accuracy_0.2 and accuracy_0.5 were 80.4% and 94.4% respectively, which achieved a high accuracy requirement. Using the trained model to solve for the minimum of the target object, all possible cases were searched for directly.

A total of 532,103 sets of solutions were calculated, and as the minimums were very close, the ten smallest of these were listed and the E_{max} truth values were found using COMSOL, as shown in Table 2.

As can be seen from the Table 3, when r_1 is 14 ~ 15 mm and θ_2 is 180, the values of r_2 fluctuate. This is because when θ_2 is 180°, the central Angle of the first arc is only 8°. The length of the arc is very small, so r_2 has little contribution to the geometric shape of the arc. It is between 58 and 70. θ_1 is the end Angle of the second arc. The value ranges from -20 to 60. It can be seen from the table that the predicted value of the model is basically equal to the calculated value of COMSOL simulation, and the error is completely within the range that can be ignored. With the initial design, E_{max} is 25.2441 kV/mm. After optimization, the results generally decrease about 7.9 kV/mm, and the minimum value of E_{max} is around 17.3 kV/mm. The average electric field intensity in the shield area is 5.43 kV/mm, so the electric field nonuniformity f decreases from the initial 5.5 to 3.2, and the highly non-uniform electric field is optimized to quasi-homogeneous electric field, with a very obvious optimization degree.

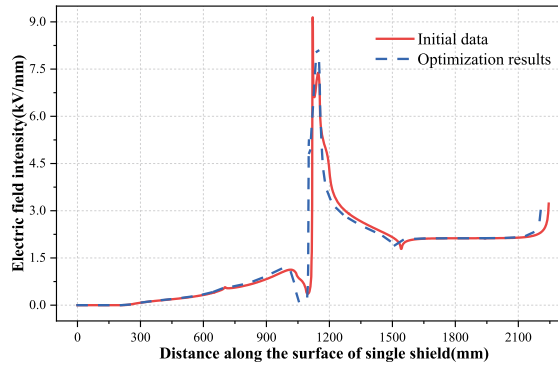
Figure 8 shows the comparison of the field strength along the shield before optimization and after optimization. After selecting appropriate parameters, the overall field strength along the surface is optimized, especially at the maximum, the initial "double peak" is transformed into "single peak", and the maximum value drops from 9.14 kV/mm to 8.2 kV/mm. After optimization, the curve is smoother and the ascending gradient is significantly reduced. Therefore, it is recommended to choose the above typical values for the shield cover structure of ± 400 kV DC wall bushing.

According to the insulation strength analysis of 4% ~ 6% C₄F₇N/CO₂ mixture gas, the breakdown field strength of 4% ~ 6% C₄F₇N/CO₂ mixture gas under lightning shock is 18.81 kV/mm at 0.5 MPa. Therefore, if 4% ~ 6% C₄F₇N/CO₂ mixture gas is used as internal insulation, the internal air pressure inside the bushing must be higher than 0.5 MPa. Because the formula is the breakdown lower limit of multiple

Table 2 Analysis table of model calculation results

r_1 (mm)	r_2 (mm)	θ_1 (°)	θ_2 (°)	Predicted value of E_{max} (kV/mm)	True value of E_{max} (kV/mm)
15	70	-24	180	17.31246	17.302
15	70	-26	180	17.31261	17.316
15	69	-26	180	17.31309	17.335
15	69	-24	180	17.31334	17.292
15	68	-26	180	17.3137	17.313
14	58	-56	180	17.31418	17.288
15	68	-24	180	17.31436	17.307
14	58	-58	180	17.31439	17.3
15	67	-26	180	17.3144	17.301
15	70	-28	180	17.31442	17.331

Fig. 8 Comparison of the field strength along the shield before optimization and after optimization



groups of tests, a part of the margin has been left, 0.5 MPa can be used as the pressure limit. However, in order to fully ensure the safe and stable operation of the ± 400 kV DC wall bushing, it is still recommended to set the internal pressure of the bushing at about 0.6 MPa under the condition that the internal mechanical structure of the bushing can bear it.

6 Conclusion

- In order to cooperate with the insulation of ± 400 kV DC wall bushings. Through simulation calculation, it is recommended to choose 4% ~ 6% C_4F_7N/CO_2 mixture gas at 0.6 MPa. At this time, the power–frequency breakdown field strength of the gas mixture is 18.03 kV/mm, and the breakdown field strength of lightning breakdown field strength is 21.56 kV/mm.
- Under the initial DC wall bushing structure, the maximum field strength is located at the end of the shield and is 25.24 kV/mm, which is significantly higher than the insulation strength of 4% ~ 6% C_4F_7N/CO_2 mixture gas under 0.6 MPa. The nonuniformity coefficient of electric field is 5.5, which is highly non-uniform electric field, so the initial structure design is unreasonable.
- Two arcs at the end of the shield are optimized based on BP neural network, and the optimal solutions of the radius and rotation angle of the two arcs are obtained. Compared with the initial design structure, the maximum electric field after optimization is generally reduced by 7.9 kV/mm, and the minimum value is around 17.3 kV/mm. The peak value on the surface of the shield is weakened. The nonuniformity coefficient of electric field is decreased from 5.5 to 3.2 indicating the obvious optimization effect.

Acknowledgements This work was funded by Science and Technology Project of PINGGAO GROUP CO., LTD. (PGKJ2021-005).

References

1. Qi, B., Yang, Z., Yang, X., et al.: Effect of different DC prestressed time on flashover characteristics of epoxy resin under polarity reversal voltage. *IEEE Trans. Dielectr. Electr. Insul.* **29**(4), 1582–1589 (2022)
2. Li, N., Peng, Z., Liu, P.: Electric field simulation and analysis of 1 100 kV DC SF6 gas-insulated wall bushing. *High Voltage Eng.* **46**(1), 205–214 (2020). (in Chinese)
3. Zhong, J., Chai, Y., Wang, S., Zhang, Y., Duan, X.: Key technology research of ± 1100 kV DC pure SF6 gas insulated wall bushing. *Elect. Power Constr.* **38**(10), 129–137 (2017). (in Chinese)
4. Yang, Y., Gao, K., Bi, J., et al.: Influence of micro-water on AC breakdown characteristics of C4F7N/CO2 gas mixture under non-uniform electric field. *High Voltage*, Early Access
5. Li, Y., Zhang, X., Chen, Q.: Study on the dielectric properties of C4F7N/N2 mixture under highly non-uniform electric field. *IEEE Access* **6**, 42868–42876 (2018)
6. Meng, Y., Ding, W., Li, Z., et al.: Surface flashover characteristics of cylindrical insulator in C4F7N/CO2 mixture under switching impulse voltage. *IEEE Trans. Dielectr. Electr. Insul.* **29**(4), 1514–1521 (2022)
7. Hu, S., Zhou, W., Zheng, Y., Yu, J., Zhang, T., Wang, L.: Experimental and synergetic analysis of the industrial frequency breakdown of C4F7N /CO2 and C4F7N /N2 gas mixtures. *High Volt.* **45**(11), 3562–3570 (2019). (in Chinese)
8. Lin, X., Zhang, J., Xu, J., Zhong, J., et al.: Dynamic dielectric strength of C3F7CN/CO2 and C3F7CN/N2 gas mixtures in high voltage circuit breakers. *IEEE Trans. Power Deliv.* **37**(5), 4031–4041 (2022)
9. Li, Y., Zhang, X., Fu, M., et al.: Research and application progress of eco-friendly gas insulating medium C4F7N, Part I: insulation and electrical, thermal decomposition properties. *Trans. China Electrotechn. Soc.* **36**(17), 3535–3552 (2021). (in Chinese)
10. Yi, L., Zhang, X., Fu, M., Song, X., Tang, J., Tang, S.: Research and application progress of eco-friendly gas insulating medium C4F7N, part II: material compatibility, safety and equipment development. *Trans. China Electrotechn. Soc.* **36**(21), 4567–4579 (2021). (in Chinese)
11. Zhang, J., Sinha, N., Jiang, M., et al.: DC breakdown characteristics of C4F7N/CO2 mixtures with particle-in-cell simulation. *IEEE Trans. Dielectr. Electr. Insul.* **29**(3), 1005–1010 (2022)